THE STANFORD TWO-MILE ACCELERATOR

THE STANFORD TWO-MILE ACCELERATOR

R. B. Neal, General Editor
Stanford University

1968 W. A. Benjamin, Inc.
New York Amsterdam

HK

THE STANFORD TWO-MILE ACCELERATOR

Library of Congress Catalog Card Number 68–24364

MANUFACTURED IN THE UNITED STATES OF AMERICA

The manuscript was put into production on October 31, 1967; this volume was published on November 20, 1968

12345M321098

W. A. BENJAMIN, INC., New York, New York, 10016

FOREWOF

This book documents the design and construction of the two-mile electron linear accelerator located at Stanford University. We have felt that the unprecedented size and complexity combined with the importance of this new installation generated a real responsibility on our part to publish in full the technical features of the installation.

The major brunt of this book has fallen on the shoulders of Dr. Richard B. Neal. He has carried out the mammoth job of collecting and editing the information, in addition to his regular work as Associate Director of the Stanford Linear Accelerator Center. We are all deeply indebted to him for this effort which extended over many long hours.

The work described in this book has been supported in its entirety by the U.S. Atomic Energy Commission and we would here like to express our gratitude and that of the entire scientific community.

W. K. H. Panofsky, Director
Stanford Linear Accelerator Center

PREFACE

Although this accelerator is the largest of its kind in the world, there are many aspects of its design which are pertinent to other shorter machines of the same type. Indeed, most accelerators whether of protons or electrons, whether large or small, whether linear or circular, share to a greater or lesser degree the problems of design, construction, and operation which are discussed herein. It is expected, therefore, that the design solutions which are described will be of general interest to a broad group of accelerator designers, builders, and users. It is hoped that the technical material in this book will also be of interest to engineers and students interested in high-power pulse techniques, special fabrication problems, and other topics of engineering interest.

The number of co-authors of this book totals more than ninety. Their efforts have been divided into twenty-seven chapters. The names of the authors contributing to each chapter are given on the title page of that chapter; one of them has generally served as the editor of the chapter as indicated. The initials of the particular author of a chapter section are given immediately after the listing of the section title. For various reasons, some individuals who made major contributions to a given topic may not appear among the listed co-authors. Attempts have been made, however, to give recognition to their work either within the appropriate chapter or among the references and acknowledgments given at the end of the chapter.

The overall preparation of this book was coordinated by an editorial committee consisting of D. W. Dupen, H. A. Hogg, G. A. Loew, and R. B. Neal. The committee has permitted a certain amount of redundancy in the presented material so that the reader will not find it necessary to turn from chapter to chapter to obtain a reasonably complete account of a given subject. Excessive overlap and repetition has, hopefully, been avoided.

Attention has been given to standardizing units, symbols, and nomenclature throughout the book. However, many exceptions to such uniformity have been made to allow descriptions and treatment of subject matters to be given in terms which are most familiar to workers in a particular field or discipline.

The editors faced the usual problems of deciding where and when to establish an information cutoff for material being prepared for publication. It was decided that the principal subject matter to be covered in this book would include the site, the buildings and utilities, and the components and systems of the accelerator and the beam switchyard. The associated physics research equipment and the research program have been described to complete the overall view, but only briefly. The descriptions and results generally apply to the status as of July 1967.

It is perhaps inevitable that the contributions of various individuals to this large and complex program have not, because of oversight, been properly recognized in this book. Regrets and apologies for these unintended omissions are hereby tendered.

February 1968 *Editorial Committee*
Stanford, California

CONTENTS

INTRODUCTION

W. T. Kirk and R. B. Neal, Editor

Design and construction of the Stanford Linear Accelerator Center (SLAC) and its principal instrument, a two-mile linear electron accelerator, occurred over a period of approximately 4 years. The first electron beam was accelerated through the entire length of this machine on May 21, 1966. Altogether, including the efforts of SLAC and subcontractor personnel, several thousand people contributed to this major undertaking. Documentation of these efforts exists in many forms including internal criteria and design reports; technical notes and laboratory notebook entries; engineering drawings and specifications; and published laboratory reports, journal articles, and conference papers. While these documents are and will continue to be valuable sources of detailed information, they are obviously inconvenient to use for general reference purposes. Moreover, these documents do not provide consistent coverage over all phases of the work and they were prepared over an extended period of time; thus many of them do not represent the final description of a particular component or system, or the final result of a test program or theoretical study.

The definite need for a single comprehensive document about SLAC at the time of completion of the accelerator has been recognized. It has been decided to prepare the document in the form of this book. It is being published approximately $1\frac{1}{2}$ years after the acceleration of the first beam through the machine. Thus, it describes the various technical features of the accelerator and the laboratory in a reasonably "final" state of completion, although it must be acknowledged that accelerators are never really complete until they approach obsolescence. Their design must continue to evolve in minor and sometimes in major ways to respond to the changing requirements of physics.

In addition to its usefulness to the SLAC staff as a ready reference and as a compendium of essential material for indoctrination of new staff

members, it is also expected that workers outside of SLAC will find this volume a repository of useful information on accelerator design and performance and on special engineering problems. Pertinent references are provided at the end of each chapter.

1-1 Comparison of SLAC accelerator with other particle accelerators (RBN)

The relative position of the SLAC machine in the international family of particle accelerators is shown in Fig. 1-1. Not noted on this graph but of interest is the fact that all of the proton machines shown accelerate their particles along approximately circular orbits. This is also true of the majority of the electron machines. But the four highest-current electron accelerators (Orsay, Kharkov, Stanford, and SLAC) accelerate their electrons along a straight path. The existing Stanford machine referred to here is the 1.2-GeV Mark III accelerator which began operation in 1950. The largest and most energetic machines now in operation are the alternating-gradient synchrotrons at the Brookhaven and CERN Laboratories, each of which accelerates protons to about 30 GeV. They will be surpassed when the Russian 70-GeV machine at Serpukhov starts operations. Two "super-energy," circular, proton accelerators of 200 to 400 GeV are presently under consideration in

Figure 1-1 Comparative graph of various accelerators.

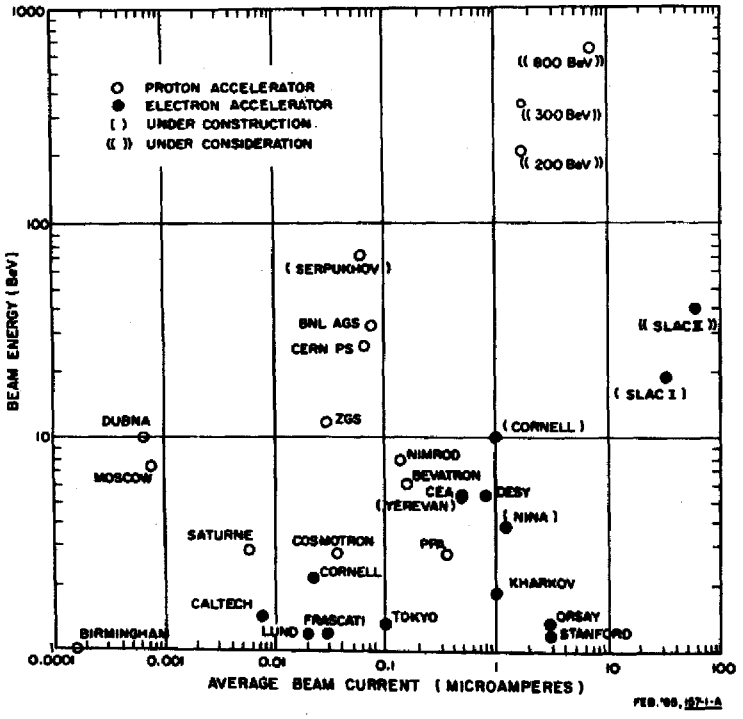

the United States and in Europe. Even larger proton machines are in initial concept stages in America and in Russia.

The two-mile Stanford accelerator is distinguished not only by its length and high energy (Stage I, 20 GeV), but also by its high current, which exceeds by an order of magnitude that of any other machine of any kind now operating. Moreover, provisions have been made in the design of this machine which permit its later expansion (Stage II) to twice the energy (40 GeV) and twice the current (60 μA) by connecting additional or higher-power radio-frequency (RF) sources along its length. If desirable, the energy increase can be accomplished in a gradual manner.

1-2 SLAC as a national facility (WTK)

The study of elementary particles through the use of high-energy accelerators became a separate and distinct aspect of physical research shortly after the end of the Second World War. During the 20-year period that has since elapsed, and as new accelerators have been built and brought into operation, there have evolved two general patterns or styles of carrying out experimental research which may be called the "university accelerator" pattern and the "national laboratory" pattern. Since SLAC does not readily fit into either category, these two "traditional" patterns will first be described so that SLAC may be compared with them.

Broadly speaking, university accelerators are those machines which are conceived and proposed by a technical group from one or two universities, are built at a university site, and are operated by the home university with the understanding that a major part of the machine's research program will be carried out by its own physicists and graduate students. This pattern began with the small group of 300- to 500-MeV accelerators that were built between 1945 and 1950; continued during the 1950's with the construction of the 1-GeV electron machine at CalTech, at Cornell, and at Stanford; and is most recently exemplified by the 3-GeV Princeton-Pennsylvania Accelerator (1961), the 6-GeV Cambridge Electron Accelerator (1961) undertaken jointly by Harvard and MIT, and the 10-GeV Cornell Electron Synchrotron (1967).

In contrast, the national laboratory pattern is associated with accelerators which at the time of their construction appear to have such exceptional research potential that extensive participation by physicists from many different institutions is expected and planned for. A further characteristic of this pattern is that each of these "forefront" accelerators is located at an Atomic Energy Commission (AEC)-supported National Laboratory which also carries out a broad program of basic and applied research in a number of scientific and technical fields other than elementary-particle physics. Three American machines fit this second pattern quite precisely: the 3-GeV Cosmotron (1952) and the 33-GeV AGS (1961) at Brookhaven National Laboratory; and the 12-GeV ZGS (1962) at Argonne National Laboratory. A fourth machine, the 6-GeV Bevatron (1953) at Lawrence Radiation Laboratory, fits

the pattern somewhat less closely than the others chiefly because of the fact that the major part of the machine's research program, particularly in its early years, was carried out by the exceptionally strong physics group at Berkeley.

It was evident from the beginning that the pattern of operation and experimental use best suited to SLAC would be neither that of the University Accelerator nor that of the National Laboratory, but rather some middle way. This was recognized in the original proposal,[1] which stated that

> . . . the unique nature of the proposed facility puts the laboratory in the role of a national facility. Even though its formal operation would remain as the responsibility of the University . . . it shall be the policy of [Stanford] to make the facilities of the laboratory available to qualified scientific workers from any institution, subject only to maintaining the quality of the research program as limited by the available facilities and funds.

As envisioned in this proposal, the concept of SLAC as a "national facility" has evolved. In this facility the pattern of the university accelerator may be seen in the fact that SLAC is a single-purpose laboratory, built and operated by one university on its own campus. At the same time similarity to the national laboratory pattern is evident. Because of SLAC's exceptional research potential and its high cost, combined with the countrywide interest in high-energy physics involving more than forty universities, it is clear that SLAC has a real responsibility to make its unique facilities available nationally and to adjust the size of its scientific staff in relation to its facilities to permit effective outside use. Effective outside participation in the experimental program by qualified physicists throughout the United States and abroad has thus been anticipated and planned for, both in terms of facilities and staff.

1-3 General policies for experimental use of the SLAC accelerator (WTK)

As a planning guideline, it has been assumed that the division of the experimental program between Stanford and outside physics groups would eventually level out at about 50% for each, with outside user participation increasing toward this level during the first year or two of operation. Early experience (as of July 1967) indicates that this working assumption is probably quite reasonable.

The SLAC Scientific Policy Committee

A key part in working out suitable policies and procedures for SLAC in its role as a national facility has been played by SLAC's Scientific Policy Committee (SPC), which was established in 1962 under the terms of Stanford

University's contract with the AEC. The terms of reference under which the SPC operates are as follows:

1. Membership of the Committee is to be between ten and twenty scientists actively engaged in the field of high-energy physics. These scientists are to be appointed for 4-year terms arranged in overlapping tenure. The composition of the Committee is to be chosen so as to strike a reasonable balance between experimental and theoretical physicists and also between scientists affiliated with universities and those affiliated with major government laboratories.
2. The members of the Committee are to be nominated by the director of SLAC and approved by the Board of Trustees of Stanford University and by the AEC.
3. The Committee will set its own agenda with the staff of SLAC providing the necessary services. The Committee should have maximum flexibility to consider all scientific and technical matters pertaining to SLAC. The Committee may include in its considerations also those administrative problems which in its view affect directly the scientific and technical work of the Laboratory.
4. The Committee will review the work of the Laboratory as well as initiate for discussion topics which it considers to be of concern to the work of the Laboratory. A major concern of the SPC is to ascertain that the facilities of the accelerator center are made available to qualified scientists from other institutions as well as Stanford University, subject only to the quality and productiveness of the research program.
5. The Committee will report to the president of Stanford University. He will transmit the findings with respect to paragraph 4, above, immediately to the director, Division of Research, AEC; he may, at his option, transmit any other findings of the Committee to the director, Division of Research, AEC.

Experimental scheduling policy

In 1965, with the advice and approval of SLAC's Scientific Policy Committee and of the Atomic Energy Commission, SLAC prepared a general statement of the policies and procedures that would be used in scheduling the assignment of time for experimental use of the accelerator's beam and the major research devices that were then being constructed. This general statement was embodied in a memorandum called "Scheduling of the SLAC Facilities," from which the following information has been extracted.

RESPONSIBILITY FOR PROGRAM. The Stanford linear accelerator is a national facility and, as such, is available to all qualified experimenters. Stanford University has the responsibility for programming the research use of this national facility according to certain basic conditions set forth in a contract

between the University and the AEC. The director of SLAC has the responsibility for decisions on all matters relating to schedules, including the administration and interpretation of these policies and procedures.

The functioning of the scheduling, and the experimental operations in general, will be reviewed periodically with the SPC, which may suggest changes in the procedures. The procedures may be amended from time to time by agreement between SLAC and the AEC.

PROGRAM ADVISORY COMMITTEE. The director will appoint a Program Advisory Committee (PAC) which will meet with him to assist him in establishing the program commitments for the use of the accelerator. It is expected that the meetings of the PAC will be scheduled at intervals of 2 to 4 weeks. The PAC will consist of eight members, at least four of whom will be high-energy physicists not employed at Stanford. The director will also appoint from the SLAC staff a program coordinator, who will act as secretary to the PAC. Appointments to the PAC will be for terms of 2 years with the possibility of reappointment. The SPC and the AEC will be informed of all changes in the membership of the PAC. At each meeting of the SPC the director will report on all scheduling decisions which have been made in the interval between meetings. It is anticipated that the SPC will also wish to review once each year the scheduling records and the operation of these scheduling procedures.

PROPOSALS FOR EXPERIMENTS. Proposals for experiments which would use beam time or for the use of any of the major research facilities intended for general use will be received by the program coordinator who will present them to the PAC on the next suitable occasion. The program coordinator will also be prepared to present to the PAC information regarding the availability and suitability of the Laboratory's resources for carrying out any particular proposal.

Proposals from staff members of SLAC will be handled on the same basis as proposals from research workers at any other institution.

CRITERIA FOR SELECTION. Stanford is contractually obligated to program the use of the linear accelerator so as to achieve "a vigorous, forward-looking research program in high-energy physics." It is further stipulated that "Scientific priority shall generally govern the allocation of machine time . . . ."

ACCEPTANCE FOR THE PROGRAM. All firm decisions to accept or reject a particular proposed experiment will be made by the director or his assigned deputy with the advice of the PAC at a scheduled meeting of the PAC, and will be announced after the meeting. A particular experiment may be discussed at several meetings of the PAC before a firm decision is reached.

An experiment accepted for the long-range operation plan will normally be assigned a specific amount of running time. Experiments will, in general, *not* be scheduled in the order of their submission or their acceptance.

EXECUTION OF THE PROGRAM. The administration of the short-range schedule, including all specific arrangements for the use of SLAC facilities will be the responsibility of the Operations Staff of SLAC. The Operations Staff will be responsible for arranging the detailed schedules so as to provide the allocated beam time to a particular experiment during a particular running period, but otherwise will be free to make adjustments in the light of day-to-day problems.

RECORDS. Records will be kept of all experiments proposed to SLAC and of the disposition of the proposals. The records will include the dates of submission and the dates of acceptance or rejection. For proposals accepted, the records will show the amount of beam time assigned and of the ultimate execution of the program, including the beam time actually received. These records will be reviewed annually with the SPC, will be transmitted to the AEC, and will be publicly available.

Early scheduling experience

As of July 1967, SLAC had received twenty-four proposals for particle-physics experiments. Of these, seventeen had been accepted for the approved experimental program, four had been rejected, one had been withdrawn, and the remaining two had not yet been acted upon. Of the seventeen approved experiments, seven were to be carried out by physics groups from Stanford, two by groups from other universities, and the remaining nine as collaborative efforts between Stanford and outside users groups. Three experiments had been completed by this time, and the results of these had been published or were being written up for publication.

1-4 Relationships among SLAC, Stanford University, and the U.S. Atomic Energy Commission (RBN)

The functional relationships among SLAC, Stanford University, the AEC, and the various advisory and coordinating committees are illustrated in Fig. 1-2. The Stanford Linear Accelerator Center has been constructed and is now being operated by Stanford University as a national facility under contracts with the U.S. Atomic Energy Commission. The AEC carries out its role as the responsible government agency administering SLAC affairs through its program and fiscal approval procedures. Contracting responsibility at Stanford resides in the Board of Trustees of the University. Construction and operating responsibility for SLAC extends from the Trustees to the president of Stanford University who has, in turn, delegated this responsibility to the director of SLAC. The director is assisted by a deputy director and by four associate directors who administer the four main divisions of SLAC: Technical Division, Research Division, Business Services Division, and Administrative Services Division.

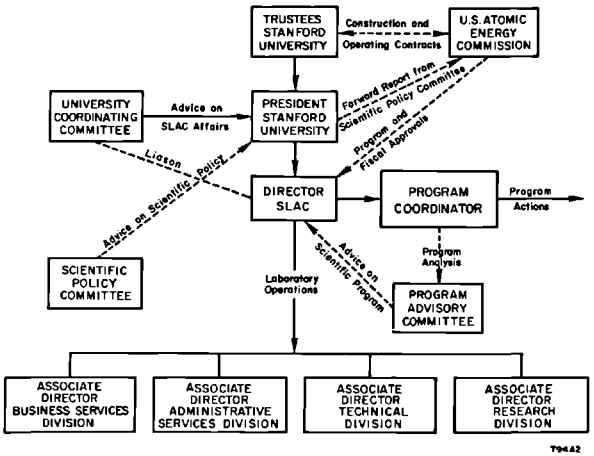

Figure 1-2 Functional relationships among SLAC, Stanford University, the U.S. Atomic Energy Commission, and various advisory and coordinating committees.

Coordination of the SLAC experimental program and liaison with the PAC are the responsibilities of the program coordinator.

The administration of the short-range schedule, including all specific arrangements for the use of SLAC facilities and for the safety of any proposed installation is the responsibility of designated members of the SLAC operating staff. The detailed day-to-day scheduling of operations of the accelerator is also the responsibility of the Operations Staff of SLAC, and is determined in consultation with the experimenters who are working on the scheduled experiments.

A University Coordinating Committee advises the president regarding the interrelationships between SLAC and the University. This Committee meets monthly.

Reference

1 *Proposal for a Two-Mile Linear Electron Accelerator*, Stanford Linear Accelerator Center, Stanford University, Stanford, California (April 1957).

2

AIMS AND PURPOSES

W. T. Kirk and R. B. Neal, Editor

Although it is not within the scope of this book to describe the physics research program at SLAC in any great detail, some knowledge of the objectives of this research and of the ways in which SLAC expects to pursue these objectives should prove helpful in understanding the reason for SLAC's existence and the general role it is likely to play as a center for particle-physics research. The intent of the present chapter, therefore, is to set out brief descriptions of the following four subjects: (a) the objectives of elementary-particle physics, (b) the machine characteristics that determine the SLAC accelerator's experimental utility, (c) the initial research program planned at SLAC, and (d) the research equipment used in conjunction with the accelerator to carry out experiments. The description of objectives given here is historical and nontechnical, since it is intended only to give the general reader a speaking acquaintance with some of the background of elementary-particle physics. The following four sections, though introductory in character, do assume some modest prior knowledge of accelerators, experimental physics techniques, and related research apparatus.

2-1 The objectives of particle physics research (WTK)

In this section a brief description of the objectives of particle physics research is presented.[1] Perhaps the simplest statement of the central goal of this work is that it is an attempt to understand how nature works on its most fundamental level. What is the basic stuff of the universe and how does it behave? These profound questions have occupied men's thoughts for as long as history has been recorded. Although the evidence of our senses presents us with an apparently limitless variety of natural objects and events in the world around us, man always sought an understanding of this rich profusion of forms

through an attempt to find some underlying simplicity—some basic pattern. Is it possible that the incredible diversity we see in nature is simply the elaborate arrangements and combinations of only a few basic substances? For the past 2500 years, starting with the Greek philosophers, men have first speculated, then later demonstrated, that the answer to this question is "yes."

Toward simplicity

About 100 years ago, the Russian scientist Mendeleev devised a comprehensive classification scheme, the Periodic Table of the Elements, which succeeded in relating to each other the seventy-odd elements that were then known, on the basis of their chemical properties and relative weights. Although the patterns of relationship revealed by the Periodic Table were striking and suggestive and, in fact, led to the prediction and subsequent discovery of several new elements, an explanation of *why* the elements should fit into such a periodic system was not given until about 1910 when Rutherford, Bohr, and others worked out the theory of the nuclear atom. This new view of matter made it clear that the chemical elements (which are now known to number about 100) were in fact not "elemental" at all, but rather were themselves composite states built up from various simple combinations of only two truly elementary particles: protons and electrons. This recognition marked a point of extreme simplicity in the search for the basic stuff of nature, and for a time it appeared that physicists would be able to describe most small-scale phenomena on the basis of only these two particles and the known electrical forces with which they acted upon each other. It was a time when so astute an observer of science as Bertrand Russell could remark that "Physical science is thus approaching the stage when it will be complete, and therefore uninteresting. Given the laws governing the motions of electrons and protons, the rest is merely geography—a collection of particular facts telling their distribution throughout some portion of the world's history."

But nature has turned out to be a good deal more elusive than that.

Toward complexity again

By the 1930's, the simplicity of the earlier view had begun to give way to a deeper and more intricate picture. The discovery of the neutron, in 1932, helped to explain several discrepancies in the earlier view; and by that time it had also been recognized that the quantum of electromagnetic radiation, the photon, could equally well be thought of as a particle or as a wave (this is true of all "particles"). Even earlier, in 1930, the theory of the electron worked out by Dirac had implied the possible existence of antiparticles (specifically, a positively charged electron), and this was soon confirmed with the discovery of the positron. It was thus believed, and later verified, that both antiprotons and antineutrons should also exist.

To be brief, the period between 1930 and the present time can be summed up as one in which each new penetration to a deeper level of nature has disclosed an unsuspected richness and subtlety. Whole new classes of particles, new properties, and new principles of conservation and symmetry have been discovered. By 1960, the list of elementary particles had increased to about thirty, and at the present time the number of different particle states that have been discovered or are predicted is about 200. Given this rich profusion, it is no longer clear which of the particles, if any, is in fact "elementary," nor even if this word still has much meaning.

The present objectives

To repeat, the central aim of elementary-particle physics is the search for an understanding of the ultimate nature of matter. Although it is somewhat misleading to divide what is essentially a unified activity into smaller parts, it is possible to describe several different aspects of the subject.

INTRINSIC PROPERTIES OF THE PARTICLES. The particles are distinguished from each other by differences in a number of intrinsic properties: mass, electric charge, spin, stability, and several others. One objective then is to determine the quantitative values of these intrinsic properties as accurately as possible.

CLASSIFICATION SCHEMES. A second objective is to devise a consistent classification scheme, perhaps analogous to the Periodic Table of the Elements, which will indicate how their intrinsic properties logically relate the particles to each other. Much progress has been made in this work in recent years. One of these recent classification schemes, called "The Eightfold Way," which is based on the mathematics of group theory, has had striking success in demonstrating that the particles occur in "families" and in predicting both the properties of known particles and the existence of new particles. A possible consequence of this scheme is that there may yet be an underlying simplicity to the variety of particle states that are now observed. In this regard, physicists are presently searching for a postulated set of three "truly" elementary objects called "quarks," which may be the building blocks from which most of the known particles are constructed.

INTERACTION FORCES. Four kinds of forces are now known in nature (see Table 2-1). The objective here is to determine the characteristics of these forces (range, strength, particles acted upon, etc.) in as much detail as possible. The electromagnetic force seems to be well understood—no discrepancies between theory and experiment have been observed so far in cases where only this force is involved. The large-scale effects of the gravitational force are well known, but its mechanism is not. Because of its relative weakness, the gravitational force is assumed to be negligible in the small-scale world of

Table 2-1 Types of forces

Force	*Relative strength*
Strong or nuclear force	1
Electromagnetic force	10^{-2}
Weak or Fermi force	10^{-14}
Gravitational force	10^{-38}

particle physics. The weak or Fermi force may be a point-force, that is, its effects may not extend over any measurable range. Recent work has made it possible to predict the effects of the weak force much more accurately than before. The strong or nuclear force appears to act through only a very short range (roughly one nuclear diameter, or 10^{-13} in.); although an understanding of this force is of critical importance, and much of the work in the field is devoted to this end, there does not yet exist any satisfactory theory for it.

THE BASIC LAWS. The ultimate objective is to formulate the basic mathematical laws that will precisely describe the behavior of matter in its most elementary forms. Except for the purely electromagnetic interactions, the present attempts to formulate such laws are approximate, speculative, and often not self-consistent. Certain conservation laws and symmetry principles appear to be broadly applicable. Although these may point toward some underlying uniformity in nature, in their present form most of them simply state what is observed to happen without greatly illuminating either mechanisms or significance.

2-2 Machine characteristics important to research (RBN)

For maximum research utility, it is essential that a particle accelerator have certain characteristics which are well matched to the experimental requirements. Among the most important characteristics are the following:

Kind of particle accelerated

Machines have been built to accelerate protons, electrons, deuterons, alpha particles, and various heavy ions. In the energy range above 100 MeV most of the existing machines accelerate either protons or electrons. Proton and electron machines are complementary in terms of applicability to research, principally because these particles interact with other particles in different ways. Electrons interact through the electromagnetic force, whereas protons interact with other particles principally through the strong nuclear force. The electromagnetic force is better understood than the strong nuclear force. Thus, the resulting interaction is in general easier to analyze when the incident particles are electrons rather than protons. However, because the nucleus force is about 100 times as strong as the electromagnetic force, the number

of events in a proton-induced interaction is correspondingly larger than in an electron-induced interaction. This situation would tend to place electron machines at a disadvantage compared to proton machines when studying processes of low cross section. However, linear electron machines usually more than compensate for this discrepancy by accelerating larger numbers of particles per second than proton machines.

For the same incident kinetic energies, electrons produce higher kinetic energies in the center-of-mass system than protons. This is because the rest mass of the electron is only about 1/1846 of the rest mass of the proton. For example, when a 10-GeV electron is incident upon a stationary proton target, the kinetic energy in the center-of-mass system is 5.3 GeV. The corresponding center-of-mass energy when the incident particle is a proton is 4.5 GeV.

Beam energy

In particle research, high energies are important for several reasons:

1. The resolution of a particular instrument used to examine the detailed structure of matter is limited by the wavelength of the "light" which illuminates the object under study. Thus, in the employment of high-energy particles for research it is not possible to resolve details which are much smaller than the de Broglie wavelength ($\lambda = h/p$), where p is the momentum of the incident particle and h is Planck's constant, 6.6×10^{-27} erg-sec. This wavelength varies inversely with the particle energy. For example, at an incident electron energy of 20 GeV, the de Broglie wavelength is 6.2×10^{-15} cm, which is roughly 1% of the diameter of the proton or neutron. In principle, this energy then permits detailed study of the fine structure of the fundamental particles.
2. In general, the number and variety of the secondary particles which are produced in a nuclear reaction increase as the energy of the bombarding particle increases. The heaviest "long-lived" particle (the Ξ^-, which has a rest mass of 1321 MeV) can be produced at an electron energy of about 6 GeV and at a proton energy of about 9 GeV. However, higher energies than these are usually desirable when studying the heavier secondary particles in order to increase the yield and to study the production of these particles at energies well above their threshold values.
3. History has shown that the advance to higher and higher energies has consistently led to interesting and often unexpected results. It is expected that such will also be the case with the SLAC two-mile accelerator.

Electron energies above 10 to 12 GeV are difficult and expensive to obtain with circular accelerators because radiation losses increase as the fourth power of the energy (for fixed radius). Since linear accelerators are not subject to radial acceleration losses, it seems quite likely that *electron* energies of 20 GeV or more will be achieved only with the linear-type machine.

Beam intensity

Many phenomena of great interest in high-energy physics occur with very low probability. Thus, a very large number of particles must be incident on the target in order that enough events occur to be statistically significant. In such cases, a large number of incident particles per unit time, i.e., a beam of high intensity, must be available if a meaningful experiment is to be accomplished in a reasonable length of time. The SLAC accelerator has a beam intensity higher by about two orders of magnitude than any other machine with energy greater than 10 GeV now in existence. Somewhat more than 10^{14} electrons/sec are available. When all of this intensity is not needed for a single experiment, the inherent capability of sharing it among several experiments simultaneously is a great advantage.

Spectrum width

When the momentum of the incident particle plays a direct role in the kinematics of an experiment, e.g., scattering experiments, it is necessary to define this momentum with great precision. This is accomplished by setting the opening of momentum-defining slits in the beam-analyzing system to a suitably small value. Only those incident particles of which the momenta lie within the desired narrow acceptance band are then able to pass through the system. Other particles with momenta outside the acceptance band are absorbed in the metallic structures forming the boundaries of the slit and are thus excluded from the experiment.

It is desirable that the spectrum width of the incident beam be as narrow as possible for the following reasons: (1) A larger fraction of the incident beam can be accepted and utilized in the experiment; (2) there is less absorbed beam and hence less trouble with unwanted background radiation; and (3) the experimental requirements can be satisfied by an accelerated beam of lower intensity; hence, there is less energy loss due to beam loading and less direct radiation and residual radioactivity along the machine and in the beam-analyzing system.

Beam duty cycle

The beam duty cycle is the fraction of the total time the beam is on.* It is given by the product (PRR) (t_p), where PRR is the pulse repetition rate and t_p is the duration of the pulse. For the SLAC machine the PRR (maximum) is 360 pulses/sec and t_p (maximum) is 1.67 μsec; thus, the maximum duty cycle is 0.06%.

* In this context, it is the macroscopic time characteristics of the beam which are referred to, not the time structure determined by the microwave (i.e., "bunched") nature of the beam.

A particular number of incident particles is required to obtain a desired number of experimental events. The average time separation of these events is proportional to the duty cycle of the machine producing the incident particles. Thus, for most counting experiments a large duty cycle is desired so that the counting equipment can discriminate between successive events and thus count all or nearly all of them. This data rate problem is even more serious when on-line computers are being used in conjunction with experiments. The limitation in this case becomes the rate at which data can be introduced into the computer.

In most counting experiments, the momentum of a particle under study is measured by requiring that it follow a precisely determined trajectory through an array of magnets. The momentum of the accepted particles is proportional to the strengths of the magnet fields which are known with great accuracy. Therefore, with a given spatial arrangement of the elements of the transport system, a wide range of momenta can be measured by variation of the fields. The fact that a particle has followed the required trajectory is ascertained by the simultaneous indication (i.e., coincidence) of counters along the path. For a given discrimination time, τ, of the counters, the probability of an accidental coincidence in two counters from two separate particles ("events") varies as $(S\tau)^2$, where S is the instantaneous counting rate. Thus, the probability of accidental events may be reduced by the use of a high beam duty cycle so that the instantaneous counting rate is low. Another way of reducing accidentals, though at added experimental complication, consists of increasing the number of counters in coincidence along the particle trajectory. For n counters in coincidence, the probability of an accidental coincidence is $(S\tau)^n$.

From the above discussion it is clear that a high duty cycle is very beneficial for most counting experiments. Duty cycle in an accelerator is limited by cost considerations. Increased duty cycle requires larger power supplies and higher average ratings of all modulator components. Operating costs are also increased roughly in proportion to the duty cycle.

In some experiments, a particle of known momentum, p, is identified by determining its relativistic mass, m, from the time, t, required for the particle to traverse a fixed distance, l, between two counters. Thus, the mass is obtained from the expression $m = pt/l$. To apply this technique successfully it is necessary to distinguish particles which truly have different transit times (because their velocities are different) from particles of the same velocity but which *appear* to have different transit times. These apparent differences in transit time can arise in either of two ways: because two or more particles pass through the counters at different instants during the pulse length or because they originate from two different pulses and are indistinguishable. Thus, to avoid confusion, it is desirable that the pulse length be short and the separation between pulses long compared to the difference in transit times of the particles being distinguished. Fortunately, it is relatively simple to adjust the injector of a high duty cycle, linear accelerator so as to obtain low beam

duty cycle conditions. The inverse situation is, of course, not possible. As an example, suppose that it is desired to distinguish among 3-GeV/c, e^-, μ^-, π^-, k^-, and $\bar{p}$ particles by time-of-flight measurements over a 45-meter distance. The transit time over a distance l for a particle of total energy E (rest energy plus kinetic energy) and rest energy mc^2 is given by:

$$t = \frac{l}{\beta c} = \frac{l}{c}\left[\frac{\gamma^2}{\gamma^2 - 1}\right]^{1/2}$$

where $\gamma = E/mc^2$.

From the known rest masses of the particles under study Table 2-2 can be calculated. The normal length of the beam in the two-mile accelerator is 1.67 μsec. However, by the use of a *beam knockout* device in the injector system, it is possible to shorten the pulse so that only single bunches are accelerated. Assuming bunching to a phase spread of 5°, the pulse length is then $1/2856 \times 5/360$ μsec $= 0.0049$ nsec. The beam knockout system also allows only 1 bunch out of each 36 to be accelerated. The bunch separation is thus 12.6 nsec. Under these conditions, it is possible to distinguish the particles in Table 2-2 by time-of-flight techniques.

Table 2-2 Transit times of various particles with 3 GeV/c momenta

Particle	*Rest energy (MeV)*	*t (nsec) for $l = 45$ meters*
e	0.51	150.000
μ^-	105.7	150.093
π^-	139.6	150.162
k^-	494	152.020
$\bar{p}$	938.2	157.164

Geometrical properties of the beam

It is desirable that the beam emerging from the accelerator have a small lateral cross section and a small angular divergence. Since these qualities can be traded to some extent, a characteristic of the beam called the *transverse phase space* occupied by the beam is more generally applicable. The phase space is given approximately by the product of the beam diameter at the beam minimum times the angular divergence of the beam. Measurements show that about 80% of the beam emerging from the SLAC accelerator is contained in a phase space of 0.03 (MeV/c) (cm). Thus, for a beam diameter of 0.4 cm the angular divergence at an energy of 20 GeV is somewhat less than 10^{-5} radian.

A small phase space is desired so that beams of good optical quality can be transported simply, inexpensively, and without excessive loss in intensity to widely separated experimental areas. A small phase space permits the use of magnets and other beam transport devices of relatively small aperture. It also requires less initial collimation of the beam. Excessive collimation results

in reduction of mean intensity and in unwanted background radiation and large residual radioactivity in the beam transport components.

A small beam cross section upon entrance into the transport and energy analyzing system is also desirable to enable precise determinations of the beam energy to be made. The characteristics of the SLAC analyzing system are such that a 6 mm diameter of the beam entering the transport system allows a $\pm 0.1\%$ energy spread in the beam accepted through an infinitely narrow energy-defining slit. (This figure applies to the A side of the transport system; the corresponding figure of the B side is twice as large.) A diagram of the beam transport system is shown in Fig. 5-23. A more complete description and design details are given in Chapter 17.

Operational flexibility

The research utility of an accelerator is greatly enhanced by the provision of certain operational features and capabilities. Examples are as follows:

1. Ease and speed of changing beam energy and intensity
2. Adjustable pulse repetition rate
3. Adjustable pulse length
4. Interlaced multiple beams, each independently controllable in pulse length, intensity and energy
5. The ability to increase the time gap between electron bunches (beam knockout)
6. Preservation of bunched beam phase quality as beam passes through beam transport system (isochronism)
7. Good beam stability in energy, current, and optical characteristics
8. Good beam transmission through accelerator (low background radiation)
9. Capability of accelerating other particles as well as primary particle (e.g., positrons)

Attention to all of these features has been given in the design of the SLAC accelerator.

2-3 The SLAC research program (WTK)

When SLAC was first proposed in 1957, it was expected that its eventual research program would have an emphasis quite different from those of the large proton accelerators. As stated in the Proposal: "Studies made with electron beams yield information which ideally complements that obtained with proton beams. In general, processes induced by electrons and photons are simpler in character than the corresponding proton reactions, and are thus more readily understood in fundamental terms." Although it was recognized at that time that the SLAC accelerator could be used to produce intense beams of secondary particles, it was assumed that experiments such as electron-scattering and photoproduction studies would tend to dominate the

SLAC program in much the same way as the work of the proton machines is dominated by strong-interaction studies done with secondary beams.

During the intervening 10 years, several factors have conspired to alter, to some extent, SLAC's original research expectations. The first factor is the increasing emphasis on strong-interaction physics brought about by the discovery of particle resonances and the subsequent proliferation in the number of meson and baryon states that have been observed, and also by the successes of such classification schemes as SU_3 in grouping the observed states into families which share certain properties. The second factor is based on a prediction by S. Drell, later confirmed experimentally, that the process of photoproduction of secondary particles would proceed, in part, through a mechanism which would result in more intense beams of high-energy secondaries at SLAC than had been previously supposed.[2] These two factors have increased the prospective importance of strong-interaction physics at SLAC.

The early program at SLAC

The first use of the SLAC accelerator for physics research began in late 1966. By the time of this writing (July 1967), many of the inevitable bugs have been worked out of the accelerator and the research equipment, and an increasingly large fraction of the machine's running time has been given over to routine production of electron and positron beams for the experimental program. The experiments that have been approved for the program as of July 1967, are listed in Table 2-3 in order to indicate the scope and variety of this initial block of work. In the remaining parts of this section, these experiments have been divided into several classes and a brief description of each class is given.[3]

Elastic scattering of electrons and positrons

One of the early experiments that will be carried out at SLAC is a study of the elastic scattering of electrons from protons. This work is an extension to higher energies of the study of the electromagnetic structure of the proton that began with the fundamental work of Hofstadter at Stanford and was continued by groups at Cornell, at the Cambridge Electron Accelerator, and recently at the Deutsches Elektronen Synchrotron (DESY), Hamburg, Germany. In general, the proton's structure is described in terms of two form factors, G_E and G_M, which refer, respectively, to the distribution of the proton's electric and magnetic properties. The values of G_E and G_M are a strong function of q^2 (q is the four-momentum that is transferred to the proton in the scattering process), and the chief purpose of the planned experiment is to extend the form factor measurements out to regions of very large q^2. Both the cross sections and the corresponding values of the form factors drop rapidly with increasing q^2; at $q^2 = 16(\text{GeV}/c)^2$, for example, a typical cross section is 7×10^{-39} cm^2/steradian. However, the high intensity of the SLAC accelerator should make it possible to obtain counting rates of 2 to 3 per hour even at this extremely small cross section.

It is also of interest to compare the scattering of positrons on protons with the scattering of electrons on protons. Most of the theoretical predictions of electron–proton scattering assume that only one photon gets exchanged in the process. This is partly because most experimental results corroborate this assumption and partly because some of the two-photon exchange calculations have not been carried out. One way to resolve this experimentally is to measure the ratio of the scattering cross sections for electrons and positrons.

Table 2-3 Approved SLAC experimental program (July, 1967)

Experiment	*Facility used*	*Participating groups*
Electron/proton elastic scattering	8-GeV/c spectrometer	Stanford, MIT, CalTech
Electron/proton inelastic scattering		Stanford, MIT, CalTech
Comparison of e^-–p and e^+–p elastic scattering		Stanford, MIT, CalTech
Inelastic spectrum of electrons scattered from carbon-12		Stanford, MIT
Photoproduction at forward angles	20-GeV/c spectrometer	Stanford
Photoproduction of asymmetric muon pairs		Stanford, MIT
Survey of photomeson production processes at backward center-of-mass angles	1.6-GeV/c spectrometer	Stanford
Photoproduction of neutral mesons		Stanford, CalTech, Northeastern
Photoproduction in a streamer chamber	2-meter spark chamber magnet	Stanford
Production of wide-angle electron pairs		Stanford, Harvard
Survey of μ–p inelastic interaction at high energy	54-in. spark chamber magnet; muon beam	Stanford
Setup of monochromatic photon beam to study photon interactions in the SLAC hydrogen bubble chamber	Positron beam	Stanford
ρ^0 photoproduction from complex nuclei at forward angles	Monochromatic photon beam	Stanford, U.C. (Berkeley)
Study of possible CP violation in f^0 photoproduction		Stanford, U.C. (Berkeley)
Flux measurements of neutral particles, and K_2^0 decay asymmetry	—	Stanford, U.C. (Berkeley)
Search for new particles	—	Stanford
Measurements pertinent to the design of a 12-GeV/c RF separated beam	—	U.C. (Berkeley)
Emulsion study of electromagnetic interactions	—	U.C. (Riverside)
A search for fractionally charged particles (quarks)	—	Stanford

If two-photon processes are observed, this will indicate a need for revision in our understanding of electromagnetism. The required accuracies have not been attainable in the past, in part because it is difficult to obtain intense positron beams. At SLAC, previous experiments can be redone with only a few hours running time with high accuracy ($\approx 1\%$). Furthermore, a two-photon contribution, if it exists, can be investigated out to higher values of momentum transfer.

Photoproduction experiments

A large number of photoproduction experiments are scheduled for the research program at SLAC. In most cases, the photon beam will be formed by letting the main electron beam strike a thin target in the beam switchyard and then deflecting the electron downward into an energy-absorbing device called a "beam dump." The gamma rays go straight ahead into a target in the end station.

The 20-GeV/c spectrometer will be used to examine photoproduction of single new particles as a function of production angle and the photon energy. This is a difficult energy-difference experiment which depends on precision measurements to isolate, by kinematics alone, processes that differ from each other in minor ways. An experiment to measure photoproduction of antiprotons is also scheduled. Counting rates as high as several per minute for 15-GeV antiprotons with a momentum spread of 1% are expected.

More complicated photoproduction events will be studied with streamer spark chambers. These include the production of very short-lived "resonance" particle states such as ρ^0 and ω. Additional photoproduction studies will make use of a quasi-monochromatic photon beam obtained from positron annihilation to look at ρ^0 production in great detail. From the knowledge of the properties of the incoming photon, it is now possible to do a photon experiment similar to that which has been done with incident pi mesons. The experiment is done with nuclei as well as protons as the target to see if at high energies the ρ^0 continue to be produced in a diffractionlike process. Such a production mechanism has been inferred from observations at lower energies.

Two other classes of photoproduction experiments will be carried out at SLAC. In the first of these, the 1.6-GeV/c spectrometer will be used to study the photoproduction of strange particles at large angles. In production processes where one of the created particles recoils in the backward direction, the momentum of the recoil particle is typically 1 GeV/c or less, which is a good match to this spectrometer. Since these low values of momentum can be measured with high precision, it is possible to specify with considerable accuracy the "missing mass" that was created in the reaction. Thus, if a resonant state is being produced, it can be detected in this way.

The last series of photoproduction experiments presently planned for the SLAC program will be carried out in the 40-in. hydrogen bubble chamber which is expected to come into operation in the latter part of 1967.

Strong-interaction experiments

As noted at the start of this section, the creation and experimental use of beams of strongly interacting secondary particles is an important part of the research program at most accelerators. Several of the early experiments that have been completed at SLAC were designed to measure the yields of these particles at various angles and momenta. A specific purpose of this work was to specify the design parameters for the high-energy beam of charged secondaries that will be used with the 82-in. hydrogen bubble chamber which is being moved from the Lawrence Radiation Laboratory in Berkeley to SLAC in the summer of 1967. In more general terms, the results of these secondary yield experiments have been published so that the information will be available to physicists outside of SLAC who may be planning to prepare proposals for experiments on the SLAC accelerator.

Muon scattering

The existence of the muon, or mu meson, is an outstanding puzzle in high-energy physics because a whole series of experiments has failed to show any difference between this particle and the electron except that the former is about 200 times heavier and that each has a different associated neutrino. At SLAC, exploration of the muon will continue by comparing electron and muon scattering at high energies. At energies where there exists no detectable difference in scattering properties, the muon is inherently a better nucleon probe than the electron because it does not radiate much energy when accelerated. The calculation of the so-called "radiative" corrections of electron scattering is both difficult and tedious.

The muons will be scattered in a liquid hydrogen target, and their momenta will be measured to within 2% at 10 GeV/c by a large-volume magnet. The muon is identified by its range or lack of interaction in a thick-plate spark chamber and iron slab, and the elastic events can be isolated by looking at the recoil proton in an opposing spark chamber. The main limitation is the intensity of the muon beam, but at SLAC this is high enough for cross sections of several microbarns to be measured in a reasonable time. For example, some 100,000 inelastic events are expected in several hundred hours of running time.

New particle search

A search for new particles will be one of the first efforts at SLAC. According to the Bethe-Heitler theory of electromagnetism, any particle having either or both electric charge and magnetic moment can be created in pairs from the field quantum (photon). The cross section for this process falls inversely as the square of the mass, so that electron–positron pair production is by far the predominant process. However with SLAC intensities it is possible to see a

"long-lived" ($>10^{-9}$ sec) beam particle in a background of 10^6 muons/particle. These may have escaped detection with proton accelerators because all experiments reported have concerned themselves with particles either made in strong interactions or decayed from such particles. If a new particle had only weak or electromagnetic interaction, it would not have been seen. Cosmic radiation, on the other hand, could contain such particles, but previous experiments would not have detected them in a ratio to muons as small as is possible in this experiment.

2-4 Initial research equipment (WTK)

In this section we give a brief description of the large experimental facilities (spectrometers, large-volume analyzing magnets, and bubble chambers) that have been built at SLAC. All this equipment is intended for general use by both SLAC and outside experimental groups. An idea of the size of these devices can be obtained from Figs. 2-1, 2-2, and 2-3.

Spectrometers

Three large magnetic spectrometers have been built for use in scattering and photoproduction experiments. The usual idea conveyed by the word "spectrometer" is perhaps inappropriate to the scale of these instruments, the largest of which is about 160 ft long and weighs 1700 tons. The three spectrometers are designed to complement each other in covering the momentum range up to 20 GeV/c and the angular range from 0° to 180°. The largest

Figure 2-1 The 8- and 20-GeV/c spectrometers.

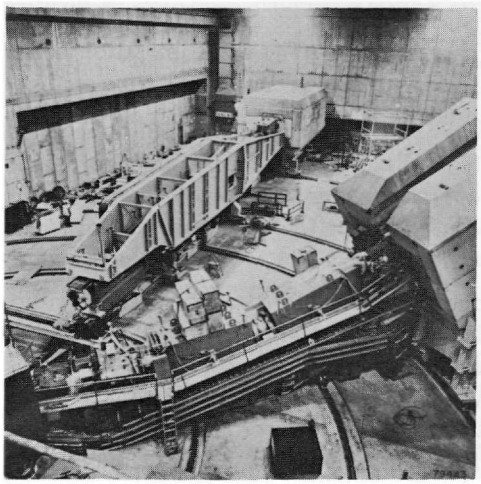

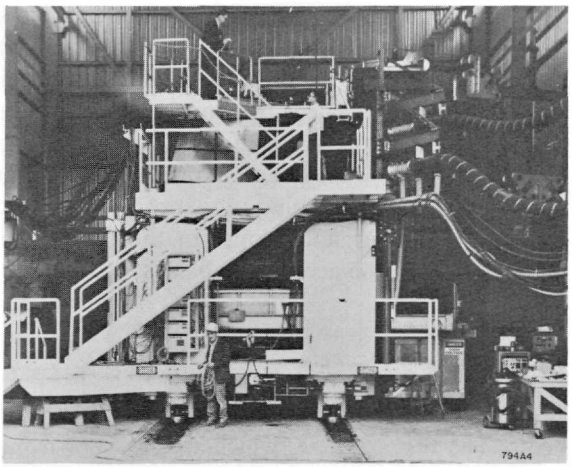

Figure 2-2 The 2-meter spark chamber magnet.

instrument can resolve momenta up to 20 GeV/c (the maximum accelerator energy) and is intended to work the forward angles from 0° to about 20° in the laboratory frame of reference. The 8-GeV/c spectrometer will handle the middle range of angles from approximately 15° to 100°. The 1.6-GeV/c, spectrometer will cover the backward angle range from about 90° to 180°.

Figure 2-3 The 40-in. hydrogen bubble chamber.

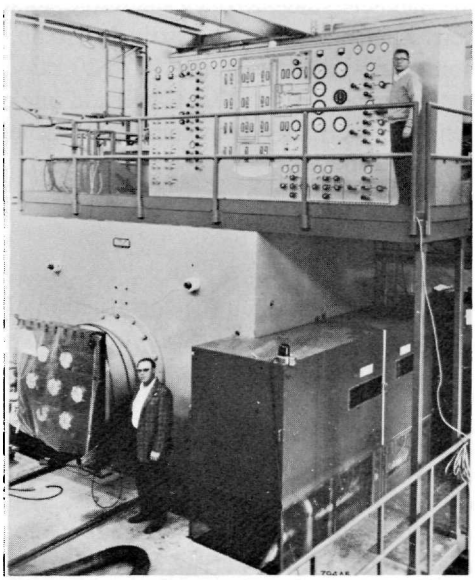

All three instruments are mounted on a common pivot point so that they can view a common target. The momentum resolution of each of the instruments is about 0.1%, and the angular resolution is about 3×10^{-4} radian. This precision is sufficient to allow the spectrometers to distinguish between elastic scattering events and those in which one or more pions are produced. Since the total solid angle and momentum acceptance of these instruments is much larger than the resolution that can be achieved, it will be common practice to use counter hodoscopes in the focal planes to resolve angles and momenta within the acceptance band.

Large analyzing magnets

Two large-volume magnets have been built for use in spark chamber experiments. The first of these, which weighs approximately 500 tons, has a pole diameter of 2 meters and can be assembled in several different configurations with gaps up to about 1 meter. The first use of this magnet will be in a photoproduction survey, where it will contain a very large streamer spark chamber, a device which permits stereophotography, has a rapid response time, and can be triggered by surrounding counters.

The second large-volume magnet has a pole diameter of 54 in. used in several configurations with gaps ranging up to about 3 ft. The first intended use of this magnet is with conventional spark chambers in an experiment to study the inelastic scattering of muons from protons.

Both of the large-volume magnets noted above are designed to permit a good deal of flexibility in setting up various field configurations. The use of movable struts and plugs simplifies access for spark chamber installation in the magnets, and provides suitable openings for stereo viewing of the chambers. Depending on the particular setup, these magnets can provide rather nonuniform fields of about 10 to 20 kG.

It is expected that SLAC will add one or two smaller magnets of this same general type to its complement of general use analyzing magnets during 1968 or 1969.

Bubble chambers

SLAC has undertaken the construction of a hydrogen (or deuterium) bubble chamber having a cylindrical volume 40 in. in diameter and 20 in. deep. It is a conventional chamber with a bellows-connected piston designed to pulse at 2 cycles/sec in a magnetic field of 20 kG. An early intended use of this chamber is in a series of photoproduction experiments in which the incoming photon beam, obtained from positron annihilation, will contain a preponderance of monochromatic photons.

The second bubble chamber is a modified version of the famous 72-in. chamber which has served so well at the Lawrence Radiation Laboratory.

The modifications, which are being carried out at Lawrence Radiation Laboratory, include extending the length of the chamber to 82 in., and increasing its cycling rate to 2 expansions/sec.

A point of interest in regard to bubble chambers at SLAC is the fact that a chamber may require very little scheduled running time. Since the accelerator delivers 360 pulses/sec, the 1 or 2 pulses/sec needed to feed a chamber can be switched, under favorable circumstances, to the chamber without noticeable effect on any other experiments that may be running.

References

1 For the general reader interested in pursuing this subject beyond the greatly simplified description given here, two recent books are especially recommended: C. N. Yang, *Elementary Particles*, Princeton Univ. Press, Princeton, New Jersey, 1961; and Kenneth W. Ford, *The World of Elementary Particles*, Ginn (Blaisdell), Boston, Massachusetts, 1963. Ford's book contains an extensive bibliography.

2 See the reports by J. Ballam and S. Drell, "Some Aspects of Target Area Design for the Proposed Stanford Two-Mile Linear Electron Accelerator," Rept. No. M-200, W. W. Hansen Laboratory of Physics, Stanford University, Stanford, California (Summer 1960).

3 Much of the information given in the remainder of this section has been adapted from Joseph Ballam, "SLAC: The Program," *Physics Today* (April 1967).

3

HISTORY AND DEVELOPMENT

D. W. Dupen

The development of linear accelerators at Stanford originated with the late W. W. Hansen's interest in x-ray problems in the mid-1930's. He sought an inexpensive way of obtaining high-voltage electrons for use in the production of x rays. The idea of a linear accelerator was an old one but required considerable advances in available techniques as well as a detailed understanding of the theory of the various components. Professor Hansen believed that the resonant-type accelerator held great promise because resonant cavities could be built with very low losses, making it possible to provide unusually high voltages with the consumption of only moderately high power. Nevertheless, in the late 1930's, the voltages of interest to the physicist could not be obtained by cavity methods even with the highest power available. The limitation on electron energy by the available RF power did not discourage Hansen in his aspirations toward higher energies. However, in 1938 and 1939, two events caused Hansen to pause in this work. The first was his participation with the Varian brothers in the invention and development of the klystron (which was destined to play an important role in the forthcoming war). The second event was Kerst's successful development of the betatron. Kerst's methods, so eminently successful, made it appear that the RF linear accelerator could not compete with the simple transformer action of the betatron, certainly not without finding unprecedented sources of power.

Technical advances during the course of the war indicated that a change in this situation might be imminent. The British development of the magnetron for radar demonstrated that new horizons of power generation were in sight.

At the end of the war, Hansen together with E. L. Ginzton and J. R. Woodyard reexamined earlier conclusions regarding the feasibility of linear accelerators. This group, among several others, recognized that the

war-developed magnetron made it practical to build linear electron accelerators in the range of several million electron volts using these available RF sources. However, it was also apparent that higher energies would require further developments in order to obtain powers in the range of several hundred megawatts.

3-1 Early developments at Stanford

In 1946, Woodyard[1] and Hansen began to explore methods of accelerating electrons using waveguide accelerator structures. Although the general concept was relatively simple, a great many details were in doubt, especially in regard to orbit stability. Equally critical was the problem of fabrication of large numbers of resonant cavities with sufficient accuracy and low loss. During 1946–47, Hansen aided by E. L. Chu, E. L. Ginzton, E. T. Jaynes, S. F. Kaisel, and W. R. Kennedy studied these problems. Hansen was able to demonstrate, both theoretically and practically, that the acceleration process was feasible.[2] In 1947, electrons were successfully accelerated in a machine known as the Stanford Mark I Accelerator which eventually became 12 ft long. This machine produced 6-MeV electrons when powered by 0.9 MW at 10-cm wavelength. A description of this accelerator was given by Kennedy[3] and later on, after various improvements, by Becker and Caswell.[4] (See Fig. 3-1.)

The early successes in acceleration of electrons at Stanford and elsewhere did not obscure the fact that sources with higher peak power were badly needed. With this in mind, and aided and encouraged by the Office of Naval Research, E. L. Ginzton and M. Chodorow began to explore possibilities of generating higher power. Being most familiar with the klystron approach, the Stanford group decided to use these tubes. Chodorow investigated the theory of operation of klystrons at relativistic velocities and found no fundamental obstacles to their operation in the multimegawatt range. Assisted by K. L. Brown, A. L. Eldredge, A. E. Harrison, N. P. Hiestand, Jr.,

Figure 3-1 The original Mark I Electron Linear Accelerator photographed in the Stanford quadrangle and being held by, left to right, S. Kaisel, C. Carlson, W. Kennedy, and W. W. Hansen.

J. H. Jasberg, C. B. Jones, R. C. Messimer, R. B. Neal, I. R. Neilsen, J. C. Soderstrom, S. Sonkin, and others, Chodorow and Ginzton demonstrated the first successful high-power klystron in the spring of 1949.

Meanwhile in 1948 a proposal was submitted to the Office of Naval Research, presenting in considerable detail arguments in favor of a gigaelectron volt linear accelerator. This proposal, framed by Hansen, Ginzton, and Chodorow, was supported by the Office of Naval Research. The project obviously involved a considerable risk because no previous experience in generation of high RF power and in accelerating electrons to high energies was available.

In the period that followed, Hansen and Chu further developed the theory of the acceleration process and the theory of disk-loaded waveguides.[5] W. W. Hansen proceeded to develop the detailed design of a gigaelectron volt machine. He was aided by many people, some of whom were responsible for major phases of this work.

E. L. Chu completed the theoretical work on many aspects of accelerator performance.[6] R. F. Post constructed the prototype machine using components designed by Hansen and others and, eventually, obtained an energy of 35 MeV with a 12-ft accelerator, the Stanford Mark II.[7,8] P. A. Pearson designed and developed power supplies, pulsers, trigger gaps, and pulse transformers suitable for a 1-GeV accelerator.[9] Ginzton, Chodorow, Sonkin, and others developed successful high-power klystrons.[10] Under the supervision of R. L. Kyhl, who was creatively assisted by F. W. Bunker, A. L. Eldredge, L. H. Franklin, W. S. Geisler, J. H. Jasberg, C. B. Jones, K. B. Mallory, R. B. Neal, and others, a complete accelerator system was planned and developed.

3-2 The Mark III 1-GeV Linear Accelerator

The construction of the 1-GeV accelerator (Stanford Mark III) began in the winter of 1949. The accelerating waveguide for the Mark III was constructed in 2 ft long subsections, each containing twenty-two cavities assembled from annular disks and 4-in. diameter tubing of selenium–copper. Five such subsections were then clamped together to form the 10-ft long accelerating waveguide sections. Each 10-ft section in the machine was to be fed by one klystron amplifier. All the klystrons were to be driven by a common magnetron oscillator.

The Mark III first operated on the night of November 30, 1950. At that time, a length of 30 ft of accelerator had been assembled, supplied by three klystrons. With each klystron providing an average of 8 MW of power, this assembly delivered an electron beam of about 75 MeV.

In the following months, the machine grew in 10-ft steps. The 4-in. diameter accelerator tube was supported on I-beams. These units were mounted on the floor of the long accelerator building. Concrete shielding blocks were piled along each side and across the top. The klystrons and their

pulse-control modulators were housed in oil baths and high-voltage cages, respectively, along one side of the resulting concrete bunker.

By April 6, 1951, the Mark III reached 80 ft in length and eight klystrons had been installed. On that date this arrangement delivered a beam of 180 MeV. During this time the klystrons were operating at no more than half their design value of 18.5 MW. The highest energy obtained with the 80-ft Mark III was about 200 MeV on January 14, 1952.

The accelerator was operated at the 80-ft length until May 8, 1952. At that date, it was disassembled. The used subsections were cleaned and assembly of the final 220-ft machine was begun. (See Fig. 3-2.)

By the end of November 1953, the Mark III had twenty-one 10-ft sections in place, but there were not yet enough reliably operating klystrons to power the entire machine. The maximum electron energy up to that time was 400 MeV with fourteen klystrons operating. At this time, Stanford Professor R. Hofstadter and his collaborators began their investigation of nuclear structure by means of electron scattering using the Mark III beam. By December 1955, the accelerator was operating routinely with a full complement of twenty-one klystrons to yield an energy of about 600 MeV.[11]

Professor Hofstadter's electron scattering program was one of many kinds of nuclear research carried out in the experimental areas of the Mark III during this time. A high point for the Laboratory was the awarding of the 1961

Figure 3-2 The first sections of the Mark III Accelerator, as seen looking in the opposite direction to beam motion (looking toward the injector). The twisted waveguide delivers power from the klystrons to the accelerator tube which is supported by the I-beams. After construction, the accelerator and I-beams were surrounded by concrete shielding.

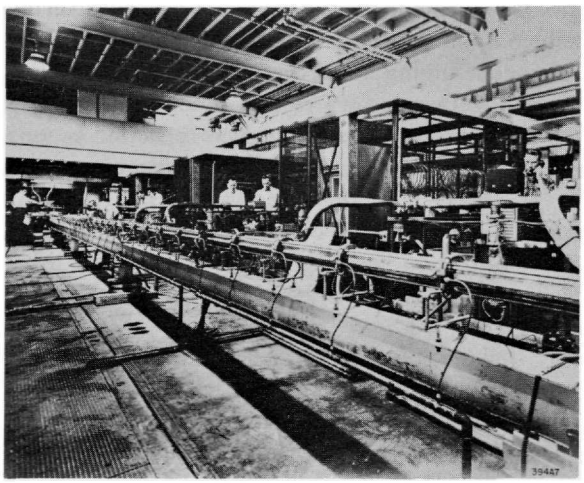

Nobel prize in physics to Professor Hofstadter "for his pioneering studies of electron scattering in atomic nuclei, and for his thereby achieved discoveries concerning the structure of the nucleons."

By December 1957, a 90-ft extension of the Mark III Accelerator was under construction. This extension was completed by July 1960, and from this time on, routine operation at energies of 900 MeV was possible. One gigaelectron volt could be obtained if all thirty klystrons along the 300-ft machine were effective and well processed.

During the latter half of 1963, the Mark III was dismantled. New accelerator sections, produced to the improved design of those to go into the two-mile machine, replaced the original Mark III sections. (See Fig. 3-3.) By March 1964, the Mark III was producing electron beams up to 1.2 GeV. The High Energy Physics Laboratory continues to operate this accelerator.

A number of other electron accelerators have also been built by Stanford for medical and other applications. During the mid-1950's, Stanford constructed a 10-ft, 35-MeV accelerator for cancer therapy at Michael Reese Hospital in Chicago, a 20-ft, 60-MeV accelerator for cancer research at Argonne National Laboratory, and a 6-ft, 5-MeV accelerator for cancer therapy at Stanford University Hospital. These machines, powered by Stanford klystrons, are used to produce electrons or x rays by electron beam

Figure 3-3 The Mark III after replacement of its accelerator sections in 1964. In this photograph all that remained was to replace the concrete shielding blocks on top of the concrete shielding walls.

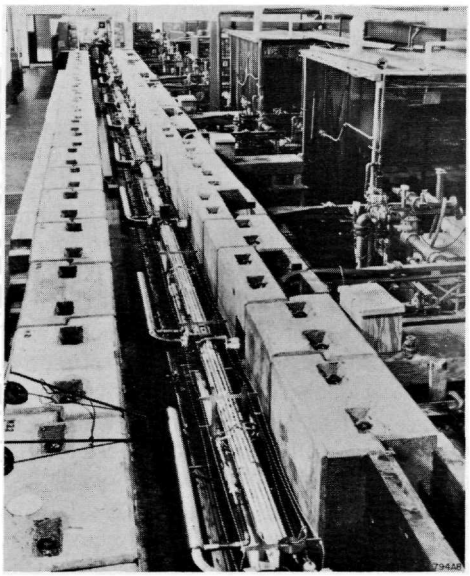

target bombardment. Many private industrial firms now specialize in building small accelerators of the Stanford design for medical research.

During the same period, Stanford built several other accelerators including two 3-ft, 2-MeV machines for radiation research, one of which was put into use at Oxford University, and a 6-ft, 5-MeV accelerator for medical research by the General Electric Company.

In 1954, with the support of the U.S. Atomic Energy Commission, Stanford started to build a 20-ft, 80-MeV accelerator. This machine, which became known as the Mark IV, was designed as a vehicle for improving accelerator components. However, it was also used at times for beta-ray cancer therapy. Under the direction of R. B. Neal, the Mark IV was invaluable in establishing many improved methods of design and construction of linear accelerators. In the early 1960's the Mark IV was used extensively testing prototype components for the two-mile accelerator. In 1964, after the big machine was well along in construction, the Mark IV was dismantled.

3-3 The beginning of the two-mile project

The immediate and resounding success of the Mark III in the early 1950's, both in operation and in application, started Stanford people thinking about a much larger accelerator.[12] Beginning in 1955, Stanford Professors, L. Schiff, R. Hofstadter, W. Panofsky, F. Bloch, and E. Ginzton met informally several times to discuss the possibilities of a "Multi-GeV" electron linear accelerator. This group decided that such a machine had good scientific justification and that the possibilities should be further investigated.

To this end, the first "Project M Meeting"* was held in the home of Professor Panofsky at 8:00 p.m. on April 10, 1956. In attendance, in addition to the five named above, were K. Mallory, W. Barber, K. Brown, R. Debs, R. Neal, R. Mozley, F. Pindar, S. Sonkin, and J. Jasberg. From the minutes of this meeting,

> The purpose of this gathering, the first in a series of weekly meetings, was to discuss plans and form objectives which will ultimately lead to a proposal for the construction of a multi-GeV linear electron accelerator. The participation of the members of this group is entirely voluntary and on their own time as there are no funds available to support this program . . . should such a program materialize, it should be administratively distinct from the Hansen Laboratories and the Physics Department. Professor Ginzton has agreed to serve as Director of the proposed accelerator activity during the design and construction phases, and Professor Panofsky as Assistant Director for at least one year.† Professors Schiff and Hofstadter would act as consultants.

* Opinion is equally divided as to whether the letter M in this early unofficial name of the project stands for Multi-GeV or for Monster.

† As things turned out, Professor Panofsky soon became Deputy Director of Project M, a post he held until assuming the directorship late in 1961, after Professor Ginzton became chairman of the Board of Varian Associates following the death of Russell Varian.

> The primary objective of the proposed large accelerator was declared to be basic physics research. There should be no security measures except to protect personnel and property, no classification and freely publishable results; the facilities should be available to qualified research visitors . . . . The following possible accelerator characteristics were listed to orient future thought: length, two miles; energy 15 GeV, expandable to 50 GeV . . . .

During 1956, much exploratory work was done by this study group* with the assistance of several other organizations. Detailed studies were made of the general problems that would be involved in the construction of such a machine. Special studies were carried out on beam dynamics, accelerator structures, and other systems and components. The Utah Construction Company and the Bechtel Corporation made voluntary independent studies of the site and tunnel problems, and submitted complete reports on their respective solutions. Technical specifications for many aspects of the project were generated. Planning and cost estimates were made for the construction and operation of a facility to design and build the huge number of klystrons which would be required. The University of California Radiation Laboratory (later the Lawrence Radiation Laboratory) provided financial and administrative information based on its experience in the operation of large accelerators. At Stanford, Professors C. Oglesby of Civil Engineering and B. Page of Geology provided civil engineering and site geology and other information.

3-4 Stanford's proposal

From these endeavors, a formal proposal for a two-mile accelerator resulted on April 18, 1957. This proposal was submitted by Stanford University President, J. E. Wallace Sterling, to the U.S. Atomic Energy Commission, to the National Science Foundation, and to the Office of the Secretary of Defense for Research and Engineering.

The proposal received consistent and impressive scientific support. The first formal endorsement of national significance came in 1958 when a panel convened by the National Science Foundation recommended that the project be initiated. Later in 1958, a joint panel drawn from the General Advisory Committee of the U.S. Atomic Energy Commission and from the President's Science Advisory Committee recommended the project. In 1960, the same joint panel, after updating its review of high-energy physics, strongly reiterated its support of the Stanford proposal. Hearings before the Joint Committee on Atomic Energy of the Congress were held in July and August 1959 and in April 1960.[13]

Two related investigations were carried out during the early planning days. One was for the selection of a suitable site. The other was for a mode

* During the year, the Project M Study Group was augmented by the addition of F. Bunker, M. Chodorow, E. Chu, D. Dedrick, L. Franklin, C. Jones, J. McIntyre, C. Olson, and H. Soderstrom.

of construction which would result in an accelerator housing shielded by 25 ft of earth.

Several methods of construction of a housing were considered. The general requirements were for two structures, each 2 miles long, one to house the accelerator itself and one to contain the klystrons and associated auxiliary equipment. The two structures were to be separated from each other by 25 ft of earth shielding. This parallel configuration was required so that equipment could be operated and maintained by personnel in one structure while the beam was on in the accelerator housed in the other structure. All equipment connections between the two structures were to be made via interconnecting penetrations in the earth shield at somewhat regular intervals along the entire machine.

One method considered was to bore two parallel tunnels through a hilly area. Another was the boring of one tunnel for the accelerator housing with the construction of a parallel building on the surface of the ground. A third plan, the one finally adopted, was to excavate a trench to the depth of the floor of the proposed accelerator housing and to construct that housing in the open trench. Then some of the excavated earth was to be dumped back into the trench to cover the completed housing. This fill was to be compacted, layer by layer, until the earth shielding was 25 ft thick. Finally, the second structure was to be built on top of this fill, parallel to, and directly over the buried accelerator housing.

Several sites were investigated, including three on Stanford University property and three on shore lands around San Francisco Bay. Because of the requirement for a bedrock foundation, the selection was narrowed to the Stanford sites. Economic considerations eventually led to the final selection of the "Sand Hill" site.

3-5 Congressional authorization

In late 1960, under congressional authorization, a contract was negotiated between the U.S. Atomic Energy Commission and the Board of Trustees of Stanford University. This contract called for Stanford to perform initial engineering and design of the accelerator, at an estimated cost of $3,000,000. Under this contract, a building on the Stanford campus to house the initial staff was planned, further studies and design work were carried out, and Stanford entered into contract to acquire architect–engineer–management services for the project. The contractor selected for this work was a joint venture known as Aetron-Blume-Atkinson (ABA). This joint venture comprised people from the Aetron Division of Aerojet-General Corporation, John A. Blume and Associates, Engineers, and the Guy F. Atkinson Construction Company. ABA began work on architectural design and planning for site and building construction.

The Congress on September 15, 1961 authorized the AEC to enter into negotiations with Stanford University for the ultimate realization of the two-

mile accelerator. In this action the amount of $114,000,000 was authorized for design and construction. Finally, in April 1962, a contract between Stanford and the U.S. Atomic Energy Commission was executed.

Although the 5 years between the proposal date and the contractual date seemed quite long to those closely identified with this program, and many cycles between states of elation and near-despair transpired during this period, the time was not wasted. Under support from the AEC, a small development program continued during this interval and progress was made in the development of klystrons, modulators, accelerator structures, and general instrumentation. Time was available for the fabrication and testing of several generations of prototypes of these basic components. In retrospect, it appears quite clear that this period of relatively small-scale but basic work contributed greatly to the performance and reliability of the accelerator as it finally materialized.

Moreover, the principal parameters of the accelerator did not remain static during the 5-year preconstruction period. For example, the 1957 proposal envisioned a two-mile accelerator powered initially by 480 klystrons giving an energy capability of 15 to 30 GeV. These tubes and the associated accelerator sections and other components were to be organized into sectors, each 250 ft in length, and the entire accelerator comprised forty such sectors. It was felt that it might be necessary to operate the klystrons initially at the conservative level of 6 MW peak in order to obtain a tenable life (2000 hours). During the preconstruction period the requirement for the initial complement of tubes was reduced to 240, organized into thirty sectors, each of 333-ft length. The corresponding beam energy for the same klystron output range became 10–20 GeV. The RF pulse length of the klystrons was increased from 2.0 to 2.5 μsec. This 25% increase resulted in a 43% increase in beam duty cycle. Many other changes in parameters and specifications, too numerous and detailed to be given here, were made during this period. The evolution of the two-mile accelerator design is discussed in a number of earlier reports.[14–17]

In general terms the contract executed in 1962 between Stanford and the U.S. Atomic Energy Commission called for the University to design and construct the two-mile accelerator. Besides authorizing $114,000,000 for design and construction of the machine, it also included provisions for spending up to $18,000,000 in preconstruction research and development. This latter sum was used for investigation of alternative methods of various design and fabrication techniques, as well as for component testing and development on the small Mark IV accelerator.

3-6 Under way

Ground breaking at the site about 2 miles west of the Stanford campus took place in July 1962. While the site was being prepared, the buildings constructed, and the underground accelerator housing built, fabrication of the

10-ft accelerator sections was begun, first in temporary quarters on the Stanford campus, then eventually in the special fabrication facility at the site.

At about the same time, SLAC's Scientific Policy Committee, chaired at that time by Professor Roger Hildebrand of the University of Chicago, held its first meeting.

By the end of 1963, two office and laboratory buildings had been built and occupied, the entire 2-mile trench had been excavated, the first 2000 ft of accelerator housing had been constructed, and filling operations had begun. (See Fig. 3-4.) In July 1964, the accelerator housing was finished and the installation of accelerator sections was begun. In the same month, the first 1000 ft of above-ground, klystron gallery was completed.

During January 1965, enough of the accelerator had been installed in the housing to permit acceleration of a 1.5-GeV electron beam through the first 666 ft. In the spring of 1965, the staff numbered 1100 people, who by then were all located on the site. In October of that year, the first "Users Conference" was held at SLAC, attended by 150 people interested in using the accelerator when completed. Installation of accelerator sections proceeded at a rate of about 40 ft/day. By the end of 1965, the entire accelerator had been installed.

Figure 3-4 SLAC accelerator housing construction continued eastward while western portions were being covered with compacted fill.

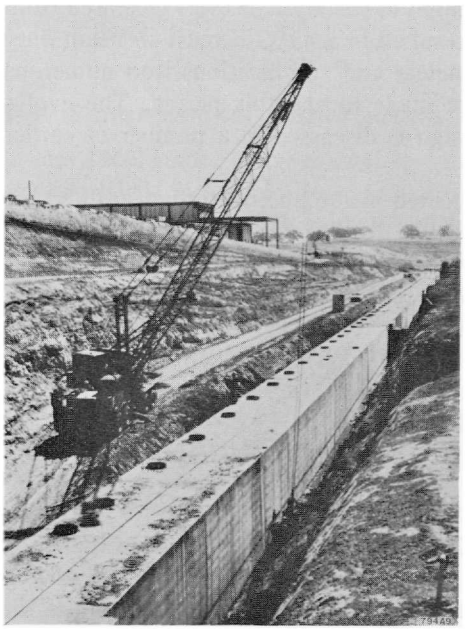

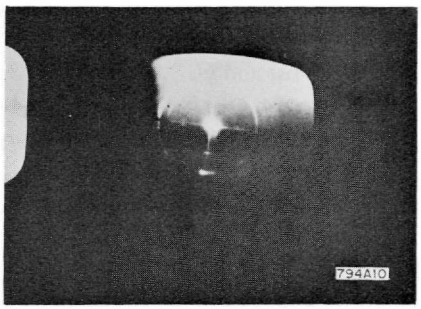

Figure 3-5 Two-mile beam centered on Cerenkov cell PR 2 (May 21, 1966).

In February 1966, the Program Advisory Committee met at SLAC to review experimental proposals and to approve and schedule the experiments to be performed at SLAC after achievement of the beam. On May 21, 1966 the entire accelerator was operated, and a 10-GeV beam was delivered to the beam switchyard.[18] (See Fig. 3-5.) Two weeks later, the beam energy had been increased to 18.4 GeV.

During the remainder of 1966, a second "Users Conference" was held at SLAC (June 22), positrons were accelerated through a portion of the machine (July 13), the electron beam was delivered through one of the end stations to the beam dump at the eastern extremity of the site (September 20), interlaced beams of different energies were delivered to the beam switchyard (October 17), and experiments with the beam began. The first experiments, carried out in November and December of 1966, were primarily concerned with measuring the intensity of the secondary particle beams produced.[19–21]

In January 1967, a beam energy of 20.16 GeV was achieved and the full research program was underway. It was just 10 years since the Stanford proposal had first been drafted. The Stanford Linear Accelerator Center was operational, completed on schedule, and within the originally authorized budget.

References

1 J. R. Woodyard, *Phys. Rev.* **69**, 50 (1946).

2 E. L. Ginzton, W. W. Hansen, and W. R. Kennedy, *Rev. Sci. Instr.* **19**, 89 (1948).

3 William Robert Kennedy, "The design and construction of a linear electron accelerator," Ph.D. Thesis, Stanford University, Stanford, California, October 1948.

4 G. E. Becker and D. A. Caswell, *Rev. Sci. Instr.* **22**, 402 (1951).

5 E. L. Chu and W. W. Hansen, *J. Appl. Phys.* **20**, 280 (1949).

6 E. L. Chu, "Theory of Linear Electron Accelerators," Rept. No. ML-140, Microwave Laboratory, Stanford University, Stanford, California (May 1951).

7 Richard Freeman Post, "A 50-MeV linear electron accelerator," Ph.D. Thesis, Stanford University, Stanford, California, October 1950.

8 R. F. Post and N. S. Shiren, *Rev. Sci. Instr.* **26**, 205 (1955).

9 P. A. Pearson, "Pulsers for the Stanford Linear Electron Accelerators," Rept. No. ML-173, Microwave Laboratory, Stanford University, Stanford, California (November 1952).

10 M. Chodorow, E. L. Ginzton, I. R. Neilsen, and S. Sonkin, *Proc. Inst. Radio Engrs.* **41**, 1584 (1953).

11 M. Chodorow *et al.*, *Rev. Sci. Instr.* **26**, 134 (1955).

12 R. B. Neal and W. K. H. Panofsky, *Proc. Intern. Conf. High Energy Accelerators and Pion Physics, CERN, 1956* (CERN, Geneva, 1956), Vol. I, p. 530.

13 *Background Information on the High Energy Physics Program and the Proposed Stanford Linear Electron Accelerator Project*, Report to the Joint Committee on Atomic Energy, 87th Congress of the United States, U.S. Govt. Printing Office, Washington, D.C., 1961.

14 R. B. Neal, *Proc. Intern. Conf. High Energy Accelerators and Instrumentation, CERN, 1959* (CERN, Geneva, 1959), p. 349.

15 K. L. Brown, A. L. Eldredge, R. H. Helm, J. H. Jasberg, J. V. Lebacqz, G. A. Loew, R. F. Mozley, R. B. Neal, W. K. H. Panofsky, and T. F. Turner, *Proc. Intern. Conf. High Energy Accelerators*, Brookhaven Natl. Lab., 1961 (U.S. Govt. Printing Office, Washington, D.C.), p. 79.

16 W. K. H. Panofsky, *Proc. Intern. Conf. High Energy Accelerators, Dubna, 1963*; p. 407 (or p. 507 in Vol. 1, AEC-CONF-114).

17 J. Ballam, G. A. Loew, and R. B. Neal, *Proc. Fifth Intern. Conf. High Energy Accelerators, Frascati, 1965* (CNEN, Rome, 1966), p. 210.

18 W. K. H. Panofsky and R. B. Neal, *Science* **152**, 1353 (1966).

19 A. Barna *et al.*, *Phys. Rev. Letters* **18**, 360 (1967).

20 A. Boyarski *et al.*, *Phys. Rev. Letters* **18**, 363 (1967).

21 S. M. Flatté, *Phys, Rev. Letters* **18**, 366 (1967).

4

PROJECT ADMINISTRATION

R. B. Neal

In this chapter the organizational structure of SLAC as it evolved during the 4-year design and construction program is discussed. This is followed by an account of the scheduling techniques used by SLAC and by ABA. Finally, fiscal and manpower experiences are recounted.

4-1 Organization

The functional relationships among SLAC, Stanford University, the U.S. Atomic Energy Commission, and the various advisory and coordinating committees were discussed in Section 1-4. It is the purpose of this section to describe the internal organization and functioning of SLAC in somewhat more detail.

The chief executive officer for SLAC is the project director, who reports administratively to the president of Stanford University. The director is assisted in his duties by the deputy director and by a small planning and coordinating staff. In case of prolonged absence of the director, his duties are assumed by the deputy director.

Throughout its existence, SLAC has consisted of four major divisions: the Research Division, the Technical Division, the Business Services Division, and the Administrative Services Division. While these divisions have been continuously in effect, their internal structures have gradually evolved to meet the changing needs of the project as its orientation has turned successively from conceptual design and development to engineering, to procurement and fabrication, to installation and checkout, to operation for accelerator testing and shakedown, and finally to operation for physics research.

Continuity of group effort has been a basic project policy. In general, the same people were involved in all phases of work associated with a given

component or system from early design to final installation, checkout, and test. This same policy has continued into the operating period so that many staff members have had an unbroken association with a particular component or system through the entire span of its conceptual and physical existence. One of the merits of this policy is its salutory effect on quality at each step through the program. This results from the continuing awareness of each staff member that tomorrow he will be required to face the consequences of today's decisions and actions. Another worthwhile result of this policy has been the breadth of experience which staff members have gained during exposure to the various phases in the evolution of a component or system. From another point of view, it can be stated with some conviction that the continuity policy being discussed influenced the project in its choice of staff. Each new member was chosen not just for his ability to design, or fabricate, or install, but to do all of these things and later play a creative and productive role during the operating phase of the laboratory.

In addition to promoting a high degree of efficiency and responsibility as discussed above, this general expectancy of personnel continuity has been an important factor in the maintenance of personnel morale during the 5 years SLAC has been in existence.

The organization of the project as it existed in January 1962 (3 months after Congressional authorization) is shown in Fig. 4-1 with the number of personnel in each group indicated in its box. The total staff at that time numbered 200, classified as shown in Table 4-1. The "professional" category

Figure 4-1 Project organization as of January 1962.

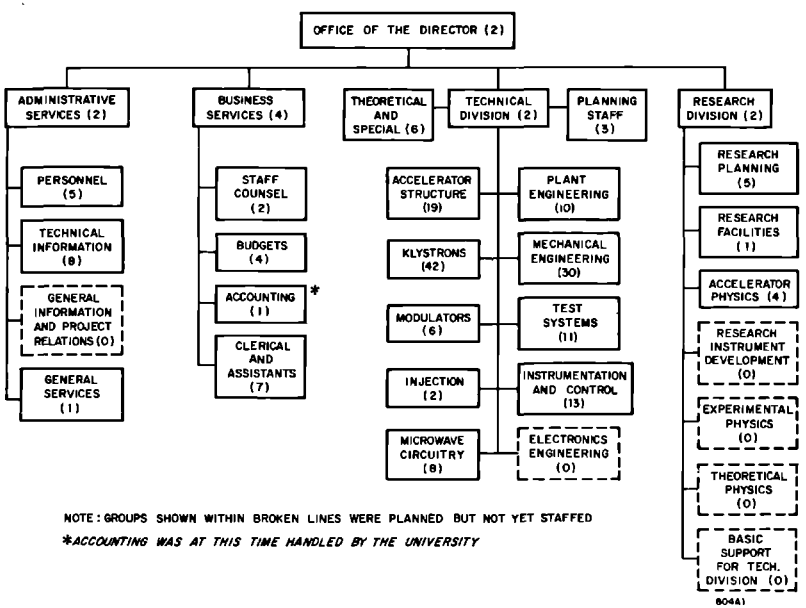

Table 4-1 Classification of SLAC staff (January 1962)

Division	*Professionals*	*Technicians*	*Draftsmen*	*Clerical*	*Total*
Director's Office	1	—	—	1	2
Research	11	—	—	1	12
Technical	60	66	16	10	152
Business Services	6	—	—	12	18
Administrative Services	7	—	—	9	16
	85	66	16	33	200

included all people with college degrees. By that date, the Technical Division had already undergone a rapid expansion and, as indicated in Fig. 4-1, the organization of this division had a strong orientation toward component and systems development. The Klystron Group was the largest group at that time, reflecting the fact that the project had put strong emphasis on klystron development during the preauthorization period. The Microwave Circuitry Group had the responsibility for development of the basic parameters of the accelerator structure and for the design of the RF drive and phasing systems. The Accelerator Structures Group was responsible for the design and fabrication of the disk-loaded accelerator tube and the rectangular waveguide system. The Plant Engineering Group was responsible for technical liaison between SLAC and Aetron-Blume-Atkinson, the architect–engineering–management organization under contract to SLAC for the design of the conventional buildings and facilities (including the accelerator housing and the klystron gallery, the beam switchyard, and the research area buildings). The Mechanical Engineering Group was responsible for layout of the various accelerator systems in the accelerator housing and klystron gallery and for engineering of the cooling water, electrical, and support systems within these structures. All project drafting was centered in this group, but provisions were made for assignment of draftsmen to other groups as required. The Test Systems Group included personnel associated with the 75-MeV Mark IV accelerator which was used as a vehicle for testing prototype components of the two-mile accelerator. In January 1962, planning of the beam switchyard and the research area had barely started. Some preliminary thinking concerning these areas had begun in the Research Planning Group within the Research Division.

Two years later, in March 1964, the SLAC organization was as shown in Fig. 4-2. By this time the project was roughly halfway through the construction period and the total SLAC staff had reached the level of 731, as shown in Table 4-2. A number of organizational changes had taken place since January 1962 (Fig. 4-1) and are shown in Fig. 4-2. The title of the Accelerator Structures Group had been changed to the Mechanical Design and Fabrication Department. This department was responsible for all project machine shops

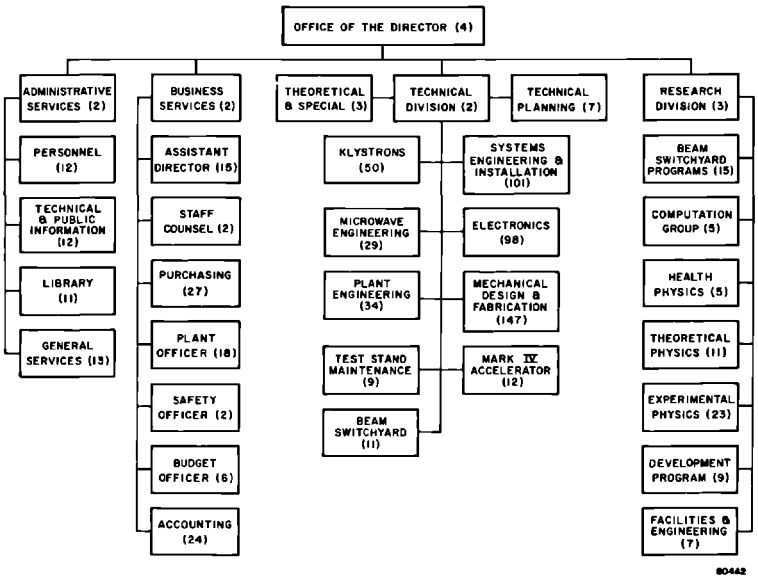

Figure 4-2 Project organization as of March 1964.

as well as for fabrication of the disk-loaded accelerator and the rectangular waveguide system. Mechanical engineering was also centralized in this department although a number of mechanical engineers were on assignment to other Technical Division groups and to the Research Division. The title of the former Mechanical Engineering Group shown in Fig. 4-1 was changed to the Systems Engineering and Installation Department. The responsibilities of the Microwave Engineering Group now included the injector system. A new *ad hoc* group responsible for the beam switchyard was now in existence. An Electronics Department consisting of Heavy Electronics, Light Electronics, and Instrumentation and Control Groups had been formed.

This is perhaps a good time to discuss another policy which has been in effect, with a few exceptions, since the project was initiated. The Technical Division has been responsible not only for the design and construction of the

Table 4-2 Classification of SLAC staff (March 1964)

Division	*Professionals*	*Technicians*	*Draftsmen*	*Clerical*	*Total*
Director's Office	2	—	—	2	4
Research	43	26	—	9	78
Technical	149	268	55	31	503
Business Services	13	16	—	67	96
Administrative Services	6	—	—	44	50
	213	310	55	153	731

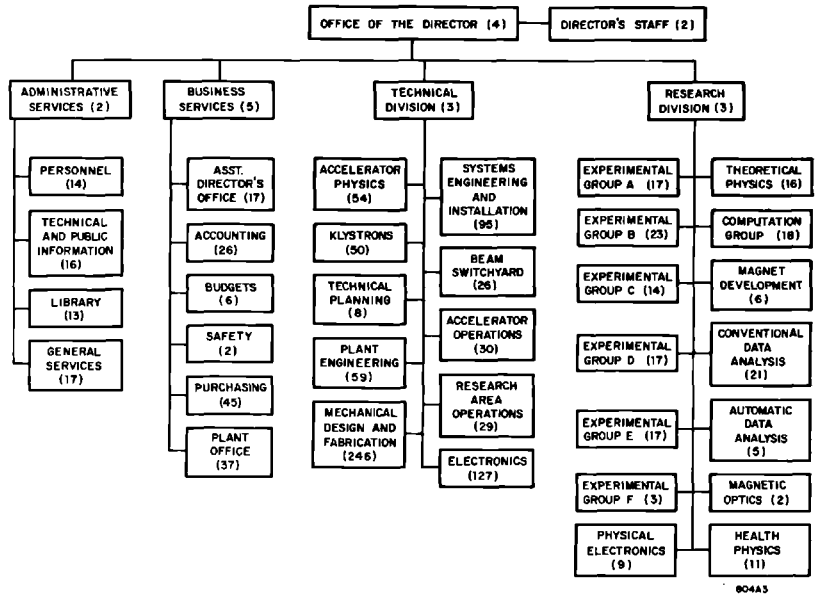

Figure 4-3 Project organization as of January 1966.

accelerator (and more recently for the operation of the accelerator and the research area facilities) but also for the technical support of the Research Division. This support has consisted of supplying machine shop and electronics shop services, and mechanical and electronics engineering and technician assistance. At the option of the customer group, the engineering and technician assistance can be given on a short-term or long-term personnel loan basis or by undertaking the job assignment within the support group itself. Both methods have been found to be effective.

The project organization in January 1966 is shown in Fig. 4-3. The total head count at that time was 1115 which was not far below the peak number reached during the construction period. The staff was divided as shown in Table 4-3.

Table 4-3 Classification of SLAC staff (January 1966)

Division	*Professionals*	*Technicians*	*Draftsmen*	*Clerical*	*Total*
Director's Office	4	—	—	2	6
Research	85	81	—	16	182
Technical	190	433	71	33	727
Business Services	27	59	—	52	138
Administrative Services	17	—	—	45	62
	323	573	71	148	1115

Six experimental groups had been activated in the Research Division. In the Technical Division, two operations groups, Accelerator Operations and Research Area Operations, had been formed and were vigorously preparing for beam turnon, scheduled to occur a few months later. A new department, Accelerator Physics, comprising the former Microwave Engineering Group, the Instrumentation and Control Group (previously in the Electronics Department), and the Theoretical and Special Group, was in effect. Other responsibilities then belonging to Accelerator Physics were magnetic measurements and the laser alignment system.

The final chart, Fig. 4-4, represents SLAC as it existed in July 1967. By this time, the machine had been operational about 14 months and the physics research program had been underway about 8 months. The number of separate organizational entities in the Technical Division had been reduced to eight. The completion of the activities of ABA and the completion of accelerator and beam switchyard installation and checkout resulted in a reduction in the scope of work for both the Plant Engineering and the Systems Engineering and Installation Departments. Therefore, it was possible to combine both of these into one department which was called Plant Engineering. Because the activities of the *ad hoc* Beam Switchyard Group were completed, this group was disbanded and its members were returned to their home groups or were reassigned to other work. Some of the key people from this group were combined with the Research Area Operations Group into a new department called the Research Area Department. The responsibilities of this department

Figure 4-4 Project organization as of July 1967.

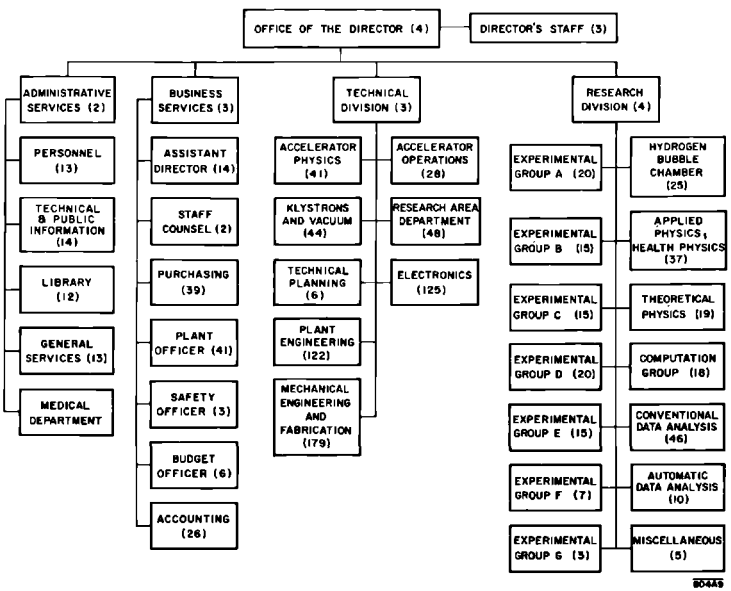

Table 4-4 Classification of SLAC staff (July 1967)

Division	*Professionals*	*Technicians*	*Draftsmen*	*Clerical*	*Total*
Director's Office	5	—	—	2	7
Research	110	86	—	63	259
Technical	165	350	54	26	595
Business Services	18	74	—	42	134
Administrative Services	12	16	—	26	54
	310	526	54	159	1049

include operation and maintenance of the beam switchyard, experimental beam planning, and construction and logistics in the research area. The responsibility for the accelerator vacuum system was transferred from the Systems Engineering and Installation Department to the Klystron Group. The name of this department then became the Klystron and Vacuum Department.

By July 1967, the project staff had decreased from the peak level of about 1200 in fiscal year (FY) 1966 to a total of 1049. It was expected that the staff would remain approximately at this level for the next year. The staff was divided as shown in Table 4-4.

4-2 Scheduling

When the SLAC project was initiated, it was recognized that the timely completion of the entire program of design and construction required the successful coordination of contributions from many individuals and organizations representing a broad spectrum of trades and disciplines. Moreover, it was clear that meeting the project's overall schedule required that much of the work proceed in a concurrent manner, e.g., the design and construction of the facilities had to be carried out in parallel with the development of criteria for the accelerator and research equipment. The mutual interaction of these key project elements required that a scheduling technique capable of dealing logically and expeditiously with the various interdependent factors and constraints be employed.

After considering several scheduling techniques, the critical path method (CPM) was selected as the most appropriate system. It was used by both SLAC and ABA during the entire design, construction, installation, and checkout phases of the project.

A basic CPM diagram shows the activities of a project arranged in logical sequences. An *activity* is a task or operation which can be clearly defined and for which a single responsibility can be assigned for its execution. Activities are separated by *event nodes* (which are merely numbered circles on the CPM diagram). Arrival at a node signifies completion of the previous activities

leading to the node and readiness to undertake the activities beyond the node. A sequence of activities and nodes from the start to the finish of a project is a *path* through the project. Usually, there are a number of parallel paths each representing a chain of activities associated with the accomplishment of a major phase of the project. Often, it is not feasible to proceed with a particular activity, A, along a certain path until other activities, say, D, F, G, associated with one or more different paths have first been accomplished. In this situation, the undertaking of activity A is said to be *restrained* by activities D, F, G.

The complete CPM logic diagram is first made up without paying attention to the time required for the various activities. After completion of the diagram, the time required for the accomplishment of each activity is then entered on the diagram opposite that activity. The times for each path are then summed up taking into account the various restraints. The path requiring the maximum total time is called the *critical path.* It is clearly the path that defines the time required to complete the entire project. Activities that are not on the critical path can start late and still finish by the time the critical path activities are completed. The amount of extra time available to complete an activity without delaying the overall schedule is called the *float time* for that activity. It is the difference between the time available for an activity and its nominal duration. From this discussion, it is evident that activities on the critical path have zero float times.

Several particular advantages accrue from the use of CPM scheduling (or other similar techniques). The interrelationships of the various activities comprising an entire project are clearly revealed. The critical items which determine the duration of the entire project are identified. Thus, any improvement in schedule requires a reduction in duration of one or more of these critical activities. Actual status of the project can easily be compared with scheduled status at any point in time during the program. The effects on total schedule of changing the logic of the CPM network or changing the durations of some of the activities can be quickly ascertained.

Calculation of the early and late starting times, the early and late finishing times, and the float times for the CPM networks can be accomplished either manually or by machine. With complex networks, the computer offers the advantages of speed, accuracy, and the ability to sort activities, e.g., by responsibility or by starting time.

The completed CPM network is basically a logical plan for accomplishing a given project. It provides indications of the proper priorities to be placed on such matters as the delivery of materials, the allocation of manpower, and the utilization of tools and equipment in order to achieve an overall schedule. By revealing which activities are on the critical path, the CPM indicates where extra manpower, overtime, or expediting should be brought to bear or where an alternative or parallel solution should be sought. It simultaneously reveals the activities with float times where extra efforts will not improve the overall schedule, but where, indeed, some relaxation in efforts may be feasible.

The use of a new scheduling technique in a complex program such as that at SLAC required that large numbers of key individuals associated with SLAC, ABA, and the AEC receive training in these methods. CPM classes were held and information was disseminated to promote a common understanding of the terminology, procedures, and interpretation of this scheduling technique. In many cases, SLAC and ABA personnel also trained members of subcontracting firms in the application of CPM.

The critical path method was utilized throughout the SLAC construction period and proved to be useful for setting up and controlling schedules. CPM continues to be used during the operating period.

During the design, construction, installation, and checkout phases, a status review meeting with one of the Technical Division groups was conducted by the Division Head each morning. The number of groups was such that each group was reviewed once every 2 weeks on a regular basis. At each of these meetings, a detailed independent report of group progress measured against the CPM schedule was presented by a member of the Technical Planning Department. Lagging activities were promptly identified and corrective steps were initiated. In some cases, alternative or "backup" programs were mounted. The status reports not only reviewed the progress of in-house work but also the progress of subcontracted components and materials. Regular visits to the plants of subcontractors were made by members of the responsible technical groups. When potential problems were recognized, the subcontractors were immediately informed of SLAC's concern, and meetings to seek possible solutions were held. If doubts persisted even after these actions were taken, separate parallel subcontractual arrangements were considered and in those cases where the overall program appeared to be threatened, these parallel programs were undertaken.

4-3 Fiscal experience

Financial support of SLAC has come principally from three funds administered by the U.S. Atomic Energy Commission: (a) a $18.1 million preconstruction research and development (R and D) fund; (b) a $114 million design and construction fund authorized by Congress in September 1961; and (c) a preoperation R and D fund totaling $26.7 million through FY 1966. The latter fund changed character from "preoperations" to "operations" starting in FY 1967. Expenditure rates for each of these funds are shown in Fig. 4-5.

Expenditures under the preconstruction R and D fund started in January 1961, about 9 months in advance of construction authorization. This work was initially a continuation of earlier R and D activities on accelerator structures and associated components already being supported by the AEC at the Hansen Laboratories. The expenditure of preconstruction R and D funds continued over a $5\frac{1}{2}$ year period, reflecting the fact that the development activities associated with some of the components for the accelerator

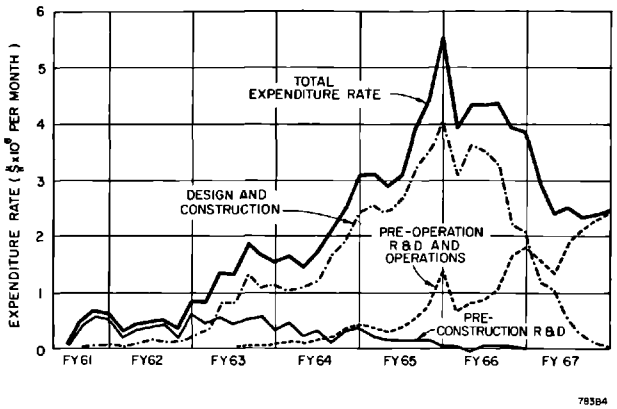

Figure 4-5 Expenditure rates for preconstruction research and development, design and construction, and preoperation research and development funds.

were completed and the designs frozen early while the development of other components and systems, particularly those utilized in the beam switchyard and research area, could not start until the programs and conceptual designs of these areas were formulated. Such considerations, stemming from the diversified nature of the accelerator and its associated research facilities, explain why the preconstruction R and D program extended through almost the whole of the construction period, although its scope was considerably diminished during the 2 final years.

Expenditure of construction funds began in March 1961, about 7 months in advance of construction authorization. The early expenditures consisted principally of money advanced by the AEC to support master planning of the accelerator site, buildings, and utilities.

This preliminary planning was very important in enabling the project to get off to a fast start after the contractual agreement between Stanford and the AEC for construction of the two-mile accelerator was reached in April 1962. For example, initial ground breaking at the accelerator site took place on July 9, 1962, and actual construction of the first two buildings, the Test Laboratory and the Administration-Engineering Building, commenced on August 2, 1962, and September 25, 1962, respectively.

In FY 1963, the construction costing rate began to increase rapidly. It continued to climb during FY 1964 and 1965, reaching a peak rate of approximately $4 million/month early in FY 1966. The rate declined rapidly after that but remained finite for some time because of modifications and extensions of facilities and settlement of contractor claims.

The number of procurement actions, i.e., subcontracts, purchase orders, and change orders per 6-month period is plotted in Fig. 4-6. These actions reached a maximum rate of approximately 2000 per month in late FY 1966. The corresponding costs incurred during each 6-month period are also shown in Fig. 4-6 for SLAC only and for SLAC plus ABA. Note that the SLAC cost

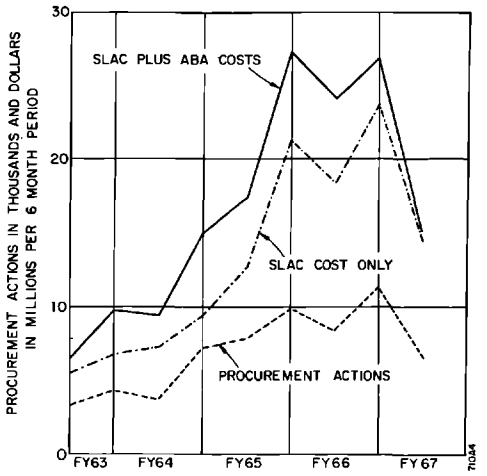

Figure 4-6 Number of procurement actions and associated costs.

rate reached a peak about 1 year after the peak of ABA's cost rate.

The integrated overall project construction costs and costs plus commitments versus time are shown in Fig. 4-7. These are in the form of classical "lazy S" curves applicable to most construction projects. These curves represent the sum of SLAC and ABA costing experiences.

The breakdown of the $114 million construction budget into the principal categories of engineering, design, inspection, and management (EDI and M), direct construction, indirect costs, and escalation and contingency is shown in Table 4-5. For comparison, these costs are given for two points in time: November 1962, shortly after the systems criteria were established and preliminary designs completed; and July 1967, when construction was substantially completed. At the earlier date, the escalation and contingency

Figure 4-7 Integrated total costs and commitments for overall SLAC construction project.

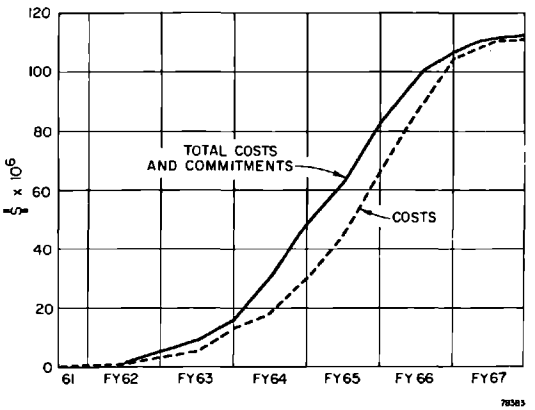

Table 4-5 Accelerator construction costs

Construction categories	*11/1962*	*7/1967*
EDI & M	$ 7,907,800	$ 13,804,835
Direct construction:		
Improvements to land	1,476,000	2,296,388
Buildings	18,778,900	24,850,066
Utilities	7,575,400	8,099,034
Equipment	6,121,200	5,759,781
Modulators	8,332,500	4,645,641
RF Systems (phase/drive)	2,197,200	2,026,807
Accelerator structures	6,326,000	6,945,585
Electrical system	1,117,400	1,605,565
Mechanical systems	5,619,500	5,965,380
Injection system	357,500	599,498
Instrumentation and control	4,295,800	4,821,827
Klystrons	2,496,000	3,392,785
Test stands (constr. and operation)	2,126,700	1,992,467
Beam switchyard equipment	2,624,500	8,538,593
End station equipment	2,436,000	2,880,463
1-meter Hydrogen bubble chamber		19,345
Total direct construction	$ 71,880,600	$ 84,539,225
Indirect Costs	11,392,300	15,404,003
Subtotal	$ 91,180,700	$113,748,063
Reserve for Escalation & Contingency	22,819,300	251,937
Total	$114,000,000	$114,000,000

reserve was kept intact and was not apportioned to the systems and components budgets in advance of proven needs for these funds. In fact, this policy was followed throughout the construction program. As can be seen in Table 4-5, the cost of EDI and M, the cost of twelve of the direct construction items, and indirect costs increased during this period. On the other hand, the cost of four of the direct construction items decreased. The reasons for these changes upward and downward include poor initial estimating, changes in scope, and changes in local or national labor or materials costs. The relative weight of these factors varied from system to system and will not be given here. From the subtotal, it may be noted that the total project estimated cost increased about 25% during the 4-year construction period. Fortunately, it was possible for this increase to be completely absorbed by the escalation and contingency reserve. The major cost increases occurred in the cases of those items (a) on which little previous experience was available and (b) for which design of prototypes was not feasible (e.g., large-one or few-of-a-kind devices such as those located in the beam switchyard) or not possible because of time limitations. Where these factors were not present, the early cost

estimates proved to be remarkably good and the increases which occurred could largely be attributed to escalation. Thus the cost of conventional construction and of the accelerator proper was kept very close to original estimates. The factors enumerated above as causes of cost increases apply principally to the beam switchyard and the target areas. Evolution of new knowledge in the areas of physics on which the accelerator was to have its maximum impact, has changed concepts of the beam switchyard and the target areas considerably from those envisaged in the original proposal, and the talent necessary to inject this new information into design concepts was not available in the earliest phases of the project. As a result it can be stated that almost the entire contingency allocated to the project has been used in those areas directly associated with the specific physical research program envisaged for the accelerator.

Schedule and cost information for the principal SLAC buildings and structures is shown in Table 4-6. This table gives the starting and completion

Table 4-6 Principal SLAC buildings and structures

Name	*Date construction started*	*Date of completion*	*Construction cost (dollars)*	*Gross area (sq. ft)*	*Cost (dollars/sq. ft)*
Test Laboratory	8/62	6/63	910,831	41,500	22
Administration-Engineering Bldg.	9/62	9/63	787,740	44,023	18
Construction Office Bldg.	12/62	6/63	188,305	15,000	13
Electronics Bldg.	2/63	11/63	341,238	26,500	13
Fabrication Bldg.	2/63	12/63	778,452	32,250	24
Accelerator Housing	6/63	10/64	4,727,632	154,355	31
Klystron Gallery	10/63	6/65	3,630,167	361,483	10
Central Laboratory	12/63	4/65	1,582,345	60,275	26
Heavy Assembly Bldg.	12/63	10/64	764,469	34,850	22
Control Bldg.	6/64	3/65	288,332	13,842	21
Beam Switchyard and D.A.B.	9/64	3/66	4,394,792	58,256	75
Cafeteria and Shop Dining Room	1/65	8/65	129,844	4,875	27
Auditorium	1/65	8/65	186,620	7,550	25
End Station A and Beam Dump East	3/65	7/66	2,623,107	32,388	81
End Station B	3/65	7/66	987,978	17,000	58
Cryogenics Bldg.	9/65	5/66	295,749	8,000	37
Fire Station	5/67	1/68	95,880	2,590	37
General Services Bldg.	12/67	8/68	543,200	30,419	18
Central Laboratory Addition	12/67	11/68	822,000	30,900	27

dates of each facility, the total construction cost, the gross area, and the cost per square foot. Engineering, design, inspection, and management costs are not included in this table. It may be noted that the cost per square foot ranged between \$10 and \$85 for the various structures. Altogether, the total gross area listed in the table is 976,056 sq ft at an average cost of \$24.67/sq ft.

4-4 Manpower

The total manpower involved in the design, construction, and operation of SLAC, including the accelerator, buildings, and facilities, is shown in Fig. 4-8. The lower curve shows the manpower associated with ABA. The second curve from the bottom gives the total of ABA employment plus their subcontractors' on-site personnel. ABA reached a manpower peak of about 140 at the end of FY 1963 and then began a gradual phaseout over a $3\frac{1}{2}$ year period. On the other hand, the manpower of ABA's subcontractors did not reach a peak until early in FY 1966 and then declined rather rapidly over a 1-year period.

Direct SLAC employment and the total of SLAC plus its subcontractors' onsite employees are shown, respectively, in the third and fourth curves from the bottom of Fig. 4-8. The bumps on the SLAC curve at the beginning of FY 1965, 1966, and 1967 represent student summer employment (typically about 60 to 75). The upper curve in Fig. 4-8 represents the total employment at the SLAC site. It reached a peak of about 1900 in July 1965. Direct SLAC employment in terms of man-months of effort is shown in the upper curve of Fig. 4-9. This plot is similar to the center curve of Fig. 4-8 but reflects the effects of vacations, overtime, and the exclusion of summer employment.

Figure 4-8 SLAC "on-site" employment.

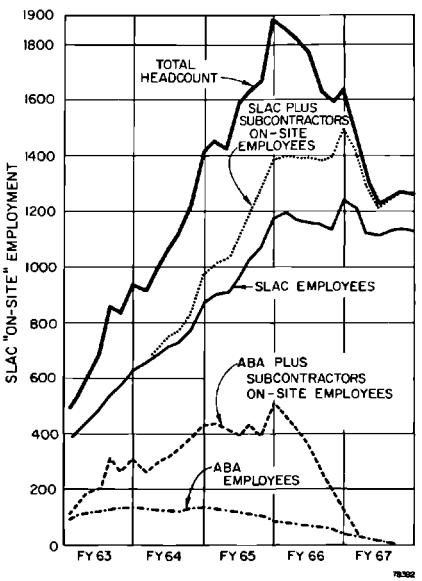

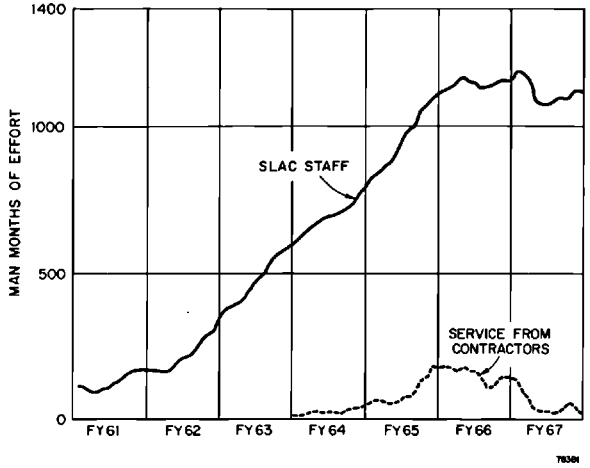

Figure 4-9 SLAC staff effort and services from contractors.

The direct SLAC effort started with a nucleus of about 30 people of all classes from the W. W. Hansen Laboratories at Stanford University. A serious effort was made to avoid excessive buildup of the long-term SLAC staff during the periods of peak manpower demand. In general, it was the intent to acquire staff members who would participate not only in the design and construction phases of the project but who would also remain as effective, continuing staff during the operating and research phases. While complete success in carrying out this objective was not achieved, the upper curve of Fig. 4-9 shows a reasonable approach to this goal. Methods used to control direct SLAC staff buildup included: (a) the hiring of approximately 140 people with appointments terminating at the end of construction (up to 6 weeks' termination pay was stipulated in the offer of employment provided the worker remained until his employment was terminated by SLAC), (b) the use of engineering services from outside engineering firms, contract draftsmen and designers, and several outside "captive" machine shops. These contract services, which reached a peak level of approximately 180 people, extended over the period from FY 1964 through 1967 as shown in the lower curve of Fig. 4-9.

The SLAC man-month effort reached a peak of 1170 in October 1965, and remained approximately constant at this level until August 1966, when it began to decline slowly. A drop to 1049 by July 1967 resulted. During FY 1965 and 1966 the project monthly turnover rate averaged about 2%. The rate was lower than this figure prior to FY 1965 and higher (up to 4% per month) during the first half of FY 1967 as the end of the construction phase approached. During the latter period, the high turnover resulted in part from the dismissal of a substantial portion of the employees with temporary appointments. A few of the latter class of workers proved to be so effective that they were offered permanent positions.

5

GENERAL DESCRIPTION OF SLAC AND TWO-MILE ACCELERATOR

R. B. Neal

This chapter presents an overall preliminary description of the accelerator site and the principal systems and components of the two-mile accelerator. More complete accounts of these systems and components are given in later chapters. In addition, accelerator performance and operating statistics obtained during the first year of operation are presented.

5-1 Description of site, principal buildings, and laboratories

The Stanford Linear Accelerator Center is located on 480 acres of land about 2 miles west of the main Stanford campus. The location of the site relative to the University and the surrounding communities is shown in Fig. 5-1. In Fig. 5-2, an air view of the site shows the research area in the foreground, the principal laboratories, offices, and shops in the center, and the accelerator and klystron gallery running west to east (top to bottom in the photograph). The injector is located at the west end of the accelerator (top of the photograph). The site is 1000 ft wide along most of the accelerator length. It increases to about 3000 ft at the target end to allow space for buildings and experimental facilities.

In the general plan for SLAC, the buildings are arranged into four major divisions. The facilities and structures are located on the site on the basis of their specific functions and interrelationships. A site plan is shown in Fig. 5-3. The "campus area" consists of buildings arranged on three sides of a landscaped open mall. The Administration-Engineering Building, the Central Laboratory, the Test Laboratory, and the Cafeteria–Auditorium are located in this area. The "accelerator complex" extends approximately 2 miles in length and traverses most of the SLAC site. In this complex are the Accelerator Housing, the Klystron Gallery, the Central Control Building, and several

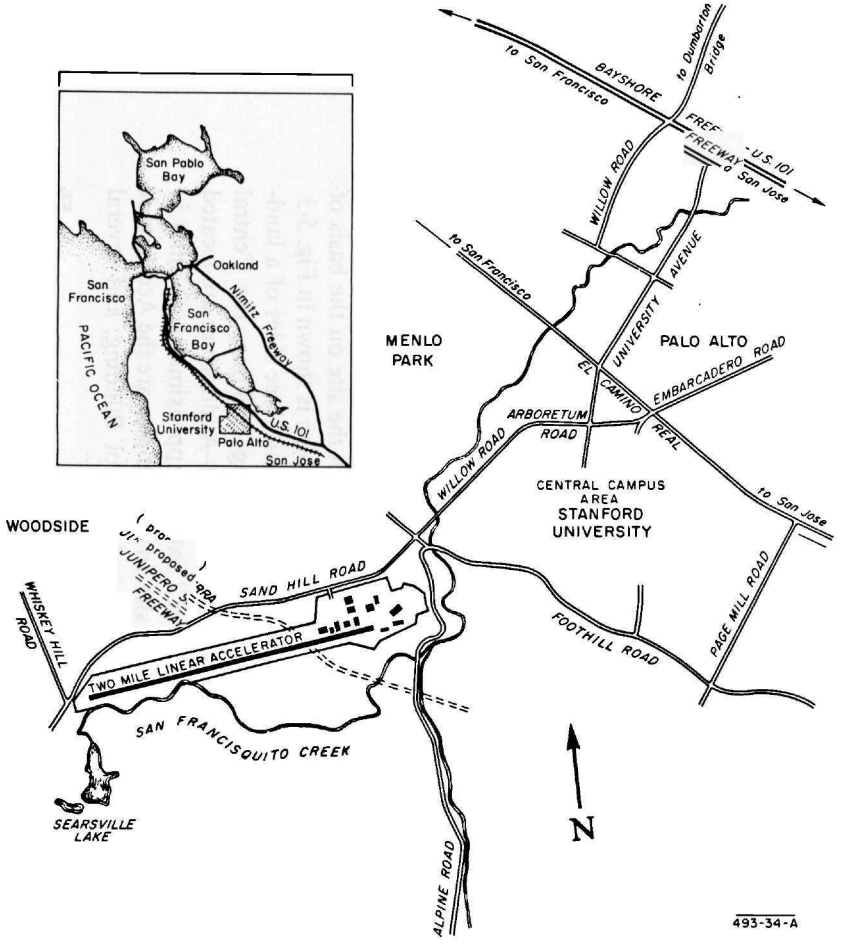

Figure 5-1 Site location relative to Stanford University and surrounding communities.

Figure 5-2 Air view of SLAC site showing the two-mile accelerator, the research facilities, and the principal laboratories and shops.

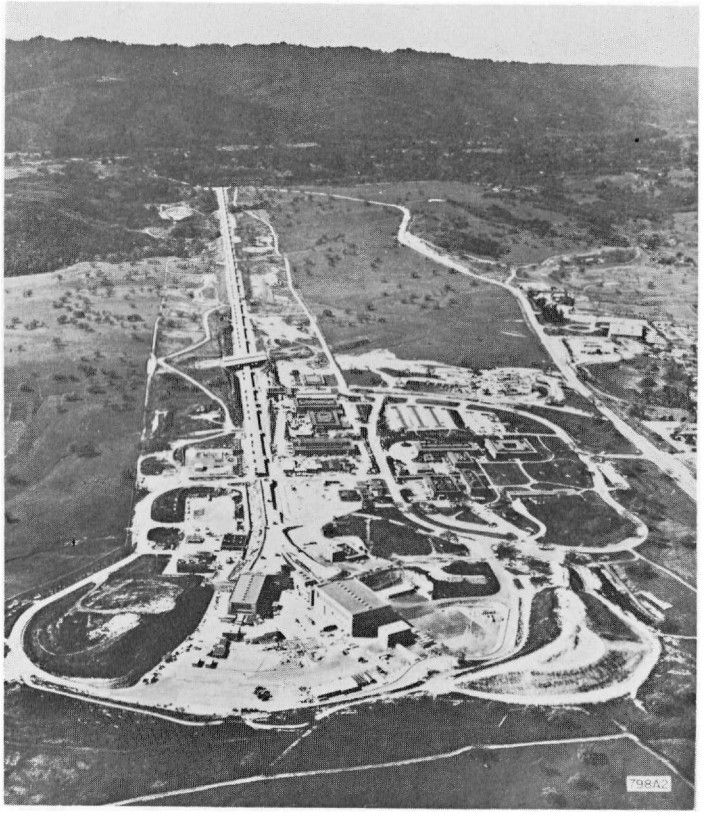

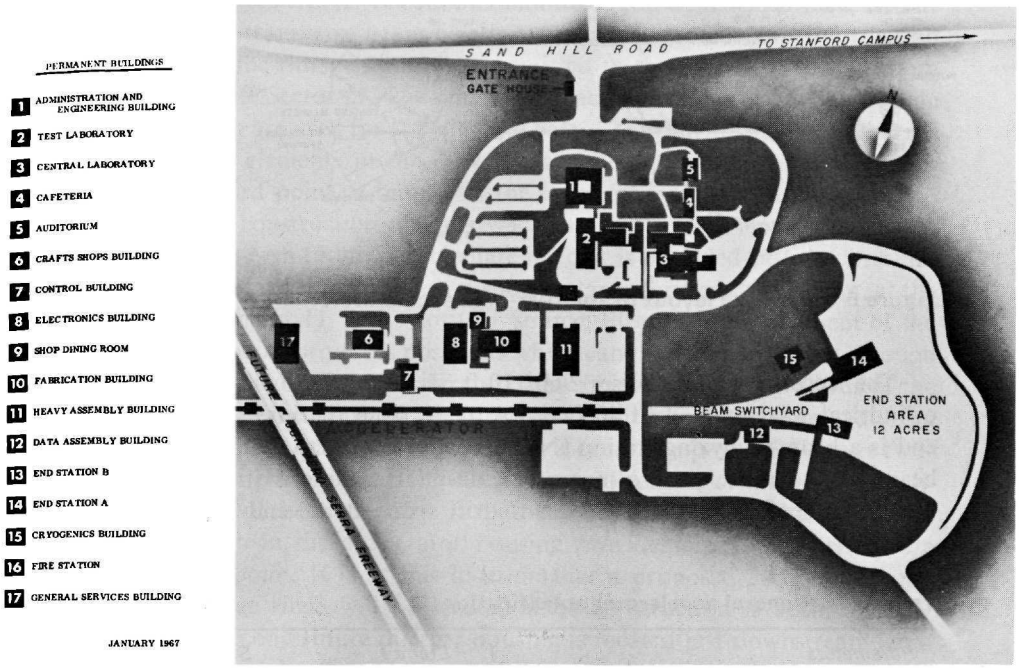

Figure 5-3 Site plan.

related electrical power, cooling water, instrumentation, and utility structures. The "support complex" is situated between the campus area and the accelerator. It includes the Fabrication Building, Heavy Assembly Building, Electronics Building, General Services Building, Fire Station, storage yards, and general service structures and facilities. These structures are located so as to be easily accessible from other areas of the project requiring their services. The "research area" occupies the eastern end of the site. Included in this area are the Beam Switchyard, End Stations A and B, "Counting House," Data Assembly Building, Cryogenic Building, and several related electrical power and utility structures.

5-2 General plan of accelerator

A diagram illustrating the entire two-mile accelerator is shown in Fig. 5.4. The overall specifications of the accelerator are given in Table 5-1. The accelerator has been authorized and built in accordance with the Stage I (20-GeV) specifications. Provisions have been made in the design to permit later expansion to Stage II (40 GeV) by connecting additional RF sources along its length. If desirable, the energy increase can be accomplished in an incremental manner.

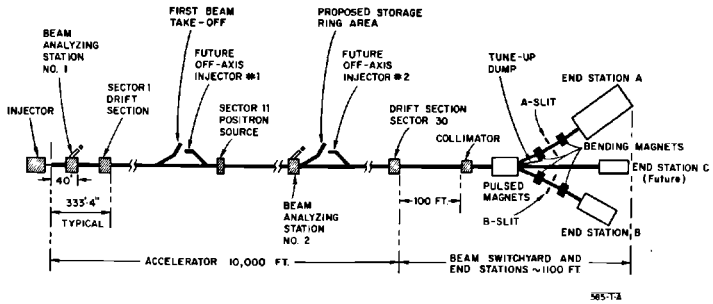

Figure 5-4 Overall layout of the two-mile accelerator.

The accelerator comprises 960, 10-ft sections of 10.5-cm disk-loaded cylindrical waveguide. Just 40 ft downstream from the injector at the west end is a beam-analyzing station (No. 1) which is used to set up the injected beam and to make precise measurements of its characteristics. An instrumentation section is located in a 9-ft drift space at the end of each 333-ft

Table 5-1 General accelerator specifications

Parameters	*Stage I*	*Stage II*
Accelerator length	10,000 ft	10,000 ft
Length between feeds	10 ft	10 ft
Number of accelerator sections	960	960
Number of klystrons	245	960
Peak power per klystron	6–24 MW	6–24 MW
Beam pulse repetition rate	1–360 pulses/sec	1–360 pulses/sec
RF pulse length	2.5 μsec	2.5 μsec
Filling time	0.83 μsec	0.83 μsec
Electron energy, unloaded	11.1–22.2 GeV	22.2–44.4 GeV
Electron energy, loaded	10–20 GeV	20–40 GeV
Electron peak beam current	25–50 mA	50–100 mA
Electron average beam current	15–30 μA	30–60 μA
Electron average beam power	0.15–0.6 MW	0.6–2.4 MW
Electron beam pulse length	0.01–2.1 μsec	0.01–2.1 μsec
Electron beam energy spread (max)	0.5%	0.5%
Positron energy	7.4–14.8 GeV	14.8–29.6 GeV
Positron average beam current[a]	0.45 μA	0.45 μA
Multiple beam capability	3 interlaced beams with independently adjustable pulse length and current	
Operating frequency	2856 MHz	2856 MHz

[a] For 100 kW of incident electron beam power at positron source located at one-third point along accelerator length.

sector of the accelerator. It contains monitoring devices which measure the beam current, transverse beam position, and beam profile. This information from each of the thirty sectors is transmitted to the Central Control Room located opposite Sector 27. The same drift space also contains the quadrupole doublets which are used for focusing the beam. These drift space components are important elements in the overall instrumentation and control system. At the one-third point, a branch in the accelerator housing is provided to allow future construction of a reduced-energy experimental facility. A structure to house a future intermediate injector is provided just downstream from the beam takeoff point. Only a short distance farther downstream, at the beginning of Sector 11, is the positron source. Electron bombardment of the target at this point produces positrons which can then be accelerated through the remaining length of the accelerator, thus achieving up to two-thirds of the maximum electron energy. At the two-thirds point is located beam-analyzing station No. 2. This station permits testing a beam of up to 3 GeV over two-thirds of the length of the machine without involvement of the beam switch-yard at the end of the accelerator. Just downstream from the analyzing station, another branch in the accelerator housing provides a second intermediate beam takeoff point. It is at this location that a proposed 3-GeV electron–positron storage ring[1] will be located if its construction is authorized by Congress. A second future injector housing is located just downstream from the storage ring takeoff.

A view of the cross section of the accelerator housing and the klystron gallery is shown in Fig. 5-5. These structures are separated by 25 ft of earth

Figure 5-5 Cross section of accelerator housing and klystron gallery.

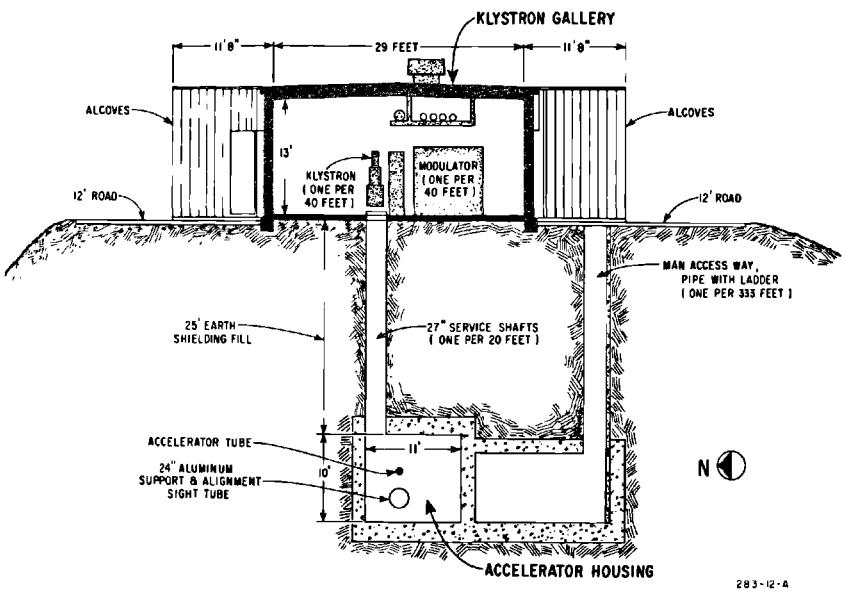

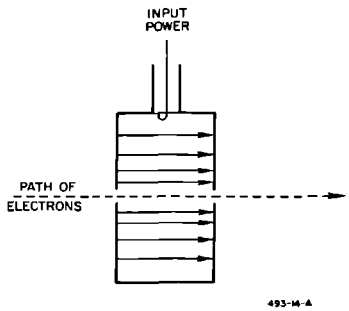

Figure 5-6
Single cavity accelerator.

for radiation shielding. Service shafts, 27 in. in diameter and spaced 20 ft apart, allow passage of waveguides, vacuum manifolds, cooling water piping, and instrumentation cables between the two housings. Man accessways are provided between the two levels at 333-ft intervals along the machine.

5-3 Elementary principles of operation

Before describing the two-mile accelerator in more detail, it may be beneficial to give a brief and rather elementary review of the operating principles of linear accelerators.

Consider a single cylindrical cavity oscillating in the TM_{010} mode at a very high (microwave) frequency, as shown in Fig. 5-6. Assume that small holes are made in the centers of the end plates and that a beam of low-energy electrons is shot in through one hole and out the other. Those electrons that pass through the cavity during accelerating phases will gain in energy by the line integral of the electric field along their path. Neglecting transit time considerations, the maximum energy gained will be

$$V = \sqrt{PR}$$

where P is the RF power dissipated in the cavity and R is the shunt impedance of the cavity which is defined by this relation.

Now suppose that instead of having a single cavity, n such cavities are placed end-to-end with the small holes aligned as shown in Fig. 5-7, so that

Figure 5-7
Multiple cavity accelerator.

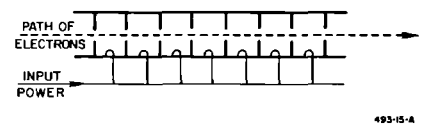

the beam can pass through. Let the cavities be excited from a transmission line which has its phase velocity adjusted so as to equal the velocity of the accelerated electrons. Then, if the available power is the same as before and equal amounts of power are distributed to each of the n cavities, the total energy gained will be

$$V = n\left(\frac{P}{n}R\right)^{1/2} = (nPR)^{1/2}$$

where perfect phasing conditions have been assumed and the transit time effect has again been neglected. This simple example illustrates a basic principle of the linear accelerator: by distributing the available power to n cavities, the net energy gain has been improved by a factor $(n)^{1/2}$. The general statement may be made that the energy gain in a linear accelerator is proportional to the square root of the product of the RF power input and the accelerator length. This conclusion applies to a single section made up of a multiplicity of cavities; it applies also to a long accelerator consisting of a multiplicity of sections.

The distribution scheme just discussed is possible in principle but difficult in execution. The design and construction of a feed system to provide equal amounts of power per cavity and to achieve the desired phase relationship between cavities would be quite complex.

Consider another system wherein the structure simultaneously serves the functions of accelerator and waveguide. Consider first an ordinary cylindrical waveguide excited in the TM_{01} mode, as shown in Fig. 5-8. If the guide is properly terminated, there will be a wave traveling in one direction in the guide which could conceivably be used for the acceleration of electrons since it has an axial component of electric field. The difficulty is that this wave has a phase velocity greater than the velocity of light, c, and material particles such as electrons cannot exceed c. Thus, being unable to keep up with the wave, they would drop behind and receive no net acceleration.

There are various ways of slowing down the phase velocity of the wave. The method used at Stanford consists of periodically loading the waveguide with metal disks, as shown in Fig. 5-9. When this structure is excited as before, it is now observed that as the excitation frequency is varied there are an infinite number of pass bands separated by attenuation bands. At a particular

Figure 5-8
Cylindrical cavity excited in TM_{01} mode.

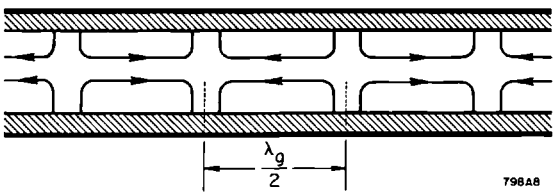

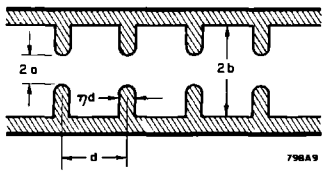

Figure 5-9 Disk-loaded cylindrical waveguide.

frequency there are also an infinite number of wave components, each traveling at a characteristic phase velocity. These additional components are required to satisfy the boundary condition imposed by the addition of the disks. The loading can be adjusted until one component is traveling at the desired phase velocity, typically the velocity of light. If this component is the one of which the velocity is closest to the phase velocity in the unloaded guide, this particular component will contain the largest share of the total RF energy, about 90%. The RF energy carried by the other wave components is wasted in the sense that it does not contribute to the useful acceleration of electrons. These components, with velocities different from those of the electrons, give rise to oscillatory forces which average to zero in a long accelerator.

Another feature of a linear electron accelerator which is important to understand is the question of orbit stability. It might be assumed that getting the electrons to pass through a pipe $\frac{3}{4}$-in. in diameter and 2 miles in length is an insurmountable problem. Even if the pipe were absolutely straight, it is virtually impossible to aim the electron gun at the beginning of the machine so accurately that the electrons will pass through such a small pipe. Fortunately these problems are not real for two reasons. First, the supposed difficulty is not based upon accurate reasoning because the effects of relativity have been neglected. According to the theory of relativity, an observer traveling with the electrons would see the pipe greatly foreshortened. However, the transverse dimensions of the accelerator are not altered, so that the $\frac{3}{4}$-in. hole retains the same dimension regardless of the axial electron velocity. Figure 5-10 indicates the degree of foreshortening of the accelerator. For example, if the machine is 10,000 ft long, then at an energy of 15 GeV it appears to the electron to be only 42 in. long. The problem of getting an electron through a hole $\frac{3}{4}$-in. in diameter and 42 in. long is a trivial one—at least as compared to the precision needed in presenting an accurate picture on the screen of a television picture tube.

Further, the straightness of an accelerator is not a critically important matter because relatively simple means can be used to redirect the electrons if a small bend in the pipe occurs. Beam position monitor devices sense the deviation of the beam from the axis of the accelerator and display this information for the operator. The operator then adjusts the current in simple dipole steering coils spaced along the accelerator to deflect the beam as needed, thus causing it to remain centered in the accelerator.

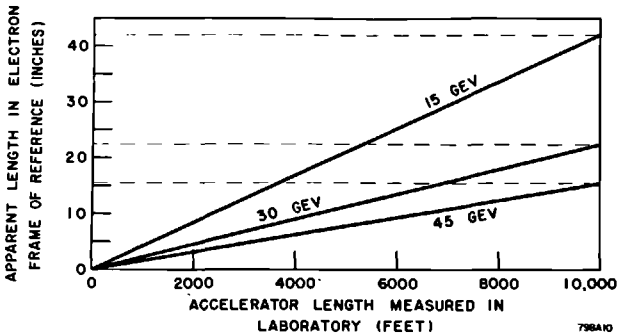

Figure 5-10 Apparent length in electron frame of reference compared to actual accelerator length.

5-4 Accelerator components and systems

A block diagram illustrating the principal components and systems of the two-mile accelerator is shown in Fig. 5-11. Most of these units are repeated many times in the entire accelerator length. For example, there are 960, 10-ft long accelerator sections, 245 klystrons, 245 modulators, 30 sub-booster klystrons, 30 power substations, and 30 vacuum systems. The instrumentation and control system is spread over the entire accelerator length, although the machine can be operated from a single Central Control Room.

Accelerator structure

The accelerator proper is a cylindrical, copper, disk-loaded structure in which an axial electric field traveling at the velocity of light is set up when the structure is excited with microwave power at a frequency of 2856 MHz. The structure is designed to produce a constant axial electric field over the length of each independently fed, 10-ft section. This constant gradient characteristic is achieved by suitable variation of the modular dimensions of the section. The shunt impedance of the structure is approximately 53 megohms/meter, which

Figure 5-11
Accelerator components and systems.

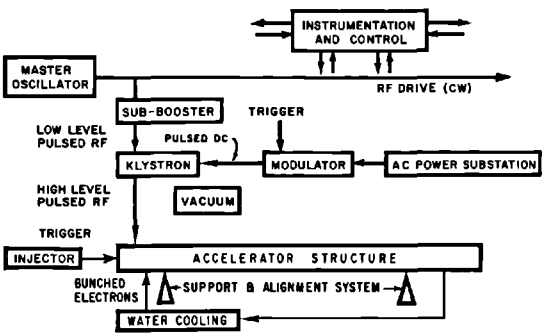

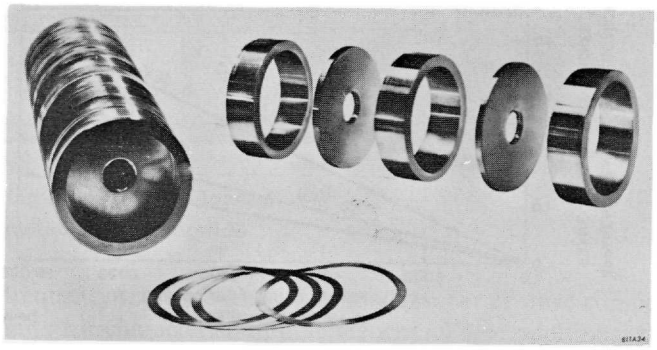

Figure 5-12 Accelerator disks and cylinders.

results in an electron energy gain in million electron volts in a 10-ft section of $\approx 10\, P^{1/2}$, where P is the input RF power to the section in megawatts.

The accelerator structure was fabricated by a brazing technique from the basic disk and cylinder elements shown in Fig. 5-12. These parts were independently machined to accuracies of ± 0.0002 in. They were then carefully stacked and clamped together on a stainless steel mandrel passing through the disk apertures. Brazing was accomplished in a special flame furnace which provided a reducing atmosphere both inside and outside of the structure to prevent oxidation. A completed 10-ft section is shown in Fig. 5-13.

Figure 5-13
View of completed 10-ft accelerator section.

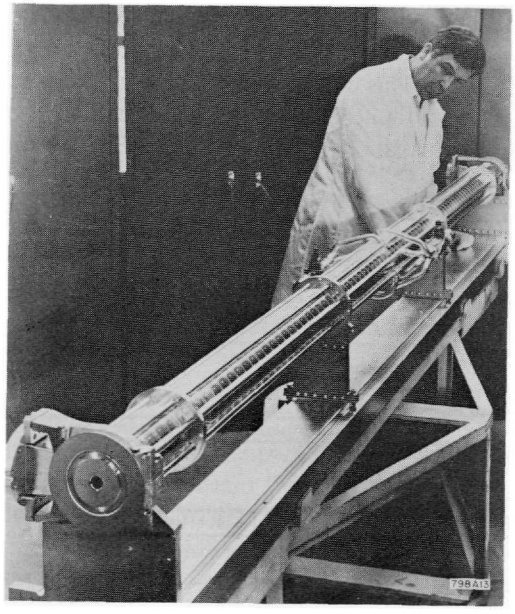

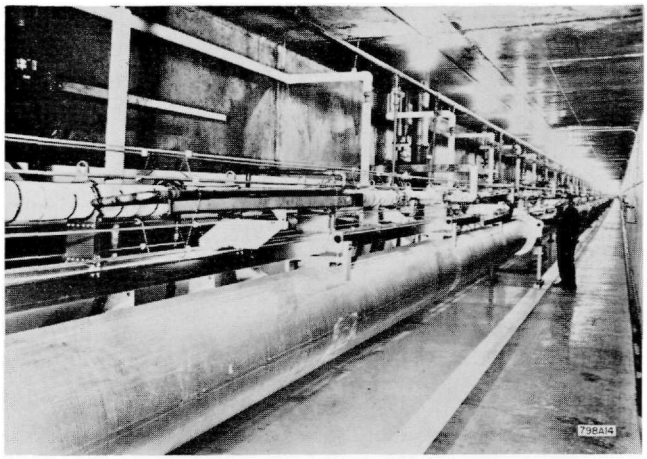

Figure 5-14 Installed basic 40-ft accelerator modules each consisting of four 10-ft sections mounted on a 24-in. diameter aluminum girder.

Four of the 10-ft sections are mounted on a 40-ft aluminum girder, 24 in. in diameter. This is the modular length of the accelerator for support and alignment purposes. The aluminum girder serves dual functions as support for the accelerator and as a "light pipe" for alignment purposes. The assembled and installed girders are shown in Fig. 5-14.

Alignment system

Each of the 40-ft support points of the accelerator is aligned with respect to a straight line defined by two end points. One of the end points is a laser light source located at the end of the accelerator near the beam switchyard and the other end point is a slit with a photomultiplier detector located upstream from the main injector. The laser light source provides a beam of light which is transmitted through the 24-in. aluminum support girder. The girder (light pipe) is evacuated to a pressure of about 10^{-2} torr to reduce refraction due to temperature gradients in the residual gas. At each 40-ft support point, a retractable Fresnel target, as shown in Fig. 5-15, images the light source on the detector. The transverse location of the image indicates the deviation of the target from its correct position. The jacks at the corresponding support point can be adjusted to bring the target into correct alignment. The correct angular rotation of the accelerator is assured by the use of precision level devices. The system described is able to align the accelerator to ± 0.5 mm. A separate laser, located in the beam switchyard, is provided to align the switchyard components using the same detector as the accelerator alignment system.

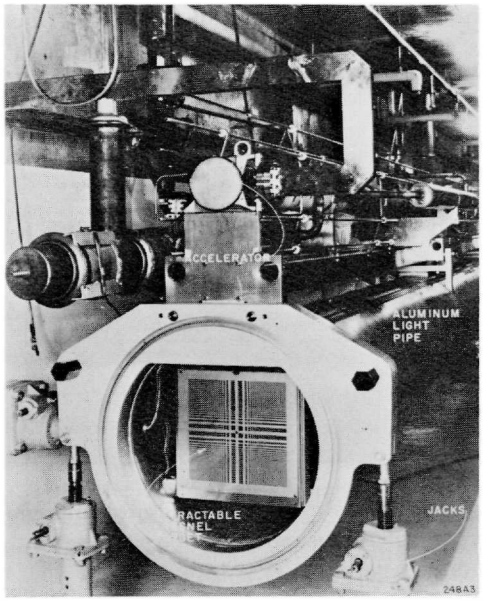

Figure 5-15 End of 40-ft girder showing retractable Fresnel target.

Klystrons

The RF power sources are high-power klystron amplifiers. A basic tube having a design capability of 24 MW peak and 22 kW average power was developed at SLAC. Four commercial companies also developed tubes for the accelerator meeting the same basic specifications as the SLAC tube. A group photograph of the five different tubes is shown in Fig. 5-16. All these

Figure 5-16 Klystron models manufactured by SLAC and by four commercial companies.

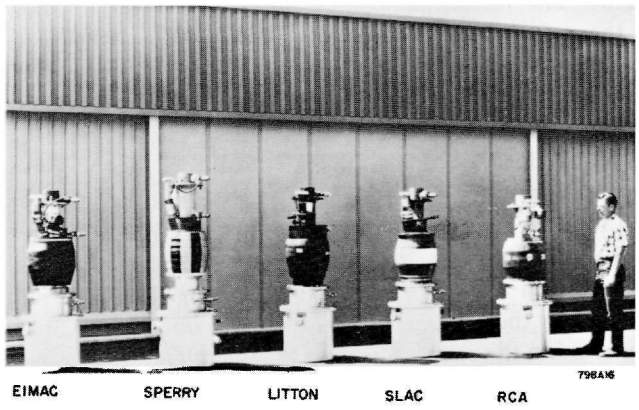

tubes have permanent magnet focusing and are electrically and mechanically interchangeable. The use of permanent magnet focusing instead of the more customary electromagnetic focusing eliminates the need for water cooling of the focusing system and for focusing power supplies. It also results in simplification of the interlock system.

The power from each klystron is divided four ways (Stage I) and is used to supply power to the four 10-ft sections located on a single 40-ft girder. The general arrangement of the klystron, the connecting waveguides, and the accelerator sections is shown in Fig. 5-17. Waveguide feeds to the accelerator connect to opposite sides of successive sections to compensate for deflecting forces due to residual coupler asymmetries. The provision of a waveguide valve just above each klystron allows the klystron to be replaced without affecting the accelerator vacuum or interfering with beam operation. If the Stage II modification is later undertaken, the number of klystrons will be increased to 960 so that each klystron will feed a single 10-ft section.

Figure 5-17 General arrangement of klystron, connecting waveguide, and four 10-ft accelerator sections.

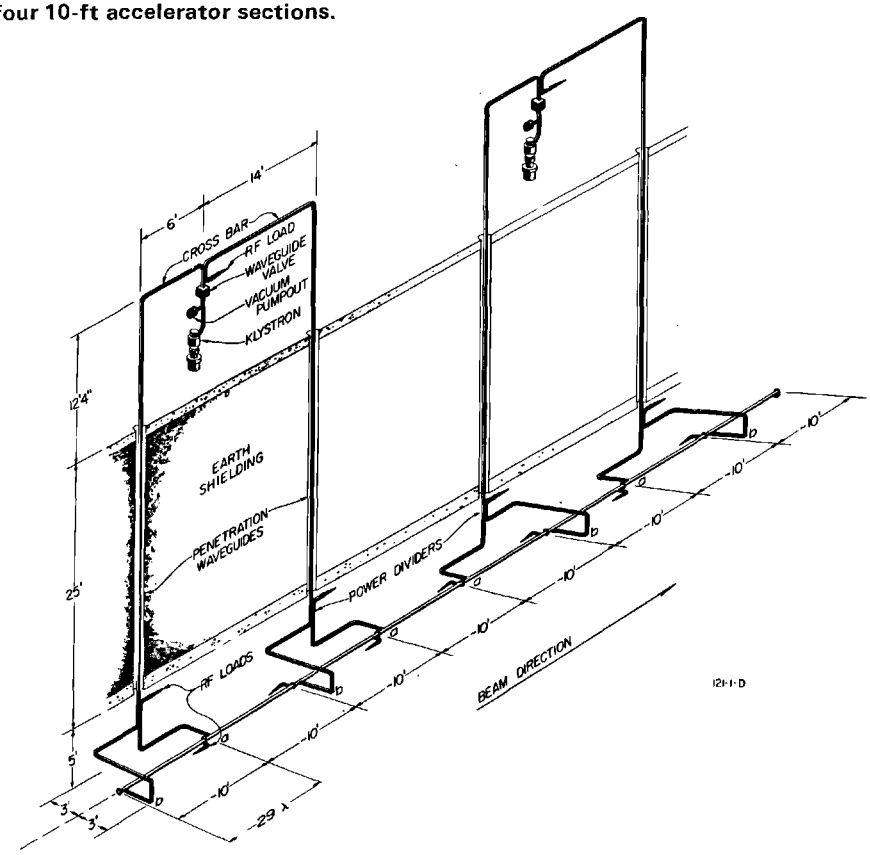

The klystron and its associated pulse transformer tank are designed to be suspended from a special support yoke. This simplifies the installation of the tube and its alignment with the rectangular waveguide system.

High-power modulators

Each klystron amplifier is provided with a "line-type" modulator rated at 65 MW peak and 75 kW average power, a pulse length of 2.5 μsec, and a maximum pulse repetition rate of 360 pulses/sec. The pulse-forming network in the modulator is discharged through a single hydrogen thyratron capable of handling the entire peak and average power requirements—the voltage of the output pulses from the modulator is increased by a factor of 12 by means of a pulse transformer, and the resulting pulses at a voltage of 250 kV (maximum) are then applied to the associated klystron.

Each modulator is provided with a "de-Q'ing" circuit which compares the charging voltage of the pulse network during each charging cycle to a reference voltage. When the level of the charging voltage reaches the reference level, the energy stored in a charging transactor is dumped into a dissipative circuit by means of a silicon-controlled rectifier switch. This effectively clamps the charging voltage at the reference level and thus stabilizes the output pulses from the modulator to $\pm 0.1\%$ even in the presence of significant (approximately $\pm 3\%$) variations in the ac line voltage.

All sixteen modulators located in each pair of 333-ft sectors are provided with power from a variable voltage substation located in the klystron gallery. The input power to each substation is provided at a 12.47-kV level by means of underground cables from the master substation located near the east end of the accelerator. The output voltage of the substation is remotely controlled over a range of 258 to 595 volts ac from the Central Control Room. All of the sixteen modulators connected to the substation receive the same voltage. However, different substations can be operated at different output voltage levels.

Injector system

A diagram of the main injector is shown in Fig. 5-18. It is designed to inject a well-bunched (5°) and well-collimated beam of electrons into the accelerator. Since the energy gain of an accelerated electron is proportional to the cosine of the phase angle that it occupies with respect to the peak of the traveling RF wave, good bunching of the electrons is essential in order to attain a narrow, electron energy spectrum at the output of the accelerator. The electron gun which operates at 80 kV is of the triode type which permits the pulse length and beam current to be selected on a pulse-to-pulse basis from any of three predetermined sets of values. This feature of the injector, together with the ability to trigger the klystrons in the various sectors in time with or after the beam (or at various repetition rates), permits carrying on several simultaneous experiments in the research areas at different incident energies, pulse

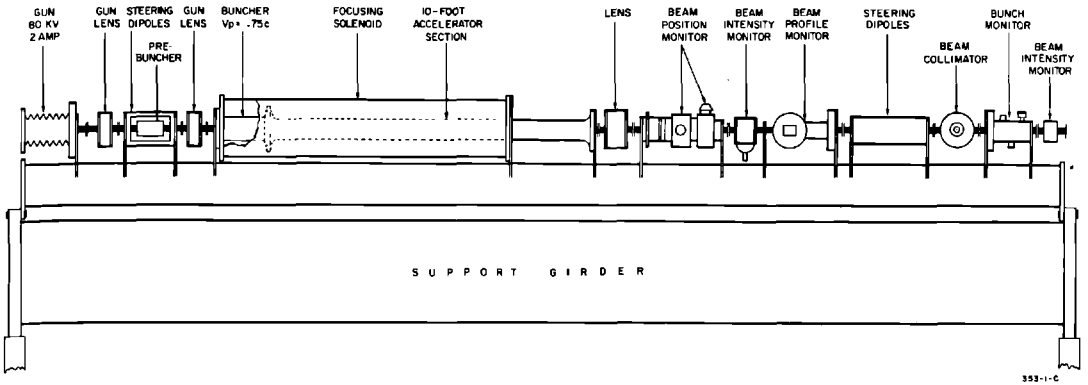

Figure 5-18 Profile view of injector.

lengths, and intensities. The prebuncher consists of a velocity modulation cavity. The bunching section is a disk-loaded section 10.5 cm long in which the phase velocity is 75% of the velocity of light. It serves to reduce the phase spread by a factor of 2.5 (while increasing the momentum spread by the same factor) and increases the beam energy to 260 keV. A 10-ft long, constant gradient, accelerator section increases the energy to approximately 30 MeV. For phase synchronization, the prebuncher, buncher, and 10-ft accelerator section are all driven by power from the same klystron, which is conservatively run at half to two-thirds of its power capability to give good life and stability.

A special beam knockout device is used when there is a need to increase the time (and space) separation of the electron bunches. This is desirable, for example, when carrying out certain experiments utilizing time-of-flight techniques. Removal of the unwanted bunches is accomplished by means of sinusoidal, transverse electric fields. These varying fields, which are developed between metal deflecting plates, deflect some of the bunches right or left into the accelerator walls while allowing other bunches to pass through undeflected. One set of these plates is located in the injector system between the prebuncher and the buncher. These plates are supplied with RF power at 39.667 MHz (the 72nd subharmonic of the 2856-MHz power which accelerates the electrons). One electron bunch passes through undisturbed at each voltage null. All other bunches are deflected and are thus effectively removed from the beam. Since two nulls occur during each cycle, one bunch out of every thirty-six entering the deflecting system survives and is accelerated through the entire machine. The peak current in this bunch can be increased until the average current in the beam is nearly equal to the maximum achievable when all of the bunches are present.

The 39.667-MHz drive power originates in one of the lower-frequency stages of the master oscillator. It is amplified by a special pulsed modulator before being applied to the deflecting plates. Other frequencies can, of course, be applied to achieve various desired spacings of the bunches. A second set

of beam knockout plates is provided for at the end of the first accelerator sector in case it is desired to reduce the phase extent (longitudinal size) of the bunch to a further degree. This second knockout stage can also serve to remove any "dark current" which may originate in the first sector. Dark current arising in later sectors can easily be eliminated in the magnetic slit system located in the beam switchyard.

Drive and phasing systems

The klystron amplifiers must receive coherent low level signals at 2856 MHz so that the RF waves in the accelerator sections will have the correct frequency and phase relationships with the individual bunches of electrons passing through the accelerator. The RF drive system consists of

a master oscillator providing 476-MHz power;
a main booster amplifier which increases the 476-MHz power to 17.5 kW, continuous wave;
a $3\frac{1}{8}$ in. diameter main drive line 2 miles long;
couplers and varactor frequency multipliers at each 333-ft sector which remove a small portion of the main drive signal and multiply the frequency by 6 to 2856 MHz;
a pulsed sub-booster klystron at each sector that amplifies the 2856-MHz power by 60 dB;
a $1\frac{5}{8}$-in. diameter coaxial line which transmits 2856-MHz drive power to the vicinity of each of the high-power klystrons in the sector;
couplers that remove approximately 4 kW peak. After attenuation, 300 watts remain to drive each klystron.

The main drive signal is transmitted at the subharmonic frequency, 476 MHz, because the low loss at this frequency ($\approx$0.25 dB/100 ft) permits transmission over 2 miles without series boosters which, if used, would lead to phase shift and reliability problems.

The RF phasing system uses the phase of the electron bunches in the accelerator as the phase reference. It is based on the principle that the wave induced by the bunched electron beam in an accelerator section is 180° out of phase with respect to the wave from a correctly phased klystron supplying power to that section. Phasing is accomplished automatically (within $\pm 5°$) by sectors when initiated by the operator.

Vacuum system

The all-metal high vacuum system capable of maintaining the accelerator and waveguides at $< 10^{-6}$ torr is shown schematically in Fig. 5-19. One such system is provided for each 333-ft sector. Four 500-liter/sec getter-ion pumps located in the klystron gallery evacuate the accelerator and waveguides through interconnecting stainless steel manifolds. A pump can be removed

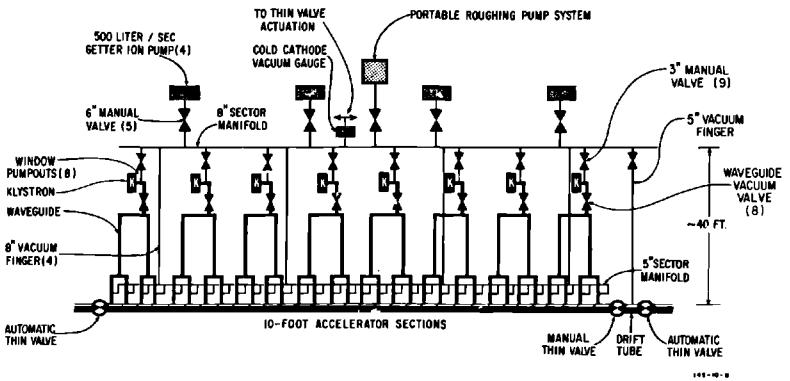

Figure 5-19 Vacuum system schematic for one 333-ft sector.

for servicing without interference with accelerator operations by closing the associated 6-in. valve. Similarly, an individual klystron can be replaced by closing the 3-in. valve connecting it to the pumping manifold and the waveguide vacuum valve in its output RF system.

Separate pumping systems are provided for rough-pumping the accelerator, for the 24-in. light pipe, and for the beam switchyard.

Cooling water systems

Most of the electrical energy consumed by the accelerator components is eventually absorbed by the cooling water systems. In addition to absorbing power, these systems serve to regulate the temperatures of critical components such as the accelerator tube, the rectangular waveguides, the RF drive line, and the klystrons.

The water systems utilize secondary loops which include the devices being cooled and primary loops containing outside cooling towers which transfer heat to the atmosphere. Heat is transferred from the secondary to the primary loops through shell-and-tube heat exchangers.

The cooling water systems are the accelerator tube cooling water system, the waveguide–drive line cooling water system, and the klystron cooling water system.

Control of accelerator tube temperature is necessary to maintain the phase velocity of the electromagnetic wave in the accelerator equal to the velocity of light. The phase shift $\delta\theta$ between the electrons and the wave in a 10-ft section is given by $\delta\theta = 2Q\tau k\,\delta T$, where Q = the unloaded Q of the accelerator cavities ($\approx$13,000), τ = attenuation parameter ($\approx$0.57), k = thermal coefficient of expansion of copper ($\approx 8.9 \times 10^{-6}$/°F), and δT is the deviation in the temperature of the accelerator structure. Thus, $\delta\theta \approx 7.5°$ for δT equal to 1°F. The accelerator tube cooling water system provides each 10-ft accelerator section with 13 gal/min. The input temperature of the cooling water

to each sector is manually adjusted to a value $[113 - 0.6\ P_{AV}(\text{kW})] \pm 0.2°\text{F}$, where $P_{AV}(\text{kW})$ is the average RF power input to the 10-ft accelerator sections of that sector. It has been empirically determined that this input water temperature will result in the design temperature of 113°F in the metal walls of the accelerator. As an example, for $P_{AV}(\text{kW}) = 4$ kW, the correct input water temperature is $113 - (0.6)(4) = 110.6°\text{F}$. Control of the input temperature of the cooling water manually is adequate for all sections which receive one-quarter of the output power of a klystron. This is the case for the vast majority of the accelerator sections. However, for those 10-ft sections in the injector and in the first sector of the accelerator, each of which receives all the power from one klystron, it is necessary to adjust the temperature of the input water over a range of about 13°F. This adjustment is made automatically so that, with the varying temperature gradients caused by changing equilibrium heat flow, the temperature of the accelerator wall remains constant. Thus, the input water temperature varies between 100° and 113°F, the lower input temperature corresponding to maximum power flow from the klystron to the accelerator section.

Except for the special constant metal temperature cases just discussed, a separate temperature-control loop is provided for each accelerator sector.

To prevent phase shift in the rectangular waveguides and in the drive lines, these lines are provided with 5 and 10 gal/min, respectively, of cooling water at a temperature of $112 \pm 1.0°\text{F}$. There is one temperature-control loop per sector.

The major sources of heat in the entire installation are the klystron amplifiers. These tubes each have a maximum rating of 75 kW of average power. Under normal conditions, about 60% of this power is dissipated in the tube itself. To prevent overheating, each tube is provided with 11 gal/min at a supply temperature of $95 \pm 1°\text{F}$. There are ten separate temperature-controlled circuits, one for every three sectors.

Each of the secondary cooling water loops is provided with a bypass demineralizer unit around its circulating pump. The accelerator tube and waveguide–drive line loops also have filters in these bypass lines. The klystron loops have full flow filters in the pump suction line.

Two large cooling towers located at approximately $\frac{1}{2}$ mile and $1\frac{1}{2}$ miles along the 2-mile housings serve to remove the heat from the primary loops. The flow in each cooling tower loop is 500 gal/min with two of the three pumps operating. In typical operation, the supply temperature is 75°F and the return temperature is 90°F at 68°F (wet bulb).

Positron source

A positron beam has to be delivered to the main experimental stations at the end of the accelerator for positron scattering experiments and the creation of a monochromatic photon beam by annihilation with electrons. In addition, a positron beam will be required at the two-thirds point along the

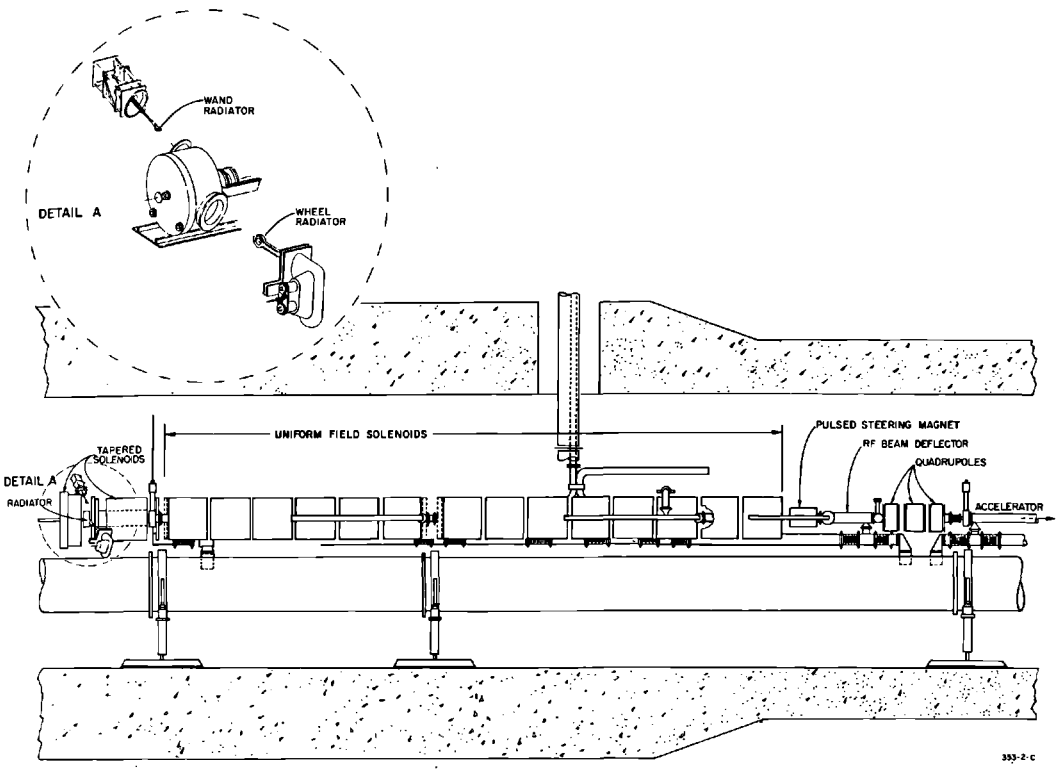

Figure 5-20 Positron source and its associated focusing and instrumentation equipment.

accelerator for injection into a proposed positron–electron storage ring. The beam is created at the one-third point along the machine by inserting a target and reversing the RF phase of the first one-third of the accelerator. With 100 kW of incident electron beam power, a positron current of approximately 0.45 μA (7.5×10^9 positrons/pulse)* can be accelerated in an energy band of about 1% and a transverse phase space of approximately 0.15 π(MeV/c)(cm).

The positron source system is shown in Fig. 5-20. Either of two separate radiators can be inserted into the beam. Each radiator has a thickness of about 4 radiation lengths of copper. A "wand" radiator is provided for intermittent positron pulses at rates up to 4 pulses/sec. It is a small target, 0.38 in. wide, driven across the beam line on command in a time equivalent to about 9 machine pulses (at 360 pulses/sec). The center pulse of this group results in a positron pulse; the other eight are suppressed by gating the main injector. All other pulses may be transmitted as a normal electron beam, if

* The maximum current actually achieved to date (July 1967) is about one-third of this amount (see Chapter 16).

desired. The second radiator is in the form of a "trolling" water-cooled wheel. It is used when continuous positron production is desired.

A magnetic lens system is used to improve the match between the source emittance and the accelerator phase space acceptance. The radiator is located in a 20-kG axial magnetic field which decreases rapidly to 2.4 kG about 2 ft downsteam of the radiator and then remains constant for the next 24 ft. Acceleration begins 2.5 ft downstream of the radiator, and the positron energy at 25 ft is about 75 MeV, at which point the solenoidal focusing is replaced by a series of thirteen quadrupole triplets and doublets of which the spacing increases with energy until this focusing system merges with the regular machine doublet system located at the end of each sector.

A pulsed RF deflector located downstream of the target is used to produce an angular deflection of the positron and electron beams. Because the beams are 180° apart in phase, they are both deflected by the same angle. Thus, depending on which beam is needed, a magnetic dipole can be used to restore the direction of either the positron or the electron beam to the axis while deflecting the other even farther.

Instrumentation and control

CONTROL LOGIC. For purposes of control, the two-mile accelerator is divided into thirty sectors. Each sector has an instrumentation alcove which serves as a data collection and transmission point. These alcoves are not manned except during maintenance or for diagnosis of troubles.

The number of signals and controls for the entire machine is so large that one operator, or even several operators, could not attend to them if they were all available simultaneously. For this reason, a system of summary alarm signals has been provided to alert the operator as to which sector requires attention. The operator can then switch a sector control panel to the sector in question. This panel displays the complete set of analog and status information for that sector and also connects the remote control system to the same sector.

The system is designed for initial control by human operators. However, the signal format has been arranged so that a control computer can be added at a later date for purposes of data logging, beam steering, and energy control.

DATA TRANSMISSION SYSTEM. Some of the data developed along the two-mile accelerator is needed only locally by maintenance personnel for periodic adjustment, diagnosis, or data logging purposes. Most of these types of data are associated with equipment which is relatively quiescent, i.e., a given status or adjustment of such equipment is ordinarily maintained for relatively long periods. Detailed operating conditions on this type of equipment are not reported to the Central Control Room (CCR) but out-of-tolerance performance is usually reported by means of a summary alarm signal.

Other data are so critical to operations that precise quantitative transmission and display at central control are essential. Examples of such data are *steering dipole current* and *sector vacuum*. Such data are transmitted as dc analog signals with a range of 0 to 5 volts on an individual wire pair. The signal is displayed at CCR on a 2% accurate, panel voltmeter. Noise pickup and cable leakage are low enough to permit display with 0.1% accuracy if a high grade meter is employed. Each circuit is grounded at only one point, usually one terminal of the voltage source. Each of the thirty accelerator sectors is provided with twenty analog signals for transmission of data to CCR.

Other information needs to be transmitted only as status signals, which are two-valued functions. For example, it may be sufficient to know whether a certain device is on or off, or within or outside a preset tolerance. Each sector is provided with 100 status channels which are time-division multiplexed and transmitted to CCR on a single wire pair as a binary-coded, frequency-shifted signal. Information is updated twice each second.

After every accelerator pulse, beam intensity and beam position signals derived from a microwave system at each sector are multiplexed and transmitted to CCR as a succession of three pulses on a single wire pair. These pulses are proportional to the x and y displacements of the beam from the axis and to the logarithm of the charge in the beam pulse. The logarithm of charge rather than the charge itself is used as a basis so that a wide dynamic range can be transmitted. However, the accuracy is correspondingly decreased (to about $\pm 30\%$). A separate accurate ($\pm 1\%$) signal proportional to charge in a beam pulse is derived from a toroidal coil in each sector drift section and transmitted to CCR by means of a precise FM (20–40 kHz) transmitter. The four beam-monitoring signals from each sector, along with similar signals from other sectors, are multiplexed in succession onto four oscilloscopes in CCR presenting beam intensity and position information to the operator for the entire two-mile accelerator.

Similar beam-monitoring signals as well as beam energy and spectrum information are transmitted to CCR from the beam switchyard.

REMOTE CONTROL SYSTEM. Most of the remote controls for accelerator equipment are actuated by an economical binary system. Three sector control panels in CCR each contain switches, status lights, and analog meters governing the most important control functions applicable to any sector. By depressing a switch, the operator can connect any one of the three panels to control any one of the thirty sectors. The transmission system for remote control consists of six parallel binary wire-pair channels, which are capable of selecting 2^6 different control functions at a sector. A seventh wire pair transmits the actual binary control command. The same seven wire pairs are bridged from sector to sector for the entire length of the machine. A separate wire pair to each sector provides means to switch the controls to a particular sector.

TRIGGER SYSTEM. Although the basic repetition rate of the accelerator is 360 pulses/sec, the trigger system permits operation of various accelerator sectors and other subsystems in a very flexible manner so that up to six beams having distinct energies, currents, and destinations in the research area can be programmed. The repetition rates of these beams can be adjusted to be any value between 1 and 360 pulses/sec. The trigger system is illustrated in Fig. 5-21. Clock pulses at 400-volt level and 360 pulses/sec are sent over the entire 2 mile length along a single, $1\frac{5}{8}$-in. diameter, coaxial cable. A small amount of power is removed from the main line by means of couplers at each station (e.g., injector, accelerator section, positron source) and is sent to the local trigger generator. A gating pulse is sent to each local trigger generator from the pattern generator in central control. Since the time precision ($\approx \pm 5$ nsec) is inherent in the clock pulses, the gating pulses do not have to be very precise and can be transmitted on ordinary wire pairs.

In Fig. 5-21, the pattern generator pulses are shown gating the clock pulses admitted to the klystron modulators of each sector. If a particular sector is not to contribute to the energy of a particular beam, the pattern gating signal causes the modulators to be triggered 25–50 μsec late, after the beam pulse has been transmitted through the sector. In other arrangements, the pattern signals may cause a particular sector to pulse at a lower repetition rate, such as 60, 120, or 180 pulses/sec.

BEAM GUIDANCE AND DIAGNOSTIC EQUIPMENT. To compensate for the earth's magnetic field and for stray ac and dc fields along the machine, parallel degaussing wires and concentric magnetic shielding are provided, reducing the average fields below 10^{-4} G. The degaussing currents are independently adjustable for each sector. The magnetic shielding material consists of 0.006-in. thick, molybdenum–permalloy material which results in a local shielding

Figure 5-21 Trigger system block diagram.

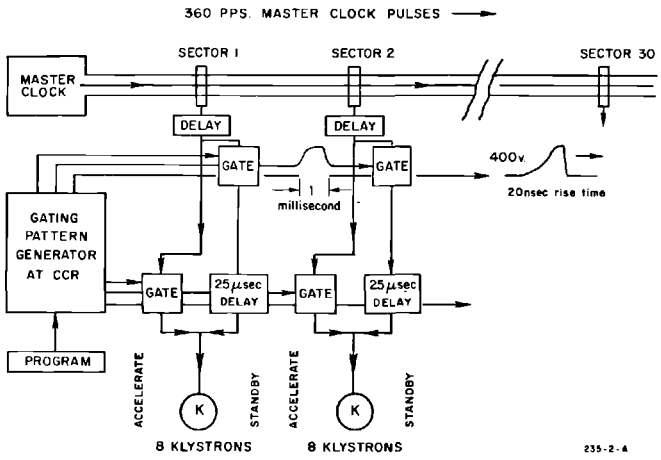

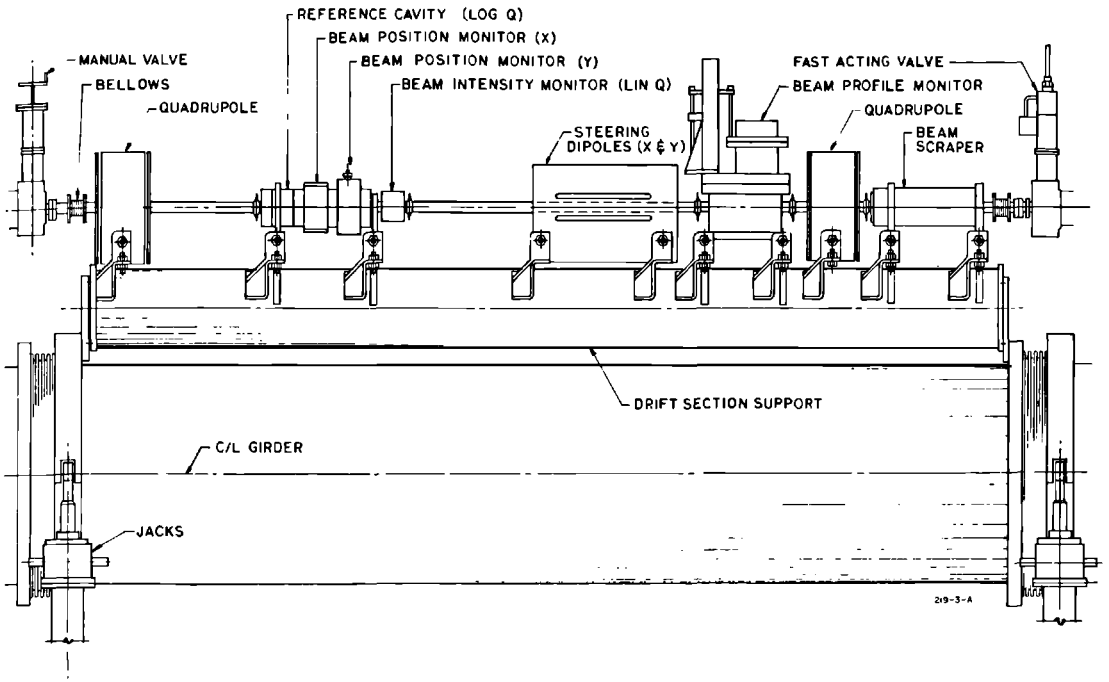

Figure 5-22 Standard instrument section located at end of each 333-ft sector.

factor of about 30 and an overall effective value of about 10, considering unavoidable gaps.

Beam monitoring, steering, and focusing devices are provided in a 10-ft drift section at the end of each 333-ft sector of the accelerator. The layout of a standard drift section is shown in Fig. 5-22. Equipment in this section consists of a quadrupole doublet, steering dipoles (X and Y), a phase reference cavity, beam position monitors (X and Y), a beam intensity monitor, a beam profile monitor, and a "beam scraper" (collimator). The beam position monitor consists of two rectangular cavities which are excited in the TM_{120} mode by an off-axis beam. Since the phase of the excitation depends on the direction of beam deviation from the axis, the sense of the deviation can be detected by comparing the phase of the wave from the beam position monitor cavities with the phase of the wave from the phase reference cavity which is excited in the TM_{010} mode. Beam positions accurate to better than 1.0 mm are displayed in central control from thirty such systems.

A long ion chamber consisting of a $1\frac{5}{8}$-in. coaxial line, filled with a mixture of argon and carbon dioxide, running the full length of the accelerator housing is provided to inform the operator regarding beam losses. From the times of arrival of the ionization signals at the injection end of the accelerator it is possible to resolve the position of the beam loss within 100 to 200 ft. The

ion chamber signal display provides a good profile of the accelerator's radiation due to beam loss. In addition, the injector is automatically turned off in case the beam loss signal at any point exceeds a preset threshold.

PERSONNEL RADIATION PROTECTION SYSTEM. Interlocking of the personnel accessways to the potentially dangerous radiation areas is the primary means of radiation protection. Opening of any of these entrances results in turning off the variable voltage substations providing power to the klystrons and also turning off the injector. The design of the protection system has to take into consideration the fact that there are approximately 100 entrances to radiation areas spread out over the entire site.

Red and green lights in the klystron gallery inform personnel when the klystrons are operating. Access to the gallery is controlled at two gates in the peripheral fencing rather than at the 150 doors of the gallery itself. Since radiation in the gallery is principally from the klystrons and is nominally quite low, the access points to the gallery are not interlocked with the electron beam or with the power supplies.

The personnel protection system consists of three major parts: the *machine shut-off system*, which prevents turn-on until the radiation areas are cleared and secured and which turns off the machine in case the security of any area is broken; the *access control system*, which prevents entry into radiation areas while the machine is on; and the "Emergency Stop" circuit which inserts beam stoppers in appropriate positions when excessive radiation is detected in the research area. In addition, the system contains warning devices and radiation monitors to help determine the state of the machine.

The machine shut-off system is based upon the integrity of double tone loops (40 and 50 kHz) which redundantly determine when the security of any radiation area is broken. If either tone loop is interrupted, all variable voltage substations and the injector are automatically turned off. If the shut-off system is tripped, the area in the vicinity of the open interlock must be searched and a reset button within the area must be actuated. Simultaneous acknowledgment by the CCR operator is required to complete the reset process. Interlocks in the shut-off system are operated from batteries so that momentary interruptions of ac power need not destroy the housing security.

The access control system contains a tone loop which is closed only if all the variable voltage substations are turned off. Only if this loop is closed can the operator release keys from the keybanks to allow personnel to enter the radiation areas.

5-5 Beam switchyard

A layout of the beam switchyard is shown in Fig. 5-23. This is a large two-level underground structure covered by 40 ft of concrete and earth for radiation shielding purposes. The beam path itself is located on the lower level. The upper level contains utility runs, instrumentation and control alcoves,

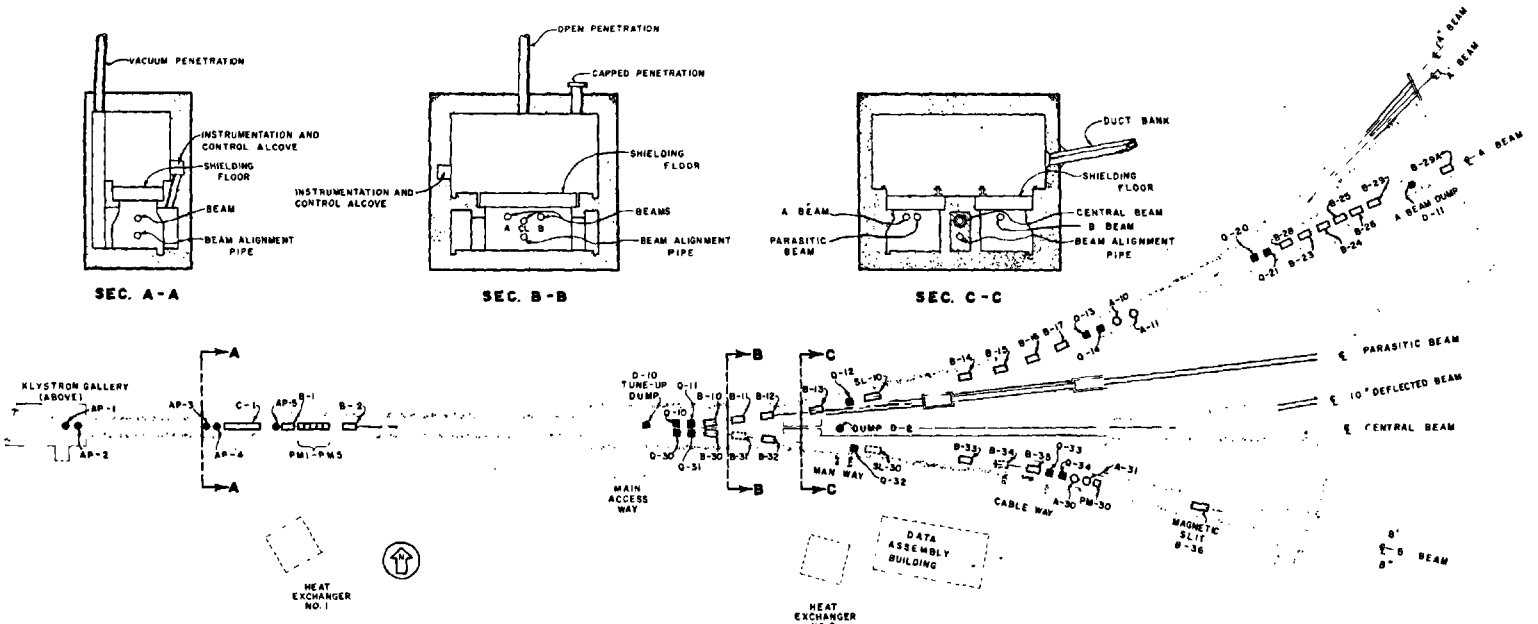

AP - Pulsed Steering Magnet
C - Collimator
B - Bending Magnet
PM - Pulsed Magnet

D - Beam Dump
Q - Quadrupole
SL - Energy Defining Slit
A - dc Steering Magnet

353-10-A

Figure 5-23 Beam switchyard plan.

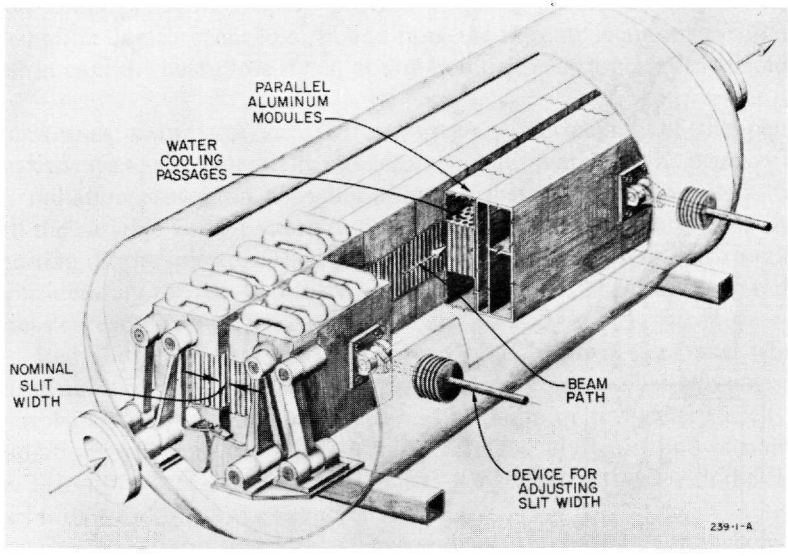

Figure 5-24
High-power energy-defining slit located in beam switchyard.

cranes, service cars, and ancillary equipment for the main beam transport devices in the lower level.

By use of a pulsed magnet system which deflects the electrons (or positrons) on a pulse-to-pulse basis into any of three large dc magnet transport systems, it is possible to carry out several experiments simultaneously in the research area using time-interlaced beams.

The unusually high-power ($\approx$1 MW in Stage I) carried by the incident beam has imposed very difficult problems in the design of the beam handling equipment. A typical example of a device capable of handling these large beam powers is the 16-ft long, adjustable, energy-defining aluminum slit shown in Fig. 5-24. Two in-line slits of the type shown, with the second rotated 90° about its axis with respect to the first, are used as an adjustable collimator at the beginning of the beam switchyard.

A small, digital, process control computer (SDS 925) is used in the control system of the beam switchyard. This computer reads data from punched cards and sends digital control information to regulators in the magnet power supplies where digital-to-analog converters generate analog reference voltages. Slits and collimators are adjusted in a similar way. When desired by the operator or experimenter, data representing the parameters of a particular beam are printed out from the computer memory for record, together with auxiliary information. About 100 signals from various sources are scanned every accelerator pulse (1/360 sec) and about 600 signals are scanned at a slower rate. The computer detects, identifies, and prints out the time and date of any changes in the interlock and status signals in proper sequence.

5-6 The research area

A layout of the research area is shown in Fig. 5-25. At this time it is divided into two general areas, one of which is centered around end station A. This end station is designed primarily for scattering and photoproduction experiments and thus the residual primary beam must be dumped outside of the building to keep background radiation acceptably low. During electron and positron scattering, the residual beam is absorbed in "beam dump east," which is located about 200 ft east of the end station. For photoproduction

Figure 5-25 Layout of the research area.

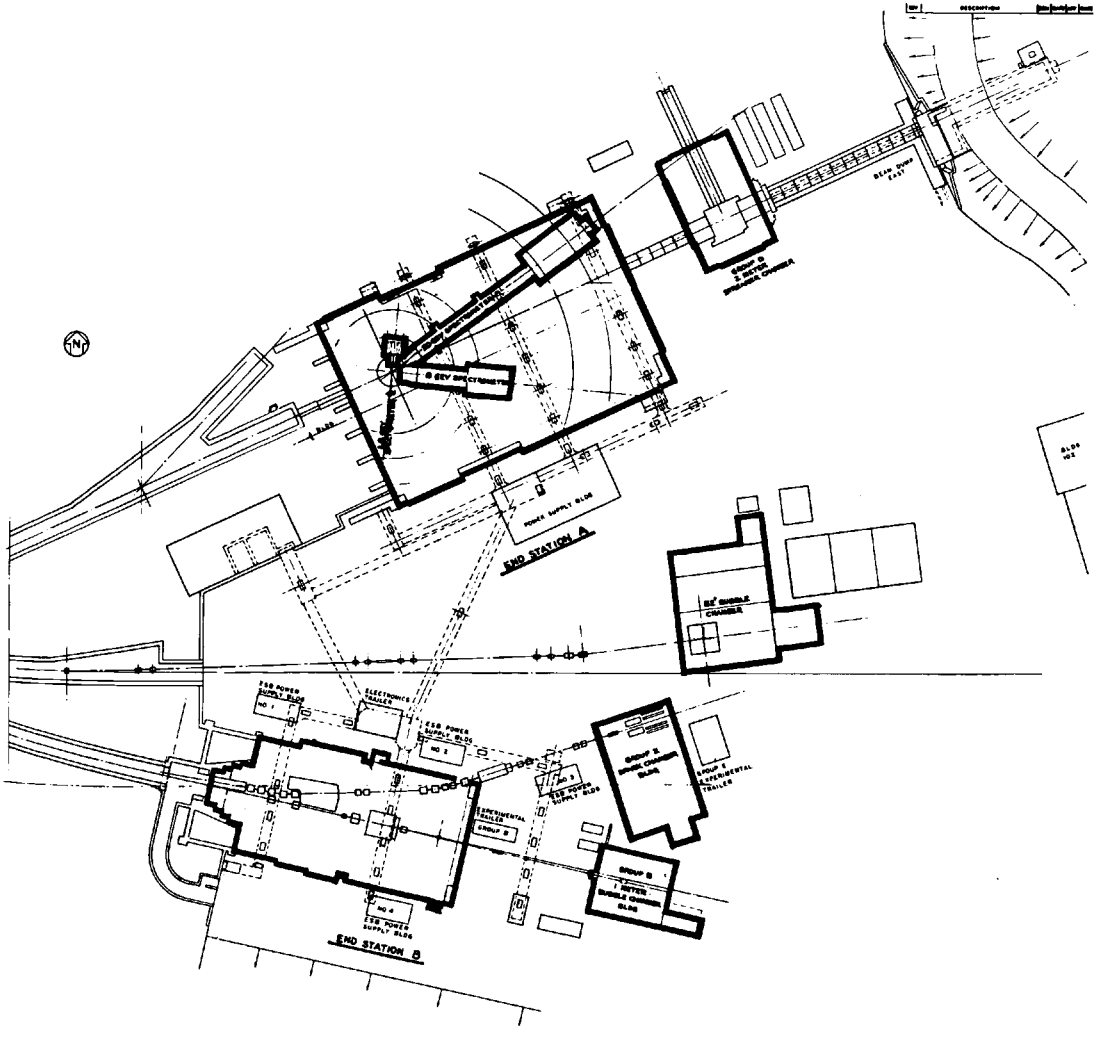

work, the primary beam creates photons in a thin target in the beam switchyard and is then deflected downward and absorbed in the "A-beam dump" located near the east end of the switchyard. This dump is isolated from end station A by thick steel shielding.

The "counting house," containing electronics equipment used in conjunction with End Station A experiments, is located in a shielded room adjacent to and immediately west of the end station at a level about 50 ft above the floor of the experimental hall. End Station A contains three spectrometers, rated at 20, 8, and 1.6 GeV/c, which are used to measure the angles and momenta of particles resulting from interactions of incident electrons or positrons with target nuclei. This area also includes (immediately east of end station A) a 2-meter streamer chamber for use in photoproduction experiments.

Large openings have been provided in the walls of end station A to permit extension of experimental equipment to the concrete pad exterior to the building if needed. When these openings are not in use they are covered with thick portable shielding blocks.

The second existing research area centers around end station B, where experiments concerned with the creation of secondary particles and determination of their characteristics are performed.

Because creation of secondary beams involves the impingement of a high-power primary beam on suitable targets, a separate well-shielded target room is provided between the beam switchyard and end station B. Ports for the passage of the secondary beam into end station B are provided in the shielding wall. As in the case of end station A, openings are provided in the outer walls of end station B to permit extension of experimental equipment to the concrete pad outside of the building, if desired. At the present time, three beams have been constructed in the end station B area: a muon beam, a neutral K beam, and a monochromatic gamma beam. Two major instruments used in these experiments are a 1-meter hydrogen bubble chamber and a spark chamber with its associated 54-in. magnet.

Both end stations A and B are provided with heavy duty cranes capable of handling equipment or shielding weighing up to 50 tons.

A third (central) experimental area includes an 82-in. hydrogen bubble chamber which has been moved from Lawrence Radiation Laboratory, Berkeley.

5-7 Initial operating results

Key dates

Perspective regarding the operating results obtained to date may be gained from an examination of the "key dates" given in Table 5-2.

An early plan called for construction of a prototype length of the machine (one or two sectors) to verify and test the mechanical, electrical, and

Table 5-2 Key dates

April 1957	Proposal for two-mile accelerator
September 1961	Authorization by Congress
April 1962	Contract with AEC
January 1965	1.5-GeV beam through two sectors
April 21, 1966	Beam to two-thirds point (Sector 20)
May 21, 1966	Beam through 30 sectors to beam switchyard
June 2, 1966	18.4-GeV beam in beam switchyard (tune-up dump)
September 16, 1966	Beam to A-beam dump in beam switchyard
September 20, 1966	Beam to research area A and beam dump east
November 1, 1966	Beam to research area B
December 20, 1966	Accelerated e^+ beam from positron source
January 10, 1967	20.16 GeV achieved
March 29, 1967	240 kW of average beam power into A-beam dump

instrumentation design features. This plan was not followed because of the associated high costs and difficulty of fitting this subproject into the design and production schedules. Instead of building separate prototype sectors, the completion of the first two sectors (666 ft) of the accelerator was pushed ahead of the rest. By January 1965 it was possible to accelerate a 1.5-GeV beam through these two sectors. As a result of these tests[2] a number of important but not fundamental changes were made in the remaining sectors. Sectors 1 and 2 were later modified to correspond to the other sectors in most respects.

It was decided after these first tests to move the beam-analyzing station originally located at the end of Sector 2 to a new location near the beginning of Sector 20. Recent operating experience has proved that this relocation was wise in that it has permitted testing up to two-thirds of the machine with a beam even when the beam switchyard is unavailable as a result of installation or maintenance activities.

The beam was first accelerated through all thirty sectors on May 21, 1966. A beam energy of approximately 10 GeV was obtained at that time. Less than 2 weeks later, on June 2, 1966, the energy was increased to 18.4 GeV by turning on more klystrons at somewhat higher levels and by better phasing of the available klystrons.

On September 20, 1966, a beam was run for the first time to Research Area A and to beam dump east (beyond end station A). The beam was first sent to end station B on November 1, 1966, and the experimental program on the B side started immediately after this date.

On December 20, 1966, positrons were first accelerated from the positron source at the one-third point in the accelerator housing to beam-analyzing station No. 2 at the two-thirds point.

The two most recent achievements shown in Table 5-2 are concerned with maximum energy and maximum beam power. On January 10, 1967, a beam

energy of 20.16 GeV was obtained with all but four of the klystrons participating. On this occasion, the klystrons were operated about 5% below their rated voltage level. On March 28, 1967, a beam having an average power of 240 kW was transmitted to the A-beam dump. The corresponding parameters were an energy of about 17 GeV, a peak current of 25 mA, 1.6 μsec beam pulse length, and a repetition rate of 360 pulses/sec.

Beam characteristics: energy, spectrum, loading, and power

The electron energy gained in the multisection accelerator of constant gradient design is given by

$$V = (1 - e^{-2\tau})^{1/2} \sum_n (P_n lr)^{1/2} - \frac{irNl}{2}\left(1 - \frac{2\tau e^{-2\tau}}{1 - e^{-2\tau}}\right)$$

where

N = number of independently fed sections
l = length of each section
P_n = input RF power to section n
r = shunt impedance per unit length
i = peak beam current
τ = RF attention per accelerator section in nepers

The first term in this equation is the "no-load" energy, i.e., the energy for negligible beam current. The second term accounts for the energy decrease caused by beam loading. Inserting the design parameters of the SLAC accelerator ($N = 960$, $l = 3.05$ meters, $r = 53$ megohms/meter, and $\tau = 0.57$ nepers) into the above equation and considering the fact that each klystron feeds its power equally into four accelerator sections and that some of the power (0.54 ± 0.1 dB) is dissipated in the waveguides connecting the klystrons to the accelerator, the result is

$$V_{\text{GeV}} = 0.020 \sum_n P^{1/2} - 0.035i$$

with P measured in megawatts and i in milliamperes. This equation is plotted in Fig. 5-26 for the case where the outputs of all klystrons are assumed to be the same and equal to 21 MW. In this case, the no-load energy is seen to be 22.0 GeV. The beam energy decreases from the no-load value at the rate of 35 MeV/mA (independent of input power levels). Also shown in the same figure is the average beam power obtained by multiplying the above energy equation by the peak beam current and then by the beam duty cycle. Theoretically, the power transferred to the beam is maximum when the peak current is such that the beam energy is reduced to one-half of the no-load value, i.e., in this case to 11 GeV. The peak current corresponding to maximum average beam power ($\approx$2.1 MW in this example) is equal to approximately 312 mA.

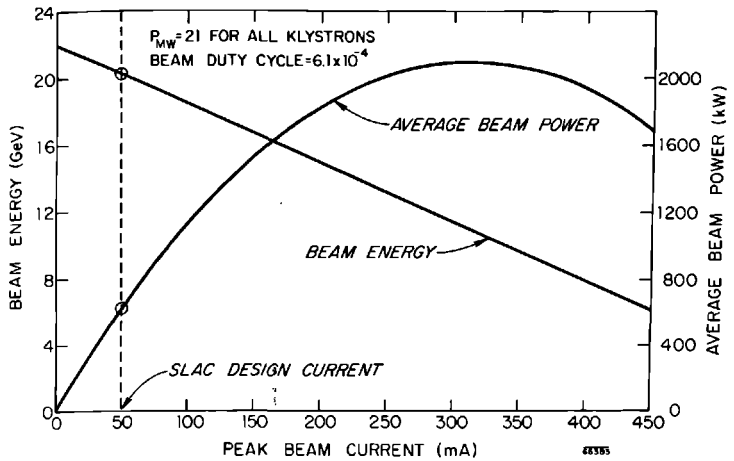

Figure 5-26 Beam energy and average beam power vs peak beam current for the SLAC accelerator.

The design current and the corresponding design energy and average beam power for the SLAC accelerator are 50 mA, 20 GeV, and 600 kW, respectively. These design values are indicated in Fig. 5-26. Design values of beam current and beam power were not initially achieved because of the onset of beam breakup phenomena as discussed in a later section. However, the coefficients in the energy design equation were verified within experimental accuracy (about 2%).

Typical energy spectra are shown in Fig. 5-27. The highest-energy spectrum resulted from relatively light beam loading ($i = 2.0$ mA). A large beam current ($i = 25$ mA) led to a beam having 0.80 GeV less energy. The low-energy spectrum is broader than the high-energy spectrum due to the presence of electrons in a high-energy tail. This tail is due to those electrons that

Figure 5-27 Energy spectra under different beam loading conditions.

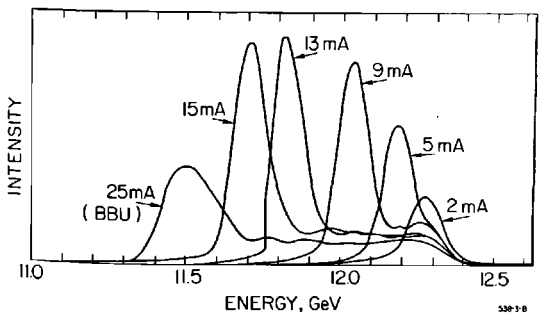

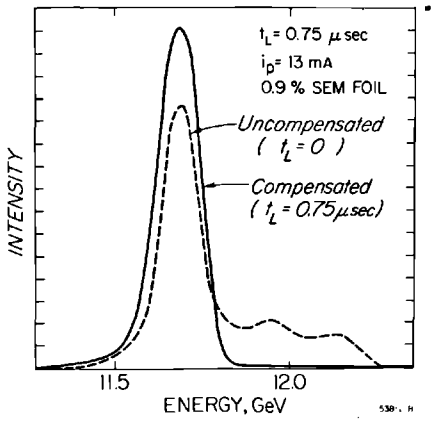

Figure 5-28 Compensation of spectrum broadening due to beam loading by trigger delay to one sector.

pass through the accelerator early in the beam pulse before the beam has extracted a significant amount of stored RF energy. Broadening of the spectrum in this manner is usually undesirable in physics applications of the beam. One useful method of compensating for this effect consists of delaying the time of triggering one or more of the accelerator sectors. When this is done, the first electrons during the pulse pass through the sector when it is not completely filled with RF energy and therefore gain less than the maximum energy potential. Later electrons encounter a situation where the sector is completely filled but some of the stored energy has been extracted by the pioneering electrons. By proper adjustment of the trigger delay to the sector, it is possible to achieve near equality in the energies of the earlier and later electrons. Compensation obtainable with this technique is indicated in Fig. 5-28 where the dotted curve represents the uncompensated spectrum and the full curve is the compensated spectrum achieved by trigger delay to one sector.

The spectrum width at half-maximum for the cases shown in Fig. 5-27 is approximately 1.3%, of which about 0.9% is attributable to resolution of the measurement devices. In more recent runs with careful adjustment of beam parameters, spectra with widths of $\approx$0.2% have been obtained.

Beam transmission

Careful measurements have shown that more than 90% of the beam current measured at beam-analyzing station No. 1, located at the 40-ft point, is preserved during passage through the entire machine. This favorable result arises from the effective performance of the beam position and intensity monitors, the steering and focusing systems, and the long ion chambers.

The microwave position monitors located in the drift space at the end of each sector are capable of indicating the transverse position of the beam within ± 0.5 mm.

Beam optics measurements at beam-analyzing station No. 1, located 40 ft from the injector, have shown that 80% of the injected beam is contained in a transverse phase space of 1.2×10^{-2} (MeV/c)(cm). A second measurement in the beam switchyard at the end of the accelerator indicates that the same fraction of the beam is contained in a transverse phase space of about 3×10^{-2}(MeV/c)(cm). Since the beam diameter at that point is roughly 0.4 cm, the angular divergence of the beam in the energy range of 10 to 20 GeV is less than 10^{-5} radian.

Tests to date have demonstrated the capability of accelerating at least three beams in a time-interlaced manner. Spectra of three low-energy interlaced beams measured at beam-analyzing station No. 2 in Sector 20 are shown in Fig. 5-29. Independent control of the energy, intensity, and pulse length of each beam is feasible. This capability permits the simultaneous performance of several independent experiments in physically separated areas. The trigger "pattern" for these beams is selected by the operator in the CCR and is sent to the appropriate destinations, namely the injector, the accelerator sectors, the beam switchyard pulsed magnets, and the experimental areas. The beam intensity presentation observed by the operator for two interlaced beams of energies 11 and 5.65 GeV is shown in Fig. 5-30. Two base line traces are shown. The height of each dot above the corresponding base line is proportional to the beam intensity at the end of a particular sector. These signals originate from toroid-type intensity monitors located in the drift space at the end of each sector. Similar displays are viewed by the operator to ascertain the vertical and horizontal beam position relative to the accelerator axis at the end of each sector. In this instance, all dots lie

Figure 5-29 Spectra of three time-interlaced beams.

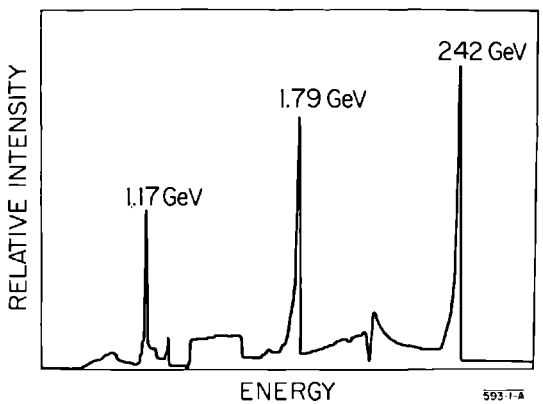

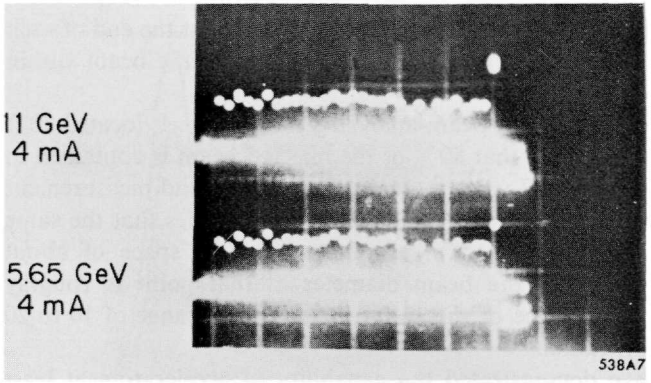

Figure 5-30 Beam intensity at end of each sector for two interlaced beams.

on the base line when the beam is perfectly centered. Displacement of a dot above or below the base line implies a right or left, or upward or downward displacement of the beam from the axis.

Beam breakup and remedial measures

Beam breakup phenomena originally limited the maximum peak current through the entire two-mile accelerator to approximately 20 mA at the maximum energy gradient. This was about 40% of the design current level. Higher currents can be accelerated to intermediate points along the accelerator. Furthermore, the maximum current transmitted to a given position along the accelerator can be increased by reducing the beam pulse length. Lower-energy gradients lead to reduced threshold current levels. In general, the product

$$\frac{it_p z}{\delta V/\delta z} \approx \text{constant}$$

where i is the peak beam current at which beam breakup occurs, t_p is the length of the beam pulse as limited by breakup, z is the distance from the injector to the closest position where current is lost at time t_p during the beam pulse, and $\delta V/\delta z$ is the average energy gradient in the accelerator.

While the current originally available was adequate for all initially scheduled experimental purposes, it was realized that some future experiments would probably require higher current. Therefore, means of increasing the beam breakup current threshold were incorporated in the accelerator.

The most significant improvement has resulted from strengthening the focusing along the accelerator. The original focusing system consisted of thirty quadrupole triplets, with one triplet being located in the drift section at the end of each 333-ft accelerator sector. In addition, thirteen special triplets were used for focusing positrons produced by the positron source at the

one-third point along the accelerator. Each triplet consisted of a collinear set of two A-type quadrupoles at the ends of the drift section and one B-type quadrupole in the center. The B quadrupoles are twice as long as the A quadrupoles and, thus, for a given current have twice the focusing strength. Originally, triplets were chosen rather than doublets because calculations showed that they would introduce less steering error in the presence of short-term misalignments due to thermal effects in the support structures. However, actual measurements with the completed accelerator showed that misalignment effects are so small that doublets can be used without difficulty. This permitted rearrangement of the quadrupoles as follows:

1. Removal of all of the longer (B) quads from Sectors 1 through 29 and from the special positron triplets.
2. Installation of doublets consisting of B-type quadrupoles in the drift sections of Sectors 10 through 29. Procurement of larger regulated power supplies capable of 15 A output for these doublets.
3. Installation of doublets consisting of A-type quadrupoles in the drift sections of Sectors 1 through 9, using standard power supplies (7 A maximum current).
4. Installation of the remaining A-type quadrupoles as singlets between 40-ft girders in the first six sectors, using standard power supplies.

With the quadrupole arrangement just described, it was possible to taper the quadrupole current linearly from Sectors 1 through 29 so as to obtain the same effective betatron wavelength for the electron orbits over the entire accelerator length. Previously, it had been possible to taper only up to 7 A quadrupole current. When the plan just discussed was completed it was possible to taper up to a normalized value of 30 A. These measures resulted in an increase of peak beam current to the value of 42 mA.

In addition to the straightforward or "brute-force" technique described above, other schemes for increasing the beam breakup thresholds are being studied. These include microwave filtering and injector noise reduction schemes. Work in these areas is still preliminary and no significant progress can yet be reported.

Klystron status and performance

Among the principal accelerator components, klystrons are being singled out for special review because of their significant role in accelerator performance and reliablity and their high cost. Because of these factors, the early decision was made to procure these tubes from several sources so that there would always be backstops against technical and production difficulties involving one or two vendors. In addition, SLAC itself chose to fabricate a reasonable number of the production tubes both for insurance purposes and also to afford a ready means of developing and testing improved models of klystrons.

Table 5-3 Klystron status as of July 27, 1967

Vendor	*Total contract*	*Accepted*	*Installed*
RCA	216	205	98
Sperry	80	80	3
Litton	144	114	90
SLAC	54	54	49
Litton[a]	6	6	3
Eimac[a]	6	5	2
Total	506	469	245

Note: 245 klystrons are required to fill all accelerator sockets.

[a] Special 6 tube contract.

A total of 245 klystrons is required to fill all the sockets along the accelerator. These tubes are rated at 21 MW peak and 21 kW average power output. Their design capability is somewhat higher than these ratings.

The status of klystron procurements and the SLAC in-house program as of July 1967 is given in Table 5-3. These procurements did not all start at the same time. Tubes from all sources are designed to be repairable. Thus, the total number of tubes being procured allows both for a quantity sufficient to fill the repair cycle and to provide a suitable reserve. SLAC has negotiated an extended warranty agreement with two of the vendors wherein, after initial purchase of a tube, SLAC pays in addition a fixed hourly rate for the first 1500 (or 2100) hours of operation of the tube and a decreased rate thereafter. Under this arrangement, the manufacturer agrees to replace a failed tube with a tube meeting original specifications at no additional acquisition cost to SLAC. The fixed hourly rate cycle described above then applies to the replacement tube.

Klystron operating experience through June 30, 1967 is summarized in Table 5-4. Tube operating hours are given by quarter and cumulatively. Also given are the number of failures and average life at failure on both a quarterly and a cumulative basis. In terms of the cumulative values, one klystron failure has occurred for each 7600 operating tube hours. This is, of course, not an accurate measure of tube life expectancy except after many generations. An attempt to predict mean life on the basis of the present meager experience is shown in Fig. 5-31, where age at failure for each tube has been plotted against the percentage of tubes which have failed. The horizontal scale is constructed so that a normal failure distribution will result in a straight line when life at failure is plotted as indicated above. The data plotted omit all failures of the tubes of one of the manufacturers since the failure rate for this company is about twelve times the average failure rate for the other two

Table 5-4 Klystron usage and failure

	Operating hours		*Quarter*		*Cumulative*	
Dates	*Quarter*	*Cumulative*	*No.*	*Avg. life at failure*	*No.*	*Avg. life at failure*
To 12/31/65	—	27,000	—	—	10	297
To 3/31/66	11,000	38,000	13	252	23	272
To 6/30/66	118,000	156,000	16	234	39	256
To 9/30/66	127,000	283,000	15	594	54	350
To 12/31/66	176,000	459,000	23	1070	76	575
To 3/31/67	228,000	687,000	28	1670	104	860
To 6/30/67	301,000	988,000	26	2166	130	1130

companies and SLAC. Where the line crosses the 50% failure coordinate, the corresponding mean time to failure may be read on the vertical scale. The predicted mean time to failure from this data is approximately 5700 hours. A better prediction of tube life must await more operating results.

SLAC has continued to do development work on klystrons during the construction and operating periods. Recently, an experimental SLAC klystron, when operated at a beam voltage of 300 kV, produced a peak power output of 42 MW with an efficiency of 45%. Although tubes having these improved characteristics are a long way from production, this result indicates that at some time in the future a significant increase in power output of production klystrons may be possible. Many questions relating to stability and life must, of course, first be resolved.

Figure 5-31
Klystron failure experience.

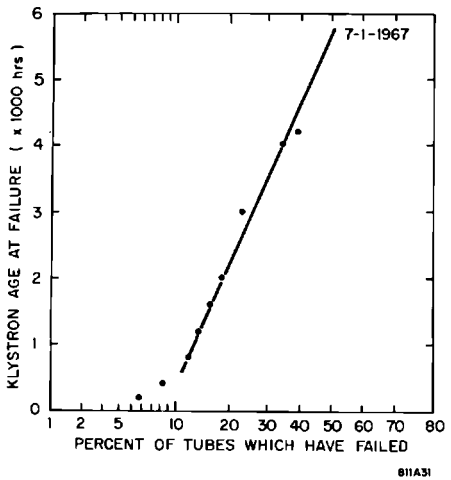

Operating statistics

Statistics for the first year of operation (FY 1967) are shown in Table 5-5 and Fig. 5-32a and b.

The total manned hours include not only operating shifts but also shifts during which the machine was shut down for scheduled maintenance, equipment modifications, and search activities. The total number of klystron hours is $\int N(t)\,dt$, where $N(t)$ is the number of klystrons in use at a given time t. Allowing about 5% reserve, approximately thirteen klystrons are needed at 1 mA beam current for each gigaelectron volt of beam energy. Thus, the number of klystron hours depends not only upon the total hours of operation but also upon the average beam energy. As noted in Table 5-5, a total of 833,413 klystron hours were run in FY 1967. This is an average of 3400 hours for each of the 245 klystron sockets on the accelerator.

The total productive beam hours given in Table 5-5 is the number of hours the accelerator was operated with one or more useful beams. Accelerator beam tuneup time and other nonproductive beam time has been excluded. The total experimental hours include actual beam hours and beam downtime requested by the experimenters. This total includes the sum of the operating times of simultaneous experiments.

Figure 5-32a shows how the total hours of manned shift time were divided during each month of the fiscal year. The accelerator was shut off for extensive installation and maintenance work during the weeks of October 23–29, December 25–31, January 1–7, February 5–11, and May 28–June 3 which explains some of the decreases in useful beam time. Figure 5-32b shows the percentage times devoted to the various activities on a quarterly basis. It is significant to note that the fraction of the manned shift time utilized for particle physics increased from 0 in the first quarter to 58.1% in the last quarter of FY 1967. During the same interval, the time devoted to machine

Table 5-5 Operating statistics for FY 1967

Manned hours	5,700
Klystron hours	833,413
Total productive beam hours	2,874
Low energy (<3 GeV)	709
Machine physics	698
Particle physics	11
High energy	2,165
Machine physics	493
Particle physics	1,672
Total experimental hours	3,466
Machine physics	1,342
Particle physics	2,124

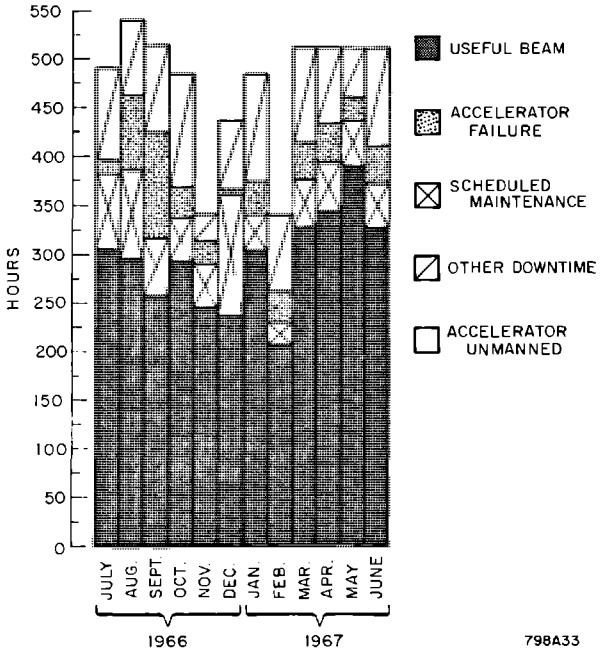

Figure 5-32a Operating statistics, hours per month.

Figure 5-32b Operating statistics, percentages per quarter.

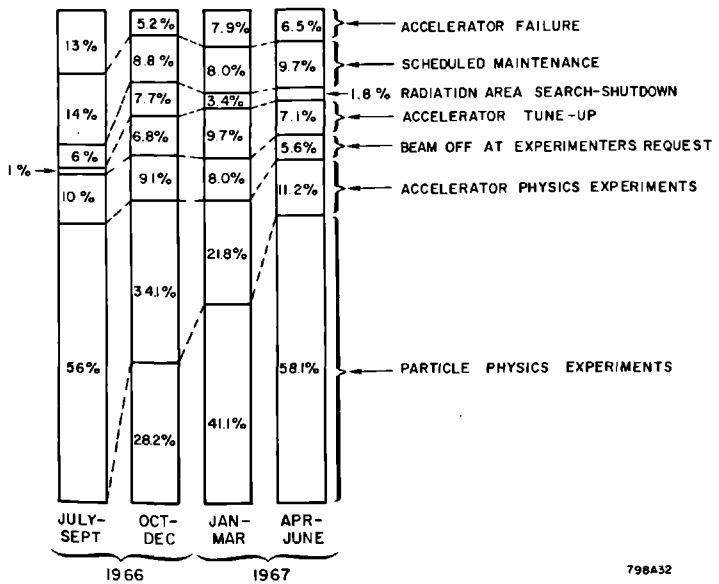

physics dropped from 56% in the first quarter to 11.2% during the final quarter. It can also be noted from Fig. 5-32b that the time consumed in other essential but unproductive activities decreased from 44 to 30.7% during the year. Steps are now being taken to reduce this unproductive time even further. It is also anticipated that the fractional time spent unproductively will decrease further as the number of operating shifts per week is increased. This improvement is expected because the productive beam time should be roughly proportional to the average number of operating shifts per week, whereas the times consumed in accomplishing several of the unproductive activities are essentially independent of the number of operating shifts.

References

1 "Proposal for a High-Energy Electron–Positron Colliding-Beam Storage Ring at the Stanford Linear Accelerator Center," Stanford Linear Accelerator Center, Stanford University, Stanford, California (revised September 1966).

2 "Consolidation of Results of Preliminary Beam Tests with Sectors 1 and 2," Rept. No. SLAC-50, Stanford Linear Accelerator Center, Stanford University, Stanford, California (September 1965).

6

DESIGN, FABRICATION, INSTALLATION, AND PERFORMANCE OF THE ACCELERATOR STRUCTURE

R. P. Borghi, A. L. Eldredge, R. H. Helm, A. V. Lisin, G. A. Loew, Editor and R. B. Neal

The purpose of this chapter is to describe the heart of the accelerator, the periodic waveguide structure which is used to accelerate the electrons. As discussed in Chapter 3, the design of the two-mile machine at SLAC is a logical extension of accelerator developments at Stanford University since 1947.[1,2] By the time the SLAC project was authorized in 1961, Stanford workers had reached a high degree of confidence and familiarity with the design and fabrication of disk-loaded waveguides. Although several other types of periodic structures were investigated as discussed later in this chapter, the disk-loaded waveguide was selected as the best overall structure meeting most design and fabrication criteria.

This chapter is divided into four parts. The first is concerned with a discussion of accelerator theory and selection of characteristic parameters. It is followed by a description of the empirical design used to achieve the selected parameters. The third part is a description of fabrication techniques, assembly, and installation. Finally, a summary of performance is given.

6-1 Theory and selection of characteristic parameters

Choice of operating frequency (RBN)

Because almost all the basic accelerator parameters have frequency dependence, it was first essential to compare the advantages and disadvantages of the various frequency bands and to choose an operating frequency. However, it was not possible to make the choice of frequency by purely analytical methods; the final selection required engineering judgment and reference to previous experience.

The laws of frequency dependence of the principal parameters involved in the design of a linac are listed in Table 6-1. To simplify the comparison, this table assumes direct scaling of the modular dimensions of the accelerating structure. For a specific accelerator some compromises must be made which modify Table 6-1 in certain details but do not alter its general implications.

The energy of electrons from a linear accelerator with negligible beam loading is given by

$$V = K(P_T L r_0)^{1/2} \tag{6-1}$$

where P_T is the total input RF power, L is the total length, r_0 is the shunt impedance per unit length, and K is a constant of which the value depends upon the net RF attenuation in each independently fed accelerator section.

Table 6-1 Frequency dependence of principal machine parameters

Parameter	*Frequency dependence*	*Frequency preference*		*Notes*
		High	*Low*	
Shunt impedance per unit length (r)	$f^{1/2}$	X		a
RF loss factor (Q)	$f^{-1/2}$		X	a
Filling time (t_F)	$f^{-3/2}$	X		a, b
Total RF peak power	$f^{-1/2}$	X		a, b, c
RF feed interval (l)	$f^{-3/2}$		X	a, b
No. of RF feeds	$f^{3/2}$		X	a, b, d
RF peak power per feed	f^{-2}	X		a, b, c
RF energy stored in accelerator	f^{-2}	X		a, b, c
Beam loading ($-dV/di$)	$f^{1/2}$		X	a, b, d
Peak beam current at maximum conversion efficiency	$f^{-1/2}$		X	a, b, c, f
Diameter of beam aperture	f^{-1}		X	a
Maximum RF power available from single source	f^{-2}		X	e
Maximum permissible electric field strength	$f^{1/2}$	X		g
Relative frequency and dimensional tolerances	$f^{1/2}$	X		a, b
Absolute wavelength and dimensional tolerances	$f^{-1/2}$		X	a, b
Power dissipation capability of accelerator structure	f^{-1}		X	a, b, d

Notes:
a. For direct scaling of modular dimensions of accelerator structure.
b. For same RF attenuation in accelerator section between feeds.
c. For fixed electron energy and total length.
d. For fixed total length.
e. When limited by cathode emission.
f. When limited by beam loading.
g. Approximate; empirical.

Since r_0 varies as $f^{1/2}$, the RF power required to produce a given final energy in a fixed length is proportional to $f^{-1/2}$. Thus, considerations of power economy indicated that the operating frequency should be as high as possible. Other advantages of the higher frequencies are the reduced filling time, which varies as $f^{-3/2}$, and reduced energy storage, which varies as f^{-2}. A shorter filling time is advantageous since electrons can be accelerated during a larger fraction of the available RF pulse length. The use of the higher frequencies also results in greater maximum field strength (as limited by breakdown) and larger relative frequency and dimensional tolerances.

From Table 6-1 it can be seen that the maximum frequency which can be used is limited by the diameter of the aperture available for the beam and by the reduced, beam current capability. Another factor against the use of very high frequencies is the increased number of power sources and feeds required. The increased cost of additional RF systems, modulators, and controls, and the increased operational difficulties which are encountered tend to offset the advantages arising from decreased power consumption at high frequencies.

An important consideration not taken into account in Table 6-1 was the degree of conservatism involved in the choice of frequency band. Although linear electron accelerators had been constructed and operated at L-, S-, and X-bands, the largest amount of experience was available at S-band. In fact, to this date all accelerators of this type having energies above 100 MeV have operated at S-band.

To illustrate the scaling laws given in Table 6-1 more specifically, design data for a 20-GeV accelerator 10,000 ft long are given in Table 6-2. Three cases are tabulated corresponding to operating at L-, S-, and X-bands. The specific values in Table 6-2 were based on relations and criteria which are developed later in this section. While each item in Table 6-2 need not be discussed individually, it may be worthwhile to emphasize the following points:

1. An important aspect of the design of the two-mile accelerator was the possibility of increasing the beam energy at some future date from its present maximum of 20 GeV to a higher level between 20 and 40 GeV. For reasons of economy and to avoid prolonged machine shutdown, it appeared desirable to make such an energy expansion possible by increasing the RF power rather than the accelerator length. According to Table 6-2, the L-band structure with a fixed length of 10,000 ft could not be expanded above about 38.4 GeV without experiencing breakdown difficulties.
2. The average RF power requirements were in the ratio 4.1/1.0/0.4 for the L-, S-, and X-band machines, respectively.
3. The maximum peak beam currents and beam powers were in the ratios of 1.7/1.0/0.6 for the L-, S-, and X-band machines, respectively.
4. The aperture available for the beam in the X-band machine (0.255 in.) would have been small enough to cause great concern about beam transmission and accelerator alignment.

Table 6-2 Design parameters of 20-GeV accelerator at three frequencies[a]

Parameter	*Frequency* (*L-Band*) *1000 MHz*	(*S-Band*) *3000 MHz*	(*X-Band*) *9000 MHz*
Shunt impedance r (megohms/meter)	31	53	92
RF loss factor (Q)	2.25×10^4	1.3×10^4	0.75×10^4
Filling time t_F (μsec)	4.31	0.83	0.16
Total RF peak power (MW)	9216	5320	3072
RF feed interval (ft)	52	10	1.92
No. of RF feeds	185	960	4988
RF peak power (MW) per feed	50	5.54	0.62
RF energy (J) stored in accelerator	21,348	2372	264
RF energy (J) required for 1.67-μsec electron beam pulse length	55,112	13,300	5,620
Total average RF power (MW) at 360 pulses/sec	19.84	4.80	2.04
Beam loading ($-dV/di$) (GeV/A)	20.5	35.5	61.5
Peak beam current (mA) at maximum conversion efficiency	544.2	314.2	181.4
Minimum diameter (in.) of beam aperture	2.292	0.764	0.255
Maximum RF peak power (MW) from single source[b]	216	24	2.7
Maximum permissible electric field strength[c] (kV/cm)	133	230	398
Maximum expanded beam energy[d] (GeV)	38.4	66.5	115.0
Relative frequency and dimensional tolerances[e]	1.11×10^{-5}	1.93×10^{-5}	3.34×10^{-5}
Absolute frequency and dimensional tolerances[e]	11 kHz 0.11 mils	58 kHz 0.06 mils	301 kHz 0.04 mils
Average power dissipated per unit area of accelerator surface[f] (W/cm^2)	0.59	0.43	0.53
Average temperature difference (°C) across accelerator wall[g]	0.42	0.10	0.04

[a] Assumptions: $2\pi/3$ mode in constant-gradient structure; $\tau = 0.57$ Np (RF attenuation); $L = 10{,}000$ ft (94.8% effective); 10% power loss in waveguides; 10% beam loading; direct scaling of modular dimensions.

[b] Based on 24 MW available at S-band, values for other frequencies based on scaling as f^{-2}.

[c] Based on maximum gradient obtained to date at S-band; values for other frequencies based on scaling as $f^{1/2}$.

[d] As limited by maximum permissible field strength.

[e] For 1% loss in beam energy.

[f] Based on 360 pulses/sec and 1.6-μsec electron beam pulse length.

[g] Based on copper wall 3, 1, and $\frac{1}{4}$ cm thick at L-, S-, and X-bands, respectively.

5. The X-band accelerator ranked highest in terms of maximum expanded energy capability, but the higher energies required X-band sources of higher peak power than were available. For example, operation at 40 GeV would have required 4988 sources each producing 2.5 MW of peak RF power.
6. Expansion of the L-band accelerator to 40 GeV would have required that each of the 185 feed points be supplied with 200 MW of peak power. Such power would have been much higher than the power output obtainable from a single L-band source and would have required parallel operation of several sources at each feed.
7. Expansion of the S-band machine to 40 GeV would have required 22.2 MW at each of the 960 feed points. Power outputs above this level had already been obtained quite easily from single S-band sources.
8. The *relative* frequency and dimensional tolerances favored the use of the higher frequencies. Relative dimensional tolerances are probably more significant than absolute tolerances, since the former are a better measure of the difficulties involved in critical machining operations.
9. The average power dissipated per unit area of accelerator surface was not significantly different in the three designs because the increased wall area at low frequency tended to compensate for the higher power required and vice versa. However, the average temperature difference across the accelerator wall, which is a measure of the degree of detuning of the structure, was highest at L-band and lowest at X-band.

It would have been possible to compare accelerator designs at the various frequencies in further detail. The designs that were chosen for illustrative purposes were based upon direct scaling of the modular dimensions of existing S-band accelerator structures. An improved design at a particular frequency from the standpoint of overall economy or performance may have been obtained by deviating from the scaling laws that were used. For example, the L-band design might have been improved by decreasing the feed interval and using a larger number of sources, and by increasing the RF and beam pulse lengths while decreasing the pulse repetition rate. However, this would not have affected the total peak power requirement or the maximum, field strength capability. Similar alterations might have been made at S- and X-bands to improve certain characteristics of these designs. However, such changes would not have modified appreciably the general conclusion that was reached, namely that S-band was the optimum choice for the two-mile accelerator for reasons implicit in the scaling laws of Table 6-1 and the illustrative examples of Table 6-2.

Product of RF power and accelerator length (RBN)

The energy of electrons from a linear accelerator with negligible beam loading was given by Eq. (6-1). To estimate the power-length product of the two-mile accelerator, the values of two important parameters discussed later in this

chapter are anticipated: the shunt impedance r_0 is assumed to be 53 megohms/meter and $K = 0.82$. The objective was an accelerator capable of producing electrons with an energy of 20 GeV under conditions of 10% beam loading. The no-load energy, therefore, had to be 22.22 GeV. To obtain a realistic estimate, 10% of the RF power was assumed to be dissipated in the RF transmission lines between the power sources and the accelerator, and 5.2% of the accelerator length was assumed to be used for auxiliary in-line devices not contributing to the acceleration process.

Substituting the above assumptions into Eq. (6-1), the required product of total RF power and accelerator length was

$$P_{OT}L = 16.12 \times 10^{14} \text{ W-cm}$$
$$= 5.30 \times 10^{7} \text{ MW-ft}$$

Selection of accelerator length (RBN)

Once the RF power–accelerator length product had been determined, these two quantities had to be chosen individually. The following factors influenced these selections:

MAXIMUM ELECTRIC GRADIENT. As discussed earlier in this chapter, the design objective was a linear electron accelerator initially capable of producing a maximum energy of 20 GeV, with an ultimate capability of 40 GeV energy by addition of RF power without increase of accelerator length. This objective required that the length of the machine be chosen so as to permit the maximum ultimate gradient. The maximum average electric gradient obtained in an operating, S-band, linear accelerator at the time the accelerator was being conceived was approximately 4.5 MeV/ft. Using this figure, a length of approximately 10,000 ft was required to satisfy the ultimate energy objective.

ECONOMIC CONSIDERATIONS. The total cost of an accelerator may be divided into three parts: (a) costs (C_P) which are proportional to the total connected RF power; (b) costs (C_L) which are proportional to the total accelerator length; and (c) fixed costs (C_F) which include research costs and administrative costs, among others.

To be meaningful, these costs had to be based on a time period that included the construction time plus a period judged to represent the useful life of the machine. A period of 10 yr of useful life was used in cost studies. From the fact that RF power and accelerator length have equal weight in the equation for electron energy, it is easy to show that the greatest overall economy results when $C_P = C_L$. Otherwise, the total cost is given by

$$C = \frac{1}{2}\left[\left(\frac{C_P}{C_L}\right)^{1/2} + \left(\frac{C_L}{C_P}\right)^{1/2}\right] C_{(P,L)_{\min}} + C_F \qquad (6\text{-}2)$$

where $C_{(P,L)_{\min}}$ is the minimum value of $C_P + C_L$ (i.e., where $C_P = C_L$).

These cost studies showed that an accelerator length of 10,000 ft was very close to the optimum value to minimize the total project costs over the initially projected 6-yr construction period and a 10-yr period of operation.

LAND AVAILABLITY. There were several potential sites available on Stanford land which seemed suitable for the accelerator project location. An accelerator length of 10,000 ft (plus another 2500 ft, approximately, for research facilities) was possible at most of these sites, but no greater length was available without high land acquisition costs.

Thus the choice of an accelerator length of 10,000 ft satisfied the several conditions discussed above: namely, it permitted operation at the ultimate, expanded energy gradient; it was near optimum from the standpoint of overall economy; and such space was available on Stanford property. Using the power-length product determined in an earlier section led to an initial total connected RF power requirement of

$$P_{OT} = 5.32 \times 10^3 \text{ MW}$$

It should be emphasized that this value of P_{OT} was based upon a particular choice of operating mode ($2\pi/3$) and a particular attenuation parameter ($\tau = 0.57$). Their selection is discussed later in this section. The value of P_{OT} would vary slightly if another mode or another value of τ had been used.

Selection of number of RF power sources and feed interval (RBN)

It was established in the previous section that a total RF peak power of 5320 MW had to be supplied by the power sources in order to achieve an electron energy of 20 GeV with 10% beam loading in a 10,000-ft accelerator. The next logical design decisions were the determination of the number of individual RF power sources and the spacing of the RF feeds along the accelerator length.

In general, it is more economical to obtain a large amount of microwave energy from a small number of high-power sources than from a large number of low-power sources. The basic reason for this fact is that the cost of a power source depends more strongly on the number and kind of operations involved in its fabrication and processing than upon its physical size and output rating. The cost of employment of the power sources in the accelerator system in terms of auxiliary equipment, such as instrumentation, controls, and waveguide equipment, also decreases as the total number of individual sources is reduced. Based upon laboratory and commercial experience with high-power klystron amplifiers, it seemed reasonable to expect that S-band tubes could be constructed to have an average life of 2000 hours or more while producing 24 MW of peak RF power and 22 kW of average RF power. Much higher, peak power levels from single S-band tubes did not appear to be readily obtainable at the time. An electron beam energy of 20 GeV could be obtained by requiring 24 MW of peak output per klystron. For a total RF power of

5320 MW, 240 klystrons producing 24 MW each were needed. For operation at the Stage II level of 40 GeV, 960 tubes producing 24 MW each would be required.

The selection of the feed spacing along the accelerator length will now be discussed. The limiting cases of feed spacing were (a) a single feed for the entire accelerator, and (b) individual feeds for each of the approximately 80,000 individual accelerator cavities. The first extreme was obviously unfeasible because the full RF power could not be transmitted through the accelerator structure. The second extreme would have been prohibitively expensive because of the multiplicity of waveguides and other microwave components and the necessary controls and instrumentation. As described in a later section, there is an optimum, or at least a preferred value, of the net RF attenuation between feed points. The choice of attenuation parameter is a compromise among many factors. The attenuation parameter can be adjusted to the desired value by properly choosing the diameter of the aperture in the disk-loaded structure and the length of the accelerator section—increasing the aperture size increases the group velocity and decreases the attenuation per unit length. Thus a given attenuation parameter can be obtained by either a short accelerator section of high unit attenuation (small aperture), or by a long section of low unit attenuation (large aperture), or by a compromise involving medium length and medium aperture. The main factor in favor of close feed-spacing is that the shunt impedance r_0 of the accelerator structure improves slowly as the group velocity is decreased. This is shown in Fig. 6-1 which applies specifically to the $2\pi/3$ mode, but the same general behavior is true for other modes.

Figure 6-1 Variation of v_g/c and r_0 as a function of cavity number along a 10-ft constant-gradient section.

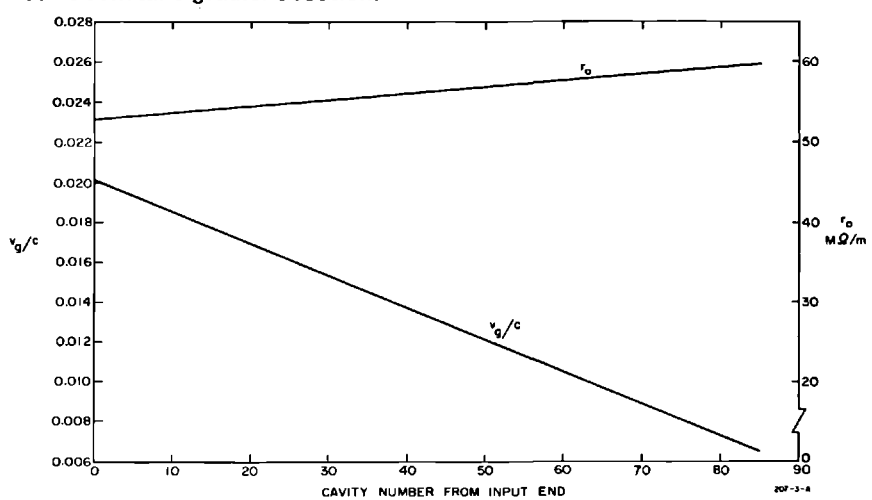

Several considerations limit how closely the feeds should be spaced. These limiting considerations are as follows:

1. Increased costs because of the larger number of components, controls, waveguides, couplers, RF loads, instruments, etc.
2. The complexity of splitting the RF power from each source many times.
3. The decreased aperture available for the electron beam as the group velocity is decreased.
4. Increased operational difficulties because of the increased number of phasing adjustments, monitors, interlocks, etc.

On the basis of these considerations, it was decided that in Stage I, 240 RF power sources supplying 6–24 MW each were to be used, as noted above, and that these sources were to be located at 40-ft intervals along the accelerator length. In Stage II (40 GeV maximum), with 960 RF sources each supplying 6–24 MW, it would not be safe (for reasons of RF breakdown) to feed the combined power outputs of two or more tubes into an accelerator section. Therefore, at least one feed every 40 ft was required in Stage I and at least one feed every 10 ft in Stage II. However, because the shunt impedance would have been reduced by about 15% in going from a 10 to a 40-ft interval, a feed interval of 10 ft was chosen for the two-mile accelerator. This meant that during Stage I operation, with 240 RF power sources, the power output from each klystron had to be divided four ways so as to supply four successive accelerator feeds. The modular arrangement of klystrons, waveguides, and accelerator sections in Stage I was shown in Fig. 5-17. With this arrangement, the number of klystrons could readily be increased to 480, a configuration sometimes called Stage "one and one-half." However, to convert to Stage II operation with 960 RF sources, it will be necessary to double the number of connecting waveguides shown in Fig. 5-17.

Choice of RF pulse length and repetition rate (RBN)

For physics research purposes, it is generally desirable to have the electron beam duty cycle (which is defined as the product of pulse repetition rate and beam pulse length) as high as possible. In fact, as this book is being written, there is a strong incentive toward developing superconducting linacs for which the duty cycle could be as high as 1. In a conventional pulsed linac, the practical upper limit of duty cycle is determined by economic considerations. The RF duty cycle must be greater than the beam duty cycle because a certain time is required to fill the accelerator with RF energy prior to injection of the beam. For the case where the electron beam is injected at a time after the start of the RF pulse equal to one filling time, the ratio of beam-to-RF duty cycles is given by

$$\frac{D_b}{D_{\mathrm{RF}}} = 1 - \frac{t_F}{t_{\mathrm{RF}}} \tag{6-3}$$

where t_F is the accelerator filling time and t_{RF} is the RF pulse length. For example, with $t_F = 0.83$ μsec (the value for $\tau = 0.57$ with the $2\pi/3$ mode) and $t_{RF} = 2.5$ μsec, the maximum duty cycle ratio as given by Eq. (6-3) is 0.67. This may be compared with the value of 0.5 for the original 1-GeV, Stanford Mark III Accelerator. An important point to emphasize is that a given fractional change in RF duty cycle, because of increasing RF pulse length, permits an even larger fractional increase in the beam duty cycle. Thus, increasing the RF pulse length from 2.0 to 2.5 μsec, an increase of 25%, allows a 43% increase in the beam duty cycle (for $t_F = 0.83$ μsec). The factors that place a practical limit on the maximum RF pulse length are the increasing costs of modulator components, such as the pulse transformers and the pulse-forming networks. On the basis of these considerations, the value of 2.5 μsec for the RF pulse length was adopted.

The maximum value of the pulse repetition rate in a linac is governed by three primary factors: (a) The initial cost of power components increases with increasing pulse repetition rate because of their higher average power ratings. (b) It is more difficult and expensive to design and construct high-power modulators at the higher repetition rates. (c) The ac power operational costs for the accelerator power sources increase almost directly with pulse repetition rate.

A maximum repetition rate of 360 pulses/sec was adopted for the two-mile accelerator, in contrast with the maximum rate of 60 pulses/sec for the Stanford Mark III Accelerator. The above combination of higher repetition rate, longer RF pulse length, and shorter filling time yielded a maximum beam duty cycle of about 0.0006, or about ten times greater than that of the Mark III Accelerator.

Selection of operating mode (RBN)

The accelerator structure is a disk-loaded cylindrical waveguide of the form shown in Figs. 5-12 and 5-13, and in Fig. 6-2a, of this chapter.(The alternative configurations in Fig. 6-2c are discussed below.) The efficiency of the structure as an accelerator of electrons is measured by a quantity called the shunt impedance per unit length. This quantity, which has already been introduced earlier and has been designated by the symbol r_0, is defined as the square of the energy gained (in electron volts) by an electron per unit length of accelerator structure for unit RF power dissipation in this same length. Gain in particle energy is used to emphasize that it is not simply the magnitude of the electric field in the accelerator structure which determines the electron energy gain per unit length; rather, it is the amplitude of the Fourier component of the axial field which travels at the electron velocity. The fundamental component is used in most linacs.

The exact value of shunt impedance for a particular configuration of accelerator structure cannot be represented in simple form but can be measured to good accuracy by microwave techniques. An approximate equation

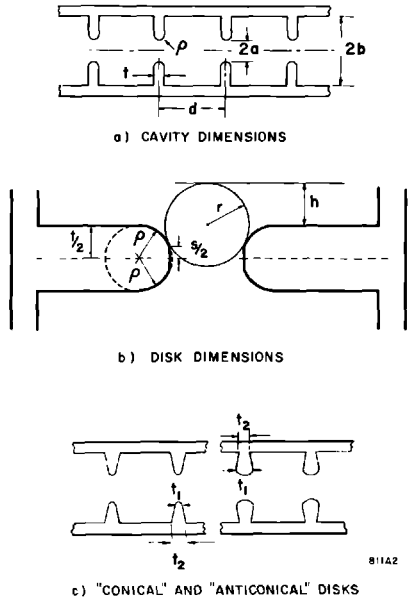

Figure 6-2 Illustration of basic modular dimensions in disk-loaded waveguide structures.

for r_0 which is suitable for studying the effects of varying the cavity dimensions is

$$r_0 = 968\left(\frac{\beta_w}{\delta}\right)\frac{(1-\eta)^2}{n + 2.61\beta_w(1-\eta)}\left(\frac{\sin D/2}{D/2}\right)^2 \tag{6-4}$$

where

β_w is the phase velocity in the structure divided by c,
δ is the skin depth,
t is the disk thickness,
d is the period of the structure,
η is the fraction of the length of the structure which is occupied by disks, i.e., $\eta = t/d = tn/\lambda$
λ is the guide wavelength,
n is λ/d, the number of disks per wavelength, and
D is the transit angle in radians of an electron passing through the cavity gap, i.e., $D = (2\pi/\lambda)(d - t)$

Equation (6-4) can be derived by considering an array of simple "pillbox" cavities. This equation gives too high a value of r_0 for two reasons: (a) the conductivity of the copper walls is never as high as the idealized value used in calculating the numerical constant (968) in the equation; (b) no account

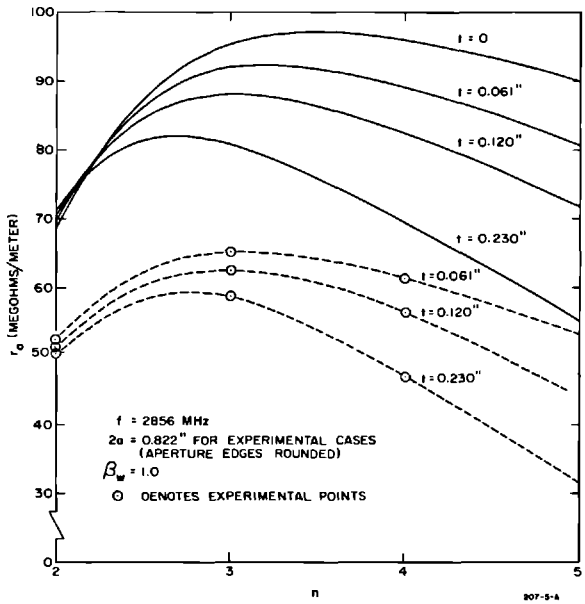

Figure 6-3 Theoretical and experimental curves of shunt impedance (r_0) per unit length versus number of disks per wavelength (n) for various disk thicknesses (t)

is taken of the effect of the disk apertures. Nevertheless, the relative variation of r_0 with the spacing and thickness of the disks given by Eq. (6-4) was confirmed by experimental measurements.

A graph of r_0 versus n for $f = 2856$ MHz based on Eq. (6-4) is shown in Fig. 6-3 for four values of disk thickness, t. Corresponding experimental values obtained from test cavity measurements are also shown. From Fig. 6-3 it is possible to draw some general conclusions. For negligible disk thickness ($t \approx 0$), the optimum number of disks per wavelength is approximately 3.5. As the disk thickness is increased, the optimum value of n decreases. The best value at $t = 0.120$ in. is about $n = 3$. It is about 2.7 for $t = 0.230$ in., which is the chosen disk thickness. The value $n = 3$, corresponding to a phase shift of $2\pi/3$ radians per cavity, was adopted. In addition to the improvement in shunt impedance, the selection of the $2\pi/3$ mode resulted in fewer disks and improved vacuum conductance compared to the $\pi/2$ mode used with the earlier Stanford structures.

The basis for the results described above may be found upon further examination of Eq. (6-4). There are three competing factors: (a) The shunt impedance of the individual cavities is improved by increasing the disk spacing. (b) The fraction of the length available for accelerating fields to act on the electrons is increased as the number of disks per wavelength is

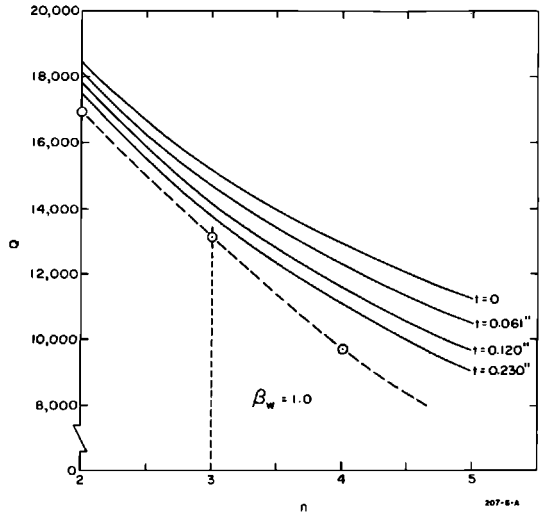

Figure 6-4 Theoretical and experimental curves of Q versus number of disks per wavelength (n) for various disk thicknesses (t).

decreased or as the disk thickness is decreased. (c) As the disk spacing is decreased, the electron transit time is decreased correspondingly, and the average or "effective" field strength acting on the electron is increased as (sin D/2)/(D/2). Thus, considerations (a) and (b) favor small n and small t, whereas consideration (c) favors large n and large t. As t increases, the fractional space occupied by the disks increases so that r_0 peaks at a lower value of n.

An expression similar to Eq. (6-4) may be given for the unloaded quality factor, Q, of an accelerator structure:

$$\frac{Q\delta}{\lambda_0} = \frac{\beta_w(1-\eta)}{n + 2.61\beta_w(1-\eta)} \tag{6-5}$$

where the symbols have the same meaning as given for Eq. (6-4). A plot of Q versus n is given in Fig. 6-4. Some measured values of Q are also shown in the same figure.

The quantity Q was measured in each case by taking two cavity lengths in the ratio of 2:1 in order to cancel out the effect of the end-wall losses as shown in a later section of this chapter. The values of Q are seen to decrease from around 17,000 at $n = 2$ to about 13,000 at $n = 3$ and 10,000 at $n = 4$.

A number of experimental curves for $n = 2$, 3, and 4 are given in Figs. 6-5 and 6-6. The data for these curves were based on disks with unrounded or "square" boundaries. For a given aperture diameter, rounding of the boundary has the effect of increasing the group velocity and decreasing the shunt impedance by about 5 to 10%.

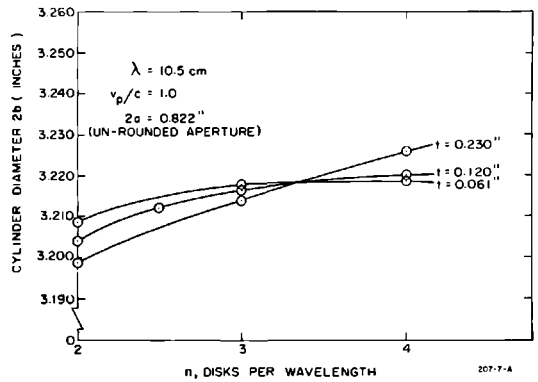

Figure 6-5 Cylinder diameter of disk-loaded waveguide as a function of number of disks per wavelength.

Another observation, which is illustrated in Fig. 6-6, is that the group velocity decreases with increasing disk thickness at a given value of n (except $n = 2$). This indicates that it may be quite misleading to compare the various cases on the basis of the same aperture diameter ($2a$). A better comparison might be made on the basis of the same value of group velocity, which would thereby insure that the filling times for an accelerator section of fixed length were equal in all cases. Alternatively, the comparison might be made on the basis of equal values of the product $v_g Q$, which would give equal values of RF attenuation per unit length in all cases. Adjusting $2a$ to give equal values of v_g would reduce r_0 more severely in the thick disk cases and would thus favor the adoption of thin disks. The limiting factors in reducing disk thickness were the increasing danger of arcing at the disk aperture boundary and the decreasing mechanical strength.

Figure 6-6 Normalized group velocity of disk-loaded waveguide as a function of number of disks per wavelength.

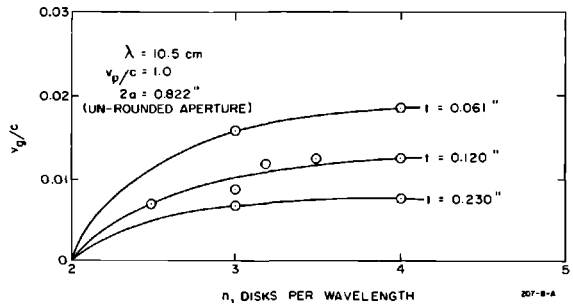

Constant-impedance vs constant-gradient structures (RBN)

When an accelerator of uniform modular dimensions ("constant-impedance" structure) is fed with RF power at one end, there is an exponential decay of power and electric field strength with axial distance from the input end. This means that the average axial electric field is less than the maximum axial field in the structure. On the other hand, it is possible to design a structure of nonuniform modular dimensions in which the axial fields will remain constant over the entire length. Such a structure is referred to as a "constant-gradient structure."

The ratio of maximum-to-average axial electric field strength is unity in the constant-gradient structure, whereas in the constant-impedance structure it is given by

$$\frac{E_0}{V_0/l} = \frac{\tau}{1 - e^{-\tau}} \tag{6-6}$$

where τ is the RF attenuation parameter which can be shown to be equal to $\omega t_F/2Q$. The parameter τ has often been called Il in the literature where I is the RF attenuation in nepers per unit length, and l is the length of the accelerator section. The dependence of τ upon filling time t_F emphasized the importance of comparing the constant-gradient and constant-impedance structures at the same value of τ for each. For equal τ, the two structures have the same filling time, the same stored energies, and the same ratios of input-to-output RF powers.[3] The ratios of maximum-to-average axial electric field strength are shown vs τ in Fig. 6-7. Thus it is clear that the constant-gradient structure

Figure 6-7 Ratios of maximum-to-average axial electric field strengths in constant-impedance and constant-gradient accelerator structures versus τ.

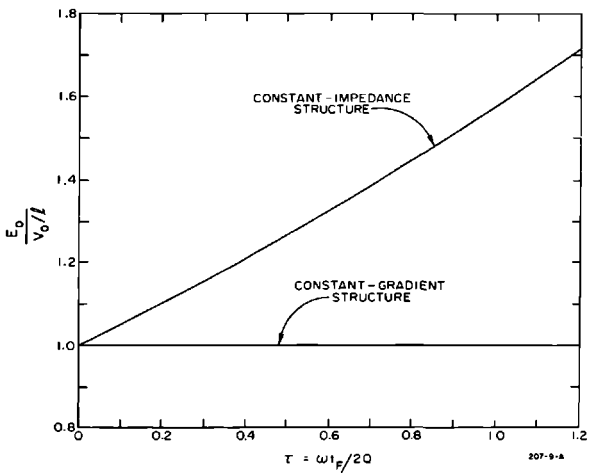

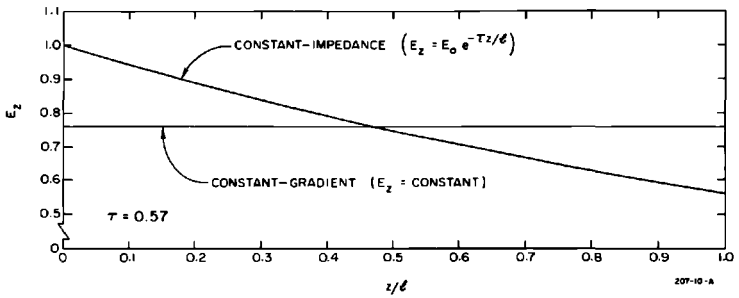

Figure 6-8 Axial field strength versus z/l for equal electron energy gain in constant-gradient and constant-impedance sections.

can produce higher electron energies than an optimized constant-impedance structure when both are operating at the breakdown limit of electric field strength. As indicated in Fig. 6-7, the relative advantage of the constant-gradient accelerator in achieving high gradients without breakdown depends upon the value of τ. Curves of field strength vs axial distance z for the two types of structures are shown in Fig. 6-8 for $\tau = 0.57$.

In addition to the advantage of the reduced ratio of maximum-to-average field strengths, the constant-gradient structure has several other advantages over the constant-impedance structure:

1. The power dissipated per unit length in the constant-gradient accelerator is constant over the entire length of the structure. In contrast, the ratio of power loss at the input end to that at the output end of a constant-impedance structure may be as high as 12.4 to 1. (This magnitude corresponds to a value of the RF attenuation constant $\tau = 1.26$ Np, which gives maximum no-load energy in the constant-impedance accelerator structure.) A plot of the power-loss ratios for the two structures is shown in Fig. 6-9.
2. The constant-gradient structure gives a slightly higher no-load beam energy than the constant-impedance structure and somewhat lower beam-loading derivative $(-dV/di)$. Thus, the constant-gradient structure has greater relative energy advantage in the loaded case than in the unloaded case. The no-load energies for the two structures are shown in Fig. 6-10 and the beam-loading derivatives in Fig. 6-11.
3. The constant-gradient structure has a higher maximum conversion efficiency (ratio of maximum electron beam power to input RF power) and a higher corresponding maximum peak beam current than the constant-impedance structure. Curves of the maximum conversion efficiency, η_{max}, and the corresponding maximum beam current, $i_{\eta_{max}}$, are shown in Fig. 6-12.
4. The constant-gradient accelerator is less frequency-sensitive than the constant-impedance accelerator, as shown in Fig. 6-13.

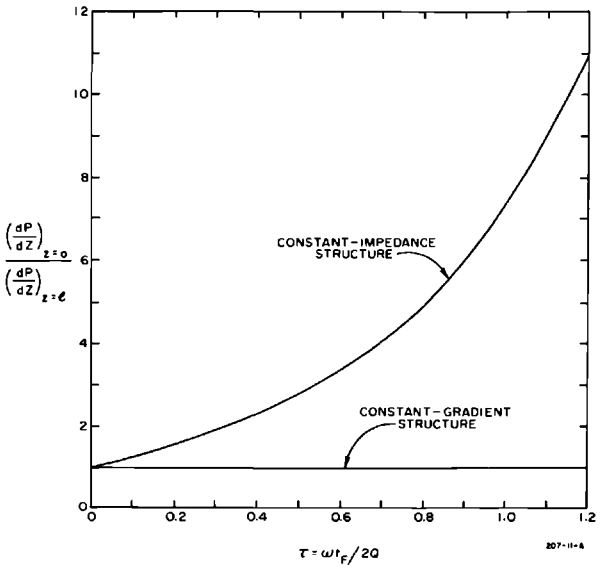

Figure 6-9 Ratio of power losses at input and output ends of accelerator section versus τ for constant-impedance and constant-gradient structures.

Figure 6-10 Unloaded beam energies versus τ for constant-impedance and constant-gradient accelerator structures.

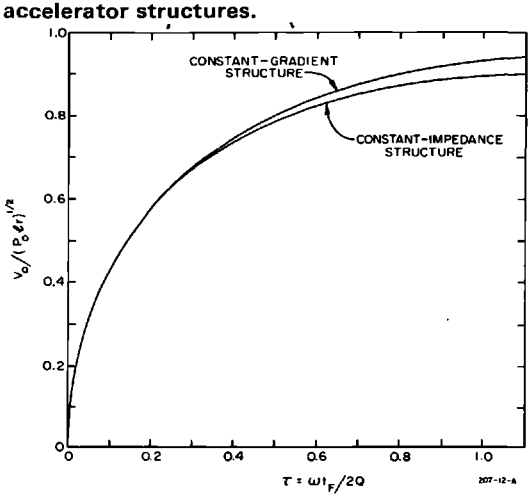

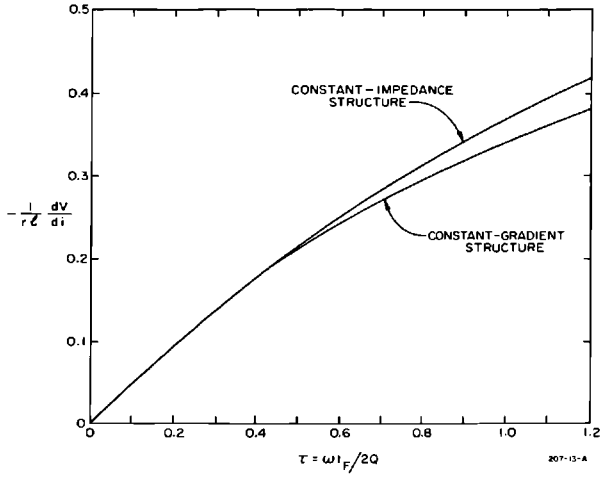

Figure 6-11 Beam loading derivatives versus τ for constant-impedance and constant-gradient accelerator structures.

Figure 6-12 Maximum beam conversion efficiencies and corresponding values of peak beam current versus τ for constant-impedance and constant-gradient accelerator structures.

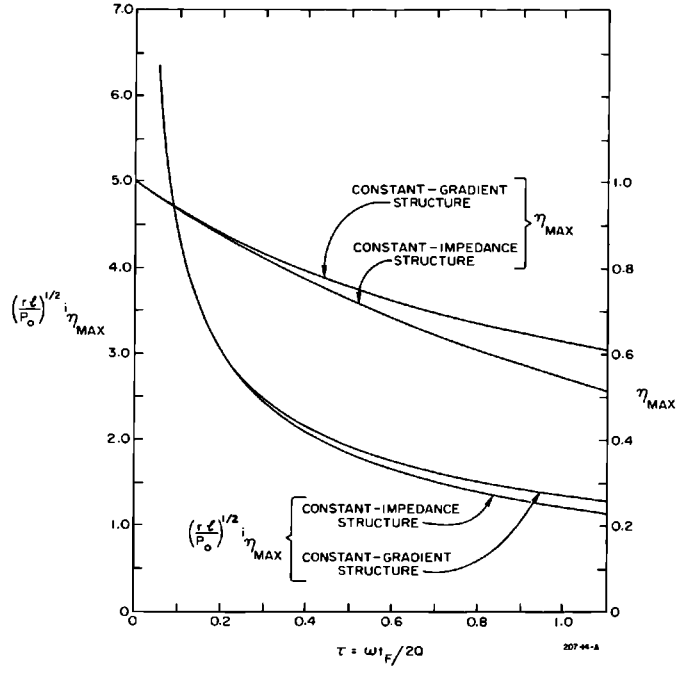

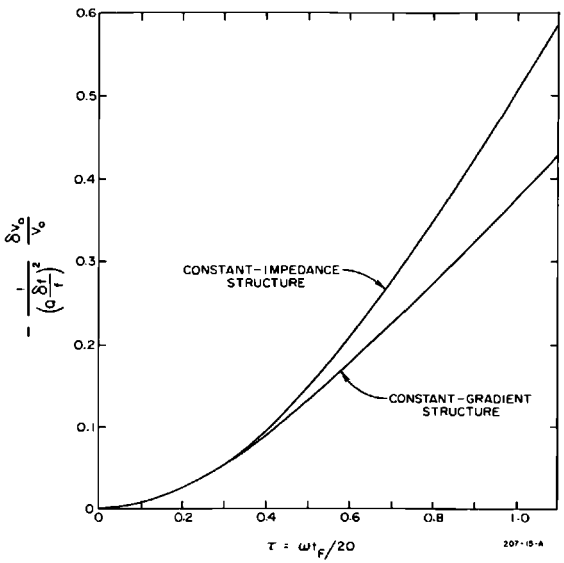

Figure 6-13 Frequency sensitivities versus τ for constant-impedance and constant-gradient accelerator structures.

The factors discussed above depend upon τ, as shown in Figs. 6-7 through 6-13. To illustrate these factors numerically, the characteristics of the two structures are shown in Table 6-3, based upon the parameters of the two-mile accelerator.

5. Amplitude and phase oscillations of the traveling wave caused by the band-pass filter characteristics of the structure may be slightly less pronounced in the constant-gradient than in the constant-impedance structure (see Fig. 6-14). This problem was first pointed out in Reference 4 and will be discussed in greater detail at the end of this section.
6. At the time the two-mile accelerator was being designed, the cumulative, multisection type of beam breakup described in detail in Chapter 7 was not known. On the other hand, experiments done at Stanford and elsewhere[5–8] had shown that the constant-gradient structure was relatively less troubled by the regenerative type of beam breakup than the constant-impedance structure. Various laboratories had reported beam breakup thresholds which were typically of the order of 300 mA with a 2-μsec pulse length for an S-band constant-impedance structure. At Stanford, it had been found that the instability could be triggered in a constant-impedance section with a current of 70 mA by injecting about 800 W of power at 4326 MHz backward into the output of the accelerator. However, the same result had not been achieved with an equal amount of power injected into a constant-gradient section of the same length, showing that the

Table 6-3 Comparison of constant-gradient and constant-impedance accelerator structures

Characteristic	*Constant gradient*	*Constant impedance*	*Ratio*[a] $\frac{g.c.}{c.i.}$
$\frac{E_0}{V_0/l}\left(\frac{\text{Peak elec. field}}{\text{Avg. elec. field}}\right)$	1.00	1.31	0.76
$\frac{(dP/dz)_{z=0}}{(dP/dz)_{z=l}}$	1.00	3.13	0.32
V_0 (no-load energy)	22.34 GeV	22.04 GeV	1.01
$-dV/di$	35.53 GeV/A	36.41 GeV/A	0.98
V (at $i = 50$ mA)	20.56 GeV	20.22 GeV	1.02
η_{max} (maximum beam-conversion efficiency)	0.73	0.70	1.05
$i_{\eta_{max}}$	314.2 mA	302.6 mA	1.04
v_g/c (normalized group velocity)	$0.0204 \rightarrow 0.0065$	0.0121	$1.68 \rightarrow 0.54$
t_F (filling time)	0.83 μsec	0.83 μsec	1.00
U (stored energy)	2372 J	2372 J	1.00
$\Delta_{z=l}$ (phase shift for $\delta f = 0.1$ MHz)	0.52 rad	0.52 rad	1.00
$\delta V_0/V_0$ (for $\delta f = 0.1$ MHz)	0.033	0.039	0.85

Assumed parameters:
$\tau = 0.57$
$P_{0T} = 5320$ MW (90% of which enters accelerator)
$L = 10{,}000$ ft (94.8% effective)
No. of sections = 960
$f = 2856$ MHz
$r = 53$ megohms/meter
$Q = 13{,}000$

[a] c.g.—constant gradient; c.i.—constant impedance.

Figure 6-14 Shapes of input and output RF pulses in constant-gradient (C.G.) and constant-impedance (C.I.) accelerator sections. Length of section = 10 ft, $\tau = 0.57$, and $2\pi/3$ mode in each case. Rise time of input pulse ≈ 0.1 μsec; time scale = 0.2 μsec/cm.

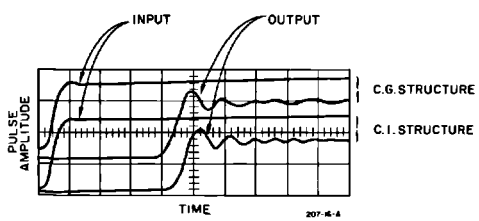

threshold must have been higher. An experiment done elsewhere[9] showed that by using a 5-ft long section of the Stanford constant-gradient design, thresholds as high as 600 mA in 3 μsec had been observed. All these results were qualitatively understood at the time in terms of the HEM_{11} dispersion diagrams which had been obtained and appear in Fig. 7-29. Indeed, in the backward-wave oscillator model, the frequency at which the $v_p = c$ line intersects the HEM_{11} dispersion diagram changes over a wide band along a 10-ft section, rather than being constant as in the constant-impedance structure. Thus buildup of the backward-wave instability is less likely to occur. Furthermore, since the currents planned at SLAC were much lower than the observed thresholds, it appeared that the constant-gradient design was assured of a reasonable degree of conservatism. As will be discussed in Chapter 7, if the accelerator were to be redesigned today, one would probably stagger accelerator sections of different designs along the 2-mile length in order to shorten the cumulative HEM_{11} interaction length at any given frequency. However, even with hindsight, it can be said that the choice of the constant-gradient design per se was correct from the beam breakup point of view since use of the constant-impedance structure, with uniform interaction along each 10-ft length, would have resulted in multisection breakup thresholds at even much lower currents than have been observed at SLAC.

The advantages of the constant-gradient accelerator discussed above had to be weighed against two disadvantages: (a) Nonuniform modular dimensions made the cavities in the constant-gradient structure more expensive to fabricate and to test. An economic comparison of the two structures showed that fabrication of the constant-gradient structure cost approximately 10% more per unit length than the constant-impedance structure. (b) At the time when the selection had to be made, there had been less operational experience with the constant-gradient structure than with the uniform structure.

It was concluded that the advantages of the constant-gradient structure outweighed its slightly higher fabrication cost. The constant-gradient structure was thus adopted for the two-mile accelerator. Subsequently, high-power tests and actual beam tests conducted with sections installed in the Mark IV and Mark III accelerators confirmed the theoretically predicted performance.

Choice of attenuation parameter (RBN)

The attenuation parameter is defined as the net attenuation in nepers in an accelerator section caused solely by resistive wall losses. It is equal to the product of the voltage attenuation per unit length and the length of the accelerator section and is designated by the symbol τ. As stated previously, $\tau = \omega t_F/2Q$, where ω is 2π times the operating frequency, t_F is the filling time, and Q is the loss factor in the RF structure. As will be evident in the following

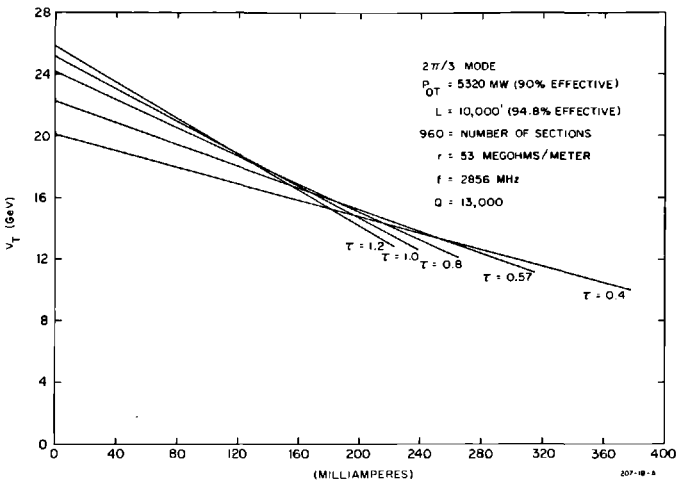

Figure 6-15 Beam loading curves for constant-gradient accelerator at various values of the attenuation parameter τ.

discussion, the value of τ influences the performance of a linac in many ways and, therefore, the proper choice of this parameter was quite important in the design of the two-mile accelerator.

The total steady-state energy gain V_T in a constant-gradient accelerator of total length L and shunt impedance r_0 is given[3] by

$$V_T = (1 - e^{-2\tau})^{1/2}(P_T L r_0)^{1/2} - \frac{i r_0 L}{2}\left(1 - \frac{2\tau e^{-2\tau}}{1 - e^{-2\tau}}\right) \qquad (6\text{-}7)$$

where P_T is the total input RF power, i is the peak beam current, and r_0 is the shunt impedance per unit length.

The first term on the right in Eq. (6-7) is the no-load energy (i.e., the electron energy at negligible current), and the second term gives the reduction in energy caused by beam loading. The reduction of energy is linear with increase in beam current, as shown in Fig. 6-15. In plotting these curves it is assumed that the electrons are situated at the peak of the traveling wave.

In the discussion which follows, the effect of τ upon the constant-gradient accelerator performance will be considered. The various accelerator characteristics are shown numerically in Table 6-4 for several values of τ.

BEAM LOADING CHARACTERISTICS. Beam loading curves for the various values of τ under consideration are shown in Fig. 6-15. The terminal point on each curve is the beam current resulting in maximum transfer of RF power to the beam. As noted, the slope $(-dV/di)$ of the beam loading curves decreases in magnitude as τ decreases. Since electrons with energies from V_{T0} to V_{Ti} emerge from the accelerator during the transient period, lower values of τ are preferred to reduce the energy spread.

Table 6-4 Calculated performance of constant-gradient accelerator at various values of attenuation parameter τ

	$\tau(Np)$				
Characteristic	0.4	0.57	0.8	1.0	1.2
(V_{To}) Unloaded energy (GeV)	20.10	22.34	24.20	25.18	25.82
($-dV/di$) Beam loading derivative (GeV/A)	26.59	35.53	45.58	52.61	58.24
(V_{Ti}) Energy at 50-mA beam current (GeV)	18.76	20.56	21.92	22.56	22.92
(ΔV)$_t$ transient energy spread (in GeV) between $i = 0$ and $i = 50$ mA	1.34	1.78	2.28	2.62	2.90
($i_{\eta max}$) Beam current at maximum conversion efficiency (mA)	377.8	314.2	265.4	239.4	221.6
(ΔV)$_e$ Energy loss in idle 10-ft section at $i = 50$ mA (MeV)	1.32	1.76	2.26	2.60	2.88
(v_g/c) Normalized group velocity[a]	0.0252–0.0113	0.0204–0.0065	0.0174–0.0035	0.0160–0.0022	0.0152–0.0014
(t_F) Filling time (μsec)	0.58	0.83	1.16	1.45	1.74
($-\delta V/V$) Energy loss for $\delta f = 0.1$ MHz	0.018	0.033	0.056	0.077	0.098

Assumptions:
$2\pi/3$ mode, constant-gradient design
$P_{OT} = 5320$ MW (90% of which enters accelerator)
$L = 10{,}000$ ft (94.8% effective)
No. of sections = 960
$f = 2856$ MHz
$r = 53$ megohms/meter
$Q = 13{,}000$

[a] The group velocity in each 10-ft accelerator section varies linearly between the limits given in each column.

MAXIMUM CONVERSION EFFICIENCY. The maximum conversion efficiency of RF power to beam power is given[3] by

$$\eta_{max} = \frac{1}{2}\left[\frac{(1 - e^{-2\tau})^2}{(1 - e^{-2\tau}) - 2\tau e^{-2\tau}}\right] \tag{6-8}$$

Maximum conversion efficiency occurs when the beam current reaches the value[3]

$$i_{\eta max} = \left(\frac{P_T}{r_0 L}\right)^{1/2}\left[\frac{(1 - e^{-2\tau})^{3/2}}{(1 - e^{-2\tau}) - 2\tau e^{-2\tau}}\right] \tag{6-9}$$

in which case the beam energy is equal to one-half of the no-load energy.

ENERGY LOSS AND POWER INDUCED WHEN THE BEAM PASSES THROUGH SECTIONS NOT SUPPLIED WITH RF POWER. When one of the klystrons along the accelerator becomes defective, it is desirable to be able to continue operation while the klystron is being changed. The amount (ΔV_e) by which the electron beam energy is reduced by excitation of an idle accelerator section of length l and the induced power P_e in this section is given[3] by

$$(\Delta V)_e = \frac{ir_0 l}{2}\left(1 - \frac{2\tau e^{-2\tau}}{1 - e^{-2\tau}}\right) \tag{6-10}$$

$$P_e = i^2 r_0 l\left(\frac{\tau^2}{e^{2\tau} - 1}\right)$$

The energy loss increases as τ increases, as shown in Table 6-4. Since each RF source supplies four accelerator sections during Stage I operation, the total energy loss given by Eq. (6-10) must be multiplied by 4. This loss must, of course, be added to the loss of beam energy incurred by the loss of the klystron (about 80 MeV under normal operating conditions).

GROUP VELOCITY. In the constant-gradient accelerator, the group velocity decreases linearly with distance along the accelerator section. It is given[3] by

$$v_g = \frac{\omega l}{Q}\left[\frac{1 - (z/l)(1 - e^{-2\tau})}{1 - e^{-2\tau}}\right] \tag{6-11}$$

FILLING TIME. A small filling time is desirable to allow the maximum available portion of the RF pulse length for the acceleration of electrons. The filling time is given[3] by

$$t_F = \frac{2Q}{\omega}\tau \tag{6-12}$$

Values of filling time for the various cases are given in Table 6-4.

FREQUENCY SENSITIVITY. The fractional beam energy loss from a fractional frequency shift $\delta f/f$ is given[3] by

$$\frac{\delta V_0}{V_0} = \left(Q\frac{\delta f}{f}\right)^2\left[\frac{2\tau e^{-2\tau}(\tau + 1)}{1 - e^{-2\tau}} - 1\right] \tag{6-13}$$

Values of $\delta V_0/V_0$ are shown in Table 6-4 for $\delta f = 0.1$ MHz.

CONCLUSIONS. From Table 6-4 it was clear that there were several advantages to using a reduced attenuation parameter τ. Except for the reduction in beam energy, the use of a low value of τ resulted in improvement of all of the factors measuring the performance of the accelerator. Moreover, the percentage improvement of each of these factors resulting from a given reduction

in τ usually exceeded the percentage loss in beam energy. In fact, if it were not for the paramount importance of high beam energy in particle physics research, the adoption of an even lower value of τ would clearly have been indicated. In conclusion, the choice of $\tau = 0.57$ was made on the basis of broad considerations, including reference to such tabulations as shown in Table 6-4, the prospective requirements of physics research, and previous accelerator experience.

[The original basis for the exact value of $\tau = 0.57$ was that this particular value resulted in a no-load energy in the constant-impedance accelerator of 10% less than the maximum no-load energy which can be obtained (occurring at $\tau = 1.26$). This was judged to be the maximum penalty in energy which one could afford to pay to obtain the advantages of low τ discussed in the text. The same qualitative reasoning held for the constant-gradient accelerator structure, and thus the value of τ selected earlier was not changed.]

Transient filter characteristics and beam loading (RHH)

PHYSICAL MODEL AND EXPERIMENTAL EVIDENCE. The band-pass filter characteristics of the accelerator structure, which were discussed briefly earlier in this chapter, will now be examined in greater detail. Both the physical model and the theory will be presented below. As already mentioned, one effect of these filter characteristics is that an impressed RF wave of finite rise time undergoes amplitude and phase oscillations as it travels down the accelerator structure. The impressed wave can come from the klystron or from beam loading. The oscillations which were illustrated in Fig. 6-14 can be understood in a simple way if one considers the symmetrical side-bands $\pm\Delta f$ of the carrier frequency (2856 MHz in this case) which are generated by the rise time of the RF wave. For an operating mode which is close to the middle of the $\omega - \beta$ diagram (see Fig. 6-21), the small side-band vectors rotate around the tip of the carrier vector in opposite directions but with approximately equal angular velocities. The resulting effect as a function of time and of distance along the structure is predominantly amplitude modulation because the sum of the two vectors remains approximately collinear with the carrier but varies in amplitude. As the operating mode gets closer to the edge of the passband, as in the $2\pi/3$ case, both amplitude and phase modulation become more apparent.

The effect of this modulation on the beam is to cause spectrum broadening. In a multisection accelerator, this spectrum broadening can be reduced by not triggering all the klystrons at exactly the same time, thereby causing the "peaks" and "valleys" to average out over a large number of sections.

Certain precautions should be taken when interpreting the pulse shapes of Fig. 6-14. It should be remembered that these pulses represent electric field amplitudes obtained at the end of a 10-ft section and that the electron beam energy results from the integral taken over the full length. Experiments done

by probing the field through small coupling holes drilled along a 10-ft section show that the evolution of the pulse shapes as a function of length is more complicated in the constant-gradient structure than in the constant-impedance structure. In addition to the side-bands caused by the rise time of the pulse, there is a frequency modulation effect. This frequency modulation is inherent in the rise time of the pulsed klystron supplying the RF power. At turn-on, the frequency can in fact be several megahertz higher than when the flat top of the modulator pulse is reached. This initial energy, which travels down the accelerator structure at a higher frequency, reaches an increasingly narrow pass-band structure as seen in Fig. 6-21. Before being attenuated, this energy travels at a group velocity which is much lower than the corresponding group velocity at 2856 MHz. When the pulse shape is examined in the middle of the section, the wiggles do not die out, i.e., the filling time is at least 2.5 microseconds long. Finally, towards the coupler end, the higher frequency energy gets attenuated or reflected and the pulse looks more and more like the simple output shown in Fig. 6-14. Because of the presence of the higher frequencies, the frequency of the wiggles is about twice as high at the input as at the output. While this effect is probably unimportant, experiments have shown that a 50% reduction in ripple amplitude can be obtained if a diode modulator at low power, preceding the klystron, is used for RF turnon. This result can be understood by the reduction in frequency modulation obtained with the *p-i-n* diode as compared with the klystron alone.

COUPLED RESONATOR WAVE EQUATIONS. The transient phenomena of wave propagation and beam loading can be described approximately by a simple theory in which the disk-loaded waveguide is treated as a continuous transmission line of which the dispersive properties are characterized by a well-defined group velocity. As has been pointed out by J. Leiss,[4] however, such

Figure 6-16 Mathematical model of a disk-loaded waveguide.

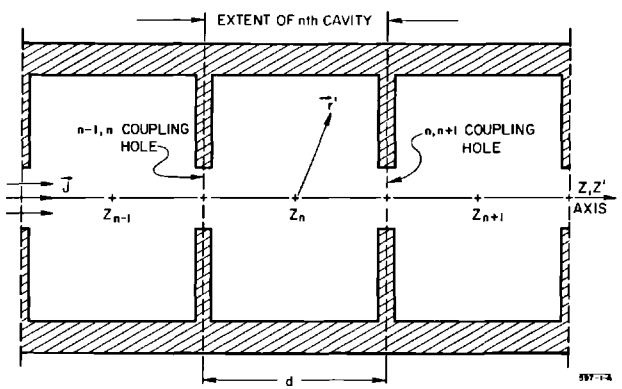

a treatment overlooks important transient effects arising from the finite passband of the periodically loaded structure.

The approach used here is an approximate version of coupled-resonator theory, equivalent to the filter-network approach of Reference 4. The wave equation may be written* (see Fig. 6-16 for geometric nomenclature):

$$\left(\frac{\partial^2}{\partial\tau^2} + 2\beta_n\frac{\partial}{\partial\tau} + \omega_n^2\right)A_n(\tau) - \omega_n\left\{\Omega_{n-1/2}A_{n-1}\left(\tau + \frac{d}{v}\right) + \Omega_{n+1/2}A_{n+1}\left(\tau - \frac{d}{v}\right)\right\}$$
$$= \frac{4\pi}{u_n}\int_{\text{cavity}} \psi_{zn}^*(\mathbf{r}')J_z\left(\mathbf{r}', \tau - \frac{z'}{v}\right)d^3\mathbf{r}' \quad (6\text{-}14)$$

where

$A_n(\tau)$ is related to the vector potential in the nth cavity by $\mathbf{A} \approx A_n(\tau)\psi_n(\mathbf{r}')$,
$\psi_n(\mathbf{r}')$ is the characteristic spatial distribution of the vector potential in the nth cavity,
$\psi_{zn}(\mathbf{r}')$ is the z-component of ψ_n,
$\tau \equiv t - \int_0^{z_n} dz/v(z)$ is the "local" time, retarded by electron transit time,
ω_n is a characteristic frequency parameter (the midband frequency),
$\beta_n = \frac{1}{2}\omega_n/Q_n$ is the loss coefficient,
$\Omega_{n\pm1/2}$ is a measure of the coupling between the nth and $(n \pm 1)$th cavities,
$u_n \equiv \int_{\text{cell}} |\psi_n(\mathbf{r}')|^2\, d^3\mathbf{r}'$ (proportional to stored energy); and
$J_z(\mathbf{r}', \tau)$ is the current density, assumed to consist of electrons traveling in the $\pm z$ direction at velocity v.

The assumptions that the parameters β_n, ω_n, and Ω_n are simple scalers is strictly valid only in the weak-coupling (small-hole) limit.

The equation may be interpreted phenomenologically by noting that, if the parameters vary only adiabatically as a function of n, then the homogeneous part has solutions of the form

$$A_n \approx A_{n-1}e^{-ik_n d}$$

where an implicit $e^{i\omega\tau}$ is understood, and

$$\omega_n^2 + 2i\beta_n\omega - \omega^2 \approx 2\omega_n\Omega_n\cos k_n d \quad (6\text{-}15)$$

Thus, if one assumes

$$\beta_n \ll \omega_n \quad \text{and} \quad \Omega_n \ll \omega_n$$

the dispersion formula is a cosine-like curve with ω_n the midband frequency and Ω_n approximately the half-bandwidth.

* In the present discussion, the units are Gaussian with $c = 1$, unless otherwise noted.

An even simpler dispersion relation results if one assumes $|(\omega-\omega_n)/\omega_n| \ll 1$; i.e., that the fields have no frequency components very far from $+\omega_n$; one may then write

$$\omega_n + \beta_n - \omega \approx \Omega_n \cos k_n d \tag{6-16}$$

In this case the wave equation may be written

$$\left(\frac{\partial}{\partial\tau} + \beta_n - i\omega_n\right)A_n(\tau) + \frac{i}{2}\left\{\Omega_{n-1/2}\,A_{n-1}\left(\tau + \frac{d}{v}\right) + \Omega_{n+1/2}\,A_{n+1}\left(\tau - \frac{d}{v}\right)\right\}$$

$$\approx \frac{2\pi}{i\omega_n u_n}\int_{\text{cavity}} \psi^*_{zn}(\mathbf{r}')J_z\left(\mathbf{r}', \tau - \frac{z'}{v}\right) d^3\mathbf{r}' \tag{6-17}$$

APPLICATION TO ACCELERATOR MODE. In the accelerator mode, the longitudinal field is transversely uniform near the axis, e.g.,

$$\psi_z \approx \psi_z(0, 0, z')$$

Defining the complex voltage gain, $w_n(\tau)$, by

$$w_n(\tau) = \int_{\text{cavity}} E_z\left(\tau + \frac{z'}{v}\right) dz' \tag{6-18}$$

or, assuming an instantaneous variation $\sim e^{i\omega_n\tau}$, and noting that $E_z \approx -i\omega_n A_z$, one may write

$$w_n(\tau) \approx -i\omega_n F_n A_n(\tau) \tag{6-19}$$

where

$$F_n = \int_{\text{cavity}} \psi_z(z')e^{i\omega_n z'/v}\, dz' \tag{6-20}$$

The voltage gain for an electron entering the structure at time $t = \tau$ is

$$V(\tau) = \sum_1^N \text{Re}\, w_n(\tau) \tag{6-21}$$

The wave equation (Eq. 6-17) may now be written

$$\left(\frac{\partial}{\partial\tau} + \beta_n - i\omega_n\right)w_n(\tau) + \frac{i}{2}\{\tilde{\Omega}_{n-1/2}\,w_{n-1}(\tau) + \tilde{\Omega}_{n+1/2}\,w_{n+1}(\tau)\} \approx -\beta_n R_n I(\tau) \tag{6.22}$$

where $I(\tau)$ is the beam current;

$$\tilde{\Omega}_{n\pm1/2} = \Omega_{n\pm1/2}\,e^{\mp i\omega_n d/v}$$

and R_n, the shunt impedance per cavity, is defined by

$$\frac{R_n}{Q_n} = \frac{2\beta_n R_n}{\omega_n} = \frac{4\pi}{\omega_n}\frac{|F_n|^2}{u_n} \tag{6-23}$$

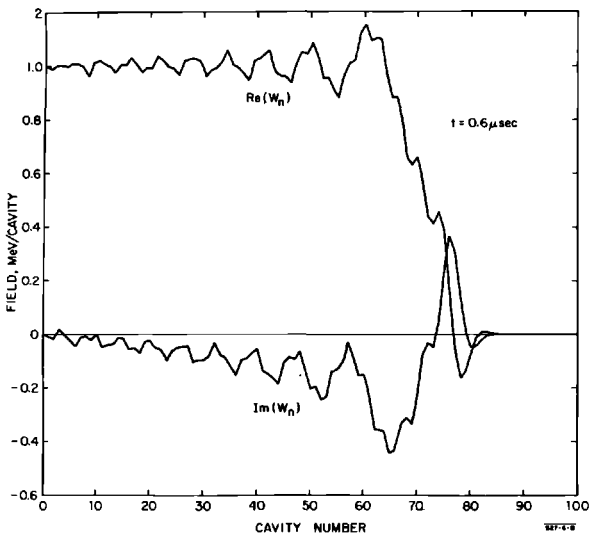

Figure 6-17a Field distribution in the accelerating mode along a constant-gradient structure, 0.6 μsec after turning on a unit step-function driving voltage in the zeroth cavity.

The transient behavior of typical disk-loaded guides has been investigated by a computer program which integrates Eq. (6-22). The program data input provides for arbitrary longitudinal variation of the waveguide parameters and choices of appropriate boundary conditions, driving sources, and beam models. As a computational convenience, the program actually calculates the function $W_n(\tau)$, defined by

$$w_n(\tau) = W_n(\tau)e^{i\omega'\tau}$$

where ω' is a constant reference frequency (e.g., the driving source frequency) and $W_n(\tau)$ is slowly varying in phase and amplitude.

Figures 6-17 and 6-18 show the results of typical computations based on the properties of the SLAC structure. The table below summarizes the pertinent initial and final values of the parameters:

Cavity No.	v_g/c	$\Omega/2\pi$ *(MHz)*	Q	R/d *(megohms/meter)*
0	0.0204	32.0	14,170	53
85	0.0061	10.41	13,220	60

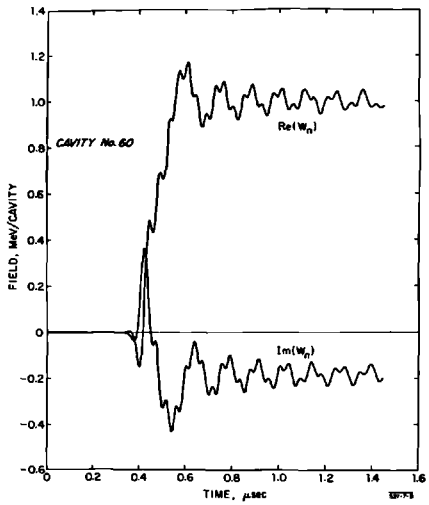

Figure 6-17b Arrival of the RF pulse at cavity No. 60 (6.9-ft point).

Figure 6-17c Arrival of the RF pulse at the 10-ft point. Note increased dispersion of the initial rise, as compared to Fig. 6-17b. The substantial out-of-phase component results from an error of ≈0.06 MHz in entering the mid-band frequency in the program input data.

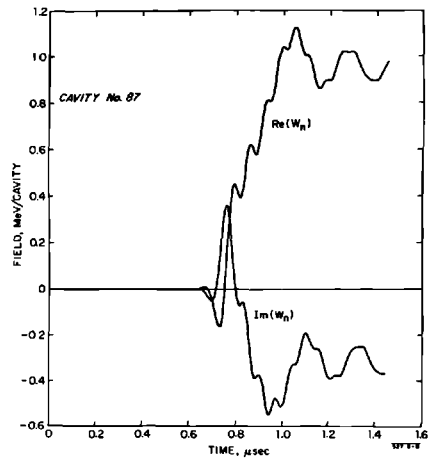

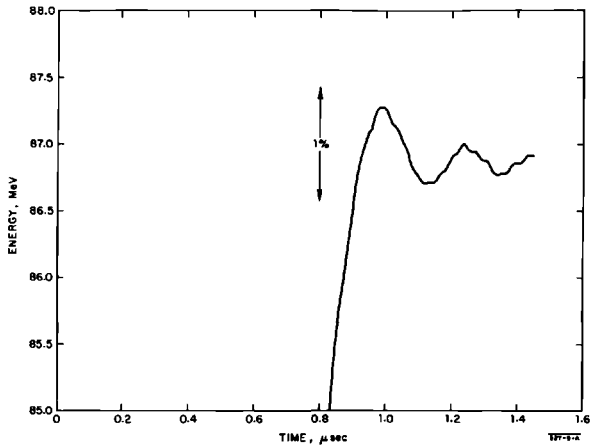

Figure 6-18 Electron energy gain versus time corresponding to the case of Figs. 6-17a, b, and c. The large ripples seen in the field plots have nearly averaged out in the summation over the cavities.

The values of half-bandwidth, Ω_n, used in the computation are derived from the design group velocity, $v_g(n)$, through the relation

$$v_g = \frac{\partial \omega}{\partial k} \approx \Omega\, d \sin k\, d$$

A step-function driving voltage applied at time $\tau = 0$ at the input boundary was assumed in all the computations. Physically, such a step function would be closely approximated by means of the *p-i-n* diode mentioned earlier. It is seen that these computations are in excellent agreement with the experimental observations mentioned above. Comparing Figs. 6-17b and 6-17c, it is seen how the wiggles evolve as a function of length, as the group dispersion increases. As the pass-band becomes narrower, certain frequency components which are shock-excited by the step-function driving voltage are reflected from the 0- or π-mode band edge at some point down the structure, propagate back to the input where they are again reflected by the constant voltage source (zero impedance) and thus set up standing-wave resonances. Such resonances would probably be much less noticeable in a more realistic case with finite rise time and source impedance matched to the guide. The appearance of a significant out-of-phase component of the field (Fig. 6-17c) results from a slight input data error of $\approx$0.06 MHz in the midband frequency. As a result, the wave is not quite synchronous at the assumed bunching frequency of 2856 MHz.

In conclusion, it is seen from Fig. 6-18 that the variation in electron energy gain is at most 1% at the beginning of the beam pulse and that it rapidly decreases from then on. Measurements made with a short accelerator length have confirmed these results.

6-2 Empirical design of the accelerator structure

Choice of the disk-loaded waveguide (GAL)

The first section of this chapter was concerned with the general determination of accelerator parameters. This section describes the procedures used to design empirically an accelerator structure that satisfies the above parameters.

The disk-loaded waveguide is not the only slow-wave structure capable of accelerating electrons. In fact, other structures (see Fig. 6-19) such as the grid-loaded ("jungle gym") waveguide yield shunt impedances about twice that of the disk-loaded waveguide. But in every case that was examined, where a large improvement in shunt impedance was obtained, the bandwidth and resulting group velocity were at least 10 times as high as desired. Efficient utilization of the available RF power under these conditions would have

Figure 6-19 Slow-wave structures proposed for linear accelerators.

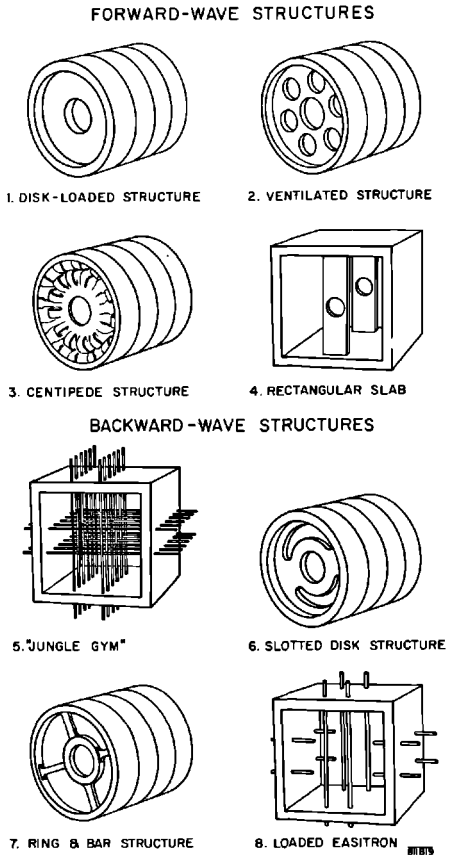

required its recirculation (feedback) or the use of extreme lengths between feeds. The former was undesirable, especially in a long multisection accelerator, because it would have resulted in undue operational complications; the latter would have required that each accelerator section transmit an excessive amount of power. Several variations of structures 2 through 8 shown in Fig. 6-19 were devised which succeeded in reducing the group velocity to the desired values (in the range of $0.01c$), but these measures also caused the shunt impedance to be reduced until no advantage remained; moreover, they would have resulted in increased cost of fabrication. For these reasons, the disk-loaded waveguide was preferred for the two-mile accelerator.

Definition and discussion of dimensions (GAL)

The modular dimensions of the disk-loaded waveguide which can be adjusted to achieve the intended parameters have already been illustrated in Fig. 6-2. Figure 6-2a and b shows the cylindrical guide diameter $2b$, the disk-hole diameter $2a$, the disk-edge radius ρ, and the land in the disk aperture s. Figure 6-2c shows further variations of the disk-loaded waveguide using so-called "conical" or "anticonical" disks. The conical disk was rejected because of its comparatively low r/Q. The anticonical disk was dismissed because of machining difficulties, although it has a 5% higher r/Q than the corresponding flat disk structure with $t = t_1 = 0.230$ in.

As indicated earlier, a 10% improvement in shunt impedance was gained by adopting the $2\pi/3$ mode rather than the $\pi/2$ mode. Figure 6-20 illustrates

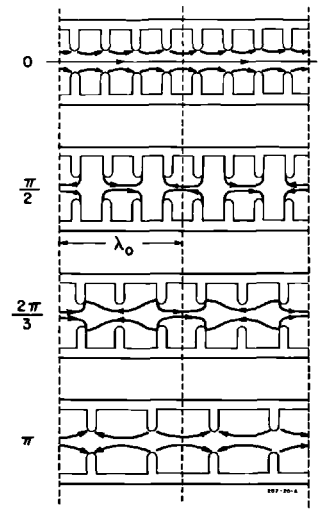

Figure 6-20 Traveling-wave electric field configurations for 0, $\pi/2$, $2\pi/3$, and π phase shift per cavity.

the respective traveling-wave field configurations at an instant in time over two wavelengths (the zero and π "standing-wave modes" are also illustrated for reference). These patterns are deformed as they slide down the waveguide but reappear in the same configuration, shifted by one cavity, at an instant $\delta t = \phi/2\pi f$ later, where ϕ is the phase shift per cavity at the frequency f.

For standard accelerator sections, the objective is to obtain a phase velocity equal to the velocity of light. Thus, specifying the operating mode and frequency (or free-space wavelength) fixes the distance between disk center lines at $d = \phi c/\omega$. After this choice, only four dimensions remain to be specified: $2b$, $2a$, ρ, and t. The lower cutoff frequency of the disk-loaded waveguide, or "zero-mode" frequency, is strongly dependent upon the waveguide diameter $2b$, whereas the bandwidth and, thus, the group velocity depend primarily on the ratio a/b at given values of ρ and t. This point is illustrated by the three ω–β (Brillouin) diagrams shown in Fig. 6–21. For experimental tests and later, in the fabrication, it was important to verify that the disk aperture edge had been properly formed; this was done through some technique such as that utilizing a steel ball (Fig. 6–2b) or a more

Figure 6-21 Brillouin diagrams for three different points in a typical constant-gradient section.

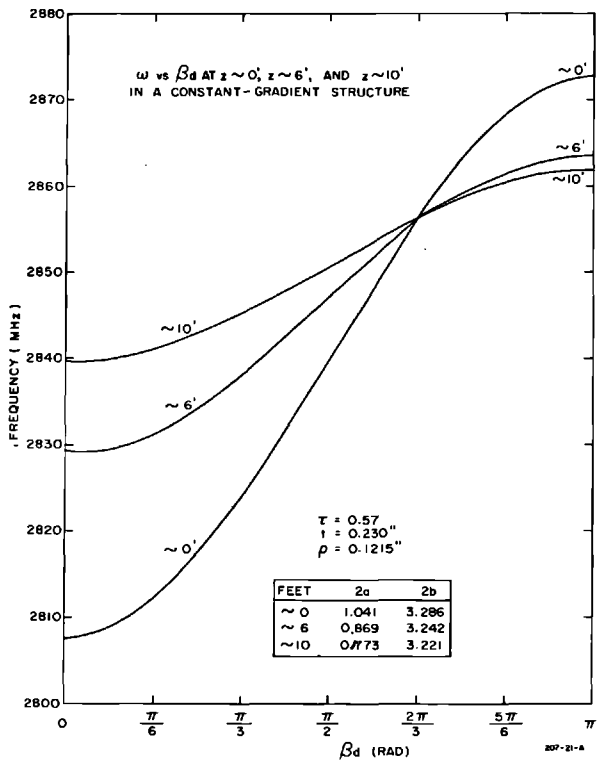

sophisticated contour plotter. Errors in the ball height h or the land s cause significant errors in the resonant frequency of test sections and hence in the resulting phase and group velocities. This fact is easily understandable because the electric field intensity is relatively strong at the disk edge. The choice of ρ can be quite arbitrary from the RF point of view so long as the tolerances are respected and electric breakdown does not result.

The choice of the disk thickness t, as discussed in the previous section, involve a compromise between the use of thin disks to increase the shunt impedance and thick disks to reduce the danger of electrical breakdown, improve heat-transfer characteristics, and increase mechanical strength.

Evolution of Stanford designs (GAL)

Prior to 1960, all Stanford accelerators had been designed to operate in the $\pi/2$ mode. Starting in 1960, the first $2\pi/3$ mode structure was tested on the 20-ft Mark IV accelerator. Until 1962, all Stanford accelerators were of the constant-impedance type. Then, in April 1962, the first constant-gradient structure was installed on the Mark IV accelerator. Finally, SLAC-type constant-gradient structures were installed on the Mark III accelerator in December 1963, replacing the earlier $\pi/2$ structures.

Table 6-5 shows a recapitulation of the respective characteristics of constant-impedance structures operating in the $\pi/2$ mode on the early Mark III accelerator and in the $2\pi/3$ mode on the Mark IV accelerator.

Table 6-5 Characteristics of Stanford constant-impedance structures

Parameters	*Mark III accelerator (1952)*	*Mark IV accelerator (1960)*
Operating mode	$\pi/2$	$2\pi/3$
Length (ft)	10	10
Waveguide inside diameter $2b$ (in.)	3.247	3.247
Disk hole diameter $2a$ (in.)	0.8225	0.890
Disk thickness t (in.)	0.230	0.230
Periodic length d (in)	1.0335	1.378
Disk edge radius ρ (in.)	0.1215	0.1215
Matching iris aperture (in.)	1.042	1.014
Frequency (MHz)	2856	2856
Group velocity v_g/c	0.0100	0.0122
Shunt impedance r_0 (megohms/meter) (corrected for fundamental space-harmonic amplitude)	47	53
Q	10,000	13,200
Attenuation τ (Np)	0.90	0.57

Constant-gradient structure dimensions (GAL)

As already discussed, the two-mile accelerator is of the constant-gradient type, propagating in the $2\pi/3$ mode. The constant field is obtained by tapering the cross-sectional dimensions of the waveguide so as to produce the required linear decrease in group velocity. The constant-field condition then results only if the shunt impedance and the Q of the cavities remain constant over the length of the section in spite of the cross-sectional variation of the structure. In practice, for a group velocity variation such as that chosen for the SLAC design, the shunt impedance r_0 (corrected for the fundamental space harmonic) increases by a small percentage over a 10-ft section, thereby yielding a structure with a gradual input-to-output field increase of 5%. Then, in the presence of beam loading, the rising field characteristic is compensated for, as will be seen later in this section.

Two constant-gradient structures were designed, one for thick disks ($t = 0.230$ in.), the other for thinner disks ($t = 0.120$ in.). Their performances were compared and the thicker disk design was chosen for the reasons already mentioned earlier. Figures 6-22 and 6-23 show the respective variations of $2b$, $2a$, v_g/c, and r_0 as a function of cavity number along a 10-ft section.

Figure 6-22 Variation of *2b*, *2a*, v_g/c, and the shunt impedance r_0 (corrected for the fundamental space harmonic) as a function of cavity number along a 10-ft constant-gradient section for $t = 0.230$ in. The values of *2b* and *2a* in this figure are those given in Table 6-6. These final values were obtained by applying several corrections to the cold test data, including those given by Eqs. (6-44) and (6-45).

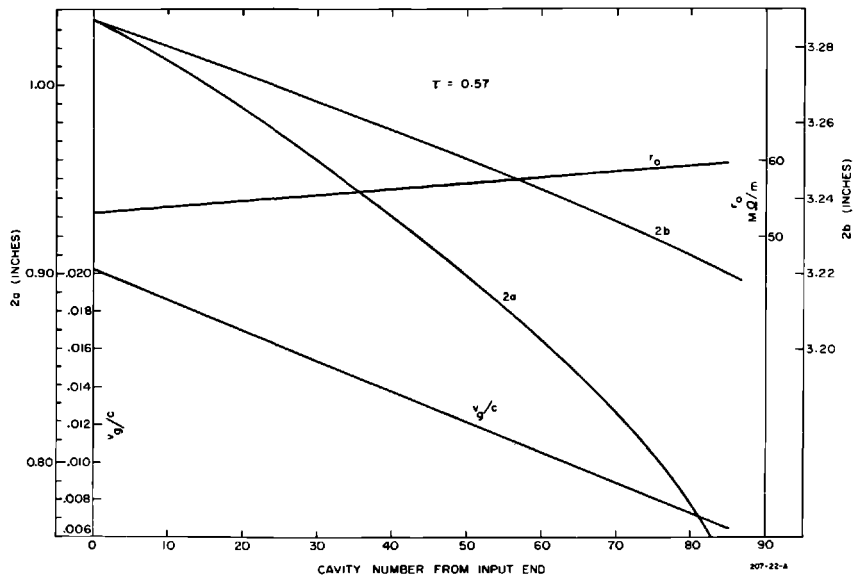

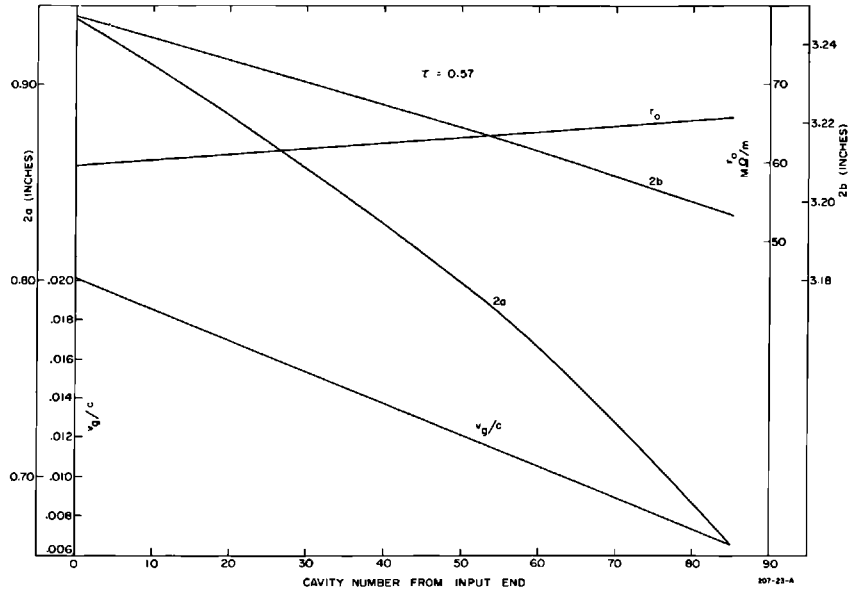

Fig. 6-23 Variation of $2b$, $2a$, v_g/c, and the shunt impedance r_0 (corrected for the fundamental space harmonic) as a function of cavity number along a 10-ft constant-gradient section for $t = 0.120$ in.

Cavities 0 and 85 are coupler cavities. It is seen that whereas $2b$ varies by less than 2%, $2a$ is reduced at the output by 30% from its input value to satisfy the group velocity variation.

When economy in fabrication is desired, a constant-gradient design can be approximated by adjusting the dimensions in steps, each step consisting of several identical cavities. However, for the two-mile Stanford accelerator, the cost of the slow-wave structure represented only a small percentage of the total cost, and the small increase incurred by varying the dimensions cavity by cavity was well justified to achieve a smooth field gradient.

Cold tests and corrections to achieve the empirical design (GAL)

OBJECTIVES AND VALIDITY OF COLD TESTS. A computer program sufficiently accurate to permit calculation of the dimensions of the constant-gradient designs shown in Figs. 6-22 and 6-23 did not exist at the time. Consequently these dimensions had to be determined experimentally from cold tests. To achieve an accurate design, a fair number of pairs of $2b$ and $2a$ values had to be determined, each set of values being obtained from a different resonant test cell. About ten different test cells were used for each of the constant-gradient designs. For each test cell, the following quantities were measured: the phase velocity v_p, the group velocity v_g, r/Q, Q, and the fundamental

space harmonic amplitude $a_0^2/\sum a_n^2$. The detailed description of these microwave measurements is beyond the scope of this book. Comprehensive treatments of this subject can, for example, be found in References 2, 10, and 11. However, a brief comment is made here on each of these measurements to outline the techniques that were used and the precautions that were taken. A discussion of the corrections applied to the experimental results is also included.

Results of cold tests on short test cells are valid if the reflection symmetries of the structure are carefully taken into account. Shorting plates must be located only in planes to which the electric-field vector is normal and in such a way that the standing wave "trapped" between them is an exact representation of the instantaneous traveling wave one wishes to study. The dotted lines in Fig. 6-20 show such planes. For observation of the $2\pi/3$ mode, sets of three or six identical cavities were used, covering one or two full wavelengths. These cavities were made of carefully machined copper or brass cups and rings, half-height rings being used at the end to apply the correct boundary conditions.

When measurements are being made, it is essential that the cavities be stacked and aligned very carefully, preferably by means of a concentric jacket, and that good electrical contact be obtained through a uniformly applied pressure.

Figure 6-24 Typical experimental setup showing cavity stack used to obtain Brillouin diagram by successive resonances.

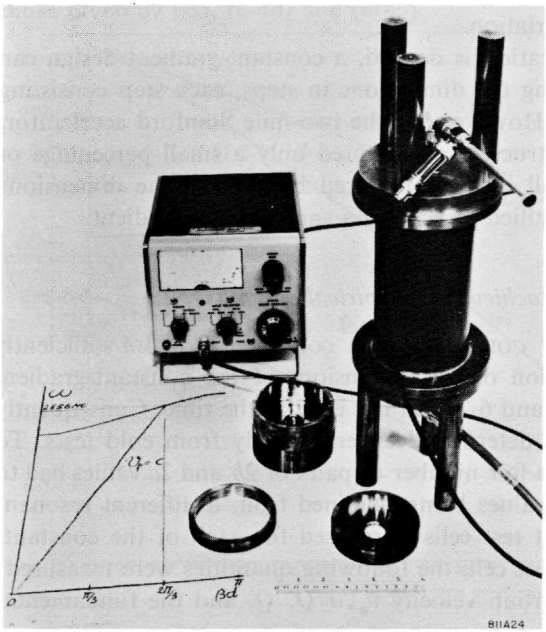

MEASUREMENT OF PHASE VELOCITY v_p. The graph in Fig. 6-24 illustrates a typical Brillouin diagram with the phase velocity $v_p = c$ for a $2\pi/3$ phase shift per cavity at $f = 2856$ MHz. The disk spacing was fixed at $\lambda/3 = c/3f = 10^4/2856$ cm. With three or six cavities of the type shown, four or seven resonant frequencies, respectively, representing $n\pi/3$ $(0 \leq n \leq 3)$ or $n\pi/6$ $(0 \leq n \leq 6)$ phase shift per cavity, can occur; these points were recorded to draw the ω–β diagram. With a moderate amount of experience, three rounds of machining correction of the diameter $2b$ were sufficient to approach the operating frequency (2856 MHz) within less than 1 MHz at $2\pi/3$ resonance. The remaining correction was done by interpolation.

MEASUREMENT OF GROUP VELOCITY v_g. The condition $v_g = c$ can be obtained for various pairs of $2b$ and $2a$ values. Each pair yields a different ω–β diagram and, hence, a different group velocity. This fact has already been illustrated in Fig. 6-21. Figure 6-25 shows the two cavity stacks for the extreme cases, the first and the last cavities of the constant-gradient section. The differences in $2a$ for $v_g/c = 0.0204$ and $v_g/c = 0.0065$ can be observed. To obtain the group velocity, the slope of the ω–β diagram was measured and, for better accuracy, a Stirling or Fourier approximation formula[12] was used with the measured resonance frequencies.

Figure 6-25 Typical cold test setup showing cavity stacks and group velocity variation as a function of length along a constant-gradient section.

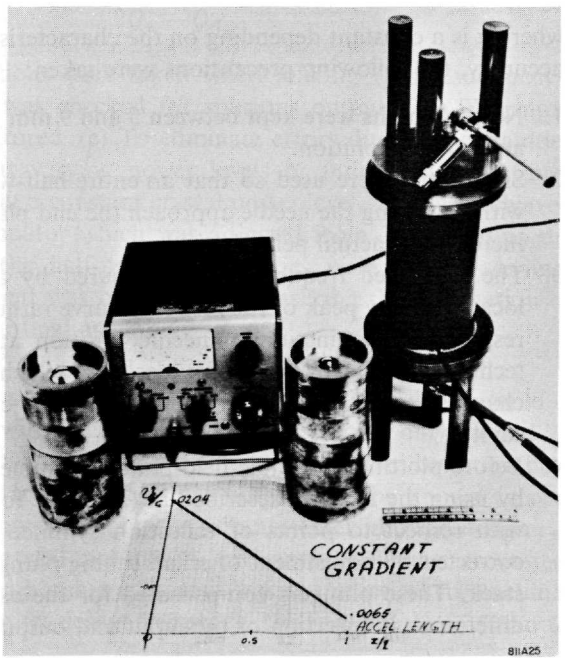

MEASUREMENT OF r/Q. The ratio of shunt impedance per unit length to Q was best measured by perturbing the axial fields in the cavity stack with a thin dielectric rod and by measuring the resonant frequency perturbation Δf. Using Slater's perturbation formula,[11,13] the value of $(r/Q)_T$ (where the index T denotes the sum of all space-harmonic components) is given by

$$\left(\frac{r}{Q}\right)_T = \frac{240c}{(\varepsilon - 1)A}\frac{\Delta f}{f^2} \tag{6-24}$$

where ε is the dielectric constant of the rod (for sapphire $\varepsilon \approx 10$), and A is its cross-sectional area. It was easiest to calibrate the dielectric rod in a simple TM_{010} cavity, for which r/Q can be calculated.

MEASUREMENT OF THE SPACE-HARMONIC AMPLITUDE. Since only the fundamental space harmonic propagates at $v_p = c$, it alone gives a net energy gain to the electrons. Thus, to obtain the effective $(r/Q)_0$, it was necessary to obtain the amplitude of the fundamental. The figure of merit by which to multiply $(r/Q)_T$ to obtain $(r/Q)_0$ is $a_0^2/\sum a_n^2$, the ratio of the square of the fundamental harmonic amplitude divided by the sum of the squares of all harmonic amplitudes. This ratio was obtained by noting the frequency perturbation caused by a short metallic or dielectric needle drawn along the axis of the resonant cavity stack. The field E_c at a given axial position in the cavity is related to the frequency perturbation Δf caused by the needle located in that position by

$$E_c^2 = k\,\Delta f \tag{6-25}$$

where k is a constant depending on the characteristics of the needle. For best accuracy, the following precautions were taken:

1. Needle lengths were kept between 5 and 9 mm to give adequate sensitivity and good resolution.
2. Six cavities were used so that an entire half-wavelength could be probed without letting the needle approach the end plates, where its image would increase the actual perturbation.
3. The perturbed frequency was measured by adjusting the frequency to locate the new peak of the response curve rather than by observing power response as a function of needle position at constant frequency. This technique avoided the difficulties[14–16] which arise from simultaneous changes in the resonant frequency and the coupling coefficients of the cavity.
4. Before plotting the whole field pattern, symmetry of the field was checked by using the method described in (3) above for a few points symmetrical with respect to points of reflection symmetry. Lack of symmetry was corrected by adjustment of small tuning plungers at the top of the cavity stack. These plungers compensated for the asymmetry created by slight differences in insertion of the input and output coupling loops.

After the field pattern was obtained, a Fourier analysis was carried out to obtain the figure of merit, which is given by

$$\frac{a_0^2}{\sum a_n^2} = \frac{1}{\lambda} \frac{\left(\int_0^{\lambda/2} E_c \cos(2\pi/\lambda)z \, dz\right)^2}{\int_0^{\lambda/2} E_c^2 \, dz} \tag{6-26}$$

It was sufficient to divide the E_c pattern into twenty-one intervals and evaluate the integral using the trapezoidal approximation.

MEASUREMENT OF Q. This was the most difficult measurement to make because the results depended on the state of the metal surface and the degree of contact between cavities. Measurements were usually taken immediately after electropolishing the cavities. Using very weak coupling, the Q's of three-cavity (Q_3) and six-cavity (Q_6) sets were successively obtained by the half-power point technique:

$$Q = \frac{f}{\Delta f} \tag{6-27}$$

where f is the resonant frequency and Δf is the frequency variation between half-power points. Although the Q's thus obtained were lowered by end-plate losses, the end effects were eliminated through use of the following expression[11]:

$$Q = \frac{Q_3 Q_6}{2Q_3 - Q_6} \tag{6-28}$$

The following precautions were taken when making Q measurements: (a) The signal generator was checked for spurious outputs. (b) The input power was carefully monitored. (c) To eliminate errors due to uncertainties in crystal law behavior at varying power levels or indicator calibrations, measurements were made at a constant crystal power level. This was achieved by using a precision attenuator which was adjusted from 3 to 0 dB as the resonant frequency and the half-power frequencies were sought. A final check of the Q measurement was obtained by measuring the attenuation of an accelerator section after final assembly.

ENVIRONMENTAL TEST CONDITIONS AND CORRECTIONS. In order to build a constant-gradient section with fixed t, d, and ρ dimensions, only $2b$ and $2a$ had to be obtained and their relationship with v_p and v_g had to be determined accurately. The quantities $(r/Q)_0$ and Q did not have to be known so precisely, because to a first approximation they do not enter into the design.

Measurements were carried out in an environment having accurately controlled temperature and humidity. Since it was not practical to machine-test cavities to attain the exact design frequency, the final value of $2b$ had to

be corrected for the residual Δf. It was usually sufficient to base the correction on the simple relation

$$\frac{\Delta 2b}{\Delta f} \approx -\frac{2b}{f} = -0.0011 \text{ in./MHz (at 2856 MHz)} \tag{6-29}$$

Another correction was required to arrive at the operating frequency for a given copper temperature differing from the room temperature at which the tests were being performed. In addition, most cold tests were done in air, and a correction had to be applied for the dielectric constant of air, which is a function of the ambient humidity and temperature (see Adam's nomograph in any engineering handbook). These problems were not very critical for short cavity-stack measurements but became important during matching and tuning operations, as discussed in a later section. For copper, the following rule of thumb can be applied at 2856 MHz:

$$\frac{\Delta f}{\Delta T} = -0.100 \text{ MHz}/2^\circ\text{C} \tag{6-30}$$

Translation from air at 80°F and 40% humidity to vacuum results in a frequency increase of about 300 parts/million.

Having applied these corrections, the values of $2a$ and $2b$ were smoothed, first by plotting the points on a curve, and then by using a simple computer program to obtain a fourth-order fit.

Basic considerations in matching and tuning an accelerator section (GAL)

If the process of machining parts and fabricating an accelerator structure could be carried out with perfect accuracy, a section such as the one shown in Fig. 5-13 would be ready for installation and use immediately after fabrication.

In practice, however, it is difficult to control the process of manufacturing to this extent; moreover, it is not economical to do so. By relaxing the tolerances on the fabrication techniques described later in this chapter, it was possible to reduce the cost of the accelerator considerably. The imperfections were corrected through the process of tuning and matching for a relatively small incremental cost.

The process of tuning an accelerator section consisted of applying external mechanical pressure to impart a permanent deformation to the wall of any cavity of which the phase shift differed from the design value. In tuning, a maximum phase excursion of $\pm 2.5^\circ$ was allowed for the 10-ft sections of the two-mile machine.

Matching the couplers of an accelerator section was done by adjusting the dimensions of the input and output coupling irises (see Fig. 6-26) so as to insure a low standing-wave ratio at the input and output of the structure. An upper VSWR limit of 1.05 was set as the matching requirement for all couplers. The main technical difficulty stemmed from the fact that the processes of

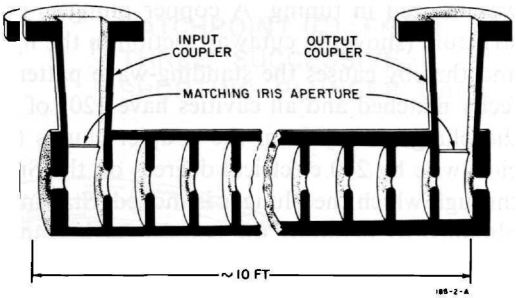

Figure 6-26 Sketch of a 10-ft long, constant-gradient, accelerator structure with input and output couplers. Notice slight taper in modular dimensions (diameter of inner wall).

tuning and matching are interrelated; the shape of the coupling iris determines both the coupling to and the phase shift of the first cavity.

A complete description of the theory and operations involved in tuning and matching an accelerator section is beyond the scope of this chapter. Good discussions on these subjects can be found in References 2, 10, 11, and 17–19. Only a few of the general principles and relevant precautions are given below.

Although the simplest mode to tune and match is the $\pi/2$, any submultiple of 2π, such as the $2\pi/3$ mode, can be handled without undue difficulty.

Figure 6-27 illustrates the principle of the nodal-shift technique which

Figure 6-27 Principle of the nodal shifting technique. Shown at left are the cutaway section with the copper plunger, and typical Smith chart plot.

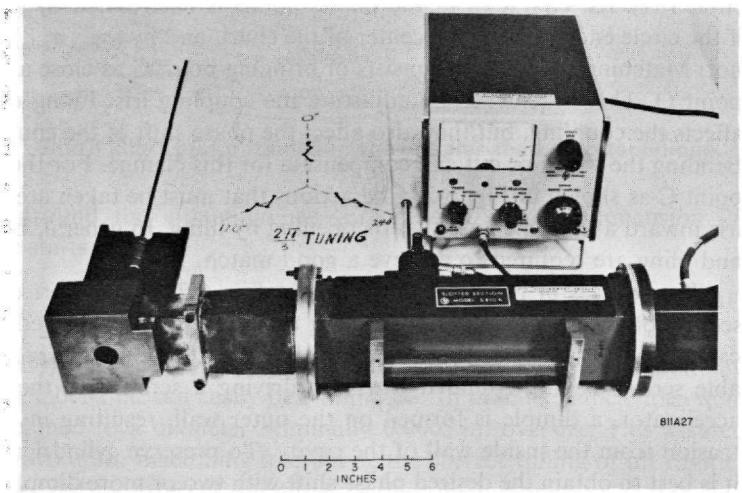

was utilized in tuning. A copper plunger, progressively pulled through the structure (shown in cutaway section in the figure), detunes successive cavities and thereby causes the standing-wave pattern to shift. If the coupler is perfectly matched and all cavities have 120° of phase shift ($2\pi/3$ mode), pulling the plunger away from the coupler causes the plotted null points to rotate clockwise by 240 electrical degrees on the Smith chart for each cavity length through which the plunger is moved. Starting from the reference point of 0°, obtained by detuning the coupler cavity (and, hence, representing the plane of the iris), the points move clockwise as shown in Fig. 6-27 from 0° to 120°, from 120° to 240°, from 240° to 0°, and so on. For the first cavities, the VSWR is nearly infinite and the points are on the rim of the chart. Farther down the section, the VSWR decreases because of the increasing net attenuation between the input of the section and the short. Thus, the plotted points move toward the center of the chart along the three radii, shown as dashed lines in Fig. 6-27. With the coupler perfectly matched but the cavities not exactly tuned, the points move erratically toward the center, as shown by the heavy lines. However, the center of the circle passing through three consecutive points still coincides with the center of the chart. When a systematic phase-shift error exists, because of an inaccurate choice of frequency, the points spiral in toward the center, clockwise if the phase shift is too large (frequency too high), or counterclockwise if it is too small (frequency too low). If the coupler is mismatched (see Fig. 6-28), the circle passing through the three points is no longer concentric with the rim of the chart. It now has two "centers"—a geometrical center and a "Smith center." Neither coincides with the center of the chart. The Smith center is the point that would be obtained if the perfectly reflecting plunger were replaced by a perfectly matched load. It can be determined mathematically[10,11] from geometric considerations. The match point (C) will lie on the extension of the straight line from the center of the Smith chart (O) to the geometric center of the circle (M). Its VSWR (σ at the match point) is determined by $(\sigma_{max}/\sigma_{min})^{1/2}$ if the circle encompasses the center of the chart, and by $(\sigma_{max}\,\sigma_{min})^{1/2}$ if it does not. Matching the coupler consists of bringing point C as close as possible to point O. This is achieved by adjusting the coupling iris. Filing or squeezing affects the coupling, but they also affect the phase shift of the coupling cavity. Bending the iris in or out can compensate for this change. For the example of point C as shown in Fig. 6-28, the actions that must be taken are to bend the iris inward and to increase the iris opening by filing. In general, both bending and filing are required to achieve a good match.

The process of tuning is illustrated in Fig. 6-29 for a short experimental section of accelerator pipe. The tuning tool here is being applied to the third cavity. It consists of a demountable collar with two or three radially adjustable screws having rounded ends. By driving a screw into the wall of the accelerator, a dimple is formed on the outer wall, resulting in a small protrusion from the inside wall of the cavity. To preserve cylindrical symmetry, it is best to obtain the desired phase shift with two or more dimples uniformly

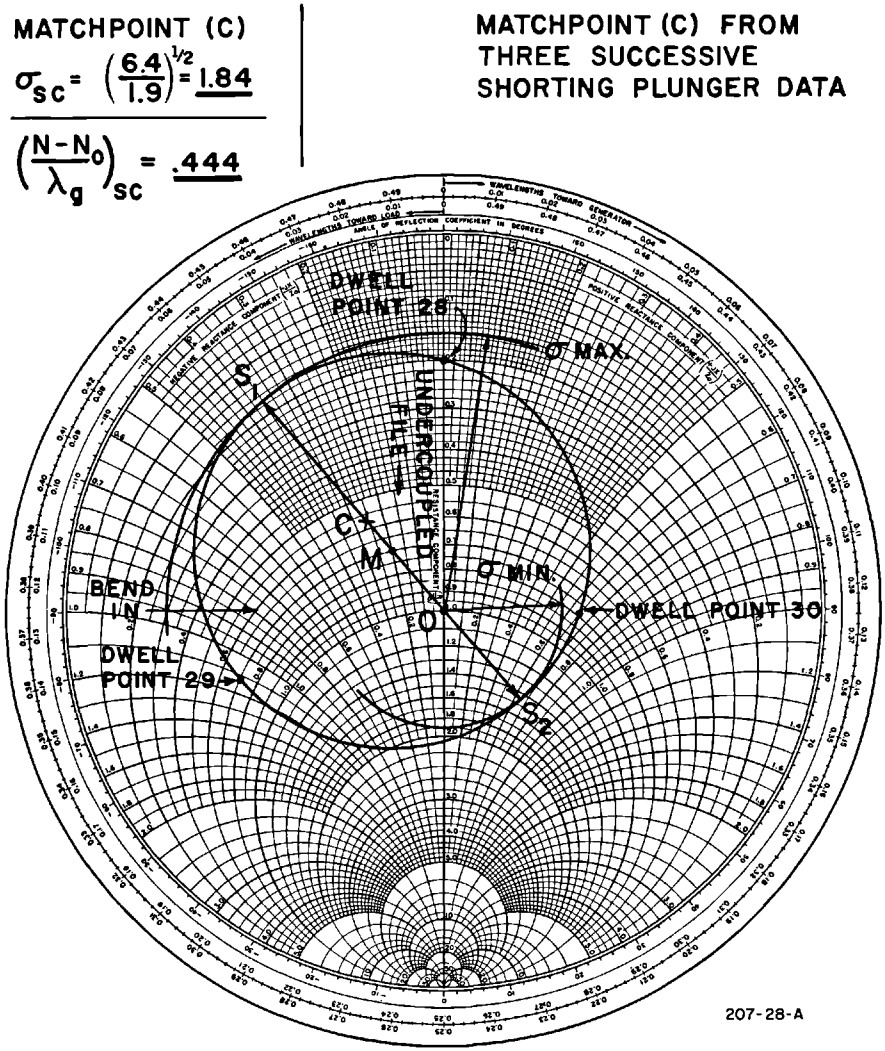

Figure 6-28 Smith chart plot obtained in the coupler-matching technique.

distributed around the circumference. Errors $\Delta(2b)$ in the dimension $2b$ create phase shifts $\Delta\phi$ by

$$\Delta\phi = \frac{2\pi}{3}\frac{c}{v_g}k\frac{\Delta(2b)}{f} \tag{6-31}$$

where $k \approx (1.0)$ MHz/0.001 in. For example, an error of 1° corresponding to a $\Delta(2b)$ of 0.0002 in. can easily be eliminated. In practice, all cavities were initially machined to a diameter nominally 0.0005 in. oversize. This assured that after allowing for machining tolerances, the correct tuning of all cavities could be achieved by external dimpling, as described above.

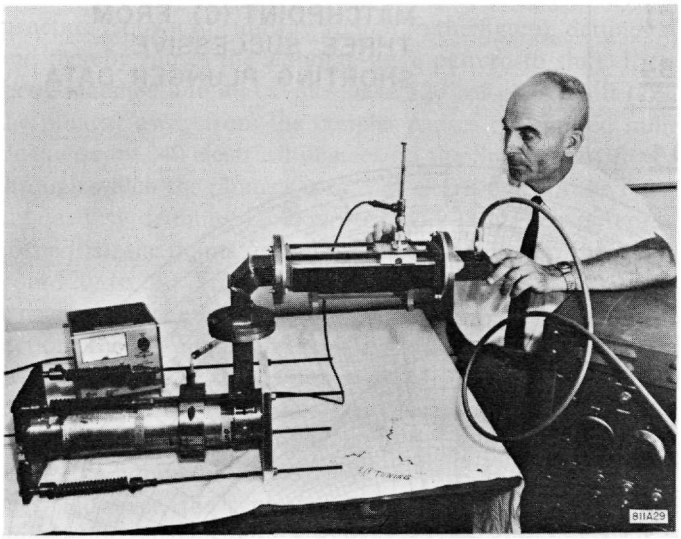

Figure 6-29 Experimental arrangement for tuning a short accelerator section, with illustration of tuning tool.

Because field lines can extend over a distance of three disks in the $2\pi/3$ mode configuration, tuning and matching strongly interact in the first cavities. It was pointed out[20] that this property can cause serious difficulties. If the coupler is not well matched, tuning the first cavities by bringing the points to the proper positions on the Smith chart can actually cause the following effect: successive cavities will have built-in cyclic phase errors $\Delta\phi_1$, $\Delta\phi_2$, $\Delta\phi_3$ which compensate for the reflection caused by the coupler. Since the VSWR for the nodal shift in the first cavities approaches infinity, the match point C is indistinguishable from the center O of the Smith chart, and the structure appears to be tuned and matched. In reality, a double or triple perodicity is built into the section, which causes passband splitting. It was predicted[20] that the split would occur at approximately the $\pi/2$ frequency for a $2\pi/3$ section. Precautions can be taken to avoid this possible ambiguity. One remedy consists of using a resistive plunger which even in the first cavities allows the position of the match point C to be identified. Another technique is to measure the phase of the wave reflected from the coupler and the adjacent (No. 1) cavity (assuming the dimensions of the latter cavity to be correct). By placing the tuning plunger alternately in cavities 1 and 2, the required condition of 120° phase shift per cavity may be approached iteratively by dimpling the coupler cavity and filing the coupling iris. In practice, this result was achieved by separately prematching the couplers with a perfect three-cavity assembly before final brazing of the section. A particular technique to prematch the coupler without a perfect three-cavity assembly has also been worked out[21] for particular use with a structure operating in the $2\pi/3$ mode.

In this technique it is necessary to know the frequency at which each cavity has $\pi/2$ phase shift. This method is useful in preventing any incorrect matching which could cause the incorrect tuning mentioned above.

A few additional remarks should be made:

1. The matching and tuning operation must be performed in a carefully temperature-controlled dry room. Sections should be allowed to stabilize thermally for several hours. Preferably, the tuning operation should be done with the section filled with dry air.

2. The detuning plunger should be light and clean in order to prevent damage or contamination of the disk edges. Notches should be provided so that the plunger always rests in the same relative position, or dwell point, around which small motions do not disturb the null. When tuning a constant-gradient section, where the $2a$ dimension changes as a function of length, the largest possible plunger compatible with the smallest $2a$ dimension should be used. It was verified that, in this manner, the dwell condition can be achieved in all cavities.

3. In the $2\pi/3$ mode it was found that moving the plunger by less than a full cavity away from the coupler causes the null on the slotted line to move toward the generator by one-half the phase shift introduced. This surprising effect is attributable to the manner in which the plunger detunes the cavity and not to any actual phase reversal. When the plunger finally moves into the dwell point in the next cavity, the null appears in the correct place.

4. Contrary to the early Mark III sections, the SLAC sections are provided with output couplers and loads to prevent a reflected wave from appearing at the klystron amplifiers. These couplers had to be tuned in the same manner as the input couplers, by switching over the whole experimental setup to the output coupler.

5. When an experimental section has been matched and tuned, three final RF checks are advisable: (1) The global match can be checked with a continuously movable short in the rectangular waveguide beyond the output coupler.[11] This measurement involves observing the image of two intersecting diameters on the Smith chart, transformed through the complete section including the two couplers. This image of the "iconocenter" must fall at the center of the chart. (2) The global match can be checked with a matched load at the output or input ends. (3) The attenuation can be measured globally for the entire section by direct substitution techniques, or for a part of the section by measuring the change in reflection coefficient as a function of plunger position.

Finally, it is often of interest to obtain a complete traveling-wave field plot for the entire accelerator section. This plot can be obtained by drawing a small metallic or dielectric needle along the axis of a disk-loaded waveguide structure which is excited at one end by a signal generator and matched at the other end with a load. The relative field amplitude is obtained by measuring either the reflection coefficient caused by the reflected wave from the bead, or the phase shift across the section caused by the forward-scattered wave from

the bead. The phase of the field can be measured by noting the phase of the reflection coefficient of the reflected wave.

It is interesting to note that if one wants to recheck the relative amplitude of the fundamental space harmonic ($a_0^2/\sum a_n^2$) by this method, both electric field amplitude and phase are needed, as shown by the derivation below. The total field is given by the expression

$$E_z(z, t) = \sum_{n=-\infty}^{n=+\infty} a_n(r) \exp[i(\omega t - \beta_n z)] \tag{6-32}$$

where β_n is the phase constant associated with the nth space harmonic. Integrating over the length of one cavity, one obtains

$$a_n = \frac{1}{d} \int_{-d/2}^{+d/2} E_z(z) \exp(j\beta_n z)\, dz \tag{6-33}$$

Notice, however, that E_z in this expression is a complex quantity of the form $|E_z(z)|e^{-j\theta(z)}$, where the plots of $|E_z(z)|$ and $\theta(z)$ are given by the perturbation measurements. Choosing the origin in the middle of a cavity and observing symmetry, it is then possible to obtain a_n and hence $a_0^2/\sum a_n^2$ by evaluating the integral

$$a_n = \frac{2}{d} \int_0^{d/2} |E_z(z)| \cos\,[\beta_n z - \theta(z)]\, dz \tag{6-34}$$

Generally, it is sufficient to calculate only three or four terms to obtain 1% accuracy.

It is also interesting to note why the traveling-wave measurement requires knowledge of both θ and $E_z(z)$ whereas the standing-wave measurement described above can be made with $E_c(z)$ alone. The reason is that in the cavity measurement, there are two waves traveling in opposite directions:

$$\begin{aligned} E_c(z, t) &= \sum_{n=-\infty}^{n=+\infty} a_n \exp[j(\omega t - \beta_n z)] + a_n \exp[j(\omega t + \beta_n z)] \\ &= \sum_{-\infty}^{+\infty} 2a_n \cos \beta_n z\; e^{(j\omega t)} \end{aligned} \tag{6-35}$$

Hence, a_n is given by

$$a_n = \frac{2}{\lambda} \int_0^{\lambda/2} E_c(z) \cos \beta_n z\, dz \tag{6-36}$$

where the quantity $E_c(z)$ is either positive or negative but contains no phase.

Dimensional correction made on the prototype section (RPB)

Final modifications in the dimensions of the disk apertures $2a$ (and accompanying changes in the cavity diameters $2b$) were made using data from completed 10-ft sections.[22] The technique consisted of comparing the

measured field variation and attenuation in a section with the field variation and attenuation required for a constant-gradient structure, taking into account the effect of beam loading. The original objective had been to arrive at a constant gradient with 10% beam loading. It was found, however, that this required too small a beam aperture. A minimum disk aperture of 0.750 in. was set, with the resulting structure having a constant gradient at about 5% loading.

For specified values of attenuation, fractional beam loading, and input power, and with known average shunt impedance of the structure, the ideal attenuation along the structure is given[23] by

$$A_n = \frac{1}{2}\frac{1}{(P_0/(\delta P)_{Tn}) - n}\left\{\frac{r_n i^2}{2(\delta P)_{Tn}} + 1 - \left[\left(\frac{r_n i^2}{2(\delta P)_{Tn}}\right)^2 + \frac{r_n i^2}{(\delta P)_{Tn}}\right]^{1/2}\right\} \quad (6\text{-}37)$$

where

A_n = loss due to dissipation in nth cavity (nepers)
P_0 = specified input power
$(\delta P)_{Tn}$ = power lost to beam and circuit in nth cavity
r_n = shunt impedance of nth cavity (assumed constant)
i = average beam current during pulse

Additionally, the average beam current during the pulse and the power lost to the beam and the circuit are obtained[24] from

$$i = (\text{fractional beam loading}) \cdot \left\{2\frac{(P_0 \sum_{n=0}^{N-1} r_n)^{1/2}(1 - e^{-2\tau})^{1/2}}{\sum_{n=0}^{N-1} r_n[1 - 2\tau e^{-2\tau}/(1 - e^{-2\tau})]}\right\} \quad (6\text{-}38)$$

and

$$(\delta P)_{Tn} = (\delta P)_{Bn} + \frac{(\delta P)_{Bn}^2}{i^2 r_n} \quad (6\text{-}39)$$

where $(\delta P)_{Bn}$, the energy absorbed by the beam in the nth cavity, is

$$(\delta P)_{Bn} = \frac{i}{N}\left\{\left(P_0 \sum_{n=0}^{N-1} r_n\right)^{1/2}(1 - e^{-2\tau})^{1/2} - \tfrac{1}{2} i \sum_{n=0}^{N-1} r_n\left(1 - \frac{2\tau e^{-2\tau}}{1 - e^{-2\tau}}\right)\right\} \quad (6\text{-}40)$$

Here τ is the total attenuation through the structure (nepers) without beam loading, and N equals total number of cavities in structure.

The power dissipated in the circuit is given by the term

$$\frac{(\delta P)_{Bn}^2}{i^2 r_n} \quad (6\text{-}41)$$

The desired values of circuit attentuation as represented by the A_n obtained from Eq. (6-37) were compared with values of A_n obtained from measurements of the relative field strength along the accelerator section and its

total attenuation. These measured values (denoted by primes) were obtained using

$$A_n' = A_0\left(\frac{E_n}{E_0}\right)^2 \exp\left(2\sum_{n=0}^{N-1} A_n'\right) \tag{6-42}$$

where E_n/E_0 is the relative strength in the nth cavity, and A_0, the loss in nepers in the first cavity due to RF dissipation, was determined, for use here, from the total attenuation measurement and data from the relative field strength plot. It is given by

$$A_0 = \frac{1 - e^{-2\tau}}{2\sum_{n=0}^{N-1}(E_n/E_0)^2} \tag{6-43}$$

The differences between the measured and required values of A_n in conjunction with group velocity measurements were used to obtain corrections for aperture diameter:

$$\Delta(2a)_n = \frac{(v_g/c)_n'[(A_n'/A_n) - 1]}{\partial(v_g/c)/\partial(2a)|_n} \tag{6-44}$$

Since changes in the disk aperture affect the phase velocity, they had to be compensated by corresponding changes in cylinder diameter ($2b$) using the relation

$$\Delta(2b) = \Delta(2a)\frac{\partial f/\partial(2a)}{\partial f/\partial(2b)} \tag{6-45}$$

The curves of $2a$ and $2b$ given in Fig. 6-22 for the thick disk case actually include the corrections made in accordance with the procedure just described. The numerical values for $2a$ and $2b$ are given in Table 6-6. These dimensions are predicated upon machining the copper disks and cylinders with the temperature of the cutting oil held at 65°F. The resulting temperature of the parts being machined was 69.7°F. Operation of the finished structure at a temperature of 113°F then results in a phase velocity in the structure equal to the velocity of light at a frequency of 2856 MHz.

The Coupler asymmetry problem and the "baba-abab" waveguide configuration (GAL)

The configuration of the waveguides feeding the accelerator, as illustrated in Fig. 5-17, was chosen as the best possible remedy to the problem of coupler asymmetry described in this section. This configuration follows the so-called baba-abab pattern, in which, looking downstream, an "a"-type waveguide feed comes from the left and a "b"-type feed comes from the right. Successive 40-ft girders alternate between the baba and the abab periodicity. How this fairly complicated configuration was arrived at is explained below.

In any normal accelerator cavity, the field configuration has cylindrical symmetry. However, the coupler cavity with its matching iris aperture is an

Table 6-6 Dimensions of constant-gradient accelerator section[a,b]

Cavity	*2b (in.)*	*2a (in.)*	*Cavity*	*2b (in.)*	*2a (in.)*	*Cavity*	*2b (in.)*	*2a (in.)*
Input coupler	3.0416[c]	0.7517[d]						
			29	3.2662	0.9631	58	3.2438	0.8713
1	3.2859	1.0323	30	3.2655	0.9603	59	3.2429	0.8677
2	3.2853	1.0300	31	3.2648	0.9575	60	3.2421	0.8640
3	3.2846	1.0277	32	3.2641	0.9547	61	3.2413	0.8603
4	3.2839	1.0254	33	3.2633	0.9518	62	3.2404	0.8565
5	3.2832	1.0231	34	3.2626	0.9489	63	3.2395	0.8527
6	3.2825	1.0207	35	3.2619	0.9460	64	3.2387	0.8488
7	3.2817	1.0183	36	3.2612	0.9431	65	3.2378	0.8449
8	3.2810	1.0159	37	3.2604	0.9401	66	3.2369	0.8409
9	3.2802	1.0135	38	3.2597	0.9371	67	3.2360	0.8369
10	3.2794	1.0111	39	3.2589	0.9341	68	3.2351	0.8329
11	3.2786	1.0087	40	3.2582	0.9310	69	3.2342	0.8288
12	3.2779	1.0063	41	3.2574	0.9279	70	3.2333	0.8246
13	3.2772	1.0039	42	3.2566	0.9248	71	3.2324	0.8204
14	3.2766	1.0015	43	3.2558	0.9217	72	3.2315	0.8161
15	3.2759	0.9991	44	3.2550	0.9185	73	3.2306	0.8117
16	3.2752	0.9967	45	3.2542	0.9153	74	3.2297	0.8072
17	3.2745	0.9943	46	3.2534	0.9121	75	3.2288	0.8027
18	3.2738	0.9918	47	3.2527	0.9089	76	3.2280	0.7981
19	3.2731	0.9893	48	3.2519	0.9056	77	3.2271	0.7934
20	3.2724	0.9868	49	3.2511	0.9023	78	3.2262	0.7886
21	3.2717	0.9843	50	3.2503	0.8990	79	3.2253	0.7836
22	3.2711	0.9817	51	3.2495	0.8956	80	3.2243	0.7786
23	3.2704	0.9791	52	3.2487	0.8922	81	3.2233	0.7735
24	3.2697	0.9765	53	3.2479	0.8888	82	3.2223	0.7682
25	3.2690	0.9739	54	3.2471	0.8854	83	3.2213	0.7628
26	3.2683	0.9712	55	3.2463	0.8819	84	3.2202	0.7573
27	3.2676	0.9685	56	3.2454	0.8784	Output coupler	3.1310[c]	0.7517
28	3.2669	0.9658	57	3.2446	0.8749	86		0.7517

[a] $2\pi/3$ mode, $\tau = 0.57$, $\rho = 0.1215$ in., $t = 0.2300$ in.

[b] Numbering convention: cavity numbers increase in the direction of beam travel; the dimension $2a$ opposite each cavity number is the diameter of the aperture in the up-beam disk of that cavity.

[c] The center for boring the half-wall of the input coupler cavity opposite the input waveguide has been displaced 0.1550 in. in a direction away from the waveguide. The purpose of this displacement is to compensate for the opening in the wall which allows power to flow into the cavity from the waveguide. The symmetry of the fields in the coupler cavity is thus approximately restored. The corresponding displacement for the output cavity is 0.0800 in.

[d] Beam entrance aperture into coupler.

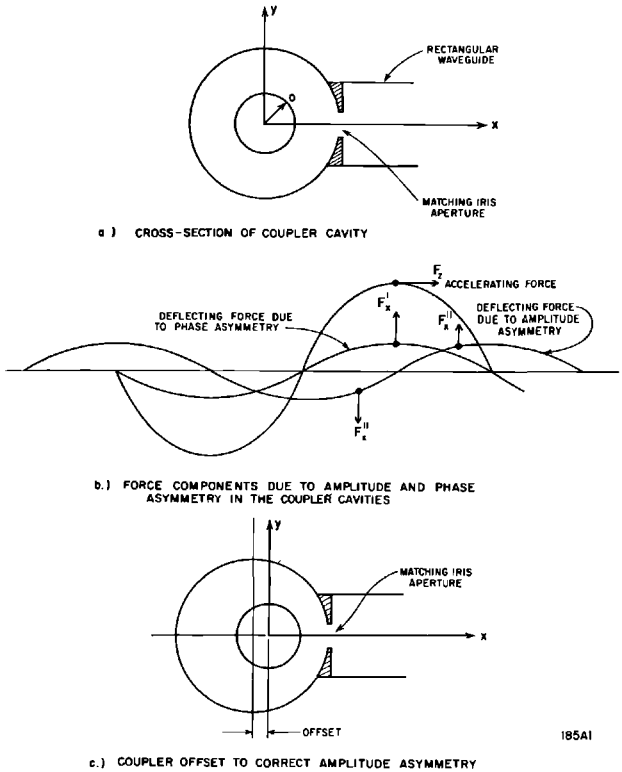

Figure 6-30 The coupler asymmetry problem.

exception. It had been known for a number of years that the longitudinal electric field in this cavity is slightly asymmetrical. Referring to Fig. 6-30a, E_z is somewhat larger on the right side, i.e., close to the iris, than on the left side. It had also been understood[25,26] that this transverse gradient of $|E_z|$ is equivalent to a magnetic field B_y which subjects the electrons to a Lorentz force F_x.

A subsequent examination of the E_z field by means of microwave perturbation measurements revealed that there were both amplitude and phase asymmetries in the transverse plane of the coupler. These measurements consisted of plotting both the amplitude and the phase of a wave reflected by a small longitudinal bead as a function of bead position in the coupler cavity. For an uncorrected cavity as shown in Fig. 6-30a, the amplitude asymmetry was of the order of 10% and the phase shift was of the order of 1.5° over the beam aperture.

To understand the effect of these asymmetries on the beam, let the spatial variation of E_z be of the form

$$E_z = \left[E_{z,0} + \frac{\Delta E}{2a}x\right] \exp\left[j\left(\frac{\Delta\phi}{2a}\right)x\right] \tag{6-46}$$

where ΔE and $\Delta\phi$ are the amplitude and phase variations in the x-direction over the aperture diameter $2a$ averaged from 0 to d, the cavity length. Then, to first order,

$$\frac{\partial E_z}{\partial x} = j\frac{\Delta\phi}{2a}E_{z,0}\exp\left[j\left(\frac{\Delta\phi}{2a}\right)x\right] + \frac{\Delta E}{2a}\exp\left[j\left(\frac{\Delta\phi}{2a}\right)x\right] \tag{6-47}$$

From Maxwell's equations, B_y and, hence, the Lorentz force F_x are both in time quadrature with $\partial E_z/\partial x$. Referring to Fig. 6-30b, the deflecting force F_x', caused by the phase asymmetry and proportional to $(\Delta\phi/2a)E_{z,0}$, is in phase with the accelerating force F_z; it produces a net deflection on a bunch traveling on the crest of the wave. On the other hand, the force F_x'', caused by the amplitude asymmetry and proportional to $(1/2a)(\Delta E/E_{z,0})E_{z,0}$, is in quadrature with the accelerating force F_z; its effect, as shown in an exaggerated form in Fig. 6-30b, is to spread transversely a bunch traveling on the accelerating wave crest. In practice, both of these effects occur simultaneously and are undesirable.

Using simple electrodynamics, it can be shown that the transverse momentum δp_x imparted to an electron traveling at an angle θ with respect to the accelerating wave crest through a coupler cavity of length d is given by

$$\delta p_x = \frac{eE_{z,0}\lambda d}{4\pi ac}\left[\Delta\phi\cos\theta + \frac{\Delta E}{E_{z,0}}\sin\theta\right] \tag{6-48}$$

This formula is also given in slightly different form in Eq. (7-107).

It was shown[26] that unless $\Delta E/E$ could be kept smaller than 0.1% and $\Delta\phi$ less than 0.06°, serious difficulties might arise in steering the beam over the 2-mile length. In particular, steering of multiple beams of different energies through accelerator sections which are powered for one beam (and hence cause a deflection) and unpowered for another (thus causing no deflection) would have been extremely difficult and probably impossible without pulsed steering magnets. To remedy these difficulties, several measures were taken.

1. Offsetting the coupler cavity as shown in Fig. 6-30c almost completely compensated for the amplitude asymmetry. The value of the offset was found through successive approximations using microwave perturbation measurements; for the input cavity it is 0.155 in. and for the output cavity, 0.080 in. Within the accuracy of the measurements, the value of $\Delta E/E$ was thereby reduced to 0.1% or less.

2. Attempts to compensate for the phase asymmetry inside the coupler cavity did not meet with a simple solution. Experiments which intentionally used slightly misaligned cavities were not successful in reducing $\Delta\phi$. The only practical solution appeared to be a symmetrically fed coupler cavity with two irises. However, such a solution would have been expensive and fairly impractical since it would have required an additional power splitter.

The baba-abab waveguide configuration shown in Fig. 5-17 is actually a practical version of the double iris coupler where the symmetrical feeding is

done on successive sections. Of all the alternative configurations, the abba-abba or baab-baab periodicities would have been the simplest because they would have re-established a parallel and axial beam over a 40-ft length. In practice, because of waveguide flange interferences, these configurations could not be adopted, and the baba-abab periodicity was chosen. Its only disadvantage is that over a 40-ft length, a beam entering on axis and parallel to it emerges parallel to the axis but with a net transverse displacement. The next 40-ft length produces the reverse effect and brings the beam back on axis. Hence this periodicity would require that klystrons be turned on and off in pairs so that over an 80-ft length the beam always remains on axis. In practice, this measure is never used. The effect is only serious at low energy in the first two or three sectors of the machine.[28] When a klystron must be turned off, the resulting steering effect is compensated by the dc magnetic steering dipoles available in the drift sections.

3. Although it was not possible to compensate for the phase asymmetry, its effect was reduced by causing the output coupler of a section to cancel part of the deflection created by the input coupler. Because the phase shift $\Delta\phi$ appears to be in the direction of power flow, this reduction in net deflection was obtained by having the input and output waveguide feeds on the same side. This remedy did not achieve total cancellation because the values of $(\Delta\phi/2a)_{\text{in}}$ and $(\Delta\phi/2a)_{\text{out}}$ differ by 30 to 40% in the constant-gradient structure.

6-3 Fabrication, assembly, and installation

Fabrication (ALE)

A number of techniques of fabricating disk-loaded waveguide capable of meeting the close tolerances necessary to obtain the correct phase and group velocities were explored at Stanford. Of the many methods considered, only three were ever used to construct accelerator sections, namely, shrinking, electroforming, and brazing. The shrinking method[2] was used at Stanford to construct the original 300-ft, 1-GeV accelerator (Mark III), but it was considered unsatisfactory for the SLAC machine when compared to the other two techniques.

Extensive work with electroforming and brazing demonstrated that satisfactory disk-loaded waveguide sections could be made by either of these techniques. The specification for maximum phase shift excursions at any point along the axis of a 10-ft section was set to $\pm 2.5°$. This corresponds to a mechanical tolerance of ± 0.00005 in. for $2b$; $+0.0002$ and -0.0000 in. for $2a$; ± 0.001 in. for d; ± 0.0002 in. for t; and ± 0.0005 in. for ρ (see Fig. 6-2). It is evident from these tolerances that special techniques had to be utilized if they were to be achieved economically.

The most exacting of the tolerances was the ± 0.00005 in. required for

the $2b$ dimension. The first step in meeting this requirement consisted of machining the parts that went into the assembly to a tolerance of $+0.0002$ and -0.0000 in. It was not sufficient simply to air-condition the room in which these parts were made; it was also essential that a temperature-controlled cutting solution be flowed over the parts during the machining operation. Hence, these parts were machined in an air-conditioned room and with a coolant oil, controlled within 0.25°C. After the assembly was completed, the equivalent of the 0.00005-in. tolerance was achieved by making slight deformations in the wall of each cavity as discussed briefly earlier in this chapter and described further below. This procedure was feasible with either the brazing or the electroforming methods of fabrication.

Satisfactory sections were obtained with both the electroforming and brazing techniques. However, extensive studies indicated that brazing was the preferable way of fabricating the 10,000 ft of disk-loaded waveguide. The decision to use the brazing technique was based primarily on the higher degree of flexibility inherent in this method; it required only a few hours to complete a brazed assembly, whereas it took 9 days to complete an electroformed assembly. However, it is significant to note that for the large-scale production required at SLAC, the cost of the electroforming technique was estimated to be the same as the cost of the brazing technique within the accuracy of the estimates. For the sake of completeness, descriptions of both fabrication techniques are included below.

Figure 6-31 shows an exploded view of the parts used for electroforming, together with a completed piece of disk-loaded waveguide made by this process. The first step in the electroforming method of fabrication was the assembly of a 10-ft array consisting of the copper disks and aluminum spacers shown in the figure. After the parts were assembled in a V-block, a mandrel was inserted through the holes to hold the assembly together. The assembly

Figure 6-31 Exploded view of parts assembled for the electroforming process.

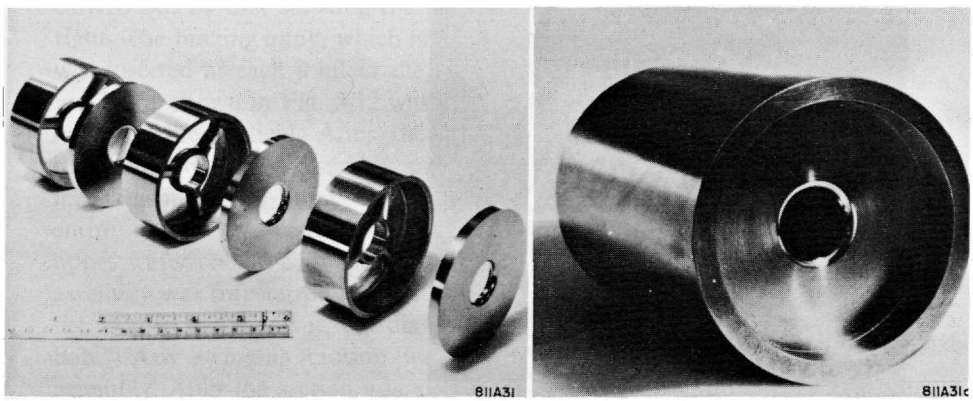

work was carried out under water to assure that the hydrostatic pressure was equalized, hence reducing the probability of solution leakage. After assembly, the array was chemically cleaned and processed, and a thickness of $\frac{3}{8}$ in. of copper was electroformed over it. Figure 6-32 shows the completed assembly in a copper sulfate electroforming bath. During this procedure, the mandrel was held horizontally with the assembly half-submerged in the solution. While plating, the assembly was rotated at approximately 30 rev/min. An agate burnisher was made to ride back and forth, continuously smoothing the surface of the plated copper. After the outer wall had been electroformed, the aluminum spacers were removed by etching in a sodium hydroxide solution. This procedure yielded an all-copper disk-loaded waveguide fabricated to very close dimensions. A comparison of the crystalline structure of copper electroformed by this technique with that of OFHC copper (oxygen-free high conductivity copper) produced by the usual, mill fabricating procedure showed that the metallurgical properties were very similar. Electroformed copper as it came from the bath had a surface finish of 6 μin. Nine days were required to deposit the $\frac{3}{8}$-in. wall thickness. Electroforming was used to produce a number of experimental 10-ft sections which exhibited excellent operating characteristics.

The study of various brazing techniques led to the development of a new type of furnace. The essential features of this furnace were a moving ring burner fired by an oxygen–hydrogen flame and a water-cooled chamber containing a reducing atmosphere in which the section was cooled. The essential

Figure 6-32 Assembly being electroformed.

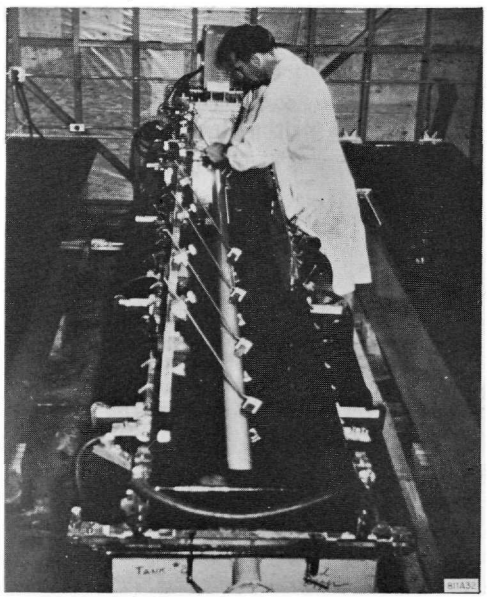

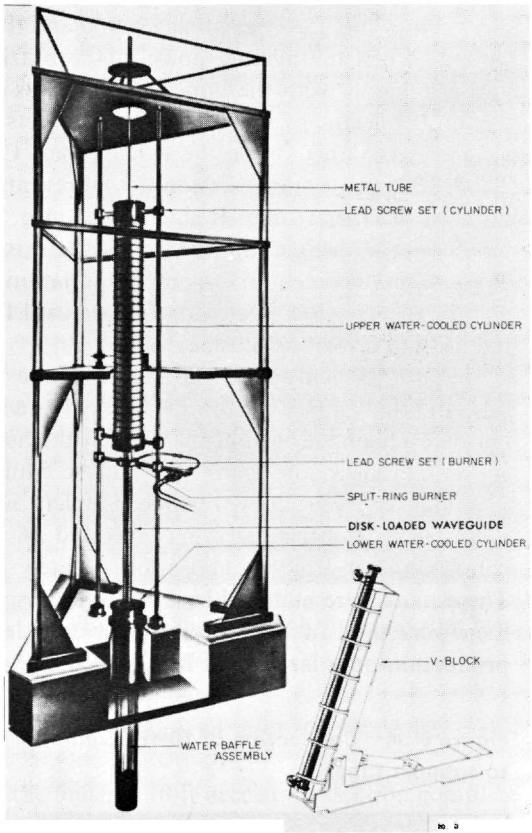

Figure 6-33 Schematic view of flame furnace.

features of the flame furnace are illustrated in Fig. 6-33 which shows a 10-ft section nearing the completion of the brazing cycle. The procedure was carried out by first stacking the parts in the V-block which is shown at the right. The brazing alloy, which is a silver–copper eutectic melting at 783°C, was inserted at each joint in the form of thin washers. The stacking of the unit parts shown in Fig. 5-12 was carried out while the V-block was at a 75° angle to the vertical. After the stacking was completed, a mandrel was inserted through the assembly and the end was clamped by a spring-loaded mechanism. The V-block was then tilted to the vertical position, and the entire assembly was moved into the furnace by means of a jib crane. The upper water-cooled cylinder was held in the fully raised position, while the assembly was transferred to the furnace and hooked onto a metal tube which then served to support it. The disk-loaded section then hung as a free "plumb bob." Any swinging motion was damped by means of the water baffle assembly. After the section was suspended, the split ring burner was closed

around the disk-loaded waveguide. The burner was then raised to the uppermost end of the disk-loaded waveguide and the oxygen–hydrogen burner was ignited. When the melting point of the brazing alloy was reached, the ring burner together with the upper cylinder was caused to move down the 10-ft section by means of the two lead screw sets. One lead screw set drove the cylinder, the other drove the ring burner. Oxidation of the interior of the disk-loaded waveguide section was prevented by flowing a reducing gas through the metal tube. Reducing gas also flowed into the upper cylinder, providing a reducing atmosphere for the exterior of the section. A period of 25 to 30 min was required from the initiation of the heating cycle to its completion. The section was ready for removal from the furnace $2\frac{1}{2}$ hours after the heating cycle was finished.

Figure 6-34 shows the connection of the 10-ft assembly to its supporting tube and the "nose" plate which served as a closure for the cylinder containing the reducing atmosphere in which the assembly was cooled. Figure 6-35 shows the furnace in operation with the flame on.

Input and output waveguide couplers were made up as separate subassemblies. Each subassembly consisted of the input or output waveguide coupler, the end flange, and approximately 8 in. of disk-loaded waveguide. These units were matched in advance as described earlier in this chapter and then were used in the stacking of a complete 10-ft section. Actually, once production on a large scale had started, the coupler parts were machined so

Figure 6-34 Connection of 10-ft assembly to support tube.

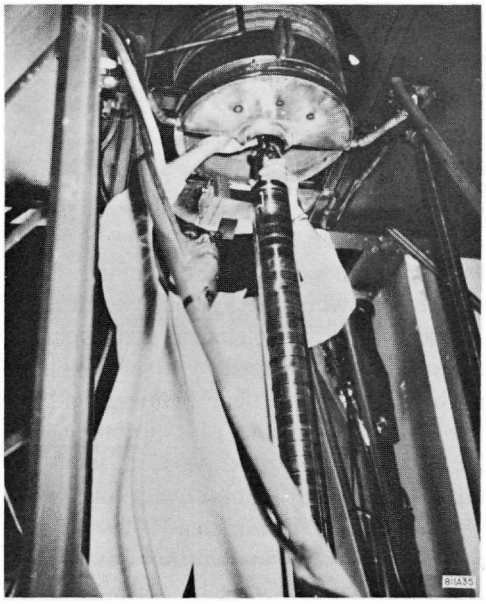

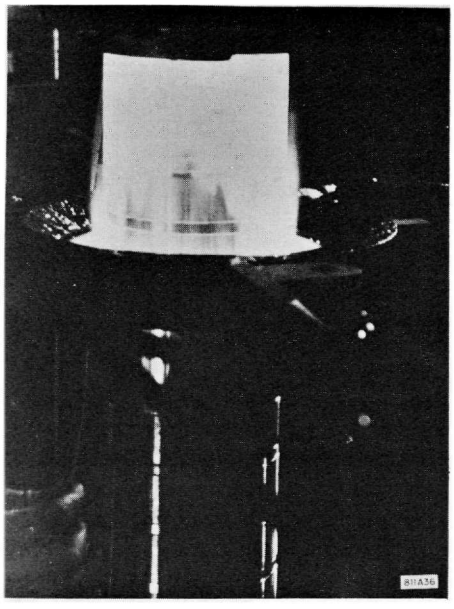

Figure 6-35 Furnace showing ring burner in operation.

accurately that no final matching was necessary to meet the maximum specified VSWR of 1.05.

Figure 5-13 shows a view of the finished 10-ft accelerator section complete with the water-cooling tubes which were attached by brazing in a separate furnace.

The maximum allowable phase tolerance per cavity of $\pm 2.5°$ was achieved by a tuning operation which consisted of indenting the walls of each cavity with four small dimples located at 90° about the axis. Figure 6-36 shows an overall view of the special tuning machine which was designed to tune the 10-ft accelerator sections while they were evacuated and at operating temperature. During the tuning procedure, the temperature was controlled to $\pm 0.1°F$. The inside diameters of the cylinders comprising the cavity walls were machined oversize, leaving approximately a 10° phase margin in each cavity for tuning.

The tuning apparatus consisted of the mechanism shown in Fig. 6-37 and a microwave bridge system[27] shown in block diagram form in Fig. 6-38. The bridge system consisted of a commercially available phase measuring unit which compared the signal reflected by a calibrated reference branch with that of a test branch containing the accelerator section. The unit utilized a double side-band suppressed-carrier technique. This technique was selected over other possible methods because it provided the required accuracy of approximately 0.1° phase and was not sensitive to changes in attenuation of

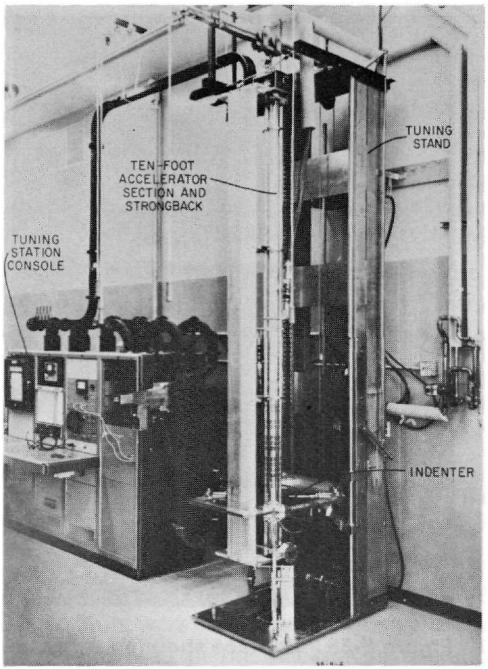

Figure 6-36 Overall view of the tuning machine.

the test signal with respect to the reference signal. Insensitivity to changes in attenuation was important because the amplitude of the wave reflected from the shorting plunger changed with the position of the plunger in the accelerator section. Furthermore, a unit was required that gave a direct phase readout so that the operator could monitor and control the amount of tuning required for each cavity. The mechanism by which the actual tuning was accomplished, illustrated in Fig. 6-37, worked in the following way: the movable carriage holding the indenters was indexed at the center of each cavity. Connected to the movable carriage was the expandable shorting plunger. The rod holding the plunger was coupled and indexed with the movable carriage by means of steel tapes. The indentation of the cavities was accomplished by means of four hydraulically driven cylinders which pushed the $\frac{3}{8}$-in. diameter indenters into the wall of the cavity. The plunger driving rod was made of Invar to insure dimensional stability in the location of the shorting plunger. Two O-ring seals allowed the rod to move into and out of the evacuated section.

The tuning of the section began with the installation of a 10-ft section as shown in Fig. 6-36. The reference arm of the bridge circuit was then calibrated by means of a reference standard which consisted of a precise, movable short with three calibrating positions corresponding to the three Smith chart

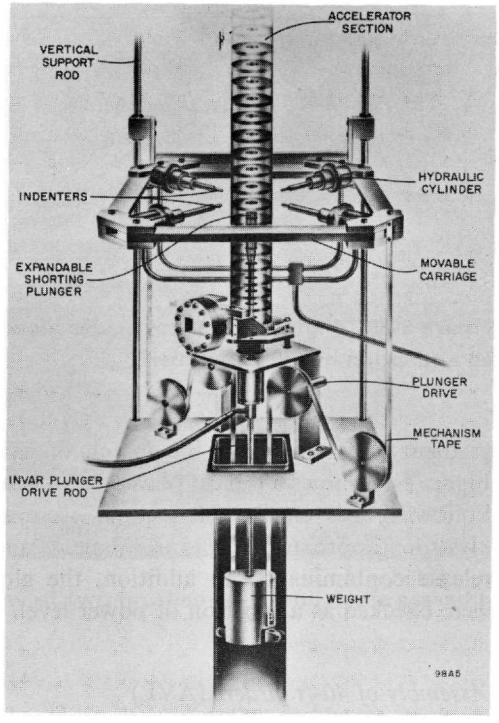

Figure 6-37 Tuning mechanism showing movable carriage and indenters.

branches for the $2\pi/3$ disk spacing of the accelerator structure. After calibration with the reference branch, the tuning of the individual cavities proceeded.

For quality control purposes, additional low-power measurements were made. Measurements were performed to check the phase of each cavity, the

Figure 6-38 Block diagram of the phase measuring system.

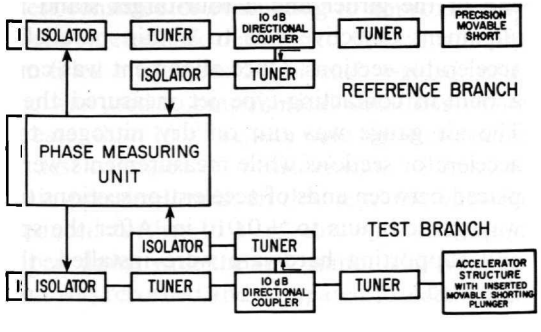

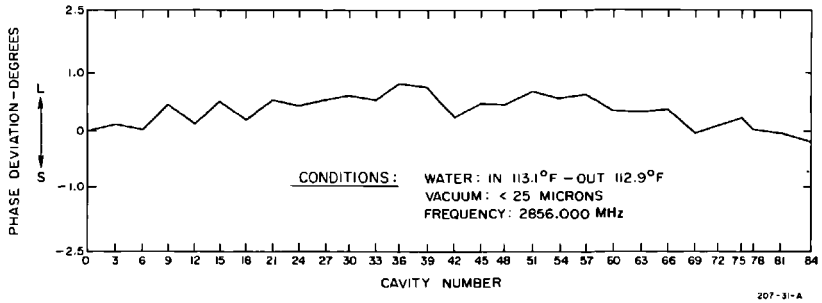

Figure 6-39 Plot of phase deviations along a 10-ft section after tuning, as a function of cavity number.

gradient along the axis, the match of each coupler, and the attenuation. Figure 6-39 shows a typical phase plot made during the quality control check. Following this check, the sections were subjected to high power from a klystron (approximately 15 MW peak and 15 kW average), primarily to release contaminants. In addition, the global phase shift and attenuation were checked as a function of power level.

Assembly of 40-ft girders (AVL)

The assembly and alignment of 40-ft lengths of accelerator were carried out in the shop (see Fig. 6-40) and these 40-ft segments were then installed in the accelerator housing. The accelerator sections were mounted on a 2-ft diameter, 40-ft long pipe which serves simultaneously as a vacuum envelope for the laser alignment system and as a support girder (see Chapter 22). Before placing the accelerator sections on the support girder, the girder was checked for vacuum leaks and the hardware for the laser alignment target was installed. The exterior of the sections was cleaned, one of the waveguide cap-off flanges was removed and a nitrogen purge line was connected, and the sections were then installed on the girder. The tooling provided for 6° of freedom, allowing the proper alignment of the sections on the girder. The alignment was achieved by means of a four-telescope alignment station at one end of the girder and a four-target stand at the opposite end. The initial alignment objective was to obtain parallelism of the mating faces of the accelerator sections. Once alignment was complete, a special air gauge using a built-in contacting-type jet measured the parallelism within ± 0.0001 in. The air gauge was run on dry nitrogen to prevent contamination of the accelerator sections while measurements were being made. Spacer rings were placed between ends of accelerator sections to adjust the distance between the waveguide inputs to ± 0.010 in. After the spacer rings and all the mounting and supporting hardware were installed, the special support tooling was removed.

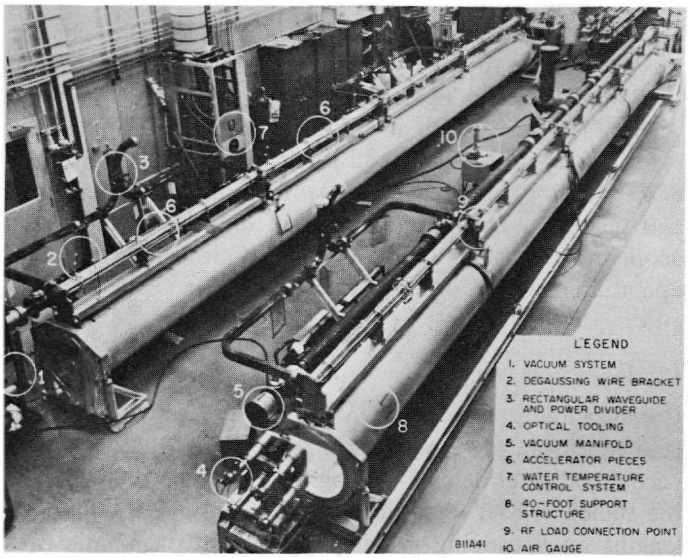

Figure 6-40 View of two finished 40-ft modules in assembly shop.

The vacuum manifold was then installed, and the accelerator sections were precisely aligned using the optical tooling holes in the 10-ft accelerator section supports. The alignment tolerance allowed only 0.001 in. displacement of any accelerator section relative to its adjoining section and a maximum of 0.005 in. total straightness error. Twist had to be avoided since the welded joints between 10-ft sections are extremely stiff in torsion, and once the weld was made, the error could not be removed. After alignment, the joints between 10-ft sections were welded using argon cover gas and nitrogen backing gas.

At this point, the rectangular waveguide S-assemblies (see Chapter 11) were installed, bolted to the waveguide input, and welded to the vacuum manifold. Then RF loads were added.

Following this installation, the assembly was vacuum tested. Two vacuum tests were performed. The first test consisted of evacuating to approximately 10^{-1} torr, connecting a mass spectrometer leak detector to the system, and leak checking by placing helium-filled enclosures about each welded, end-bolted joint. A fine helium probe was used to pinpoint leak locations where necessary. Any detected leaks (greater than 10^{-10} cc/sec) were repaired before proceeding. The second vacuum test consisted of measurements of pressure and time required to attain certain pressure levels. In this test, the vacuum was roughed down to 1 torr, reduced further to 10^{-4} torr with the liquid nitrogen thimble, and then pumped down with the ion pump. The time required to reach each pressure point was recorded and compared to a standard.

The vacuum envelope had to attain 3×10^{-7} torr in less than 8 hours to be acceptable. Upon completion of the vacuum checks, the accelerator was pressurized to 2 psig with dry nitrogen and pinched off.

Several parallel operations were carried out simultaneously with the vacuum tests. These included the connection of all plumbing to the accelerator sections, waveguides, and loads, and installation of magnetic shielding, demagnetizing, and degaussing wires. Final alignment was then carried out, and the girder assembly was loaded onto a transporter for the trip to the accelerator housing. A more detailed description of the girder assembly operation can be found in Reference 29.

Installation (AVL)

Completed girder assemblies were transported from the assembly area to the accelerator housing on a special trailer. The trailer length was adjustable to accommodate girders of varying lengths (from the 9-ft drift section girder to the standard 40-ft long girder) by placing girder support frames of various lengths on a running gear equipped with pneumatic tires. The maximum acceleration of the girder assembly in transit was specified to be 0.3 *g*. An accelerometer was mounted on the girders during transport and the dynamic loading was recorded. The maximum allowable loading of 0.3 *g* was not exceeded and nearly all girder assemblies were subjected to a dynamic loading of less than 0.2 *g*.

The girder assemblies were transported on the special trailer over the road to the west portal of the accelerator housing and up the aisle in the accelerator housing to their approximate final location. Two air-film supported pallets were then placed under the girder support frame and the running gear was removed. The air-film supported pallets allowed the entire assembly to be slipped sideways from the aisle into the beam line and adjusted to the correct position. Figure 6-41 shows a girder being moved from the aisle side of the accelerator housing into the beam line position. The girder was raised to the correct elevation by means of jacks built into the pallets. The girder weight was then transferred to the floor jacks, and the girder support frame and air-film supported pallets were removed.

After the girders were set in place and roughly aligned, connections were made to the penetration waveguides. The vacuum manifold was welded to the vacuum finger and to the vacuum manifold on the adjoining girders, and the beam line intergirder bellows were welded. When all the girders within a sector were installed and the vacuum system was completed as described above, the entire sector was evacuated. After evacuation and connection of the water-cooling lines to the accelerator sections and waveguide, the waveguide was phase tuned (see Chapter 11).

Subsequently, the downbeam end of each girder was accurately positioned with respect to the upbeam end of the following girder in the cross-joint alignment process. This process is described in Chapter 22. Upon completion,

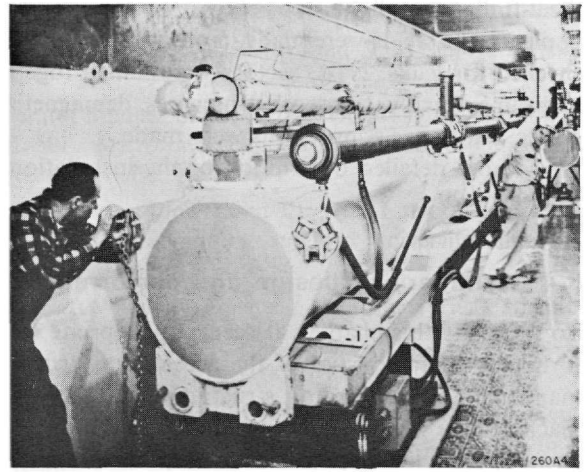

Figure 6-41 Positioning of a 40-ft girder in the accelerator housing.

Table 6-7 Final design and performance of the SLAC accelerator structure

No. of standard 10-ft sections	940
No. of 7-ft sections	12
No. of cavities in each 10-ft section	84 + 2 couplers
Distance between inputs of two consecutive sections on a girder	29λ or 87 cavities
Phase shift per cavity	$2\pi/3$
Operating frequency (nominal)	2856 MHz
Measured frequency for maximum electron energy at 113°F operating temperature	2855.980 MHz
Accelerator wall temperature increase with average input power	0.42°C/kW
Frequency change necessary to track temperature change	100 kHz/2°C
Normalized group velocity range, v_g/c	0.0204–0.0065
Range of shunt impedance r_0 (for fundamental space harmonic) in 10-ft section obtained by microwave measurements	53–60 megohms/meter
Attenuation parameter τ in 10-ft section	0.57
Filling time t_F	0.83 μsec
Efficiency[a] $K = V/P^{1/2}$, where V is in MeV per 10-ft section and P is in MW into the section	
Theoretical, based on $\bar{r}_0 = 56.5$ megohms/meter	10.75 MeV/(MW)$^{1/2}$
Experimental (average over entire accelerator)	10.65 MeV/(MW)$^{1/2}$
Beam loading derivative	35 MeV/mA

[a] When the output power from a single klystron supplying four 10-ft sections is referred to, the respective numbers are ≈20.2 and 20. The rectangular waveguide loss is ≈0.54 ± 0.1 dB.

the 2-ft diameter, light pipe bellows were inserted between girders and welded in place. The welds were made in one sector at a time and the sector was then checked for leaks. Next, sectors were joined together and checked for leaks in groups. Finally, the degaussing wires, demagnetizing wires, phase reference cables, and other connections were made.

A more detailed description of the installation process can be found in Reference 29.

6-4 Summary of design and performance (GAL)

To conclude this chapter, it seems appropriate to summarize the main performance characteristics of the accelerator structure. Of course, the performance of the accelerator structure cannot be divorced from that of the machine as a whole, and hence, many of the operational results have already been reported in Chapter 5. In retrospect, it can be said that, so far, the accelerator structure has lived up to all the expectations and specifications for which it was designed. It has failed only in one respect in that the cumulative, multisection-type of beam breakup was not foreseen in advance. This problem continues to be under intensive investigation as this book is being written and a detailed up-to-date discussion can be found in Chapter 7. The final design and performance data of the accelerator structure are summarized in Table 6-7.

Acknowledgments

The authors would like to thank those members of the Stanford Linear Accelerator Center staff who have contributed to the work reported here. In particular, they wish to acknowledge the contributions of O. Altenmueller, W. J. Gallagher, B. Kendall, A. Kirshbaum, C. Kruse, J. Abraham, L. Cain, R. Chapton, M. Heinz, D. Jeong, F. Patton, J. A. Pope, C. Rasmussen, D. Robertson, D. Rogers, K. Skarpaas, H. Soderstrom, and B. Stillman.

References

1 E. L. Ginzton, W. W. Hansen, and W. R. Kennedy, *Rev. Sci. Instr.* **19**, 89 (1948).

2 M. Chodorow *et al.*, *Rev. Sci. Instr.* **26**, 134 (1955).

3 R. B. Neal, "Theory of the Constant Gradient Linear Electron Accelerator," Rept. No. ML-513, Microwave Laboratory, Stanford University, Stanford, California (1958); and "Comparison of the Constant Gradient and Uniform Accelerator Structures," Rept. No. M-259, Stanford Linear Accelerator Center, Stanford University, Stanford, California (1961).

4 J. E. Leiss and R. A. Schrack, "Transient and Beam Loading Phenomena in Linear Electron Accelerators," Internal Report, Natl. Bur. Standards, Washington, D.C. (October 30, 1962).

5 M. G. Kelliher and R. Beadle, *Nature* **187**, 1099 (1960).

6 M. C. Crowley-Milling, T. R. Jarvis, C. W. Miller, and G. Saxon, *Nature* **191**, 483 (1961).

7 "Linear Electron Accelerator Studies; Status Rept. 1 October to 31 December, 1958," Rept. No. ML-581, Microwave Laboratory, Stanford University, Stanford, California (February 1959).

8 P. B. Wilson, "A Study of Beam-Blow up-in Electron Linacs," Rept. No. HEPL-297, High Energy Physics Laboratory, Stanford University, Stanford, California (June 1963).

9 R. Kingsland, Hughes Aircraft Company, Fullerton, California (private communication).

10 E. L. Ginzton, *Microwave Measurement*, McGraw-Hill, New York, 1957.

11 W. J. Gallagher, "Measurement Techniques for Periodic Structures," Rept. No. M-205, Stanford Linear Accelerator Center, Stanford University, Stanford, California (November 1960).

12 P. N. Robson, "Fourier Series Representations of Dispersion Curves for Circular Corrugated Waveguide Used in Traveling-Wave Linear Accelerators," Rept. No. 5105, Metropolitan-Vickers Electrical Company, Ltd., Manchester, England (1956).

13 W. R. Ayers, E. L. Chu, and W. J. Gallagher, "Measurements of Interaction Impedance in Periodic Circuits," Rept. No. ML-403, Microwave Laboratory, Stanford University, Stanford, California (June 1957).

14 "Linear Electron Accelerator Studies and Proposed Two-Mile Accelerator Project; (combined) Status Report, 1 October to 31 December 1960," Rept. No. M-246, Stanford Linear Accelerator Center, Stanford University, Stanford, California (January 1961).

15 K. B. Mallory, "A source of error in the use of slope detection for perturbation measurements," *Inst. Radio Engrs. Trans. Microwave Theory Tech.*, **10**, 146 (1962).

16 Renée Hirel, "Space-Harmonic Content of the $2\pi/3$ Accelerator Structure," Rept. No. M-270, Stanford Linear Accelerator Center, Stanford University, Stanford, California (1961).

17 G. A. Deschamps, *J. Appl. Phys.* **24**, 1046 (1953).

18 Kenneth Brandt Mallory, "A comparison of the predicted and observed performances of a billion-volt electron accelerator," Ph.D. Thesis, Stanford University, Stanford, California (1955), p. 68 *et seq.*

19 R. Belbéoch, "Problèmes posés par l'adaption du coupleur d'entrée d'une structure en guide chargé par des iris," Rept. No. LAL-13, Laboratoire de L'accélerateur Linéaire, Orsay, France (1961).

20 R. Kyhl (private communication).

21 E. Westbrook, "Microwave Impedance Matching of Feed Waveguides to the Disk-Loaded Accelerator Structure Operating in the $2\pi/3$ Mode," Tech. Note SLAC-TN-63-103, Stanford Linear Accelerator Center, Stanford University, Stanford, California (December 1963).

22 R. Borghi and D. Jeong, "Gradient Corrections for the SLAC Accelerating Structure," Tech. Note SLAC-TN-63-60, Stanford Linear Accelerator Center, Stanford University, Stanford, California (1963).

23 R. B. Neal, "Theory of the Constant Gradient Linear Electron Accelerator," Rept. No. ML-513, Microwave Laboratory, Stanford University, Stanford, California (1958), p. 4, Eq. (3.6).

24 R. B. Neal, "Comparison of the Constant Gradient and Uniform Accelerator Structures," Rept. No. M-259, Stanford Linear Accelerator Center, Stanford University, Stanford, California (1961), p. 5, Eq. (7).

25 R. H. Helm, "A Note on Coupler Asymmetries in Long Linear Accelerators," Rept. No. M-167, Stanford Linear Accelerator Center, Stanford University, Stanford, California (1960).

26 R. H. Helm, "Effects of Stray Magnetic Fields and RF Coupler Asymmetry in the Two-Mile Accelerator with Sector Focusing," Rept. No. SLAC-20, Stanford Linear Accelerator Center, Stanford University, Stanford, California (October 1963).

27 R. Borghi, F. Patton, and M. Heinz, Phase velocity adjustment of the SLAC accelerating structure (private communication).

28 SLAC Staff, "Consolidation of Results of Preliminary Beam Tests with Sectors 1 and 2," Rept. No. SLAC-50, Stanford Linear Accelerator Center, Stanford University, Stanford, California (1965).

29 A. Lisin, "Girder Assembly and Installation," Tech. Note SLAC TN-67-17, Stanford Linear Accelerator Center, Stanford University, Stanford, California (May 1967).

7

BEAM DYNAMICS

R. H. Helm, G. A. Loew, and W. K. H. Panofsky, Editor

This chapter deals with the general features of particle motion[1] through the standard sectors of the two-mile accelerator. The special problems associated with the injector and positron source are described in Chapters 8 and 16, respectively. The approach in this chapter is to identify those general features of particle motion which do not depend on details of design of the disk-loaded waveguide configuration. Emphasis is, therefore, placed on general formulation rather than detailed computation.

The first portion of the chapter deals with vacuum trajectories of single particles and thus ignores any effects that depend on beam intensity. The analysis is first made assuming no external focusing. Then the magnetic lens system now employed in the accelerator is taken into account. For this purpose the matrix formalism applying to beam transport problems is briefly reviewed; not only are orbits for the ideal accelerator derived, but the effects of misalignments and other perturbations are also studied.

The second part of the chapter deals with those phenomena resulting from the influence of the electron current upon individual particle behavior. The dominant item in this category is the beam breakup phenomenon which is discussed first in terms of a general asymptotic theory identifying the phenomena involved and is then examined through more detailed numerical computations. The chapter concludes with a summary of experimental observations taken to date on the beam breakup phenomena.

7-1 The "ideal" linear accelerator (WKHP)

Consider an ideal accelerator having cylindrical symmetry about the z axis. Let total differentiation with respect to z and referred to the moving electron be denoted by a prime ($'$); let γ be the energy of the electron in

units of the rest energy m. Equating the velocity of light c to unity yields

$$\gamma' = \frac{eE_z}{m} \tag{7-1}$$

where E_z is the axial component of the electric field. In this chapter, $\beta = (1 - 1/\gamma^2)^{1/2}$ will be used for the velocity and the usual notation will be adopted for the components of electric and magnetic fields. It will be assumed that γ and γ' are given functions of z, resulting from the integration of Eq. (7-1) in a given accelerating field E_z.

The radial equation of motion is[2,3]

$$(\beta\gamma r')' = \frac{e(\mathbf{E} + \boldsymbol{\beta} \times \mathbf{B})_r}{m\beta} \tag{7-2}$$

In the absence of external focusing, the electric and magnetic terms in Eq. (7-2) almost cancel for a traveling-wave accelerator in which the phase velocity of the wave matches the particle velocity; in the relativistic limit ($\beta \approx 1$) the right-hand side of Eq. (7.2) becomes small. Thus in the usual description all radial forces are neglected and the integral of Eq. (7-2) becomes

$$r = r_0 + \theta_0(\beta\gamma)_0 \int_{z_0}^{z} \frac{dz}{\beta\gamma} \tag{7-3}$$

where θ_0 is the slope dr/dz at an arbitrary starting point and the subscript zero identifies the values of the other variables at that point. If the energy gain is uniform, $\gamma = \gamma' z$, where γ' is constant; furthermore if the energy is sufficient to make $\beta \approx 1$, Eq. (7-3) becomes

$$r = r_0 + (\theta_0 z_0) \ln\left(\frac{z}{z_0}\right) \tag{7-4}$$

where z_0 is defined by $\gamma' z_0 = \gamma_0$. These logarithmic orbits are a simple consequence of the transverse momentum being a constant while the longitudinal momentum increases linearly; such a momentum relationship implies $r' = \theta_0 z_0/z$ from which Eq. (7-4) follows. Equation (7-4) can be interpreted in terms of an "effective length" L given by

$$L = z_0 \ln\left(\frac{z}{z_0}\right) \tag{7-5}$$

which would be the length given by $r = r_0 + \theta_0 L$, i.e., the length over which a corresponding radial excursion in the absence of acceleration would occur (Fig. 7-1). The quantity L will also be recognized as the "contracted" length of the accelerator as seen from a frame of reference moving with the electron.

The right-hand side of Eq. (7-2) does not vanish exactly in the relativistic limit. To illustrate this, the "paraxial" equation will be formed, carrying terms linear in r only. With this approximation, the transverse field components can be expressed in terms of the longitudinal electric field as follows.

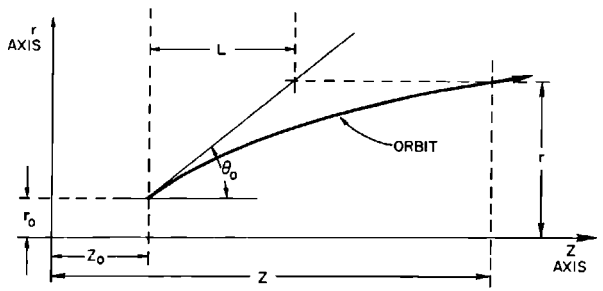

Figure 7-1 Orbit geometry.

In the absence of space-charge effects,

$$0 = \nabla \cdot \mathbf{E} = \frac{1}{r}\frac{\partial}{\partial r}(rE_r) + \frac{\partial E_z}{\partial z}$$

Therefore, remembering that E_z is circularly symmetric and thus has no first-order dependence on r, one obtains

$$-eE_r = \frac{er}{2}\frac{\partial E_z}{\partial z} = \frac{mr}{2}\frac{\partial \gamma'}{\partial z} \tag{7-6}$$

Similarly,

$$\frac{\partial E_z}{\partial t} = (\nabla \times \mathbf{B})_z = \frac{1}{r}\frac{\partial (rB_\phi)}{\partial r}$$

from which it follows that

$$eB_\phi = \frac{er}{2}\frac{\partial E_z}{\partial t} = \frac{mr}{2}\frac{\partial \gamma'}{\partial t} \tag{7-7}$$

Hence the general first-order paraxial equation of motions is*:

$$\begin{aligned}(\beta\gamma r')' &= -\frac{r}{2\beta}\left(\frac{\partial \gamma'}{\partial z} + \beta\frac{\partial \gamma'}{\partial t}\right) \\ &= -\frac{r}{2\beta}\left(\gamma'' - \beta^{-1}\gamma^{-2}\frac{\partial \gamma'}{\partial t}\right)\end{aligned} \tag{7-8}$$

since

$$\frac{d}{dz} \equiv ' = \frac{\partial}{\partial z} + \frac{1}{\beta}\frac{\partial}{\partial t}$$

is the total derivative with respect to z. As γ becomes large the last term

* Note that $(\mathbf{E} + \boldsymbol{\beta} \times \mathbf{B})_\phi = 0$, i.e., the Lorentz force has no azimuthal component.

vanishes (corresponding to cancelation of electric and magnetic forces in the relativistitic limit); the differential equation then becomes, with $\beta = 1$,

$$(\gamma r')' + \frac{r}{2}\gamma'' = 0 = \left(\gamma r' + \frac{r}{2}\gamma'\right)' - \frac{r'\gamma'}{2} \tag{7-9}$$

Integrating from a point denoted by the subscript zero to a final point, where the initial point is assumed to be in field-free space, one finds

$$\gamma r' - (\gamma r')_0 = \frac{1}{2}\int_{r_0}^{r} \gamma' \, dr - \frac{r}{2}\gamma'$$

or

$$\gamma r' - (\gamma r')_0 = \tfrac{1}{2}\{-r_0\overline{\gamma'} + r(\overline{\gamma'} - \gamma')\} \tag{7-10}$$

where $\overline{\gamma'}$ is a mean value of the rate of energy gain γ'. Hence the radial momentum differs from being a constant of the motion by the two terms on the right-hand side of Eq. (7-10). The first term $-\frac{1}{2}r_0\overline{\gamma'}$ represents the converging lens effect at the beginning of the accelerating region. The effective thin-lens focal length f_0 at entry is simply

$$\frac{1}{f_0} = +\frac{1}{2}\frac{\overline{\gamma'}}{\gamma} \tag{7-11}$$

The second term gives an alternating focusing–defocusing action due to the fluctuations in γ' about the mean value of $\overline{\gamma'}$. The result is a net "strong focusing" action the strength of which can easily be computed by conventional strong focusing theory. Note that even if the term in $\overline{\gamma'} - \gamma'$ is negligible within the accelerator section, the exit fringe field still contributes a radial impulse $+\frac{1}{2}r\overline{\gamma'}$ and is thus equivalent to a diverging lens of focal length

$$\frac{1}{f} = -\frac{1}{2}\frac{\overline{\gamma'}}{\gamma} \tag{7-12}$$

Thus the field-free gaps between sections are equivalent to weak, alternating gradient doublets. These effects will not be analyzed further here, since the strength of the radial forces discussed in this section for the parameters of the SLAC accelerator is small compared with the action of the external lenses which will be discussed in the next section.

7-2 External focusing (RHH)

In real accelerators the transverse position and quality of the beam are affected by numerous small perturbations, such as stray magnetic fields, misalignments, RF asymmetry effects, scattering by residual gas, and in some cases a transverse instability ("beam breakup") resulting from electromagnetic interaction with the accelerator structure. In addition, the finite phase space volume of the injected beam imposes limits on the distance the beam

can be transported before filling the entire radial aperture, even in an ideal accelerator.

External focusing is a practical means of containing the initial phase space which has the additional advantage of suppressing the various perturbing effects to a considerable extent. A major disadvantage arises from the beam deflection caused by misalignment of focusing lenses, which, therefore, must be aligned to very tight tolerances.

In the present section the principles of linac focusing are discussed, with special emphasis being given to problems affecting very long accelerators, and to the design of the focusing system for SLAC.

Phase space

The general definition of phase space volume which will be employed in this chapter is

$$U_6 = \iiint\iiint dx\, dp_x\, dy\, dp_y\, dt\, d\gamma \tag{7-13}$$

where (x, p_x), (y, p_y), and (t, γ) are the conjugate coordinate pairs appropriate to a Hamiltonian system in which the independent variable is the longitudinal coordinate, z, and in which there is no scalar potential.* According to Liouville's theorem, the coordinates of a given set of particles are contained in a volume which is invariant provided that only nondissipative forces act on the particles.

In beam transport (i.e., the motion of streams of charged particles through a complex accelerating, steering, and focusing system) it often happens that one or more components of the motion are decoupled from other motions, so that phase volumes are conserved in certain subspaces; e.g., the projected phase plane areas

$$u_x = \iint dx\, dp_x \qquad u_y = \iint dy\, dp_y \qquad u_t = \iint dt\, d\gamma \tag{7-14}$$

might each be conserved. Frequently the coupling between different components is weak enough to permit the use of perturbation calculations in which such subspace projections of the phase volume are conserved as a first approximation.

Because of the conservation, whether exact or approximate, the concept of phase space *emittance* of a beam source is useful as a figure of merit. For example, a small transverse emittance implies that the beam may be focused in such a way as to have simultaneously a moderate size and a very small transverse momentum, so that it may consequently be transmitted for long distances without further focusing. Small transverse emittance also implies

* If a scalar electric potential were present, the longitudinal canonical momentum could not be equated with the energy γ.

that the beam may be focused to very small size without excessive angular spread—a desirable property for allowing a small target size for physics experiments.

The concept of phase space is also useful in specifying the properties of a beam transport system. Here the *admittance*, the maximum phase space which can be transmitted through the system, serves as a figure of merit. Clearly, the emittance of the beam to be transmitted imposes a lower limit on the required transport system admittance.

The transverse emittance of the SLAC injector (described in Chapter 8) has been measured. It is found that 90% of the beam, in a projection of the phase volume on the x, p_x plane, is contained within an ellipse of area

$$u = 3.6\pi \times 10^{-3}\,(\mathrm{MeV}/c)(\mathrm{cm}) \tag{7-15}$$

To illustrate the effect of the initial phase space, suppose that the beam is injected as an erect ellipse in the x, p_x plane (solid curve in Fig. 7-2). Then if all transverse forces can be neglected, the transformation to a later point in the machine is given by

$$p_x = \text{constant} \qquad \text{and} \qquad x = x_0 + \zeta p_{x_0}$$

where

$$\zeta(z, z_0) = \int_{z_0}^{z} dz'/P(z') \tag{7-16}$$

and $P(z)$ is the longitudinal momentum.

It is then readily shown that the maximum size of the transformed ellipse is given by

$$x_{\max} = [(x_0)^2_{\max} + \zeta^2 (p_0)^2_{\max})]^{1/2} = \left((x_0)^2_{\max} + \zeta^2 \left[\frac{u}{\pi (x_0)_{\max}}\right]^2\right)^{1/2} \tag{7-17}$$

As an example, consider uniformly accelerated relativistic electrons, for which $P/m = \beta\gamma \cong \gamma$, $\gamma' = d\gamma/dz = \text{constant}$, and $\zeta = (1/m\gamma') \ln(\gamma/\gamma_0)$. Taking

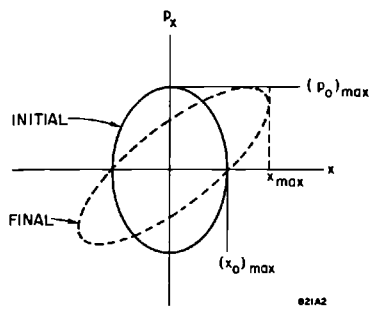

Figure 7-2 Injection of initial phase space as erect ellipse.

$m\gamma' = 0.06$ MeV/cm, $m\gamma_0 = 35$ MeV, $m\gamma = 18$ GeV, $u = 3.6\pi \times 10^{-3}$ (MeV/c)(cm), and the initial beam size $(x_0)_{max} = 0.5$ cm, it is found from Eq. (7-17) that

$$x_{max} = 0.81 \text{ cm}$$

On the other hand, if the beam were initially accelerated to 2 GeV and allowed to coast the rest of the way through the machine, the result would be

$$x_{max} = 1.63 \text{ cm}$$

It is evident that very little focusing along the machine would suffice to contain the small emittance of the injector. However, the positron system (Chapter 16), with a design admittance of 0.15π (MeV/c)(cm), imposes a much stronger focusing requirement. Further, as will be seen, a rather large admittance is also desirable for transport of the normal electron beam because of the various perturbing effects.

Formulation of the ideal accelerator focusing and transport system

THE EQUATION OF MOTION. Consider first an ideal system in which there are no misalignments or other perturbing effects. It will be assumed that the x and y motions are decoupled, e.g., any focusing elements presumably would be magnetic quadrupoles of which the symmetry planes include the x and y axes. The first-order paraxial equation of motion for a typical transverse coordinate, x, is of the form

$$p_x' = (Px')' = xC(z) \tag{7-18}$$

where

$$C \approx 0 \text{(in a drift section or an accelerator section)} \tag{7.19}$$

or

$$C = e\frac{\partial B_y}{\partial x}\left(\text{in a quadrupole field of transverse gradient } \frac{\partial B_y}{\partial x}\right) \tag{7-20}$$

THE MATRIX FORMULATION.[4,5,6,7,8] Because the differential equation (7-18) is linear and homogeneous, its solution may always be written as a linear transformation

$$\begin{aligned} x(z) &= a_{11}(z)x_0 + a_{12}(z)p_{x_0} \\ p_x(z) &= a_{21}(z)x_0 + a_{22}(z)p_{x_0} \end{aligned} \tag{7-21}$$

or in matrix notation

$$\begin{bmatrix} x \\ p_x \end{bmatrix} = \begin{bmatrix} a_{11} & a_{12} \\ a_{21} & a_{22} \end{bmatrix} \begin{bmatrix} x_0 \\ p_{x_0} \end{bmatrix} \tag{7-22}$$

which may be written schematically as

$$\mathbf{x} = \mathbf{A}\mathbf{x}_0 \tag{7-23}$$

The determinant of any transport matrix is unity; e.g., in the present 2×2 representation

$$|\mathbf{A}| = a_{11}a_{22} - a_{12}a_{21} = 1 \tag{7-24}$$

Combinations of transport elements then are generated by the usual rules of matrix multiplication.

THE PERIODIC SYSTEM. If the elements of a transport system repeat periodically, then

$$\mathbf{A}(n, 0) = \mathbf{A}^n \tag{7-25}$$

where $\mathbf{A}(n, m)$ is the transformation from the mth to the nth reference plane, and $\mathbf{A}$ is the transformation for one period. The resulting well-known eigenvector problem for a 2×2 matrix has the solution

$$\tilde{x}_n = \tilde{x}_0 e^{in\theta} \tag{7-26}$$

where the eigenvalues $e^{\pm i\theta}$ are given by*

$$\cos\theta = \tfrac{1}{2}(a_{11} + a_{22}) \tag{7-27}$$

and a suitable representation of the eigenvector, if θ is real, is

$$\tilde{x}_n = x_n - \frac{i}{\sin\theta}\left[\tfrac{1}{2}(a_{11} - a_{22})x_n + a_{12}p_{xn}\right] \tag{7-28}$$

The betatron phase shift is invariant under translation of the reference planes; in fact, for any nonsingular transformation $\mathbf{T}$ it is easy to show that the trace of the transformed matrix is conserved. Thus

$$b_{11} + b_{22} = a_{11} + a_{22} \tag{7-29}$$

where

$$\mathbf{B} = \mathbf{T}^{-1}\mathbf{A}\mathbf{T} \tag{7-30}$$

Two conclusions may be drawn from Eqs. (7-26) through (7-28): (1) The condition for stable orbits is that θ be real, i.e.,

$$\begin{aligned} &|a_{11} + a_{22}| < 2 \text{ means stable orbits} \\ &|a_{11} + a_{22}| > 2 \text{ means divergent orbits} \end{aligned} \tag{7-31}$$

(2) The quantity

$$\begin{aligned} |\tilde{x}_0|^2 = |\tilde{x}_n|^2 &= x_n^2 + \frac{a_{12}^2}{\sin^2\theta}\left[p_{xn} + \frac{a_{11} - a_{22}}{2a_{12}}x_n\right]^2 \\ &= \frac{a_{12}}{\sin^2\theta}\left[-a_{21}x_n^2 + (a_{11} - a_{22})x_n p_{xn} + a_{12}p_{xn}^2\right] \end{aligned} \tag{7-32}$$

is invariant as a function of n.[9]

* In the accelerator literature, the parameter θ is commonly called the *betatron phase shift*.

Now in the case of stable orbits it is evident that the curve $|\tilde{x}_n|^2 = \text{constant}$ represents an ellipse in the (x_n, p_{xn}) phase plane. The area of this ellipse is†

$$u = \frac{\pi \sin \theta}{a_{12}} |\tilde{x}_n|^2 \tag{7-33}$$

From Liouville's theorem we conclude that the phase plane area u is invariant, so that

$$u = \frac{\pi \sin \theta}{a_{12}} |\tilde{x}|^2 = \frac{\pi}{\sin \theta} [-a_{21}x^2 + (a_{11} - a_{22})xp_x + a_{12}p_x^2] \tag{7-34}$$

may be considered to remain invariant under an arbitrary translation of the periodic reference planes.

The maximum amplitude of a given orbit is thus

$$x_{\max}^2 = \frac{a_{12}^*}{\sin \theta} \frac{u}{\pi} \tag{7-35}$$

where $|a_{12}^*|$ is the value of $|a_{12}|$ maximized with respect to translation of the reference planes. The admittance, U, of the periodic system is designated as the area of the maximum phase ellipse which can be transmitted through the defining aperture; e.g., in a system of constant aperture, a,

$$U = \pi a^2 \frac{\sin \theta}{a_{12}^*} \tag{7-36}$$

Physically, in a transport system consisting of lenses and drift spaces, the maximum orbit size always occurs in a converging lens.

ADIABATICALLY VARYING (ALMOST PERIODIC) SYSTEM. The next case to be considered is a repetitive transport system which is almost periodic in the sense that the matrix elements, dependent on parameters such as lens strengths, beam energy, and spacing of reference planes, vary slowly from period to period. Since the characteristic function u given by Eq. (7-34) is an invariant, the transformation

$$\mathbf{A}(n, 0) = \mathbf{A}(n, n-1)\mathbf{A}(n-1, n-2) \cdots \mathbf{A}(1, 0) \tag{7-37}$$

has an approximate eigenvector solution

$$\tilde{x}_n \cong \tilde{x}_0 \left(\frac{\sin \theta}{a_{12}}\right)_0^{1/2} \left(\frac{a_{12}}{\sin \theta}\right)_n^{1/2} e^{i\mu_n} \tag{7-38}$$

where

$$\mu_n = \sum_{m=1}^{n} \theta_m$$

and θ_n and $\tilde{x}_n$ are defined by Eqs. (7-27) and (7-28) but with the matrix elements now dependent upon the index n.

† The sign of $\sin \theta$ is defined to be the same as that of a_{12}.

The function u defined by Eq. (7-34) now becomes an adiabatic invariant. The local maximum orbit size is given by Eq. (7-35). The admittance of the system is defined by

$$U = \pi\left(\frac{a^2 \sin\theta}{a_{12}}\right)_{\min} \tag{7-39}$$

where the minimum value which the function takes anywhere in the system is to be used.

The beam is said to be *optically matched* to the transport system if the beam phase space distribution is matched as nearly as possible to the characteristic admittance ellipse, Eq. (7-34). The transverse fluctuations in beam size then are minimized. The adiabatic invariance of the characteristic admittance ellipse implies that a beam which is initially optically matched to the system will remain matched through an adiabatically varying system.

TYPICAL TRANSPORT ELEMENTS.[10,11] The accelerator transport system elements are accelerator sections and drift sections containing magnetic quadrupoles. In the representation being used, the dynamic vectors are

$$\mathbf{x} = \begin{bmatrix} x \\ p_x \end{bmatrix} \quad \text{and} \quad \mathbf{y} = \begin{bmatrix} y \\ p_y \end{bmatrix} \tag{7-40}$$

Transfer matrices for these basic transport elements will now be given.

DRIFT AND ACCELERATOR SECTIONS. To the approximation that radial forces may be neglected, the transformation from z_1 to z_2 is

$$\begin{bmatrix} 1 & \zeta \\ 0 & 1 \end{bmatrix} \tag{7-41}$$

where ζ is given by Eq. (7-16), i.e.,

$$\zeta = \frac{1}{m\gamma'} \ln \frac{\gamma_2}{\gamma_1} \tag{7-42a}$$

for relativistic electrons accelerated by a uniform energy gradient, and

$$\zeta = \frac{z_2 - z_1}{P} \cong \frac{z_2 - z_1}{m\gamma} \tag{7-42b}$$

for electrons at constant energy.

QUADRUPOLES.[1,12,13] The following definitions are needed:

$$\left.\begin{aligned} Z &= \text{effective length of quadrupole field} \\ Q &= \text{"quadrupole strength"} = e\int \frac{\partial B_y}{\partial x}\, dz \\ k &= \left(\frac{e}{P}\frac{\partial B_y}{\partial x}\right)^{1/2} \end{aligned}\right\} \tag{7-43}$$

The appropriate transformations through the quadrupole are

$$\begin{bmatrix} \cos kZ & \dfrac{\sin kZ}{kP} \\ -kP \sin kZ & \cos kZ \end{bmatrix} \quad \text{(in the focusing plane)} \tag{7-44a}$$

and

$$\begin{bmatrix} \cosh kZ & \dfrac{\sinh kZ}{kP} \\ kP \sinh kZ & \cosh kZ \end{bmatrix} \quad \text{(in the defocusing plane)} \tag{7-44b}$$

If small-angle expansions ($kZ \ll 1$) are used, the matrix corresponding to two equal drift spaces and one "thin" lens may be written as the product of three matrices, as follows:

$$\begin{bmatrix} 1 & \zeta_2 \\ 0 & 1 \end{bmatrix} \begin{bmatrix} 1 & 0 \\ -P/f & 1 \end{bmatrix} \begin{bmatrix} 1 & \zeta_1 \\ 0 & 1 \end{bmatrix} \tag{7-44c}$$

where

$$\zeta_1 = \zeta_2 = \frac{1}{2}\frac{Z}{P}\left(1 + \frac{QZ}{12P} \cdots\right) \tag{7-45}$$

and

$$\frac{P}{f} = Q\left(1 - \frac{QZ}{6P} \cdots\right) \tag{7-46}$$

with the understanding that $Q > 0$ in the focusing plane and $Q < 0$ in the defocusing plane. In the present discussion it will turn out that the expansion parameter, $QZ/P \approx Z/f$, is always small and the quadrupole is optically equivalent to a thin lens at its geometric center.

IDEAL PROPERTIES OF ALTERNATIVE ACCELERATOR TRANSPORT SYSTEMS. Three different systems have been analyzed for magnetic focusing in the accelerator at SLAC: (1) the *alternating singlet* system, consisting of alternating gradient quadrupole singlets at the beginning of each 40-ft girder; (2) the *sector doublet* system, a quadrupole doublet in each of the drift sections* at the ends of the 333⅓-ft sectors; (3) the *sector triplet* system, a quadrupole triplet in each drift section.

Two variations of each of the sector focusing schemes were studied, one in which the quadrupoles of the multiplet were spread as far apart as possible in the 10-ft drift section and one in which the quadrupoles were placed essentially end-to-end. The latter alternative proved undesirable† not only

* See "The 10-ft Girder Components" under Section 7-3.

† An exception occurs in the positron transport system (Chapter 16) where a number of compact multiplets are used in matching the large phase space of the positron beam into the standard accelerator focusing system.

because of greater quadrupole power requirements but also because of tighter alignment tolerances. Consequently, only the widely spaced doublet and triplet cases will be considered here.

ALTERNATING SINGLETS. The basic section is shown in Fig. 7-3. In this discussion, the quadrupoles are treated as thin lenses and the reference planes are placed just ahead* of them. The two types of quadrupoles are assumed to have the same strengths and to be equally spaced along the machine. The relative energy change is assumed to be small so that a parameter l can be defined such that

$$l \cong \int_{z_1}^{z_1+L} \frac{dz}{P} \cong \int_{z_1+L}^{z_2} \frac{dz}{P} \cong \frac{L}{P} \cong \frac{L}{m\gamma} \tag{7-47}$$

The transfer matrix for one section is

$$\mathbf{A} = \begin{bmatrix} 1 & l \\ 0 & 1 \end{bmatrix} \begin{bmatrix} 1 & 0 \\ Q & 1 \end{bmatrix} \begin{bmatrix} 1 & l \\ 0 & 1 \end{bmatrix} \begin{bmatrix} 1 & 0 \\ -Q & 1 \end{bmatrix} \tag{7-48}$$

$$= \begin{bmatrix} 1 - Ql - Q^2l^2 & 2l(1 + \frac{1}{2}Ql) \\ -Q^2l & 1 + Ql \end{bmatrix} \tag{7-49}$$

where the quadrupole strength Q is defined by Eq. (7-43). The betatron phase shift, by Eq. (7-27), is

$$\cos\theta = 1 - \tfrac{1}{2}Q^2l^2 \tag{7-50}$$

It may be shown that the present choice of reference planes maximizes the a_{12} matrix element. [Refer to Eq. (7-22).] Therefore, if the amplitude is limited by the system aperture to a value a, the admittance of the system as defined in Eq. (7-39) is given by

$$U = \frac{\pi}{2} Qa^2 \left(\frac{1 - \frac{1}{2}Ql}{1 + \frac{1}{2}Ql}\right)^{1/2} \tag{7-51}$$

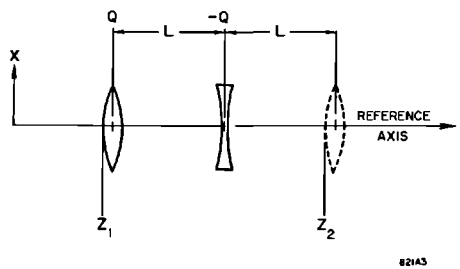

Figure 7-3 Typical period of alternating singlet system.

* The expression "just ahead," as used here and subsequently, should be interpreted to mean at the beginning of the effective length Z [see Eq. (7-43)], i.e., "squaring off" the fringing field.

The admittance as a function of quadrupole strength for a fixed value of the spacing parameter l is maximized for $Ql = \sqrt{5} - 1$. Under this condition, the optimum admittance becomes

$$U_{\text{opt}} = 0.300 \frac{\pi a^2}{l} \tag{7-52}$$

and the betatron phase shift is

$$\theta_{\text{opt}} = \cos^{-1}(\sqrt{5} - 2) = 76.34^\circ \tag{7-53}$$

which implies a wavelength of 9.44 L.

A stop band occurs if $Ql \geq 2$, where the admittance and betatron phase shift become imaginary. Therefore, a *low-energy* cutoff occurs at

$$m\gamma_{\text{co}} \approx P_{\text{co}} \approx \tfrac{1}{2}QL \tag{7-54}$$

In the high-energy limit, $Ql \to 0$ and the asymptotic admittance U_∞ becomes, from Eq. (7-51)

$$U_\infty = \lim_{Ql \to 0} U = \frac{\pi}{2} Qa^2 \tag{7-55}$$

SECTOR DOUBLETS. Figure 7-4 shows the basic section in the plane of initial focusing (the **x** plane). The transfer matrix per sector in this case is

$$\mathbf{A} = \begin{bmatrix} 1 - Qd - Q^2\lambda\, d & \lambda + d + Q\lambda\, d \\ -Q^2\, d & 1 + Q\, d \end{bmatrix} \tag{7-56}$$

where

$$d = \frac{D}{P} \qquad \text{and} \qquad \lambda = \int_{z_1 + D}^{z_2} \frac{dz}{P} \approx \frac{\Lambda}{P} \tag{7-57}$$

As noted above, the present choice of reference planes maximizes the a_{12} matrix element. The matrix from z_1 to z_2 in the initially defocusing (**y**) plane results from Eq. (7-56) by changing the sign of Q. The maximum value of the

Figure 7-4 Typical period of sector doublet system; the period $(\Lambda + D)$ = total length of one sector.

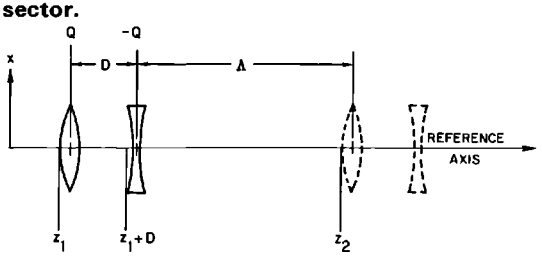

821A4

a_{12} matrix element is the same in the **y** plane as in the **x** plane, but occurs when the basic period is defined so that the doublet is located at the end of it rather than at the beginning. In either case, the sector doublet has the following properties:

Betatron phase angle,

$$\cos\theta = 1 - \tfrac{1}{2}Q^2\lambda\, d \tag{7-58}$$

Admittance,

$$U = \pi Q a^2 \frac{[(d/\lambda)(1 - \tfrac{1}{4}Q^2\lambda\, d)]^{1/2}}{1 + d/\lambda + Q\, d} \tag{7-59}$$

Low-energy cutoff,

$$(Q^2\lambda\, d)_{co} = 4$$

or

$$m\gamma_{co} \approx P_{co} \approx \tfrac{1}{2}Q(\Lambda D)^{1/2} \tag{7-60}$$

Asymptotic admittance as $\gamma \to \infty$,

$$U_\infty = \frac{\pi Q a^2}{1 + D/\Lambda}\left(\frac{D}{\Lambda}\right)^{1/2} \tag{7-61}$$

If the doublet is treated as a thin lens, i.e., if

$$D \ll \Lambda \qquad \text{and} \qquad Qd \ll 1$$

the admittance is optimized with respect to quadrupole strength when $(Q^2\lambda\, d)_{opt} \approx 2$. It follows from this that

$$\begin{aligned} U_{opt} &\approx \frac{\pi a^2/\lambda}{1 + (2D/\Lambda)^{1/2}} \\ &\approx \pi Q a^2\left(\frac{D}{2\Lambda}\right)^{1/2} \cong \left(\frac{1}{2}\right)^{1/2} U_\infty \end{aligned} \tag{7-62}$$

and $\theta_{opt} \approx \pi/2$ (betatron wavelength = 4 sectors).

SECTOR TRIPLETS. The sector triplet period is shown in Fig. 7-5 in the plane of initial focusing (the **x** plane). The transfer matrix is

$$\mathbf{A} = \begin{bmatrix} 1 - Q^2\lambda\, d\left(1 + \frac{1}{2}\frac{d}{\lambda} - \frac{1}{2}Q\, d\right) & \lambda + d + \tfrac{1}{2}Q\, d^2 - \tfrac{1}{2}Q^2\lambda\, d^2 \\ -Q^2\, d(1 - \tfrac{1}{2}Q\, d) & 1 - \tfrac{1}{2}Q^2\, d^2 \end{bmatrix} \tag{7-63}$$

where λ and d are defined as in the doublet case. The reference planes have again been chosen to maximize the a_{12} matrix element.

In the **y** plane (initially defocusing), the orbit maxima would occur at the center of the triplet rather than at the ends; however, in the present application, it is assumed that the quadrupole has sufficiently larger aperture than

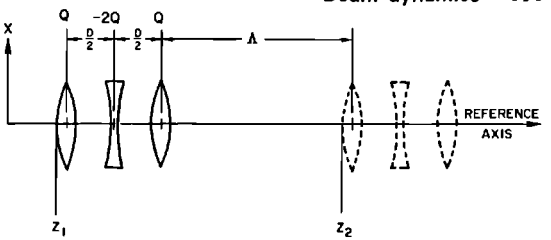

Figure 7-5 Typical period of sector triplet system; the period ($\Lambda + D$) = total length of one sector.

the accelerator so that the ends of the triplet essentially define the limiting aperture. Hence, the above matrix with reversed sign of the quadrupole strength Q is appropriate for calculating the y plane properties.

The properties of the sector triplet are

Betatron phase shift,

$$\cos\theta_{x,y} = 1 - \frac{1}{2}Q^2\lambda\, d\left(1 + \frac{d}{\lambda} \mp \frac{1}{2}Q\, d\right) \tag{7-64}$$

Admittance,

$$U_{x,y} = \pi Q a^2 \left(\frac{d}{\lambda}\right)^{1/2} \frac{\{(1 + d/\lambda \mp \frac{1}{2}Q\, d)[1 - \frac{1}{4}Q^2\lambda\, d(1 + d/\lambda \mp \frac{1}{2}Q\, d)]\}^{1/2}}{1 + d/\lambda \pm \frac{1}{2}Q\, d^2/\lambda - \frac{1}{2}Q^2 d^2} \tag{7-65}$$

Asymptotic admittance as $\gamma \to \infty$,

$$U_\infty = \pi Q a^2 \left(\frac{D}{\Lambda}\right)^{1/2} \tag{7-66}$$

Assuming that the lenses are thin, so that $d/\lambda \ll 1$ and $Q\, d \ll 1$, the following approximate results may be derived:

Low-energy cutoff,

$$m\gamma_{co} \approx P_{co} \approx \tfrac{1}{2}Q(\Lambda D)^{1/2} \tag{7-67}$$

Optimum quadrupole strength,

$$(Q^2\lambda\, d)_{opt} \approx 2 \tag{7-68}$$

$$(U_{x,y})_{opt} \approx \frac{\pi a^2}{\lambda}$$

$$\approx \pi Q a^2 \left(\frac{D}{2\Lambda}\right)^{1/2} \approx \left(\frac{1}{2}\right)^{1/2} U_\infty \tag{7-69}$$

$$\theta_{opt} = \pi/2 \text{ (betatron wavelength} = 4 \text{ sectors)}$$

NUMERICAL COMPARISON OF FOCUSING SYSTEMS. Some typical numerical properties of the three systems discussed above are listed in Table 7-1. The following parameters are assumed:

L = spacing of alternating singlets = 12 meters
D = center-to-center length of multiplets = 2 meters
$\Lambda \approx$ sector length = 100 meters
a = radius of defining aperture = 0.85 cm

A typical asymptotic admittance of 0.3π (MeV/c)(cm) has been chosen to be compatible with the positron transport system (Chapter 16) for which the design admittance is 0.15π (MeV/c)(cm).

Another comparison is seen in Table 7-2, in which the locations of the *equivalent planes* of the system are shown. Employing the well-known equivalent-plane expansion yields

$$\begin{bmatrix} a_{11} & a_{12} \\ a_{21} & a_{22} \end{bmatrix} = \begin{bmatrix} 1 & -\zeta_2 \\ 0 & 1 \end{bmatrix} \begin{bmatrix} 1 & 0 \\ -P/F & 1 \end{bmatrix} \begin{bmatrix} 1 & \zeta_1 \\ 0 & 1 \end{bmatrix} \tag{7-70}$$

where $P/F = -a_{21}$, $\zeta_1 = (a_{22} - 1)/a_{21}$, and $\zeta_2 = (1 - a_{11})/a_{21}$. Here ζ_1 and ζ_2 are measures of the distances to the equivalent plane from the respective ends of the system.

A number of conclusions may be drawn from the comparisons listed in Tables 7-1 and 7-2:

1. All of the three systems considered are capable of adequate asymptotic (high-energy) admittance with quadrupoles of rather trivial size.

Table 7-1 Typical optical properties of alternative transport systems

Properties	*Alternating singlet*	*Sector doublet*[a]	*Sector triplet*[a]
Quadrupole strength[b] for $U_\infty = 0.3\pi$(MeV/c)(cm)			
per quadrupole	2.7 kG	9.7 kG	9.7, 19.4, 9.7 kG
per sector	22 kG	19.4 kG	38.8 kG
gradient[c]	0.68 kG/in.	2.4 kG/in.	2.4 kG/in.
Low-energy cutoff for $U_\infty = 0.3\pi$(MeV/c)(cm)	0.49 GeV	2.1 GeV	2.1 GeV
Beam energy at which $U_{opt} = 0.15\pi$(MeV/c)(cm)	0.83 GeV	2.1 GeV	2.1 GeV
Quadrupole strength at which $U_{opt} = 0.15\pi$ (MeV/c)(cm)	2.8 kG	6.8 kG	6.8, 13.6, 6.8 kG
Limiting admittance through Sector 2 ($m\gamma_1 = 0.6$ GeV, $m\gamma_2 = 1.2$ GeV)	0.11π(MeV/c)(cm)	0.05π(MeV/c)(cm)	0.06π(MeV/c)(cm)

[a] Doublet and triplet properties are based on the thin-lens approximation.
[b] Quadrupole strength is defined as gradient times effective length (Eq. 7-43).
[c] It is assumed that the singlet and doublet quadrupoles have effective lengths of 4 in. and that the triplet quadrupole effective lengths are 4, 8, and 4 in.

2. The singlets and doublets require comparable total quadrupole strength per sector and the triplets about twice as much. The singlet system would be considerably more expensive in initial cost because of the larger number of quadrupoles (8 per sector vs 2 or 3 for sector multiplets).
3. The singlets would, however, require considerably less total excitation power because the gradients are smaller.
4. The singlet system is appreciably broader band, i.e., for a given asymptotic admittance, the cutoff energy is lower.
5. The triplet has a rather strong appeal because of the fact that the equivalent planes are located very close to the physical center of the lens; i.e., the triplet acts very much like an ideal thin lens.
6. The triplet also has slightly larger admittance than the doublet [compare Eqs. (7-62) and (7-69)] amounting to a factor of 1.2 in the above example.

The general conclusion from these comparisons is that there is no compelling reason for deciding among the alternative systems on the basis of ideal beam optics alone. The problems of tolerances in magnet construction and alignment will now be considered as a possible basis for a choice.

Effects of quadrupole misalignments[14,15]

GENERAL NOTATION. Misalignments and other extraneous effects will tend to perturb the electrons from their ideal orbits. Using the matrix notation

Table 7-2 Location of equivalent planes relative to initial plane

			Numerical[b]	
	General formula[a]	*Optimal focusing*	*x plane (meters)*	*y plane (meters)*
Alternating singlet				
ΔZ_1[c]	$\mp f$	$\mp \dfrac{L}{\sqrt{5}-1}$	−9.7	9.7
ΔZ_2	$L \mp f$	$L \mp \dfrac{L}{\sqrt{5}-1}$	2.3	21.7
Sector doublet				
ΔZ_1	$\mp f$	$\mp \frac{1}{2}(\Lambda D)^{1/2}$	−7.1	7.1
ΔZ_2	$D \mp f$	$D \mp \frac{1}{2}(\Lambda D)^{1/2}$	−5.1	9.1
Sector triplet				
ΔZ_1	$\dfrac{D}{2 \mp D/f}$	$\dfrac{D/2}{1 \mp (D/\Lambda)^{1/2}}$	(1 + 0.165)	(1 − 0.124)
ΔZ_2	$D - \Delta Z_1$	$D - \Delta Z_1$	(1 − 0.165)	(1+ 0.124)

[a] $f = P/Q$ = quadrupole singlet focal length.

[b] Numerical values are for the optimal focusing case.The parameters as given in the text are $L = 12$ meters, $D = 2$ meters, $\Lambda = 100$ meters.

[c] ΔZ_1 and ΔZ_2 are defined as follows [see Eq. (7-70)]:

$\Delta Z_1 = P\zeta_1$

$\Delta Z_2 = P\zeta_2 + 2L$ (alternating singlets)

$= P\zeta_2 + \Lambda + D$ (sector multiplets)

employed previously [Eq. (7-21) ff.], one obtains

$$\mathbf{x}_n = \mathbf{A}(n, n-1)\mathbf{x}_{n-1} + \delta\mathbf{x}_n \tag{7-71}$$

where the perturbation vector,

$$\delta\mathbf{x}_n = \begin{bmatrix} \delta x_n \\ \delta p_{xn} \end{bmatrix} \tag{7-72}$$

depends on the local imperfections in a manner which need not be specified for the moment.

Equation (7-71) is readily expanded to the formal solution

$$\mathbf{x}_n = \mathbf{A}(n, 0)\mathbf{x}_0 + \sum_{m=1}^{n} \mathbf{A}(n, m)\,\delta\mathbf{x}_m \tag{7-73}$$

which may be written alternatively

$$\mathbf{x}_n = \mathbf{X}_n + \boldsymbol{\xi}_n \tag{7-74}$$

where

$$\mathbf{X}_n \equiv \begin{bmatrix} X_n \\ P_{xn} \end{bmatrix} = \mathbf{A}(n, 0)\mathbf{X}_0 \tag{7-75}$$

$$\boldsymbol{\xi}_n \equiv \begin{bmatrix} \xi_n \\ \rho_n \end{bmatrix} = \sum_{m=1}^{n} \mathbf{A}(n, m)\,\delta\mathbf{x}_m \tag{7-76}$$

That is, the perturbed orbit is given by the sum of the unperturbed solution $\mathbf{X}_n$ and a perturbation term $\boldsymbol{\xi}_n$ which is a particular solution of the inhomogeneous difference equation (7-71) under the boundary condition $\mathbf{x}_0 = 0$.

PERIODIC OR ALMOST PERIODIC (ADIABATIC) SYSTEM. For a periodic or adiabatic system, the complex eigenvector solution may be written in terms of equations which are analogous to Eqs. (7-26) through (7-28), (7-37), and (7-38). Thus

$$\tilde{X}_n \approx \tilde{X}_0 \left(\frac{\sin\theta}{a_{12}}\right)_0^{1/2} \left(\frac{a_{12}}{\sin\theta}\right)_n^{1/2} e^{i\mu_n} \tag{7-77}$$

$$\tilde{\xi}_n \approx \left(\frac{a_{12}}{\sin\theta}\right)_n^{1/2} \sum_{m=1}^{n} \left(\frac{\sin\theta}{a_{12}}\right)_m^{1/2} \delta\tilde{x}_m e^{i(\mu_n - \mu_m)} \tag{7-78}$$

where

$$\tilde{X}_n \equiv X_n - i\left[\frac{1}{2}\left(\frac{a_{11} - a_{22}}{\sin\theta}\right)_n X_n + \left(\frac{a_{12}}{\sin\theta}\right)_n P_{xn}\right] \tag{7-79}$$

$$\delta\tilde{x}_n \equiv \delta x_n - i\left[\frac{1}{2}\left(\frac{a_{11} - a_{22}}{\sin\theta}\right)_n \delta x_n + \left(\frac{a_{12}}{\sin\theta}\right)_n \delta p_{xn}\right] \tag{7-80}$$

$$\tilde{\xi}_n \equiv \xi_n - i\left[\frac{1}{2}\left(\frac{a_{11} - a_{22}}{\sin\theta}\right)_n \xi_n + \left(\frac{a_{12}}{\sin\theta}\right)_n \rho_n\right] \tag{7-81}$$

INDEPENDENT RANDOM ERRORS. If the errors in different focusing sections are random and uncorrelated, the mean square amplitude perturbation of the orbit may be estimated as

$$\langle \xi_n^2 \rangle = \tfrac{1}{4}\langle (\tilde{\xi}_n + \tilde{\xi}_n^*)^2 \rangle = \tfrac{1}{2}\langle |\tilde{\xi}_n|^2 + \operatorname{Re} \tilde{\xi}_n^2 \rangle \tag{7-82}$$

since, from Eq. (7-81), ξ_n is the real part of $\tilde{\xi}_n$. Then, by Eqs. (7-76) and (7-78),

$$\langle \xi_n^2 \rangle \approx \frac{1}{2}\left(\frac{a_{12}}{\sin\theta}\right)_n \sum_{m=1}^{n} \left(\frac{\sin\theta}{a_{12}}\right)_m \{\langle |\delta\tilde{x}_m|^2 \rangle + \operatorname{Re}\{\langle \delta\tilde{x}_m^2 \rangle \exp[2i(\mu_n - \mu_m]\}\} \tag{7-83}$$

The oscillatory term in Eq. (7-83) makes only a small contribution if the sum is over a number of orbit wavelengths; hence a fair estimate of $\langle \xi_n^2 \rangle$ is

$$\langle \xi_n^2 \rangle \approx \frac{1}{2}\left(\frac{a_{12}}{\sin\theta}\right)_n \frac{1}{\pi} \sum_{m=1}^{n} \langle \delta u_m \rangle \tag{7-84}$$

where the phase space increment $\langle \delta u_n \rangle$ is defined by

$$\langle \delta u_n \rangle = \pi\left(\frac{\sin\theta}{a_{12}}\right)_n \langle |\delta\tilde{x}_n|^2 \rangle \tag{7-85}$$

$$\langle \delta u_n \rangle = \frac{\pi}{\sin\theta_n}\{-a_{21}\langle \delta x^2 \rangle + (a_{11} - a_{22})\langle \delta x\, \delta p_x \rangle + a_{12}\langle \delta p_x^2 \rangle\}_n \tag{7-86}$$

from Eq. (7-32).

Error analysis of alternative transport systems

ELEMENTARY PERTURBATIONS DUE TO ACTUAL QUADRUPOLE ERRORS. The effects of the principal error components in an individual quadrupole are presented below. Application to specific systems will be given in later paragraphs. (See Fig. 7-6 for definition of the misalignment components.)

1. *Transverse displacement.* The perturbation vector (Eq. 7-72) is readily found by a transformation from the symmetry axis of the quadrupole to the reference axis. The result referred to the quadrupole principal plane is

$$\delta\mathbf{x} = \begin{bmatrix} \delta x \\ \delta p_x \end{bmatrix} = \begin{bmatrix} 0 \\ Q \end{bmatrix}\varepsilon \tag{7-87}$$

using the lowest-order thin-lens approximation (Eq. 7-44c). The momentum impulse, $Q\varepsilon$, is of course just the line integral of eB_y at a distance ε from the quadrupole axis.

2. *Skew, or rotation about a transverse axis.* The perturbation is again calculated by a simple coordinate transformation. To the lowest-order lens thickness approximation, the result is

$$\delta\mathbf{x} \approx \frac{Q\,\Delta Z}{12P}\varepsilon'\begin{bmatrix} -2 \\ Q \end{bmatrix} \tag{7-88}$$

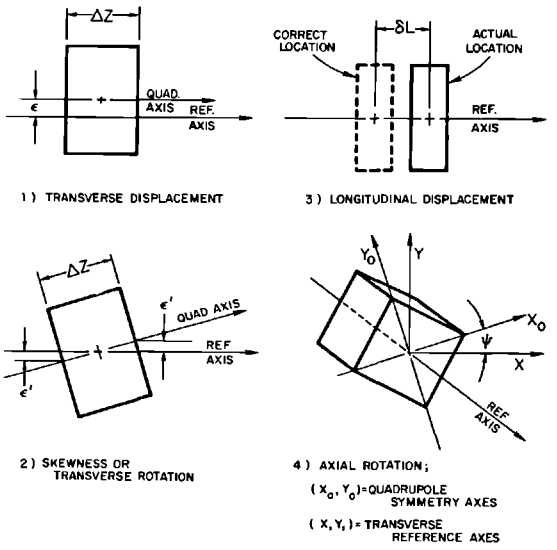

Figure 7-6 Quadrupole misalignment components. 821A6

(Note that ε' is defined as the transverse displacement of the ends of the quadrupole relative to the center.) The effect becomes very small in thin lenses, for which $\Delta Z \ll P/Q$, were P/Q is the quadrupole focal length.

3. *Longitudinal displacement.* By transforming the perturbed orbits to the unperturbed reference plane, it is found to first order that the displacement is

$$\delta \mathbf{x} \approx -\frac{Q\,\delta Z}{P}\mathbf{X} \tag{7-89}$$

where $\mathbf{X}$ is the unperturbed orbit just ahead of the quadrupole.

4. *Axial rotation.* In this case the perturbation introduces a coupling between x and y motions. Again, as a first-order approximation, it is found that for an axial rotation ψ,

$$\delta \mathbf{x} \approx -2QY\psi\begin{bmatrix}0\\1\end{bmatrix} \tag{7-90}$$

where Y is the unperturbed orbit amplitude in the y plane.

5. *Quadrupole strength error.* In the thin-lens approximation, the perturbation is

$$\delta \mathbf{x} = -X\,\delta Q\begin{bmatrix}0\\1\end{bmatrix} \tag{7-91}$$

where the quadrupole strength error δQ might result from an error in construction or in excitation current.

SAMPLE CALCULATION FOR RANDOM TRANSVERSE DISPLACEMENTS IN THE ALTERNATING SINGLET SYSTEM. As an illustration of the general method used in calculating orbit perturbations and error tolerances, consider the alternating singlet system with transverse displacement errors as shown schematically in Fig. 7-7.

The unperturbed transformation is given by Eq. (7-48). The net perturbation is found by transforming the effect of the individual impulses, given by Eq. (7-87), to the end of the section:

$$\delta \mathbf{x}_n = \begin{bmatrix} 1 & l_n \\ 0 & 1 \end{bmatrix} \begin{bmatrix} 1 & 0 \\ Q_n & 1 \end{bmatrix} \begin{bmatrix} 1 & l_n \\ 0 & 1 \end{bmatrix} \begin{bmatrix} 0 \\ Q_n \end{bmatrix} \varepsilon_{n_1} + \begin{bmatrix} 1 & l_n \\ 0 & 1 \end{bmatrix} \begin{bmatrix} 0 \\ -Q_n \end{bmatrix} \varepsilon_{n_2}$$

$$= \begin{bmatrix} 2Ql(1 + \frac{1}{2}Ql) \\ Q(1 + Ql) \end{bmatrix}_n \varepsilon_{n_1} - \begin{bmatrix} Ql \\ Q \end{bmatrix}_n \varepsilon_{n_2}$$

Assuming that the errors are random and uncorrelated, i.e.,

$$\langle \varepsilon_{n_1} \rangle^2 = \langle \varepsilon_{n_2} \rangle^2 \qquad \text{and} \qquad \langle \varepsilon_{n_1} \varepsilon_{n_2} \rangle = 0$$

the elementary phase space increment defined by Eq. (7-86) may be calculated; the result is

$$\langle \delta u_n \rangle = \frac{4\pi Q_n \langle \varepsilon^2 \rangle}{(1 - \frac{1}{4}Q_n^2 l_n^2)^{1/2}} \tag{7-92}$$

Hence, the mean-square orbit displacement, by Eq. (7-84), is

$$\langle \xi_n^2 \rangle \approx \frac{4}{Q_n} \left(\frac{1 + \frac{1}{2}Q_n l_n}{1 - \frac{1}{2}Q_n l_n} \right)^{1/2} \sum_{m=1}^{n} \frac{Q_m \langle \varepsilon^2 \rangle}{(1 - \frac{1}{4}Q_m^2 l_n^2)^{1/2}} \tag{7-93}$$

If the beam is coasting at constant energy with equal quadrupole settings, the result is

$$\langle \xi_n^2 \rangle = \frac{4n \langle \varepsilon^2 \rangle}{1 - \frac{1}{2}\frac{QL}{m\gamma}} \qquad \begin{cases} Q_n = Q = \text{constant} \\ \gamma_n = \gamma = \text{constant} \end{cases} \tag{7-94}$$

Figure 7-7 Alternating singlet system with transverse displacement.

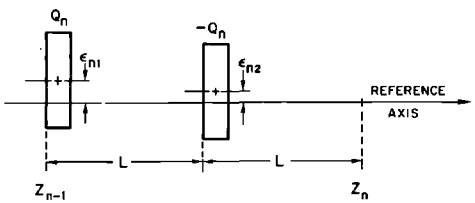

The beam would be very unstable if the beam energy were near the stop band, where $QL/m\gamma \approx 2$, but would be rather insensitive to energy above the optimum condition, i.e., if from Eq. (7-51) $Ql \leq \sqrt{5} - 1$.

SUMMARY OF QUADRUPOLE ERRORS AND ESTIMATE OF TOLERANCES. The basic algebra and the elementary perturbation expressions developed in the preceding paragraphs have been used to analyze the effects of various quadrupole errors for the alternative focusing systems and to assign tolerances to the error components on the basis of allowable beam perturbation.

In the case of doublets and triplets, certain correlations appear among the errors in the elements of a multiplet because of motions of the common supporting member. Figure 7-8 shows some of the error components associated with the multiplet systems, whereas Fig. 7-6 shows the basic components of independent quadrupole misalignment.

The misalignments considered here arise from the essentially random effects of fabrication, mounting, and alignment. Correlated misalignments over large distances, such as might arise from earth motions, tend to produce beam effects depending essentially only on total admittance, the effective average focusing force, and do not form a basis for comparison of alternative systems.

Figure 7-8 Misalignment components associated with common support structure in multiplets.

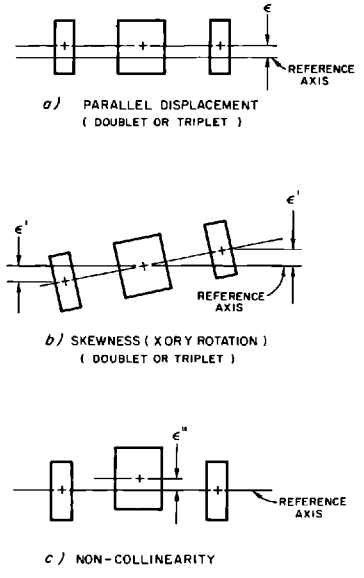

The "worst" conditions are, of course, minimum energy and maximum quadrupole strength. The following set of standard conditions, representing a constant-energy beam coasting through about half the machine, has been chosen for assigning tolerances:

Maximum allowable beam deflections, $|\xi|_{max} = 0.1$ cm
Beam energy, $m\gamma = 2$ GeV (assumed constant)
Quadrupole strength (optimal)
for alternating singlets, $Ql = L/f = \sqrt{5} - 1$
for sector multiplets, $Q^2\lambda\, d \approx \Lambda/F \approx 2$
(Here f is the singlet focal length, and F is the multiplet focal length.)

The numerical constants, as before, are

Spacing of alternating singlets, $L = 12$ meters
Doublet and triplet length, $D = 2$ meters
Sector length, $\Lambda = 100$ meters
Number of focusing periods in half the machine
alternating singlets, $N = 60$
sector multiplets, $N = 15$
Maximum orbit radius, $X_{max} = Y_{max} = a = 0.85$ cm

Table 7-3 lists the approximate dependence of mean-square orbit deviation $\langle \xi^2 \rangle$ on system parameters and error components for three systems considered in the coasting beam, constant parameter case. Table 7-4 gives the tolerances derived from these expressions.

The following observations may be made on the data presented in Table 7-4:

1. The most critical *transverse* alignment tolerances—*singlet displacement* ($\approx$1.6 mils),* *doublet skew* ($\approx$0.7 mil), and *triplet collinearity* ($\approx$0.7 mil) —all result primarily from the dipole field component of displaced quadrupoles and, therefore, will be compensated almost completely by the magnetic steering dipoles† along the machine. Thus it may be concluded that these very tight tolerances actually apply only to short-term instability of the support system.
2. The other rather critical transverse tolerance ($\approx$7 mils for parallel displacement of the multiplets) probably cannot be maintained in an absolute sense. Magnetic steering solves the problem partially; however, some dispersion between multiple beams at different energies would remain because the energy dependence of deflection by the displaced multiplet differs from that of a dipole. The alignment objective has been to meet the 7-mil figure as nearly as possible in order to facilitate multiple beam operation.

* 1 mil = 0.001 in.

† The steering dipoles are described in Section 7-3.

Table 7-3 Mean-square orbit uncertainties $\langle \xi^2 \rangle$ for various quadrupole error components, assuming coasting beam and constant parameters

Error	*Alternating singlet*	*Sector doublet*	*Sector triplet*
Parallel displacement	$\dfrac{4N\langle \varepsilon^2 \rangle}{1-\frac{1}{2}Ql}$	$\dfrac{1}{2}N\dfrac{Q^2\lambda d}{1-\frac{1}{4}Q^2\lambda d}\langle \varepsilon^2 \rangle$	$\dfrac{1}{2}N\dfrac{Q^2\lambda d}{1-\frac{1}{4}Q^2\lambda d}\langle \varepsilon^2 \rangle$
Skew (multiplet)	—	$2N\dfrac{\lambda}{d}\dfrac{\langle \varepsilon'^2 \rangle}{1-\frac{1}{4}Q^2\lambda d}$	$\frac{1}{2}NQ^2 d^2\langle \varepsilon'^2 \rangle$
Collinearity (triplet)	—	—	$2N\dfrac{\lambda}{d}\dfrac{\langle \varepsilon''^2 \rangle}{1-\frac{1}{4}Q^2\lambda d}$
Longitudinal displacement (independent)	$2NX_{\max}^2 Q^2 l^2 \dfrac{1+\frac{1}{2}Ql}{1-\frac{1}{2}Ql}\dfrac{\langle(\delta L)^2\rangle}{L^2}$	$\dfrac{1}{4}NX_{\max}^2\dfrac{Q^2\lambda d}{1-\frac{1}{4}Q^2\lambda d}\dfrac{\langle(\delta D)^2\rangle}{D^2}$	$\dfrac{1}{2}NX_{\max}^2\dfrac{Q^2\lambda d}{1-\frac{1}{4}Q^2\lambda d}\dfrac{\langle(\delta D)^2\rangle}{D^2}$
Longitudinal displacement (multiplet)	—	$\dfrac{1}{2}NX_{\max}^2(Q^2\lambda d)^2\dfrac{\langle(\delta\Lambda)^2\rangle}{\Lambda^2}$	$\dfrac{1}{2}NX_{\max}^2(Q^2\lambda d)^2\dfrac{\langle(\delta\Lambda)^2\rangle}{\Lambda^2}$
Axial rotation (independent)	$16NY_{\max}^2\langle \psi^2 \rangle$	$NY_{\max}^2\dfrac{\lambda}{d}\dfrac{\langle \psi^2 \rangle}{1-\frac{1}{4}Q^2\lambda d}$	$2NY_{\max}^2\dfrac{\lambda}{d}\dfrac{\langle \psi^2 \rangle}{1-\frac{1}{4}Q^2\lambda d}$
Axial rotation (common)	—	$2NY_{\max}^2 Q^2 d^2\langle \psi^2 \rangle$	(Small)
Quadrupole strength (independent)	$4NX_{\max}^2\dfrac{1+\frac{1}{4}Q^2l^2}{1-\frac{1}{4}Q^2l^2}\dfrac{\langle(\delta Q)^2\rangle}{Q^2}$	$\dfrac{1}{2}NX_{\max}^2\dfrac{\lambda}{d}\dfrac{1}{1-\frac{1}{4}Q^2\lambda d}\dfrac{\langle(\delta Q)^2\rangle}{Q^2}$	$\dfrac{3}{2}NX_{\max}^2\dfrac{\lambda}{d}\dfrac{1}{1-\frac{1}{4}Q^2\lambda d}\dfrac{\langle(\delta Q)^2\rangle}{Q^2}$
Quadrupole strength (multiplet)	—	$NX_{\max}^2\dfrac{Q^2\lambda d}{1-\frac{1}{4}Q^2\lambda d}\dfrac{\langle(\delta Q)^2\rangle}{Q^2}$	$NX_{\max}^2\dfrac{1}{1-\frac{1}{4}Q^2\lambda d}\dfrac{\langle(\delta Q)^2\rangle}{Q^2}$

Table 7-4 Summary of comparative error tolerances for alternative focusing systems[a]

Error	*Alternating singlet*	*Sector doublet*	*Sector triplet*
Parallel Displacement	1.6 mils[b]	7.3 mils	7.3 mils
Skew			
independent[c]	(Large)	(Large)	(Large)
multiplet	—	0.73 mil	73.0 mils
Collinearity (triplet)	—	—	0.73 mil
Longitudinal displacement			
independent	2.1 in.	2.4 in.	1.7 in.
multiplet	—	7.2 ft	7.2 ft
Axial rotation			
independent	0.21°	0.17°	0.12°
multiplet	—	6.1°	(Large)
Quadrupole strength			
independent	0.51%	0.43%	0.25%
multiplet	—	1.5%	1.5%

[a] See text for numerical values of system parameters appropriate for SLAC.
[b] 1 mil = 0.001 in.
[c] The orbit perturbation due to transverse rotation of an individual quadrupole is negligibly small.

3. The seemingly critical requirements on independent axial rotation and individual quadrupole strength are based on the pessimistic assumption that typical beam orbit amplitudes fill the whole available aperture. If moderately good phase space matching can be maintained along the machine, there should be a reasonable factor of safety beyond the figures given.

CHOICE OF FOCUSING SYSTEM FOR SLAC. Historically, the alternating singlet system was considered first but was rejected as being too complicated and requiring a transverse alignment tolerance of <2 mils on a very large number of independently supported quadrupoles.

The sector multiplet concept had the advantage that the focusing, steering, and beam-sensing instrumentation for each sector could all be contained in a single package; interaction between steering and focusing would be directly correlated, and operating adjustments would be easily understood.

Finally, triplets were initially chosen in preference to doublets primarily on consideration of alignment tolerances. For doublets, the critical tolerance on skewness, 0.7 mil in 40 in., is equivalent to an aiming stability of $\approx 2 \times 10^{-5}$ rad, and there was no certainty that this could be maintained stably with any reasonable support structure. Triplets, on the other hand, are very insensitive to skewness, and it was felt that the critical internal stability tolerances—in particular on the collinearity—could be held by a suitably rigid and thermally stable support structure. The triplet also has greater optical symmetry and slightly larger admittance.

Accordingly, triplets were originally chosen for the transport system and were used during early beam operation beginning in April 1966. Subsequently, the discovery of the beam breakup phenomenon and the resulting need for stronger focusing led to a rearrangement of the existing sector triplet quadrupoles into a combination of the alternating singlet and sector-doublet systems. This changeover is discussed under "The Magnetic Fix Program" in Section 7-5. No serious effects due to singlet and doublet misalignments have been encountered in actual machine operation, indicating great conservatism in the initial design.

Other transverse perturbations

SCATTERING BY RESIDUAL GAS.[16] The residual gas in the accelerator can spread the beam by single and multiple nuclear Coulomb scattering. It is interesting to note that these processes do not conserve beam phase space.

Nuclear form factors and recoil corrections can be neglected because the momentum transfers involved are small. Writing the Coulomb scattering cross section for single scattering in small-angle approximation as[17]

$$\frac{d\sigma}{d\Omega} \approx \frac{4r_0^2 Z^2}{\gamma^2(\theta^2 + \theta_1^2)^2} \tag{7-95}$$

where Z is the atomic number of the residual gas, $r_0 = e^2/m = 2.81 \times 10^{-13}$ cm is the classical electron radius and

$$\theta_1 = \frac{\lambda\!\!\!^{-}}{Z^{-1/3}\hbar^2/(me^2)} \approx \frac{Z^{1/3}}{137\gamma} \tag{7-96}$$

is the minimum effective scattering angle for a screened Coulomb field in the Fermi-Thomas model. If it is assumed that the transverse momentum acceptance, proportional to $\gamma\theta_m$, is independent of z, the total fraction of electrons lost is simply given by

$$\frac{4\pi N_s r_0^2 Z^2}{\gamma^2\theta_m^2 + (Z^{1/3}/137)^2} \tag{7-97}$$

where N_s is the total number of gas atoms per unit area.

The momentum acceptance is estimated as $m\gamma\theta_m \approx U/\pi a$, where U is the admittance and a is the aperture radius. If $U = 0.05\pi$ (MeV/c)(cm), then $\gamma\theta_m = 0.115$; let the residual gas be nitrogen at 10^{-6} torr or $N_s \approx 2 \times 10^{16}$ atoms/cm^2 for the 2-mile length; the fraction lost by single scattering is then 0.74×10^{-4}, which is negligible.

On the other hand, if it is assumed that $\theta_m = 0$, then the total fraction of electrons undergoing any single scattering (based on $\gamma\theta_1 = Z^{1/3}/137 = 0.014$) is $0.005 = \frac{1}{2}\%$.

Since this number may be interpreted as the total probability of single scattering for a given electron, it is concluded that the effects of plural and multiple scattering must be negligible also.

STRAY MAGNETIC FIELDS.[17] To estimate the effect of magnetic fields along the accelerator axis, consider the equation of motion of an electron in the absence of other transverse forces:

$$(Px')' = e(B_y - y'B_z) \approx eB_y \tag{7-98}$$

The $y'B_z$ term is negligible. The formal solution is

$$x = x_0 + \zeta(z, 0)p_{x_0} + e\int_0^z B_y(z_1)\zeta(z, z_1)\,dz_1 \tag{7-99}$$

where $\zeta(z, z_1)$ is given by Eq. (7-16).

As an example, consider the effect of a uniform field on a relativistic beam with uniform energy gradient in the absence of focusing. The magnetic deflection is

$$\Delta x = \frac{eBz}{m\gamma'}\left(1 - \frac{\gamma_0}{\gamma - \gamma_0}\ln\frac{\gamma}{\gamma_0}\right) \tag{7-100}$$

For $z = 3 \times 10^5$ cm, $m\gamma' = 0.06$ MeV/cm, $\gamma \gg \gamma_0$, and $B = 0.5$ G, we find $\Delta x \approx 750$ cm, i.e., the average transverse field would have to be reduced by a factor of 10^4 to keep the deflection to ≈ 1 mm; the tolerable field would be $\approx 6 \times 10^{-5}$ G.

The effect of external focusing on the deflection by stray magnetic fields may be calculated by the perturbation formulation used in the quadrupole error analysis [Eq. (7-71) ff.]. Considering the sector–multiplet type of focusing, the perturbation vector for one sector is obtained from Eq. (7-99):

$$\delta\mathbf{x}_n = \begin{bmatrix}\delta x \\ \delta p_x\end{bmatrix}_n \tag{7-101}$$

where

$$\delta x = \frac{e}{m\gamma}\int_{z-\Lambda}^{z} B_y(z_1)(z - z_1)\,dz_1 \tag{7-102}$$

and

$$\delta p_x = e\int_{z-\Lambda}^{z} B_y(z_1)\,dz_1 \tag{7-102}$$

on the assumption that the variation in γ per sector is adiabatic.

Two cases are considered explicitly:

1. *Uniform magnetic field over the entire length.* In this case it turns out that, if the quadrupole strengths are held essentially constant for compatibility with simultaneous beams of high and low energy, then the greatest deflection is at the highest beam energy. The result, based on the thin-lens approximation for sector multiplets, is

$$\xi_n \approx \frac{e}{m}\frac{B_y\Lambda^2\gamma_n}{(\Lambda\gamma')^2 + 2\gamma_0^2} \tag{7-103}$$

where $m\gamma_0 = Q(\frac{1}{2}\Lambda D)^{1/2}$ is the energy at which the quadrupole strength is optimized [Eq. (7-62) or (7-68)]. For a typical case where $m\gamma_0 = 2$ GeV, $m\Lambda\gamma'$ = energy gain per sector = 0.7 GeV, $m\gamma_n = 20$ GeV, and $\Lambda = 100$ meters, one finds

$$B_y = 1.4 \times 10^{-3}\ \text{G}$$

as the field which produces a deflection of $\xi = 0.1$ cm.

2. *Random variation from sector to sector.* This could result, for example, from errors in setting or regulation of the degaussing system (see the paragraphs on the degaussing and magnetic shielding system below). Again constant quadrupole strength is assumed for compatibility with multiple beams. The mean-square deflection is found to be

$$\langle \xi_n^2 \rangle \approx \frac{n}{4}\frac{e^2}{m^2}\frac{\langle B^2\rangle \Lambda^4}{\gamma_0^2} \tag{7-104}$$

which is nearly independent of beam energy. The Λ and γ_0 are defined above, and n is the number of sectors. Again taking $m\gamma_0 = 2$ GeV and $\Lambda = 100$ meters, it is found that

$$\langle B^2\rangle^{1/2} = 2.4 \times 10^{-3}\ \text{G}$$

for an orbit uncertainty of $\langle \xi_n^2\rangle^{1/2} = 0.1$ cm at $n = 30$. A reduction of the external field by a factor approaching 10^3 is therefore required.

COUPLER ASYMMETRY.[18,19] The coupling of RF between the rectangular waveguide and the disk-loaded accelerator is accomplished through side slots in the end cavities of the 10-ft structure. (See Fig. 6-26.) The asymmetry of these couplers introduces transverse gradients in the accelerating field, which can deflect the beam in the manner of an RF separator.

The transverse impulse imparted by one coupler is related to the vector potential A_z and the electric field E_z accelerating the beam particle by[20]

$$\delta p_{xc} = e\int \frac{\partial A_z}{\partial x}\,dz = \frac{ie}{k}\int \frac{\partial E_z}{\partial x}\,dz \tag{7-105}$$

in which the integral extends over the region of the perturbation and k is the RF wave number.

The complex amplitude of the field acting on the particle at a particular point in the cavity is of the form

$$E_z = E(x)e^{i\Delta(x)} \tag{7-106}$$

where both the field amplitude $E(x)$ and the phase angle $\Delta(x)$ of the electron relative to the accelerating crest depend on x, the transverse coordinate in the coupler cavity.

The real part of Eq. (7-105) is then simply

$$\delta p_{xc} = -\frac{e\,\Delta z}{k}\left[\left\langle\frac{\partial E}{\partial x}\right\rangle_{AV}\sin\Delta + \left\langle E\frac{\partial\Delta}{\partial x}\right\rangle_{AV}\cos\Delta\right] \tag{7-107}$$

where $\langle\ \rangle_{AV}$ refers to the average value of the quantity in question over the coupler cavity of length Δz.

Thus an amplitude asymmetry would produce a dispersive effect proportional to the bunch width, whereas a transverse phase variation of the field would produce a uniform deflection of the whole bunch, in phase with the accelerating field.

The effect of such momentum impulses, repeated coherently in each powered accelerator section of length ΔL, is mathematically equivalent to a uniform magnetic deflecting field of magnitude

$$B_c = \frac{1}{\Delta L}\frac{\delta p_{xc}}{e} \tag{7-108}$$

Hence the results obtained above for stray magnetic fields apply directly. Let the numerical values be $k = 2\pi/10.5 = 0.598\ \text{cm}^{-1}$, Δz = disk spacing = 3.5 cm, $\Delta \approx 5^\circ \approx 0.1$ rad (typical RF bunch width), $\Delta L = 300$ cm, $E \approx$ 0.06 MV/cm. Take $B_c \approx 1.4 \times 10^{-3}$ G corresponding to the tolerance from Eq. (7-103) for uniform magnetic field with moderate focusing, interpreted to give a betatron wavelength of four sectors at 2 GeV. The tolerances on coupler symmetry

$$\left|\frac{2a}{E}\left\langle\frac{\partial E}{\partial x}\right\rangle_{AV}\right| \le 0.72\%$$

and (7-109)

$$2a\left|\left\langle\frac{\partial\Delta}{\partial x}\right\rangle_{AV}\right| \le 0.04^\circ$$

are obtained where $2a$ = disk hole diameter $\approx$ 2 cm.

Quantitative effects of measured asymmetries of the SLAC couplers, and the cure by alternating the coupler orientations, are discussed in Chapter 6.

ACCELERATOR MISALIGNMENT. The misalignment effects to be considered here are associated with the accelerator structure itself, as distinguished from the special problems of the quadrupole misalignments discussed above.

Accelerator misalignments arise from fabrication errors, limitations of alignment precision, and environmental changes. The 10-ft accelerator sections are initially aligned on the 40-ft girder assemblies to a straightness of $\pm$0.010 in.; the accelerator axis at the beginning of each 40-ft girder is referenced to the laser alignment system* to perhaps $\pm$0.005 in.; absolute precision of the laser system itself is probably better than $\pm$0.005 in. Mechanical

* See Chapter 22, "Support and Alignment."

loading by the rectangular waveguide and thermal distortions can contribute perhaps 0.010 to 0.020 in. to the intragirder deviations. Tolerances on the linkage between girders allow a maximum discontinuity of 0.015 in. in the accelerator axis.

In over a year of experience it has been found that the maximum motion of any point in the machine due to earth settlement is about 0.040 in. during a 3- to 4-month realignment cycle; maximum relative motion between any adjacent pair of support jacks is on the order of 0.005 to 0.010 in. in the same period.

The main effect of the initial random misalignment of the accelerator subassemblies is simply a loss in aperture of perhaps 10% in radius. This effect is not serious for the electron beam, which is kept to a radius of a few millimeters by the focusing system. Positron beam transmission, which is proportional to the fourth power of aperture, may be reduced appreciably.

Magnetic steering will cause only slight dispersion between interlaced beams of different energies. Transverse components of the accelerating field introduced by misalignment have a slight steering effect. This may contribute to the dispersion between interlaced beams and will generate slight motions of the beam when klystrons are turned on or off. To illustrate the latter effect, consider a misaligned 40-ft module, powered by a single klystron, and assumed to be internally straight. Figure 7-9 shows the optical equivalent of the module. The net deflecting impulse is due to the combination of the transverse component of the misaligned E-field and the fringe-field lens effect given by Eqs. (7-11) and (7-12). It is given to first order by

$$\delta p_x = eE \cdot \tfrac{1}{2}(\varepsilon_2 - \varepsilon_1) = \tfrac{1}{2}m\gamma'(\varepsilon_2 - \varepsilon_1) \tag{7-110}$$

As a rather extreme example, assume a segment with a relative misalignment $\varepsilon_2 - \varepsilon_1 = 0.2$ cm, and an energy gain of $m\gamma' = 0.06$ MeV/cm. The impulse would be $\delta p_x \approx 0.006$ MeV/c, and the maximum beam deflection under focusing conditions corresponding to a betatron wavelength λ_β of four sectors at 1 GeV would be

$$\delta x \approx \frac{\delta p_x}{m\gamma}\frac{\lambda_\beta}{2\pi} \approx 0.04 \text{ cm}$$

Thus the steering effect in turning klystrons on or off can be appreciable.

Figure 7-9
Misaligned accelerator segment.

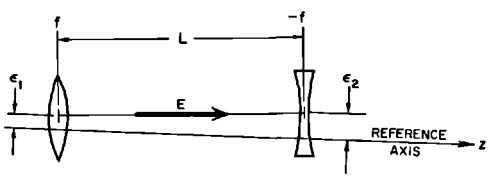

821A9

7-3 The beam control system

General description (RHH)

The major components used in beam control and monitoring will be reviewed briefly.

BEAM-ANALYZING STATIONS (BAS). These are two special instrumentation packages primarily intended for beam diagnostics; full details are given in Chapter 15. BAS-1 is located in the last 10-ft of the first 40-ft module of Sector 1 and BAS-2 occupies the first 40-ft of Sector 20. The most important features of both stations are magnetic spectrometers used in checking beam energy and spectrum. Beam current and position monitors also are included (see "Standard Drift Section" below). BAS-1 also contains a special, short quadrupole triplet which is part of the main focusing system; this is described under "Transport System" below.

LONG ION CHAMBER. The long ion chamber (commonly called "PLIC") consists of a coaxial transmission line, operated as an ion chamber, running the full length of the machine. Details are given in Chapter 21. The primary function of PLIC is to provide a signal used in the machine protection system. Another useful feature is that arrival time of signals at the injector end of the machine provides information as to location of sources of radiation and thus aids the operator in diagnosing the causes of beam loss.

DEGAUSSING AND MAGNETIC SHIELDING. Magnetic compensation is effected by degaussing wires and magnetic shielding along the accelerator and by steering dipoles at the end of each sector. Details are given below.

STANDARD DRIFT SECTION.* The layout of a typical instrumentation package (drift section) located at the end of each 333⅓-ft sector was shown in Fig. 5-22. The components include:

1. A *quadrupole doublet* (discussed under "Transport System" below).
2. The *reference cavity*, a TM_{010} resonant cavity driven by the beam current to generate a signal for phase reference and normalization of beam position monitor output (below). A portion of the signal from this cavity is logarithmically amplified and sent to central control as a broad-range beam current indication.
3. The *beam position monitor*, which consists of two TM_{120} rectangular cavities oriented to give signals proportional to the x or y displacements of the beam from the cavity axis, respectively. The phase of the signal

* The handling of signals from the various beam-sensing elements of the drift section is described in Chapter 15.

relative to the phase of the reference cavity tells the sign of the displacement, while the amplitude normalized by the reference-cavity amplitude is a measure of the amount of displacement.

4. The *beam intensity monitor*, which is a current transformer with a toroidal ferrite core, gives an accurate (1 %) measure of absolute beam current.
5. The *steering dipole*, which consists of Helmholtz-type coils rated at $\approx$2000 G-cm, equivalent to 0.6 MeV/c transverse momentum. It provides a final correction for all uncompensated deflections. The steering dipoles are designed for dc or pulsed operation.
6. The *beam profile monitor*, designed to display the transverse distribution of the beam. A retractable Čerenkov radiator of thin quartz, viewed by a television pickup, has been used, but this device is severely limited by heat dissipation in the radiator and by multiple scattering. A scanning device using a small (1 mm^3) beryllium bead on a fine wire has been developed, intercepting about 1 % of the beam. Detection of the scattered radiation provides a signal proportional to the beam intensity at the position of the bead.
7. The *beam scraper*, or protective collimator. This is a water-cooled copper collimator approximately 12 in. long with an aperture of 0.675 in. diameter, which is 2 mm smaller than the accelerator aperture. It tends to localize beam interception in case of mis-steering or poor focusing. The scrapers can dissipate 20 kW of average power (1 % of maximum design beam power) and can withstand a few beam pulses at full power. Indication of beam scraping is provided by PLIC and local discrete ion chambers. In the event of sudden beam interception by the scraper, the radiation information from PLIC will be used to shut the beam off within a few pulses.

The degaussing and magnetic shielding system[21,22] (RHH)

DESCRIPTION AND SPECIFICATIONS. Transverse stray magnetic fields result from several causes: the earth's magnetic field, magnetized reinforcing or structural steel, equipment in the klystron gallery, power line fields, and ground currents in the accelerator support girder. As shown in the previous section, the field tolerance is of the order of 2 mG, averaged over a sector, under moderate external focusing. Table 7-5 summarizes tolerances on the various magnetic effects.

Magnetic compensation was specified to limit the residual transverse field averaged over a given sector to 10^{-4} G.

Figure 7-10 shows the degaussing wires and shielding system. The degaussing currents in each sector are adjustable independently.

The magnetic shield was adopted primarily to compensate for the observed, short-range variation in the field (see the paragraphs on effects of magnetic fields, below). The shield also reduces ac fields, degaussing field fluctuations, and temporal variations in the earth's field which may amount to many

Table 7-5 Tolerances on magnetic effects under moderate focusing conditions[a]

Effect	*Tolerance*[b]
Uniform transverse field (full length)	1.4×10^{-3} G
Random sector-to-sector variations	2.4×10^{-3} G
Stray currents in the 24-in. diameter support girder	
dc	4 A
60 Hz[c]	40 A

[a] Betatron wavelength: four sectors at 1 GeV.
[b] The tolerances are set by allowing a maximum beam deflection of 1 mm.
[c] Increased shielding factor at 60 Hz due to skin effect in the accelerator pipe

milligauss per hour during magnetic storms. The shielding material is moly-Permalloy sheet, 6 mils thick. The inherent shielding factor is greater than 20 when the material is carefully demagnetized in an essentially null ambient field. However, the average dc shielding factor along the machine is on the order of 10 because of unavoidable gaps in the shielding at waveguide and water connections. At 60 Hz (skin depth $\approx$ 1 cm in copper), the shielding factor is larger by a factor of 10 due to skin effect.

Possible circulation of large ground currents, e.g., from power circuits and chemical EMF through the 24-in. aluminum support structure was once viewed with considerable alarm, and breaking up of ground loops by insulating gaps was considered. However, careful balancing and grounding procedures in the power distribution systems have kept the ac ground currents within tolerance; and chemical EMF were found to be insignificant.

EFFECTS OF MAGNETIC FIELDS. Figure 7-11 shows field measurements in the first few sectors of the tunnel before installation of the accelerator. Average field components are about 0.4 G vertical and 0.2 G horizontal, but short-range local fluctuations of over 0.5 G peak-to-peak are observed.

Figure 7-10 Magnetic shielding and degaussing system.

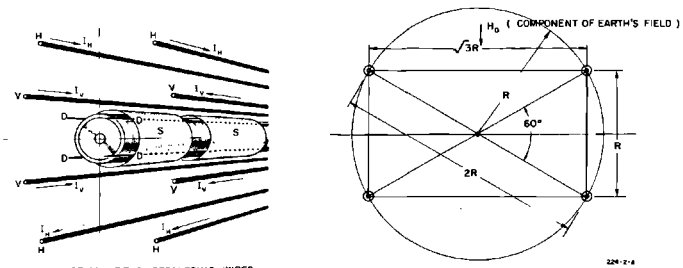

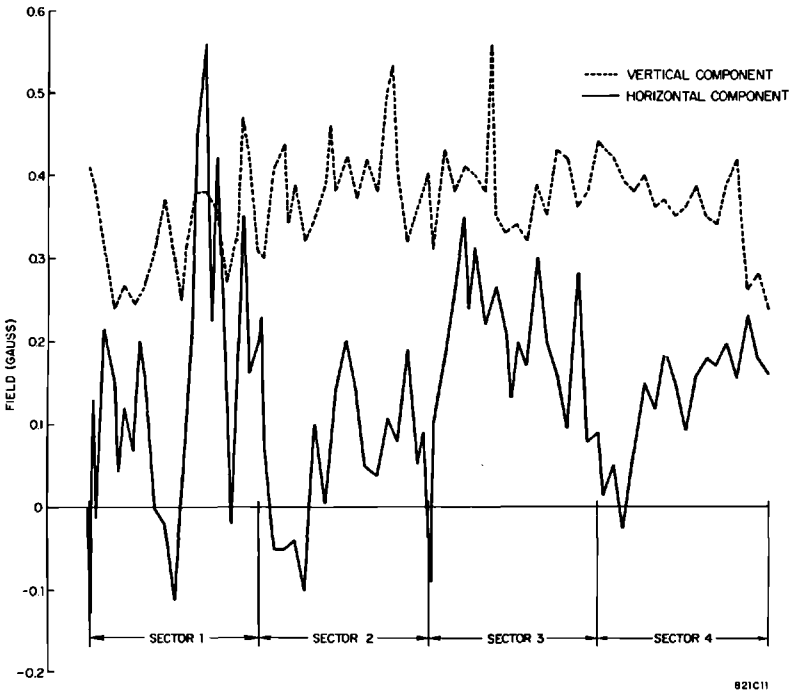

Figure 7-11 Magnetic field measurements in accelerator tunnel.

Figure 7-12 Beam deflections due to actual magnetic field.

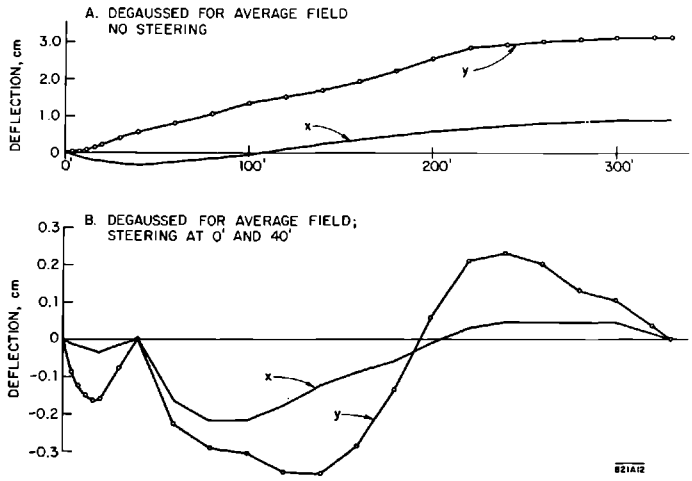

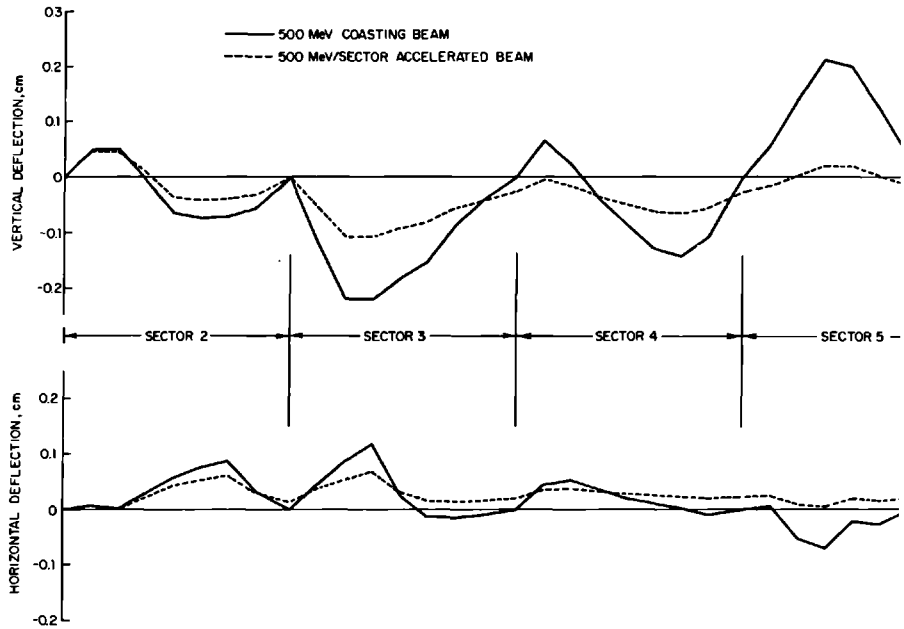

Figure 7-13 Dispersion between accelerated and coasting beams due to actual magnetic fields in early sectors.

Figure 7-12 shows computed deflections of the beam in Sector 1, neglecting focusing and shielding: (A) with the average field (but not the fluctuations) balanced out by the degaussing system and (B) with steering at the 0-ft point and at the 40-ft point (BAS-1), so that the beam is centered at BAS-1 and at the end of Sector 1. It is seen that with the latter conditions, the maximum deflections are greatly reduced. It is evident that a shielding factor of 10 would reduce the deflections to well within tolerance.

Figure 7-13 shows dispersion between a beam coasting at 500 MeV and a beam accelerated by 500 MeV per sector, based on measured fields in the first several sectors. The sector average fields are again assumed to be nulled by degaussing, and the steering is optimized for a 500-MeV coasting beam.

Transport system (RHH)

Here the existing accelerator transport system is described. The original sector triplet configurations of quadrupoles was rearranged into a combiantion of the alternating singlet and sector doublet schemes* in order to improve the beam current limit imposed by the transverse instability (see Section 7-4).

* See "Choice of Focusing System for SLAC," Section 7-2, and "The Magnetic Fix Program," Section 7-5.

Table 7-6 Quadrupole specifications for SLAC accelerator transport system

Specifications	*QA*	*QB*
Effective length[a]	4 in.	8 in.
Bore radius	0.6 in.	0.6 in.
Strength[a]		
nominal[b]	10 kG	20 kG
maximum	≈17 kG	≈40 kG
Energizing current		
nominal	6 A	6 A
maximum	≈12 A	≈15 A
Power (nominal)	45 W	72 W
Cooling	natural convection	

[a] Strength is given as $\int(\partial B_y/\partial x)\,dz$ and effective length is strength divided by central gradient.
[b] Excitation (strength vs energizing current) is linear up to at least the nominal values.

PHYSICAL DESCRIPTION. Two quadrupole designs are used. These are designated as types *QA* and *QB* and have effective lengths of 4 and 8 in., respectively; specifications are given in Table 7-6.

The optical elements of the system, in order of distance along the machine, are:

1. The BAS-1 triplet, consisting of quadrupoles *QA*, *QB*, *QA*, with each *QA* spaced 10.5 in. (center-to-center) from the *QB*. The electrical connection is series, with astigmatism control being provided by selective shunting of the *QB* or the *QA*'s.
2. Alternating singlets of type *QA* at 40-ft spacing through the rest of Sector 1, and at the same spacing in Sectors 2 through 6. The first singlet is at the 80-ft point of Sector 1 and the last is at the 280-ft point of Sector 6. Electrically the first singlet is run from a separate power supply, whereas in the remainder of Sector 1 and Sector 2 successive pairs are powered as independent doublets. In Sectors 3 through 5, quadruplet connections are used, and Sector 6 contains one quadruplet, one doublet, and one singlet, in that order. The disposition of the quadrupoles in Sectors 1 and 6 is shown schematically in Fig. 7-14.
3. Sector doublets of type *QA* in the drift sections DS-6 (end of Sector 6) through DS-9. Center-to-center spacing of the quadrupoles is 80.75 in.
4. Sector doublets of type *QB* in drift sections DS-10 through DS-29. Center-to-center spacing is 71 in.
5. A doublet of type *QA* in DS-30.

In all doublets, astigmatism control is available through selective shunting of either quadrupole.

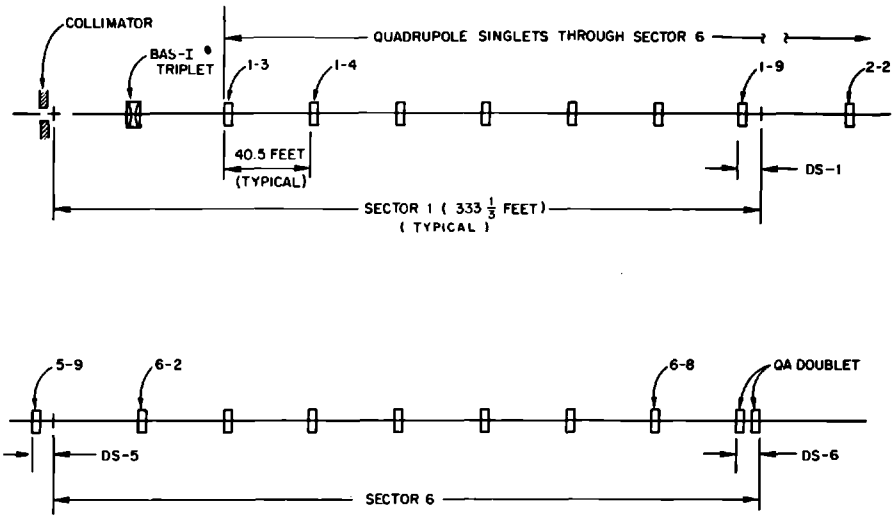

Figure 7-14 Schematic layout of quadrupoles in Sectors 1 and 6.

TRANSPORT PROPERTIES. The limiting admittance of the system occurs in the initial match into the alternating singlets, and is about 0.04π (MeV/c)(cm), compared to injector emittance of $\approx 0.004\pi$ (MeV/c)(cm). Typical quadrupole strengths in the singlet region are given by

$$Ql \approx \frac{QL}{m\gamma} = \frac{L}{f} \leq \sqrt{5} - 1$$

where $\sqrt{5} - 1$ is the "optimum" value. Using the numerical value $L = 40.5$ ft, one finds

$$Q \leq \frac{(\sqrt{5} - 1)}{L} m\gamma \approx \frac{m\gamma}{1000} \text{ (singlets)}$$

where Q is expressed in MeV/cm and $m\gamma$ in MeV. Corresponding betatron wavelengths [Eq. (7-53)] are $\lambda_\beta \geq 9.44L = 1.18$ sectors.

In the sector doublet region, typical quadrupole strengths are given by

$$Q(\lambda\, d)^{1/2} \approx \frac{Q(\Lambda D)^{1/2}}{m\gamma} \approx \left(\frac{\Lambda}{F}\right)^{1/2} \leq \sqrt{2}$$

where $\sqrt{2}$ is the "optimum" value. Corresponding betatron wavelengths are $\lambda_\beta \gtrsim 4$ sectors. In this case, the parameters $D \approx 200$ cm and $\Lambda \approx 10^4$ cm give

$$Q \lesssim \left(\frac{2}{\Lambda D}\right)^{1/2} m\gamma \approx \frac{m\gamma}{1000} \text{ (doublets)}$$

Thus, relationship between quadrupole strength and beam energy is practically the same for the singlets and doublets.

The maximum strength of the QB doublets, ≈ 40 kG or ≈ 12 (MeV/c)/cm, allows the optimum (4-sector) betatron wavelength to be maintained up to the 12-GeV point.

TYPICAL OPERATION. Usually most of the quadrupoles are set according to the above relationships between quadrupole strength and estimated beam energy. When interlaced beams of different energies are used, the quadrupoles must be set for the lowest energy.

The problem of phase space matching, between the injector and the singlet system and between the singlet system and the doublet system, has been solved approximately by use of the TRANSPORT computer program. In the computer fit, the BAS-1 triplet and the first singlet are varied to match the injector emittance to the remainder of the singlet system; the match of the singlets to the doublets is effected by tapering down the singlet fields in Sector 6, with independent adjustment of the last singlet and the drift section (Sector 6) doublet. When the actual quadrupoles are preset according to the computer fit, it is usually found that only minor readjustments are needed to establish good transmission.

Figure 7-15 shows typical beam envelope traces from the TRANSPORT computations in the region of the injector match and the singlet-to-doublet transition.

The quadrupoles always show some steering effects due to misalignments, but because of the high standards of prealignment and the excellent precision of the laser alignment system, these effects have not been very troublesome.

Figure 7-15a Computed envelope of matched beam through Sectors 1 through 5.

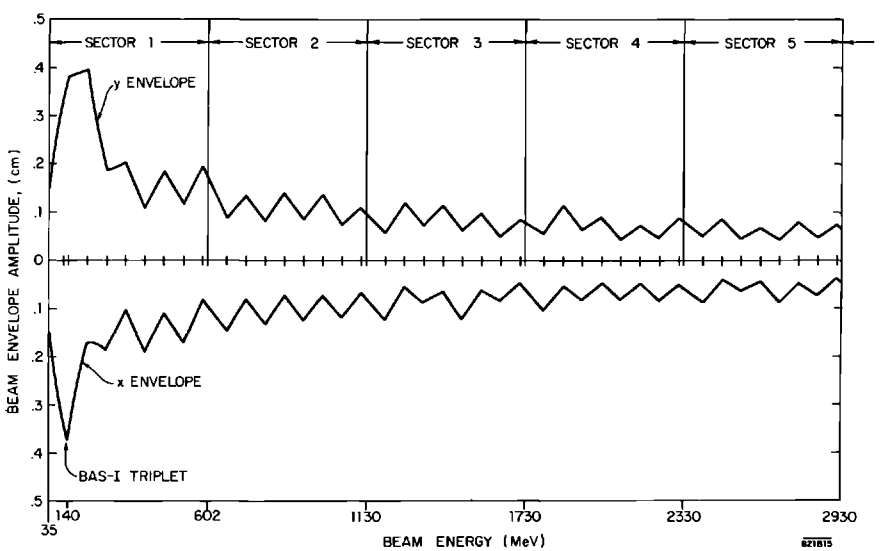

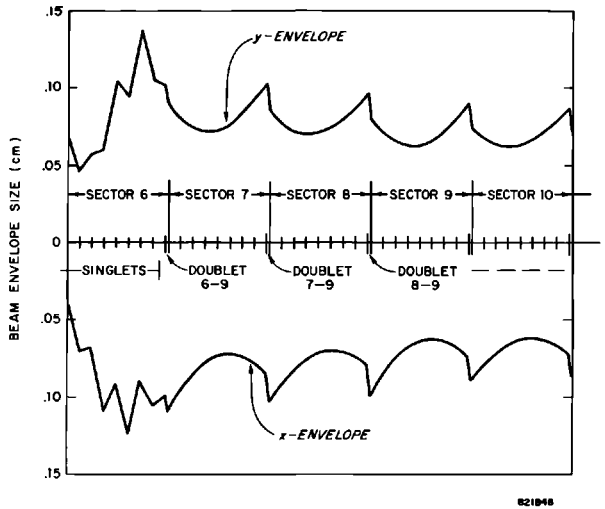

Figure 7-15b Computed envelope of matched beam —transition from singlet to doublet system.

*Phase space measurement**

The emittance of the accelerator was measured at the input to the beam switchyard. The equipment used in the measurement is shown schematically in Fig. 7-16. The beam from the accelerator was focused to achieve a minimum spot on the profile monitor. The beam diameter was measured at collimator No. 1 by steering the beam so as to scrape the beam on the collimator. The current through the collimator was measured with a toroid behind the collimator as a function of horizontal and vertical steering currents. Similarly, the current through collimator No. 2 was measured as a function of the steering currents. The first step in the measurement process was to adjust the quadrupole lens to minimize the beam diameter at the profile monitor. The beam

Figure 7-16 Equipment used in the measurement of accelerator emittance.

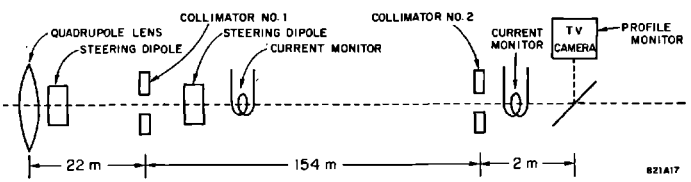

* This subsection written by R. H. Miller.

Figure 7-17 Emittance plane.

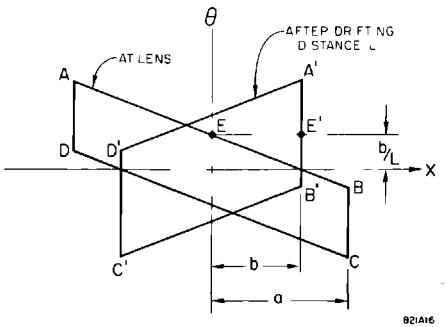

radii (a at the lens and b at the profile monitor) were then measured. As can be seen in Fig. 7-17, the radii a and b define a parallelogram in x, θ phase space, the area of which is

$$A = \frac{4ab}{L} \tag{7-111}$$

where L is the drift distance from the lens to the monitor. In Fig. 7-17 the parallelogram $ABCD$ represents the area in phase space at the lens limited by the radii a and b, whereas $A'B'C'D'$ represents the same area after transformation through the drift distance L. It is evident from the figure that the beam radius after the drift L is minimized by adjusting the beam convergence with the lens (and thus the slope of line segment AEB) until its image $A'E'B'$ is a vertical line since the θ coordinate of the point E' is unaffected by the lens. It is also evident that the beam passes through a waist somewhere between the lens and the end of the drift space. Similar considerations apply if the beam is represented by an ellipse in phase space. Following convention, the area of the largest ellipse contained within the parallelogram defined by the beam radii a and b will be used here. This area is

$$A = \frac{\pi ab}{L} \tag{7-112}$$

or in the conserved form

$$U = \gamma A = \frac{\pi ab\gamma}{L} \tag{7-113}$$

where γ is the energy of the beam.

The emittance of a 9.3-GeV beam with a peak current of 3.8 mA was measured. A sample of the data is shown in Fig. 7-18. Using Eq. (7-113), the fraction of beam current contained in the emittance ellipse of variable area was computed; the result is shown in Fig. 7-19. Ninety percent of the current is contained in 0.1π (MeV/c)(cm). This measured emittance is approximately one order of magnitude larger than the injector emittance reported in Chapter 8.

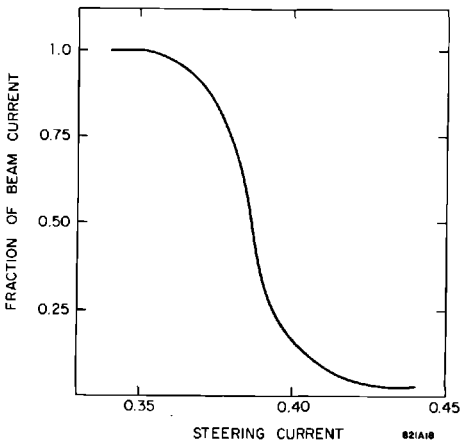

Figure 7-18 Beam current through collimator No. 2 vs steering current.

Figure 7-19 Beam current contained in a given accelerator emittance at $E = 9.3$ GeV, $I = 3.8$ mA peak.

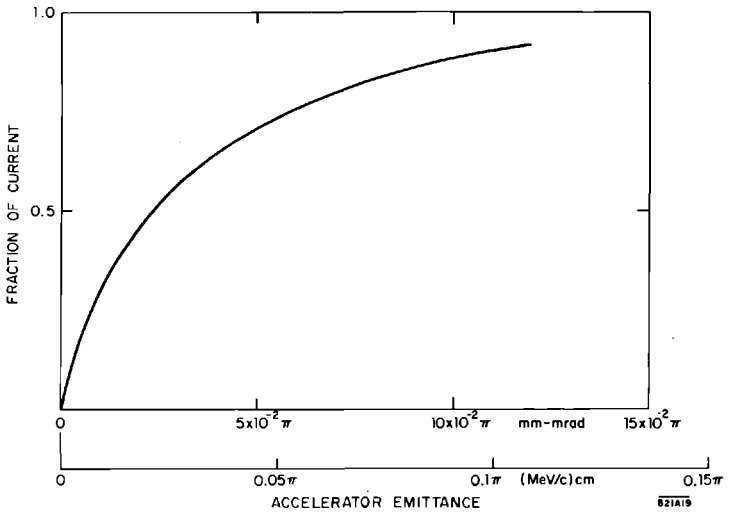

7-4 Theory and calculations of beam breakup

Effects of the beam on radial particle motion (WKHP)

In the previous sections, orbit motion has been treated as single particle dynamics in external fields. In all accelerators available, intensity is ultimately limited by instabilities produced by the action of beam-induced fields on the particle motion—and the electron linear accelerator is no exception.

SPACE CHARGE. If the effects of the currents induced in conducting surfaces surrounding the beam are ignored, the problem is reduced to analysis of conventional space-charge action. Let J be the current in particles per unit length in the beam,* concentrated in a cylinder of radius b and concentrated longitudinally into a bunch of phase length $\Delta\phi$. Using Eq. (7-2), the effect of the radial space charge can easily be shown to be described by

$$\beta(\beta\gamma r')' = \frac{J}{\gamma^2}\frac{rr_0}{b^2}\frac{4\pi}{\Delta\phi} = Ar\gamma^{-2} \tag{7-114}$$

where the γ^2 factor originates from the cancelation of electric and magnetic space-charge forces, and where r_0 is the classical electron radius. With reasonable numerical constants ($J = \frac{2}{3} \times 10^7$ electrons/cm, $b = 0.2$ cm, $\Delta\phi/2\pi = 0.015$) the constant A in this case becomes $A = 0.008$. The WKB solution of Eq. (7-114) indicates an exponential radial increase for $\beta \approx 1$ given by

$$r \approx \exp\left\{A^{1/2}\int_{z_0}^{z}\gamma^{-3/2}\,dz\right\} = \exp\left\{\frac{2A^{1/2}}{\gamma'}(\gamma_0^{-1/2} - \gamma^{-1/2})\right\} \tag{7-115}$$

for constant energy gain γ'. Numerically $\gamma' \approx 0.12$ cm^{-1}; the radial increase due to space charge is small if γ_0 at injection from the bunching section is large enough. If $\gamma_0 = 60$, then the radial growth factor after the injector is about 1.2.

RESISTIVE WALL EFFECTS. If the effects of currents in the conducting walls induced by the beam are considered, the phenomena are more complex. In general, the radial motion of individual particles will be affected by the so-called "wake field" of each bunch falling off inversely as the square root of the distance behind the bunch. This wake field is due to the induced currents in the tube wall and gives rise to the "resistive wall instability" observed in circular accelerators and storage rings. Calculation of this effect has been carried out only for a tube of smooth bore having walls of conductivity σ and, therefore, can be applied to SLAC only by the use of an "effective" radius R of somewhat uncertain magnitude. Calculation by Sessler[13,23] predicts an asymptotic amplitude increase described by

$$\exp\{Azt^{1/2}R^{-3}\sigma^{-1/2}\}^{2/5} \tag{7-116}$$

where A is a numerical constant. If $R = 1$ cm, a current of 530 mA causes the beam radius to increase from an initial misalignment offset of 0.05 cm to a radius of 1.0 cm at which beam loss would occur. Note that this is not a very large factor of safety beyond the rated current of 50 mA specified for SLAC.

* Note that $c = 1$.

BEAM BREAKUP. Considerably lower threshold currents are observed for the onset of instabilities. These instabilities are due to beam excitation of specific electromagnetic modes which produce a regenerative transverse deflection. Such instabilities have been observed in smaller linear accelerators for some time. However, one should clearly recognize that there are two quite distinct mechanisms by which such modes can lead to an exponential "blowup" of radial motion. The first mechanism, which is extensively discussed in the literature,[24–27] results from the negative group velocity of the HEM_{11} mode. This is the mode nearest in frequency to the TM_{01} mode used for accelerating. The HEM_{11} mode has a field configuration producing a transverse deflection of the beam[28] (Fig. 7-20).

The negative group velocity of the HEM_{11} mode will feed energy from the field excited by the beam in the end of each accelerating section toward the front. There it will produce additional transverse modulation in the beam which will, in turn, increase the excitation of the mode. This sequence of events leads to the regenerative action responsible for the conventional "backward-wave oscillator." This phenomenon characteristically occurs in a given section at currents of several hundred milliamperes.

The buildup mechanism which is dominant in limiting beam currents in the SLAC accelerator involves amplification from section to section and is coupled only through the electron beam. Of course, both mechanisms will contribute to transverse modulation buildup, but by way of introduction to the problem, a simple, but very general, model of the multisection buildup phenomenon is presented next.

Figure 7-20 (a) A ω–β diagram of conventional disk-loaded structure. (b) Field configuration of the HEM_{11} and TM_{01} modes in the disk-loaded structure.

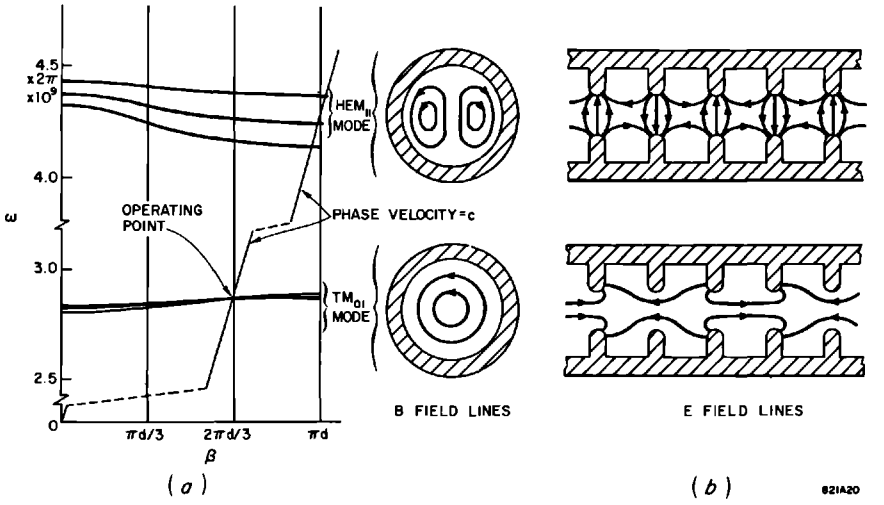

The multicavity model of beam breakup[29] (WKHP)

Let each accelerator section be represented by a single cavity. Let each cavity be excited in a mode of frequency ω_0 and quality factor Q; let the mode have a vanishing accelerating field E_z along the axis. Furthermore, let the rate of buildup be small compared to ω_0. Consider a particle of charge e to cross the nth cavity at a distance x from the z axis at a time t, and let the distance between cavities be L (Fig. 7-21). Let the fields (**E**, **B**) in the nth cavity be derived from a vector potential **A**. The transverse momentum per cavity is given as in Eq. (7-105) by[20,30]

$$\delta p_x = e \int \frac{\partial A_z}{\partial x} dz \tag{7-117}$$

giving rise to a radial differential equation of motion,

$$\frac{d}{dn}\left(\gamma \frac{dx}{dn}\right) = \frac{eL}{m} \int \frac{\partial A_z}{\partial x} dz \tag{7-118}$$

If the particle is deflected a distance x from the axis, in general it will do work against the field and thus the field amplitudes will be increased. Succeeding particles will then meet a larger deflecting field. This combined action of deflection by suitable fields and excitation of such fields by deflected particles gives rise to a buildup of transverse motion both in time and with distance along the accelerator.

A current eJ will deliver energy to the field at a rate

$$-eJ \int \mathbf{E} \cdot \mathbf{dz} = -Jxe \int \frac{\partial E_z}{\partial x} dz$$

Since $E_z = 0$ on the axis, the rate of buildup of energy U in a deflecting mode is then controlled by the relation

$$\frac{\partial U}{\partial t} + \frac{\omega U}{Q} = \mathrm{Re}\left\{-\frac{eJ}{2} x \int \frac{\partial E_z^*}{\partial x} dz\right\} \tag{7-119}$$

Figure 7-21 Radial orbits in multicavity model.

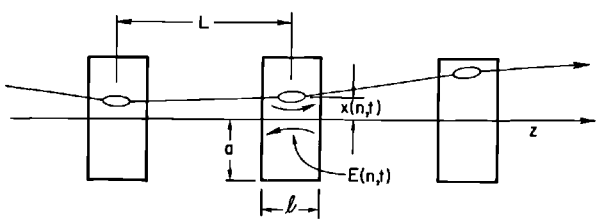

In general, the field energy U depends quadratically on the field integral

$$I = \int \frac{\partial E_z}{\partial x}\, dz$$

Specifically,

$$U = \tfrac{1}{2} \operatorname{Re} \{KII^*\} \tag{7-120}$$

where the constant K is given by

$$K = \frac{a^4}{181l} \tag{7-121}$$

for a simple cylindrical cavity of radius a and "interaction length" l.

When Eqs. (7-118) through (7-121) are combined, the basic beam breakup equation is obtained,

$$\left[\left(\frac{\partial}{\partial t} + \beta\right)\frac{\partial}{\partial n}\left(\gamma \frac{\partial}{\partial n}\right) + iCJ\right]x = 0 \tag{7-122}$$

where the dimensionless constant C is given by

$$C = 14.4\left(\frac{r_0 l\lambda L}{a^4}\right) \qquad \text{and} \qquad \beta = \frac{\omega}{2Q}$$

and where the vector potential $\mathbf{A}$ is assumed to relate to the electric field $\mathbf{E}$ through $\mathbf{E} = -i\omega\mathbf{A}$. These equations govern the buildup of the displacement x with time from section to section, starting from initial disturbances. Among such starting sources are

Shot noise in beam
Shock excitation through misalignments
Thermal noise in early sections
Noise or spurious signals from klystron power sources
Electrical discharges in high microwave fields

Present experimental evidence is not conclusive as to which of these initial driving terms are important. However, all experimental data are consistent with a factor of 10^7 to 10^9 (e^{16} to e^{20}) increase from initial amplitude leading to loss of beam.

The solution of the beam breakup differential equation (7-122) can best be carried out by numerical computations as indicated in a later section. However, the general behavior of such solutions and the applicable scaling can be determined from the asymptotic solution, which can be derived analytically. Such a solution can be obtained by expressing the transverse displacement x as a Laplace transform along an appropriate contour C in the complex μ plane:

$$x(n, t) = e^{-\beta t} \int_C f(n, \mu) e^{\mu t}\, d\mu \tag{7-123}$$

where $f(n, \mu)$ obeys

$$\mu(\gamma f')' + iCJf = 0 \tag{7-124}$$

This has a WKB solution, valid for adiabatic variation of γ,

$$f(n, \mu) \sim \gamma^{-1/4} \exp\{\pm i(iCJ)^{1/2}\mu^{-1/2}g\} \tag{7-125}$$

where g is the integral

$$g(n) = \int_{n_0}^{n} \gamma^{-1/2}\, dn' \tag{7-126}$$

which is a known function of n for a given acceleration program $\gamma(n)$. The aymptotic solution valid for a large blowup factor can be generated by evaluating the integral (7-123) along a contour C along a path of "steepest descent" through the "saddle point" of the exponent located at

$$\mu = (CJ)^{1/3}\left(\frac{g}{2t}\right)^{2/3} e^{-i\pi/6} \tag{7-127}$$

The contour C passes through this point at an angle of $5\pi/12$ to the real axis. Evaluation of the integral gives

$$x(n, t) = x_0(n, t) \exp\left\{3\left(\frac{2^{1/3}}{4}\right)(\sqrt{3} - i)(CJt)^{1/3}g^{2/3} - \beta t\right\} \tag{7-128}$$

where $x_0(n, t)$ is a relatively slowly varying function given by

$$x_0(n, t) \approx J^{1/6}t^{-5/6}g^{1/3}\gamma^{-1/4} \tag{7-129}$$

The growth is thus controlled by the exponent

$$1.64C^{1/3}(tJg^2)^{1/3} \tag{7-130}$$

in the highly transient breakup observed at SLAC, where the term βt is small compared to the previous term. The effective onset of beam breakup corresponds to this exponent, assuming a value of 16 to 20. The exponent defines the scaling laws for beam breakup. The threshold of beam instability will occur for specific values of the quantity

$$s = CtJ\left[\int_{n_0}^{n} \gamma^{-1/2}\, dn'\right]^2 \tag{7-131}$$

This approximate treatment describes the principal qualitative features of the phenomenon and gives a good representation of the scaling laws. It ignores the multiplicity of modes which can generate the phenomenon, and it does not include contributions from the "backward-wave oscillator" mechanism, which is, however, relatively small in the SLAC accelerator. An analytical solution derived by iteration of Eq. (7-122) has been obtained by Bander[31] in the form of a series expansion; extensive results similar to the ones outlined here have been obtained by Voskresenskii, Koroza, and Serebryakov.[32–34]

Effect of focusing on beam breakup (WKHP)

Equation (7-122) describes the particle motion as affected by the beam-induced fields but omits the effect of any external focusing magnetic lenses. Their effect can be included by introducing a smoothed focusing term $\gamma k^2 x$ into Eq. (7-124), where k is the "betatron" wave number discussed earlier. The equation becomes

$$\mu[(\gamma f')' + \gamma k^2 f] + iCJf = 0 \tag{7-132}$$

which has the WKB solution

$$f(n, \mu) = \gamma^{-1/4} \exp\left\{\pm i \int_{n_0}^{n} \left[\frac{iCJ}{\mu\gamma} + k^2\right]^{1/2} dn'\right\} \tag{7-133}$$

Analytical evaluation of this expression by the "steepest descent" method appears difficult in general except for small values of k^2. If only terms linear in k^2 are carried, it is found that the beam breakup threshold is raised by a factor K given by

$$K = 1 + \frac{0.6}{s^{2/3}} \left(\int_{n_0}^{n} \gamma^{-1/2}\, dn'\right)\left(\int_{n_0}^{n} k^2 \gamma^{1/2}\, dn'\right) \tag{7-134}$$

where s is the scaling parameter given previously in Eq. (7-131). This equation gives a fair description of the corrective effect of weak external focusing.

Numerical computation of beam breakup[35] (RHH)

Two different formulations have been used in computational studies of the beam breakup phenomenon: (1) a coupled resonator model, analogous to the treatment of transient wave propagation in the accelerator mode, as discussed in Chapter 6 and (2) the separated cavity model used in the analytical solutions discussed in the previous section.

COUPLED RESONATOR MODEL. Here the notation of Chapter 6 relating to transient filter characteristics and beam loading will be used. The simplified phenomenological wave equation, Eq. (6-17), is employed to describe the details of the interaction of the beam with the deflecting mode in the disk-loaded structure. It is assumed that the cavity wave function characteristic of the HEM_{11} mode is linear in x near the accelerator axis, i.e.,

$$\psi_{zn}(r) \approx x\psi_n^{(1)}(z)$$

where

$$\psi_n^{(1)} = \left[\frac{\partial \psi_{zn}}{\partial x}\right]_{x=0}$$

The transverse momentum impulse for an electron traversing the nth cell in terms of the z component of the vector potential A_{zn} from Eq. (7-117) is

$$g_n(\tau) = \frac{1}{m}\,\delta p_{x,n} = \frac{e}{m}\int_{\text{cell}}\left[\frac{\partial A_{zn}}{\partial x}\right]_e dz' \tag{7-135}$$

where $[\partial A_{zn}/\partial x]_e$ implies evaluation along an electron trajectory. On the assumption that the time variation of A_z is instantaneously sinusoidal, i.e.,

$$[A_{zn}]_e = A_n(\tau)\psi_{zn}\,e^{i\omega_n(\tau+z'/v)}$$

the following is obtained

$$g_n(\tau) = \frac{e}{m}\int_{-l/2}^{l/2}\psi_n^{(1)}(z')A_n(\tau + z'/v)\,dz' \approx \frac{e}{m}\,F_n\,A_n(\tau) \tag{7-136}$$

where

$$F_n = \int_{-l/2}^{l/2}\psi_n^{(1)}(z')e^{i\omega_n z'/v}\,dz' \tag{7-137}$$

is the "form factor" of the nth cell. With this substitution into Eq. (6-17), the wave equation

$$\left(\frac{\partial}{\partial\tau} + \beta_n - i\omega_n\right)g_n(\tau) + \frac{i}{2}\{\tilde{\Omega}_{n-1/2}\,g_{n-1}(\tau) + \tilde{\Omega}_{n+1/2}\,g_{n+1}(\tau)\} = -iC_n J(\tau)x_n(\tau) \tag{7-138}$$

is obtained, where

$\tilde{\Omega}_{n\pm1/2} = \Omega_{n\pm1/2}\,e^{\mp i\omega_n l/v}$,

$\Omega_{n\pm1/2}$ is the half-bandwidth of the structure, related to the coupling between adjacent cells,

$J(\tau)$ is the (slowly varying) beam current amplitude expressed as electrons per unit time,

$x_n(\tau)$ is the RF component of the centroid of the transverse beam displacement which has an instantaneous frequency close to ω_n.

C_n is defined by

$$C_n = \frac{2\pi r_0}{\omega_n}\frac{|F_n|^2}{u_n} \tag{7-139}$$

where $r_0 = e^2/m$ = the classical electron radius, $u_n = \int_{\text{cell}}|\psi_n|^2\,d^3\mathbf{r}'$ as defined in Chapter 6, and F_n is defined by Eq. (7-137).

The geometric constant C_n of Eq. (7-139) is essentially the C of Eq. (7-122) except that the definition here is for a single cell of the disk-loaded waveguide, and transit-angle correction of the cavity has been included through the form factor (Eq. 7-137). The constant C_n may also be related to the

"transverse shunt impedance" defined by Altenmueller, Larsen, and Loew,[30] which is given in the present notation by

$$\left(\frac{r_\perp l}{Q}\right)_n = \left(\frac{R_\perp}{Q}\right)_n = 29.98\,\frac{\lambda_n^3 |F_n|^2}{\pi^2 u_n} \tag{7-140}$$

where $R_\perp$ is the transverse shunt impedance per cavity in ohms, Q_n is the unloaded quality factor of the structure, and λ_n is the RF wavelength.

Evaluation of F_n and u_n by approximating the field as a simple TM_{11} cavity mode gives

$$\frac{r_\perp}{Q} \approx 29.98\,\frac{8\pi}{\lambda_n}\left[\frac{\sin(\pi l/\lambda_n)}{\pi l/\lambda_n}\right]^2\left(\frac{1}{\alpha_{11}J_0(\alpha_{11})}\right)^2 \tag{7-141}$$

where $\alpha_{11} = 3.823\ldots$ is the first root of $J_1(\alpha)$. SLAC parameters give $r_\perp/Q \approx 20$ ohms/cm.

The orbits, in the absence of external focusing, are given by simple recursion formulas:

$$p_{x,n+1/2} = p_{x,n-1/2} + mg_n(\tau) \tag{7-142}$$

$$x_{n+1/2} \approx x_{n-1/2} + \frac{l}{m\gamma_n}\,p_{xn} \tag{7-143}$$

in which the $n \pm \frac{1}{2}$ indices refer to the cell boundaries, and the midcavity values x_n, p_{xn} are appropriate averages.

A computer solution of the above formulation has been developed. The numerical method and boundary options for the wave equation (7-138) are as described in the discussion of transient filter characteristics and beam loading in Chapter 6. Simultaneous evaluation of the beam dynamics equations [(7-142) and (7-143)] is straightforward. For convenience in the numerical integration, the substitutions

$$x_n(\tau) = X_n(\tau)e^{i\omega'\tau} \qquad p_{xn}(\tau) = P_{xn}(\tau)e^{i\omega'\tau} \qquad g_n(\tau) = G_n(\tau)e^{i\omega'\tau} \tag{7-144}$$

are used, where ω' is an arbitrary reference frequency (independent of n) such that $|\omega_n - \omega'| \ll \omega_n$; the complex amplitudes X_n, P_{xn}, and G_n are assumed to vary slowly in phase and magnitude.

The simple dispersion equation, implied by the wave equation (7-138), i.e.,

$$\Omega_n \cos k_n l \approx \omega_n + i\beta_n - \omega \tag{7-145}$$

does not fit the measured dispersion curve over the entire passband (see Fig. 7-20a). However, useful results may be obtained by employing a fit of the parameters Ω_n and ω_n which is valid over a restricted frequency range. Figure 7-30 shows a result, obtained in this way, which simulates several resonant modes characteristic of the first few cavities of the SLAC disk-loaded structure. The existence of such resonances is explained by reference to Fig. 7-29 where it is seen that the π-mode cutoff frequency in the tapered structure increases with distance along the structure; thus a band of frequencies is trapped between the stop band and the input coupler, which is a large mismatch except at the frequency of the accelerating mode. For certain frequencies within this trapped band the round-trip phase shift is a multiple

of 2π, and resonance occurs. The resonances near the beginning of the structure, and particularly the lowest one ($\approx$4140 MHz), are most nearly synchronous with the electrons and, consequently, are the most serious in exciting the breakup effect.

The computer experiments by which these resonances were found were performed by simulating a transverse beam modulation of constant amplitude and by varying the modulation frequency until resonance conditions were satisfied. Comparison of the computed resonances with experimental values are shown in Table 7-7. The "effective lengths" of the modes were found by comparing the net transverse impulse at each resonance with that of a single cell cavity.

Table 7-7 Comparison of computed and experimental resonant modes in the HEM_{11} passband in SLAC waveguide

Computed resonant frequency (MHz)	*Experimental resonant frequency (MHz)*	*Computed effective interaction length (cm)*
4139.4	4139.64	23.2
4147.8	4147.50	8.9
4154.5	4154.00	11.2
4160.5	4159.72	8.1
4165.7	4164.82	8.1

By combining the effective length computed in this way with the shunt impedance per unit length as estimated above [Eq. (7-141)], it was possible to find the interaction impedance for an entire resonating region considered as a single cavity. For the dominant ($\approx$4140 MHz) mode,

$$\frac{R_{\text{eff}}}{Q} = \frac{r_\perp l_{\text{eff}}}{Q} \approx 460 \text{ ohms} \tag{7-146}$$

or in terms of the geometric constants defined in the previous section [Eq. (7-122)],

$$C \approx \left(\frac{\pi^2 r_0 L}{\lambda_n^2}\right) \frac{R_{\text{eff}}/Q}{30\,\Omega} \approx 2.5 \times 10^{-10}$$

A determination of R_{eff}/Q based on experimental beam breakup data is presented in a later paragraph; the result is

$$\frac{R_{\text{eff}}}{Q} = 400 \text{ ohms } (\pm 40 \text{ ohms})$$

which is in reasonably good agreement with the estimate.

Another interesting computer experiment done under the beam breakup theoretical program was an investigation of the regenerative type of blowup in coupled resonator structures. Figure 7-22 shows typical results under

Figure 7-22a Computed regenerative breakup in the first 30 cells of the SLAC injector showing growth of field during regenerative breakup. The quantity plotted is $|g_n|$ or $|A_n|$. Conditions: $I_0 = 3.0$ A; injection energy = 260 keV ($v/c = 0.75$); $Q = 8000$; $r_\perp = 0.16$ megohms/cm. The accelerating field varies approximately in accordance with steady-state beam loading. The starting signal is a delta function impulse of transverse modulation. The breakup takes place at a natural frequency of 4148.5 MHz, about 1 MHz above the second normal mode.

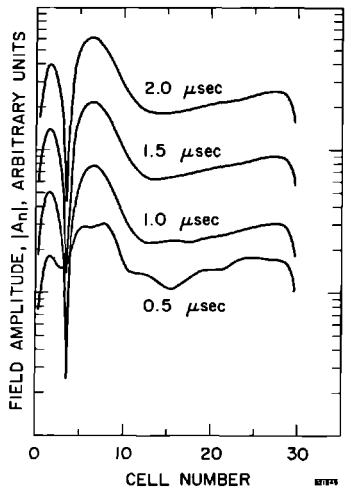

Fig. 7-22b Computed regenerative breakup in SLAC injector showing growth of beam deflection during regenerative breakup at several currents. Conditions same as in Fig. 22a.

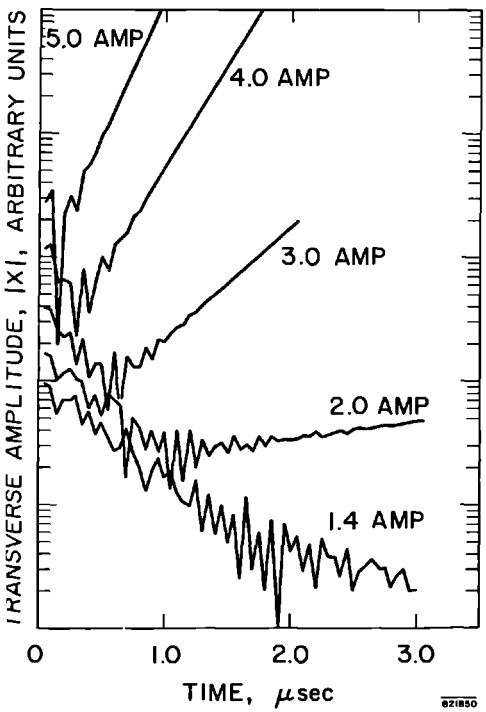

Figure 7-22c Computed regenerative breakup in SLAC injector showing exponential buildup rate of regenerative breakup as a function of beam current. Same conditions as in Fig. 22a.

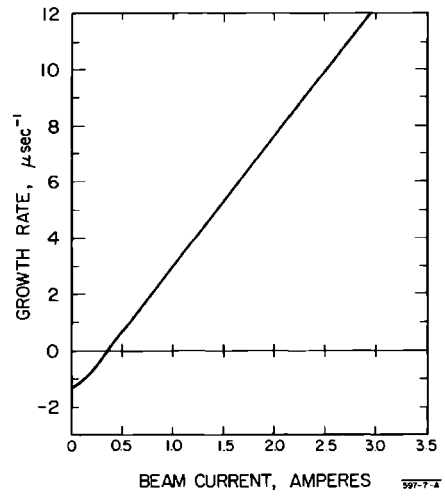

conditions simulating the SLAC injector. As discussed previously, regenerative breakup in a coupled cavity structure does not occur very readily in the SLAC accelerator design.

ISOLATED CAVITY MODEL. Formulation of multisection beam breakup in the previous sections treat the transverse modulation of the beam as a continuous, nearly sinusoidal wave with slowly varying amplitude and phase. Any effects of the longitudinal bunching of the beam are ignored in such a treament because of the implicit assumption that the beam charge is uniformly distributed over RF phase angle. Similarly, nonlinear focusing elements, such as sextupoles, are precluded by the assumption that the modulation is essentially sinusoidal. (It should be noted that the electromagnetic interaction between the beam and the RF deflecting mode is described by an essentially linear theory.)

It is of considerable interest to include these effects in the beam breakup theory. For example, the longitudinal structure of the beam, coupled with accidental misalignments, could contribute to the "shock excitation" of a driving signal to start the breakup. In cases where the bunching frequency and breakup frequency happen to be sufficiently close to a small-integer ratio, there may be important interference effects which could either enhance or dampen the rate of breakup. The effects of longitudinal structure might be of particular importance in the case of subharmonic bunching schemes.

On the other hand, nonlinear focusing elements could provide a mechanism, analogous to Landau damping, whereby the coherence of the transverse modulation would be partially destroyed by dependence of the betatron wavelength on transverse phase space.

As in the previous formulation of isolated cavity breakup, each accelerator section is treated as a short resonant "cavity," which is resonant in one of the modes described above. The form of the wave equation given by Eq. (6-14) is used. For a particular mode in the nth cavity, this becomes

$$\left(\frac{\partial^2}{\partial\tau^2} + 2\beta_n \frac{\partial}{\partial\tau} + \omega_n^2\right) A_n(\tau) = \frac{4\pi}{u_n} \int_{\text{cav}} \psi_{zn}(\mathbf{r}') J_z\left(\mathbf{r}', \tau - \frac{z'}{v}\right) d^3\mathbf{r}' \quad (7\text{-}147)$$

where the various quantities may all be considered real, and the wave function now characterizes the normal mode rather than a single cell. In terms of the normalized momentum impulse [Eq. (7-135)] it may be shown that

$$g_n(\tau) \approx 2C_n \int_0^\tau J(t') x_n(t') e^{-\beta_n(\tau - t')} \sin\left[\omega_{rn}(\tau - t')\right] dt' \quad (7\text{-}148)$$

where the quantities are defined formally in the previous section except that now in the definition of g_n, F_n, and u_n the integrals are over all the cavities participating in the resonance instead of over just a single cavity, and

$$\omega_{rn}^2 \equiv \omega_n^2 - \beta_n^2 \approx \omega_n^2$$

(the loss coefficient, $\beta_n = \omega_n/2Q_n$, is assumed $\ll \omega_n$).

Assuming that the beam current is bunched at a frequency $\omega_b = 2\pi/t_b$ so that

$$J(\tau) = \bar{J}(\tau)t_b \sum_{j=0}^{\tau/t_b} \delta(\tau - jt_b) \tag{7-149}$$

where $\bar{J}$ is the electron current averaged over the bunching cycle and using Eq. (7-148), one finds that the normalized impulse for the jth bunch is

$$g_n(j) = 2C_n t_b \sum_{j'=0}^{j} \bar{J}(j')x_n(j') \{\exp[-\beta_n t_b(j - j')]\} [\sin \omega_n t_b(j - j')] \tag{7-150}$$

This may be expressed more compactly as the imaginary part of a complex function $h_n(j)$,

$$h_n(j) = 2C_n t_b \sum_{j'=0}^{j} \bar{J}(j')x_n(j') \exp[i\theta_n(j - j')] \tag{7-151}$$

where

$$\theta_n = (\omega_n + i\beta_n)t_b \tag{7-152}$$

Figure 7-23 Computed beam breakup (BBU) growth as function of time and distance with typical SLAC parameters. Conditions: acceleration at 600 MeV/sector; $R_\perp/Q = 400$ ohms/active length in a 10-ft section; $Q = 8000$; beam breakup frequency = 4140 MHz; beam current = 7 mA; no focusing.

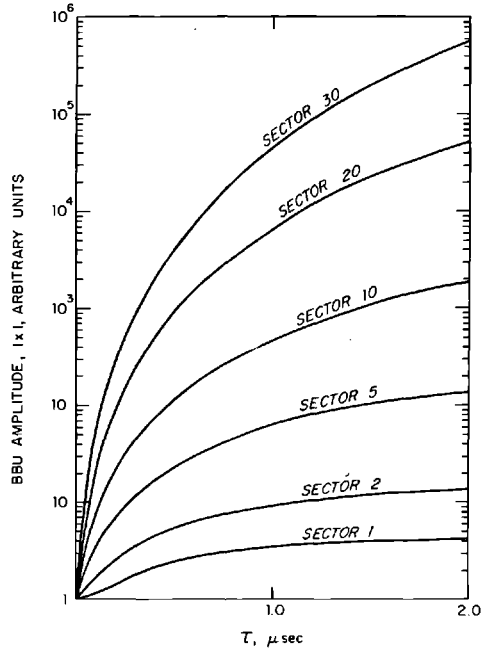

The function h_n satisfies the recursion relation

$$h_n(j) = 2C_n t_b \bar{J}(j) x_n(j) + h_n(j-1) \exp(i\theta_n) \tag{7-153}$$

which is useful for efficient numerical computation because it avoids the necessity of recomputing the entire summation [Eq. (7-150)] with every increment in time (or j).

The transformation of the jth bunch through the nth cavity to an impulse approximation, is

$$\left.\begin{aligned} P_{x,n+1}(j) &= p_{xn}(j) + m \operatorname{Im}[h_n(j)] \\ x_{n+1}(j) &= x_n(j) \end{aligned}\right\} \tag{7-154}$$

The numerical computation is carried out by tracing each successive bunch through the various elements of the system—cavities, accelerator and drift sections, lenses, etc.—starting with initial conditions such as $h_n(0) = 0$ and

Figure 7-24 Effect of external focusing on beam breakup threshold with typical SLAC parameters. Conditions: total length = 30 sectors; one sector = 333 ft; uniform acceleration at 600 MeV/sector; $R_\perp/Q = 400$ ohms/10-ft section; $Q = 8000$; f(beam breakup) = 4140 MHz; $\mu = 1.6$ μsec; constant betatron wavelength. The computed curve is based on sector focusing, i.e., discrete lenses at sector intervals, whereas Eq. (7-134) assumes a uniform and weak focusing force.

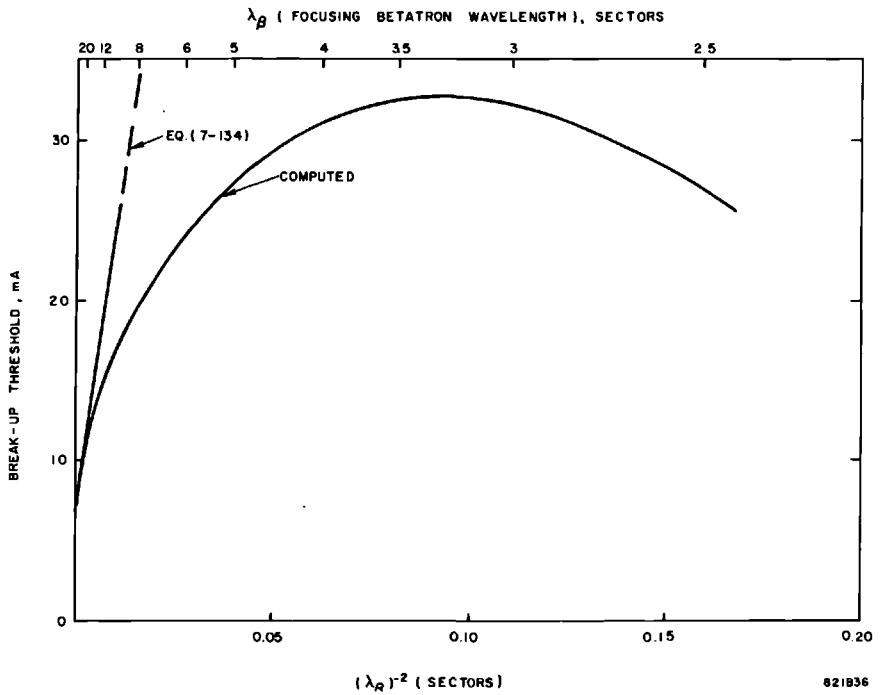

with boundary conditions such as $x_0(j)$ and $p_{x0}(j)$ being given functions of time (bunch number). Numerical calculations for the beam breakup for typical SLAC parameters are shown in Fig. 7-23, plotted in the absence of focusing. Curves computed when focusing is included are shown in Fig. 7-24.

7-5 Beam breakup: observations, experimental laws, and remedies

Qualitative observations (GAL)

The first observation of beam breakup at SLAC was made on April 27, 1966, 1 week after the beam was first turned on over two-thirds of the accelerator's 2-mile length.[36,37] Manifestations of the regenerative phenomenon known alternatively as beam breakup, beam blowup, or pulse shortening had been observed as early as 1957 in various, short, commercially built linacs operating in the 500-mA range. However, it was the surprisingly low current thresholds in the 10 to 20-mA range discovered with the SLAC accelerator which led to the analysis and understanding of the multisection type of interaction presented in the previous section of this chapter. Although the dates are not exactly known, it appears that similar observations made on the 2-GeV Kharkov linac in the U.S.S.R.[38,39] and on another linac in Japan[24] prompted the parallel studies already mentioned above.

The basic manifestation of the beam breakup effect at SLAC is illustrated in Fig. 7-25. As seen from the three video pulses, the injected beam pulse length, shown here to be 1.5 μsec for the top pulse, is shortened erratically when the beam current is increased above a certain value. The shortening becomes more pronounced as the current from the injector is increased. The pattern of pulses shown here can be observed at any location along the accelerator and the onset of breakup is determined by the beam current

Figure 7-25 Oscillograms of beam pulses below and above beam breakup threshold.

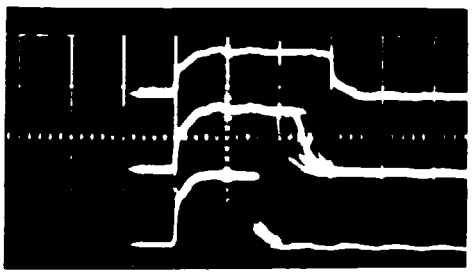

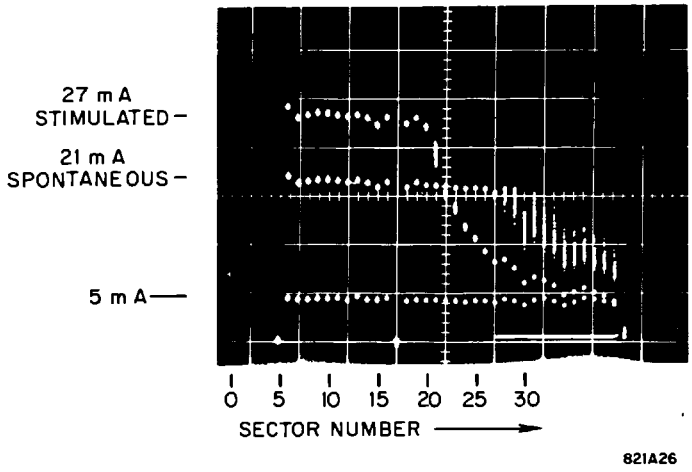

Figure 7-26 Transmitted beam profiles below and above beam breakup threshold (energy: 2 GeV; pulse length; 1.5 μsec).

transmitted through that point. Figure 7-26 shows an example of three different beam profiles along the machine. The ordinates of the dots represent the amount of charge transmitted past the end of each of the thirty accelerator sectors. In the lower trace (5 mA), the beam current from the injector is at a level below the breakup threshold for this particular set of energy, pulse length, and focusing conditions, and no current is lost along the accelerator. In the middle trace (21 mA), the injected current has been increased to a level above the natural breakup threshold. As can be seen, the current transmitted past Sector 20 becomes erratic and an increasingly large fraction of the electron bunches is lost to the accelerator walls and to the beam collimators. Thus, bunches which get transmitted to sectors beyond Sector 20 correspond to increasingly earlier parts of the injected pulse. In the upper trace (27 mA), the injected current has been further increased and, in addition, a few milliwatts of CW power at 4140 MHz have been injected onto the beam by means of an in-line cavity, 40 ft downstream of the injector. It is seen that breakup now occurs as early as Sector 14 and the external stimulation causes the breakup pattern to be less erratic, the amplitude of the driving term of the breakup mode having been stabilized. Still another manifestation of the beam breakup effect is illustrated in Fig. 7-27. This figure is a profile of the pulse obtained from the long ion chamber described earlier in this chapter. The peaks on the fine structure of the display correspond to ionization maxima resulting from beam scraping by the collimators, one of which is located at the end of each of the thirty sectors. In this example scraping starts at Sector 12, and there are 18 peaks to the end of the machine. Finally, Fig. 7-28 shows photographs of beam cross sections as observed at the end of the accelerator on a profile monitor. Various cases are shown. At the top, the current is below

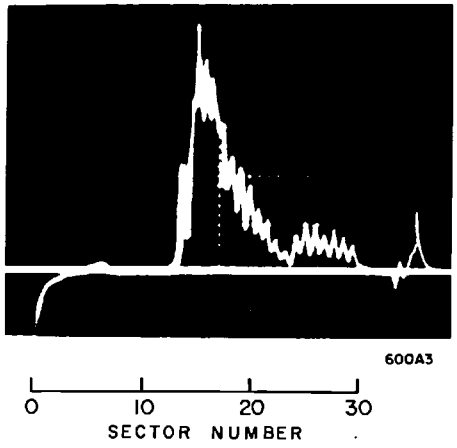

Figure 7-27 Long ion chamber profile for beam breakup at Sector 12 (5 GeV, 1.6-μsec pulse)

threshold for breakup. In the next picture, the breakup appears predominantly in the vertical direction. This direction is approximately perpendicular to the plane of the couplers. As will be discussed below, spontaneous breakup always starts in this plane because the Q of the HEM_{11} mode is greater in the vertical than in the horizontal plane. In the lower figures, the current has been increased even further and breakup now occurs more and more at random in all directions.

As this book is being written, more than a year has gone by since the first observation of beam breakup in the accelerator. Numerous measurements to compare theory and experiment have been performed. In the next two sections, an attempt will be made to summarize the experiments carried out to understand the microwave properties of the HEM_{11} mode and to verify the laws of breakup on the two-mile machine.

Microwave observations and experiments (GAL)

As discussed earlier in this book and particularly in this chapter, one of the important characteristics of the SLAC accelerating structure is that it is of the constant gradient design. Because of the tapered dimensions, the phase shift per cavity for any frequency other than 2856 MHz changes from cavity to cavity. Brillouin dispersion diagrams for specific cavities can be obtained with equivalent cavity stacks. Experimental data for the HEM_{11} mode in cavities at five different locations along a 10-ft section are shown in Fig. 7-29. The lowest resonant frequency at which beam breakup has been observed at the present operating currents (< 100 mA) is 4139.6 MHz, roughly 4140 MHz.

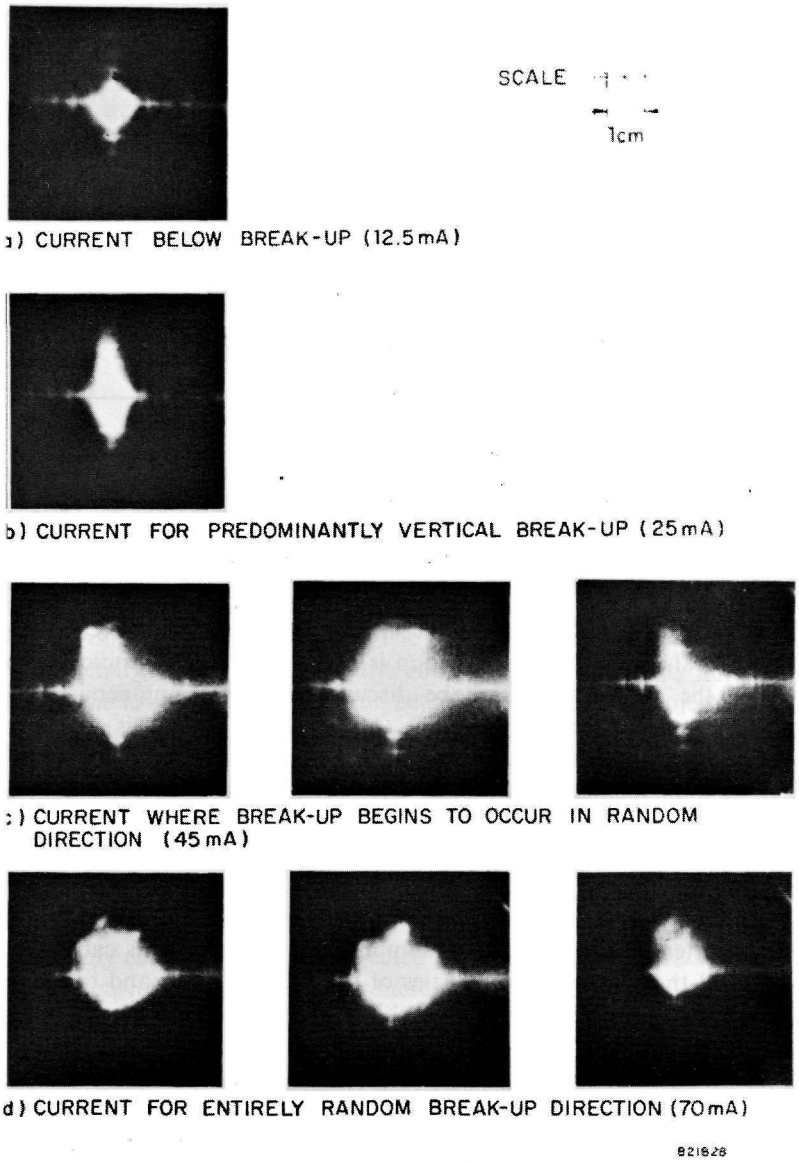

Figure 7-28 Beam cross sections as seen on profile monitor at the end of the accelerator (1.6-μsec beam pulse). These photographs were obtained from a 16-mm movie and represent frames taken at the rate of 24 frames/sec.

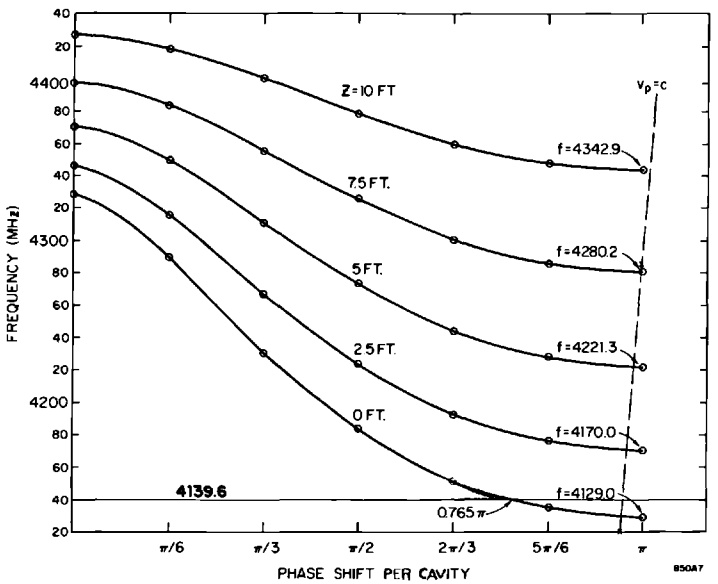

Figure 7-29 Brillouin diagrams for the HEM_{11} mode at five locations along a constant-gradient section.

Since the electrons are bunched at 2856 MHz, the growing sine wave representing the envelope of their displacement appears not only at 4140 MHz but also at the difference frequency, 4140 − 2856 = 1284 MHz. It also appears at the difference between 4140 and the third harmonic of 2856, namely, 4428 MHz, and at 4428 − 2856 = 1572 MHz (etc.). Hence, although the basic microwave interaction takes place only at 4140 MHz, the other frequencies are always present on the beam. They can be detected by means of microwave probes and can also be used to precipitate and sharpen the breakup by artificially stimulating the beam with an external source. The mechanism by which the first and higher resonances can be excited is understood by further examining Fig. 7-29. At 4139.6 MHz, the phase shift of the first cavity beyond the coupler is 0.765π. As the wave at this frequency progresses along the guide, the phase shift per cavity reaches π and then becomes cut-off. As has been illustrated in Table 7-7, the lowest frequency resonance occurs when the phase shift through the first 8 to 10 cavities adds up to a multiple of π. Figure 7-30 shows that there is excellent agreement for the first three resonances between the computer calculations (Fig. 7-30b) and the VSWR measured at the input of the structure (Fig. 7-30a). The amplitude of the electric field intensity for the first mode nearest to the coupler has also been measured by means of a bead perturbation test and is illustrated in Fig. 7-31. The phase angle in Fig. 7-30b is plotted for the wave with respect to a relativistic beam. The fact that this phase angle is not zero can be understood since in Fig. 7-29, the crossover of the $v_p = c$ line allows only quasi-synchronism.

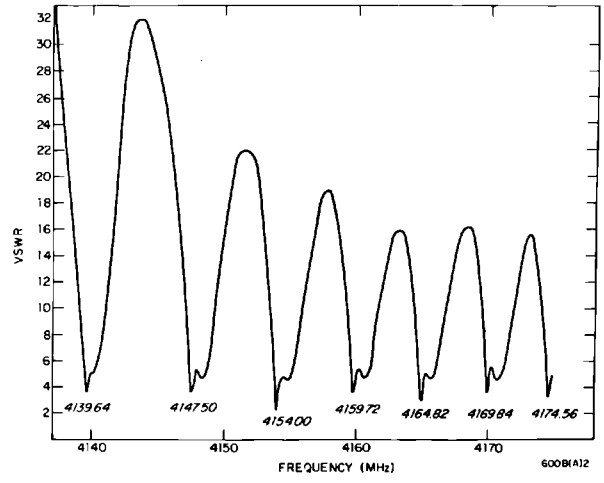

a) VSWR LOOKING INTO SECTION INPUT

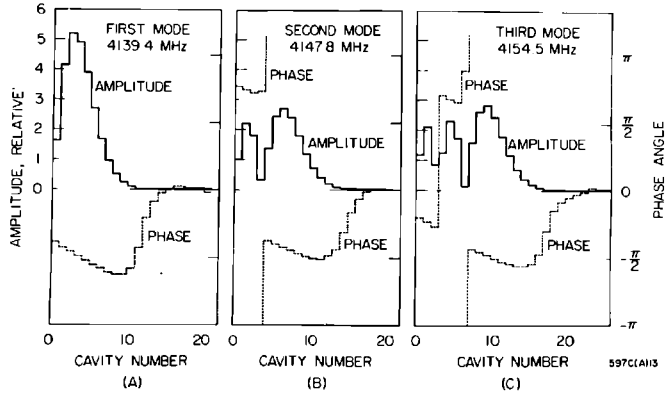

b) EXAMPLES OF COMPUTED AMPLITUDE AND PHASE DISTRIBUTION

Figure 7-30 Measured and computed HEM_{11}-mode resonances in SLAC constant-gradient section. (a) Measured VSWR; (b) computed.

Another important observation to be made in Fig. 7-30a is the fact that the valleys in the VSWR curve exhibit two minima. Although this fact is not yet completely understood, it appears that the two minima correspond to the horizontal and vertical HEM_{11} mode polarizations. Whether beam breakup starts from noise or is stimulated through some external source, both horizontal and vertical polarizations are possible. This fact is further illustrated in Fig. 7-32 where the mode polarization of the HEM_{11} wave excited through the horizontal input coupler of an accelerator section is plotted as a function of frequency. As already shown in Fig. 7-28, for low beam currents and long

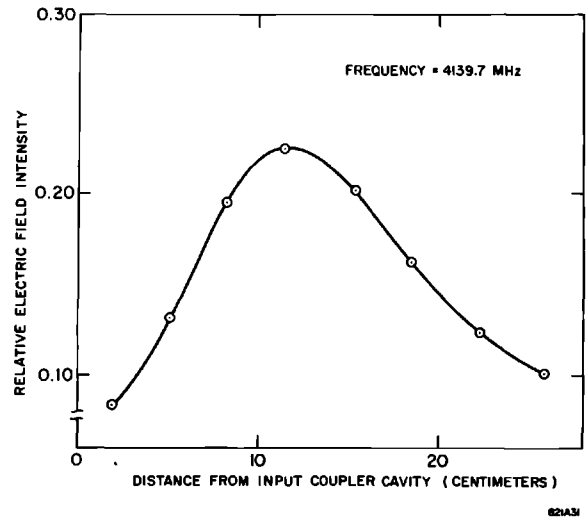

Figure 7-31 Measured electric field variation in the first eight cavities of a 10-ft accelerator section, when excited at 4139.7 MHz through the input coupler.

Figure 7-32 Axial electrical field intensity for the HEM_{11} mode in the first eight cavities of a 10-ft accelerator section as function of azimuthal angle, when excited through the input coupler. Plots are shown for five different frequencies.

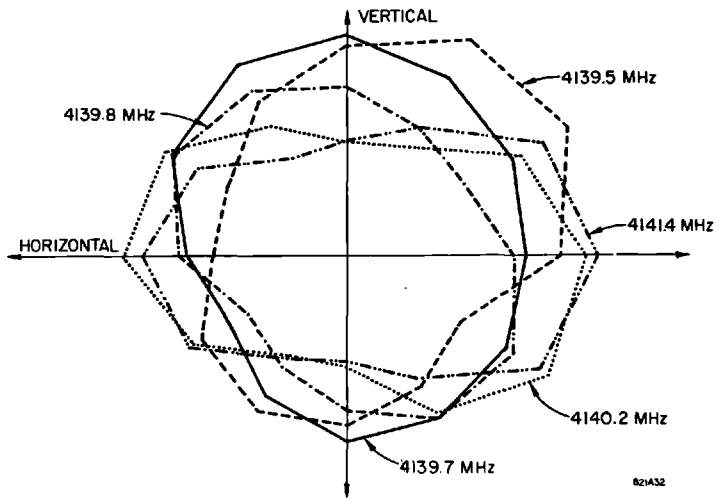

pulses, breakup appears first in the vertical plane, and it is only after increasing current above the vertical threshold in a ratio of approximately 3 : 2 that the orientation of the breakup plane becomes random. Although a definitive measurement of Q has not yet been made, it appears that the value in the vertical plane, Q_0, is of the order of 8000 and that Q_L, the loaded Q in the horizontal plane, is roughly two-thirds of this value. The one-way travel time of the resonant wave is of the order of 50 nsec. Hence, for very short high-current injector pulses, the beam still breaks up in one plane, but since there is no time for resonant buildup, the orientation of the plane is random from pulse to pulse.

In addition to the cold tests described so far in this section, several other microwave experiments were conducted directly on the accelerator. These experiments included the measurement of beam breakup gain and investigation of the effects of external stimulation, as will be described in the next paragraph, and the "feedback" described below. For this purpose several in-line cavities were installed along the accelerator in available space in the drift sections. An example of two such C-band cavities is shown in Fig. 7-33. Similar cavities resonant at the difference frequency, 1284 MHz, were also installed at discrete locations for the purpose of performing feedback experiments. The object of the feedback experiments was to derive a beam-induced signal proportional to the beam transverse displacement in one cavity, to amplify the signal, and feed it back into an adjacent cavity so as to impart a corrective transverse momentum impulse to the beam. One such experiment, illustrated in Fig. 7-34, was performed at 1284 MHz with a 10-kW pulsed output amplifier. The total gain and time delays in the feedback chain were approximately 100 dB and 50 nsec, respectively. Measurements on frequency modulation through the 1284-MHz pulse indicated that a 50-nsec time delay introduced only 12° phase slip between induced and fed-back signals. With

Figure 7-33 Cavities (4140 MHz) used in breakup experiments.

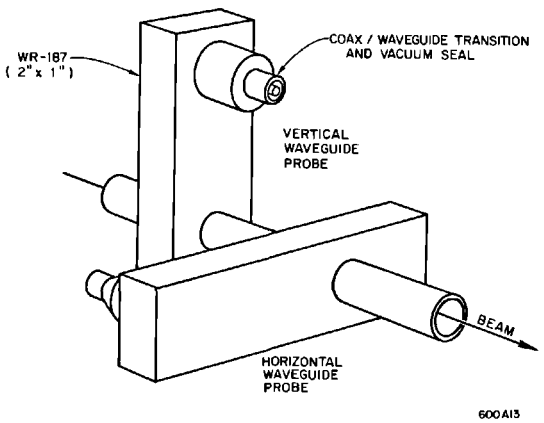

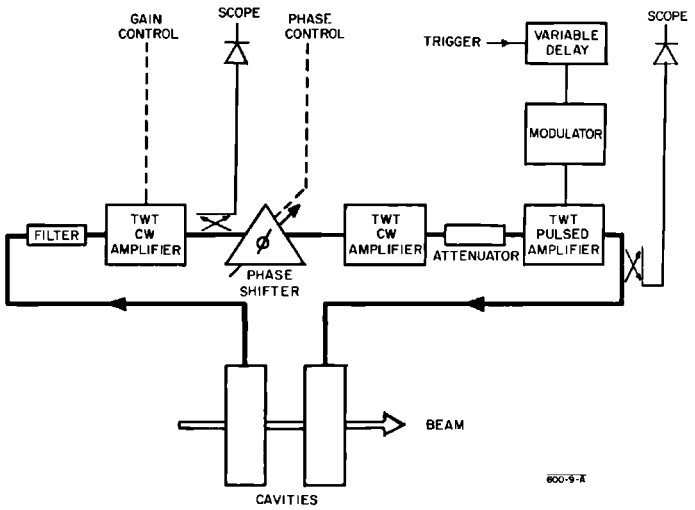

Figure 7-34 Block diagram of beam breakup, feedback experiment.

the equipment installed at the end of Sector 3, after very careful phase and gain adjustments, it was barely possible to move the location of natural breakup for a given current by as much as one sector length. When the current was increased by 20%, cancellation was no longer obtained. From this experiment, it was concluded that to make the feedback system workable, several stages would be necessary along the machine, perhaps as many as five to ten. Since the cavities only pick up one polarization, both horizontal and vertical cavities would be required. The gain and bandwidth of the amplifier chains would have to be considerable, and the system would, thus, be very expensive and complex. For these reasons, as will be discussed below, feedback cancellation was not adopted as a beam breakup remedy at SLAC.

Experimental verification of beam breakup laws (GAL)

The analytic expressions and computational studies presented early in this chapter have been tested experimentally on the SLAC accelerator under a variety of conditions. The degree to which these laws have been verified will now be discussed.

Referring to Eqs. (7-128) and (7-131), it is seen that for uniform acceleration, the variation of beam breakup current as a function of inverse distance should be approximately linear. This fact, verified by computer calculations, is illustrated in Fig. 7-35. Similarly, it can be shown that for a beam accelerated to a given point and coasting from there on, proper integration of Eq. (7-126) gives a parabolic variation of log x as a function of the cube root of the distance where x is the transverse amplitude of the beam. This fact is shown in Fig. 7-36. If, on the other hand, distance and pulse length are kept

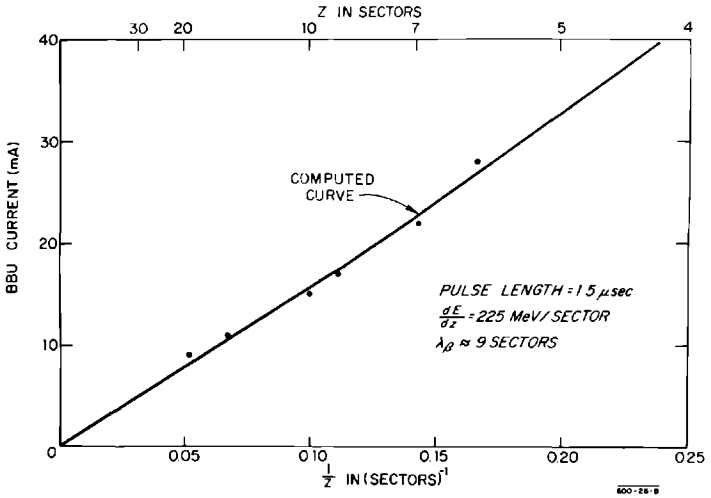

Figure 7-35 Beam breakup (BBU) current vs inverse length.

Figure 7-36 Logarithm of square root of induced beam breakup power (proportional to transverse beam amplitude) vs sector number, for a coasting beam with moderately strong focusing. The solid curve was found by simulating the experimental conditions (including focusing) with the computer program and agrees moderately well with the simple analytical formula [Eq. (7-126)].

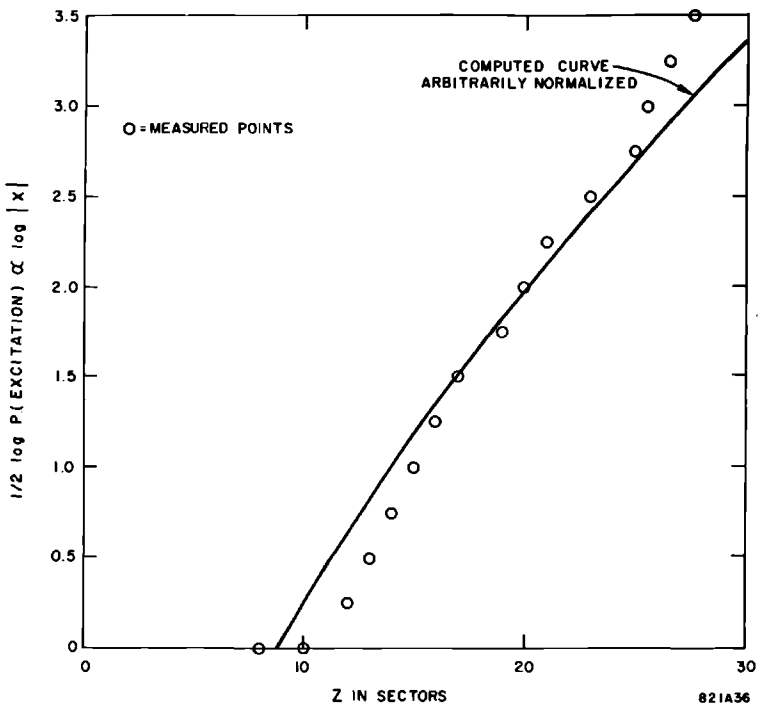

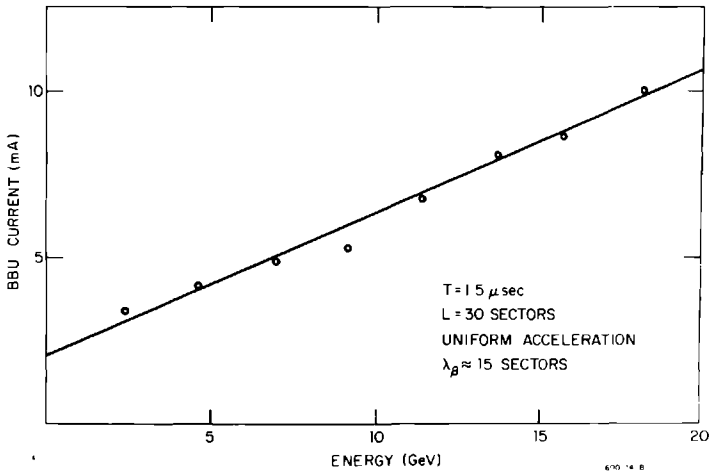

Figure 7-37 Beam breakup (BBU) current vs energy; weak focusing.

constant, then in the case of weak focusing, the variation of beam breakup threshold current as a function of energy gradient γ', should be linear as illustrated in Fig. 7-37. When stronger focusing is applied, Eq. (7-132) is no longer easy to solve, and one must resort to the computer calculations. Figure 7-38 shows a plot of beam breakup current as a function of betatron phase shift per sector. It is seen that when the theoretical data is normalized to one given experimental point, the agreement with experiment is excellent. For relatively weak focusing, the curves for different energy gradients are close to straight lines.

Further examination of the solution of Eq. (7-122) prompts one to examine the variation of the pulse length t as a function of the variable* $(tIz)^{1/3}$ evaluated at the beam breakup threshold. This is done in Fig. 7-39, and it is seen that for fixed focusing conditions, the curves are close to straight lines. This result is understandable because, neglecting focusing and the slowly varying coefficient $x_0(n, t)$ of Eq. (7-128), the slope of these curves should be a function of the loss term β, which is constant. A curve which is probably of greater interest to accelerator users who wish to know the maximum current obtainable as a function of pulse width is given in Fig. 7-40. Both experimental and computed total charge and peak beam current are plotted. For example, for a 50-nsec pulse, the maximum obtainable current below breakup is 250 mA peak.

Another way of verifying the laws of beam breakup is to measure indirectly the relative amplitude of the transverse modulation. A particular variable of interest is $(Iz)^{1/3}$. In Fig. 7-41, the experimental points for the ordinate x,

* The term (tIz) is analogous to the earlier term (tJg^2) of Eq. (7-130).

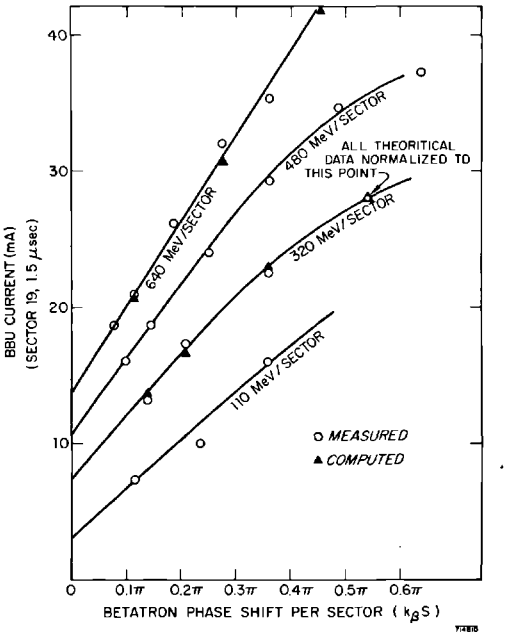

Figure 7-38 Beam breakup (BBU) current vs focusing strength expressed as betatron phase shift per sector.

Figure 7-39 Curves of $(tIz)^{1/3}$ vs t at beam breakup threshold.

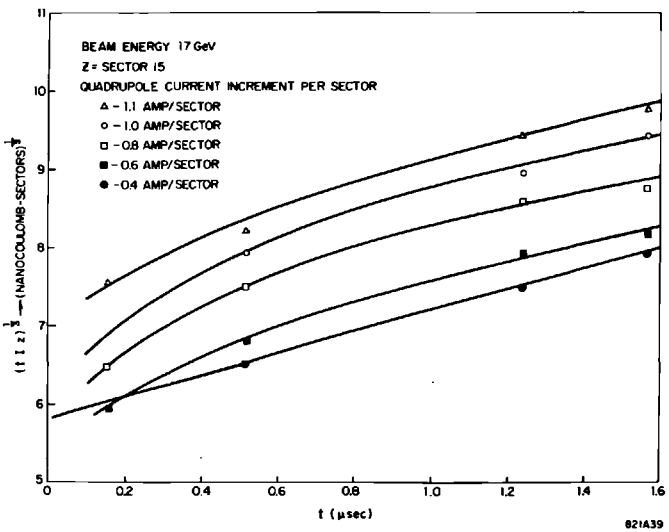

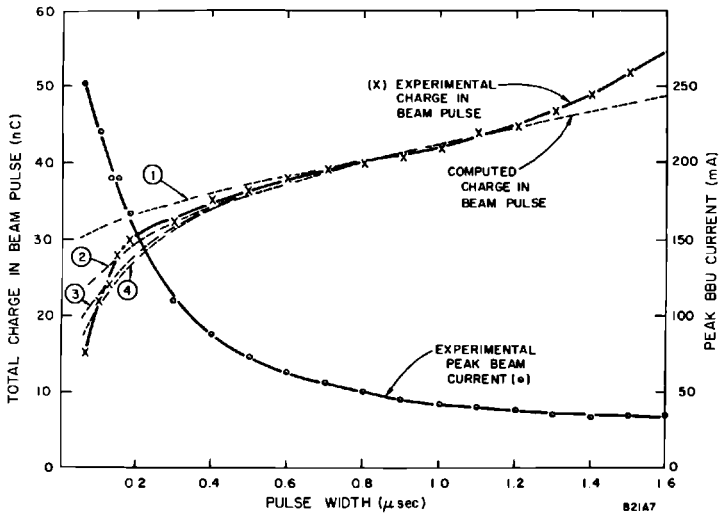

Figure 7-40 Experimental and computed beam breakup threshold as a function of pulse width. Curve 1 is computed, considering only the dominant (4139.64 MHz) resonant mode; curve 2 includes the effect of the first two modes (4139.64 and 4147.50 MHz); curve 3 includes the first three modes (4139.64, 4147.50, and 4154.00 MHz); and curve 4 includes the first four modes (4139.64 through 4160.5 MHz). It is assumed in the computation that $Q = 8000$ for all modes and that $R_\perp/Q = 400$ ohms/10-ft sections for the dominant mode. The values of $R_\perp/Q$ for the other modes are scaled according to the computed "effective lengths" given in Table 7-7. The failure of the computation to predict the time dependence in detail is probably due in part to the effects of transient beam loading and beam current pulse shape, which are not taken into account in the computation.

were obtained indirectly from the microwave power induced in one of the C-band cavities described in the previous paragraph. Computed values are also shown. Similarly, it has been possible to verify the law of beam breakup gain as illustrated in Fig. 7-42. The experimental points were obtained by successively disconnecting klystrons along the accelerator and measuring the amount of injected microwave power at 4140 MHz required barely to affect pulse shortening at a fixed point along the machine, namely the end of Sector 19. Again, it is seen that agreement with the computed power is quite good.

In the experiments discussed so far, the beam breakup starting conditions have not been considered. As mentioned earlier in this chapter, there appear to be several competing noise sources at the beginning of the accelerator which are illustrated in somewhat simplified form in Fig. 7-43. As this book is being written, experiments are still being conducted to discover if one of

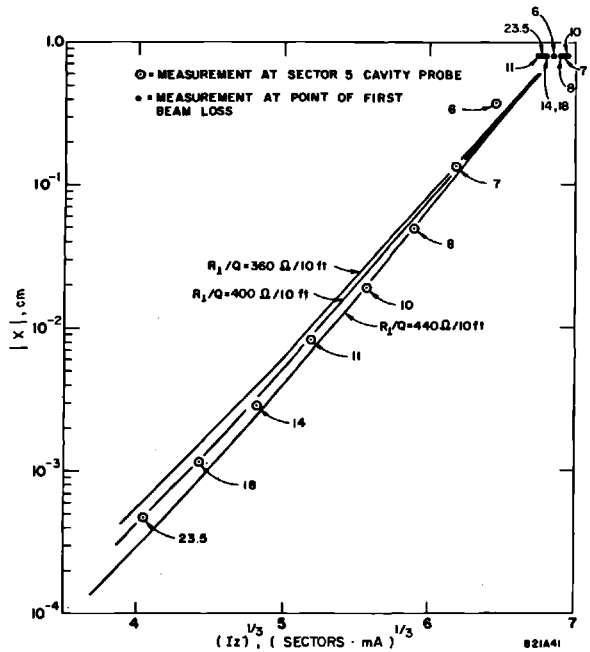

Figure 7-41 **Transverse modulation in beam breakup as a function of $(Iz)^{1/3}$. The circled points were measured by means of a C-band cavity probe at the end of Sector 5; the solid points correspond to points along the machine at which breakup occurred at $\tau = 1.6$ μsec. The number attached to each point represents the sector at which breakup was first observed at a given beam current. The three curves for different values of $R_\perp/Q$ were calculated by the computer program. Comparison indicates an experimental value of $R_\perp/Q \approx 400 \pm 40$ ohms/10-ft accelerator section.**

the sources is dominant. However, whether this is the case or not, it should be pointed out that it would take a significant reduction in noise power before the effect on the current threshold would become noticeable. Hence, letting the exponent given by Eq. (7-130) be called F, it can be shown that a reduction in noise power R in decibels corresponds to a relative increase in beam breakup threshold

$$T = \left(1 + \frac{R_{\text{dB}}}{8.68\,F}\right)^3 \tag{7-155}$$

Thus, for example, letting $R \approx 20$ dB and $F \approx 20$, it is seen that $T = 1.39$, giving less than 40% improvement in current.

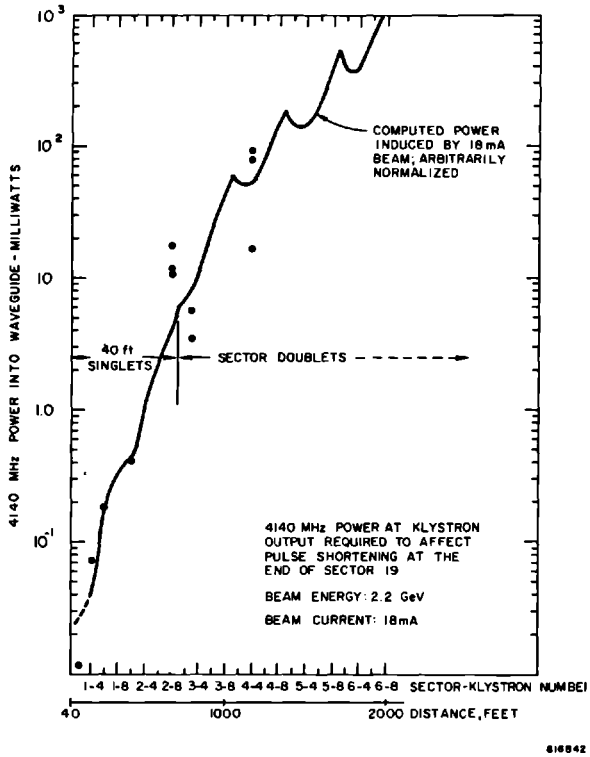

Figure 7-42 Beam breakup power vs distance.

Figure 7-43 Diagram of beam breakup, noise excitation mechanisms.

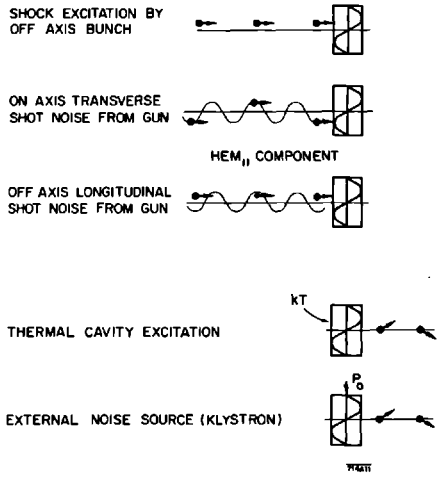

If shock excitation were the dominant driving term, the breakup threshold should be particularly sensitive to misalignment or mis-steering in the beginning of the accelerator. The threshold should also be strongly dependent on gun pulse shape. Finally, if x_0 in Eq. (7-128) is at least linear with J, the initial equivalent noise power would have to be quadratic with J. None of these assumptions has yet been clearly verified. On the other hand, if shot noise were the dominant source, the equivalent noise power would be linear with injected current. To test this idea, the following experiment was devised. At the 40-ft point, downstream of the injector, power P_0 at 4140 MHz was injected into the in-line C-band cavity mentioned earlier. At the end of Sector 5, roughly 1600 ft downstream, beam-induced power P_5 was extracted from a similar cavity. In the absence of any external excitation, this induced power P_5 was measured for a given beam current. Then, the injected power P_0 was increased until P_5 was roughly doubled. This measurement was repeated over a range of beam currents and at different times. Since that fraction of injected power P_0 which actually acts on the electron bunches must be of the same order of magnitude as the natural noise power carried by the beam, a relative, normalized measure of noise can be inferred. The results, which are plotted in Fig. 7-44, do not allow one to distinguish whether the normalized noise

Figure 7-44 Injected noise power equivalent to interval noise vs beam current.

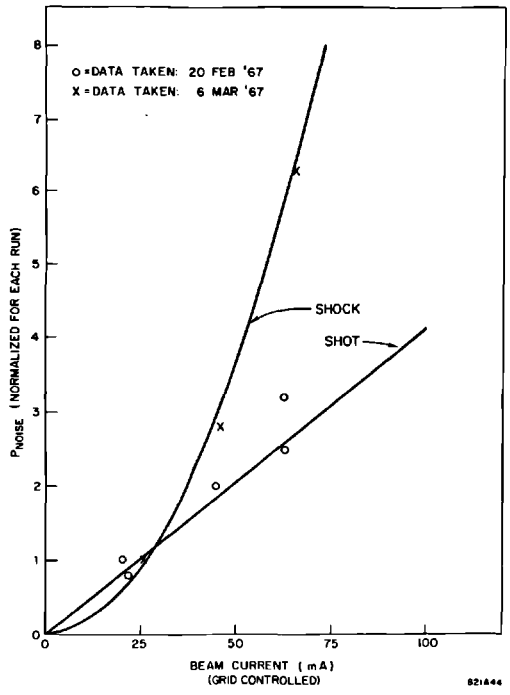

power is linear or quadratic with beam current. However, it can be concluded with fair certainty that this power is not entirely independent of current and, hence, that neither klystron noise nor cavity thermal excitation are the only sources of beam breakup noise. This conclusion is further confirmed by another experiment where the operation of the injector gun was taken from the temperature-limited region into the space-charge-limited region. As seen in Fig. 7-45, an improvement in beam breakup threshold of about 12% was found by increasing the cathode filament power from the temperature-limited to the space-charge-limited case. Unfortunately, under normal conditions, the gun is already operating under space-charge-limited conditions and straightforward improvements do not seem easily obtainable. Attempts are presently being made to design a cathode with a smaller radius which may, if shot noise is dominant, increase the present threshold. Finally, referring back to Fig. 7-42, it should be noticed that in the position where the first klystron was disconnected, an equivalent noise power of 12 μW was required. This value sets an upper limit to the allowable noise power from a high-power klystron. Above this value, klystron noise power would certainly become the dominant driving term for beam breakup. As this book is being written, it has not been possible to ascertain whether, indeed, the noise power from the klystrons is above or below this value. However, high-power filters capable of selectively attenuating signals at 4140 and 4428 MHz are being designed and will eventually be installed in the outputs of the early klystrons in the accelerator.

Figure 7-45 Beam breakup current vs cathode temperature (filament power).

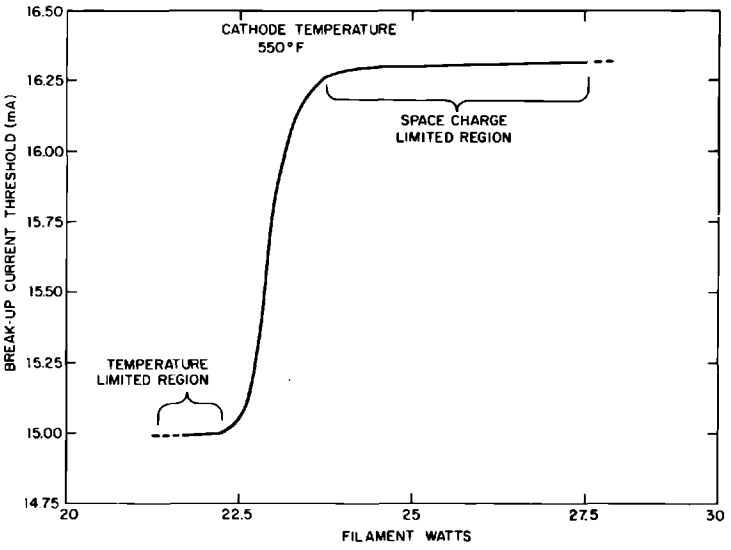

The magnetic fix program (RHH)

SUMMARY OF ALTERNATIVE BEAM BREAKUP REMEDIES. We list here some of the schemes which have been considered for suppression of the beam breakup at SLAC, and the reasons for rejecting most of them:

1. "*Landau damping*" *mechanisms.* Here we refer to any mechanism which destroys the coherence of the transverse beam oscillations. Two possibilities have been considered: (a) varying the focusing strength as a function of time during the RF pulse, e.g., by addition of ferrite quadrupoles modulated at a few MHz; and (b) nonlinear focusing, e.g., by addition of sextupole or octupole magnetic lenses. Computer investigation has indicated that both these schemes would be very ineffective under SLAC conditions. The key to this failure is the fact that the Landau mechanisms can be effective only if the instability grows adiabatically over many betatron wavelengths. In the SLAC transport system, the maximum number of betatron wavelengths in the entire machine is on the order of 10, whereas the *e*-folding distance for the beam breakup is on the order of a sector or less at onset of beam loss.
2. *RF cancellation.* The positive result of the RF cancellation experiment, described in an earlier section, proves that active RF suppression can work in principle. The expense and operational complexity appear to be prohibitive, however. We note in passing that true feedback, over a significant fraction of the machine, is ruled out (for low duty factor linacs) by the transit time problem.
3. *Starting-noise suppression.* Some effort has been devoted to the possibility of filtering the klystron output to remove frequency components in the 4140-MHz band. This is likely to give only marginal improvements, however, because both statistical beam fluctuations (shot noise) and shock excitation through misalignments appear to be of sufficient magnitude, even under best conditions of gun operation, steering, and alignment, to initiate the instability.
4. *RF "fixes" (passive).* Some possibilities are: (a) modification of the RF structure to decrease the coherence (effective length); (b) using several different accelerator modifications that resonate at different frequencies in the HEM_{11} band, so that the amplification in different sections is incoherent; (c) "Q-spoiling," i.e., coupling power selectively out of the HEM_{11} fields. The use of some sort of passive structure, which is excited by the transverse modulation and imparts a net demodulating impulse, also has been suggested. The most promising sort of passive RF fix for SLAC appears to be a selective detuning of the first cells of existing accelerator sections, over a finite fraction of the machine. These various approaches are under continuing study, but as of this writing (July 1967), no definite conclusions have been reached.

5. *Brute force* (*external focusing*). As has been seen in the previous sections, this approach gives a demonstrable improvement in the beam breakup threshold. Focusing has the additional advantage of nonselectively suppressing instabilities associated with other HEM_{11} resonances, higher transverse modes, and wake-field interaction.

THEORETICAL CONSIDERATION; CHOICE OF FOCUSING MODIFICATION. As was shown in a previous section, the improvement in beam breakup current threshold from external focusing is proportional (in the weak-focusing limit) to the quantity

$$\int \gamma^{1/2} k^2 \, dz$$

[see Eq. (7-134)] where k is the betatron wave number. In terms of the quadrupole strength, this integral is proportional to

$$\int \gamma^{-3/2} S^2 \, dz \tag{7-156}$$

where S is the quadrupole strength (gradient × length) referred to as Q in Section 7-2.

Thus, if the focusing is limited by the low-energy stop band, so that the quadrupole strength can be increased in proportion to beam energy, then the integrand goes as $\gamma^{1/2}$, and it is advantageous to increase the focusing at the high-energy end of the machine.

If, on the other hand, the limitation is imposed by available quadrupole strength so that $S \approx$ constant, then the integrand goes as $\gamma^{-3/2}$, and it is advantageous to concentrate the relatively weak quadrupoles at the low-energy end.

In order to take advantage of these considerations, a scheme was evolved for a more efficient arrangement of the original sector triplet quadrupoles.* In the first phase of the conversion, all the sector triplets were reconnected as doublets, using only the outer two, weaker, QA quadrupoles. The stronger QB quadrupoles were then removed from the drift sections and used to convert the doublets in the last two-thirds of the machine to QB doublets (this required changing some of the special positron triplets to doublets, also). Finally, the excess QA's which were thus released were then used to convert the first six sectors to the 40-ft alternating singlet system.

IMPROVEMENTS IN BEAM BREAKUP THRESHOLD; COMPUTED AND OBSERVED. Figures 7-46 and 7-47 illustrate computer results from which improvement factors were predicted, based on the best estimates of the deflecting mode parameters as of September 1966 and June 1967, respectively. In these figures, "Phase 0" refers to the system as originally designed, capable of being

* See Section 7-3 for detailed description of the existing transport system.

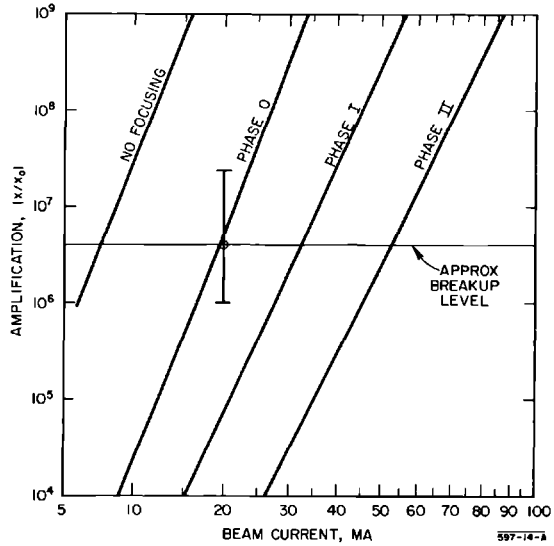

Figure 7-46 Beam breakup gain vs beam current for various earlier focusing schemes.

Figure 7-47 Similar to Fig. 7-46 but based on parameters as of June, 1967. Conditions: uniform acceleration to 18 GeV; $R_\perp/Q = 400$ ohms/10-ft section; $Q = 8000$; $\tau = 1.6$ μsec. "Phase I-A" differs from the "Phase I" of Fig. 7-46 in that the quadrupole singlets had been installed in Sectors 1 and 2. "Phase II-A" differs from the "Phase II" of Fig. 7-46 in that "Phase II-A" is based on the actual 40-ft spaced quadrupole singlets in Sectors 1 through 6, while "Phase II" was based on the assumption of 80-ft spaced doublets in Sectors 1 through 6. The circled points represent observed maximum currents under conditions similar to those for which the curves were computed.

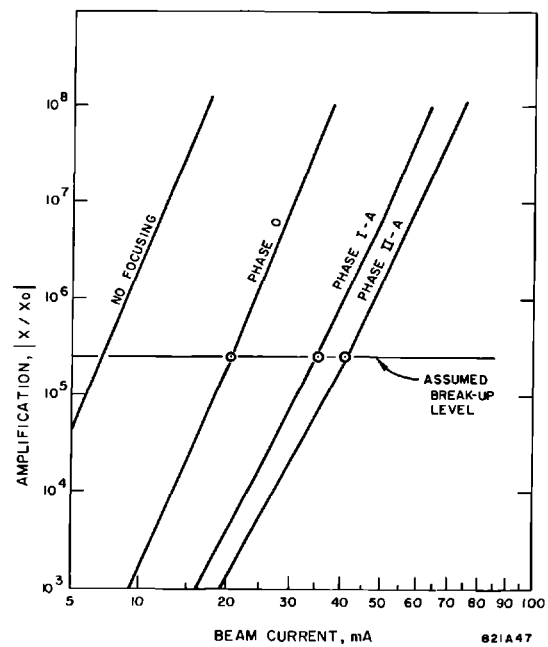

focused to optimum strength only up to Sector 7; "Phase I" refers to the first stage of quadrupole rearrangement in which the optimum focusing taper could be carried through most of the machine; and "Phase II" means the final stage in which additional lenses have been placed at closer spacing in the first six sectors.

(Actually, Phase I never existed; the alternating singlets were installed in the first two sectors before the doublet conversion was completed. This is taken into account in the "Phase I-A" line in Fig. 7-47.)

The experimental beam current thresholds, shown for comparison, are seen to be in reasonable agreement with the predictions.

References

1 M. S. Livingston and J. P. Blewett, *Particle Accelerators*, McGraw-Hill, New York, 1962.

2 W. K. H. Panofsky, "Note on Radial Beam Dynamics," Tech. Note No. SLAC-TN-63-89, Stanford Linear Accelerator Center, Stanford University, Stanford, California (1963).

3 R. H. Helm, "Notes on Electromagnetic Forces in Linear Accelerators," Tech. Note No. SLAC-TN-63-107, Stanford Linear Accelerator Center, Stanford University, Stanford, California (1963).

4 J. S. Bell, "Basic Algebra of the Strong Focusing System," Rept. No. AERE-T/R 1114, Atomic Energy Research Establishment, Harwell, Berkshire, England (January 1953).

5 A. P. Banford, *The Transport of Charged Particle Beams*, E. and F. N. Spon, London, 1966.

6 Klaus G. Steffen, *High Energy Beam Optics*, Wiley (Interscience), New York and London, 1965.

7 P. A. Sturrock, *Static and Dynamic Electron Optics*, Cambridge Univ. Press, London and New York, 1955.

8 E. D. Courant and H. S. Snyder, *Ann. Phys. N.Y.* **3**, 1 (1958).

9 P. A. Sturrock, "A New Interpretation of the Adiabatic Approximation," Rept. No. AERE-TM-88, Atomic Energy Research Establishment, Harwell, Berkshire, England (September 1953).

10 R. H. Helm, "Discussion of Focusing Requirements for the Stanford Two-Mile Accelerator," Rept. No. SLAC-2, Stanford Linear Accelerator Center, Stanford University, Stanford, California (August 1962).

11 R. H. Helm, "Optical Properties of Quadrupole Multiplets for Sector Focusing in the Two-Mile Accelerator," Rept. No. SLAC-14, Stanford Linear Accelerator Center, Stanford University, Stanford, California (February 1963).

12 Albert Septier, "Strong Focusing Lenses," *Advan. Electron. Electron Phys.* **14**, 85.

13 A. Sessler, Lecture given at the Stanford Linear Accelerator Center, May 26, 1966 (unpublished).

14 R. H. Helm, "Misalignment and Quadrupole Error Effects in a Focusing System for the Two-Mile Accelerator," Rept. No. SLAC-11, Stanford Linear Accelerator Center, Stanford University, Stanford, California (January 1963).

15 R. H. Helm, "Misalignment and Quadrupole Error Problems Affecting the Choice of Multiplet Type for Sector Focusing of the Two-Mile Accelerator," Rept. No. SLAC-15, Stanford Linear Accelerator Center, Stanford University, Stanford, California (March 1963).

16 H. C. DeStaebler, Jr., "Scattering of Beam Electrons by the Residual Gas in the Accelerator," Rept. No. M-281, Stanford Linear Accelerator Center, Stanford University, Stanford, California (1961).

17 Bruno B. Rossi, *High Energy Particles*, Prentice-Hall, Englewood Cliffs, New Jersey, 1952, p. 65.

18 R. H. Helm, "A Note on Coupler Asymmetries in Long Linear Accelerators," Rept. No. M-167, Stanford Linear Accelerator Center, Stanford University, Stanford, California (March 1960).

19 R. H. Helm, "Effects of Stray Magnetic Fields and RF Coupler Asymmetry in the Two-Mile Accelerator with Sector Focusing," Rept. No. SLAC-20, Stanford Linear Accelerator Center, Stanford University, Stanford, California (October 1963).

20 W. K. H. Panofsky and W. A. Wentzel, *Rev. Sci. Instr.* **27**, 967 (1956).

21 W. B. Herrmannsfeldt and B. L. Salsburg, *Rev. Sci. Instr.* **35**, 906 (N) (1964).

22 W. B. Herrmannsfeldt, *IEEE Trans. Nucl. Sci. NS-12*, 929 (1965).

23 A. Sessler, "Instabilities of Relativistic Particle Beams," *Proc. 5th Intern. Conf. High-Energy Accelerators, Frascati, 1965* (C.N.E.N., Rome, 1966), pp. 319–329.

24 H. Hirakawa, *Japan J. Appl. Phys.* **3**, 27 (1964).

25 M. G. Kelliher and R. Beadle, *Nature* **187**, 1099 (1960).

26 T. R. Jarvis, G. Saxon, and M. C. Crowley-Milling, *Proc. Inst. Elec. Engrs. (London)* **112**, 1795 (1965).

27 P. B. Wilson, "A study of Beam Blow-up in Electron Linacs," Rept. No. HEPL-297 (Rev. A), High Energy Physics Laboratory, Stanford University, Stanford, California (June 1963).

28 H. Hahn, *Rev. Sci. Instr.* **34**, 1094 (1963).

29 W. K. H. Panofsky, "Transient Behavior of Beam Break-up," Tech. Note No. SLAC-TN-66-27, Stanford Linear Accelerator Center, Stanford University, Stanford, California (1966).

30 O. H. Altenmueller, R. R. Larsen, and G. A. Loew, "Investigations of Traveling-Wave Separators for the Stanford Two-Mile Linear Accelerator," Rept. No. SLAC-17, Stanford Linear Accelerator Center, Stanford University, Stanford, California (August 1963).

31 M. Bander, "Solution of the Beam Break-up Equation," Tech. Note No. SLAC-TN-66-28, Stanford Linear Accelerator Center, Stanford University, Stanford, California (June 1966).

32 G. V. Voskresenskii, V. I. Koroza, and Yu. N. Serebryakov, "Transverse Instabilities of a Beam in a Linear Accelerator prior to Increasing Injection

Current," *Uskoriteli* (Accelerators), Vol. 8, p. 136, Moscow Inst. Eng. Phys., Atomizdat, Moscow, 1966.

33 G. V. Voskresenskii *et al.*, *Soviet At. Energy* **20**, 3 (1966).

34 G. V. Voskresenskii, V. I. Koroza, and Yu. N. Serebryakov, "Toward the Investigation of the Radial Instability of a Beam in a Linear Electron Accelerator," *Uskoriteli* (Accelerators), Vol. 9, Moscow Inst. Eng. Phys. Atomizdat, Moscow, 1966.

35 R. H. Helm, "Computer Study of Wave Propagation, Beam Loading and Beam Blowup at the SLAC Accelerator," *Proc. 1966 Linear Accelerator Conf.*, Rept. No. LA-3609, Los Alamos Scientific Laboratory, Los Alamos, New Mexico (1966), p. 254.

36 O. H. Altenmueller *et al.*, "Beam Break-up Experiments at SLAC," *Proc. 1966 Linear Accelerator Conf.*, Rept. No. LA-3609, Los Alamos Scientific Laboratory, Los Alamos, New Mexico (1966), p. 267.

37 G. A. Loew, *IEEE Trans. Nucl. Sci. NS-14*, No. 3, p. 529 (June 1967).

38 V. A. Vishnyakov, A. I. Zykov, I. A. Grishaev, and L. A. Makhnenko, "Questions Concerning the Increase of the Limiting Current in Multisection Linear Accelerators," Rept. No. 309/VE-072, the Academy of Sciences, U.S.S.R. Physics and Engineering Institute, Kharkov (1967).

39 V. A. Vishnyakov, A. I. Zykov, I. A. Grishaev, N. I. Mocheshnikov, and G. D. Kramskoi, "An Investigation into the Effects of Current Pulse Shortening in Multisection Linear Accelerators," Rept. No. 276/VE-062, the Academy of Sciences, U.S.S.R. Physics and Engineering Institute, Kharkov (1966).

40 J. E. Bjorkholm and R. F. Hyneman, *IEEE Trans. Electron Devices ED-12*, p. 281 (1965).

41 H. S. Butler, S. K. Howry, and C. H. Moore, "Specifications for the Beam Transport Systems to End Stations A and B," Rept. No. SLAC-29, Stanford Linear Accelerator Center, Stanford University, Stanford, California (June 1964).

42 G. H. H. Chang, Pulse shortening in electron linear accelerators, M.Sc. Thesis, University of California, Berkeley, California (1964); see also E. L. Chu, "A Crude Estimate of the Starting Current for Linear Accelerator Beam Blow-up in the Presence of an Axial Magnetic Field," Tech. Note No. SLAC-TN-66-17, Stanford Linear Accelerator Center, Stanford University, Stanford, California (1966).

43 M. C. Crowley-Milling, "A 40-MeV Electron Accelerator for Germany," *AEI Eng.* **2**, No. 2 (1962).

44 R. L. Gluckstern and H. S. Butler, *IEEE Trans. Nucl. Sci. NS-12*, p. 607 (1965).

45 J. A. McIntyre, R. L. Kyhl, and W. K. H. Panofsky, "External Magnetic Focusing Devices for the Mark III Accelerator," Rept. No. ML-202, Microwave Laboratory, Stanford University, Stanford, California (July 1953).

8

INJECTOR

J. Berk, R. F. Koontz, and R. H. Miller, Editor

Many of the dominant features which determine the ultimate qualities of the electron beam emerging from a linear accelerator depend on the proper design and operation of the injector system. Thus, the ease with which the beam can be transported over long distances, the width of the energy spectrum, the precision with which the beam energy can be measured, and the precision with which scattering angles of particles can be determined in a physics experiment all depend on the phase space of the beam. The injector which was designed to help optimize these desirable requirements as the beam gets launched into the accelerator is the subject of this chapter.

8-1 Introduction and specifications (RHM)

The SLAC injector, is a short one-section linear accelerator consisting of the following components, shown schematically in Fig. 8-1:

1. A spherical triode gun and gun modulator.
2. A velocity modulating cavity or prebuncher.
3. A short bunching section with phase velocity equal to three-quarters the velocity of light.
4. A 10-ft long, constant-gradient, accelerator section with phase velocity equal to the velocity of light.
5. A focusing solenoid surrounding the buncher and the accelerator section.
6. Two 24-MW klystrons, one of which drives the injector. The other remains as a standby driver which can be switched onto the injector in less than a minute.
7. Steering dipoles and thin lenses.
8. RF deflection plates to add a 20–80 MHz structure to the beam.
9. Beam monitoring devices.

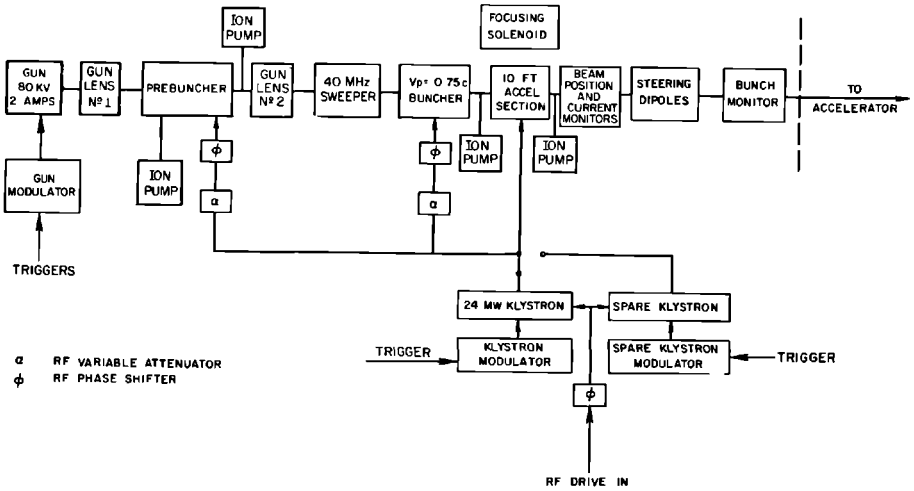

Figure 8-1 Main injector, schematic diagram.

A beam of 80-keV electrons from the gun is initially bunched by the resonant cavity prebuncher. It is further bunched and accelerated to 250 keV in a 10-cm long, travelling-wave buncher. The beam then enters the 10-ft long, accelerator section in which it is still further bunched into less than a 5° phase interval and accelerated to 40 MeV.

The most important objectives of the SLAC injector design were excellent bunching and beam optics, and maximum flexibility and reliability of operation. The bunch size is important since it sets the ultimate limit on the narrowness of the energy spectrum which can be achieved with the two-mile accelerator. A broad spectrum reduces the number of useful electrons for many experiments and also increases the radiation background against which these experiments must discriminate. The contribution of the bunch size to the energy spectrum spread of an otherwise perfect accelerator has been set at 0.1%. For optimum phasing of the injector relative to the rest of the accelerator, the relative energy spectrum is given by

$$\frac{\Delta E}{E} = 1 - \cos\frac{\Delta\phi}{2} \approx \frac{\Delta\phi^2}{8} \tag{8-1}$$

where $\Delta\phi$ is the bunch length in radians. For a 0.1% spectrum, a 5° bunch is required.

The ease with which a high-energy beam can be transported over long distances, the precision of beam energy measurements, and the accuracy to which scattering angles of particles can be determined all depend on the transverse phase volume occupied by the beam. Since the volume in phase cannot be reduced (except by throwing away part of the beam), these factors set restrictions on the injector emittance.

Flexible operation of the injector is mandatory for good utilization of the beam from the accelerator. A triode gun and its modulator permit the beam

Table 8-1 Injector specifications

Klystron peak power	14 MW
power to prebuncher	$\approx$1 kW
power to buncher ($v_p = 0.75c$)	$\approx$1 MW
power to accelerator	13 MW
Beam radius	0.5 cm
Radial phase space ($\pi r \times p_r$)	$\leq 5\pi \times 10^{-3}$ (MeV/c) (cm)
Bunch length (80% of accelerator current)	$\leq 5°$
Phase coherence of bunches	$\pm 5°$
Loaded beam energy	27.5 MeV (at 0.3 A)
Unloaded beam energy	38 MeV
Energy spectrum width	1%
Peak beam current	Programmable from 10^{-9} to 0.3 A
Allowable current variation	
within pulse	$\pm$0.5%
pulse-to-pulse	$\pm$0.75%
Current pulse length	Adjustable within a range of 0.04 to 2.1 μsec
Repetition rates	1–360 pulses/sec
Multiple beam capability	Three interlaced beams with independently adjustable pulse length and current

current and pulse length to be selected on a pulse-to-pulse basis from any of the three preset levels. Each of the three preset pulse lengths can be continuously varied from 0.04 to 2.1 μsec, and each current level can be varied from $\approx 10^{-9}$ to 0.3 A. In addition, the energy of the accelerator beam can be varied from pulse-to-pulse by switching klystrons beyond the injector in and out of time with the beam. These combined features permit several experiments to be carried on simultaneously. They also enable the operator to set up a new beam at a low repetition rate while current experiments are using most of the pulses.

These injector requirements are reflected in the specifications presented in Table 8-1. The klystron driving the injector is conservatively run at one-half to two-thirds full power to improve its life and reliability. To further improve reliability, a standby klystron and klystron modulator are installed. A waveguide "switch," consisting of two 3-dB hybrids and a hybrid phase shifter in the configuration commonly used for variable directional couplers, permits switching from one klystron to the other in less than 1 min.

8-2 Electron gun (JB, RHM)

General characteristics

The pulse characteristics of the accelerator beam are initially determined by the electron gun system. SLAC requires a range of pulse widths of from 0.04 to 2.1 μsec, rise and fall times of 0.2 μsec, and a range of beam current

amplitude from 2 A, for use with beam choppers, down to the dark current threshold of the accelerator which is less than 1 nA. Any combination of these pulse widths and heights has to be available on a pulse-to-pulse basis at repetition rates from 1 to 360 pulses/sec.

Several common techniques are available to vary the amplitude of the emitted current. The simplest methods are (1) controlling the cathode temperature and (2) controlling the space-charge-limited current allowed to reach the anode by varying the anode voltage in a diode or the grid voltage in a triode. Here the "grid" can be either an intercepting wire mesh or a nonintercepting modulator anode. The temperature-limited emitter cannot be considered, because the thermal time constant of a practical cathode would not permit current changes to be made on a pulse-to-pulse basis. Varying the cathode-to-anode voltage cannot be used for current control, since a changing injection energy is not compatible with tight bunching. An advantage of the intercepting grid over the nonintercepting anode is that it is capable of a greater range of beam current control. The nonintercepting anode and the intercepting grid can also provide the on–off control of the beam pulse. Another common technique, transverse deflection of the beam across an aperture, can also be used to define the pulse duration. Such a system is used for subharmonic pulse selection as will be described later in this chapter. The intercepting grid has the disadvantage that it intercepts 10–20% of the cathode current and, consequently, has a heat dissipation problem. However, the mesh grid was chosen in preference to the nonintercepting anode because it was clear that an order of magnitude higher gain could be achieved with a mesh grid. Anticipation of a need for rise and fall times of the order of a nanosecond favored a high gain triode.

Computer design

The gun electrode configuration was developed using a computer program written by W. B. Herrmannsfeldt[1] to solve the Poisson equation. Using this program, the computer iteratively calculates electron trajectories through the gun in the presence of space charge. The program begins by solving the Laplace equation in the gun (i.e., it maps the field distribution with no space charge present). It then calculates the cathode emission densities and electron trajectories for that Laplace potential distribution. Then the charge distribution resulting from the trajectory calculation is inserted in the potential-solving subprogram, and the process is iterated. With suitable damping (accomplished by averaging cathode emission between successive trials) the calculation converges in about six iterations.

Gun electrode spacings were originally calculated using a spherical diode model. The electrode shapes were modified until the computed trajectories closely approximated those of the ideal spherical diode. Computed potentials along the beam edge agree with the analytic solution for a spherical diode to within 1% for over 90% of the distance from the cathode to the anode.

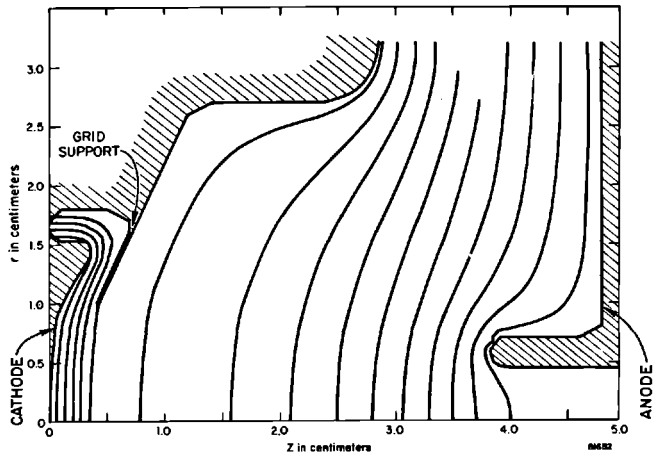

Figure 8-2 Computed equipotential plot.

The mesh grid was contoured to follow the equipotential surface which is nominally 1% of the cathode-to-anode voltage. This position allowed the highest gain consistent with a 2:1 ratio of mesh size to grid–cathode spacing. The closer the mesh grid is to the cathode, the more sensitive are the beam optics to perturbations in grid shape and spacing due to fabrication errors and thermal expansion.

The computer program treats the grid as an equipotential which does not intercept beam current. The computed equipotentials are shown in Fig. 8-2. The computed electron trajectories in the triode are shown in Fig. 8-3.

Phase space

The minimum emittance a gun can have is determined by the area and temperature of the cathode. The electrons emitted from the cathode

Figure 8-3 Computed electron trajectories.

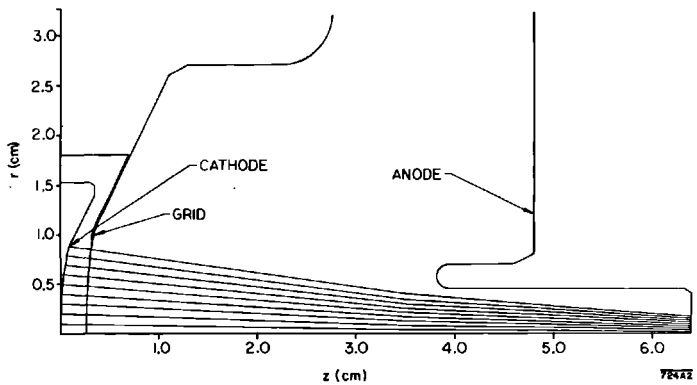

have a mean-square transverse velocity due to thermal energy given by

$$v_r^2 = \frac{kT}{m} \tag{8-2}$$

where k is Boltzmann's constant (1.38×10^{-16} erg/deg), T is the absolute temperature of the cathode, and m is the rest mass of the electron. So the emittance area due to thermals is

$$A_T = \pi r_c mc\left(\frac{kT}{mc^2}\right)^{1/2} \tag{8-3}$$

where r_c is the cathode radius.

For thermal electron emitters, kT varies from ≈ 0.1 eV for oxides to ≈ 0.2 eV for pure metals. The cathode radius in the SLAC gun is approximately 1 cm so the minimum emittance achievable is

$$2.3\pi \times 10^{-4}\,(\text{MeV}/c)\,(\text{cm})$$

The focusing elements of the gun also contribute to phase space. The computer program assumes that electrons have zero velocity at the cathode surface, so a measure of the focusing contribution can be obtained from the computed trajectories. The computer output includes the radius r and the slope dr/dz of each trajectory at the exit plane. These data are plotted in Fig. 8-4. In order to obtain a quantitative evaluation of various electrode configurations, it was necessary to calculate[2] an effective emittance area, for sets of discrete points, such as that shown in Fig. 8-4. The computed electron trajectories shown in Fig. 8-3 have an effective emittance of

$$5.7\pi \times 10^{-4}\,(\text{MeV}/c)\,(\text{cm})$$

Mechanical design

Figure 8-5 illustrates the physical configuration of the gun. On the right is the vacuum flange which is the mechanical and electrical interface with the

Figure 8-4 Computed gun emittance.

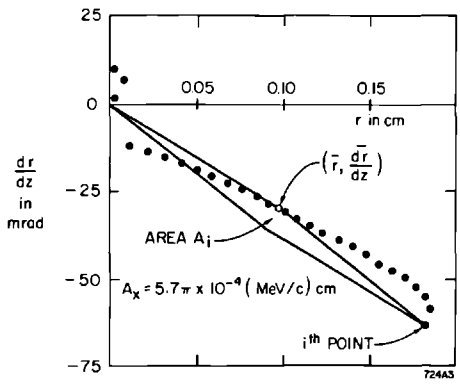

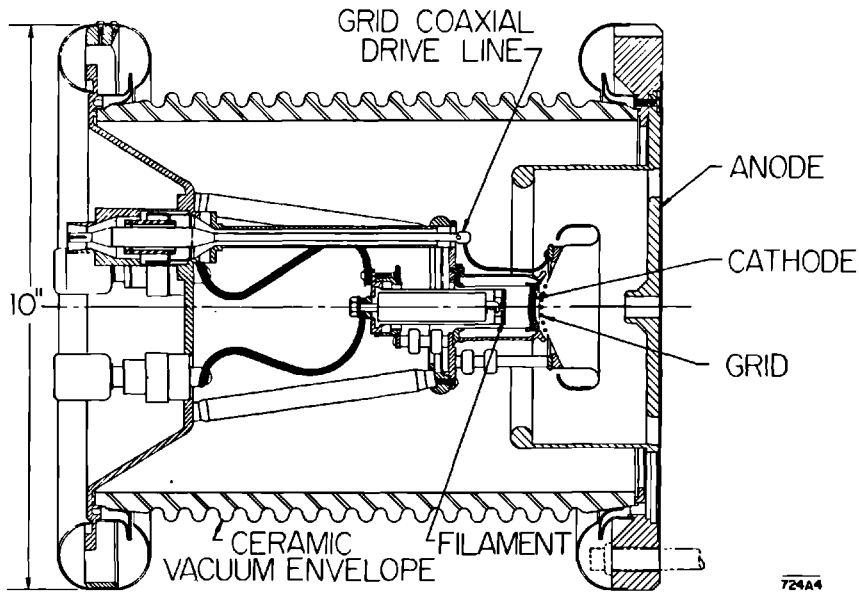

Figure 8-5 Electron gun assembly.

grounded accelerator structure. On this flange is mounted the anode, removal of which permits access to the inner gun. On the left is the rear deck which operates at cathode potential and is separated from the vacuum flange by the alumina insulator. With the corona shields shown the gun can be operated at 100-kV dc without arcing. Potential plotting on a conductive paper analog permitted adjustment of the corona shield on the anode flange to limit the maximum potential gradient in the ceramic to less than 890 volts/mm.

The rear deck is a recessed vacuum wall penetrated by the two filament feedthroughs and the grid, coaxial, drive line. The 50-ohm grid drive line has its outer conductor at cathode potential and its inner conductor connected to the grid structure. Inside the vacuum envelope the rear deck provides a structural support for the inner gun.

The inner gun can be replaced as a unit simply by connecting the two filament leads and the grid to the new unit. The mounting interface with the rear deck is the cathode deck on which the cathode assembly, the inner heat shields, and the beam-forming electrode are mounted. Two decks, each supported from the cathode deck with three insulated legs, support the grid structure and the bombarder.

The bombarder is a spiral "pancake" filament supported by a coaxial structure made from molybdenum and alumina. Two tantalum screws for clamping the filament legs allow convenient, but secure, filament installations. With suitable spacers installed at the rear of the bombarder the distance of the filament from the back of the cathode can be adjusted permitting either bombardment or radiant heating of the cathode.

The gun is designed to be baked as an assembly at temperatures in the range of 400 to 600°C for vacuum processing. Materials, therefore, are restricted to stainless steel, cupric nickel, oxygen-free high-conductivity copper, and refractory metals such as tungsten, tantalum, and molybdenum. Fixed joints are brazed wherever possible. Joints between components that can be reused several times are inert-gas welded or screwed together.

Mechanical thermal expansions are, of course, significant. The 3.95-cm distance between the cathode and the anode changes to 3.89 cm (1.5%) when the cathode temperature is raised from room temperature to its operating level. Temperature distributions on all components were estimated or measured. Room temperature dimensions were then calculated so that the computed electrode geometry would be assumed at the operating temperature.

GRID. The operating voltage chosen for the grid results in a grid–cathode spacing of 2.5 mm. The mesh is woven with 0.05-mm diameter, molybdenum wires at 1-mm spacing resulting in a ratio of interception area-to-total area of 10%. The mesh disk is stress relieved at 1000°C brightness for 1 min in a molybdenum jig, thereby forming it into a spherical cap. The individual wire ends are then spot-welded to the supporting 0.18-mm thick, molybdenum, focus electrode in an assembly jig. When the cathode is oxide coated and is operated at a temperature of 950°C brightness, the grid temperature measures about 410°C.

CATHODE. Considerations of the maximum beam pulse current requirement when operating with subharmonic pulse selection led to specifying a gun which would deliver 2 A at 80 kV, corresponding to a perveance of 0.0885×10^{-6} A/V$^{3/2}$. A cathode diameter of 1.90 cm and area of 2.84 cm^2 requires a maximum, homogeneous emission density of 0.775 A/cm^2 (assuming 10% grid capture). This emission level can, for a 2.5-μsec pulse and a maximum 0.001 duty factor, be obtained from several emitter materials.[3]

The technology of thin-film emitters, applied to a conducting base as a mixture of barium, strontium, and sometimes calcium carbonates and later thermally converted to oxides is well developed and reliable. The first SLAC guns used a carbonate emitter material sprayed on a nickel cathode base. Bases with either a fine nickel mesh or a fine nickel powder sintered to the surface provide adequate bonding interfaces for the carbonates.

The cumbersome and sometimes slow conversion processes required and the sensitivity of these emitters to poisoning in vacuums worse than 10^{-5} torr has led to a gun design which can accept a carburized, thoriated, tungsten cathode similar to that described by Haimson and Brodie.[4] The initial production of the 0.2-mm thick, carburized layer using colloidal graphite is as involved as the preparation of the oxide cathode. However, it can be done in a vacuum bell jar as this emitter can be exposed to air and reconverted (with a quick temperature flash) several times.

The carburized tungsten cathode has the disadvantage of requiring a higher operating temperature. Whereas the oxide cathode operates below about 900°C, the tungsten cathode requires up to 1600°C. The effect of the higher temperature on the heater power required can be seen by calculating the power radiated by the electron-emitting surfaces of the different cathodes. Assuming the cathodes face a cold wall with no additional heat shielding, the oxide cathode at 900°C radiates 10 W, whereas the tungsten cathode at 1600°C radiates 100 W.

HEATER. The oxide cathode temperature can easily be achieved using a radiant-heating spiral filament. Heaters with 0.6-cm spacing between center leg and outer leg, $9\frac{1}{2}$ turns of 0.25-mm diameter tungsten (2% thoria) wire and 0.50-mm turn-to-turn spacing have a resistance of about 2.57 ohms at 1720°C. In the SLAC gun, they require about 40 W to maintain the oxide cathode at 780°C. Depending on the bombarder emitter efficiency, about 150 to 200 W is required to maintain the tungsten cathode at 1600°C. The same filament is used in carburized form as a bombarder diode emitter.

The filaments are wound two at a time, interleaved, and back-to-back, in a molybdenum jig. They are then stress relieved by heating to 1500°C for 2 min in a vacuum bell jar. For use as electron emitters, they are sprayed with colloidal graphite in an aqueous solution and then carburized by firing in vacuum to 1800°C for 30 sec.

In bombarder service these filaments are mounted 1 cm from the cathode back. With 1.4 kV applied between filament and cathode, a bombarder beam current of 150-mA dc provides 210 W of power with only 5 W of applied filament power. The filament operates at a temperature of 1450°C with a cathode temperature of 1600°C. Most of the power required to heat the bombarder filament is derived from back-heating from the hotter cathode. Temperature stability of the main cathode is controlled by regulating the bombarder beam current. This is achieved by operating the bombarder filament temperature limited and controlling the power used to heat it by means of a feedback circuit which senses the bombarder current.

Performance

BEAM OPTICS. The beam profiles shown in Fig. 8-6 were measured using a SLAC Model 4-1 gun with an oxide cathode and the SLAC beam analyzer. Cross sections of the beam current density were determined using a 0.25-mm diameter hole in front of a small Faraday cup. The radii at which the beam current density had dropped to 10% of its maximum value were then measured. Thus the profiles should contain about 90% of the beam current.

The profiles illustrate a beam minimum diameter of 0.76 cm at about 2.5 cm downbeam from the gun vacuum flange for the 0.10 microperveance ($K = 10^{-7}$ A/V$^{3/2}$) beam which is approximately the gun design perveance.

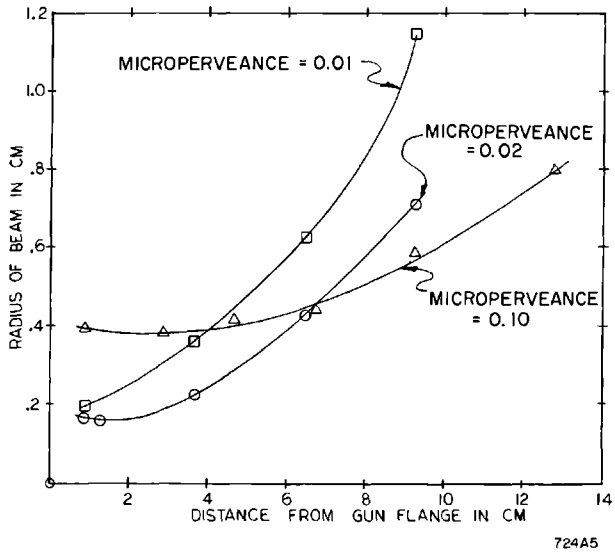

Figure 8-6 Measured beam profiles for three gun currents.

Space-charge spreading is an important effect at this perveance. The figure shows that the beam minimum moves back toward the cathode and becomes smaller with decreasing perveance.

ELECTRICAL CHARACTERISTICS. The transfer characteristics shown in Fig. 8-7 were taken using a SLAC Model 4-2 gun with an oxide cathode at a cathode–anode voltage of 40 kV. Therefore, the 1 % grid drive current of 1.2 A at 40 kV is a perveance of 0.15 microperveance. At 80 kV, this would give 3.4 A.

The cutoff characteristic shown in Fig. 8-8 was measured on a SLAC Model 4-2 gun with a tungsten cathode at a cathode–anode voltage of 70 kV. The cutoff value of 0.5-nA beam current was voltage dependent and may be due to grid emission. Use of the gun on the SLAC accelerator has indicated that the cutoff current is $\lesssim 0.1$ nA.

CATHODE LIFE. Although oxide cathodes have useful lives in excess of 10,000 hours in sealed tubes, their lifetimes in continuously pumped, linear accelerators have frequently been much less. For the last several years, however, since installation of a differential pumping system between the accelerator and the gun, the Mark III accelerator at Stanford University (1 GeV, 100 meters long) has been achieving oxide cathode gun lives of about 1 yr, or 6000 operating hours. No statistics are yet available for the SLAC gun. The first gun installed, which has an oxide cathode, is still in service and its performance is very encouraging. It now (July 1967) has been installed for 21 months and has been operated approximately 8000 hours.

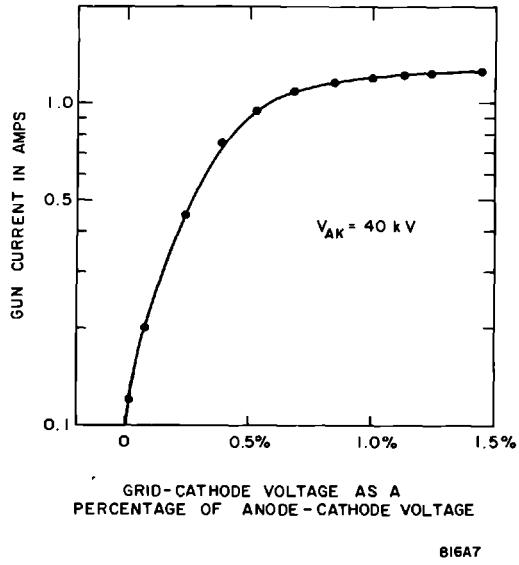

Figure 8-7 Gun transfer characteristic.

Figure 8-8 Gun cutoff characteristic.

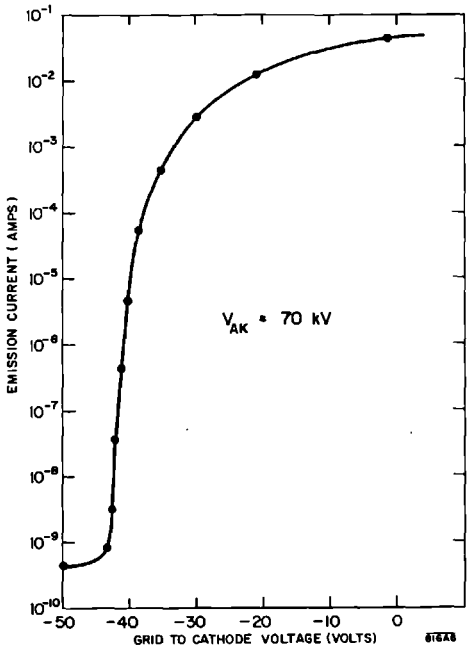

8-3 Multiple beam capability (RFK)

Beam parameters required

Early in the design of the accelerator, the problem of full beam utilization by the experimenters was considered. Some experiments such as bubble chamber studies cannot use the full repetition rate capability of the machine (360 pulses/sec), while other experiments require large amounts of integrated beam time, but are not concerned with a small percentage of missing pulses. Time is also required for setting up new beam configurations or experiments and this ideally should not represent wasted accelerator time. The outgrowth of these considerations was a beam switchyard concept with a capability of directing beams on a pulse-to-pulse basis to the several different target areas where the physics experiments are installed. Along with the capability of directing the beam to different experimental areas on a pulse-to-pulse basis came the requirement of programming the various beam parameters on a pulse-to-pulse basis. In addition to pulse repetition rate, the significant beam parameters from an experimenter's viewpoint are beam energy, beam spectrum, beam intensity, pulse duration, beam structure, and beam timing. Of these parameters, the injector influences or determines all but the beam energy. Beam energy depends on the number of klystrons used to accelerate the beam, and the machine control system makes provision for programming this number on a pulse-to-pulse basis. If the accelerator is properly phased, the beam spectrum is determined by the microwave properties of the injector structure. This is discussed in the following section. Of the remaining parameters, beam intensity and pulse duration are controlled by varying the output of the gun through control of the gun modulator. Beam structure refers to further intensity modulation within a single beam pulse. Various time-of-flight experiments require different structuring of the beam and, so far, two structuring systems have been built at SLAC and will be described below. Additional systems are being studied and designed and in time will become available for experimental use. The last parameter mentioned is beam timing. Control of beam timing and transmission of timing information to the experimenter is accomplished by the machine trigger system. The injector is required to maintain a stable relationship between machine trigger and the gun output.

The appropriate beam specifications associated with the injector gun and modulator system are given in Table 8-1. The gun has been discussed in detail in the preceding section.

The following gun characteristics are pertinent to the modulator design. The Pierce triode gun operates at a dc cathode potential in the range of 40 to 100 kV with 80 kV the nominal operating voltage. It requires about 700 volts, positive grid drive to achieve a 2-A peak current output. Grid current is about 10% of cathode current. Grid-to-cathode capacity is in the range of 20 to 25 pF, and the input structure looks like a 50-ohm transmission line terminated in this capacity. Virtually complete gun cutoff (less than 10^3 electrons/pulse) is achieved at a negative bias of 100 volts on the grid.

Gun modulator physical design

The SLAC accelerator is housed in a tunnel 25 ft below ground level. The moderate amounts of radiation present in the tunnel dictate that electronic equipment, especially that containing semiconductors, be installed if at all possible above ground in the klystron gallery and not in the tunnel. Since the gun must be in the tunnel, the choice had to be made whether to install all the gun pulser electronics in the gallery and face the problem of getting the pulser output to the gun by some transmission system or to mount portions of the pulser electronics in the tunnel close to the gun in a radiation environment and, therefore, inaccessible for maintenance during operation.

The first modulator system, a prototype, used at SLAC had a 300-ohm, distributed, amplifier pulser which was mounted in the tunnel. A large "box within a box" structure was built. The inner box contained instrument racks and was insulated from the outer box. The structure was installed in the tunnel directly behind the injector. An aperture in the outer box wall permitted the structure to be fitted over the gun so that the gun insulator spanned the gap between boxes. The inner box was floated at the dc cathode potential and was connected to the floating deck electronics in the gallery by a specially constructed 100-kV multiconductor cable which contained coaxial cables as well as individual wire pairs. The prototype modulator components previously mentioned were mounted in this box in close proximity to the gun and connected to electronics in the gallery through the multiconductor high-voltage cable. The present modulator has all of its electronics in the gallery as shown in Fig. 8-9, but it is anticipated the deck in the tunnel will be used later to mount fast grid driving pulsers associated with future beam structuring schemes. Recent developments in fast rise-time, high-voltage, dc,

Figure 8-9 Gun pulser block diagram.

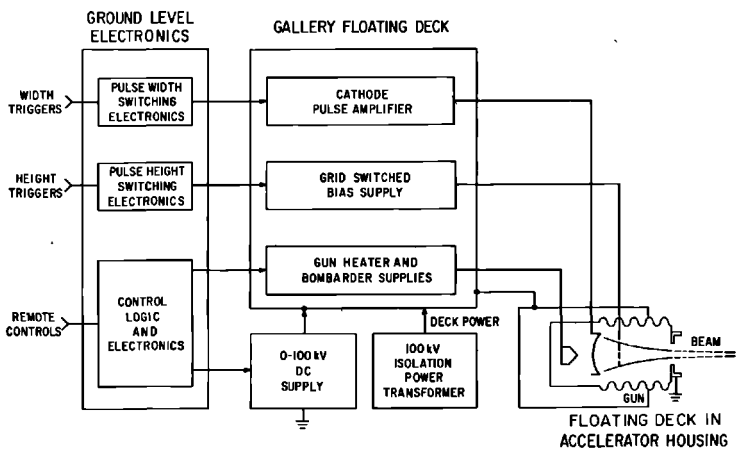

isolation transformers may even allow fast grid driving pulsers to be mounted in the gallery at ground level, in which case the large floating deck in the tunnel will be unnecessary.

Electrical requirements

BIAS PROGRAMMING. The present modulator is capable of selecting one of three remotely programmable grid bias settings in response to one of three pretriggers. The bias, in turn, controls the current output of the gun. A pretrigger is supplied to the gun modulator in advance of each machine pulse as required by the multiple beam pattern set up for the machine. If no trigger is received, or if two or more simultaneous triggers due to a programming error are received, the bias reverts to a high, but remotely controllable level which either cuts off the beam or reduces it to an extremely low intensity. The bias control channels are not part of either the personnel or machine protection interlock system, so this fourth channel feature guarantees an experimenter only that he will not receive a damagingly intense beam if a multiple trigger programming error or a missed trigger condition occurs. The fourth channel with its remote control capability also allows experiments which require very low electron densities (10^4–10^8 electrons/pulse) to be run while using the bias channel as a higher current "steering" channel. The low electron density beam is not seen by the machine beam-steering monitors, but an occasional pulse on the "steering" channel makes the orbit of the low-intensity beam visible on the monitors.

The switched grid bias electronics consists of a fast regulating, power supply and four, remotely controlled, reference potentiometers which can be switched into the power supply regulator circuits. These circuits and the receiving circuits of the RF pattern generator are mounted on the gallery

Figure 8-10 Bias control circuits.

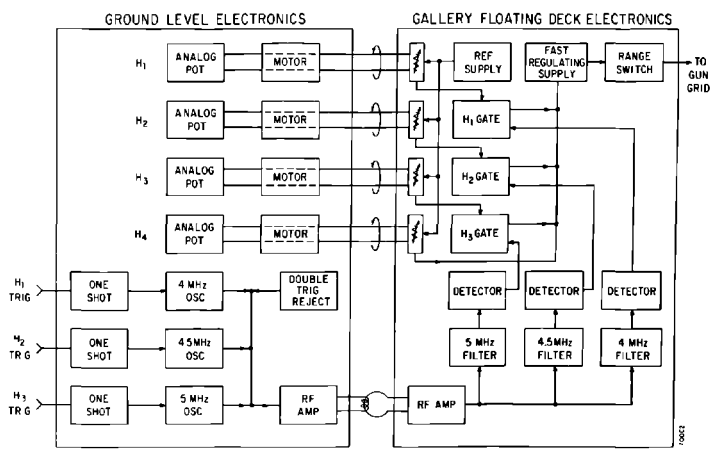

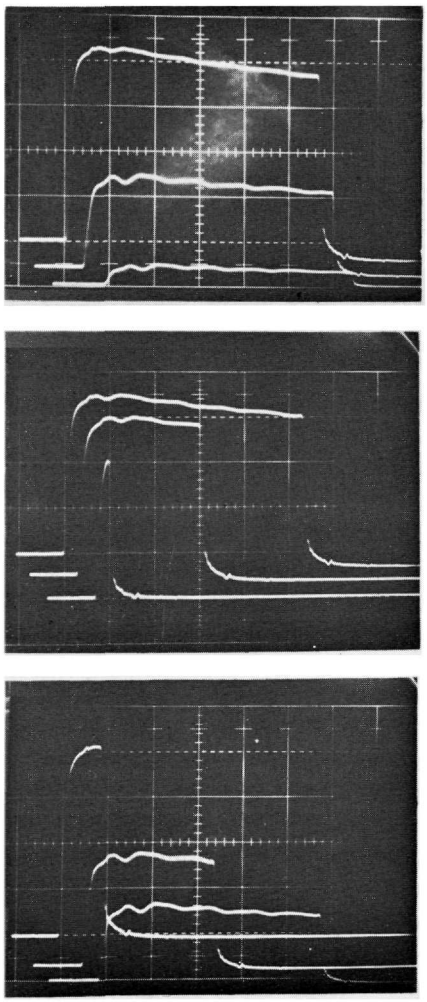

Figure 8-11 Gun pulse profiles (sweep speed 0.25 μsec/cm).

floating deck. An RF pattern corresponding to the selected beam intensity profile is generated in ground level electronics and coupled to the floating deck via an isolation transformer. Figure 8-10 shows a block diagram of the complete bias control system. Figure 8-11a shows a picture of three, typical, gun pulse-height profiles which are selectable on a pulse-to-pulse basis in response to the appropriate input triggers.

PULSE WIDTH PROGRAMMING. Beam pulse width is also selectable from pulse-to-pulse. Separately triggered, low-level pulsers generate three pulses, remotely controllable in width, which can be selected as the machine beam pattern requires. These channels can be triggered in parallel, and, since each

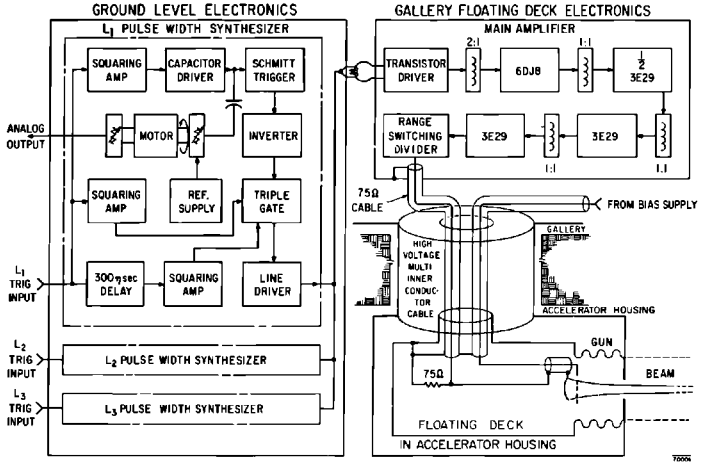

Figure 8-12 Gun pulser circuits.

has a separate timing control, three current pulses can be accelerated during one machine RF pulse. There is no ambiguity in driving all three of these pulsers during the same machine pulse either concurrently or sequentially, and this mode of operation has been used for some experiments. The pulse width circuits are part of the machine protection system so special effort is made to prevent triggering on noise or producing output pulses when there is no trigger. The outputs of all three pulse synthesizers are combined in a diode matrix to drive a high-voltage isolation transformer used to span the ground-to-floating deck gap.

On the gallery floating deck, the isolation transformer output is amplified and squared in a three-transistor driver whose output is a 30-volt pulse at a 50-ohm impedance level with rise and fall times of less than 20 nsec. This signal drives the four-tube saturated amplifier which produces an output of 800 volts into an impedance of 75 ohms. The four tubes of this amplifier all operate normally cut-off, and the last stages run from a separate power supply so that the tube plate has the correct dc reference level to drive the gun cathode directly. The polarity of the output is such that it directly drives the gun cathode. The block diagram of this system is shown in Fig. 8-12.

A set of typical pulse width profiles is shown in Fig. 8-11b. When the pulse-width and pulse-height programming capabilities are jointly used, gun beam profiles such as are shown in Fig. 8-11c are the result.

Beam structure equipment

Subharmonic beam sweeper systems are used to impress further structure on the electron beam pulse. The electron beam already has a fine structure corresponding to electron bunching at the machine frequency, 2856 MHz. For time-of-flight experiments, it is desirable to eliminate most of the electron

bunches and accelerate an equivalent amount of charge in a train of widely separated bunches or bunch groups, spaced apart by a time long enough to avoid ambiguities and to permit measurement of the time of flight using time stretching techniques. To obtain single bunches, a deflector system phase-locked to the accelerator frequency is employed to eliminate all but the desired bunches. For bunch groups consisting of several bunches, phase-locking is not necessary and the experimenter can vary his group spacing at will by changing the deflector frequency.

Two early scheduled time-of-flight experiments generated requirements for a structured beam of single bunches periodic at 12.5 nsec and a structured beam of three bunches periodic in a range from 25 to 50 nsec. The 12.5-nsec period corresponds to a $\approx$40-MHz drive frequency and the 25–50 nsec periodicity corresponds to a variable frequency drive of from 10 to 20 MHz.

The single bunch system is shown in Fig. 8-13. It consists of a 50-kW RF amplifier and a resonant beam deflection structure close to the gun. The operating frequency of this system is, at the seventy-second subharmonic of the machine, 39.667 MHz. The master oscillator of the machine has an output at this frequency and this signal is used to drive the 50-kW peak pulsed RF amplifier. Pulsing is required since in multiple beam operation, the experiment requiring the structured beam may be assigned only a portion of the total machine pulses.

INITIAL BEAM DEFLECTOR. The first beam deflector is a pair of plates in the beam line following the gun and prebuncher. At this point the beam may not be sufficiently bunched for the plates totally to eliminate electrons in bunches

Figure 8-13 Subharmonic sweeper system.

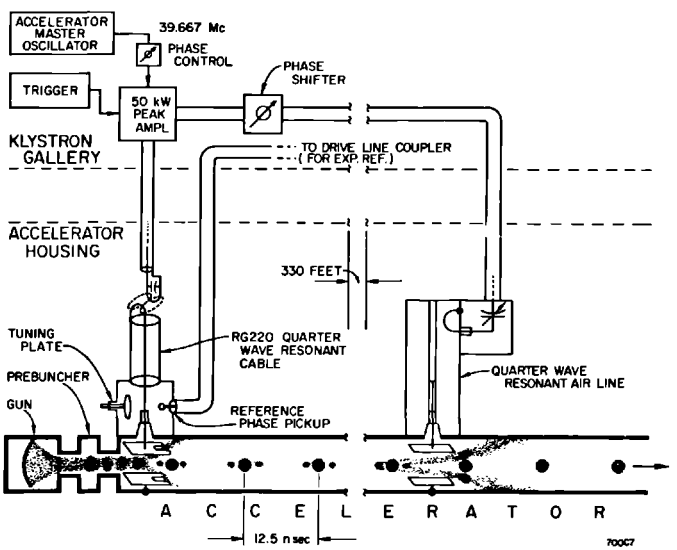

adjacent to the desired bunch, so provision has been made for later installation of a cleanup deflector downstream at the end of Sector 1. Early elimination of unwanted electron bunches prevents their loading the following buncher and accelerator structures. Consideration of these loading effects dictated the location of the first deflector. A quarter-wave section of RG 220 cable forms the deflector resonant circuit and steps the RF drive voltage up to 40 kV peak. This deflects all but the central bunch and vestiges of adjacent bunches into the walls of the deflector structure. The deflector phase is adjusted so that the central bunches occur at the zero crossings of the RF cycle. There are two of these per RF cycle, so only one out of every thirty-six bunches is transmitted.

A typical chopped beam is seen in Fig. 8-14a and b. This is the output of a single-turn toroid, 15 ft downstream of the first deflector as viewed on a 100-MHz bandwidth oscilloscope. If the beam is not precisely centered, and is improperly phased, electron bunches corresponding to alternate zero crossings will not have the same orbit and will suffer unequal transmission losses. This is observable in the photographs.

A capacitor divider samples the drive phase and transmits this information to the experimenter via the machine master drive line. The machine drive line frequency is 476 MHz and transmission of a 39.667-MHz signal does not

Figure 8-14 A 39.667-MHz structured beam.

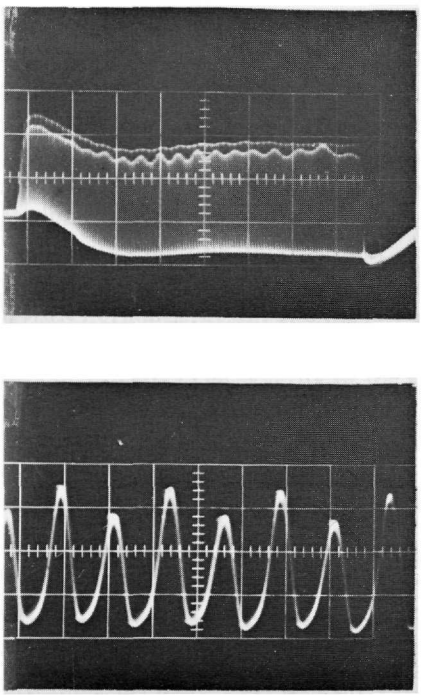

degrade its primary function of providing phase coherent drive for the machine sub-boosters, which, in turn, drive the 2856-MHz klystrons.

The resonant circuit for the 40-MHz system is not compatible with the 10–20 MHz chopping system at the present time. Work is proceeding on developing a broad-band voltage stepup transformer which will be useful over the range of 10 to 40 MHz.

SECOND BEAM DEFLECTOR. The second beam deflector, if installed, will be used only with the 40-MHz system and so does not have broad-banding problems. Its design will be similar to the first deflector, but the Q of its resonator will be higher since beam interception losses are not a factor. This deflector serves two purposes. It eliminates the residual adjacent bunches missed by the first deflector; it also eliminates all random electrons captured and accelerated in the injector and first 333 ft of the machine. Preliminary measurements of this "dark current" electron count indicate quantities of from 10^2 to 10^3 electrons/pulse. Eliminating these "dark current" electrons at the end of the first 333 ft of the machine effectively eliminates them from the experiment since all electrons captured downstream have insufficient energy to pass through the energy-analyzing slits of the machine.

8-4 Microwave system (RHM)

Buncher

Bunching in the SLAC injector occurs in three lumped components: the prebuncher, the 10-cm long, traveling-wave buncher, and the first 10 cm or so of the 10-ft accelerator section. A bunching system having several lumped components was chosen in preference to a tapered buncher because the former is easier to design, fabricate, and cold-test and because provision of independent phase and power controls to the components permits correction for design or fabrication errors. This flexibility also permits tuning to achieve optimum bunching despite malfunctioning equipment, such as a gun modulator or a gun that cannot achieve the design voltage, a low-power klystron, or stable but improper temperature control of the RF components.

The buncher design concept is one suggested by Lichtenberg.[5,6] It consists of matching the longitudinal phase space emittance of a prebuncher to the admittance of the accelerator with a quarter-wave transformer. Consider the following: (1) a prebuncher the emittance of which can be approximated by an erect* ellipse with a momentum extent of p_1 and phase extent ϕ_1; (2) an accelerator the admittance of which, for the desired final bunch, can be represented by an erect ellipse p_3 by ϕ_3; and (3) an intermediate traveling wave structure, or buncher, which can be characterized by the fact that a

* In this case, "erect" means that the principal axes of the ellipse are parallel with the p and ϕ axes, respectively.

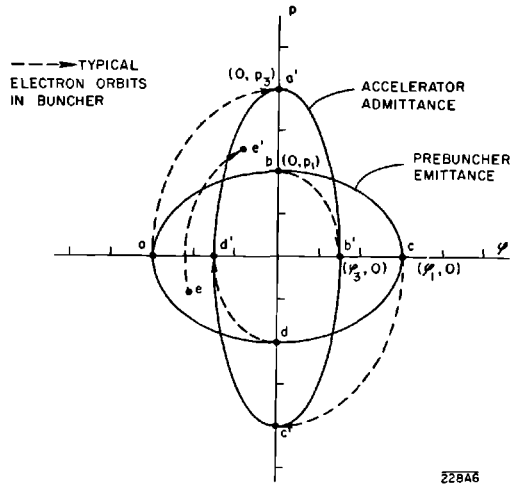

Figure 8-15 Buncher phase space.

particle performing phase oscillations with a maximum phase excursion of ϕ_2 will have a maximum momentum excursion p_2. The problem is to find the essential properties of the buncher so that it will transform the prebuncher emittance ellipse into the accelerator acceptance ellipse.

It has been shown by a number of authors[7,8] that an electron bound to a wave having a constant phase velocity less than the velocity of light oscillates in phase and also, of course, in momentum. For reasonably small oscillations and field strengths the equations can be linearized, and the oscillations in phase and in momentum are sinusoidal and in quadrature with each other. Consequently, in a plot of momentum against phase, an electron traces out a closed path which is an erect ellipse. Electrons with differing initial values trace out concentric, linearly scaled ellipses.

The function of the buncher is presented graphically on the momentum-phase plane in Fig. 8-15. The coordinate system chosen is one in which the electron in the middle of the bunch is at rest. The ellipse labeled "prebuncher emittance" with principal semiaxes p_1 and ϕ_1 encloses the initial conditions of all electrons considered to be within the bunch. The ellipse labeled "accelerator admittance" with semiaxes p_3 and ϕ_3 encloses the desired end points of all electrons in the bunch. The dashed lines represent electron orbits in the buncher which will map initial points a, b, c, d, and e within the prebuncher emittance into points a', b', c', d', and e' in the accelerator admittance. The orbits are segments of concentric similar ellipses. If p_2/ϕ_2 is the ratio of the semiaxes of the orbit ellipses within the buncher, then to map points a and c to a' and c', p_2/ϕ_2 must satisfy the condition

$$p_3 = \frac{p_2}{\phi_2}\phi_1 \tag{8-4}$$

Since the transformation maps a point on the ϕ axis onto a point on the p axis, the buncher must be $(2n + 1)/4$ phase oscillations long. Similarly, in order to map b and d into b' and d', p_2/ϕ_2 must satisfy

$$\phi_3 = \frac{\phi_2}{p_2} p_1 \tag{8-5}$$

From Eqs. (8-4) and (8-5) the conditions for the mapping are found to be

$$p_3 \phi_3 = p_1 \phi_1 \tag{8-6}$$

and

$$\frac{p_2}{\phi_2} = \left(\frac{p_1 p_3}{\phi_1 \phi_3}\right)^{1/2} \tag{8-7}$$

From the linear nature of the mapping, it follows that the entire prebuncher emittance is mapped into the accelerator admittance. Equation (8-6) requires the areas of the two ellipses to be equal. Equation (8-7) is analogous to the condition on the impedance of a quarter-wave matching transformer in transmission line theory. The buncher orbit ellipticity p_2/ϕ_2 is the analog of the transformer impedance, whereas the ellipticity of prebuncher emittance p_1/ϕ_1 and the ellipticity of accelerator admittance p_3/ϕ_3 are analogs of the input and output impedances, respectively. The ratio p_2/ϕ_2 must be the geometric mean of p_1/ϕ_1 and p_3/ϕ_3.

In the buncher design for the present injector the buncher increases the momentum spread by a factor of about 2.5 while reducing the phase spread by a factor of about 2.5.

The phase velocity of the wave in the buncher is $0.75c$, and the field strength is 25 kV/cm. The buncher is 10.5 cm long. In this distance the electrons oscillate a quarter of a cycle about the phase stable point. The mean velocity of the electrons entering the buncher is $0.50c$. For electrons leaving the buncher, it is $0.75c$. Thus the buncher accelerates the electrons as well as transforming the ratio of the momentum extent to the phase extent. The phase velocity in the 10-ft accelerator section is $1.00c$, and the field strength is 120 kV/cm.

The precise electrical parameters for the prebuncher, buncher, and accelerator, and the resulting theoretical performance were determined by numerical integration of the following longitudinal and radial equations of motion[9] and by summing over space harmonics:

$$\frac{d\gamma}{dZ} = -\sum_n \alpha_n \left\{ J_0(k_{\rho n}\rho) \sin\left(\phi + \frac{2\pi n Z}{l}\right) - \frac{k_{zn}\rho p_\rho}{\beta\gamma} \cos\left(\phi + \frac{2\pi n Z}{l}\right) \right\} \tag{8-8}$$

$$\frac{d\phi}{dZ} = k_{z0} - \frac{2\pi}{\beta} \tag{8-9}$$

$$\frac{dp_\rho}{dZ} = \sum_n \frac{J_1(k_{\rho n}\rho)}{k_{\rho n}} \left[\alpha_n \left(\frac{k_{zn}}{\beta} - 2\pi \right) \cos\left(\phi + \frac{2\pi n Z}{l} \right) + \frac{1}{\beta} \frac{\partial \alpha_n}{\partial Z} \sin\left(\phi + \frac{2\pi n Z}{l} \right) \right] \tag{8-10}$$

$$\frac{d\rho}{dZ} = \frac{p_\rho}{\beta\gamma} \tag{8-11}$$

where

$Z = z/\lambda$

$\rho = r/\lambda$

$\beta = \frac{v}{c}$ for the electrons

$\gamma = \frac{1}{(1-\beta^2)^{1/2}}$ = total energy in rest mass units

p_ρ = radial momentum in units of mc

$\alpha = \frac{eE\lambda}{mc^2}$ = normalized electric field strength

n = space harmonic index and runs from $-\infty$ to $+\infty$ with 0 designating the fundamental space harmonic

k_{z0} = axial propagation constant of the fundamental space harmonic

$k_{zn} = k_{z0} + \frac{2\pi n}{l} = \frac{2\pi}{\lambda_g/\lambda}$

l = periodic length of the disk-loaded guide

$k_{\rho n} = [(2\pi)^2 - (k_{zn})^2]^{1/2}$ = radial propagation constant

These equations are appropriate for either traveling-wave or standing-wave structures with suitable choice of the periodic length l. The computer program written by W. Herrmannsfeldt using these equations was used to calculate electron orbits through the prebuncher, buncher, and accelerator section and intervening drift spaces. The values of the space harmonic amplitudes α_n were obtained from cold test measurements of disk-loaded structures which have been made at Stanford over a period of years.[10] Only three space harmonics were used in the injector calculations: $n = 0, -1, +1$.

Microwave components

The microwave power for the injector prebuncher, buncher, and accelerator comes from either of two standard SLAC 24-MW klystrons driven by standard modulators. The rectangular waveguide system consisting of a high-power switch for switching from one klystron to the other, directional couplers for splitting off power for the prebuncher and buncher, and a waveguide phase shifter and phase-compensated attenuator for the buncher, are described in Chapter 11. The prebuncher drive has a commercial, rotary vane attenuator. This type of attenuator was chosen because it introduces practically no phase shift as the attenuator is varied over a wide range. The prebuncher phase

shifter is a Fox phase shifter of the type used in the RF drive system described in Chapter 9. The fact that the prebuncher and buncher attenuators do not introduce appreciable phase shifts greatly speeds the process of converging on optimum phase and power settings for the prebuncher and buncher.

PREBUNCHER. The prebuncher is a re-entrant resonant cavity machined from stainless steel. Stainless steel is used to lower the Q to approximately 500 so as to minimize the effects of temperature, mechanical distortions, and electron beam loading on the fields in the cavity. The peak gap voltage in the cavity is about 10 kV at the design drive power of 1 kW. The velocity modulation introduced by the prebuncher causes 70% of the electrons to be bunched into a 75° interval in the 30-cm drift space between the prebuncher and the buncher.

BUNCHER. The buncher and accelerator are copper disk-loaded structures fabricated by means of the brazing technique described in Chapter 6. The buncher is a traveling-wave structure only four cavities long, including the input and output couplers. It operates in the $2\pi/3$ mode (i.e., three cavities per guide wavelength) with a phase velocity of $0.75c$, so it has a length of one free space wavelength (10.5 cm). The buncher is brazed to the injector accelerator section to form a single assembly with a 1.9-cm thick, copper spacer between them. Each has a separate input waveguide, output waveguide, and load. The buncher and accelerator section have common water-cooling tubes brazed to the outer surface and they are supported in a common concentric stainless steel tube, which also supports the solenoid coils surrounding the buncher and the accelerator section. The buncher has a peak field of 25 kV/cm in the fundamental space harmonic at the design drive power of 0.5 MW. The desired electrons enter the buncher within a phase interval of 75° with an average velocity of $0.5c$ (79 keV). They leave the buncher within a phase interval of 30° and at a wave velocity of $0.75c$ (260 keV).

ACCELERATOR SECTION. The accelerator section in the injector is a standard constant-gradient section identical to all other sections except for external mechanical changes required to accommodate the buncher and the surrounding focusing coils. The 30° bunches are caused to enter the accelerator section around the phase stable field null, become bunched to less than a 5° width, and asympotically approach the crest of the wave as they are accelerated.

A simple analytic expression can be derived[7,9,11] for the asymptotic phase of an electron injected into a constant-gradient accelerator with the phase velocity equal to the velocity of light:

$$\cos \phi_\infty = \cos \phi_0 - \frac{2\pi}{\alpha} \left(\frac{1 - \beta_0}{1 + \beta_0} \right)^{1/2} \tag{8-12}$$

where ϕ_∞ is the asymptotic phase angle relative to the wave of an electron entering the accelerator with phase ϕ_0, and velocity $v_0 = c\beta_0$. The phase

origin is taken at the field null, 90° ahead of the crest. The electric field parameter α is the energy in units of rest mass gained per free space wavelength λ by an electron on the crest of the wave:

$$\alpha = \frac{eE\lambda}{mc^2}$$

When $(2\pi/\alpha)[(1 - \beta_0)/(1 + \beta_0)]^{1/2} = 1$, an electron, entering the accelerator at $\phi_0 = 0$, asymptotically approaches the crest, $\phi_\infty = -\pi/2$. This condition produces optimum bunching of the electrons entering in the region of the null forward of the crest since

$$\left(\frac{d\phi_\infty}{d\phi_0}\right)_{\phi_0=0} = 0 \tag{8-13}$$

Expanding ϕ_∞ in a Taylor series about $\phi_0 = 0$, we get for this case

$$\phi_\infty \approx -\frac{\pi}{2} - \frac{\phi_0^2}{2} \tag{8-14}$$

For example, all electrons entering in the $\frac{1}{2}$ radian phase interval $-\frac{1}{4} \leq \phi_0 \leq +\frac{1}{4}$ have their asymptotic phase in the interval $-\pi/2 \geq \phi \geq -[(\pi/2) + (1/32)]$. Thus a phase compression factor of 16 is achieved in this example.

Bunch monitor

The function of the bunch monitor is to provide a signal which is simply related to bunch size and, hence, enables the operator to optimize bunching. Among the parameters that affect the energy spectrum of a long linear accelerator, one of the most basic is the bunch size. If the bunch length is θ radians and the phasing of the injector relative to the rest of the accelerator differs from the optimum by ϕ radians, the spectrum of the accelerator exclusive of other influences will be

$$\frac{\Delta E}{E} \approx \frac{1}{2}\left(\frac{\theta}{2} + \phi\right)^2 \qquad \text{for } \phi \leq \theta/2 \tag{8-15}$$

and

$$\frac{\Delta E}{E} \approx \theta\phi \qquad \text{for } \phi > \theta/2 \tag{8-16}$$

If $\theta = \phi = 5°$

$$\frac{\Delta E}{E} = 0.0085$$

Since the bunch forms in the first 10-ft accelerator section and remains substantially constant in size throughout the rest of the accelerator, it is meaningful to measure the bunch size at the output of the first section. This makes possible an evaluation of the bunching independent of the operation of the rest of the accelerator.

The bunch monitor consists of two RF induction cavities through which the beam passes, one resonant at 2856 MHz and one resonant at the fifth harmonic, 14280 MHz. The RF power from each cavity is detected with broadband detectors. The difference between the two detected signals is amplified and presented on an oscilloscope. It can be shown that this difference is proportional to the square of the bunch length.[12]

Measurement of bunching

The bunch monitor is intended to be an aid to optimizing bunching but is not intended to give an absolute measure of the bunch length. However, two absolute bunch length measurements have been made. The first, performed on a prototype of the injector, measured the bunch by sweeping the beam from the injector transversely with RF from the klystron which was feeding the injector.[13] Beyond the RF sweeper the electrons transverse position depends linearly on its phase relative to the RF at the sweeper. The bunch structure was measured by measuring the current through a slit as a function of the phase of the sweeper. The results shown in Fig. 8-16 indicate a bunch length of 2.7° full width at one-third maximum.

The second measurement of bunching was made after installation of the first sector of the accelerator. It was performed by measuring the increase in the width of the spectrum from the injector when a second 10-ft accelerator section was turned on 90° out of phase.[14] This measurement, which includes the effect of phase modulation present in the output of the injector 24-MW klystron relative to the phase modulation present in the output of the second 24-MW klystron, gave bunch widths ranging from 4° to 8° full width at half-maximum. The klystrons each have about 3° phase modulation.

Figure 8-16 Charge distribution in bunch.

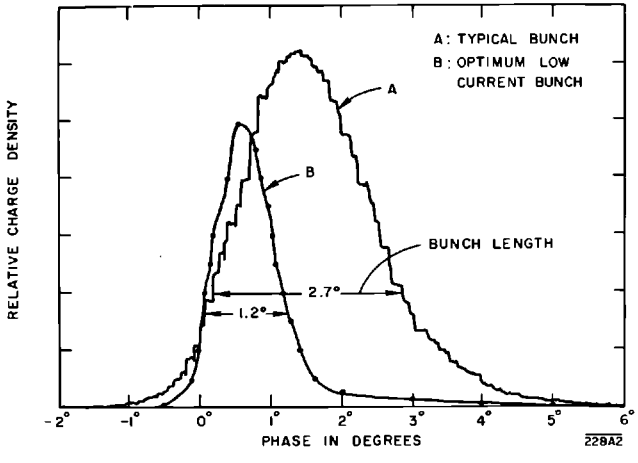

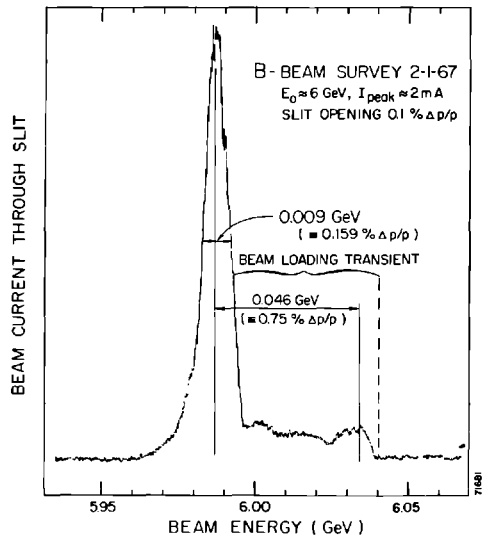

Figure 8-17 Low-current energy spectrum at the end of the accelerator.

Finally, the spectrum from the accelerator indicates the quality of the buncher. Figure 8-17 shows a typical spectrum for a low current beam immediately after phasing all klystrons and then adjusting the injector phase for best spectrum. This final adjustment of injector phase corrects for the average phase error resulting from small errors in the phasing of each klystron. Changing the injector phase by 1° or 2° from the optimum causes an obvious degradation of spectrum. The electrons on the high-energy side of the main peak are those accelerated during the beam-loading transient period. The energy of these electrons can be lowered by delaying the turn-on of an appropriate number of klystrons.

8-5 Beam transport (RHM)

Aside from the accelerating field, the electron beam from the gun is acted upon by its own space charge forces, by radial RF fields in the prebuncher, buncher, and accelerator, by the earth's magnetic field, and by stray magnetic fields caused by local currents and magnetic objects. For this reason it is necessary to incorporate steering, degaussing, and focusing devices into the design of the injector.

System description

In the region between the gun and the buncher, two magnetic thin lenses are used to focus the beam. The prebuncher gap is located at the beam waist (i.e., the point of minimum beam diameter) formed by the first lens. This location

of the prebuncher minimizes the effects of the radial fields and the radial dependence of the longitudinal fields in the prebuncher. Use of a magnetic thin lens permits adjustment of the position of this first beam minimum and hence, permits relaxation of the gun fabrication tolerances and also allows for a variation of gun optics with a change in gun current. Since the lens is dc, whereas the gun current can be changed on a pulse-to-pulse basis, the lens must be set for the best compromise for the range of gun currents in use at a given time. Another magnetic thin lens is located 15 cm downstream from the prebuncher gap and produces a second waist at the entrance of the buncher.

Solenoid

At the second waist, a Brillouin focusing magnetic field is introduced. It is obtained by means of a focusing solenoid which encompasses the buncher and the first accelerator section. The confining field is terminated by shaping the field to produce a convergent magnetic lens at the end of the Brillouin field. By this method a slightly convergent beam can be emitted from the injector 10-ft accelerator section.

The solenoid is assembled from 34 3-in. thick, pancake coils. Each pancake consists of 540 turns of $2\frac{3}{4}$-in. wide, 0.0065-in. thick anodized aluminum foil interleaved with 0.00025-in. Mylar tape. This type of construction produces coils of which the mechanical and magnetic axes almost exactly coincide. The solenoid was assembled by sliding the pancakes onto the concentric stainless steel tube which supports the buncher and 3-meter accelerator section. The assembly is held together by four stringer bolts. Compression forces are applied through a stack of conical washers on each bolt. The pancakes are edge cooled by conduction through a thin layer of loaded epoxy to water-cooled plates between each pair.

At the beginning of the solenoid, where the electrons are not very energetic, the pancakes are individually driven by separate power supplies. In the downbeam half of the solenoid, the pancake coils are coupled together in sets of four, each set being energized by one power supply. This arrangement permits the optimum magnetic field configuration to be found experimentally.

Radial phase space

The dominant feature of the injector optics is that there are strong phase-dependent radial forces which act on the electrons, as seen in Eq. (8-10). Using an impulse approximation in which one assumes the radius ρ to be constant while the forces are applied, it is easy to integrate Eq. (8-10) through a prebuncher, buncher, or accelerator section.

For a prebuncher the answer is

$$\Delta p_\rho \approx \pi\rho \, \Delta\gamma \left(\frac{1-\beta^2}{\beta^2}\right) \cos \phi_m \tag{8-17}$$

where $\Delta\gamma$ is the peak cavity voltage in units $m_0 c^2/e$, and ϕ_m is the phase when the electron reaches the middle of the cavity. For a short buncher with the phase velocity of the wave equal to $\beta_w c$, one obtains

$$\Delta p_\rho \approx \frac{\alpha\rho}{2} \frac{\beta_w(1-\beta^2)}{\beta(\beta_w - \beta)} (\sin\phi_0 - \sin\phi_1) \tag{8-18}$$

where ϕ_0 and ϕ_1 are the phases of the electron entering and leaving the structure. Finally, for the capture region of an accelerator with $\beta_w = 1$ and initial electron velocity $\beta_0 c$, the radial impulse is

$$\Delta p_\rho \approx \frac{\alpha\rho_0}{2} \left\{1 + \left(1 + \frac{1}{\beta}\right) \sin\phi_0\right\} \tag{8-19}$$

For the accelerator section the radial impulse produced by the fringing fields at the output end is not included since the radius has probably changed and the electrons are tightly bunched into a short phase interval so the output has very little effect on the emittance. Since the radial impulses are phase dependent and the electrons enter the prebuncher, buncher, and accelerator with phase spreads of about 4, 1.2, and 0.5 rad, respectively, it is clear that these effects increase the area occupied by the beam in radial phase space. Furthermore, since the radial impulse depends linearly on the radius ρ, the radial emittance $\pi p_\rho \rho$ will vary as the square of the radius of the beam if these dominate. Because of the nonlinear property of the bunching action, electrons entering a bunching element at several different phases and undergoing differing radial forces leave the element at the same phase. As a result the increases in the radial momentum spread are not removed by subsequent RF elements but are cumulative.

Inserting a beam radius of 1 mm into Eqs. (8-17), (8-18), and (8-19) and using phase intervals of 4, 1.2, and 0.5 rad, respectively, for the prebuncher, buncher, and accelerator, one obtains the following values for the range of momentum impulse received:

$$\begin{aligned} &\text{prebuncher} \quad (\Delta p_\rho) \approx 1 \times 10^{-3} \text{ MeV}/c \\ &\text{buncher} \quad\ (\Delta p_\rho) \approx 7 \times 10^{-3} \text{ MeV}/c \\ &\text{accelerator} \quad (\Delta p_\rho) \approx 8 \times 10^{-3} \text{ MeV}/c \end{aligned}$$

This produces an estimated injector emittance of the order of $1.6\pi \times 10^{-3}$ (MeV/c)(cm).

The radial emittance of the injector has been measured.[14] About 90% of the current from the injector is contained in an area of $4\pi \times 10^{-3}$ (MeV/c)(cm) in radial phase space for beam currents of 13.2 and 153 mA.

Acknowledgments

The authors wish to acknowledge the contributions of a number of persons who assisted in the design, fabrication, and installation of the injector. The klystrons, klystron modulators, microwave drive components, and 10-ft

disk-loaded waveguide were substantially identical to those used throughout the two-mile accelerator, and the responsible groups handled their procurement and installation in the injector. D. D. Tsang designed and supervised installation of most of the microwave system and special vacuum components. T. O. McKinney, J. Crew, W. P. Schulz, and J. Zink all made vital contributions to the gun development and testing program. R. A. Leeman supervised the installing of the electronics and cabling. E. F. Roskowski and R. R. Cochran did most of the mechanical engineering.

References

1 W. B. Herrmannsfeldt, "Poisson Equation Solving Program," Rept. No. SLAC-51, Stanford Linear Accelerator Center, Stanford University, Stanford, California (September 1965).

2 R. H. Miller, J. Berk, and T. O. McKinney, *IEEE Trans. Nucl. Sci. NS-14*, No. 3, p. 98 (June 1967).

3 G. A. Haas, "Thermionic Electron Sources," Rept. No. NRL-5657 (AD 266 039), Naval Research Laboratories, Washington, D.C. (October 1961), Fig. 1, p. 5.

4 J. Haimson and I. Brodie, *Nature* **199**, 795–797 (August 24, 1963).

5 A. J. Lichtenberg, Ph.D. Thesis, Oxford University, Oxford, England, 1961.

6 A. J. Lichtenberg, "The Application of Phase Space Concepts to the Design of an Electron Linac Buncher," Engineering Design Laboratory, Oxford University, Oxford, England (no date).

7 J. C. Slater, *Rev. Mod. Phys.* **20**, 473 (1948).

8 M. Chodorow *et al.*, *Rev. Sci. Instr.* **26**, 134 (1955).

9 E. L. Chu, "The Theory of Linear Electron Accelerators," Rept. No. ML-140, Microwave Laboratory, Stanford University, Stanford, California (May 1951).

10 W. J. Gallagher, "Measurement Techniques for Periodic Structures," Rept. No. ML-767, Microwave Laboratory, Stanford University, Stanford, California (November 1960), Appendix B, p. 55.

11 G. Dôme, "Electron Bunching by Uniform Sections of Disk-Loaded Waveguide. Part A: General Study," Rept. No. ML-780-A, Microwave Laboratory, Stanford University, Stanford, California (December 1960).

12 R. H. Miller, "Proposed Bunch Monitor," Tech. Note SLAC-TN-63-65, Stanford Linear Accelerator Center, Stanford University, Stanford, California (August 1963).

13 R. H. Miller, R. F. Koontz, and D. D. Tsang, "The SLAC Injector," *IEEE Trans. Nucl. Sci. NS-12* (No. 3), 804 (1965).

14 R. H. Miller, "Measurements of the SLAC Injector Emittance," *Proc. 1966 Linear Accelerator Conf.*, Rept. No. LA-3609, Los Alamos Scientific Laboratory, Los Alamos, New Mexico (1966), p. 65.

9

THE DRIVE SYSTEM

Z. D. Farkas, C. J. Kruse, G. A. Loew, Editor, and R. A. McConnell

When the operation of a multisection linear accelerator is considered, among the first images to come to mind is that of an array of klystrons and accelerator sections, all working in phase synchronism so that the electron bunches which pass through the accelerator are always on the crests of the traveling wave. This desired situation is provided by the combination of the drive system and the phasing system. Although these two systems are closely intertwined, they are described in separate chapters. The drive system is the subject of this chapter, the phasing system is described in Chapter 12.

9-1 Introduction (GAL)

Three basic requirements were originally placed on the RF drive system for the accelerator klystrons:

1. A drive signal of at least 240 W had to be supplied to each 24-MW klystron.
2. The RF phase of the drive signal to each of these klystrons had to be adjustable so that the traveling RF wave crests in the accelerator and the electron bunches could be made to coincide within $\pm 5°$. This phase relationship had to be preserved in the presence of environmental changes.
3. The phase relationship had to be maintained over a tuning range of ± 0.1 MHz centered around 2856 MHz.

The system which was built to meet these power and frequency stability requirements is the "drive system," the subject of this chapter. The system which actually determines the phase of the electron bunches and automatically optimizes the RF phase of each drive signal is called the "automatic phasing system," which is described in Chapter 12.

In this introduction, the origin of the above basic requirements will be explained, alternative design approaches will be briefly reviewed, and the overall system which was ultimately built and put into operation will be outlined.

The minimum drive requirement for each 24-MW klystron was dictated by the need to operate each tube at saturation.[1] The input power required to do this was specified at 240 W. In order to operate with a comfortable safety margin, the corresponding specification imposed on the drive system was 1 kW per high-power klystron. In addition, it appeared desirable from the beginning to design a system capable of operating under Stage II conditions, i.e., driving as many as 960 high-power klystrons.

For maximum energy gain, the electron bunches in the accelerator must ride on the RF wave crests. There are several reasons why this condition may not be fulfilled, such as incorrect initial phasing, asynchronism of the RF wave with the electrons caused by incorrect frequency or incorrect accelerator temperature, and poor bunching.

To start out, assuming perfect synchronism, the accuracy to which the klystrons must be phased depends upon how closely one expects the output energy to approach the ultimate performance level (perfect phasing). The total electron energy V_T is the sum of the individual contributions of the N accelerator sections,* i.e.,

$$V_T = \sum_{0}^{N} V_n \cos \theta_n \tag{9-1}$$

where V_n is the maximum possible energy gain for a given RF power input, and θ_n is the relative phase angle between the electrons and the wave crests in section n. For small values of θ_n and equal values of V per section, Eq. (9-1) may be written

$$V_T = VN[1 - \tfrac{1}{2}\overline{\theta^2}] \tag{9-2}$$

where $\overline{\theta^2}$ is the average value of θ_n^2. Thus, for the accelerator energy to attain 99.5% of its maximum value, it is necessary that $\theta = 0.1$ rad (approximately 5°). This goal was the origin of the $\pm 5°$ specification on phasing accuracy.

Even in the case of perfect initial phasing ($\theta = 0$), it is possible for a drift or slippage between the RF wave crests and the electron bunches to take place within a 10-ft accelerator section. This slippage occurs either when the entire accelerator is at a single temperature but the frequency is incorrect (asynchronous case) or when the temperature differs from section to section, resulting in deviations of the phase velocity from the velocity of light. The latter condition can occur when different sectors operate at different repetition rates and the constant temperature cooling water causes them to stabilize to different copper temperatures. For the 10-ft constant-gradient section, it can

* This calculation assumes that the four-way rectangular waveguide split introduces no systematic differential phase shifts. For a further discussion of the phase shifts in the rectangular waveguide, see Chapter 11.

be shown that a temperature error of 2°C is equivalent to a frequency error of 0.1 MHz or a maximum slippage of 31 electrical degrees. The resulting energy loss is of the order of 1.5%. In the Stage I configuration, it has been found that the maximum energy dissipated per accelerator section is of the order of 5 kW average, which results in a temperature excursion of slightly over 2°C from maximum to zero repetition rate. In a practical operating case, the differences are less severe, and any frequency averaging or adjustment is less than 0.1 MHz. However, to be prepared for larger power and temperature excursions which would be encountered under Stage II operation, it was decided that the drive system should be capable of frequency adjustment over the range of 2856 ± 0.1 MHz. In turn, for such frequency adjustments to result in measurable energy increases without having to rephase the entire accelerator, the frequency change δf necessary to eliminate a phase slippage $\delta\theta$ within each accelerator section must cause only a negligible phase slippage $\delta\phi$ of the wave along the 2-mile long drive system. This condition must be satisfied because for small angles the change in beam energy varies as the square of the phase shift whether the phase shift occurs in the accelerator sections ($\delta\theta$) or in the transmission line ($\delta\phi$). To assure that frequency and phase adjustments remain essentially orthogonal, it is necessary that

$$(\delta\phi)^2 \ll (\delta\theta)^2$$

As has been shown in Chapter 6,

$$\frac{\delta\theta}{(\delta f/f)} = 8.5 \times 10^5 \text{ deg}$$

Hence, $\delta\phi/(\delta f/f)$ has to be negligible in comparison with this number to meet the third basic requirement of the drive system. Because, as will be seen below, this requirement puts severe restrictions on the allowable group delay deviation from an ideal TEM line, an arbitrary upper limit of $\delta\phi = 1$ electrical degree was chosen for $\delta f = \pm 0.1$ MHz.

The problem of imperfect bunching and the associated problems of energy spectrum width and phase closure are discussed elsewhere (Chapters 8 and 12).

Turning now to the various design approaches which were examined on the basis of the above requirements, it should be noted that work on this system was started in 1958 so that design and engineering had time to evolve through many cycles. A good summary of early ideas can be found in Reference 2. The order in which decisions were made was as follows. First, one had to consider the choice of a main drive line.[3-6] In earlier accelerators, standard rectangular waveguides had been used. However, S-band waveguide was rejected primarily because of its low group velocity ($\delta\phi = 162°$ in a 2-mile length for $\delta f = 0.1$ MHz), but also because of its high attenuation (64 dB for 2 miles) and expensive temperature control requirements. Several types of L-band size waveguides were then considered. For example, a TE_{01} circular waveguide with a 65 cm diameter results in a phase shift error of

10° (for $\delta f = 0.1$ MHz) and an attenuation of 0.12 dB for two miles. However, these special waveguides were rejected for many reasons: their cost, including couplers, would have been 10 times as high as those for coaxial lines; the prevention of cross-sectional expansions would have required very careful temperature control; multimoding would have been difficult to suppress; and finally, the mechanical complications caused by size and weight would have been prohibitive. Point-to-point communication in air was considered but rejected because of the number and cost of antennas and receivers, phase shift problems, and overall noise. Similar difficulties and the status of technology at the time weighed against a modulated laser system with numerous demodulators, one at each feed point. In contrast, a coaxial line system appeared much more appealing. The only major obstacle seemed to be the inherent attenuation (over 100 dB for 2 miles at 2856 MHz for a $1\frac{5}{8}$-in. line). This obstacle could have been surmounted by using a number of booster amplifiers along the way, but overall reliability of the system would have suffered. The timely advent of reliable, high-efficiency varactor multipliers led to the idea of transmitting the main drive signal at a subharmonic of the accelerator frequency. Both the twenty-fourth (119 MHz) and the sixth (476 MHz) subharmonics were considered. The lower attenuation favored 119 MHz, whereas the smaller number of multiplier stages with the reduction of their inherent phase instabilities weighed in favor of 476 MHz.

The drive system which was finally arrived at is shown in Fig. 9-1, and consists of the following subsystems:

1. One on-line "master oscillator" tunable within 476 ± 0.017 MHz, with a second switchable unit on standby for reliability purposes.

Figure 9-1 RF drive system.

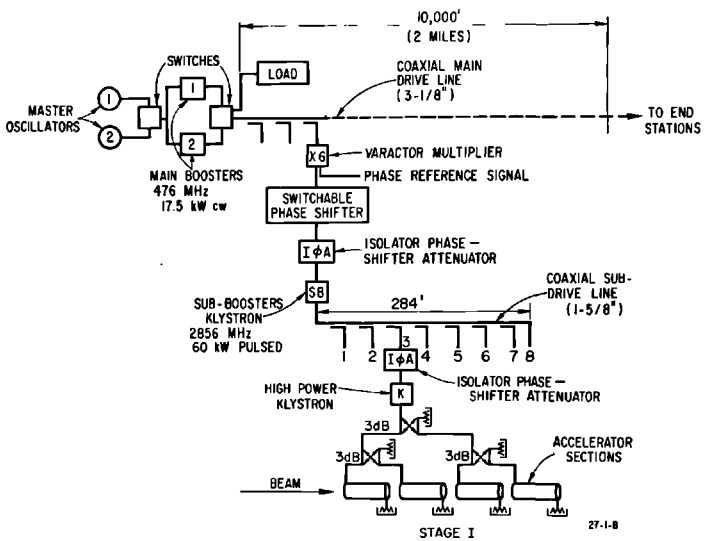

2. One on-line "main booster" which amplifies the signal from the master oscillator to a level of 17.5-kW cw, with a second switchable unit on standby, also for reliability purposes.
3. A 2-mile long, $3\frac{1}{8}$-in. diameter, coaxial drive line which transmits this cw signal at 476 MHz over a 2-mile length from the injector end to the experimental end-station areas, and includes thirty coupling points to supply 4 W of cw power to each of the thirty sectors.
4. For each sector (a) a varactor multiplier unit which multiplies the 476-MHz signal by 6 to 2856 MHz, the operating frequency of the accelerator, (b) an "isolator, phase shifter, attenuator" unit ($I\phi A$) which controls the signal at the output of each varactor multiplier, and a switchable phase shifter capable of introducing a predetermined phase shift for positron acceleration or electron deceleration on a pulse-to-pulse basis, (c) a pulsed sub-booster which amplifies the cw signal from the varactor multiplier to a 60-kW, 2.5-μsec pulse with a repetition rate of 360 pulse pairs*/sec, (d) a $1\frac{5}{8}$-in. diameter coaxial drive line with eight coupling points along its length to supply each of the eight 24-MW klystrons in a sector.
5. At each coupling point, a cable with high phase stability feeding an $I\phi A$ unit (which controls the drive signal to each 24-MW klystron), followed by another cable to the input of the klystron.

Each of these subsystems will be described in the following sections. A summary of operating experience to date is given at the end of each section.

9-2 The master oscillator (RAM)

Function and specifications

The master oscillator is the starting point and frequency standard of the RF drive system. The specifications of the master oscillator are summarized in Table 9-1.

Table 9-1 Summary of master oscillator specifications

Output frequency	476 MHz
Output power	0–8 W
Tuning range	$\pm$16.7 kHz
Frequency stability	$\pm$50 Hz/hour; $\pm$200 Hz/day
Harmonic and spurious frequency suppression	60 dB
Amplitude Stability	$\pm$0.2 dB/24 hours; $\pm$0.5 dB/week.

* The reason for using pairs of pulses is explained later in this chapter, in the section on the sub-booster klystron and its modulator.

The output power was chosen so as to provide at least 2W to each of the two klystron amplifiers driven by the master oscillator, with ample margin for losses in the division and distribution of the master oscillator power. The tunability requirement was chosen to provide ± 100 kHz tuning range at 2856 MHz. It is imposed by the necessity of tracking accelerator temperature variations in order to maintain the phase velocity equal to the speed of light. The stability specification on the master oscillator was chosen to reduce random frequency variations below the level at which they could affect the operation of the accelerator. Harmonic and spurious signal generation specifications were also low enough to have negligible effect on accelerator operation. This point is discussed in detail below. Amplitude stability requirements were such that the drive level to the subsequent amplifiers would be kept well within the saturation region, maintaining maximum amplitude stability throughout the entire drive system. As will be seen in the discussion of the frequency multipliers, small amplitude variations at the frequency multiplier inputs are converted to large phase excursions at the outputs.

Design

The master oscillator consists of a crystal oscillator at 39.67 MHz, followed by a multiplier–amplifier chain and a vacuum tube power amplifier with an output of 8W at 476 MHz. With the exception of the power amplifier, the entire unit is solid state. In addition, there is an electronic frequency control

Figure 9-2 Master oscillator block diagram.

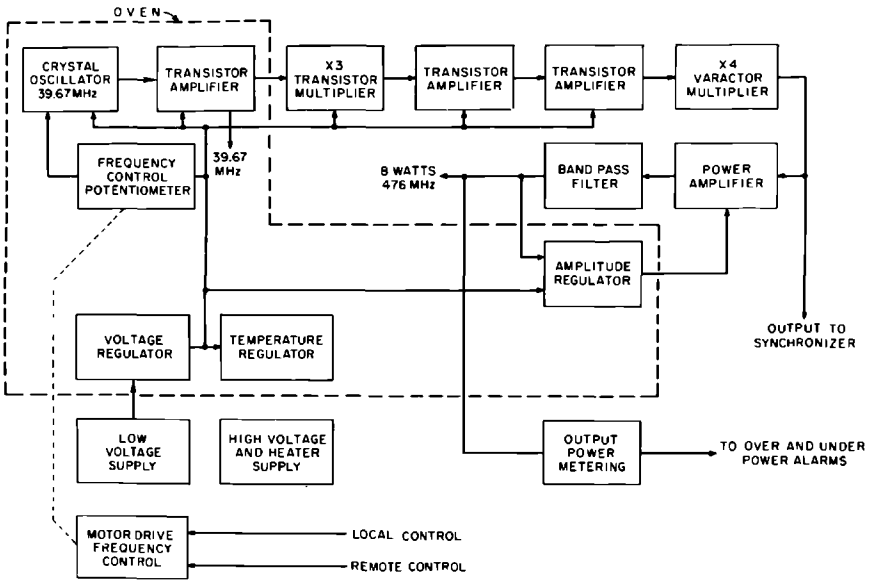

system, an amplitude regulation system, an oven in which the crystal oscillator is housed, a low-level 39.67 MHz output to drive the "beam knockout" deflector in the beam injector system, and regulated high- and low-voltage dc power supplies. The frequency can be changed either at the master oscillator or from the accelerator central control room. Over–under power alarms are provided locally and at the central control room. A block diagram of the master oscillator is given in Fig. 9-2.

The frequency stability of this oscillator, when combined with a tunability of ± 16.7 kHz, is somewhat above average. The crystal used is of the third overtone type with the crystal in the series resonant mode. A varactor diode in parallel with the oscillator collector tank circuit provides ± 1.5 kHz tuning around the crystal frequency of 39.67 MHz by means of a regulated voltage applied to the varactor through a motor-driven potentiometer. Long-term stability is obtained by enclosing the crystal oscillator and the operating and tuning voltage-supply regulator in an oven which stabilizes the temperature to better than $\pm 0.1°C$.

The requirement for suppression of spurious emission was determined from the following considerations.

Suppose that a maximum deviation of 5° is allowed between the electron bunch in the accelerator and the RF wave crest. Let the master oscillator be phase-modulated by a small noise signal. At some time the phase of the carrier will be displaced from its proper position by an angle θ. Then

$$\tan \theta = \frac{e_1 + e_2}{e} \tag{9-3}$$

where e_1 and e_2 are the upper and lower side-bands and e is the carrier.

Since phase angles are multiplied in the frequency multiplication process, the angle θ at the 476 MHz must be one-sixth that at 2856 MHz, or 0.83°. Assuming e_1 equal to e_2, one finds $e_1/e = 0.0073$. In this case, a side-band suppression of 42.8 dB at 476 MHz is required.

The above analysis disregards higher-order phase modulation side-bands, but these can be shown to be negligible for small phase modulation indices.

With 60 dB suppression at 476 MHz, as specified for the master oscillator, the phase deviation contribution of the master oscillator is 0.7°.

Additional features

Since the master oscillator is an indispensable part of the accelerator RF drive system, a standby unit has been provided for use in the event of failure of the on-line unit. A frequency locking system causes the standby oscillator to track the frequency of the active unit. In case of failure, the standby unit is automatically switched in, remaining on the last frequency of the failed unit until it is retuned by the accelerator operator. In addition, either oscillator can be selected manually from the central control room.

A direct reading counter is provided locally for each master oscillator, so that a continuous watch may be maintained on frequency stability and tracking. In addition, a direct reading counter is installed in the central control room. A small sample of RF from the main drive line in Sector 28 is multiplied to 2856 MHz and applied to the counter. Thus the operator reads the actual accelerator operating frequency, which is more meaningful to him than the main drive line frequency.

Physical description

The master oscillator is built on a standard rack mounting panel, 19 in. wide by $8\frac{3}{4}$ in. high. The weight is approximately 40 lb. One front panel meter with a selector switch monitors critical voltages and currents within the unit. A second meter displays output power level, and meter relays on this instrument provide switching signals in the event of over- or underpower output. Front panel controls include an on–off standby switch, a power adjustment, a frequency control, and a meter relay reset switch. Figure 9-3 is a photograph of the unit.

Performance

After initial shakedown difficulties, there have been only minor problems with the master oscillators. Since the drive requirements of the klystron amplifiers fed by the master oscillator turned out to be substantially lower than anticipated, it has been possible to reduce the master oscillator output power to 4 W, and the resulting life of the final amplifier tube (an Amperex 5894) is now in excess of 10,000 hours. The power reduction has also improved amplitude stability. The frequency stability specification has been easily met, with typical frequency drifts being on the order of 100 Hz/week.

Figure 9-3 Master oscillator.

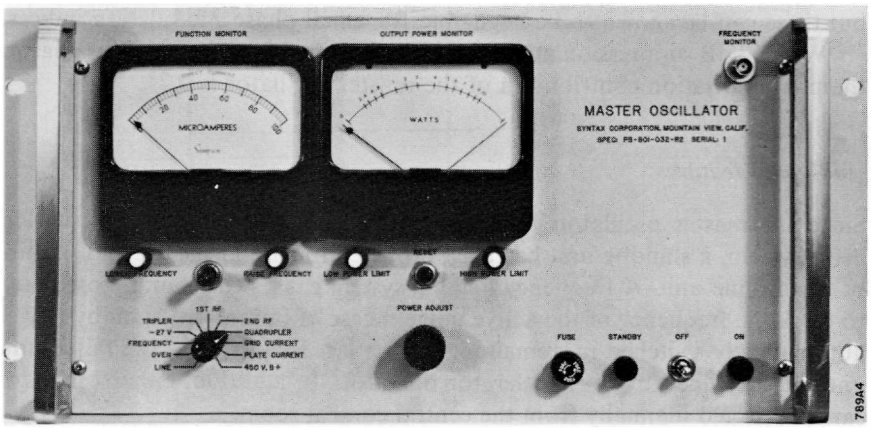

9-3 The main booster amplifier (RAM)

Function and specifications

The function of the main booster is to amplify the output of the master oscillator from several watts to 17.5 kW for delivery to the main drive line.

The output power of 17.5 kW was selected to allow approximately 4 W to be extracted from the main drive line at each of thirty sectors with couplers having no closer coupling than 10 dB, and to permit about 50 W to be received at the far end of the 2-mile main drive line for distribution into the end stations.

A stringent output power stability requirement was dictated by the fact that the varactor frequency multipliers driven by the main booster amplifier show substantial amplitude to phase conversion, as was mentioned previously in connection with the master oscillator amplitude stability specification.

Design

The main booster amplifier uses a uhf TV klystron (Eimac 4KM70LA). This tube has four external cavities and a gain greater than 40 dB. It is rated at 17.5-kW cw for SLAC's application. Amplitude stabilization is accomplished through collector voltage regulation by means of a series regulator tube in the collector high-voltage supply. The control grid of the regulator tube (Eimac 4CW50,000) receives a signal which represents the difference between a reference voltage and the output of an RF detector diode coupled to the output of the amplifier. Careful design of the reference voltage source and the following dc amplifiers, and temperature stabilization of the RF detector have made it possible to hold the output power to ± 0.1 dB/week. In the event of failure of the RF detection diode, a backup regulation system is provided in which the high voltage, rather than the rectified RF voltage, is compared to the reference voltage. In addition, the water used to cool both the klystron and regulator tube is stabilized to within a few tenths of a degree centigrade, and the amplifier is operated at saturation.

The amplifier power supply is a conventional three-phase full-wave bridge circuit using solid-state rectifiers.

Cooling is accomplished with deionized water and forced air. The klystron requires 20 gal/min, and the regulator tube 10 gal/min. Water is drawn from the same supply that furnishes water for the 24-MW klystrons. Fans provide cooling for the high-voltage rectifier stacks and the vacuum tubes which are part of the regulator circuit dc amplifiers.

A block diagram of the amplifier is given in Fig. 9-4.

Standby equipment

Like the master oscillator, the main booster amplifier is an indispensable part of the RF drive system. Accordingly, a standby unit is available within seconds

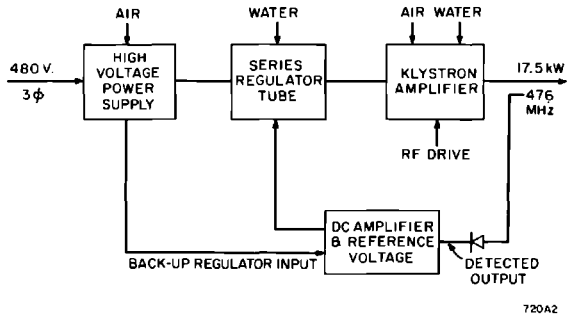

Figure 9-4 Main booster amplifier block diagram.

after a failure of the on-line unit. An automatic switching system removes RF drive from both units, interchanges a dummy load and the main drive line, and returns RF drive to both units. The switching time is determined by a coaxial transfer switch which requires about 2 sec to operate. Rapid switching is necessary in order to prevent the accelerator structure from changing temperature because of the absence of RF power. Further details on the switching system are given in a later section.

Physical description

The main booster amplifier is housed in an enclosure approximately 8 ft high by 4 ft deep by 10 ft long. Important voltages and currents can be monitored on front panel meters. An extensive interlock circuit provides for safe operation, and indicator lights in the interlock chain aid in the location of trouble. Power supplies and the regulator circuit are located in the left-hand portion of the enclosure. The center panel contains metering circuits, while the klystron and cooling systems are located to the right. Figure 9-5 is a photograph of the unit.

Performance

As of July 1967, approximately 28,000 hours of operating time had been accumulated on the main booster amplifiers. Up to that time, there had been four klystron failures, one at 3 hours, one at 2500 hours, one at 3600 hours, and one at 8800 hours.

The high-voltage rectifier stack in one amplifier failed at 4000 hours, possibly because an accumulation of dust and a water leak through the roof of the klystron gallery caused high-voltage breakdown across one of the rectifiers. Changes have been made to prevent recurrence of these faults.

Furthermore, the regulator circuits have been relocated away from the regulator tube, where they were subject to water damage from the regulator tube cooling system.

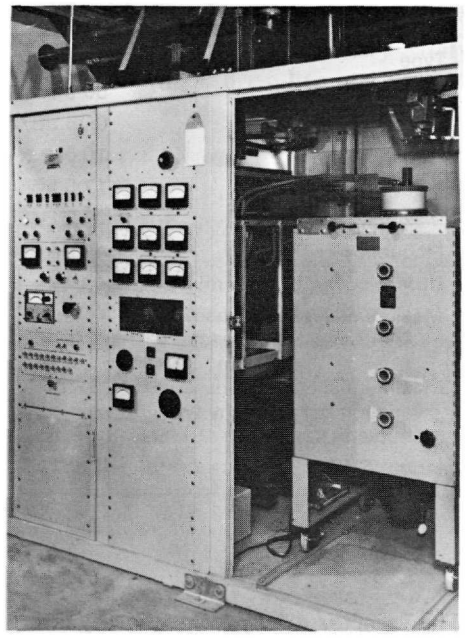

Figure 9-5 Main booster amplifier.

The important specification of amplitude stability has been well maintained, and modifications in the dc amplifier portion of the regulator have further improved amplitude stability.

9-4 Main drive line (ZDF)

Function and specifications

The main drive line transmits the 476 MHz power from the main booster, located in the injector area, to the end of the accelerator. It includes thirty equally spaced couplers to feed 4.1 W of cw power to each of the thirty frequency multipliers, one of which is located at the beginning of each of the thirty sectors that make up the machine. The remaining power, at the end of the main drive line, is transmitted by means of 1200 ft of $\frac{7}{8}$-in. semirigid coaxial line to the end stations.

An extra coupler at Sector 28 provides 1 W for monitoring the power and frequency of the drive signal in the central control room.

In addition, with the aid of multiplexers, the main drive line has the capability of transmitting dc to 100 MHz signals from the injector area to the end stations.

The specifications of the main drive line are summarized in Table 9-2.

Table 9-2 Summary of main drive line specifications

Type	$3\frac{1}{8}$-in. EIA standard copper line
Impedance	50 ohms
Attenuation	0.25 dB/100 ft
Length	10,049 ft
Input power	17.5 kW (cw)
Maximum power	25.0 kW (cw)
Frequency	476 ± 0.0167 MHz
Output power to each multiplier	4.1 W
Maximum allowable phase variation with frequency	$\pm 0.167°$ deviation from that of an ideal TEM line of equal length for ± 0.0167 MHz.
Maximum allowable phase variation between any two couplers	$\pm 0.167°$/24 hours
Input VSWR	1.05 : 1.00

Power input requirements

The varactor multiplier at the beginning of each section has to be driven by 4.1 W at 476 MHz in order to provide enough output power to saturate the sub-booster klystron. This requirement, coupled with the minimum end-station power needs, determines the power input to the main drive line.

The input power required was determined in the following manner:

If a transmission line has N couplers, and each coupler removes P_n watts, then the total input power is the summation from 1 to N of the power from the nth output, multiplied by the attenuation factor from the input to the nth output.

Expressed mathematically

$$P_T = \sum_{1}^{N} P_n r_n \tag{9-4}$$

where P_T is the total input power, P_n is the power output from the nth coupler, and r_n is the attenuation factor from the input to the nth output.

The power input necessary to provide P_o output power at equally spaced coupling points along the line with an attenuation factor r between coupling points is

$$P_T = P_o \frac{r^N - 1}{r - 1} \tag{9-5}$$

This expression led to a required line input power of 8 kW. However, in addition to the couplers feeding each of the thirty sector frequency multipliers, there is a coupler in Sector 1 to drive redundant equipment peculiar to only that sector and an extra coupler in Sector 28 as already mentioned. Finally,

it was desired to have about 50 W at the end of the main drive line to be distributed to the end stations. These requirements and a necessary safety factor resulted in setting the input power to the main drive line at 17.5 kW.

Environmental phase stability

Environmental factors affect the phase stability of the main drive line in the following ways:

1. The length varies as a function of temperature.
2. The dielectric constant of the gas inside the lines varies because of changes in the pressure to temperature ratio, that is, in the density, and changes in moisture content.
3. The dielectric constant of the teflon supports for the center conductor changes with temperature. The bulk of the teflon supports was kept low and the effect on phase variations with temperature was found to be negligible.

The total electrical length of the drive line is

$$\phi = \sqrt{\varepsilon_a}\,\frac{l_a}{c}\,\omega + \sqrt{\varepsilon_t}\,\frac{l_t}{c}\,\omega \tag{9-6}$$

where

ε_a = relative dielectric constant of air
ε_t = relative dielectric constant of teflon center conductor supports
l_a = length of that portion of the line filled with air
l_t = length of that portion of the line filled with teflon
$l = l_a + l_t$ = total length of line

Defining

$$\sqrt{\varepsilon_a} = 1 + \delta_a \qquad \sqrt{\varepsilon_t} = 1 + \delta_t$$

one obtains

$$\phi = \frac{l + l_a\,\delta_a + l_t\,\delta_t}{c}\,\omega = \tau\omega \tag{9-7}$$

where τ is defined as time delay. δ_t has negligible variation, and δ_a is given by[7]

$$\delta_a = 105 \times 10^{-6}\,\frac{P}{T} \tag{9-8}$$

where P is air pressure in torr and T is air temperature in °K. From Eqs. (9-7) and (9-8) for small δ_a:

$$\frac{d\tau}{\tau} = \frac{dl}{l} + \delta_a\left[\frac{dP}{P} - \frac{dT}{T}\right] \tag{9-9}$$

Table 9-3 Time delay in drive line as a function of air temperature and pressure variations

Initial condition	*760 torr, 80°F*	*760 torr, 112°F*	*10^{-3} torr, 80°F*
δ_a	266×10^{-6}	252×10^{-6}	0.35×10^{-12}
$\frac{d\tau}{\tau}$	-0.492×10^{-6}/°F 18.1×10^{-6}/lb/in.^{2}	-0.440×10^{-6}/°F 17.15×10^{-6}/lb/in.^{2}	-0.648×10^{-12}/°F $0.35 \times 10^{-12}/10^{-3}$ torr
$d\tau$	−4.92 psec/°F 181 psec/lb/in^2	−4.41 psec/°F 171.5 psec/lb/in.^{2}	−0.648 psec/°F 0.35 psec/10^{-3} torr

The relative and absolute changes in time delay for the 2-mile line ($\tau = 10^{-5}$ sec) per unit change in temperature and pressure are given in Table 9-3 for three initial conditions of the air inside the line. The time delay errors are readily converted into phase delay errors since at 2856 MHz they are nearly equal numerically (1 psec = 1.026°).

The relative and absolute changes in time delay because of length variations with temperature are

$$\frac{d\tau}{\tau} = \frac{dl}{l} = 9.7 \times 10^{-6}/°\text{F}$$

$$d\tau = 97 \text{ psec}/°\text{F}$$

To control the length variations, all output ports are rigidly anchored to the concrete floor of the klystron gallery.[8] The line is supported on rollers at 10-ft intervals to avoid excessive stresses, and changes in line length are taken up by expansion sections which allow both inner and outer conductors to slide past each other. Thus the length variation, which causes the greatest phase error, is eliminated.

To control the phase shift due to changes in dielectric constant of the gas inside the line, the pressure is maintained constant within ± 0.01 lb/in.^{2}, and the temperature is regulated to within ± 1°F. These variations correspond to phase variations of $\pm 1.81°$ and $\pm 4.92°$, respectively, for the 2-mile line. Dry air is used so that moisture content is not a factor in determining the dielectric constant. If necessary, the phase variation from pressure and temperature effects can be further reduced by partial evacuation of the main drive line, or by filling the line with helium whose relative dielectric constant is one-tenth that of air.

Environmental performance

A portion of main drive line consisting of five sectors was short-circuited at one end, and at the other end the forward and reverse power were sampled with two directional couplers. The outputs of the couplers were fed to a phase

bridge to monitor the phase between the forward and reflected signals. The temperature of the line was also monitored.

A three-day continuous test showed the following variations:

Water temperature, 113.2–113.4°F
Water temperature inside insulation, 113.3–114°F
Main drive line temperature near water tracer, 111.5–112.6°F
Main drive line temperature far from water tracer, 110.6–108.0°F
Air temperature inside insulation, 105.5–99.8°F
Gallery temperature, 50–80°F
Phase variation in about 60 hr, $\pm 35°$ (projected to 2856 MHz and 2 miles)

The above-measured phase variations can be accounted for by the change in dielectric constant of the air in the line as a function of temperature. Normally, as will be discussed in Chapter 12, the entire accelerator is rephased at least once every 24 hours and these variations are automatically compensated for.

Phase frequency response

Since the coincidence of the RF drive signal wave crest and arrival of the electron bunches must be preserved over a tuning range of ± 0.1 MHz, and the maximum allowable phase error is 1°, the restriction imposed on the relative group delay of the drive line is as follows[9]: Let ϕ_e be the total phase shift of the beam, ϕ_w the total phase shift of the RF wave, τ_e the total group delay of the beam (beam length divided by beam velocity), and τ_w the total group delay of the RF wave. From the definition of group delay:

$$\delta\phi_e = \tau_e\,\delta\omega, \qquad \delta\phi_w = \tau_w\,\delta\omega \tag{9-10}$$

and the phase error is

$$\delta\phi = \delta\phi_w - \delta\phi_e = \tau_e\left(\frac{\tau_w}{\tau_e} - 1\right)\delta\omega \tag{9-11}$$

The relative group delay of the drive line is related to the phase error tolerance by

$$\frac{\tau_w}{\tau_e} = 1 + \frac{\delta\phi}{2\pi\,\delta f\,\tau_e} \tag{9-12}$$

For an allowable error of $\delta\phi$ of 1°, a time delay τ_e of 10^{-5} sec, and a frequency change δf of ± 0.1 MHz, the relative group delay of the wave must fall between 0.997 and 1.003. If the lengths of the beam and wave travel are made identical, the relative group velocity of the RF with respect to the beam,

v_w/v_e, must fall within the same range. The relative group velocity of the beam differs from unity by $1/2\gamma^2$, where γ is the ratio of total mass to the rest mass of the electron. Thus, after the first few feet of acceleration it can be assumed that $v_e = c$.

The relative group delay of the wave is affected by the dielectric loading due to inner conductor supports. These supports slow down the wave and the group velocity is reduced. In addition, the supports present periodic discontinuities along the line. The reflection from the discontinuities may increase or decrease group delay. Of these two effects, the larger is dielectric loading which adds a delay on the order of 2 psec/ft. The reflections add a relative group delay proportional to the product of individual reflection coefficients. The magnitudes of the reflection coefficients are of the order of 0.025 and they add a group delay of ± 0.625 psec/ft. Thus, an additional 2.625 psec/ft is added to the 1000 psec/ft of an ideal line.

Phase frequency performance

The test setup used for the phase-temperature measurements was also used for measuring the phase-frequency response. The frequency was varied around 476 MHz until two successive nulls were obtained from a phase bridge output. A similar measurement was made by bending a sector of main drive line into a U and using a slotted line to monitor the phase of the incident power at each end of the line. The length from the coupling points to the detector probe was made equal, and the frequency was changed around 476 MHz until two successive minima were obtained. The frequency change δf was noted. Using Eq. (9-10), the total group delay was then given by $\tau_w = 1/2\delta f$. The relative group velocity was obtained by measuring l and forming the ratio $(l/\tau_w)/c$. The values obtained were within the specified range.

The measured reduction of beam energy for a 0.1 MHz frequency change is 1.5%. This can be accounted for by considering the slippage of the electrons with respect to the RF wave within individual accelerator sections, indicating that frequency and phase adjustments are essentially orthogonal.

Physical description

The main drive line consists of an assembly of $3\frac{1}{8}$-in.-diameter rigid copper coaxial line sections, each 20 ft, 3 in. long. The sections are joined together with EIA flanges, and directional couplers and expansion sections are fitted at appropriate intervals.

A typical sector consists of sixteen 20-ft-3-in. sections and one 8-ft-4-in. section containing the expansion joint. Section lengths were measured at room temperature and extrapolated to 112°F. As installed and operating at 112°F, the expansion section can contract 1 in. and expand 3 in. Because a sector expands 1 in./25°F, the above limits allow for a temperature range of 112°F(+25°, −75°F).

Because much of the main booster power is dissipated in the first few sections, larger temperature excursions are experienced. To accommodate this, an additional expansion section is fitted in each of the first five sectors.

The first 20-ft section of each sector contains a directional coupler which supplies the input drive to the frequency multiplier. The coupling ratios range from 35.5 dB at the beginning of the drive line to 12 dB at the end.

Drive line extension to end stations

Signals synchronous with the beam bunches are needed in the experimental areas for timing, supplying RF to particle separators, and for other purposes as yet unforeseen. For these reasons the drive line was extended into the end stations. Because of the unavailability of convenient anchor points and the lack of inexpensive means of temperature control, a $\frac{7}{8}$-in. semirigid aluminum coaxial transmission line was used instead of the rigid line. Whenever possible the cables were buried 2 ft underground. Tests showed that the daily temperature variation at that depth is less than a degree centigrade.

The time delay variation with temperature of the semirigid cable is less than that of rigid coaxial line because the linear expansion of the conductors is partially compensated by the expansion of the dielectric support of the inner conductor. The measured variation of time delay with temperature is 0.005 psec/°F/ft. For a length of 1200 ft and an estimated temperature variation of 2°F, a maximum time delay variation of 12 psec can be expected. If this variation should prove excessive, it may be reduced by connecting in series with the line an appropriate length of RG-214/U cable which has a negative coefficient of time delay versus temperature, or by phase-locking the output signal to the beam at a point relatively close to the end stations.

9-5 Subdrive line (ZDF)

Function and specifications

Each of the thirty subdrive lines transmits the 60-kW-peak 2856-MHz power output from the sub-boosters and distributes this power equally to eight 24-MW peak power klystrons. The first seven klystrons are supplied by means of directional couplers. The last one is fed directly by using all the power remaining at the end of the line. A summary of the subdrive line specifications is given in Table 9-4.

Design

Because the length of each subdrive line is one-thirtieth of the length of the main drive line, the restrictions on the relative phase-frequency response and phase-temperature variation per unit length can be relaxed by the same factor.

Table 9-4 Summary of subdrive line specifications

Type	$1\frac{5}{8}$-in. EIA standard copper line
Impedance	50 ohms
Attenuation	1.13 dB/100 ft
Length	284 ft $\pm$ $\frac{1}{2}$ in. at 112°F
Input power	60 kW (peak), 113 W (average)
Maximum power	100 kW (peak), 200 W (average)
Frequency	2856 $\pm$ 0.1 MHz
Output power from each coupler	4 kW (peak), 8 W (average)
Variation of phase with frequency	$\pm 1°$ deviation from an ideal TEM line of equal length for 0.1 MHz frequency change
Phase stability	$\pm 1°$/24 hours
Input VSWR	1.05 : 1

Expansion sections are not required. With use of Table 9-3 and Eq. (9-10), allowing 1° phase error, the following restrictions are imposed on the subdrive line:

Allowable range of relative group velocity, 0.99–1.01
Temperature stabilization, $\pm 1°$F
Pressure stabilization, ± 0.1 lb/in.^{2}

These specifications were met.

9-6 The Frequency Multipliers (RAM)

Function and specifications

The function of the frequency multipliers is to multiply the 4.1-W, 476-MHz input power from the main drive line by a factor of 6 to 2856 MHz, and supply approximately 400 mW to drive the sub-booster klystrons. As with most parts of the RF drive system, good phase stability is a prime requirement. At the time the RF drive system was being designed, varactor diode multipliers were quite new and the phase stability properties of such devices were unknown. Consequently, measurement systems had to be devised to determine their capabilities before design work could continue on other major parts of the drive system.

The output power of the multiplier was chosen to be sufficient to provide adequate drive power for the sub-booster klystron and to provide a phase reference signal for the automatic phasing system.

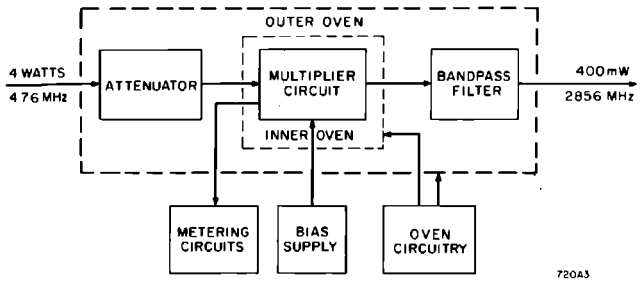

Figure 9-6 Frequency multiplier.

The input power specification was dictated by the efficiency of the multiplier and the output power requirement.

The phase stability specification was chosen on the following basis. The total allowable phase difference between electron bunches and RF wave crests in the accelerator was set at $\pm 5°$. Of this 5°, the frequency multipliers were allowed to contribute 1°. That is, the phase difference between the outputs of a reference multiplier in an invariant environment and a second multiplier subjected to various environmental changes was not to differ by more than $\pm 1°$.

Design

A block diagram of the frequency multiplier is given in Fig. 9-6. The function of the input attenuator is to adjust the input power to the precise value required for maximum phase stability. The double oven maintains the temperature of the multiplier circuit at $68 \pm 0.1°C$. The band-pass filter eliminates spurious outputs, mainly fifth and seventh harmonics of the input frequency. A bias supply rather than a self-biasing circuit is used for two reasons: starting problems are reduced by the use of fixed bias, and it has been found possible to minimize phase shift as a function of drive power by small adjustments of bias.

A simplified diagram of the multiplier RF circuit is given in Fig. 9-7.

Physically, the input circuits are composed of lumped elements, the idler circuits are strip line, and the output circuit is a cavity.

Figure 9-7 Varactor frequency multiplier simplified circuit diagram.

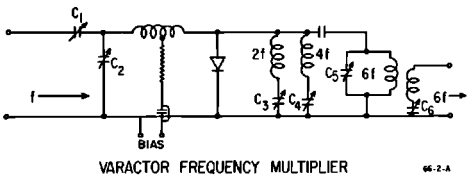

Adjustment

To obtain optimum phase tracking among the thirty-one multipliers used along the accelerator, it was necessary to develop the following technique to ensure that all multipliers were tuned in an identical manner.

Referring to Fig. 9-7, it is convenient to consider C_1, C_2, and the bias voltage as input tuning controls and C_3, C_4, C_5, and C_6 as output tuning controls. Initially, a rough adjustment of all controls is made for maximum output power. Then the input controls are adjusted for minimum reflected input power, and the output controls are adjusted for maximum output power. The above procedure results in a separation of tuning control functions which greatly reduces the time required for tune-up, and also results in multipliers being nearly identically tuned.

Since the capacitance of the varactor diode is a function of applied voltage, it is to be expected that changes in input power to the multiplier will result in changes in tuning, with a resulting phase shift through a single multiplier. When drive power variations occur to two or more multipliers driven in parallel, variations among diodes, circuit Q's, and tuning conditions cause a loss of phase tracking at the multiplier outputs. The tuning technique described above contributed greatly to improvement of the phase tracking and, in addition, it was found that fine adjustments of bias voltage resulted in a minimization of phase shift with drive power. In many cases, the phase tracking between two multipliers could be improved to better than $\pm 0.1°$ for drive power variations of ± 0.1 dB.

Physical description

The frequency multiplier is built behind a standard rack panel, $8\frac{3}{4}$ in. high by 19 in. wide. Front panel controls are limited to a power on–off switch, a screwdriver-adjust attenuator, and a meter function selector switch. The meter monitors line voltage, bias voltage, and input power. A second meter measures output power. Two pilot lights indicate presence of primary power and cycling of the oven heater.

Measurement techniques

Since phase stabilities of better than 1° per week were to be measured, it was necessary to develop phase measuring instruments capable of 0.1° per week stability.[10] A two-detector direct comparison phase bridge, employing a matched magic T and having mechanical and electrical symmetry in both arms, was constructed. The whole structure was built on a heavy pressed-wood table top. Supporting brackets for the waveguide components were placed at frequent intervals. Dowel pins were used to assure proper alignment of all flanges. It was necessary to use coaxial lines at the inputs and outputs of the multipliers. Rigid or semirigid temperature-compensated cables were

used in these places. Tunnel diode detectors which required only −15 dBm input and which had better temperature characteristics than crystal diode detectors were used. The detector outputs were combined in a resistive network and fed to a stable dc voltmeter–amplifier–recorder system. Through the use of diode loading and level controls, the detectors were made identical in laws of response and output. As a result, the bridge response to amplitude variations was reduced to a second-order effect. Finally, the whole apparatus was operated in a temperature-controlled room with maximum variations of ±2°F. The result was a phase bridge capable of a stability of better than ±0.01° for measurements requiring only a few minutes, and better than ±0.1° per week.

The bridge was also used in the optimization of phase tracking with drive power changes. About 1% modulation at 500 Hz was applied to the RF source driving two multipliers in parallel. The multipliers themselves caused amplitude-to-phase conversion which was measured at the bridge output with a tuned voltmeter. Very small adjustments in the fixed bias of one multiplier resulted in a minimization of the phase shift between the two multipliers. This was apparently accomplished by shifting the operating point of the diode to a position at which the C–V curves of the two diodes more nearly matched.

Performance

The frequency multipliers have met all their specifications. Phase stability of ±1° between a reference multiplier and all other multipliers has been maintained under the following input and environmental fluctuations simultaneously applied:

Line voltage, ±5%
Temperature, +40° to +120°F
Frequency, ±100 kc (at output)
Drive power, ±0.1 dB

A test period of 1 week was used in all cases.

The diodes are being operated at the upper edge of their power handling capability. Diode life, however, has been good. A number of diodes have been operating with no apparent change in characteristics for more than 15,000 hours. On one occasion the drive power to the multipliers was increased by 1.5 dB because of a failure in the main booster amplifier regulation circuit, resulting in a failure of about half the diodes connected to the main drive line.

An early difficulty was the variation in diode quality resulting in marginal power output. This problem has been solved by closer control of diode characteristics in the manufacturing process.

As more life information has become available, a new problem has appeared. Some diodes exhibit a slow change in characteristics which makes it impossible for a multiplier to meet the input VSWR specifications even after retuning. This condition is at present determining end of life.

9-7 Sub-booster klystron and modulator (CJK)

The sub-booster klystron supplies the subdrive line with 60 kW of pulsed power at 2856 MHz.

In this section only the RF features of the modulator and klystron will be discussed. Details of the modulator electronics will be found in Chapter 13.

Klystron specifications

A summary of the sub-booster klystron specifications is given in Table 9-5.

The output power was designed to be sufficient for Stage II operation, the drive power requirement was based upon the klystron design, and the phase and power stability requirements were determined from the allowable contributions of the sub-booster to the overall phase error in the accelerator.

Physical description of the sub-booster klystrons

The initial complement of sub-booster klystrons was supplied by the Eimac Company and used periodic–permanent magnet focusing, built as an integral part of each tube. Including magnets, the klystrons are approximately 6 in. in diameter, 23 in. long, and weigh 35 lb. The second generation of klystrons was supplied by Litton Industries. These are focused by conventional "barrel" uniform field, permanent magnets, interchangeable from tube to tube. Including the magnets, the tubes are approximately 9 in. in diameter, 23 in. long, and 100 lb in weight. Cooling-water connections are of the Hansen

Table 9-5 Summary of sub-booster klystron specifications

Power output	60 kW (peak)
Drive power	60 mW (cw)
Gain	60 dB
Peak beam voltage	28 kV (maximum)
Pulse length (maximum)	10 μsec
Pulse length (normal)	2.5 μsec
Frequency range	2848–2864 MHz
Efficiency	23.5% (minimum)
Perveance	$\approx 2 \times 10^{-6}$ A/V$^{3/2}$
Allowable phase variations	
pulse-to-pulse	$\pm 0.5°$ (maximum)
during pulse	$\pm 0.5°$ (maximum)
with voltage	0.5°/10 V
Power drift	Less than 0.05%/°C temperature change of inlet water
Phase drift	Less than 0.8°/°C temperature change of inlet water

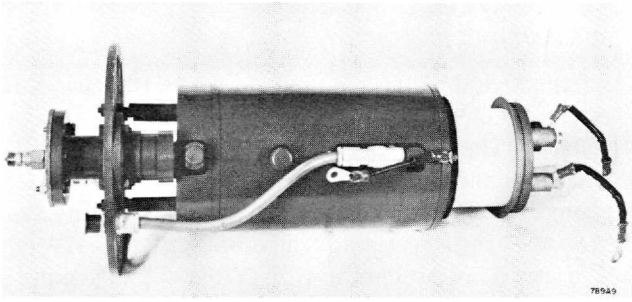

Figure 9-8a Eimac sub-booster klystron.

quick-disconnect type. The klystrons are cooled with deionized water at 113°F. They operate with the isolated cathodes downward and the collectors grounded. The RF input connectors are type N, whereas the outputs are EIA standard $1\frac{5}{8}$ inch. The EIMAC klystron is shown in Fig. 9-8a, and the Litton klystron in Fig. 9-8b.

Sub-booster modulator specifications

A summary of the sub-booster modulator specifications is given in Table 13-8.

Figure 9-8b Litton sub-booster klystron.

Pulse pairing

An explanation of the requirement for pulse pairs is necessary at this time. The sub-booster klystron produces two output pulses separated in time by 20 to 50 μsec. The first pulse is referred to as the accelerating pulse, the second is called the standby pulse. If it is desired to remove a sector from acceleration for phasing, energy control, or maintenance purposes, and yet maintain the sector at normal operating temperature, the 24-MW klystrons of that sector are triggered in synchronism with the standby pulse rather than with the accelerating pulse. Because no beam is present at that time, no acceleration takes place, but the average RF input to the sector and the temperature of the accelerator structure remain constant. In the same manner, a single klystron and its associated accelerator sections can be removed from acceleration and placed on standby.

Provision for longer pulses

Under normal operating conditions, the leading edge of the sub-booster RF pulse occurs about 0.1 μsec after the leading edge of the 24-MW klystron voltage pulse, and the sub-booster pulse is slightly shorter than the 24-MW klystron pulse. Under special operating conditions where, for example, thyratrons within a sector might fire at slightly different delay times, it might be desirable to have a longer RF drive pulse to overlap all 24-MW klystron voltage pulses. For this reason, provision was made to allow operation of the sub-booster klystron and modulator with a voltage pulse length of 3.5 μsec.

Voltage stability requirements

The total phase shift tolerance during a pulse and from pulse to pulse allotted to the sub-booster klystron was $\pm\frac{1}{2}°$. This requirement allowed a corresponding voltage change of $\pm 0.04\%$, as shown by the following derivation.

The phase shift ϕ across a klystron of length L is given by

$$\phi = \frac{\omega}{v} L \tag{9-13}$$

where v is the electron velocity.

Letting V be the klystron beam voltage, e the electron charge, and m its rest mass, and equating the energy supplied to the electron to its gain in kinetic energy, one obtains

$$eV = mc^2[(1 - \beta^2)^{-1/2} - 1] \tag{9-14}$$

where $\beta = v/c$.

Equation (9-14) may be written

$$v = c\left[1 - \left(1 + \frac{eV}{mc^2}\right)^{-2}\right]^{1/2} \tag{9-15}$$

Substituting Eq. (9-15) in Eq. (9-13),

$$\phi = \frac{\omega L}{c}\left[1 - \left(1 + \frac{eV}{mc^2}\right)^{-2}\right]^{-1/2} \tag{9-16}$$

At $V = 26\ kV$ and $eV/mc^2 \approx 0.05$, Eq. (9-16) simplifies to

$$\phi = \omega L(2e/m)^{-1/2}V^{-1/2} \tag{9-17}$$

so that

$$\frac{d\phi}{\phi} = -\frac{1}{2}\frac{dV}{V} \tag{9-18}$$

Substituting the initial parameters for ϕ yields

$$d\phi = -180^\circ \frac{L_{cm}}{0.657(V_{kv})^{1/2}}\frac{dV}{V} \tag{9-19}$$

For a voltage V of 26 kV, a length L of 21.2 cm, and a phase excursion of 1°, the total voltage variation permissible across the pulse is 0.088%.

Voltage measurement technique

Tests have shown that the phase variation across the tube from all factors other than beam voltage variation was less than 0.05°. Hence the phase shift across the tube is a very sensitive and accurate method of measuring the voltage droop, ripple, and pulse-to-pulse characteristics of the applied pulse voltage, and a phase measurement was used to verify that the sub-booster modulators met the specifications of ±0.04%, or 22.8 V out of 26 kV peak. The phase bridge was identical to that used in the frequency multiplier phase measurements, with the addition of an oscilloscope for display of the bridge output. Part of the cw input to the sub-booster was coupled into the reference arm of the bridge, while a sample of the pulsed output was fed to the signal arm. Figure 9-9 is a photograph showing the phase-versus-time behavior of

Figure 9-9 Phase versus time in the sub-booster RF pulse.

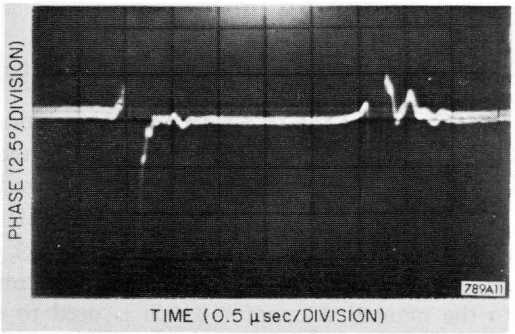

the RF pulse. The central 5 cm represent that time during which the sub-booster RF pulse is present. The large spikes at the beginning and end of the pulse are indicative of the very large phase excursions that occur during the rise and fall of the voltage pulse. The regions to right and left of the spikes at the edges of the picture represent the time during which only the cw reference signal is present. From Fig. 9-9 it is seen that the sub-booster modulator klystron contributes a negligible amount of phase shift error to the drive system.

Physical description of modulator

The sub-booster modulator is housed in a cabinet 30 in. deep, 72 in. long, and 90 in. high. The sub-booster klystron is mounted within this cabinet. The varactor frequency multiplier and the sub-booster $I\phi A$ unit are installed in two $10\frac{1}{4}$-in. panels in the top of the cabinet.

Performance

A serious shelf life problem became apparent in the early sub-booster klystron procurement program. In general, tubes which were placed in service immediately after delivery performed excellently. However, those stored for several months became gassy and exhibited mechanical detuning. At some times, rejection rates were as high as 50%. Fortunately, the good performance of tubes which were immediately placed in service has eased the situation. For the latter tubes, the MTBF has been greater than 6000 hours.

The sub-booster modulator has proved capable of meeting its stringent voltage stability specifications over long periods of time. Short life on the part of the 4PR1000 switch tubes was initially a problem. The life was improved by the addition of a third such tube to the two in the original design. Later, an improved version of the 4PR1000 was procured, and the life was further increased.

For a more detailed discussion of modulator performance the reader is referred to Chapter 13.

9-8 Isolator, phase shifter, attenuator ($I\phi A$) unit (CJK)

The function of the $I\phi A$ is to provide isolation, phase control and drive level control both to the sub-booster klystrons and to the 24-MW klystrons. The specifications of the $I\phi A$ unit are summarized in Table 9-6.

In the operation of the Stanford Mark III Accelerator it was found that a slow application of RF drive to high-power klystrons upon turn-on greatly reduced the incidence of output window damage. Consequently, in addition to the manual attenuator which is used to set drive level, a "protection"

Table 9-6 Summary of $I\phi A$ specifications

Phase shifter range	0°–360°(+0.0°, −0.5°)
Manual attenuator range	0–25 dB minimum
Protection attenuator range	0–25 dB maximum
Isolation	30 dB minimum
Complete $I\phi A$ unit	
frequency range	2856 ± 0.1 MHz
total insertion loss	3 dB (with attenuators set to minimum attenuation)
Input VSWR	1.1 : 1.0 maximum

attenuator is included in the $I\phi A$ unit. The protection attenuator can remove drive in 1 to 2 sec and restore drive in 5 to 6 sec.

Isolation was required to prevent reflections from causing phase shifts in the subdrive line. Consideration of coupling ratios and cable attenuation indicated that an isolation of 30 dB was needed.

The design of the automatic phasing system required a phase shifter which could continuously and cumulatively vary in phase starting from any arbitrary setting. The phase shift had to be a linear function of mechanical setting. The Fox phase shifter,[11] of which the SLAC unit is a modification, has these characteristics. It consists of three sections: a launching section, a half-wave phase shifting section, and a receiving section. The launcher takes a coaxial TEM wave and converts it to a circularly polarized wave. The half-wave center section reverses the direction of rotation of the circularly polarized wave. The receiver section then converts it back to a TEM wave. In the launcher and receiver sections, the instantaneous time phases of the TEM waves are linearly related to the instantaneous angular positions of the field vector in the circularly polarized waves. Mechanical rotation of the half-wave center section through an angle δ increases the angle between input and output field vectors by 2δ, and, hence, increases the phase angle between input and output TEM waves by the same amount.

The isolator, the phase shifter, and the two attenuators are packaged as a unit. A block diagram and photograph of the unit are given in Figs. 9-10 and 9-11, respectively, and additional information is given in Chapter 12.

Figure 9-10 Isolator, phase shifter, and attenuator block diagram.

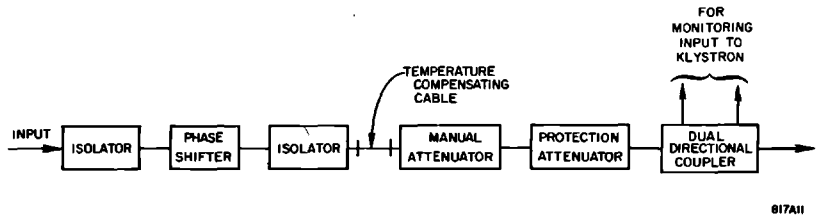

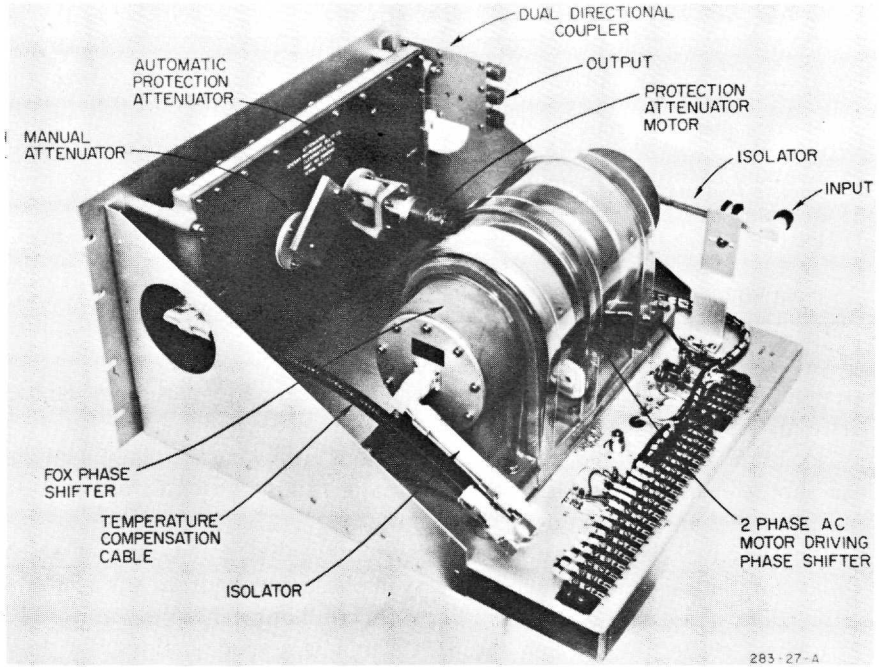

Figure 9-11 Isolator, phase shifter, and attenuator unit.

Switchable phase shifter

For purposes of positron acceleration or electron deceleration, the phase of the RF to each sector can be shifted by a preset amount within the interpulse period.

The switchable phase shifter consists of a three-port switching circulator, an adjustable short circuit, and a transistorized driver which controls the polarity of the current through the circulator control windings, and, hence, the path of the RF through the circulator. One polarity of control current causes the RF to pass directly through the circulator from Port 1 to Port 2. The opposite polarity causes the RF to pass from Port 1 to Port 3. At Port 3 the signal is reflected from an adjustable short circuit and from there out to Port 2. The phase shift of the second path can be set to any desired value by means of the adjustable short circuit. This value is normally in the vicinity of 180° to permit positron acceleration or electron deceleration for multiple beam operation at widely varying energy levels.

9-9 Dropout cables (CJK)

The so-called "dropout" cables are used to interconnect the various components of the system. Since great care was taken to ensure phase stability in all these components, the dropout cables also had to have stable characteristics.

The cables connect the main drive line to the varactor multipliers, the varactor multiplier to the sub-booster $I\phi A$, the sub-booster $I\phi A$ to the sub-booster klystron, the subdrive line to the 24-MW klystron $I\phi A$, and the $I\phi A$ to the 24-MW klystron.

The drop-out cables are semirigid $\frac{1}{2}$-in. coaxial lines having a foam dielectric. The cable has an attenuation of 7.6 dB/100 ft, and meets the following phase shift-versus-temperature specification:

Absolute (one cable)
$\pm 0.60°$ per foot between 60° and 100°F
$\pm 0.91°$ per foot between 100° and 130°F

Relative (cable-to-cable)
$\pm 0.30°$ per foot, 60° to 100°F
$\pm 0.45°$ per foot, 100° to 130°F

9-10 Standby equipment and switching (CJK, RAM)

To improve the reliability of the RF drive system, several items of equipment in the injection area and Sector 1 are backed up by standby units. One operating spare is available at all times for each of the following: master oscillator; main booster amplifier; sub-booster modulator; and frequency multiplier. For the first three of these items, automatic switching is provided in the event of failure. Manual switching is also provided, either from the Central Control Room or locally at the master oscillator rack in Sector 1.

At the output of each of the above units, RF power is sampled and detected. The detected signal is used to control switching relays through appropriate time delay circuits. Each switching unit also provides status information to the Central Control Room. In the sections immediately following, each switching circuit is described in some detail.

Master oscillator switching

Each master oscillator is coupled into its switching network and then to line or load through a 476-MHz circulator which serves to isolate the output stage of the master oscillator. With this isolation, and because the output power is only a few watts, the coaxial relay which performs the switching can be actuated while RF power is present. Switching occurs in the 2 msec or so required to operate the coaxial relay. The switching time is so short that the subsequent switching circuits for the main booster and sub-booster do not have time to initiate switching at those points erroneously.

Main booster switching

The switching unit detects the presence of RF power at the output of the main booster, and, upon loss of RF power, generates a signal which is sent to the main booster transfer switch. The logic is as follows:

1. Loss of RF power is sensed.
2. The transfer switch actuating signal is delayed a few seconds to allow for momentary failures and switching of the master oscillators.
3. The RF drive is removed from both main boosters.
4. The main booster transfer switch is actuated, placing the standby main booster in service.
5. The RF drive is restored.

Sub-booster switching

As with the other units, RF output is sampled, detected, and used to control switching. The logic is as follows:

1. Loss of RF power is sensed at the output of the sub-booster.
2. The relay actuating signal is delayed a few seconds to allow for momentary failures and switching of the master oscillators.
3. The sub-booster modulator trigger is removed.
4. The sub-booster transfer switch is actuated, placing the standby unit in service.
5. The sub-booster modulator trigger is restored.

Since switching of the main booster results in a loss of RF output from the sub-booster, a signal is derived from the main booster switching unit which inhibits sub-booster switching while the main booster is being switched.

Also, since the sub-booster output will disappear if the frequency multiplier preceding it fails, the standby sub-booster is provided with its own frequency multiplier, and failure of a frequency multiplier causes switching to occur as it would if a sub-booster had failed.

Acknowledgments

The authors of this chapter wish to thank Dr. R. B. Neal, who initiated many of the early design ideas for the drive system, and Dr. J. Dobson and Mr. W. J. Gallagher who participated in some of the early experiments. They also wish to thank Mr. J. R. Bordenave for his work on the master oscillators, frequency multipliers, and $I\phi A$ units, Mr. R. R. Hanselman for his work on the main booster amplifiers, and Mr. R. G. Wilson for his work on the drive lines.

References

1 C. B. Williams and R. Belbéoch, "Some RF Characteristics of the Present Mark IV High Power Klystrons," Tech. Note No. SLAC-TN-62-13, Stanford Linear Accelerator Center, Stanford University, Stanford, California (March 1961).

2 M. H. Blewett, ed., *Proc. Intern. Conf. High Energy Accelerators, Brookhaven, 1961*, U.S. Govt. Printing Office, Washington, D.C., 1961, p. 96.

3 R. B. Neal, "Drive Line Considerations for Project M," Rept. No. M-105, Stanford Linear Accelerator Center, Stanford University, Stanford, California (December 1958).

4 G. A. Loew, "Requirements for a Possible Coaxial Drive System for Project M," Rept. No. M-107, Stanford Linear Accelerator Center, Stanford University, Stanford, California (October 1959).

5 R. B. Neal, "Note on Phase Shift in Transmission Lines Due to Ionizing Radiation," Rept. No. M-106, Stanford Linear Accelerator Center, Stanford University, Stanford, California (October 1959).

6 G. A. Loew, "Possible Drive Systems and Sub-booster Procurement," Tech. Note No. SLAC-TN-62-4, Stanford Linear Accelerator Center, Stanford University, Stanford, California (January 1962).

7 C. G. Montgomery, *Techniques of Microwave Measurements*, McGraw-Hill, New York, 1947, p. 391.

8 C. J. Kruse, "Temperature Stabilization and Support of the RF Drive Lines," Tech. Note No. SLAC-TN-62-55, Stanford Linear Accelerator Center, Stanford University, Stanford, California (October 1962).

9 Z. D. Farkas, "Phase Error between RF Drive Signal and Electron Beam," Tech. Note No. TN-62-62, Stanford Linear Accelerator Center, Stanford University, Stanford, California (October 1962).

10 R. A. McConnell, "Phase and Power Measurements on Varactor Frequency Multipliers," Tech. Note No. SLAC-TN-63-93, Stanford Linear Accelerator Center, Stanford University, Stanford, California (November 1963).

11 A. Gardner Fox, *Proc. Inst. Radio. Engrs.* **35**, 1489 (1947).

10

KLYSTRONS

R. W. Bierce, J. Jasberg, and J. V. Lebacqz, Editor

The klystrons used on the Stanford two-mile accelerator were developed specifically to operate in permanent magnets with reasonable efficiency, as well as to achieve long life and minimum operating costs. The feasibility of permanent magnet focusing at peak powers in excess of 20 MW was demonstrated by development programs undertaken at SLAC and in industry. Extensive window development work undoubtedly contributed to the achievement of long life and reliability of the tubes now in use. The operating experience to date has been very good, with a predicted mean time to failure in excess of 8000 hours.

10-1 Selection of RF sources (JVL)

Three main types of RF sources were considered for use at SLAC: the magnetron, the amplitron, and the klystron. Even though Slater and his colleagues were successful in demonstrating the use of a large number of magnetron oscillators in an operating machine,[1] the system is complicated and inefficient. The main difficulty arises from the relative instability of heavily loaded oscillators and the problems of accurately phasing a large number of oscillators. In addition, it was felt that the rather short life expectancy and the relatively low peak power of magnetrons would make this type of tube unsuitable for use in a large accelerator.

The amplitron has the advantages of high efficiency and low phase sensitivity to input voltage. Its main disadvantages result from very low gain and low isolation between input and output, requiring the use of amplifier chains and high-power isolators. In addition, amplitrons can oscillate in spurious modes unless the drive power is applied for a longer time than the cathode power. In case of drive failure, the resulting oscillations can produce failures of both the input and output windows.

The klystron amplifier has been used on almost all linear electron accelerators having multiple power sources and operating at microwave frequencies. It appears most suitable for the following reasons: (1) it is a high gain amplifier, which simplifies phasing and driving problems, particularly in a very long machine; (2) the necessary average and peak powers can easily be obtained; (3) the efficiency is reasonable, although not as high as that of other tube types; (4) the high degree of isolation between input and output makes it more stable under conditions of load mismatch; and (5) experience on the Stanford Mark III accelerator over the past 15 years and in many radar applications indicates the potentially long life of this device.

However, the amplitron appeared sufficiently promising to warrant an extensive study of its possible applications. The results of that study[2] indicated that, although there would be a slight reduction in power costs, the disadvantages of the amplitron system made its adoption inadvisable for the SLAC accelerator. The main reasons are outlined below:

1. From a general system standpoint, it is essential to evacuate the waveguide between the RF source and the accelerator. Amplitrons at that time (1961) were known to be susceptible to failures of both the input and output windows. Consequently, it would have been necessary to evacuate not only the output waveguides but also the drive line to the amplitron to prevent losing the vacuum in the accelerator in case of double window failure.
2. Although the amplitron by itself has a very good phase stability, the low gain requires the use of a waveguide drive line and additional amplifiers in series. Unless the waveguide temperature is controlled to better than $\pm 1°C$, the resulting overall phase stability is inferior to that of the klystron system.
3. The possible effects of amplitron oscillations or spurious signals on the behavior of the accelerated beam are not well understood and made the consequences of adopting this RF source uncertain.
4. The added complexity of the amplitron system as visualized for the Stanford accelerator and the attendant increase in initial installation cost would not be offset by reduced power cost resulting from high amplitron efficiency.

The above comments are not meant to imply that amplitrons should not be considered in other linear accelerators where the design requirements (e.g., high duty cycle or small number of RF sources) might favor adoption of this tube.

Another factor influencing this decision was the well-advanced stage of development of high-power klystrons. In 1944, E. L. Ginzton suggested that it would be possible to build klystron amplifiers each delivering 15–30 MW of pulsed power at S-band. By 1948, the basic design of a three-cavity high-power klystron had been established, and tests confirmed the general validity of the theory and assumptions made.[3] The same basic design is still used in

some of the sockets of the Mark III accelerator at Stanford, and considerable development work was carried on at Stanford.[4] During the 1950's, development work on high-power klystrons was carried on at Sperry, Varian, Eimac, Litton, and General Electric in this country, at CSF and CFTH in France, and at EMI and AEI in England. In this country, tubes were produced capable of 3-MW peak power and 50-kW average power at C-band, 20-MW peak and 54-kW average power at L-band, and 10-MW peak and 20-kW average power at S-band. The French development work resulted in tubes capable of 20- to 30-MW peak power at S-band, with average power capabilities in excess of 20 kW.

One of the major considerations in the design of all systems for the accelerator including the RF sources was the desire to obtain maximum reliability. In addition, the potential operating costs were also carefully considered. It was felt that the reliability of the klystron system would be much greater than that of an amplitron system since the total number of components in the former system is much lower. From a standpoint of accelerator operating expense, one of the major factors is tube replacement cost. Although meaningful operating experience at peak power outputs of $\approx$20 MW was not available for either amplitrons or klystrons, it was felt that, based on radar system experience, the life of a conservatively designed klystron would probably be greater than the life of the amplitron. In addition, it was known that klystron tubes can be repaired many times, thus reducing the average cost per hour below that obtained if only new tubes could be used.

For all the reasons mentioned above, it was decided to use klystrons to provide the RF power for the Stanford linear accelerator.

10-2 Specifications (JVL)

The experience acquired in operation of the Stanford Mark III accelerator indicated the desirability of further improvements in the klystron design and performance characteristics. For example, to achieve the desired narrow beam energy spectrum from the Stanford two-mile accelerator it was necessary to limit the maximum phase deviation at any of the 960 feed points of the machine to $\approx 5°$. This phase deviation can be caused by any of the RF components between the main drive source and the feed point of the accelerator, including the stable sources, the drive lines, the preamplifier (booster and sub-booster) klystrons, the final amplifier klystrons, and the waveguide system to the accelerator. Thus, along with other stringent systems requirements, extremely tight specifications had to be imposed on the phase modulation within the final klystron amplifier. Furthermore, amplitude modulation on the RF output pulse would also result in spectrum broadening, and the maximum allowable amplitude modulation had to be limited.

Although the simplified theory indicates complete isolation between the amplifier stages in a klystron, in practice some oscillation or feedback mechanisms are possible, due either to reflected electrons or to a tendency for cavities

to oscillate at frequencies above the driving frequency. Moreover, in many klystrons operating at this power level, oscillations in the gun structure have been observed which can cause phase and amplitude instability in the output.

The number of klystrons involved in the SLAC operation necessitated some deviations from normal practices. For example, a careful study of the focusing problems indicated that there was a potential saving to be obtained from eliminating electromagnets and their power supplies with their attendant water cooling and interlock requirements. Hence, it was decided to design the tube in such a way that it could be focussed by permanent magnets. Following the Stanford Mark III practice, it was also deemed desirable to evacuate the waveguide runs between the klystron and the accelerator.

Another deviation concerns the method of mounting the tube. Because of slow lateral movements of the long accelerator housing and the necessity of accurate accelerator alignment, it is expected that it may be necessary to move the feed points gradually with respect to the housing by as much as several inches. To maintain phase stability in the waveguides, the whole waveguide system must be moved with the accelerator; hence, it was necessary to attach the klystron to a movable frame. The solution has been to hang the klystron and pulse transformer tank from the frame to minimize the tolerance problems in making the klystron-to-waveguide vacuum joint. This method has the additional advantage of allowing variations in overall klystron length without having to change the mechanical installation system. Hence, there is flexibility for continuing improvements in the klystron design.

The cooling requirements of the tube are met by use of low-conductivity deionized water. To simplify the water and interlock systems, it was decided that the tube body and collector would be cooled in series, and that the available flow and pressure drop would be 10 gal/min and 30 psi, respectively.

Table 10-1 gives the objective specifications of the klystrons for SLAC and a comparison of these specifications with those of the klystrons used at Stanford on the Mark III accelerator.

10-3 Procurements (JVL)

Because it was decided that the SLAC tube should be focused by a permanent magnet and no such tubes existed at SLAC power levels, it was obviously necessary to instigate an extensive development program. The majority of the tubes used to power the accelerator were to be procured from industry, and it appeared essential to have two sources of supply for such tubes to insure a continuing supply in the event of delays from one vendor. To achieve the lowest possible operating costs, it was decided to follow the experience of the Mark III accelerator and use tubes which could easily be repaired and rebuilt after failure.

Consequently, the development effort had a double objective. The first was to demonstrate that the peak and average powers required for the SLAC accelerator could be obtained with permanent-magnet-focused klystrons. The

Table 10-1 Comparison of Mark III and SLAC klystron specifications

Parameter	*Unit*	*Mark III accelerator klystron*	*SLAC klystron*
Operating frequency	MHz	2856	2856
RF pulse width	μsec	2	2.5
Repetition rate	pulses/sec	60	60–360
Peak power output	MW	20	24[a]
Heater power	W	600	270
Beam voltage	kV	325	250
Beam current	A	185	250
Microperveance	10^{-6} A/V$^{3/2}$	1	2
Peak drive power	kW	10	0.24
Gain	dB	33	50
Amplitude modulation	%		1 (max)
Phase modulation, maximum	deg		1 (heater hum) 8 (for 1 % beam voltage varia 1 (any other cause)
Noise power (with respect to fundamental power)			<-40dB in any 1 MHz band 5000 MHz <-25dB in any 1 MHz band 5000 MHz
Focusing		Electromagnet	Permanent magnet
Radiation	mR/hour		3 maximum at 3 ft
Faults			Less than 10 in 8 consecutive ho

[a] Acceptance specifications: 21 MW at 250 kV, 12 MW at 200 kV.

second was to achieve an economical design of an easily repairable tube that could be readily transferred to manufacturing.

Accordingly, the development effort was divided among Stanford and two tube manufacturers, RCA and Sperry. It was hoped that at the end of a development period of approximately 1 yr, SLAC could procure tubes at a minimum cost on the basis of performance specifications after supplying the detailed designs resulting from the development programs to the various tube manufacturing companies. Unfortunately, at the end of the development program a full specification tube had not been achieved, but sufficient knowledge had been acquired to dispel any doubts about the feasibility of meeting the specification with a permanent-magnet-focused klystron.

During the initial phases of procurement of production tubes, both vendors (RCA and Sperry) encountered difficulties which resulted in delays in deliveries, and Stanford procured a few experimental tubes from two additional companies, Eimac and Litton. In order to meet construction schedules, it was necessary to increase the klystron delivery rate by having a third industrial supplier (Litton). Hence, there are now on the machine tubes from three production suppliers (RCA, Litton, and Sperry) as well as SLAC-built tubes.

10-4 Design considerations and development work (JVL)

The following summary of the design considerations and development work done on the klystrons for SLAC will be primarily concerned with the Stanford development; parallel work has been done in industry and the main differences between the various approaches and results will be pointed out. In this review, the various components of the klystron will be considered separately.

The electron gun

Stanford's klystron initially used a gun designed by J. Picquendar of CFTH.[5,6] This gun, designed as a magnetic field-free (magnetically shielded) gun, took advantage of the fringing magnetic field to reduce the beam diameter at the entrance to the anode. Although the results observed at Stanford with this gun were in general satisfactory, some gun oscillation problems were encountered after a modification of the physical length of the anode enclosure.[7] As a result, G. K. Merdinian designed a gun specifically for use with the Stanford klystron.

This new gun (Merdinian gun) was designed following Pierce's theory,[8] with the introduction of an additional correction factor to compensate for the presence of a large anode hole. The design of electrode shapes was carried out in an electrolytic tank, after which the gun was analyzed on an IBM 7090 computer, where Laplace and Poisson's equations were solved simultaneously. The electrostatically focused, minimum beam diameter is approximately 0.9 in. After the beam passes through the magnetic pole plate, the beam diameter converges to approximately 0.8 in. It was also found experimentally that this gun operates extremely well under partially confined flow conditions, and that the permanent magnets which have been procured exhibit the proper field shape in the gun region to satisfy these conditions. For this type of operation, it is believed that the beam diameter is still approximately 0.8 in. For Brillouin flow,[9] the magnetic field required to focus the beam is approximately 600 G. In practice, because of the density bunching near the output cavities, the field needs to be increased to approximately 1000 G. The same field should also be adequate for focusing the beam under partially confined flow conditions.

With this design, gun oscillations have been virtually nonexistent. It is believed that in most high-voltage and high-perveance guns, Llewellyn-type diode oscillations[10] are prevalent. Because these oscillations take place between the cathode and anode noses in a cavity formed between the cathode support and the anode housing, loading of this cavity tends to decrease or suppress the oscillations. A smooth transition between the high-voltage bushing and anode nose is intended to provide loading by the pulse transformer tank oil. In the early work with permanent magnets, the anode housing had been lengthened, and under these conditions oscillations were detected in the gun region.

It has also proven easier to design permanent magnets to provide a small threading field at the cathode rather than to obtain a true zero-field condition as required by the Brillouin gun theory. A combination of the Merdinian gun and the experimental magnets which were procured gave, in general, much better results than the combination of the Picquendar gun and the experimental magnets. For these various reasons, the SLAC-built tubes during the past several years have utilized the Merdinian gun. The only further improvement made on that gun consisted of minor modifications in the cathode button radius of curvature to compensate for thermal expansion and of mechanical changes in heat-shielding arrangements and heater position.

The present layout of the gun is shown schematically in Fig. 10-1. The cathode button diameter is approximately 7.94 cm and the spherical radius 6.9 cm, giving a solid angle of 35°. The total cathode emitting area is approximately 54 cm^2 resulting in a very conservative cathode loading of less than

Figure 10-1 Stanford electron gun layout.

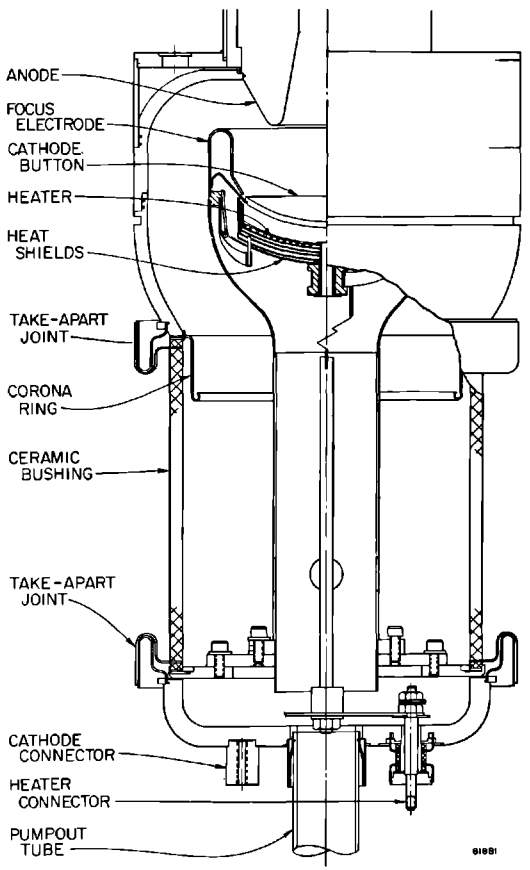

5 A/cm^2. The area convergence ratio of the gun is approximately 16 (depending on the actual beam diameter achieved).

Like Stanford, RCA started their development program by using Picquendar's gun. Unlike Stanford, RCA has found practically no oscillation problems with this gun and has gradually been able to improve the entrance conditions to the point where the tube performance using their gun is very similar to that of the Stanford tube using the Merdinian gun.

Sperry is using a gun of their own design which operates in a field-free region to achieve Brillouin focusing for the beam. Originally, many oscillations were observed with this gun, but the problem was cured by the use of judiciously placed one-half wavelength slots in the focus electrodes, and loading in the anode housing.

Eimac initially was planning to use a gun which had been designed specifically for operation under fully confined flow conditions. The advantage of a confined flow gun is the potential improvement in efficiency. Unfortunately, strong oscillations were observed with this gun, and lack of time to determine the cause and cure of the oscillations forced Eimac to use the Merdinian gun.

Litton is using the Merdinian gun. The first tube they built showed strong gun oscillations. The cause of these oscillations was traced to a change in geometry of the gun support structure. The structure has since been modified to duplicate that used at Stanford, and no further oscillation problems have appeared.

The interaction space

With the beam diameter given at 0.8 in., a drift tube diameter of $1\frac{1}{8}$ in. was chosen as a compromise between optimum coupling and minimum interception. The conventional plasma theory for operation at 250 kV with a microperveance of 2 gives, for these conditions, a reduced plasma frequency of 160 MHz or a reduced plasma wavelength of 55 in. The normalized drift tube and beam radii are $\gamma_a = 0.775$ and $\gamma_b = 0.551$ rad, respectively.[11] Theoretical design based on Webber's model[12] indicates that optimum gain and efficiency should be achieved for a total interaction length between 20 and 24 in. However, it appeared certain that a reasonably uniform magnetic field of between 800 and 1000 G could not be achieved over an interaction length of 20 in. by permanent magnets. Hence, since gain and efficiency near the optimum do not vary rapidly with length, the first tubes built at SLAC were designed with a total interaction length of approximately 17 in., as a compromise between magnet design and electrical tube design requirements.

These tubes operated with electromagnetic focusing at an efficiency of approximately 35% in the voltage range between 200 and 250 kV. The measured field requirements were approximately as expected, but discussions with permanent magnet manufacturers indicated that it would not be feasible to achieve the required fields over a length of 18 to 20 in. without unacceptable increases in size, weight, and cost. Accordingly, a further reduction in tube

length was decided upon and the interaction space was designed to fit within a total magnet length of approximately $16\frac{1}{2}$ in. The first tubes built to this new length were still using the Picquendar gun and gave rather disappointing results: the efficiency rarely exceeded 32%, and the power output never exceeded 19 MW. Using the same body with the Merdinian gun, the output and efficiency both improved, but were still disappointing. A series of modifications were then undertaken to bring the performance up to desired levels.

The coupling coefficients were computed as being approximately 0.383 for the buncher cavities and 0.707 for the output cavities (although the cavity gap lengths and gap diameters were approximately the same, the relativistic computation resulted in the large difference in coupling coefficients). Table 10-2 gives the successive modifications introduced in the interaction dimensions. The overall drift distance increase was achieved without modification in permanent magnet length by reducing the distance between the pole plates and cavities to the minimum compatible with stable operation. The maximum possible reduction was determined mostly experimentally.

The change in output Q was first determined by recomputation and was then confirmed experimentally. Normal variation in power output from tube to tube makes it difficult to optimize the output coupling unless a large sample of tubes is used.

The potential problems of oscillations in the tube body were recognized when the design was started, although not fully appreciated. The initial design included cavities with different aspect ratios (height-to-diameter ratios). In this way, the frequencies of the second and third resonant modes are different from cavity to cavity, and there is little possibility of producing oscillations by drift tube coupling at these higher mode frequencies. In spite of these precautions, some tubes exhibited higher mode oscillations. Analysis showed that these oscillations were probably of a monotron type, caused by a TM_{12} mode which is strongest with symmetrical cavities. A redesign of the cavities with opposing noses of different length has apparently solved that oscillation problem. Some oscillations which produced an amplitude ripple on the RF output pulse were also observed. These apparently result from feedback between the first stages of the tube and were observed only on two tubes

Table 10-2 Drift distances

Drift distance	*XM-1 (in.)*	*XM-2 (in.)*	*XM-3 (in.)*	*XM-7 (in.)*	*XM-12 (in.)*
L_{1-2}	3.0	2.875	2.894	2.894	2.894
L_{2-3}	3.0	3.000	2.857	2.857	2.857
L_{3-4}	3.5	4.250	4.842	4.568	4.568
L_{4-5}	3.5	3.750	3.726	4.000	4.000
Total	13.0	13.857	14.319	14.319	14.319
Q_e Output	25–30	20–25	18–20	18–20	18–20

where the cavities were tuned to the same frequency—a frequency which was different from the drive frequency. Because of the overall length limitation, the drift distances in the voltage amplifier portion of the klystron are very small and the cavities are not completely decoupled from one another. Thus it is possible to have, in effect, a two-cavity oscillator, the output of which combines with the drive frequency to give a beat at the frequency of the amplitude ripple observed on the RF output.

Under certain conditions, one can also observe oscillation caused by returning electrons. Whether these originate from the output gap or from secondaries emitted in the collector region is not clear. However, it is known that the magnetic field through the collector region will tend to focus secondaries back into the drift section. With permanent magnet focusing as used in SLAC tubes, there is an appreciable magnetic field at the collector.

The vendors have also experienced the same kind of oscillations observed in SLAC tubes. In general, the sources have been the same and similar corrective steps have been taken. In addition, cavity oscillations have been suppressed by introducing losses either by plating the whole cavity with lossy material (Litton technique) or by introducing a frequency selective loss by means of pins or loops in the cavity (RCA technique).

Collector design

The design of a collector for operation with permanent magnet focusing required some special attention due to the high stray magnetic fields existing in the collector region. Because of the focusing caused by these stray fields, it was desirable to reduce the collector diameter below what would normally be considered optimum for the usual electromagnetic focusing. As observed above, focusing of secondary electrons by this stray field may also cause unwanted reactions with the main beam in the output section of the klystron.

Collector oscillations can exist because of the propagation of waves in the collector and drift tubes at frequencies above the cutoff frequencies corresponding to their diameters. As a result, there can be regeneration in the cavity oscillation mode described previously. However, it was found possible to change the phase of the reflected waves to the cavity by adjusting collector length and, thus, to eliminate the oscillations.

Although SLAC has never observed oscillations which were demonstrably caused by the collector, both Sperry and RCA have been troubled by unwanted collector phenomena. These may appear as regeneration at the drive frequency, resulting in an output pulse length independent of the drive pulse length, or in spurious outputs at frequencies other than the drive frequency.

The SLAC collector is approximately 4 cm in diameter and 37 cm long, giving a total area of approximately 470 cm^2 exposed to the beam. When the tube is operating without drive and without focusing, the average power density over the collector would be approximately 170 W/cm^2 at full beam voltage. With electromagnetic focusing, the maximum power density is

computed as approximately 1 kW/cm^2 at no drive. Although accurate calculations have not been made for the maximum power density with permanent magnet focusing, it is believed to be approximately 0.7 kW/cm^2 and, hence, quite conservative.

From a mechanical standpoint, the SLAC collector is an integral part of the tube and cooling is obtained by flowing water through a spiral groove on the outside of the collector with a very high Reynolds number to achieve efficient heat transfer.

In general, there have been few problems with the collector design, although some tubes have shown erosion caused either by beam focusing near the tip of the collector or by a skewed beam probably due to transverse fields.

The permanent magnet

The magnets used to focus the SLAC klystron are barrel shaped and are designed for a gap length of 16½ in. with an inside diameter of approximately 8½ in., providing space for insertion of lead shielding and for easy removal of the tube from the magnet. The maximum outside diameter is approximately 18 in., and the total weight is nearly 800 lb. The magnetic material used is Alnico 8.

The typical reversal of the magnetic field on both ends of the magnetic barrel was a problem in designing the magnets, because the gun design requires a reasonably accurate field shape in the gun region. Field shaping has generally been accomplished by using a magnetic shield to reduce the reverse field and by incorporating a series of bar magnets in the gun area. These bar magnets are polarized in the same direction as the main field to compensate for the inverse field remaining in spite of the shield. By careful adjustment of the location and number of these bar magnets, the desired field for proper electronic beam forming can be obtained.

One of the main problems remaining with permanent magnets is that of cross or transverse magnetic field. The transverse fields can be reduced either by very careful magnetizing or by using magnetic shunts. These shunts consist of either thin magnetic plates normal to the main field axis or thin steel cylinders coaxial with the main field axis. Even so, it is still possible to produce permanent transverse fields in an initially well-behaved magnet by local demagnetization on the surface caused by contact of magnetic objects with the side of the magnet. The magnet can usually be restored to proper operating condition by judicious location of small magnetic pieces around the pole plates. In addition, SLAC has built a magnetizer to bring magnets back to full specifications if they are accidentally weakened below the useful range of magnetic fields.

RCA is procuring magnets to specifications that carefully limit the maximum amplitude of transverse fields as well as the range of acceptable magnetic fields. Sperry uses magnets that match the requirements for a Brillouin focused beam.

10-5 Klystron mechanical design (JVL)

As mentioned earlier, the SLAC klystron is designed so that a vacuum seal can be made to the waveguide system in spite of the possible variation in height and location of the waveguide feed of several inches with respect to the floor of the klystron gallery. To achieve this result, the klystron is suspended from a yoke to which the waveguide is attached. The whole yoke is mounted on an I-beam frame which is adjustable in height and position.

The klystron output waveguide flange is accurately located with respect to three mounting hemispheres on the mounting plate of the klystron (see Fig. 10-2). The mounting yoke, in turn, has three accurately located V-blocks in which the hemispheres are set, thus giving complete control for the alignment of the klystron output waveguide with respect to the permanent waveguide system installed in the klystron gallery. A total vertical motion of a few

Figure 10-2 Cutaway view of Stanford klystron in permanent magnet (No. 135-5-D).

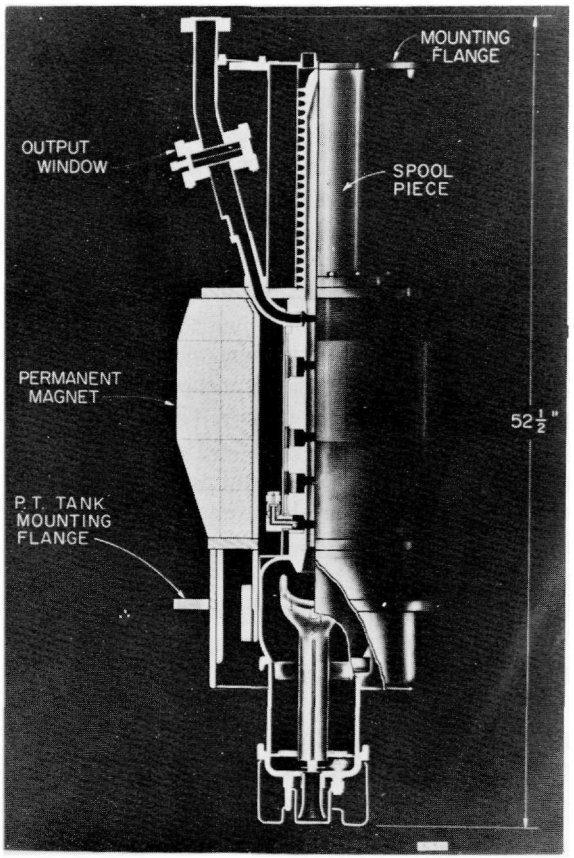

inches, controlled by hydraulic jack, enables one to lower and raise the tube until the flange mates with the corresponding flange of the waveguide system. The whole klystron assembly, consisting of the tube and the pulse transformer tank, is brought into location on an "air-bearing" platform so that the locating hemispheres and V-grooves can easily be mated.

A combined vacuum and RF joint is made at the waveguide output flange by means of a rectangular copper gasket. The flange design is different from that used for other waveguide joints on the accelerator because of the high temperature of the flange during the baking of the tube. Little difficulty has been experienced in obtaining a satisfactory leak-free joint at the output flange.

The klystron body and the permanent magnet are bolted to a spool piece, the upper end of which is the mounting flange (see Fig. 10-2). The permanent magnet, in turn, is built with supporting stainless steel rods between the upper and lower pole plate and a flange welded to the magnetic shield to which the pulse transformer tank assembly can be connected. It was fortunate that the Electronics Department was able to procure a pulse transformer of much smaller dimensions than had been previously achieved at these operating voltages and powers. As a result, the overall height of the klystron-pulse transformer tank assembly varies from 6 to 7 ft, depending on the specific tube length. Figure 5-16 is a photograph of the klystrons supplied by the various manufacturers, mounted on pulse transformer tanks. Figure 10-3 shows a typical klystron installation in the klystron gallery.

One more design point has not been covered; it concerns the lead shielding required to keep radiation levels below a specified maximum value (3 mR at a distance of 3 ft from the tube). The majority of the tubes now installed have

Figure 10-3 Typical klystron installation in klystron gallery.

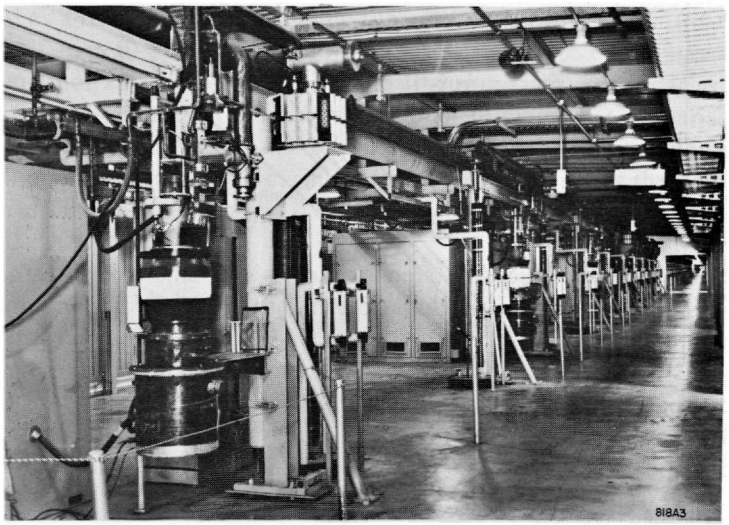

$1\frac{3}{4}$ in. thickness of lead shielding around the collector and 2 in. of lead shielding above the collector. Calculations have indicated that between $1\frac{1}{4}$ and $1\frac{1}{2}$ in. of lead is probably adequate collector shielding.

In addition, there is a $\frac{1}{2}$-in. cylindrical lead shield inside the magnet extending down approximately to the top of the high-voltage cathode bushing. In general, the shielding provided in this fashion is adequate, except for radiation coming out parallel to the output waveguide or to the water-cooling connections. Additional shielding has been provided around these areas and the radiation level meets the specifications. After a few months of operating experience, some radiation appeared to be escaping around the pulse transformer tank, and a small quantity of lead shielding has been added to keep all tubes within specifications.

10-6 Klystron performance (JVL)

In spite of early difficulties encountered by the vendors, all tubes operating on the accelerator meet the minimum specifications. Figure 10-4 shows the power output versus beam voltage for all tubes installed as of November 1966. The mean power output is approximately 12 MW at 200 kV and 21.7 MW at 250 kV. The standard deviation is from 11.4 to 12.8 MW at 200 kV and from 20.6 to 23.0 MW at 250 kV. Accordingly, there is no question that the electrical performance is entirely satisfactory from a power output standpoint. Similarly, the gain requirement has been met or exceeded in all cases, and the stability is generally excellent. However, it is difficult to give statistical information on these parameters.

Figure 10-4 Average performance of installed klystrons in November 1966.

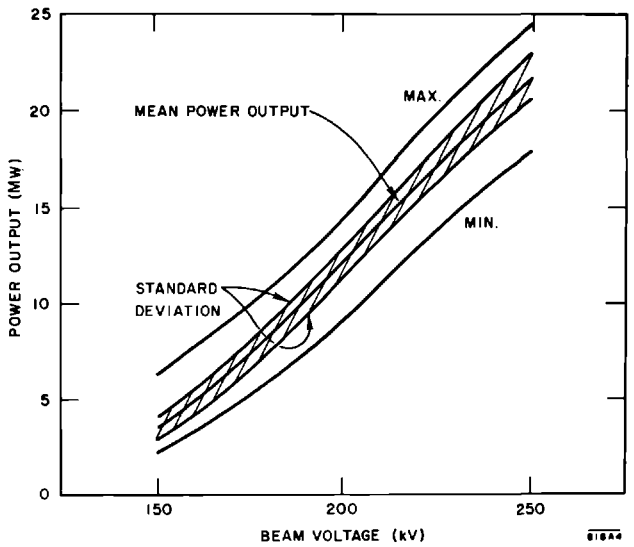

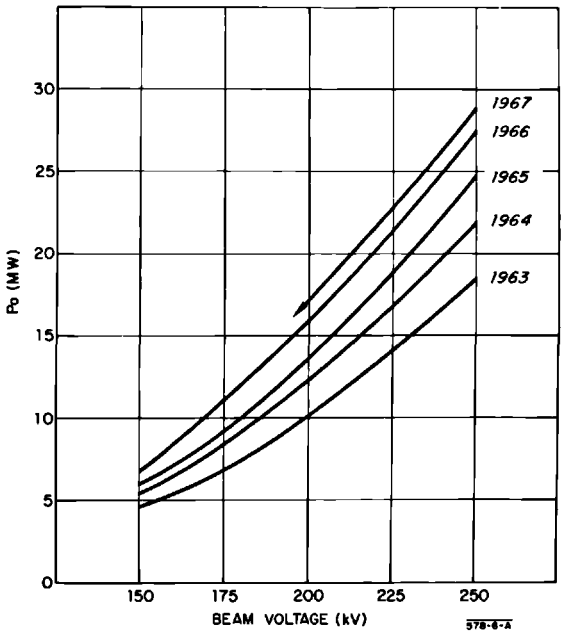

Figure 10-5 Comparison of SLAC klystron performance in electromagnet. Drive and focusing optimized at each voltage.

Although the present performance of all tubes on the line is eminently satisfactory, a brief review of the experimental results obtained during the development program is probably in order.

Figure 10-5 shows the improvement in performance of experimental tubes built at SLAC when operated in electromagnets. The improvement can also be expressed as a function of experimental tube type as shown in Fig. 10-6. A comparison of Fig. 10-6 with Table 10-2 indicates the effect of changes of drift tube length on tube performance. Figure 10-7 shows the performance of the XM-7 and XM-12 tubes in "standard" permanent magnets. Comparison of Figs. 10-6 and 10-7 shows that the power output of the XM-12 design at 250 kV with permanent magnet focusing is less than 1 MW below the power output with electromagnet focusing. The difference in these outputs is about 3 MW for the XM-7 design.

The reason for this smaller decrease in power output of the XM-12 is obvious upon analysis of the magnetic field plots (see Fig. 10-8). Curve 1 of Fig. 10-8 is the standard, permanent magnet curve which closely approximates the optimum electromagnet focusing measured initially on tubes of the XM-1 and XM-3 variety. Optimum electromagnet performance was obtained with the XM-7 tubes with a field plot which approximates curve 2 of Fig. 10-8. With the permanent magnets commercially available at present, it does not appear feasible to obtain fields similar to that of curve 2 in Fig. 10-8.

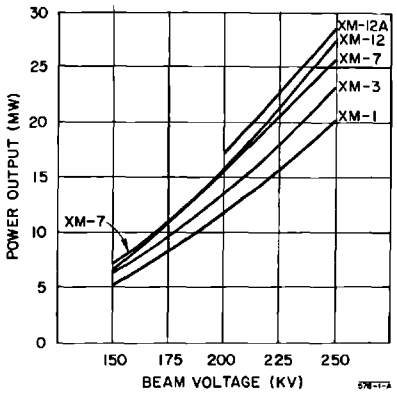

Figure 10-6 SLAC klystron performance in electromagnet. Drive and focusing optimized at each voltage.

The high fields necessary near the third drift tube indicated that the electron beam was scalloping. It appeared possible that, by increasing the drift tube diameters between the third and fifth cavities, a reduction of magnetic field requirements could be achieved without impairing the output gap coupling coefficient and tube performance.

Accordingly, experimental tubes (XM-12) were built with the third and fourth drift diameters increased from $1\frac{1}{8}$ to $1\frac{1}{4}$ in., but with all other parameters equal to those of the XM-7 tubes. Upon test in electromagnets, both tubes exhibit performance essentially equal to that of the best XM-7 tubes (as shown by curve XM-12, Fig. 10-6), but the magnetic field requirements had been drastically reduced as indicated by curve 3 of Fig. 10-8. These tubes were

Figure 10-7 SLAC klystron performance in permanent magnets.

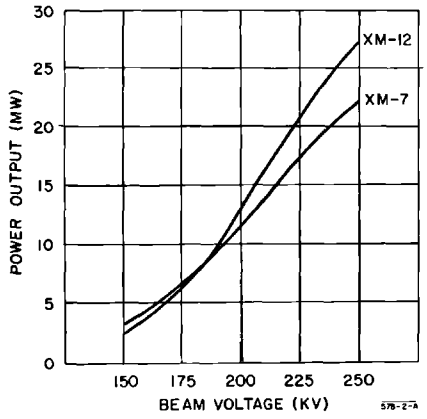

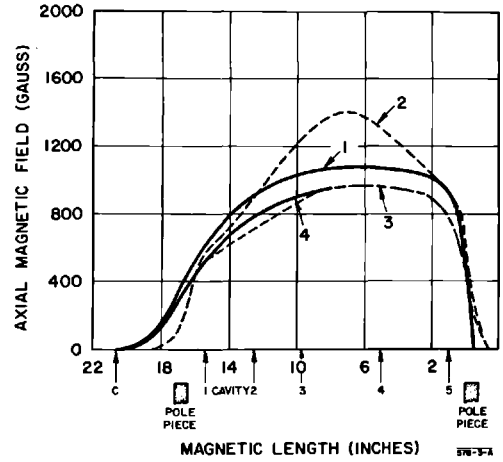

Figure 10-8 Axial magnetic fields for SLAC klystrons.

then tested in permanent magnets which had been demagnetized by approximately 100 G from their standard value. The actual magnetic field plot is given by curve 4 of Fig. 10-8 and the average performance of the XM-12 experimental tubes in a permanent magnet is shown in Fig. 10-7. By comparing Figs. 10-6 and 10-7, it can be seen that their performance in permanent magnets is substantially the same as in electromagnets at the higher-voltage levels.

One experimental tube has been built with the XM-12 dimensions, but with the output gap length decreased from approximately 1 to approximately 0.8 rad. The performance of that tube in an electromagnet up to 250 kV is shown in Fig. 10-5 (1967) and Fig. 10-6 (XM-12A). In a permanent magnet, the same tube produced almost 28 MW at 250 kV. Other tubes will be built with similar modifications to prove whether or not the observed improvement can be duplicated.

A serious effort was made to improve tube efficiency by taking advantage of extended interaction cavities. The first tubes built in this fashion had slightly higher output than the standard tubes built at that time (XM-7), but the extended interaction cavities tended to produce oscillations which could only be eliminated by extremely critical focusing adjustment. Although it is theoretically possible to achieve higher performance with an extended interaction tube, the necessity of extremely stable output of the klystron used on the accelerator may render the extended interaction klystron design impractical.

For these reasons and in view of the efficiency improvements already achieved, the effort is now concentrated on further improvement of the standard klystron. It appears that the drift distances are not yet fully optimized. One limitation at present is the overall length of the magnetic field. However, it appears feasible to operate klystrons at these power levels with magnetic field reversal. This would eliminate the restrictions on total drift distances.

In addition, the possibility of building tubes for higher-power output is being examined. One experimental tube (XM-12A) has been operated up to 300 kV in an electromagnet. At that level, the tube was producing in excess of 40 MW at 45% efficiency. The same tube in a specially shunted permanent magnet was also operated to 270 kV with a power output of 34 MW and an efficiency of approximately 42%.

10-7 Window development (JHJ)

The window effort at SLAC has been a continuation of work which started at Stanford University with the design of the first high-power klystrons which were used on the Mark III accelerator. Additional window studies were done in connection with the construction and operation of the Mark IV accelerator and in conjunction with other high-power tube work at the W. W. Hansen Laboratories of Physics, Stanford.[3,13] It seems desirable to present briefly some of this initial work to put the present studies in proper perspective.

Breakdown and overheating of the output windows has been common during the operation of all high-power klystrons. In the first Stanford experimental high-power klystron representing a power extrapolation 1000 times that available from existing klystrons of that era, the window problem was avoided by constructing the tube with a load as an integral part of the vacuum envelope. Somewhat later, as had been feared, the first output window (a resonant glass window from a commercial magnetron) failed, and a series of designs were then tried, all of which had very short lives. Finally a 3-in. diameter alumina disk in a pillbox structure* was developed which performed reasonably well.[14] When this model was mounted so that secondary electrons from the output cavity of the klystron could not directly strike it, window life of the order of cathode life was achieved (approximately 1500 hours). These klystrons were operated on the Mark III accelerator at levels of approximately 15-MW peak and 2-kW average power. Because these tubes were continuously pumped, a small leak could be tolerated, and it was possible to replace windows by keeping the tube filled with dry nitrogen during the change. The dominant mode of failure of these windows was by puncturing through the ceramic. Although cracking occurred, it always appeared on windows which had been badly damaged by punctures. The windows became darkened on the load side by carbon deposited from the diffusion pump oil vapors in the system. Life data on these windows had an exponential distribution, indicating that their failure was random and independent of previous history.†

Because radiation from the klystron and the awkward geometry cause

* Similar to Fig. 10-9.

† More recently the Mark III accelerator has been operated in a mode in which the power from the klystrons is always reduced to a low value after a load breakdown. The power is then slowly raised to full value. This operating change has increased window life to well over 10,000 hours. The data on these recent window failures are understandably too scanty to indicate a statistical trend.

difficulties in testing windows on tubes, and because of the high cost of such tests, a resonant ring was built to facilitate these studies.[15] The ring also made it possible to test windows at powers far above those available directly from a klystron. This ring was pumped to about 10^{-5} torr by an oil diffusion pump with a liquid nitrogen trap. A viewing port allowed observation of one surface of the window. Although much was learned about the glow observed on the surface of all windows tested, no windows failed in ring tests at the power then available (25 MW peak).

To summarize the window status as of 1960: At the Mark III facility it had been found possible to make a window which would withstand 15-MW peak and 2-kW average power and which would have a reasonable life. There were still many window failures due to punctures, but techniques had been developed to allow replacements of windows on operating tubes. No design had been found which was superior to the initial pillbox construction, and alumina from different manufacturers gave essentially identical performance. Tests with 50% greater peak power than used on the Mark III had failed to damage windows.

The SLAC window program

Because new window problems were foreseen at SLAC power levels, which are 50% higher in peak power and 10 times higher in average power than the Mark III requirements, a program to study window failure mechanisms was started in 1958. It was hoped that the mechanisms causing window failures could be identified and that designs and operating conditions could be specified which would give long window life. A testing program was also set up to evaluate promising window materials by testing them to destruction. In the course of this program, excessive heating caused by multipactor at the window surfaces was recognized, and a study of methods of eliminating this effect was started. Some work was also done on window matching techniques and on the optimum window structure for SLAC use.

Test apparatus

Initially the diffusion pumped ring, described above, was used to test completed window assemblies. A more powerful driver tube was used giving ring powers between 70 and 80 MW peak, and average powers up to 45 kW. Because vacuum-tight window assemblies are expensive and time-consuming to make, a method of shrink-fitting window materials into copper (or copper-plated stainless steel) sleeves was devised. Although the dielectric-to-metal joint is not vacuum tight, it is very good from an RF standpoint. This technique allowed testing of materials for which sealing techniques did not exist and eliminated possible degradation of performance caused by a standard metal-to-ceramic type seal.

To allow testing at higher powers and to investigate the effect of better vacuum conditions, an all-metal ring was built incorporating a number of

improvements.[16] It was pumped by a sputter-ion pump which eliminated contamination by oil vapors and achieved pressures of 10^{-8} torr at the window (without RF). Extensive water cooling was provided to reduce the detuning effects of heating at high powers. The ring was equipped with two viewing ports to allow both surfaces of the test window to be observed. Two ionization gages measured the pressures close to both sides of the window. This ring was initially baked to reduce contamination to a minimum. It was hoped that each window assembly could be baked with the ring prior to testing. This procedure proved to be too difficult and time-consuming, but good vacuum conditions were maintained by using clean window assemblies, keeping the ring pumped except when making window changes, and by always letting up to dry nitrogen. When the ring was driven by a SLAC klystron, powers up to 170 MW peak and 150 kW average were attained.

Because, in a resonant ring, windows are tested with a traveling wave that is essentially reflection-free under high gain conditions, an all-metal ion-pumped cavity was built to evaluate possible differences in window behavior in highly mismatched cases.[16] Because of its high Q, this cavity proved very difficult to keep well matched and in tune. It was used for a relatively small number of tests. The behavior of samples in this cavity was very similar to that observed in rings.

Both the rings described above were carefully matched without test windows. The windows were separately tuned before insertion into the rings, eliminating the need for expensive impedance matching transformers in the rings. When needed, a small amount of matching could be done by squeezing the waveguide near the test piece or by shifting the frequency slightly. Using these procedures, it was relatively easy to keep the rings in good tune as the power was raised or as the losses changed.

At high peak powers, a considerable quantity of x rays are generated within the ring, particularly at the test window and at other discontinuities such as the tuner. It was found necessary to provide some lead shielding and to place lead glass in front of the viewing ports. It was also found that power at harmonic frequencies came either from the driver klystron or from generation within the ring, making it necessary to provide metal screens on the viewing ports to avoid possible eye injury.

Choice of window materials

Probably the most stringent specification for the SLAC klystron windows is the requirement for a vacuum environment on both sides of the window. This completely eliminates convection gas cooling commonly used on high-power windows and allows multipactor heating to occur on both sides of the disk. Radiation cooling is negligible until the window has reached temperatures where most materials will fail due to thermally induced stress. Therefore, the loss tangent in the window material must be as small as possible, and the thermal conductivity and the tensile strength should be as high as possible.

Since the fields are high, the dielectric strength should also be high.[17] In addition, the material must be capable of being assembled into a vacuum-tight, bakeable seal of high reliability.

Table 10-3 lists a group of dielectric materials which were considered promising for window use.[18] With the exception of beryllia and pyrolytic boron nitride, all have very poor thermal conductivities. The loss tangent, with several exceptions, is sufficiently low to allow use at SLAC powers. A few of these materials present practical problems which preclude their use, as long as other suitable materials are available. Although quartz has a very low dielectric loss tangent, its thermal conductivity is also very low. It is very difficult to seal quartz to metals because of its very low thermal expansion coefficient. Pyrolytic boron nitride had not been made into vacuum-tight seals and was not readily available. Sapphire, due to its anisotropic nature, must be used in zero-oriented form which makes it expensive. It is also a difficult material to make into large vacuum seals because of its tendency to crack.

At peak powers above 35 MW, many windows failed by puncturing during ring testing. In addition, some failures by cracking occurred at average powers over 2 kW. Many of the windows on experimental klystrons (including both alumina and beryllia) also cracked at powers as low as 6 kW. A large number of samples of alumina from one commercial source were tested to destruction to determine the mechanism of failure. These tests revealed a general pattern for two types of failure.

One type, dielectric breakdown within the material, occurs when the *peak* power reaches a critical value which is apparently determined by the individual sample. The second type of failure occurs when the *average* power through the window exceeds a critical level. The window usually fails by cracking in a manner controlled by the constraints at the edge of the disk. In a few cases, a single puncture directly through the disk has been found. In all tests, some glow appears at the surface of the window, either as a bright oval at the center of the disk or as a fainter set of arcs the shape of which is determined by the power level and the intensity of which decreases during the test.

Table 10-4 shows the results of a series of tests done on window materials. The following standard testing procedure was used. At a 60-cycle pulse rate and a 2.5-μsec pulse length, the peak power was raised to the maximum available (70–90 MW) or until dielectric failure occurred. The power was reduced to a low level while the pulse rate was increased to 360 cycles, after which the power was again raised to the limit of average power available (40–45 kW) or until thermal failure occurred (by cracking or melting). These tests were done with samples shrunk into sleeves to eliminate any effects from sealing techniques. All samples were tested in a pillbox-type geometry.*

* The cooperation of manufacturers of these dielectrics contributed greatly to the success of these tests. In particular, Western Gold and Platinum, Union Carbide, and Norton Refractories have supplied courtesy samples of materials made by them for evaluation.

Table 10-3 Physical properties of window materials

Material	*Manufacturer*	*Dielectric strength (V/mil)*	*Dielectric constant*	*Dielectric loss factor*	*Thermal conductivity (cal/cm²/sec/°C)*	*Thermal expansion coefficient (°C)⁻¹*	*Tensile strength (psi)*	*Compressive strength (psi)*	*External strength (psi)*
Alumina									
AL-300	Wesgo	1100[a]	9.4[b]	0.005[b]	0.064	8.5×10^{-6}	—	250,000	46,000
AL-995	Wesgo	800[a]	9.4[b]	0.002[b]	0.070	6.9×10^{-6}	—	300,000	62,000
AD-96	Coors	220–240	8.9	0.073	0.048	3.7×10^{-6}	26,000	300,000	49,000
AD-99	Coors	220–240	9.4[b]	0.002[b]	0.070	3.5×10^{-6}	34,000	300,000	54,000
4462	Frenchtown	225	9.2	0.003	0.071	6.11×10^{-6}	—	425,000	55,000
Sapphire	Linde	1700	9.4[b]	0.002[b]	0.06	7.7×10^{-6}	58,000	300,000	65,000
Beryllia BD-96	Coors	238	6.6	0.003	0.60	9.23×10^{-6}	—	225,000	32,000
Fused quartz									
Amersil	Engelhard	410	3.72[b]	0.001[b]	0.0033	0.54×10^{-6}	7,000	190,000	—
Boron nitride									
Hot-pressed	Union Carbide	300	4.78[b]	0.0015[b]	0.045	0.33×10^{-6}	—	—	15,000
Pyrolitic	Union Carbide	>3000	5.12[b]	0.0005[b]	0.15	0.1×10^{-6}	—	—	15,000
Magnesia	Norton	—		—	0.100	—	—	—	—
Zirconia	Norton	—	~20	—	0.02	9.1×10^{-6}			2,300
Pyroceram 9606	Corning	—	5.8	0.002[b]	0.009	5.7×10^{-6}	—	—	20,000[c]
Glass	Corning	900	4.1	0.01	—	3.2×10^{-6}	—	—	~10,000[c]

[a] Measured in oil.

[b] Values are at 3 to 6 GHz and were taken from Reference 23. (All other values are quoted from manufacturer's data sheets.)

[c] Surface abraded.

Table 10-4 Comparative material test data

Material	Samples tested	Surviving samples[a]	Failure samples: Dielectric failures	Failure samples: Thermal failures	Remarks
Alumina	46	13	18	10[b]	Multipactor on 60% of windows tested
Untreated Grooved	7	1	4	2	Multipactor reduced, more susceptible to dielectric failure
Grooved and coated	7	3	4	—	No multipactor, still susceptible to dielectric failure
Beryllia	1	0	—	1	Multipactor
Quartz					
Flat	5	0	—	5	Multipactor-heating, high-temp. gradient, catastrophic failure
Grooved	6	5	1	—	Only failure during mismatch at 80 MW, no multipactor
Boron nitride					
Hot-pressed	8	0	8	—	No multipactor
Pyrolitic	3	1	2	—	Interlaminar breakdown in two samples,[c] new sample survived
Magnesia	5	0	5	—	Most failed at low peak power (<7 MW)
Zirconia	3	0	—	3	All failed at low average power (≈ 2 kW)
Pyroceram 9606	2	0	—	2	Melted at ~ 30 kW average power (loss apparently related to reduced resistance)
Glass 7070	2	0	—	2	Melted at average power ≤ 10 kW

[a] Surviving maximum available powers ≥ 70 MW peak (1.8×10^{-4} duty factor) and 40 kW at 1.08×10^{-3} duty factor.

[b] Five samples which were not tested at high average power had been damaged by severe multipactor during peak operation and would most likely have failed thermally.

[c] Very early experimental samples.

These tests showed that multipactor can be expected on all uncoated materials except possibly boron nitride. They also indicated that the best thermal conductivity available (beryllia) is not sufficiently high to prevent thermal failure. Poor thermal conductivity, however, results in catastrophic failure. Glass (7070), Pyroceram, and zirconia, tested because of their high dielectric strength, melt at low powers due to their high loss tangents. Both magnesia and hot-pressed boron nitride were found to be unsuitable for SLAC use because of low dielectric strength. Boron nitride (in the pyrolitic form) would possibly be suitable if sealing techniques could be devised. Quartz, treated to prevent multipactor, shows promise, but suffers from the same sealing problem and has been found to be highly variable from sample to sample. Sapphire, not shown on this chart, was tested in a cavity where the samples failed by cracking at disappointingly low powers. Similar low resistance to thermal shock has been found at the W. W. Hansen Laboratories of

Physics, Stanford, during attempts to make sapphire-to-metal seals. Thus, alumina and beryllia, treated to prevent multipactor were found to be the two most promising materials tested. There has been a continual improvement in dielectric materials, such as alumina, concurrent with their use in power tubes. It should be stressed that the data presented here show the performance of the materials available at the time of the tests.[18] Improvement in material and different conditions of operation (i.e., with gas under pressure on the load side of the window) may allow use of substances not suitable in the SLAC environment.

Although low dielectric constant is desirable from the matching standpoint, the only factor of major importance for SLAC windows is the ability to handle the output power. Although beryllia would appear to be desirable because of its greater thermal conductivity, uncoated samples of beryllia have failed on klystrons at as low an average power as have alumina. Beryllia is also a difficult material to handle because of its high toxicity in powder and vapor forms. Therefore because alumina coated with titanium had been shown to handle more than twice the power needed, this material was chosen.

Design of window assemblies

Many high-power window designs have been employed at Stanford and in the tube industry.[3,6,13,19–21] Half-wave blocks of material, while attractive from the matching standpoint, have been avoided because of difficulties in construction. Slanted slabs and conical designs, which provide a bandwidth which is not needed at SLAC, all have two-surface multipactor problems which cause excessive heating. All of the above designs may also have ghost modes[22] and trapped resonances which can cause dangerously high fields. In the simple narrow-band pillbox structure, such modes can be placed well away from the operating frequency. The relatively thin ceramic disk can be readily and reliably sealed into a suitable metal sleeve. Variations of the pillbox design, such as increasing the spacing between the window and the transitions, were tried at the Mark III accelerator[14] without improving performance.

Some of the first experimental klystrons built at SLAC were constructed with two identical output windows to reduce the chance of failure by halving the power each must handle. This system did not prove any more successful than a single window, and the two outputs only added to the complications of testing. All SLAC-built klystrons now use a single output window* of the pillbox type shown in Fig. 10-9. A high-purity alumina disk, A, is copper brazed into a cupronickel sleeve, B. The sleeve is brazed to a stainless steel cylinder designed to mate with two special flanges, thus forming a complete demountable window assembly. Vacuum sealing is provided by copper gaskets located between the cylinder and the flanges. The window is matched by proper choice

* Designed by G. K. Merdinian.

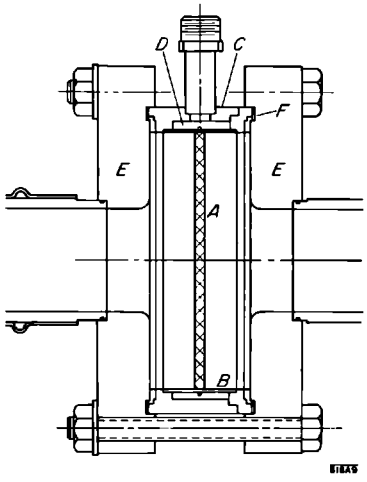

Figure 10-9 Window used on SLAC-built klystrons.

of dimensions and by using the reactance produced by the discontinuity between rectangular and cylindrical waveguide; the resulting VSWR is less than 1.04. The alumina disk is coated by sputtering with titanium after it is brazed to the sleeve assembly, but before it is bolted onto the klystron.

Of the four klystron vendors, three (RCA, Litton, and Eimac) have used a pillbox type of window design similar to that described above. In two of these the ceramic is brazed into a cylinder. The third design (RCA) uses a technique in which the disk is shrunk into a thin copper cylinder surrounded by a band of high tensile strength steel. The force produced presses the ceramic sufficiently far into the copper to produce a vacuum-tight bakeable seal. This force is great enough to cause the ceramic disk to become slightly dished. The fourth vendor (Sperry) has chosen a design using a disk slightly greater than a half-wave length thick. It is a modified pillbox and is water-cooled. All of these designs use the discontinuities at the junction between the two types of waveguide as part of the provisions for matching. All vendors use alumina and have developed coating processes to prevent heating by multipactor. These different designs, when properly made, have operated successfully on the SLAC accelerator.

10-8 Types of window failure (RWB)

On the basis of experience to date, window failures can be separated into three basic categories: (1) dielectric failure (punctures and/or internal failure), (2) thermal failure (cracking or melting caused by excessive heating of the window material), and (3) boundary failure. Thermal failure has been the predominant form of window damage on SLAC klystrons. In many instances

a window failure cannot easily be classified in one of the three groups, but will combine the symptoms of two or more types. In such cases, the question of which failure mechanism occurred initially is often difficult to resolve.

Dielectric failure

Dielectric failure occurs in a window when the electric field gradient exceeds the dielectric strength of the window material and the ensuing electrical breakdown causes permanent damage to the material. The path of the breakdown may be entirely confined within the dielectric in the case of internal failure or may extend from the dielectric to the adjoining medium in the form of a puncture. The two types of failure are usually found together since the occurrence of one will often immediately initiate the other.

Internal failure may be expected to follow the direction of maximum dielectric stress, as determined by the electric field configuration in the propagating mode. This form of dielectric failure determines the ultimate limitation of any window material. Since the computed electric fields present in SLAC windows are below[16] the published value of dielectric strength[23] of the alumina used, internal failure should not be a problem. Internal breakdown did occur occasionally in higher-power tests performed in the window study program. Internal failure in process and the damage resulting from it are shown in Fig. 10-10a and b, respectively. The cause of internal failure where electric fields in the propagating mode do not exceed the intrinsic dielectric strength has not been established, but two possible explanations have been postulated. The presence of randomly occurring voids in the body of the window material is believed to increase the probability of internal breakdown. Consistent dielectric failures observed at relatively low-power levels in a

Figure 10-10 (a) Internal failure (view of a failure in process). (b) Internal failure (view of the damage caused, lighting from behind).

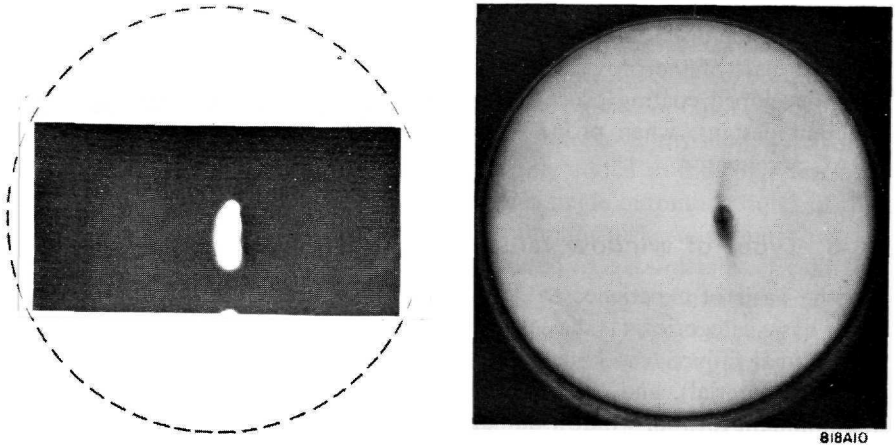

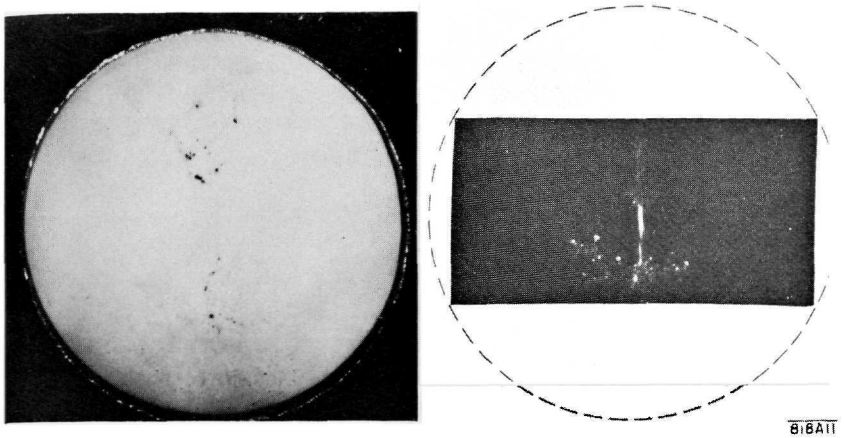

Figure 10-11 (a) Window punctures (Mark III window). (b) Surface discharge.

group of alumina specimens known to include voids gave some weight to this hypothesis. One possible mechanism for this form of failure has been described by Nergaard.[24] Another possible explanation involves the presence of "ghost" modes[22] in the dielectric or "trapped" resonances in the window structure, either of which could produce electric field gradients considerably higher than those in the propagating mode.

The more common form of dielectric failure at SLAC and at the Mark III accelerator has been puncturing, as illustrated in Fig. 10-11a. The exact nature of the puncture mechanism is still unknown, but several possible explanations have been advanced. Both the presence of voids and the effect of spurious resonances could account for puncturing as well as for internal dielectric breakdown. Occasional punctures appear to be related to surface discharge phenomena of the type shown in Fig. 10-11b. Breakdown in this manner is frequently observed on windows operating at high peak power and does not often damage the dielectric. There are indications that multipactor may also contribute to puncture formation, but the mechanism involved is not yet understood.

Thermal failures

The thermal failure category includes all window damage caused by excessive heat produced in the window material. Thermal damage may consist of melting or cracking of the dielectric. With some exceptions, melting is usually caused by violent electrical breakdown at the window. In most cases of failure, the window cracks when stresses due to temperature gradients exceed the mechanical strength of the material. Because of the mechanical properties common to most dielectric materials (see Table 10-3), windows crack under tension. In the SLAC window, which is brazed into a thin metal sleeve, failure occurs when the temperature gradient from the center to the edge of the

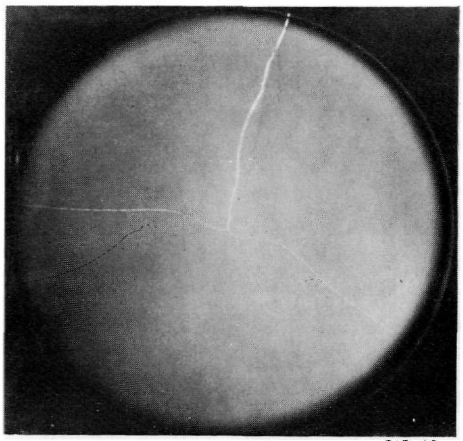

Figure 10-12 Typical example of a SLAC window cracked due to overheating (lighting from behind).

window produces tensile stress circumferentially. In cases where heat loss is relatively uniform, a window will usually crack in a pattern similar to that shown in Fig. 10-12. A special case is that of a vendor tube window mounted in a compression seal, to bow the ceramic. In this configuration, mechanical failure often begins at the center where a tensile force tangential to the surface is produced as the window heats, and the compressive forces at the boundary of the disk increase the dishing of the ceramic (see Fig. 10-13).

Figure 10-13 An example of the mechanical failure of a window in a compression seal (lighting from behind).

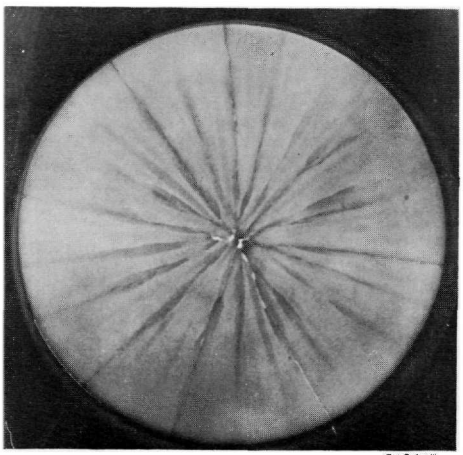

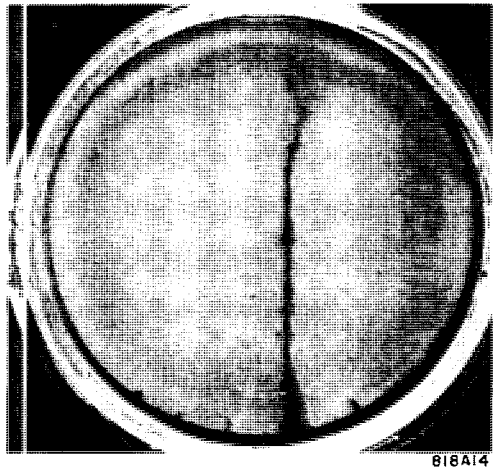

Figure 10-14 Window cracked because of a seal failure.

Cracks may also be caused by local thermal stress, and will often occur in cases of dielectric or seal failure (see Fig. 10-14). In the former instance, it may be difficult to determine which type of failure occurred first. Usually, in cases where the window cracks first, punctures which may then appear as a secondary effect will all be located on the crack (as in Fig. 10-15). Where dielectric failure precedes cracking, punctures will often be scattered randomly on the window surface, many of them far removed from any crack

Figure 10-15 Seal failure in early stage of development. (Magnified approximately 4 times.)

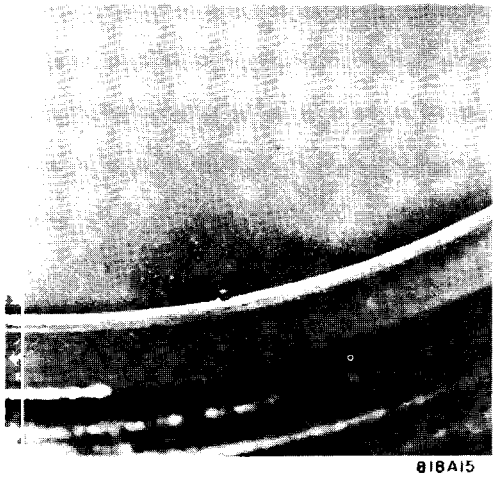

which may result from thermal stress produced at the site of a particularly active puncture.

The classification of thermal failure can also be subdivided according to the method by which the dielectric is heated. Four identifiable sources of window heating are: dielectric loss, electrical breakdown, multipactor, and resistive loss in a coating layer. The latter two are discussed in the section on the multipactor effect and its suppression. The heat-producing effects of electrical breakdown have been described in the foregoing treatment of crack formation.

Excessive heating due to dielectric loss has not been a primary problem with SLAC windows. The relatively low duty factor (0.9×10^{-3}) of the klystron output and the low dielectric loss factor of the alumina ceramic used as window material have combined to confine dielectric loss heating within safe limits,* despite the relatively poor heat transfer capability of the SLAC window design. An aspect of dielectric loss heating is the possibility of "runaway" heating due to an increase of the dielectric loss factor with increasing temperature.[21]

Boundary failure

The final classification of window failure concerns phenomena which depend not on the window itself, but on the boundary region between the dielectric and the metal sleeve containing it. Boundary failures can be further broken down into those associated with flaws built into the ceramic–metal seal and others caused by the presence of foreign matter at the seal boundary in an area of high electric field. The problem of avoiding flaws in the ceramic–metal seal is strictly a question of proficiency in fabrication techniques. The technology of metal–dielectric seals has been extensively studied and reported.[26,27] One potential source of seal trouble is excessive penetration of the dielectric by the metalizing material. This condition can cause severe heating at the seal and possibly lead to thermal failure.[28] A fillet of brazing material should not be allowed to encroach on the surface of the window because an electrical discharge may start at the fillet. The discharge will gradually sputter additional metal onto the window surface, electrical activity will be increased in turn, and the cumulative effect will eventually produce a thermal failure. A large fillet will simply accelerate the process.

Some boundary failures have been caused by accumulation of foreign material in high field areas of the seal. The electrical breakdown which results is similar to that associated with a protruding braze fillet, as is the typical cumulative development to eventual failure. Figures 10-14 and 10-15 show two illustrations of this type of trouble, one of which depicts a thermal failure.

* The center-to-edge temperature gradient produced by the transmission of 20-kW average power through the SLAC window calculated from an expression derived by Caryotakis[25] is ≈ 10 C. The value corresponds well to measured gradients. The gradient should be expected to vary linearly with power transmitted.

The other illustrates an early stage of development of failure. If recognized in time, this condition can often be corrected simply by cleaning the contaminated and sputtered portion of the window surface. This type of damage can be prevented by careful tube handling procedures. The external surface of the window must be inspected and cleared of all contaminants each time the klystron is installed.

10-9 Window multipactor and suppression techniques (RWB)

A significant recent improvement in high-power microwave tube window development has been the use of thin film coatings to reduce secondary emission and thus prevent electron multipactor. Prior to the use of window coatings, SLAC klystron windows often failed because of multipactor heating at average power levels as low as 2 kW. Effective coating techniques have virtually eliminated the window multipactor problem.

Description of multipactor

Electron multipactor is produced by secondary electron emission in an alternating electric field. The phenomenon requires a secondary electron emission coefficient greater than unity to maintain itself and rapidly builds up to avalanche proportions at high frequencies, if certain resonance conditions obtain. In its most common form, multipactor occurs between two surfaces (which serve as terminals of the alternating field) wherever the voltage and distance between the two surfaces combine to produce a secondary electron transit time equal to one-half period at the operating frequency.[29] However, multipactor may be a single-surface phenomenon in the event of transverse electric fields as on the SLAC klystron window. As first described by Priest and Talcott,[30] single-surface multipactor is a secondary electron resonance between portions of a dielectric surface parallel to the alternating electric field. The resonance is maintained by a restoring force which returns energetic secondaries to the window surface after they have been accelerated by the RF field. The energy of the returning secondaries is dissipated upon impact producing heat in the window material and releasing photons as well as new secondary electrons from the window surface.

Recognition of multipactor symptoms

In view of the damaging potential of multipactor, it is important that its presence be recognizable. Multipactor is most easily distinguished by its visible symptoms and by the elevated window temperature it induces. Apart from multipactor, high window temperature can also be caused by dielectric loss or resistive loss. Since dielectric loss is predetermined by the choice of window material, there is little danger of its being confused with multipactor heating. In window operation at SLAC, the more likely alternative cause of

window heating has been surface resistance loss, which is readily distinguishable from multipactor by visual observation of the window surface.

The visible characteristic of multipactor is the illumination produced at the window surface by the electron bombardment. This "multipactor glow" can be confused with another light-producing window phenomenon apparently associated with the release of adsorbed gas from the window surface. The "gas release glow" is much less intense than multipactor glow, depends upon the electric field configuration in the propagating mode, varies its shape with changing field strength, and has a diffuse appearance which gives the impression that the glow has depth. The gas release glow has a tendency to diminish and eventually disappear with continued operation, apparently indicating its relation to adsorbed gas.

In contrast with the gas release phenomenon, multipactor glow is much more intense and seems to emanate from the window material itself, giving the impression of a distinctly detailed pattern of illumination. In general, multipactor glow has a central pattern, most intense where electric field is highest, but is also somewhat affected by window geometry. Multipactor glow may also assume irregular shapes in instances when the surface has not been uniformly coated or when portions of a coating have been removed, as by an electrical discharge. Multipactor and gas release glow may appear simultaneously, but the intensity of the multipactor glow is likely to obscure the dimmer gas release pattern superimposed upon it.

Multipactor suppression techniques

The problem of suppressing or reducing electron multipactor has been solved by the use of thin films of materials with low secondary emission coefficient deposited on the window surface. Other techniques for reducing multipactor have been devised or suggested, but to date none has proven to be as convenient or effective as coating. The principle involved in window coating is simply a matter of superimposing a surface whose secondary emission coefficient is less than unity over the surface of the untreated window material which has a high secondary emission ratio. Only a very thin layer (≈ 50 Å) of coating film is required effectively to substitute the surface characteristics of the coating material for those of the window substrate. Because such a minute amount of coating is required to suppress secondaries, the bulk properties of the substrate material are not significantly affected. Coatings may be applied by a variety of methods most of which are variations of sputtering or evaporation of the coating material.

Multipactor prevention techniques other than coating include the use of superimposed electric or magnetic fields or of shaped electric fields. A number of alternative techniques are described in reports on window study programs conducted at Eimac[31] and Sperry.[32] One interesting possibility, the use of grooved windows, was the subject of a series of tests at SLAC in collaboration with Dr. O. Heil of Eimac. Grooved specimens of alumina and quartz were tested

at high power and the amount of multipactor was compared with that observed on coated and uncoated windows with flat surfaces. With the window grooves oriented perpendicularly to the main component of electric field in the propagating mode, multipactor was greatly reduced on grooved alumina windows, although a significant amount of electron activity continued to occur on the ridges of the grooves. Only when titanium coating was deposited on these ridges was the multipactor eliminated entirely. The grooved alumina windows usually failed by puncturing in or near the areas of highest electric field gradient, i.e., in the dielectric at the bottoms of the grooves. Aside from the higher fields, loose particles of alumina or other material often became lodged at the bottoms of grooves and provided circumstances favorable to local arcing which, in turn, led to puncture of the ceramic. Grooved quartz windows were somewhat more successful, operating without multipactor even without coating on the ridges of the grooves. The different comparative behavior of grooved quartz may have been due to a lower secondary emission coefficient than that of alumina or possibly to impurity coatings picked up by the quartz. Despite the good results of grooved quartz, the difficulty of fabricating a bakeable quartz window has discouraged its further consideration as a practical alternative to the present window.

Window coating

The use of titanium-based window coating films is at the time of this writing still the most convenient, effective, and widely used method of multipactor suppression. There are, however, numerous possible variations in window coatings which remain to be explored before an optimum solution can be claimed. The question of coating material is still completely open. A few materials other than titanium have been tried; none have been thoroughly evaluated. The matter of optimum coating method and thickness is also unsettled. Finally, one of the most vital criteria of an ideal coating, its stability through exposures to high-temperature cycles, is yet to be satisfied.

Because of its low secondary emission coefficient, titanium was the original choice as a window coating and is still the most widely used material.[33] The most comprehensive investigation to date of coating material alternatives, made as part of a window study at Sperry,[32] tested a variety of materials which successfully suppressed multipactor. The problem of choosing a coating material does not appear to be difficult insofar as multipactor suppression is concerned; many materials will do the job including carbon-based impurity films.* At present, the optimum choice of material seems to depend more upon its thermal stability than its secondary emission coefficient.

The question of whether evaporation or sputtering is preferable as a coating method is yet to be resolved. There is no positive evidence to indicate that

* Multipactor did not occur on nearly half of the uncoated window samples tested (see Table 10-4). Though not recognized at the time, it was later shown that a thin layer of oil film from the oil diffusion pump of the original ring could prevent multipactor completely.

either method produces a more effective window coating film. There is perhaps an advantage to be gained from better coating adherence of sputtered films, but this has not as yet been established experimentally. The coatings on SLAC klystron windows are applied by ac sputtering with a discharge between shaped titanium electrodes in an argon atmosphere.[34] Windows on other SLAC tubes supplied by vendors have been coated by evaporation from heated titanium wire or by RF sputtering.

Coating thickness is a critical variable. The minimum effective coating thickness is not precisely established, but is approximately 50 Å. Insufficient coating has not been a problem on SLAC windows. Marginally thin coating will perhaps permit enough multipactor to be easily visible, but even partial protection is usually sufficient to prevent significant multipactor heating at SLAC operating levels. Excessive coating poses a more difficult problem. Following the vacuum bake cycle, the electrical resistance of a thick coating may be reduced sufficiently to cause excessive heating due to resistive loss. Although a thin coating is identifiable by the increased multipactor glow intensity, a thick coating is indistinguishable by visual observation. Neither will temperature measurement during preinstallation test in the resonant ring usually indicate a thick coating, because the increase of resistive loss in the coating will not become apparent until its oxygen content is reduced during vacuum bake exposure. An accurate method of measuring coating thickness is, therefore, a vital adjunct to the coating process.

There are numerous thin-film thickness measurement techniques,[35,36] but few of them can be employed during the coating process. The most practicable method for measuring films deposited on SLAC windows appears to be the use of a crystal resonator as a microweighing device. Placed adjacent to the surface of the window being coated, the crystal picks up a proportionate amount of the window coating, and its resonant frequency shifts in a linear relation with its increase in mass. Unfortunately, it has not yet been possible to calibrate the crystal monitor readings against an independently determined absolute value of coating thickness. However, on the basis of experience with tube window performance and resonant ring tests, arbitrary limitations of coating thickness have been established in terms of the relative thickness readings indicated by the crystal monitors. The relative limits now being used are 80 Å minimum and 130 Å maximum. There has been a consistent tendency to lower the maximum thickness limitation as more has been learned of the instability of titanium coatings at high temperatures.

Window coating stability

The greatest single problem involved in the use of window coatings at SLAC has been their lack of stability when exposed to high-temperature cycles. With windows on klystrons built at SLAC, the problem has been limited to vacuum bake cycle exposure, but with some of the vendor tubes exposure to braze cycle temperatures in hydrogen atmospheres has also been involved.

In the case of vacuum bake exposure, the effect upon the coating is essentially one of reduction of the original coating layer to form a film with lower electrical resistance. This behavior is typical of titanium coatings but has also been observed with other window coating materials. Following application and subsequent exposure to air, a titanium coating assumes a resistivity greater than 10^{12} ohms/square. During a vacuum bake, this resistivity will decrease to 10^6 ohms/square or less, depending upon the thickness of coating. Even after cooling, the surface of the window which remains in vacuum will maintain a relatively low surface resistance which may contribute a significant amount of resistive loss to overall window heating. Only when the inside surface of the window is exposed to air will its resistance approach its initial high value. If the same window coating is again exposed to vacuum bake, the inside surface resistance will assume lower values at the bake temperature and after cooling than it did as a result of the initial bake. The ability of titanium coatings to reoxidize whenever exposed to air made it quite difficult to recognize the resistance drop caused by vacuum bake. Only when thermal failures began to occur consistently on windows exposed to two or more vacuum bake cycles was the phenomenon identified.

Comparative evaluations of window coating stability were first made by means of surface resistance measurements in simulated vacuum bake cycles. These measurements verified the mode of coating resistance behavior postulated from the observed pattern of tube window failure. Further verification was provided by means of a "double-window" test technique, in which two standard klystron windows are joined by a short section of waveguide evacuated by an independent ion pump. Using this configuration, it is possible to conduct resonant ring tests on windows exposed to vacuum bake, while maintaining a vacuum on only one side of each window. In this way the conditions of vacuum bake exposure encountered by a tube window are simulated.

Apart from the effect of vacuum bake, experience with klystrons built for SLAC by outside vendors has shown that titanium-based coatings may react with a hydrogen atmosphere at braze cycle temperatures. The effects of exposing a coating to braze conditions are much less clearly understood than are those associated with the vacuum bake, but seem to be critically dependent upon the water vapor content of the hydrogen atmosphere. A braze cycle in dry hydrogen appears to affect the coating in much the same way as a vacuum bake cycle, reducing the resistance of the coated surface and causing relatively high resistive loss heating during operation. Brazing in wet hydrogen has an entirely different effect, resulting in a noticeable increase in window multipactor, as if the coating has been partially removed.

10-10 Operational conditions (JVL)

The SLAC klystrons have been designed to be able to operate at beam voltages between 150 and 250 kV, corresponding to peak power outputs of approximately 3.5 to 22 MW (see Fig. 10-4). The tubes are capable of being turned

on directly at any voltage level within that range. However, in general, after a station has been inoperative for a few days, it is the practice to turn on near the lower voltage limit and at the minimum repetition rate (60 pulses/sec). Both beam voltage and repetition rates are then increased gradually to the required operating level.

The main reasons for the slow turn-on are to protect the components of the station, including the klystron, and prevent excessive gassing in the waveguides and in the accelerator pipe which could occur after a reasonable period of idleness.

The details of the protection system are covered in Chapter 21, but the principle of the protection is based on prevention of damage to the tube components. One set of protection devices and interlocks ensures that the beam voltage cannot be turned on until adequate heater power has been established for a predetermined time, and that there is water cooling in the system. Another protection circuit prevents the repetition of arcing in the tube should such arcing occur. In the present system, a single beam fault from either cathode overcurrent or overvoltage stops the trigger to the modulator for approximately 2 sec. After that time, the beam pulse comes back on. If arcing occurs again, the procedure is repeated until a predetermined number of faults have taken place (1–15 per hour), after which the modulator stops until it is reset manually.

Since it was suspected that the window could be a major cause of klystron failures, the vacuum system for the SLAC accelerator was specified as an all-metal, ion-pumped system. It has proven extremely reliable, achieving pressures in the 10^{-8} torr range. It is believed that this good vacuum inhibits window failures, especially those which might be caused by window overvoltage due to load breakdown. In addition, two circuits were incorporated to protect the window under adverse conditions. One measures the vacuum close to the window and stops the modulator when the pressure rises above a preset level (presently 10^{-6} torr). When the pressure again falls below this level, the modulator is automatically turned on again. The second system turns off the modulator when the reflected power exceeds a preset level (now 2 MW peak). After the first outage, the klystron is turned on at full power, if conditions are normal within 2 sec. After the second outage, or if vacuum pressures remain high for more than 2 sec, the RF drive to the klystron is reduced to give a low output before the modulator is turned on again. The drive is then increased in a period of 5 to 6 sec to the value which gives full output power. This system is similar to that used successfully on the Mark III accelerator at Stanford. The maximum number of allowable vacuum or reflected energy faults is determined by the same counting circuit used for beam fault protection.

10-11 Klystron operating experience (JVL)

As of July 1, 1967, the accelerator had been in operation for somewhat more than 1 yr, in addition to approximately 6 months shakedown of individual

sectors. The total klystron hours accumulated was close to one million, and the total number of failures was 130. A total of approximately 400 tubes have been accepted from outside vendors, all meeting the same electrical and mechanical specifications. Tubes from a given vendor are interchangeable in all permanent magnets supplied by that vendor, although they are not interchangeable with magnets from other vendors.

Because the actual operating cost of the machine will be greatly affected by the klystron replacement costs, a special test (endurance run) was initiated in April 1966 and ended in August 1966, in an attempt to obtain information on tube life and equipment reliability as a function of operating level. Seven pairs of sectors (eight tubes per sector; i.e., 112 klystrons) were operated under substantially constant conditions of both beam voltage and repetition rate for 130,000 socket hours. The operating conditions, the average number of accumulated hours per socket during the endurance run, the number of klystron failures under the different operating conditions, and the average life at the time of failure are given in Table 10-5.

The number of failures experienced during this endurance run was so small that no meaningful statistical information was obtained. However, the fact that the number of failures was much higher in sector pair 5–6, running at maximum voltage and repetition rate, led to the conclusion that it would be desirable to limit the normal operating level to somewhat below 240 kV. During the first 6 months of 1967, one-half of the klystrons were nominally operated at 236 kV, the other half were nominally operated at 218 kV. To date there appears to be no significant difference in failure rate under these operating conditions.

Table 10-6 gives a summary of tube usage and failures since the beginning of operation. Although the mean age at failure is still low, it is predicted that the mean time to failure of klystrons will be in excess of 8000 hours at the present operating levels. This prediction is based on statistical analysis assuming a standard distribution of failure and a mean deviation equal to half of

Table 10-5 Klystron endurance run results

	Operating level					
Sector pair	*Reference voltage*	*Klystron beam voltage*	*Klystron peak output power (MW)*	*Repetition rates*	*Average operating hours per socket*	*Cumu klyst failu*
3/4	115	240–250	19–22	60	1175	1
5/6	115	240–250	19–22	360	1050	6
7/8	105	220–230	16–18	60	1200	—
9/10[a]	105	220–230	16–18	180	1140	—
13/14	105	220–230	16–18	360	1135	2
15/16	90	195–205	11–14	60	1200	1
17/18	90	195–205	11–14	360	1190	—

[a] This pair of sectors began the run approximately 60 hours after the others.

Table 10-6 Klystron usage and failure

	Operating hours		*Failures*			
			Quarter		*Cumulative*	
Dates	*Quarter*	*Cumulative*	*No.*	*Avg. life at failure (hours)*	*No.*	*Avg. life at failure (hours)*
To 13/31/65	—	27,000	—	—	10	297
To 3/31/66	11,000	38,000	13	252	23	272
To 6/30/66	118,000	156,000	16	234	39	256
To 9/30/66	127,000	283,000	14	594	53	350
To 12/31/66	176,000	459,000	23	1070	76	575
To 3/31/67	228,000	687,000	28	1670	104	860
To 6/30/67	301,000	988,000	26	2166	130	1130

the mean time to failure. This prediction has to be hedged by the fact that up until now only a small percentage of tubes have failed from old age, i.e., from such causes as lack of emission. Between one-fourth and one-third of the total failures were caused by output window failure, and at least one-third were caused by tube gassiness as evidenced by excessive arcing, pulse breakup, pulse droop, and/or oscillations. There were also a few failures caused by high-voltage seal punctures.

Another indication that the mean time to failure will probably exceed 8000 hours can be obtained from the plot of age distribution of tubes installed in the gallery (Fig. 10-16). This figure shows that the mean age on March 1, 1968, was 5600 hours, and the median age was 6200 hours.

Figure 10-16 Klystron age distribution (all vendors) in 1000-hour increments.

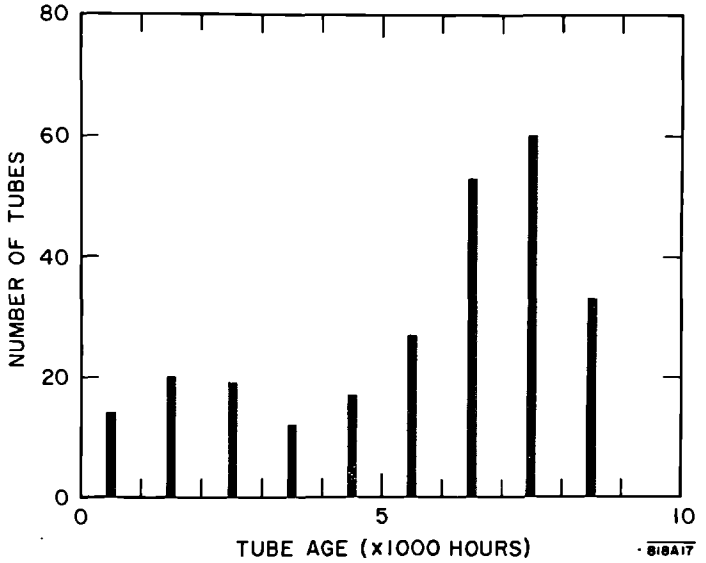

The good operating experience to date probably results not only from the high quality of the tubes procured and the quick-acting protection circuits installed, but also from the careful maintenance while the tubes are being installed in the accelerator. Further, it appears that the stringent specifications for SLAC klystrons have resulted in the high quality of the accepted tubes. For instance, the specifications on instabilities (phase and amplitude modulation) and faults probably result in rejection of any tube which would be marginally gassy.

In addition, a regular preventive maintenance program has been instigated in which each klystron receives a thorough check after every 500 hours of operation. Sometimes small instabilities are observed which can be eliminated by retuning the magnet. Sometimes a tube appears to be close to temperature-limited operation and an appropriate increase in heater power is introduced. In any case, the preventive maintenance is essential because the total instrumentation at each station in the gallery is minimal and it is essential for satisfactory operation of the accelerator that each klystron installed should operate within specifications.

In general, there have been few operational difficulties with klystrons. As noted above, the instrumentation on the machine is not as complete as might be desired for complete analysis of potential troubles. For this reason, many tube and pulse transformer tank assemblies are removed from the gallery for retest in the test laboratory. To date, the average number of tube removals is equal to twice the number of tube failures.

One of the main questions initially concerned the stability of the permanent magnets. At this time, there is no indication that the permanent magnets deteriorate in any way. Accordingly, it is felt that the total maintenance effort is greatly reduced by the use of permanent magnets compared to the conventional electromagnets and their power supply systems.

10-12 Extended operating life warranty (JVL)

When the klystrons were initially purchased from our vendors, they carried no warranty except for the guarantee of performance during the acceptance tests, including a 20-hour heat run at full power. The failed tubes were returned to vendors for repair. The vendor analyzed the tube and quoted a repair price based on the work to be done to the tube. The main disadvantage of the repair contract, from SLAC's standpoint, is the possibility of wide fluctuations in number of failures and, hence, in operating costs. In addition, there is no real incentive for the vendor to improve the life and quality of his products.

A modification of the initial procurement contracts has now introduced an extended warranty covering the tubes used at SLAC (in sockets on the accelerator). This extended warranty provides that all tube failures (except those caused by equipment malfunction or human error) will be replaced at no cost to SLAC. In return, SLAC makes a warranty payment for each operating hour of the tube on the accelerator. There are two hourly rates, a high

initial rate and later a lower rate which continues until the tube fails. The rates have been negotiated so that the payments on the warranty would be about equal to those on the repair contract calculated on the basis of the mean time to failure expected at the time of the negotiations.

From an operational standpoint, the main advantage of the extended warranty is that a maximum hourly operating cost per socket is set by the terms of the agreement. In addition, at the end of the extended warranty period, all tubes initially contracted for will still be operable. With a repair contract, some tubes would be considered nonrepairable and the resulting attrition would considerably reduce the number of tubes available for operation.

Acknowledgments

The successful development of permanent-magnet-focused klystrons would not have been possible without the full cooperation of the members of the Klystron Department at SLAC and corresponding personnel of the vacuum tube companies having development contracts with SLAC in the early 1960's. Nor would the final machine performance have been possible without the cooperation of the klystron vendors who supplied the majority of the tubes being used on the machine.

Some members of the Klystron Department who have not been involved in the preparation of this chapter deserve special commendation for their outstanding contributions. First on the list should be G. K. Merdinian who not only designed the gun now used on the SLAC tube but was instrumental in the electrical and mechanical design of the window, as well as in the computations from which the major modifications of drift distances and improvement in efficiency resulted. The tube fabrication itself would not have been possible without the untiring efforts of J. P. Meloni. Tube testing has been principally the responsibility of R. L. Stringall. R. S. Callin has helped solve the mechanical handling problems and installation in the gallery, and T. Johnston has contributed greatly to the solution of operational and maintenance problems. K. Welch and B. G. Ryland by their continuing visits to tube manufacturers have helped maintain the flow of deliveries.

The window improvement work has been greatly assisted by the contributions of W. R. Fowkes (ring design), W. P. Schulz (sputtering techniques), and S. Sonkin (consultation on major problems).

References

1 P. T. Demos, A. F. Kip, and J. C. Slater, *J. Appl. Phys.* **23**, 53 (1952).

2 J. V. Lebacqz and R. B. Neal, "A Comparison of Amplitrons and Klystrons as Radiofrequency Power Sources for the Proposed Stanford Two-Mile Accelerator," Rept. No. M-256, Microwave Laboratory, Stanford University, Stanford, California (March 1961).

3 M. Chodorow, E. L. Ginzton, I. R. Neilsen, and S. Sonkin, *Proc. Inst. Radio Engrs.* **41**, 1584 (1953).

4 M. Chodorow, E. L. Ginzton, J. Jasberg, J. V. Lebacqz, and H. J. Shaw, *Proc. Inst. Radio. Engrs.* **47**, 20 (1959).

5 J. E. Picquendar, *Rev. Tech. CFTH* No. 32, p. 62 (1960).

6 R. Metivier, "Les klystrons amplificateurs de grande puissance de la Compagnie Francaise Thomson-Houston," *Rev. Tech. CFTH* No. 32, p. 85 (1960).

7 G. Merdinian and J. V. Lebacqz, "High-Power, Permanent Magnet Focused, S-Band Klystron for Linear Accelerator Use," *Proc. Fifth Intern. Conf. Microwave Tubes, Paris, 1964*, Dunod, Paris, 1965.

8 J. R. Pierce, *Theory and Design of Electron Beams*, Van Nostrand, Princeton, New Jersey, 1949.

9 L. Brillouin, *Phys. Rev.* **67**, 260 (1945).

10 F. B. Llewellyn, *Electron-Inertia Effects*, Cambridge Univ. Press, London and New York, 1941.

11 J. V. Lebacqz, *IEEE Trans. Nucl. Sci.* **NS-12**, p. 86 (June 1965).

12 S. E. Webber, "Large Signal Analysis of the Multicavity Klystron," Rept. No. 58-RL-1897, General Electric Research Lab., Technical Information Section, The Knolls, Schenectady, New York (January 1958).

13 J. V. Lebacqz, J. Jasberg, H. J. Shaw, and S. Sonkin, *Proc. Inst. Elec. Engrs. (London)* **B105**, Suppl. 11, p. 617 (1958).

14 J. Jasberg and J. V. Lebacqz, "Problems Related to Very High Power Windows at Microwave Frequencies," in *Advan. Vacuum Sci. Technol.: Proc. First Intern. Congr. Vacuum Techniques, Namur, Belgium, June 1958*, Macmillan (Pergamon) New York, 1960, Vol. II, p. 667.

15 L. Milosevic and R. Vautey, *Vide* **11**, (65), 410 (September–October 1956).

16 J. Jasberg and J. V. Lebacqz, "High-Power Microwave Windows," *Proc. Fifth Intern. Conf. Microwave Tubes, Paris, 1964*, Dunod, Paris, 1965.

17 A. Von Hippel, ed., *Dielectric Materials and Applications*, Wiley, New York, 1954.

18 R. Bierce, W. R. Fowkes, and J. H. Jasberg, *IEEE Trans. Nucl. Sci.* **NS-12**, No. 3, p. 180 (June 1965).

19 "Superpower Microwave Windows; Final Report, 2 Jan. 1963 to 1 Jan. 1964," Rept. No. NA-8240-8372, AD 438 452, Sperry Gyroscope Co., Great Neck, New York (January 1964).

20 F. Johnson, "High Power RF Window Study Program; Final Technical Report," Rept. No. RADC-TDR-63-510, AD 433 791, Varian Associates, Palo Alto, California (November 1963).

21 C. E. Muehe, "Some Aspects of High Power Window Design," MIT Lincoln Lab. Rept. No. 46G-0003, Lincoln Laboratories, Massachusetts Institute of Technology, Lexington, Massachusetts (October 1960).

22 M. P. Forrer, "On the Boundary Value Problem of Waveguide Windows," Rept. No. ML-575, Microwave Laboratory, Stanford University, Stanford, California (March 1959).

23 W. B. Westphal, "Dielectric Constant and Loss Measurements on High-Temperature Materials," Tech. Rept. No. 182, Laboratory for Insulation Research, Massachusetts Institute of Technology, Cambridge, Massachusetts (October 1963).

24 D. A. Daly, H. B. Law, and L. S. Nergaard, "Study of Aspects of Failure of Klystron Windows," Final Rept. No. RCA-94963-FR, David Sarnoff Research Laboratory, Radio Corporation of America, Princeton, New Jersey (April 1963).

25 G. Caryotakis, "RF Heating in Disc Windows," Rept. No. EMI-TR-65-5, Eitel-McCullough, Inc., San Carlos, California (February 1965).

26 L. Reed *et al.*, "Metallurgical Research and Development for Ceramic Electron Devices, Final Report, 1 July 1962 to 30 June 1965," Rept. No. EMI-TR-66-1, AD 636 950, Eitel-McCullough, Inc., San Carlos, California (January 1966).

27 A. C. Grimm and P. D. Strubhar, "Dielectric to Metal Seal Technology Study," RCA Tech. Rept., RADC-TDR 63-472, AD 432 199, Radio Corporation of America, Industrial Tube and Semiconductor Division, Lancaster, Pennsylvania (October 1963).

28 D. E. Stutz, "A Survey of the High Power Microwave Tube Window Problem," BMI-197-11-1, AD 292 082, Battelle Memorial Institute, Columbus, Ohio (November 1962).

29 S. C. Brown, *Basic Data of Plasma Physics*, Technology Press of MIT and Wiley, New York, 1959.

30 D. H. Preist and R. C. Talcott, *Inst. Radio Engrs. Trans. Electron Devices*, **ED-8**, p. 243 (May 1961).

31 R. Hayes, "Research on Microwave Window Multipactor and Its Inhibition, Final Report, 1 July 1962 to 30 June 1964," Rept. No. AD 256 295, Eitel-McCullough, Inc., San Carlos, California (June 1964).

32 A. Saharian, A. Kiefer, and P. Lally, "High Power Microwave Tube Window Investigations, Final Report, September 15, 1964–September 14, 1965," Rept. No. AD 477 679, Electronic Tube Division, Sperry Rand Corporation, Gainesville, Florida (September 1965).

33 R. C. Talcott, *Inst. Radio Engrs. Trans. Electron Devices* **ED-9**, p. 405 (September 1962).

34 W. P. Schulz, "Apparatus for coating substrates by cathode sputtering," U.S. Patent No. 3,293,168 (December 20, 1966).

35 O. S. Heavens, *Optical Properties of Thin Solid Films*, Butterworth, London and Washington, D.C., 1955.

36 L. Holland, ed., *Thin Film Microelectronics*, Wiley, New York, 1965.

WAVEGUIDES

A. L. Eldredge, Editor, and V. G. Price

This chapter describes the rectangular waveguide system which transfers microwave power from the klystrons to the disk-loaded accelerator. In addition to the transfer of microwave power, this system provides for monitoring the power level of the klystron outputs. The phase of a beam-induced wave in the disk-loaded waveguide is also monitored once in each 40 ft of accelerator length.

A key boundary condition for the design of the waveguide network is based upon the decision to feed four 10-ft sections of the disk-loaded waveguide from one klystron. Consequently, the waveguide network must either have a high-power phase shifter in each 10-ft accelerator feed or be made with sufficient accuracy and temperature stability to make independent phase adjustment of the separate waveguide feeds unnecessary. Consideration of cost and operational factors led to the latter design solution. During operation, phase adjustments are made only at the RF inputs to the klystrons.

High emphasis was placed on reliability. A major reliability question concerned the RF windows in the waveguide system between the klystrons and the accelerator. A window is needed at each klystron to provide a vacuum seal which is transparent to RF in the output waveguide. This allows each klystron to be independently evacuated, processed, and tested, and then stored until it is needed for service on the accelerator. Early in the design program there was doubt regarding the feasibility of designing a window capable of handling the high-peak and average powers needed for the accelerator without providing gaseous cooling on the output side of the window. However, the use of gaseous cooling within the waveguide system demanded that a second window be provided in series to prevent the gas from entering the accelerator. Moreover, it would have been necessary to pressurize the gas to enable it to withstand the high-voltage gradients in the waveguide without breakdown.

A puncture or crack in any of the 245 secondary windows in the waveguide system would then result in the accelerator becoming filled with gas, which would immediately make it inoperable. Consideration of this serious consequence led to the decision to use only a single in-line window (attached to the klystron) and to evacuate the waveguide region between the klystron and the accelerator. This decision, of course, complicated the window design problems but, in spite of formidable difficulties, a window meeting these requirements was designed, as discussed in Chapter 10. A further consequence of the decision to use a single in-line window was the necessity of developing a waveguide valve. This valve would allow reflectionless transmission of RF power when in the open position but would be an effective vacuum seal when it was closed, thus allowing klystron replacement without disturbing the accelerator vacuum. Such a valve was successfully developed and is described later in this chapter.

For reasons outlined above, the rectangular waveguide system was designed to operate in high vacuum ($\approx 10^{-8}$ torr). The decision to evacuate the waveguide system also necessitated the development of reliable vacuum directional couplers, loads, power dividers, and vacuum pumpout orifices with high conductance and negligible RF coupling. Special fabrication techniques also had to be developed to provide the nominal 48,000 ft of rectangular waveguide.

A fundamental requirement for the overall machine design was that it should allow the initial energy specification to be doubled without requiring significant structural changes in the klystron gallery and accelerator housing, and without increasing the length of the disk-loaded waveguide. To be compatible with this design philosophy, the rectangular waveguide network was designed to have sufficient flexibility to accommodate any subsequent addition to the number of klystron stations with minimum accelerator downtime, while keeping the cost of the initial network as low as possible. The flexibility was achieved by careful planning of the waveguide layout and by the use of additional flange joints that allow the network to be disassembled and reconnected to accommodate an increased number of klystron stations.

General specifications established to meet the waveguide system requirements are given in Table 11-1.

11-1 Waveguide layout

The specific configuration for the waveguide network was determined by the conformations of the principal elements of the system and by the requirement for flexibility to add, conveniently, additional klystron stations with little accelerator downtime. The primary elements affecting the layout included microwave loads, RF couplers, power dividers, vacuum pumpouts, waveguide valves, and the mechanisms allowing rapid replacement of the klystrons.

The short-slot hybrid junction was used for the power dividers in preference to a simple shunt or series T-junction because it is much less sensitive

Table 11-1 General specifications of waveguide system

Operating frequency	2856 MHz $\pm$ 3 MHz
Input reflection coefficient	$\lvert S_{11} \rvert < 0.07$
Power transmission capacity	24 MW peak, 21 kW average
Phase deviations of output signals relative to an input reference phase	$\pm 3°$ ($+360° n$, where n may be as high as 23)
Vacuum operating level	10^{-7} torr at full RF power, 10^{-8} torr at zero RF power
Gas burst rate	Less than 1 burst/hour average at full RF power after processing
Temperature tolerances	$\pm 2°$F

to load impedance variation. More specifically, a T-junction subjected to impedances that produce VSWR's of 1.10 in each of the two outputs will have a power division difference that can, in the worst case, be 0.8 dB. For the same load condition the power output imbalance from the short-slot hybrid is 0.1 dB in the worst case.

Folded hybrids and short-slot, sidewall hybrids were much easier to adapt to the waveguide network than either the top-wall hybrids or magic T's. Furthermore, sidewall hybrids were found to have higher-peak power handling capacity[1] than magic T's, folded hybrids, or simple T-junctions. The short-slot hybrid of the Riblet[2] design proved to be the most suitable because of its relatively simple configuration and good electrical characteristics.

The basic module of the waveguide network consists of the waveguide components necessary to connect two klystrons to 80 ft of accelerator structure. Figure 5-17 illustrates this basic rectangular waveguide network module. The rectangular waveguide system for the injector, designed by Tsang and Keicher,[3] is shown in Fig. 11-1. This network provides for switching from the on-line klystron to a standby klystron within seconds and provides power to the prebuncher and buncher as well as to the injector disk-loaded waveguide section. The prebuncher and buncher feeds have independent phase and power adjustments. The special waveguide network for the positron sources is illustrated in Fig. 11-2.

A fundamental problem concerned the relative motion of the klystron gallery and accelerator housing due to normal earth shifting and settling. In addition to accommodating this relative motion, the waveguide network had to function properly in the presence of temperature excursions encountered during installation and start-up, shut-down cycles associated with machine operations. To accommodate these conditions, the waveguide layout was designed so that the only fixed tie points were at the klystrons. The fixed point was achieved by reinforcing the directional coupler with stainless steel plates and bolting it to the klystron frame. The klystron frame consists of two vertical cylindrical steel pipes 20 ft apart, bridged by a steel I-beam. The I-beam has a yoke which supports the klystron, together with its permanent magnet and

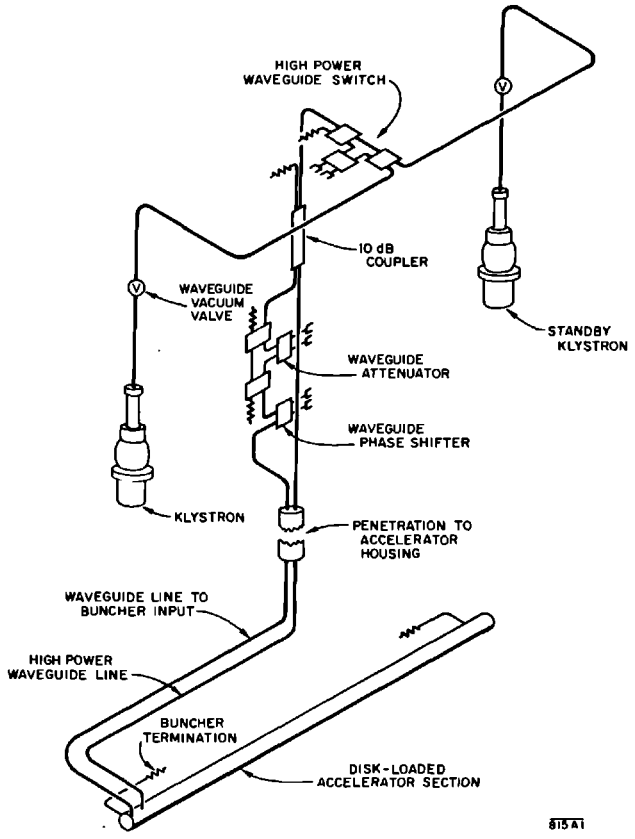

Figure 11-1 Waveguide network in the injector area.

pulse transformer tank. The yoke design provides an indexing system which insures that the klystron vertical output waveguide matches the flange of the rectangular waveguide network. The reinforced directional coupler also provides the connection point of the vacuum system to the waveguide network in the klystron gallery.

The rectangular waveguide crossbar assembly is supported as shown schematically in Fig. 11-3. The flexible supports at points A and B are achieved by spring couplings to the klystron frame. The vertical loads due to the weight of the waveguides in the vertical penetrations are transferred to the klystron frame by the same springs. The klystron frame is adjustable both vertically and horizontally by means of a jack pad between the floor and the bottom of the steel vertical pipes. Hence any changes in the relative positions of the klystron gallery and accelerator housing can be compensated for by adjusting the klystron frame. This arrangement and procedure prevent the waveguide network from producing loads on the 40-ft girders, which could cause serious misalignment of the accelerator structure. Figure 11-4 is a photograph of the klystron, the support frame, and the crossbar assembly.

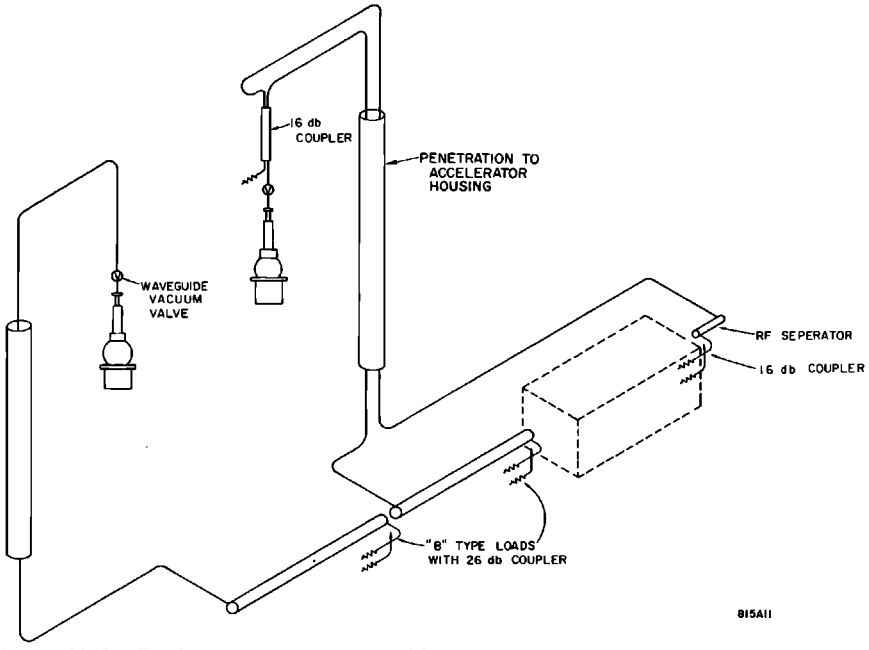

Figure 11-2 Positron source waveguide arrangement.

The waveguide layout was designed to be as nearly symmetrical as possible, in spite of the restrictions imposed by the need for alternating the direction of the input feeds to the 10-ft accelerator sections and by the decision to have flexibility to accommodate additional klystron stations. The primary asymmetry is caused by the latter requirement which necessitated locating the klystron

Figure 11-3 Schematic of waveguide attachment to klystron support frame.

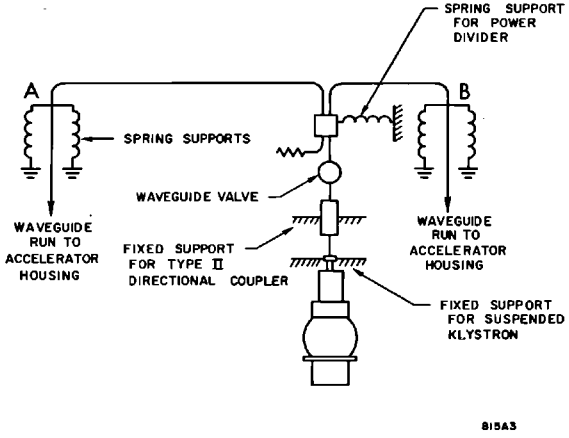

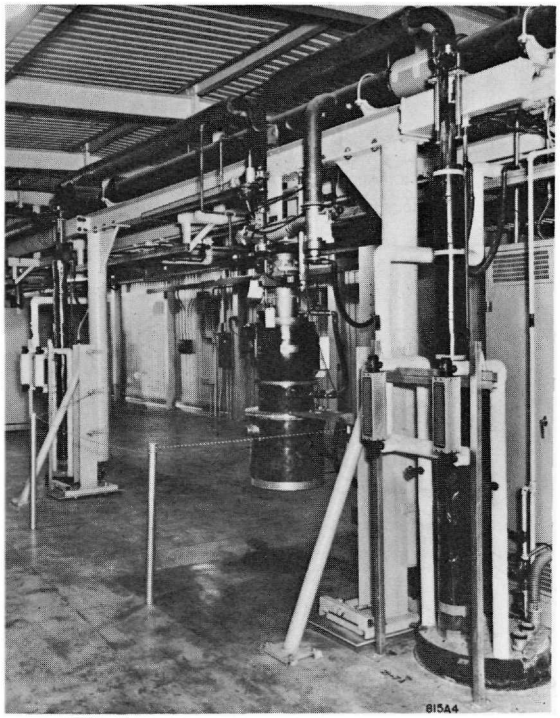

Figure 11-4 Klystron support frame with waveguide and klystron attached.

so that one waveguide run from the klystron is about twenty guide-wavelengths longer than the other run from the same klystron. The resultant asymmetry required careful attention to the design of the waveguide network, including the methods of cooling, phase adjustment, and mechanical support.

11-2 Waveguide selection

Cross section

The internal dimensions for the rectangular waveguide cross section were set at 1.340 × 2.840 in., with a tolerance of ± 0.005 in. Factors leading to this cross-section included both microwave and vacuum considerations.

Initial technical design considerations suggested the possibility of using the rectangular waveguides both as the microwave transmission system and as the evacuation lines between the klystron gallery and the accelerator housing for the accelerator structure. In addition to possible reduction and simplification in vacuum components, the larger cross section that would be

necessitated by vacuum conductance requirements would give some microwave advantages such as lower dispersion and attenuation. However, economic consideration established that it was far less expensive to use the smallest waveguide cross section that could reliably meet the microwave requirements and use separate periodic stainless steel manifolds to evacuate the accelerator structure. These factors led to the design of the vacuum system as described in Chapter 23.

The factors involved in determining the waveguide cross section, in addition to those already discussed, included material selection, cooling methods, phase stability, and fabrication methods to process approximately 48,000 ft of waveguide. Consideration of the vacuum requirements, electrical performance, and fabrication problems led to the selection of high-purity low-oxygen content (not more than 10 parts per million) copper as the waveguide material. The only other suitable materials were silver and aluminum. The use of silver would yield a waveguide with 2% less attenuation than one made from copper; however, its extreme cost outweighs such a small improvement in attenuation. An aluminum waveguide has an attenuation 15% greater than copper, which is an intolerable increase, and particularly so in view of the relatively small difference in the cost of the two materials for a fabricated, installed, rectangular waveguide network.

The waveguide network design makes it essential to have excellent phase stability because there are no high-power phase shifters (with the exception of the one in the injector). This requirement places critical dimensional stability tolerances on the waveguide cross section. Pressures and forces that can produce mechanical deflections are due to evacuation of the waveguide, the loads imposed by the waveguide weight, and changes in distance between the klystron gallery and the accelerator housing. The change in distance between the klystron gallery and the accelerator housing due to normal earth motion is a very slowly varying function; hence periodic mechanical adjustment of the klystron support frame can maintain this force at a very small value. The principal source of waveguide dimensional change is the elastic deformation of the copper caused by atmospheric pressure when the waveguide is evacuated.

Elastic deformation can be minimized by making the waveguide walls sufficiently thick. However, there is a reasonable balance between allowable deformation and the cost of the waveguide. The cross section of an unperturbed rectangular waveguide of inside width a and height b is shown in Fig. 11-5. Virgile[4] studied deformation of waveguide subject to internal pressure. Experimental data showed that evacuated waveguide deforms as illustrated in Fig. 11-6. Virgile's data gives $\Delta a_0/\Delta b_0$ as 0.21 for pressurized WR-284 waveguide, which has the same internal dimensions as the SLAC waveguide. Assuming sine wave deformation, the phase shift per unit length caused by such perturbations of the waveguide walls may be shown to be[5]

$$\frac{\Delta\phi}{L} = \frac{2\lambda_g}{a^2}\left[\frac{\Delta a_0}{a} + \frac{1}{3}\frac{\Delta b_0}{b}\right] \tag{11-1}$$

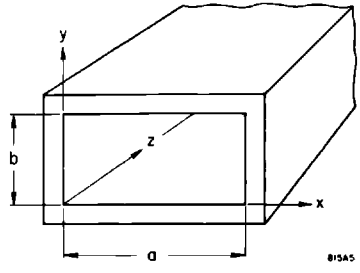

Figure 11-5
Waveguide dimensions.

where λ_g is the guide wavelength and the other symbols have meanings as illustrated in Figs. 11-5 and 11-6. Substituting $\lambda_g = 6.023$ in., $a = 2.840$ in., $b = 1.340$ in., and $\Delta a_0/\Delta b_0 = 0.21$ in Eq. (11-1) yields the result $\Delta\phi/L = 0.17°/\text{ft}/0.001$ in. change in the dimension b at the center of the broad face of the waveguide.

Experimental, evacuated, waveguide cavities, 4 ft long, were fabricated to provide empirical data on the variation in phase shift as a function of wall thickness and atmospheric pressure. The results of measurement and computation of phase shift per unit length are plotted on Fig. 11-7 using values of Δb_0 which were determined by Skarpaas.[6] The shift in resonant frequency, corrected for the dielectric constant of the air-water vapor in the cavity, was measured when the cavity was evacuated. The measured, incremental phase shift for the 0.157-in. sample waveguide approached the value that was accepted as the maximum allowable; hence this wall thickness was specified as the minimum. The nominal wall thickness was specified as 0.173 in. with tolerances on the internal dimensions of ± 0.005 in. and tolerances on the external dimensions of ± 0.010 in.

Barometric pressure at SLAC seldom falls outside the limits of 29.0 to 30.5 in. of mercury. By interpolation of the upper experimental curve of Fig. 11-7, a phase shift of 0.023°/ft/in. of mercury change in barometric pressure can be predicted for a waveguide with 0.173-in. wall thickness. A 12-ft length of waveguide was fitted with vacuum windows on its ends and inserted in a chamber in which the external pressure could be varied while maintaining an internal vacuum. The incremental phase shift per unit length measured by a

Figure 11-6 Waveguide deformation when evacuated.

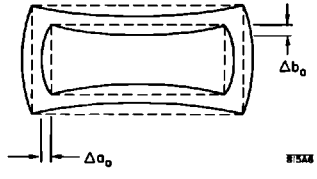

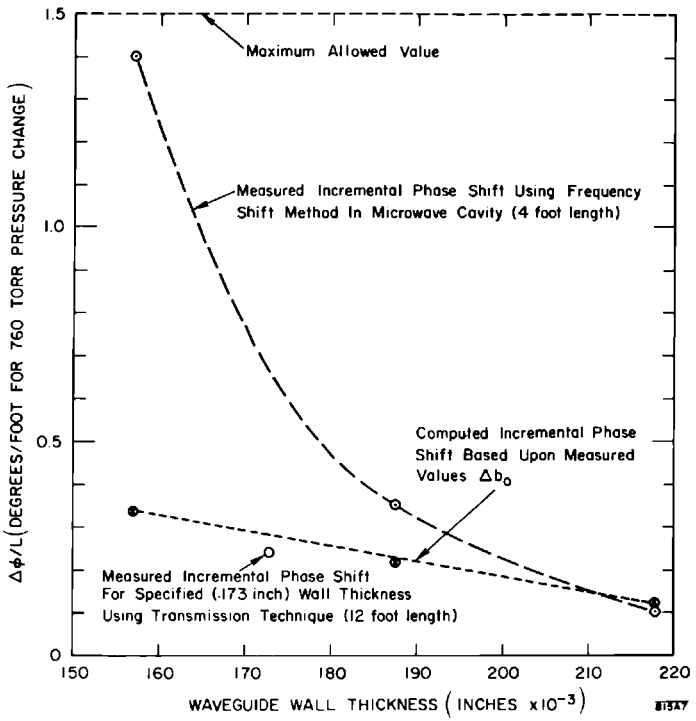

Figure 11-7 Measured and computed values of incremental phase shift for evacuated waveguide with wall thicknesses of 0.157, 0.187, and 0.218 in.

transmission method was found to be approximately 0.008°/ft/in. change in barometric pressure. Work hardening of the annealed copper, from repeated cycling, produced some difficulty in repeating the measurements but reflected what would actually be encountered in operation. It was concluded that the expected differential phase shifts due to changes in atmospheric pressure in the SLAC area with the asymmetric waveguide should be no greater than 0.2°.

The long-term plastic creep of the copper in the rectangular waveguide under operating conditions is estimated to be sufficiently small that it will be 8 to 10 yr before any trim tuning of the waveguide will be required.

The cooling necessary for temperature and, hence, for length stability is provided by water flowing through a 1 × 1½-in. rectangular tube brazed on one broad wall of the waveguide, as shown in Fig. 11-8. Phase shift measurements versus water pressure in the cooling water tube were made, using the cavity frequency shift method, on two 6-ft samples. The frequency shift in the evacuated 6-ft waveguide cavity was measured as the coolant channel was pressurized to 80 psi. A large initial inelastic deformation was observed, but after reaching the elastic deformation region, the furnace-brazed samples

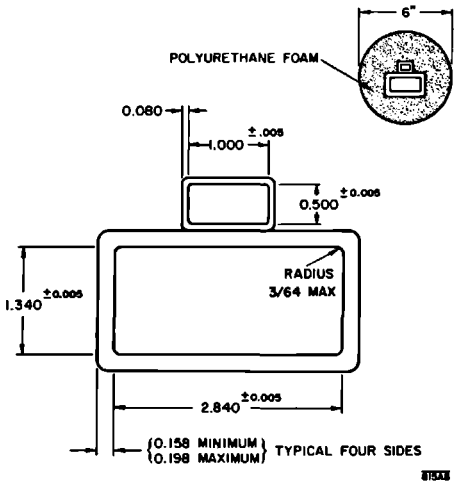

Figure 11-8 Specified waveguide and cooling tube dimensions. Cooling tube is shown in its brazed position on the rectangular waveguide.

showed an incremental phase shift of 8.3×10^{-4} deg/ft/psi of variation in water pressure. It was concluded from this that no significant phase error would be incurred due to coolant pressure fluctuations or to turning the water off and on.

Key factors in the successful fabrication of the rectangular waveguide network and the disk-loaded waveguide were the quality of copper used and the choice of fabrication techniques. The copper requirements for these two components of the accelerator were more than 2 million lb in ingot form. To assure quality, steps in the copper processing were controlled from the refinery state through fabrication of the mill shapes, including the special cross sections for the rectangular waveguide and cooling tube.

The entire 48,000 ft of waveguide was processed at SLAC. All operations culminating in the final installation of the waveguide network were performed using the same quality-control standards and techniques as used in high-power vacuum tube manufacture. These techniques include high-quality chemical cleaning and high-temperature hydrogen brazing procedures. The rectangular water cooling tube was brazed to the rectangular waveguide in a 17-ft deep hydrogen furnace. A substantial saving in the cost of the waveguide was achieved by specifying that random lengths would be acceptable. Long lengths were made by butt brazing shorter pieces of the rectangular waveguide together after the cooling tube brazing was completed. Precise joints were made possible by sizing the male and female ends of the rectangular waveguides to a tolerance of ± 0.001 in. and then brazing them together as shown in Fig. 11-9.

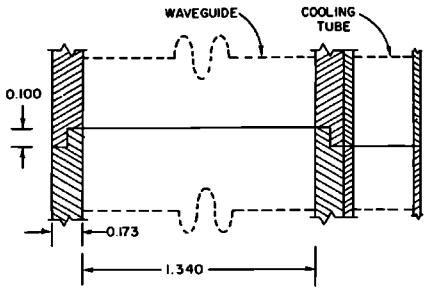

Figure 11-9 Waveguide butt-joint configuration.

Several random lengths of waveguide (with brazed cooling tubes) were arranged in a closed horizontal array and brazed together to form the required long lengths, such as the 38-ft pieces needed to extend through the penetrations between the klystron gallery and the accelerator housing. Before brazing the array of short pieces, they were filled with hydrogen through a capoff flange, and the hydrogen was burned at the output capoff flange. The series of brazes necessary to complete the assembly were then sequentially made with an oxygen–hydrogen ring flame burner. The silver–copper eutectic used in the braze was hand fed when the joint reached the proper temperature; no preplaced alloy was employed in the butt joints. This method produced excellent joints as verified by metallographic cross sections from samples and by the overall operating success of the machine to date. (At this writing, some of the joints are already 4 yr old).

11-3 Waveguide insulation and heat control

Accuracy of phase relationships and phase stability make it essential that the rectangular waveguide be closely temperature controlled during accelerator operation. The electrical length of a waveguide of length L is given by

$$\phi = \beta_g L \tag{11-2}$$

where β_g is the waveguide phase constant. Differentiating Eq. (11-2) with respect to temperature, T, gives

$$\frac{d\phi}{dT} = \beta_g \frac{dL}{dT} + L\frac{d\beta_g}{dT} \tag{11-3}$$

In the TE_{10} mode, β_g can be expressed as

$$\beta_g^2 = \beta_0^2 - \left(\frac{\pi}{a}\right)^2 \tag{11-4}$$

where $\beta_0 = 2\pi/\lambda_0$ is the free-space phase constant and a is defined in Fig. 11-5.

Therefore,

$$\frac{d\phi}{dT} = \beta_g \frac{dL}{dT} + \frac{L\pi^2}{\beta_g a^3} \frac{da}{dT} \tag{11-5}$$

From the coefficient of linear thermal expansion of the metal, α, one obtains

$$\alpha = \frac{da}{a\,dT} = \frac{dL}{L\,dT} \tag{11-6}$$

Combining Eqs. (11-5) and (11-6) gives

$$\frac{d\phi}{dT} = \frac{\alpha L}{\beta_g} \left[\left(\frac{\pi}{a} \right)^2 + \beta_g^2 \right] \tag{11-7}$$

Combining Eqs. (11-4) and (11-7) gives

$$\frac{d\phi}{dT} = \frac{\alpha L \beta_0^2}{\beta_g} = \frac{2\pi\alpha L \lambda_g}{\lambda_0^2} \tag{11-8}$$

where λ_g is the guide wavelength and λ_0 is the free-space wavelength. The value of α at the operating temperature of 113°F is 9.26×10^{-6}/°F, hence Eq. (11-8) gives $(d\phi/dT) = 0.0141$ electrical degree/ft/°F at the SLAC operating frequency.

Equation (11-8) was experimentally verified over a temperature range of 30°F, with very good agreement between theory and experiment.

Heat is generated in the high-power waveguide by the RF currents flowing in the waveguide walls. The rectangular waveguide itself has a resistive attenuation of about 6.3×10^{-3} dB/ft. In addition, each stainless steel flange pair has an attenuation of about 6.8×10^{-3} dB while the other components of the system have a total attenuation below 0.1 dB. The calculated average loss through a network from a klystron to an accelerator section is 0.54 ± 0.10 dB. Measurements using sliding shorts on the four outputs of a full-scale model gave a network attenuation of 0.5 dB. This attenuation will cause a heat dissipation of approximately 2.4 kW in the rectangular waveguide fed from a klystron delivering 21 kW average power. This power dissipation was verified using a full scale model of the waveguide layout. It is, therefore, necessary that the cooling system should provide close temperature control while dissipating 2.4 kW per accelerator feed and should be capable of handling higher powers when additional klystron stations are added.

The design work done by Lisin[7] led to a cross section for the temperature-stabilized cooling waveguide as illustrated in Fig. 11-8. Water flow rates are 10 gal/min in the full power waveguide and 5 gal/min in the waveguide carrying half-power or less. The 2°F temperature stability requirements made it necessary to use a polyurethane foam insulating jacket as shown in Fig. 11-8 to reduce the cost of temperature control. Insulation was applied to the cross-bar and penetration waveguides. It was unnecessary to insulate the waveguide in the accelerator housing because there is good temperature stability in this area due to the temperature control of the disk-loaded waveguide.

Table 11-2 Calculated power levels at accelerator input ports relative to klystron output

Waveguide network configuration	*Imbalance*	*Branch 1 (dB)*	*Branch 2 (dB)*	*Branch 3 (dB)*	*Branch 4 (dB)*
ABAB	Minimum	−6.52	−6.53	−6.57	−6.58
	Maximum	−6.42	−6.53	−6.57	−6.68
BABA	Minimum	−6.53	−6.51	−6.58	−6.56
	Maximum	−6.53	−6.41	−6.68	−6.56

Asymmetrical division of power from a klystron would result in unequal power dissipation in the accelerator sections and waveguide feeds. This would give rise to temperature and phase shift differentials. Consequently, considerable care was taken to obtain equal power distribution to the four branches of the waveguide network. Table 11-2 gives the best and worst cases of RF power imbalance obtained in the waveguide network, the worst case being due to imperfect division by the power dividers which have a 0.1 dB tolerance. This table gives the total attenuation (including power division) in each of the four branches from any one klystron to an accelerator section. Inspection of Table 11-2 shows that the maximum imbalance between any two feeds is 7% (0.27 dB).

11-4 Electrical phase length considerations

The schematic diagram (Fig. 11-10) of a 40-ft waveguide module defines N_n, the number of guide wavelengths between the klystron output and the four accelerator input ports. If the four branches of the waveguide network are tuned properly, a signal at 2856 MHz at the input will arrive in phase at each of the four output ports. The design phase length of the network is given in Table 11-3 for the two general configurations (ABAB and BABA, identifying the alternating accelerator input coupler orientation shown in Fig. 5-17).

The half-cycle phase length difference between the N_1 and N_2 branches and between the N_3 and N_4 branches corrects for the half-cycle inversion of the signal in passing through a right-handed E-plane bend as compared to the same wave through a left-handed E-plane bend with the same center-line

Table 11-3 Design phase lengths of branches of the wavelength layout

Waveguide network configuration	*Branch phase length in No. of λ_g's*			
	N_1	N_2	N_3	N_4
ABAB	118	$121\frac{1}{2}$	134	$137\frac{1}{2}$
BABA	123	$116\frac{1}{2}$	139	$132\frac{1}{2}$

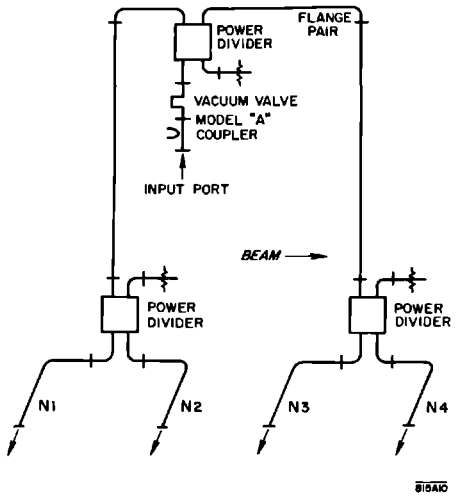

Figure 11-10 Schematic of a 40-ft unit of waveguide network.

length. There is one left-hand E-plane bend in the N_1 and the N_3 branches and one right-hand E-plane bend in the N_2 and N_4 branches. All of the other waveguide bends are H-plane types which do not exhibit this phase reversal.

The manufacturing tolerances of ± 0.005 in. on the internal dimensions of the waveguide correspond to an equivalent phase shift tolerance of $\pm 1.42°$/ft. Prior to phase adjustment of the waveguide layout, the above phase shift tolerance permits the phase shift through one branch of the network to differ as much as 170° from that through another branch. During installation of the waveguide layouts, the pretuning tests showed the phase differences between branches to be typically less than 60° although several with differences close to 180° were encountered.

The phase lengths at 2856 MHz of some waveguide components, such as bends, power dividers, and valves, relative to a reference straight length of waveguide, are given in Fig. 11-11.

Phase length adjustment of the waveguide branches for each klystron was accomplished by Weaver and Alvarez[8] by using a modulated reflection method similar to one suggested by Schafer[9] and later further developed and used by Swarup and Yang[10] to adjust a radio astronomy antenna array.

Each klystron is individually phased by an automatic system to obtain the correct phase relationship between the bunched beam and the wave in one particular accelerator section driven by that klystron. However, the high-power waveguide network must be permanently adjusted so that when the wave is phased correctly with respect to the beam in that one accelerator section, it is also phased correctly in the other three sections driven by that same klystron. Since the accelerator RF input ports are spaced by an integral number of wavelengths (29), the waveguide network branches must be

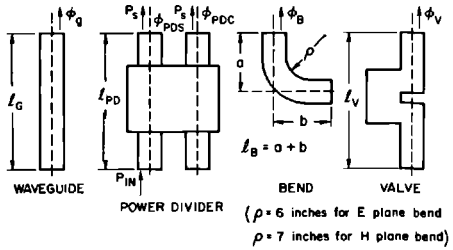

$\Delta\ell_g$	$\Delta\ell_{PDS}$	$\Delta\ell_{PDC}$	$\Delta\ell_B$ "E"	$\Delta\ell_B$ "H"	$\Delta\ell_v$
±0	+0.500"	+2.006"	−3.380"	−4.240"	+10.385"

Figure 11-11 Phase lengths of some waveguide components relative to straight waveguide at 2856 MHz.

adjusted to be equal in phase length, or to differ by only integral numbers of wavelengths.

The modulated reflection method for phase adjustment uses a separate diode-modulated reflector, or "modulator flange," at each of the four accelerator output ports. A 2856-MHz cw signal was fed to the input port of the waveguide network (see Fig. 11-12), then one reflector at a time was modulated at 1 kHz, and each return signal was compared in a phase bridge with a much larger unmodulated reference signal. The resultant signal will not exhibit a

Figure 11-12 Block diagram of phasing machine.

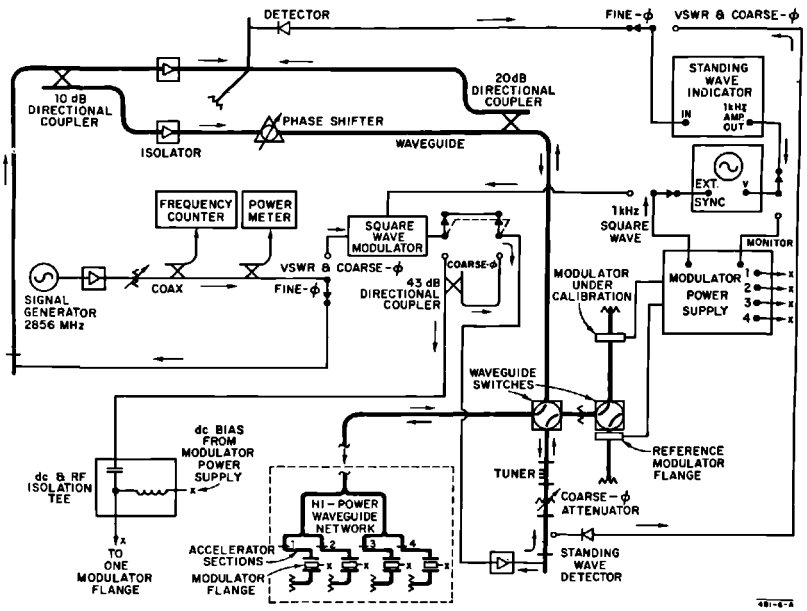

1-kHz amplitude modulation when the reference signal and the carrier of the modulated reflected signal are out of phase by 90°. While measurements are being made on one branch, the diodes in the other three modulator flanges are not switched, but are dc biased to cause little reflection. This allows comparison of the phase lengths of the four branches, subject to the half-cycle ambiguity of the reflection method. The half-cycle ambiguity is then resolved by a standard, transmission phase measurement using the modulator flanges as waveguide-to-coax adapters with a long coaxial cable providing the return path to the input port of the waveguide network. Instability in the coaxial cable limits the accuracy of this method to about 10°.

In the fine-phase (modulated reflection) measurement, the modulator power supply switches one of the four modulator flanges at a 1 kHz rate, forward-biases the other three, and triggers the oscilloscope sweep. The calibrated, dielectric slab phase-shifter is adjusted to produce a null in the 1-kHz amplitude modulation of the sum signal at the detector. The differences in phase shifter settings for the four branches of the network are direct measures of the phase length differences. The standing-wave indicator conveniently doubles as a 1-kHz tuned preamplifier for the detected amplitude modulation of the sum signal. The oscilloscope displays this amplitude modulation and serves also as the synchronous detector which resolves the quarter-cycle ambiguity. The standing-wave detector is used also in a separate measurement to measure the input reflection of the network after tuning. Additional facilities permit calibration of the reflection phases of the modulator flanges and monitoring of drift in the phasing machine.

The modulator flange (Fig. 11-13) consists of a diode switch mounted in a special stainless steel, S-band waveguide flange. Both sides of the flange are machined to form vacuum seals with the waveguide flanges. A point-contact germanium diode is spring loaded against the end of a post across the waveguide. Two adjustable tuning screws in the plane of the diode are used for

Figure 11-13 Modulator flange.

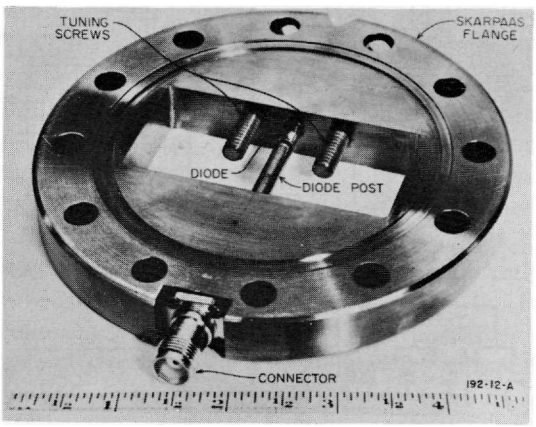

matching. The tuning screws and the diode post, which connects to the center conductor of a TNC fitting on the flange circumference, are vacuum sealed with Teflon O-rings. Thin gold plating on top of copper plating improves the calibration accuracy and the shelf life of the stainless steel flanges. When the flange is properly tuned, reverse biasing of the diode creates a large shunt admittance across the waveguide, which causes almost complete reflection. Forward biasing creates only a small shunt admittance, which causes little reflection. The tuning screws are adjusted so that the phases of the sums of the small and large reflections are the same in all four modulators. Because the diodes exhibit a nonlinear phase-versus-voltage characteristic, square-wave modulation simplifies understanding and analysis of the circuit. The modulator power supply switches the diode bias signal at a 1 kHz rate from -20 V to $+100$ mA. When the diode is reverse biased, the modulator flange serves as a waveguide-to-coax adapter with stable phase characteristics and a transmission loss of about 20 dB. Between the diode support post and the flange body, there is a capacitive reactance of about 1.4 ohms at 2856 MHz, which provides some isolation between the bias circuit and the microwave reflector circuit. Since a modulator flange is primarily a precision reflector, and only incidentally a waveguide-to-coax adapter, the 20-dB transmission loss is preferable to less isolation. Frequent recalibrations locate the position of the equivalent plane of reflection to better than $\pm 0.3°$. The major source of calibration error is the small movement due to slight distortion of the internal parts of the flange modulator during its installation. The modulator flange is the most critical component of the system.

The actual phase adjustments of the network were performed by permanently indenting the waveguide walls with special C-clamps having 12-in. jaws. Smooth indentations over a length of several feet easily produce phase shifts up to 60° between branches, which is generally the maximum correction required. A few networks were out of adjustment by almost 180° and required clamping over longer lengths to prevent significant reflections. Bowing in of the narrow wall of the waveguide decreases its phase length, and bowing in of the broad wall (with consequent bowing-out effects on the narrow wall) increases its phase length.

It was found that measurements could be repeated within $\pm 0.1°$. The modulator flanges have a calibration accuracy of better than $\pm 0.3°$, and the networks have a phase stability of better than $\pm 0.5°$. The accelerator sections are within $\pm 2.5°$ of their design lengths. Thus, the overall accuracy of phase adjustment is better than $\pm 4.5°$, allowing $\pm 1.0°$ for temperature instabilities for the accelerator sections.

11-5 Components of the waveguide system

Stringent specifications were applied to the rectangular waveguide components. Consequently, all components had to be specially developed, including the rectangular waveguide itself as discussed above. Because of the anticipated

addition of more klystron stations in the future, all components had to be capable of handling at least 24-MW peak and 21-kW average power. This meant that all reflection coefficients had to be below −30 dB and all component transmission losses had to be not greater than 0.1 dB for the above peak and average powers. Each component was tested at low and high power before installation to insure that the microwave and mechanical characteristics had been achieved.

During the development period, preproduction models of each component were tested and fully evaluated prior to writing final specifications and initiating production. Because only fully developed and tested designs were produced and because the amount of tuning and other operations required during production to produce satisfactory components was minimized, substantial cost savings resulted. Special facilities were set up to simplify production, tuning operations, and testing.

Flow charts were prepared for each item used in the waveguide layout. The charts showed all the detailed steps needed to fabricate, inspect, test, store, and install the various components. The following paragraphs provide brief descriptions of the principal specially developed components of the waveguide system.

Waveguide vacuum valve (Fig. 11-14)

The vacuum valve[11] is an all-metal structure which is used to isolate the evacuated waveguide layout and the accelerator from exposure to air during replacement of the high-power klystron tube used to drive the accelerator.

The microwave structure consists of a resonant iris in the common broad wall of the two adjacent waveguides. The positions of the shorting plates were determined empirically and are the same in all valves. The positions were adjusted so that, in conjunction with the E-plane 90° miter joints, a bilateral standing-wave ratio of 1.08 or less was obtained at the operating frequency prior to tuning. All production units were tuned by squeezing the walls of the input and output waveguide so that the VSWR was reduced to 1.02 or less.

Continuity of wall currents in the upper waveguide section is achieved through the copper gasket and copper-plated mating surfaces in the backseat region.

The vacuum structure of the waveguide valve is composed of the brazed body and plunger subassemblies. The vacuum seal between these subassemblies is made by means of a crush seal joint and a copper gasket. The recurrent vacuum seal for klystron replacement is made by forcing the plunger assembly's circular stepped knife edge into an indium-filled groove concentric with the circular resonant iris in the common broad wall between the two waveguides. The closing force is provided by a lead screw actuator which attaches directly to the plunger assembly. By using concentric machined steps, several sealing edges are achieved simultaneously. More than 200 closures have been obtained on a single seal (i.e., with leak rates $< 24 \times 10^{-8}$ std cm^3 He/sec) in

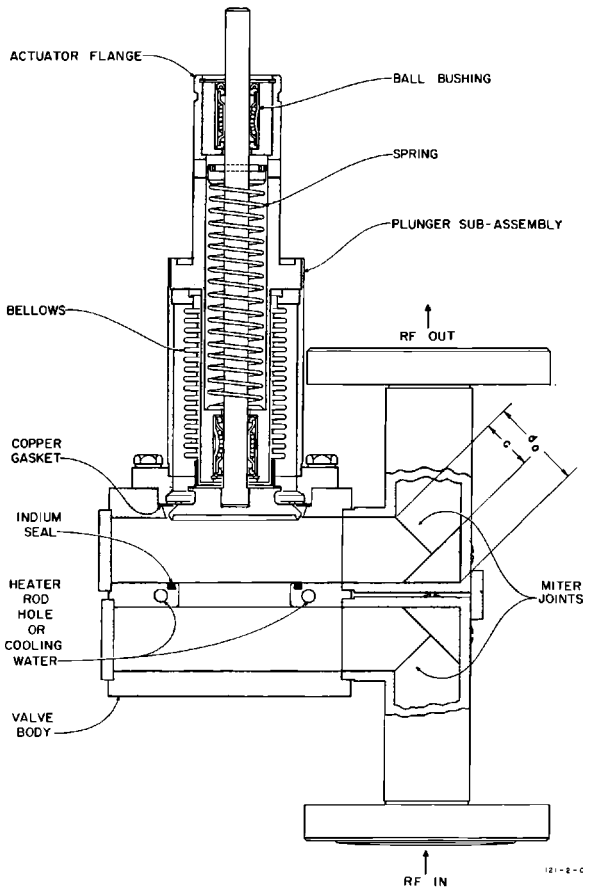

Figure 11-14 Cross-sectional view of waveguide valve assembly.

test units. When the indium seal has become heavily indented after many closures, the surface can be readily renewed by remelting the metal (melting point, 156.6°C) so that it re-forms smoothly in the groove. To achieve this, heater rods are installed in the valve body. The remelting process requires approximately 1½ hours (including cool-down) and can be performed while the valve is installed and operating at low pressures in the accelerator vacuum system.

Considerable attention was given to the problem of casting good indium seals, i.e., achieving an indium-to-stainless steel interface which is free of leak paths and stable under repeated closures. The process which was developed is composed of two steps: a casting or wetting of the indium into the stainless steel groove in a dry hydrogen atmosphere and a remelting of the indium while it is under vacuum. The first step is performed at temperatures

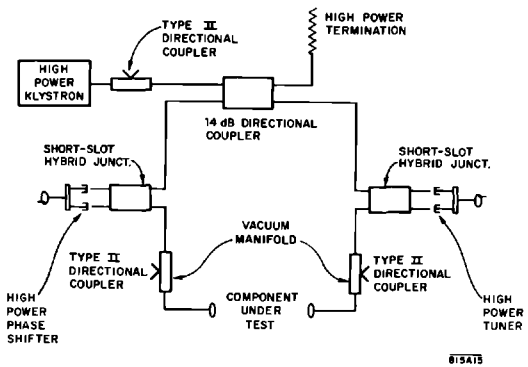

Figure 11-15 Schematic representation of resonant-ring test facility for waveguide vacuum valves.

between 750° and 850°C. The dry hydrogen atmosphere reduces the oxides both on the indium and the stainless steel so that a wetting or interface alloying of the metals can take place. Two runs are made, the first using only a small amount of indium to wet the surfaces of the groove, and the second with the groove filled to the desired level. This entire process is visually monitored since the length of time required and the temperature are not easily specified. They are affected by the dew point of the hydrogen as well as by the initial conditions of the stainless steel, the indium, and even the furnace.

Upon completion of the furnace processing, the assembly is placed on a vacuum station evacuated by an ion-getter pump where the newly cast indium is remelted using external heaters. Vacuum levels on the order of 10^{-5} torr are maintained, but bursts of gas are detectable as the indium melts. The release of these entrapped gases is sometimes accompanied by sputtering of indium onto the surrounding surfaces. The sputtered indium is prevented from reaching the copper-plated inner surfaces of the valve (where it would cause etching) by covering the seal with a hood during this first vacuum remelt. Subsequent remelting of the seal while the valve is installed does not result in significant sputtering.

Each vacuum valve was tested at RF powers of 60-MW peak and 24-kW average power using the resonant ring illustrated in Fig. 11-15. In addition, each valve is cycle-tested 5 times with a maximum allowable leak rate of 1×10^{-8} std cm^3 He/sec.

Directional couplers

A directional coupler is a four-port junction (Fig. 11-16). Providing all ports of this junction are matched, the coupling between ports 1 and 3 and between ports 2 and 4 is zero. Montgomery, Dicke, and Purcell[12] prove that any matched four-port junction is a directional coupler.

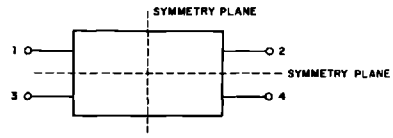

Figure 11-16 Directional coupler schematic.

Three types of directional couplers were used in the waveguide layout. These couplers are listed in Table 11-4 by type, coupling ratio, isolation, and application in the waveguide system. In each case the designs were guided by the necessity to achieve good vacuum performance, compact structure, high isolation, electrical characteristics that are stable with time, and uniformity of coupling ratio.

The properties of the couplers used in the waveguide layout are expressed succinctly by means of the scattering matrix notation. Let $[b_i]$ be a column vector representing the scattered voltages from the four ports, $[a_j]$ be a column vector representing the input voltages, and $[S_{ij}]$ be a 4×4 scattering matrix of the junction. Then

$$[b_i] = [S_{ij}][a_j] \tag{11-9}$$

When $i \neq j$, S_{ij} is the transmission coefficient between ports i and j, and when $i = j$, S_{ii} is the reflection coefficient of port i. Each of the coupler types are reciprocal and symmetrical. Therefore:

$$\begin{aligned} S_{ij} &= S_{ji} \\ S_{11} = S_{22} &= S_{33} = S_{44} \\ S_{12} = S_{21} &= S_{34} = S_{43} \\ S_{13} = S_{31} &= S_{24} = S_{42} \\ S_{14} = S_{41} &= S_{23} = S_{32} \end{aligned} \tag{11-10}$$

Table 11-4 Types and applications of directional couplers in the waveguide layout

Type	*Directional coupler type*	*Nominal coupling ratio (dB)*	*Typical isolation (dB)*	*Waveguide layout application*
I	Short-slot hybrid junction	−3	40	Power divider
II	Modified Bethe hole	−52	80	Sample forward and reflected power at klystron output to monitor klystron performance and provide protection against waveguide arcing
III	Cross guide	−20	40	Sample beam-induced power out of 10-ft accelerator section for use as a reference signal in the automatic phasing system

From Eq. (11-10) the scattering matrix is simplified to

$$S = \begin{bmatrix} S_{11} & S_{12} & S_{13} & S_{14} \\ S_{12} & S_{11} & S_{14} & S_{13} \\ S_{13} & S_{14} & S_{11} & S_{12} \\ S_{14} & S_{13} & S_{12} & S_{11} \end{bmatrix} \tag{11-11}$$

In an ideal well-matched coupler $S_{11} = 0$ and $S_{13} = S_{24} = 0$ representing complete isolation. In this case the scattering matrix reduces to

$$S = \begin{bmatrix} 0 & S_{12} & 0 & S_{14} \\ S_{12} & 0 & S_{14} & 0 \\ 0 & S_{14} & 0 & S_{12} \\ S_{14} & 0 & S_{12} & 0 \end{bmatrix} \tag{11-12}$$

The directional couplers are essentially lossless, and, therefore, the scattering matrix is unitary, i.e.,

$$[S_{ij}][S_{ij}^*] = 1 \tag{11-13}$$

Inserting matrix Eq. (11-12) into Eq. (11-13),

$$|S_{12}|^2 + |S_{14}|^2 = 1 \tag{11-14}$$

$$S_{14}S_{12}^* + S_{12}S_{14}^* = 0 \tag{11-15}$$

If one inserts $S_{14} = |S_{14}|e^{j\phi_4}$ and $S_{12} = |S_{12}|e^{j\phi_2}$ into Eq. (11-15), then

$$\cos(\phi_4 - \phi_2) = 0 \tag{11-16}$$

giving a 90° phase shift between the signals in the output of a matched lossless symmetrical coupler with perfect isolation. Levy[13] shows that with slightly imperfect couplers the phase shift deviation from 90° is related to the isolation. For example, the output signals will deviate 0.1° from 90° in a coupler of which the isolation I is 30 dB, where I in decibels is defined as

$$I_{\text{dB}} = 10 \log_{10} \frac{1}{|S_{13}|^2} \tag{11-17}$$

Levy[13] further shows that in an imperfect coupler the magnitude of the reflected signal at an input port is nearly equal to the magnitude of the signal emerging from the decoupled port as follows;

$$|S_{11}| \approx |S_{13}| \tag{11-18}$$

Measurement of the match looking into a port in a directional coupler provides by Eq. (11-18) a very useful check of the isolation.

In two of the couplers used in the waveguide layout, directivity of coupling is an important consideration. Directivity of a coupler in decibels is defined by the equation

$$D_{\text{dB}} = 10 \log_{10} \frac{|S_{14}|^2}{|S_{24}|^2} \tag{11-19}$$

and is a measure of the capability of the coupler at, say port 4, to distinguish

a "forward" unit signal incident at port 1 from a "backward" unit signal incident at port 2. If the coupling of a directional coupler C in dB is

$$C_{dB} = 10 \log_{10} |S_{14}|^2 \tag{11-20}$$

then the coupling, isolation, and directivity of the coupler are related as follows:

$$D_{dB} = C_{dB} + I_{dB} \tag{11-21}$$

With the relationships developed in the above paragraphs, one can now turn to the design of the couplers used in the network.

Power divider

The three power dividers used in each of the waveguide modules have the function of dividing the power output from a klystron into four equal parts. These power dividers are directional couplers with

$$|S_{12}| = |S_{14}| \tag{11-22}$$

Directional couplers in which Eq. (11-22) holds true are called hybrid junctions because they are analogous to the hybrid repeating coils used in telephone technology. Of the various hybrid junctions available, the short-slot, narrow wall, coupled junction[14,15] was considered to be the most satisfactory because it has high-power handling capacity and each of its ports lies in the same plane. For example, tests indicate that a short-slot hybrid can operate without voltage breakdown at more than 70% of the power capacity of the terminal waveguides. The corresponding power levels in top-wall hybrids and magic T's are 40% and 17%, respectively.

The design of short-slot hybrid junctions (Fig. 11-17) is simplified by analysis of the coupling region using a superposition of even and odd modes. The TE_{10} mode is used as the even mode and the TE_{20} mode is used as the odd mode (Fig. 11-18). The width of the hybrid junction in the coupling region must be large enough to propagate the TE_{20} mode but must be small enough to prevent propagation of the TE_{30} mode (a higher-order even mode) at the operating frequency.

Figure 11-17 Cutaway view of a short-slot hybrid junction showing coupling iris.

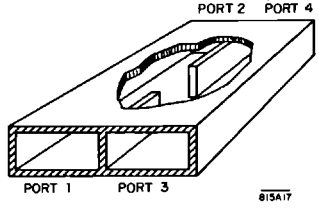

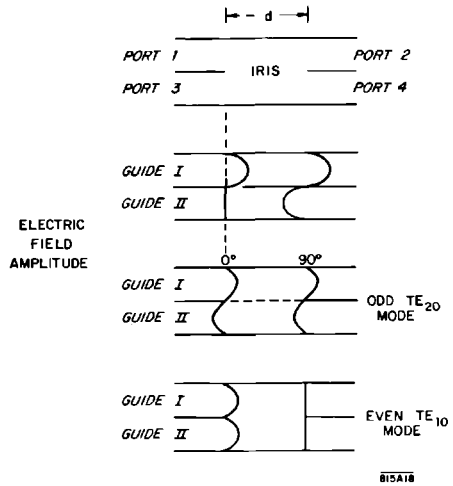

Figure 11-18 Superposition of even and odd modes in a hybrid junction.

The coupling iris is made long enough to provide just 90° phase shift between the even and odd modes as required by Eq. (11-16). Thus, if d is the length of the coupling iris,

$$\frac{2\pi d}{\lambda_{g_e}} - \frac{2\pi d}{\lambda_{g_0}} + \phi_r = \frac{\pi}{2} \tag{11-23}$$

where λ_{g_e} is the guide wavelength in the coupling region of the even TE_{10} mode, and λ_{g_0} is the guide wavelength of the TE_{20} odd mode. The phase shift ϕ_r accounts for reflections at the ends of the coupling iris. At first, ϕ_r is neglected and Eq. (11-23) is solved for d

$$d = \frac{\lambda_0}{4}\left\{\frac{1}{[1-(\lambda_0/\lambda_{c_e})^2]^{1/2} - [1-(\lambda_0/\lambda_{c_0})^2]^{1/2}}\right\} \tag{11-24}$$

where λ_{c_e} and λ_{c_0} are the cut-off wavelengths in the even and odd modes, respectively.

Equation (11-24) is plotted (Fig. 11-19) to provide the initial design length for the coupling iris after a choice is made for the cavity width within the constraints shown for TE_{30} and TE_{20} mode propagation.

An arbitrary choice of cavity width at 5.500 in. permitted operation of the hybrid sufficiently below cutoff for the TE_{30} mode. Hybrid junctions were fabricated with this width and with several different iris lengths near the value 3.850 in. indicated in Fig. 11-19 in order to determine empirically the value ϕ_r and the proper length d to give the desired 90° phase shift.

Fabrication of the hybrid junctions for high-vacuum application required the spacing between the terminal waveguides to be larger than is usual in

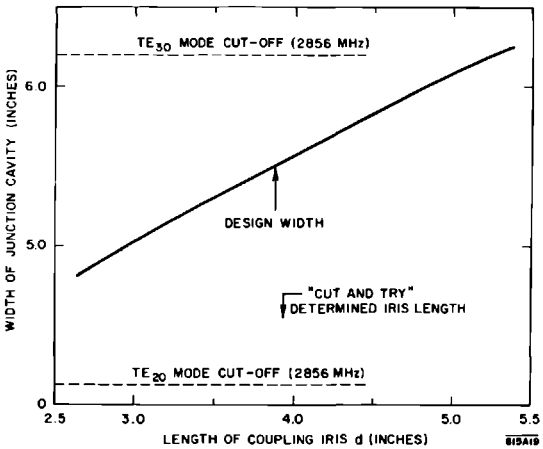

Figure 11-19 Plot of short-slot hybrid junction iris length d as a function of cavity width (assumes $\phi_r = 0$).

nonvacuum junctions. This resulted in a very thick septum at the terminals of the coupling iris. The thick septum gives an appreciable reflection coefficient not only for the even mode but also for the odd mode and this reflection must be cancelled. Stoesser[16] indicates that a septum whose width is 5% of the terminal waveguide width may be corrected by increasing the iris length by 10% above that predicted by Eq. (11-24). It was necessary to use a septum of which the width (0.400 in.) is 14% of the terminal guide width (Fig. 11-20), and compensation for this width was accomplished not only by lengthening the iris to 3.930 in. but also by using capacitive loading at the center of the coupling iris. The centrally located capacitive buttons more strongly affect the even mode guide wavelength than they do the wavelength of the odd mode.

Figure 11-20 Cross-sectional view of hybrid junction showing critical dimensions.

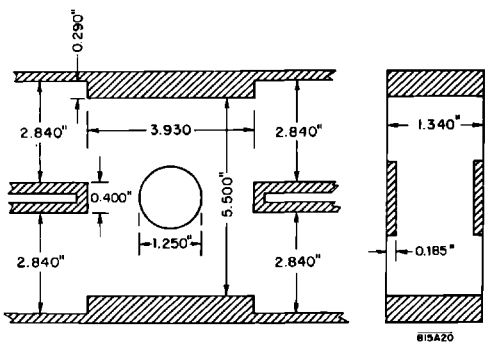

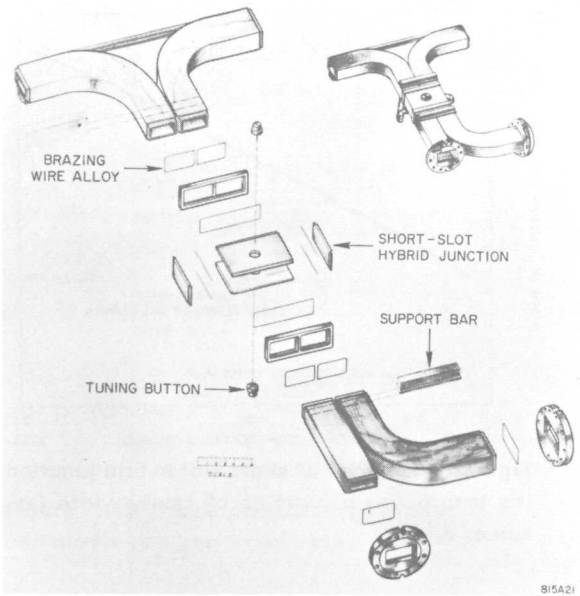

Figure 11-21 "Exploded" view of Type I, 3-dB, directional coupler.

Figure 11-22 Photograph of Type I directional coupler mounted in place in the klystron gallery.

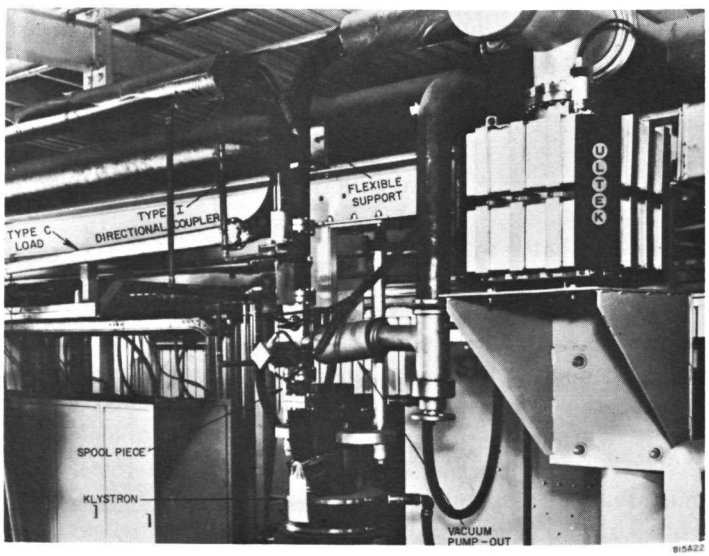

On the other hand, small changes in width of the iris region strongly affects the guide wavelength of the odd mode. It was found by experiment that buttons 1.250 in. in diameter and 0.185 in. high on both bottom and top walls of the junction gave satisfactory performance.

The copper parts for the junctions were designed to be brazed together in a self-jigging method to give near uniform electrical characteristics with little required tuning. Figure 11-21 is an "exploded" view of the hybrid junction. Figure 11-22 is a photograph of a typical power divider with its terminal waveguides and water-cooling connections.

Approximately 800 hybrid junctions were fabricated. The junctions were measured and, after slight tuning by wall deformation, each junction gave a maximum deviation from equal power division of 0.1 dB and isolation values no less than 40 dB (typically 40–50 dB). These values of isolation correspond to input reflection coefficients ($|S_{11}|$, $|S_{22}|$, $|S_{33}|$, and $|S_{44}|$) of less than 0.01.

Modified Bethe hole coupler

A modified Bethe[17] hole coupler was used at the output of the klystron for power sampling. The coupling ratio is -52 dB with 80 dB isolation. In addition to the power sampling function, the Bethe hole coupler unit contains the pump-out for the vacuum connection, the vacuum gauge, and the only fixed tie point of the waveguide system. Figure 11-23 is a photograph of the complete unit.

The modified Bethe hole coupler, which henceforth will be referred to as the "Type II directional coupler," differs from a conventional Bethe hole

Figure 11-23 Photograph of Type II directional coupler.

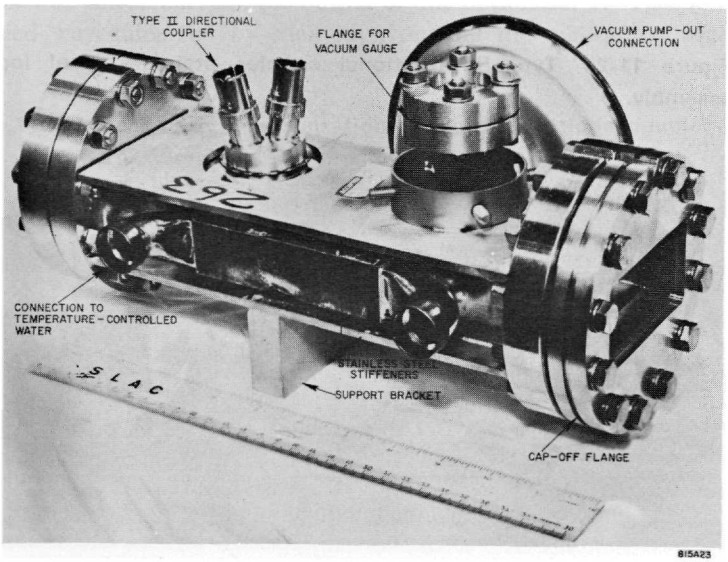

coupler in that the secondary waveguide has been replaced by a coaxial strip line loop which is external to the primary waveguide. The motivations leading to the development of this new type coupler stemmed from the necessity for conserving space and reducing costs. The design used allowed the inclusion of a waveguide pump-out and vacuum gauge in the same space that would have been occupied by a conventional-type coupler. It was possible to design the coupler so that the coaxial strip line loop operated in air while the coupling hole and primary waveguide were a part of the evacuated system. This was made possible by using a dielectric window, as shown in Fig. 11-24. The coupling loop was designed to be a strip line terminated by 50-ohm coaxial cables. The dimensions of the strip line and spacing between the line and ground plane were determined empirically. The dimensions chosen minimized the reflection coefficients $|S_{33}|$ and $|S_{44}|$. The coupling loop was mounted on the primary waveguide in such a way that it could be installed by welding two stainless steel eyelets together. Once a coupling loop assembly (Fig. 11-24) had been fabricated and was found to have a reflection coefficient less than $|0.02|$, the loop was mounted on the waveguide and rotated for optimum directivity which was at least 25 dB and typically 28 dB. The loop assembly was then clamped in the proper orientation and tack-welded. The directivity was then remeasured and if found unchanged the coupling loop assembly was completely heliarc-welded, and the coupler was then ready for final calibration.

The Type II couplers were calibrated using three independent approaches; the intermediate frequency (IF) substitution method (see Fig. 11-25), the calorimetric method at high power, and the RF substitution method after installation in the waveguide network. The coupling values of 250 couplers, as determined by the three techniques, were all identical within a spread of 0.3 dB. Two of the Type II couplers were used as monitors in the resonant

Figure 11-24 Type II directional coupler—stainless steel loop assembly.

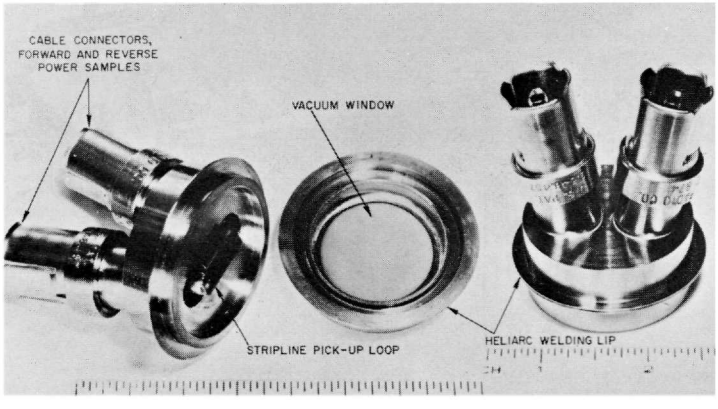

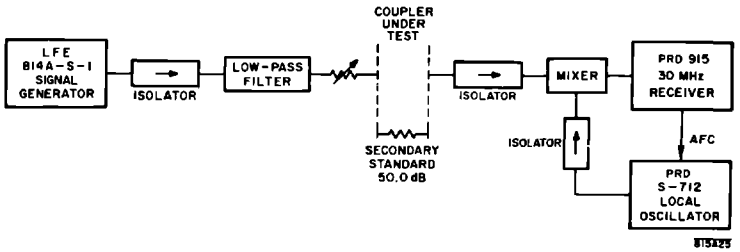

Figure 11-25 Intermediate frequency substitution technique for calibration of Type II directional couplers.

ring to measure ring power. These two couplers operated satisfactorily in the ring at power levels of 90 MW peak and 40 kW average.

The coaxial cables terminating the Type II couplers were 20 ft long, with an approximate attenuation of 3 dB per cable. The coaxial cables from a given coupler were terminated by low-pass filters and strip-line directional couplers (Fig. 11-26) to distribute samples of the forward and reflected power with minimum interaction to a waveguide breakdown detector, and to ports which may be used for monitoring power and pulse shape. The 20-ft cables and the strip-line power distribution package provide the necessary low VSWR termination for the Type II couplers.

Cross guide coupler

In order to provide beam-induced RF signals to operate the automatic phasing system which phases the input to each klystron, a Moreno-type,[18] cross guide coupler was placed between the output of one of the four 10-ft sections of disk-loaded waveguide fed by each klystron and the high-power load

Figure 11-26 Schematic representation of Type II directional coupler—signal sampling network.

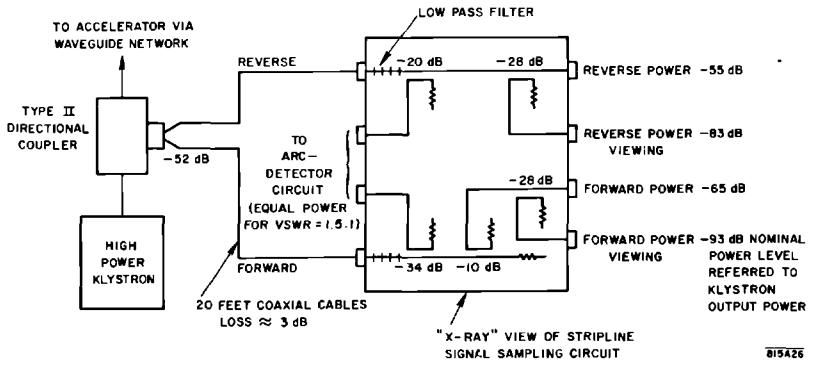

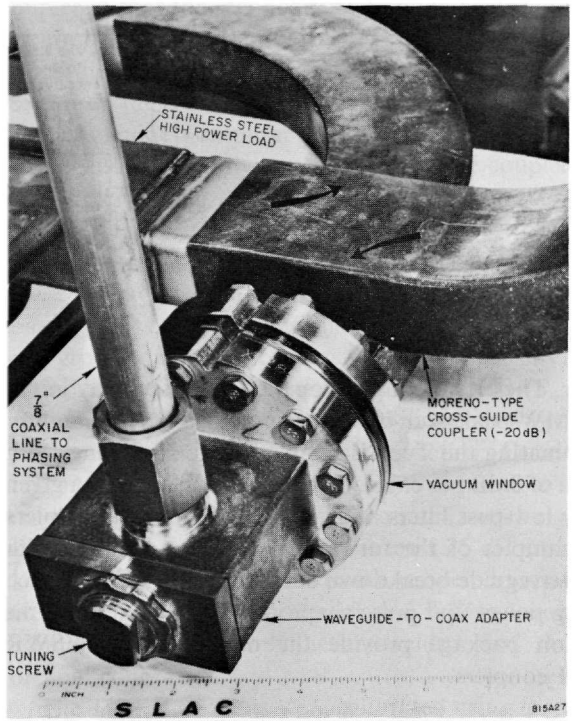

Figure 11-27 Type III directional coupler.

terminating that section. The section used is alternately the second (in an "ABAB" module) and the third (in a "BABA" module). The coupler has a −20 dB coupling coefficient and a directivity of 20 dB. This same coupler design is also used for two applications in the positron source area. The Moreno coupler operates in vacuum, the decoupled port being terminated in an all-metal high vacuum load. The coupled port is connected to a vacuum window (Fig. 11-27) and then to a waveguide-to-coaxial line transition. The coaxial line is a standard $\frac{7}{8}$-in. 50-ohm impedance cable. The assembly of the coupler window and waveguide-to-coaxial line junction was tested to 100-kW peak power without evidence of failure. The 100-kW peak is in excess of the maximum power expected at the coupler when all the power from a klystron drives a single accelerator section.

Waveguide flanges

To facilitate installation, maintenance, and repair of the rectangular waveguide network, it was necessary to develop a rectangular waveguide flange joint which would make a high vacuum seal and handle high RF powers.

The specifications established for the flanges were as follows:

1. No organic seals or gaskets were to be used in the flange joints.
2. The flange pair when assembled with a gasket should provide a joint which has a VSWR of 1.015 or less at a frequency of 2856 $\pm$ 100 MHz.
3. The flange pair should be capable of transmitting 40-kW average and 90-MW peak power.
4. The flange pair should withstand at least twenty opening and closing cycles, provided a new gasket was used each time the seal was remade.
5. The completed seal should have a leak rate not greater than 2×10^{-10} std cm^3 He/sec.
6. The assembled flange pair should be leak tight when subjected to a bake-out cycle consisting of heating at a rate of 100°C/hour to a peak of 560°C, holding at this temperature for 48 hours and cooling at a rate of 100°C/hour.
7. The maximum angular mismatch between two assembled flanges should not exceed 0.25°.
8. The maximum offset between two assembled flanges should not exceed 0.010 in. in any symmetry plane.

The specification regarding leak rate during a bake-out cycle resulted from klystron manufacturing experience. Paradoxically, the final flange used in the rectangular waveguide network is not yet in use on the klystrons because klystron manufacture was started prior to the development of the rectangular waveguide network, and a different flange design is used. In order to transform to the klystron flange, a spool piece is inserted between the terminal point of the rectangular waveguide and the klystron. The spool piece comprises a short piece of waveguide with the specially developed Skarpaas[19] flange on one end and a Merdinian[20] flange matching the klystron on the other end. An additional reason for use of the spool piece is to protect the flange on the end of the major waveguide system. When a klystron is being replaced, only the spool piece flange is subject to risk of accidental damage. If this occurs, it can easily be replaced.

It is easier to make a reliable vacuum joint with a circular seal. However, microwave continuity requires a high current joint which follows the rectangular periphery of the waveguide, at least across the broad walls. The RF currents for the dominant TE_{10} mode flow longitudinally on the broad walls and only in the transverse direction on the narrow walls. Hence good contact is not necessary on the narrow walls of the waveguide at the joint. Good contact along the broad walls of the waveguide is achieved by making the male flange slightly conical and the female flange flat. The vacuum requirement is met by a circular male–female configuration on the mating flanges which shears into the copper gasket. In assembly, the first points of contact with the gasket are in the center of each of the strips forming the rectangular aperture in the gasket. As the bolts are tightened, a near line contact is obtained along each strip. It can be seen from Fig. 11-28 that the only regions of

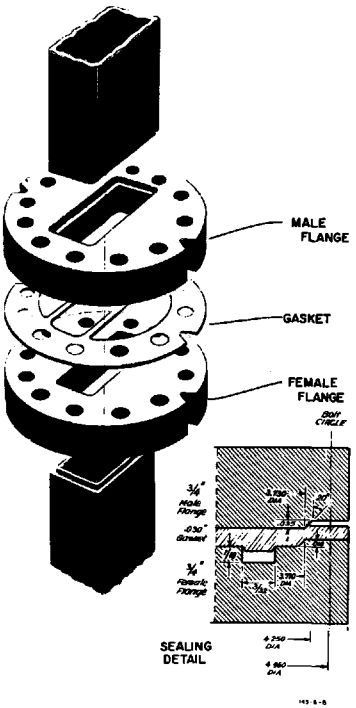

Figure 11-28 Waveguide flange (Skarpaas) vacuum seal and copper gasket.

high-pressure contact between the flanges and the gasket are these two narrow strips of copper coplanar with each broad wall of the waveguide and an outer copper ring which forms the vacuum joint. The width of the copper strips was kept small to insure high contact pressure and to minimize the vacuum virtual leak problem. The void between the flanges that is formed between the strips and the circular vacuum seal is evacuated by means of a pump-out groove which opens into the narrow wall of the waveguide.

The critical alignment of the flanges during assembly is achieved by a clamp band which holds two precision dowels in the precision alignment "V" slots during the operation of inserting and torquing the bolts. Approximately 6000 pairs of flanges were fabricated and installed in the waveguide network with no difficulties during installation or failures to date, which is 2 yr after installation.

Waveguide loads

High-power and low-power vacuum RF loads were required to terminate each 10-ft section of the disk-loaded accelerator waveguide and to terminate the power dividers. A number of design approaches were considered, some

of which used lossy dielectrics. An all-metal design was finally adopted, using a resistive coating on the inside walls of tapered rectangular waveguide to dissipate the RF power in the form of skin losses. The basic construction used was the same for both the low-power and the high-power loads. The high-power loads were water cooled by means of copper tubes brazed onto the outside walls.

The heat exchange problem for the high-power load was simplified by making the rate of heat dissipation along the length of the load as uniform as practical.

The power, $P(z)$, in the load should decrease linearly from the input power P_0 at $z = 0$ to zero at $z = L$, where L is the length of the load. Thus,

$$P(z) = P_0\left(1 - \frac{z}{L}\right) \tag{11-25}$$

Differentiating Eq. (11-25) gives

$$\frac{dP(z)}{dz} = -\frac{P_0}{L} \tag{11-26}$$

The attenuation constant, $\alpha(z)$, is defined as follows:

$$\alpha(z) = -\frac{1}{2P(z)}\frac{dP(z)}{dz} \tag{11-27}$$

Combining Eqs. (11-26) and (11-27) gives

$$2\alpha(z)P(z) = \frac{P_0}{L} \tag{11-28}$$

Substituting Eq. (11-25) into Eq. (11-28) gives

$$\alpha(z) = \frac{1}{2(L - z)} \text{ Np/unit length} \tag{11-29}$$

The attenuation constant α for the TE_{10} mode in rectangular waveguide is given by the following relationship:

$$\alpha = \frac{2R_s v^2}{a\eta[1 - v^2]^{1/2}} + \frac{R_s}{b\eta[1 - v^2]^{1/2}} \tag{11-30}$$

where

R_s is the surface resistivity of the waveguide walls
a and b are the waveguide cross section dimensions (Fig. 11-5)
η is the intrinsic impedance of the medium
v is λ/λ_c, the ratio of the free space wavelength to the cutoff wavelength in the waveguide

Equation (11-30) illustrates that $\alpha(z)$ may be controlled by varying dimensions a and b of the cross section if the surface resistivity is held constant. Large values of α can be obtained by reducing the cross section as a function of length.

Ideally, a load should absorb all incident waves with no reflection, which requires $\alpha(z)$ to be infinite when $z = L$. However, in a practical load a one-way attenuation of 15 dB produces a reflection coefficient $|S_{11}|$ of 0.03. A tapered load, 5 ft in length, that is properly coated can be readily made to give 15 dB attenuation.

Surface resistivity is defined as

$$R_s = \frac{1}{\sigma\delta} = \left(\frac{\pi f \mu}{\sigma}\right)^{1/2} \text{ohms/square} \tag{11-31}$$

where

σ = conductivity in mhos/meter
δ = skin depth, in meters
f = frequency in hertz
μ = permeability in henrys/meter

Equation (11-31) indicates that for good attenuation, an absorbing material should have low electric conductivity and high permeability at a given frequency. In addition, the absorbing material must be stable and have good vacuum properties for evacuated waveguide networks. Kanthal,* an iron alloy (iron, 20–30% chromium, 5% aluminum, and traces of manganese), meets these requirements reasonably well. There is also considerable vacuum experience with the material as an absorber in high-power microwave tubes. Accordingly, Kanthal was selected as the absorber material. Nalos[21] measured the resistivity of Kanthal to be 1.2 ohms/square for a film 0.002 in. thick on a copper base using a resonant cavity technique. Experiments with films 0.006–0.010 in. thick on a stainless steel base with WR-284 waveguide configuration indicated that 0.7 dB/ft attenuation could be achieved at 2856 MHz. This attenuation corresponds to a surface resistivity of 1.86 ohms/square. In both cases, Kanthal wire was flame-sprayed onto the base material. The higher resistivity apparently resulted from the greater thickness of the film and from increased surface roughness that accompanied the thick film. Films thicker than 0.008 in. did not result in increased attenuation. Conductivity of Kanthal was measured to be 7.32×10^3 mhos/meter ($\pm 10\%$). From Eq. (11-31) the skin depth of Kanthal at 2856 MHz is approximately 0.003 in.

To achieve the most economical load design, a straight taper in both the a and b dimensions from the WR-284 waveguide size was used down to a cross section $a' = 2.08$ in. (just above cutoff at 2856 MHz) and $b' = 0.280$ in. The stainless steel walls used to fabricate the taper were prepared for welding

* Registered by the Kanthal Corporation, 1 Wooster, Bethel, Connecticut; special electric resistance alloys.

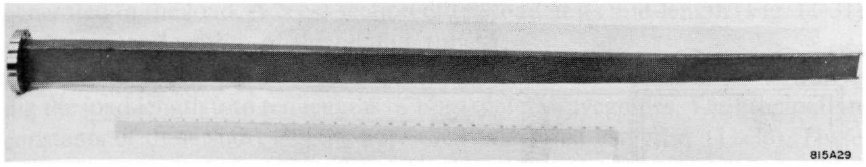

Figure 11-29 Photograph of stainless steel low-power vacuum load.

by cleaning for vacuum, then by sandblasting (to increase the surface roughness for good bonding to the Kanthal film), and then by flame-spraying Kanthal wire to a uniform depth inside a mask that protected the edge to be welded. The walls were then tack-welded together to form a taper, using an aluminum mandrel. The final welding took place in an automatic heliarc welder to insure a full penetration weld along the corners.

After welding, the loads were vacuum baked at 600°C for 24 hours with the terminal vacuum level at 10^{-6} torr. Approximately 2000 loads, half high-power and the other half low-power, were fabricated. The loads typically had an input reflection coefficient $|S_{11}| = 0.05$ before tuning. The low-power loads (Fig. 11-29) were tuned to give $|S_{11}| < 0.02$ by dimpling the stainless steel walls. The high-power loads (Fig. 11-30) were tuned under high-power operation on a test stand. Processing the load at high power is a procedure in which the input power is increased slowly in steps to outgas the load with RF. Foreign materials with low work functions cause multipactoring and require

Figure 11-30 Photograph of stainless steel high-power vacuum load.

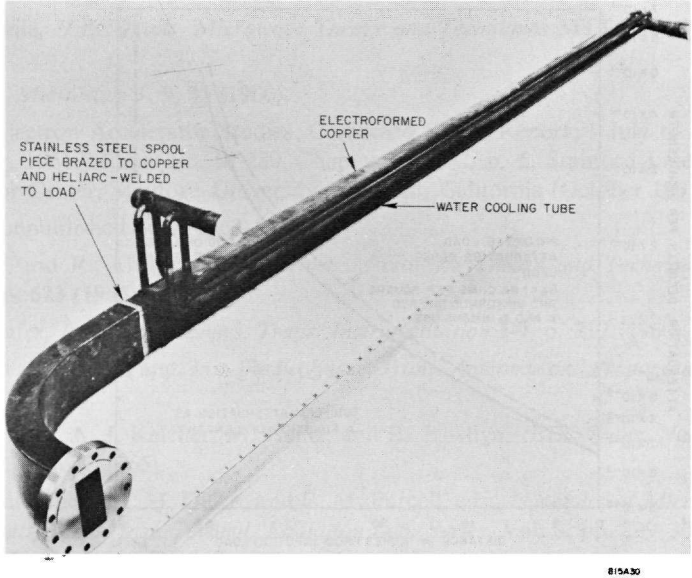

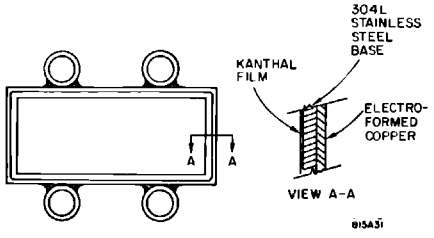

Figure 11-31 Cross-sectional view of high-power RF load.

sufficient local heating to burn them off. After processing, the high-power loads were tuned to minimize the reflection coefficient. Some of the high-power loads were tested at power levels of 18 MW peak with reflection coefficients less than 0.17. Most of the high-power loads were tested only to power levels of 8 to 10 MW peak power. The maximum input power to the loads is approximately 2 MW peak, when one klystron is used to drive four 10-ft sections of disk-loaded waveguide.

Attachment of cooling tubes to the high-power loads was accomplished by first electroforming a thick layer of copper onto the outside walls of the load and then brazing the copper tubes to the surface. The electroformed copper provides a good thermal conduction path to the water-cooling tubes for heat

Figure 11-32 Comparison of predicted load attenuation with uniform attenuation per unit length of load.

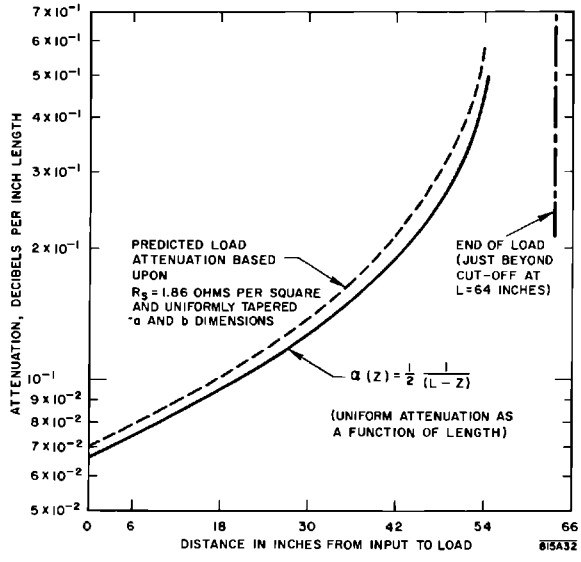

generated in the load. A cross section of the load at its mid-length (Fig. 11-31) illustrates the location of the cooling tubes.

The predicted rate of heat dissipation of the load was determined by dividing the load length into ten lengths of nontapered waveguides. The attenuation constants of these short lengths were then calculated using Eq. (11-30). These constants were compared to the desired values from Eq. (11-29). (See Fig. 11-32). No hot spots in the loads were observed, and the minimum one-way attenuation of 15 dB was achieved. During 2 yr of operation only one load failed due to multipactoring problems.

Acknowledgments

The authors would like to acknowledge the creative contributions of the following people whose efforts were instrumental in the successful completion of the rectangular waveguide network: M. Adams, R. Alvarez, C. Angelos, R. Borghi, R. Chapton, M. Gan, A. Guidi, A. Keicher, R. Lam, A. Lisin, E. Marshall, R. Messimer, J. Pope, C. Rasmussen, K. Skarpaas, H. Soderstrom, B. Stillman, J. Weaver, and H. Zaiss.

References

1 G. L. Matthaei, L. Young, and E. M. T. Jones, *Microwave Filters, Impedance-Matching Networks, and Coupling Structures*, McGraw-Hill, New York, 1964, p. 910.

2 H. J. Riblet, *Proc. Inst. Radio Engrs.* **40**, 180–184 (1952).

3 D. Tsang and A. Keicher, unpublished notes.

4 L. G. Virgile, *IEEE Trans. Microwave Theory and Techniques* **MTT-5**, p. 247 (1957).

5 L. Young, *Microwave J.* **9**, 45 (1966).

6 "Linear Electron Accelerator Studies; Combined Status Report; 1 July to 30 September, 1961," Rept. No. M-280, Chapter III, F-2, p. 5, Stanford Linear Accelerator Center, Stanford University, Stanford, California (October 1961).

7 A. Lisin, unpublished note (1963).

8 J. Weaver and R. Alvarez, *IEEE Trans. Microwave Theory and Techniques* **MTT-14**, p. 623 (1966).

9 G. E. Schafer, *Inst. Radio Engrs. Trans. Instrumentation* **I-9**, p. 217 (1960).

10 G. Swarup and K. S. Yang, *Inst. Radio Engrs. Trans. Antennas and Propagation* **AP-9**, p. 75 (1961).

11 A. L. Eldredge, A. J. Keicher, M. Heinz, and R. J. Allyn, *IEEE Trans. Nucl. Sci.* **NS-12**, p. 694 (1965).

12 C. G. Montgomery, R. H. Dicke, and E. M. Purcell, eds., *Principles of Microwave Circuits, Mass. Inst. Technol. Radiation Lab. Series*, Vol. 8, pp. 299–301, McGraw-Hill, New York, 1948.

13 R. Levy, "Directional Couplers," in *Advan. Microwaves* (L. Young, ed.), Vol. 1, p. 124, Academic Press, New York, 1966.

14 M. Surdin, *J. Inst. Elec. Engrs.* (*London*) (Pt. IIIA) **93**, 725 (1946).

15 H. J. Riblet, "Waveguide hybrid," U.S. Patent No. 2,739,288 (filed March 17, 1950).

16 W. Stoesser, *Frequenz* (*Berlin*) **14** (4), 117 (April 1960).

17 H. A. Bethe, "Theory of Side Windows in Waveguides," MIT Radiation Lab. Rept. No. 43-27, Massachusetts Institute of Technology, Cambridge, Massachusetts (1943); also, H. A. Bethe, "Theory of Diffraction by Small Holes," *Phys. Rev.* **66**, 163 (1944); also, R. L. Kyhl, "Directional Couplers," in *Techniques of Microwave Measurements, Mass. Inst. Technol. Radiation Lab. Series* (C. G. Montgomery, ed.), Vol. 11, p. 858, McGraw-Hill, New York, 1947.

18 T. Moreno, "A New Directional Coupler for Waveguides," unpublished report, Sperry Gyroscope Co., Inc., Garden City, New York, July 17, 1946.

19 K. Skarpaas, "Microwave waveguide coupling seal," U.S. Patent No. 3,212,035, (filed December 20, 1963).

20 G. Merdinian, unpublished notes.

21 E. J. Nalos, "Loss for High Power TWT's," unpublished note, General Electric Microwave Laboratory, Palo Alto, California, March 1955.

12

THE PHASING SYSTEM

H. A. Hogg, Editor, M. J. Lee, G. A. Loew, and A. R. Wilmunder

The function of the phasing system is to adjust the phases of the 245 klystrons so that the energy of the accelerated electron beam is maximized and the energy spectrum width is held to a minimum. To achieve this, the design objective of the automatic phasing system was to make the crests of the RF traveling wave in the accelerator coincide with the electron bunch centers within $\pm 5°$. This objective has been met by the system described in this chapter.

During the initial design phase of the SLAC project, detailed studies were made of various proposals for phasing the machine.[1–10] Evaluation of these proposals, which are briefly reviewed here, led to the choice of the *beam induction* technique as the *modus operandi* for the automatic phasing system.

The drive system and the phasing system are covered in separate chapters of this book. However, a complete understanding of the automatic phasing system cannot be obtained without at least partial reference to the drive system described in Chapter 9. The reader who wishes to understand the basic motivations behind the design criteria imposed on the phasing system should at least read the introduction to that chapter. Hereinafter, the justifications for these criteria will be assumed. Hence, the discussion on phasing accuracy and the desire to maximize the energy of the accelerator to within 0.5% of its maximum value will not be repeated.

The energy spectrum width depends on phasing in the following way. If all accelerator sections are perfectly phased and the electrons are bunched with a uniform distribution within an angular spread α, the energy spectrum width expressed as a fraction of maximum energy is

$$\frac{\Delta V_{\text{Tot}}}{V_{\text{Tot}}} = 1 - \cos\frac{\alpha}{2} \approx \frac{\alpha^2}{8} \tag{12-1}$$

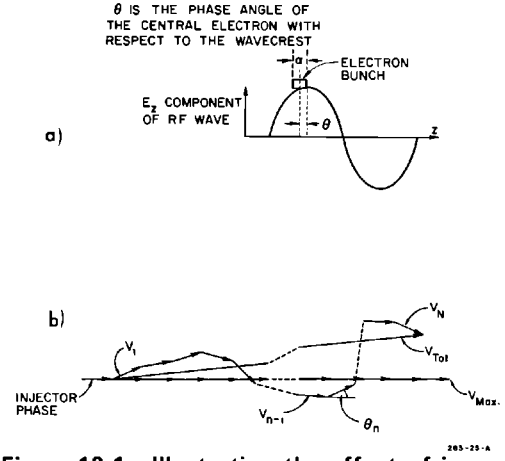

Figure 12-1 Illustrating the effect of imperfect phasing.

However, if phasing is imperfect as shown in Fig. 12-1a, the fractional energy spread for small α and θ can be shown[8] to become

$$\frac{\Delta V_{\text{Tot}}}{V_{\text{Tot}}} \approx \frac{1}{2}\left[\frac{\alpha}{2} + \frac{\sum \theta_n}{N}\right]^2 \tag{12-2}$$

where N is the number of sections and $\sum \theta_n$ is the algebraic sum of the individual phasing errors. (See Fig. 12-1b.) Thus, the minimum obtainable energy spectrum width is determined by the bunching angle α, but the energy spread is further degraded by the term $\sum \theta_n/N$. Fortunately, this term can experimentally be made equal to zero even if the individual values of θ_n are not known. It is only necessary to adjust the phase of the injector klystron until the energy spectrum width out of the machine is minimized. This operation is commonly called "phase closure." It is performed manually after the automatic phasing system has been operated.

Some alternative methods of phasing, either automatically or manually, will now be mentioned before proceeding to a detailed discussion of the adopted technique.

12-1 Survey of earlier phasing methods (GAL)

Beam energy maximization

With the exception of the 2-GeV Kharkov Linear Accelerator in the U.S.S.R., no linear electron accelerator built or conceived before the SLAC machine ever required an automatic phasing system. In multisection accelerators, the practice so far has been to optimize the phase of each klystron individually

by maximizing energy output and minimizing spectrum width. This corresponds to setting all θ_n equal to zero in Fig. 12-1b, so that V_{Tot} coincides with V_{Max}. The method, known as "beam energy maximization," has the disadvantage that its sensitivity is inversely proportional to the number of klystrons in operation. A change in phase of $\pm 5°$ about the optimum for 1 klystron in 240 gives a fractional energy change of 0.0016%. From this it is clear that beam energy maximization is not a very good way of phasing a long machine. The sensitivity can be improved by observing the current in part of the electron beam after dispersion by a momentum spectrometer. The change in current in a certain energy width is observed as the RF phase is rotated. However, this method, which is known as the "current variation detection (CVD) technique,"[1,6,7] is also insufficiently sensitive and interferes with the beam available for physics experiments. In addition, both methods are slow and require the establishment of a beam through the entire machine prior to phasing—a condition which is probably impossible to fulfill.

Direct phase comparison

A method based on direct phase comparison between adjacent RF feed lines just before they connect to the accelerator was considered. It is apparent that, in order to be sure that the waves in successive accelerator sections are correctly phased within the allowed tolerance, the electrical lengths of all RF lines involved must be known very precisely, not only at the time of installation, but subsequently when the temperature has changed and building movements may have occurred. In any case, such a direct comparison ensures only that all the RF waves are correctly phased with respect to each other but not necessarily with respect to the beam. The later phase alignment has to be achieved by another method, such as the CVD technique mentioned above. (It should be remembered that the CVD technique has a workable sensitivity when it is applied to whole sectors of the machine instead of individual klystrons.)

Interaction between electron beam and RF wave

Two further methods of phasing were proposed. These depend upon measurement of changes in resistive and reactive beam loading as the relative phases of beam and RF wave are changed in an accelerator section.

When an electron beam passes through an accelerator section filled with RF energy, a fraction of this energy is delivered to the beam, and the RF power at the output of the section decreases. This effect is known as *resistive beam loading*. The section is correctly phased when the power reduction is a maximum. If a phase error θ exists between the electron bunches and the wave, the steady-state RF power flow at the exit of a constant gradient accelerator section is

$$P = P_0 e^{-2\tau} + rLi^2\left[\frac{\tau^2}{e^{2\tau}-1}\right] - 2i\left[P_0 rL\left(\frac{\tau^2}{e^{2\tau}-1}\right)e^{-2\tau}\right]^{1/2}\cos\theta \quad (12\text{-}3)$$

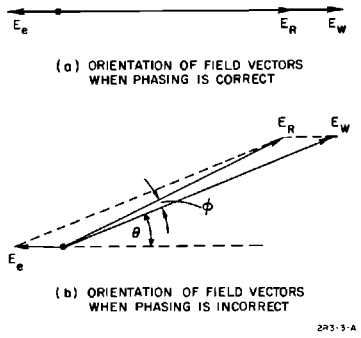

Figure 12-2 Vector diagram illustrating principle of phasing accelerator section by reactive beam-loading method.

where P_0 is the RF input power, and all other symbols have been defined in Chapter 6. Unfortunately, the cosine term makes the effect a poor criterion for correctness of phasing, since $dP/d\theta$ is proportional to sin θ. Thus the sensitivity tends to zero as the optimum phase relationship is approached.

Reactive beam loading may be understood by referring to Fig. 12-2. Here $\mathbf{E}_W$ is the electric field vector of the impressed RF wave from the klystron power source. The magnitude of $\mathbf{E}_W$ is approximately constant along a constant gradient accelerator section. The beam induces a wave of which the electric field vector is represented by $\mathbf{E}_e$. The magnitude of this vector grows with distance as[11]

$$E_e = \frac{ir}{2} \ln \left[1 - \left(\frac{z}{L} \right) (1 - e^{-2\tau}) \right] \tag{12-4}$$

where again, the symbols are defined in Chapter 6. $\mathbf{E}_R$ is the vector sum of $\mathbf{E}_W$ and $\mathbf{E}_e$, and its magnitude is given by

$$E_R^2 = E_e^2 + E_W^2 - 2E_e E_W \cos \theta \tag{12-5}$$

Figures 12-2a and b show the vector orientations for correct and incorrect phasing, respectively. ϕ is the phase angle between E_R (beam on) and E_W (beam off). It is the quantity which has to be measured and adjusted to zero in this method of phasing. It may be seen that

$$\lim_{\theta \to 0} \left| \frac{d\phi}{d\theta} \right| = \frac{1}{E_W/E_e - 1} \tag{12-6}$$

The ratio E_W/E_e at the end of a 10-ft accelerator section fed by a 24-MW klystron, with 1 mA of accelerated beam current is approximately 500. Therefore the sensitivity of this method of phasing is also low.

12-2 Theory of beam induction technique (HAH, MJL)

Examination of the reactive beam loading method of phasing, which involves an indirect measurement of the phase of the beam-induced wave in an accelerator section, led to the *beam induction* method which was chosen for the two-mile machine.

The principle of the beam induction technique is as follows:

1. With the klystron wave turned off, the phase of the beam-induced wave in the particular accelerator section to be phased is compared with a coherent cw reference signal of the same frequency.
2. The phase of the reference signal is adjusted to be the same as the phase of the beam-induced signal at the place where the comparison is made. See Fig. 12-3a.
3. The phase of the reference signal is then locked.
4. The klystron is turned on, and the phase of the klystron wave in the accelerator section is compared with the reference signal.
5. The phase of the klystron signal is adjusted to be 180° away from the phase of the reference signal. (See Fig. 12-3b.)

For the reasons explained above and illustrated in Figs. 12-1 and 12-2, the klystron is then optimally phased.

Actually, for clarity in the statement of the principle of operation, one oversimplification of the system was made which requires correction: when the phase comparison between beam-induced and reference signals is being

Figure 12-3 Illustrating beam-induction method of phasing accelerator.

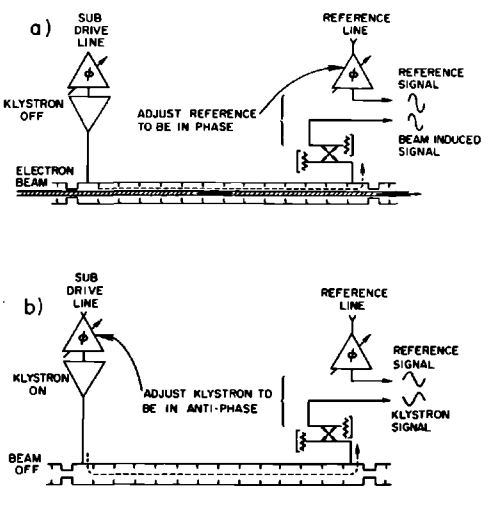

made, there is no need to turn the klystron off. Indeed, to do so is undesirable because removal of RF power from an accelerator section allows it to cool down, with a consequent change in its dimensions and propagation characteristics. Since the accelerator is a pulsed machine, it is only necessary to delay the klystron pulse by a suitable interval, typically 50 μsec, during the phasing operation instead of turning it off.

The delayed position of the klystron pulse with repect to the beam pulse is referred to as the "standby" position.

The beam-induction method has a number of advantages but also poses certain problems that will be discussed below. The advantages are

1. It has the best sensitivity of all the methods which were studied. Since θ is measured directly,

$$\frac{\text{sensitivity (beam induction method)}}{\text{sensitivity (reactive beam loading method)}} = \lim_{\theta \to 0} \left(\frac{1}{|d\phi/d\theta|} \right) = \frac{E_W}{E_e} \tag{12-7}$$

   As mentioned above this ratio can be as large as 500 : 1.
2. The beam-induced and klystron signals are sampled directly at the accelerator and are transmitted along a common cable to the phase detection circuit in the klystron gallery. The phase comparison is, therefore, essentially direct; the length of the cable does not need to be known, and the attainable sensitivity and accuracy are good.
3. There need be very little interference with physics experiments, because only one klystron at a time need be "set to standby" as the phasing operation progresses along the machine.
4. Klystrons which are placed on "standby" for reasons other than phasing can be maintained correctly phased with respect to the beam so that they are instantly available for acceleration, on demand.

Among the problems, the most serious relates to the very large difference between the power levels of the beam-induced and the klystron signals. The extremes of the specified conditions under which the phasing system will be required to operate have to be considered, viz., a beam current pulse as low as 1 mA and a klystron peak power input to one 10 ft accelerator section as high as 24 MW. The attenuation per 10-ft section is approximately 5 dB and the beam-induced power at the output of the section is 26 W/(mA)^2, so that the largest power ratio of the two signals at the end of the 10-ft section is roughly 54 dB.

Well-known devices such as the slotted line, "magic T," and hybrid ring are normally used for the phase comparison of two signals. A minimum or a null in the detected output from one arm of these devices indicates a given phase relationship between the two signals. A null is obtained only if the two signals are of equal amplitude. As the difference between the amplitudes of

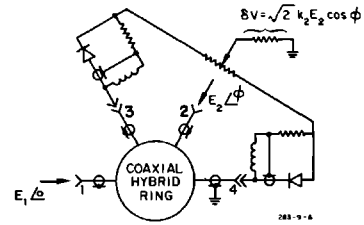

Figure 12-4 Hybrid ring phase comparator.

the two signals increases, the phase-indicating null is replaced by a broad minimum, and the balance point becomes increasingly difficult to detect. The method is unreliable when the signals differ by more than 10 dB. Moreover, the *overall* phase detection system that is required is one which will develop an error signal depending only upon the phase difference between the two input signals. Considering that the phase comparison network is just a *part* of the overall system, it will be shown later that its error signal can be permitted to vary by not more than 4 to 1 over the entire range of input signal levels.

The performance of a perfect hybrid ring used as a phase comparison network will now be examined (Fig. 12-4). The signals to be compared are applied to arms 1 and 2, and arms 3 and 4 are terminated in matched detectors. Let the electric field amplitudes of the input signals be E_1 and E_2. Then the outputs to the detectors are given by

$$E_3^2 = \frac{E_1^2}{2} + \frac{E_2^2}{2} + E_1 E_2 \cos \phi \tag{12-8}$$

and

$$E_4^2 = \frac{E_1^2}{2} + \frac{E_2^2}{2} - E_1 E_2 \cos \phi \tag{12-9}$$

where ϕ is the phase difference between E_1 and E_2 at arms 1 and 2.

Let E_2 represent the reference signal and E_1 either the beam-induced or the klystron signal, and let $E_1 \geq E_2$.

If the detectors have an index n, their responses are

$$V_3 = kE_3^n \tag{12-10}$$

and

$$V_4 = kE_4^n \tag{12-11}$$

where k is a constant.

It follows that the difference between the detected signals is given by

$$\delta V = \frac{k}{2^{n/2}} [(E_1^2 + E_2^2 + 2E_1E_2 \cos \phi)^{n/2} - (E_1^2 + E_2^2 - 2E_1E_2 \cos \phi)^{n/2}] \tag{12-12}$$

so that

$$\delta V_{\max} = \frac{k}{2^{n/2}} [(E_1 + E_2)^n - (E_1 - E_2)^n] \tag{12-13}$$

Two cases are of special interest. If the detectors are "square-law" ($n = 2$),

$$\delta V = 2k_1E_1E_2 \cos \phi \tag{12-14}$$

where k has been set equal to k_1. Then

$$\delta V_{\max} = 2k_1E_1E_2 \tag{12-15}$$

Thus, for square-law detectors, the differential ouput voltage δV for a given phase error is proportional to both E_1 and E_2. The reference E_2 can be constant, but E_1^2 is variable over a 54-dB range; therefore, square-law detectors are quite unsuitable for use in the phasing system.

On the other hand, if the detectors are linear, $n = 1$ and Eq. (12-13) becomes

$$\delta V_{\max} = \sqrt{2}k_2E_2 \tag{12-16}$$

where k has been set equal to k_2.

When $n = 1$ and $E_1 \gg E_2$, Eq. (12-12) becomes

$$\delta V = \sqrt{2}k_2E_2 \cos \phi \tag{12-17}$$

and the sensitivity, $\partial(\delta V)/\partial\phi$, is $-\sqrt{2}k_2E_2$ at $\delta V = 0$.

When $n = 1$ and $E_1 = E_2$, Eq. (12-12) becomes

$$\delta V \mp \sqrt{2}k_2E_2\left(\cos \frac{\phi}{2} - \sin \frac{\phi}{2}\right) \tag{12-18}$$

and the sensitivity at $\delta V = 0$ is $-k_2E_2$.

In Fig. 12-5, δV is plotted as a function of ϕ for both cases. It is seen that the use of linear detectors removes the δV dependence on E_1, so that with constant E_2, δV is a function of ϕ only. As E_1 decreases from very large values to equality with E_2, the sensitivity of null detection decreases by a factor of only $1/\sqrt{2}$.

It should be mentioned now that no detector will remain perfectly linear over the specified range of input powers. The best approximation presently available is a coaxial thermionic diode, which maintains an index of less than 1.2 over the required range.

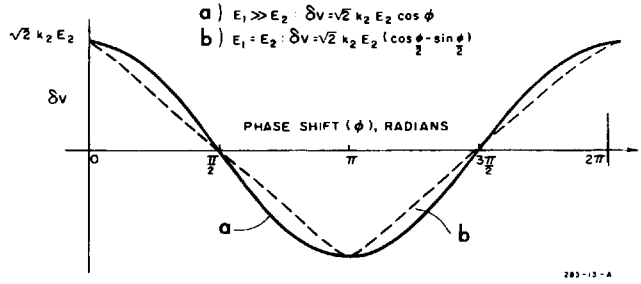

Figure 12-5 Plot of δV vs ϕ for linear diodes.

The effect of diode nonlinearity may be estimated as follows. Let the range of E_1 be $E_b \leq E_1 \leq E_a$, and let $E_b = mE_2$, where $m \geq 1$. Assume that the diode index n changes from $1 + \varepsilon$ to 1 as E_1 changes from E_b to E_a. The ratio R of $(\delta V)_{\max}$ at the extremes of the range of E_1 is given by

$$R = \frac{(\delta V)_{\max}\,|_{n=1,\,E_1=E_a}}{(\delta V)_{\max}\,|_{n=1+\varepsilon,\,E_1=E_b}} < R_{\max}$$

where

$$R_{\max} = \frac{(\delta V)_{\max}\,|_{n=1+\varepsilon,\,E_1=E_a}}{(\delta V)_{\max}\,|_{n=1+\varepsilon,\,E_1=E_b}}$$

Substituting from Eq. (12-13) and expanding the numerator gives

$$R_{\max} = \frac{2(1+\varepsilon)(mE_a/E_b)^{\varepsilon}}{(m+1)^{1+\varepsilon} - (m-1)^{1+\varepsilon}} \tag{12-19}$$

which becomes $(E_a/E_b)^{\varepsilon}$ for large m. The extreme operating conditions are $m = 1$ and $(E_a/E_b)^2 = 54$ dB. When $\varepsilon = 0.2$, these conditions give $R_{\max} \approx 3.4$. From this, it will be seen that the coaxial thermionic diode is acceptable.

The detector used is an RCA Type 6173 coaxial thermionic diode mounted in a special housing designed at SLAC (see Fig. 12-6). The anode is held in

Figure 12-6 Thermionic diode and housing.

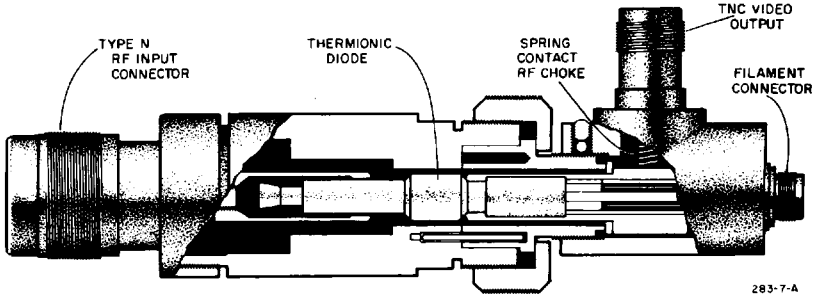

position by spring fingers and connected to the center conductor of the Type N input RF connector. The detected output is taken from the cathode to a TNC connector on the side of the diode housing. The filament power is supplied through a separate twin-axial connector.

The diode resistive loads are connected in opposition by a balancing potentiometer, the wiper of which may be adjusted to offset asymmetries in the hybrid ring, diodes, and diode loads. In theory, the differential diode output as described contains the required phase information. If the diodes are balanced, then as the phase angle ϕ rotates, the differential output will oscillate about zero, passing through zero when $\phi = (p \pm \frac{1}{2})\pi$, where p is an integer. The direction from which zero is approached with increasing ϕ may be used to avoid π ambiguity in phase setting (see Fig. 12-5). However, such a system is impracticable because it depends on dc balancing. The long-term stability required of the diodes and the following dc amplifiers would be very difficult to achieve. This difficulty constitutes the second serious problem in the development of the beam-induction phasing system. The problem is avoided by the use of a technique which has become known as "phase wobbling."

12-3 The principle of "phase wobbling" (HAH, MJL)

The dc phase-detection system described above is converted to an ac system by phase-modulating the reference signal, E_2. This artifice immediately removes most of the problems of drift in dc levels and provides a method of instructing the automatic servo system whether the phase of E_1 is leading or lagging the phase of the reference, E_2.

Phase wobbling is achieved by the use of a three-port switching circulator in the reference line (see Figs. 12-7 and 12-8). The reference signal enters through one port and propagates to the output port either directly or through a third port, depending upon the polarity of the field used to magnetize the ferrite material. The third port is terminated by an adjustable short circuit, so that the difference between the two path lengths to the output port can be made one-half wavelength. The direction of current flow in the magnetizing coil is reversed before the arrival of each successive beam-induced or klystron

Figure 12-7 Switching circulator used as phase wobbler.

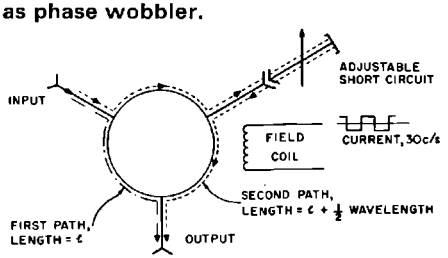

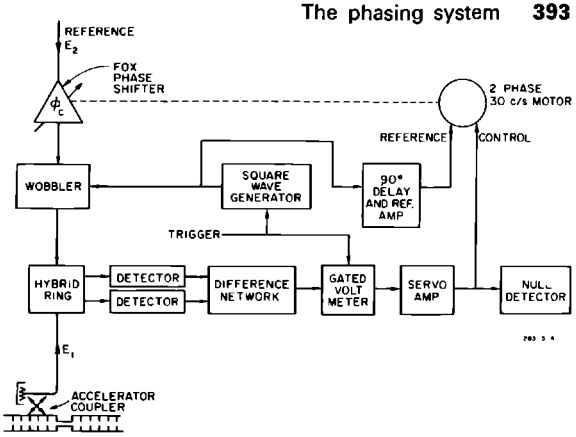

Figure 12-8 Block diagram of phase-wobbling system.

RF pulse. Hence the cw reference signal, E_2, is square-wave, phase-modulated at 30 Hz so that successive beam-induced or klystron pulses are compared with reference signals which differ in phase by π.

The principle of the phase wobbling technique is essential to the automatic phasing system which has been developed, so that a description of the former introduces the main features of the latter.

A block diagram of the system is shown in Fig. 12-8. The cw reference signal E_2 is transmitted to the wobbler through a "Fox"-type rotary phase shifter,[12] ϕ_c. This design of phase shifter was chosen because the phase shift it introduces is a linear monotonically increasing function of the angle of rotation of the phase-shifter drum. There are no discontinuities or end stops. The wobbler is driven by a 30-Hz square-wave generator, synchronized by a 60-pulses/sec trigger. The wobbler output is connected to the hybrid ring, where the accelerator signal E_1 interacts with reference E_2 as described above. The output ports are terminated by the two thermionic diode detectors, and the differential output is fed into a gated voltmeter.

To understand the operation of the system so far described, the reader is referred to Figs. 12-8 and 12-9. Let the drum of the Fox phase shifter be slowly rotated so that the phase difference ϕ between E_1 and E_2 at the hybrid ring increases from 0 to 2π in a time $2T_p$, where $2T_p$ is a few seconds. See Figs. 12-9a and b. The wobbler is phase-modulating E_2 by $\pm\pi/2$ at 30 Hz, so that the phase of E_2 at the hybrid ring changes by π every 1/60 sec. Pulses of signal E_1 are arriving from the accelerator at the rate of 60 per second, the pulse length being 1–2.5 μsec. The trigger for the wobbler driver assures that E_2 changes phase in the interval between the arrival of E_1 pulses.

It was shown above that the balanced differential output from two linear diodes is $\sqrt{2}k_2 E_2 \cos\phi$. It follows that, as E_2 is wobbled, the differential output pulse amplitudes will change from $\sqrt{2}k_2 E_2 \cos[\phi + (\pi/2)]$

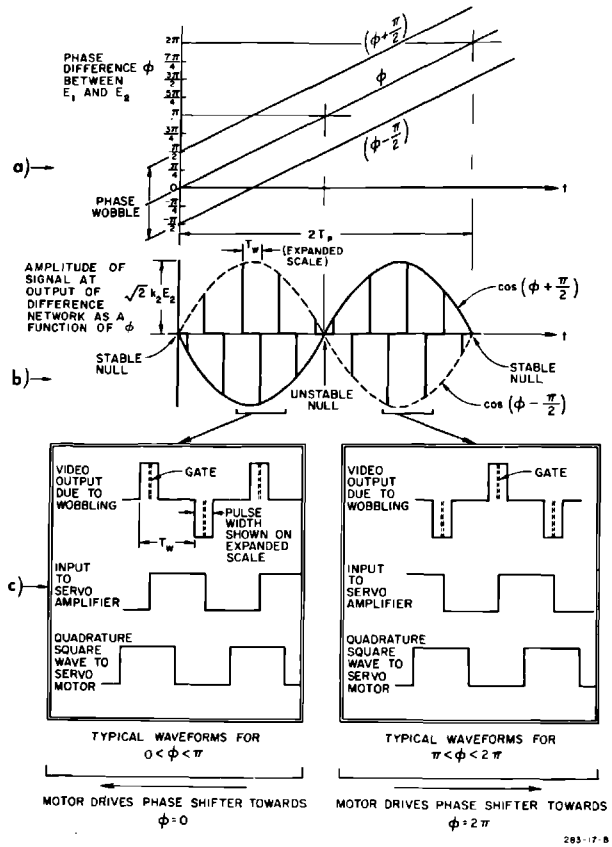

Figure 12-9 Illustrating the application of phase wobbling to an automatic phasing system.

to $\sqrt{2}k_2 E_2 \cos[\phi - (\pi/2)]$ in a time $T_W = 1/60$ sec. (For clarity, the "wobbled" time scale in Fig. 12-9b has been expanded.)

To see what happens next, the output pulses are further expanded in the top line of Fig. 12-9c. To avoid beginning and end-of-pulse transients, the pulse amplitudes are sampled by a "gate," 0.2 μsec wide, located near the center of the pulse. The sample is held until the next pulse arrives, so that a 30-Hz square wave is formed with amplitude proportional to $\cos[\phi + (\pi/2)]$. This wave is amplified and fed to the control winding of a two-phase motor which drives ϕ_c.

Going back to the wobbler driver (square-wave generator in Fig. 12-8), part of the square-wave output is fed to a 90° delay circuit followed by an amplifier stage, giving a constant amplitude square-wave output which is in quadrature with the wobbler drive signal. This signal energizes the reference winding of the two-phase motor. The motor will develop a torque proportional to the product of the amplitudes of the applied square waves. The

direction of rotation will depend upon whether the control wave leads or lags the reference wave.

From Figs. 12-9a and b, when $0 < \phi < \pi$,

$$E_2 \cos\left(\phi + \frac{\pi}{2}\right) < 0 < E_2 \cos\left(\phi - \frac{\pi}{2}\right) \tag{12-20}$$

Therefore the motor is connected so that, under these conditions, the phase shifter rotates towards $\phi = 0$.

It follows that when $\pi < \phi < 2\pi$,

$$E_2 \cos\left(\phi + \frac{\pi}{2}\right) > 0 > E_2 \cos\left(\phi - \frac{\pi}{2}\right) \tag{12-21}$$

and the phase shifter rotates toward $\phi = 2\pi$, which is identical with $\phi = 0$.

The system thus connected always drives ϕ_c away from the unstable null at $\phi = \pi$ toward the stable null at $\phi = 0$. It should be noted that an identically connected phase shifter in the *other* input arm to the hybrid ring will rotate toward a stable null at $\phi = \pi$.

Before proceeding to a description of the complete automatic phasing system, two further comments on the wobbler technique will be made.

First, it is easy to show that errors which would otherwise be introduced by differing diode conversion efficiencies are eliminated by phase wobbling. This is an important advantage, because it is not possible to obtain a perfectly matched pair over the entire range of signal levels.

Let the output voltages of the two diodes be

$$V_3 = k_3 E_3^n$$

and

$$V_4 = k_4 E_4^n$$

For the two wobbler positions ($\pm\pi/2$) the difference between the output voltages is given by Eq. (12-12)

$$\delta V|_{(\phi \pm \pi/2)} = \frac{k_3}{2^{n/2}} \left[E_1^2 + E_2^2 + 2E_1E_2 \cos\left(\phi \pm \frac{\pi}{2}\right)\right]^{n/2} - \frac{k_4}{2^{n/2}} \left[E_1^2 + E_2^2 - 2E_1E_2 \cos\left(\phi \pm \frac{\pi}{2}\right)\right]^{n/2} \tag{12-22}$$

The automatic system indicates a phase balance when the difference between the detected outputs in the two wobbler positions is zero, i.e.,

$$\delta V|_{(\phi + \pi/2)} = \delta V|_{(\phi - \pi/2)}$$

This occurs when $\phi = 0 \pm p\pi$, independently of the values of k_3 and k_4.

The second point to be made is that imperfections in the switching circulator do not affect phasing accuracy. It can be shown[13] that if the phase difference introduced by switching from one path to the other is not exactly π, or if the two paths have different insertion losses, no phase error is introduced.

12-4 Functional description of the system (HAH, ARW)

Sector phasing equipment

As for most other systems, a sector was chosen as the subdivision of the machine for the purpose of phasing. This division is convenient since all the necessary status signals concerning the modulators and klystrons are available at the "instrumentation and control" alcove located approximately in the middle of a sector. It also reduces the length of the control wires and RF cables, thereby reducing attenuation and phase drift.

Figure 12-10 is a schematic of the RF drive system in one sector. The 476-MHz main drive signal is multiplied to 2856 MHz, at which point -10 dB of the power is coupled off to provide the reference signal, E_2, for the phasing system. The remainder of the signal is used to drive the sub-booster amplifier, which feeds 360 pulse-pairs/sec into the subdrive line.

As described in Chapter 9, power is coupled from the subdrive line at eight points, each coupler feeding one 24-MW klystron through an isolator, phase-shifter, attenuator unit. The phase shifter in this unit is of the type already described. It is coupled to the automatic phasing system and will be referred to as the "klystron phase shifter," ϕ_k. The RF ouput from each klystron feeds four 10-ft accelerator sections, as shown. As discussed in

Figure 12-10 Drive system schematic for one module of the machine, showing how the signals for the phasing system are derived.

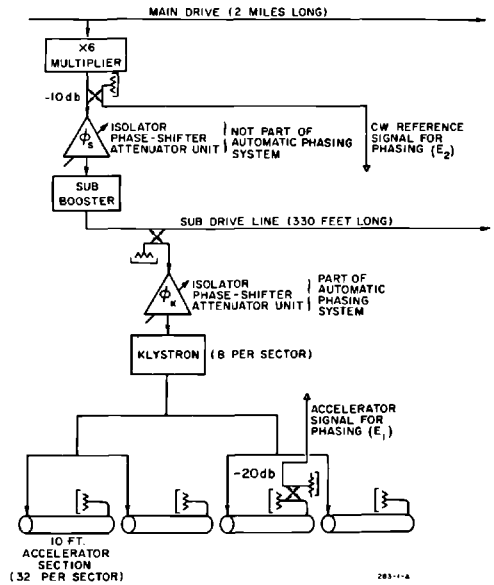

Chapter 11, the lengths of waveguide runs between the klystron and the four sections are carefully controlled to give the correct phase relation between each section at the design frequency and temperature. No adjustment of the relative phases within each group of four sections was made after completion of installation. Of course, because of the small differences in the lengths of the waveguide feeds, a change in frequency results in a phase shift between sections, but this is negligible. In addition, it can be shown that the loss of beam energy due to a frequency change is a minimum if the phasing signal is taken from the second or third section of each group of four sections. A 20-dB, cross-guide coupler is placed in front of the matched termination at the end of the second or third 10-ft section and is used to sample the klystron wave and beam-induced wave for phasing purposes.

Figure 12-11 is a block diagram of the automatic phasing system for an entire sector. The outputs from one 10-ft section of each module are transmitted to a nine-position switch which selects one channel at a time and transmits the E_1 signal to the hybrid ring–wobbler–detector system which has been described previously. The switch, wobbler, and phase detector are housed in the RF detector panel. The phase shifter in the reference line to the wobbler is known as the "control phase shifter," ϕ_c.

The gated voltmeter, servo amplifier, wobbler driver, 90° delay, and reference amplifier are housed in an electronics panel together with a null detector which determines when the phasing operation is complete by measuring the servo control voltage. The function of the electronics panel has also been described in connection with phase wobbling. The programmer

Figure 12-11 Block diagram of automatic phasing system for one sector.

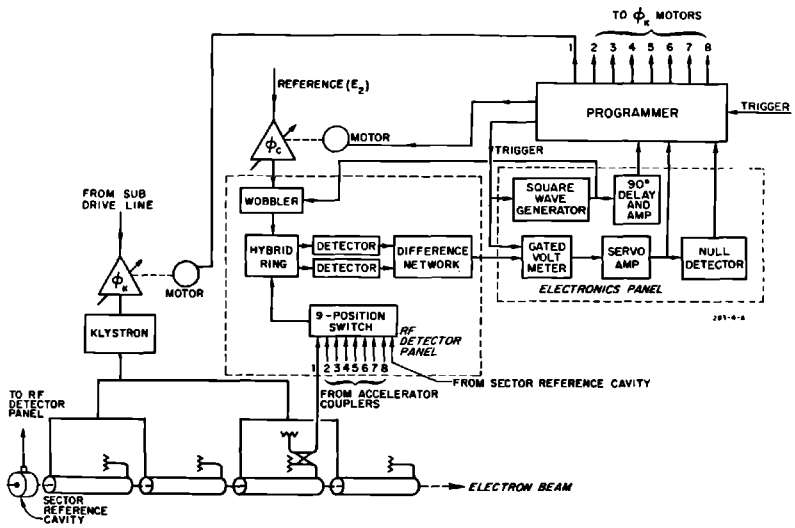

is a special switching unit which ensures that the steps described in the previous section are carried out in sequence, and repeated "down the line" until all eight klystrons in one sector are properly phased.

Basic operation

The operation of the complete system is as follows:

1. When the programmer is activated by pressing either the local or Central Control Room (CCR) "start" button, klystron No. 1 is set to the "standby" pulse position. Switches in the RF detector panel connect the appropriate accelerator section output to the hybrid ring, and the phase of the beam-induced wave is compared with the reference signal. A typical CRO trace of the video signal at the output of the diode network before phasing is shown in Fig. 12-12a.

2. The control phase shifter, ϕ_c, rotates towards a stable null until the servo amplifier output drops below 4 V. The motor then stops and the null detector indicates that the programmer may advance to the "klystron-phase" position. [See the CRO trace in Fig. 12-12b.]

3. A brake is applied to ϕ_c.

Figure 12-12 RF detector panel video output traces at three stages of phasing.

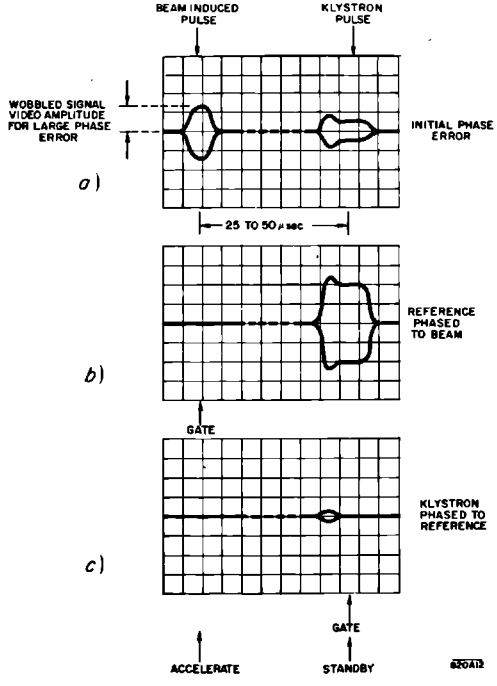

4. Provided that klystron No. 1 is operating properly, the "gate" of the gated voltmeter shifts to sample the standby klystron pulse, so that the phase of the klystron wave is compared with the reference.

5. The klystron phase shifter, ϕ_k, preceding klystron No. 1 is connected to the electronics panel by the programmer and rotates to a stable null which is π away from the stable null of ϕ_c because it is in the other signal input arm to the hybrid ring. A typical CRO trace of the video signal at the output of the diode network after phasing is shown in Fig. 12-12c.

6. When the null detector indicates that the phasing error is within the accepted tolerance, the programmer switches to klystron No. 2, setting it to standby and returning No. 1 to accelerate. The phasing cycle is then repeated.

7. The phasing operation continues until all eight klystrons are phased.

8. When the null detector indicates that the last klystron in the sector has been phased, the programmer energizes switches in the RF detector panel, connecting a sample signal from the sector subdrive line to ϕ_c. At the same time, the other input arm of the hybrid ring is switched to the output of a reference cavity located in the drift section at the end of the previous sector (shown schematically in Fig. 12-11). This reference cavity is a re-entrant cavity resonant at 2856 MHz, the axis of which is collinear with the accelerator axis, so that the bunched beam passes through it. Part of the beam-induced output signal from the cavity is used as a normalizing signal for the beam position monitoring system, and part is used to provide a sector phase reference signal. (For more details, see Chapter 25.)

9. The phases of the cavity and subdrive line signals are compared at the hybrid ring, and the automatic servo system rotates ϕ_c until a stable null is reached with the servo amplifier output voltage below 4 V. At this point, the brake is applied to lock the position of ϕ_c and the programmer switches itself off. However, the electronics and RF detector panel are not de-energized so that the phase balance between the cavity and subdrive line signals continues to be monitored. If a phase drift occurs such that the servo amplifier output voltage exceeds 4 V, a warning light appears in the sector instrumentation alcove and in the central control display. The phase drift may be corrected either by automatically rephasing the sector or by rotating the phase shifter preceding the sub-booster (Fig. 12-10).

Special features

The simple logic enumerated above is complicated by the following features:

1. Signals are received at the programmer from each modulator/klystron control unit (see Chapter 15) indicating whether the modulator is on or off and whether there is an RF output from the klystron. If both "no modulator" and "no RF" signals are received, no phase adjustments are attempted, and the programmer steps on to the next klystron. If, however, the indication is

that the modulator is available but there is no RF output, the programmer waits for recycling of the modulator to be completed. When RF again appears, it is phased. If the modulator goes off, the programmer steps to the next klystron.

2. If the "no RF" indication persists, or the phasing system fails to reach a null for any reason, the programmer may be stepped to the next klystron by pressing the "fault override" button (again, either on the programmer panel or in CCR).

3. The programmer may be made to step through without setting klystrons to standby or phasing by pressing a "don't phase" button in CCR, or holding down the "fault override" on the programmer panel.

4. The programmer may be stopped at any position by pressing a "stop" button in CCR or pressing and holding the "start" button on the programmer panel.

5. The programmer stops if the video ouput of one coaxial thermionic diode detector falls below a preset level (corresponding to a 1-mA peak beam current) or if the beam pulse repetition rate in the first time slot is lower than 60 pulses/sec.

6. Any phase shifter in one sector may be rotated locally by means of a manually controlled power supply built into the programmer.

Special phasing systems

1. In sectors containing more than eight klystrons, subprogrammer units are used to quadruple the capacity of the main programmer. This means that at a future date the phasing system can be expanded to handle up to thirty-two klystrons per sector. At present, subprogrammers are used only in Sectors 1 and 11, where extra klystrons are required for initial acceleration of electron and positron beams, respectively.

2. When the "standby" injector klystron is brought on line, it is necessary to ensure that it has the same phase as the one it replaces. This is achieved by the system shown in Fig. 12-13. A special RF detector panel compares the phase of the subdrive-line signal (after the injector phase shifter) with the phase of the high-power signal in the common waveguide output. The differential video output is fed to a standard phasing electronics panel which generates the reference and control servo waveforms. These are routed to the $I\phi A$ unit in the drive to the "on-line" klystron. A control panel in the injector alcove allows the $I\phi A$ unit to rotate the klystron phase until the electronics panel indicates a null, then removes the control signal and applies the phase-shifter brake. When the klystron changeover switch is actuated, servo control is momentarily applied to the other $I\phi A$ unit, so that the original phase relationship at the RF detector panel is restored. The overall injector phase is controlled by the injector phase shifter.

3. In addition to the standard two-phase ac motor in the phasing servo system, the $I\phi A$ units in Sector 27 can be driven by stepper motors controlled

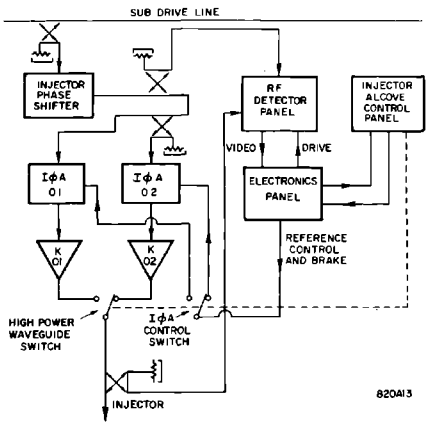

Figure 12-13 Automatic injector klystron phase control.

from CCR. When required, these motors are coupled to the Fox phase-shifter drums by electromagnetic clutches. The system allows fine phase control for vernier energy adjustments to multiple beams.

12-5 Description of main and auxiliary components (HAH, ARW)

Cables for transmission of phasing signals

In order to transmit the RF signals from the accelerator to the RF detector panel with the minimum of loss and yet with some flexibility in installation, $\frac{7}{8}$-in. coaxial cables are used. The 50-ohm cable has an attenuation of 2.8 dB/100 ft and a peak power handling capacity of over 60 kW.

The variation in phase shift through the cable due to ionizing radiation has been calculated and has been shown to be negligible for the radiation levels in the accelerator housing and for the lengths of cable which are exposed.

The IφA units

As already mentioned in Chapter 9, *IφA* is a convenient abbreviation for isolator, phase shifter, attenuator. A typical unit is shown in Fig. 9-11. The input is connected by a $\frac{1}{2}$-in. semirigid coaxial cable to a subdrive-line coupler. The RF signal (360 pulse-pairs/sec, pulse width 2.5 μsec, 4-kW peak power) travels through the phase shifter, which is protected from mismatches by two coaxial isolators. The signal is then coupled into the strip-line dual attenuator

assembly through a flexible cable whose phase shift-versus-temperature characteristic is of opposite sign to the rest of the unit. The cable length is chosen to keep the phase shift below 0.1°/°F in the range of 70° to 130°F. The function of the manual and protection attenuators is described in Chapter 9. Before the output is connected to the main klystron, there is a dual directional coupler for monitoring forward and reflected power.

The control phase shifter

A control phase-shifter unit consists of a Fox phase shifter, identical to the *IφA* phase shifter, mounted on a smaller chassis. Isolators are provided on the input and output.

The RF detector panels

A simplified schematic of the microwave circuit in an RF detector panel is shown in Fig. 12-14. The wobbler and phase detection components have already been described. The nine-position selector switch is actually made up as a tree of coaxial switches. This arrangement has the advantages that it can be constructed from readily available commercial switches and gives an interchannel cross-talk isolation of about 100 dB, which is in excess of this system's requirements. The RF switches are operated either automatically by the programmer or manually by a control switch on the front of the panel. Provision is also made for monitoring various RF and video signals. A completed unit is shown in Fig. 12-15.

Figure 12-14 Simplified schematic diagram of RF detector panel.

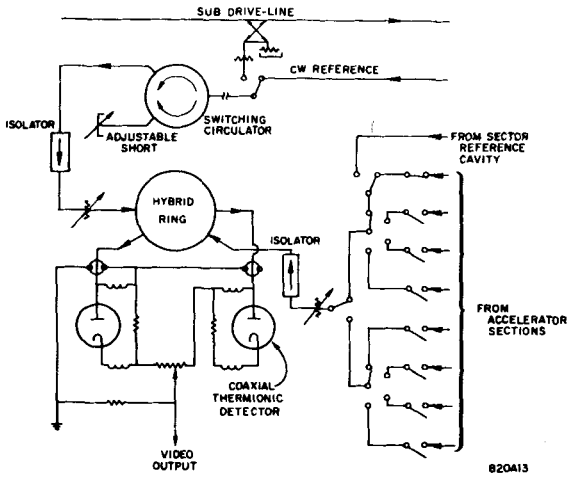

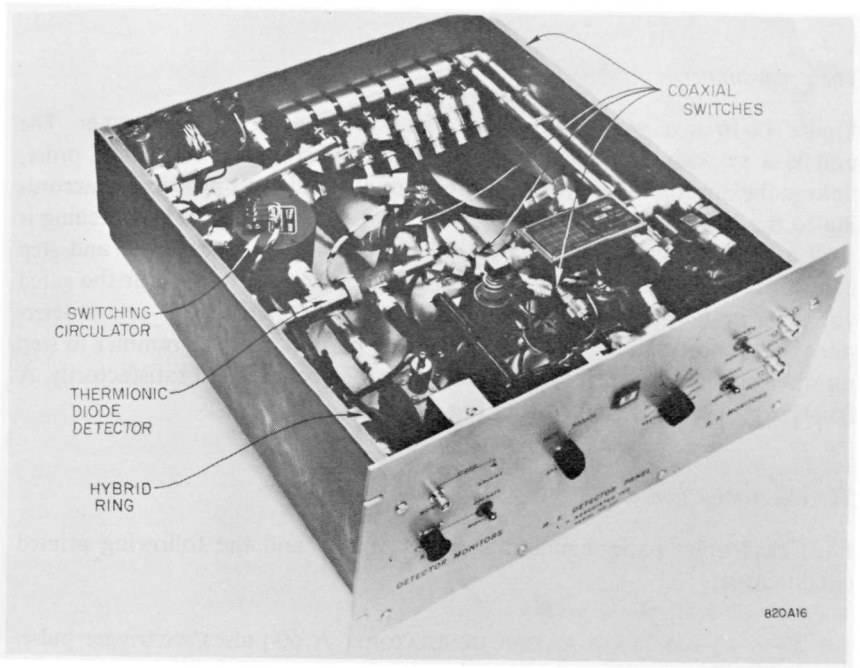

Figure 12-15 An RF detector panel.

Figure 12-16 Block diagram of phasing programmer.

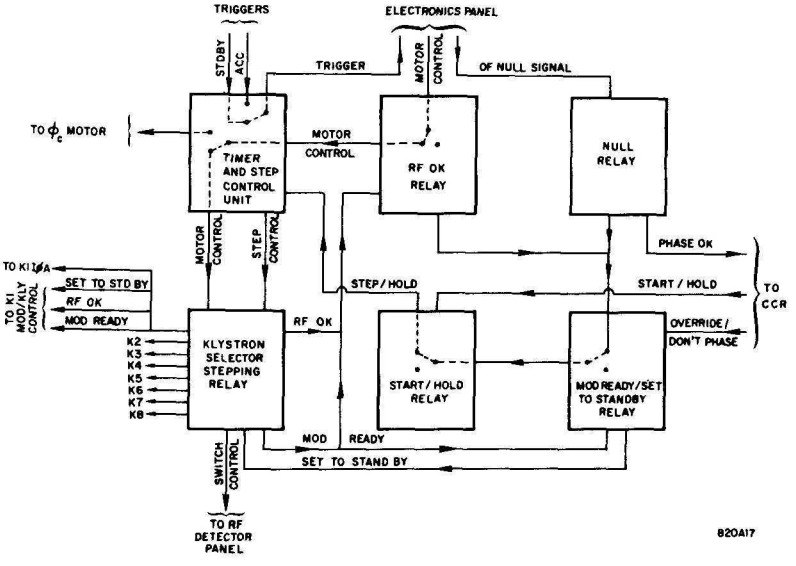

The programmers

Figure 12-16 is a greatly simplified block diagram of a programmer. The unit is a switching system which selects the klystrons in numerical order, linking the appropriate control and readout channels and proceeding according to the logic described under Section 12-4. Station-to-station switching is performed by a single stepping relay, which is driven by a timer and step control unit. The latter unit also selects the appropriate trigger for the gated voltmeter in the electronics panel. "RF OK" and "mod ready" relays determine the station status, and the "null" relay permits the programmer to step on when a particular phasing operation has been completed satisfactorily. A finished programmer is shown in Fig. 12-17.

The electronics panels

Each electronics panel contains a power supply and the following printed circuit cards:

THE 30-HZ SQUARE WAVE MASTER GENERATOR. A 60-pulses/sec trigger pulse, selected by the programmer, is used to trigger a master divide-by-two multivibrator. The output of this multivibrator drives an amplifier to provide power to operate the phase wobbler and the 90° delay and servo reference amplifier.

THE 90° DELAY AND REFERENCE AMPLIFIER. The unit consists of two monostable multivibrators and an amplifier identical to the one in the master generator. The first multivibrator is triggered by a signal from the master "divide-by-two" and acts as a quarter-cycle time delay. At the end of a quarter-cycle, the second multivibrator is triggered, and its output is amplified

Figure 12-17 Phasing programmer.

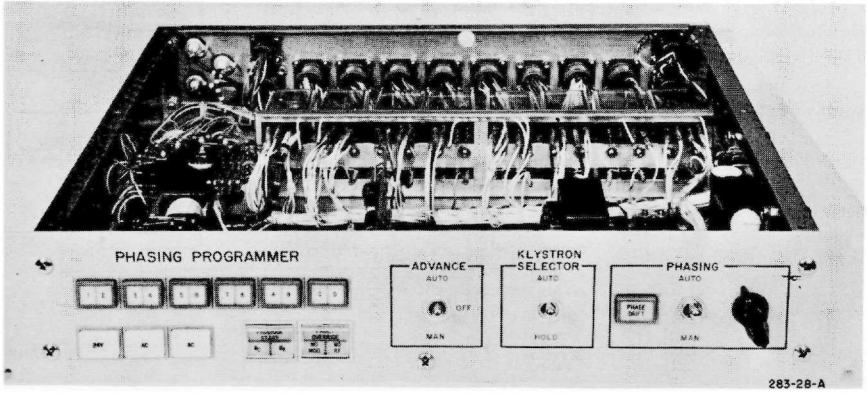

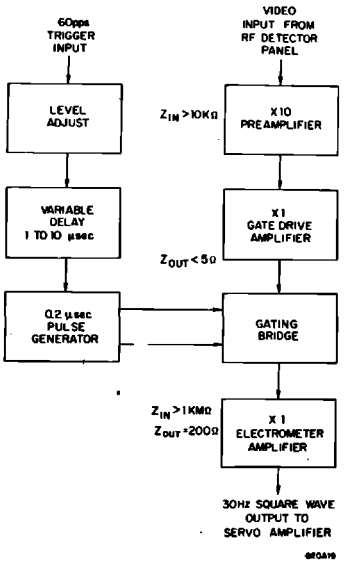

Figure 12-18 Block diagram of gated voltmeter.

to give a 30-Hz square wave in quadrature with the master generator. This waveform is applied to the reference winding of the two-phase motors which turn the phase shifters.

THE GATED VOLTMETER. A block diagram of this circuit is shown in Fig. 12-18. The video output from the RF detector panel is amplified in a $\times 10$ preamplifier and fed into a sample-and-hold circuit, where a gating bridge takes a 0.2-μsec sample, 0.5 μsec after the beginning of the video pulse. The time constant of the sampling circuit is 40 μsec, so that the hold circuit voltage (with a time constant of 10 sec) rises to over 95% of the sampled video voltage. The gate occurs after the appropriate trigger, selected by the programmer. The delay is adjustable so that it may be properly positioned in the video pulse. The sampled voltage is held essentially constant until the next sample is taken, so that a 30-Hz square wave is formed. As has been shown, its amplitude is proportional to the cosine of the phase across the hybrid ring.

THE SERVO AMPLIFIER. This amplifier increases the output of the gated voltmeter to a level which will drive the control winding of the two-phase motor. Its gain is adjusted to saturate at 20 V corresponding to a phase error of 30°.

THE NULL DETECTOR. This device is a voltage-doubling rectifier driving a back-biased saturating dc amplifier. When the servo amplifier output is

greater than 4 V peak-to-peak, the voltage out of the doubler exceeds the back-bias and a relay in the programmer is pulled in.

THE VIDEO AMPLIFIER AND BEAM CURRENT INTERLOCK. The amplifier, which is identical to the gated voltmeter preamplifier, boosts the level of the video output from the RF detector panel and feeds it to the video transmission system to CCR.

A beam current interlock operates from the video output of one of the coaxial thermionic diodes in the RF detector panel. The video pulse is superimposed upon a multivibrator pulse (timed by the "accelerate" trigger). If the video pulse amplitude exceeds a preset level (corresponding to 1-mA beam current), the combined voltages lift a tunnel diode and transistor amplifier circuit into conduction. The multivibrator pulse ends after 20 μsec, biasing the tunnel diodes off and resetting the circuit. It should be noted that this circuit conducts only if a video pulse of sufficient amplitude arrives in coincidence with a multivibrator pulse. Thus, if there is no beam in the first time-slot (using for phasing), the circuit will not conduct. When there is an adequate beam, successive current pulses close a relay which enables the phasing program to proceed. Time constants are chosen so that the relay will not close if the beam repetition rate is a less than 60 pulses/sec.

12-6 Operational procedures (HAH, ARW)

Central Control Room operation

Phasing is initiated by selecting the required sector on a switched sector panel, after having checked that the beam current through the sector in Time Slot 1 is not less than 1 mA, 1.6 μsec pulse width, and 60 pulses/sec, and by pressing the "phase" button and the "start" button.

If required, the RF detector panel video output may be viewed by operating the video selector, although phasing is frequently initiated in many sectors in quick succession without video monitoring. However, when it is examined, the video display is very useful in diagnosing faults, as is shown in Table 12-1.

By pressing the "don't phase" button before pressing the "start" button, the programmer is made to step through without setting klystrons to standby or phasing them. This feature enables the operator at the maintenance console to examine the amplitude and phase stability of any klystron without disturbing machine operation. The "stop–start" buttons hold the programmer at any step for prolonged examination.

Appropriate use of these buttons and the "phase–don't phase" buttons permits the phase of one klystron to be adjusted without disturbing its neighbors.

As previously explained, the "fault override" button causes the programmer to proceed to the next step.

Table 12-1 Video display and diagnosis of faults

Video indication	*Possible cause*
No wobbled pattern (refer to Fig. 12-12)	1. No cw Reference available to phasing system—varactor multiplier off or disconnected. 2. Fault in wobbler or master generator. 3. Klystron already phased (no fault).
Wobbled pattern does not close, or "phase not OK" light stays on.	1. Trigger or gate mistimed. 2. Gated voltmeter or servo amplifier gain too low. 3. Phase shifter sticking (or brake not releasing). 4. Thermionic diode unbalance greater than 1.5 V (indicated by a large unsymmetrical "pedestal" on the klystron pulse). 5. Rapid phase jitter on beam or klystron pulse (can be seen on video pattern).

Operation in the sector alcove

All the above operations can be carried out from the sector alcove by manipulating the "start" and "fault override" buttons on the programmer. However, to monitor klystrons and diode balance, it is only necessary to rotate the selector switch on the front of the RF detector panel, and the programmer is more easily controlled by using the "advance" and "klystron selector" switches.

As previously mentioned, phase shifters may also be rotated manually from the programmer.

12-7 Operational results (HAH, ARW)

Correct operation of the automatic phasing system is essential to the rapid tuneup and spectrum optimization of the long accelerator.

Since the days of the first beam tests in Sector 1, it has always been possible to phase a sector locally (from the alcove) with speed (less than 1 min) and confidence (by monitoring the video on an oscilloscope), with residual phase error spread of less than $\pm 3°$. However, random recurrence of many faults (mostly included in Table 12-1) over the full thirty sectors of the machine led to initially unreliable performance when phasing was done from CCR with no video display available there.

Experience has led to the diagnosis and elimination of recurrent faults in the programmers and electronics panels, such as programmers skipping steps because of switching transients from the phase-shifter motors, noise on the video input to the gated voltmeters, and servo loop instability due to crossover distortion in the gated voltmeters.

With the installation of the video readout in CCR and beam current interlock, most malfunctions due to improper operating conditions have been eliminated.

Thermionic diode unbalance in the RF detector panel has always been a weakness in the reliability of the system. The trouble stems from the fact that the diode characteristics change with signal level and with time. While the wobbled signal amplitude stays within acceptable limits, as discussed earlier, divergence of the two diode characteristics at high signal levels (as produced by the klystrons) can easily result in a dc offset to the wobbled pulse which saturates the gated voltmeter preamplifier.

The present solution is to rebalance each diode pair once a week. However, for testing purposes, a "switched attenuator" has been added to the RF detector panels in two sectors. This device adds 20-dB attenuation to the RF path when the klystron is being phased and substitutes a low-attenuation, trombone phase shifter when the reference signal is being phased to the beam. The two paths are brought to the same electrical length by a fixed adjustment of the trombone. The switched attenuator certainly solved the diode unbalance problem but has the disadvantage that it could introduce an inherent phase error if the fixed length of either of the two paths should drift. Other solutions are still being sought.

In conclusion, it may be stated that the automatic phasing system is now recognized at SLAC to be an invaluable tool in the routine phase optimization of the machine, in setting up special phase conditions for positron acceleration, and for diagnosing klystron faults and intrasector beam loss.

Acknowledgments

Many people contributed to the conceptual and technical development of the automatic phasing system. The authors are particularly indebted to R. B. Neal, D. J. Goerz, and W. J. Gallagher for their contributions in formulating the idea of beam-induction phasing and to C. B. Williams and J. Dobson for much of the initial planning of the system. G. Jackson, Jr., J. R. Bordenave, P. V. Lee, K. E. Holladay, and C. E. Bolden were responsible for much of the work involved in designing, procuring, and testing system equipment.

References

1 D. J. Goerz and R. B. Neal, "Method of Phasing a Long Linear Electron Accelerator," Rept. No. ML-550, Microwave Laboratory, Stanford University, Stanford, California (October 1958).

2 W. J. Gallagher, D. Goerz, G. Loew, K. Mallory, R. Neal, and J. Pine, "Methods for Phasing Long Linear Accelerators," Rept. No. M-101, Stanford Linear Accelerator Center, Stanford University, Stanford, California (November 1958).

3 W. J. Gallagher, D. Goerz, G. Loew, K. Mallory, R. Neal, and J. Pine, "Methods of Driving Long Linear Accelerators," Rept. No. M-102, Stanford Linear Accelerator Center, Stanford University, Stanford, California (December 1958).

4 D. J. Goerz and R. B. Neal, "Phasing a Linear Accelerator from RF Phase Shift Due to Beam Loading Interaction," Rept. No. M-103, Stanford Linear Accelerator Center, Stanford University, Stanford, California (December 1958).

5 W. J. Gallagher, D. Goerz, G. Loew, K. Mallory, R. Neal, and J. Pine, "Comparison of Methods of Phasing Long Linear Accelerators," Rept. No. M-104, Stanford Linear Accelerator Center, Stanford University, Stanford, California (December 1958).

6 R. Belbéoch and C. B. Williams, "Current Variation Detection Technique of Phasing Linear Electron Accelerators," SLAC-TN-62-75, Stanford Linear Accelerator Center, Stanford University, Stanford, California (November 1962).

7 G. A. Loew, "Phasing System," Section III.E of the SLAC Source Book, Stanford Linear Accelerator Center, Stanford University, Stanford, California (March 1963).

8 K. L. Brown, A. L. Eldredge, R. H. Helm, J. H. Jasberg, J. V. Lebacqz, G. A. Loew, R. F. Mozley, R. B. Neal, W. K. H. Panofsky, and T. F. Turner, "Linear Electron Accelerator Progress at Stanford University," *Proc. Intern. Conf. High Energy Accelerators, Brookhaven, September 1961*, p. 101, U.S. Govt. Printing Office, Washington, D.C.

9 R. B. Neal, "Transient Beam Loading in Linear Electron Accelerators," Rept. No. ML-388, Microwave Laboratory, Stanford University, Stanford, California (May 1957).

10 G. A. Loew, "Non-synchronous Beam Loading in Linear Electron Accelerators," Rept. No. ML-740, Microwave Laboratory, Stanford University, Stanford, California (August 1960).

11 G. A. Loew, "Beam Induced Power in a Constant Gradient Accelerator Section," Tech. Note No. TN-63-19, Stanford Linear Accelerator Center, Stanford University, Stanford, California (March 1963).

12 A. G. Fox, "An Adjustable Waveguide Phase Changer," *Proc. Inst. Radio Engrs.* **35**, 1489 (1947).

13 J. Dobson and M. Lee, "The Beam Induction Technique of Phasing Linear Electron Accelerators over Large Ranges of Beam Current," Tech. Note No. TN-63-70, Stanford Linear Accelerator Center, Stanford University, Stanford, California (1963).

13

MODULATORS

R. W. Bradford, P. C. Edwards, C. W. Olson, Editor, R. M. Rowe, W. T. Tomlin, F. T. Veldhuizen, and A. L. Williams

This chapter describes two pulse modulators developed for the SLAC accelerator. The first is the "main modulator," one of which is associated with each high-power klystron. The second is the "sub-booster modulator," one of which is located in each of the thirty sectors of the machine to pulse a sub-booster drive klystron.

13-1 Main modulator

History (CWO)

During the initial design phase, several different types of modulators were considered. The one selected and built for the accelerator was the line-type modulator.[1] This was chosen not only because of its high efficiency and relatively low cost but also because of the large reservoir of practical experience on the line-type modulator which had accumulated at Stanford during the development of klystrons and earlier accelerators.

The original concept was to use eight large power supplies, each of which would be rated at approximately 3 MW output at 23 kV and would furnish dc on a common buss to thirty modulators. Each modulator was to have a fuse and a switch to disconnect it from the line for maintenance purposes. In addition, each modulator was to have a vacuum relay to remove it rapidly from the common dc buss in the event of switch tube faults. A power scavenging de-Q'ing system was to be included for fast regulation of the pulse-forming network voltage. Induction voltage regulators were to be used to regulate output voltage by feedback to the ac input.

Because spark gaps were not very reliable at 360 pulses/sec and would,

consequently, require considerable maintenance, the switching device considered for use in the modulators was the multigrid, mercury pool ignitron. No large single hydrogen thyratron capable of handling the specified power levels (65-MW peak, 75-kW average output) existed at that time. Initially, the ignitron appeared to be a good solution, but experiments revealed serious disadvantages such as excessive fault rate, excessive anode time delay, low holdoff voltage, short life, and complicated triggering. During the period of experimental work with ignitrons, the state of the art for hydrogen thyratrons was advancing, and, by 1963, tubes which would satisfy our requirements became available.

That same year, the large megawatt power supply concept was re-evaluated with respect to high-voltage stability during switch tube faults. It was recognized that large switch tubes will occasionally fault. During such occurrence a short circuit would be placed on the 23-kV supply. Although a vacuum relay would be incorporated to clear such faults, the buss voltage supplying the remaining twenty-nine modulators would vary during the fault duration. This would, in turn, cause the output of the modulators to change and klystron phase shift and power decrease to occur. A direct consequence of this phase shift and decrease in RF power would be degradation of the beam energy spectrum. This problem and the inflexibility of adjusting the voltage of individual modulators to compensate for different klystron perveances resulted in changing the design concept from large dc power supplies feeding many modulators to small ones for each modulator.

In the adopted system, ac power at 12.47 kV is fed the length of the accelerator into induction voltage regulators which step this voltage down to a selected value between 258 and 595 V. Each induction voltage regulator supplies ac power to sixteen modulators. This system provides improved isolation from modulator to modulator, better fault clearing because ac faults are easier to clear than dc faults, and the capability of making minor voltage adjustments on each modulator by changing primary taps on the local rectifier transformer to compensate for different klystron perveances.

General description (CWO)

The modulator built for the two-mile accelerator, shown in Figs. 13-1 and 13-2, was designed by SLAC personnel and fabricated and assembled from SLAC-supplied drawings and specifications.

The modulator and its associated pulse transformer was designed to meet or exceed the performance specifications given in Table 13-1.

The SLAC modulator is called a "line-type modulator." It is so named because it uses a capacitance–inductance network (pulse-forming network) constructed so as to simulate electrically a transmission line. A simplified diagram of the modulator is shown in Fig. 13-3. The main pulse and charging circuits have been drawn in schematic form to aid in the explanation of these circuits.

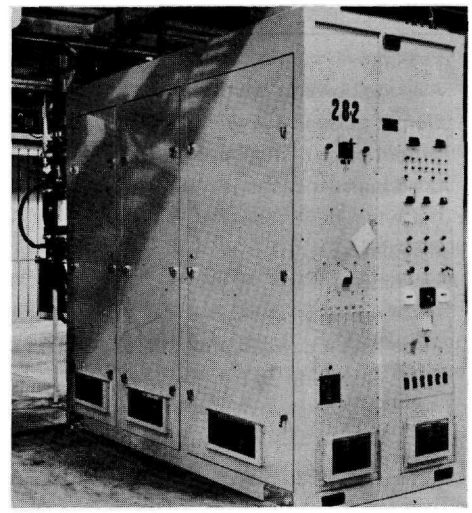

Figure 13-1 The SLAC modulator, view 1.

After each output pulse, the pulse-forming network (PFN) capacitors charge to approximately twice the dc power supply voltage because of the resonant charging characteristics of the charging transformer and the total PFN capacitance. The charging current flows from power supply ground, through the primary of the pulse transformer, the PFN inductors, the charging diodes, and the charging transformer to the positive side of the dc power supply. Because of the low values of inductances of the pulse

Figure 13-2 The SLAC modulator, view 2.

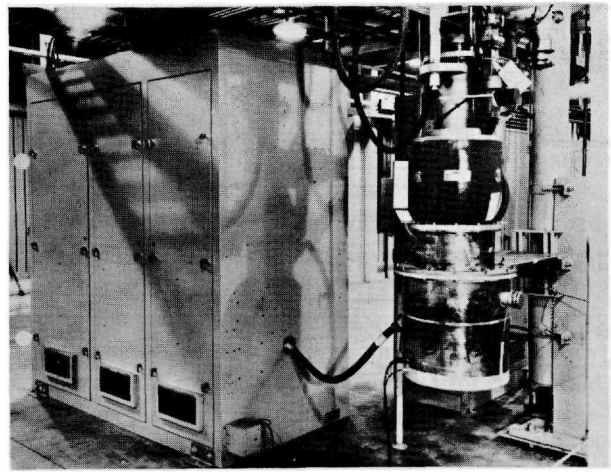

Table 13-1 Overall specifications of modulator (including pulse transformer)

Peak power output (max)	65 MW
Average power output (max)	75 kW
Output pulse voltage range	150–250 kV
Output pulse current range	110–262 A
Load impedance range	1365–955 ohms
Pulse length, flat top	2.5 μsec
Rise time	0.7 μsec
Fall time	1.2 μsec
Pulse repetition rates	360, 180, 120, 60 pulses/sec
Pulse height deviation from flatness (max)	$\pm$0.5%
Pulse amplitude drift	
Long term	$\pm$1.5%/hour
Short term	$\pm$0.25%/5-min period
Time jitter	$\pm$10 nsec

transformer primary and the PFN inductors, they have negligible effect on the charging cycle.

The PFN capacitor retains the voltage level of nearly twice the dc power supply voltage until the hydrogen switch tube is triggered. Once this occurs the PFN capacitors discharge through the primary of the pulse transformer, the switch tube, and PFN inductors. Since the reflected impedance of the klystron into the pulse transformer primary is approximately equal to the characteristic impedance of the PFN, half of the voltage on the PFN capacitors appears across the pulse transformer and half is dropped across the

Figure 13-3 Block diagram of modulator.

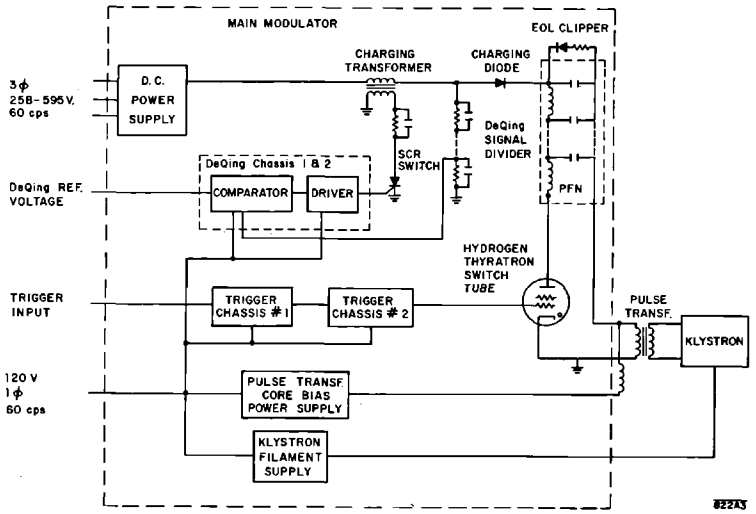

PFN. The time for complete discharge of the PFN is approximately 3.5 μsec. Once the discharge is complete, the positive plate voltage on the hydrogen thyratron extinguishes and conduction ceases.

In addition to the main pulse and charging circuits described above there are additional supporting circuits as shown in Fig. 13-3. Trigger chassis Nos. 1 and 2 receive the input trigger pulse and shape and amplify it to the value required to trigger the hydrogen thyratron switch tube.

The de-Q'ing chassis in conjunction with the silicon controlled rectifier (SCR) switch and the charging transformer regulates the value of the charge placed on the PFN. If this charge were allowed to vary, the subsequent output pulse to the klystron would, in turn, be affected. Without some form of regulation any short-term ac line variations would show up as changes in the output of the dc supply which would cause the network charge and output voltage to vary accordingly.

The de-Q'ing circuitry regulates as follows. The PFN voltage is sampled by means of a voltage divider. This PFN voltage analog is fed to the comparator together with a dc reference voltage. The dc reference voltage is also fed to the variable voltage substation (VVS), where it sets the level of the ac voltage fed to the modulators. When the sampled PFN voltage exceeds the dc reference voltage, the comparator generates an output pulse which is shaped by the driver chassis to trigger the SCR. The energy left in the charging transformer at the time the SCR conducts is dissipated in the secondary load resistor. The reverse blocking action of the charging diode causes the PFN voltage to be maintained at the value it had when the de-Q'ing circuit fired.

The de-Q'ing circuit is normally adjusted to dissipate a few percent of the charge in each cycle. It can, on a pulse-to-pulse and long-term basis, regulate the PFN voltage to 0.1% for line voltage changes of 3% or less, and for any repetition rate from 60 to 360 pulses/sec. Also, since the ac voltage from the VVS tracks the de-Q'ing reference voltage, the de-Q'ing system stays within range for all modulator output voltages.

A klystron filament power supply and a pulse transformer core bias supply are also included within the modulator. The output of both can be adjusted by controls and monitored by meters at the modulator's control panel.

The design, with the exception of the de-Q'ing circuitry, was patterned after conventional line-type modulators. Ideas from previous modulators procured from industry and from previous Stanford units were utilized.

The choice of the main high-voltage level in the modulator was governed by several factors. The major one was the ratings of the available switch tubes, which at the time the modulator was being designed, was 50 kV. In order to get the required rise time out of the pulse transformer, it was necessary to keep the turns ratio as low as possible. The klystron requires a maximum of 250 kV on its cathode. Therefore, using a turns ratio of 1:12, the modulator is required to produce a pulse of 21 kV. This pulse voltage demands about 40 kV maximum on the pulse-forming network which gives a comfortable margin with

50-kV thyratrons. Since the Q of the charging system is high, there is approximately 2:1 step-up in voltage from power supply to pulse-forming network. The power supply voltage required is, therefore, 20 kV plus about 3% for de-Q'ing. Approximately 5% "positive" mismatch is used at full voltage, i.e., the load impedance is about 5% higher than the PFN impedance.

The cabinet which measures 4 ft wide × 8 ft deep × 8 ft high is built of heavy gauge sheet steel. Three doors are provided on each long side to provide easy access to all components inside. Cooling for the components inside the cabinet is provided by three 1500-ft^3/min fans mounted just below exhaust ports in the roof of the modulator.

Radio frequency interference (RFI) was recognized as a problem because of the high pulse voltages involved. Precautions are taken to minimize RFI originating from high-energy pulse radiation. The cabinet is divided into two parts, the high and the low noise regions, with a steel bulkhead separating the two. As much of the low level circuitry as possible is placed in the low noise part so as to minimize RFI pickup on its wiring. The doors are equipped with RFI metal gasketing so as to form good conductive seals around the door edges. In addition, latches are provided around the edges of the doors to force them against the gasketing thus providing better conduction between mating parts. The air intakes and exhaust ports are covered with RFI filters of the honeycomb type to prevent radiation through these openings. All wires, ac and control leads, passing through the top of the cabinet are filtered with RFI filters to reduce conducted noise.

The control panel contains all the necessary controls, meters, and interlock lights to operate the modulator. The main circuit breaker on the left control panel is used for fault protection as well as for connecting and disconnecting the modulator from the main feeder buss which feeds fifteen additional modulators. The modulator is sufficiently stable to make run-up from low voltage unnecessary. It may be placed on the line at any VVS voltage setting within the operating range. For maintenance purposes, an auxiliary power input socket on the left control panel, just above the air intake, is used to supply power to the modulator from a portable power source. Access to this socket is made by unlatching its protective cover with the same key that, upon removal, locks out the main circuit breaker. This provides personnel protection and, in addition, prevents simultaneous excitation from two power sources.

The lethal voltages present within the modulator when the unit is operating made it mandatory to incorporate a number of personnel safety features. The modulator has a total of six lock-equipped doors. The key for five of these doors is located inside the modulator on the support post adjacent to the left rear door. The key for the latter door is attached by welded ring to another key normally inserted into a key interlock mounted on the front control panel. In order to remove the two keys it is necessary to rotate the key interlock to the "off" position. This electrically opens the interlock and prevents excitation of the high voltage. When the left rear door is opened, a spring-loaded two sectional high-voltage shorting switch closes and places a short across the

filter and PFN capacitors. In addition, a door microswitch in series with the five remaining door interlocks releases and electrically opens the interlock chain. Grounding hooks are also provided inside each door with an attached cable that drapes across the door opening to remind the individual gaining access to use the hook to ground out any potentially hazardous circuits.

It was recognized early in the design phase that each modulator–klystron station would be subject to various faults during operation, such as klystron arcs, vacuum system gas bursts, thyratron faults, high-voltage power supply overloads, and end-of-line clipper overcurrents. A circuit was incorporated in the modulator interlock chain which works in conjunction with an external klystron protection chassis. It recycles the modulator up to a predetermined number of faults (from 1 to 15 as set by a rotary switch on the control panel) in 55 min. If the actual faults exceed the predetermined number in the 55-min period, the modulator is shut down automatically and must be reset manually. Faults external to the modulator merely interrupt the trigger for approximately 1 sec or longer in case of continuous faults. Faults originating in the modulator interrupt the high voltage by opening a contractor in the primary of the main rectifier transformer. If the fault clears in 1.5 sec, the high voltage is turned on automatically and operation is resumed.

As can be seen in Fig. 13-2, the pulse transformer tank is external to the modulator cabinet and is an appendage hanging from the bottom of the klystron. A special triaxial cable feeds the pulse power from the modulator to the pulse transformer tank.

Figure 13-4 shows modulator-characteristic curves of the dc power supply output voltage and current, the de-Q'ing current, and the klystron beam voltage for various pulse repetition rates.

Figure 13-5 is an oscillogram of the klystron beam voltage pulse.

Figure 13-4 Modulator characteristics.

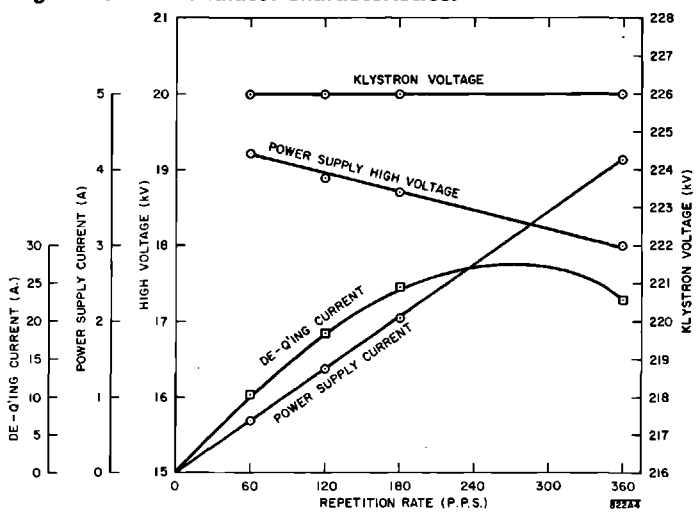

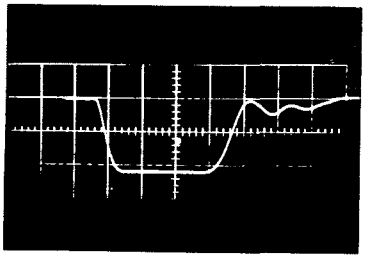

Figure 13-5 Klystron beam voltage pulse. (Time scale: 1 μsec/large division.)

Modulator power supplies (PCE)

The three-phase ac input to the modulator can be any level from 258 to 595 V, depending on the setting of the external induction voltage regulator. This regulator furnishes the ac power to a total of sixteen modulators. The input ac enters the modulator through three 125-A line filters which decouple high-frequency noise from the ac lines, thus preventing possible RFI.

The power supply used in the modulator is a conventional, three-phase, double-way, dc power supply. The three-phase variable voltage is delivered through a circuit breaker and contactor to a step-up rectifier transformer (see Fig. 13-6). The secondary of this transformer feeds power to a semiconductor rectifier assembly. The rectified output, proportional to the ac input, is delivered to the pulse-forming network via the inductance-capacitance (LC) rectifier filter and charging transformer.

Figure 13-6 Schematic diagram of modulator power supply.

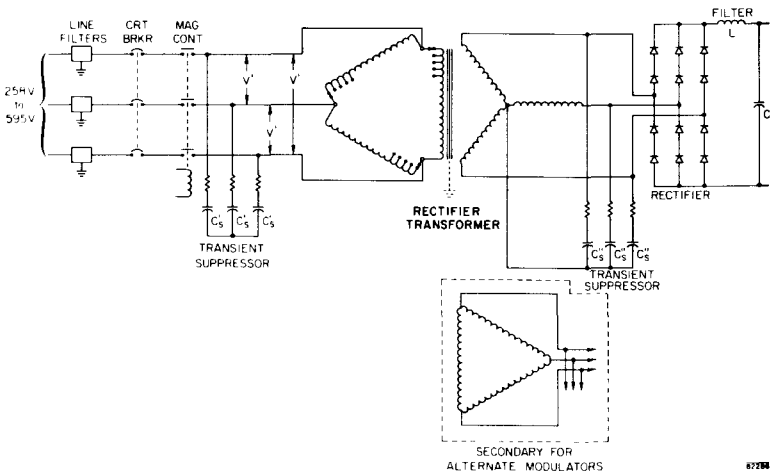

The rectifier transformer is an oil-filled, hermetically sealed, floor-mounted unit. It is rated to provide 3.8 A (rms) at 17.3 kV with 595 V in the primary. The primary has taps brought out to external terminals to allow reduction of dc output voltage in steps of 2.5, 5, 7.5, and 10%. The dc regulation is 8% (maximum) for a range from 5 to 100% full load. The reactance of the transformer was selected to be $10 \pm 0.75\%$. This fairly high leakage reactance was chosen to limit the load current during short circuit faults in order to protect rectifier units from damage. The transformer excitation does not exceed 5% at 595 V.

The secondary of the rectifier transformer is connected to a three-phase, double-way, semiconductor rectifier assembly. This assembly consists of six stacks of 100 silicon diodes, each capable of delivering 3 A average at 600 V. Each diode is paralleled with a resistance and a capacitor to equalize voltage distribution across the series string. The entire rectifier assembly is rated to deliver 23 kV at 4.5 A dc when the modulator is running at the maximum repetition rate of 360 pulses/sec.

The rectifier transformers for half of the 240 modulators are connected with a delta primary and a delta secondary while the remainder are connected delta–Y. The result is a phase shift in the harmonic currents of one group with respect to the other. The characteristic fifth and seventh harmonics of a six-phase rectifier effectively cancel one another.

Low-frequency transient suppressor networks are connected from line to line in the primary and secondary of the rectifier transformer. These suppressors not only reduce transients resulting from rectifier commutation action in the secondary but also prevent the occurrence of overvoltage caused by the interruption of exciting current in the primary.

If these transients are not suppressed, damage to the solid-state rectifier assembly can occur, and dielectric insulation failure can result from the repetition of transient overvoltages caused by the action of rectifier commutation. The capacitors in the primary suppressor are sized to maintain the transformer exciting current magnitude by resonating with the transformer's inductance at a frequency not greater than 60 cycles/sec for a short period after the primary voltage is disconnected from the transformer by opening the line circuit breaker. The transformer excitation and primary transient suppressor capacitor circuits are analyzed as follows:

1. The transformer excitation equivalent inductance for Δ winding connection is calculated from

$$L_e' = \sqrt{3}\, V'/2\pi f I_e$$

where

L_e = the equivalent inductance of the transformer excitation circuit in henrys
I_e = the exciting current measured in the supply lines, rms amperes
V' = the supply line to line voltage, rms volts
f = the frequency (=60 Hz)

2. The primary line to line suppressor capacitance, C_s', is calculated from

$$C_s' = [(2\pi f)^2 L_e']^{-1} \text{ farads}$$

The primary side suppressor circuit is connected in Y (with the neutral isolated). Therefore each capacitance has to be twice the value calculated from (2) above. The voltage rating of the capacitors is 660 V ac in order to provide sufficient safety factor. The transformer core loss serves as a damping feature for $L_e'C$, so that only a nominal value of resistance is needed in series with the suppressor capacitance to provide proper damping.

Transients due to rectifier commutation tend to cause ringing in the secondary circuit comprising the transformer winding leakage inductance and the coil inherent capacitance. The purpose of the secondary suppressors is not only to reduce this ringing frequency but also to damp the transient oscillation by the insertion of series resistance. Because resistance cannot be placed in a load current circuit, it is included in series with the capacitor. The secondary circuit is connected in Y with the neutral isolated. Thus, the suppressor is a series resistance–capacitance network shunted across the 17-kV lines. Analysis of the secondary circuit includes the following steps:

1. The capacitance C_2, reflected into the secondary from the suppressor capacitance C_s' in the primary, is given by

$$C_2 = \frac{2C_s'}{N^2}$$

where N = the secondary-to-primary turns ratio.

2. The secondary suppressor capacitance C_s'' is calculated from

$$C'' = [(2\pi f_1)^2 L_s'']^{-1}$$

and

$$C_s = [(2\pi f_0)^2 L_s'']^{-1}$$

where

C'' = the total capacitance formed by C_2 in series with the parallel combination of the suppressor capacitance C_s'' and C_s
L_s'' = the equivalent transformer leakage inductance in henrys
C_s = the coil inherent equivalent capacitance in farads
f_1 = the desired ringing frequency in hertz
f_0 = the natural frequency of the coil in hertz

Note that the transformer inherent frequency is typically 10–50 kHz, and $C''/C_s = (f_0/f_1)^2$. In order to reduce f_1 by one order of magnitude to avoid frequencies within the $L_s''C_s$ frequency bandwidth, the ratio C''/C_s has to be 100:1. The value of the damping resistance is calculated using $R_s = 2(L_s''/C'')^{1/2}$ ohms, where R_s is the series damping resistance including the transformer equivalent copper load loss resistance.

The LC filter in the dc circuit performs two functions. It attenuates the 360-Hz rectifier ripple to an acceptable value and reduces the ac power line

Table 13-2 Alternating current power-line harmonic currents at master substation

Pulse repetition rate (pulses/sec)	*For harmonic[a] frequency (Hz):*									
	120	180	240	300	420	660	780	1380	1500	*Total rms*
360	0.3	0.5	—	0.7	0.5	0.2	0.2	0.8	0.6	1.5
180	0.4	0.4	0.3	0.4	0.2	0.1	0.1	0.4	0.3	1.2
60	0.8	0.3	0.2	0.3	0.2	—	—	0.2	0.2	1.1

[a] Harmonic current expressed as percent of 60-Hz full load current at 360 pulses/sec.

harmonics, which result from resonant charging of the modulator PFN to less than 3% (total rms) of full modulator line current. The largest harmonic current occurs at 120 Hz when the modulator is operating at 60 pulses/sec.

The ac power line harmonic currents associated with operation of the accelerator are individually less than 1% of the fundamental (60-Hz) line current when the modulator is operating at full load. Table 13-2 lists the harmonics resulting from accelerator runs at 360, 180, and 60 pulses/sec. The maximum of all the harmonics is 1.5% rms and occurs at 360 pulses/sec. These harmonics flowing in the power system source impedance produce a 3% distortion of the line frequency sine wave. This amount of distortion is acceptable from the standpoint of interference with communications and control systems.

Typical harmonic current characteristics of an individual modulator are shown in Fig. 13-7. The result of using delta–delta and delta–Y transformer connections together with a phase-shifting transformer in the variable voltage substation is shown in Figs. 13-8 and 13-9. These circuit arrangements and the 12.47-kV cable itself attenuate the harmonic currents so that the master substation carries only a small fraction of the harmonics generated by the individual rectifiers in each modulator. This can be seen by comparing Table 13-2 with Fig. 13-7. Typical harmonic voltages in the 12.47-kV distribution system that result from operating the modulators at 360 pulses/sec are shown in Fig. 13-10.

The total power demand of the modulator system when operating at a level which produces 20-GeV beam energy at 360 pulses/sec is 20.4 MW as listed in Table 13-3. The wattless reactive component required to supply core excitation for the VVS induction voltage regulators as well as that resulting from the rectifier commutation phase angle lag is 10.4 MVAR. Table 13-3 lists the overall accelerator power loads typical for various repetition rates. The power demand load for klystron gallery conventional facilities and auxiliaries is less when the klystrons are operating at 360 pulses/sec than it is when they are being pulsed at 180 or 60 pulses/sec because the waveguide heaters shut off when the heating from RF system losses is sufficient to

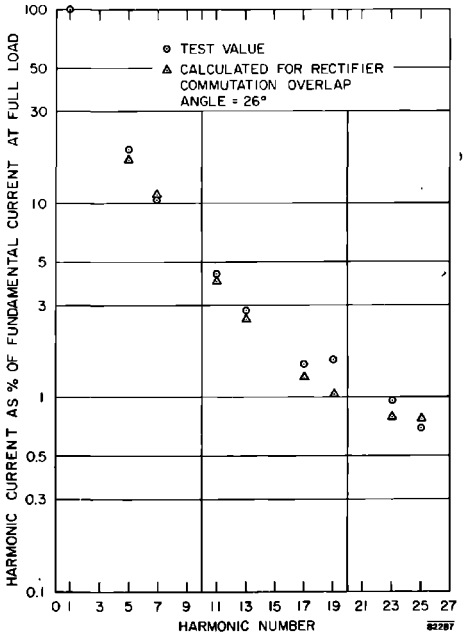

Figure 13-7 Individual modulator ac line-current harmonics.

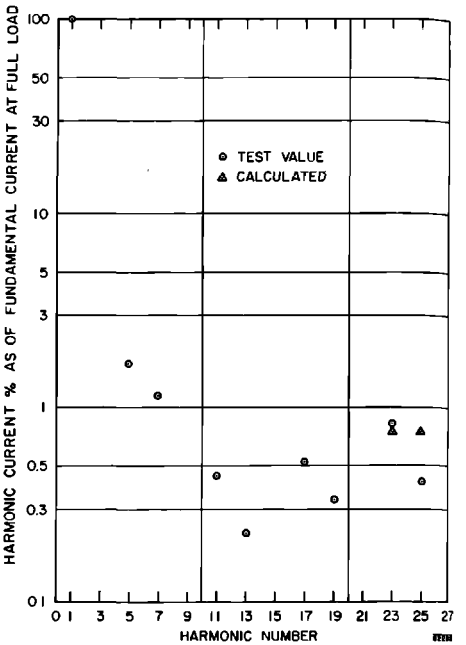

Figure 13-8 Plots of 12.47-kV line current harmonics at VVS input for 360 pulses/sec operation.

Figure 13-9 Plots of 12.47-kV line current harmonics at VVS input for 60 pulses/sec operation.

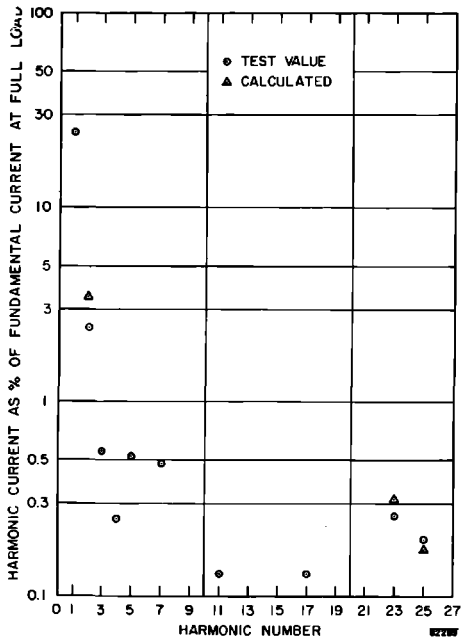

Figure 13-10 Plots of 12.47-kV line voltage harmonics at variable voltage substation input for 360 pps operation.

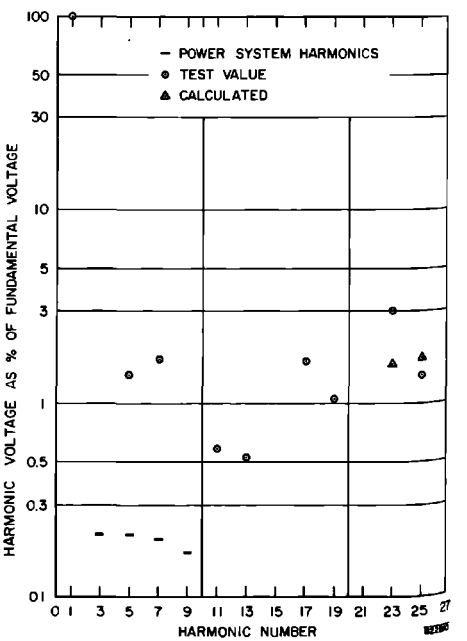

Table 13-3 Alternating current power requirements[a] at master substation for 20 Gev

Pulse repetition rate (pulses/sec)		*Power load (kW)*	*Reactive load (KVAR)*
360	Modulators (240) (ref. 105 V) plus injector	20,400	10,400
	Klystron gallery conventional facilities	4,141	1,900
	Total	24,541	12,300
180	Modulators (240) (ref. 105 V) plus injector	10,600	6,530
	Klystron gallery conventional facilities	5,128	1,870
	Total	15,728	8,400
60	Modulators (240) (ref. 105 V) plus injector	3,700	3,300
	Klystron gallery conventional facilities	5,128	1,870
	Total	8,828	5,170

[a] Not including cable or power factor correction capacitance.

hold the temperature. At 360 pulses/sec and 105 V reference the VVS output voltage is 502 V, the current is 92 A, and the power demand is 75 kW per modulator.

Pulse-forming network (ALW)

The pulse applied to the high-power klystron is specified to be a maximum of 250 kV at 262 A, with a rise time of 0.7 μsec, a fall time of 1.2 μsec, and a duration of 2.5 μsec, during which time the voltage is to be constant within ±0.5%. The pulse is supplied by a pulse transformer, which is driven by the modulator.

To drive the primary of the pulse transformer, a two-terminal device, the PFN, is used. The PFN simulates the characteristics of a transmission line by the use of lumped capacitive and inductive elements. The PFN used in this modulator is a modified type-E circuit consisting of two parallel networks of ten fixed-value capacitors and ten essentially uncoupled slug-tuned inductors (see Fig. 13-11).

Figure 13-11 Schematic diagram of simplified modulator.

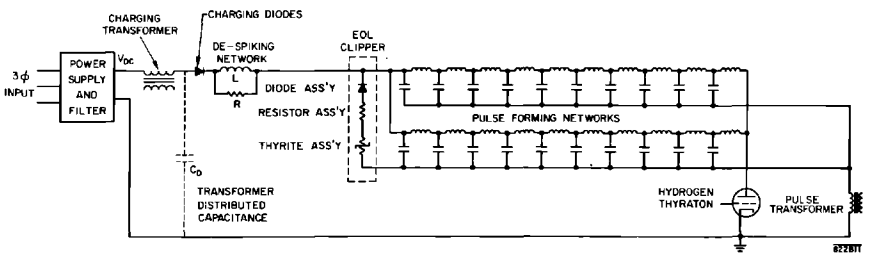

The PFN stores energy in the capacitors at a slow rate and discharges it rapidly in the form of a rectangular pulse of short duration when the hydrogen thyratron is triggered. The duration of the pulse and its approach to an ideal rectangular shape depends on the circuit constants of the PFN.

Although the circuit values of the individual *LC* sections for a particular pulse shape can be derived theoretically, it is much simpler to start off with the total value of capacitance and inductance required and experimentally derive the individual values. In a strictly theoretical approach, it is difficult to account for parameters such as stray capacitance and inductance that are always present in an actual circuit. In the PFN of this modulator, the total capacitance was derived from the energy equation below which states that the energy stored in the PFN before discharge must equal the energy supplied to the load, i.e.,

$$\tfrac{1}{2}CV_c^2 = \int_0^T V_p I_p \, dt$$

or

$$C = \frac{2V_p I_p T}{V_c^2} \tag{13-1}$$

where

C = the total PFN capacitance
V_c = the voltage across PFN capacitance (41.6 kV)
V_p = the pulse transformer primary voltage (20.8 kV)
I_p = the pulse transformer primary current (3000 A)
T = the duration of pulse (3.35 μsec, which includes the equivalent duration of rise and fall times).

The total inductance is found from the PFN characteristic impedance equation, viz.,

$$Z_0 = \left(\frac{L}{C}\right)^{1/2} \tag{13-2}$$

The choice of individual capacitance and inductance values and their number is influenced by previous knowledge of PFN characteristics. Pulse rise time is dependent on the number of *LC* sections. The greater the number, the faster the rise time. The way the leading edge turns into the flat top is mainly controlled by the value of the inductance nearest the switch tube. A comparatively large value for this coil rounds off the top of the leading edge. Small values give a sharp overshoot which trails off into the flat top. Flat-top irregularities are smoothed out by adjusting for symmetry between *LC* sections.

In this modulator it was determined that a dual ten-section PFN with fixed capacitors of approximately 0.014 μF and tunable inductors of a

maximum inductance of 4.5 μH would satisfy the pulse requirements. The dual section PFN was initially used in a split configuration, one section for each of two smaller switch tubes. When the large single switch tube became available, the two PFN's were paralleled. Had the single tube been available during the early design phase, a single ten-section PFN, with larger capacitors, would have been used. The use of tunable inductors allows adjustment over discrete portions of the output pulse. Pulse characteristics such as duration, rise time, droop, flat-top ripple, and fall time can be varied in a coarse manner by locating the interconnecting strap to the desired coil turn, and fine adjustments are made by varying the depth of insertion of a copper-tuning slug in the coil.

The fixed capacitors are specified to be between 0.013 and 0.015 μF and 50-kV operating voltage. The dielectric and impregnant used in these capacitors are polyethylene and silicone oil, respectively. The losses with these materials were found to be approximately one-third the losses in equivalent paper–oil capacitors.

The tunable inductors are mounted on the capacitor's high-voltage bushing stud. The inductor consists of ten turns of $\frac{3}{8}$-in. o.d. copper tubing with a center-to-center spacing of 4 in. and a length of 7 in. A three-fingered spacer of molded insulating material is mounted inside the inductor and supports a $2\frac{1}{2}$-in. diameter, $5\frac{1}{8}$-in. long, tubular copper slug. Each of the capacitor–inductor assemblies are interconnected by braided straps, one end of which is attached to the capacitor high-voltage bushing and the other end to the inductor using a cable clamp. Figure 13-12 shows the PFN installed in the modulator.

The PFN can be adjusted while the modulator is operating by installing in the modulator door opening a protective Lucite–wire screen. A Lucite tuning rod with a protective grounding ring midway along its length can be inserted through holes in this screen to adjust the copper tuning slugs.

End-of-line clipper (ALW)

The end-of-line clipper consists of a series combination of diodes, power resistors, and Thyrite resistors. (See Fig. 13-11.) The entire assembly is connected across the last (farthest removed from the switch tube) PFN capacitor. The function of the end-of-line clipper is to provide a low-impedance load for the collapsing field of the PFN inductors after a klystron fault. Without the end-of-line clipper, the excess energy on the PFN inductors would be transferred as an inverse charge to the PFN capacitors. Such a negative charge on the capacitors would have two adverse effects. The thyratron switch tube could be damaged by reverse arc-through and the PFN capacitors could be over voltaged (in the absence of de-Q'ing) during the next charging cycle. While accomplishing the objective of preventing a high inverse voltage being placed on the PFN capacitors after a load fault, the end-of-line clipper must present essentially an open circuit to the normal PFN positive charge and also

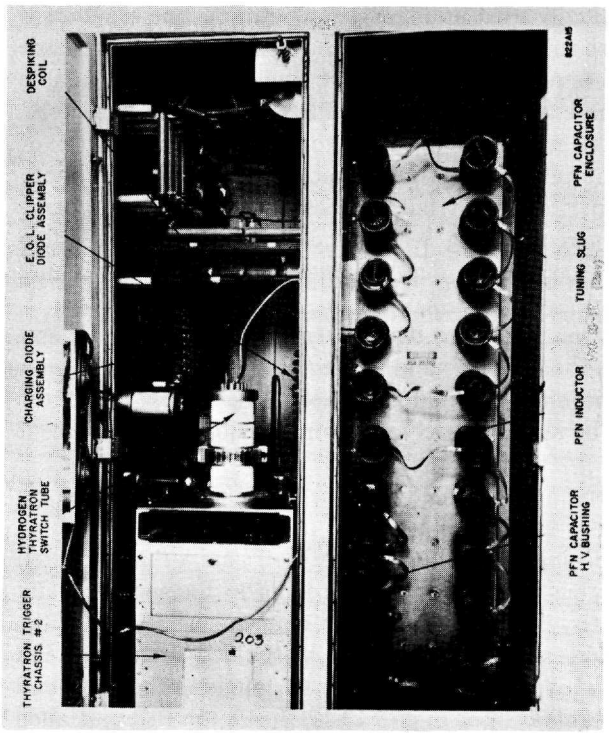

Figure 13-12 Pulse-forming network, installed.

present a high impedance to the low inverse voltage required for thyratron deionization.

The diode section of the end-of-line clipper consists of a series string of one hundred and fifty resistance-capacitance (RC)-compensated, 600-V, 20-A silicon diodes. These diodes provide a low-impedance path for inverse voltages and essentially an open circuit to the normal PFN positive voltage.

The resistor assembly comprises four parallel legs of two 10-ohm, 200-W resistors in series to give an equivalent resistance of 5 ohms. These resistors along with the Thyrite assembly provide essentially a matched power dissipating load to the PFN for the high inverse charge.

The Thyrite assembly is made up of four parallel legs of six 6-in. diameter Thyrite disks in series. Thyrite is a nonlinear resistive material in which the resistance varies inversely as a power function of the voltage. With a negative deionization voltage of say, 3.6 kV the resistance of this Thyrite assembly is approximately 2 kohms. When the high negative fault voltage is impressed on the Thyrite assembly, the resistance drops to an extremely low value, and the

series combination of diodes, power resistors, and Thyrites provides a low impedance to dissipate the negative charge on the PFN. A monitoring device consisting of a current transformer–relay combination senses end-of-line clipper current each time a load fault occurs. In this event, the recycle circuit mentioned earlier in this chapter causes the modulator to be turned off for approximately 1.5 sec and then turned on again.

Pulse-forming network voltage regulation (de-Q'ing) (WTT)

Regulation of the klystron pulse voltage is accomplished by controlling the voltage to which the PFN is charged. This method, although somewhat indirect, is much simpler than working directly with the 250-kV klystron pulse. It has the disadvantage, however, that the actual regulation occurs sometime prior to pulsing the klystron, and leakage in the PFN capacitors or external leakage paths across the network will allow the PFN voltage to discharge slightly. In the SLAC modulators, operating from 60 to 360 pulses/sec, the time delay between regulation and pulsing varies from approximately 14.7 to 0.75 msec. As the discharge or leakage rate is constant, regulation is not affected at fixed repetition rates. The PFN voltage and, consequently, the klystron voltage will decrease slightly, however, when the repetition rate is changed from 360 to 60 pulses/sec.

Regulation against two causes of PFN voltage variation is necessary to insure klystron pulse stability. As the PFN voltage is a direct function of the dc power supply voltage (Eq. 13-5) and this, in turn, is proportional to the ac input voltage, any change in the input is reflected as a change in the PFN voltage. Although the modulators are fed in groups of sixteen by an induction voltage regulator, this unit has a minimum response time of several seconds and cannot regulate for pulse-to-pulse amplitude variations. The second need for regulation arises from either misfiring of the main thyratron during the charging cycle or arcing in the load during the output pulse. Either will result in an increase in PFN voltage for the succeeding charging cycle although the latter effect is greatly reduced by use of a negative discharge circuit (end-of-line clipper) for the PFN as discussed earlier.

A simplified diagram of the PFN charging and regulating circuits is shown in Fig. 13-13 along with the pertinent waveforms. In the conventional method of regulation or de-*Q*'ing, the charging transformer is a single-winding inductor shunted by a parallel *RC* network in series with a switch, usually a thyratron tube. Because the charging inductor voltage rises to approximately twice that of the dc power supply, the tube, its filament and reservoir transformers, and the *RC* network all rise to a very high voltage above ground, requiring large insulators and component separation. It is also necessary to insulate the tube from its trigger circuitry. Space was not available for insulating these components to 45 kV, so the step-down transformer circuit of Fig. 13-13 was developed. An additional advantage of the low-voltage regulating circuit was that a solid-state switch could be employed, offering longer life and more trouble-free operation.

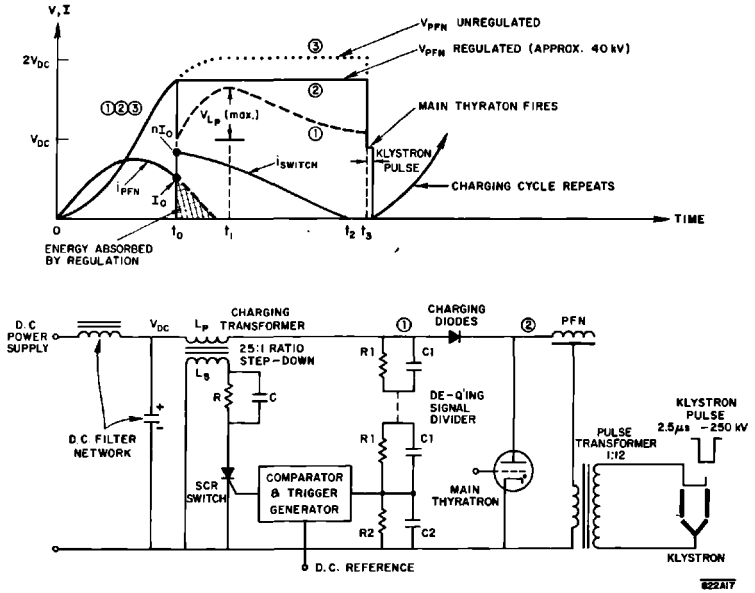

Figure 13-13 Pulse-forming network charging and regulating circuits with waveforms. Regulation occurs at t_0. Maximum silicon controlled rectifier switch current $= nI_0$, where $n = 25$.

The operation of either circuit is basically the same, the major difference being the leakage inductance present in the charging transformer. For the lossless (infinite Q) case, the charging current flowing into the PFN capacitors and the resultant voltages across the charging transformer primary and the PFN are given, respectively, by

$$i_{\text{PFN}} = \frac{V_{\text{DC}}}{\omega L_p} \sin \omega t \tag{13-3}$$

$$V_{L_p} = -L_p \frac{di_{\text{PFN}}}{dt} = -V_{\text{DC}} \cos \omega t \tag{13-4}$$

$$V_{\text{PFN}} = \frac{1}{C_{\text{PFN}}} \int_0^t i_{\text{PFN}}\, dt = V_{\text{DC}}(1 - \cos \omega t) \tag{13-5}$$

where $\omega = (L_p C_{\text{PFN}})^{-1/2}$, and L_p is the inductance of the charging transformer primary.

The charging current is restricted to a unidirectional flow by the presence of the charging diode and thus forms the basis for this method of regulation. If the current is forced to stop flowing into the PFN, then the voltage will remain at the level reached except for the small leakage present. This is accomplished by "loading" the charging transformer (or inductor) with a parallel resistor and capacitor. The voltage across the inductor then becomes a function primarily of its inductance, the magnitude of the current when the switch was

closed, and the added resistance and capacitance. Initially the uncharged capacitor in the secondary circuit appears as a short circuit and the voltage across the inductor drops to zero as shown in Fig. 13-13. It will then assume one of three possible forms, depending upon whether the *R–L–C* combination is overdamped, critically damped, or underdamped. Lowering the transformer primary voltage drop thus causes the anodes of the charging diodes to become negative with respect to their cathodes, and conduction ceases.

Considering the underdamped or damped oscillatory case with the resistance and capacitance reflected into the transformer primary, and assuming that current flow to the PFN is zero, the voltage across the inductance is given by

$$V_{L_p} = \frac{I_0}{\omega_0 C} \exp\left[-\frac{\omega_0(t-t_0)}{2\omega_0 RC}\right] \sin \omega_0(t-t_0) \tag{13-6}$$

where

$$\omega_0 = \left(\frac{1}{L_p C} - \frac{1}{4R^2C^2}\right)^{1/2}$$

and

$$I_0 = \frac{V_{DC}}{\omega L_p} \sin \omega t_0$$

that is, I_0 is the magnitude of the charging current i_{PFN} at the instant of regulation (t_0 in Fig. 13-13). This analysis has neglected any resistance in the charging transformer, wiring, or semiconductor switch as these would normally be so small as to have a negligible effect on the resultant voltage and would merely serve to complicate the calculation. It has also neglected transformer secondary leakage reactance as this is a small inductance and contains no initial stored energy. Equating the time derivative of Eq. (13-6) to zero indicates that V_{L_p} is maximum when $2\omega_0 RC = \tan \omega_0(t_1 - t_0)$. The equation for $V_{L_p}(\max)$ can then be written as follows:

$$\begin{aligned} V_{L_p}(\max) &= I_0 R\left[2 \exp\left(-\frac{\omega_0(t_1-t_0)}{\tan \omega_0(t_1-t_0)}\right) \cos \omega_0(t_1-t_0)\right] \\ &= I_0 R[K_E] \end{aligned} \tag{13-7}$$

where $(t_1 - t_0)$ = the time required after t_0 to reach $V_{L_p}(\max)$. The values of K_E, the bracketed expression of Eq. (13-7), can be calculated as a function of $\omega_0(t_1 - t_0)$ and are given in Table 13-4.

Table 13-4 Values of K_E of Eq. (13-7) for different values of $\omega_0(t_1 - t_0)$

$\omega_0(t_1 - t_0)$	Deg.	30	35	40	45	50	55	60	65	70	75	80
	Rad.	0.533	0.611	0.698	0.785	0.873	0.960	1.047	1.134	1.222	1.309	1.396
K_E		0.688	0.684	0.666	0.645	0.618	0.583	0.545	0.496	0.438	0.364	0.281

From Eq. (13-7),

$$R = \frac{V_{L_p}(\max)}{I_0 K_E} \tag{13-8}$$

and from the maximization condition,

$$C = \frac{\tan \omega_0(t_1 - t_0)}{2\omega_0 R} \tag{13-9}$$

To obtain the actual values required in the transformer secondary, R must be divided by the square of the turns ratio and C multiplied by this value. Since a damped oscillatory condition was chosen to insure i_{L_p} reaching zero before the start of the next charging cycle, ω_0 should be selected so that

$$\omega_0(t_3 - t_0) + \omega_0(t_1 - t_0) \geq \pi \tag{13-10}$$

The time between pulses for the fastest repetition rate should be used for t_3. If the repetition rate is lowered, t_3 will increase and V_{L_p} and the switch current will have time to reverse unless the switch is unidirectional. The silicon-controlled rectifier is essentially unidirectional except for a short turnoff or recovery time. From Eq. (13-6) it is clear that the lower the value of $\omega_0 RC$, the more damped will be the negative half-cycle of the waveform and, consequently, the less will be the strain on the switching device. The charging current, which was flowing through the transformer primary L_p to the PFN, is diverted to the RC network at t_0. For the conventional method with a single-winding inductor, it has the form:

$$i_{L_p} = I_0 \exp\left[-\frac{\omega_0(t - t_0)}{2\omega_0 RC}\right] \frac{\sin[\omega_0(t - t_0) + \omega_0(t_1 - t_0)]}{\sin[\omega_0(t_1 - t_0)]} \tag{13-11}$$

This current has an initial value of I_0 and then decays as a damped sinusoid with its phase and magnitude determined by the value of $\omega_0(t - t_0)$.

From the definition of ω_0, Eq. (13-6), L_p must be less than $4R^2C$ for the underdamped or oscillatory condition to exist. It should also be noted that L_p must be selected in conjunction with the total PFN capacitance so that sufficient time is allowed to dissipate the energy remaining in the charging transformer. Energy remaining at the beginning of the next charging cycle will result in the charging current starting at some nonzero value. This can result in transients in the circuit and will also cause the PFN to charge at a faster rate which will affect the recovery of the main thyratron. An additional term, $\omega L_p I_{t_3} \sin \omega t$, must be added to Eq. (13-5) as a result of the current still flowing at t_3.

The choice of $V_{L_p}(\max)$ is somewhat arbitrary and depends upon the difference between the maximum PFN voltage (without de-Q'ing) and the desired regulated level of PFN voltage. This does not mean that regulation will cease for voltages even higher than the design maximum but, that under certain

circumstances, some charge may pass to the PFN with a resulting increase in voltage. Referring to Fig. 13-13, it is obvious that V_{L_p} should not be allowed to rise above the regulated value of V_{PFN} for some allowable increase in V_{DC}. The normal operating magnitude of $V_{L_p}(\text{max})$ must be somewhat less than this. A value of $V_{L_p}(\text{max})$ equal to approximately 25% of the power supply voltage V_{DC} will provide for regulation over a considerable increase in voltage. The normal operating value of regulated PFN voltage is selected to take care of the maximum decrease expected in ac line voltage and should usually be set for a range of 3 to 5 % regulation. Percentage regulation is here defined as follows:

$$\% \text{ regulation} = \frac{V_{\text{PFN}}(\text{unreg}) - V_{\text{PFN}}(\text{reg})}{V_{\text{PFN}}(\text{unreg})} \times 100 \tag{13-12}$$

It should be remembered that the greater the percentage regulation, the higher the power dissipation so that some discretion is necessary in making this choice. Another point to be considered is the "dead" region resulting with very low values of regulation; that is, where the time rate of change (dV_{PFN}/dt) approaches zero. Most comparator circuits respond in proportion to this rate of change. This region of uncertainty in de-Q'ing performance cannot be accurately defined but measurements indicate that it includes values of regulation below about 0.25%.

To complete the selection of the two required parameters, resistance and capacitance, it now remains to discuss power dissipation and energy. A comparison between the inductive voltage and current, Eqs. (13-6) and (13-11), shows that the current leads the voltage by the angle $\omega_0(t_1 - t_0)$. The current, therefore, reaches zero when $\omega_0(t - t_0) + \omega_0(t_1 - t_0) = \pi$ and the energy in the inductance becomes zero at the same time. The initial energy $(\frac{1}{2}L_p I_0^2)$ is then stored in the capacitor, less the amount which was dissipated in the resistance. The current will try to flow in the reverse direction, with the voltage still positive across the switching device. The semiconductor switch will turn off when the current drops below a certain level, known as the holding current. A short recovery period or turnoff time is involved, but this is a matter of a few microseconds, approximately 25 in the large, high-current devices. The capacitive energy is then isolated from the inductance and is dissipated at a rate determined by the RC time constant, which is the same rate at which the damped voltage and current sinusoids were attenuated. In the actual circuit, a series RC protection against voltage spikes is placed across the switch so that a small amount of negative current continues to flow. The average power dissipated over the entire charging period is determined from the inductive energy as follows:

$$P = \frac{\frac{1}{2}L_p I_0^2}{t_3} = \tfrac{1}{2}(\text{PRR})L_p I_0^2 \tag{13-13}$$

where PRR is the pulse repetition rate.

The magnitude of I_0, as defined in Eq. (13-6), can also be calculated in terms of V_{PFN} and V_{DC} by combining Eqs. (13-3) and (13-5), in which case

$$I_0 = \left[\frac{C_{PFN}}{L_p} V_{PFN}(2V_{DC} - V_{PFN})\right]^{1/2} \tag{13-14}$$

where V_{PFN} represents the voltage at t_0, i.e., the regulated value.

So far, transformer leakage reactance has not been introduced into the analysis. The secondary leakage, which will be quite small for the low-voltage winding, has only a very minor effect on the regulation. Primary leakage inductance, on the other hand, contains energy due to the flow of charging current which is not extracted by the process of loading the secondary. The transformer should, therefore, be designed so that this leakage is as small as possible. The complexity of the circuit prevents an exact explanation of its behavior. In the first place, it was assumed that the semiconductor-charging diode was a perfect unidirectional switch and this is not exactly true—a recovery time of 10 to 15 μsec is typical in medium-sized diodes. Second, the exact nature of the circuit is not known; only an approximate equivalent circuit can be considered. Referring to Fig. 13-13, the following simplified explanation can be given, again assuming that the charging diode ceases conduction at t_0. The primary leakage reactance will appear as a series inductance in the charging circuit, not shunted by the secondary resistance and capacitance, and having a stored energy of $\frac{1}{2}L_L I_0^2$ joules. There is also a distributed capacitance, C_D in Fig. 13-11, from both primary and secondary to ground. This distributed capacitance on the primary side of the SLAC transformer is approximately 0.0025 μF and can be considered in parallel with the de-Q'ing signal divider and, therefore, charged to a voltage V_{DC} at t_0. The R–L_p–C combination can be transformed approximately into a two-element series equivalent circuit and, due to the low Q of the combination, one element will be a resistor of sizable value. The leakage inductance is, therefore, still contained in a closed path which will prevent an abrupt interruption of its current flow. If transferred directly to the distributed capacitance, the inductive energy would cause a voltage rise equivalent to $I_0(L_L/C_D)^{1/2}$. However, the derived low-Q, series R–L–C network results in a damped sinusoidal current which is initiated by an impulse function equal in magnitude to $L_L I_0$. The voltage which this current develops across the distributed capacitance is then superimposed on V_{L_p} of Fig. 13-13. It is considerably more damped than V_{L_p} and has a much higher frequency. Unfortunately, the exact magnitude of this voltage cannot be determined, but it could very well reach a value in excess of the regulated PFN voltage. It is, therefore, necessary to reiterate that the transformer leakage reactance should be as small as possible in order to minimize this voltage.

From the foregoing analysis, it is apparent that the entire design procedure is clouded with a certain degree of arbitrariness. Furthermore, the complexity of the equations encountered, even after simplifying assumptions are made, makes a rigorous generalized analysis of the circuit impossible. Some

insight into the problems involved, though, and a knowledge of the general approach will aid considerably in performing the circuit design.

The de-Q'ing signal divider plays an important part in the accuracy obtained. Accuracy is best described as percentage error and is defined as follows:

$$\% \text{ error} = \frac{\Delta V_{PFN}(\text{reg})}{V_{PFN}(t_0)} \times 100 \tag{13-15}$$

Certain fixed delays are inherent in the system, both in the comparator and trigger circuits and in the turn-on time of the semiconductor switch. The turn-on time is typically 10 μsec or more for high-current devices although the exact definition of full turn-on may vary somewhat. The delay in the comparator and trigger generator depends upon the circuit used and is not necessarily constant for different percentages of regulation. For a high degree of accuracy, the desired level of the attenuated V_{PFN} waveform must be compared to a very stable, highly regulated dc voltage. For small percentages of regulation, near its maximum value, the time rate of change of this voltage is very small, and the rise time of the comparator output pulse may be greater than it would be with a faster rising input signal. Nevertheless, a certain delay does exist, and assuming that it is fixed, the result of it can be seen by studying Fig. 13-14.

The solid line of waveform 1 represents a normal-amplitude PFN voltage. The command to commence regulation is given at point B, and it is assumed that the de-Q'ing signal divider is exactly compensated (zero phase shift) and the system requires about 10° delay, an exaggerated figure for the purpose of illustration. Therefore, 10° later the regulation process is complete, and the PFN voltage is set at the level represented by C. Next, consider a cycle in

Figure 13-14 Compensated de-Q'ing signal divider waveforms.

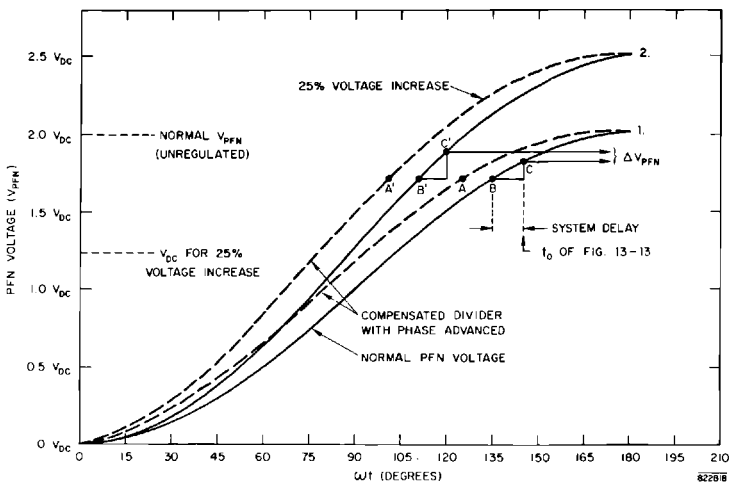

which all conditions remain the same but a 25% increase in unregulated PFN voltage occurs as represented by waveform 2. The command to regulate, now B′, is given at the same voltage level although occurring earlier in time. The regulated level, again reached after a 10° delay, is set at C′. It is readily seen that this latter level represents an increase over the value attained with normal voltage, and this increment is identified as the numerator of Eq. (13-15). The denominator is taken as point C which represents t_0 of Fig. 13-13.

If the waveform from the de-Q'ing signal divider is now advanced in phase by the required amount, the commands to regulate are given at points A and A′ for the normal and increased PFN voltage, and the regulation occurs at points B and B′. These points now represent the same level of voltage, and the regulation is ideal; that is, the percentage error is zero. It should be noted that if the phase were advanced further, so that overcompensation existed, the regulated value of the increased voltage would be less than for the normal voltage.

To calculate the phase shift associated with the divider network, consider a divider consisting of n identical sections of R_1 and C_1 and an output section of R_2 and C_2. This results in $n+2$ simultaneous integral equations and, if driven by the PFN voltage of Eq. (13-5), the solution for the output voltage across R_2 is represented by the following equation. For $V_{in} = V_{DC}(1 - \cos \omega t)$,

$$V_{out} = V_{DC} \frac{R_2}{nR_1 + R_2} [1 - K_1 \cos(\omega t + \theta) + K_2 e^{-t/\tau_p}] \qquad (13\text{-}16)$$

where

$$\theta = \tan^{-1} \frac{\omega(\tau_1 - \tau_p)}{\omega^2 \tau_1 \tau_p + 1}$$

$$\tau_p = \frac{nR_1R_2}{nR_1 + R_2} \left(\frac{C_1}{n} + C_2 \right) \approx R_2 C_2$$

$$\tau_1 = R_1 C_1$$

$$K_1 = \left[\frac{\omega^2 \tau_1^2 + 1}{\omega^2 \tau_p^2 + 1} \right]^{1/2}$$

$$K_2 = \frac{\omega^2 \tau_p (\tau_1 - \tau_p)}{\omega^2 \tau_p^2 + 1}$$

An examination of this expression indicates that it reduces to the input waveform, reduced by the resistive ratio, when τ_1 equals τ_p. For a constant phase shift, which is necessary for the greatest accuracy, the last term in the equation should be zero. Although this is not possible, the term will essentially vanish after five time constants so that the earliest reference to the waveform should be made after a time $\geq 5\tau_p$. In calculating R_2 and C_2, consideration must be given to the input resistance and capacitance of the comparator circuit and any cable capacitance between the divider and comparator. The choice of R_1 in

high-voltage circuits must take into consideration power dissipation and voltage rating, in conjunction with the desired time constant, and the number of sections required is determined by these factors. The resistors must also be noninductive with low temperature and voltage coefficients and low thermal noise. A further consideration is corona, which is associated with circuits operating above approximately 30 kV. This may make it necessary to immerse the divider in oil, as was the case with SLAC modulators. As the system time delay is never known exactly when the original modulator design is made, the practical approach is to calculate the resistors and C_1 and then adjust C_2 for best regulation when the circuit is tested.

The final selection to be made is the choice of semiconductor switch. This requires a knowledge of the maximum voltage to be expected across the device and the average and rms currents. Root-mean-square current is not easily determined but can be approximated closely enough for practical purposes by calculating the current for the much simpler case when the system is critically damped and ω_0 is zero. This results in

$$I_{\text{switch}}(\text{rms}) \approx I_0\left(\frac{(\text{PRR})L_p}{1.6R}\right)^{1/2} \tag{13-17}$$

where R is the secondary resistance for the transformer-coupled circuit. Average current can be calculated by an integration of Eq. (13-11) and is accomplished by referring this current to the transformer secondary to give the following form:

$$i_{\text{switch}} = \frac{nI_0 \exp\left[-\dfrac{\omega_0(t-t_0)}{2\omega_0 RC}\right] \sin[\omega_0(t-t_0)+\omega_0(t_1-t_0)]}{\sin[\omega_0(t_1-t_0)]} \tag{13-18}$$

and

$$I_{\text{switch}}(\text{AV}) = \frac{(\text{PRR})}{\omega}\int_0^{\pi-\omega_0(t_1-t_0)} i_{\text{switch}}\, d(\omega_0 t) \tag{13-19}$$

The upper limit of integration is obtained by solving Eq. (13-18) for the angle $\omega_0(t_2 - t_0)$ at which the switch current becomes zero. This will always be in the second quadrant and can, therefore, be written as $\omega_0(t_2 - t_0) = \pi - \omega_0(t_1 - t_0)$. The lower limit is identified as the angle $\omega_0 t_0$ when the de-Q'ing circuit is fired and represents zero on the $\omega_0 t$ angular scale. Inserting Eq. (13-18) in Eq. (13-19) and carrying out the integration yields

$$I_{\text{switch}}(\text{AV}) = (\text{PRR})nI_0(L_p C_{\text{PFN}})^{1/2}\left\{\exp\left[-\frac{\pi-\omega_0(t_1-t_0)}{\tan\omega_0(t_1-t_0)}\right] \times \sin\omega_0(t_1-t_0) + \sin 2\omega_0(t_1-t_0)\right\} \tag{13-20}$$

where n is the charging transformer turns ratio. The value of the term in braces $\{K_I\}$ is evaluated in Table 13-5, using the same values of $\omega_0(t_1 - t_0)$ as in Table 13-4.

Table 13-5 Values of K_I of Eq. (13-20) as a function of $\omega_0(t_1 - t_0)$

$\omega_0(t_1 - t_0)$	Deg.	30	35	40	45	50	55	60	65	70	75	80
	Rad	0.533	0.611	0.698	0.785	0.873	0.960	1.047	1.134	1.222	1.309	1.396
K_I		0.871	0.955	1.020	1.066	1.100	1.118	1.124	1.122	1.109	1.091	1.066

The triggered semiconductor devices, commonly known as silicon controlled rectifiers and Trinistor controlled rectifiers, are available with current ratings up to approximately 500 A rms and voltages of 1200 V and more. The transformer turns ratio, in conjunction with the PFN voltage and current, determine the operating conditions for the switch. It should be remembered that, as a rule, the higher the current rating, the slower the turn-on time; and forcing a fast-rising current through the switch before it is fully turned on will create excessive peak power dissipation. Another precaution to be observed concerns high-voltage transients, which are prevalent in pulse modulators.* A series *RC* network across the switch affords protection against such voltage spikes. If the choice between series and parallel operation of switches arises, the series connection appears to be preferable. This requires a voltage-dividing network across the two devices but ensures that the current rate-of-rise through each one is very nearly equal. Parallel operation, unless the devices are very closely matched, usually requires current-equalizing elements which are located in series with the individual switches. Furthermore, even though originally matched, it is not assured that they will remain so during their lifetime. In calculating the currents for selection of the switch, the worst-case conditions should be considered, that is, the fastest repetition rate and greatest percentage regulation that the circuit will be subjected to.

In the SLAC system, the dc reference voltage controls both the output of the ac induction regulators and the level at which PFN regulation occurs. This ensures that the percentage regulation remains about constant for any set input voltage level. The reference power supply is regulated to better than 0.01% against line and load changes and has a maximum peak ripple of 0.7 mV. This is further attenuated in the comparator to less than 0.03 mV. Regulation errors as small as 0.045% have been achieved without making a concentrated effort to reach the minimum possible. This represents a change of approximately 110 V in the 250-kV klystron pulse.

Some specific data on the de-*Q*'ing components used in the SLAC modulators are as follows:

CHARGING TRANSFORMER—25:1 step-down ratio.

Primary: 1.8 H inductance, 25 mH leakage inductance referred to primary, 5.7 ohms resistance.

Secondary: 0.03 ohm resistance, isolated from the primary by a grounded electrostatic shield.

* One such voltage spike, which can be particularly harmful to the semiconductor switch, is described in the section on despiking networks.

RESISTOR—2 ohms, 8 kW. Eight 0.25-ohm, 1000-W edgewound ribbon-type resistors in series.

CAPACITOR—50 μF, 660 V rms. Two 25 μF ac motor-run capacitors in parallel.

SEMICONDUCTOR SWITCH—Type 2N3895 controlled rectifier, 1200 V, 175 A average, 275 A rms. Two series-connected units with voltage dividing networks across each. A series despiking network, 0.5 μF capacitance and 25 ohm resistance, connected across the combination.

The transformer–semiconductor circuit offers two distinct advantages over the conventional method of regulation. The components are operated at relatively low voltage which requires much less space for insulation and the low-voltage components are generally smaller. The life of the controlled rectifier far exceeds that of gaseous tubes. An accurate projection of the lifetime cannot be made at this time; however, some of the devices at SLAC have now accumulated approximately 9000 hours operating time.

Despiking network (WTT)

The function of the despiking network is to protect the charging transformer from excessive voltage spikes and the charging diodes from excessive peak current when the main thyratron fires. The following explanation refers to the simplified schematic diagram of Fig. 13-11. The network is shown mounted in the modulator in the photograph of Fig. 13-12.

The charging transformer (or inductor) has an inherent distributed capacitance, C_D, to ground. For simplicity, this is shown as a lumped capacitance although the actual equivalent circuit is of a more complicated nature. This capacitance is charged to approximately V_{DC} when the main thyratron fires. The exact value will depend upon whether the de-Q'ing cycle is complete. If it is, then the voltage reached will be V_{DC} plus V_{L_p} as shown in Fig 13-13. In the absence of the de-Q'ing, the value reached will depend upon whether C_D in conjunction with the charging transformer and filter capacitance has had time to reach a stabilized condition after the PFN current has stopped flowing.

When the main thyratron fires and the PFN has discharged, which is approximately 3.5 μsec later in the SLAC modulators, the PFN is left with a small positive potential and the thyratron remains in the conducting state. This is owing to the fact that the characteristic impedance of the PFN is purposely made slightly smaller than the reflected impedance of the klystron. Referring to Fig. 13-11, it is seen that a conduction path then exists from C_D through the charging diodes, the PFN, and the thyratron back to C_D. Most of the PFN inductance will be bypassed by its capacitance so that only one section of the inductance of each network is in the circuit. A rather complicated parallel path also exists through the PFN and the pulse transformer primary, although the inductance of the transformer is large enough to prevent a fast-rising current from flowing through this circuit. As the resistance of the conduction path is very low, being mostly the forward resistance

of the charging diodes, the peak current in the absence of a despiking network can reach magnitudes of many hundreds of amperes. This current, on a repetitive basis, would normally far exceed the surge current rating of the charging diodes.

Because of this current flow, the charge on C_D reverses and the voltage becomes very nearly $-V_{DC}$. The frequency of the waveform is a function of the equivalent series inductance and capacitance of the circuit and is approximately 500 kHz in the SLAC modulators without the despiking network. This high-frequency waveform creates excessive turn-to-turn and layer-to-layer voltages on the PFN side of the charging transformer. It is also transferred to the secondary and appears as a reverse voltage across the semiconductor switch. The ideal remedy would be a low-pass filter which offers no attenuation to the PFN charging frequency but presents very high attenuation to the high-frequency waveform. Such a filter is best approximated by a parallel LR network in series with the charging circuit as shown in Fig. 13-11. If L is some small percentage of the charging transformer primary inductance, it will have little effect on the PFN charging waveform other than to lower the frequency slightly. The resistance is selected to have a value which is much higher than the reactance of L at the charging frequency and yet lower than the reactance at the high frequency discussed above. The equivalent series network will then appear as an inductance to the charging frequency and as a resistance in series with a smaller inductance at the high frequency.

A lumped capacitance analysis of the circuit does not yield results which are useful in the design of the network. An empirical approach, used with a knowledge of the circuit behavior resulting from the added elements, is the most practical design procedure. The resistance, which serves to attenuate the high-frequency current and dissipate the energy initially stored in C_D, should be as large as possible. However, a large resistance requires a very large value of inductance as its reactance must be much greater than the resistance to allow most of the high-frequency current to flow through the resistor. From the standpoint of the PFN charging circuit and also the de-Q'ing circuit, the inductance should be as small as possible. The choice of L, then, involves attempting to satisfy these two opposing requirements. A compromise is possible because the two frequencies are generally separated by two to three decades. Experience indicates that a value of inductance in the range from 0.05 to 1.0% of the charging transformer inductance will provide a network with considerable attenuation to the high-frequency waveform. The frequency will also be lowered by the impedance of the added circuit. The resistance is selected by trial to give minimum negative voltage, $-V_{C_D}$, at the charging transformer.

The following data on the SLAC network illustrates the variation of V_{C_D} with resistance under operating conditions:

R(ohms)	250	500	1000	1500	2000	2500	3000	3500	4000
$-V_{C_D}$(kV)	25	20	11	8	8	8	9	11	12

For this test, the dc power supply voltage was 20 kV, the charging transformer primary inductance was 1.8 H, the transformer distributed capacitance, C_D, was 0.0025 μF, and the despiking inductance, L, was selected to be 15 mH or 0.83% of the charging transformer inductance. It is seen that the negative voltage rises rapidly for resistances less than optimum. Also of interest is the minimum value of negative voltage obtained with four different designs of essentially the same charging transformer, each enclosed in an oil-filled case of approximately the same size. The dc power supply voltage was again 20 kV, when the following comparative data were taken:

C_D (μF)	0.0007	0.0025	0.005	0.0185
L (mH)	19.5	15	19.5	11.5
R (ohms)	3000	2000	900	250
$-V_{C_D}$(kV)	9	8	11.4	15.75

The range of distributed capacitance varies by a factor of 26 to 1, and the minimum negative voltage obtainable increases with the capacitance. This indicates that the capacitance should be kept reasonably small. The smaller capacitance will also reduce the high-frequency current that must flow through the charging diodes. Furthermore, it will reduce the stored energy, some of which is dissipated with a consequent reduction of the modulator efficiency.

Switch tubes (RWB)

Early in 1963, efforts were concentrated upon the evaluation of hydrogen thyratrons for the SLAC modulators, because spark gaps and ignitrons did not meet system requirements.

No single hydrogen thyratron which would meet all the SLAC specifications was available, so the modulators were constructed to permit the use of hydrogen thyratrons known to exist at that time, including two of the smaller tubes in a parallel PFN configuration. The two-tube system was used for initial beam tests in Sectors 1 and 2 and, in some modulators, during full beam operations for over a year with good performance.

SPECIAL SLAC REQUIREMENTS. The most stringent requirements imposed upon the SLAC thyratron centered around the anode delay time, variation (variation in switching time from minimum voltage and pulse rate to maximum voltage and pulse rate), instantaneous starting at full voltage, and long mean time between faults.

The variation in delay time through the SLAC modulators is an important parameter because it is desirable to utilize as much of the flat-top portion of the pulse as possible for beam acceleration.

The instantaneous start requirement is necessary because it would be impracticable to spend extra time varying operating voltages to get modulators back on whenever a fault occurred.

Table 13-6 Hydrogen thyratron specifications

Peak anode forward voltage (e_{py})	46 kV (max)
Peak anode inverse voltage (e_{px})	5 kV (max)
Pulse duration (T_p)	4 μsec (max)
Peak anode current (i_b)	4000 A (max)
Average anode current (I_b)	5 A (max)
Rms anode current (i_p)	140 A (max)
Anode delay time (T_{ad})	0.4 μsec (max)
Anode delay time jitter (T_j)	0.01 μsec (max)
Anode delay time drift (ΔT_{ad})	0.04 μsec (max)
Anode delay time variation (ΔT_{adv})	0.15 μsec (max)
Anode dissipation factor (P_b)	70×10^9 (max)
Pulse repetition rate (PRR)	60 to 360 pulses/sec
Number of kickouts	4 (max)in 96 hours
Operating life (objective)	10,000 high-voltage hours

The long mean time to fault is required for beam stability. There are 245 modulators in the accelerator and even at four faults per 96 hours, which is the maximum fault rate specified, the mean time to fault for all the tubes in the accelerator would be approximately 6 min.

The principal specifications for the hydrogen thyratrons are shown in Table 13-6.

In order to meet the SLAC specifications the manufacturers incorporated a pretrigger electrode and modified the grid and baffle configurations for optimum switching time and low kickout rate.

PRETRIGGER ELECTRODE. The maximum anode delay in the hydrogen thyratron is largely determined by the time it takes the plasma in the relatively large cathode region to build up to a critical density in the control grid aperture region. When this point is reached, the tube begins to conduct. In order to reduce the ionization build-up time in the cathode region, a pretrigger electrode was installed between the cathode and the control grid (see Fig. 13-15). This electrode is connected to the trigger transformer through a 250-ohm resistor. The control grid is connected to the trigger transformer through an *LC* filter network. There is a delay through this network of approximately 0.1 μsec which allows current to flow to the pretrigger electrode and partially ionize the cathode region prior to application of the grid trigger. This mode of operation reduces the cathode ionization time from approximately 600 to 230 nsec and reduces the cathode ionization time variation from a nominal 350 to 100 nsec.

KEEP-ALIVE OPERATION. During the development phase, experiments were done with a constant dc voltage applied to the pretrigger electrode. The effect of the keep-alive voltage was to reduce the ionization time in the cathode

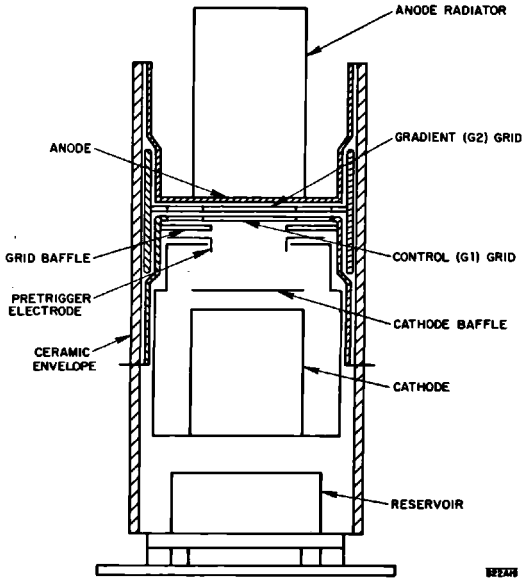

Figure 13-15 Typical SLAC hydrogen thyratron, showing grid structure and pretrigger electrode.

ı to approximately 80 nsec and the cathode ionization time variation to ıan 10 nsec. The effect of the three trigger modes on anode delay time can :n in Fig. 13-16.

; can be seen in Fig. 13-17, the anode delay time is essentially stable : 180 mA of keep-alive current on a new tube and is stable above 200 mA bes with 7000 hours, or more, of operation. About 2A through this

Figure 13-16 Anode delay time vs repetition rate for three trigger modes.

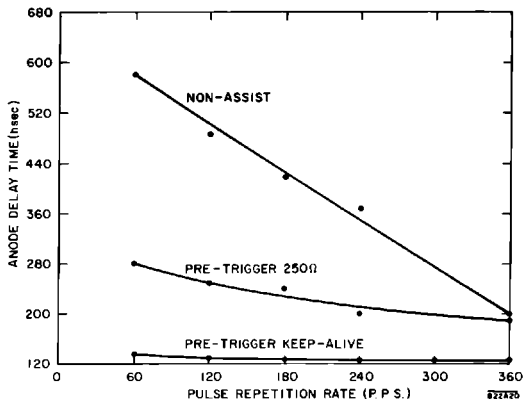

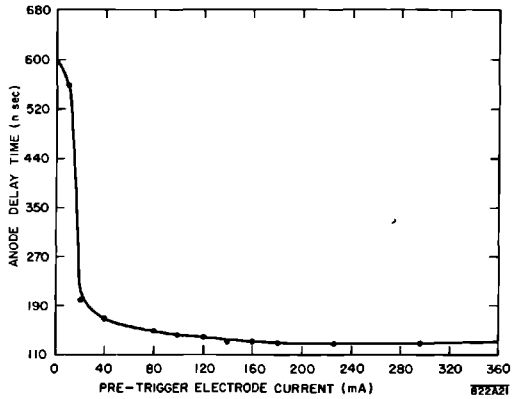

Figure 13-17 Anode delay time vs pretrigger electrode current.

electrode are required to fire the tube. It was decided to run the SLAC thyratron at a keep-alive current of 350 mA.

An additional benefit from operation of these tubes in the keep-alive mode was a marked increase in operating life. It is believed that a 3–5 times increase might be expected for a tube in this power class.

In order to help the manufacturers meet specifications, the effects of varying element spacings were studied at SLAC, and it was possible to correlate the delay times attributed to the different electrodes in the thyratron with tube dimensions. Several tubes with varying dimensions were built so that these effects could be studied. Manufacturing tolerances were minimized through direct measurements of interelectrode spacing from x-ray prints using high-energy, cobalt-60, x-ray techniques. It was noted for instance[2] that the spacing between the control grid G_1 and the cathode baffle was most critical (being the longest portion of the discharge path). The separation also varied critically with the focusing effect of the cathode aperture. A change of 0.020 in. (10%) in some cases accounted for delay changes of 170 nsec through this space. It was found that a spacing between 0.170 and 0.200 in. for a given cathode aperture was satisfactory for one type tube. The effect of G_1 to G_2 (gradient grid) spacing was studied, and a spacing of 0.125 to 0.135 in. was found to be optimum. Greater spacings produced greater delay time in G_1 to G_2 transfer which was probably due to the reduced field intensity or penetration in the G_1 slot. Closer spacing than 0.120 in. produced excessive kickouts. The anode to G_2 spacing was optimized between 0.115 and 0.120 in. Larger spacings produced excessive time delay. Spacings less than 0.115 in. caused arcing and kickouts. Of course, the dimensions vary for other tube types, but the effects are the same.

CIRCUIT CONSIDERATIONS AFFECTING THYRATRON OPERATION. In order to achieve good performance and long life, it was necessary to tailor the modulator circuit and operating conditions to the tube. Two important thyratron

characteristics affecting the modulator design are recovery time and anode delay time stability. Also, the PFN charging circuit affects switch tube recovery. As slow a charging rate as possible was allowed, consistent with ability to de-Q the charging transformer at the highest repetition rate. Even so, the charging current does not start at zero, which has the effect of reducing recovery time from 300 to 225 μsec.

The end-of-line clipper protects the switch tube and modulator from high inverse voltages due to load arcing and also has a pronounced effect on the normal inverse recovery voltage.

The thyratron trigger affects the anode delay time. A high amplitude trigger from a low impedance source reduces anode delay time. It was found that about 2000 V from a 25-ohm source was adequate.

Stored energy in the shunt inductance and capacitance of the pulse transformer affects the switch tube recovery and dissipation. The resulting currents during recovery time tend to force reconduction of the thyratron after the main pulse. Energy stored in the leakage inductance of the pulse transformer is another principal source of postpulse current. It causes "spikes" on the anode voltage waveform during the recovery period and results in tube faults.

The impedance match between the PFN and load is important for proper operation of the thyratron. One of the more common methods of obtaining inverse voltage is the "negative mismatch" mode of operation. In this mode, the load impedance is less than the PFN impedance, causing a reflected negative voltage to appear on the anode of the switch tube immediately after the pulse. The disadvantages of this are (1) increased anode dissipation due to ion bombardment as a result of negative voltage on the anode immediately after the main pulse, while the tube is still in a heavily ionized state; (2) high spikes on the anode during recovery time, as a result of the energy stored in the pulse-transformer leakage inductance; (3) the pulse-transformer stored energy cannot be transferred to the PFN in the negative mode and must be dissipated in an additional circuit (primary pulse-transformer clipper) if klystron backswing voltage and pulse-transformer losses are to be minimized.

A second method of obtaining inverse voltage (the one used at Stanford) is the "positive" mismatch mode of operation, where the load impedance is higher than the PFN impedance, and some positive voltage is left on the PFN network after the main pulse.

The energy stored in the pulse-transformer shunt inductance is transferred through the thyratron to the PFN in a time period determined by the pulse-transformer shunt inductance and the total PFN capacitance. In the SLAC modulator the thyratron is kept conducting for approximately 50 μsec after the end of the main pulse. This is followed by the application to the anode of a 4-kV negative pulse which decays in about 175 μsec. (See Fig. 13-18).

The thyratron in this mode performs the function of a pulse-transformer primary clipper, but since the pulse-transformer stored energy adds to the next charging cycle instead of being dissipated, the overall modulator efficiency is improved. Other advantages of positive mismatch mode operation

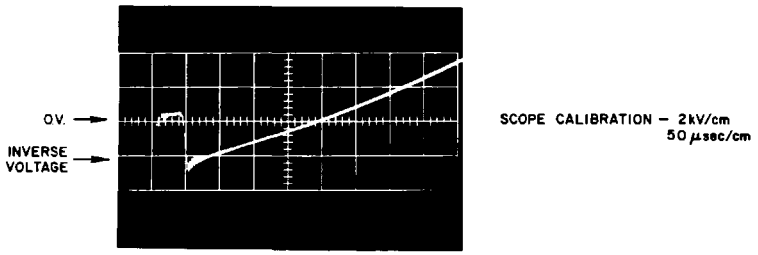

Figure 13-18 Typical postpulse thyratron anode voltage waveform.

are reduction in anode spike amplitude and a marked increase in time between tube faults. In some tube types a 10:1 reduction in the number of tube faults for a given period has been observed.

RANGING. In order to obtain stable high-voltage operation and long life, the switch tubes are operated at optimum hydrogen pressure for that particular tube.

Lower pressures improve high-voltage holdoff characteristics but at the same time increase tube voltage drop and cause cathode stripping or depletion due to excessive ion bombardment and excessive anode temperatures. High pressure, on the other hand, decreases tube dissipation but results in excessive fault rates.

The pressure in the hydrogen thyratrons is controlled by varying the heater power to titanium reservoirs. The SLAC thyratrons have a typical reservoir range of $\pm 10\%(\pm 0.4$ V) from the center of the range. It is necessary to check the center point at 500-hour intervals to insure optimum life because the reservoir center point may shift due to hydrogen cleanup. This checking and adjustment procedure is known as "ranging." The shift in reservoir set point cannot be predicted and in some instances there has been no significant shift. Figure 13-19 is a plot of reservoir center range versus age for three typical tubes at full SLAC power. Ranging is a time-consuming maintenance problem because 245 thyratrons are involved and it takes about 15 min to range each one.

Two methods have been investigated. The first method is the traditional hot ranging technique whereby the reservoir voltage is lowered by 0.1-V intervals until grid hash or commutation spikes are observed on the grid waveform which indicates the low pressure limit. The reservoir is then raised in 0.1-V intervals until the thyratron faults, which is the high pressure limit. Halfway between the extremes is the reservoir center point or optimum hydrogen pressure. The disadvantage of this method is that it is time consuming.

A second method developed at SLAC is the thyratron RF noise detector. There are numerous frequencies generated within the tube which change in amplitude with tube pressure and which are independent of the external

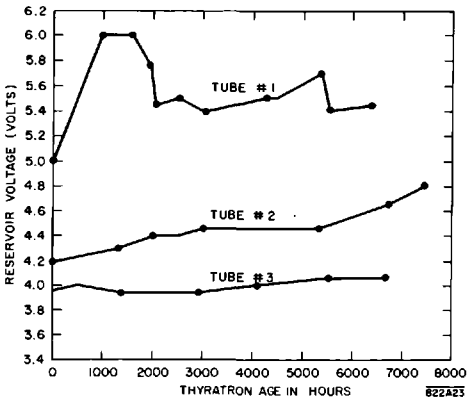

Figure 13-19 Typical reservoir center range vs thyratron age in hours.

circuit. The useful frequency for pressure setting in the SLAC thyratron occurs at 24 MHz. At this frequency the RF power peaks at the center of the pressure range and drops off about 4 dB at the range limits. Figure 13-20 shows a plot of RF pickup at 24 MHz versus reservoir voltage for a typical SLAC thyratron. The principal advantages of this system are greater speed and accuracy in ranging. The optimum pressure can be determined accurately in less than one-third the time required by the old method.

Figure 13-20 Plot of RF amplitude at 24 MHz vs reservoir voltage.

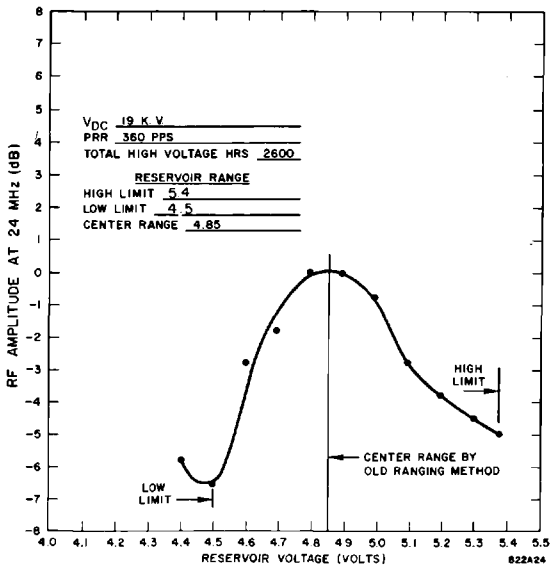

THYRATRON LIFE. At this writing insufficient life information is available to estimate accurately the life of the hydrogen thyratrons in the accelerator. Some life-test tubes have been run 7000 hours at full power and some have been run 5000 hours, but it is expected that the average life of the first generation of tubes will be 3000 to 4000 hours. It is hoped to achieve the design objective of 10,000 hours within three tube generations when the failure modes are identified and the necessary modifications are incorporated.

Thyratron trigger system (RWB)

The trigger circuit incorporated in the modulator to furnish a grid trigger pulse to the high-power hydrogen thyratron switch tube consists of two separate units identified as trigger chassis Nos. 1 and 2. Schematic diagrams of these units are shown in Figs. 13-21 and 13-22.

Trigger chassis No. 1 consists of two power supplies, a driven blocking oscillator, a cathode follower output stage, and a fault interlock and gating circuit. This unit accepts the input pulse from the sector trigger generator and amplifies it to a level sufficient to drive trigger chassis No. 2. The input pulse has an amplitude of approximately 50 V, a duration of 2 μsec, and a rise time of 50 nsec. The output pulse is approximately 200 V, has a duration of 3 μsec, and a rise time of 50 nsec.

Trigger chassis No. 2 is a scaled-down version of the modulator's high-power pulse circuit. Specifically, the circuit consists of a 5-kV dc supply, a charging choke and diode, a PFN, a pulse transformer, a hydrogen thyratron switch tube, and other supporting components. The circuit functions the same

Figure 13-21 Thyratron trigger chassis No. 1.

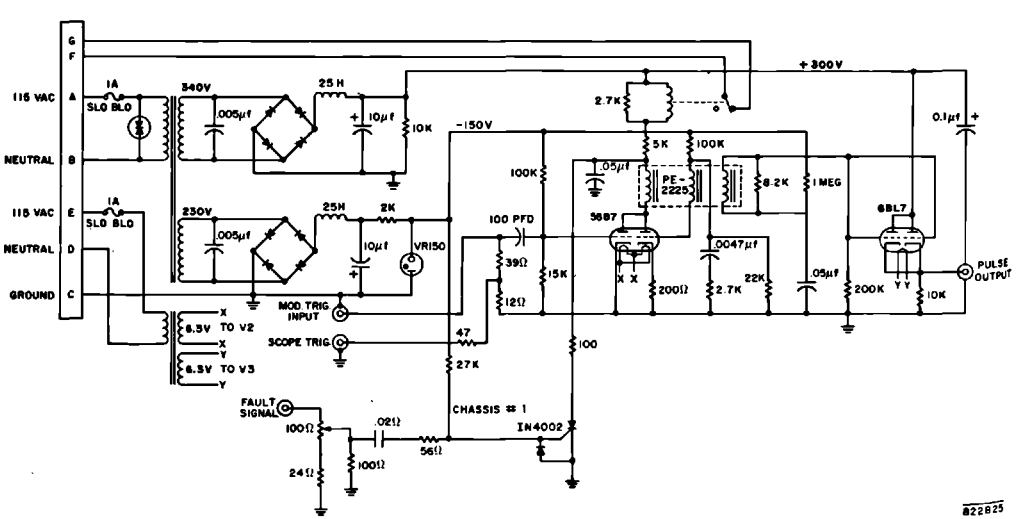

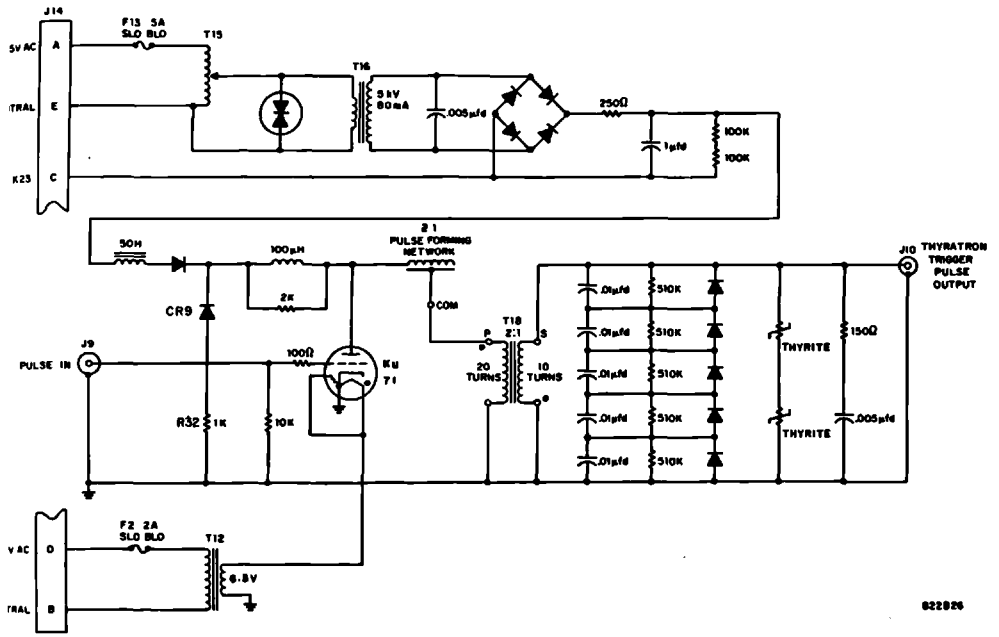

Figure 13-22 Thyratron trigger chassis No. 2.

as a line-type modulator. The 5 kV from the power supply is increased to approximately 8 kV across the PFN capacitors by dc resonance charging. When the driver hydrogen thyratron switch tube is triggered by the pulse from trigger chassis No. 1, the PFN capacitor's stored energy is discharged through the primary of the pulse transformer, the switch tube, and the PFN inductors. Half of the voltage on the PFN capacitors is dropped across the pulse transformer to produce the output pulse and half appears across the PFN when working into a matched load. However, this circuit works into a high impedance load until the main thyratron fires, at which time the load impedance drops to a low value, so most of the PFN charge is reflected back to the PFN where it is dissipated in the inverse diode circuit consisting of CR 9 and R 32.

When the main switch tube fires, its control grid assumes a potential dependent on the voltage gradient from plate to cathode and its relative position between these two elements. During tube commutation this potential may vary from 2 kV for normal operation to 10 kV during load faults. To safeguard the driver from possible damage due to these high-voltage transients, protective circuits consisting of a low-pass *LC* filter, spark gap, and a Thyrite assembly were added on the secondary side of the pulse transformer.

The output pulse has a maximum voltage level of 4 kV when the main thyratron switch tube is nonconducting and supplies about 200 A when the switch tube is in conduction. Its pulse width is 2 μsec and rise time 0.2 μsec (maximum).

Pulse transformer (RMR)

The pulse transformer is the link between the modulator and the main klystron amplifier (see Fig. 13-23). Therefore, its band pass and power handling characteristics have to be such that the modulator output pulse will be transmitted with minimum distortion and attenuation.

With this requirement in mind, the operating specifications shown in Table 13-7 were developed for the pulse transformer.

In order to obtain a transformer of minimum volume and weight, the manufacturer made use of a reset core. In this design, the core is held near negative saturation during the interpulse interval by a steady, direct bias current of approximately 12 A. This current is supplied to the primary of the pulse transformer through a 2.5-mH inductor. The inductor is required to isolate the bias power supply from the high-voltage primary pulse. This scheme permits a flux swing of 17.5 kG at 250 kV and 3.5-μsec effective pulse width.

The core of the pulse transformer is made up of 3 smaller "subcores" strapped together. Each subcore is wound from 0.002-in. thick, grain-oriented silicon steel ribbon, $1\frac{5}{8}$ in. wide. The buildup of the winding is $2\frac{3}{8}$ in. The window opening in the core is $7\frac{1}{8}$ in. long and $3\frac{3}{4}$ in. wide.

The primary winding of the pulse transformer consists of six turns of five No. 16 AWG conductors in parallel on each leg of the core. The two primary

Figure 13-23 Klystron and pulse-transformer tank.

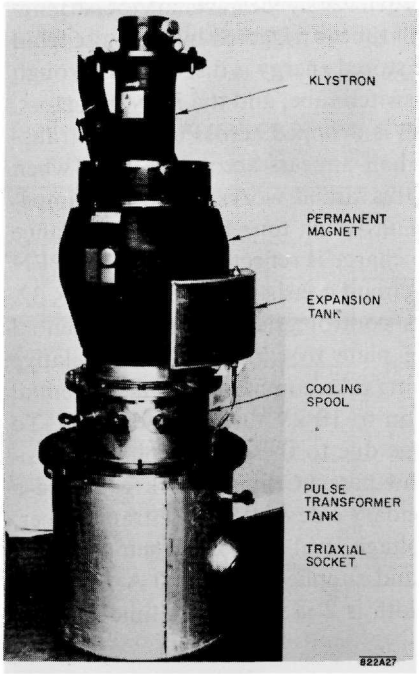

Table 13-7 Pulse transformer specifications

Input		*Output*	
Peak voltage	20.8 kV (negative)	Load	Perveance $2 \times 10^{-6} \pm 5\%$ (klystron)
Peak current	3000 A (nominal)	Load shunt capacity	$90 \pm 20\%$ pF
Rise time (5–95%)	0.5 μsec (max)	Peak voltage	250 kV (negative)
Pulse duration	3.7 μsec (max at 70% amplitude)	Peak current	250 A (nominal)
Fall time (95–5%)	0.5% μsec (max)	Rise time (5–95%)	0.7 μsec (max)
Flat-top duration	2.8 μsec (min)	Flat-top duration	2.5 μsec (min)
Pulse repetition rate	360 pulses/sec (max)	Pulse top ripple	$\pm$0.5% (max)
Pulse top ripple	$\pm$0.3% (max)	Droop of flat top	2% (max) with isolation inductor
Turns ratio	1 : 12 (exact)	Fall time (95–5%)	1.2 μsec (max)
		Pulse undershoot	15% (max)
		Pulse return swing	10% (max)

windings are connected in parallel. There are two secondary windings of seventy-two turns each, connected in parallel. One secondary is wound on each leg. The secondary conductors are No. 18 AWG.

In a step-up pulse transformer, pulse rise time is proportional to the square root of the product of leakage inductance and shunt capacitance (transformer distributed plus load strays). The leakage inductance in the SLAC pulse transformer was minimized by employing a "constant gradient"[3] or tapered secondary winding. (See Fig. 13-24). In this type of winding, the volume enclosed by the leakage flux (and hence the leakage inductance) is approximately one-half of what it would be if the coils were of conventional, parallel-sided, concentric construction. The leakage inductance was further reduced by winding a complete primary and secondary on each leg of the core and then connecting them in parallel[1] as noted above. This technique also simplified the problem of feeding low-voltage ac power to the klystron filament transformer, since the pulse-transformer secondary windings provided the necessary high-voltage pulse isolation. The pulse-transformer equivalent circuit parameters are summarized in Fig. 13-25. With the realization that few if any transformer manufacturers had facilities to check the wave-shape characteristics of this transformer under full voltage operating conditions, a low-voltage, pulse-shape acceptance test was specified for rise time and pulse top ripple. The theoretical basis for this type of test has been well established.[4] Correlation between low-voltage pulse tests and high-voltage operation was excellent.

The klystron filament power is supplied by a 325-VA toroidal transformer housed within the klystron socket. The transformer is the "auto" type and

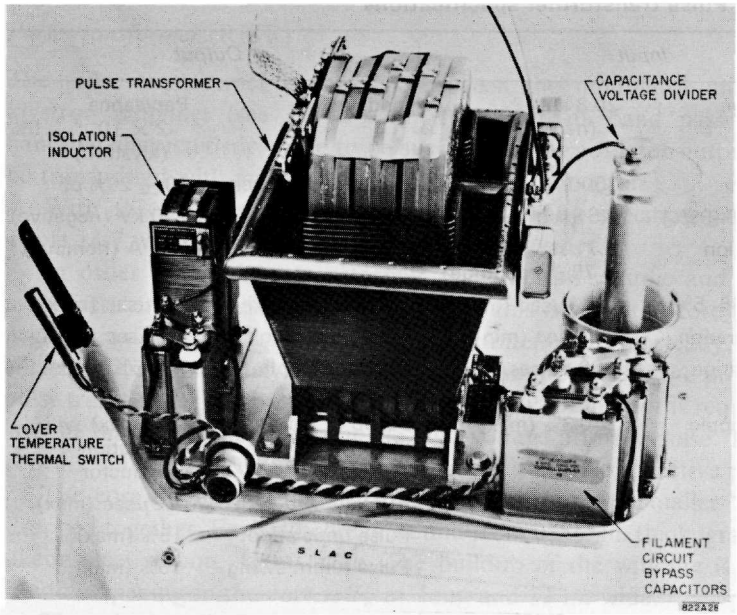

Figure 13-24 Pulse transformer and associated components.

floats at high voltage. There was no room in the transformer tank for a low-capacitance, filament isolation transformer of the type conventionally used in cathode-modulated power tube circuits. The filament transformer can be seen on top of the pulse transformer in Fig. 13-26.

The capacitance voltage divider with a division ratio of 5000:1 allows direct viewing of the klystron cathode pulse. The divider, which can be seen in Figs. 13-24 and 13-26, is coaxial and has a fully shielded pickup ring. The characteristics and advantages of this type divider are discussed in References 5 and 6.

For ease of assembly and servicing, the pulse transformer, pulse isolation inductor, capacity voltage divider, and filament circuit bypass capacitors are

Figure 13-25 Equivalent circuit of the pulse transformer.

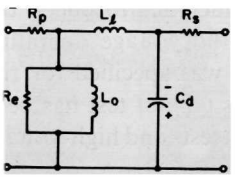

ALL VALUES ARE REFFERED TO HIGH VOLTAGE SIDE

R_p = 0.6Ω PRIMARY DC RESISTANCE
R_e = 58KΩ EQUIVALENT CORE LOSS
L_o = 110 mH TRANSFORMER OPEN CIRCUIT INDUCTANCE
L_ℓ = 224 μH LEAKAGE INDUCTANCE
C_d = 100pf DISTRIBUTED CAPACITANCE
R_s = 1.05Ω SECONDARY DC RESISTANCE (SUM OF BOTH WINDINGS)

822A25

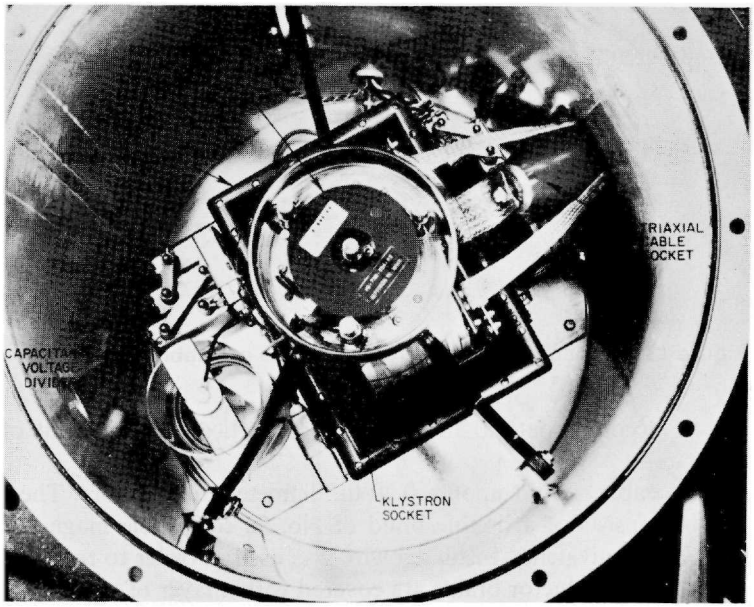

Figure 13-26 Pulse transformer tank, top view.

mounted on an aluminum base plate (Fig. 13-24). This assembly is housed in a 22-in. diameter × 22-in. deep aluminum tank. The klystron socket assembly is supported on epoxy insulating arms from the sides of the tank (Fig. 13-26). The klystron tube is supported on a flanged double-walled stainless steel cooling spool which is bolted to the top flange of the tank. Cooling for the insulating mineral oil, with which the entire assembly is impregnated, is provided by the klystron collector cooling water which circulates between the double walls of the cooling spool. The maximum temperature rise of the oil is 42°C under full power operating conditions (250 kV, 360 pulses/sec), maximum cooling water inlet temperature (35°C), and maximum ambient air temperature (43.5°C). This temperature rise causes an increase in oil volume of approximately 230 $in.^3$. The increase is accommodated by an external expansion tank bolted to the klystron mounting flange. The pulse transformer tank and its contents are protected from overtemperature operation by a thermal switch (extreme left of Fig. 13-24) set to open at 85°C. The thermal switch is part of the modulator interlock chain. The klystron pulse tank assembly is shown in Fig. 13-23.

Triaxial pulse cable assembly (RMR)

The pulse power from the main modulator is delivered to the pulse transformer tank by means of a high-power, triaxial, pulse cable assembly. This assembly is required to be sufficiently flexible to allow easy coupling and uncoupling

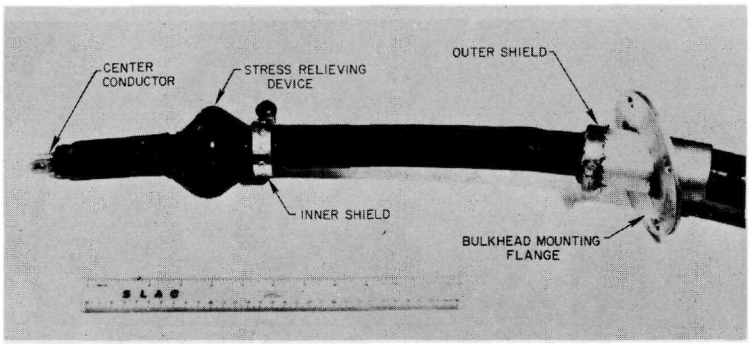

Figure 13-27 Modulator end of pulse cable assembly.

and to accommodate a 2 ft variation in vertical displacement of the pulse tank.

The cable is built upon a 0.70-in. diameter, rubber core. The center conductor consists of a double braid of No. 30 solderable magnet wire (No. 4 AWG dc equivalent). Insulated wire was used in order to reduce skin effects. The center conductor braids are covered with a layer of semiconducting tape, and then served with layers of oiled polyethylene tapes to build the major insulation to a thickness of 0.050 in. The second braid, also No. 4 AWG dc equivalent, provides the pulse current return path. The outer braid is the RFI shield braid and assures that the modulator cabinet and pulse-transformer tank remain at the same potential.

The pulse cable assembly consists of an air end termination and a stress-relieving device (Fig. 13-27) which are installed in the modulator, and an oil end termination (Fig. 13-28). The oil end termination consists of two parts: a socket which is installed in the pulse tank and a male plug which is built up on the end of the cable. The socket contains the stress-relieving device for the oil end of the cable assembly.

Figure 13-28 Pulse-transformer tank end of pulse cable assembly.

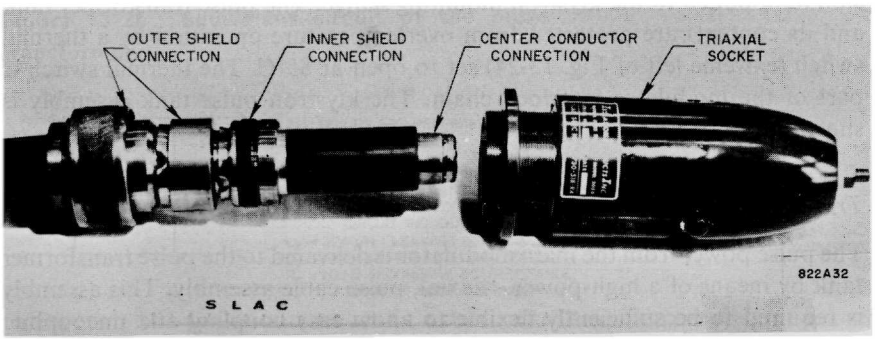

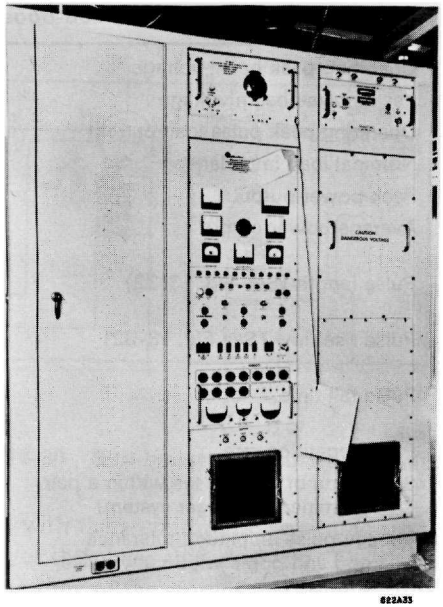

Figure 13-29 Sub-booster modulator.

13-2 Sub-booster modulator (FTV)

General description

The sub-booster modulator, shown in Fig. 13-29, is part of the drive system of the accelerator. In conjunction with a sub-booster klystron, its main function is to amplify a 2856-MHz RF signal from approximately 60 mW to a minimum of 60 kW with strict requirements relating to rise and fall times and amplitude tolerances.

The stringent specifications established for the beam voltage pulse are of primary importance because the pulse shape determines the rise and fall time of the RF output pulse, and its phase shift, which ultimately has a large effect upon the energy spectrum of the electron beam.

One unit per sector (total 30) supplies the RF power through a coaxial subdrive line to the eight 24-MW klystrons of a sector.

The klystron tube used in the sub-booster modulator is a 60-kW, S-band, fixed tuned, pulsed amplifier with coaxial input and output connectors. For more details see Chapter 9.

The characteristics of the sub-booster modulator are given in Table 13-8.

The sub-booster modulator circuit

The sub-booster modulator is of the hard tube type.[1] The plates of the switch tubes are connected to a storage capacitor C_n and the filaments are at

Table 13-8 Specifications of sub-booster modulator

Operating peak beam voltage	26 to 28 kV (negative)
Peak inverse beam voltage	1 kV (max)
Operating peak pulse load current	7–12 A
Nominal load impedance	2333–3328 ohms
Peak power output	336 kW
Average power output	660 W for 2.5-μsec pulse length 890 W for 3.5-μsec pulse length
Pulse length (See Fig. 13-32)	$2.5 \pm 0.020\,\mu$sec $3.5 \pm 0.1\,\mu$sec
Pulse rise time (See Fig. 13-32)	0.2 μsec (max) (10–100%) 0.1 μsec(max) (75–100%)
Pulse fall time	1.5 μsec (max) (100–10%) 0.15 μsec (max) (100–75%)
Pulse repetition rate	360 pulse-pairs/sec
Separation of two pulses within a pair (determined by trigger system)	20–100 μsec
Voltage pulse amplitude tolerance	
Droop and ripple within any pulse or pulse pair	0.08% (max)
Amplitude variation and drift	0.04% (max)/5 min 0.08% (max)/1 hour 0.16% (max)/24 hours 0.32% (max)/168 hours
Pulse delay time	0.4 μsec (max)
Pulse delay time jitter	$\pm$10 nsec (max)
Pulse delay time drift	15 nsec (max)/hour 60 nsec (max)/24 hours

ground potential (see Fig. 13-30). The other side of the capacitor is connected to the klystron load.

A resistor is used as an isolating element between the pulser circuit and its associated high-voltage power supply.

When the grids of the switch tubes are driven positive and the tubes start to conduct, a large proportion of the voltage across the capacitor C_n appears across the klystron, since it is the highest impedance in the series circuit, consisting of the switch tubes, the storage capacitor C_n, and the klystron.

One of the major design considerations was the requirement for an extremely flat pulse to minimize the phase shift in the RF output of the klystron tube. Any change in the amplitude of the beam voltage pulse applied across the klystron causes phase shift in the RF output pulse of the klystron. For the particular klystron used in the sub-booster, a change in beam voltage amplitude of approximately 26 V (0.1 %) corresponds to a phase shift of 1°. This is the maximum allowed for all possible deficiencies, such as ringing, droop, and overshoot. Radio-frequency phase measurements were made on all sub-boosters to check that they met these stringent requirements.

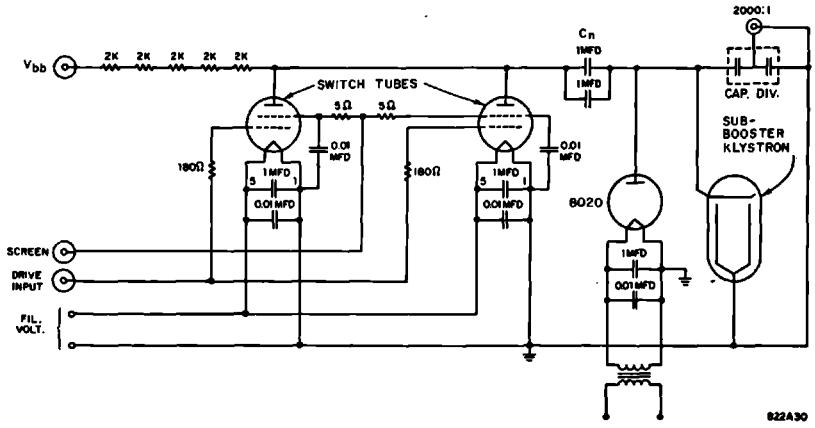

Figure 13-30 Sub-booster modulator circuit.

The requirement of a pair of pulses, with the second pulse separated from the first by 20 to 100 μsec, also aggravates the phase shift problem. The short interpulse period relative to the charging time of the storage capacitor results in an amplitude difference between the two pulses. The magnitude of this difference and the amount of droop in each pulse can be minimized by selecting a large value for C_n. This will be evident by the example given below.

From the simple circuit diagram of Fig. 13-31, it may be deduced that the voltage across the klystron changes according to the formula,

$$V_L = V_{bb} \cdot \exp\left\{-\left[\frac{\tau}{(R_L + r_p)C_n}\right]\right\} - V_p \qquad (13\text{-}21)$$

where

V_{bb} = the initial voltage across C_n
τ = the duration of the pulse
R_L = the load resistance (klystron)
$V_p = I_p \times r_p$ = the voltage drop across the switch tubes
r_p = the effective resistance of the switch tubes.

If the pulse width $\tau \ll (R_L + r_p)C_n$, only a small fraction of the energy in C_n is discharged. The change in the amplitude of the beam voltage pulse is

Figure 13-31 Simplified circuit diagram of sub-booster modulator.

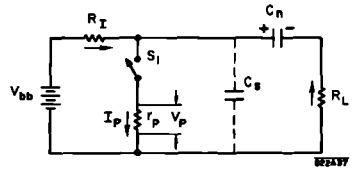

called "droop," ΔV_L, and its magnitude can be reduced by making the storage capacitor C_n larger for a given value of pulse current and pulse width. This follows from the relation,

$$\Delta V_L = \frac{I_L}{C_n} \cdot \tau \tag{13-22}$$

which is valid if $\tau \ll (R_L + r_p)C_n$. A large value for C_n reduces the difference in amplitude between the two pulses of a pair, because the delay time of 20 to 100 μsec is very small compared to the recharge RC time constant of the modulator.

These calculations on storage capacitor discharge during a pulse are made assuming a resistive load. For all practical purposes, the results can be applied to the use of biased diode-type loads such as the klystron.

A disadvantage of the large physical size of the storage capacitor is the stray capacitance to ground C_s, of the capacitor case (see Fig. 13-31). This stray capacitance appears as a shunt capacitance across the klystron load. A major effort has been made to keep the total stray capacitance C_s to a minimum, in order to obtain the required rise time. A list of the capacitances to ground for various circuit components is given in Table 13-9. The total stray capacitance, including connecting straps, is approximately 160 pF.

The stray capacitance of the circuit determines to a large extent the peak current the switch tubes have to supply if a fast pulse rise time is a prerequisite. This current is in addition to the load current and the current drawn by the isolating resistors between power supply and pulser during the pulse.

The peak current required to discharge the stray capacitance must satisfy the formula,

$$I_c = C_s \cdot \frac{\Delta V_B}{\Delta t}$$

where

C_s = the stray capacitance
V_B = the beam voltage
Δt = the rise time

Table 13-9 Capacitances to ground for various circuit components

Component	*Capacitance (pF)*
Klystron tube input capacitance	16
Filament transformer	16
Pulse voltage divider	5
Current viewing transformer	5
Recharge diode	5
Charging resistor assembly	13
Switch tubes, output capacitance	32
Storage capacitor case to ground	60

For the sub-booster modulator under consideration,

$$V_B = 28 \text{ kV}$$
$$C_s = 160 \text{ pF}$$
$$\Delta t = 200 \text{ nsec}$$
$$I_c = 160 \times 10^{-12} \cdot \frac{28 \times 10^3}{200 \times 10^{-9}} = 22.4 \text{ A}$$

The current drain in the 10-kohm isolating resistors during the pulse is 2.8 A. (See Fig. 13-30.) The sub-booster modulator requires approximately 30–32 A for a rise time of 180 to 200 nsec (10–100%). In this case, it is clearly shown that the peak switch tube current in a fast rise time pulser will be several times the value of the load current (7–12 A).

It can also be shown that if the grid drive pulse to the switch tubes has a finite rise time (in the present case 0–800 V in 100 nsec), the switch tube current will increase linearly during part of the rise time and then decrease when the beam voltage reaches its minimum value, or "bottoms out." The current during the remainder of the pulse duration is determined by the klystron and the current lost in the isolating resistors. (See Fig. 13-32). For this to be true,

Figure 13-32 Effect of peak current capability of switch tubes on rise time of beam voltage and RF output.

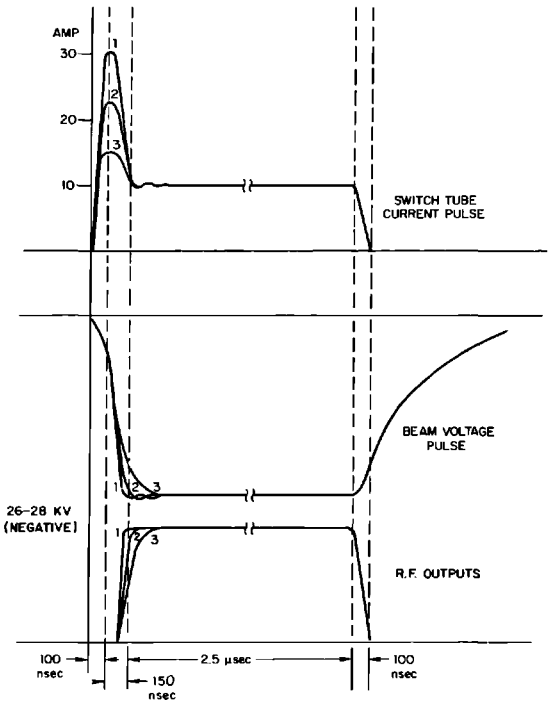

the cathodes of the switch tubes must be capable of supplying this large peak current.

The peak current capability of the switch tubes depends on the cathode or filament emission, most often expressed in milliamperes per filament watt. A drop in this peak current emission capability, due to decarburization of the thoriated tungsten filaments, for example, will result in increased rise time.

A drop in the peak current capability will also cause a corresponding decrease in the width of the flat-top portion of the pulse and a sharp increase in the rise time of the RF output pulse, due to the $\frac{5}{2}$ power law behavior which the klystron exhibits (see Fig. 13-32).

To eliminate any trace of ac ripple in the RF output pulse, the filaments of the switch tubes and the klystron are supplied with dc power.

The fall time of the beam voltage pulse

The value of the stray capacitance also has an important effect on the pulse fall time for the following reason.

Referring to Fig. 13-31, it can be seen that upon opening switch S_1 the stray capacitance charges through R_I in parallel with R_L. (C_n can be considered a short circuit during this time because its voltage does not change appreciably during the fall time.)

The only way to improve the fall time in an arrangement where the klystron load is one determinant and the stray capacitance has been kept to a bare minimum value, is to reduce the resistance value of the isolating element between the pulse circuitry and its power supply. However, a lower resistance value means an increase in the current lost in this element during the pulse, and it necessitates an increase in peak current requirements for the switch tubes.

The compromise value for R_I of 10 kohms that was finally arrived at keeps the current loss to a reasonable value (2.8 A) and allows a fall time of approximately 100 nsec from the 100 to 75% level.

With these values it was possible to obtain an RF output pulse with rise and fall times which are approximately the same (100 nsec maximum).

Choice of switch tubes

The choice of the switch tubes (Fig. 13-30) for the modulator was based upon a consideration of the following requirements:

1. A high-voltage rating compatible with the maximum beam voltage required for the klystron, with a reasonable safety margin.
2. A peak current capability, as determined by the maximum value of the current for the specified rise time and load.
3. A suitable plate resistance, which, of course, is related to the efficiency of the modulator and the anode dissipation of the tube. It is also a factor in determining the high-voltage power supply specifications.

4. Suitable drive characteristics, which are determined to a large extent by the input capacitance and the cutoff point of the tube as well as transconductance.
5. Flatness of the pulse obtainable. The characteristics of the tube play a major role at this point.
6. Freedom from arcing for extended periods of operation, taking into account that most vacuum tubes for pulse service suffer from this irregularity.
7. Minimal cost of replacement of a sizeable number of tubes on a year-round 24-hour basis. The economics play an important role when so many modulators are involved.

A tetrode was chosen in preference to a triode, because the grid drive power is considerably less for the tetrode—an important factor for fast rising pulses. Another reason for selecting the tetrode was because of the stringent pulse flatness requirement which could only be met by the tetrode tube type.

The tube decided upon was the 4PR1000A, which is an excellent tube when properly processed. The disadvantages in the choice of this particular tube are that three tubes have to be used in parallel to handle the current, and the high-voltage hold-off safety margin is on the low side. However, there are only a very limited number of tubes available in this high-voltage and current range.

Initially two 4PR1000A's were used in parallel. However, due to an unknown mechanism, possibly because of positive ion bombardment when the tubes are operated at or near the saturation knee of the e_p/i_p curve, the thoriated tungsten filaments are decarburized. This results in a steady decrease in peak current capability and at the same time in an increase in rise time of the beam voltage pulse and a shortened flat-top portion. A three-tube parallel arrangement alleviates this problem to some degree, because the load on each tube is decreased.

The main disadvantage of the third tube is the addition of its output capacitance to the stray capacitance of the circuit. There is also a small decrease in reliability of the equipment because of added complexity.

A developmental tube (Y448) with increased filament power and corresponding peak current output capability has been successfully tested and has shown satisfactory life expectancy under the present operating conditions. Two of these tubes are a satisfactory substitute for three 4PR1000H's.

It is clear that, at this time, no tube fully meets the SLAC requirements. Work aimed at improving performance and life expectancy is continuing.

Driver circuit

The driver circuit for the switch tubes is shown in Fig. 13-33. It consists of a delay line-controlled blocking oscillator V_1 and a bootstrap amplifier V_2. Bias for both tubes is developed across a common cathode resistor and a

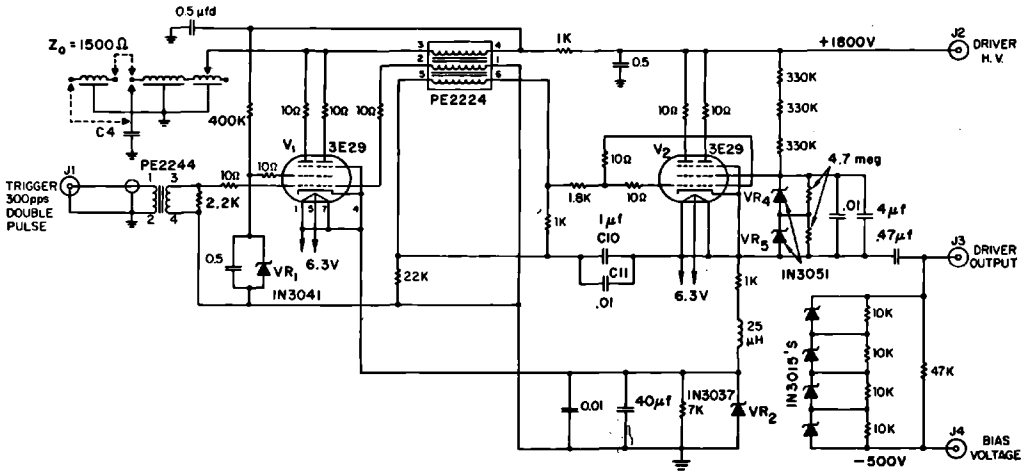

Figure 13-33 Sub-booster driver circuit.

822838

zener diode VR_2. The screen voltage of V_1 is stabilized by VR_1, and the bootstrap amplifier screen voltage is determined by the zener diodes, VR_4 and VR_5.

Stabilization of these voltages is important in reducing the recovery time required by the blocking oscillator V_1. A minimal recovery time is essential to meet the requirement for identical pulse shapes in pulse pairs at minimum separation (20 μsec).

The operation of the circuit is straightforward. A 50-V positive trigger at the first grid of V_1 results in an amplified negative pulse at the plate. This negative pulse, in turn, drives the control grid of the right-hand section more positive, through polarity reversal by the transformer. The anode begins to draw current through the pulse transformer which, in turn, drives the grid further positive, thus providing positive feedback. The right-hand section of V_1 is now fully turned on, and the negative pulse at the plates progresses down the delay line, is reflected by C4, and travels back with opposite polarity through the transformers turning the tube off via its grid and returning it to a stable condition.

The two-way travel time along the delay line determines the width of the pulse. A fine adjustment for the delay is provided, and long-term stability is obtained by the excellent temperature characteristics of the line.

The tertiary winding on the blocking oscillator transformer is connected to the grids of the bootstrap amplifier, V_2. The output of the blocking oscillator is effectively applied between the cathode and grids of V_2 through the capacitors C10 and C11.

The bootstrap cathode follower V_2 provides a positive output pulse for a positive input. Stabilization of the screen voltage reduces pulse droop and makes it feasible to obtain two very nearly identical pulses in a pair.

The output pulse is capacitively coupled to the grids of the switch tubes and is superimposed on their cutoff bias voltage. Bias voltage is provided by a highly regulated power supply and applied to the grids through a series resistor.

The amplitude of the drive pulse can be clipped to approximately 800 V by a zener diode arrangement to limit overshoot, ripple, and droop to a very low level. The switch tubes also help to clip the pulse when their grids are driven sufficiently positive.

The plate voltage for the driver unit is supplied from a highly regulated power supply.

Power supplies

The power supplies used in the sub-booster modulator are divided into two groups: (1) Main high-voltage power supply with a separate high-voltage regulator and (2) three separate high-voltage supplies, in one package, but with individual controls and meters.

The various outputs are

Bias: 0 to −800 V, 0–3 mA
Driver: 0 to +2100 V, 0–27.5 mA
Screen: 0 to +2100 V, 0–47.5 mA

These supplies are very well-regulated to obtain the required stability of the RF output pulse under varying ac line conditions. Temperature compensation in the regulating circuits of these supplies minimizes the instability caused by the widely varying temperatures in the gallery where this equipment is located.

For increased reliability, silicon solid-state devices are used in these power supplies, with the exception of the series-regulating tubes.

The power supplies are protected from overload conditions, such as shorts in a damaged switch tube, by a current-limiting circuit.

Main high-voltage power supply

The main high-voltage power supply consists of a single phase, full wave bridge rectifier with a series regulator. Its output dc level is regulator-controlled in the voltage range from 24 to 29 kV. Below 24 kV the output is controlled by varying the rectifier ac input by a motor-driver variable transformer.

The nominal output of the unregulated section is 32 kV at 40 mA and the maximum output after the regulator is 29 kV at the same current rating. Overcurrent and overvoltage protection is provided for the power supply and its associated pulser circuit, complete with automatic recycling. This enables the modulator to recycle after a momentary overcurrent condition, i.e., arcing in a switch tube. If more than three faults occur in a 5-min period, the modulator

will be turned off, in which case it must be reset manually. The motor-driven variable transformer is interlocked to prevent turn-on unless it is set for minimum output.

High-voltage regulator circuit

The high-voltage regulator circuit is of the conventional series type, with one special feature. All amplifier and low-voltage power supply circuits are near ground potential, which makes servicing and trouble shooting not quite as dangerous as in circuits floating at the 30-kV level. This is made possible by the application of a 6BK4A shunt voltage regulator tube between the last amplifier stage and the grid of the 4PR400A series regulator.

The 4PR400A tube and its screen supply are the only components mounted on a floating chassis. This regulator will only function in a limited range, 24–29 kV, thus eliminating the need for a larger tube with a considerably greater anode dissipation rating to accommodate a larger voltage range. The 24–29-kV range is ample for this application.

References

1 G. N. Glasoe and J. V. Lebacqz, eds., *Pulse Generators, Mass. Inst. Technol. Radiation Lab. Series*, Vol. 5, McGraw-Hill, New York, 1948.

2 R. W. Bradford, "Hydrogen Thyratron Performance in the SLAC Two-Mile Accelerator," Rept. No. SLAC-PUB-192, Stanford Linear Accelerator Center, Stanford University, Stanford, California (May 1966).

3 T. F. Turner, "An Improved Pulse Transformer for High-Voltage Applications," Rept. No. ML609, Microwave Laboratory, Stanford University, Stanford, California (May 1959).

4 P. R. Gillette, K. W. Henderson, K. Oshima, and R. M. Rowe, "Pulse Transformer Design and Test Methods," Final Report, Part I (AD 79 221), Part II (AD 79 222), Part III (AD 79 223), Project No. 782, Stanford Research Institute, Menlo Park, California (May 1959).

5 K. Dedrick, "Measurement of High Voltage Pulses with Co-axial Voltage Divider," Rept. No. ML-556, Microwave Laboratory, Stanford University, Stanford, California (1958).

6 W. R. Fowkes and R. M. Rowe, *IEEE Trans. Instrumentation and Measurements* **IM-15**, p. 284 (December 1966).

14

TRIGGER SYSTEM

A. Barna, E. J. Faust,
K. W. Henderson, and K. B. Mallory, Editor

The trigger system must provide appropriate timing signals to the injector, the RF drive system, the klystron modulators, the beam transport system, the end-station equipment, and the data-transmission system. Two independent timing functions are to be provided: one is *pulse-rate selection* and the other is *synchronization*—the adjustment of the relative timing of various devices with respect to a single master trigger pulse.

14-1 System design (KBM)

Principles of operation

Three major operational requirements govern the general philosophy of the trigger system design: low jitter, variable repetition rates, and protection and maintenance routines.

First, the relative jitter of the outputs of components (gun, klystrons, etc.) contributing to a beam pulse must be 15 nsec maximum. The synchronization of different trigger pulses must, therefore, be accurate, stable, and independent of the repetition rate of the beam or of the number of klystrons in use.

The second requirement is that the accelerator shall normally operate at repetition rates from 60 to 360 pulses/sec and that beams at lower rates shall be available for special experiments. Operation with interlaced beams of different energy and intensity is also required. It is, therefore, necessary that various pieces of equipment be driven at different repetition rates.

The small jitter and flexibility of repetition rate are obtained by using a single, master clock signal at 360 pulses/sec from which all synchronization is derived, and by using slow gating signals at each piece of equipment to determine which pulses in the 360-pulses/sec clock train are used.

The third requirement is that certain protection, standby, and maintenance functions must be provided through the trigger system:

1. In case of a gas burst in an accelerator section, the trigger must be removed from the corresponding klystron modulator.
2. In case of serious deterioration of vacuum or failure of certain water circuits, the beam must be turned off promptly by removing the trigger to the injector. The beam must also be shut off when the personnel protection interlocks are interrupted.
3. In case of excessive radiation, the beam must be turned off.
4. For phasing, the accelerator structure must be kept at normal operating temperature (by supplying RF power to the section) while the beam-induced signal is observed.
5. Newly installed klystrons must be tested without interfering with the beam operation.
6. Reserve klystrons must be warmed up and ready for operation to take the place of failures.

The three latter items are handled using an auxiliary, delayed trigger signal which does not coincide with the beam. The "delayed" trigger is 25–50 μsec later than the normal "prompt" trigger. The delay at successive sectors is staggered so as to prevent appreciable acceleration of stray electrons during the delayed pulse.

The protective circuits associated with the klystron and its modulator are described in detail in Chapter 15. These circuits are located in the instrumentation rack adjacent to each modulator and are provided as part of the actuation and measurement equipment, not as part of the trigger system.

Special circuits are provided to shut off the gun in case of excessive radiation, pulse-magnet malfunction, or other cause or sympton of undesirable beam loss. These circuits interact with the gun trigger through equipment described in Chapter 21.

SYSTEM LOGIC. A simplified diagram of the trigger system is shown in Fig. 14-1. The entire trigger system is slave to a clock composed of the sequence generator and the master trigger generator. The sequence generator, located

Figure 14-1 Trigger system block diagram.

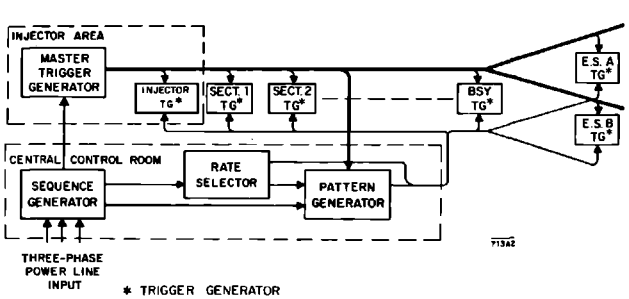

in central control, locks the master trigger generator to the 60-Hz line frequency and supplies gating pulses to the rate selector and pattern generator. The master trigger generator, located at the injector end of the klystron gallery, creates the 360-pulses/sec clock pulses which are transmitted to trigger generators located wherever trigger signals are required.

The pattern generator in central control generates for each piece of equipment a millisecond pulse "pattern signal" which determines whether the next clock pulse is or is not to be used. Each trigger generator uses the gating information from the pattern generator and the precise timing of the clock pulse from the master trigger generator to generate the appropriate output trigger pulses.

MASTER CLOCK AND MAIN DISTRIBUTION. The synchronization of all events associated with a given pulse of electrons in the accelerator is determined by clock signals from the master trigger generator. It operates at 360 Hz, locked to the power line frequency. The clock output is a train of pulse pairs consisting of a negative pretrigger followed 25 μsec later by a positive main trigger pulse.

The clock output pulses are distributed by a $1\frac{5}{8}$-in. diameter, high-velocity, low-loss coax line to trigger generators in each sector, in central control, in the switchyard, and in each end-station area. The main trigger line is isolated from the equipment by coupling transformers in the line and by gates and buffer amplifiers in the trigger generators. The trigger generators can be programmed to select the proper pulse rate and pattern for each piece of equipment.

Programming for multiple beams

As will be shown below, the patterns occasionally will be irregular during multiple-beam operation. The klystron modulators are designed to be operated at regular rates (60, 120, 180, or 360 pulses/sec). Special gating signals, called "rate signals," are synthesized at the rate selector in central control. These signals enable the trigger generator to furnish "delayed" trigger pulses with a small delay of, say, 25 μsec, which fill in gaps in an irregular pattern but do not contribute unwanted acceleration energy to the beam.

In order to limit the range of regulation for power supplies and water systems, 60 pulses/sec was chosen as the minimum klystron operating rate (360 pulses/sec is the design maximum). It is evident that one can operate half the klystrons at 360 pulses/sec and the rest at 60 pulses/sec, thus producing two interlaced beams—one full-energy pulse followed by five half-energy pulses. A pulsed, magnetic deflection system for steering the beams to different targets was determined to be feasible and led to the multiple-beam concept.

A problem arises when one attempts the reverse situation: the case in which 60 pulses/sec are to be at half-energy and the remainder are to be at full energy. In this case, half of the klystrons are to skip one pulse out of

every six. With the best of regulators, the first RF pulse after the skipped one will not be of exactly the same magnitude as the others. In order to avoid skipping a pulse, a small pulse-position modulation was introduced to delay a modulator pulse for a few microseconds when it was not desired for acceleration. This "delayed" pulse occurs after the beam has passed, so that it cannot affect the electron energy, but it serves to keep the average power and the repetition rate of the klystron constant.

The pattern signals are described in detail below. Briefly, the desired pattern of beam pulses is set up within the pattern generator, and a set of selector switches connects each beam pattern to the equipment which contributes to that beam. The sum of all beam patterns required for a piece of equipment is its pattern signal.

The following additional features are required:

1. Provision must be made for resolving overlapping requests, i.e., two or more requests for the same beam pulse.
2. It must be possible to switch back and forth between any two beams of the same energy but differing in other characteristics such as pulse length, intensity, and repetition rate.
3. It must be possible to program klystrons, pulse magnets, experimental equipment, etc., for a new beam before prior experiments are terminated.

It has been determined that it can take as long as 2 hours to set up a high-energy run after a low-energy run. Most of this time may be eliminated if the new beam is programmed while the former experiments are still in progress, and tuned up by stealing a few pulses per second from the prior experiments.

USE WITH MULTIPLE BEAMS. Since a pattern signal impulse is transmitted to a piece of equipment only when it is to be triggered, it is possible to turn on different combinations of klystrons or steer the beam by means of the pulse magnets to different targets on successive pulses. Each different program of pieces of equipment to be triggered for a given pulse can be considered the program of a separate beam. Consider the following example, chosen to illustrate pattern signal logic—not a real experiment. A spark chamber operating in area B requires 60 pulses/sec at 10 GeV, but there must be no beam pulse in the accelerator 1/360 sec before, in order to reduce the probability of stray background trails. The experimenters in area A desire 20 GeV, using every available leftover beam pulse.

It is clear that the entire accelerator must contribute to four successive beam pulses to area A, the entire accelerator must be off for the next pulse, and half the accelerator will then contribute to one beam pulse for area B. Typical pattern signals for this type of operation are shown in Fig. 14-2.

The pulse patterns are irregular; this is a natural result of using multiple beams. However, the klystrons will be triggered by the "delayed" trigger when the pattern signal is off and thus will operate at a regular rate (in this example, 360 pulses/sec for all klystrons).

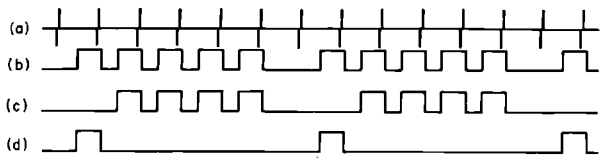

(a) Clock pulses
(b) Pattern signals for Injector and Sectors 1–15
(c) Pattern signals for Sectors 16–30, Target Area A trigger generator and Pulse Magnet A
(d) Pattern signals for Target Area B trigger generator and Pulse Magnet B

7I3AI

Figure 14-2 Pattern signals for a 60-pulses/sec beam at 10 GeV to area B, following a 60 pulses/sec "null beam," with the remaining beam pulses at 20 GeV to area A.

In order to produce the desired pattern signals, it is first necessary to determine which beams are desired. In the example above, area A is willing to use all leftover pulses; it is "requesting" a 360 pulses/sec beam. Area B is requesting a 60-pulses/sec beam, but it is also requesting no beam on the preceding pulse. Such a required "null beam" must be programmed just like any other beam.

Since it is impossible to handle two different beams during one pulse, it is necessary to cancel area A's request for a 20-GeV beam whenever area B requests its null beam or its 10-GeV beam. A "priority circuit" sorts out the requests to determine which beam shall be delivered on each machine pulse. The resultant output signals are the "beam pattern signals" which are then used to generate the pattern signals for the equipment. The purpose of the priority circuit is twofold: (1) It provides a very simple means of generating the irregular beam pattern signal for area A, and (2) it allows area A to receive all pulses automatically any time B interrupts experiments and cancels its requests. There need be no wasted pulses; an area willing to accept all leftover pulses will, indeed, get a beam pulse, of the proper energy, every time another experiment is not using the beam.

Trigger generators

"STANDARD" TRIGGER GENERATOR CHANNEL. A typical trigger generator channel is diagrammed in Fig. 14-3. Its operation is as follows.

A sampling device couples a portion of the clock output from the main trigger line to each trigger generator. A diode network blocks low-level noise from the trigger line and separates the positive main trigger pulse from the negative pretrigger pulse.

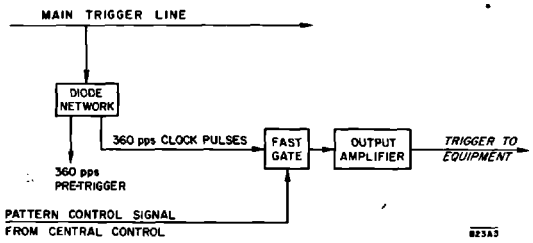

Figure 14-3 Standard trigger generator channel.

The main trigger is fed through a fast gate controlled by the two-state pattern signal sent from central control. If the pattern signal is "on," a trigger signal is passed on to the equipment. If the pattern signal is "off," no trigger output will exist. A delay network, if required, produces the proper timing with respect to the beam. A final amplifier produces a trigger signal of 10-volt amplitude, 50-nsec rise time, and 400-μsec duration which is delivered via a 50-ohm cable to a 50-ohm input in the equipment to be triggered.

This output level is the nominal standard for all trigger generators. As previously stated, the output pulse pattern is determined entirely by the pattern control signal from central control. It may be completely arbitrary—anything from a single pulse on demand, one pulse per year, to 360 pulses/sec, any combination of bursts of pulses, skipped pulses, regular rates, etc. It is at central control that these patterns must be generated. The local generator is strictly a slave to its pattern control signal.

SECTOR TRIGGER GENERATOR. Although the sector trigger generator is basically a group of standard trigger channels as described above, the modulator trigger is handled somewhat differently. The klystron modulators must operate at regular rates of 60, 120, 180, or 360 pulses/sec in order to satisfy specifications on pulse-to-pulse stability. For this equipment, therefore, the arbitrary pulse patterns required for multiple-beam operation are provided by using the pattern control signal to shift the timing of the modulator triggers. When the pattern signal is "on," the modulator is triggered by "prompt" pulses coincident with the beam. When the pattern signal is "off," the modulator is triggered by "delayed" pulses, just after the beam has passed by. The overall pattern is, therefore, a uniform pulse rate with a small pulse-position modulation. The "prompt" pulses contribute to the beam, the "delayed" pulses do not. (A different delay is used at each sector in order to minimize the energy to which stray electrons can be accelerated during the "delayed" pulse.)

In addition to the normal "accelerate" trigger output, which may contain prompt and delayed pulses according to the requirements for multiple beams, a "standby" output containing only delayed pulses is required for klystrons being held in reserve, cycling after gas bursts, being tested, phased, etc. The

standby output is controlled by the rate selector setting only; it is not affected by the pattern signal.

The drive sub-booster must provide delayed as well as prompt drive pulses for the klystrons. To keep its phase shift constant, it delivers 360 pairs of drive pulses per second no matter what rate the klystron modulators use. Hence, neither rate setting nor pattern control signal affects sub-booster operation.

In order to compensate for beam loading (discussed in Chapter 5), a 0–1 μsec remotely adjustable delay, common to the modulator and sub-booster pulses, is provided for each sector. This allows compensation for the energy droop of the beam which occurs within each pulse, at high beam current.

The automatic phasing equipment requires both the prompt and the delayed pulse at 60 pulses/sec. The data-handling system requires the ungated 360-pulses/sec standard trigger only.

Analysis of trigger system delays

The various delays which must be considered in determining the synchronization relationships of the trigger system are discussed below, and shown in Figs. 14-4a through d. Delays are designated by the symbol τ plus a subscript for identification. Compensations are designated by the symbol T plus a subscript.

The sum of all the necessary delays (τ_M, τ_T, ...) plus the fixed compensation T_C is a minimum of $L/c + l/c + 3.26$ μsec and a maximum of $L/c + l/c + 3.96$ μsec. T_F allows optional insertion of up to 0.775 μsec additional delay so that the RF pulse will fill the accelerator exactly $L/c + l/c + 4.0$ μsec after the trigger pulse starts down the main line.

1. *Main line delay* $= \tau_M$. The trigger signal travels from the main trigger generator to the individual sector in a time $\tau_M = L/0.921c$, where L is the distance to the sector and c is the velocity of light. The clock signal at Sector 30 is delayed 0.843 μsec more with respect to the electron beam than the clock signal at Sector 1.
2. *Compensation for main line delay* $= T_C$. The compensation varies from 1.00 μsec at Sector 1 to 0.16 μsec at Sector 30. The trigger signal is arranged to arrive at the sector trigger generator 3.00 μsec before the beam arrives at a point directly below.
3. *Trigger generator delay* $= \tau_T$. A delay of 0.20 μsec is allowed through the gates and power amplifiers in the trigger generator.
4. *Sector trigger distribution delay* $= \tau_d$. The delay in the sector distribution cables is $\tau_d = l/0.67c$, where l is the variable distance from the sector trigger generator to the klystron fiat racks.
5. *Sector distribution compensation* $= T_d$. Compensation for the low group velocity is accomplished by supplying increased cable lengths to the first few fiat racks. The excess delay is 0.16 μsec.

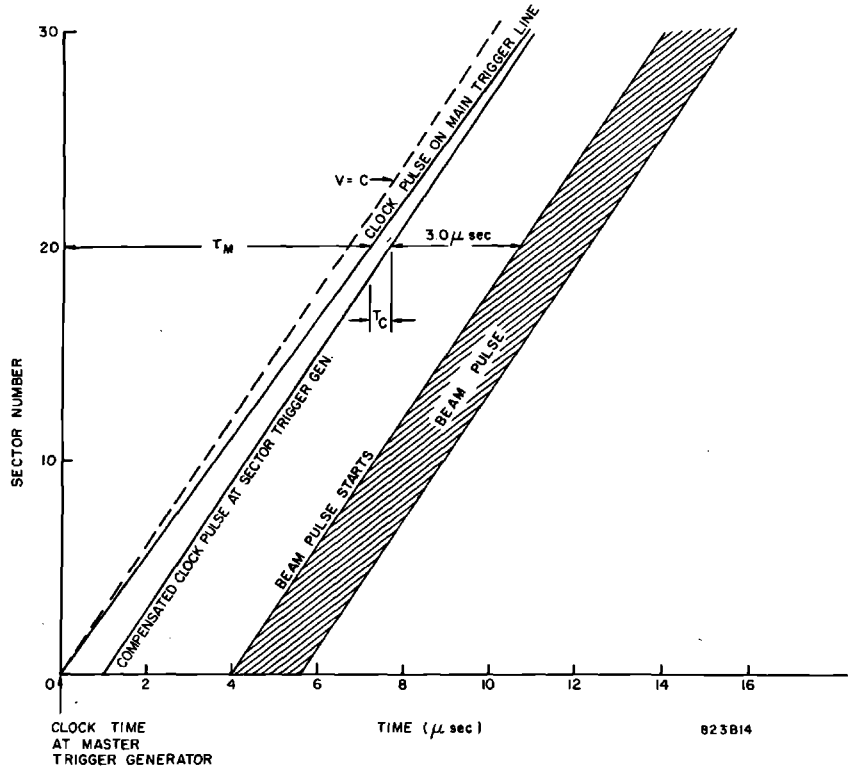

Figure 14-4a Intersector timing diagram showing trigger system delays and compensations τ_M and T_c.

Figure 14-4b Intrasector timing diagram showing trigger system delays and compensations τ_T, τ_d, T_d, τ_m, T_F, τ_r, τ_f.

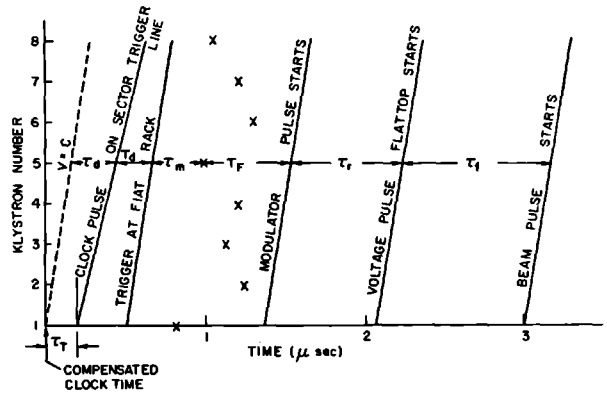

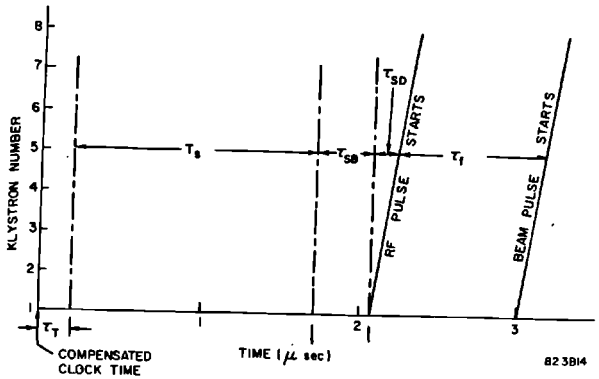

Figure 14-4c Intrasector timing diagram showing trigger system delays and compensations τ_T, T_S, τ_{SD}, τ_{SB}, τ_f.

Figure 14-4d Two first-order approaches to beam-loading compensation, showing use of trigger system delay T_L.

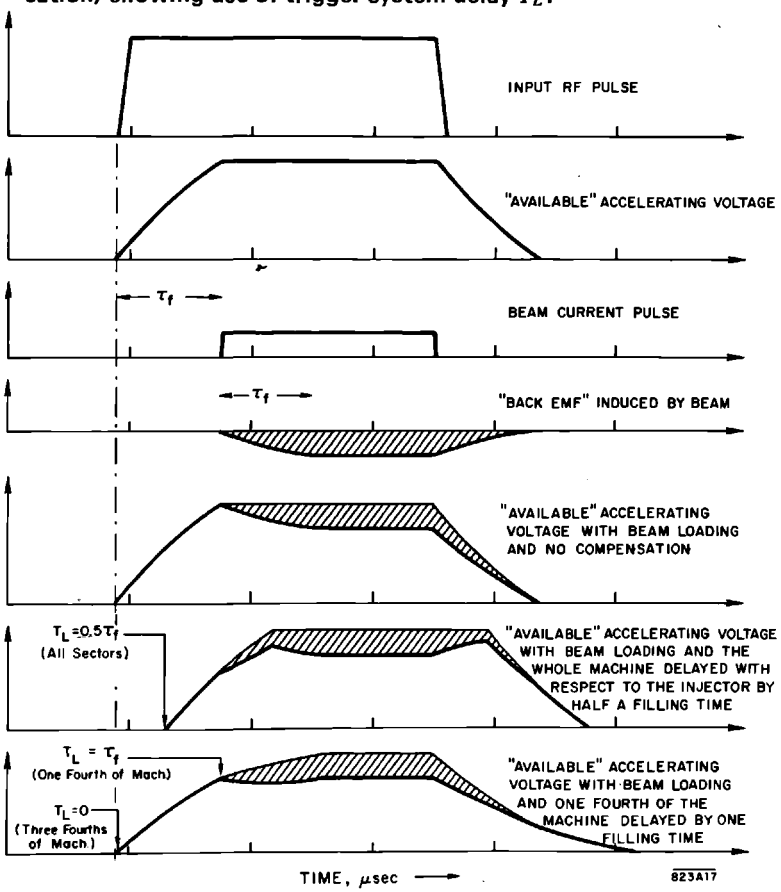

6. *Modulator delay* $= \tau_m$. A delay of 0.1 to 1.0 μsec (including up to 0.40 μsec thyratron anode delay) must be allowed. The compensation is accomplished in T_F.
7. *Fiat rack compensation* $= T_F$ (see Chapter 15). A 0–0.775-μsec delay (steps of 400, 200, 100, 50, and 25 nsec) is provided at each fiat rack to compensate for thyratron anode delay which differs from one thyratron to another and varies during the life of any individual thyratron.
8. *Modulator rise time delay* $= \tau_r$. The modulator rise time is taken to be 0.70 μsec. It is assumed that there may be individual differences between modulators of ± 0.10 μsec.
9. *Filling time* $= \tau_f$. The filling time of the accelerator input waveguide is about 0.10 μsec and of the accelerator proper, 0.83 μsec.
10. *Subdrive line delay* $= \tau_{SD} = l/c$. The group velocity of the subdrive line is taken to be virtually equal to the velocity of light. There is, therefore, no excess delay in the subdrive line.
11. *Sub-booster modulator delay* $= \tau_{SB}$. The delay in the trigger and driving circuit of the sub-booster modulator is assumed to be greater than 0.10 μsec but less than 0.50 μsec.
12. *Sub-booster timing adjustment* $= T_S$. In order to make the sub-booster and the main klystron pulse overlap properly, it is necessary to satisfy the equation:

$$T_F + T_d + \tau_d + \tau_m + \tau_r = T_S + \tau_{SB} + \tau_{SD}$$

The equation is satisfied by adjusting T_S, which is composed of a fixed delay of 1.30 μsec plus a variable 0.0–0.775-μsec delay identical to T_F. On the average, all of the above delays add up to $L/c + l/c + 3.10$ μsec.

13. *Beam-loading adjustment* $= T_L$. The beam-loading adjustment for each sector is remotely controlled from central control. The minimum delay is labeled 0.0 μsec; the maximum delay is labeled 1.0 μsec.
14. *Standby delay* $= T_D$. At each sector, the standby delay is fixed at a value between 25 to 50 μsec. As previously explained a different standby delay is used in each sector.

Beam-loading compensation

The reduction in electron energy and deterioration in spectrum width which are caused by beam current loading are discussed in Chapter 5, in the section dealing with beam characteristics. Figure 5-27 illustrates the development of a high-energy tail on the spectrum as the beam current is increased.

A fair degree of compensation for the deleterious effects of beam loading may be achieved by using the trigger system delay T_L. Two simple approaches are illustrated in Fig. 14-4d. The heavy lines in the lower three diagrams indicate the magnitude of the available accelerating voltage. Some compensation is afforded by delaying the whole machine with respect to the injector. A better solution, however, is to delay one or more sectors by approximately one filling

time. Since the rise of the available voltage pulse approximates a truncated exponential and the rise of the "back emf" is roughly parabolic, perfect compensation cannot be achieved by varying a single parameter. Nevertheless, the spectrum may be considerably improved, as illustrated in Fig. 5-28.

Signal waveforms

The system uses two types of signals: trigger pulses and programming pulses. The trigger pulses have nominal length 400 nsec, rise time 20 nsec, and timing precision ± 5 nsec. The programming pulses have nominal length 1000–1700 μsec, rise time 30 μsec, and timing precision 50 μsec. Trigger pulses are transmitted on 50-ohm coaxial cables, at a level of 10 V (except in the main distribution system). Details of the ± 400-V output pulse train from the master trigger generator are given in Fig. 14-5. Programming pulses are transmitted on balanced telephone pairs, at a level of about 10 V into 1000 ohms. Examples are shown in Fig. 14-6.

Two types of programming pulses have been distinguished: rate signals and pattern signals. The rate signals originate in the sequence generator and rate selector and have rates of 60, 120, 180, and 360 Hz. They are used primarily to trigger equipment that must operate at a uniform rate (such as klystron modulators) regardless of the specific repetition rate of a beam. They are centered about the beam pulse as shown in Fig. 14-6c.

The pattern signals are associated with a particular beam or group of beams and may be irregular—a pattern at 300 pulses/sec would contain five pulses at 360 Hz, followed by a gap of twice the normal interpulse interval.

The pattern signal is used to gate both the prompt and the delayed klystron trigger pulses; it, therefore, overlaps the beam pulse, Fig. 14-6a, by about 100 μsec. It also is used to switch dc levels in the positron phase shifters and to trigger the pulsed magnets in the switchyard; these circuits must be allowed

Figure 14-5 Master trigger generator, output pulse

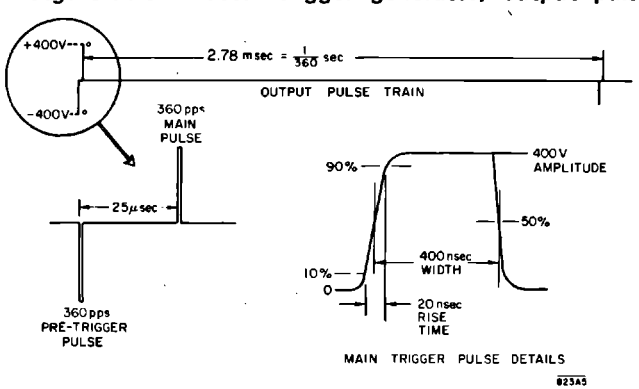

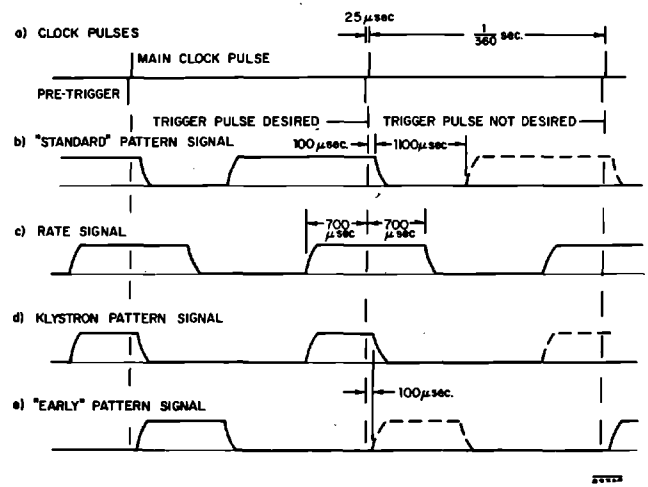

Figure 14-6 Typical pattern signals.

an advance warning of about 1500 μsec. The normal pattern will, therefore, be a chopped signal of Fig. 14-6b. It is always off from the time 100 μsec after the beam to the time 1200 μsec after the beam, and it is on for the remaining interval if the pattern calls for the use of the next pulse. The signal duration is thus about 1677 μsec for each beam pulse required.

The pattern signal transmitted to each sector trigger generator for the klystrons is first combined with the "rate signal," Fig. 14-6c, for that sector at CCR. Since the rate signals from the sequence generator are of shorter duration than the normal pattern signals, the resultant "klystron pattern signals" will be shortened to approximately 1-msec duration, as shown in Fig. 14-6d. They must also overlap the beam pulse by 100 μsec.

For certain functions, an "early" pattern signal is required. This signal consists of pulses starting 100 μsec after the preceding beam pulse and continuing for 1100 μsec, as shown in Fig. 14-6e.

14-2 Description of system components (EJF)

The trigger system has four groups of components: the clock, the distribution system, the trigger generators, and the programming equipment.

The clock produces main trigger clock pulses at 6 times line frequency (nominally 360 Hz). The special distribution system transmits the clock pulses to the trigger generators where they are gated by the programming pulses to yield trigger pulses at the appropriate repetition rate for each piece of equipment. The programming pulses thus determine which pieces of equipment are operated for each beam pulse; they are controlled by the operator at the pattern generator in central control.

Master clock

Associated with the clock are the sequence generator, the master trigger generator, and the comparator.

SEQUENCE GENERATOR. The functions of the sequence generator are (a) to produce a 360 pulses/sec pulse train to drive the master trigger generator (the source of "clock" pulses) and (b) to produce the six different phases of 60-pulses/sec pulses needed to form the rate pulses.

Figure 14-7 shows the time relationships of the input and output waveforms of the sequence generator. The six, equally spaced phases of 60-pulses/sec output pulses are formed from the positive-going and negative-going zero crossings of the input. These sine waves of input current are changed to voltage pulses by the saturating transformers, of which the cores have the property of becoming quickly saturated with flux as the magnetizing current increases. Inductors in series with each transformer limit the surge current during the time when the core is saturated and the transformer impedance is negligibly low. The output pulses are properly channeled by diodes.

Figure 14-7 Sequence generator waveforms and schematic.

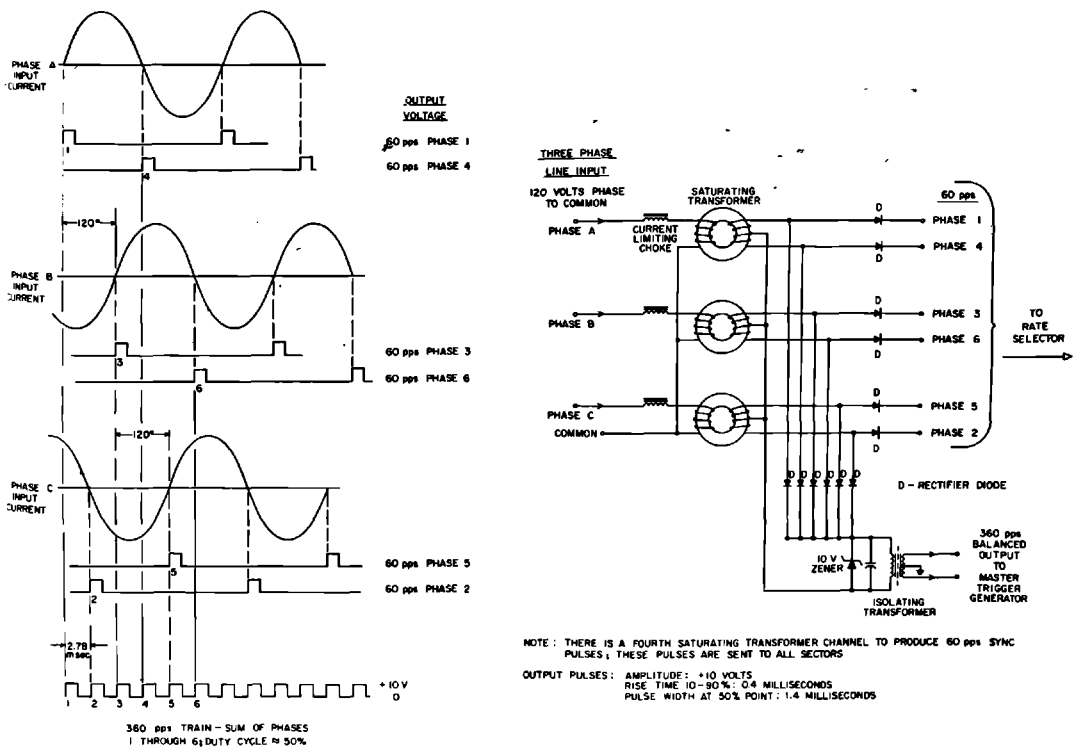

An important function that the sequence generator fills is the locking of the output pulses to the incoming 60-cycle line frequency. (These pulses define the timing of the "clock" pulses for the machine.) This technique is useful in eliminating noise caused by beat frequencies that would be present with a system not locked to line frequency.

There is a high degree of reliability obtained by using the three-phase line as an input. In the event of the failure of any phase, a filter in the master trigger generator has a sufficiently long time constant to maintain a train of output clock pulses from the master trigger generator. This guards against a sudden dumping of the entire 245-modulator power load.

The use of three sequence generators is a further aid to reliability. Each generator supplies rate signals for one-third of the machine, another safeguard against a sudden loss of the entire modulator power load. Each sequence generator also supplies pulses to one of the three master trigger generators; thus, the system for generating clock pulses is triply redundant from power line input to clock pulse output.

MASTER TRIGGER GENERATOR. The master trigger generator (MTG) is the source of precisely timed pretrigger and main clock pulses for the trigger system. The block diagram, Fig. 14-8, shows how the master trigger generator converts the slow-rising, 360-pulses/sec pulses from the sequence generator into fast, low-jitter, positive and negative output pulse pairs.

The input pulses are first carefully filtered with a 360-Hz, band-pass filter into a relatively pure and jitter-free sine wave. A phase shifter retards the phase of the wave to ensure that the clock pulses derived from this wave will be centered relative to the input pulses. A pulse shaper then converts the 360-Hz sine wave to a negative 360-pulses/sec pulse train. This output splits into an undelayed and a delayed channel and is regenerated and amplified to form the pretrigger and main trigger pulses. These pulses are combined in the output pulse transformer and sent down the main trigger line.

COMPARATOR. Failure of the sequence generator or the master trigger generator could produce a complete system failure. Sudden failure of the master

Figure 14-8 Block diagram of master trigger generator.

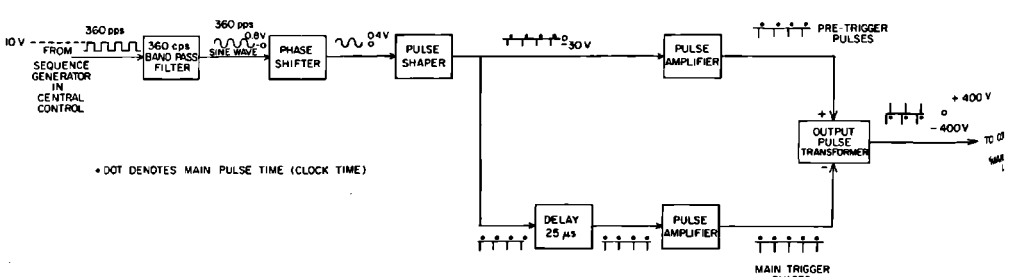

clock when all the klystron modulators are in operation would produce significant power line transients which are to be avoided. Three redundant sequence generators and MTG's are furnished. The comparator monitors the outputs of the three MTG's and switches a reserve MTG to the main trigger line when the active one fails.

The basic requirements for the comparator are that it will

1. detect a missing pulse from a MTG;
2. detect an extra pulse from a MTG;
3. operate a transfer switch when such a fault occurs in the MTG on the line;
4. have a limited recycling capability.

A missing pulse fault condition is defined to exist when no pulse occurs within 3.0 msec of the previous clock pulse. An extra pulse fault condition exists when a pulse occurs within 2.5 msec after the previous clock pulse.

Figure 14-9 shows a block diagram of one of the monitor circuits and indicates typical waveforms. Only the positive clock pulse is monitored. The clock pulse triggers an asymmetrical multivibrator which has a long dead time (2.5 msec) followed by a short active time (0.5 msec) during which it may be triggered again. Normally a clock pulse arrives after 0.28 msec of active time and resets the multivibrator. An extra pulse which arrives too soon cannot reset the multivibrator. If a clock pulse does not arrive during the short active interval, the multivibrator resets itself automatically after 0.5 msec of active time.

Figure 14-9 Monitor circuit for comparator.

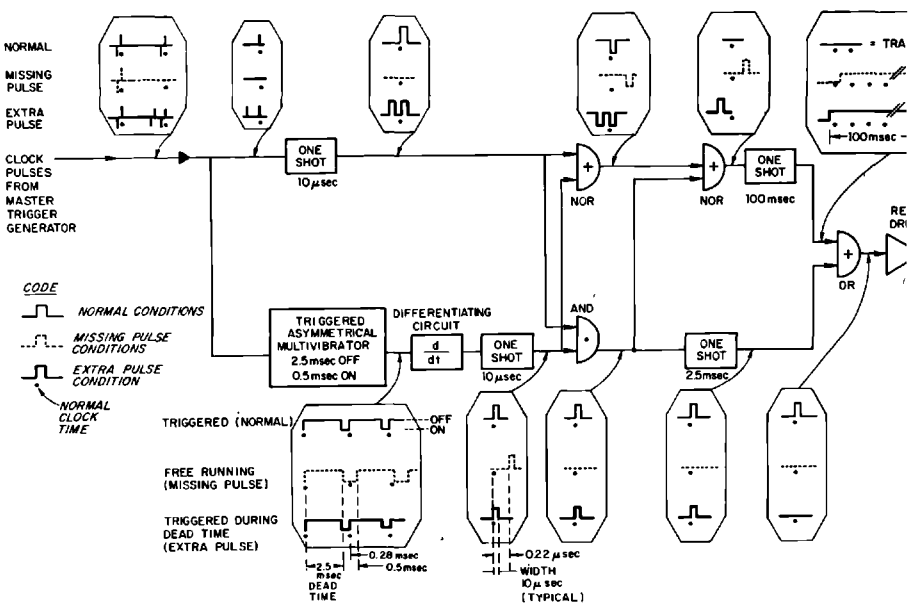

There are three conditions to consider: (1) normal—no faults; (2) missing pulse; and (3) extra pulse.

Referring to Fig. 14-9, and *assuming the normal condition* it is seen that the multivibrator is off for the standard "dead time" of 2.5 msec, at the end of which it automatically turns itself on. The arrival of a clock pulse 0.28 msec later turns the multivibrator off again. The differentiating circuit produces a narrow pulse coincident with turnoff, which in this case is at clock time. The one-shot multivibrator stretches this narrow pulse to 10 μsec, which is sufficiently wide for accurate summing in the gates. The AND gate receives two coincident clock time pulses; it, therefore, transmits a pulse at clock time. NOR_1 (an inverting OR gate) also receives both pulses and sends out an inverted replica of the input pulses. NOR_2 algebraically adds the pulses from the AND gate and NOR_1. Because these are coincident pulses of opposite polarity, zero output results. The 100-msec one-shot inhibit signal is, therefore, not triggered in the normal mode. The 2.5-msec one-shot, however, is triggered regularly at 360 pulses/sec. These pulses pass through the OR gate and relay driver to hold the relay contacts closed.

In the *missing pulse condition*, the absence of a trigger pulse at clock time causes the narrow pulse in the asymmetrical multivibrator waveform to continue past clock time, until the multivibrator turns itself off. The differentiating circuit now produces a pulse 0.22 msec later than normal. Tracing this late pulse through the AND gate, it is seen that there can be no output because there is only one input signal. However, the NOR_1 gate does transmit the late pulse, as does the NOR_2, so that the 100-msec inhibit signal is initiated. This allows the relay to drop out and causes the comparator to switch to another MTG.

In the *extra pulse situation*, the asymmetrical multivibrator operates normally, because the extra pulse arrives at a time when the multivibrator is insensitive to triggering. The AND gate receives two simultaneous inputs at clock time and, therefore, transmits an output pulse. NOR_1 sends out an inverted double pulse, the clock pulse, and the extra pulse. NOR_2 sends out only the extra pulse, because the erect and inverted clock pulses cancel each other. The extra pulse initiates the 100-msec inhibit signal which stops transmission of the 2.5-msec pulses through the OR gate, causing the relay contacts to open. After the 100-msec interval, the relay closes again until another fault occurs. The transfer switches are fast enough to ensure that no clock pulses are lost during transfer.

Distribution system

The clock output pulses are distributed by a high-velocity, low-loss, coaxial line to trigger generators in each sector, at the injector, at central control, in the switchyard, and in each end-station area and physics laboratory.

MAIN TRANSMISSION LINE. The electron beam specifications require that the pulse-time jitter shall be ± 15 nsec maximum. Assuming that some jitter is

introduced in modulators and in amplifiers in the trigger system, a specification of about ± 5 nsec must be placed on the transmission system between the master clock and the trigger generators. With good discriminators, it is possible to hold 5-nsec jitter with about 50-nsec rise time of the input pulse to the trigger generators.

The clock pulse must arrive at every sector somewhat ahead of the beam pulse in order to turn on the klystron modulators. It was decided that the clock pulse should arrive at every sector exactly the same amount in advance (3.0 μsec). An adjustable delay at each sector then triggers the equipment at each sector at the correct time.

The beam requires approximately 10.2 μsec to travel 10,000 ft. In a cable, it will take a clock pulse slightly longer to travel the same distance. With an air dielectric cable, the difference in transit time between beam and clock pulse is negligible. With a solid polyethylene dielectric, the propagation velocity of the clock pulse is about two-thirds the velocity of the beam, and the transit time of the clock pulse will be 5 μsec greater. A compensating delay must, therefore, be inserted at the first sector (and a proportionately reduced delay at later sectors) in order to trigger the equipment at the proper moment.

It is difficult to introduce a delay as great as 5 μsec without introducing more than 5-nsec jitter. It is uneconomical to use a cable with $v = c$ in order to eliminate this delay. The practical solution is to use a cable with moderately high velocity, $v = 0.91c$, which introduces 1.0-μsec extra transit time for the trigger pulse. The 1.00-μsec delay required at Sector 1, the 0.97-μsec delay required at Sector 2, etc., may be introduced by extra delay cables that degrade the rise time of the pulse to just such an extent that the received pulse is of the same quality at every sector.

For most cables useful in pulse transmission, attenuation below approximately 1000 MHz is due mainly to skin-effect losses and varies as the square root of frequency.[1] For such cables, the output response to a step-function input has a rise time that varies as the square of the attenuation at a given frequency.

The 0–50% rise time, T_0, is given by the formula

$$T_0 = 4.56 \times 10^{-12} A^2 l^2 \text{ sec}$$

where A is attenuation in decibels per unit length at 1 GHz, and l is the length of the cable.

Cables of different sizes or types were compared for cost vs loss. For a 50-nsec rise time, the total attenuation Al is 105 dB. Therefore, the cable must have a loss at 1 GHZ of 1.05 dB/100 ft or less. The least expensive cable which approached this requirement was found to be a $1\frac{5}{8}$-in. diameter, Heliax cable. This cable has a velocity of $0.91c$ and requires some compensation.

TAKEOFF TRANSFORMERS (AB). The purpose of the takeoff transformers[2] is to provide timing pulses for the trigger generators without appreciably disturbing the pulses propagated along the main trigger line.

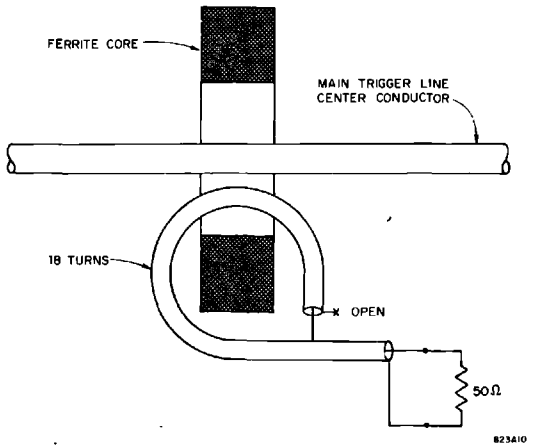

Figure 14-10 Schematic diagram of takeoff transformer.

A current transformer has been designed with the center conductor of the 50-ohm main trigger line as primary; the secondary winding consists of 18 turns of coaxial cable on a 1-in. ferrite core. This cable is terminated with its characteristic impedance of 50 ohms at the far end (see Fig. 14-10).

Measurements of the transient response show a 10–90% rise time of 2 nsec with 20% overshoot and ringing. The frequency response is down by 3 dB at 30 kHz and at 115 MHz.

The series impedance is reflected by the transformer into the main trigger line. The pulse height at the last sector is 87% of that at the first sector, resulting in takeoff voltages of 22.5 to 19 V along the entire accelerator for a MTG output voltage of 400 V.

Trigger generators

A number of different trigger generators are used, of which the outputs are determined by the requirements of the local equipment to be triggered. The most specialized trigger generators are to be found in the klystron gallery, where the requirements are fixed. The least specialized trigger generators are to be found in the research area where the requirements are frequently changed and where the experimenters are accustomed to providing their own gating and delay circuits.

The sector trigger generator is described in detail below; the other trigger generators use similar circuits, stripped down to the essential requirements.

SECTOR TRIGGER GENERATOR. The sector trigger generator must perform the following functions:

1. Trigger the sub-booster modulator at a constant, double 360-pulses/sec repetition rate, i.e., a pair of 360-pulses/sec pulses spaced 25–50 μsec apart.
2. Trigger the main modulators at a regular rate; specifically, 60, 120, 180, or 360 pulses/sec.
3. Deliver a regular or irregular train of "prompt" pulses to the main modulators on demand. (These pulses are timed so that the modulator output will accelerate the beam.)
4. Deliver a regular or irregular train of "delayed" or standby pulses to the main modulators to fill in gaps in the train of "prompt" pulses, thus satisfying requirement (2) above. These pulses are timed late, so that the modulator output will not accelerate the beam.
5. Deliver pulses to components or subsystems as follows: (a) 60-pulses/sec "prompt" and "delayed" pulses to phasing system; (b) 360-pulses/sec pulses to beam monitor equipment; and (c) 360-pulses/sec pulses to data-handling system.

In addition to the above requirements, the sector trigger generator must also perform the essential function of delaying modulator pulses as noted earlier.

Figure 14-11 is a block diagram of the sector trigger generator. Its input is a train of positive 360-pulses/sec "clock" pulses supplied by the MTG via the main trigger line and the sector takeoff tee.

The pulses coming off the tee are exact replicas of the clock pulses on the main trigger line except that they are reduced in amplitude from 400 to 20 V. The negative pretrigger pulse is shunted to ground by a diode. The remaining +20-V, 360-pulses/sec pulses (clock pulses) are passed through a pulse transformer that matches the 200-ohm impedance of delay T_C to the 50-ohm line. Delay T_C compensates for the slowness of the main trigger line relative to the electron beam, varying the amounts of delay in successive sectors in order to achieve synchronism.

The pulses leaving T_C are fanned out into three paths: (1) through delay T_D to produce "delayed" pulses, (2) through delay T_L to produce "prompt" pulses that are corrected for beam-loading effects; or (3) to synchronize most of the accessories, i.e., the phasing pulses, the data equipment pulses, and the beam monitoring pulses.

The sub-booster modulator trigger pulses are formed by combining prompt and delayed pulses in the OR_1 gate. These pulses are delayed by T_S, amplified to 40-V pulses, and sent out.

The "accelerate" trigger pulses for the main modulators are formed by combining prompt and delayed pulses in the OR_2 gate, but the process is a bit more complex. The prompt pulses are gated by pattern pulses in AND_1; there can be no transmission of "prompt" pulses through AND_1 without the simultaneous appearance of a pattern pulse. Therefore, the output of AND_1 is, in general, an irregular train of prompt pulses corresponding to the pattern

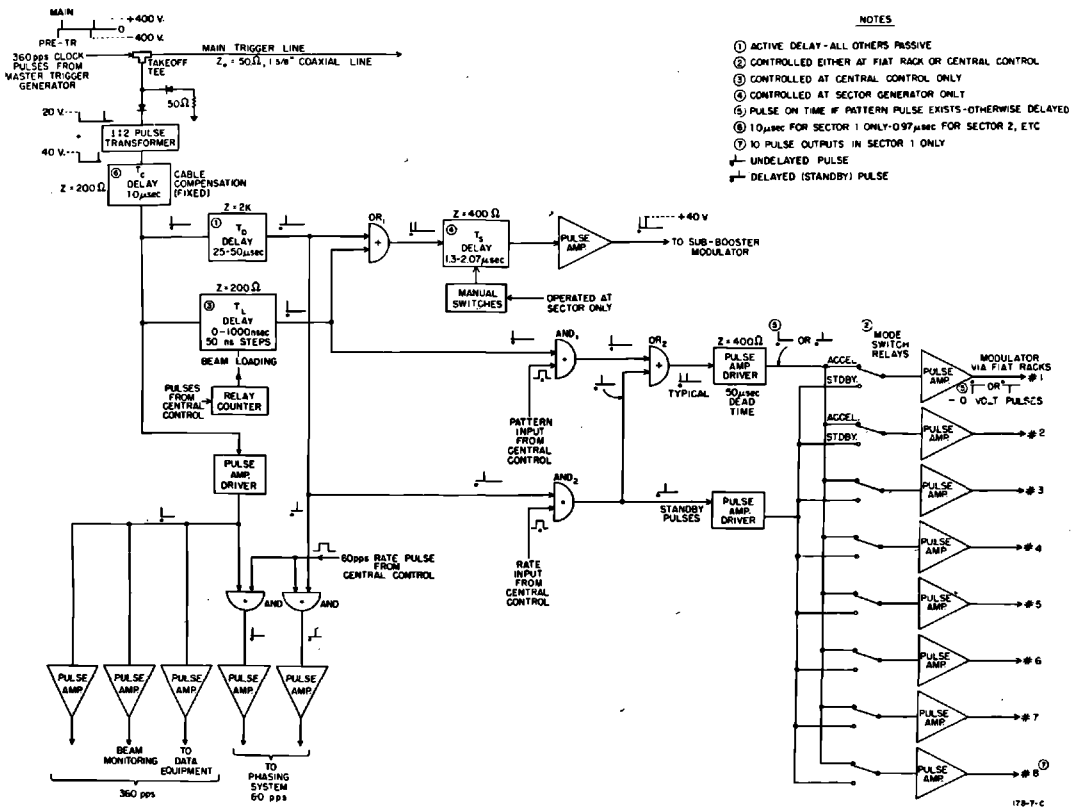

Figure 14-11 Block diagram of sector trigger generator.

pulse train. The AND_2 gate combines delayed pulses and rate pulses such that its output is a train of delayed pulses identical to the rate pulse train. The two outputs from AND_1 and AND_2 are then summed in the gate OR_2. When "prompt" and "delayed" pulses occur within 50 μsec of each other, the delayed pulse is suppressed in the pulse amplifier driver.

The output is an irregular pulse train which will, in general, have prompt and delayed pulses in various combinations. These pulses pass through the mode switch, are amplified to 10-V pulses, and are sent to the modulators via the respective FIAT racks. The other mode switch position is standby. The standby line delivers delayed pulses at the rate determined by the rate signals. The operation of the mode switch is described in Chapter 15.

INJECTOR TRIGGER GENERATOR. The injector trigger generator must provide sets of timing pulses for equipment associated with each of several beams. Some equipment is pulsed every time a beam pulse occurs. Some equipment is pulsed only for one beam or another. In general, the pulse repetition pattern may be different for each piece of equipment. A block diagram is shown in Fig. 14-12.

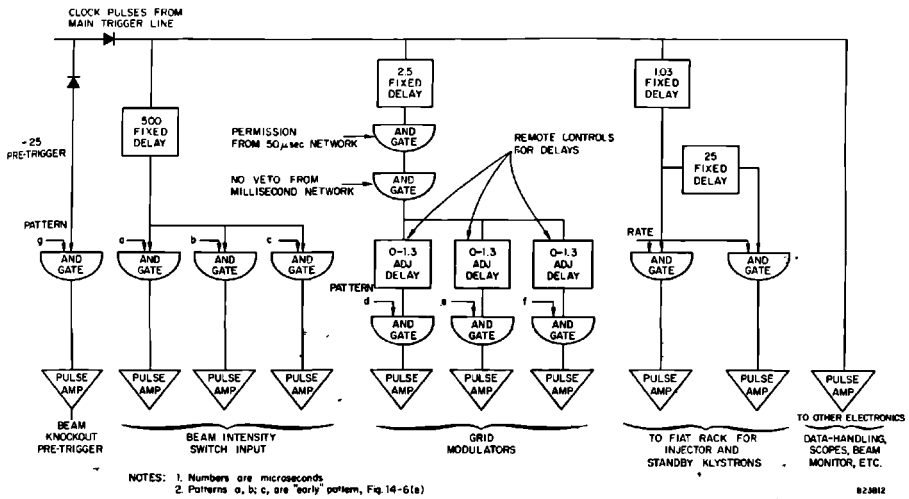

Figure 14-12 Block diagram of injector trigger generator.

The pulse intensity control requires special pretriggering. The injector trigger generator, therefore, requires a set of special pretrigger channels differing from the types found in the sector trigger generator.

The intensity control requires a trigger signal 2.3 msec before a new level is required. There are provisions for three levels, which may be called for in any sequence.

The previous clock pulse is fed through a delay line. The output of the delay line is gated by an "early" pattern signal to trigger the intensity control switch for the next pulse.

The injector modulator has three separate grid pulse modulators which allow selection of three different pulse lengths (see Chapter 8). This selection is independent of the selection of beam current. The circuit requires an input pulse of approximately 3.0 μsec duration, instead of the standard 400 nsec. Each channel has a separate, remotely controlled, delay adjustment from 2.5 to 3.8 μsec. The minimum delay within the grid modulator is 0.5 μsec. The leading edge of the grid pulse is, therefore, adjustable from 3.0 to 4.3 μ sec after the clock. The trigger system is designed to use a nominal leading edge of the beam pulse 4.0 μsec after the clock. The earlier triggering allows for one variety of beam loading compensation. All three grid pulses are shut off by the millisecond network of the machine protection system and are gated by the output of the 50-μsec network of the machine protection system.

The beam knockout system requires a 25 μsec pretrigger gated by a pulse pattern signal. Many other pieces of electronic equipment require standard clock pulses. These trigger channels are handled in the same manner as in the sector trigger generator.

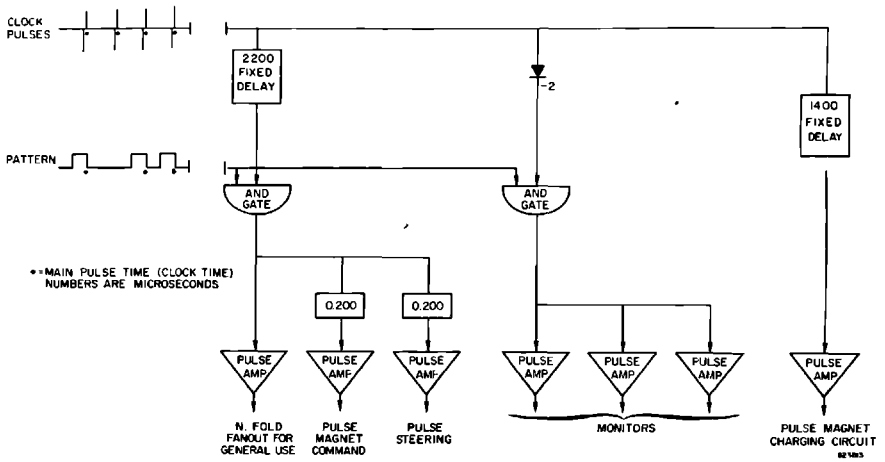

Figure 14-13 Block diagram of trigger channels for beam A (a portion of the switchyard trigger generator).

SWITCHYARD TRIGGER GENERATOR. The switchyard trigger generator must provide sets of timing pulses for equipment associated with each of several beams. Some equipment is pulsed only for one beam or another. In general, the pulse repetition pattern may be different for each piece of equipment. A block diagram of that portion of the switchyard trigger generator devoted to the A-beam is shown in Fig. 14-13.

The pulse magnets require special pretriggering. The switchyard trigger generator, therefore, has a set of special pretrigger channels differing from the types found in the sector trigger generator.

The previous clock pulse is fed through two delay lines. The output of the first delay line occurs at -1400 μsec to recharge the storage capacitors in the magnet modulators. The output of the second line is gated by the appropriate pattern signal and yields a 500-μsec pretrigger to trigger the pulse magnet modulator for the next pulse.

Many other pieces of electronic equipment require 25-μsec pretrigger or standard clock pulses. These trigger channels are handled in the same manner as in the sector trigger generator.

Pattern generator (KWH)

The pattern generator subsystem in CCR enables the operator to produce separate pulse patterns for as many as six interlaced beams of different repetition rates, energies, and destinations, and to transmit each pulse to appropriate points along the accelerator (injector, sectors, beam switchyard, end stations, etc).

The pattern generator consists of four principal components, performing four principal functions (Fig. 14-14):

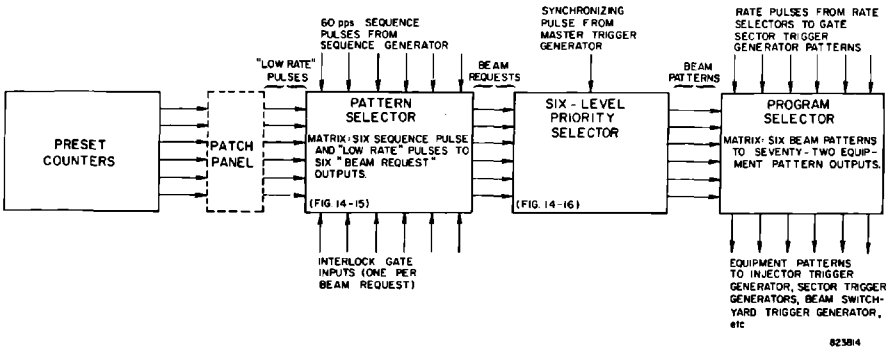

Figure 14-14 Block diagram of pattern generator subsystem.

1. A pattern selector which enables the operator to distribute any or all of the six sequence pulses to any or all of six "beam lines."
2. A set of counters to provide submultiples of 60 pulses/sec and to create pulse sequences of arbitrary complexity.
3. A priority selector which enables a priority (1–6) to be assigned to each beam line, so that whenever there are time-coincident pulses on two or more beam lines, only the one of highest relative priority is permitted to pass and all others are blocked.
4. A program selector which enables the pulses on each beam line to be transmitted to the desired points along the accelerator.

Suppose that the three interlaced beams given in the example under Section 14-1, entitled "Programming for Multiple Beams," are required, i.e., beam A—all available pulses, high energy (all thirty sectors), beam B—60 pulses/sec, medium energy (fifteen sectors), and null beam—60 pulses/sec. These requirements can be achieved by the settings shown in Table 14-1.

Since beam B and the "null beam" use different sequence pulses, none of their pulses coincide, and their relative priorities are immaterial. This is not true for beam A. On beam line 1, the priority selector passes only sequence pulses 3, 4, 5, and 6, yielding an irregular pulse pattern of 240 pulses/sec (Fig. 14-2c).

It is not necessary to use the first fifteen sectors for beam B. Any combination of sectors could be used, but it is generally easier to focus and steer a

Table 14-1

Beam	*Beam line*	*Pattern selector (sequence pulses)*	*Priority selector (priority)*	*Program selector (sectors)*
A	1	1, 2, 3, 4, 5, 6	3	1–30
B	2	2	2 or 1	1–15
Null	3	1	1 or 2	None

high-energy beam than a lower-energy beam, and it is customary to bring each beam pulse up to its final energy in the earliest available sectors.

In two sectors (27 and 28) near CCR, however, the sector trigger generators have been modified, and programming switches are provided in CCR for creating independent patterns for each of the sixteen klystrons, thus enabling beam energies to be adjusted in smaller increments than can be done by programming entire sectors.

Normally only two or at most three beams are in operation at a time. The ability to program as many as six beams facilitates switching back and forth as required between two beams of different energies or repetition rates destined to the same target. Provisions have been made for easily increasing the number of beam lines and priority levels if and when required.

Each of the three principal pattern generator units also performs certain other functions.

A functional logic diagram of the pattern selector is shown in Fig. 14-15. A 6 × 7 array of toggle switches allows synthesis of six beam request signals. A "high" rate may be created from the six 60-pulses/sec inputs from the sequence generator or a "low" rate from the counter–frequency dividers may be selected, for each beam request. The pattern selector also contains an interlock relay in each beam line by which each beam can be disabled from a number of remote points such as the beam switchyard and end stations. The

Figure 14-15 Functional logic diagram of pattern selector. A 6 × 7 array of toggle switches allows synthesis of six beam requests from six 60-pulses/sec inputs or from the counter inputs.

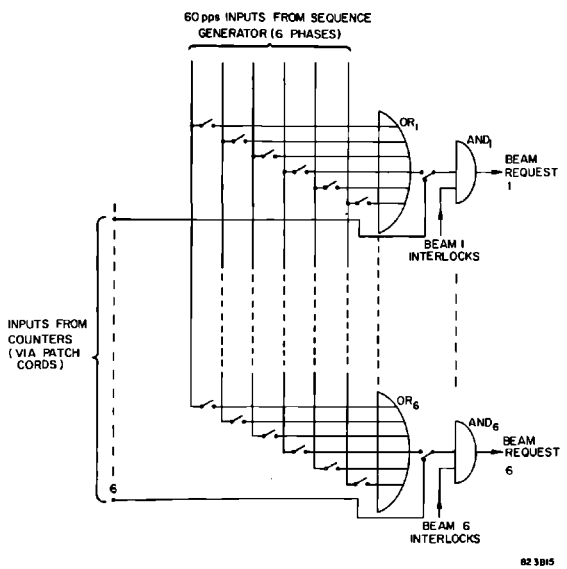

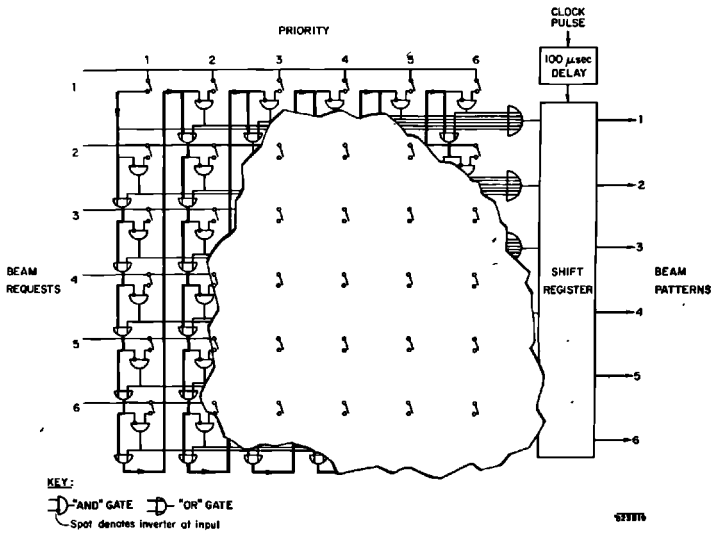

Figure 14-16 Simplified logic diagram of priority selector. The "veto circuit" (heavy line) insures that any output pattern cancels every lower-priority request. The shift register changes the output pattern immediately after a beam pulse and prevents scrambling of patterns when toggle switches are changed.

relay prevents the pattern selector from transmitting any pulses for a desired beam until all such remote points indicate permissible conditions of personnel and machine safety and experimental readiness for that particular beam. Alternatively, once the beam is operating, it can be turned off within one pulse period from any of these remote points in case of an emergency.

The operation of the priority selector is illustrated in Fig. 14-16 (the actual mechanization is somewhat more complex). A "veto" circuit (heavy line) insures that any output pattern inhibits any simultaneous lower-priority request. Thus, in case of time-coincident requests on two or more beam lines, the priority network blocks all such pulses but the one of highest relative priority. If the output of the priority network were used directly for the beam patterns, the patterns would change at some arbitrary time between beam pulses when a toggle in the pattern selector or the priority selector is changed. If the patterns changed after the pulsed magnets in the switchyard were triggered but before the klystrons were triggered, the resultant scrambled beam pulse could cause trouble. Immediately after each beam pulse, the output of the priority network is loaded into a shift register, which then cannot be changed until after the next beam pulse. The effect of this register is to make the actual beam patterns 1/360 sec later than the corresponding requests.

The program selector has a 6 × 72 array of toggle switches in a circuit similar to the pattern selector to allow synthesis of equipment patterns from the six beam patterns. An additional array of switches at the operator's

console allows creation of individual patterns for the sixteen klystrons of Sectors 27 and 28. The equipment patterns are chopped at 360 pulses/sec to allow ac-coupled transmission to the trigger generators. The normal chopper output produces the standard pattern of Fig. 14-6b; an inverted chopper signal can be used to produce the early pattern of Fig. 14-6e. The patterns for the klystrons are also gated by the appropriate signal from the rate selector, to provide the klystron pattern of Fig. 14-6d, thus providing protection against inadvertently applying accelerated pulses to the klystrons at higher repetition rates than those of the respective standby pulses from the rate selectors. Since they are changed very infrequently, the chopping and gating at each program selector output are not determined by switch settings but by jumper connections inside the selector.

Subsidiary components include a six-channel counter–frequency divider, whose counting cycle lengths are easily and independently adjustable. The channels may be interconnected with one another and with the pattern selector through an associated patch panel, for numerous special purposes.

Operated as frequency dividers, they may be used to produce any desired submultiples of any of the six sequence pulse trains.

Operated as counters, they may be used to produce aperiodic pulse trains of different lengths for timing sequences of events that must occur during a relatively long pulse period. For example, the starting times of a wand target and bubble chamber and the starting time and duration of a quiet (null beam) period can be adjusted independently with respect to the occurrence of a low-frequency positron beam.

References

1 Counting Note, File No. CC2-1 in "Radiation Laboratory Counting Handbook," Rept. No. UCRL 3307 (Rev.), Lawrence Radiation Laboratory, University of California, Berkeley, California (1959).

2 A. Barna, "Sector Takeoff Transformer for the 2-Mile Accelerator," Technical Note No. SLAC-TN-64-69, Stanford Linear Accelerator Center, Stanford University, Stanford, California (Aug. 1964).

INSTRUMENTATION AND CONTROL

K. E. Breymayer, K. F. Crook, E. V. Farinholt, Z. D. Farkas, L. Genova, H. A. Hogg, R. S. Larsen, M. J. Lee, K. B. Mallory, Editor, and D. D. Reagan

Early in the history of SLAC, it was decided that the injector, the alignment system, and the beam switchyard should be developed as independent units. As a result, they are but weakly integrated with the instrumentation and control systems for the rest of the machine. They are discussed in detail in other chapters.

Instrumentation and control (I & C) includes the trigger and protection systems, which extend over the whole machine and are described in Chapters 14 and 21. It also includes a number of other systems extending from the injector to Sector 30. These systems, covered in this chapter, are data handling, central control, beam monitoring, guidance, and analysis systems, and local control and protection for klystrons and modulators. I & C also includes coordination of the multitude of interfaces between these systems and the injector, alignment system, phasing system, beam switchyard (BSY), water, power, and vacuum systems, discussed in other chapters.

15-1 Criteria and requirements

General criteria (KBM)

The control system for the SLAC accelerator was largely shaped by two sets of criteria, one physical and one operational. The primary physical criteria are the 25-ft shielding requirement between the accelerator and maintenance people during operation, the 2-mile length of the machine, and the presence of a large number of noise sources such as the high-power modulators. The principal operational criteria are the requirement for multiple beams and the

need to centralize enough controls so that one person, possibly assisted by a computer, can operate the machine.

The accelerator housing is buried under 25 ft of shielding and is inaccessible while the machine is operating. Therefore, to the greatest extent possible, all equipment requiring maintenance (certainly all electronics) must be located in the gallery above. The gallery cannot be full of technicians; therefore, equipment must run unattended for long periods. The equipment must be self-protecting, self-resetting where feasible, and should give remote alarms calling for help when required. A large number of status monitoring signals is required to alert the operator to the existence of trouble and to indicate at least the first step toward repair.

The number of signals is so large and the distances are so great that multiplexing becomes an attractive method for handling both control and status monitoring signals. The signals transmitted to central control must pass along the gallery, filled with high-power modulators. The transmission system must have a high immunity to radiofrequency interference (RFI) and, considering the distances involved, to cross-talk. Coaxial cables or individually shielded pairs are extravagant; twisted pairs, with balanced circuits where practical, were chosen for transmitting all but video signals. Voice communications and "high-level" signals, greater than 10-V peak, are transmitted in separate cables from the low-level signals. In general, circuit impedances are low, 1000 ohms or less. Both in monitor and control circuits, relays are preferred to solid-state circuits, when suitable, not only because of lower cost but also for their greater tolerance to momentary overloads.

Multiple beam operation of the accelerator yields beams of different currents and energies, interlaced in some complicated pattern. An adequate beam monitoring system must do better than averaging the characteristics of all beams; it must measure the characteristics of each beam independently. This is accomplished by measuring the parameters (current and position profiles along the accelerator) of each beam pulse and by arranging the display so that each beam may be examined independently.

CENTRAL CONTROL. Central control contains controls and displays for all thirty sectors, trigger programming equipment, radiation monitor readouts, and display and control panels for specialized equipment such as the master trigger generators, the master oscillator and main booster, and water-cooling towers. The operations console contains injection controls, beam monitoring displays, beam guidance controls, a panel which can be switched to display status and analog signals and to operate controls in any one sector at a time, and summary indications to alert the operator as to which sector is likely to contain the source of trouble when he cannot obtain a beam.

DATA ASSEMBLY BUILDING. The control room in the Data Assembly Building operates the switchyard magnets, monitors all interlocks in the switchyard, and has complete information about the beam from the end of the accelerator

through the beam switchyard and target areas to the ultimate beam dump. It is manned continuously during operation. It is described in detail in Chapter 19.

LOCAL CONTROL AREAS. In general, complete local control and monitoring exists for ease of maintenance of all equipment. Only those operational adjustments which are expected to require attention from day to day are duplicated in central control.

The alignment system is controlled from the alignment observation room at the end of the accelerator housing behind the injector. The wiring for this system is separate from the controls for the rest of the accelerator. Alignment is, in principle, an off-line process; there is no need for central control to be involved.

A complete console for operation of the injector, 40 ft of accelerator, and the first beam-analyzing station (BAS 1) is located in the injector area. For the first 2 months of operation, the injector console was manned. Since that time, the injector has been operated satisfactorily from central control, and the injector console has been visited only at the beginning and end of shutdown periods of a weekend or more.

An I & C alcove in each sector serves as a data assembly point for all signals to and from central control. Local interlock logic and automatic control equipment are also located in the alcove. All signals to and from central control can be monitored and tested, and it is possible to operate the entire sector from the alcove. Initial tests of the accelerator were made using the injector, Sectors 1 and 2, and a temporary beam-analyzing station located at the beginning of Sector 3. The Sector 2 I & C alcove served as temporary "central control" for these tests.

The I & C alcove in Sector 11 has been fitted with a console for control of the positron source and of special beam guidance equipment in the next four sectors. Once some operational experience has been gained, the necessary signals will be transmitted to central control; the Sector 11 console will thereafter, like the injector console, be manned only for troubleshooting during major shutdown.

Analysis of control requirements (KEB)

The signals required for beam operation were determined after an extensive study of the anticipated operational and control problems of the accelerator. The development of basic concepts will be outlined briefly, in order to explain the selection of particular signals. The study was not restricted to the accelerator control problems alone but included consideration of relations with all other areas which might affect the layout of the control system. Such areas were the experimental physics work, maintenance, data collection of component performance, and others. These interrelationships had to be understood so that the control system could meet their demands.

It was natural that operational experience with the Stanford Mark III accelerator should be used as a guide in these initial studies.

OPERATIONAL CONCEPTS. The guidelines given for the development of the control system stated that beam operation was planned to be continuous with infrequent scheduled shutdowns and that all operational controls for the accelerator should be directed from one place, known as the Central Control Room (CCR). Local operations were to be on a temporary basis only.

The concept of continuous beam operation required that maintenance and repair of critical components (mostly electronic) be possible while the beam was on. As a consequence, such equipment was not to be installed in high-radiation areas which would not be accessible during operation. In the klystron area, the radiation level was to be kept low enough so that maintenance personnel could be present during operation.

A further consequence of these concepts was the specification that all equipment contributing to beam operation should operate unattended and with proper self-protecting features. However, the idea of continuous unattended operation was not inconsistent with the assumption that such equipment would initially be started up and adjusted locally.

The close relationships between operating a beam and performing maintenance and repair on components along the machine made it necessary to postulate a "maintenance" center in the control room, so that these activities could be coordinated most efficiently.

With the development of these concepts, ideas on the communication system between the CCR and the accelerator equipment began to take shape. After a detailed study of the cost involved in transmitting data from the accelerator to CCR, it was decided to divide the accelerator into thirty sectors, each 333 ft long. In each sector, data would be collected at the I & C alcove and transmitted to CCR. The sector concept was applied to the main injector, which became known as Sector 0, and also to the beam switchyard. Initially, the concept included means for local operation. This idea was dropped later when the control requirements were understood better. Although the I & C alcove is primarily a data collection point, it provides a full display of sector status signals and allows access to analog and control signals for analyzing the system performance.

BEAM CONTROL CONCEPTS. Major factors in beam operation include energy control, phase control, and beam guidance. Some fundamental decisions had to be made regarding the methods and layout of these controls. Regarding energy control, it was decided that a variable voltage substation (VVS) with a circuit breaker on the secondary should be placed in every second sector, with the ac output distributed to the modulators in the two sectors. This scheme provides continuous energy control over the operating range of the klystrons.

The basic concept also provides for control over the energy contribution of a single klystron. This is achieved by the use of two trigger signals at each

modulator. The first, or "accelerate," trigger operates the modulator so that the klystron RF output contributes to the beam energy. The second, or "standby," trigger is sufficiently delayed so that the klystron RF pulse does not contribute to beam energy. The RF energy in a standby pulse is entirely dissipated in the disk-loaded waveguide and its termination. It serves to maintain the waveguide temperature and the VVS load and is also used for phasing and maintenance purposes.

With respect to phasing, it was recognized that individual, remote phase-control of each klystron using energy maximization as the phasing criterion was unworkable. An automatic phasing system was conceived that could phase the klystron with respect to the electron bunches in the beam. The formalization of this system was strongly influenced by requirements of the centralized control system. The phasing system is described in Chapter 12.

Beam guidance did not offer any particular problems with regard to centralized control. It had straightforward sector-by-sector control and dc analog requirements. The beam monitoring problem, however, was more complex. It had to provide beam position and intensity information per sector with simultaneous display at CCR. The system finally adopted provides for two types of signals from each sector. One signal contains the logarithm of the beam pulse charge Q together with the horizontal and vertical displacements of the beam. The other contains a signal linearly proportional to the charge of the pulse. Both signals have bandwidth small enough to be transmitted to CCR on a normal telephone-type wire pair. The information from all sectors is displayed on four scopes: one each for horizontal (X) displacement, vertical (Y) displacement, log Q, and linear Q.

The necessity of keeping variations of the principal operating parameters within permissible limits was also recognized. Analysis of the effect of klystron beam voltage variations led to the requirement for individual de-Q'ing circuits in each modulator so that the necessary pulse-to-pulse amplitude stability could be achieved. These circuits are described in Chapter 13.

The temperatures of the disk-loaded waveguide and waveguide drive line systems are kept within acceptable limits by automatic control of the cooling-water temperature. The cooling-water system is described in Chapter 24.

INTERLOCKS. All equipment subsystems along the accelerator were examined for susceptibility to damage caused by failure or malfunction of other subsystems. This work resulted in the specification of protection systems. Examples are the machine protection system (MPS) and the modulator–klystron package (M–K package). The MPS shuts off the beam to protect components in the beam line, such as accidentally closed vacuum valves, and to protect beam scrapers or the disk-loaded waveguide against severe mis-steering of the beam is case of a degaussing power supply failure. The beam switchyard is protected from beam energy changes which fall outside the acceptance band. Such changes in energy result from failures of equipment controlling the energy contributions of eight or more klystrons. The MPS, thus, monitors the operation

of the vacuum system, cooling-water systems, RF drive system, and the ac voltage system and shuts off the beam when system components are endangered. The M–K package is described below. The MPS is described in Chapter 21.

The personnel protection system (PPS), like the MPS, extends over the whole accelerator. Its requirements state simply that access to the housing shall be possible only when all variable voltage substations and the injector are off, i.e., there is no RF power and no beam. The system has strong ties with the control system. The PPS is also described in Chapter 21.

CRITERIA FOR THE SIGNAL SELECTION. The development of the equipment layout in the accelerator and of the basic control concepts for establishing a beam resulted in a number of well-defined subsystems with specified performance and protection features. The actual selection of the signals used in operating the accelerator from CCR was based on this layout. The large number of signals involved and the cost of obtaining, transmitting, and displaying them made it mandatory to select critically and to handle only the minimum necessary for efficient operation.

The first set of signals was obtained by listing the basic operational steps to obtain a beam. This analysis selected the control and analog signals necessary to obtain voltage, current, and related adjustments. These signals were supplemented by status signals which would indicate that a piece of equipment had been turned on locally and was available for operational control. The resulting set of signals was designed to permit the operator to set the essential beam parameters and to steer and monitor the beam. Any piece of equipment contributing to the beam and failing during operation could be located by sector and type via the change in its status signal. The cause of the trouble would have to be identified at the location of the equipment in question. This concept eliminated a lot of secondary information which would be of limited use at CCR.

The problem of monitoring in-tolerance operation of the various subsystems proved to be more complex. The objective was to obtain the status of the most significant characteristics at acceptable cost. This was possible for temperature-controlled systems and the master oscillator output power limits. In other cases, a sufficiently accurate analog signal was obtained, such as the frequency of the master oscillator. No easy solution appeared to be possible for the important information on klystron output pulse amplitude and phase stability. A system that could transmit all relevant information with the accuracy deemed necessary was found economically unreasonable. For this reason, a scheduled local monitoring procedure was assumed, to supplement the subsystem performance monitoring from CCR.

STANDARDIZATION OF SIGNALS. Concurrent with the evaluation of the operational signals, the means for transmitting these signals to CCR were defined. Status signals were to be transmitted via a time division multiplex system, and analog and control signals via hard wire. The I & C alcove in each sector

was planned to accommodate the necessary terminal equipment and a 24-V battery to supply power to the signal circuits.

In order to standardize the signal sources, the following arrangements were made with the designer of each piece of equipment. For status signals, a contact closure with ungrounded contacts was to be provided to indicate the proper operating state. A 1-kohm source providing a 0–5-V signal analog of the quantity to be measured or a 1-kohm potentiometer was specified for analog signals. For on-off or up-down control, a floating bipolar latching relay or two separate relays with diode steering for momentary bipolar control were required.

A different technique was adopted for the control of the dc steering power supplies. These were equipped with stepping motors controlled directly from CCR.

SIGNALS AVAILABLE AT CCR. The transmission capacity for the data flow to and from each sector was specified to provide for 100 status, 20 analog, and 24 control signals. The simultaneous display at CCR of all these signals from thirty sectors would have been rather costly. An analysis of operational needs indicated that not all of these signals had to be available simultaneously. The key to the solution was in the fact that the signals in the sectors are repetitive. It was, therefore, decided to locate all status, analog, and control signals from one sector on a panel with selector switches so that it could be connected to any of the thirty sectors. Three such panels were made available. In order to warn of changes in a sector not connected to any of these panels, two additional alarm signals were provided from each sector, i.e., 2×30 sets. One signal indicates that the beam has been shut off from a sector by the MPS; the other signal warns of an out-of-tolerance operation that needs attention. The sources of the alarms can be identified when the panel is switched to the sector so indicated.

The switched sector panel is of greatest use during initial adjustments or when the beam is off. After the beam is established, interest is focused on the subsystems that are needed for maintaining the beam, the most important being beam steering and monitoring. Speed of action requires that controls and information from such systems be available continuously.

The essential status of the klystrons in each sector and important information about the PPS are also displayed continuously.

Signals for control of the injector and the beam switchyard are all "one of a kind" and are displayed continuously on separate panels.

Signal and controls made available at CCR from the above concept proved to be adequate and useful when beam operation started. During the first 8 months of operation, energy control was accomplished only by changing the number of klystrons in use. At the end of 8 months, the only major changes were that a vernier control of energy, based on adjustment of the RF phase of pairs of klystrons, was being installed; a limited video system was being connected to allow CCR viewing of the RF pulse envelope for each klystron.

15-2 Modulator-klystron logic (KEB)

Concurrent with the formulation of the energy control concept, as applied to the 240 accelerator klystrons, an analysis was made to determine what information from the klystron modulators had to be sent to CCR to operate the machine effectively.

The particular subject of this section is the problem of the remote and local control requirements converging at each klystron and modulator and the integration of the fault protection and recycling concepts. The resulting solutions provided a control circuit for each klystron modulator, the M–K package, and a control circuit for all klystrons in one sector. The latter determines the mode of operation either of individual klystrons or of all the klystrons of the sector. It was called the "modulator trigger mode switch control logic" (MTMSCL) to the bewilderment of the uninitiated.

Before going into details of these circuits, the method used for controlling energy and evaluation of the operational information from each modulator–klystron will be described.

The basic energy control concept

VVS CONTROL. As mentioned above, a VVS is installed in every second sector, supplying the operating voltage to the klystron modulators in two sectors. In each of the fifteen sector pairs, it is necessary to remove or to add the energy contribution of individual klystrons. This arrangement defines the scope of the basic energy control. It provides for continuous VVS control over the operating range, complete disconnection of the VVS output, and individual klystron "on-off" control.

The operational concept requires that all klystron-modulator units be turned on and initial adjustments be made locally and that thereafter all controls for beam operation be exercised from central control.

Another control requirement was added, resulting from the de-Q'ing circuit which maintains the klystron pulse-to-pulse output stability within specified limits. This requirement was that the de-Q'ing level should follow the modulator operating level to keep the power dissipation in this circuit within tolerable limits.

The layout which provides for mutual tracking of the VVS output and the de-Q'ing level utilizes an adjustable dc reference source. The VVS control circuit regulates the ac output to match this reference. The same dc reference is also fed to the modulators in the two sectors and is used as the de-Q'ing reference. Small corrective adjustments for ac input and de-Q'ing level are provided at each modulator to take care of individual circuit variations and to insure uniform operation.

This control scheme was analyzed in great detail with respect to its suitability for remote operation and reliability. One point of concern was the

possibility of failure of the reference, thus removing the de-Q'ing voltage, which could cause substantial damage to the de-Q'ing circuits. In order to offset this possibility, a unit called the "monitor rectifier" was connected to each dc reference source. Its purpose is to monitor the source and to provide the necessary de-Q'ing level in case the source should fail. In order to match the established de-Q'ing level, this rectifier is fed from the actual VVS output voltage. Its output is set somewhat below the reference voltage to avoid interference with normal operating conditions. If the reference voltage source fails, the monitor rectifier thus causes the VVS to regulate its output to the lowest level.

THE INDIVIDUAL KLYSTRON CONTROL. The need to change the beam energy in each sector by an amount corresponding to the contribution of a klystron is resolved by the "accelerate–standby" concept. It simply provides accelerate and standby triggers for each modulator. With the accelerate trigger selected, the klystron RF power adds energy to an electron beam present in the accelerator waveguide. In the standby mode, the trigger is sufficiently delayed so that the RF power does not contribute to the beam energy. This concept maintains the thermal equilibrium in modulator, klystron, and attached waveguides and is fast enough to change mode of operation from pulse to pulse. It serves as a basic feature in multiple beam operation, recycling of modulators under faults, klystron phasing, and other applications.

Klystron–modulator information for Central Control Room

The selection of these signals was largely based on economic considerations. Any signal proposed was carefully analyzed with respect to the "need to know," the cost of obtaining, transmitting, and displaying it at CCR. It was recognized that, for operation, it is sufficient to know that the modulator–klystron is "on" or "off" and, when on, that it is operating within specification. The on-off requirement is fully satisfied by three status signals from each unit.

The three status signals selected from each klystron-modulator unit have the following information content:

1. "Modulator available" (Mod available) indicates that the local startup is completed, all interlocks are closed, and filaments are turned on. The unit is ready for operational control from CCR, such as turning on and setting the klystron voltage and applying the trigger. When this signal changes state, it indicates that the respective unit is not available for operational control. This can be due to a fault that shut off the modulator or because maintenance work is being performed on the modulator. Details of faults are not given to CCR and have to be identified from the information at the unit.

2. When the klystron voltage is set, the trigger can be applied to the units in a sector. When this is done, the average klystron current is monitored and a signal "modulator on" (Mod on) is transmitted to CCR from each unit. This signal was selected to confirm that the modulator trigger has become effective, because the generation of RF output power is delayed until an attenuator in the drive input is removed, which takes several seconds and serves to protect the klystron output window.
3. The final signal selected reads "RF OK" and indicates the attenuator is fully removed and that a preset value of RF output power has been exceeded. The unit is now fully operational; it can be operated in the accelerate or standby mode as defined previously. With the set of signals, "Mod available, Mod on, RF OK," the essential operating states of the klystron-modulator unit can be identified from CCR.

Proper performance can be monitored best by looking at the RF output waveform of the klystron. A system that could transmit to CCR all the pulse information considered necessary was at first found to be too costly. For the same reason, the idea of monitoring the RF signal locally and transmitting a status signal about its shape could not be realized. In order to get the necessary information to CCR, the concept of local turn-on and tune-up was extended to include scheduled monitoring. This monitoring routine was to be an integral part of operation.

Modulator–klystron protection (M–K logic)

The operational requirements of the klystrons and modulators involve local start-up and initial adjustments, local monitoring of performance and fault diagnostics, self-protection, accelerate–standby control, and derivation of three status signals from each unit.

A special rack was added at each modulator–klystron to accommodate the equipment resulting from these requirements, such as klystron output monitoring, drive-line controls, vacuum gauge power supplies, and fault protection. The specifications for these items were determined by the need to integrate the operational and fault protection requirements of the klystron. The two key items were the M–K logic and the accelerate–standby mode control.

The major development was focused on the protection of the pulse transformer, the klystron proper, and its waveguide window. Experience has shown that klystron window life can be prolonged when the RF output is gradually increased during start-up, which can be achieved by slowly removing a protection attenuator in the input drive line. Furthermore, unfavorable operating conditions on the load side of the window should be avoided, such as poor vacuum or reflected energy due to arcing in the waveguide.

For klystron protection, safety limits were set for the beam voltage measured at the cathode and the current into the pulse transformer.

The criteria for the operation of the protection attenuator specify that full attenuation shall become effective every time the klystron RF output

disappears for more than a few seconds. Removal of attenuation is initiated when RF drive power exists at the klystron input and the modulator has started pulsing the klystron.

Modulator operation, in turn, is interlocked with the protection requirements for the klystron. When these conditions are met, modulator–klystron operation may start and the attenuator is removed. If, during operation, any of the interlocks in the modulator open, pulsing stops, and the drive input power is attenuated.

The protection concept discontinues operation temporarily in case of a fault and resumes operation automatically when safe operational conditions for the klystron are restored. Some fault conditions in the modulator are handled by this fault protection cycle.

When a preset number of such faults is exceeded in a given time interval, modulator operation is discontinued. Such an event is indicated to CCR by the "modulator not available" signal. Fault tracing and restarting has to be done locally.

The signals monitoring the safe operation of the klystron act upon a switch controlling the trigger to the modulator. The sequence of operations in this trigger control and the signals acting are as follows: Fault signals from the klystron, i.e., reflected energy, overvoltage, and overcurrent, are compared with a preset threshold signal. When this threshold is exceeded, they act on a gate in the trigger circuit and shut off the trigger. This condition is held for about 1 sec, and the gate is opened again. The trigger can enter the modulator and, if the fault has cleared in the meantime, operation will continue; otherwise, the first klystron pulse will generate a new fault input and again remove the trigger.

The reflected energy fault indication may be followed by an unsatisfactory vacuum condition on the load side of the window. This latter signal will withhold the trigger in a relay circuit until the vacuum improves above a preset value; operation then resumes automatically. A vacuum gauge failure, however, will hold this relay circuit open until the gauge is replaced.

Any of the above fast or slow interlocks will advance the fault counter in the modulator.

The two signals acting in the attenuator control circuit are the "RF drive" and "modulator on" signals. The first is established at the output of the sector drive sub-booster, the second is derived at each modulator. When either one or both signals disappear, attenuation is applied in the drive line. The relay indicating the "modulator on" condition in the attenuator motor control circuit has a delay circuit which keeps it energized for about 2 sec after the "modulator on" signal is removed.

Klystron operation can, therefore, be resumed immediately when fast-acting fault inputs clear within the 1-sec time interval when the trigger is removed. When the fault is repeated at the next pulse or a slow input removes the trigger, the delay time expires and the attenuator is dropped in. Removal of the attenuator prolongs the restarting by about 10 sec.

The above arrangement has proved very successful in coping with fault situations that can be cleared by temporarily suspending operation of klystron or modulator.

Modulator trigger mode switch control logic

Several criteria are involved in defining when a klystron shall operate in the accelerate or standby mode. The latter mode always applies when a klystron is off and during the turn-on period until the attenuator is fully out, since the RF output pulse of the klystron displays substantial phase variations during this period.

When the attenuator is out, the RF pulse is fully established and either mode can then be selected, depending on the operational objectives. For example, the standby mode must be used while the phasing system samples the beam-induced voltage in the accelerator and the phase of the RF wave. Beam energy adjustments can be made by selecting the appropriate mode. It is also possible to place all klystrons into the accelerate state simultaneously, subject only to the phasing needs.

The mode control is achieved by selecting in the sector trigger generator the accelerate or standby trigger for the modulator in question. One mode control relay is provided for each modulator. These relays are controlled from inputs at the local level and from CCR. All control, monitoring, and logic functions are performed by relays. They are assembled in a special unit (MTMSCL) located in the I & C alcove of each sector. In addition, they provide status input to the transmission system to central control.

The operating state of each modulator is monitored from its status signals. The operating state of the klystron determines when the mode switch can be set to accelerate. This is permitted when the RF OK signal exists, and the operating voltage for the mode relay is made available. The phasing system has standby control only; it cannot set to accelerate. It cancels, however, any individual accelerate control from CCR. The CCR also has standby control. The "all-accelerate" control is common to all modulators in one sector. The phasing system can override this control in order to set a klystron being phased to standby, but the klystron immediately returns to accelerate when phasing is completed.

15-3 Beam monitoring system

An important problem with the SLAC accelerator is to determine accurately the transverse position of the beam within the accelerating structure. Moreover, since multiple beams of widely different charge will be used, it is essential to be able to observe the position of each beam independently.

Sensors are in use which produce video output signals proportional to the horizontal and vertical position coordinates of the beam measured from the

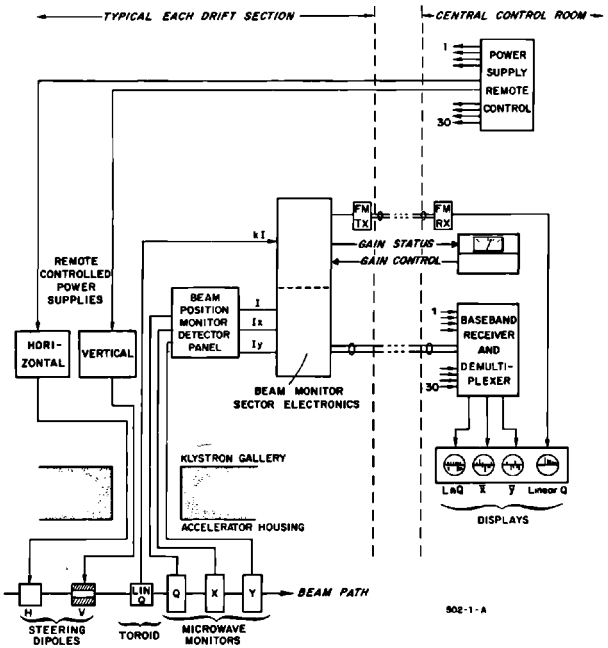

Figure 15-1 Block diagram of beam monitor system.

central axis. In the two-mile SLAC accelerator, however, the transmission of large numbers of such wide-band signals to the control room would be difficult and costly. The approach taken here has been rather to develop a system in which video pulses are processed locally, i.e., at the drift section at the end of each 330-ft sector, to obtain high-level average position signals suitable for transmission over a hard-wire telemetry link.

Figure 15-1 illustrates the main components of the beam monitoring system located at a drift section in the SLAC accelerator, and the connections to the CCR. Three microwave resonant cavities provide RF outputs which are functions of beam intensity (I), intensity times horizontal displacement from the accelerator central axis (Ix), and intensity times vertical displacement (Iy). These are fed to microwave detector circuitry which produces video outputs directly proportional to I, Ix, and Iy. These signals are processed by the beam monitor sector electronics unit to give ln Q, x, and y in a serial form, where Q is the total charge in the pulse. This signal is sent by a baseband telemetry system to a demultiplexer at the CCR, together with similar signals from the remaining twenty-nine sectors.

The demultiplexer first samples each of the thirty signals and channels ln Q, x, and y into three separate oscilloscope displays. A remote control system allows the operator to adjust the steering dipole currents at any sector while monitoring the resulting beam position displacements for the entire machine.

More accurate charge monitoring is accomplished by means of a ferrite toroid through which the beam passes. After processing in the beam monitor sector electronics panel, a signal proportional to total charge in a pulse is sent from each sector to central control by means of a FM transmission system using one wire pair in a fifty-pair telephone cable. At central control, the accurate charge signal from each sector is demodulated, fed to a multiplexer along with similar signals from other sectors, and finally presented on an oscilloscope.

Beam monitoring sensors (HAH, EVF, ZDF)

MICROWAVE SENSORS. Initial SLAC requirements called for two designs of beam position monitors. The first was to have an aperture not smaller than the accelerator structure. Monitors of this design were to be installed principally in the drift sections at the end of each of the thirty sectors of the linear machine and to be capable of detecting 0.020-in. horizontal and vertical beam deviations with respect to the machine axis, for beam pulse currents in the range of 1 to 300 mA. A second design was required for position monitors to be installed in the beam switchyard. Performance requirements here were similar to the first design, but the monitor aperture had to be as large as possible.

Much of the early exploratory and design work on the SLAC monitors was done by Brunet *et al.*[1] and Lee.[2] Some of the types of beam sensors

Figure 15-2 Beam position sensors.

TYPE OF MONITOR	SCHEMATIC	REMARKS	REFERENCE
SYMMETRICAL MATCHED WAVEGUIDE	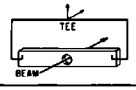	LOW SENSITIVITY. DIFFICULT TO CALIBRATE.	15-1
RESONANT WAVEGUIDE RING	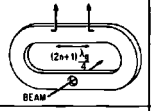	GOOD SENSITIVITY. CUMBERSOME STRUCTURE.	15-1
SHORTED WAVEGUIDE	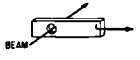	LOW SENSITIVITY. REQUIRES TWO SENSORS PER COORDINATE.	15-1
TM_{120} CAVITY	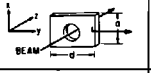	GOOD SENSITIVITY. ZERO OUTPUT WHEN BEAM CENTERED. SMALL SIZE.	15-1
SACLAY LOOPS		VERY LOW SENSITIVITY. COMPACT. 4 LOOPS CAN BE PLACED IN ONE SECTION.	15-3
TM_{010} CAVITIES	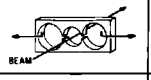	LOW SENSITIVITY. CAVITIES MUST BE EXACTLY MATCHED.	15-3
DIFFERENTIAL PULSE TRANSFORMER	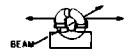	LOW SENSITIVITY.	15-4

considered are illustrated schematically in Fig. 15-2. They are discussed in the references given.[1,3,4] In spite of greater complexity and cost, microwave monitors were preferred to ferrite-cored differential pulse transformers because much higher sensitivity could be obtained with high-Q resonant cavities. Theoretical and experimental investigation led to the choice of TM_{120} resonant cavity sensors for the "in-line" monitors to be installed along the linac. It was also decided that the beam aperture in the monitor should be 0.8 in. in diameter.

The resonant waveguide ring was initially chosen for the beam switchyard monitors, but its sensitivity deteriorated rapidly as the beam aperture size was increased. It was found that the TM_{120} cavities operated well with a 2-in. diameter aperture, so these were used in the switchyard.

Each monitor assembly comprises two orthogonally mounted position cavities and one circular cavity operating in the TM_{010} mode. The output of the latter cavity is independent of beam position and is used to normalize the position cavity output signals with respect to beam current.

The most important parameters of the in-line and switchyard monitors are given in Table 15-1.

THEORY AND DESIGN: IN-LINE MONITORS. The RF-video system is shown in Fig. 15-3. Semirigid coaxial cables with low loss and good phase stability are used to transmit the RF signals from the cavities up to the detector panel in the klystron gallery. Here, the RF signals are converted to video pulses proportional to beam current I_0 and beam current times displacement ($I_0 x$ and $I_0 y$). The signs of $I_0 x$ and $I_0 y$ indicate the displacement directions. The video signals are processed in the sector electronics described below.

IN-LINE CAVITY DESIGN. The TM_{120} cavity is formed from a section of waveguide—broad dimension a, narrow dimension b. The guide is closed by shorting planes which are separated by a distance d (approximately one guide wavelength at the accelerator operating frequency). Circular apertures are placed in the centers of the broad faces to permit passage of the electron beam

Table 15-1 Parameters of in-line and beam switchyard monitors

Parameters	*In-line monitors*		*Switchyard n*	
	Reference	*Position*	*Reference*	
Sensitivity	250 mW/mA²	100 μW/mA²mm²	40 mW/mA²	4
Loaded Q	1200	600	1200	
Unloaded Q	9000	15,000	5000	
Frequency	2856 ± 0.3 MHz	2856 ± 0.6 MHz	2856 ± 0.3 MHz	2
Operating temperature	110°F	110°F	90°F	
Temperature detuning	25 kHz/°F	25 kHz/°F	25 kHz/°F	

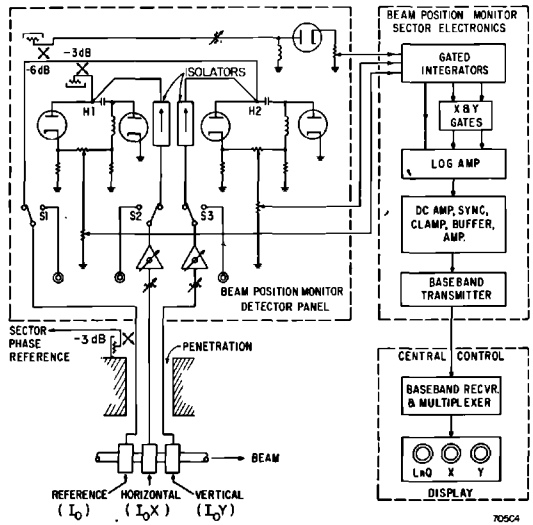

Figure 15-3 In-line beam position monitor system.

(see Figs. 15-2 and 15-4). The beam is tightly bunched at the accelerator frequency.

Power extracted from the beam is given by

$$P_b = \tfrac{1}{2}\,\mathrm{Re}\int_{-\infty}^{\infty} E_z I_{\mathrm{RF}}^{*}\,dz \tag{15-1}$$

where E_z is the peak value of the electric field along the axis of the electron beam, and I_{RF} is the peak value of the fundamental frequency component

Figure 15-4 In-line monitor cavity assembly.

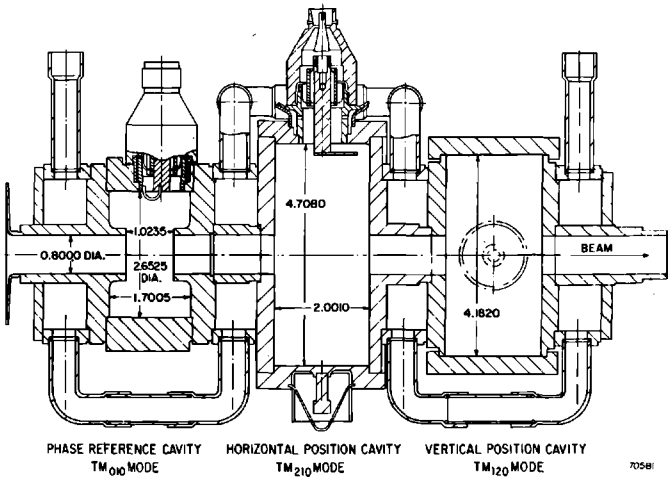

of beam current. Because E_z and I_{RF} are in phase, and I_{RF} is twice the average beam current during the pulse I_0,

$$P_b = E_z I_0 b \tag{15-2}$$

E_z is related to $E_m(y')$, the maximum electric field in the cavity for a given beam position, y', by

$$E_z = E_m(y') \sin \frac{2\pi y}{d} \tag{15-3}$$

$y' = 0$ when the beam axis coincides with the center of the waveguide apertures, and E_z changes phase by π as the beam crosses the center.

Since the power induced must equal the total dissipated power, P_b may also be expressed in terms of the loaded shunt resistance, R_L, of the cavity,

$$P_b = \frac{1}{2R_L}\left[\int_{-\infty}^{\infty} E_z\, dz\right]^2 = \frac{[E_m(y')b]^2}{2R_L} \sin^2\left(\frac{2\pi y}{d}\right) \tag{15-4}$$

so that

$$\frac{R_L}{Q_L} = \frac{E_z^2 b^2/2P_b}{2\pi f U/P_b} = \frac{[E_m(y')b]^2}{4\pi f U} \sin^2\left(\frac{2\pi y}{d}\right) \tag{15-5}$$

where Q_L is the loaded quality factor, f is the frequency, and U is the energy stored in the cavity.

Since

$$U = \frac{\varepsilon_0 abd[E_m(y')]^2}{8} \tag{15-6}$$

where ε_0 is the dielectric constant in vacuum, one obtains

$$\frac{R}{Q} = \frac{2b}{\varepsilon_0 \pi f a d} \sin^2\left(\frac{2\pi y}{d}\right) \tag{15-7}$$

The subscripts are dropped because R/Q is independent of the load. P_b must equal the sum of the power P_0 coupled out of the cavity and the power P_j lost in the cavity walls, so that

$$P_0 = \frac{P_b \beta}{1+\beta} \tag{15-8}$$

where

$$\beta = \frac{P_0}{P_j}$$

Combining Eqs. (15-2), (15-3), (15-4), (15-7), and (15-8) yields

$$P_0 = \frac{4Q_L}{\varepsilon_0 \pi f} \cdot \frac{b}{ad} \cdot \left[\frac{\beta}{1+\beta}\right] I_0^2 \sin^2\left(\frac{2\pi y}{d}\right) \tag{15-9}$$

Equation (15-9) has to be corrected for cavity detuning Δf, finite bunch

width α, electron transit time τ, and field variation across the cavity. The corrected output, P_0', is

$$P_0' = \left[\left(\frac{1}{[1 + (2Q\,\Delta f/f)]^{1/2}}\right)\left(\frac{\sin \alpha/2}{\alpha/2}\right)\left(\frac{\sin \pi f\tau}{\pi f\tau}\right)\cos\frac{\pi x}{a}\right]^2 P_0 \quad (15\text{-}10)$$

A further correction has to be applied for the field perturbation caused by the beam aperture. In the case of the in-line monitors, however, the variation in R/Q from the sine-squared distribution [Eq. (15-7)] was too small to measure.

The circular re-entrant TM_{010} cavity used for phase reference and normalization is discussed in detail by Altenmueller and Brunet.[5] The power output from the cavity is calculated in the same way as for the position cavities. One obtains

$$P_0 = 2\frac{R}{Q}Q_L\left[\frac{\beta}{1+\beta}\right]I_0^2 \quad (15\text{-}11)$$

The first three correction factors of Eq. (15-10) apply. The cavity is made re-entrant to maximize the product $[\sin(\pi f\tau)/\pi f\tau]^2 R/Q$.

IN-LINE MONITOR DETECTOR PANELS. A schematic of this unit is included in Fig. 15-3. It can be seen that the TM_{010} reference cavity signal is divided four ways—part is used as a reference for sector phase stability, part is used for current normalization, and the remainder is divided and used as phase reference in two hybrid rings. The second input arms to these hybrid rings are connected via attenuators and phase shifters to the horizontal and vertical position cavities, as shown. The output signals are detected by coaxial thermionic diodes, which have a linear detection range (index less than 1.15) large enough to monitor beam currents between 1 and 300 mA. The differential video output from a balancing network between each pair of diodes is fed to the beam monitor sector electronics panel. Each network is adjusted to give zero output when the position cavities are disconnected, and each phase shifter is adjusted to maximize the video output (and to select the desired polarity) when a signal is received from a position cavity. In this condition, each hybrid ring is insensitive to small phase changes in the input signals.

CONSTRUCTION AND INSTALLATION: IN-LINE MONITORS. Details of the three-cavity assembly are shown in Fig. 15-4. The cavities, internal drift tubes, and water jackets are constructed from OFHC copper. Stainless steel–copper–water interfaces were avoided because of electrolytic erosion. Specified tolerances on resonant frequency and assembly alignment made close dimensional tolerances unavoidable. All dimensions determining cavity size were held to ± 0.0005 in. for the reference cavities and ± 0.001 in. for the position cavities. The latter were fabricated from plates rather than being milled out of solid stock. This method was preferred for reasons of economy and avoidance of leakage "pipes" across the cavity walls. All internal cavity surfaces were machined to a 32-μin. finish. A total indicated runout up to 0.010 in. was allowed between cavity apertures in a completed assembly.

Details of the coupling probe assemblies can also be seen in Fig. 15-4. The hybrid L-coupling was used in the position cavities because it afforded a wide range of β adjustment by rotating the probe assembly, without being critically dependent upon the current contact between the probe outer conductor and the cavity wall. A conventional loop coupling proved to be more suitable for the reference cavity. The inner conductors of both probe types pass through coaxial-sleeve ceramic vacuum seals. The probe assemblies are welded to stainless steel cups brazed into the cavity walls. Conical taper sections adapt the position probes to type-N connectors and the reference probes to type-HN connectors.

Each brazed cavity was checked for Q_L and resonant frequency with standard probes before final braze assembly. Probes selected for that assembly were then inserted and rotated to give the desired Q_L. Measurements of Q were made rapidly and accurately using a swept frequency display with double side-band suppressed carrier modulation to provide frequency markers at the 3-dB points on the Q curve. The probe positions were marked and then the probes were welded in place. For final testing, the complete assembly was evacuated and water at 110°F was circulated around the cavities. The resonant frequency of each cavity was adjusted by distorting a specially weakened area of one wall (shown on the middle cavity in Fig. 15-4).

After final testing, each monitor assembly was clamped in an aluminum support bracket and attached by adjustable bolts to an accelerator drift section.

In each installation, the support bracket is aligned by optical tooling apertures with the drift section support girder, which contains a Fresnel zone plate for alignment with a laser beam. The rms misalignment between the electrical center of the position cavities and the theoretical beam axis is 0.010 in.

BEAM SWITCHYARD MONITORS. Beam position monitors are located at six places in the switchyard. Microwave signals from each cavity assembly are transmitted via semirigid coaxial cables to a detector chassis mounted nearby and shielded from direct radiation. Polystyrene dielectric is used in the coaxial cables and as much as possible elsewhere in each installation, to minimize susceptibility to radiation damage. Video signals from the detector chassis are transmitted to the Data Assembly Building (DAB), where they are processed and displayed (see Fig. 15-5).

SWITCHYARD CAVITY DESIGN. The theory of operation is the same as for the in-line monitors. The 2-in. diameter beam aperture reduces the slope of E_z versus position at the center, and increases field penetration from each cavity into the connecting drift tubes. For the latter reason, drift tube lengths had to be increased to 4 in. to avoid cross-coupling.

BSY BEAM POSITION MONITOR DETECTOR CHASSIS DESIGN. This chassis is similar to the in-line detector panel discussed above, with the following exceptions: (1) the signal from the TM_{010} cavity is used only for amplitude and phase

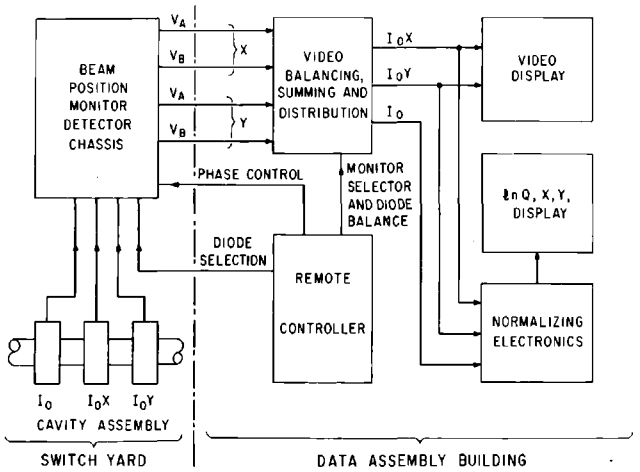

Figure 15-5 Switchyard beam position monitor system.

reference at the hybrid rings, and not separately detected for normalization; (2) the hybrid ring outputs can be remotely switched either to coaxial thermionic diode detection or to tunnel diode detectors (tunnel diodes are used for low-level detection, and are chosen primarily because their radiation resistance is better than that of other semiconductor devices); (3) the diode video outputs are transmitted directly to DAB; and (4) the phase shifters are motor-driven and remotely controlled.

Equations (15-9) and (15-11) may be rewritten, for small beam displacements,

$$P_p = K_p I_0^2 p^2 \tag{15-12}$$

and

$$P_r = K_r I_0^2 \tag{15-13}$$

where P_r is the power from the reference cavity at one input to a hybrid ring, and P_p is the power from one position cavity (either horizontal or vertical) at the second input to the hybrid ring. In this section, all K's are constants; p is the beam displacement, horizontal or vertical. The phase shifters are adjusted so that the two input signals at each hybrid ring are in phase for beam displacements up and to the right. This condition allows the signal powers at the two output ports of one hybrid ring to be written

$$P_A = \frac{P_r}{2}\left[1 + \left(\frac{P_p}{P_r}\right)^{1/2}\right]^2 = u^2(1+v)^2 \tag{15-14}$$

and

$$P_B = \frac{P_r}{2}\left[1 - \left(\frac{P_p}{P_r}\right)^{1/2}\right]^2 = u^2(1-v)^2 \tag{15-15}$$

P_A and P_B are detected by diodes of which the output voltages are given by $V_A = K_A(P_A)^{n/2}$ and $V_B = K_B(P_B)^{n'/2}$, i.e., the diodes have different conversion efficiencies and different laws of detection. Three quantities are of interest: the difference voltage $V_D = V_A - V_B$, the sum voltage $V_S = V_A + V_B$, and the normalized voltage $V_N = V_D/V_S$. Using the above equations and $K = K_B u^{n'}/K_A u^n$, one obtains for $(n-1)\,v/2 \ll 1$ and $(n'-1)\,v/2 \ll 1$,

$$V_D = K_A u^n[(1-K) + v(n + Kn')] \tag{15-16}$$

and

$$V_S = K_A u^n[(1+K) + v(n - Kn')] \tag{15-17}$$

Note that V_N formed from Eqs. (15-16) and (15-17) is a slowly varying function of K. If, however, the normalizing voltage $V_C = K_C(P_r)^{n''/2}$ is derived from a separate diode, then V_N will change much more rapidly with varying diode characteristics. If the diodes are balanced ($K = 1$) and matched ($n = n'$), then Eqs. (15-16) and (15-17) simplify to

$$V_D = 2K_A nvu^n = K_D I_0^n P \tag{15-18}$$

and

$$V_S = 2K_A u^n = K_S I_0^n \tag{15-19}$$

hence

$$V_N = K_N p \tag{15-20}$$

If the diodes are unbalanced, the position error p_e (i.e., the distance by which the beam is displaced when the monitor indicates that it is centered) is easily calculated by equating Eq. (15-16) to zero, giving $v(n + Kn') = K - 1$, or

$$p_e = \left[\frac{K-1}{n+Kn'}\right]\left[\frac{K_r}{K_p}\right]^{1/2} \tag{15-21}$$

Referring to Eqs. (15-12) and (15-13), $[K_r/K_p]^{1/2}$ is that value of p for which $P_p = P_r$ at a given current. For the switchyard monitors, $[K_r/K_p]^{1/2}$ is found to be 20 mm. Assuming both diodes are linear (the worst case), this means that the unbalance ratio must not be greater than 1.1/1 if p_e is to be kept below 1 mm.

In the switchyard, the position monitors are used primarily as beam-centering devices, so it is sufficient to display V_D on an oscilloscope. However, provision exists for forming V_S and V_N and displaying ln Q, x, and y.

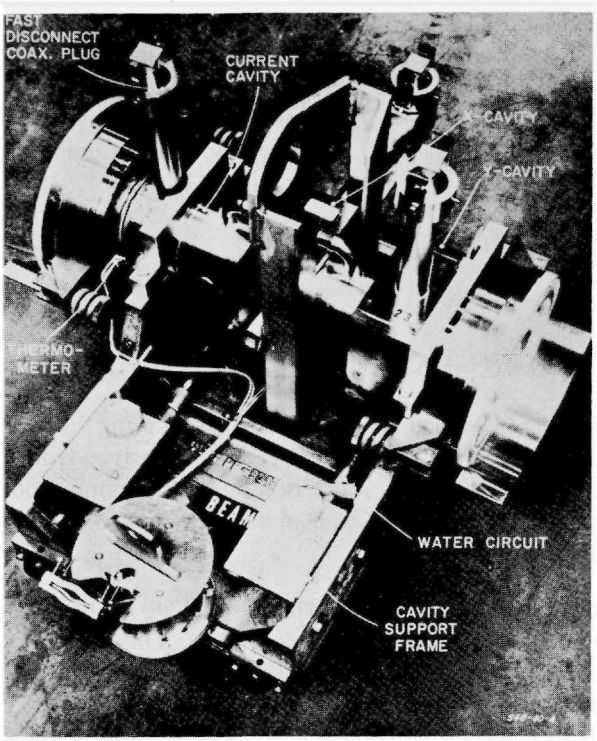

Figure 15-6 Switchyard position monitor.

CONSTRUCTION AND INSTALLATION: SWITCHYARD MONITORS. Construction of the switchyard cavities is very similar to the in-line cavities. Specially developed RF connectors and vacuum seals are used, so that the cavity assemblies can be quickly disconnected and removed by means of remote-handling tools. The support and alignment system is also modified to permit quick removal. A completed monitor is shown in Fig. 15-6.

OPERATIONAL RESULTS. The two position monitor systems described above perform in accordance with initial design concepts and are invaluable aids to establishing and maintaining electron beams through the long machine. No troubles have been experienced with the RF cavities. Some inconvenience is caused by imperfect matching of the coaxial thermionic diodes used for video detection. In Eq. (15-16), K is a function of RF power, so that even if the diode outputs are balanced at one power level, making $V_D = 0$ for $v = 0$, then K differs slightly from unity at other power levels. This gives rise to a spurious position error signal, as has been discussed. K also changes with time, as the diodes age. The problem is of no consequence in the switchyard monitors, as a remote balancing control is included in the system. However, in the in-line monitors, it has proved necessary to add a control which enables all RF

position signals to be disconnected from the hybrid rings. The CCR display then shows the zero errors for each monitor at a given time and beam current. In addition, motor-driven balancing potentiometers have been installed in each beam position monitor detector panel. The CCR control which disconnects all RF position signals also switches all control signals from the steering power supply control motors to balancing potentiometer motors. The steering controls in CCR can then be used to balance all diode pairs along the machine at a particular current. Zero errors are thus eliminated, and the operator can steer to a straight display line.

EXPERIMENTAL END-STATION MONITOR. A very large aperture, high-sensitivity monitor has been built for measuring horizontal displacements in SLAC end stations. The system is illustrated in Fig. 15-7. The beam sensor is a 3-in. diameter drift tube brazed into the broad walls of S-band waveguide. Common walls are removed to permit beam passage and electromagnetic coupling. The two beam-induced waves travel around the waveguide arms and are combined in a hybrid tee, accurately positioned so that the output signals are equal for a centered beam. The RF signals are converted to 120-MHz IF, logarithmically amplified, detected, and differentially displaced on an oscilloscope. It can be shown that the output for a displacement x is

$$V(x) = 20S \log \tan\left[\frac{2\pi x}{\lambda_g} + \frac{\pi}{4}\right]$$

where λ_g is the guide wavelength and S is the slope of the logarithmic amplifiers in volts per decibel.

The power flow in each arm of the waveguide was measured as 10 μW/mA^2. A 0.004-in. change in position of a 0.01-mA beam pulse could be detected. It is known that greater sensitivity can be achieved at the cost of electrical aperture size by introducing symmetrical reflections in the waveguide arms. This increases the slope of phase versus position near the center of the monitor.

Figure 15-7 End-station beam position monitor system.

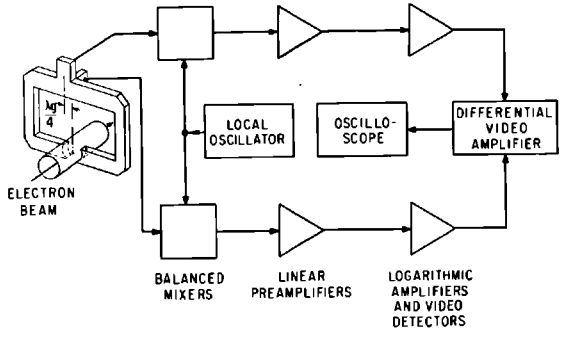

Early tests indicated a response time of 50 nsec, but a long trailing edge appeared on the position pulse after the monitor was installed in one end station. The trouble was traced to a resonance in the drift tube. It was cured on cold test by inserting a narrow ring of lossy material. The inside of the tube has been coated with lossy iron alloy, but at the time of writing the monitor has not been retested in the beam line.

Beam monitor sector electronic (RSL)

The sector electronics unit[6,7] performs two functions: (1) it processes the microwave position monitor video outputs into stretched pulses proportional to average x displacement, average y displacement, and the logarithm of charge and (2) it processes the video signal from a toroidal monitor to obtain a 1% accurate measure of beam charge. Both measurements are made at every sector on a pulse-to-pulse basis in order to operate with interlaced beams. Therefore, a measurement must be completed in less than 2.78 msec, with essentially no interference between measurements of successive pulses.

POSITION MONITORING CIRCUITS. For a pulse of instantaneous beam current $I(t)$, displacement $x(t)$ and duration T, the circuit evaluates an average position given by

$$\bar{x} = \frac{\int_0^T Ix\, dt}{\int_0^T I\, dt}$$

To simulate this equation requires separate integration of the two quantities $Ix(t)$ and $I(t)$, followed by division using a logarithmic approximation.

First, the three microwave position monitor pulses are integrated in three separate, gated, RC integrators followed by field effect transistor (FET), buffer amplifiers, to yield the quantities:

$$\int_0^T I\, dt = Q \qquad \int_0^T Ix\, dt = Q\bar{x} \qquad \int_0^T Iy\, dt = Q\bar{y}$$

The quantities are held on the integrating capacitors because of the extremely high impedance of the FET buffer and are, therefore, available for the entire interpulse period. The charges are cleared shortly before the arrival of the next beam pulse.

By appropriate gating into a logarithmic amplifier (an operational amplifier with diode feedback), the following circuit operations are performed:

$$\ln(Q + kQ\bar{x}) - \ln Q = \ln(1 + k\bar{x}) \approx k\bar{x}$$

$$\ln(Q + kQ\bar{y}) - \ln Q = \ln(1 + k\bar{y}) \approx k\bar{y}$$

where k is selected to make $k\bar{x}, k\bar{y} \ll 1$.

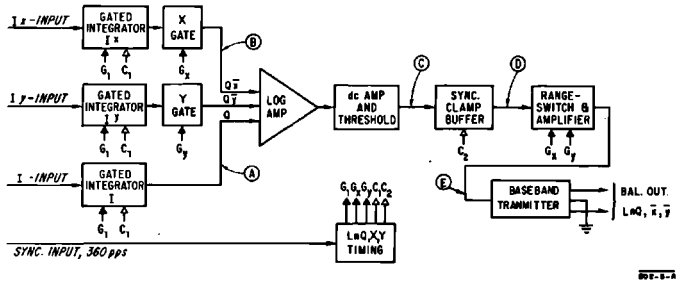

Figure 15-8 Position monitor circuits in beam monitor sector electronics.

The value of k is easily controlled in the resistive summing network feeding the logarithmic amplifier. The gating is arranged to obtain $\bar{x}$, $\bar{y}$, and ln Q serially for transmission over a single pair of wires to a demultiplexer in CCR. The basic circuit and its waveforms are shown in Figs. 15-8 and 15-9.

The system can handle a 1000:1 (60-dB) range of signals, from 100 mA 2 μsec down to 100 μA, 2μsec, or any equivalent charge. The range of position covered is ± 1 cm; the accuracy of the electronics alone is limited by offsets to ± 0.2 mm for a 1-mA, 2-μsec beam, and degrades to ± 1 or 2 mm for a 100-μA, 2-μsec beam. Additional offsets from the microwave diodes degrade the system further.

Because of the logarithmic approximation, the position signals are nonlinear at large values. Similarly, because of diode nonlinearities, the ln Q measurement is accurate only to about ± 1 dB over the 60-dB range. Complete details and error analyses are given in the references cited.

CHARGE MONITORING CIRCUITS (LINEAR Q). The basic sensor for accurate charge monitoring[7] is a 2-in. o.d. ferrite toroid, through which the beam passes. The 25-turn toroid sends an initial current of $I_b/25$ into a 95-ohm matched cable, to give an output at the receiving end which represents the instantaneous beam current vs time.

Figure 15-9 Waveforms in beam monitor sector electronics. (See Figure 15-8.)

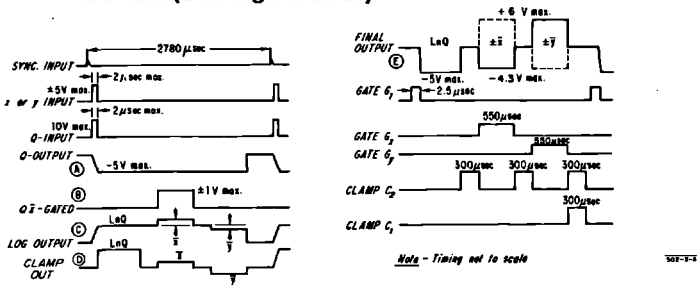

The circuit function is to derive a quantity

$$\int_0^T I\,dt = Q$$

for each beam pulse and to transmit each such signal via FM telemetry to CCR for both oscilloscope and meter display.

Circuit operation is straightforward. The toroid signal is amplified and integrated in a gated, dual *RC*, self-damping integrator. The peak output of the integrator, which is proportional to Q, is further amplified and then stretched in a sample-and-hold circuit to a full 2.2 msec. The output of the sample-and-hold drives a local FM transmitter.

Gain-switching is provided in the amplifiers, including the preamplifier, to cover a range of 54 dB in 6-dB steps. A 6-dB range of signals can be arranged to lie within the desired 2.5–5-V output range. The gains are switched by the CCR remote control system; a 0–5-V gain status signal is monitored at CCR.

At the bottom of the range, a remote-controlled switch can reverse the input polarity for monitoring positron currents.

The system is calibrated by injecting a known charge of 5×10^{-8} C into a separate 1-turn winding around the toroid. The gating, sample timing, and gain are then adjusted to give the appropriate output. The total system calibration is most easily verified on the CCR monitor in the presence of a beam, by observing the relative outputs of all units for the same nominal input charge.

Complete circuit design details are given in reference 7.

Beam monitoring, data transmission and display (KFC)

The function of the beam monitoring system is to provide the central control operator with a display of beam position and intensity as measured at the injector, each sector, and at several locations in the BSY. The major units of the system at each transmitting location are the beam monitors, the signal conditioning equipment, and the transmitters. At central control, the major units are the receivers, the display electronics, and the oscilloscope and meter displays.

REMOTE LOCATIONS. At each measuring location, beam information is obtained from two types of monitors: (1) a ferrite, toroid charge monitor for the precise determination of Q, and (2) microwave monitors for position (x and y) and intensity normalization. The pulses are conditioned to produce four analog signals on a pulse-to-pulse basis. These are (a) a signal Q proportional to the total integrated charge (linear Q), (b) a signal ln Q, proportional to the logarithm of the total integrated charge, (c) and (d) signals x and y, proportional to the horizontal and vertical displacement of the beam from the accelerator axis. The linear Q signal is transmitted as a pulse, 2250 μsec long.

The pulse is generated each time a beam pulse passes the current monitor. The transmitter is a stable voltage-controlled, FM oscillator.

The remaining three signals, ln Q, x, and y, are transmitted in serial form, as a return-to-zero, pulse-amplitude-modulated (PAM) wave train. The group of three pulses occupies 2.78 msec and is generated each time a beam pulse passes the microwave monitor.

TRANSMISSION MEDIUM. Each remote location transmits information to central control over two pairs of a 50-pair telephone cable. One pair is used for the FM transmission and the other pair is for the PAM wave train. In addition, one pair is required for remote control of the linear Q amplifier, gain switch, and another pair for analog readback of switch setting.

CENTRAL CONTROL. Signals transmitted from the remote locations are received at central control and handled as follows (see Fig. 15-10):

For linear Q channels, the carrier signal received at central control from each transmitting location is demodulated in an FM receiver. The output pulse waveform is fed to a channel multiplexer which sequentially samples all inputs once in each interpulse period. (See Fig. 15-11 for waveforms.)

The multiplexer output is a serial PAM wave train containing linear Q information from all remote locations. The output drives an oscilloscope

Figure 15-10 Beam monitoring system, CCR block diagram.

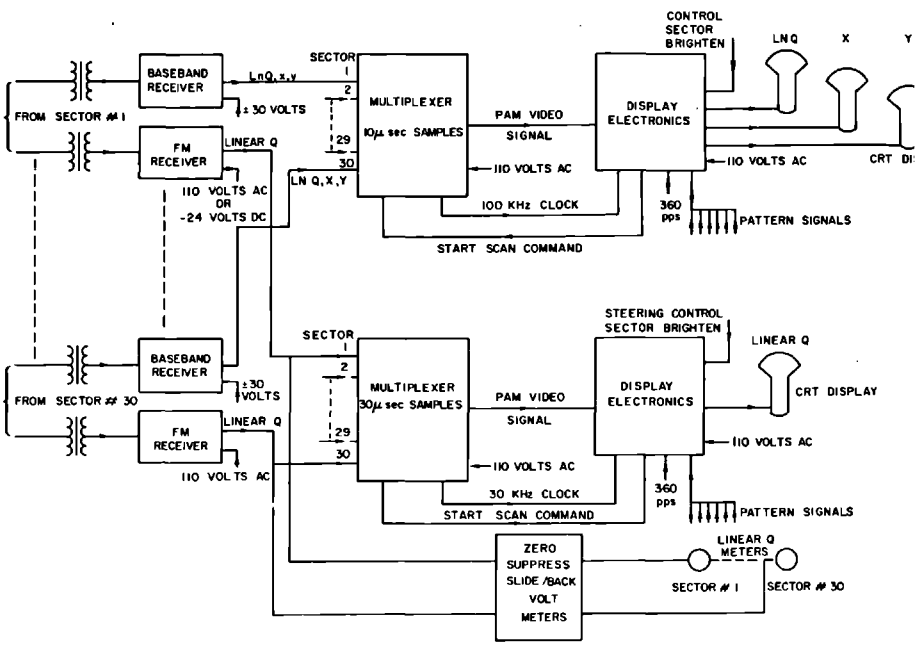

display unit which presents the linear Q signals in the form of a series of dots. The display unit provides a "scan start" signal to the multiplexer, and, in turn, receives 36 "brightening" pulses from the multiplexer.

Pattern signals from the CCR pattern generator provide appropriate gating waveforms to the display unit for trace displacement when multiple beams are being displayed.

In addition to the oscilloscope display, linear Q signals are presented on panel meters, one for each remote location. The meter inputs are not gated for selection of a specific beam when running multiple beams.

For ln Q, x, and y signals, the PAM wave train from each sector is transformer-coupled from the transmission line to a pulsed clamp which restores the dc level by clamping the waveform to ground during the interval between information pulses. (See Fig. 15-11.)

The clamped waveform is sampled by a multiplexer in a similar manner to the linear Q system except that the sampling rate is 3 times higher (approximately 100 kHz). Sequential sampling of the ln Q signals commences 150 μsec after the 360-pulses/sec master trigger pulse, and it continues for 320 μsec. The x-position signals are sampled for 320 μsec, starting 1000 μsec after the trigger pulse, and the y-position signals are sampled for 320 μsec starting 1860 μsec after the trigger pulse. Sampling is initiated by pulses generated in the display unit. Trace brightening pulses at a 100-kHz rate are supplied to the display unit by the multiplexer.

The display equipment consists of three CRT monitors, one each of ln Q, x, and y. Provision has been made for display of up to six beams by arranging the traces in different vertical positions on the screen.

Figure 15-11 Beam monitoring system, CCR waveforms.

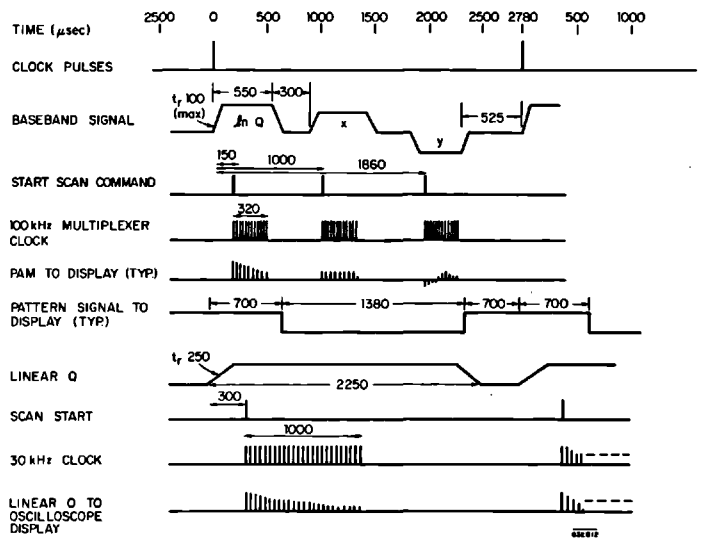

15-4 Beam guidance system (LG)

The power supplies and associated controllers required to power the steering dipole magnets, the quadrupole magnets, and the degaussing coils are mounted in the beam monitor rack in the klystron gallery at the end of each sector. This location was chosen to minimize the length of interconnecting wires to the quadrupole and steering dipole magnets which are mounted in the drift section in the accelerator housing below.

Each power supply has a controller which permits adjustment of its output current from either a local or a remote location. The local controls are mounted on the front panel of the controller. Remote control may be exercised either from the I & C alcove or from CCR, except for the degaussing power supply, which can only be controlled from a local position.

Power supplies

All the beam guidance power supplies are current-regulated, using all-silicon solid-state circuitry. The original beam guidance power supplies were custom-built and were purchased on a performance specification from one manufacturer. A more recent set of high-current quadrupole power supplies are commercially available units, procured to reduce beam breakup by increasing the quadrupole magnet focusing. The ratings of each of the five power supplies are listed in Table 15.2.

Table 15-2 Comparison of power supply ratings

Type	*Regulated output current*		*Output voltage*	*Nominal current regulation*
	Min	*Max*		
Degaussing	1 A	20 A	1.8–44 V dc	±10 mA
Steering dipole	18 mA	18 A	20 mV–20.5 V dc	±0.1% or 5 mA, whichever is greater
Quadrupole	120 mA	7 A	0.45–43.4 V dc	±7 mA
Positron quadrupole	120 mA	14 A	0.45–82.6 V dc	±14 mA
High-current quadrupole	120 mA	15 A	0–60 V dc	±35 mA

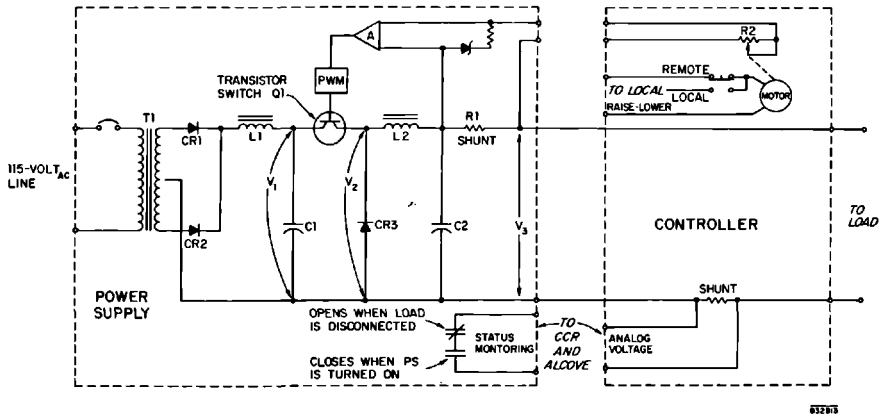

Figure 15-12 Beam guidance power supply and controller.

The degaussing, steering dipole, quadrupole, and positron quadrupole power supplies are current-regulated by pulse width modulation (PWM; see Fig. 15-12). The 115-V ac line is fed to a transformer, full-wave rectifier and *LC* filter to produce unregulated dc voltage V_1. Transistor switch $Q1$ is opened and closed at a rate of approximately 1.5 kHz. The duration of closure determines the magnitude of the output voltage of the power supply. Voltage V_2 appears as a square wave having a constant period and a pulse width directly proportional to the output voltage. Voltage V_2 is smoothed by the *LC* filter composed of L2 and C2, and the output voltage V_3 is a dc voltage with a minute amount of ripple modulation. Diode CR3 is a free-wheeling diode that permits current to continue to flow through L2 when transistor switch Q1 is in the "off" position.

Regulation is achieved by sampling the output current through shunt R1 and comparing the voltage across R1 with a reference voltage set by current control potentiometer R2. The difference between the two voltages is amplified by differential amplifier A and its output is fed into pulse width modulator PWM which drives the series transistor switch to the "on" position for a time directly proportional to the magnitude of the desired output current. The described negative feedback circuitry produces an output current which is almost completely dependent on the value of the set resistance of potentiometer R2.

The power supplies have been used with moderate success in the gallery. Difficulty was experienced by the manufacturer in meeting the overall current regulation specification listed in Table 15-2, and the regulation of the average power supply is approximately a factor of 2 times the values listed in the table. Overall current regulation was specified as the envelope within which the output current had to remain when subjected to either one or all of the following conditions: (a) $\pm 10\%$ change in line voltage; (b) $\pm 10\%$ change in load resistance; and (c) $\pm 20°C$ change in ambient temperature.

The only problem area remaining at the present time is the occasional loss of power transistors used in transistor switch Q1 in Fig. 15-12.

The high-current quadrupole power supply is a commercially available unit using a Class A series regulator and a silicon controlled rectifier (SCR) preregulator to limit the dissipation of the series regulator transistors. The high-current quadrupole power supply is capable of delivering up to 15-A dc while the normal quadrupole power supply is capable of only 7-A dc. The two units take up the same amount of panel space, and the high-current supply may be conveniently used instead of the normal power supply when quadrupole currents in excess of 7 A are desired.

Controllers

The controllers used to set the output current level of each beam guidance, power supply provide two functions: (a) they permit local or remote control of the output current of each supply and (b) they contain 0.1%, 1-V shunts of which the outputs are used for metering the power supplies' currents in the I & C alcove and in CCR.

The degaussing and all quadrupole controllers are basically identical and will be described first. The steering dipole controller is different in several aspects and will be described last.

DEGAUSSING, QUADRUPOLE, AND POSITRON QUADRUPOLE CONTROLLERS. The controller (see Fig. 15-12) consists of a motor-driven potentiometer to set the output current of the associated power supply, local controls and a remote input to operate the motor, and a precision shunt is used for remote metering. The slight differences among the different controllers are given in Table 15-3.

The local controls are available on the controller's front panel. Normally the "local–remote" switch is in the remote position, and control may be

Table 15-3 Comparison of controllers

Type of controller	*Remote controls*	*Remote metering*	*Shunt output*
Degaussing	None	I & C alcove only	1 V at 20 A
Quadrupole	Raise–lower, power supply on–off from alcove and CCR	I & C alcove and CCR	1 V at 7.5 A
Positron quadrupole	Raise–lower from alcove	Sector 11 I & C alcove only	1 V at 15 A
Steering dipole	Raise–lower from alcove and CCR	I & C alcove and CCR	1 V at 20 A
High-current quadrupole	Raise–lower from alcove and CCR	I & C alcove and CCR	1 V at 15 A

transferred to the local position by keeping the switch depressed. By then pushing either the increase or decrease push buttons, proper polarity is fed to the dc motor to cause it to increase or decrease the resistance of the 10-turn potentiometer, causing the output current of the associated power supply to change. The power supply's output current is directly proportional to the potentiometer's resistance. When pressure is removed from the "local–remote" switch, control reverts automatically to the remote location which, by transmitting the proper voltage polarity, sets the output current of the associated power supply.

The analog voltage from the shunt is used in the local alcove and in CCR to measure the output current of the power supplies.

STEERING DIPOLE, POWER SUPPLY CONTROLLER. The steering dipole, power supply controller is different from the ones already described because it uses a stepping motor instead of a dc motor and it also uses a reversing relay to change the direction of current through the steering dipole coils.

A stepping motor is used to permit the output current of the power supply to be varied at a slow, medium, or fast rate. A pulse generator in CCR may be set to generate pulses at either 1, 10, or 100 pulses/sec. The pulses are transmitted through a pair of telephone wires to the controller. Electronic circuits inside the controller drive the stepping motor, causing the potentiometer to turn. Reversal of current direction through the magnet is accomplished by a relay when the load current is below 10-mA dc. Minimum current sensing is accomplished by ganging another 10-turn potentiometer on the same shaft as the control potentiometer and sensing when the control potentiometer is at zero, and, therefore, power supply output current is at minimum.

15-5 Beam analysis

Profile monitors (DDR)

Beam profile monitors for use along the accelerator must meet requirements that differ appreciably from those for the BSY and research areas.[8] Some kinds of monitors are ruled out because of possible harmful effects upon the performance of the disk-loaded waveguide. Zinc sulfide screens, for example, might outgas, and might release harmful substances which could form deposits on the surfaces of the RF structure. The foils of a gas Cerenkov cell might rupture and leave fragments inside the critically tuned cavities. On the other hand, since the electron beam in the accelerator is confined to a small cross section, relatively high specific beam intensities can be expected, so that the monitors for the accelerator need not be so sensitive as those for the research areas.

Two types of profile monitors have been constructed for this application. One type, useful at relatively low beam power levels, makes use of a thin-quartz Cerenkov radiator which is viewed by a TV camera. The other type

was designed for use at very high beam power levels. In the high power or scanning monitor,[9] a small bead, typically a 1 × 1-mm molybdenum cylinder hung on a fine wire, is scanned over the beam profile. The bead scatters a small part of the beam, which hits the inner wall of the accelerator, making a shower downstream. The shower is measured by means of an ion chamber. The high-power monitor is poorly suited for the beam breakup (BBU) studies which have so far preoccupied experimenters who study the accelerator and its beam, since BBU does not repeat accurately from pulse to pulse. Apart from the BBU phenomenon, the beam profile has seemed to be well behaved and well understood. As a result, the scanning monitor has not, as of July 1967, been used as a tool for accelerator studies.

The Cerenkov TV monitors, illustrated in Fig. 15-13, have been installed at beam-analyzing station (BAS) 1 and in drift sections 1, 10, and 19. When one of these monitors is in operation, the electron beam passes through a 0.75-mm-thick fused quartz plate, producing light by the Cerenkov effect. The quartz radiator is mounted at a 45° angle to the electron beam so that the useful light will emerge at right angles to the quartz surface. Part of this light is reflected upward by a mirror and passes out of the accelerator vacuum region through a glass window. The light is observed by means of a closed-circuit TV system. Indicator units can be connected locally and are installed permanently at the injector control room and at CCR. To give reference marks, tungsten has been evaporated on the downstream surface of each quartz radiator to form a grid of 0.25 × 0.25-in. squares, as seen when viewed along the beam axis.

Figure 15-13 Cerenkov-TV profile monitor for use along the accelerator.

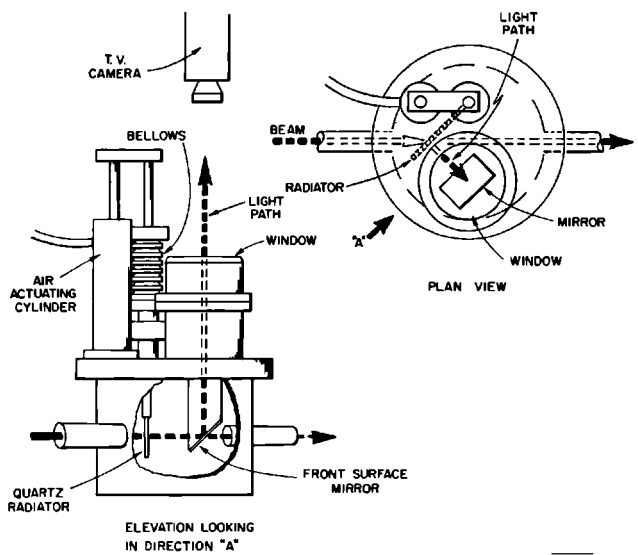

Unlike ordinary light, Cerenkov light is not radiated isotropically, but in a well-defined conical sheet. A description of this effect and other features of Cerenkov monitors is given by de Raad.[8] Due to the cone effect, it is necessary to take precautions to avoid mistakes when a TV camera is used to view a Cerenkov target. In early tests at BAS 1, for example, a very odd "profile" was once observed[10] which resulted from TV camera misalignment. After some confusion, it was found that the Cerenkov cone had been missing the camera entirely and that the TV camera automatic gain control had been operating in such a way that some very weak scattered light was visible, resulting in the misleading picture. In this case, a 25-mm wide-angle lens was installed so that the remotely operated camera pan and tilt mechanism could give adequate lateral motion and the camera could be properly aligned with the Cerenkov cone.

For regular installation along the accelerator housing, it was desired to use a lens of 75-mm focal length, so that the camera could be mounted well away from the beam line and yet give a fairly large image at the viewing screen. To eliminate the need for complicated camera positioning gear, the downstream surfaces of the Cerenkov targets have been roughened by sandblasting, to diffuse the Cerenkov light. When new *f*/1.8 lenses and 7735*B* vidicons have been available, the systems, as of July 1967, have always been sufficiently sensitive to meet experimental demands.

Since the lenses become brown and the vidicons deteriorate seriously in a few months in the accelerator housing, it has become the practice to install cameras only when required, and to remove them when they are not in use. Nonbrowning vidicons are not used, since it appears that browning is not the life-determining factor. For initial installation, ordinary lenses were used. It is planned (July 1967) to procure and install some nonbrowning lenses, so that the browning rates of the two types can be compared. The quartz Cerenkov radiator itself remains in the accelerator vacuum; it is inserted into and withdrawn from the beam path by means of an air cylinder. The motion is accommodated by a stainless steel bellows which forms part of the accelerator vacuum wall. Some of the quartz radiators have been removed and have been found to have suffered some radiation damage. There is typically an oval brown spot, about 2 × 3 cm, with an annealed clear spot near the center. In some cases, the quartz has been melted enough to smooth out part of the rough sandblasted surface. As of July 1967, the evaporated tungsten grids seem to have suffered no ill effects.

Beam analysis stations (HAH, MJL)

Two BAS have been built and installed on the accelerator. The first station, BAS 1, analyzes the beam after it has left the injector and has been accelerated through the first 40 ft of the machine. It is designed for energies up to 200 MeV. The second, BAS 2, was initially installed at the end of Sector 2, and served as beam dump and beam analyzer during the early tests while the

Table 15-4 Summary of parameters for the beam analyzer stations

Parameter	*BAS 1 (injector)*	*BAS 2 (Sector 2 test)*	*BAS 2 (Sector 20)*
Maximum energy	200 MeV	1.45 GeV	3.0 GeV
Maximum field required	8 kG	15 kG	15 kG
Maximum current required	120 A	300 A	300 A
Energy calibration	25 MeV/kG	96.7 MeV/kG	200 MeV/kG
Energy acceptance	25%	25%	25%
Bending radius	32.8 in.	126.9 in.	262.5 in.
Bending angle	30°	7.7°	3.75°
Pole-face rotation			
Entrance face	−1.5°	−12.4°	−14.4°
Exit face	−1.5°	−12.4°	−14.4°
Focal point location coordinates[a] $z' =$	60.5 in.	230.9 in.	465.8 in.
$y' =$	30.3 in.	30.2 in.	30.0 in.

[a] Position is measured relative to the point of intersection of the magnet entrance pole face and the beam axis.

remainder of the machine was being built. In this location, it could accept beam energies up to 1.45 GeV. At the beginning of 1966, BAS 2 was modified to enable it to analyze beam energies of 3 GeV, and it was moved to its permanent home at the beginning of Sector 20.

Both stations were invaluable tools for testing operation of the accelerator prior to its completion. Their utilization has tended to decline as operational experience and skill increase, permitting beams to be set up and passed directly to the switchyard for analysis. However, BAS 1 is used regularly for injector tune-up, and BAS 2 enables low-energy accelerator physics experiments to proceed while modifications are being made in the switchyard and end stations.

A summary of magnetic and optical design parameters for BAS 1 and the two forms of BAS 2 is given in Table 15-4. The basic optical arrangement of BAS 1 is shown in Fig. 15-14, which may also be used to identify parameters listed in Table 15-4 for BAS 2.

OPTICAL DESIGN: DETERMINATION OF FOCAL POINTS For electron energy $E \gg m_0 c^2$, the field intensity B_1, bending radius ρ, and energy E are related by[11]

$$\rho = \frac{E}{0.3B} \text{ (cm, MeV, kG)} \tag{15-22}$$

Similarly, the field intensity integral along the particle path is related to the bending angle α and the energy by

$$\int B \cdot dl = \frac{\alpha E}{0.3} \text{ (kG, cm, rad, MeV)} \tag{15-23}$$

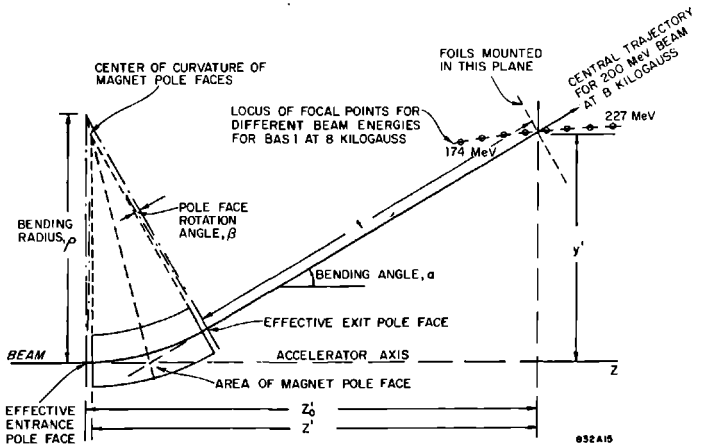

Figure 15-14 Basic optics: BAS 1.

The effective length l_{eff} of a trajectory through a magnet is defined to be the arc length of a trajectory through an ideal magnet (with uniform field $B_{\max}$ equal to the maximum field in the real magnet) which has the same bending angle. From Eqs. (15-22) and (15-23),

$$l_{\text{eff}} = \frac{1}{B_{\max}} \int B \cdot dl = \frac{\alpha E}{0.3 B_{\max}} \tag{15-24}$$

Referring to Fig. 15-14, it may be shown[12] that, for equal pole-face rotation angles, β, first-order theory gives

$$\begin{bmatrix} x \\ \theta \end{bmatrix} = \begin{bmatrix} \dfrac{\cos(\alpha - \beta)}{\cos \beta} & \rho \sin \alpha \\ \dfrac{-(1 + \tan^2 \beta) \sin(\alpha - 2\beta)}{\rho} & \dfrac{\cos(\alpha - \beta)}{\cos \beta} \end{bmatrix} \begin{bmatrix} x_0 \\ \theta_0 \end{bmatrix} \tag{15-25}$$

where x_0, θ_0 and x, θ are the position and angle coordinates of beam trajectories at the entrance and exit pole faces, respectively, relative to the central trajectory at the same energy. The relative coordinates a distance t from the exit pole face will then be

$$\left.\begin{aligned} x' &= x + t\theta \\ \theta' &= \theta \end{aligned}\right\} \tag{15-26}$$

Now the focal point will be such that $x' = 0$ for a parallel incident beam ($\theta_0 = 0$). Inserting Eq. (15-26) into Eq. (15-25) with these conditions gives

$$\frac{\cos(\alpha - \beta)}{\cos \beta} - \frac{t(1 + \tan^2 \beta) \sin(\alpha - 2\beta)}{\rho} = 0$$

and, hence,

$$t = \frac{\rho \cos(\alpha - \beta) \cos \beta}{\sin(\alpha - 2\beta)} \tag{15-27}$$

From the geometry of Fig. 15-14, it is seen that

$$y' = t \sin \alpha + \rho(1 - \cos \alpha) \tag{15-28}$$

and

$$z_0' = y' \cot \alpha + \rho \tan \frac{\alpha}{2} \tag{15-29}$$

Equations (15-27), (15-28), and (15-29) are used to calculate the position of the focal point. (Note that $z' = z_0' - d$, where d is the separation of real and effective pole faces.)

A more general form of Eq. (15-25), to cover unequal entrance and exit pole-face rotations, was used to calculate the focal points for other energies. The locus of these points for BAS 1 is shown in Fig. 15-14.

The method outlined above was used to calculate the parameters in Table 15-4. For BAS 1, however, it was practicable to confirm the calculated values by the floating-wire method.[13] The trajectory of a beam of energy E through a magnet may be simulated by a fine wire under tension W carrying a current I_W. The relation is

$$E = 2.94 \frac{W}{I_W} (\text{MeV, g, A}) \tag{15-30}$$

The annealed wire was clamped at a point along the central trajectory ($\alpha = 30°$) corresponding approximately to the calculated value of t. The wire passed through the magnet and over pulley supported on air bearings. Weights on the free end supplied a suitable tension (approximately 50 g), and I_W was adjusted to satisfy Eq. (15-30) for $E = 200$ MeV; B was adjusted so that the wire between the pulley and the entrance pole face coincided with the accelerator axis. Then, by trial and error, the value of t was found for which, when the pulley was moved up and down, the wire between it and the magnet remained strictly parallel to the accelerator axis. This value of t defined the focal point. Theoretical and experimental focal points coincided within 1%. The floating-wire test could not be used for BAS 2 because of the large values of t involved. It was used, however, to check the calculated value of the effective length of the magnet.

ELECTROMAGNET CHARACTERISTICS. The same design of magnet was used for both BAS 1 and BAS 2. Each magnet has a U-shaped yoke, with arcuate pole pieces (mean radius 30 in., angle of arc 30°) fitted inside the yoke and carrying the energizing coils. The field variation is less than 0.1% over a zone $\frac{3}{4}$ in. wide on each side of the central arc. The field is 15 kG for a current of 300 A, with about 20% saturation at that level.

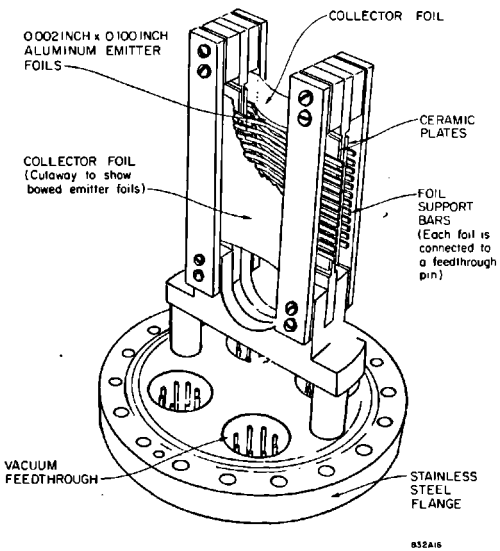

Figure 15-15 Secondary-emission foil assemblies: BAS 1 and 2.

ENERGY ANALYZER FOILS. The beam, deflected and spread out into an energy spectrum by the magnet, is detected by a series of secondary-emission monitors. The monitor assembly is shown in Fig. 15-15. Twenty-four aluminum foils, each 0.002-in. thick and 0.100 in. wide, are mounted horizontally in the plane shown in Fig. 15-14, normal to the central trajectory. The top foil, for which the analyzer is calibrated, crosses the central trajectory. The remaining twenty-three foils are mounted immediately below alternately, on opposite sides of alumina support strips, so that they are insulated from each other and yet beam interception is continuous. From Eq. (15-24),

$$\frac{\Delta E}{E} = -\frac{\rho}{l_{\text{eff}}}\Delta\alpha = -\frac{\rho}{l_{\text{eff}}}\cdot\frac{w}{t} \tag{15-31}$$

where w is the foil width. All foils are 0.100 in. wide, giving $\Delta E/E \approx 0.33\,\%$. The foils are bowed to avoid "oil-canning" when they are heated by the beam. Large collector foils biased 120 V positive with respect to the emitter foils are mounted on each side.

Each emitter foil is connected to the center conductor of a low-capacity coaxial cable which runs up to the foil scanner in the klystron gallery. The outer conductors of all twenty-four cables are connected to the two collector foils. All cables are terminated in 100-megohm loads, giving an RC time constant of about 0.1 sec. in each case.

Assuming that 10% of the analyzed beam current strikes one foil[14] and that the secondary emission efficiency (both sides) is 4%, the foil current for a 1-mA beam is 4 μA. Thus, for a 1.6-μsec beam pulse length and 1000-pF

distributed cable capacity C, the pulse voltage is $\Delta V = 6.4$ mV. If the time T between beam pulses is approximately 17 msec (60 pulses/sec), then the steady-state voltage built up across the terminating resistor is

$$V = \frac{\Delta V}{1 - e^{-T/RC}} = 41 \text{ mV}$$

If the voltage is sampled every twenty pulses, it will rise to about 95% of its steady-state value.

The output of the top foil is amplified and applied to the y channel of an $x - y$ recorder. A voltage proportional to the electromagnet current is applied to the x channel. Thus, as the magnet current is raised, a detailed plot of relative beam current versus energy is obtained.

Voltages from the remaining twenty-three foils are scanned sequentially by means of a series of reed delays driven by a ring counter. The circuit is designed to allow adequate time for one relay to open before the next one closes, preventing charge leakage between foils. The scanned outputs are displayed on an oscilloscope, appearing as a histogram of beam current in each 0.33% energy interval.

The foils for BAS 2 are longer than for BAS 1; otherwise, the two assemblies are identical.

GENERAL DESCRIPTION OF BAS 1. The main features of BAS 1 can be seen in Fig. 15-16. The station is mounted on a 10-ft drift-section girder. The beam runs through a stainless steel "Y" vacuum envelope inside the magnet, allowing the beam to go straight ahead when the magnet is degaussed or to be

Figure 15-16 Layout of BAS 1.

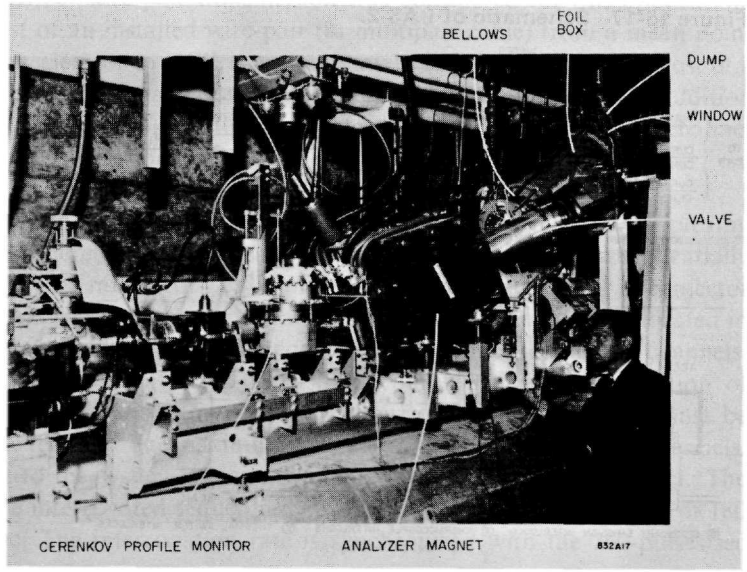

bent up into the large cylindrical chamber known as the foil box. A large manual valve permits the foil box to be isolated from the accelerator vacuum system. The foil assembly is mounted on the underside of the foil box just below the copper vacuum window, through which the beam passes to be absorbed in the beam dump. A large bellows permits adjustment of the foil box position. The copper window is water-cooled and reduced in thickness along the beam interception area to minimize heating. The lead-shielded dump is a complex design of stacked copper plates (to prevent the cracking which could occur at the shower maximum in a solid block), peripherally water-cooled. It will dissipate 40 kW. The system is protected by thermal switches on the magnet cooling water, flow switches on all water supplies, thermocouples (operating meter-relays) on the dump, window, and valve, limit switches on the valve and the dump (which can be moved for maintenance), and secondary-emission foils[15] (operating in air) to protect the "Y" from beam interception. Tripping any interlock shuts off the beam. The station can be controlled from either the rack containing the magnet power supply or from the injector console.

GENERAL DESCRIPTION OF BAS 2. Figure 15-17 shows the layout of BAS 2 in schematic form. The station, which is mounted on the first girder in Sector 20, has the same main components as described for BAS 1, with the exception of the manual valve to isolate the foil box. The "box" is an 8-in. diameter stainless steel pipe about 38 ft long. The magnet, the large "Y" section, and a beam stopper (for emergency protection of people working in the switchyard while a beam is being run into BAS 2) occupy the first 10 ft of the girder. These are followed by a 10-ft drift tube. Two accelerator sections are mounted in the last 20 ft. The beam stopper, which is a copper bar inside the vacuum

Figure 15-17 Schematic of BAS 2.

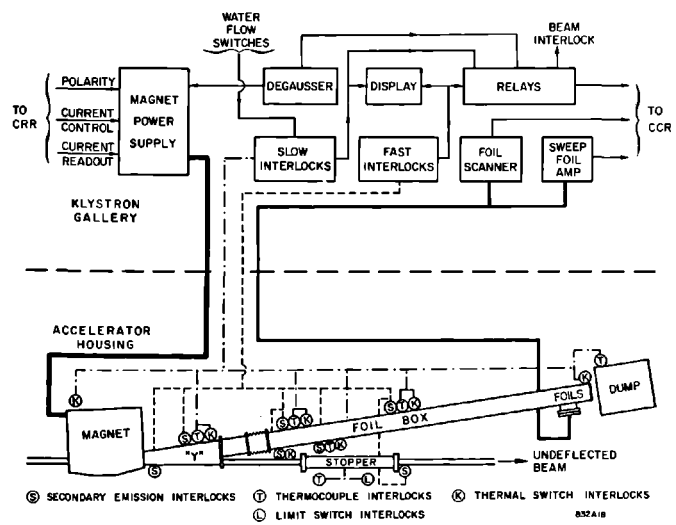

system, can be remotely moved into and out of the beam line. The dump for BAS 2 is attached to the ceiling of the accelerator housing. It consists of six copper blocks, each 2 in. thick. The first four blocks are water-cooled. The dump is rated at 35 kW, and is lead-shielded for personnel protection from residual radioactivity.

The station is protected by an extensive system of interlocks of the types described for BAS 1 and located as shown in Fig. 15-17. The secondary-emission foils mounted in air around the vacuum envelope trigger a fast fault system which will trip on a single pulse and reset after 1 sec. All other protection devices operate a "slow fault" circuit. A fault summary panel in the local rack indicates the location of the trouble.

The BAS 2 is normally operated from CCR. All incoming control signals are amplified by SCR circuits which drive dc relays. A PWM signal is applied to a dc motor regulating the current level of the bending magnet power supply, giving a very wide range of speed control for exploring and plotting spectra. A current and polarity programmer automatically degausses the analyzer magnet when a straight-ahead beam is required.

15-6 Data-handling systems (KFC)

Status monitoring system

There are approximately 3000 status signals generated in the sectors, the injector, and the BSY. The signals represent, typically, the condition of valves (open–closed), vacuum (OK–not OK), modulators (OK–not OK), etc. It is the function of the status monitoring system to (1) collect these data, (2) transmit the signals to the CCR, and (3) provide drive voltages for lamps on the display consoles. Direct wire-pair transmission was considered for this application, but the cost of an installed wire-pair (in multipair cable) from a mean point along the accelerator to CCR is approximately $150. The equivalent cost of a solid-state multiplex transmission system is $40–$50 per signal. In addition to the cost advantage, multiplex equipment can be expanded in channel capacity quickly and conveniently by plug-in cards.

SYSTEM DESCRIPTION. The selected system employs time-division multiplexing techniques, whereby each input at a remote location is sampled sequentially every 600 msec. Transmitting equipment is located in each sector, the injector and the DAB in the beam switchyard. All receiving equipment is located in the CCR. As initially installed, the equipment is strapped to scan 108 channels. Expansion to 156 inputs can be easily accomplished without addition of equipment at the transmitting location; however, output modules must be added at the receiver. The maximum capacity of the equipment is 252 channels. Each input to the system is made available as a floating relay contact. The contacts are interrogated sequentially by a digital multiplexer at a rate of 180 contacts/sec. The interrogation rate is synchronized with the 360-pulses/sec

accelerator clock. The multiplexer output is processed in an encoder which inserts the frame synchronizing signal (three binary "ones" followed by a binary "zero") and generates the binary data wave train. A closed status contact is represented by a logic "1" followed by "0," and an open contact is a "0" followed by "1." This type of code has two important features: (1) it provides redundancy for simple error checking at the receiving location, and (2) it carries its own bit-synchronizing signal.

The binary wave train modulates a frequency shift transmitter which has a nominal frequency of 18.8 kHz and a frequency shift of ± 250 Hz. The carrier signal is transmitted on a wire-pair to CCR where the binary signal is demodulated in a frequency shift receiver. The receiver output is checked for transmission errors in a decoder and converted to parallel format in a serial-to-parallel converter. The parallel outputs feed to output modules. The module consists of a memory flip-flop to prevent relay dropout between successive data scans and a driver to operate an external relay.

TRANSMITTING EQUIPMENT. The transmitting equipment consists of an encoder and a frequency shift transmitter (see Fig. 15-18). The function inputs at the remote station are provided by up to 156 normally open or normally closed contacts. In the open condition, a scanning current of 2 mA is provided in turn to each of these contacts. When open, the voltage across the contacts is 18 V.

The encoder scans all input functions and generates a binary coded pulse train as shown in Fig. 15-19. The scanning operation is accomplished by a basic counter and matrix which sequentially scans the sixteen input functions in each group. Each group is enabled in sequence by a group counter and

Figure 15-18 Remote station (transmitter), 252-channel system.

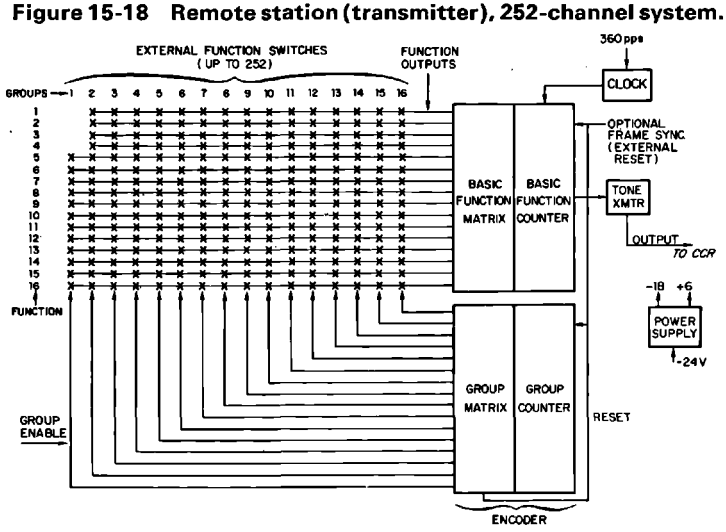

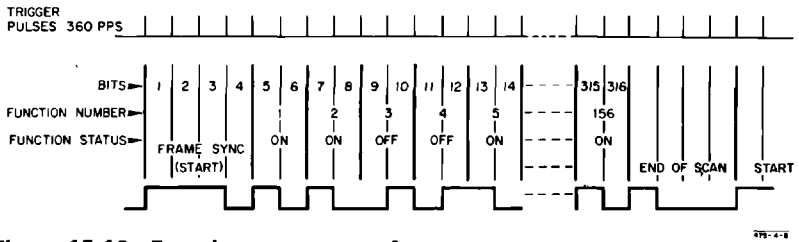

Figure 15-19 Encoder output waveform.

matrix. Ten group outputs have been provided, but as many as sixteen groups can be installed. The counters are continually advanced by pulses from an internal clock which is synchronized with the accelerator 360-pulses/sec trigger. If the 360-pulses/sec trigger input fails, the internal clock will continue to run at approximately 350 pulses/sec.

The binary pulse train from the encoder is used to shift the frequency of a transmitter between 18.550 and 19.050 kHz. Carriers in other frequency bands can be transmitted on the same wire-pair if expansion of the system is required. The transmitter output voltage is 1.3 V rms maximum, into a balanced 135-ohm wire-pair. Harmonic distortion is 5% maximum and amplitude modulation is less than 20%.

The input power is from the local −24-V battery. The supply output is +6 V regulated, and −18 V unregulated.

RECEIVING EQUIPMENT. The receiving equipment consists of a frequency shift receiver and a decoder for each transmitting location and an additional decoder for each switched sector panel (see Fig. 15-20).

Figure 15-20 Receiving equipment—252-channel system.

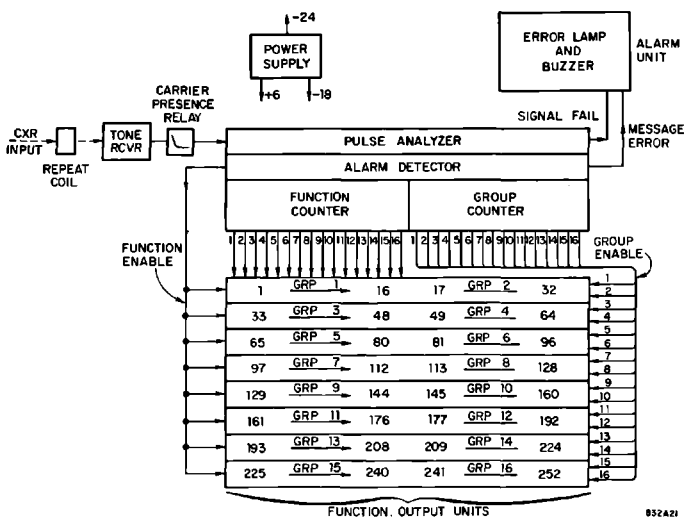

The receiver delivers a voltage output that is a reproduction of the pulse train applied to the remote transmitter. If the carrier level drops below a preset level, audible and lamp alarms are generated.

The decoder consists of the following subassemblies:

PULSE ANALYZER—decodes message to provide function status display and extracts frame synchronizing and bit synchronizing signals

ALARM DETECTOR—performs error checks on the message. If message contains extra pulses, extra spaces, missing pulses, missing spaces, or wrong parity count, an alarm signal is generated

COUNTER UNITS—Contain basic function counter and group counter

AUDIBLE ALARM UNIT—Sounds internal alarm buzzer when error is detected or carrier fails

OUTPUT MODULE—Provides memory and drive for external relay

POWER SUPPLY—Operates from local −24-V battery; generates 6 V regulated, and −18 V unregulated.

The arrangement of equipment in CCR is shown in Fig. 15-21. Continuous decoding and display are provided for the injector and the BSY. In addition, thirty-two channels are continuously displayed from each sector. All status channels (156 maximum) from any three sectors can be monitored on display panels, one on the operator's console and two on the maintenance console.

Figure 15-21 Block diagram of status monitoring system.

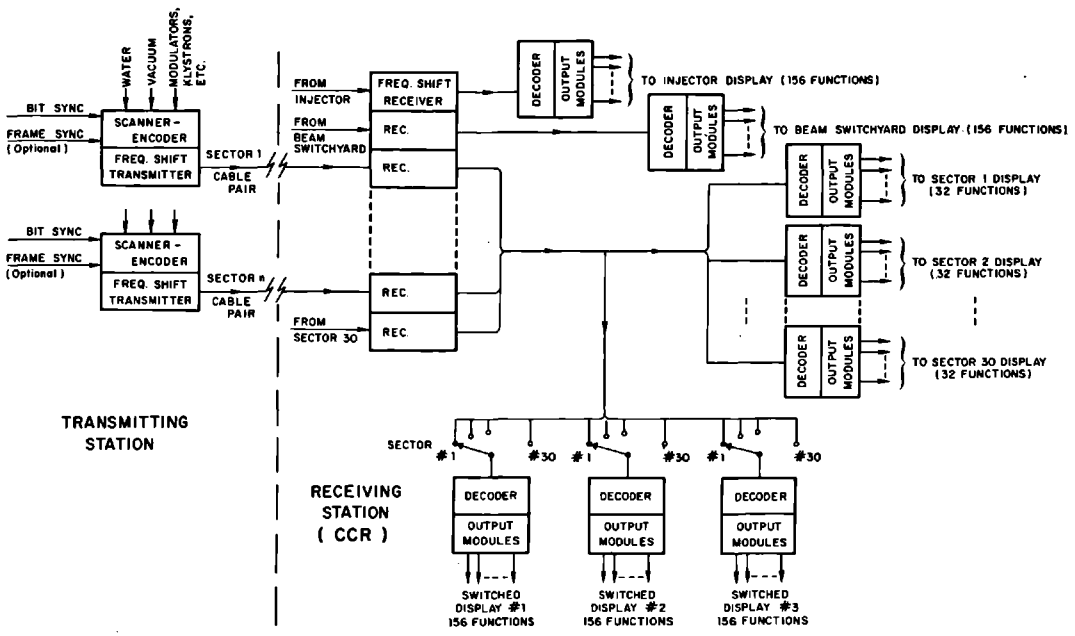

Remote control system

For efficient operation of the accelerator, it is essential that the CCR operator be provided with the means for remotely controlling equipment in the sectors, the injectors, and the BSY.

The system adopted for the accelerator uses binary coded relays. A code applied in parallel to six wire-pairs looped from sector to sector is decoded by a relay tree at the selected sector. Sixty-four channels are thus available. A control voltage applied to a seventh pair determines whether the remote device is turned on or off. Response time for the system is approximately 200 msec.

SYSTEM DESCRIPTION. The CCR console switches are grouped on the injector, BSY, and sector panels. (See Fig. 15-22.) There are three identical switched sector panels, allowing access to any three different sectors simultaneously.

Operation of the injector system will be described first. The description applies equally to the BSY system. When a control switch is pressed, one of sixty-four encoding relays in CCR operates. This relay, corresponding to the decimal number of the channel, operates to apply a code to the six wire-pairs and to "lock out" all but the selected channel. A binary "one" is transmitted as a "tip-positive" 48-V signal and a binary "zero" is transmitted as a "tip-negative" 48-V signal.

One of the two control relays also operates, depending on the command, "on" or "off." The control relay applies 48 V to the seventh pair.

Figure 15-22 Block diagram of remote control system.

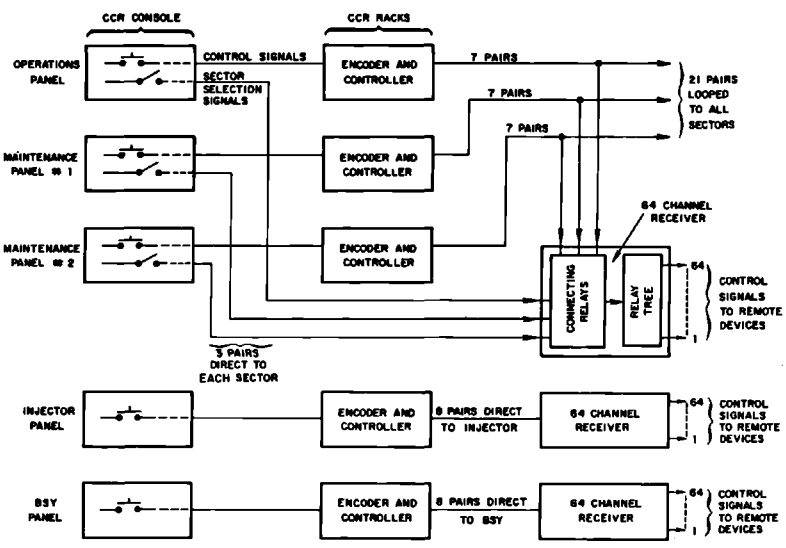

At the injector, a relay tree decoder converts the six binary inputs to the appropriate decimal number and completes a circuit from the local 24-V battery to the selected device via contacts of a control relay. This relay, operated by the seventh pair, serves to reverse the local battery depending on the "on" or "off" command from CCR. The load current available to remote devices is fused at 2A. The applied voltage is present only while the CCR switch is depressed. For devices requiring a holding current, external latching relays are added.

Operation of the sector system is similar except for the requirement that only one switched sector panel at a time can operate in a particular sector. The operator's console has priority over maintenance No. 1, and maintenance No. 1 has priority over No. 2. Only the highest priority panel can control or monitor a selected sector. Seven looped pairs (6 binary, 1 control) are associated with each panel. In addition, each panel has thirty long-haul pairs to the sector receivers, one for each sector-select button. When a sector is selected, the long-haul pair applies voltage to one of three relays in the receiver. The relay acts to connect the relay tree to the appropriate set of looped cables. Control of remote devices can then be exercised by operating the control switch. If the same sector is selected by a panel of higher priority, the first connecting relay drops out and the second connects the receiver to the second set of looped cables.

Provision has been made for pulsing of remote stepping motors. A strap is added to the particular channel so that a control pulser is started whenever the channel is selected. The pulser breaks the control pair at any one of several preset rates (1, 2, 5, 10, 50 pulses/sec).

SPECIAL CONTROL CHANNELS. In certain cases, the "one channel at a time" feature of the relay tree is undesirable because simultaneous access is required for two or more functions at a particular location. Vertical and horizontal steering is an example of this. Separate hard wire pairs are used for these applications. The transmitting voltage is 48 V, pulsed at 1, 10, or 100 pulses/sec.

Analog system

The analog system provides the CCR operator with D'Arsonval meter displays of dc signals from remote information sources. Typical sources are steering coil currents, quadrupole current, and VVS reference voltage. The method adopted for the accelerator is a simple dc transmission system using one wire-pair per signal. The transmission level is 0–5 V dc, 0–1 V dc, or ± 1 V dc, depending on the source characteristics.

A number of possible approaches were examined in detail before selecting this straightforward system. These included remote multiplexing of the signals with time-division transmission, using pulse amplitude, pulse duration, or pulse code modulation. Other proposed methods would have used frequency-division techniques. The overriding factors in the choice of hard wire were

lower cost and adequate accuracy. For most signals, $\pm 3\%$ of full scale appears to be satisfactory. In cases where short-term accuracy of better than 3% is required, digital voltmeter or slideback voltmeter circuits are used.

SYSTEM DESCRIPTION. There are thirteen signals from a typical sector. Six of these are displayed continuously in CCR and the remainder are displayed on three identical panels on the CCR console. Each of these panels can be switched to display the analog signals in any one sector.

Seven injector signals are displayed continuously on console meters and eighteen are displayed on one meter via a selector switch. Beam switchyard signals are also divided into continuous displays (10) and switched displays (20).

EQUIPMENT DESCRIPTION. All analog sources are basically voltage sources of low impedance (1000 ohms maximum). Line current is approximately 105 μA at full scale, determined by a multiplier at the CCR meter. For the switched analog displays from the sectors, the signal can be displayed on any one of three switched panels. The three meters are connected in series, and when a meter is switched out of circuit, the total circuit resistance is restored by switching in a fixed resistor. Figure 15-23 is a simplified circuit of the three-meter arrangement.

In most cases, the source voltage is provided by the equipment itself. For example, the variable voltage transformer is supplied by a dc rectifier in the reference voltage subsystem. When an internal voltage source is not available, voltage is supplied by a Zener regulator in the analog metering panel located in each sector alcove. The metering panel also allows sector monitoring of signals without disturbing the CCR reading and provides a series potentiometer for current adjustment of each signal circuit.

SOURCES OF ERROR. The long-haul cable pair is 22 gauge which, for a 2-mile run, has a nominal loop resistance of 380 ohms. Over a temperature range of

Figure 15-23 Simplified functional schematic diagram of a typical analog signal circuit.

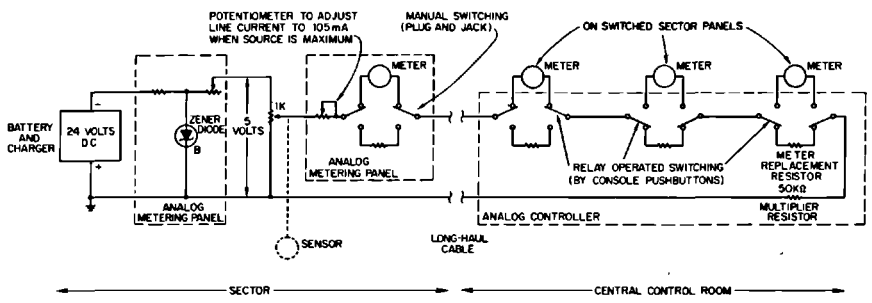

$\pm 20°C$, the maximum error introduced by temperature is $\pm 0.08\%$ of full scale.

Several analog voltage sources utilize shaft position potentiometers. The change of source impedance with change in shift position introduces 0.3% of full scale error.

The small panel meters used have an accuracy of $\pm 2\%$ of full scale (100 μA). The system accuracy has been improved by shunting all meters to read full scale when the circuit current is 105 μA. Thus differences on individual meters can be eliminated at full-scale reading. Nonlinearity at readings less than full scale are still present, however, and are of the order of $\pm 1\%$. The 5-V source in the analog metering panel has a stability of $\pm 0.13\%$ over $\pm 25°C$ and will hold the voltage to $\pm 0.2\%$ with normal variations of input voltage from the 24-V battery system.

The CCR equipment for selecting a particular sector for display is mounted in the rack area of CCR. It consists of six relay chassis called "analog controllers." The function is to select any group of 45 signals (up to 15 signals from each of three sectors) from 450 input signals (up to 15 signals from each of thirty sectors). A block diagram is shown in Fig. 15-24.

Video cable system

There are a number of video signals generated in the sectors, injector, and BSY which are made available to the CCR operator. The signals include toroid pulses, video pulses from the phasing system, and TV signals. The cost of

Figure 15-24 Central Control Room equipment analog system.

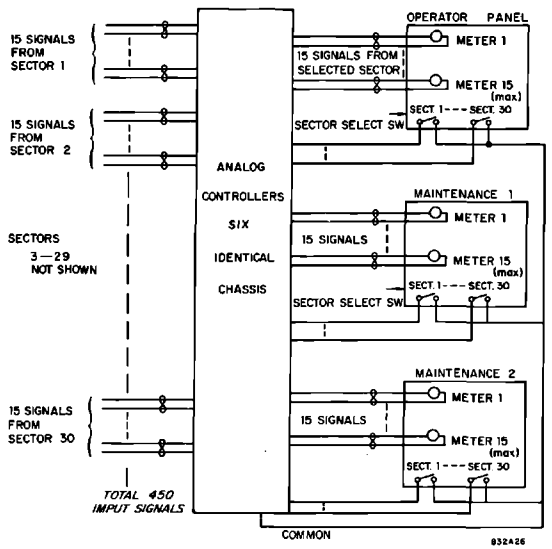

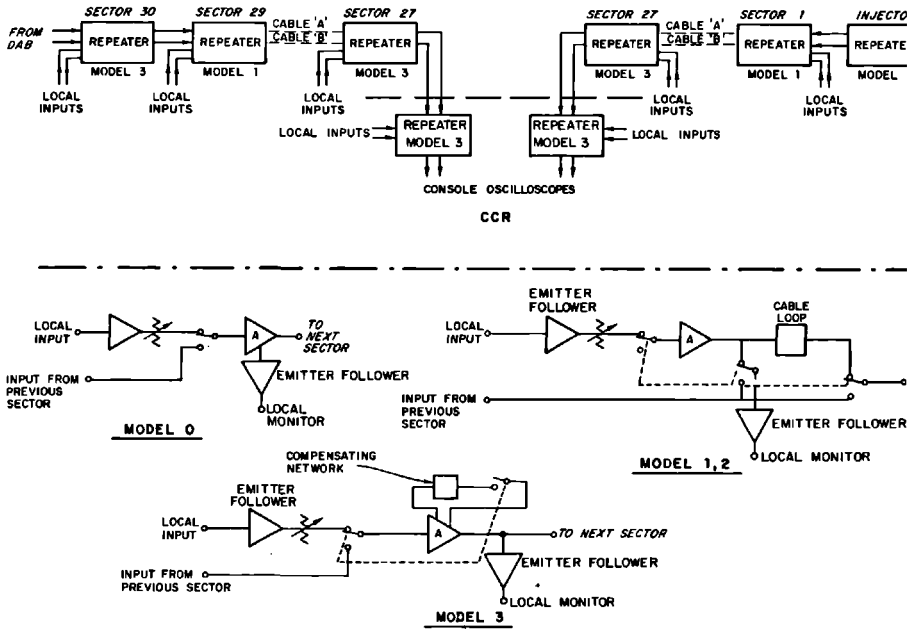

Figure 15-25 Video cable system.

high-quality coaxial cable with a rise time of the order of 100 nsec over 10,000 ft would have been prohibitive. The system adopted for the accelerator uses a lower-quality cable in conjunction with compensating techniques.

SYSTEM DESCRIPTION. There are four independent cable channels—two from the DAB via Sectors 30–27 to CCR and two from the injector via Sectors 1–27 to CCR. (See Fig. 15–25.)

Signals may be transmitted from the injector to CCR, CCR to the injector, or introduced at any intermediate sector and transmitted in either direction. The same flexibility exists for the CCR–DAB cable.

A system rise time of approximately 50 nsec has been achieved by the use of compensated repeaters every third sector (Sectors 3, 6, 9, etc.).

Four different repeater models have been installed. Model 0 in the injector consists of an amplifier with gain steps of 0.5, 1, 2, 5, and 10. Model 1 in Sectors 1, 4, etc., is used only to introduce local signals through an amplifier identical to model 0, except that the signal passes through a coaxial cable loop. The coaxial cable has loss characteristics equal to the loss of a signal transmitted 333 ft from the previous sector. For signals transmitted from the injector to CCR, the repeater is bypassed completely.

Similarly, a model 2 is installed in Sectors 2, 5, etc. For locally introduced signals, a coaxial cable loop simulates the loss of transmission over two sectors. For through transmission, the repeater is bypassed.

Model 3, in Sectors 3, 6, etc., contains a compensation network in the amplifier feedback network. The network is in the circuit for signals transmitted from a previous sector but is not used for local signals.

Provision has been made for remote control of local gain, the selection of one of a number of available local inputs, and for the reversal of input and output connections. System operation is returned to the normal mode, injector to CCR or DAB to CCR, by operation of a "clear" button on the CCR console. Rotary switches in each repeater step to a "home" position and transfer command to the next repeater down the line.

SYSTEM PERFORMANCE

Rise time: 50 nsec 0–90%
Droop: less than 10% in 10 μsec
Signal amplitude: ± 2.5 V peak-to-peak maximum
Cable type: FHJ450 $\frac{1}{2}$-in. foam heliax.

15-7 Central control (DDR)

Introduction

The accelerator control system is arranged so that, after the necessary components are made ready for use by operations performed along the klystron gallery, all controls necessary to normal operation can be operated from the CCR. In addition to controls and indicators required for normal operation, some equipment has been provided in CCR for use in detection, evaluation, and location of abnormalities, so that maintenance personnel can efficiently be dispatched for necessary repairs. Other equipment has been provided for the coordination of accelerator control with activities in the beam switchyard and in the experimental area.

When the SLAC control system is compared with those of smaller accelerators, it will be noted that the number and quality of signals exchanged between CCR and remote components have been stringently limited. No pulse shape information is ordinarily transmitted from accelerator components to CCR. Instead, a few pulse channels have been made available for occasional special use. Whenever possible, analog signals, such as voltmeter readings, have been replaced by status, or "go–no go" signals. Klystrons and modulators, for example, do not originate any analog signals in the CCR. The number of status signals transmitted to CCR has also been reduced by eliminating some signals and by transmitting logical combinations of certain others on single channels. In all, about 500 slow analog signals and 3000 status signals are available for display on meters and lamps in CCR. The response time of status and analog channels is nominally 1 sec. In addition, some 200 PAM signals are received in CCR from beam position, intensity, and spectrum monitors for display on oscilloscopes. Most of these signals are updated 360 times/sec. An important part of CCR instrument design has been aimed at

coping with multiple beams. Special oscilloscopes have been provided, in which base line position and trace intensity modulation can be used to distinguish data belonging to different beams.

Roughly 1200 remote control channels fan out from CCR to the injector, positron source, thirty sectors, beam switchyard, and other remote points. These channels transmit pulses of 5 msec and longer, originating in a 48-V dc source, over telephone wire-pairs. For wiring economy, most of these channels make use of relay trees, which operate remote equipment in accordance with binary coded control signals, each transmitted upon several wire-pairs. Response times of relay tree control operations are in the 0.1–0.5-sec range. The remote control channels for the beam-steering dipole controls are each assigned a separate wire-pair and give faster response.

General description

The CCR for the accelerator is arranged as shown in Fig. 15-26. Much of the space is devoted to signal-handling equipment which is connected, mostly by means of telephone cables, to components along the accelerator. The controls and indicators that terminate the communications systems in CCR are located in the console area. The console area is divided into four regions, corresponding to four kinds of activities. These activities are operation, maintenance, programming, and studies. Each of the first two activities is provided with a separate console. Much of the programming is done at the so-called backup

Figure 15-26 Central control layout.

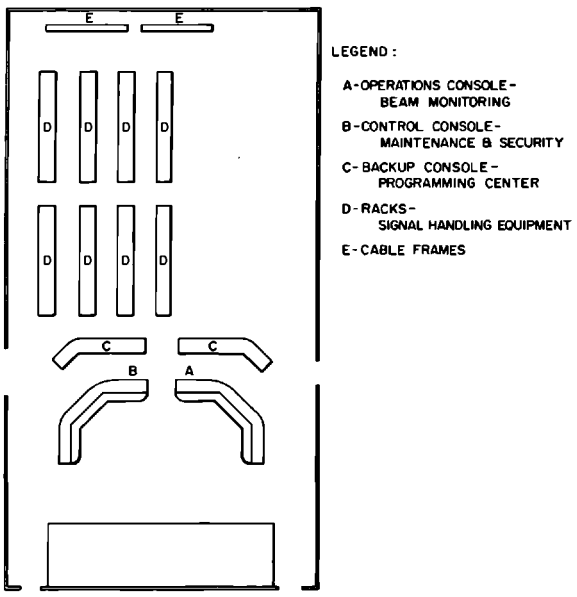

console. The studies area consists of extra space, centrally located in the consoles, to provide mounting space for special instruments, with convenient accessibility to a large number of the permanently installed instruments.

Because of the structure of the signal-handling equipment, it is generally most convenient and economical to arrange control panels on a geographic basis in CCR. Three identical panel assemblies called " switched sector panels," two in the maintenance console and one in the operations console, contain transmitting and receiving terminals for connection to the thirty sectors which comprise the greater part of the accelerator. Any of these panels can be connected to any sector. A priority arrangement prevents more than one panel at a time from being connected to any sector. Similar panel assemblies terminate monitoring and control channels connected to the injector, DAB, and other remote locations.

Some instruments are arranged on a subsystem basis. There are long rows of meters in the backup console which show vacuum gauge readings, radiation levels, and steering current values along the accelerator. In the maintenance console all the most urgent, sector alarm status indicators are arranged on two panels, side by side. Two more panels contain essential status information for all the klystrons along the gallery except certain special ones. In the beam operator's console, many of the controls and displays are arranged on a subsystem basis, notably the steering controls, some alarm signal lamps, and the multiplexed displays presented by the steering and spectrum oscilloscope.

Operation

At least one man sits at the beam operator's console (Fig. 15-26) and is responsible for making adjustments so that the electron beam can meet the requirements of the experiments. Controls and indicators not necessary for adjusting and monitoring beam parameters have largely been excluded from the panel space within easy reach of the beam operator. In this way, it has been possible to place within arm's reach those instruments that he uses most frequently.

INJECTOR ADJUSTMENTS. In the injector panel, the beam operator has controls and indicators to adjust beam pulse heights, lengths, and delays, focusing coil and quadrupole currents in the injector, and the frequency of the master oscillator. The same panel contains status lamp indicators for the principal injector components. Another panel, called the phase closure panel, contains remote controls for several phase shifters belonging to the injector system. These are used to optimize electron bunch parameters and the beam energy spectrum. In addition to meters that verify the action of remote controls, there are pulse oscilloscopes which may be connected to selected pulse sources in the injector and elsewhere. These oscilloscopes have controls to displace base lines and to brighten or dim traces to help distinguish pulses belonging to different beams.

BEAM GUIDANCE AND MONITORING. One of the beam operator's major jobs is to steer the beam, using adjustable magnetic dipole deflection coils, so that it can travel 3 km through a 2.2-cm diameter hole without striking the wall anywhere. Two long rows containing thirty-nine lever switches each are provided for the control of the vertical and horizontal steering dipoles installed along the accelerator waveguide. Above the steering switches are four oscilloscopes which display multiplexed signals, originating from beam intensity and position monitors installed along the accelerator. Each indicator can be made to display up to six rows of dots, corresponding to beam intensity or position along the machine for up to six electron beams. Two of these units indicate vertical and horizontal steering errors. One displays beam intensity or linear Q, measured by toroidal ferrite core monitors. The other unit shows log Q, a signal generated as a by-product in the normalizing circuits that convert 2856-MHz signals to vertical and horizontal steering error signals. To help reduce error and confusion in the beam steering operation, a special brightening circuit has been provided. When a steering switch is operated this circuit brightens a dot on the appropriate position monitoring oscilloscope which corresponds to the position monitor readout at the end of the next sector. Another oscilloscope displays a video pulse train, originating in the machine protection, long ion chamber (PLIC); its signal indicates beam power loss as a function of distance along the machine. The PLIC oscilloscope is frequently very useful in beam steering and focusing adjustments. The PLIC signal is also connected to a discriminator which shuts off the beam whenever the PLIC signal exceeds a preset level.

The electron beam is focused by quadrupoles installed at intervals along the accelerator, which are adjusted by means of controls in a switched sector panel, located to the beam operator's left. Quadrupole currents can also be adjusted through the two similar panels in the maintenance console.

ENERGY SPECTRUM MONITORING AND ADJUSTMENT. In the BSY the electron beam is magnetically deflected and its spectrum analyzed. The spectrum signals are multiplexed in the DAB, transmitted to CCR, and displayed on two oscilloscopes, one for each end station, in the beam operator's console. To produce a good energy spectrum, the beam operator must first switch to the "accelerate" state as many klystrons as are necessary to produce slightly more than the required beam energy, making sure that all klystrons are properly phased. Then, he must misphase two klystrons, adjusting by equal and opposite amounts until the beam energy is correct. In this way, he can make the length of the effective accelerating voltage vector of the whole machine equal to the required beam energy per electron. To produce a narrow spectrum, he must also make sure that the phase of the machine voltage vector and the mean phase of the electron bunch are identical. In addition, he must correct for beam loading by a timing adjustment, making some klystrons fire about 0.8 μsec late. Producing a good spectrum is sometimes a "cut-and-try" process. Upon occasion, the operator must make small adjustments in each

parameter, and watch the effect of each upon the spectrum shape before he proceeds to make another trial adjustment.

For the purposes of energy control, high-power klystrons along the machine can be divided into four classes. Klystrons belonging to the injector, Sector 1, and the positron source are not ordinarily manipulated for energy control. Klystrons in Sector 28 have special pattern controls, so that they can each be assigned to any beam or combination of beams, or switched to "standby." Klystrons in Sector 27 have pattern controls like those in Sector 28, and in addition each has a phasing control that is manually adjustable by the beam operator. The remaining klystrons are all divided, for pulse pattern purposes, into sector groups of eight. All klystrons in each ordinary sector are constrained to pulse on the same pattern when they are in the "accelerate" state. Any of these klystrons can be switched to the "standby" state by the beam operator. In this state, a klystron continues to pulse, producing its normal RF power output at its normal rate, but with its trigger timed to be 20 to 30 μsec too late to accelerate the beam. Unlike the practice with some linacs, at SLAC the klystron pulse heights are not ordinarily adjusted to control beam energy.

The spectrum oscilloscopes, the special controls, and indicators for Sectors 27 and 28, the phase closure panel, and certain other indicators related to the BSY and DAB are all located in one rack immediately to the right of the beam operator's switched sector panel, which forms the extreme left end of the operations panel cluster. The switched sector panel contains controls and indicators used for switching klystrons to "accelerate" or "standby," and for sector timing and phasing adjustments. At the time of writing (July 1967), it is planned to install circuits along the machine which would reduce the time and effort required to select and switch klystrons to "accelerate" or to "standby" by making these operations largely automatic. Controls and indicators for this system will be mounted to the operator's right. With this system, it is hoped to reduce the downtime occasioned by malfunctioning klystrons and modulators.

Maintenance and servicing

The success of the beam operator depends upon satisfying many preliminary requirements. The maintenance supervisor is responsible for seeing that the hardware requirements are met and for dispatching maintenance men and materials along the klystron gallery as required. He is also responsible for monitoring and controlling the personnel and machine protection systems. In the maintenance console (Fig. 15-26), he has two switched sector panels, similar to the one provided for the beam operator. Each has detailed indicators which report such faults as open interlocks, faulty klystrons, closed valves, defective power supplies, and other obstacles to satisfactory beam operation, in any sector to which it is connected. Each has many remote control buttons. Some remote control functions are adjusting klystron pulse voltage and sub-booster phasing and timing, initiating the automatic phasing program,

switching klystrons to "accelerate" or "standby," and operating safety interlock relays. In each case, a status lamp or a panel meter indicates the response to the control action. Panels similar to switched sector panels are provided in the maintenance console which terminate signal channels between CCR and the injector and BSY. Other panels provide indications of the status of special elements of the machine and personnel protection systems, and the remote controls belonging to these systems.

Programming

Preliminary adjustments must be made upon occasion in order to establish a new set of electron beam parameters so that a new experiment may be brought into operation. These changes must be made in such a way as to cause the least possible interference with experiments in progress. Part of this problem can be solved by proper switching of pulse pattern circuits and indicator circuits. This activity is carried out largely in the programming area in the backup console, indicated in Fig. 15-26. The backup console also contains remote controls and indicators which are less frequently used than those which are mounted in the operations and maintenance consoles.

Acknowledgments

The successful completion of the two beam analyzer stations in time for the early beam tests was largely due to the work of E. L. Roskowski, who did almost all the mechanical design work and supervised fabrication, installation, and testing. The control and readout electronics systems were designed and tested by A. R. Wilmunder. Thanks are also due H. Brechna, who, although deeply involved in magnet design work for the beam switchyard, found time also to design the magnet for the analyzer stations.

References

1 P. Brunet, J. Dobson, M. J. Lee, and C. B. Williams, "Microwave Beam Position Monitors," Tech. Note No. SLAC-TN-64-45, Stanford Linear Accelerator Center, Stanford University, Stanford, California (July 1964).

2 M. J. Lee, "The Effect of Rotation of a TM_{120} Cavity on the Amplitude and Phase of the Beam-Induced Signal," Tech. Note No. SLAC-TN-64-66, Stanford Linear Accelerator Center, Stanford University, Stanford, California (October 1964).

3 R. Bergere, A. Veyssiere, and P. Daujat, *Rev. Sci. Instr.* **33**, 1441 (1962).

4 L. H. Johnston, J. Faust, W. Pierce, and M. Stangenes, *IEEE Trans. Nucl. Sci.* **NS-14**, No. 3, 1106 (June 1967).

5 O. Altenmueller and P. Brunet, "Some RF Characteristics of the Beam Phase Reference Cavity," Tech. Note No. SLAC-TN-64-51, Stanford Linear Accelerator Center, Stanford University, Stanford, California (September 1964).

6 R. S. Larsen and H. A. Woods, *IEEE Trans. Nucl. Sci.* **NS-12**, No. 3, 862 (June 1965).

7 R. S. Larsen, "Design of Beam Position and Charge Monitoring Circuits for the Stanford Two-Mile Accelerator," Rept. No. SLAC-63, Stanford Linear Accelerator Center, Stanford University, Stanford, California (May 1966).

8 B. de Raad, "Some Visual Beam Observation Methods of Interest for the Beam Switchyard," Tech. Note No. SLAC-TN-64-4, Stanford Linear Accelerator Center, Stanford University, Stanford, California (January 1964).

9 D. Reagan, *Rev. Sci. Instr.* **37**, 1190 (1966).

10 SLAC Staff, "Consolidation of Results of Preliminary Beam Tests with Sectors 1 and 2," Rept. No. SLAC-50, pp. 66, 69, Stanford Linear Accelerator Center, Stanford University, Stanford, California, (September 1965).

11 See, for example, J. J. Livingood, *Principles of Cyclic Particle Accelerators*, Van Nostrand, Princeton, New Jersey, 1961.

12 S. Penner, *Rev. Sci. Instr.* **32**, 150 (1961).

13 M. J. Lee and A. W. Burfine, "Magnetic Field Measurements and Energy Calibration of the Beam Analyzing Station Spectrometers," Tech. Note. No. SLAC-TN-65-21, Stanford Linear Accelerator Center, Stanford University, Stanford, California (1965).

14 M. J. Lee, "Some Calculations on the Aluminum SEM Foils," SLAC Internal Memorandum, Stanford Linear Accelerator Center, Stanford University, California (1965).

15 M. J. Lee, "An Ion Chamber in Air for the Beam Analyzing Station Interlocks," Tech. Note No. SLAC-TN-65-30, Stanford Linear Accelerator Center, Stanford University, Stanford, California (April 1965).

16

THE POSITRON SOURCE

H. Brechna, K. E. Breymayer, K. G. Carney, H. DeStaebler, R. H. Helm, and C. T. Hoard

The purpose of this chapter is to describe the positron source and all its associated subsystems. Following the introduction, the chapter is divided into three major parts: (1) a discussion of general design considerations including the radiator, the focusing system, and predicted yields; (2) a description of the system including the various radiators, the focusing magnets, and special instrumentation and controls; and (3) a summary of early operating experience.

16-1 Introduction (HDeS)

The positron beam at SLAC is generated by a technique similar to that used at other electron linacs.[1,2] An electron beam is accelerated in the first third of the machine and, at an energy of about 5 GeV, it strikes a radiator located on the axis of the machine. The radiator is several radiation lengths thick. A small fraction of the positrons emerging from the radiator is focused and accelerated in the remaining two-thirds of the machine in which the RF phase is shifted by about 180°. The positron beam is characterized by a maximum energy which is two-thirds of the maximum electron beam energy, by an intensity which is a small percentage of the intensity of the electron beam striking the radiator, and by a transverse phase space which is much larger than that of the usual electron beam. In fact, the phase space is about the maximum that the machine will transmit, 0.15π (MeV/c)(cm).

The SLAC system differs from other positron systems largely because of the high power available in the incident electron beam (up to several hundred kilowatts) and the high energies involved. The high power gives rise to severe thermal problems, both pulsed and steady-state and also to significant radiation problems. Levels on the order of 10^7 rad/hour are anticipated near the radiator

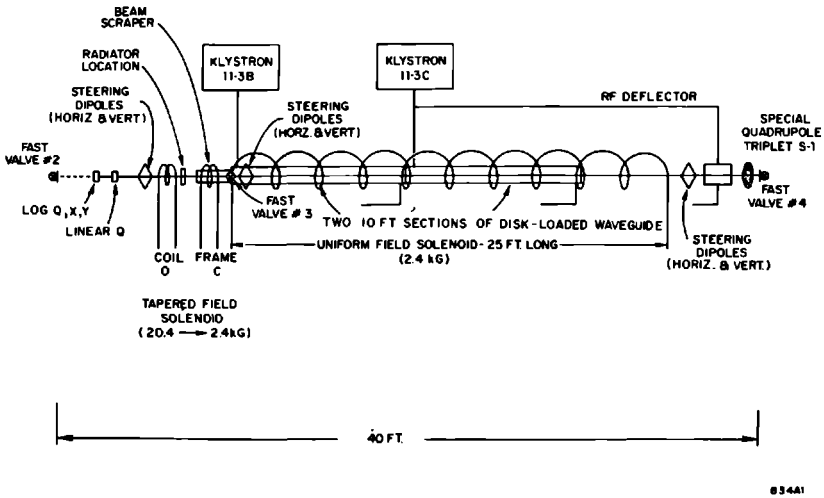

Figure 16-1 Positron source overall layout.

when it is in use at full beam power, and residual radiation levels of 10 rad/hour have frequently been encountered in early operation at about one-tenth of full power. Since the incident electron beam has an energy of 5 to 6 GeV, the radiator should have a thickness about equal to the shower maximum at this level; in copper, for example, this thickness is several inches. The system that has been built has a wide positron energy acceptance. Such a system seemed promising because the initial energy spread of the positrons at the source

Figure 16-2 Positron focusing system layout.

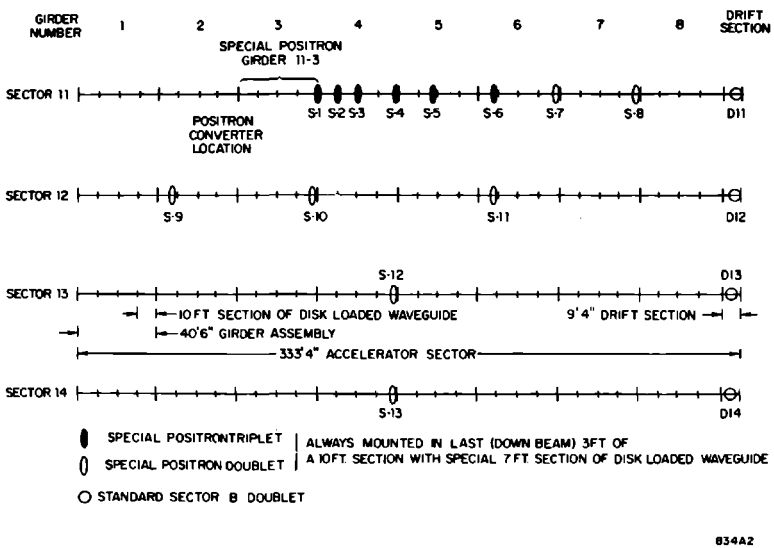

(typical useful range between 5 and 15 MeV) becomes unimportant at the end of the machine in relative value, when the positrons emerge at energies of several gigaelectron volts.

The decision to locate the radiator one-third of the way from the injector was rather arbitrary. It represented a compromise between the conflicting desires of high positron intensity, which requires high electron power incident on the radiator, and high final positron energy, which requires that the radiator be placed toward the front end of the accelerator. The experimental uses anticipated for the positron beam were for the scattering of positrons on protons, for a monochromatic photon beam arising from positron–electron annihilation, and possibly for injecting into a positron–electron storage ring.

Figures 16-1 and 16-2 show a layout of the major in-line elements in the positron source system.

16-2 General design considerations

Radiator (HDeS)

The basic design of the radiator is conditioned by the development of the electromagnetic cascade shower. The rate at which energy is absorbed determines the thermal problems. The positron distribution in energy, angle, and transverse position determines the source emittance for the positron beam.

All present SLAC radiators are being made of copper. Preliminary considerations indicated that materials with a large atomic number, Z, would be best, but in such materials the specific heat is low and the linear dimensions are small so that the heating problems are very severe. Furthermore, the positron yield at 0° from copper is only about 20% less than that from lead. The positron yield per incident electron is approximately proportional to the electron energy so that the positron current is proportional to the incident power.

The rate of energy deposition in copper according to a one-dimensional Monte Carlo calculation is shown in Fig. 16-3.[3] The incident electron beam is typically 1 mm in diameter, and near shower maximum the effective radius is 2 or 3 mm.[4] An elementary and approximate steady-state heat transfer calculation for a "slug" radiator suggests that it should melt in the neighborhood of 100-kW incident power.[5] Under test conditions, one "slug" melted between 120 and 140 kW,[5] and this empirical knowledge is guiding the design of future solid copper radiators.

The maximum azimuthal and radial thermal stresses, $(\sigma_\theta)_{\max}$ and $(\sigma_r)_{\max}$, arising from one pulse may be estimated from the formulas derived for a thin circular plate:

$$(\sigma_\theta)_{\max} = -(\sigma_r)_{\max} = \frac{E\alpha\,\Delta T_p}{2} \tag{16-1}$$

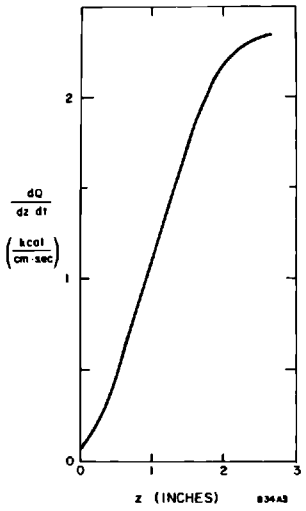

Figure 16-3 Heat deposition as a function of depth for 100 kW of 5-GeV electrons incident on copper.

where E is Young's modulus, α is the coefficient of thermal expansion, and ΔT_p is the temperature rise accompanying one beam pulse. This temperature rise is approximately

$$\Delta T_p = \frac{1}{\rho C_p \pi a^2} \frac{dQ}{dz\ dt} \frac{1}{v} \tag{16-2}$$

where

ρ = the density ($\rho = 8.9$ for copper)
C_p = the specific heat (0.09 cal/g°C for copper)
a = the radius of energy deposition (3 mm)
$dQ/(dz\ dt)$ = the rate of heat deposition from Fig. 16-3
v = the accelerator repetition rate (360 pulses/sec)

For an incident beam of 100 kW,

$$\Delta T_p = 27^{\circ}\text{C/pulse}$$

and

$$\sigma_{\max} = 3600 \text{ psi}$$

which is near the tensile strength for OFHC copper at high temperature (700°C). This implies that cyclic fatigue failure may take place. So far, no failure has been observed after limited operation at 30 to 40 kW.

A liquid radiator was also considered. It has various conceptual advantages but, at present, the accompanying practical uncertainties and complexities seem to outweigh the advantages. In general, experience at SLAC has indicated

Table 16-1 Measured positron yields

E_0 (*in GeV, e^-*)	*Material*	*Thickness (in radiation lengths)*	$\left(in \frac{\frac{dn}{E_0\, dP\, d\Omega}}{e^+}\right)$ $\left(\frac{}{(GeV, e^-)(MeV/c) \cdot Steradian}\right)$	*Reference*
0.22	Lead	Optimum (1.7)	0.22	Orsay (Ref. 6)
0.165	Lead	Optimum (1.7)	0.22	Orsay (Ref. 6)
1.0	Lead	2.9	0.175	SLAC (Ref. 7)
1.0	Copper	3.0	0.143	SLAC (Ref. 7)

that simplicity, ruggedness, and reliability are preferable to a sophisticated, nonconservative design even though such a design may promise somewhat higher performance.

The detailed distribution in energy, angle, and transverse position of positrons from the radiator is not known very well. It is difficult to compute, even by Monte Carlo techniques, because there are so many variables. A useful quantity that has been measured is the specific positron yield at zero degrees, that is, the number of positrons per steradian at 0° per million electron volt (E) of positron energy per incident electron of energy E_0(GeV). The measured yields are given in Table 16-1. The SLAC yields may be slightly low because of excessive multiple scattering. They dropped somewhat for angles greater than zero; they were fairly constant for E from 5 to 16 MeV but dropped at 35 MeV. The Orsay yields peaked around E equal to 10 to 15 MeV.

Calculated yield (HDeS)

A calculation of the yield of positrons at the end of the machine depends on the beam transport properties of the focusing system of the accelerator as well as on the source emittance. In principle, the beam transport could be calculated; however, at present, there is insufficient information about the five-dimensional source emittance. The five variables are the position and momentum in both transverse directions, and the longitudinal momentum (or total energy divided by c which nearly equals the longitudinal momentum). However, a rough estimate of the yield may be obtained using simple approximations of both the beam transport and the source emittance.

An approximation of the source emittance is obtained by integrating separately over the positron beam cross section, the transverse momentum, and the longitudinal momentum. The integration over cross section is done, effectively, by using the specific yield measured at 0°. The maximum value of transverse momentum at the source that is transmitted is about 0.5 MeV/c. This number may be estimated by noting that the product of maximum transverse momentum and maximum transverse displacement is constant throughout the accelerator, with numerical value 0.15 (MeV/c)(cm), and that an

approximate value for the source radius is 0.3 cm. It seems reasonable to make a rough correction for the way the multidimensional source emittance is handled. The volume of a four-dimensional ellipsoid is $(\pi^2/2)(abcd)$, where a, b, c, d are the semiaxes. The integration over cross section is done as if the area were πab, so that the integration over angle should contain the extra factor of $\frac{1}{2}$, $(\pi/2)cd$. A reasonable range of longitudinal momentum is 6–11 MeV/c because this initial energy spread by itself would give rise to a spread in RF phase angle leading to a final energy spread equal to 0.75% (full width), and it is plausible to assume that general machine operation would broaden this to 1%.

Based on these assumptions, the yield can be calculated as follows:

$$\begin{aligned}\frac{n}{E_0} &= f\int_{P_1}^{P_2} dP \int_0^{p/P} \frac{dn}{E_0\, dP\, d\Omega}\, 2\pi\theta\, d\theta \\ &\approx f\pi\left(\frac{dn}{E_0\, dP\, d\Omega}\right)\int_{P_1}^{P_2}\left(\frac{p}{P}\right)^2 dP \\ &= f\pi p^2\left(\frac{dn}{E_0\, dP\, d\Omega}\right)\left(\frac{1}{P_1}-\frac{1}{P_2}\right)\end{aligned} \tag{16-3}$$

Numerically, one obtains

$$\frac{n}{E_0} = 4.5 \times 10^{-3} e^+ \qquad \text{into} \quad 1\%/\text{GeV incident } e^-$$

where

$f = 0.5$ is the correction factor for the four-dimensional phase space
$dn/E_0\, dP\, d\Omega = 0.15\ e^+/\text{GeV (MeV}/c\text{) steradian}$ is the measured specific yield at 0°
$p = 0.5$ MeV/c is the maximum acceptable transverse momentum
$P_1, P_2 = 6$ MeV/c, 11 MeV/c are the limits of the acceptable longitudinal momentum

Thus, the estimated specific yield, which is probably an upper limit, is 4.5×10^{-3} positron in a final energy width of 1%/GeV of an incident electron; this number is about 3 times larger than the observed yield.

It is interesting to note that a broad phase spectrum can still give a rather sharp energy spectrum although perhaps of low intensity. For example, if the number of positrons per unit RF phase angle is $dn/d\phi$, then the number per unit final energy is

$$\frac{dn}{dE} = \frac{d\phi}{dE}\frac{dn}{d\phi} = -(E_{\max}^2 - E^2)^{-1/2}\frac{dn}{d\phi} \tag{16-4}$$

where

$$E = E_{\max}\cos\phi$$

For constant $dn/d\phi$ (the least favorable case)

$$n = \int_E^{E_{max}} \frac{dn}{dE}\, dE = \frac{dn}{d\phi} \int_0^{\cos^{-1}(E/E_{max})} d\phi = \left(\cos^{-1} \frac{E}{E_{max}}\right) \frac{dn}{d\phi}$$

$$\approx \left[2\left(1 - \frac{E}{E_{max}}\right)\right]^{1/2} \frac{dn}{d\phi} \quad \text{for} \quad \frac{E}{E_{max}} \approx 1 \qquad (16\text{-}5)$$

This formula shows that the particle density per unit energy interval is maximum close to the crest. Thus, for example, 45% of the beam that is within 5% of E_{max} is actually within 1% of this energy.

Focusing (RHH)

GENERAL PROPERTIES. The positron focusing system functions as a phase-space transformer between the low-energy and large transverse momentum particles emitted by the radiator, and the transport systems of the accelerator and beam switchyard (BSY) which have admittances characterized by small transverse momentum acceptance even at high beam energies.

Table 16-2 lists some parameters relevant to the SLAC positron transport system. The arbitrary design admittance of 0.15π (MeV/c)(cm) is a reasonable compromise between positron yield and the admittance limitations of the BSY and accelerator.

Note that the BSY admittance is compatible with the design admittance at momenta down to $P \approx 2$ GeV/c. The admittance of the accelerator transport system becomes 0.15π (MeV/c)(cm) at a momentum of about 2.5 GeV/c, or four sectors of acceleration; this means that special focusing provisions are required for about four sectors following the positron radiator.

Table 16-2 Parameters affecting positron transport design

Beam switchyard (A-beam)[a]	
Vertical (y) admittance[b]	$0.7\pi\, P \times 10^{-4}$
Horizontal (x) admittance	$1.15\pi\, P \times 10^{-4}$
Accelerator (sector doublets)[c]	
Admittance (x and y)	$0.6\pi\, P \times 10^{-4}$
Radial aperture	0.85 cm
Radiator emittance	
Typical transverse momentum	$\sim$15 MeV/c
Inherent shower radius (normal density Cu radiator)	$\sim$1 mm
Typical source radius (dependent on focusing of e^- beam)	1–3 mm
Nominal design admittance for positron transport	0.15π (MeV/c)(cm)

[a] See Chapter 17 for details of BSY design. B-beam admittances are approximately a factor of 2 greater than A-beam admittances.

[b] Admittances are expressed as phase ellipse areas in units of (MeV/c)(cm), where P, the longitudinal momentum, is expressed in MeV/c.

[c] See Chapter 7 for details of accelerator transport system.

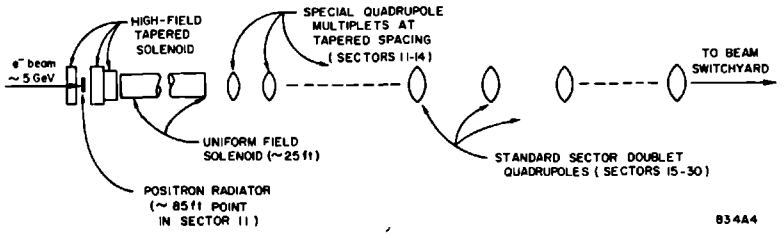

Figure 16-4 Schematic diagram of positron transport components.

Figure 16-4 illustrates schematically the overall layout of positron transport components. Briefly, the operation is as follows: the high-field tapered solenoid transforms the large divergence, small radius emittance at the radiator into a more nearly parallel beam at somewhat larger radius. The uniform-field solenoid then holds the beam together through several accelerator sections, until the energy is high enough for injection into a system of quadrupole lenses at finite spacing. The spacing of the quadrupole lenses tapers up approximately in proportion to the increasing beam energy, thereby maintaining constant admittance, until a match in the standard (sector doublet) focusing system is attained.

SHORT-RANGE FOCUSING—SOLENOIDS. First, a short digression will be made to review briefly the beam optical properties of a solenoidal magnetic field.[8-11] Consider the solenoid to have cylindrical symmetry about the z axis, in which case the field is derivable from a vector potential given by

$$\begin{aligned} A_r &= A_z = 0 \\ A_\phi &= J_1\left(r\frac{d}{dz}\right)\int_{-\infty}^{z} B(z_1)\,dz_1 \\ &= \tfrac{1}{2}rB(z) - \tfrac{1}{16}r^3B''(z) + \cdots \end{aligned} \tag{16-6}$$

where the "prime" denotes differentiation with respect to z;

$$\mathbf{B} = \nabla \times \mathbf{A} \tag{16-7}$$

and $B(z)$ is the z component of $\mathbf{B}$ evaluated along the z axis.

The general equation of motion*

$$m\frac{d}{dt}(\gamma \mathbf{v}) = e\mathbf{v} \times \mathbf{B} \tag{16-8}$$

may be rewritten in terms of the canonical momentum $\mathbf{p}$:

$$\begin{aligned} \mathbf{p} &= m\mathbf{v} + e\mathbf{A} \\ \frac{d\mathbf{p}}{dt} &= e\nabla(\mathbf{v} \cdot \mathbf{A}) \end{aligned} \tag{16-9}$$

* Gaussian units with $c = 1$ are used throughout this paragraph.

The well-known invariance of the canonical angular momentum, which ;ults from the cylindrical symmetry of **A**, may be expressed as

$$p_\phi = xp_y - yp_x = \text{constant} \tag{16-10}$$

Assuming that the motion is predominantly in the $+z$ direction and that ; transverse momentum is much smaller than the longitudinal momentum, .e can write the equations of motion in *first-order paraxial* expansion, using ıs. (16-6) and (16-9):

$$\begin{aligned} p_x' &= (Px' - \tfrac{1}{2}eBy)' = \tfrac{1}{2}eBy' \\ p_y' &= (Py' + \tfrac{1}{2}eBx)' = -\tfrac{1}{2}eBx' \end{aligned} \tag{16-11}$$

ıere the scalar momentum is

$$\begin{aligned} P &= m(\gamma^2 - 1)^{1/2} \\ &\approx p_z \text{ (first-order approximation)} \\ &\approx m\gamma \text{ (for relativistic electrons or positrons)} \end{aligned}$$

A useful simplification is found by transforming the above equations into ·otating coordinate system (ξ, η) (see Fig. 16-5), where the angle of rotation is the Larmor angle

$$\mu = \frac{1}{2}\int \frac{eB}{P}\,dz \tag{16-12}$$

The transformation in four-dimensional phase space is

$$\begin{bmatrix} \xi \\ p_\xi \\ \eta \\ p_\eta \end{bmatrix} = \begin{bmatrix} \cos\mu & 0 & \sin\mu & 0 \\ 0 & \cos\mu & 0 & \sin\mu \\ -\sin\mu & 0 & \cos\mu & 0 \\ 0 & -\sin\mu & 0 & \cos\mu \end{bmatrix} \begin{bmatrix} x \\ p_x \\ y \\ p_y \end{bmatrix} \tag{16-13}$$

d the equations of motion become simply

$$\begin{aligned} p_\xi' &= (P\xi')' = -\frac{1}{4}\frac{e^2B^2}{P}\xi \\ p_\eta' &= (P\eta')' = -\frac{1}{4}\frac{e^2B^2}{P}\eta \end{aligned} \tag{16-14}$$

Figure 16-5 Definition of rotating coordinate system (ξ, η).

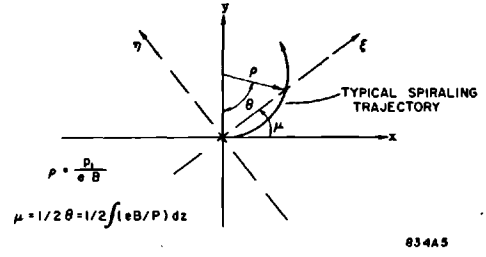

i.e., in the rotating coordinate system, the ξ and η motions are decoupled and are expressed by the differential equation of a simple linear oscillator. Thus, the essential properties of solenoid optics may be described in terms of a one-dimensional motion.

If the parameter $B(z)$ is slowly varying, one may employ the well-known WKB approximation for the solution of Eq. (16-14); the result is

$$\begin{bmatrix} \xi \\ p_\xi \end{bmatrix} = \begin{bmatrix} \left(\frac{B_i}{B}\right)^{1/2} \cos\mu & \frac{2\sin\mu}{e(B_i B)^{1/2}} \\ -\tfrac{1}{2}e(B_i B)^{1/2}\sin\mu & \left(\frac{B}{B_i}\right)^{1/2}\cos\mu \end{bmatrix} \begin{bmatrix} x_i \\ p_{xi} \end{bmatrix} \tag{16-15}$$

where the subscript i denotes initial values, $\mu(z_i) = 0$ so that $x_i = \xi_i$ and $p_{xi} = p_{\xi i}$. The result for (η, p_η) is analogous. It may be shown that a sufficient condition for validity of the WKB approximation is

$$|B'| \ll |\mu' B|$$

or

$$\left|\frac{B'}{B^2}\right| \ll \frac{e}{2P} \tag{16-16}$$

The transformation in (x, p_x, y, p_y) space may be found from Eqs. (16-13) and (16-15),

$$\begin{bmatrix} x \\ p_x \\ y \\ p_y \end{bmatrix} = \mathbf{R}^{-1} \begin{bmatrix} \mathbf{A} & \mathbf{O} \\ \mathbf{O} & \mathbf{A} \end{bmatrix} \begin{bmatrix} x_i \\ p_{xi} \\ y_i \\ p_{yi} \end{bmatrix} \tag{16-17}$$

where $\mathbf{R}$ is the 4×4 rotation matrix in Eq. (16-13), and $\mathbf{A}$ is the 2×2 matrix in Eq. (16-15).

It can be shown from Eq. (16-15) that the quantity

$$I_2 \equiv \tfrac{1}{2}eB\xi^2 + \frac{2}{eB}p_\xi^2 \tag{16-18}$$

is conserved along a given trajectory if Eq. (16-16) holds, i.e., I_2 is an *adiabatic invariant*. The area enclosed by this elliptical phase orbit is

$$u \equiv \pi I_2 = \pi\left(\frac{1}{2}eB\xi^2 + \frac{2}{eB}p_\xi^2\right) \tag{16-19}$$

Similarly, it may be shown from Eq. (16-17) that

$$I_4 \equiv \tfrac{1}{2}eB(x^2 + y^2) + \frac{2}{eB}(p_x^2 + p_y^2) = \tfrac{1}{2}eB(\xi^2 + \eta^2) + \frac{2}{eB}(p_\xi^2 + p_\eta^2) \tag{16-20}$$

is conserved. Another invariant function may be found by combining Eqs. (16-10) and (16-20):

$$J_4 \equiv I_4 - 2p_\phi$$

$$= \frac{2}{eB} P^2(x'^2 + y'^2) \equiv \frac{2}{eB} p_\perp^2 \tag{16-21}$$

It follows from Eq. (16-19) that the maximum (ξ, p_ξ) or (η, p_η) admittance of an adiabatically tapered solenoid of uniform radial aperture, a, is

$$U = \frac{\pi}{2} eB_{\min} a^2 \tag{16-22}$$

where $B_{\min}$ is the minimum value of B within the solenoid. The maximum initial transverse size and momentum which can be contained are

$$(x_i)_{\max} = \left(\frac{B_{\min}}{B_i}\right)^{1/2} a \tag{16-23}$$

$$(p_{xi})_{\max} = \tfrac{1}{2} e(B_i B_{\min})^{1/2} a \tag{16-24}$$

A fundamental limitation on the final energy spectrum of accelerated positrons is imposed by RF debunching caused by differences in transit time. If one neglects the bunching forces in the RF accelerating field, then to second order in the dynamic variables the relative phase slip is given by

$$\delta\phi = \omega\, \delta t \approx \frac{\pi}{\lambda} \int \left(\frac{1}{\gamma^2} - \frac{1}{\Gamma^2}\right) dz + \frac{\pi}{2\lambda} J_4 \frac{e}{m^2} \int \frac{B}{\gamma^2} dz + \cdots \tag{16-25}$$

where $m\Gamma$ is a reference energy, λ is the RF wavelength, and J_4 is the invariant function defined by Eq. (16-21).* Here the first term represents the effect of different velocities, and the second term represents the second-order path-length differences of trajectories with finite transverse phase space.

The above formulation can now be applied to actual design concepts. Two types of systems will be described: the "quarter-wave transformer" and the "tapered field solenoid."

Several existing or proposed positron facilities† use the "quarter-wave transformer" principle, so called because of its analogy with transmission line theory. Figure 16-6 illustrates the idealized operation of this type of system. The low-field region, B_f, is assumed to extend along a finite fraction of the accelerator, while the high-field region, B_i, which performs the matching function, turns out to be only a few centimeters long, as shown in Fig. 16-6a. In the phase-space diagram [Fig. 16-6b], the shaded area represents the "effective" radiator emittance, or region which is filled more or less uniformly with positrons. The erect ellipse (admittance) represents the accepted phase

* It may be shown that the limiting values of J_4 are 0 and $2U/\pi$.

† For example, linacs such as those at Frascati, DESY, and Saskatchewan, designed to give low or medium energy positrons.

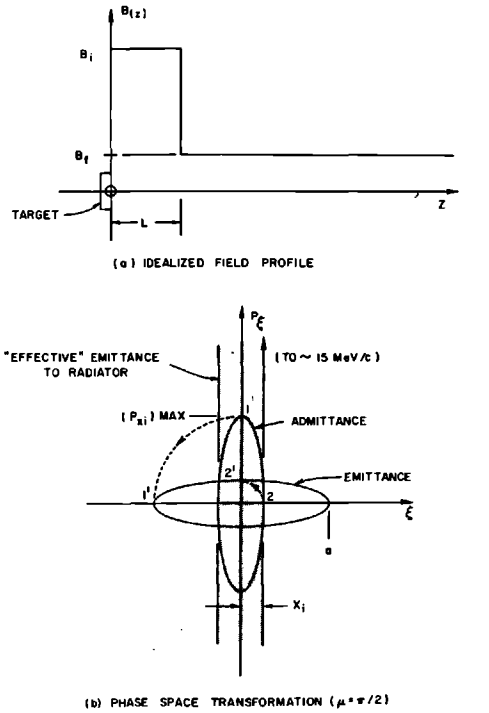

Figure 16-6 Illustration of the quarter-wave transformer principle ($\mu = \pi/2$) in positron matching.

space as seen at the radiator. The flat ellipse (emittance) represents the phase space accepted by the low-field region. The dashed curves 1–1′ and 2–2′ represent typical phase orbits through the high-field region ($\mu = \pi/2$).

The following relations represent optimum conditions for the quarter-wave transformer:

admittance

$$U = \frac{\pi}{2} eB_f a^2 \tag{16-26}$$

initial field strength

$$B_i = \frac{a}{x_i} B_f \tag{16-27}$$

effective length for $\mu = \pi/2$

$$L = \frac{\pi m \Gamma}{eB_i} \tag{16-28}$$

where a is the limiting aperture, x_i is the effective source width at the radiator, and $m\Gamma$ is the energy for which $\mu = \pi/2$. The energy spread that is satisfactorily matched, i.e., the bandwidth, is estimated as

$$\frac{\Delta\gamma}{\Gamma} \approx C\frac{B_f}{B_i} \tag{16-29}$$

where C is a geometric constant of order unity. The above relations are best illustrated by taking a numerical example. Using $U = 0.3\pi$ (MeV/c)(cm), $a = 0.95$ cm, $x_i = 0.2$ cm, and $m\Gamma = 8$ MeV, one obtains $B_f = 2.2$ kG, $B_i = 10.5$ kG, $L = 8$ cm, and $\Delta\gamma/\Gamma \approx 0.2$. The maximum transverse momentum captured from the radiator is $(p_{xi})_{max} = 1.5$ MeV/c, which, as assumed, is less than the effective transverse momentum at the radiator. The RF debunching through the high-field region is estimated to be about 0.2° from the velocity spread, the first term of Eq. (16-25), and about 2° from the phase-space-dependent term. Additional debunching in the low-field region will depend on how far the beam drifts before entering the accelerating field but will tend to be small because of the small value of $\Delta\gamma/\Gamma$.

The SLAC positron system makes use of a somewhat different initial matching scheme in that it has an adiabatically tapered solenoid rather than a quarter-wave transformer. The principle of the tapered solenoid may be understood from Eq. (16-19) which shows that the admittance area remains constant under a slow change in $B(z)$. The maximum size and maximum transverse momentum are $\xi_{max} = \{2u/[e\pi B(z)]\}^{1/2}$ and $(p_\xi)_{max} = [euB(z)/(2\pi)]^{1/2}$ from which it can be seen that, as $B(z)$ decreases, the size of the beam increases and the transverse momentum decreases. The interesting feature is that the transformation is independent of energy, so that the system is inherently broad-band in energy acceptance and can accept a large fraction of the initial positron spectrum.

The optimum conditions for the tapered solenoid are

admittance

$$U = \frac{\pi}{2} eB_f a^2 \tag{16-26}$$

initial field

$$B_i = \frac{a^2}{x_i^2} B_f = \frac{2}{\pi}\frac{U}{ex_i^2} \tag{16-30}$$

field profile

$$B(z) = \begin{cases} \dfrac{B_i}{1+\alpha z} & z \le L \\ B_f & z \ge L \end{cases} \tag{16-31}$$

length of tapered field

$$L = \frac{1}{\alpha} \frac{B_i - B_f}{B_f} \tag{16-32}$$

where

$$\alpha = \varepsilon \frac{eB_i}{m\Gamma} \tag{16-33}$$

and ε is an arbitrary small number of order 0.1; the other parameters have been defined earlier. The specified field profile results from the adiabatic validity condition, Eq. (16-16), with the assumption that the inequality should be equally well satisfied everywhere.* The useful energy bandwidth is limited at low energies by phase slip and at high energies either by phase slip, by failure of the adiabatic approximation, or by cutoff of the natural positron spectrum.

On the basis of the SLAC parameters, namely a design admittance of $U = 0.15\pi$ (MeV/c)(cm) and an accelerator aperture $a = 0.95$ cm, and assuming an effective source radius of $x_i = 0.2$ cm, one obtains $B_f = 1.1$ kG and $B_i = 25$ kG for the "optimum" final and initial fields. Actually a value of $B_f = 2.4$ kG has been chosen; this choice has the consequence that the useful positron beam in the uniform field region is confined to a radial size of $(x_f)_{\max} \approx 0.64$ cm which presumably makes the beam steering less critical in this region. On the other hand, the initial field is limited by practical considerations to a value of $B_i = 20.4$ kG, so that the initial matching is not quite optimum. The useful initial transverse momentum acceptance under these conditions is

$$(p_{xi})_{\max} \approx 0.7 \text{ MeV}/c$$

The field profile is based on an arbitrary choice of $L = 25$ in. for the tapered region, so that

$$B(z) = \frac{20.4 \text{ kG}}{1 + 0.118z(\text{cm})} \tag{16-34}$$

Taking the design energy to be $m\Gamma = 8$ MeV, one then finds that the adiabatic parameter, ε, is

$$\varepsilon = \alpha \frac{m\Gamma}{eB_i} = 0.154$$

The total Larmor angle through the tapered region is

$$\mu = \frac{1}{2} \int \frac{eB}{m\Gamma} dz = \frac{1}{2\varepsilon} \ln \frac{B_f}{B_i} = 2.2\pi \text{ rad}$$

* It is assumed that the taper takes place at constant positron energy, i.e., before entering the accelerating field.

There is an additional 5 in. of uniform field making a total of 30 in. between the radiator and the start of acceleration.

The useful energy acceptance is limited to a band from about 6 to about 11 MeV by velocity-dependent debunching, the first term of Eq. (16-25). The phase-angle spread in this band is about 14°, corresponding to a final spectrum width of $\approx 0.75\%$ for accelerated positrons. The maximum slip introduced by the phase-space-dependent effect, the second term in Eq. (16-25), is estimated as about 7°, which should not deteriorate the final spectrum seriously.

Figure 16-7 shows (a) the idealized field profile of the SLAC tapered solenoid and (b) the theoretical phase-space transformation from the source plane (admittance) into the uniform solenoid (emittance).

In summary, it is interesting to compare the properties of the quarter-wave transformer and the adiabatically tapered solenoids used as positron matching devices.

The quarter-wave transformer is characterized by rather moderate field strength requirements [note that $B_i = (a/x_i)\, B_f$], efficient use of magnetic field

Figure 16-7 Parameters of SLAC tapered positron solenoid.

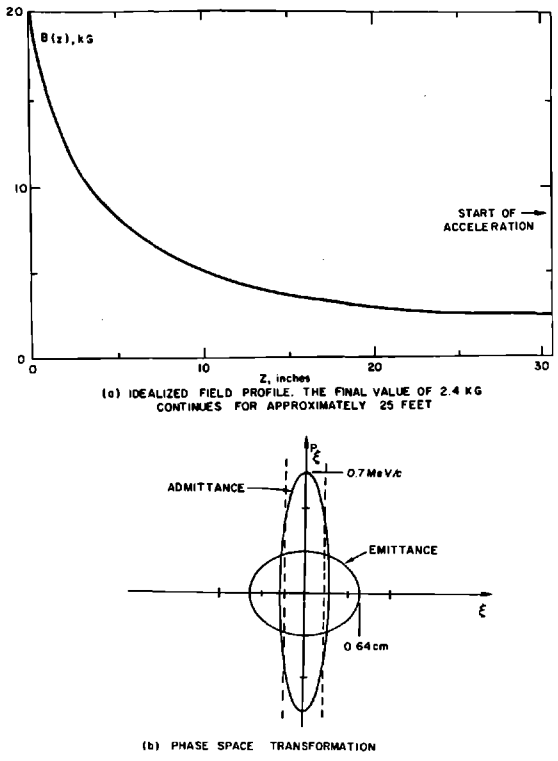

(e.g., relatively small stored energy), small RF debunching, and narrow-band acceptance of positron energies. These features tend to make this scheme ideal for machines in which the final positron energy is to be moderate or low, e.g., less than 1 GeV.

In the tapered solenoid, on the other hand, the field strength requirement tends to be rather extreme [note that $B_i = (a/x_i)^2 B_f$], and the magnetic energy is rather large (e.g., in the SLAC case, the power required for the 25-in. tapered field is comparable to that for the 25-ft uniform field section). The RF debunching tends to be severe, although the SLAC design is by no means optimized in this respect. The great advantage of the tapered system, for a very high energy machine, is its broad-band energy acceptance leading to theoretical positron yields of about an order of magnitude greater than for the quarter-wave transformer design.

Another advantage of the tapered system is that the field profile is quite uncritical. Because there is no need for a rapid transition from maximum to minimum field, the coil apertures may be quite large, thus providing space for protective collimators to shield the coils and accelerator structures from radiation. This feature is important in the SLAC case, where the power sprayed out of the radiator may be in excess of 100 kW; in fact, the need for the protective collimator is the main reason for placing the radiator 30 in. ahead of the first accelerator section, even though the debunching is worsened by this rather long drift length.

The validity of the adiabatic approximation has been probed by computer ray-tracing. It is found that the adiabatic approximation, with the field profile given above, is valid up to energies of about 30 MeV which corresponds to a value of ε of 0.58.

LONG-RANGE FOCUSING—QUADRUPOLES. In order to avoid the expense of extending the solenoids along the entire machine, a transition to quadrupole focusing is made as soon as the positron energy is high enough to permit reasonable spacing between the quadrupoles. For operational convenience, it was decided to use quadrupole multiplets—triplets or doublets. If the multiplets are short compared to their spacing, they may be treated to a first approximation as ideal, circularly symmetric, thin lenses.

The transport properties of such systems are summarized in some detail in Chapter 7. In the thin-lens approximation, the maximum phase ellipse which can be transported between two lenses located at z_n and z_{n+1} is

$$U_n = \frac{\pi a^2}{l_n} \tag{16-35}$$

where

$$l_n = \int_{z_n}^{z_{n+1}} \frac{dz}{P} = \frac{1}{m\gamma'} \ln \frac{\gamma_{n+1}}{\gamma_n} \text{ (assuming uniform acceleration)} \tag{16-36}$$

a is the limiting aperture, and $\gamma' = d\gamma/dz$.

Thus, to maintain a given admittance U through the system, the optimum lens spacing is

$$L_n = z_{n+1} - z_n = \frac{\gamma_n}{\gamma'}(e^{\beta} - 1) = L_0 e^{n\beta} \tag{16-37}$$

where

$$\beta = \frac{\pi a^2 m\gamma'}{U} \tag{16-38}$$

and

$$L_0 = \frac{\gamma_0}{\gamma'}(e^{\beta} - 1) \tag{16-39}$$

The focal lengths of the lenses are, then,

$$F_n = \tfrac{1}{2}\gamma_n l_n = \frac{\pi a^2 \gamma_0}{2U} e^{n\beta} \tag{16-40}$$

With the SLAC design parameters, $a = 0.85$ cm, $U = 0.15\pi$ (MeV/c)(cm), $m\gamma' \approx 0.06$ MeV/cm, and an arbitrary assumption of $L_0 = 300$ cm for one accelerator section, one obtains $m\gamma_0 \approx 53$ MeV for the positron energy at which the quadrupole focusing can begin. About twelve lenses would be required to taper up to a spacing of one sector $\approx 10^4$ cm, to match into the regular sector doublet focusing system.

The actual SLAC system uses compact, small aperture quadrupoles (0.6-in. bore radius, 4 and 8 in. in effective length). The overall physical length of the special multiplets is about 28 in. To make space for these multiplets, special, short (7 ft long) accelerator sections were fabricated. This system avoids the necessity of large aperture quadrupoles to fit around the accelerator sections ($\approx$3-in. radius) but makes it impossible to place the lenses with precisely the theoretical optimum spacing given above. Rather, the theoretical spacings were used as a guide in selecting the maximum allowable spacing between any pairs of lenses.

Figure 16-2 shows the locations of the various special focusing elements. Here S-1, S-2, . . . , S-13 are the special short multiplets and D11, D12, etc. are the regular sector doublets. Note that the regular doublets D11 through D14 are used as elements in this focusing system. In the original design concept, all of the multiplets were triplets. However, as part of the beam breakup improvement program,* all the sector lenses and some of the special positron lenses were converted to doublets. As of the present time (July 1967), lenses S-1 through S-6 are triplets and the remainder are doublets.

The TRANSPORT computer program has been used to determine the correct quadrupole settings. Figure 16-8 shows the theoretical admittance plots obtained by mapping the various defining apertures to the output end of the uniform field solenoid.

* See "The Magnetic Fix Program" in Section 7-5.

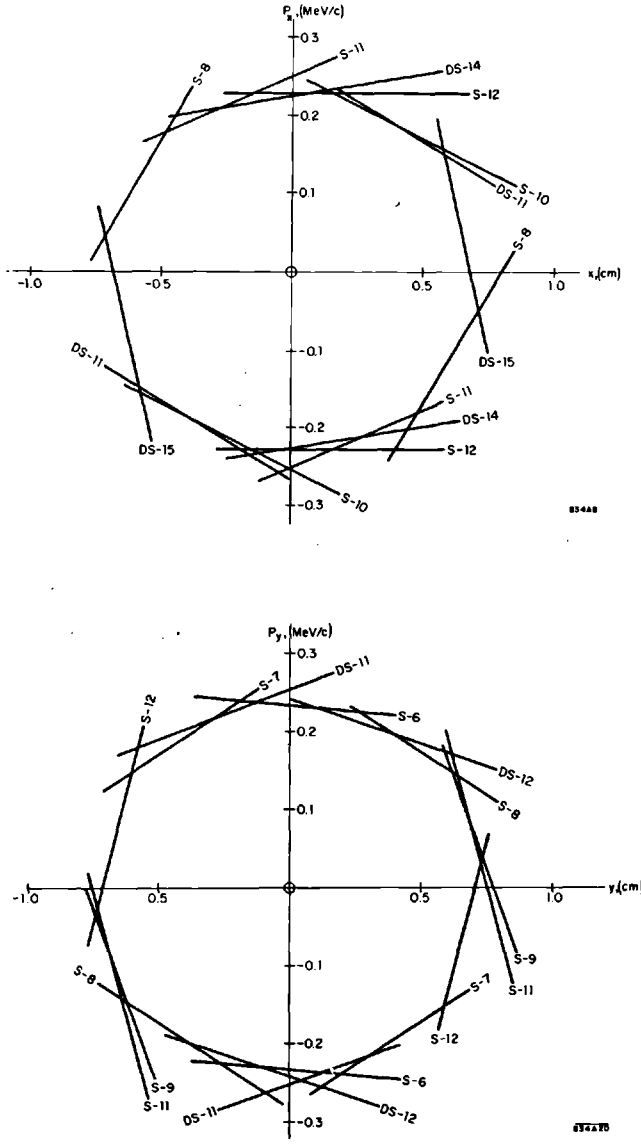

Figure 16-8 Computed admittance of long-range positron transport system, referred to the output end of the uniform solenoid; quadrupole strengths approximately optimized. Only those apertures that actually affect the admittance have been mapped on these plots (see Figure 16-2 for lens designations). (a) x, p_x plane; admittance $\cong 0.163\pi$(MeV/c)(cm); (b) y, p_y plane; admittance $\cong 0.166\pi$ (MeV/c)(cm).

16-3 Radiators (CTH)

Three different radiators are described in this section: the "slug" (temporary source), the "wand" (a few pulses per second source) and the "wheel" (continuous source). An overall view of the positron radiator area is shown in Fig. 16-18.

Before the construction of the wheel radiator could be completed, a continuous source of positrons was needed that could accept higher-power levels than the wand target is capable of handling when held stationary in the beam. This was the function of the slug.

Slug radiator

The slug radiator is a water-cooled copper block that can be held in the beam or retracted to allow operation of the wand.

TARGET. The target is a cylindrical block of OFHC copper (see Fig. 16-9) which has been slotted radially to provide water channels in a spiral configuration, but to a depth that keeps solid copper throughout the beam path. The block is brazed into a stainless steel case that forms the water chamber. The copper block is exposed only at the entrance and exit of the beam. Cooling water from a manifold (visible in Fig. 16-10) is injected at three points around the stainless steel case and flows axially through the slots to output tubes leading to a second manifold.

RETRACTION. A commercial pneumatic cylinder slides the support rod through pillow blocks for insertion and retraction. A bellows seals the vacuum chamber. To hold the vacuum load when air is turned off, a mechanical latch engages the support rod in the retracted position. The latch is lifted by a solenoid.

The control valve for the actuator is solenoid-operated and is mounted on the actuator stand. Flow control valves (needle and ball check) between the control valve and the actuator prevent rapid motion of the target.

SENSORS. Limit switches are tripped at each limit of travel. Signals appear on the instrumentation and control panel indicating "slug in," "slug out," and "in transit," and interlocks with the wand and with the beam are activated.

The exit face of the copper block carries three thermocouples that monitor the steady-state temperature at the edge of the beam and also indicate centering of the beam.

FLANGE. The flange for the slug radiator is the same as that for the wheel radiator described below.

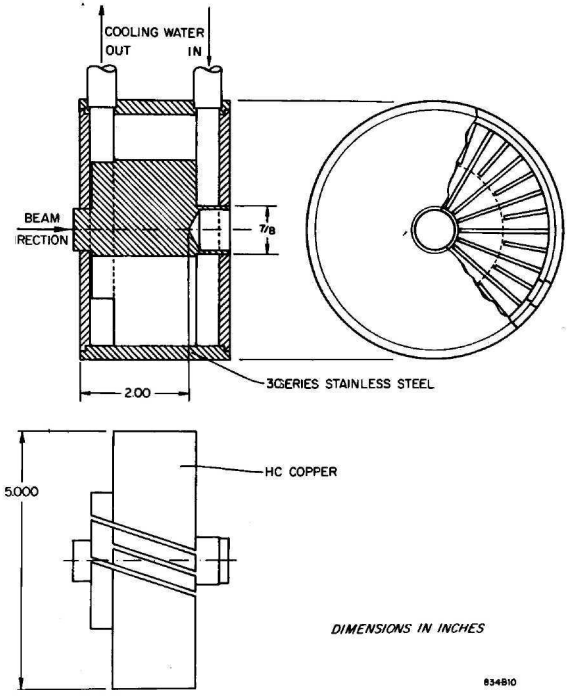

Figure 16-9 Assembly of slug radiator.

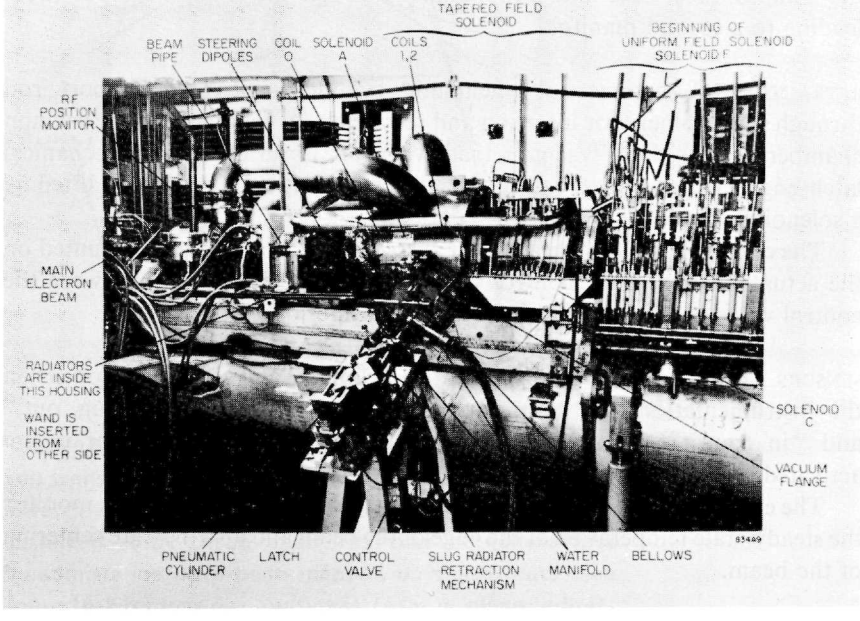

Figure 16-10 Overall view of positron radiator area with slug radiator installed.

Wand radiator

The wand radiator converts a particular electron beam pulse to positrons while allowing free passage to the other electron pulses. In operation, a slim arm swings the target through the beam. The speed of passage could not be too high because of the difficulty of synchronizing the center of the swing to the electron pulse timing. In actual operation, nine consecutive electron pulses (at the 360-pulses/sec repetition rate) are interrupted by inhibiting the trigger to the injector. This inhibition is lifted for the fifth pulse which produces the positrons. Positrons can also be produced on the return swing, and up to several positron pulses per second are possible. For some operating conditions, more than nine electron pulses must be interrupted because eddy currents in the radiator steer the electron beam which is only a fraction of an inch away.

TARGET. The target which is inserted into the beam consists of a solid copper block, 2.25 in. long in the beam direction (see Fig. 16-11). It is 0.38 in. wide in the direction of its swing and maintains this width over a height such that even a poorly centered beam is intercepted. Then it widens to 0.75 in., the width of five fins with 0.03-in. cooling-water slots. A stainless steel baffle plate covers the top edge of the slots to force the water to run along the full length.

A rectangular cover, also of stainless steel, is brazed to a shoulder around the copper block. The cover is the structural attachment for the target and also confines and directs the cooling water. After brazing the cover to the copper block, the end of the copper where the beam leaves the target is cut away about 0.26 in. to give the desired length of 2.25 in. Because showering increases through the block, the exit face has maximum heating; the removal of part of the copper has the effect of increasing the available cooling where it is most needed.

Figure 16-11 Wand target with stainless steel baffle plate and cover.

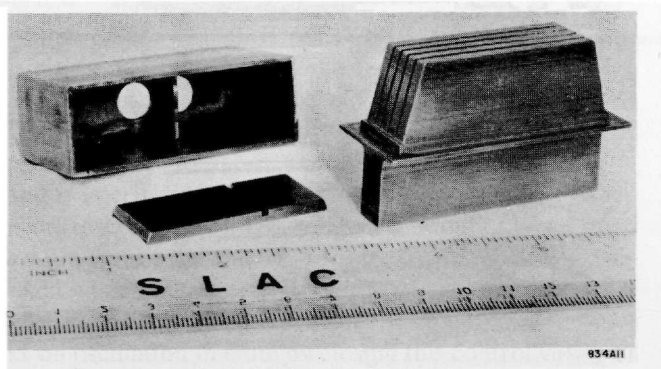

An alternative target, consisting of eleven plates normal to the beam with cooling water flowing between them, was built and tested. It had the disadvantage of requiring thin windows to separate water and vacuum along the beam line and its output of positrons gave only two-thirds of the production obtained from solid copper. This alternative target is shown in Fig. 16-12, attached to the wand actuation mechanism.

WAND. The wand itself is a pivoted support arm for the target case. It consists of two water tubes of 321 stainless steel (see Fig. 16-13) which are welded through the vacuum plate and end in flexible metal hoses. The vacuum plate is supported by two rocking brackets from the pivot. A drive arm connects the vacuum plate to an adjustment link on the oscillating actuator. Vacuum integrity is maintained by an oscillating bellows that seals the vacuum plate to the floor of the box. The pivot bearings straddle this bellows so that its midpoint lies on the pivot center line. When the wand oscillates, the bellows follow a simple rocking motion with stresses low enough to assure long life. Because of the rocking motion, journal bearings were used for the pivot. In order to withstand radiation, the bearings were turned from sintered bronze and vacuum impregnated with Shell VRT fluid E.

OSCILLATING ACTUATOR. The oscillating actuator consists of a pneumatic piston and cylinder, with air cushions at each end operating through the entire stroke. The cushion plungers are integral with the piston and nearly as large in diameter. The piston and plungers, as well as the piston rod seal, are made

Figure 16-12 Wand radiator and actuation mechanism ready for installation in the accelerator (target shown, requiring thin windows, was later replaced by the target shown in Figure 16-11).

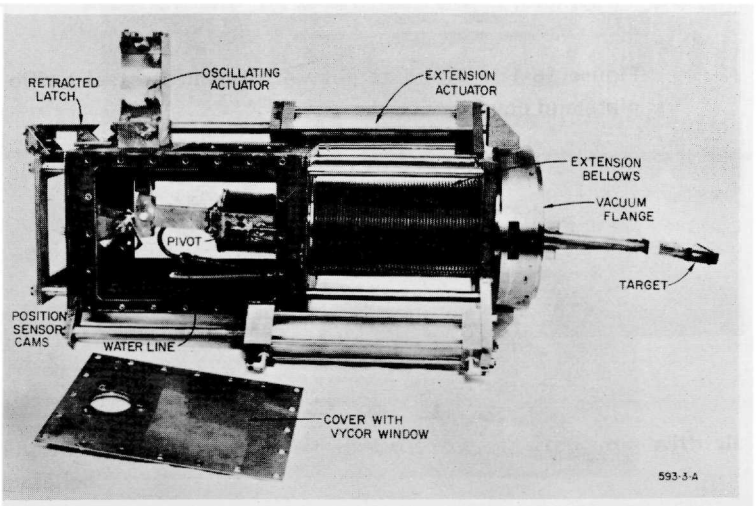

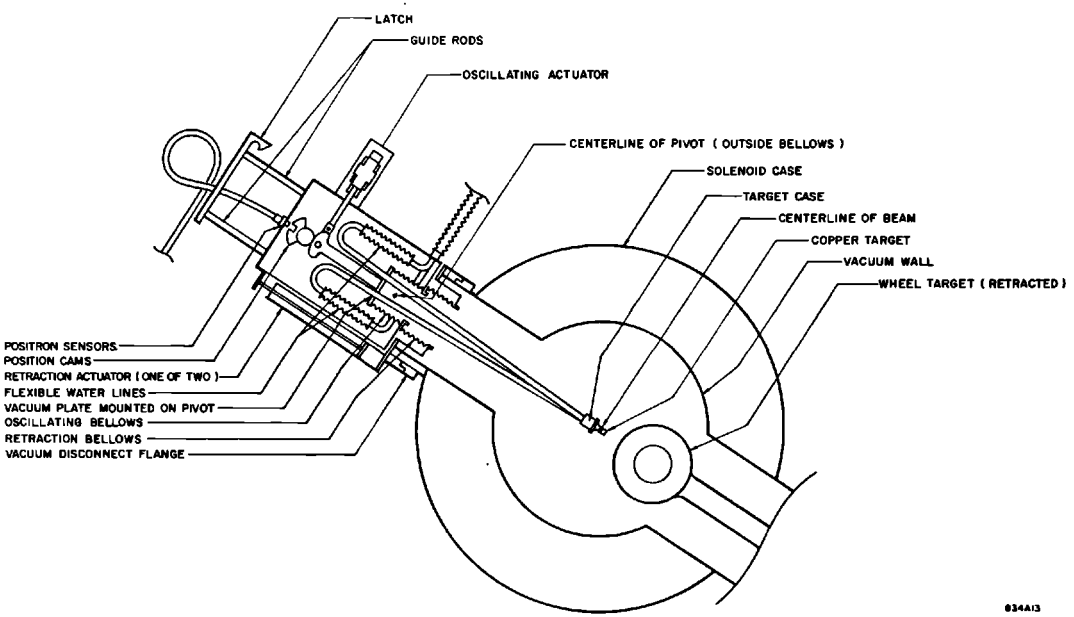

Figure 16-13 Diagram of wand target, positron source.

of impregnated bronze. Air leakage is controlled by close fits to the stainless case. Ball and needle valves in each end of the case control the cushioning. An adjustable link connecting the piston rod to the drive arms allows the wand to be roughly centered. Exact centering is not needed; it is necessary to know only when the wand passes through the beam and this is accomplished by adjustment of the position cams. An air valve, selected for fast response, controls the air to the oscillating actuator. The two solenoids that drive the valve spool are rated for ac power but are energized by a dc pulse to avoid time lags due to phasing. This valve must be connected by short lines to the actuator and is, therefore, mounted on the side of the positron strongback in the tunnel.

FLANGE. The wand flange carries a shallow, polished groove while the mating flange on the solenoid case has a deep, polished groove. The grooves were designed for a commercial seal ring but a solid indium ring of square cross section has proven superior.

OPERATION. The wand is interlocked to prevent insertion if the wheel target is occupying the chamber, to prevent oscillation if either wand or wheel microswitches change to an "in transit" signal, or if the vacuum, air, or water fail. The beam is interlocked while the target is close to the beam center line. Air to the oscillating valve in the tunnel passes through a control valve in the gallery. All interlocks on oscillation operate by closing this control valve. The

speed of the wand travel may be varied somewhat by altering the air pressure into the control valve by means of the regulator on the air panel in the gallery. Large changes in pressure require resetting of the cushion needle valves in the oscillating actuator to prevent impact or bounce. The latch and the centering bellows are actuated by air from the same regulator but their functions are independent of the air pressure within wide limits.

The wand moves across the beam line at a speed of 50 cm/sec, and it may be driven across up to 3 or 4 times/sec.

A small, spring-return bellows is mounted on the lower side of the wand box. The moving end of the bellows is connected by a small cable to the driving arm inside the box. When this bellows is actuated, the cable is pulled down to a stop and holds the wand target in the beam center line. This "hold" is used if the wand is to function as a fixed target. The flexibility of the actuating cable prevents the "hold" system from interfering with the normal oscillating motion of the wand.

Figure 16-14 Diagram of wheel target, positron source.

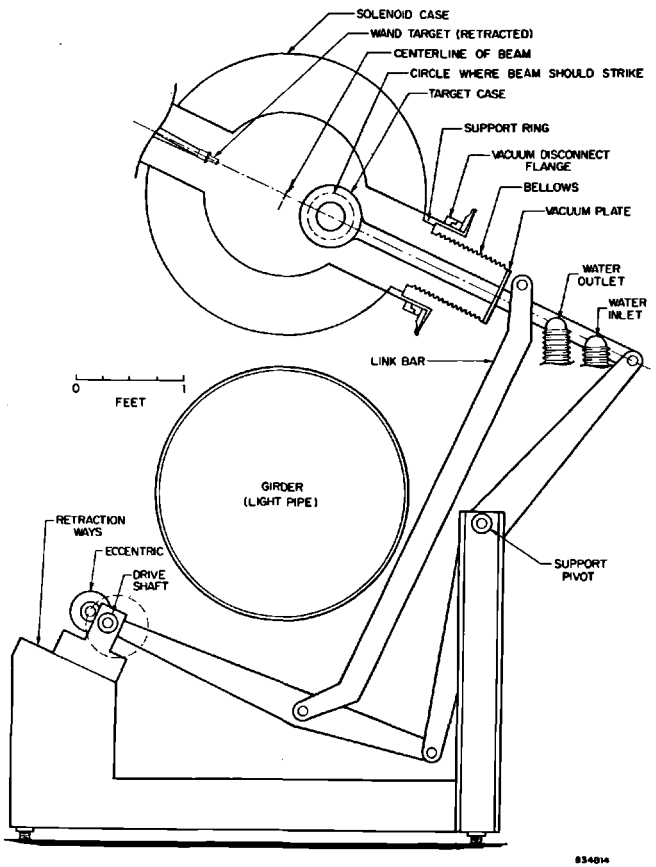

Wheel radiator

The wheel radiator is designed to provide positrons up to a repetition rate of 360 pulses/sec, using full electron beam power at Sector 11. The target moves in a circle with sufficient speed to minimize the overlap by successive incident beam pulses. Because of concomitant sealing problems, the driving mechanism was designed not to rotate but to "troll" the target (see Fig. 16-14.)

TARGET. The target is a solid copper ring, 2.1 in. thick along the beam axis with circumferential water-cooled fins. A stainless-steel case covering the fins contains the cooling water and is welded to the drive arm (see Fig. 16-15). The case is brazed to the copper at a radius sufficient to prevent the beam from hitting the joint under any condition of steering.

A series of pins blocks the water slots at the junction with the drive arm to prevent short-circuiting between inlet and outlet water flows. Because of the increased particle flux from showering, heat deposition increases through the ring. The downbeam face of the ring has, therefore, been counterbored so that, in effect, two additional fins cool the hotter section. The design assumes a 50-kW thermal deposition in the last third of the ring and a total of 100 kW in the entire ring.

The peak temperature of the copper depends, of course, on the thermal path length to the nucleate boiling level. For this reason, the solid ring is only 0.375 in. wide radially, and the center line of the beam pipe is just 0.150 in. from the edge of the central hole in the target ring. If the beam is misdirected,

Figure 16-15 Details of wheel target, positron source.

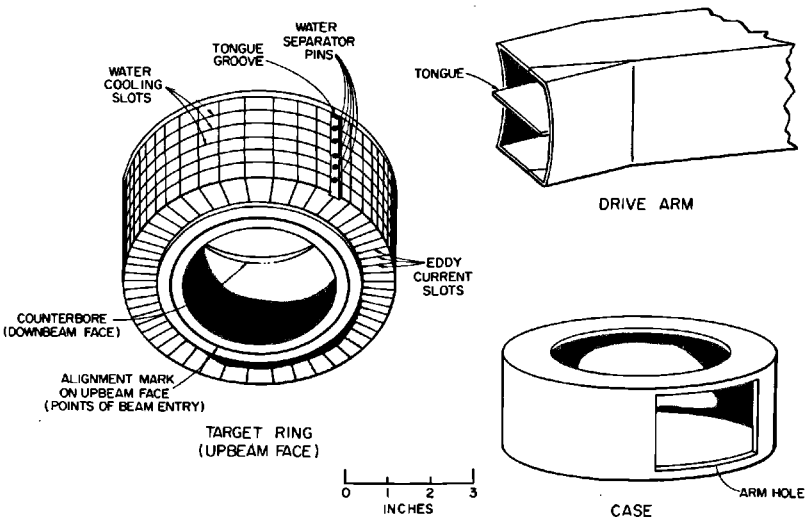

on half of the trolling cycle it will hit closer to the cooling fins, and on the other half, it will miss the target entirely.

In a continuous copper ring trolling in a magnetic field, eddy current drag could be substantial. A series of radial slots at right angles to the cooling fins are made to reduce these currents.

TROLLING DRIVE. Several methods for generating circular motion without rotation were studied. A true pantograph linkage could have provided perfectly circular motion, but either large forces or interference with the overall structure would have resulted. A modified pantograph was chosen (Fig. 16-14) in which the offsets of the support pivot and the link pivots reduce the target deviation from a circle to 0.072 in.

A three-phase induction motor drives a worm reducer (15 : 1) through an electric clutch-brake. A pair of replaceable gears transfers the 116-rpm output of the worm to the drive shaft of the eccentric. For the present target, which requires a 5.25-in. diameter trolling circle, the transfer gears have a 1 : 1 ratio. For other targets or a wider beam spot spacing, the transfer gears can be replaced for stepped speed changes.

RETRACTION. The transfer gears are connected to the drive shaft of the eccentric by means of two universals and a spline. Since the eccentric bearings are mounted on ways, the shaft arrangement permits the eccentric mounting to be shifted 3.25 in. (up to the left in Fig. 16-14) without disturbing the gears or motor. Through the linkage, this movement retracts the wheel target from the beam center line to permit the passage of electrons or to leave room for the wand target. Travel is controlled by limit switches which also actuate interlocks on wand insertion or beam pulses and which light three indicators in the instrumentation and control alcove: "wheel in," "wheel out," and "in transit." The motor has a spring brake that releases when power is turned on.

SENSORS. In order to retract the wheel, it must stop trolling in the zero position in which it is shown in Fig. 16-14. To accomplish this, a ferrite "proximity sensor" follows a cam on the downbeam extension of the drive shaft. The cam edge is a solid circle except for one notch which generates a square pulse in the sensor at the zero position on each revolution. Upon the retract command, a delay is activated which starts timing at the next sensor pulse. At the end of the adjustable delay interval, the drive clutch is opened and the brake applied. The linkage stops in the zero position with the proximity sensor signaling the presence of the notch. This signal releases an interlock and starts the retraction motor.

Two pulses in the same spot on the target ring would increase the chance of thermal fatigue; more than two pulses would be needed to distort or melt the copper. In the event of clutch slippage or motor overload, the most likely causes for loss of speed, the beam must be interrupted. A small gear acts as a second cam and is mounted next to the first. A timing circuit checks the period

between teeth passing under a second proximity sensor and interrupts the beam if the period lengthens. If the transfer gears are changed to run at a different speed, the speed cam is changed to match it.

FLANGE. The vacuum disconnect flange is similar to flanges used in the BSY with minor modifications. Two hooks on eccentrics clamp the flanges together by means of two ring springs. These rings have been machined with six equally spaced lands that contact the flange lip at different level of clamp pressure. Fully clamped, the rings distribute equal forces to the flanges at each land. The two-point actuation allows the flanges to be opened easily from a distance.

The seal is a ring of solid indium of rectangular cross section. It is trapped in a groove and forced to extrude slightly.

To prevent the varying spring forces generated by the bellows from disturbing the indium seal, a support ring is attached to the solenoid case inside the flange to provide a rest for the bellows terminal. The connection between the flange and the bellows terminal is welded from flat, light, stainless sheet, so that the flange is effectively isolated from the bellows forces transmitted through the support ring.

OPERATION. To run the wheel target, a switch on the instrumentation and control panel is turned. If the wand cooling-water and vacuum interlocks are clear, the retraction motor inserts the wheel to the zero position. The limit switch both stops the retraction motor (and switches its line connections to reverse) and actuates the trolling clutch. The last interlock clears when the speed sensor indicates trolling speed.

If the wand slips from the retracted position or if the vacuum interlock is activated, wheel rotation stops automatically. Other interlocks interrupt the beam. To retract the wheel manually, the panel switch is again turned and the trolling stops with the wheel in the zero position. The retraction limit switch stops the motor, reverses it, and clears the interlocks.

FLOOD CONTROL. The large water capacities, separated from the accelerator vacuum by stressed metal and brazed or welded joints, pose a hazard. The working bellows are an additional hazard but because they separate air from vacuum, the consequences of a failure are less severe. To limit damage, the first 10-ft positron girder has a separate vacuum system with its own ion pump. The accelerator vacuum header skips this girder. A fast valve at each end of the girder isolates the positron section from the accelerator sections on either side. In addition to these passive design features, an active system responds automatically to pressure increases in the positron chamber.

An ion gage monitors the vacuum line a few feet from the positron chamber. If the pressure rises to 10^{-5} torr, the beam is interrupted. An increase to 5×10^{-5} torr is assumed to be a small leak; the fast valves close to isolate the section, and solenoid valves cut off the water supply to both wheel and wand.

If the wand is in use, the oscillating air is vented and the wand settles by gravity to the lower end of its swing. If the wheel is in use, it stops trolling and retracts out of the beam line.

If the pressure continues to rise to 10^{-2} torr, dry nitrogen is released into the chamber and allowed to build up to 5 psig. At this point, drains open at the lowest point in the water lines, so that flow through either an air or water leak is reversed.

16-4 Design and construction of the solenoids (HB and KGC)

The principle of the tapered-field solenoid has been described earlier in this chapter. It was decided to build a solenoid that generates a longitudinal field along the beam axis as shown in Fig. 16-16. If $z = 0$ is taken at the target face of the positron radiator, the desired field for positron focusing at any point z (in centimeters) downbeam has been shown to be given by the expression

$$B_z = \frac{20.4}{1 + 0.118z} \text{ kG} \tag{16-34}$$

Thus, the 20.4-kG longitudinal field at $z = 0$ must be tapered to 2.4 kG at $z = 63.5$ cm. A uniform field with an amplitude for 2.4 kG should be maintained for another 7 meters downbeam.

To help fulfill these requirements, an additional magnet (coil 0 in Fig. 16-16) with a central field of 37 kG, generating 12 kG at $z = 0$, was added upbeam from the radiator chamber. Superposition of fields originated by coil

Figure 16-16 SLAC positron solenoid.

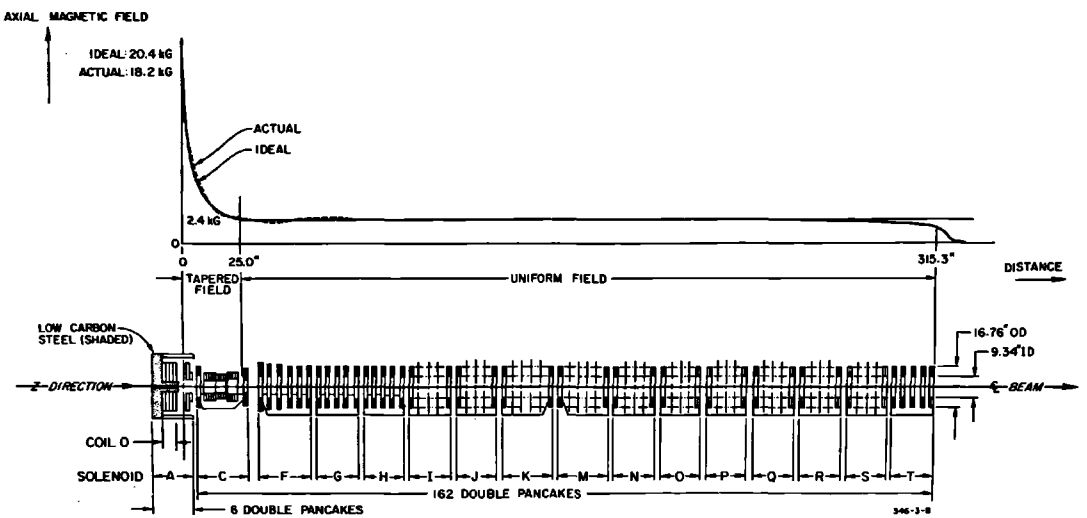

0, iron, and downbeam coils, yields a total field at $z = 0$ of 18.2 kG, which corresponds to 89% of the specified field value.

Much of the difference between the ideal and calculated field at $z = 0$ is due to limitations on the size and location of coil 0. The outside diameter of coil 0 was severely restricted to avoid blocking two lines of sight for optical tooling. These lines extend uninterrupted over the full length of the accelerator, 25.4 cm below and 13.7 cm on each side of the beam axis. The location of the center of the coil at $z = -16.71$ cm was dictated primarily by mechanical and heat transfer considerations. To force the maximum field downbeam, an iron return path (see Fig. 16-16) was provided along the inside diameter and the upbeam face of the coil. The measured field contribution from coil 0 and iron at $z = 0$ is 13.7 kG, i.e., approximately 1 kG less than calculated. The discrepancy is believed to be primarily due to the poor magnetic quality of commercially available low-carbon (1010) steel, used without previous annealing.

By balancing the magnetic requirements with those for mechanical support of the disk-loaded waveguides and associated cooling water, vacuum and RF connections, a constant 9.91-cm center-to-center spacing was maintained between matched pairs of double coil "pancakes" throughout the uniform field. The dip in the field curve between double pancake pairs was on the order of 4 G. For ease in manufacturing, 142 of the 146 hollow conductor double pancakes in the uniform field had identical dimensions. The other four differed only in outside diameter.

The double pancakes adjacent to the positron radiator are subjected to a relatively high integrated radiation dose. Since it was difficult to make correct estimates of the maximum dose rate, the insulation which was chosen was of the type developed at SLAC for maximum radiation resistance, using glass tape impregnated with alumina-loaded epoxy.[12]

Because of the high-power density and heat flux, 32.5 W/cm^3 and 121 W/cm^2 (maximum), respectively, edge-cooling was required in coil 0. Chromium plating was applied over a nickel substrate to protect coil surfaces exposed to erosion by water with a velocity as high as 6.5 meter/sec.

Figures 16-10 and 16-17 through 16-19 show the solenoids installed in the positron source station in Sector 11. Solenoids A and C are identified in Fig. 16-10. Although unidentified, solenoid F appears just to the right (downbeam) of solenoid C. Access to the radiator chamber is through the flanged opening in the side of the solenoid A housing. Labels indicate the relative position of edge-cooled coils 0, 1, and 2 within the housing.

Figure 16-17 includes the full complement of uniform-field solenoids. In this view, the upbeam cover and all but one of the double pancakes of coil 0 have been removed from solenoid A, exposing the four feedthroughs and the shaft upon which the double pancakes are centered.

Figures 16-10 and 16-18, looking at the same general area, illustrate the complex array of power, water, and other utility connections required to service a solenoid installation of this magnitude. Figure 16-19 was taken looking upbeam at the downbeam end of the positron source station.

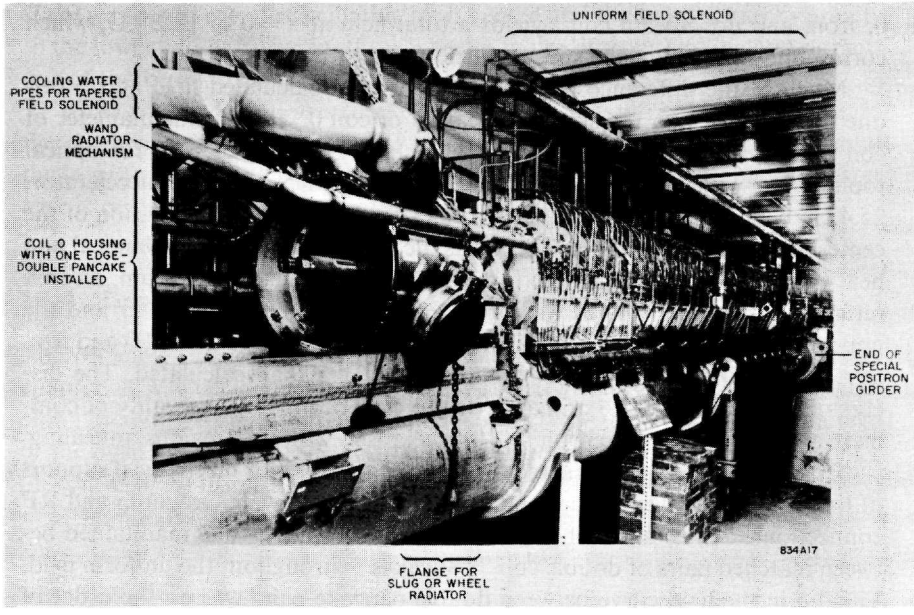

Figure 16-17 General view of positron radiator area. Coil 0 housing open, wand radiator installed; wheel or slug radiator not installed.

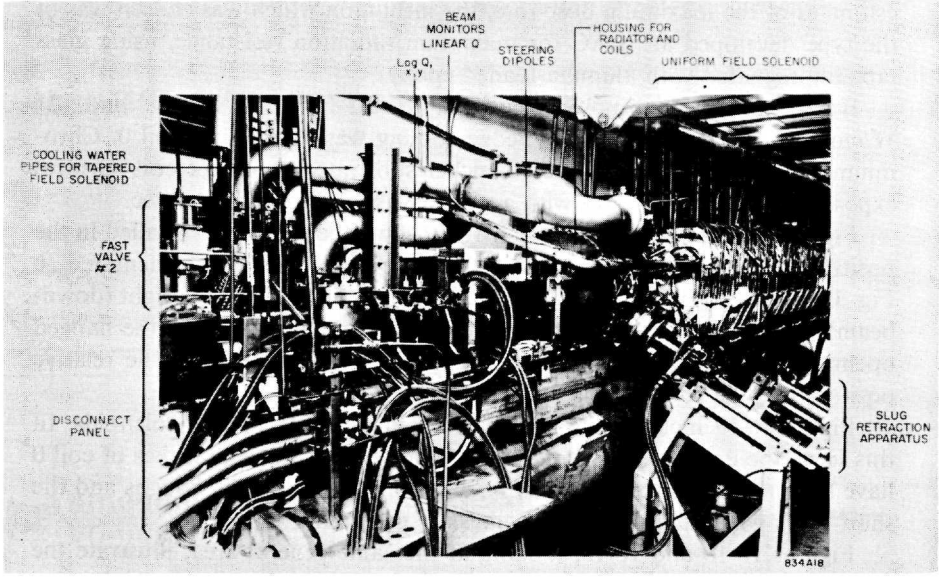

Figure 16-18 General view of positron radiator area. Slug radiator installed; wand radiator not installed.

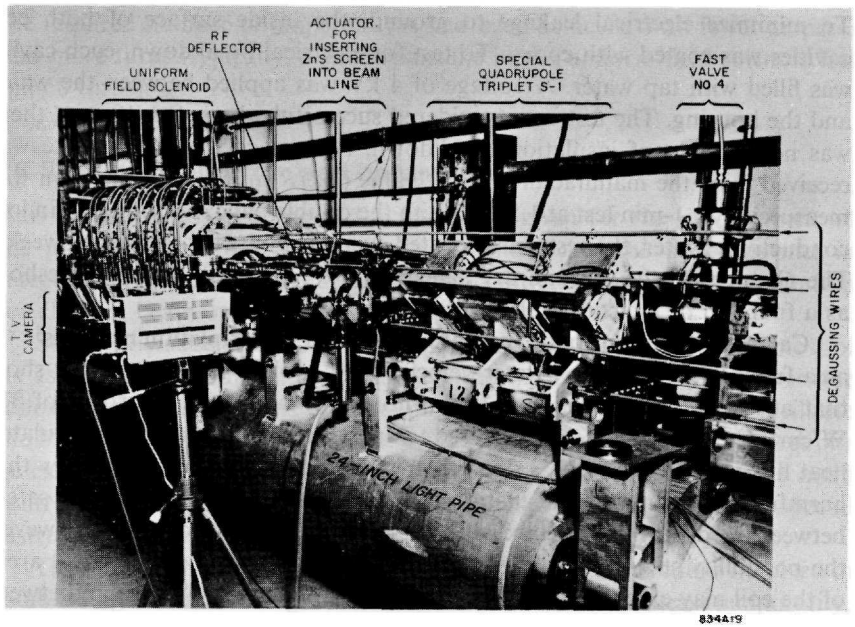

Figure 16-19 General view of downstream end of special positron girder. Beam direction left to right.

Coil design

Double pancake design for a succession of coils producing a specified longitudinal field is generally governed by Fabry geometry factors.[13] Since mechanical obstacles prevented full optimization, trial and error calculations performed on the computer were used to give the best results to obtain a satisfactory field distribution.

No major problems were encountered in cooling the seventy-eight hollow conductor coils in the uniform-field solenoid and in frame C of the tapered-field solenoid. Values of heat flux, an order of magnitude higher than in the hollow conductor wires, required that considerably more attention be given to the cooling of coils 0, 1, and 2. To improve mechanical strength between double pancakes and reduce the danger of electrical breakdown due to creeping along immersed surfaces, water cooling was confined to the conductor edges on the two outside faces of each double pancake. As finish-machined, the conductor is 0.635 × 1.59 cm in cross section and slightly tapered toward the ends to leave more room for insulation between the edge exposed to water flow. The glass tape and cloth used as insulation was prefilled with alumina-loaded epoxy. After winding and vacuum impregnation, double pancake faces were carefully machined. To insure that all surface cracks and minute voids exposed by machining were filled, each double pancake was then reimpregnated.

Coil 0 is a stack of four edge-cooled double pancakes, three dividers, and two end spacers mounted in the upbeam coil cavity of the solenoid A housing.

To minimize electrical leakage to ground, the inside surface of both coil cavities was coated with epoxy. To test for electrical breakdown, each cavity was filled with tap water. A voltage of 4 kV was applied between the water and the housing. The test was considered successful when after 10 min, there was no evidence of insulation breakdown. After each double pancake was received from the manufacturer, its Q value ($\omega L/R$) in the dry condition was measured by a 1-min test at 1.5 kV. With the double pancake immersed in low conductivity water, the test was repeated every 24 hours for the next 2 weeks. The Q values of the wet and dry pancake were compared. Corona threshold as a function of interturn voltage was also recorded.

Calculations of burnout temperatures by various correlation methods[14–17] as a function of heat flux, water velocity, and coolant slot dimensions show that at the design water-flow rate, burnout may occur at a heat flux of 371 W/cm^2. Comparison of the measured temperature gradient and the calculated heat flux indicates (1) a heat flux under operating conditions well below that harmful to the interturn insulation and (2) a considerable margin of safety between the operating heat flux and the corresponding burnout flux. However, the possibility still exists that the operating heat flux in certain critical areas of the coil may exceed 121 W/cm^2, thereby justifying a 300% margin between calculated values of heat flux and burnout heat flux.

The shape of the measured magnetic field agrees well with the calculated field; the absolute values agree within about 5% which is comparable with the uncertainties in the calibrations of the measuring equipment.

The power supplies for the solenoids have silicon controlled rectifiers and are current regulated to about 1% at full power. Since the energy acceptance of the focusing system is broad, good regulation is not required. One supply powers coil 0 to 700 kW (3720 A, 188 V); another powers coils 1 and 2 and frame C, the remainder of the tapered-field solenoid, to 116 kW (2000 A, 58 V); and a third one powers the uniform-field solenoid to 253 kW (two solenoids in parallel, each at 600 A, 211 V).

Because the positron beam has a rather low energy while it is in the solenoids, it was desirable to minimize stray, transverse magnetic fields which could mis-steer the beam. Therefore attention was given to the cancellation of stray fields from the leads and to the alignment of the various magnetic elements that give rise to the longitudinal field. Typically, the tolerance on the angular alignment of the axis of a magnetic element was 2 mrad.

The uniform field solenoid was divided into fourteen separate frames, each of which contained five or six pairs of double pancakes. Within a frame, the double pancakes were aligned to minimize the transverse field, and the alignment of each frame on the strongback was checked by verifying that the net steering effect was small. Asymmetries arising from the leads, crossovers within double pancakes, and cross-connects between double pancakes were cancelled to a large extent because the solenoid was actually made of two interlaced solenoids, each with opposite helical pitch. The problems associated with alignment and stray field effects would probably have been less severe if

the required number of ampere-turns had been achieved with fewer amperes and more turns (typically, a single pancake in the uniform-field solenoid has only 8 turns).

16-5 Instrumentation and control (KEB)

This section discusses some of the guidelines given for the development of the positron beam instrumentation and control and the problems met in integrating the necessary signals and controls with the existing instrumentation for electron beam operation from the CCR.

Sector 11 was selected for the location of the positron source with most of its associated equipment. The beam monitoring and steering system in the following four sectors was to be augmented by special devices to facilitate the monitoring and guidance of the established positron beam. The need for quick access to the special equipment made it desirable to locate the main control point in Sector 11. This location also made it possible to set up special instrumentation quickly.

The overall operational concept assigned to CCR all functions involved in establishing and controlling the electron beam. However, at least temporarily, when the positron beam is being generated, all subsequent operations are to be directed from Sector 11, with CCR assistance only when requested. Later on, it is anticipated that positron operation will be feasible from CCR when all special routines have been established. For this reason, all local instrumentation for positron operation in Sector 11 had to be made compatible for remote control.

Instrumentation requirements

The positron control and instrumentation requirements called for individual RF power control and monitoring of the two klystrons following the positron source. Suitable controls, monitoring, and protection were required for the "wheel" and the "wand." Current control and monitoring for each of the three power supplies servicing the focusing solenoids were also specified.

In addition, instrumentation was required for the thirteen special quadrupole packages following the solenoids. Eight of these are located in Sector 11, three in Sector 12, and one each in Sectors 13 and 14. Access to the standard beam guidance and monitoring equipment in Sectors 11 through 14 is required. The phasing system in Sector 11 had to be modified to permit both local, individual, and remote automatic operation.

The positron control system resulting from the above requirements was installed in the instrumentation and control (I & C) alcove of Sector 11. The alcove is the data collection point in every sector and is, thus, the local interface between the accelerator and CCR. This location permitted easy access to the new equipment and interconnections with existing systems and CCR. Some of the major control features provided are described below.

Klystron voltage control and phasing

Two separate power supplies were installed to supply the operating voltage for the two klystrons following the positron source. The on–off and voltage control were of the same basic design as used in the control of the standard substations. The combination of standard reference voltage power supply and monitor rectifier could, therefore, be used to set the klystron voltage and to provide the "de$Q$'ing" level for the associated modulators. Two identical sets were installed.

A special panel was built for the power supply on–off control, which also displays the power supply and operating status of the special klystrons. These controls are presently operated from Sector 11 only. The contactors of the power supplies are interlocked with the personnel protection system and can be energized only when all interlocks to the accelerator housing are closed. The operating status of the special klystrons also controls the red–green warning lights in Sector 11.

All klystrons in Sector 11 can be phased from CCR in the usual manner. Local phasing of the klystrons is possible from a special local phasing panel; additional controls permit the "accelerate–standby" selection of individual klystrons.

Wand control

The essential operational and monitoring features for the wand control are located on one panel. It controls and monitors the movement of the wand from the retracted position, where it is normally held when not in use, into the operating position and vice versa.

When the wand has been moved "in," another control permits it to operate in an oscillatory mode or in a stationary position in the beam line. The control selecting the oscillatory mode functions only when the wand is "in," and operates into the wand driver unit which generates the drive pulses for the solenoids in the air system. An air-operated system, described earlier, is used to move the wand across the beam and to return it to its starting position.

Wheel controls

The wheel controls and monitoring signals are assembled on one panel. Ancillary equipment needed for the operation of the wheel and to monitor its movements is located in a special rack near the "penetration" to the wheel.

Similarly to the wand, the wheel is in a retracted position when not in use and is moved into an operating position where it can "troll" when a positron beam is to be generated. Two electrical motors are provided, one for the "in–out" motion and the other for the trolling motion. The motor for the trolling motion is coupled to the wheel through an electrically operated clutch-brake device.

The following operations take place when the control switch is placed into the "wheel in" command position. The motor assigned to this function is energized and moves the wheel in. When it is completely in, the motor is stopped and the trolling motor is started. Simultaneously, the brake is released and the clutch is engaged. The trolling motion starts, its speed is monitored and when a preset value is exceeded, an interlock is closed which in conjunction with other wheel interlocks permits the beam to be turned on. This sequence of operation is completely automatic, except for the beam turn-in. The individual stages are monitored and indicated on the control panel.

Solenoid power supply controls

Three power supplies for the operation of the tapered- and uniform-field solenoids were specified and procured from an outside vendor, who also furnished the control panel for the supplies. It provides for on–off and voltage control for each supply.

The solenoids have a very large number of interlocks which monitor the flow and temperature of the cooling water in individual coils. To facilitate fault location, these interlocks are monitored individually on a hold basis; i.e., when a fault has been cleared, the fault indication does not disappear until a reset button is actuated, which closes the interlock chain and permits resumption of operation.

Additional monitoring is done on a special panel summarizing the operating relations between the pump supplying cooling water to the solenoids and their power supplies.

Steering and quadrupole power supply controls

The above title is the name of a panel for beam guidance control. It was desired to control six steering dipoles and eighteen quadrupoles between Sectors 10 to 14. Because of the large number of access points, one set of instrumentation for quadrupole and steering current control was mounted on a panel with selector switches permitting the selection of the control point chosen. Four of these points were part of the standard beam guidance system controlled from CCR. Special relays were added in these locations to disconnect the CCR control temporarily while adjustments were made from the positron control point in Sector 11.

Beam monitoring

The standard beam monitoring system generates one signal proportional to the charge of the beam pulse (linear Q) and another signal indicating in sequence the logarithm of the charge and the horizontal (x) and vertical (y) positions of the pulse (see Chapter 15). These signals are normally transmitted to CCR and displayed with the signals from other sectors in such a way as to show the sector-to-sector variations of each quantity.

One set of FM receiving equipment for linear Q is installed locally in Sector 11, and a selector switch is provided on a special panel to connect the receiver to the location to be monitored. The output can be displayed on a scope.

Similarly, the composite signal (log Q, x, y) is made available at Sector 11 for scope display by connecting the appropriate receiving equipment to the point chosen. A separate selector switch is provided on this panel.

The linear Q amplifier in each sector is adjustable in gain to cover the full range of the beam current. It also has a provision for reversing the input when a positron beam is to be monitored. The appropriate controls are also furnished on this panel.

Supplementary beam monitoring is provided by ionization chambers, sensitive toroid beam monitors, and fluorescent screens that can be inserted into the beam path at the special quadrupole multiplets. The screens are viewed with TV cameras (see Fig. 16-19). Several such cameras can be preset. The insertion and retraction of these special monitors is controlled from Sector 11. When a monitor is inserted, the copper walls of its vacuum enclosure cause so much scattering that the beam is no longer transmitted.

Radio-frequency deflection system

Under typical operating conditions, both positrons and electrons would be captured and accelerated at the same time, with the bunches of opposite sign riding one-half wavelength apart in the machine. The standard position and intensity monitoring devices cannot respond separately to these two beams, and special devices that could do so seemed complicated to build. A relatively simple solution was to utilize the RF structure of the beams and to deflect the unwanted particle bunches out of the machine.

One part of the deflection system is a traveling wave structure that gives the same horizontal impulse of about 0.5 MeV/c to the bunches of both signs. The other part is a standard sector steering dipole adjacent to the deflector, which is pulsed to cancel the impulse on the desired bunches and to double the impulse on the unwanted bunches. These are, then, deflected into the walls of the machine, about 10 ft farther downstream.

The deflection occurs after about 70 MeV of acceleration, when the two beams are well formed. The RF deflector is about 24 in. long and operates in the HEM_{11} mode at 2856 MHz.[18] Its power (typically about 1.5 MW peak) comes from the same klystron that powers the second 10-ft section of disk-loaded waveguide downbeam of the radiator. Since the magnet is triggered on a pulse-to-pulse basis, either a positron beam or an electron beam can be accelerated while the radiator remains fixed in the "in" position.

Central Control Room Signals

A minimum number of signals is presently transmitted to CCR until such time when positron operation can be performed from this point. The basic

concept for selecting signals considers two cases. For positron operation, CCR is to stay in close contact with Sector 11 and to be kept informed about the status of the operation. When positron beam operation is discontinued, CCR is to have sufficient information that equipment used for generating and monitoring the positron beam is shut off and, therefore, cannot interfere with the electron beam.

Supplementary status information is given about systems that either have to be kept in operation or are needed both for electron and positron operation. Examples of these are the vacuum and cooling-water systems.

The special phase shifters which can introduce an extra predetermined phase shift ($\approx 180°$) on a pulse-to-pulse basis for positron acceleration are discussed in detail in Chapter 9.

16-6 Early positron operating experience (HDeS)

To date (July 1967) the positron beam has been set up about 15 times with an integrated operating time of about 150 hours at incident power levels up to about 40 kW. For the time being, it takes more time and effort to set up this beam than the usual electron beam, partly because the positron beam occupies a larger transverse phase space and adjustments are more critical. Customarily, the beam is tuned by sequentially optimizing the transmission near the radiator and empirically adjusting focusing and steering to maximize the positron current at the sector drift sections, using the same instrumentation as for the main electron beam. The intensity monitors (linear Q) work well at maximum positron intensity, but the RF position monitors operate very close to their thresholds of usefulness. From run to run, the optimum settings reproduce fairly well, but each time a final optimization is required to obtain the best beam. Tuning by using special intensity monitors within Sector 11 has not increased the final positron intensity. This procedure is complicated because, close to the source, there are still many particles inside the machine that are *not* useful positrons but which activate whatever detecting device is being used. After the positron beam is momentum analyzed, the amount of RF phase shift is finely tuned to get the best momentum spectrum.

Typically, the positron yield observed at the end of Sector 11 is 2 or 3% of the incident electron current (at 5 to 6 GeV). Of this, perhaps 75% is gradually lost as the beam is accelerated to Sector 20; from Sector 20 to the end of the machine the transmission is about 100%. About 30 to 50% of the beam leaving the accelerator proper goes through 1% (full-width) momentum slits, and spot sizes in the target area on the order of a few millimeters are common. This represents a specific yield of $1.5 \times 10^{-3} e^+/\text{GeV}$ of e^- and it corresponds to an average positron current of 0.15 μA for 100 kW incident on the radiator.

The positron yield as a function of RF phase shift shows a rather sharp peak near 165°; hence, conceptually, the RF must be reversed in phase by exactly 180° and then retarded by 15° with respect to the positron beam being accelerated. Another peak of similar magnitude is obtained if the RF is

simply retarded by about 15°, which corresponds to relativistic positrons being decelerated, slipping in phase by about 180°, and then being captured and accelerated.[19] The turning point occurs within the solenoid so that the particles are contained while their longitudinal velocities are low, and few positrons are lost. However, this mode of operation is not generally used because the beam energy is somewhat lower and the energy spread effects in the focusing system are worse.

The radiator is a source of electrons, as well as of positrons. The RF deflector system transmits only one particle or the other, which greatly simplifies the problem of beam monitoring. The deflector has been a useful and worthwhile part of the system. The best electron beam is 5–10 times greater than the best positron beam. If the system is tuned for positrons and then slight compromises are made to transmit electrons, the intensities are comparable. Under these conditions, the phase shifters in the first third of the accelerator and the steering dipole current in the RF deflector area must be switched on a pulse-to-pulse basis to select the sign of the accelerated beam.

Acknowledgments

J. Pine (Caltech) has been, and still is intimately involved in all phases of the positron system and has contributed many of the ideas that have been incorporated. J. Mar (Caltech) constructed much of the sensitive monitoring equipment used in the early tuning of the positron beam. A. L. Eldredge provided much counsel, direction, and stimulus. C. L. Rasmussen has overseen the materialization of numerous ideas and the rectification of a few bad ones. A. V. Lisin has contributed valuable criticism and advice.

References

1 D. Yount and J. Pine, *Nucl. Instr. Methods*, **15**, 45 (1962).

2 J. Pine in "1963 Summer Study Report," Rept. No. SLAC-25, Part I, Section D, Stanford Linear Accelerator Center, Stanford University, Stanford, California (January 1964).

3 C. D. Zerby and H. S. Moran, *J. Appl. Phys.* **34**, 2445 (1963).

4 J. Pine and H. DeStaebler, "Pulse Thermal Stresses in the Positron Radiator," Tech. Note No. SLAC-TN-66-31, Stanford Linear Accelerator Center, Stanford University, Stanford, California (July 1966). This note includes measurements of shower size with 1-GeV electrons incident on a layered radiator.

5 J. Pine and H. DeStaebler, "Heating Test of Positron Slug Radiator," Tech. Note No. SLAC-TN-67-18, Stanford Linear Accelerator Center, Stanford University, Stanford, California (June 1967).

6 T. L. Aggson and L. Burnod, "Production de positrons à l'accélérateur d'Orsay: détermination de la section efficace à 0° sur cibles epaisses." Rept. No. LAL-27, Laboratoire de l'Accélérateur Linéaire, Orsay, France (October 1962).

7 H. DeStaebler, "Remarks on Positron Intensities," Tech. Note No. SLAC-TN-65-23, Stanford Linear Accelerator Center, Stanford University, Stanford, California (March 1965).

8 P. A. Sturrock, *Static and Dynamic Electron Optics*, Cambridge Univ. Press, London and New York, 1965.

9 E. Ferlenghi and L. Mango, "Calcoli per L'Ottica di Trasporto dei Positroni nell 'Acceleratore Lineare di Frascati," Rept. No. LNF-63/70, Laboratori Nazionali di Frascati, Rome, Italy (November 1963).

10 D. E. Lobb, "A Study of a Focusing System for Positron Beams," Rept. No. SAL-5 (Ph.D. Thesis), Saskatchewan Accelerator Laboratory, University of Saskatchewan, Saskatoon, Saskatchewan (March 1966).

11 C. S. Nunan, "A Positron Linear Accelerator Design," *IEEE Trans. Nucl. Sci.* **NS-12**, No. 3, p. 465 (June 1965).

12 H. Brechna, "Effect of Nuclear Radiation on Organic Materials; Specifically Magnet Insulation in High-Energy Accelerators," Rept. No. SLAC-40, Stanford Linear Accelerator Center, Stanford University, Stanford, California (March 1965).

13 H. Brechna, "Electromagnets for High Energy Physics Applications," in *Proc. Intern. Symposium Magnet Technol., Stanford Linear Accelerator Center, September 1967* (H. Brechna and H. S. Gordon, eds.), Conf-650922, p. 1, Clearinghouse for Federal Scientific and Technical Information, Springfield, Virginia.

14 F. C. Gunther, *Trans. Am. Soc. Mech. Engrs.* **73**, 115-123 (1951).

15 H. Brechna and D. B. Montgomery, "A High Performance dc Magnet Utilizing Axial Cooled Discs," Rept. No. NML-62-1, p. 18, National Magnet Laboratory, Massachusetts Institute of Technology, Cambridge, Massachusetts (September 1962).

16 S. Mirshak, W. S. Durant, and R. H. Towell, "Heat Flux at Burnout," Rept. No. DP-355, Du Pont de Nemours (E.I.) and Co., Savannah River Laboratory, Augusta, Georgia.

17 Wm. McAdams, W. E. Kennel, C. S. Minden, R. Carl, P. M. Picornell, and J. E. Dew, *Ind. Eng. Chem.* **41**, 1945–1953 (1949).

18 A technical description of the RF deflector is given in O. H. Altenmueller, R. R. Larsen, and G. A. Loew, *Rev. Sci. Instr.* **35**, 436 (1964). A more detailed description of the whole deflection system is given in G. A. Loew and O. H. Altenmueller, "Design and Applications of RF Deflecting Structures at SLAC," in *Proc. Fifth Intern. Conf. on High-Energy Accelerators, Frascati, Italy, 1965*, pp. 551-553 (C.N.E.N., Rome, 1966).

19 The theory of capture in a traveling wave structure was developed by J. C. Slater, *Rev. Modern Phys.* **20**, 473 (1948).

17

BEAM SWITCHYARD DESIGN AND OPERATION

J. L. Harris, S. K. Howry,
E. J. Seppi, Editor, and H. A. Weidner

As previously discussed, the accelerator is capable of providing interlaced electron and/or positron beams at various pulse rates, currents, and energies. The beam switchyard (BSY) is designed to separate the various beams coming from the accelerator and deliver them to the appropriate experimenters' locations. A beam transport system consisting of pulsed and direct current magnets channels the beam through the switchyard to the various experimental setups on a pulse-to-pulse basis. This transport system and the associated instrumentation provides momentum analysis and control of the high-power beams up to the points where they are dissipated in targets or beam dumps. Figure 5-25 shows the arrangement of the research structures and experimental setups; Fig. 5-2 is an aerial view of the research area. Accelerator beams are delivered to two shielded and physically separated buildings known as end stations A and B. These buildings are located in a large research area which is available for the erection of other permanent and temporary buildings containing bubble chambers, spark chambers, and counting equipment. Three spectrometers are available in end station A. The central C-beam system transports the accelerator beam to targets and dumps within the beam switchyard housing, providing secondary beams for a bubble chamber and other experimental equipment located in the central part of the research area. Present beam arrangements are capable of delivering electron, photon, positron, μ-particle, π-meson, and K-meson beams to various experimental setups.

Considerable flexibility has been provided in the BSY for future beams and experimental facilities. Figures 5-23 and 17-1 through 17-3 show the locations of the equipment and beams in the switchyard. Provisions have been made for future development of a gamma-ray beam which could operate parasitically off the A system. In addition, the tunnel configuration provides

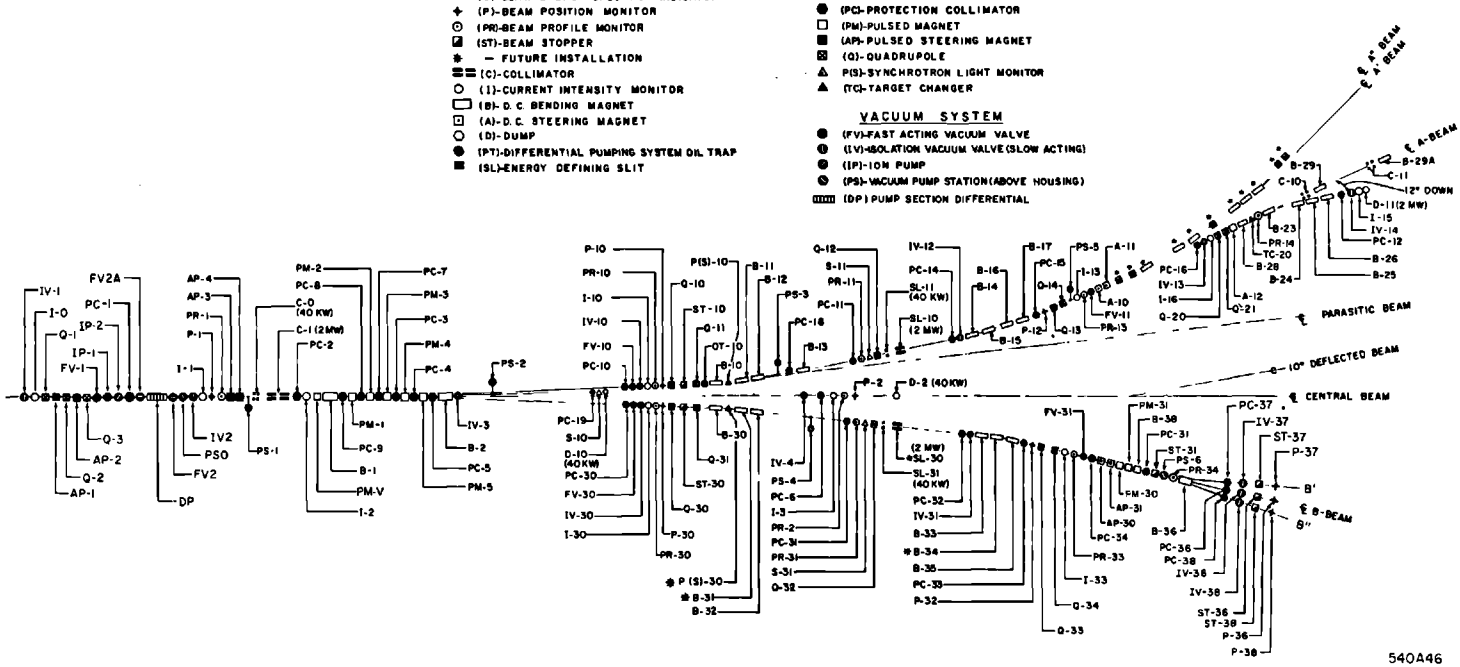

Figure 17-1 Schematic illustration showing the relative locations of magnets, energy absorbers, and beam instrumentation in the beam switchyard.

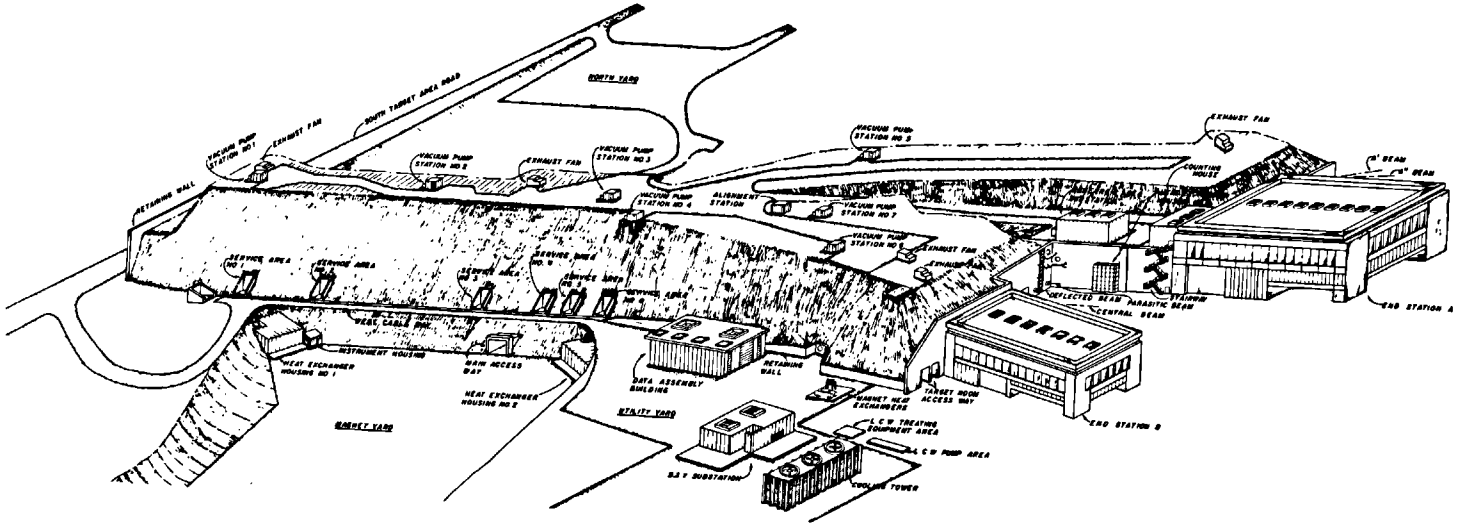

540-47-A

Figure 17-2 Isometric drawing of the beam switchyard area and end station building design.

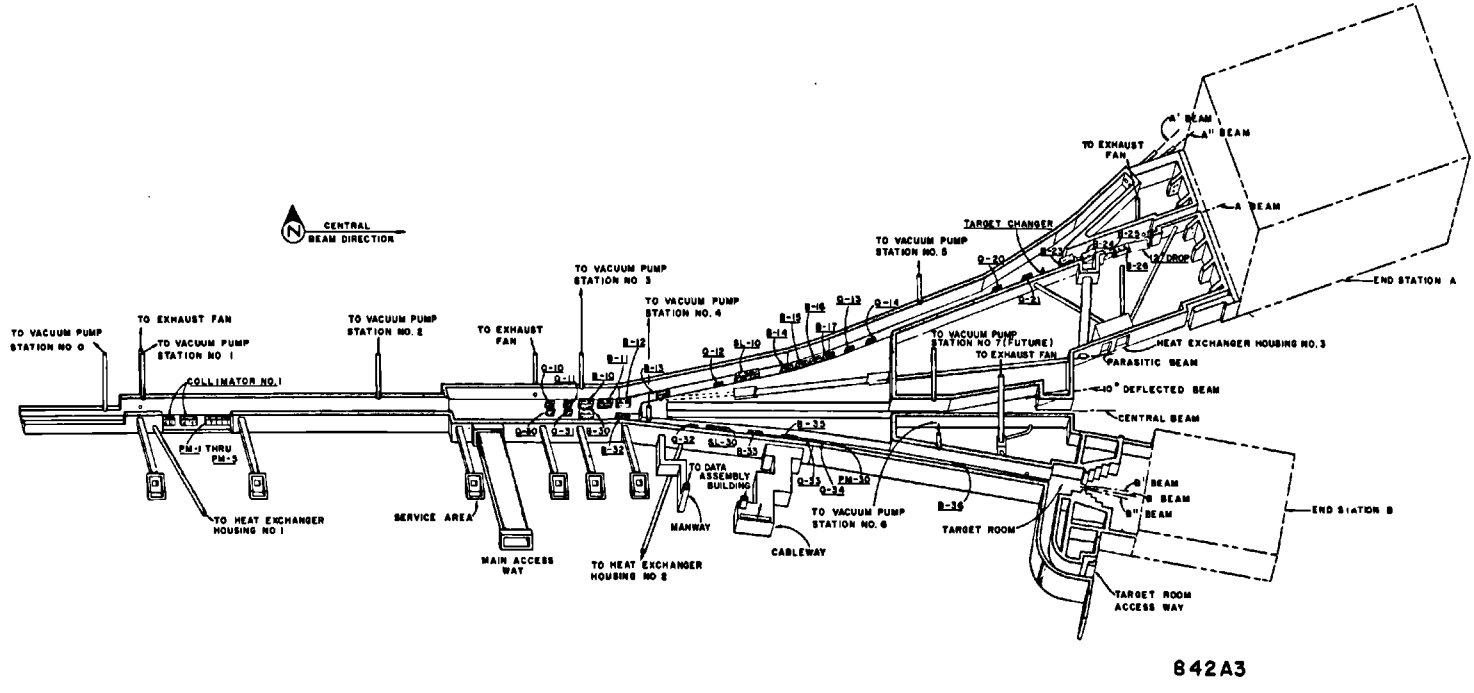

Figure 17-3 Isometric drawing of beam switchyard housing.

Table 17-1 Provisions for beam switchyard beams

Beam	*Status: July 1967*
Momentum analyzed electron or positron beam to end station A	Developed
A′ and A″ beams	Undeveloped
Momentum analyzed electron or positron beam to end station B with B-beam switching	Developed
Photon beam, end station A	Developed
Central beam	Being developed
10° deflected beam	Undeveloped
Parasitic beam	Undeveloped

for future beams (designated A′, A″) off the A system. Table 17-1 gives a list of arrangements which have been made for particle and photon beams from the beam switchyard. The table indicates the status and planned development of beams as of the fall of 1967.

The design of systems capable of handling the high beam power available from the accelerator and also using the accelerator's multiple beam flexibility presents numerous problems in instrumentation, mechanical design, and physical layout. The following discussion includes a description of the BSY, primary transport system and the optics of momentum analysis, an outline of the problems associated with the transport of high-intensity beams, a description of the beam switchyard design which was developed to solve these problems, and the results of BSY tests and early operation experience. Problems associated with BSY transport magnets and momentum calibration, instrumentation and control, beam energy absorbers, component alignment, and radiation shielding are discussed in Chapters 18, 19, 20, 22, and 26, respectively. Descriptions of the BSY vacuum system, cooling-water system, electrical system, and physical plant have been included in chapters covering these topics for the entire accelerator facility.

17-1 Beam switchyard transport and momentum analysis (SKH)

The magnets in the BSY and transport systems provide the deflection and focusing necessary to deliver momentum-analyzed beams to the A and B experimental areas. The essential optics of the systems were proposed by K. L. Brown.[1] System A was studied on a semiquantitative basis by Penner,[2] who concurred that it would be an acceptable system subject to more precise calculations. These two transport systems are illustrated in Figs. 17-1 and 5-23. The design criteria for systems A and B are summarized in Table 17-2. Since the A and B systems are nearly identical, only the transport system for beam A will be described. Methods of optimizing the A system and differences between the A and B systems will be described.

Table 17-2 Design characteristics of the beam switchyard transport systems A and B

Parameter	*System A*	*System B*
Momentum	The transport system will operate in the momentum range from below 1 GeV/c to 25 GeV/c.	The transport system will operate in the momentum range from below 1 GeV/c to 25 GeV/c. The system can easily be modified to operate up to 40 GeV/c.
Acceptance	The system will accept and pass without loss a beam with the following phase space: beam radius 0.3 cm, angular divergence 10^{-4} rad, momentum width up to 2.6% total. Actually, the accelerator provides an electron beam of considerably smaller phase space, but the positron beam has the above phase space.	The system will accept and pass without loss a beam with the following phase space: beam radius 0.3 cm. angular divergence 10^{-4} rad, momentum width up to 5.2% total.
Beam characteristics	The transport system is capable of handling 0.6 MW of beam power continuously. The pulse repetition rate is 0 to 360 pulses/sec, and the pulse width is 0.020–1.7μsec.	The transport system is capable of handling 0.1 MW of beam power.
Resolution	The transport system is capable of resolving $\pm$0.05% in momentum at the slit. The mean momentum of the beam is reproducible to $\pm$0.02%. The momentum width and mean momentum passed by the system is independent of the operation of the accelerator and the performance of the pulsed magnets.	The transport system is capable of resolving $\pm$0.1% in momentum at the slit. The mean momentum of the beam is reproducible to $\pm$0.05%. The momentum width and mean momentum passed by the system is independent of the operation of the accelerator and the performance of the pulsed magnets.
Momentum calibration	The absolute value of the mean momentum passing through the system is determined to $\pm$0.2%. The dispersion at the momentum defining slit is 0.15%/cm	The absolute value of the mean momentum passing through the system is determined to $\pm$0.5%. The disperion at the momentum defining slit is 0.3%/cm.
Achromaticity	The system is achromatic; that is, after leaving the last bending magnet, the momentum and transverse position distribution within the beam are uncorrelated.	The system is achromatic; that is, after leaving the last bending magnet, the momentum and transverse position distribution within the beam are uncorrelated.
Isochronism	After passing through the system, the longitudinal extent of the bunch does not exceed $\pm$20° RF phase (at 2856 MHz) for $\Delta P/P = \pm 1\%$; this is equivalent to a bunch length of $\pm$0.6 cm.	After passing through the system, the longitudinal extent of the bunch does not exceed $\pm$20° RF phase (at 2856 MHz) for $\Delta P/P = \pm 3\%$; this is equivalent to a bunch length of $\pm$0.6 cm.

The A and B transport systems

Functionally, the A transport system is characterized by the following features, which are illustrated in Fig. 17-1. The beam from the accelerator is directed through the collimator C-1 by the pulsed steering magnets AP 1-4. After its size and position have been determined by the collimator, its beam enters the pulsed magnets PM-1 through PM-5 and is deflected to the quadrupole doublet, Q-10, Q-11. For monoenergetic beams, the doublet Q-10, Q-11 forms images as follows: the beam cross section at the center of the pulsed magnet PMV is focused vertically to form an image in the horizontal axial plane at the symmetry quadrupole Q-12; the beam cross section at the center of the pulsed magnet group PM-1 through PM-5 is focused horizontally to form an image in the vertical axial plane at the front of the slit SL-10. The horizontal focus at the entrance to the slit optimizes the momentum resolution of the system. The bending magnets B-10 through B-13 disperse the beam horizontally for momentum resolution at the slit. Vertically, the symmetry quadrupole has little effect on the beam because of the small vertical size of the beam resulting from the vertical focus at the symmetry quadrupole. In the horizontal plane the symmetry quadrupole recombines the different momenta, so that after passing through the second set of bending magnets B-14 through B-17, the beam is achromatic. The quadrupole doublet, Q-13, Q-14, produces a low-divergence beam by imaging (approximately) the slit to infinity. The final beam then drifts to the end station without appreciable spreading. A small adjustment of the final location and direction of this beam can be made using the steering magnets A-10 and A-11.

Essentially, the transport system up to this point has maintained a constant phase volume. In the A-beam, a target, beam dump, and the associated magnets and instruments for generating a photon beam are located in the drift space following Q-20, Q-21. The pair of doublets (Q-13, Q-14 and Q-20, Q-21) can be used to achieve a desired spot size, or for phase-matching either the electron beam or, to some extent, the photon beam to experiments. The drift space following the latter doublet is chosen in conjunction with the focal length of the doublet to give the desired spot size or the proper phase match into the experiment or auxiliary system. At 15 meters from the doublet, an electron beam spot size of 1 mm is possible.

In the B-beam, after passing through the doublet Q-33, Q-34, which corresponds to Q-13, Q-14 in the A line, the beam is steered by two pulsed steering magnets, AP-30, AP-31, into two pulsed magnets PM-30 and PM-31, which can deflect the beam either left or right by 0.35° or let the beam pass undeflected. The beam then encounters the slit magnet B-36, which is actually two C-type deflecting magnets which perform the function of adding a further deflection of 1.7° to a beam deflected to the left or right by PM-30, PM-31. In addition, the properties of the C-type magnets are such that they will allow an undeflected incident beam to pass with no added deflection. Thus, the

B-beam can be provided in end station B along three different beam lines on a pulse-to pulse basis.

Selection of fixed parameters

Certain parameters of the transport systems were fixed at the outset by considerations not entirely optical. Compromises involving spatial clearance, magnet design, economy, and the like, fixed the criteria of the system. Each of the fixed parameters of the system will now be discussed. The total bending angle of the pulsed magnets PM-1 through PM-5 was set at 0.5°. The magnitude of this angle is optically not significant. The difficulties in designing a pulsed magnet system with the necessary stability and reliability at a reasonable cost, and of which the magnetic field can be programmed on a pulse-to-pulse basis, set the upper limit for the bending angle.

After passing through the pulsed switching magnets, the deflected beam must drift until it is sufficiently offset from the center line of the straight-ahead beam to allow insertion of the next magnets of the system, namely the Q-10, Q-11 doublet. Assuming the 0.5° deflection from the pulsed magnets above, a drift of 78.5 meters gives an offset of 70 cm (27.5 in.) which is sufficient. This drift distance D_1, essentially the distance from the source to the focusing quadrupole doublet Q-10, Q-11, is also important because it fixes the monochromatic beam image size at the slit. This image size determines the ultimate (or zero slit width) momentum resolution of the system. It should be small so that similar images of neighboring momenta do not overlap excessively. To a first approximation, the momentum range passing through a vanishingly small width slit in system A is

$$\frac{\Delta P}{P} \approx \frac{x_0}{D_1 \gamma} \tag{17-1}$$

where P is the momentum, γ is the total angle of bend of the first group of magnets B-10 through B-13, and x_0 is the horizontal extent of the beam spot at the collimator. For $\gamma = 12°$ (see below), $x_0 = 0.3$ cm, and $D_1 = 78.5$ meters, the ultimate resolution is roughly

$$\frac{\Delta P}{P} \approx 0.018\% \tag{17-2}$$

The bending magnets B-10 through B-13 serve a dual purpose, deflecting the beam so that the end stations can be physically separated, and dispersing it for momentum analysis. The angle of bend was fixed at 12° as a rather loose compromise between two conflicting requirements. The first was economic—increasing the bend angle decreases the overall cost of creating a given separation between the two end stations (although more magnets are needed, tunnel length is decreased). The second constraint was optical—the greater

the angle of bend, the greater the deterioration of beam isochronism. For a momentum band pass of $\pm 1\%$, a 24° bend increased the bunch spread by $\pm 15°$ in RF phase. This increase, when combined with the initial bunch length, makes the total bunch length spread near the limiting value of $\pm 20°$ (see Table 17-2). The bend is accomplished using identical 3-meter magnets, each bending 3°. Optically, they should be as close to the doublet, Q-10, Q-11, as possible in order to maximize the dispersion. A distance of 1.5 meters between magnets is sufficient for standard instrumentation. To provide for the parasitic gamma beam, the separation between the second and third magnets was increased to 2 meters to allow insertion of a thin radiator for gamma production. Moreover, the fourth magnet (B-13) was moved 9 meters downstream to create clearance between the gamma beam and the magnet. As a result, the resolution deteriorated about 0.5% from its ideal value for closely spaced magnets; this is an acceptable loss. The bend angle of the magnet group B-14 through B-17 was chosen equal to that of B-10 through B-13 because this leads to the smallest loss of isochronism in the beam. Also, this bend is necessary to separate the defined electron beam from the off-energy background radiation generated at the slit. The magnets B-14 through B-17 are also 3-meter long magnets and are spaced 1.5 meters apart.

The beam is dispersed in energy in traversing B-10 through B-13. The distance D_2 from the vertex of the bending group B-10 through B-13 to SL-10 is fixed by the momentum spread desired to pass through a fixed slit width. The distance was chosen to give a dispersion of 6 cm for a momentum spread of 1%.

Given the angle of bend for bending magnets and the distance D_2, then the distance D_3 from Q-12 to the doublet Q-13, Q-14 and the focal length of this doublet are fixed by the requirement that the emergent beam be made achromatic and dispersionless. The final determination of D_3 and the strength of the quadrupole setting will be discussed later. Another requirement on D_3 was that it had to be at least long enough to house the high-power slits SL-10 and SL-11 and associated equipment. The drift distance D_4 to the experimental end station was selected on the basis of giving the various experimental areas enough physical and radiological separation. Because the beam is made parallel in this region, there is no appreciable increase in beam size after drifting through the selected distance.

17-2 Quantitative determination of transport system parameters (SKH)

The detailed analysis of the beam switchyard transport system was performed by a general purpose digital computer program, TRANSPORT, which was developed at SLAC in 1962. It seems appropriate to outline in some detail the mathematical methods used in the program. Further details are to be found in Reference 3. A quantitative discussion of the parameters and specifications will also be given.

Beam transport analysis

The following notation has been adopted in discussing the differential beam coordinates of a particle with respect to the central ray of the transport system. The quantities x and θ refer to the differential position and divergence, respectively, in the horizontal (axial) plane. The quantities y and ϕ refer to the vertical plane. The variable z is the differential path length from the center of a particle bunch. The quantity $\delta = \Delta p/p$ is the differential momentum of the particle with respect to the momentum of a particle in the central ray. The transformation equation for the six differential coordinates of a particle in passing from one point, $\mathbf{X}_0$, in the transport system to another, $\mathbf{X}$, can be written

$$\mathbf{X} = R\mathbf{X}_0 \tag{17-3}$$

or

$$\begin{pmatrix} x \\ \theta \\ y \\ \phi \\ z \\ \delta \end{pmatrix} = \begin{pmatrix} (x\,|\,x_0) & (x\,|\,\theta_0) & 0 & 0 & 0 & (x\,|\,\delta_0) \\ (\theta\,|\,x_0) & (\theta\,|\,\theta_0) & 0 & 0 & 0 & (\theta\,|\,\delta_0) \\ 0 & 0 & (y\,|\,y_0) & (y\,|\,y_0) & 0 & 0 \\ 0 & 0 & (\phi\,|\,y_0) & (\phi\,|\,\phi_0) & 0 & 0 \\ (z\,|\,x_0) & (z\,|\,\theta_0) & 0 & 0 & 1 & (z\,|\,\delta_0) \\ 0 & 0 & 0 & 0 & 0 & 1 \end{pmatrix} \begin{pmatrix} x_0 \\ \theta_0 \\ y_0 \\ \phi_0 \\ z_0 \\ \delta_0 \end{pmatrix} \tag{17-4}$$

The matrix R in the above equation is called the transformation matrix. The zeros which have been placed in the matrix depend on some rather general assumptions about the transport systems which will not be discussed here.

Transformation matrices for quadrupoles, bending magnets, and other fields are found in the literature.[1,2,3] For example, in a field-free region the matrix for a drift section of length L is

$$D = \begin{bmatrix} 1 & L & & & & \\ & 1 & & & & \\ & & 1 & L & & \\ & & & 1 & & \\ & & & & 1 & \\ & & & & & 1 \end{bmatrix} \tag{17-5}$$

The transformation matrix through an entire system is found by successive multiplication of individual matrices. It is now possible to formulate mathematically what is meant by the image of a source. Any particle leaving the source plane with a given displacement x_0 will arrive at the image plane with the displacement x regardless of the divergence θ_0, i.e., x is independent of θ_0, or $(x\,|\,\theta_0) = 0$.

The other optical conditions also translate into transformation matrix constraints:

1 Point-to-point horizontal image requires $(x \mid \theta_0) = 0$
2 Point-to-point vertical image requires $(y \mid \phi_0) = 0$
3 Horizontal image from infinity requires $(x \mid x_0) = 0$
4 Vertical image from infinity requires $(y \mid y_0) = 0$
5 Achromatic beam (horizontal) requires $(x \mid \delta_0) = 0$
6 Dispersionless beam (horizontal) requires $(\theta \mid \delta_0) = 0$.

These are a few special cases of constraints on the transformation matrix R. This matrix clearly depends on values of parameters such as drift region lengths, dipole strengths, and quadrupole gradients of elements making up the system. The computer program, TRANSPORT, solves the general problem of varying these parameters to find numerical solutions, if any, to given sets of constraints applied to given systems.

The behavior of the envelope of a group of particles is important in the design of any system in that it fixes the apertures of all the magnet elements and vacuum pipes. Given that the six differential coordinates are necessary to describe a particle, a group of particles will occupy a certain volume in this six-dimensional phase space. An ellipsoid volume in this phase space is a reasonable approximation for particles in a beam distributed about some ideal particle. Such an ellipsoid may be represented as a quadratic form.

$$\sum_{i=1}^{6} \sum_{j=1}^{6} a_{ij} x_i x_j \leq 1 \tag{17-6}$$

where x_i for $i = 1$ through 6 denotes $(x_0, \theta_0, y_0, \phi_0, z_0, \delta_0)$, the differential coordinates represented by $\mathbf{X}_0$ in Eq. (17-3).

Equation (17-6) may be written in matrix notation

$$\mathbf{X}_0^{\dagger} \sigma_0^{-1} \mathbf{X}_0 \leq 1 \tag{17-7}$$

where the matrix σ_0^{-1} denotes the matrix elements a_{ij} and the dagger superscript denotes the transpose vector. The matrix σ_0 uniquely characterizes the ellipsoid and, hence, the beam of particles. For convenience in what follows, σ, with or without subscripts, will be referred to as the beam matrix. Two observations can be made which follow from the properties of the quadratic form defined by σ: (1) The volume of the six-dimensional ellipsoid defined by σ is $(16/3)\pi(\det \sigma)^{1/2}$—this is the "phase space" occupied by the beam; (2) σ is a real, positive-definite symmetric matrix.

As a particle passes through a system of magnets it undergoes a transformation given by Eq. (17-3). The transformation for the beam matrix is

$$\sigma = R \sigma_0 R^{\dagger} \tag{17-8}$$

This can be seen by substituting into Eq. (17-7) as follows:

$$\begin{aligned} \mathbf{X}_0^{\dagger} \sigma_0^{-1} \mathbf{X}_0 = \mathbf{X}_0^{\dagger} [R^{\dagger} (R^{\dagger})^{-1}] \sigma_0^{-1} [R^{-1} R] \mathbf{X}_0 &= (R\mathbf{X}_0)^{\dagger} (R \sigma_0 R^{\dagger})^{-1} (R\mathbf{X}_0) \\ &= \mathbf{X}^{\dagger} \sigma^{-1} \mathbf{X} \leq 1 \end{aligned} \tag{17-9}$$

This leads to the following principle: Given the beam entering a magnet system and given the transformation matrix of the system, the beam leaving the system may be readily obtained by the transformation of Eq. (17-8).

To examine the significance of these symbolic transformations, consider the two-dimensional (x, θ plane) representation of the beam matrix,

$$\sigma = \begin{pmatrix} \sigma_{11} & \sigma_{12} \\ \sigma_{12} & \sigma_{22} \end{pmatrix} \tag{17-10}$$

with (det σ) $= \varepsilon^2$. Then

$$\sigma^{-1} = \frac{1}{\varepsilon^2} \begin{pmatrix} \sigma_{22} & -\sigma_{12} \\ -\sigma_{12} & \sigma_{11} \end{pmatrix} \tag{17-11}$$

and the expansion of $x^\dagger \sigma^{-1} x$ becomes the equation of an ellipse,

$$\sigma_{22} x^2 - 2\sigma_{12} x\theta + \sigma_{11} \theta^2 = \varepsilon^2 \tag{17-12}$$

The coefficients of the ellipse and, hence, the elements of the σ matrix can be given an interpretation with the aid of Fig. 17-4. The square root of the diagonal elements gives the projection of the ellipse upon the coordinate axes and this is the extent of the beam in the various coordinates. The correlation between components depends upon the off-diagonal term. It is defined as

$$r_{12} = \frac{\sigma_{12}}{(\sigma_{11})^{1/2}(\sigma_{22})^{1/2}} \tag{17-13}$$

The correlation measures the tilt of the ellipse and the intersection of the ellipse with the coordinate axes. The area of the ellipse is π det σ. Because the determinant of a product is the product of the determinants, so long as (det R) $= 1$, the area is invariant under

$$\sigma = R\sigma_0 R^\dagger \tag{17-14}$$

This is essentially a statement of Liouville's theorem for the magnetostatic fields employed. In the (important) case that the ellipse is upright, the area becomes $\pi(\sigma_{11})^{1/2}(\sigma_{22})^{1/2} = \pi x\theta$, a more familiar measure of phase volume.

Figure 17-4 Beam ellipse.

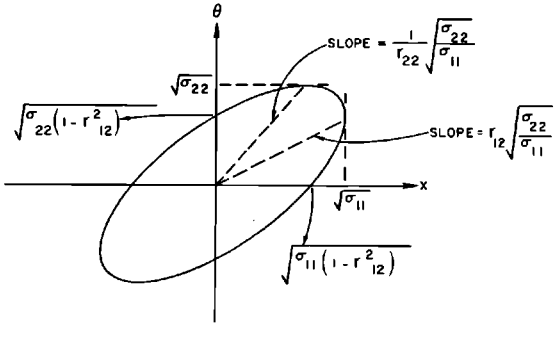

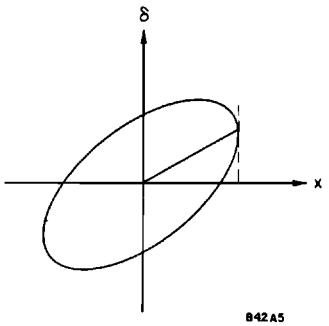

Figure 17-5 Projection of three-dimensional phase ellipsoid on x, δ plane.

The three-dimensional $(x, 0, \delta)$ extension of ray optics as published by Penner[2] requires a three-dimensional phase ellipsoid. Here again, in the units employed and for an upright ellipsoid, the volume of phase space becomes $\frac{4}{3}\pi x\, 0\delta$. The element σ_{13} defines the correlation between displacement and momentum and measures the *dispersion* in the beam. The projection of this ellipsoid on the x, δ plane is shown in Fig. 17-5. Thus, there obviously exists a correlation between particles with positive displacements and particles with positive momenta. This is the effect produced by deflecting the beam in a bending magnet.

Several other facets of the physical interpretation of the beam matrix warrant emphasis. The first point relates to the definition of the ellipsoid representing the beam. From the derivation of the transformation affecting the beam, it is apparent that particles cannot cross the surface of the ellipsoid. If their coordinates initially lie within the ellipsoid, they will remain within the ellipsoid through any number of linear transformations. This leads to a second point. The square roots of the diagonal elements indicate the maximum excursion of the particles in the beam from the reference trajectory. In particular, $(\sigma_{11})^{1/2}$ measures the horizontal extent of the beam. A plot of $(\sigma_{11})^{1/2}$ versus distance along the system is, therefore, the envelope of the beam and is the controlling factor in determining horizontal magnet apertures.

A characteristic of the beam envelope that becomes apparent upon plotting is the waist. This is a point where the horizontal (or vertical) extent of the beam is a minimum; in a field-free region it also happens to be a point where the ellipse is upright in the x, 0 plane, that is, $\sigma_{x\theta} = 0$ (see Fig. 17-6). At this point the beam is momentarily neither converging nor diverging. The fact that the minimum corresponds to an uncorrelated beam may be verified by determining the drift length that yields the minimum width,

$$\frac{\partial \sigma_{11}}{\partial L} = 0 \tag{17-15}$$

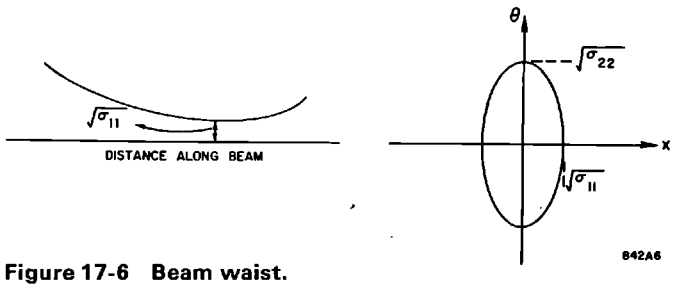

Figure 17-6 Beam waist.

The position of a waist depends upon the initial beam shape. However, it bears no useful relationship to the focal point of the magnets that may be used to produce the waist. For nonzero phase volumes, the location of a waist does not coincide with the location of a focus—that point at which the (x, θ) or (x, x) element of the transformation matrix vanishes. Evidently, if a small spot size at a target is desired, the target should be placed at a waist rather than a focus. The field-free drift distance to a waist is given by

$$L = -\frac{\sigma_{11}}{\sigma_{22}} = -r_{12}\left(\frac{\sigma_{11}}{\sigma_{22}}\right)^{1/2} \tag{17-16}$$

On the other hand, if L is a fixed distance from a quadrupole Q to a target, T, the optimum adjustment of Q to produce a small spot size at the target need not dictate a waist at the target, as Fig. 17-7 indicates.

Second-order effects

The previous paragraphs described a first-order model of beam optics. To establish, for a given beam transport system, the validity of approximations used in first-order theory, it is necessary to show that second-order aberrations for that system are negligible or at least sufficiently small. For this reason, a second-order beam optics model was developed and incorporated into

Figure 17-7 Effect of waist location on spot size.

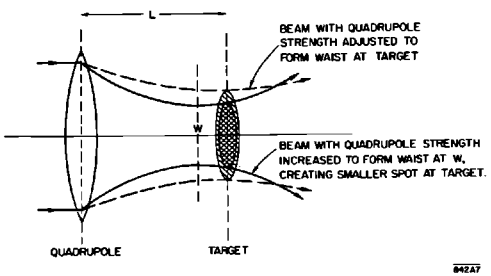

TRANSPORT. The approach is similar to the first-order case. One obtains a larger second-order transformation matrix for individual magnet types (e.g., bending magnet, quadrupole, sextupole), then combines them by matrix multiplication to get the second-order transformation of the system. Suppose that through a given magnet the transformation is

$$(x)_i = \sum_{l=1}^{6} R_{il} x_l + \sum_{l=1}^{6} \sum_{j=1}^{6} T_{ilj} x_l x_j + \cdots \tag{17-17}$$

The R_{il} form the first-order matrix described earlier. The T_{ilj} are the second-order coefficients of the transformation. For each individual magnet type, the T_{ilj} must be derived by expanding to second order the paraxial form of the general equations of motion of a charged particle through the magnet. Closed-form expressions for the T_{ilj} were obtained for various types of magnetic fields by different workers[1,4,5] and implemented into TRANSPORT. Then, with T available, a second-order transformation matrix through an individual magnet can be written. The product of such matrices, representing the magnets of the system in the appropriate order, yields the second-order transformation matrix of the entire system. The useful part of this matrix is the "T" partition. For example, the T_{236} element will give the effect on the final θ due to the product $(y_0\ \delta_0)$ of the initial ray. For this reason it is sometimes convenient to call T_{236} the $(\theta | y_0\ \delta_0)$ aberration. The reader is referred to Reference 1 for a complete discussion of second-order effects.

17-3 Optimization of system A (SKH)

In Section 17-1, the basic engineering criteria were given for the bending angles and drift distances D_1 and D_2. The remaining parameters of system A are the distance D_3 and the gradients of all five quadrupoles. The input acceptance requirements and other parameters fixed in the previous section together with certain constraints are used to determine values for these parameters. In practice, it is usual for a certain condition, e.g., a small beam cross section, to be required at some fixed position. The various conditions at different locations have been solved using the program TRANSPORT to yield a number of solutions to the beam design problem which have been collected to form a beam catalog.

The constraints which are common to almost all solutions are the following: (1) the transformation matrix element R_{12} from the center of the pulsed magnet group PM-1 through PM-5 to the front face of SL-10 is set equal to zero; (2) the matrix element R_{34} from the vertical pulsed magnet to the back face of the quadrupole Q-12 is set equal to zero (these two conditions determine the settings for Q-10 and Q-11 with two solutions; either Q-10 focuses horizontally and Q-11 vertically or vice-versa; (3) the matrix elements R_{16} and R_{26} to a point after the final bend at B-17 are set equal to zero. The location of the point is unimportant because once equal to zero [see Eq. (17-5)], these matrix elements remain equal to zero as the beam passes through

drift sections and quadrupoles. (The conditions $R_{16} = R_{26} = 0$ are, respectively, the achromatic and dispersionless conditions and their solution is essentially the same for all problems. These conditions determine the strength of Q-12 and the ratio of D_3 to D_2.)

To get a desired beam condition at a given distance D_4, the appropriate constraints are entered at that distance. The constraints may be for a waist ($\sigma_{12} = \sigma_{34} = 0$) or for a focus ($R_{12} = R_{34} = 0$) or for a parallel beam ($\sigma_{22} = \sigma_{44} = 0$) or perhaps for a given spot size such as ± 0.5-cm radius ($\sigma_{11} = \sigma_{33} = 0.5$). The parameters that are adjusted to fit these constraints are the gradients of the quadrupole doublet Q-13, Q-14 or of the doublet at Q-20, Q-21, the latter doublet being closer to the experimental area. Each of these may have either the focus–defocus or the defocus–focus order as in Q-10, Q-11. Between the choices of constraints and quadrupole order there are a large number of possible beam configurations. The beam catalog is simply a collection of some of these choices.

Second-order effects

There are two types of second-order aberrations—geometrical and physical. The two together make up the T_{ijk} array (previously discussed) for an individual magnet. The physical aberrations are the result of magnet imperfections, including the failure of first-order magnet parameters to describe adequately the magnetic field in the magnet. The geometrical aberrations are important when linear approximations are no longer valid. This occurs when any of the following conditions fail: $x/p \ll 1$; $y/p \ll 1$; $\theta \ll 1$; $\phi \ll 1$; $\delta \ll 1$.

For system A, $x/p \approx y/p \approx 10^{-3}$, $\theta \approx \phi \approx 10^{-4}$, and $\delta \approx 10^{-2}$. One would expect that if any second-order aberrations are important they would be chromatic in nature, namely, dependent on δ. However, because all second-order aberrations involve products of the above quantities, it is to be expected that second-order effects are negligible for the highly paraxial system A. This is, indeed, true except for bending magnet imperfections, and these alone will be discussed below. For a more detailed treatment, see Reference 6.

A dipole magnet with midplane symmetry has the following magnetic field components away from the fringe area:

$$\begin{aligned} H_z(x, y) &= 0 \\ H_y(x, y) &= H_0\left[1 - \frac{nx}{\rho} + \frac{\beta x^2}{\rho^2} + \left(\frac{n}{2} - \beta\right)\frac{y^2}{\rho^2} + \cdots\right] \\ H_x(x, y) &= H_0\left[-\frac{ny}{\rho} + \frac{2\beta xy}{\rho^2} + \cdots\right] \end{aligned} \tag{17-18}$$

where ρ is the radius of curvature of the reference trajectory in the magnet (for the 3° 3-meter magnets, $\rho = 57.296$ meters), H_0 is the field of the reference particle (at $x = 0$), n is the gradient or linear field index, and β is the quadratic

field index. The parameters H_0 and n are first-order field parameters. The quantity n can usually be made to vanish by symmetry of magnet design. Even if this is not the case, nonzero n effects can be countered by the gradients Q-10, Q-11. Since no term involving β in Eq. (17-18) is linear in the coordinates x and y, the first-order theory is independent of the value of β. If β is too large, differences between first-order theory and the actual field will appear. These differences will be seen in the second-order model.

There are three criteria for judging size and effect of second-order aberrations. They must not (1) affect the resolution of the system, (2) cause the beam to exceed magnet apertures, or (3) cause the minimum beam cross section at the target to be appreciably enlarged.

TRANSPORT second-order simulations on system A show that if the input beam divergence is $\approx 10^{-4}$, then noticeable second-order aberrations affecting resolution begin to appear for $|\beta| \approx 1500$. Also, the final beam cross section increases by a factor of 2 (over the $\beta = 0$ case) to 0.25 cm. This value of β determines the field homogeneity requirements.

The value of β for an actual magnet can be obtained from magnetic measurement data relating the field in the median plane $H_y(x, 0)$ to x, the horizontal displacement. The method by which such data are obtained is described below. These data may be fitted by least squares to a parabola,

$$H_{y(x,0)} = H_0\left(1 - n\frac{x}{\rho} + \frac{\beta x^2}{\rho^2}\right)$$

In this way estimates of β were calculated for all bending magnets. It was found that $|\beta| \leq 1600$ at all magnet currents. For magnet currents corresponding to momenta less than 20 GeV/c, $|\beta|$ is always less than 400. For $|\beta| \leq 400$, the quadratic field change at a distance of 1 cm from the reference trajectory on the median plane of the magnet is less than 2 parts in 10^5. The estimates of $|n|$ were in all cases less than 1 and were negligible.

The B transport system

The design philosophy for system B is identical to that for system A. The values of the design parameters are given in Table 17-2. The total angle of bend is 12.5°, derived from two 6° bends and a 0.5° deflection by the pulsed switching magnet. Magnets of the same design are used in both A and B systems. Two 3-meter magnets, each bending 3°, are used to obtain the 6° bend. The two magnets in each set are separated by 6 meters to allow the future insertion of a third magnet for expansion to the Stage II accelerator energy of 40 GeV/c. Each magnet then will bend only 2°. The effects of second-order aberrations are essentially the same as those for system A. The alignment criteria are also similar to those of the A system because the apertures in the second bending magnet group, as well as the reproducibility requirement on momentum definition, are equivalent to those of system A.

Alignment tolerances

The preceding discussion assumes that all the magnet axes coincide perfectly with the axis of the beam transport system. In practice this is not the case, so the mathematical model must be extended to deal with misalignments and to predict their effect on overall beam quality.

A rigid magnet has six degrees of freedom, three translational and three rotational. These are conveniently represented by six dependent quantities

$$\mathbf{m} = \begin{pmatrix} \delta x \\ \theta_x \\ \delta y \\ \theta_y \\ \delta z \\ \theta_z \end{pmatrix} \tag{17-19}$$

where δx, δy, δz are the displacements in the x, y, and z directions and θ_x, θ_y, θ_z are the rotations about the x, y, and z axes, respectively. The origin of the xyz coordinate system is taken as the magnet center, i.e., the point in a magnet of length L at which the reference particle has traversed length $L/2$. At that point the magnet axes coincide with the x, y, z components of the differential $\mathbf{X}$ vector discussed earlier. The vector $\mathbf{m}$ is a convenient quantity to use when discussing misalignment tolerances.

The problem is how to relate $\mathbf{m}$ to the transformation Eq. (17-3). When the magnet is misaligned, this becomes

$$\mathbf{X} - \mathbf{D} = R(\mathbf{X}_0 - \mathbf{D}_0) \tag{17-20}$$

The vectors $\mathbf{D}_0$ and $\mathbf{D}$ are the entrance and exit differential 6-vectors, respectively, of a ray traversing the path of the reference particle in a perfectly aligned magnet (see Fig. 17-8). Misalignment is a rigid transformation; therefore, the length and curvature of arc ACB are fixed and $\mathbf{D}$ and $\mathbf{D}_0$ are uniquely

Figure 17-8 Beam displacement due to magnet misalignment.

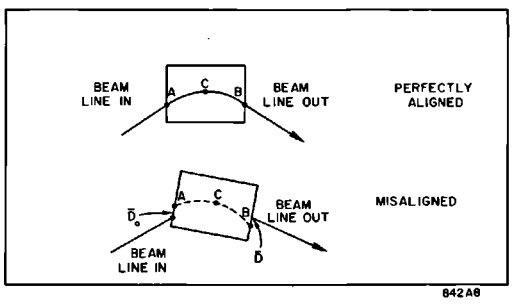

determined by **m**. For small |**m**| the relationship is

$$\begin{aligned} \mathbf{D}_0 &= A_0\,\mathbf{m} \\ \mathbf{D} &= A\mathbf{m} \end{aligned} \tag{17-21}$$

where

$$A = \begin{pmatrix} \cos\alpha & 0 & 0 & \rho\sin\alpha & \sin\alpha & 0 \\ 0 & 0 & 0 & 1 & 0 & 0 \\ 0 & -\rho\sin\alpha & 1 & 0 & 0 & -\rho(1-\cos\alpha) \\ 0 & -\cos\alpha & 0 & 0 & 0 & -\sin\alpha \\ -\sin\alpha & 0 & 0 & -\rho(1-\cos\alpha) & \cos\alpha & 0 \\ 0 & 0 & 0 & 0 & 0 & 0 \end{pmatrix} \tag{17-22}$$

and

$$A_0 = \begin{pmatrix} \cos\alpha & 0 & 0 & -\rho\sin\alpha & -\sin\alpha & 0 \\ 0 & 0 & 0 & 1 & 0 & 0 \\ 0 & +\rho\sin\alpha & 1 & 0 & 0 & -\rho(1-\cos\alpha) \\ 0 & -\cos\alpha & 0 & 0 & 0 & +\sin\alpha \\ +\sin\alpha & 0 & 0 & -\rho(1-\cos\alpha) & \cos\alpha & 0 \\ 0 & 0 & 0 & 0 & 0 & 0 \end{pmatrix} \tag{17-23}$$

α is one-half the angle of bend of the magnet, and ρ is the radius of curvature. For a quadrupole magnet, $\alpha = 0$ and $2\alpha\rho = L$, the magnet length, and the matrices reduce accordingly.

Substituting Eq. (17-21) into Eq. (17-20) gives a ray transformation through a magnet misaligned by **m**,

$$\mathbf{X} = RX_0 + (A - RA_0)\mathbf{m} \tag{17-24}$$

This completes the model for known misalignment **m**. Consider now an uncertainty in the magnet position and let the covariance matrix $\langle mm^\dagger \rangle$ measure the resulting distribution of magnet positions. If the position of the reference particle upon entering the magnet is $\langle xx^\dagger \rangle$ (due to, say, uncertainties introduced by misalignments of preceding magnets) and if there is no correlation of errors between two magnets, then from Eq. (17-24)

$$\langle xx^\dagger \rangle = R\langle xx^\dagger \rangle_0 R^\dagger + (A - RA_0)\langle mm^\dagger \rangle (A - RA_0)^\dagger$$

This equation expresses the resultant distribution in uncertainty upon leaving the magnet. This model for misalignment has been implemented in TRANSPORT. It enables one to introduce a displacement uncertainty δx, say of Q-10, and trace its effect through the system. The computer was used to generate tables of misalignment effects.

Alignment criteria

The two main concerns in establishing alignment tolerances on the system are related to apertures and momentum definition. In general, magnet apertures are kept small to reduce cost. This means that the uncertainty of the

reference axis must be kept small so that the beam will pass through all magnet apertures. A radial displacement of the reference axis at the slit corresponds to passing a different mean momentum through the slit; hence, the uncertainty of this quantity must be small enough to prevent significant deterioration in the momentum-defining ability of the system.

Using the alignment model discussed in a previous section, the effects on the horizontal and vertical aperture at any point due to any type of misalignment of any preceding magnet were computed. Starting with zero phase space (i.e., the reference trajectory only), a small misalignment uncertainty of a specified type, say δx, is introduced at magnet j. The resulting horizontal and vertical phase space at points $k > j$, i.e.,

$$(\sigma_{11}(k))^{1/2} \quad \text{and} \quad (\sigma_{33}(k))^{1/2}$$

are computed. These represent the uncertainty in the reference trajectory due to the alignment error. In this way the partial derivatives

$$H_{ijk} \equiv \frac{\partial[(\sigma_{11}(k))^{1/2}]}{\partial(\mathbf{m})_i} \qquad k > j,\ i = 1, 2, \ldots, 6$$

$$V_{ijk} \equiv \frac{\partial[(\sigma_{33}(k))^{1/2}]}{\partial(\mathbf{m})_i}$$

are approximated for each magnet j and are tabulated in Reference 6. The units are centimeters per mil and centimeters per milliradian for the displacement and rotation misalignment derivatives, respectively. The unit "mil" denotes 0.001 in. and was the convenient unit when actually aligning the magnets. With this detailed information available, sensible compromises between aperture sizes and alignment tolerance specifications were made at an early stage of BSY development.

A look at the values H_{ijk} and V_{ijk} for system A showed that the alignment requirements amount to controlling the vertical displacement of the beam at B-17 and the horizontal displacement at the slit. The significant alignment errors contributing to vertical displacement at B-17 are the vertical displacements of Q-10, Q-11, and Q-12, and rotations of bending magnets B-10 through B-17 and pulse magnets PM-1 through PM-5. Individual vertical uncertainties due to misalignments given in Table 17-3 added on an rms basis to the beam envelope at B-17 give an increased phase space which still passes through the usable aperture of ± 2.4 cm after this magnet. The significant alignments contributing to horizontal uncertainty at the slit are also given in Table 17-3. At the slit, the dispersion in the A system is $r_{16} = 6.3$ cm/percent momentum spread. Therefore, a momentum bite of $\pm 0.05\%$ will pass through a ± 0.32-cm slit. If this definition is to be reproducible to $\pm 0.02\%$ over long periods of time, then alignment errors must not shift the central trajectory in excess of $6.3 \times 0.02 \approx 0.13$ cm. Individual radial displacements due to the misalignments of Table 17-3 when added on an rms basis result in a displacement less than 0.13 cm. Other misalignments did not

Table 17-3 Tolerances controlling vertical uncertainty at B-17 and horizontal uncertainty at the slit

Quadrupoles	$\delta y \leq 5$ mils	$\delta x \leq 10$ mils
Bending magnets	$\theta z \leq 0.33$ mrad	$\delta z \leq 170$ mils
Pulsed magnets	$\theta z \leq 3$ mrad	

significantly affect these two criteria, i.e., their alignment derivatives were very small. For further discussion of alignment tolerances and alignment techniques, see Chapter 22.

17-4 Problems associated with transport of high-intensity beams (HAW)

Thermal effects

The high-intensity beams delivered by the accelerator posed severe problems to the designers of beam transport equipment. Direct impingement of the electron beam on solid materials results in rapid temperature rise and prompt damage due to thermal stress or melting (see Chapter 20). For example, a 600-kW, 20-GeV, 0.6-cm diameter beam resulting from 1.7-μsec long, 50-mA peak current electron pulses at 360 pulses/sec will cause a rise of 50°C/pulse at shower maximum in copper. A material having low thermal conductivity, high atomic number, or low melting point will sustain severe damage after only a few pulses. Consequently, the beam cannot be allowed to impinge directly on vacuum chamber components for more than a few pulses. The usual causes of accidental impingement are change in beam position, direction, or beam cross section at the end of the accelerator; incorrect setting of bending magnets; and incorrect setting of focusing magnets.

Although the energy spectrum from the accelerator is good, at high beam current there is a considerable intensity of off-energy electrons. These electrons are deflected into the walls of the vacuum chambers in and downbeam of bending magnets, and the equipment, therefore, has to be designated to withstand continuous bombardment by these electrons. These electrons create all the problems of a mis-steered high-intensity beam, though to a lesser degree.

Beam power is continuously absorbed in dumps, targets, slits, collimators, and protection collimators where the latter are located to intercept the off-energy electrons. Some beam energy is also unavoidably absorbed in vacuum chamber walls. When the power density exceeds about 1 W/in.^{2}, water cooling is required.

There were some fears that the high rates of energy deposition would give rise to shock waves which would cause fracture or spallation. Tests of aluminum samples have shown that this does not occur at the power levels expected in the electron beam. However, thermal fatigue due to temperature

cycling is a recognized cause of failure of materials. Some parts of the power absorbers may reach temperatures high enough to cause thermal fatigue within the useful lifetime of the equipment. Thin, water-cooled sections are used to reduce temperatures where high-energy deposition rates may occur.

The pulsed magnets require vacuum chambers of low electrical conductivity to minimize eddy current heating. Materials having a low electrical conductivity usually have a low thermal conductivity and are, therefore, subject to failure by thermal shock. These chambers must be protected from excessive heating. Also, nonconductive materials are subject to failure due to buildup of internal electrical charge when irradiated with charged particles.

Primary radiation

In addition to thermal effects, the electron beam can cause radiation change. Organic materials (vacuum gaskets, electrical insulation, electronic equipment, etc.) are very sensitive to radiation. For example, the epoxy material commonly used for magnet coil insulation will become brittle and develop cracks after absorbing about 10^{12} ergs/g—the epoxy[7] used in SLAC magnets will lose strength after absorbing about 10^{14} ergs/g; polyethylene and polystyrene cable insulation become brittle and crack at about 10^{11} ergs/g; Teflon, butadiene, and polyurethane insulation become embrittled at about 10^{10} ergs/g; Neoprene and rubber become embrittled at about 10^{9} ergs/g; semiconductors change their electrical characteristics significantly at 10^{6} to 10^{8} ergs/g. None of these materials can be used in the beam or in its immediate vicinity. Most of them cannot be used in regions where the beam is absorbed or lost unless they are suitably shielded.

Metals and ceramics are highly radiation resistant. Even direct impingement of the beam on thin sections of low-Z metals and ceramics will not cause radiation damage in reasonable lengths of time. Significant changes in properties do not occur until doses exceed 10^{18} ergs/g. For example, a 1-MW, 5–20-GeV, 0.6-cm diameter beam will deposit about 0.8 kW/cm^3, or 3×10^{9} ergs/g/sec at a depth of 4.5 cm in a block of aluminum.

Secondary radiation

Beam loss in the beam transport system causes intense radiation. Continuous beam losses occur at the slits, collimators, protection collimators located after magnets, and, of course, in dumps. DeStaebler[8] has estimated the integrated radiation exposure 10 ft from a shielded slit to be about 10^{10} ergs/g in 10 yr. This figure was confirmed by Neet,[9] whose tests also showed that the integrated radiation dosage inside the shielding would be as high as 10^{13} ergs/g in 10 yr. Thus, of the available organic materials, only the SLAC epoxy[7] can be used near places where beam is absorbed. Cables for magnets, instruments, switches, etc., must be fiberglass or mineral insulated; vacuum feedthroughs must be ceramic insulated. Since these solutions are expensive, it is desirable

to make a transition to more conventional insulation as close to the equipment as possible.

Conventional electrical and electronic equipment cannot survive for long periods of time in high radiation, so this equipment must be removed to a safe distance. This creates difficulties for electronic equipment where the signal level is very low.

Glass becomes brown and opaque after about 10^6 ergs/g, so viewing windows and lenses cannot be used in or near the beam.

Lubricating oils and greases harden when irradiated. In tests at SLAC,[10] a polyphenyl ether oil hardened at about 10^{12} ergs/g. Thus, equipment in high radiation areas can be lubricated if the proper lubricants are used. Dry lubricants have greater radiation resistance, but none of those investigated proved reliable. The usual problem was that continuous coverage could not be maintained.

Induced radioactivity

Material that absorbs beam will become radioactive. DeStaebler[11] has estimated the radiation levels in the vicinity of beam scrapers along the accelerator. For 5 kW of beam power absorbed in a scraper, he estimated saturation radiation levels of 2.2×10^3 mrem/hour from the concrete walls of the accelerator housing. Measurements have shown that these estimates are approximately correct. Shielding of the sources and addition of boron to the concrete are discussed by DeStaebler as possible methods of reducing radiation levels. Radioactivity will make access for modification and repair very difficult. Provision must be made for shielding radioactive equipment and for working at a distance. The air surrounding the beam transport will absorb some energy and will become radioactive. Fortunately, most of this activity is due to short-lived isotopes. It is thus possible to seal the housing in operation and to ventilate at shutdown, after a short decay period. Water that is used to absorb beam energy or to cool energy absorbers will become radioactive.[12] The ^{13}N, ^{15}O, ^{11}C, and ^{7}Be are produced by irradiation of ^{16}O. Tritium (^{3}H) will also be produced. The ^{13}N, ^{15}O, and ^{11}C have short half-lives, but ^{7}Be and ^{3}H activity will build up to high levels.

FORMATION OF CORROSIVE GASES. When air is irradiated, ozone and oxides of nitrogen are formed. In the presence of moisture, the nitrogen oxides will convert to nitric acid. The production of nitric acid can be estimated as follows: Reference 13 gives a production rate of one molecule of HNO_3 for each 35 eV absorbed. It is estimated that for a 600-kW beam, 3–20 W are absorbed in air in the BSY. Since 1 W equals 6.23×10^{18} eV/sec, 18×10^{16} HNO_3 molecules/W-sec are formed. For 20 W of power absorbed in air, 33 g of HNO_3 are produced each day. This is equivalent to about 0.06 liter/day of 35% concentrated acid. After 5 days of continuous operation, 165 g will have been produced, giving a concentration of about 6 parts per

million if evenly distributed throughout the switchyard housing. The greatest concentration of absorbed radiation will be in the vicinity of the high-power beam absorbers. It is difficult to predict whether the nitric acid will be uniformly distributed or will be concentrated near the energy absorbers. Continuous or frequent ventilation would reduce the concentration of nitric acid in the air, as would chemical scrubbing or chemical neutralization. Removal of water vapor from the air or exclusion of oxygen from the housing would reduce the production of nitric acid.

Very few materials are nitric acid-resistant, and most of these are expensive. Stainless steels, glass, ceramics, and high-silicon cast iron are very good at all concentrations of acid. Certain plastics such as phenolics, vinyls, and epoxies are fairly good at some levels. Plating is not very useful at high concentrations of acids. Very few plating materials are nitric acid-resistant (gold, chromium), and minute plating flaws can destroy the effectiveness of even these materials.

LIMITED ACCESS. During operation, radiation levels in the switchyard housing are so high that human occupancy is ruled out. Equipment must be designed to operate unattended. Beam instrumentation must be remote-reading and remotely operable. Personnel and equipment protection must be automatic.

After running at high-power levels, time must be allowed for decay of radioactive isotopes in the air and for subsequent ventilation. Thus, diagnosis and repair of equipment failures is very time-consuming, making high reliability a necessity. It is also very desirable to locate marginally reliable equipment and equipment requiring frequent adjustment or servicing in accessible areas.

After long periods of operation at high power, equipment in the vicinity of the beam will become radioactive. This will make modification and repair increasingly difficult. Equipment must be designed for quick adjustment and removal and for ultimate removal by personnel shielded from the high radiation. Again, high reliability and minimum maintenance must be incorporated into the design of all equipment.

Shielding

Shielding problems in the BSY are primarily of two kinds: (1) for primary and secondary radiation, and (2) for radioactivity. In operation, the shielding must be adequate to protect personnel from photon, neutron, and mu radiation produced when the primary electron beam is intercepted. Thick concrete walls and earth fill will stop the photons and neutrons. The neutrons will tend to "duct" out of even mazed or baffled openings, so provisions must be made for shielding all openings. The muons have a very long stopping distance (equivalent to 50 ft of steel for 25-GeV incident electrons), so that high-density shielding must be used where muons are produced close to inhabited areas.

Cooling water from energy absorbers will be highly radioactive during operation, so these water lines must be shielded. Equipment absorbing beam inside the BSY will become radioactive, so local shielding will be required to permit access for maintenance and modifications during shutdown.

17-5 Beam switchyard design (HAW)

The beam switchyard transport system is a permanent part of the accelerator. It was designed to provide reliability, precision, and flexibility under the severe conditions of operation described above. The arrangement of the beam switchyard and some of the components and subsystems unique to the beam switchyard will be described.

The BSY equipment is installed in a 1000-ft long concrete housing buried under 30 ft of earth. Figure 5-23 shows typical BSY housing cross sections. The housing walls are reinforced concrete. Sections around targets, dumps, slits, and collimators are boron-loaded to reduce activation by neutrons. The walls, floor, and ceiling are painted with white radiation-resistant paint. Normal access is limited to a large opening suitable for trucks and two smaller accessways suitable for personnel. These openings are shielded, locked, and interlocked during operation.

An underhung crane riding on rails suspended from the ceiling has access to all equipment. The crane runs the full length of each leg. In the section where the beams diverge, the rails are interlaced and a transfer bridge is provided to shift cranes from one leg to another. Steel rails for a future shielded car are laid above the shielding ledge. Up to 4 ft of shielding may be placed on the shielding ledge to protect cables and electronics in the upper level from radiation during operation and to protect personnel from radioactivity during shutdown. Large air exhaust ducts are located at the end of all beam runs at both levels, making it possible to admit air through the main accessway, which has a large filter door and to ventilate every part of the housing.

All beam transport equipment is located in the lower level. All vacuum, water, and electrical connections can be made from the upper level through holes in the shielding, if necessary.

The nominal beam height is 5 ft, 6 in. above the floor. All equipment is supported on adjustable stands. Provision is made for 6 in. of precise jack adjustment from the upper level. Greater adjustments require insertion and removal of spacers. Radiation-resistant materials were used in the design of equipment for the lower level. Magnets, stands, and other equipment, which are not in high-radiation areas and could not economically be made of stainless steel, are coated with epoxy paint. Carbon steel parts in high-radiation areas are coated with special radiation-resistant paint (see Chapter 20).

The primary subsystems and components of the BSY include the vacuum system, water systems, power distribution systems, magnets and power supplies, instrumentation and control, beam absorbers, and targets and stands of various types.

The system of vacuum chambers for the transport equipment is entirely inorganic. All chambers are aluminum or stainless steel weldments with the exception of the pulsed magnet vacuum chambers which are discussed below. The quickly replaceable vacuum parts use indium gaskets with a SLAC-designed coupling. Water cooling of the vacuum chamber is provided where beam heating is expected. The vacuum pumps and gages are located on top of the shielding fill for ease in servicing. The pumps are conventional oil diffusion pumps with refrigerated baffles and mechanical backing pumps. The accelerator vacuum system operating at 10^{-7} torr is separated from the switchyard vacuum of 10^{-4} torr by a differential pumping system including ion pumps, a refrigerated baffle at $-40°C$, and fast vacuum valves. Radiation-resistant fast valves and isolation valves are scattered throughout the switchyard to protect the accelerator vacuum and delicate BSY equipment and to minimize pump-down time.

Two types of water systems are required: magnet water systems and radioactive water systems for beam energy absorbers. The magnet water system is fabricated from copper and stainless steel. Headers in the upper level of the housing supply low conductivity water to individual pieces of equipment. Flexible copper hoses supply water to each piece of equipment in the lower level. A remotely disconnectable stainless steel pipe union is installed in each line to permit removal of equipment. Individual return lines are brought through the shielding to return headers on the outside of the beam switchyard structure. Flowmeters, flow switches, valves, and thermometers are located in each return line where they can be reached in operation. All heat exchangers, pumps, surge tanks, and controls are also outside the housing. Separate water systems are provided for the A-beam and the B-beam. In an emergency, either heat exchanger can be used with either beam; each heat exchanger can handle both beams.

The radioactive water systems are stainless steel with copper in some systems and aluminum in others. The heat exchangers, pumps, surge tanks, and instruments are outside the switchyard. The radioactive water system equipment is shielded to protect personnel from radiation due to radioactivity in the water during operation. Radiation levels of 110 R/hour have been measured inside this shielding during operation. The heat exchanger pad floor is so arranged that leakage of radioactive water will drain into the switchyard housing where it can be stored until it has "cooled" and can be disposed of. No provision was made initially to handle evolved gases. A hydrogen recombiner system has since been developed (see Chapter 20). Connection to equipment is by commercial couplings with metal gaskets. It was feared that radioactivity in the water would build up to levels which would make repairs and maintenance of water system equipment difficult or impossible. This has not proved to be so. The ^{7}Be is captured in the demineralizers which are shielded and can be safely disposed of.[14] Tritium levels can be kept low by periodic changes of water, the period depending on the power deposition. Other activities are short-lived.

Magnets are of conventional design but are manufactured to tight tolerances to maintain the uniformity required. Coils are potted in radiation-resistant, alumina-loaded epoxy.[7] Each coil is protected by overtemperature switches. Insulators in the magnet water circuits are alumina. Pulse-to-pulse switching is done by five 0.1° laminated-core pulsed magnets with 0.1° bending angles.[15] The power supplies for these magnets consist of capacitor banks charged by vacuum tube rectifier power supplies and discharged through SCR switches (see Chapter 19). Pulse-to-pulse steering is accomplished similarly using smaller magnets and power supplies. The pulsed magnets have ceramic vacuum chambers because even low conductivity metals such as stainless steel and Hastelloy overheat in the pulsing magnetic field. Some apprehension was felt about damage due to accumulation of stray electrons and attempts were made to obtain ceramics with increased electrical conductivity. The attempts were unsuccessful, and subsequent tests of $\frac{1}{4}$-in.-thick samples of alumina in an electron beam produced no failures by this mechanism although 1 W/cm^2 was absorbed. (Samples did fail due to thermal shock.) The alumina has a very low thermal conductivity and is subject to damage due to shock, so protection collimators in the equipment protection system (see Chapter 20) prevent the beam from striking the chamber walls, but low-energy electrons can be deflected around the collimators, heating the walls. Thermometers were installed to turn off the accelerator upon excessive temperature indication. The alumina chambers are oval in cross section with stainless steel bellows and flanges at each end. The transition from alumina to metal is via thin stainless steel cuffs brazed to alumina. The alumina has a proprietary conductive coating both inside and outside to prevent surface charge buildup.

The pulsed steering magnets have Hastelloy vacuum chambers. The maximum field intensity is lower than in the 0.1° pulsed magnets and the maximum temperature in the Hastelloy is acceptable.

The vacuum chambers in the precise bending magnets are 316L or 304L stainless steel especially selected for low permeability to minimize local distortion of the magnetic field.

All the power supplies for the beam switchyard magnets are located in the Data Assembly Building next to the control room for ready accessibility. Direct current cables run outside the shielding as far as possible, then through duct banks into the upper level of the housing. They are connected to radiation-resistant, fiberglass-insulated cables which run to the magnets in the lower level. A SLAC-developed remote power disconnect is used to hook up to the magnets. The power disconnects are protected by locked covers; it is necessary to shut off the power supply before this cover can be removed. Power supply disabling switches and warning lights are provided in the vicinity of each magnet.

The instrumentation and control cables are similarly run outside the shielding to a point near the associated instrument, and then through a duct bank into the upper level. The connection to the instruments in the lower level is made by mineral-insulated coaxial cable or fiberglass-insulated wire. Both

Cerenkov cells and zinc sulfide screens are used in the beam, so optics and TV cameras are required. Front surface mirror optics are used to avoid problems with darkening of glass due to radiation. Radiation-hardened TV cameras are very expensive, so cameras are shielded and easily replaceable. All beam line instruments are adjustable and removable from the upper level. Where electric motors are required, they are located above the shielding floor and are replaceable. Air actuators are metal-bellows sealed.

As mentioned above, the ceramic vacuum chambers are protected from the electron beam by protection collimators. Other vacuum chambers, instruments, etc., are similarly protected. Each protection collimator has an associated ionization chamber which is in the interlock chain and which serves to shut off the accelerator when the collimator is hit by the beam.

Beam instrumentation is provided to monitor beam position, beam current, and energy spread (see Chapter 19). The instruments read out in the Data Assembly Building where power supplies and controls are also located.

17-6 Early operating experience and design evaluation (EJS and JLH)

The first electron beam was delivered through the A-beam transport system and end station A to beam dump east on September 20, 1966. Since that date, numerous tests and experiments have been performed on the beam switchyard transport system. In addition, several preliminary experiments of a survey nature have been completed and others are in progress. In general, the operation of the system has been exceedingly satisfactory. The maximum electron energy to date is 20.16 GeV. A momentum spectrum of the electron beam obtained using the beam switchyard momentum analyzing system is shown in Fig. 8-17. The first positron beam was delivered to end station B on February 22, 1967. The maximum beam power which has been transported through the system is 240 kW. It is anticipated that the power level will soon be more than doubled. Multiple beams of various energies, currents, pulse lengths, and repetition rates are now routinely delivered to experimenters in the end stations. Electron beam spot sizes of 1 mm diameter have been achieved. Various early checks on the momentum calibration of the transport system have been made by comparing the A and B transport systems, by using a quantameter and Faraday cup, by comparing the end station spectrometer with the A transport system, and by calorimeter measurements. Although much more refined tests are required, the early tests indicate that the beam switchyard system satisfies the design criteria for momentum calibration and resolution given in Table 17-2. Early experimental studies of beam optics and beam isochronism indicate that the transport system behaves in agreement with the predictions of the SLAC TRANSPORT computer program, which was used to design the system. However, optics tests indicate that the transport system solid-angle acceptance is less than expected. This effect is not clearly understood, but is probably the result of misalignment of

components and certain known differences in the bending magnets of the system. Since the emittance phase space of the accelerator is much smaller than the achieved acceptance of the beam switchyard transport system, there is no difficulty in delivering the beam to the experimental areas.

Operating experience to date has emphasized the need for high reliability of equipment. Problems that hamper delivery of the beam are the usual ones of getting such a system to operate—e.g., interlock faults, power supply failures, slit drive failure, browning of TV camera lenses, vacuum failure, and personnel protection system failure. Since the initial turn-on, equipment has been damaged by the electron beam on two occasions: (1) a spring in a vacuum quick-disconnect valve was overheated, resulting in loss of elasticity and a vacuum leak, and (2) a vacuum quick-disconnect was overheated, causing the indium seal to melt, again resulting in a vacuum leak. At the power levels run to date, usually about 1 to 10 kW, no serious radiation or radioactivity problems have been encountered. The radioactivity induced in the radioactive water systems is already sufficient to restrict system ventilation during operation. Some of the cooling water becomes intensely radioactive, but most of the activity is short-lived (^{15}O, ^{11}C). The ^{7}Be is produced in the water and removed by the demineralizers. Demineralizers have been found to have about 100 μCi of activity when depleted. Equipment close to the beam is becoming radioactive, but remote operations have not yet been necessary. It is too early to evaluate the radiation resistance of special components.

Acknowledgments

The fundamental principles of the beam transport systems were proposed by K. L. Brown. The proposal was studied and recommended by S. Penner. R. Taylor was responsible for the development of the basic layout of all equipment and systems and for the basic criteria for all components. He was aided by many people in many areas: D. A. G. Neet, control and instrumentation; B. DeRaad (CERN), instrumentation and equipment protection; F. Bonaudi (CERN), general layout, services, and utilities; H. Brechna, magnets and radiation-resistant coil insulation; Bengt Hedin (CERN), magnets; Julius Muray, magnet instrumentation and pulsed power supplies; E. Garwin, vacuum, energy absorbers, and water systems; H. DeStaebler, radiation and radioactivity; H. Butler, beam optics and computer programming; S. Howry and C. Moore, computer programming; D. Coward, all areas; K. Trigger, alignment; A. Odian, parasitic gamma beam; D. Drickey, A photon beam; W. B. Johnson, physics (B-beam); R. Larsen, physics (B-beam); Z. Guiragossián, radiation and shielding; D. Fries, muon shielding.

The engineering of the switchyard was done under the direction of the *ad hoc* beam switchyard group. The contributions of support groups are acknowledged elsewhere. Beam switchyard group staff and their areas of responsibility were as follows: C. R. Johnson, equipment installation; C. A. Harris, power supplies; E. K. Johnson, electrical distribution and water;

E. Oster, magnets (this later became the responsibility of the Magnet Engineering Group under J. Gunn); L. Lucas, energy absorbers; D. A. G. Neet, instrumentation and control; J. Voss, supports and alignment; R. Allyn, mechanical engineering; R. Gould, plant engineering liaison; R. Pedersen and R. Short, technical planning liaison. Dorothy Ellison was group secretary during its entire lifetime.

References

1 K. L. Brown, "A First- and Second-Order Matrix Theory for the Design of Beam Transport Systems and Charged Particle Spectrometers," Rept. No. SLAC-75, Stanford Linear Accelerator Center, Stanford University, Stanford, California (July 1967).

2 S. Penner, *Rev. Sci. Instr.* **32**, 150 (1961).

3 C. H. Moore, S. K. Howry, and H. S. Butler, "TRANSPORT—A Computer Program for Designing Beam Transport Systems," Rept. No. SLAC-54, Stanford Linear Accelerator Center, Stanford University, Stanford, California (to be published).

4 R. Helm, "First- and Second-Order Beam Optics of a Curved, Inclined Magnetic Field Boundary in the Impulse Approximation," Rept. No. SLAC-24, Stanford Linear Accelerator Center, Stanford University, Stanford, California (November 1963).

5 S. Howry, "Second-Order Aberration Coefficients of a Quadrupole," Tech. Note, No. SLAC-TN-62-45, Stanford Linear Accelerator Center, Stanford University, Stanford, California (1962).

6 H. Butler, S. Howry, and C. Moore, "Specifications for the Beam Transport Systems to End Stations A and B," Rept. No. SLAC-29, Stanford Linear Accelerator Center, Stanford University, Stanford, California (1964).

7 H. Brechna, "Effect of Nuclear Radiation on Organic Materials; Specifically Magnet Insulations in High-Energy Accelerators," Rept. No. SLAC-40, Stanford Linear Accelerator Center, Stanford University, Stanford, California (1965).

8 H. DeStaebler, "Rough Estimates for Radiation inside the BSY When the Beam Is on," Tech. Note, SLAC-TN-63-69, Stanford Linear Accelerator Center, Stanford University, Stanford, California (1963).

9 D. A. G. Neet, "Radiation Exposure in the Switchyard," Tech. Note, SLAC-TN-65-9, Stanford Linear Accelerator Center, Stanford University, Stanford, California (1965).

10 D. R. Walz and E. J. Seppi, "Irradiation of Highly Radiation-Resistant Organic Lubricants and a High Temperature Paint," Tech. Note, SLAC-TN-67-13, Stanford Linear Accelerator Center, Stanford University, Stanford, California (1967).

11 H. DeStaebler, "Radiation Levels in the Vicinity of the Beam Scrapers," Tech. Note, SLAC-TN-64-23, Stanford Linear Accelerator Center, Stanford University, Stanford, California (March 1964).

12 H. DeStaebler, "Photon-Induced Residual Activity," Tech. Note No. SLAC-TN-63-92, Stanford Linear Accelerator Center, Stanford University, Stanford, California (1963).

13 S. C. Lind, C. J. Hochanadel, and J. A. Ghormley, *Radiation Chemistry of Gases*, Am. Chem. Soc. Monograph No. 151, Reinhold, New York, 1961.

14 R. McCall, "Activation of Water during Beam Tests," Tech. Note No. SLAC-TN-66-4, Stanford Linear Accelerator Center, Stanford University, Stanford, California (1966).

15 H. Brechna, "A Pulsed Bending Magnet for the Beam Switchyard Area of the Stanford Two-Mile Linear Electron Accelerator," Rept. No. SLAC-28, Stanford Linear Accelerator Center, Stanford University, Stanford, California (1964).

18

BEAM SWITCHYARD MAGNETS

H. Brechna, W. O. Brunk, A. W. Burfine, J. K. Cobb, Editor, D. R. Jensen, E. L. Oster, E. J. Seppi, and M. T. Stangenes

The purpose of this chapter is to describe the extensive system of magnets installed in the beam switchyard (BSY). Following a brief description of the overall system in which the major components are identified, a detailed discussion of the design, fabrication, and performance of each type of magnetic element is presented. Design parameters and costs are summarized in tables. The magnetic characteristics of the momentum-analyzing systems are described in the next section, together with a discussion of magnetic measurements and data reduction. Criteria used in selecting the location of each magnet are given, and the chapter ends with a comparison of three methods of setting magnet fields for momentum analysis.

18-1 Qualitative description of system elements (HB, WOB, ELO, MTS)

Each of the magnets in the beam switchyard transport systems is a discrete element performing a separate function. The most prominent magnets are the 3° bending magnets for momentum analysis and beam deflection and the 8-cm quadrupole magnets for beam focusing. These basic elements are used in both A and B systems of the BSY (see Fig. 17-1). In addition, there are five 0.1° pulsed deflection magnets used to switch the beam into system A or system B on a pulse-to-pulse basis, two 0.25° dc emergency deflection magnets which are used if the pulsed magnets fail, and two 18.6-cm quadrupoles used as field lenses at the symmetry positions in the two transport systems. Four dc magnets are used when it is required to deflect the A-beam down into a dump preceding end station A. In the B system, two 0.17° pulsed deflection magnets and a magnetic slit are used to select the destination of the beam in end station B on a pulse-to-pulse basis. The optical characteristics of the BSY are discussed in Chapter 17.

All of the momentum-analyzing magnets in the A and B beams of the BSY are identical in physical and magnetic characteristics except for relatively minor magnetic differences which will be discussed later in this chapter. These magnets are 3° bending magnets and are used in positions B-10, -11, -12, -13, -14, -15, -16, -17, -30, -32, -33, and -35 in the BSY. All of the quadrupole magnets used in doublets in the BSY are also identical in physical and magnetic characteristics. These magnets are located at positions Q-10, -11, -13, -14, -20, -21, -30, -31, -33, and -34. Continuing the catalog, the five 0.1° pulsed magnets PM-1, -2, -3, -4, -5, and the two 0.17° pulsed deflection magnets PM-30 and -31 are all the same, as are the dc emergency magnets B-1 and -2, the 18.6-cm symmetry quadrupoles Q-12 and -32, the pulsed steering magnets AP-1, -2, -3, and -4, the dump magnets B-23, -24, -25, and -26, the dc steering magnets A-10, -11, and -12, and the pulsed steering magnets AP-30 and -31. The remaining magnets in the BSY are all one of a kind. The most important magnets will be discussed in some detail, whereas the less critical ones will be dismissed with only a few words about general magnetic and physical characteristics.

Of all component groups in the BSY, the magnet and power supply system is predominantly the most expensive. Major considerations in the development of new types of magnet configurations were economy while still maintaining safety and reliability of operation. It was also essential that the magnet characteristics dictated by second-order beam optics be achieved. These included field homogeneity over a given area in the gap of bending magnets and constant field gradient over at least 90% of the aperture in focusing magnets. Design objectives of greatest concern were: (1) control of fringing field by shaping pole-piece ends; (2) achieving specified field homogeneity by pole shimming[1] in bending magnets; (3) optimization of core and coil sizes for the required dimensions of useful gaps and apertures; (4) suppression of dipole and higher-order multipole fields in quadrupoles[2]; (5) development of appropriate coil insulation to withstand integrated irradiation doses of 10^{11} to 10^{12} rad.[3]

In the case of the pulsed bending magnets, although specifications with regard to irradiation resistance and field homogeneity are essentially the same as in the dc magnets, a few additional factors are added. The pulsed magnets operate at a frequency of 360 pps, and fatigue problems over a period of at least 10 yr due to the effects of the oscillating magnetic field must be considered. The coils operate at a voltage of 2 to 3 kV with respect to ground and with approximately 1.0 kV between turns. They must, therefore, be insulated in such a way that no voids are left in the insulating material, because such voids could permit corona discharges leading to breakdown. As the conductor has to be of a multistranded water-cooled construction to prevent excessive eddy current losses, an impregnation process had to be developed which insured thorough penetration of the thermoset. In addition, of course, the insulating material had to have proven irradiation resistance. The vacuum chambers inside the pulsed magnet gaps are specially designed and constructed ceramic tubes, which withstand irradiation effects and do not crack

from charge accumulations. The use of metals or combinations of metallic and organic materials in the vacuum chambers had to be avoided because of eddy-current heating which would occur in the fluctuating, transverse magnetic fields.

With these special requirements, systematic development work was needed. Simple calculations based on known engineering practices and rough model magnet work were inadequate. A team effort was needed not only to design, build, and test prototypes, but also to enforce very stringent quality control to insure that all magnets of the same design would be closely identical. Uniformity of steel ladle analysis, mechanical tolerances, and quality of workmanship were closely scrutinized throughout the fabrication program.

General design consideration

The function of the BSY magnet system is threefold: (1) provision of bending forces to keep the particle moving in a predetermined path; (2) provision of focusing forces to restrict horizontal and vertical motion of electrons, so that they remain inside vacuum chambers of relatively small cross sections; and (3) provision of steering forces to compensate for the malfunction or misalignment of certain components and for residual magnetic fields.

The design of the BSY magnets was influenced by their interaction with the other components along the beam, such as control and monitoring systems, slits, and collimators.

All BSY magnets have iron cores which are very resistant to damage by radiation. Therefore the problem of irradiation resistance centered principally upon the choice of coil insulation material. When organic materials are irradiated, covalent bonds are broken by ionization causing displacement of atoms in the lattice structure. In electron machines the production of fast neutrons is approximately two orders of magnitude smaller than in proton machines of the same beam power, but the ionizing radiation fields are more intense. Therefore, standard organic materials cannot be used near beam absorbers. Since many magnets were to be located near beam absorbing units, a new coil insulation had to be developed.

The coil insulation is based on heat-treated and chemically treated glass fiber tapes as structural material and alumina-loaded thermosets as impregnants. The ratio of organic to inorganic materials in the composite insulation is low, yielding a surface distribution without too many detrimental changes in mechanical properties, reduced shear stress and adhesion to the conductor, and decreased hygroscopic absorption.

The final formulation which was used for interturn and ground insulation is

Thermoset: pure epoxies, 100 pbw (parts by weight).
Hardener: aromatic Amine, 3 pbw or Anhydride, 80 pbw.
Wetting agent: epoxy functional glycidoxylpropyl trimethoxy silane, 1–2 pbw.
Filler: pure granulous alumina with grain size 1–10 μ, 100–200 pbw.

Table 18-1 Design features of the beam switchyard magnets

Parameters	*Pulsed magnet*	*3° Bending magnet*	*8-cm quadrupole magnet*	*18.6-cm quadrupole magnet*	*3° dump magnet*	*Magnetic slit*	*Emergency magnet*
Beam energy (GeV)	25	25	25	25	25	20	25
Deflection angle (degs)	0.1	3	—	—	3	± 1.8	0.25
Combined units	5	Beam A: $4+4$ Beam B: $2+2$	Doublets	Singlet	4	1	2
Gap height (meters)	0.05	0.06027	—	—	0.076	0.0508	0.07
Aperture (meters)	—	—	$r=0.04$	$r=0.092$	—	—	—
Useful gap dimensions (meters)	—	—	$r=0.037$	$X=\pm 0.1$ $Y=\pm 0.01$	—	—	—
Gap width (meters)	0.16	0.3	—	—	0.12–0.24	0.178	0.07
Flux density (T)	0.17	1.455	—	—	1.455	± 0.85	0.56
Field gradient (T meters^{-1})	—	—	7.5	4.33	—	—	—
Effective length (meters)	0.85	3.025	2	2	3	2.5	0.0648
Overall length (meters)	1.08	3.47	2.30	2.33	3.58	2.82	0.93
Field homogeneity	10^{-3} (over $x=\pm 4$ cm)	$\approx 10^{-4}$ ($x=\pm 4$ cm)	—	—	—	10^{-3} ($x=\pm 2.5$ cm)	10^{-3} ($x=\pm 4$ cm)
Gradient linearity (%)	—	—	0.1 ($r=\pm 3.7$ cm)	0.1 ($X=\pm 10$ cm) ($Y=\pm 1.$ cm)	—	—	—
Peak current (A)	300	800	850	550	1000	700	360
Current density (A cm^{-2})	346	552	2600	700	700	560	572
Turns per pole	24	48	6	29	48	26	49
Terminal voltage (V)	2500	75	65	75	80	42	20

All coils were vacuum impregnated and cured under pressure at temperatures between 100 and 180°C. The high radiation environment also made it necessary to eliminate organic materials including natural and synthetic rubber from the magnet water-cooling circuits. Stainless steel connectors were used, with ceramic sleeves where electrical insulation was needed.

The magnet core and poles consist of forged or rolled steel with the following impurity composition: C—0.12% maximum; total A + Mo + S + P—0.1% maximum; total Mn + Ni + Cr + Cu + Si—0.7% maximum.

Manufacturing tolerances (deviations from calculated contours) were kept within 0.0002 in. on straight pole surfaces, and 0.0025 in. on contoured surfaces. In general, gap errors obtained in manufacturing were a factor of 2 or 3 better than the specified tolerances.

All magnets except the steering magnets and photon beam magnets are equipped with magnetic mirrors which confine the fringing field area and define the effective magnetic length. To eliminate second-order effects on the beam due to iron saturation and fringing fields, the pole ends and pole contours are shimmed. With the exceptions noted, the above remarks apply to all BSY magnets. In the following sections, design and construction details of each of the main types of magnets will be given.

The pulsed magnet system

The pulsed magnet system is designed to deflect an electron or positron beam of momentum up to 25 GeV/c by 0.5° to either side of the central axis. The deflection is achieved on a pulse-to-pulse basis by a series of five identical pulsed magnets. The main features of these magnets are given in Table 18-1.[4]

The core was manufactured from 0.035-cm cold reduced, grain oriented, silicon steel laminations which were stamped to the required tolerances. Epoxy was applied to one surface of each lamination, and the laminations were stacked in a rigid fixture to form the core. The assembly was evacuated to approximately 1 torr, vacuum impregnated, and cured under a pressure of 0.2 to 0.5 kg-cm^{-2} at a temperature of 125°C. The core consists of two E-shaped parts, welded at the outside surfaces to structural channels and bolted rigidly to each other. A pulsed magnet with its magnetic mirror attached is shown in Fig. 18-1. The stainless steel water connections and the structural parts are clearly visible. The normalized induction integrated over the length ($\int B\,dz$) at the median plane, as a function of horizontal displacement x perpendicular to the beam axis, is given in Fig. 18-2.

Multistranded water-cooled cable was wrapped in medium-weave glass tape and the wound coil was spaced by means of small glass fiber blocks from the mold walls and bottom plate. The assembly was vacuum impregnated with alumina-loaded thermoset, and cast in a single operation. Great care had to be taken during impregnation, casting, and curing to prevent any voids and fissures in the insulation. As mentioned above, these could lead to corona discharges and thus to a total destruction of the coil.

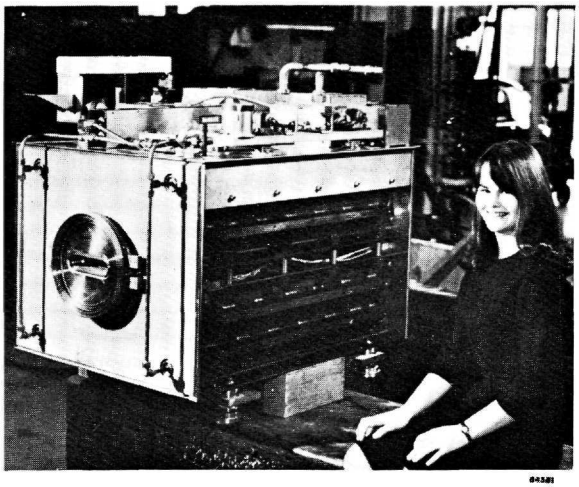

Figure 18-1 0.1° pulsed magnet.

Figure 18-2 Field plot of 0.1° pulsed magnet.

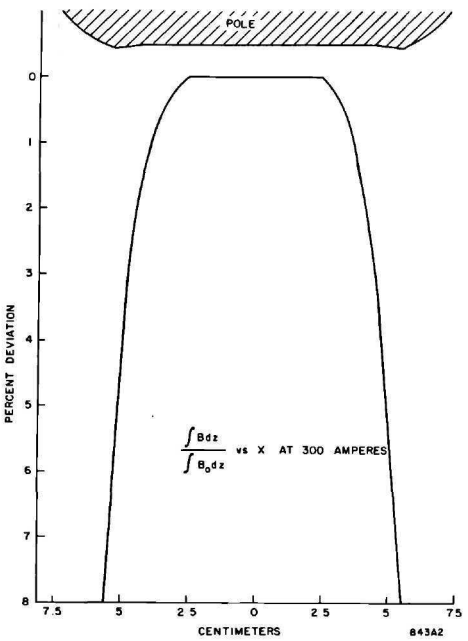

Prior to manufacturing the coils, a prototype coil was sectioned and tested for impregnation quality. The manufactured coils for all pulsed magnets were tested by means of a sensitive corona tester[5] and other nondestructive high-voltage methods to check for voids and poorly impregnated spots. A few details are worth mentioning. Stainless steel end plates providing compressive stress on the cores led to excessive induction heating and were eliminated at the pole ends. The thermoset between laminations provided adequate adhesion. The remainder of the end plates, the purpose of which was to keep the core under constant pressure, were not removed. Because of initial procurement difficulties with the ceramic vacuum chamber to be placed in the gap, the pulsed magnet cores were designed so that they could be sealed in a vacuum-tight envelope to permit the entire magnet assembly to be evacuated. This step became unnecessary as the ceramic chambers proved to be satisfactory as noted below. The ceramic vacuum chamber in the gap has an oval cross section with a height of 4.76 cm, a width of 17.5 cm, and wall thickness of 0.476 cm. It consists of 96% alumina and is coated with a low resistivity titanium compound inside and out. Welding the vacuum chambers to adapter flanges proved to be very difficult, but the job was finally completed successfully, using a heliarc welding technique.

In case of pulsed magnet failure, an emergency dc magnet is provided at each end of the row of pulsed magnets. The two emergency magnets are also capable of bending the beam 0.5° either side of the incident beam line. They are designed with 0.32-cm-thick laminations in order to permit the field polarity to be reversed within 2 sec. The emergency magnets are H-type with a gap height of 7 cm and a central field of 0.56 T.

The 3° bending magnets

Twelve of these magnets are used in the switchyard; two groups of four in the A-line bend the beam through 24°, and two groups of two in the B-line bend the beam there through 12°. For the purpose of design, the beam was assumed to have a diameter of 0.6 cm, a divergence of 10^{-4} rad, and a momentum spread of 2.6%. These figures are for the A-beam. The corresponding values are the same for the B side except a momentum width up to 5.2% is acceptable. Because of magnet resolution, the emergent beam would then be 4.8 cm wide at the exit of the magnet system. Such a beam was required to be deflected without appreciable loss in quality.

To conform with these requirements, the gap height was chosen to be 6 cm, and the pole ends in the x-y plane were shimmed to avoid saturation at operating fields of $B_{0,0,0} = 1.45$ T.[1,6] For the required homogeneity of $B_y/B_{0,0,0} = 10^{-4}$ over $x = \pm 4$ cm, the pole width was chosen to be 30 cm. A few of the most important design features are given in Table 18-1.

The main dimensions of the 3° bending magnet can be obtained from Fig. 18-3. Measured curves of B_y versus x at various z coordinates are given in Fig. 18-4. The deviation of B_y from $B_{0,0,0}$ at various excitation currents is

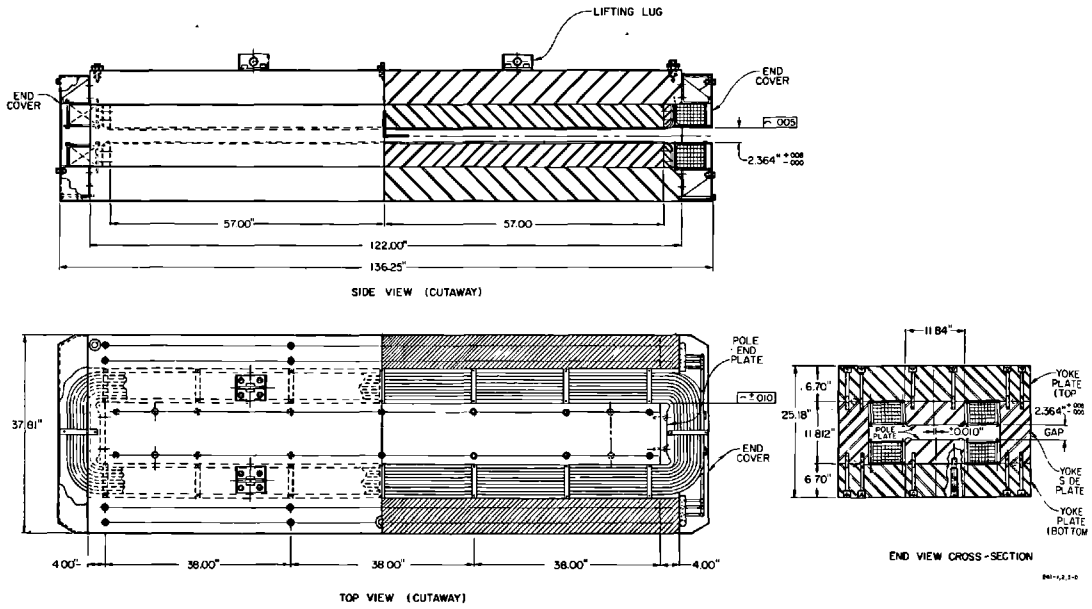

Figure 18-3 Diagram of 3° bending magnet.

Figure 18-4 Field plot of 3° bending magnet No. 7 at 800 A and at longitudinal positions measured from the center of magnet ($z = 0$, $x = 0$).

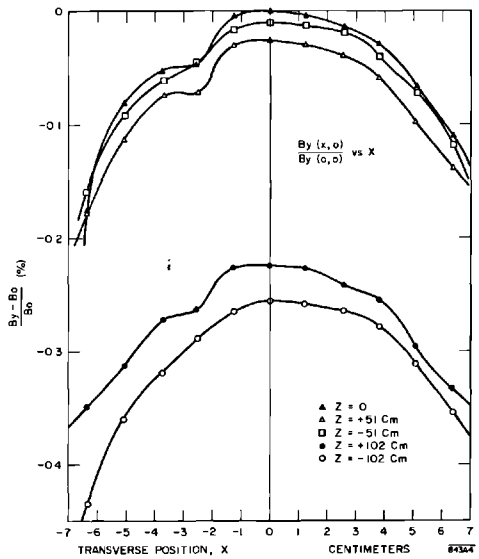

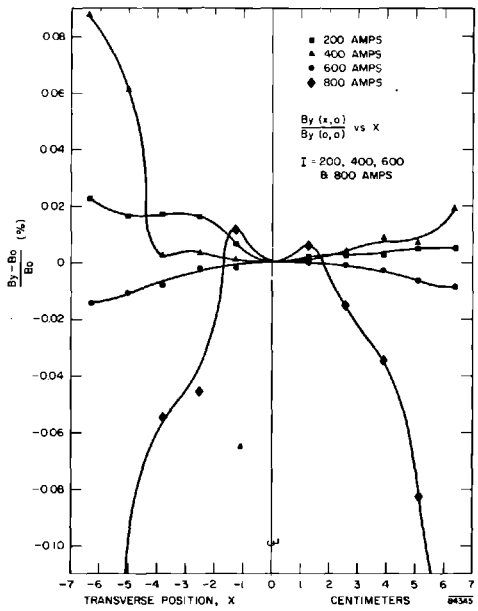

Figure 18-5 Field plot of 3° bending magnet No. 7 at various currents, one longitudinal position ($z = 0$).

given in Fig. 18-5. To prevent saturation effects at the entrance and exit of the magnet, the pole ends were circularly shaped with a radius equal to five-twelfths of the gap height. The magnet is provided with mirrors. For a given actual magnet length, the use of rounded pole ends leads to a somewhat shorter "effective length," but the field homogeneity in the gap is preserved over wider field ranges.

COIL CONSTRUCTION. The excitation coils consist of six double pancakes, each having sixteen turns. The hollow square-section copper conductor has an open-weave glass tape insulation which is treated with Volan-A and applied by a wet lay-up technique. This insulation method was necessary to ensure thorough wetting of the conductor surface. The insulation was applied as follows. The coil without ground insulation was placed in a mold with movable sides. The highly loaded thermoset was pulled through the insulation under a vacuum of ≈ 1 torr for 4 to 8 hours at about 40°C to guarantee uniform interturn impregnation. After this, mechanical pressure was applied through the movable mold walls onto all surfaces of the double pancake, and the assembly was given a primary 12-hour cure at 100°C. Unfortunately, a semicuring of the interturn impregnant was not possible due to manufacturing problems. Thus, prior to the application of the ground wrap the double pancake surfaces had to be cleaned and sandblasted. After the wet lay-up

of the ground insulation, the second impregnation was performed identically to the interturn impregnation. The insulation process was a delicate one, requiring skill, care, and close supervision to eliminate the inclusion of voids in the finished casting.

CORE STRUCTURE. The required gap-field homogeneity made it necessary for the core-iron to meet stringent specifications regarding impurity content, size and distribution of voids, and gas enclosures and fissures. Gap tolerances on the finished cores were required to be within 1.5×10^{-3} cm. Low-field measurements[7] also revealed that the silicon content had a significant influence upon the low-field behavior of the various magnets.

Owing to irradiation effects the pole surfaces were supposed to be nickel-plated to inhibit corrosion. However, due to lack of time, only an organic protective surface was utilized.

MAGNET ASSEMBLY. It was apparent that the air gap could not be reset to the specified close tolerances if the core had to be disassembled and reassembled to permit coil installation. For this reason, the coil supports were designed so as to allow insertion of coils and supports without disturbing the core steel assembly. Figure 18-6 illustrates a 3° bending magnet prior to installation in the BSY.

The 8-cm quadrupole magnet

In order to realize near-perfect focusing in quadrupole magnets, the field gradient in the central magnet region must be constant and the field shape at the entrance and exit of quadrupoles must follow a predetermined pattern.

Figure 18-6 Photo of 3° bending magnet—lead end.

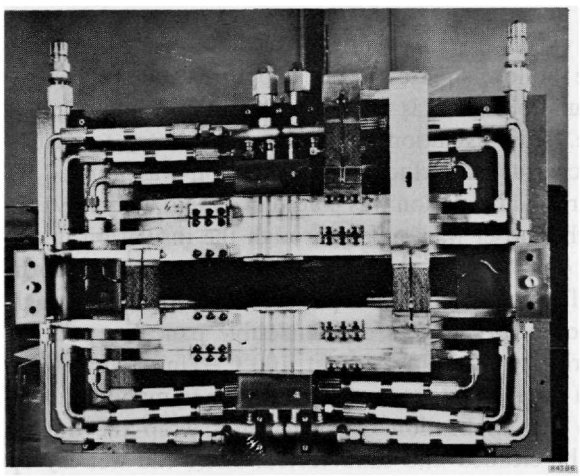

Excellent focusing is achieved if the field gradient along the z axis over the entire lens length and in the boundary region changes linearly with excitation and is practically zero at the mirrors.

In calculating the focusing properties of magnetic fields, a common approximation is to assume that the field is constant over the length of the magnet to virtual boundaries located a certain distance from each pole end.[8] In ordinary quadrupole magnets, the distance between virtual field boundaries, the effective length, changes with magnetic field intensity in a nonlinear fashion. This proves to be troublesome if the magnet must focus over a wide energy range. To compensate for this deficiency, the main design objectives for the BSY quadrupoles were: (1) to guarantee a constant gradient with a negligible harmonic content over 90% of the useful aperture area; (2) to make the "gradient-length product" change as a linear function of the excitation current. The first requirement was accomplished by using hyperbolic pole shapes and physically placing the excitation coils with respect to the poles in such a way that coil dipole effect in the useful aperture was negligible. The second requirement was met by using three-dimensional hyperbolic pole ends that satisfy the potential functions.

Let the coordinates X, Y be designated as the magnet axis and x, y as the pole symmetry axis.

The potential function inside the magnet ($x = R$) is given by

$$V_1 = k_1 XY \tag{18-1}$$

The pole ends are shaped as three-dimensional hyperbolas yielding a potential function

$$V_2 = k_2 XYz \tag{18-2}$$

At $\theta = 45°$ (pole symmetry axis), this potential function is written

$$V_2 = k_2 z \frac{x^2}{2} \tag{18-3}$$

Using the center of the mirror as the origin of a new coordinate system and designating $z = l_p$ as the distance of the point P (transition point from the constant pole aperture to the variable pole end aperture) results in

$$V_1|_p = V_2|_p = k_1 XY = k_1 \cdot \frac{x^2}{2} = k_2 \cdot l_p \cdot \frac{x^2}{2} \tag{18-4}$$

where R = aperture radius inside the magnet. Then

$$k_1 = k_2 \cdot l_p$$

Combining Eqs. (18-3) and (18-4) yields

$$x^2 = \frac{2V_2^2}{k_2 z} = \frac{2V_2 \cdot l_p}{k_1 \cdot z} \tag{18-5}$$

Differentiating Eq. (18-5) yields

$$\frac{dx}{dz} = -\frac{1}{2}\left(\frac{2V_2 \cdot l_p}{k_1}\right)^{1/2} \cdot z^{-3/2} = -\tan\alpha$$

Again, at the transition point $z = l_p$,

$$V_2 = V_1 = k_1 XY = k_1 \cdot \frac{R^2}{2} \tag{18-6}$$

we get

$$l_p = \frac{R}{2\tan\alpha} \tag{18-7}$$

where α is the angle between the tangents at the transition point P for $x = R$ and $x = x(z)$. The choice of α is governed by two considerations: (1) At the transition point the field disturbance should be tolerably small, and (2) to keep the length of the quadrupole to a minimum, the pole end should not extend too much in the z direction. A good initial guess is $\alpha = 8$ to 12°.

Combining Eqs. (18-6), (18-7), and (18-4), we get the equation for the pole-end contour at $X = Y = x/\sqrt{2}$:

$$zx^2 = \frac{R^3}{2\tan\alpha} \tag{18-8}$$

For a pole-end surface with

$$x = \sqrt{2}X = \sqrt{2}Y$$

we get

$$XYz = \frac{R^3}{4\tan\alpha} \tag{18-9}$$

The practical approach was to approximate the pole ends close to the excitation coil by a spherical dome, as illustrated in Fig. 18-7.

The magnet cores were manufactured from sixteen separate steel pieces, which gave the manufacturer more opportunity to salvage out-of-tolerance components, permitted greater flexibility during assembly, and saved machining time. As might be expected, this increased the quality control work appreciably. The hyperbolic pole-end shapes were manufactured by means of templets and computer-controlled milling machines. These pole ends were bolted to the main pole body.

Main features of the 8-cm quadrupole are given in Table 18-1. Measured field and gradient differences integrated over z as a function of θ are illustrated in Figs. 18-8a and b. The multiple field distribution parallel to the z axis at $x = y = a$, where a is the aperture radius, is given in Fig. 18-9.

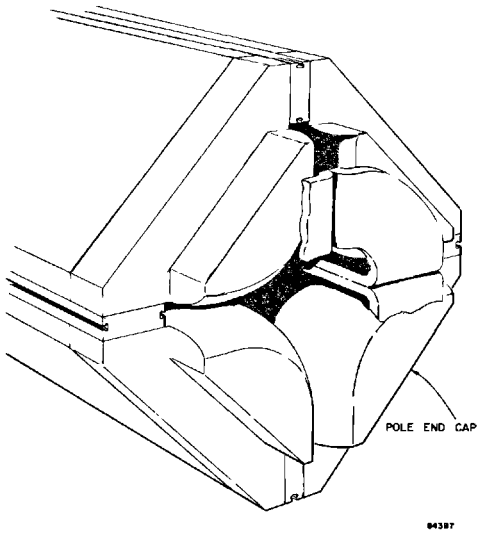

igure18-7 Poledetailsof 8-cmquadrupole iagnet.

'he 18.6-cm quadrupoles

'he main features of these lenses are generally the same as those of the smaller -cm quadrupoles, and the poles are shaped in the manner described above.)ne additional feature of the 18.6 cm-quadrupoles is the coil design. The urrent density distribution is such that the dipole component induced by the xcitation current is compensated so that it does not effect the useful aperture

igure 18-8a Field plot of 8-cm quadrupole No. 10.

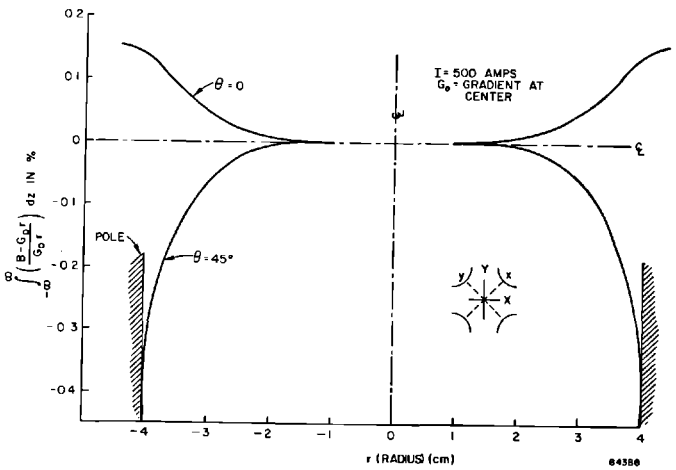

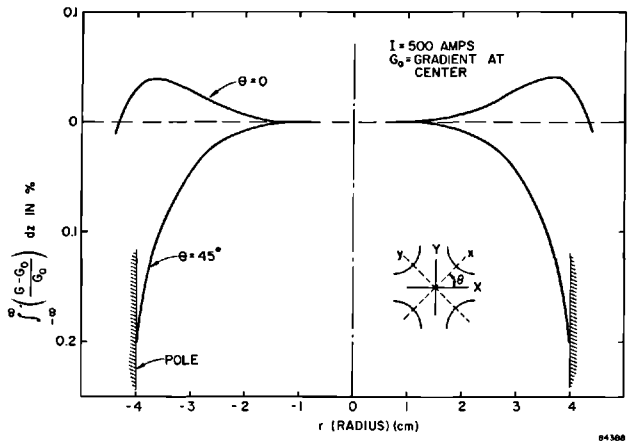

Figure 18-8b Gradient plot of 8-cm quadrupole No. 10.

area.[8] The cross sections of the coils for the large BSY magnets are shown in Fig. 18-10. Figure 18-10a shows how the current density of the coil in the region of the aperture for the 18.6-cm quadrupole is reduced by wider spacing of conductor.

The main design parameters of the magnet are given in Table 18-1. The coil and core designs are similar to those of the 8-cm quadrupole. The quadrupole front view is illustrated in Fig. 18-11, and Fig. 18-12 gives a typical fringing field plot at one end of the magnet.

Figure 18-9 Multipole content of 8-cm quadrupole No. 10.

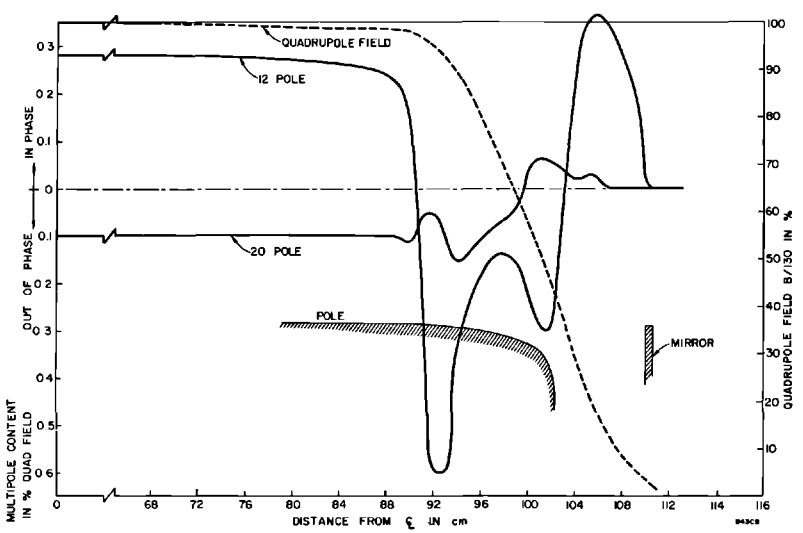

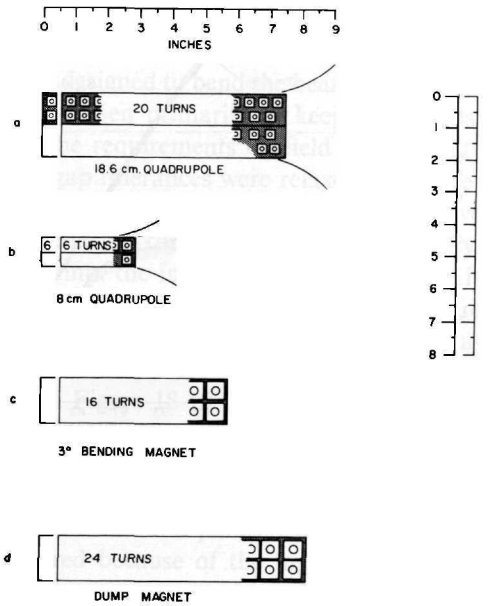

Figure 18-10 Some beam switchyard magnet coil sections.

Figure 18-11 Partial assembly of 18.6-cm quadrupole.

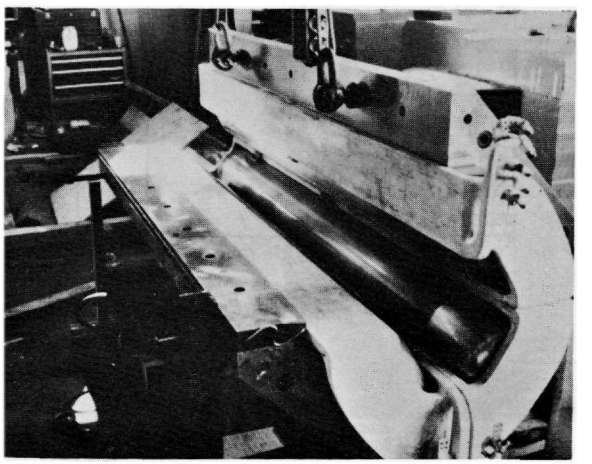

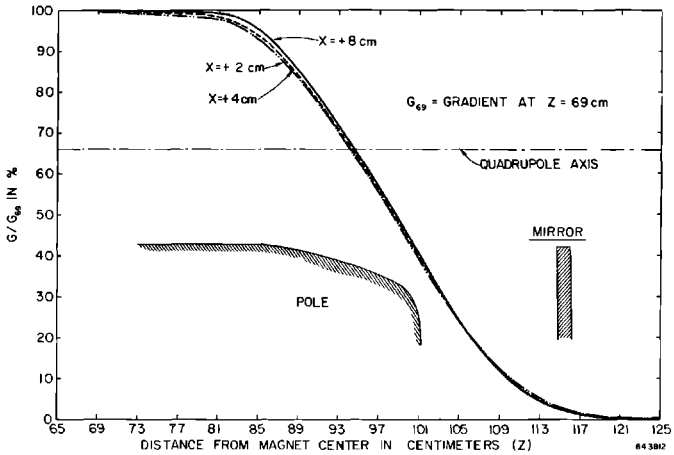

Figure 18-12 Gradient plot of 18-6-cm quadrupole at 600-A current.

Figure 18-13 Dump magnet.

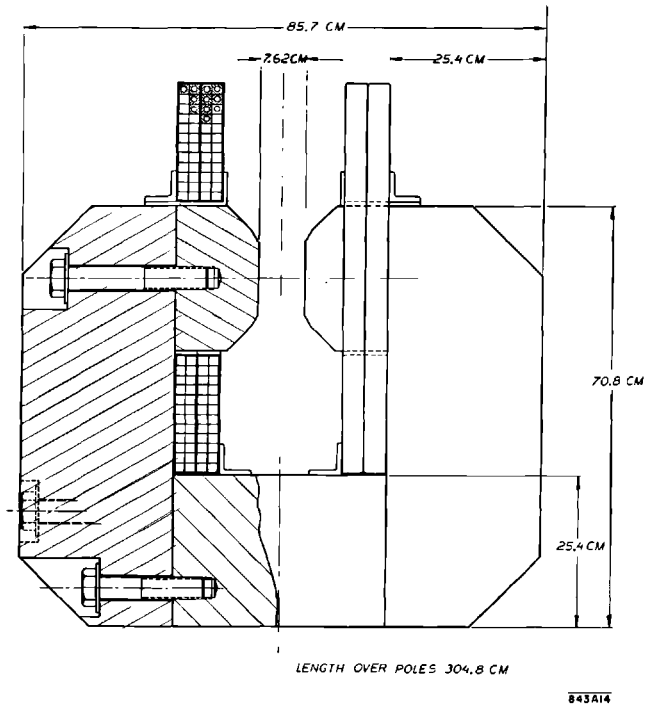

The dump magnets

The dump magnets are C-type magnets designed to bend the beam in a vertical plane. The C-type configuration was chosen primarily to keep the vertical plane free of obstacles on one side. The requirements on field homogeneity were not stringent and, therefore, the gap tolerances were relaxed. The poles are tapered and the yoke cross section is related to the pole area to achieve optimum flux distribution in the iron and maximum ampere-turn efficiency. As the magnet is close to the beam dump, the integrated irradiation dose is expected to exceed 10^{11} rad in a period of 10 yr. Coil and core designs are similar to those of the other BSY magnets. The interturn and ground insulations were applied using the wet lay-up technique described earlier. They were impregnated and cured simultaneously. Figure 18-13 is an assembly drawing of a dump magnet, and Table 18-1 gives the main design features.

The core material for these units was specified to be fully annealed plates of commercially available low-carbon (1010) steel.[9]

It may be pointed out that in most of the double pancake designs, counterflow heating problems were encountered because of the high thermal conductivity of the loaded thermoset used as interturn and interlayer insulation. In order to protect the coils against overheating, two thermoswitches were generally used for each hydraulic circuit. In the dump magnets one additional thermal switch, not anticipated in the initial design, was installed in each hydraulic circuit near the location of a hot spot discovered during test runs. Figure 18-14 shows a partially assembled dump magnet during magnetic field testing.

Figure 18-14 End view of dump magnet.

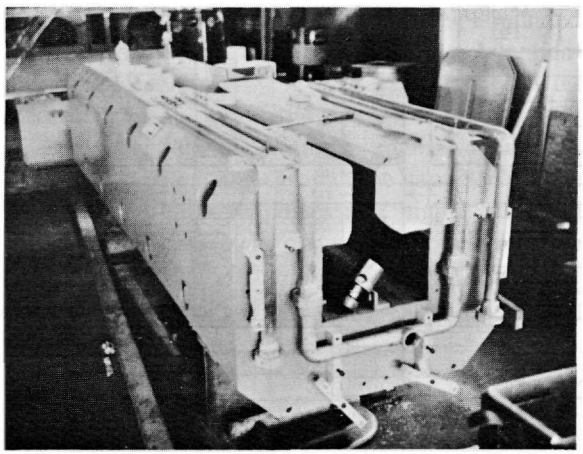

643413

The 2.5-meter magnetic slit

Near the output end of the B-beam transport system, a dc bending magnet (to be replaced in the near future by a pulsed magnet, similar to the 0.1° pulsed magnet) and a magnetic slit[10] are used to deflect the beam along any of three separate beam lines. The magnetic slit, essentially a combination of two C-type magnets separated by auxiliary poles and having a common gap (Fig. 18-15), is used to bend an initially deflected 20-GeV/c electron beam horizontally by an additional $\pm 1.8°$ or allow an initially undeflected beam to pass undeflected.

In the central part of the slit, a maximum field gradient of $\pm 3 \times 10^{-4}$ T/cm over a width of ± 1 cm was measured. The maximum field in the gaps

Figure 18-15 SLAC magnetic slit used in the beam switchyard.

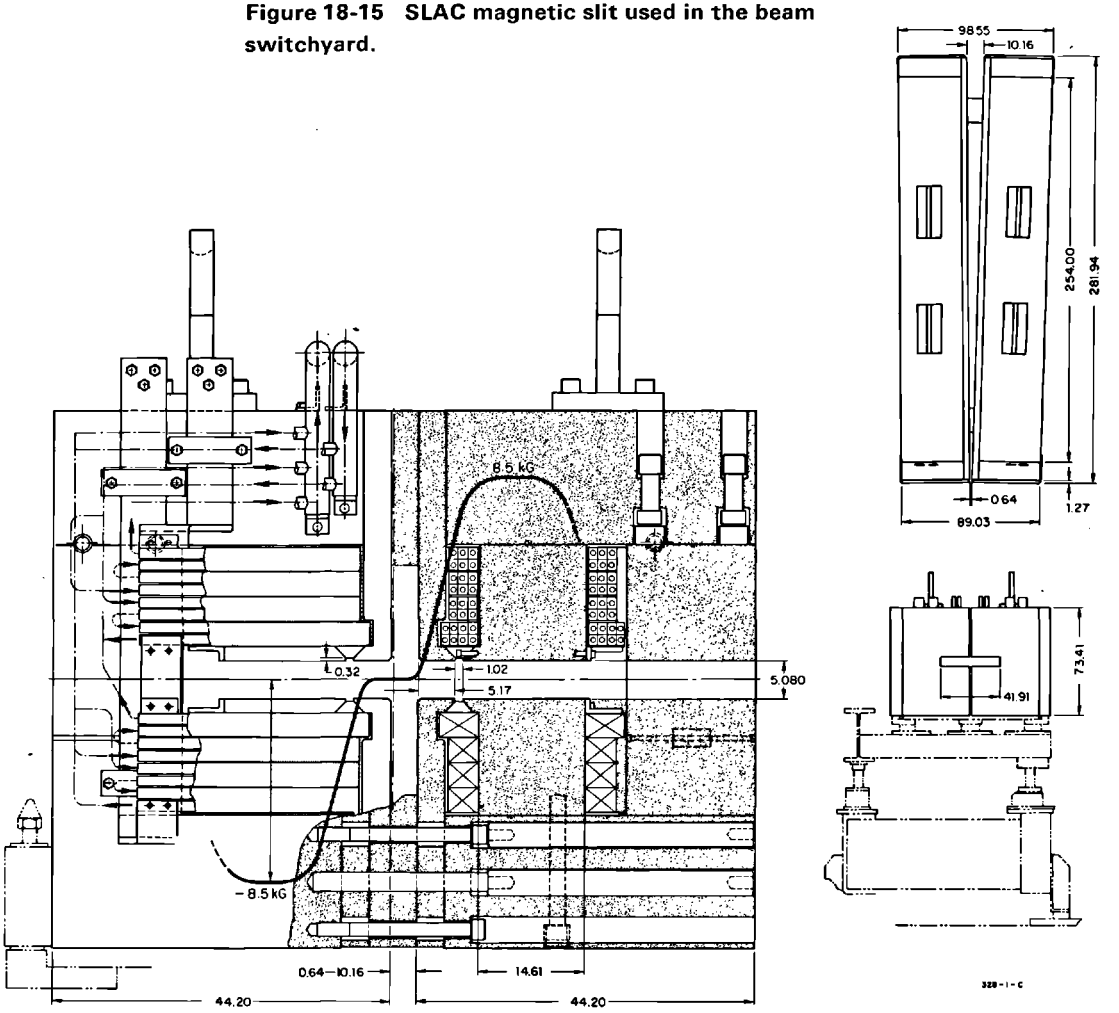

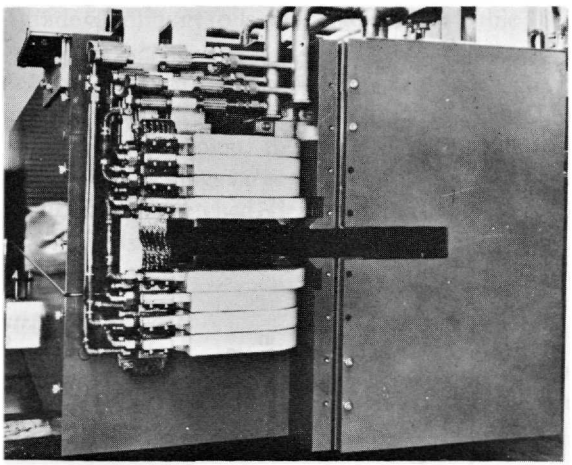

Figure 18-16 End view of magnetic slit magnet with one-half mirror removed.

is ± 0.85 T, corresponding to a beam deflection angle of $\pm 1.8°$. The gap area, where the beam is swept over $x = \pm 10$ cm, is free of obstacles and current sheets. The main features of the magnetic slit are given in Table 18-1. Figure 18-16 shows the 2.5-meter magnetic slit with part of the front mirror removed.

The pulsed steering magnets

These magnets are part of the common beam (prior to deflection into the A and B channels) and are used for beam steering on a pulse-to-pulse basis. Since the magnets are pulsed (600-cycle full sine wave, 360 pulses/sec maximum), the cores were built of 0.035-cm, grain-oriented silicon steel, laminated with Carlite insulation. The core dimensions are small and, thus, the laminations could be stamped as a single piece, simplifying the core assembly. After the laminations were stacked in proper fixtures, they were vacuum impregnated with a low-viscosity thermoset and cured. Mounting angles were welded to the outside core faces. The beam pipe passing through the gap should have a high electrical resistance to keep eddy-current losses low, high mechanical strength in order to keep the wall thickness down to a minimum, and must be able to be welded or brazed to stainless steel. After some searching, Hastelloy B proved to be the best choice. Table 18-2 illustrates the main features of the pulsed steering magnet.

The dc steering magnets

The magnets are used for horizontal and vertical steering in the A- and B-beam areas. The cores are manufactured of low-carbon (1010) steel plates.

Table 18-2 Main features of the beam switchyard pulsed and dc steering and photon beam stripping magnets

Parameters	*Pulsed steering magnets*		*dc steering magnets*			*Photon beam stripping magnets*	
	AP-1, ..., 4	PMV[a]	A-10, 11, 30, 31 400, 401	A-12	B-28	B-29	B-29A
Max. beam energy (GeV)	25	25	25	25	25	25	NA[b]
Deflection angle (deg)	0.0172	0.0143	0.0573	0.086	0.475	1.02	NA
Flux density in gap (T)	0.065	0.052	A-10, 11, 30, 31 0.33 A-400, 401 0.40	0.324	1.26	1.1	0.5
Effective length (meters)	0.384	0.405	0.254	0.266	0.38	1.09	1.09
Total length (meters)	0.482	0.482	0.365	0.362	0.622	1.37	1.37
Field uniformity (%)	0.1 ($x=\pm 1.3$ cm)	0.1 ($x=\pm 1.3$ cm)	0.25 ($x=\pm 4$ cm)	1.0 ($x=\pm 4$ cm)	0.6 ($x=\pm 2.5$ cm)	1.0 ($x=\pm 2.5$ cm)	1.0 ($x=\pm 2.5$ cm)
Gap height (meters)	0.0388	0.052	A-10, 11, 30, 31, 8 cm; A-400, 401, 10.15 cm	0.127	0.0762	0.114	0.152
Gap width (meters)	0.127	0.1524	0.2014	0.203	0.1524	0.1524	0.170
Current (A)	21	23.8	25	36	500	850	850
Current density (A cm^{-2})	183	207	353	486	880	580	580
Turns per pole	48	48	462	462	104	158	132
Terminal voltage (V)	1340	1445	118	170	46	52.8	39.6
Weight (kg)	227	286	186	193	582	3110	2230

[a] Vertical pulsed magnet.

[b] Not applicable.

The coils are wound of EC grade aluminum foils and edge-cooled. Table 18-2 gives the main features of these magnets.

To compensate for the effect of the earth's magnetic field on the electron beam, two steering magnets with one single excitation coil made of aluminum foil were utilized. After curing the impregnant, the coils were machined to produce a saddle shape and provide openings large enough to pass the beam pipe through. The machined surfaces were etched, cleaned, and reimpregnated to prevent interturn shorts. The coils are air-cooled by natural convection.

Photon beam steering and stripping magnets

Three additional magnet elements are employed in the BSY magnet system as a part of the photon beam system. These units are of conventional design except for the use of radiation-resistant components.

Magnet costs

Table 18-3 gives a cost breakdown for engineering, coil and core procurement, and assembly for the major BSY magnets.

18-2 Magnetic characteristics of the momentum analyzing systems (JKC, DRJ, EJS)

To achieve the requirements for momentum calibration placed on the transport system, it was necessary to make magnetic measurements commensurate with a reproducibility of magnetic field setting of $\pm 0.02\%$ and an absolute field determination of $\pm 0.1\%$. Field distribution measurements were required to ensure that the magnet design achieved the field uniformity necessary to transport the beam without introducing significant aberration. Using the SLAC TRANSPORT[11] computer program, analysis of beam optics requirements indicated that $\int B(x, y, z)\, dz$ could vary no more than 3 parts in 10^4 for $-2.5 \leq x \leq 2.5$ cm, where B is the magnetic field in the magnet, x is measured in the traverse direction, y is measured perpendicular to the pole face, and z is measured along the longitudinal axis of the magnet. Another requirement placed on the transport system is that the direction of the beam leaving the system should be independent of particle momentum, i.e., the system should be achromatic.

Magnetic measurements (JKC, DRJ)

THE 3° BENDING MAGNETS. Magnetic measurements on the 3° bending magnets were performed in the laboratory. Later, they were repeated in the BSY with the magnets in final position and using the power and control systems provided for beam operations. The measurements were made using standard instruments; most were performed with a long-coil system. Two long coils

Table 18-3 Beam switchyard dc magnet procurement costs

Magnets	*Quantity*	*Core*	*Coil*	*Assembly*	*Hardware*	*Total*
3° Bending magnet	14	$165,479	—	$96,000 (incl. coils)	$30,000	$291,479
8-cm quadrupole	12	87,912	—	39,397 (incl. coils)	18,800	146,079
18.6-cm quadrupole	2	54,264	—	24,340 (incl. coils)	8,410	87,014
Dump magnets	4	—	$95,871 Total (coil, core assy.)		19,930	115,801
$\frac{1}{4}$° Emergency magnets	2	—	29,000 Total (coil, core assy.)		4,700	33,700
Magnetic slit	1	22,500	17,500	(In house)	1,510	41,510
DC steering magnets	7	2,500	3,632	(In house)	680	6,812

were used for measurements in the BSY. One of these is permanently located in the reference magnet, which will be discussed in Section 18-4 below, and the other was moved from magnet to magnet for comparison purposes.

The search coil consisted of a 3.75-meter long, epoxy–fiberglass coil form wound with copper wire. The coil rested in a cradle with roller supports at many points. The cradle in turn rested on the lower pole of the magnet being tested; it was adjusted so that the coil was in the central plane of the magnet. An electric motor rotated the coil upon command through slightly more than 180°. The coil output was fed into an integrating digital voltmeter which was set to integrate either positive or negative signals only. As the coil rotated, integration was inhibited until the coil plane was perpendicular to the direction of B. Integration then commenced and continued until the coil had rotated 180° and the output voltages had changed sign. This method required no accurately set limit stops on the coil flipping mechanism and improved the accuracy of the measurement. The long coils were periodically placed in 3° magnets with field profiles determined by direct measurements to check the coil constant. The readings of magnet excitation current were made with a 0.1 mohm, high-accuracy (0.02%) shunt in series with the magnet. The power supply run-up rate and current level were controlled by a stepping motor.

In order to make magnetic measurements reproducible, it was necessary to degauss the magnets before each test. It was found experimentally that the magnets could be consistently degaussed by the use of a reverse current held for some definite time and then decreased to zero. This technique of degaussing works very well if the magnet has been excited to at least 400 A. The reverse current necessary to degauss the magnet is dependent upon rate of change of current. A reverse current of 165 A held for 30 sec degausses all of the magnets to less than 0.5 G.

Long-coil measurements of two types were performed: (1) $\int B\,dz$ versus transverse position at several excitation currents I_{ex} and (2) $\int B\,dz$ versus I_{ex} at the center of the pole transversely and in the center plane. The measurements of $\int B\,dz$ versus I_{ex} were performed in 50-A increments and with two modes of current run-up, starting with a degaussed magnet. The modes were (a) "direct," in which the current is run up from zero current to the desired current with no intermediate steps, and (b) "incremental," in which the current is run up from zero to a current I_1, then to current I_2, etc., and a long-coil measurement is made at each current level. "Direct run-down" and "incremental run-down" measurements have also been made. In this case the measurements are made by decreasing the magnet current from an initial, well-defined magnetic state at 800 A. A 6-A/sec rate was chosen and, unless otherwise indicated, all measurements were made using that rate of excitation.

A typical graph of homogeneity of $\int B\,dz$ versus x is shown in Fig. 18-17. The dependence of run-up rate on the $\int B\,dz$ achieved for a given final current is shown in Fig. 18-18 for three different run-up rates. In Fig. 18-18 the line of zero deviation is the 6-A/sec rate, and it can be seen that the $\int B\,dz$ values for 9 A/sec are higher than the 6-A/sec values, while the 3-A/sec rate gives

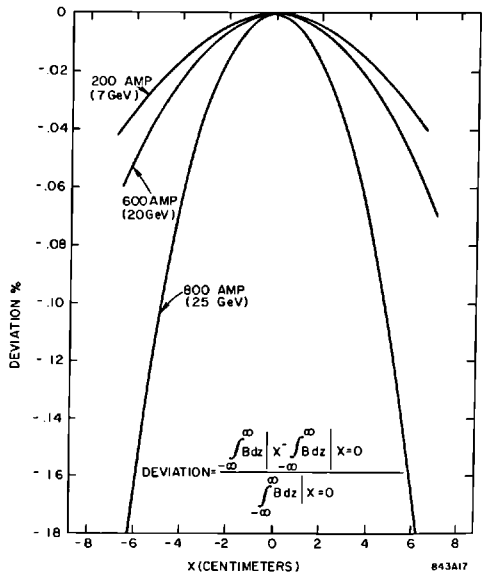

Figure 18-17 Field plot of 3° bending magnet.

lower values of $\int B\,dz$. This illustrates the need for using a single run-up rate. It has been mentioned before that measurements of B at a point in the magnet show a dependence on run-up rate which is different from that obtained for $\int B\,dz$. This can be seen by comparing Figs. 18-18 and 18-19. At other points in the magnet different B dependences are observed such that the integrated effect is consistent with that given by the long coil.

Figure 18-18 Average 3° bending magnet long coil measurements vs current.

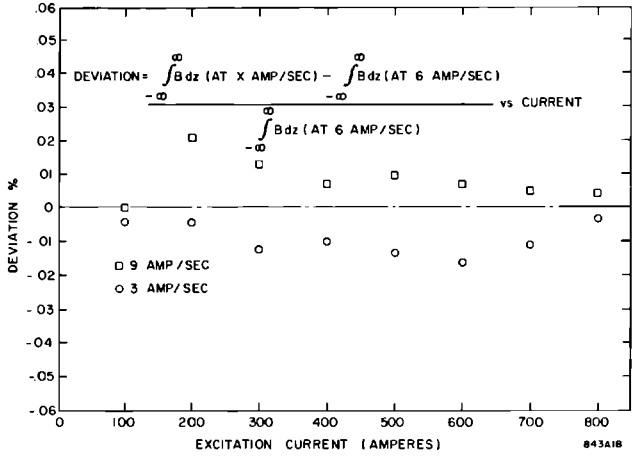

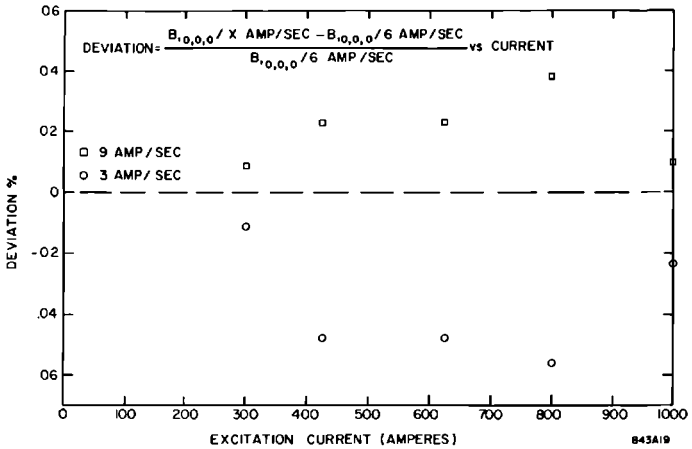

Figure 18-19 Average 3° bending magnet NMR measurements in center of magnet.

Differences of $\int B\,dz$ between magnets at a given I_{ex} can be attributed to differences in gap width, core length, and core impurities. Measurements of $\int B\,dz$ versus I_{ex} were made on each magnet, and it was found that the differences between magnets could be separated into two types: those that were current dependent and those that were not. The noncurrent-dependent differences were characterized by a nearly constant percentage offset of $\int B\,dz$ over the whole range of excitation current. The percentage offsets compared to magnet No. 4 are listed for each magnet in Table 18-4. Superposed on

Table 18-4 Summary of differences in $\int B\,DZ$ of magnets

Core No.	*Beam switchyard position*	$\frac{\langle \int B\,dz\ \text{Magnet}\ N \rangle}{\langle \int B\,dz\ \text{Magnet}\ 4 \rangle}$ *(in %)*
1	B-33	+0.347
2	A-ref	+0.193
3	B-10	−0.050
4	B-16	0
5	B-13	−0.020
6	B-12	+0.131
7	B-32	+0.015
8	B-11	+0.110
9	B-17	+0.120
10	B-ref.	−0.017
11	B-14	−0.049
12	B-15	−0.031
13	B-30	+0.084
14	B-35	+0.304

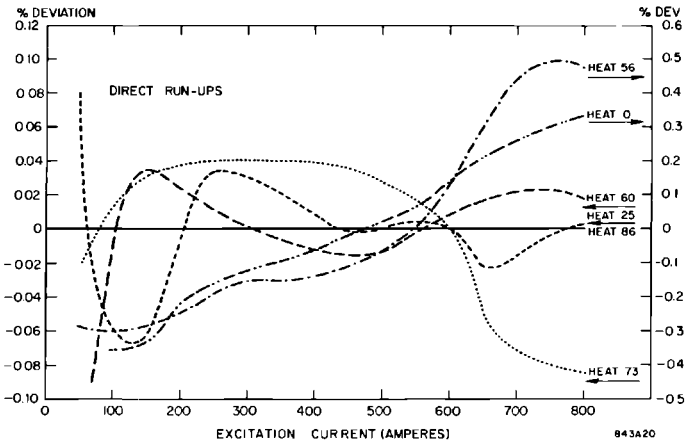

Figure 18-20 3° bending magnet—relative differences in $\int B\,dz$ caused by differences in steel impurities. Direct current run-ups.

these differences are current-dependent differences which group themselves according to the heat number of the steel from which the cores were fabricated. These differences, which are shown in Figs. 18-20 and 18-21, are seen to be quite large in the case of some heats. Figure 18-20 shows the relative differences attributable to steel impurities based on measurements of $\int B\,dz$ using direct run-up of current. Figure 18-21 shows similar data for incremental run-up of current. In these figures heat 86 is taken as the standard of

Figure 18-21 3° bending magnet—relative differences in $\int B\,dz$ caused by differences in steel impurities. Incremental current run-ups.

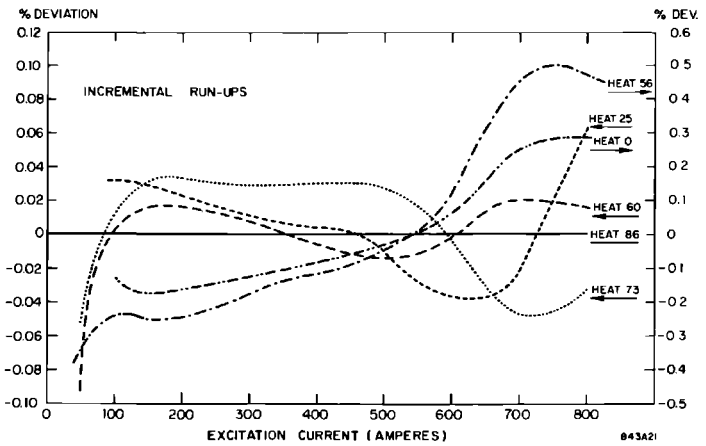

Table 18-5 Chemical ladle analysis, percent impurities in steel for 3° bending magnet cores

Impurity	*Heat No.* 56	60	86	0	73	25
C	0.06 %	0.06 %	0.06 %	0.05 %	0.08 %	0.07 %
Mn	0.29	0.26	0.30	0.15	0.28	0.30
P	0.009	0.009	0.008	<0.03	0.008	0.008
S	0.029	0.025	0.017	0.025	0.025	0.022
Si	0.004	0.18	0.18	0.08	0.13	0.16
Ni	0.02	0.01	0.04	0.06	0.04	0.01
Cr	0.03	0.05	0.04	0.01	0.04	0.03
Mo	—	0.01	0.01	0.01	0.02	0.01
Cu	0.05	0.04	0.04	0.04	0.04	0.03
Al	0.005	0.008	0.012	<0.005	0.009	0.004
Magnet	1	2, 3	4, 5	14	7, 9	12
Cores		6, 8	11		10, 13	

comparison and is plotted as zero deviation. Table 18-5 gives a chemical ladle analysis of the various heats of steel from which the magnet cores were made.

THE 8-CM AND 18.6-CM BSY QUADRUPOLES. The BSY quadrupoles were individually measured in the laboratory after assembly had been completed. Harmonic analysis was used to determine the deviation of $B\ (r, z)$ from the ideal B expressed by $G_0\ (0, z)r$, where G_0 is the field gradient at the magnet center. The nonlinearity of B integrated over the length was obtained by numerical integration of the nonlinearity of B over all values of z. It was found that the magnetic characteristics of all of the 8-cm quadrupoles were within the required tolerances of small aberrations for the size of the beam envelope at each position in the switchyard. The gradient length product versus the excitation current of each quadrupole was measured by a Hall probe gaussmeter using numerical integration of $B_r(r, z)$ over the length z to find the effective lengths and a Hall probe gaussmeter to find $B(r, 0)$ as a function of I_{ex}.

OTHER MAGNETS. All of the other magnets in the BSY were measured using long integrating coils to determine $\int B\,dz$ versus I_{ex} at $x = y = 0$ and $\int B\,dz$ versus x at several currents I_{ex}. The 0.1° pulsed magnets were also measured with a long coil, but instead of flipping the long coil the field was pulsed to obtain a measurement.

18-3 Reduction of data on beam switchyard magnets (JKC, AWB)

The 3° bending magnets

HYSTERESIS. The $\int B\,dz$ taken as a function of the excitation current I_{ex} was normalized to 50-A increments. The method used to normalize the data was a two-point linear interpolation using the points:

$$[(\textstyle\int B\,dz)_i, (I_{ex})_i] \quad i = 0, 1, \ldots, N$$

and

$$[(\textstyle\int B\,dz)_{i-1}, (I_{ex})_{i-1}]$$

with the assumption that $\int B\,dz|_{I_{ex}=0} = 0$.

This method was chosen in preference to a second- or third-order approximation because the difference between the normalized and unnormalized values was only several parts in 10^4.

A least-squares polynomial fit was made from the data points (both $\int B\,dz$ versus I_{ex} and I_{ex} versus $\int B\,dz$) on three different incremental run-up rates and on the direct run-up rate. From the polynomials, points were calculated using normalized current values and then compared with the data points. The parameters for the fit were as follows: decree—eighth; absolute error—2×10^{-4} (for a weight of 1.0); sum of errors—10^{-20}.

The calculated points were compared to bending magnet No. 4 (considered the standard magnet) for both direct and incremental run-up at a 6-A/sec run-up rate. Finally, the $\int B\,dz$ resulting from incremental current run-up was compared with $\int B\,dz$ resulting from the direct current run-up.

All data points were not given equal weight because less significant digits were obtained at low currents, and power supply regulation, current resolution, and $\int B\,dz$ resolution were also poor. The weights used for fitting were as follows:

50 A—0.1	200 A—0.6
100 A—0.2	250 A—0.9
150 A—0.4	≥ 300 A—1.0

HOMOGENEITY. The parameters η and ε for each magnet were calculated from $\int B\,dz$ versus transverse position x, using the least-squares method where η and ε satisfy the equation

$$K = 1 + \eta x + \varepsilon x^2 \qquad (x \text{ in centimeters})$$

and K is defined by

$$K = \frac{\int B\,dz\,|\,x = x_n}{\int B\,dz\,|\,x = 0}$$

MOMENTUM ANALYZING SYSTEM. For a momentum analysis of the A-line series B-10, -11, -12, and -13, the beam displacement, momentum expected, and momentum obtained are given by the following equations. Let

$$A_I = \left[\frac{\sum_{m=1}^{N} \int_I B\, dz[m]}{N}\right]$$

The error (DX_I) is then,

$$DX_I = \sum_{J=1}^{N} \left[R[J] \sum_{K=1}^{J} \frac{(Y[\Sigma K, I] - A[\Sigma I]}{A[\Sigma I]}\right]$$

where

R = magnet displacement along beam line
J = magnet position
I = current level
$Y = \int B\, dz$

The measure of error is

$$E[I] = 1 + DX[I] \cdot 0.0015625$$

The expected momentum is

$$PE[I] = A(I) \cdot \frac{25}{4.3663374}$$

and the momentum obtained is

$$P[I] = PE(I) \cdot E(I)$$

In this calculation no correction was made for synchrotron radiation losses due to their very small magnitude. In the A-line the fractional energy loss in the bending magnets is about 1.6×10^{-4} and in the B-line the fractional energy loss is about 0.8×10^{-4} at 25 GeV.

THE 8-CM AND 18.6-CM QUADRUPOLES. From the measurements of $B_r(r, z)$ versus I_{ex} which were taken on the BSY quadrupoles the gradient $B_r/r = G_r$ was formed. The gradient versus I_{ex} was normalized to even current increments in the same manner as was done for the 3° bending magnets, and a least-squares polynomial fit was made from the data for gradient versus I_{ex} and I_{ex} versus gradient. The effective lengths were measured separately. The product of gradient and length was compared with the gradient length as calculated from TRANSPORT[11] and was used to determine the excitation current required to produce a given gradient–length product.

OTHER MAGNETS. The data taken from these magnets was normalized, and a least-squares fit was found for the polynomials $\int B\, dz$ vs I_{ez} and I_{ex} vs $\int B\, dz$ or $G_0 L$ vs I_{ex} and I_{ex} vs $G_0 L$ for quadrupoles. An eighth-order fit was used

for each of the magnets unless the computation was limited to a lower-order fit by the amount of memory available in the control computer used for setting magnet currents.

18-4 Selection of magnet location (EJS)

Initial TRANSPORT calculations made to design the BSY transport system assumed identical magnets, each bending the beam by 3°. However, in practice, the magnets are required to have identical current, and measurements show that small but significant differences exist in the $\int B\,dz$ magnetization versus current data for the individual magnets. (See Figs. 18-20 and 18-21 and Table 18-4.) The result is that the bending angle at each element in the system is not exactly 3° and, furthermore, the ratios of the various actual deflections produced by the magnets vary with current and, therefore, with the momentum setting of the system. Because the current through the system must be set to define the momentum, the exit angle from the system varies slightly with the momentum.

Because there were fourteen magnets to be assigned to fourteen positions, there were 14! ($\approx 8.7 \times 10^{10}$) possible permutations from which the optimum arrangement was selected. A number of magnetic features such as degaussing characteristics, transverse magnetic homogeneity, magnetization characteristics, etc., needed to be considered in determining the optimum permutation. However, measurements and calculations indicated that magnets were sufficiently identical that consideration of magnetic features other than magnetization was not necessary. The number of permutations was reduced significantly by imposing the requirements that momentum-defining magnets (the first four in A-beam and the first two in B-beam) and the respective reference magnets in each system have similar magnetization curves. This choice gives more confidence that future measurements on the reference magnets will indicate the behavior of the nearly inaccessible, momentum-defining magnets in the system. Also, since the requirements for optical quality are more stringent for high-energy experiments planned using the A-beam, this beam was given priority in the selection of the remaining magnets. Based on these requirements, the four magnets from heat 60, the magnets from the magnetically similar heat 86, and the magnet from heat 25 were assigned to A-beam. The magnetization data for these magnets and the heat-73 magnets was supplied to a computer program designed to select the permutation of magnet assignment which would result in a minimum deviation of the deflection of the exit beam from the ideal beam as the beam momentum was changed from one value to another. The program was required to select three magnets from heat 60 plus one magnet from heat 86 for the first four momentum-defining magnets. The remaining heat 60 magnet was assigned as the A-beam reference magnet. The last four magnets in A-beam were selected by the program from heats 86, 73, and 25, with the requirement that three

heat-73 magnets remain unused. This completed the assignment of magnets to the A-beam. The program was then used in a similar manner to assign the remaining magnets to location in the B-beam. Heat-73 magnets were used in the first two momentum-defining positions and as the B reference magnet. Table 18-5 gives the chemical ladle analysis for the steel from which the 3° bending magnet cores were made.

As a result of the magnet differences, the beam exit angle from the installed A-transport system varies from the design figure of 24.5° depending on the momentum setting of the system. If not compensated by the steering magnets provided at the end of the transport system, the extremes of angular variation for momentum settings between 3 and 20 GeV are sufficient to cause a motion of about 1 cm in the location of the beam spot in end station A. The corresponding displacement in end station B is about 4 cm.

18-5 Magnetic field setup for momentum analyses (EJS, JKC)

There are three methods of setting up the deflection magnets in the BSY transport system, two of which are presently in use and are being tested to determine their relative advantages. The first and operationally preferable method is to adjust the current in the deflecting magnets until the desired $\int B\,dz$ is achieved in the reference magnet. For this measurement, the long coil permanently installed in the reference magnet is used, and its integrating digital voltmeter measures the volt-second integration resulting from a flip of the coil. In this method, the $\int B\,dz$ of the reference magnet is related to the $\int B\,dz$ (and, hence, the momentum setting) of the transport system through the previous magnetic measurements on the individual magnets of the system. Obviously, this method requires that the $\int B\,dz$ in the transport system should track with the $\int B\,dz$ of the reference magnet. As has been discussed, magnets assigned to the momentum analysis locations of the transport system were chosen to have nearly identical $\int B\,dz$ magnetization variation with current. Tests have been performed to study the tracking characteristics of these magnets. It has been found that over the measured range of parameters, these magnets track each other to within 0.02%, independently of the run-up rate and the mode of operation (direct or incremental, up or down). Although the evidence is incomplete and further tests are planned, it seems that this method makes it possible to set up for a desired momentum analysis in a precise, quick, and flexible way.

The second method of setting the transport system to a specified momentum uses the current reading from a precision shunt in series with the transport magnets. The accuracy of this method depends upon the stability and accuracy of the current-monitoring shunt and associated voltmeter. This method requires that the magnets be degaussed and then set via direct run-up to the current corresponding to the desired momentum setting. This current setting is determined from analysis of the direct run-up magnetic measurements. To allow step increases in the momentum setting, tables giving the

required current change have been prepared from the incremental run-up measurements. These should give good results provided that increases in momentum of only a few steps are made and that the steps are not too large. All the tables were prepared by fitting eighth degree polynomials to the magnetic data. A similar scheme has been worked out using the run-down data. In using this method, the available data are only sufficient to allow changes in one direction during a single run. In principle this method for setting up the BSY momentum analysis system should be as accurate as the $\int B\,dz$ measurements outlined above. In particular, the direct run-up technique, although it is long and tedious, is based on a well-defined sequence on the hysteresis loop of the magnets. It should yield reliable results when a check on other methods is necessary.

A third method for establishing fields in the transport system magnets is based on readings from nuclear magnetic resonance (NMR) probes which are installed in the gap of each of the momentum-defining magnets. These probes give the induction at that point in the magnet. They can be used to set up the required magnetic fields for the deflection systems, but the accuracy is not as good as the long flip-coil measurements because the induction is sensitive to local variations in field and to gap changes caused by temperature variation. The installed NMR's, however, serve as a basic check against shunt changes or electrical shorts in the magnets and may detect anomalous behavior of a magnet which would not be reflected in the reference magnet readings.

Acknowledgments

The contributors to the work discussed in this chapter are many and all could not possibly be mentioned here but several deserve special mention. The overall criteria and basic calculations for a great part of the beam switchyard magnets were furnished by R. Taylor and by B. deRaad who is now at CERN. The design of the beam switchyard 3° bending magnets was a contribution of B. Hedin who also is now at CERN. The measurements program was initiated by J. Murray. G. Loew, R. Miller, and W. Herrmannsfeldt assisted greatly by contributing valuable advice during many hours of discussion.

References

1 B. Hedin, "A Bending Magnet with Nonsaturating Shimming," Rept. No. SLAC-19, Stanford Linear Accelerator Center, Stanford University, Stanford, California (September 1963).

2 J. Cobb and R. Cole, "Spectroscopy of Quadrupole Magnets" in *Proc. Intern. Symposium on Magnet Technol., Stanford Linear Accelerator Center, September 1965* (H. Brechna and H. S. Gordon, eds.), CONF-650922, p. 431, Clearinghouse for Federal Scientific and Technical Information, Springfield, Virginia.

3 H. Brechna, "Effect of Nuclear Radiation on Organic Materials; Specifically Magnet Insulations in High Energy Accelerators," Rept. No. SLAC-40, Stanford Linear Accelerator Center, Stanford University, Stanford, California (March 1956).

4 H. Brechna, "A Pulsed Bending Magnet for the Beam Switchyard Area of the Stanford Two-Mile Linear Electron Accelerator," Rept. No. SLAC-28, Stanford Linear Accelerator Center, Stanford University, Stanford, California (May 1964).

5 H. Brechna and E. Oster, "Insulation Structure and Coil Reliability," in *Proc. Intern. Symposium on Magnet Technol., Stanford Linear Accelerator Center, September 1965* (H. Brechna and H. S. Gordon, eds.), CONF-650922, p. 313, Clearinghouse for Federal Scientific and Technical Information, Springfield, Virginia.

6 J. K. Cobb, "The Prototype BSY 3° Bending Magnet," Tech. Note No. SLAC-TN-56-20, Stanford Linear Accelerator Center, Stanford University, Stanford, California (March 1965).

7 E. J. Seppi, J. K. Cobb, and D. R. Jensen, *IEEE Trans. Nucl. Sci.* **NS-14**, No. 3, p. 473 (June 1967).

8 H. A. Enge, *Rev. Sci. Instr.* **35**, 278 (1964).

9 H. Brechna, "Electromagnets for High Energy Physics Applications," in *Proc. Intern. Symposium on Magnet Technol., Stanford Linear Accelerator Center, September 1965* (H. Brechna and H. S. Gordon, eds.), CONF-650922, p. 1, Clearinghouse for Federal Scientific and Technical Information, Springfield, Virginia.

0 H. Brechna and J. Cobb, *Rev. Sci. Instr.* **38**, (9), 1289 (September 1967).

1 H. S. Butler, S. K. Howry, and C. H. Moore, "Specifications for the Beam Transport Systems to End Stations A and B," Rept. No. SLAC-29, Stanford Linear Accelerator Center, Stanford University, Stanford, California (June 1964).

19

INSTRUMENTATION AND ELECTRONICS IN THE BEAM SWITCHYARD

R. W. Coombes, J. N. Hall, C. A. Harris, S. K. Howry, M. J. Hu, I. C. Lutz, D. R. Olsen, R. A. Scholl, Editor, and E. J. Seppi

The instrumentation for the SLAC beam switchyard (BSY) can be grouped into four basic categories: beam monitors, transport control system, equipment protection system, and magnet power supplies.

19-1 Introduction (RAS)

Beam monitors include current-measuring toroids, beam position monitors, equipment for observing beam profile by optical (TV) means, and secondary-emission monitors for measurement of intercepted beam current on energy absorbers, for observing energy absorbers, and for observing energy spectrum.

The *transport control* system controls magnet currents and slit and collimator position, and also includes associated measurement equipment for monitoring magnet currents and fields and the positions of energy-absorbing devices. This system includes a control computer for automatic setup of the transport parameters.

The *equipment protection system* consists of sensors in the BSY to monitor radiation, temperature, water flow, the positions of energy absorbers and other movable instruments, vacuum system pressures, and so on; sensor electronics in the control room for signal conditioning; and a summary circuit to provide the necessary signals for the master machine protection circuitry at the Central Control Room (CCR) and the injector. This system protects the instruments from beam-induced damage and is not intended for protection of personnel. (Personnel protection is described in Chapter 21.)

The *magnet power supplies* provide the pulsed and dc power for all of the magnets in the transport and deflection system.

Each of these four will be described in greater detail below, but a few general remarks will be made here. Because of the high radiation levels

associated with the interception of the beam by energy absorbers, the BSY is a closed structure under many feet of earth and concrete shielding. This closed structure causes several problems in the design of equipment and sensors to be located there. First, radiation-induced chemical reactions between the nitrogen, oxygen, and water vapor in the air cause a slow buildup of nitric acid fumes. These fumes attack copper and aluminum, especially in thin sections. For this reason, extensive use was made of stainless steel and other inert materials, particularly for thin elements and for components that are difficult to replace or repair.

The high radiation levels also prevent frequent access to the BSY for maintenance purposes; delays of many days could easily be required if the device needing service were near a beam dump, for example. This situation made it necessary to design each instrument for high reliability, using radiation-resistant components, and prevented the use of materials or parts that require routine service (vacuum tubes, for example). Where this principle could not be adhered to for reasons of economy or lack of availability of suitable materials, the component was placed either in an alcove or other partially shielded area. Certain pieces of equipment were mounted so that removal could be effected remotely by the use of special tools produced for that purpose.

The layout of the major components and instruments in the BSY was shown in Fig. 17-1. As can be seen in the figure, the switchyard is roughly Y-shaped. The upper leg leads to the "A" experimental area and is called the A analyzing channel; similarly, the lower leg is called the "B" channel, whereas the beam transport system collinear with the accelerator is called the "C" beam channel. This terminology will be used below when discussing instrumentation differences in the various areas. For a complete discussion of the criteria and analysis of the optical properties of the system, see Chapter 17.

19-2 Beam monitors

Beam current monitors (BCM's) (DRO)

Current transformers are used for measuring the beam pulse current at various locations throughout the switchyard. A toroidal transformer can be considered approximately as a current source supplying a pulse current I/N into the cable with impedance R. The output voltage on the cable is, thus,

$$V = \frac{I}{N} \cdot R \tag{19-1}$$

where I = the beam pulse current; N = the number of turns on the toroid; and R = the cable impedance.

Equation (19-1) is approximately true for a current pulse as long as

$$\frac{L_T}{R} > t_p$$

where

$$\frac{L_T}{R} = \frac{\mu\mu_0 N^2 \cdot A}{2\pi r R} \text{ sec} \tag{19-2}$$

in which

L_T = the toroid inductance
t_p = the beam pulse length (1.6 μsec)
A = the cross section of the core
r = the mean radius of the core
μ = the initial permeability of the core

The droop in the output voltage is

$$D = \left|\frac{\delta V}{V}\right| = \frac{R t_p}{L_T} = \frac{2\pi r \cdot R}{\mu\mu_0 N^2 \cdot A} \cdot t_p \tag{19-3}$$

It is desirable to have a large output voltage V and a small droop D, so it is necessary to compromise on R and N. The values selected are given in Table 19-1.

The 3-in. beam aperture current intensity monitor assembly incorporates two toroids. One toroid is used in the current monitoring system. The other is used in the precise integrator system or serves as a spare. Each core is surrounded by an open aluminum case which acts as a Faraday shield and also as a support for the core inside the vacuum housing. The two core assemblies are insulated from each other and from the vacuum housing by ceramic beads. The signals are brought out through standard ceramic-to-metal sealed vacuum feedthroughs to radiation-resistant, 95-ohm, fiberglass-insulated twinaxial cables. These cables extend to the upper housing of the switchyard, where they are spliced (and matched) to RG/22/U polyethylene cables.

A current transformer with an aperture of 6.35 in. is needed in front of beam dump D-11 and in front of beam dump east. The core data for this transformer are shown in Table 19-1 and the construction is very similar to the 3-in. transformer. The 6-in. transformer is built into one housing with the four-quadrant secondary-emission monitor. The assembly of these two monitors is called the dump monitor.

Electronics

There are three readout systems associated with the beam current transformers.[1] The most fundamental one is the video or dynamic scope display of the actual beam pulse waveform. The video display provides a direct observation of the beam structure as a function of time and is used also to

Table 19-1 Data on beam current monitors

Item	*Description*
3-in. aperture current transformer	
Core	Four rings: 6 in. o.d., 3.675 in. i.d., each $\frac{1}{2}$ in. thick
Core material	Mn-Zn ferrite; Ceramag 24 (Stackpole Carbon Comp.)
Beam aperture	3 in.
Initial permeability	3600 (measured value); catalog value = 2500
Radiation threshold	$>2 \cdot 10^{11}$ ergs/g
No. of turns	48 for output signal; 1 for calibration input
Windings	Fiberglass insulated stranded copper wire
Cables	Output signal 95-ohm twinaxial (T-95 and RG/22/U); calibration signal 50-ohm coaxial (B-50 and RG/63/U)
Shielding	Transformer—aluminum can insulated from vacuum housing; cables—copper shield up to preamplifier
Inductance	24 mH
Sensitivity	2 mV/mA
Noise level	100 μV (equivalent input noise of system)
Droop	0.8% (2-μsec long beam pulse)
Rise time	Transformer proper—10 nsec; on scope in control room—30 nsec.
6-in. aperture current transformer	
Same as 3-in. transformer with the following exceptions:	
Core	Three rings: 10 in. o.d., $7\frac{1}{2}$ in. i.d., each $\frac{1}{2}$ in. thick
Beam aperture	6.35 in.
Droop	Approximately $2\frac{1}{2}$%
Feedthrough	Stainless steel, MgO-insulated cables welded into housing

measure the beam peak current. The second readout system displays average beam current (microamperes) on a meter. By comparing average beam current readings at various points in the BSY, an indication of the magnitude and location of beam losses may be obtained. The third readout is an integrator system which reads average current and total charge with higher precision. The characteristics of the three readout systems are summarized in Table 19-2. A block diagram of the current monitoring system is shown in Fig. 19-1a.

The local preamplifier (BCM local electronics chassis) is placed as close as possible to the current transformer but outside the switchyard shielding so that it is accessible when the electron beam is turned off even when there

Table 19-2 Characteristics of current monitor readout

Monitor readout	*Description*
1. Dynamic pulse readout	
Display	On 647 oscilloscope
Amplitude measurement	Can be measured with 0.3% precision using a comparator circuit
Absolute calibration accuracy	3%
Frequency response	30 nsec with compensated cables
Range	Min. 50-μA peak current, signal/noise = 1; max. 100-mA peak current
Electrons–positrons	Polarity of scope signal reverses; polarity of comparator on control chassis can be changed
2. Average current readout	
Display	4-in. scale meter
Precision	2%
Range	0.03–100 μA full scale
Electrons-positrons	Polarity can be switched on front panel
3. Integration circuit	
Display	Digital (Nixie tubes)
Precision	0.3% relative; 1% absolute
Range	0.001 and 100 μA
Readouts	Total charge over any time period (manual start–stop); Q/sec measured over 0.1, 1, 10 sec (μA); Q/pulse averaged over 10, 100 beam pulses (coulombs)
Electrons–positrons	Polarity can be switched on front panel

Figure 19-1a Beam current monitoring system.

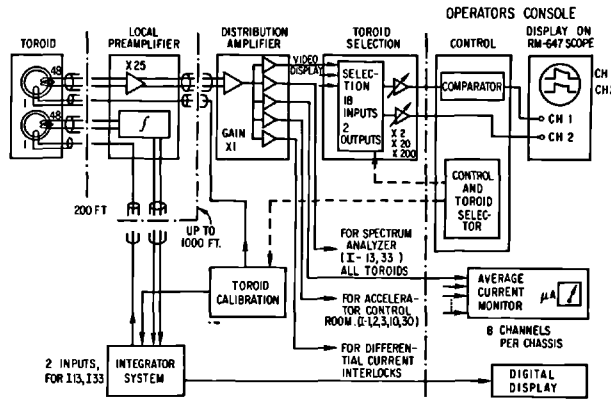

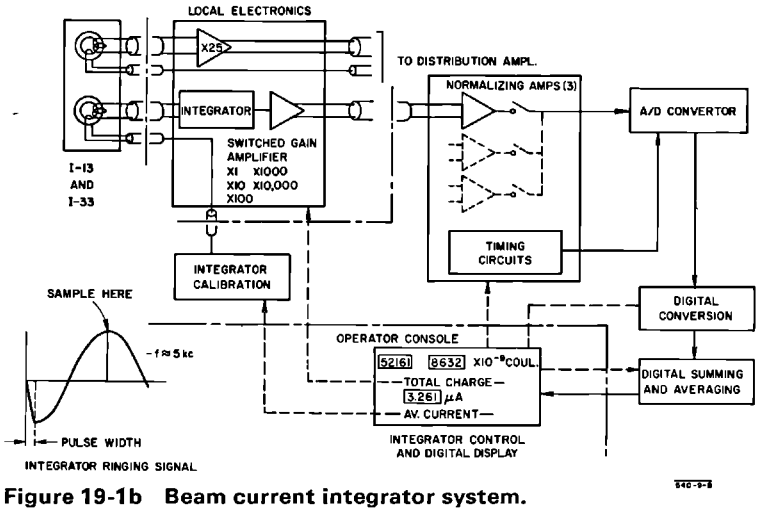

Figure 19-1b Beam current integrator system.

is significant residual radioactivity at the location of the monitor. The preamplifier has a gain of 25 and a balanced input and output. The purpose of the preamplifier is to minimize the effect of noise pickup in the long cable runs to the control room.

Twinaxial cable (RG/22/U) is used to minimize noise pickup over the long transmission distances (400 to 1000 ft) after the preamplifier. The cable from the toroidal current transformer to the preamplifier is totally shielded by a combination of flexible bronze tubes and copper pipes. The frequency response of all the amplifiers in one channel from the current transformer to the oscilloscope is approximately 20 MHz. This corresponds to a 10–90% rise time of 17 nsec. The limiting element is the twinaxial cable. The frequency response of the cables may be equalized, but for the longer cable lengths (1000 ft) the rise time might be as long as 50 nsec. The total linearity of all amplifiers is better than 0.3% over the operating range. The gain stability is better than 0.3% for the anticipated temperature fluctuations.

The distribution amplifier shown in Fig. 19-1a serves to adjust the gain of each transformer channel to 50 mV/mA and to provide five separate buffered outputs. The buffered outputs are typically used for the following:

1. Video display system.
2. Average current display system.
3. Current display system in the accelerator control room. The signals from I-1, -2, -3, -10, and -30 are processed by the linear-Q circuit[2] in the sector electronics. This circuit integrates the video signal and sends a signal which is proportional to the charge per pulse to the CCR.
4. Differential current interlock circuits.
5. Other purposes: the analyzed beam current signals from I-13 and -33 are combined with other signals in the display of the spectrum analyzer.

The monitor calibration circuit (BCM system calibration chassis) can send a pulse through the calibration winding of the transformer. The controls for this circuit are integrated with all other controls in one panel (BCM video control chassis). The calibration pulse is delayed 100 μsec with respect to the beam pulse in order to allow calibration during beam operation. The absolute accuracy of the calibration system should be better than 3%.

The basic criterion of the video display is to observe on an oscilloscope simultaneously the output signal of any two current monitors along one beam, e.g., either I-10 and -13 or I-10 and -15. It is also possible to display simultaneously monitor signals from two different beams. The total linearity and stability of all amplifiers is better than 0.3%.

The control chassis shown in Fig. 19-1a (BCM video signal control) contains thirty-six current monitor selection switches, eighteen for oscilloscope channel 1 and eighteen for channel 2, in such a way that any monitor may be displayed on either channel. A comparator circuit in this chassis produces a precise dc offset voltage which is used to measure the pulse amplitude.

The switches for monitor selection and two amplifiers each with gains of $\times 2$, $\times 20$, and $\times 200$, are mounted in a separate chassis (BCM video selector chassis). The purpose of these amplifiers is to present a reasonably high voltage which is a decimal function of the beam current (0.1 V/mA, 1.0 V/mA, 10 V/mA) to the oscilloscope. They also provide filtering which can reduce the high- and low-frequency noise.

The average beam current display consists of three chassis, each of which contains eight separate meter displays. Each chassis is separately synchronized by a synchronization pulse 1.5 μsec before beam time. The chassis has a front panel switch which allows the selection of two synchronization pulses. With this arrangement it is possible to display alternatively the current from two interlaced beams on the same meter.

The maximum zero offset on the meters is due to system noise, and dc drift is less than 10% of the most sensitive reading (0.003 μA). The precision is about 2%.

The purpose of the beam current integrator[2,3] is to provide a precise measurement of the beam current at the end of the beam energy analyzing system. At present, one integrator readout system is built which may be switched to read the current in either the A or B beam (I-13, I-33). The integrated current can be displayed on two digital readouts. One display represents the total charge over an arbitrary period of time (selected by the operator pushing a "start" and a "stop" button). The second readout displays the average beam current in either microamperes or average charge per pulse.

The integrator circuit is located in a local electronics box as close as possible to the current transformer but outside the radiation restricted area and consists of a capacitor connected directly across the twinaxial cable from

the second transformer of the current monitor. The sensitivity of this resonant integration is

$$V_{\text{out}} = \frac{I \cdot t_p}{N \cdot C} \tag{19-4}$$

where C = the integrating capacitance.

After the integration period t_p, the capacitor and transformer inductance L_T produce a damped oscillation, as shown in Fig. 19-1b.

The local switched gain amplifier is provided to build the signal level to the highest possible value before transmission to the control room. In the control room, each of the two inputs (I-13 and -33) goes to a separate amplifier which compensates for differences in gain as a result of differences in cable length.

The integrator control and display chassis selects the integrated signal from any of the three monitors and connects it to the analog-to-digital (A/D) converter. The A/D converter includes a sample-and-hold circuit which samples the second peak of the oscillation [Fig. 19-1b]. This quantity is measured with a precision of 0.1% and is proportional to the integral of the beam pulse current.

The A/D converter is a 14-bit bipolar unit with binary output. The output of the A/D converter goes to the digital circuit, which converts the binary signal to a decimal form and connects to the two readouts mentioned above.

The linearity and reproducibility of the system is better than 0.1%. The accuracy between the various ranges is better than 0.05%. The absolute calibration will at best be of the order of 0.3 to 1%. The minimum observable signal is limited by the amount of coherent noise in the system.

The integrator calibration chassis discharges a precisely known amount of charge through the toroid calibration winding.

Position monitors (DRO)

A block diagram of the beam position monitor system is shown in Fig. 19-2a. The basic position detector is a microwave cavity; these cavities and the diode detectors are discussed in Chapter 15.

The calibration curves shown in Fig. 19-2b are based on measurements taken on position monitors P_1 and P_2 during a beam test run in June 1966. They were taken with a gain setting equal to 1. The curves depend on the system gain which can be adjusted internally.

The microwave position monitor has two display systems: the video or dynamic oscilloscope display system and the average or normalized display system. The primary use of the microwave cavities in the switchyard is for beam centering. A secondary use is to measure the actual displacement of the beam.

The output of the video display system provides the most sensitive indication for beam centering. As shown in Fig. 19-2a the x and y position signals of any two monitors may be viewed simultaneously on the Type 551 oscilloscope.

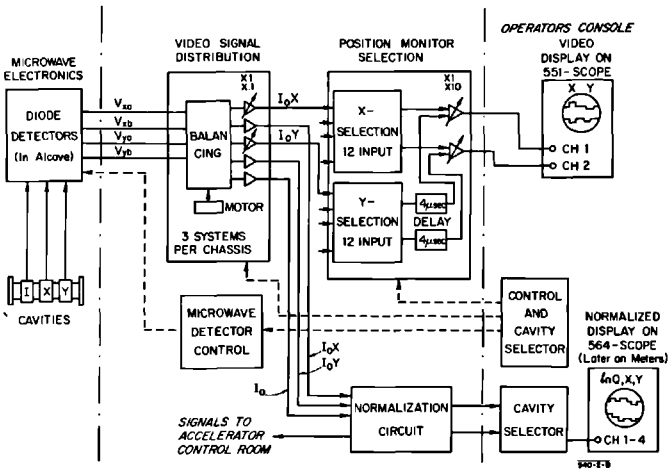

Figure 19-2a Beam position monitoring system.

In this display, the y signal is delayed by 4 μsec and combined with the x signal so that both are displayed on the same trace of the oscilloscope.

The video signal distribution circuit [beam position monitor (BPM) video distribution chassis] reduces the outputs from the microwave detector diodes. This chassis combines the signals V_{xa}, V_{xb}, V_{ya}, V_{yb}, and produces five output signals: two position signals proportional to Ix, two position signals proportional to Iy, and one current signal I (I = beam peak current measured in the beam current monitor cavity).

Because the diodes do not track over the operating range, the signals V_{xa} and V_{xb} must be balanced each time the beam current I is changed.

The output to the video system may be range-switched through relative gains of 0.1, 1, and 10 so that the operator can adjust the scope display to suit his requirements.

Figure 19-2b Microwave position monitor calibration.

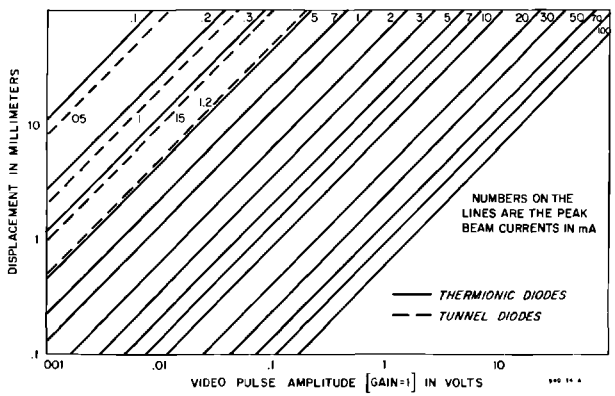

The control chassis (BPM video signal control) selects the cavities that are displayed on the scope and provides controls for balancing, phase adjustment, and diode switching in the microwave detector chassis.

The chassis marked microwave detector control in Fig. 19-2a is used to multiplex the control chassis to the various position monitors.

A position signal independent of the beam current is produced in the normalization circuits. These circuits are the same as those used for the position monitors along the accelerator (see Chapter 15). The inputs to these circuits are the video position signals *Ix*, *Iy*, and *I* signal. The outputs produce three pulses, each 500 μsec wide. The first is proportional to the logarithm of the charge of the beam pulse, the second is proportional to the x displacement, and the third to the y displacement. They are displayed in a row on one trace of a Type 564 oscilloscope. The oscilloscope has four traces so that the outputs of four monitors are displayed simultaneously.

Beam profile monitors (RWC)

In the BSY, three different types of monitors are used to measure the cross-sectional profile of the beam as it is shaped by the accelerator and the transport system. Although the principles of operation of the three devices are quite different, they share the common characteristic of producing a beam of light, which when focused onto a suitable detector (in this case the vidicon tube of a television camera) gives an image of the profile of the beam. The three sources of light are synchrotron radiation, Cerenkov radiation, and beam-induced phosphorescence. Each effect and the way it is used in the BSY will be described separately. It should be mentioned, however, that the optical and TV system is basically the same for the three monitors. The light is reflected by a series of mirrors from its source in the lower half of the double tunnel structure of the switchyard to a radiation-resistant telescope and television camera mounted in a shielded sleeve in the upper part of the tunnel.

SYNCHROTRON LIGHT. Electromagnetic radiation is emitted tangentially to the path of an electron deflected in a magnetic field. For most of the magnets in the beam switchyard, the wavelength of this radiation covers the visible spectrum. This phenomenon has been used after the first bending magnet B-10 in the A-beam of the switchyard as a nonintercepting means of visual observation of the beam spot.[4] The radiation covers a wide frequency spectrum which is dependent upon the bending radius in the magnet and which shifts toward the shorter wavelengths with the third power of the beam energy:

$$\lambda_c = 5.59R \cdot \left(\frac{1}{E}\right)^3$$

where λ_c is the shortest wavelength in angstroms radiated, E is the energy in gigaelectron volts, and R is the bending radius in meters.

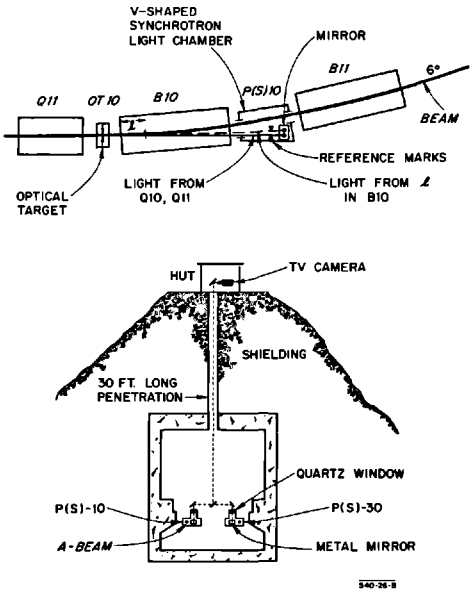

Figure 19-3
Synchrotron light observation.

The bending magnet has a bending radius of 57 meters, and the synchrotron radiation is, therefore, in the visible spectrum if

$$E = \left(\frac{5.59 \times 57}{5000}\right)^{1/3} = 0.4 \text{ GeV or higher}$$

The photons are emitted in a forward cone with an angular distribution extending to 1.5 mrad (half-angle),[4] the number of photons in the visible range emitted per second for each microampere of beam current being

$$N = 2.4 \times 10^{12} \frac{l}{R^{2/3}} \text{ photons/sec}/\mu\text{A}$$

where l = length of the path the electrons travel in the magnetic field. The optical system is arranged to accept light from the first 12 in. of the effective magnetic length of bending magnet B-10 (Fig. 19-3).

The theoretical light production in this length is 4.9×10^{10} photons/sec/μA and all of the transmitted light will be collected by a 4-in. diameter mirror at a distance of 7 meters. The light is reflected by four front surface aluminized mirrors (reflectivity = 90%), and passes through one $\frac{3}{8}$-in. quartz window (transmission 95%). Assuming a beam spot size in B-10 of 2 × 15 mm and a demagnification from the beam to the vidicon faceplate of 1/30, we find a light level on the photocathode of approximately 18.5×10^{11} photons/cm^2/sec/μA. The RCA 7735A vidicon tube, when adjusted for maximum

sensitivity, operates with a faceplate illumination (highlight) of 0.1 ft-c = 4×10^{11} photons/cm^2 (according to the manufacturer's brochure). This corresponds to a beam current of 0.22μA. For our purposes, a useable image can be obtained with lower light levels and we have observed experimentally that the beam is still visible at average currents of less than 0.01 μA.

The special V-shaped vacuum chamber located after B-10 contains a mirror which is adjustable manually via a three-point support from outside the vacuum box. Initial alignment of the mirror is accomplished by using the optical target OT-10 in front of B-10 and the reference marks (cross wires) fixed inside the V-shaped chamber (see Fig. 19-3). The mirror consists of a $\frac{1}{4}$-in. thick piece of polished, high-purity, fused silica, the front surface of which is aluminized. A 12-in., quick disconnect, vacuum flange enables the section containing the mirror and quartz viewing window to be replaced easily.

CERENKOV LIGHT. Cerenkov light is emitted by charged particles moving through a medium with a speed greater than the phase velocity of light in that medium. In the profile monitors for the switchyard[5] the Cerenkov light is observed when the electrons pass through a gas at atmospheric pressure. The number of Cerenkov photons produced in a gas and their angle of emission are given by

$$N_\phi(3500\ \text{Å} < \lambda < 6000\ \text{Å}) \approx 900(n\beta - 1)\ \text{photons/cm/electron}$$

Figure 19-4 Principle of Cerenkov light monitor.

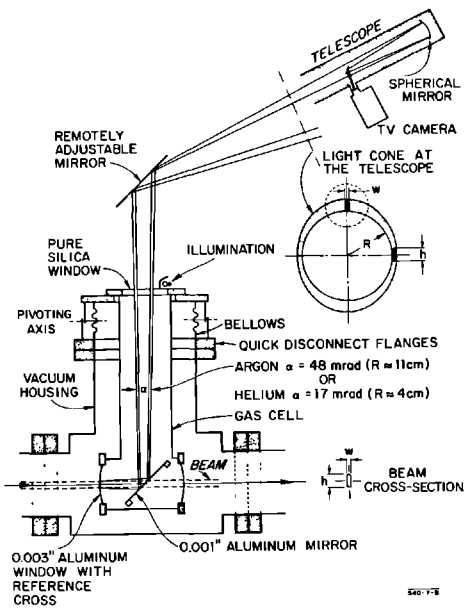

and

$$\theta = \cos^{-1} \frac{1}{\beta n}$$

where n = the refractive index, and $\beta = v/c$ so that a light cone is developed in the gas with an opening angle $\alpha = 2\theta$. The beam image is observed by looking along one part of the cone. This introduces a distortion along one axis equal to $l \sin \theta$, where l is the effective length of the gas cell. The construction of the Cerenkov profile monitor is shown schematically in Fig. 19-4. The gas in the cell flows through when the monitor is in the beam at a flow rate of 1 cm^3/sec. Both argon and helium have been used at different times. Argon produces more light, but helium reduces the distortion as well as the beam scattering. The gas cell is built in a tubular hammerhead configuration and has 0.003-in. thick hard aluminum beam entrance and exit windows. The light cone is reflected vertically by a mirror placed in the beam at 45°. The mirror consists of a 0.001-in. thick mechanically and chemically polished foil stretched over a ring, using a drumhead tightening principle. The gas cell swings about a pivot axis and is moved into the beam by the application of air pressure to a small cylinder. A counterweight (see Fig. 19-5) moves the cell out of the beam when the air pressure is released. Except for a beam position reference cross, the input window is blackened using a graphite spray (Aquadag, ammonium hydroxide, and water).[6] The blackening

Figure 19-5 Cerenkov light profile monitor.

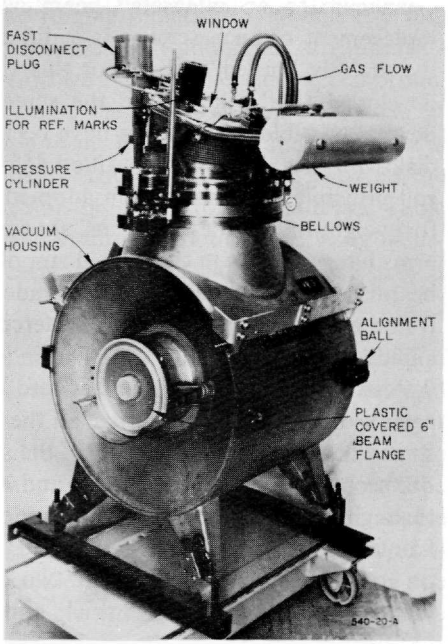

Table 19-3 Comparison of two types of multiscreen monitors

Characteristics	*Cerenkov cell*	*ZnS screen*
Sensitivity	(He)10^{-9} A/cm^2 (Ar) 3×10^{-10} A/cm^2	10^{-9} A/cm^2
Spot definition	1 mm	1 mm
Max. aperture	3 in. in diameter	8 in. wide, 2 in. long
Material in beam	2 Al windows 0.003 in.; 1 Al mirror 0.001 in.; 20 cm gas; 0.001 in. graphite (Aquadag) on one window	0.002-in. Al foil at 65° or 90° to beam 0.001-in. and 0.004-in. thick zinc sulfide Sylvania (P-402)
Rad. length in Beam	6×10^{-3} rad l (Ar); 2×10^{-3} rad l (He)	1.3 to 3.5×10^{-3} rad l
Mechanical	Moved into beam by air pressure, out by gravity	Selected and operated by electric motors
Expected life	Mirror 1.5×10^4 μA hour/cm^2	10 μA hour/cm^2 per screen

carbon is molecularly bonded to the window and is, therefore, permanent. The cross can be illuminated with a lamp mounted outside the viewing window. Table 19-3 gives the characteristics of both the Cerenkov cell and the zinc sulfide screen profile monitors.

ZINC SULFIDE SCREENS. Zinc sulfide screens are easy to make and have good sensitivity; however, they have the disadvantage of losing luminescence after exposure to an integrated beam current of about 10 μA/hour/cm^2. The replacement of such screens is a difficult task in the switchyard because of the severely limited access. For this reason, an automatic device has been developed that will replace the screens after they have become inactive. Several possible mechanisms have been considered, among which are a large disk with its axis of rotation tilted 45° with respect to the beam, and the film roll principle. The mechanism adopted for the switchyard is a carrousel with forty-eight independent screens, shown in Fig. 19-6. The forty-eight screen arms hang on balls in the slotted rim of a 10-in. wheel. The screen frames can be raised into the beam by the blade lift mechanism. The U-shape of the frame ensures that the beam is intercepted only by the 0.002-in. thick zinc sulfide-coated aluminum foil. The index drive mechanism rotates the wheel 7.5° so that a new screen comes into the lift position. The carrousel can be removed from its housing when all the screens have been used. The individual screen frames can be lifted out of the slotted rim for replacement. The image of the beam spot on the screen and position reference marks are observed through a fused silica vacuum window at the top of the light pipe and a front surface mirror at the lower end of the light pipe. The adjustable mirror on top of the light pipe and the two drive motors, shown in Fig. 19-7, protrude into a slot in the 2-ft thick concrete shielding floor. In this way they

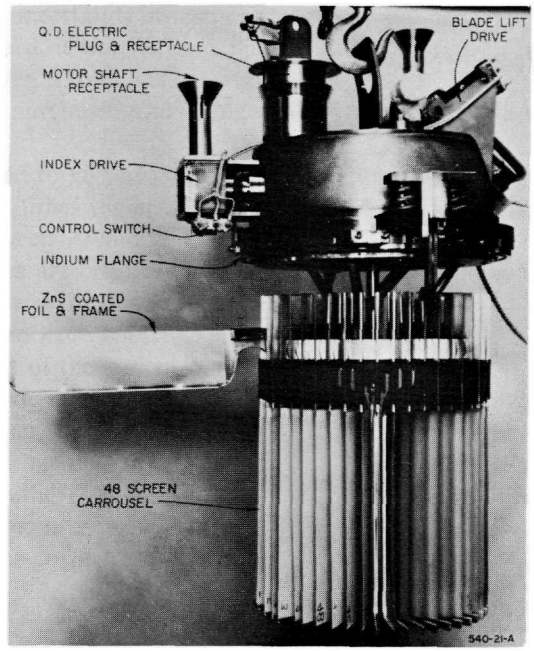

Figure 19-6 The ZnS screen changer lifted out of vacuum housing.

are shielded from radiation and are easily accessible. Figure 19-7 shows various other details designed to make remote replacement possible: a fast disconnect, two plug-in-type drive motors, assembly guide rods, a 12-in. fast-disconnect, vacuum flange, and lift eyes. Two types of the multiscreen profile monitors described above have been built, the carrousel being identical in each case. One is for a 6-in. beam pipe (4-in. wide screen) and the other is for a 12-in. beam pipe (8-in. wide screen). The only difference between the two types is the angle at which the screen is presented to the beam (see Table 19-3). The screens are sprayed at a temperature of about 80°C, using a suspension of 10-μ P-4 phosphor in glycerin, sodium silicate, and water, by a process developed by W. Schultz.[6]

OPTICS AND TV SYSTEM. A 735 scan line I.T.T. closed-circuit television system is used, its optimum resolution of 520 lines both horizontal and vertical being below that of the optical system. There are a total of eight cameras in the switchyard, and the video signals and the controls for the instruments are multiplexed into two display channels. The vidicon tube selected for the television cameras is the RCA 7735A, which is available either with a standard faceplate or (at a much higher price) with a non-browning faceplate. Radiation levels in the switchyard are still low and the standard tubes will be used until faceplate browning rather than photocathode

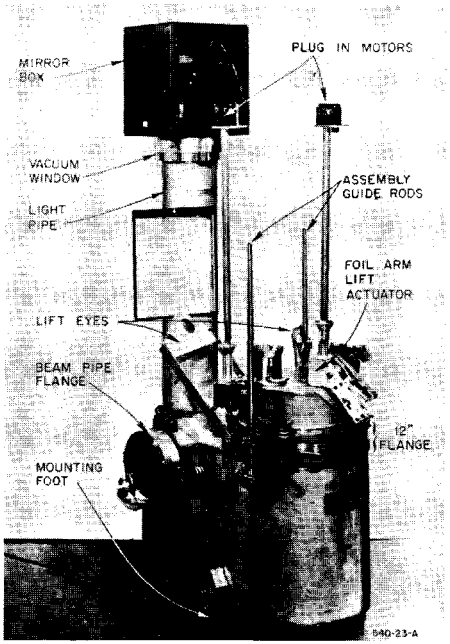

Figure 19-7 Complete multiscreen ZnS monitor.

degradation limits tube life. The photocathode of this tube has a fairly sharp spectral sensitivity curve with a peak at 5500 Å, so that other optical components in the system were chosen to match this wavelength where possible. The light is focused on the vidicon tube with a reflector telescope using spherical, front surface, aluminized mirrors (Liberty Mirror No. 756). The advantages of the telescope are that the mirrors are less expensive, are better resistant to radiation than nonbrowning lenses, and, using the Newtonian arrangement with the camera perpendicular to the telescope, the camera can easily be shielded from radiation. Light from the monitors passes in each case through a radiation-resistant vacuum window (Corning pure fused silica, code 7940) and is directed into the telescope by a remotely adjustable front surface mirror. This mirror can be rotated through small angles about two axes by electric motors driving cams, the cams being contoured to give two speeds. The front surface aluminized mirrors are unaffected by radiation but are very sensitive to nitric acid corrosion. Other metallic coatings such as gold, titanium, and chromium are resistant to nitric acid corrosion but have a low reflectivity. The reflectivity of a front surface chromium-on-glass mirror was increased to about 90% at 5500 Å by the application of several quarter-wavelength-thick layers of magnesium fluoride and titanium dioxide. This mirror was found to be unaffected by nitric acid and no significant changes in reflectivity could be found after exposure to a radiation dose of

10^{10} ergs/g. Because of the uncertainty in estimating the nitric acid vapor concentration in the switchyard, it was felt that the expense of these mirrors could not be justified. However, a fully dielectric commercial mirror (Liberty Mirror No. 90-500) has been purchased and installed on one of the Cerenkov cells for further evaluation.

The telescopes are designed to give an overall magnification on the 17-in. TV monitor between 1 and 2 times the actual beam size. The spherical mirrors vary in focal length between 10 and 20 in. for the different monitors in the switchyard. The telescopes are constructed in such a way that they will accept any $4\frac{1}{4}$-in. diameter mirror in this range. Coarse focusing is provided by means of a thumbscrew on each telescope; fine focusing is provided by remote control of the position of the vidicon tube inside the TV camera.

In the case of the zinc sulfide screen changers, where viewing angles introduce different distortions along the two axes, an elliptical disk is mounted just out of the beam path in such a way that it corresponds to a circular beam spot and can be seen on the TV monitor when there is no screen in the beam. By adjusting the TV monitor so that this disk appears circular, the distortion of the system can be corrected.

Secondary-emission monitors (SEM's) (JNH)

Low-energy secondary electrons (<30 eV) are emitted from the surfaces of material when it is traversed by high-energy (>75 keV) charged particles. The secondary emission shows little dependence on primary particle energy above 150 keV. It is linear with current and there is no saturation. SEM's are useful in the switchyard for their linearity and wide dynamic range but can be used only where an intercepting-type monitor is permissible.

Secondary-emission monitors are used in the switchyard, in the following applications:

1. The tune-up spectrum monitor (TSM).
2. A- and B-beam spectrum analyzers (SA).
3. For beam centering into the high-power dumps (four-quadrant SEM) and collimators.
4. On the slits to provide spectrum centering information (spectrum drift indicator—SDI).
5. Applications 3 and 4 above are also used to provide interlock signals to the summary interlock system for equipment protection.

The theoretical secondary-emission coefficient, η, is approximately 4% for aluminum. The coefficient is very dependent on surface conditions. Aluminum foils are used for all SEM's in the switchyard, and for calculation purposes η was assumed to be 3%.

SEM FOILS ON SLITS, COLLIMATORS, AND TUNE-UP DUMP. Sets of three parallel SEM foil emitters are mounted on the front and back of C-0, C-1, and SL-10

and on the front of SL-31. Two of the foils on the front of C-0, C-1, and SL-10 are experimental gold-plated conduction foils. Two sets of parallel SEM foils are mounted at each edge of the tune-up dump. These protect the dump edge from beam powers above 50 kW.

FOUR-QUADRANT SEM (4-Q SEM). This SEM is a circular structure 8 in. o.d. × 3 in. i.d. It is divided into four quadrants: top, bottom, right, and left. Each quadrant consists of a set of three 0.005-in. thick emitting foils in parallel.

A 4-Q SEM is mounted in front of the window of the A-beam dump and beam dump east. The monitor is used to steer the beam into the center of the window. The permissible power density on the window is highest in the center. Very intense beams must be carefully centered to avoid overstressing the window near its edge.

ELECTRONICS. The SEM electronics provide two signals, an interlock level and a dynamic presentation of SEM signals. Each foil is connected to an RC integrator (T = 200 msec). The integrator voltage is monitored by a variable threshold comparator (+20 mV to + 2.0 V). The comparator outputs are connected to an OR gate and used as the SEM interlock signal.

For dynamic presentation, the integrator voltages may be viewed on an oscilloscope which is connected to the electronics through a multiplexer and a selector panel (see Fig. 19-8).

Beam spectrum instrumentation (JNH)

A low-resolution spectrum measurement can be made with the tune-up spectrum monitor S-10, located in front of the tune-up dump D-10. A more precise measurement of the deflected A- and B-beam spectrum is made with identical analyzers S-11 and -31, located in front of the slits SL-10 and -31. (See Table 19-4.)

Figure 19-8 Secondary-emission monitor electronics.

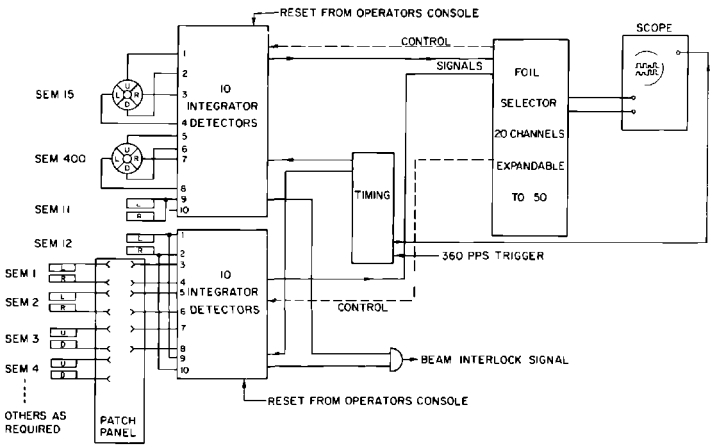

Table 19-4 Data on spectrum instrumentation

	Spectrum monitor S-10
1. Data on foils	
Material	Aluminum 0.005 in. thick
High-resolution side	22 foils covering $\alpha = 4.0$ to 7.5 mrad deflection
Low resolution side	16 foils covering $\alpha = 1.58$ to 4.0 mrad deflection
SEM-11 A and B	SEM protection foils
2. Signal integrator	
Time constants	$\frac{1}{3}$, 1, 3 sec
Signal attenuation	$100\times$ (1μF), $10\times$ (0.1μF), $1\times$ (0.01μF)
Noise level	0.5 nA avg. beam current
Trigger rate	60 pulses sec synchronized with beam
Scan time	270 μsec/channel—low-resolution foil 100 μsec/channel—high-resolution foil
Display	Oscilloscope (shared with spectrum analyzer 2 and 4)

Spectrum analyzers S-11 and -31													
1. Data on foils													
Width	mm,	40	24	12	12	6	6	6	6	12	12	24	48
S-11 $\Delta P/P$	%,	0.8	0.4	0.2	0.2	0.1	0.1	0.1	0.1	0.2	0.2	0.4	0.8
S-31 $\Delta P/P$	%,	0.16	0.8	0.4	0.4	0.2	0.2	0.2	0.2	0.2	0.2	0.8	1.6
Maximum opening between foils	6 in.												
Material	Aluminum 0.001 in. thick												
2. Average spectrum display	See detail 2 of spectrum monitor												
A-beam	12 foils from S-11 + current signal from I-13												
B-beam	12 foils from S-31 + current signal from I-31												
Scan time	100 μsec/channel												
3. Video spectrum display	Any combination of four out of the 26 video signals can be displayed on a Tektronix 551 scope												
Equivalent input noise	30 μV												
Response time	30 nsec												
4. Sampled spectrum display	See detail 2 of spectrum monitor												
Synchronization	Every beam pulse												
Sample width	100 nsec; sample can be taken at any point of beam pulse length : 0–2.2 μsec												

TUNE-UP SPECTRUM MONITOR S-10. The TSM consists of a row of SEM foils mounted in a wide vacuum chamber in front of the tune-up dump D-10. The TSM and the tune-up dump were made as wide as possible to provide maximum energy acceptance during accelerator tuning.

The TSM has been split into two halves. This allows each half to mount on a standard 12-in. fast disconnect vacuum flange. The half located closest to the A-beam is shown in Fig. 19-9. It contains six narrow high-resolution foils each corresponding to $\Delta P/P = 0.86\%$. The beam is normally tuned on these foils before deflecting into the A- or B-beam vacuum pipe. The other half of the TSM is constructed in the same way but has no high-resolution foils.

The foils are 0.005-in. aluminum. They are spot-welded to nickel tabs which are, in turn, brazed to metallized areas on a rectangular ceramic bar. Each foil is brazed on the alternate side of the ceramic bar, allowing the foils to be positioned with no gap or overlap between them.

At each edge of the TSM there is a stack of interlock SEM foils (SEM-11). These are used for interlock protection of the edges of the tune-up dump (see above).

The tune-up dump spectrum monitor electronics is shown in Fig. 19-10. Each of the thirty-eight individual foils is connected to an integrator in the local electronics box. The low leakage coaxial cable between the foil and this

Figure 19-9 High-resolution tune-up spectrum monitor.

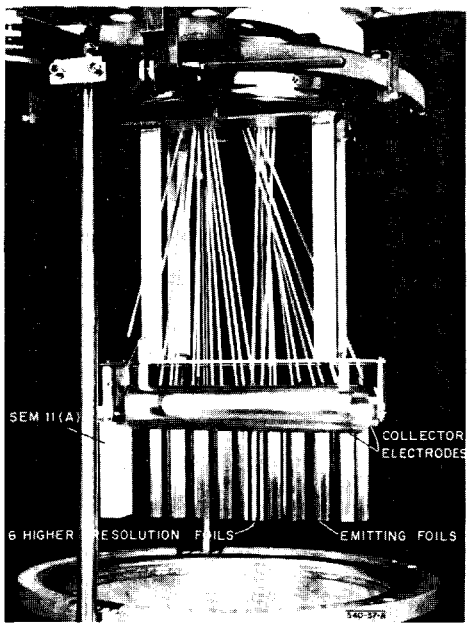

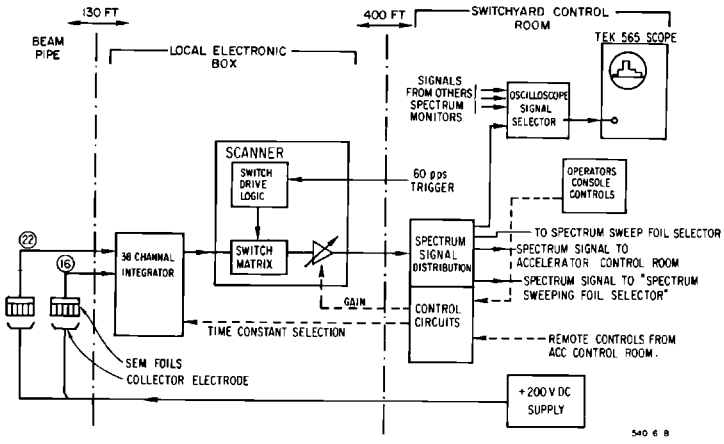

Figure 19-10 Tune-up spectrum monitor system.

circuit is part of the integrating capacitor. The discharge time constant and integrating capacitor of each integrator are remotely adjustable.

The scanner sequentially samples the voltage on each integrator and amplifies the output signal (gain adjustable from 1 to 20). The spectrum signal is then transmitted to the switchyard and accelerator control rooms.

A selector is used to separate one foil signal in the spectrum display for plotting the spectrum as a function of deflecting magnet current. To obtain a spectrum using this procedure, one has to sweep the beam across the foil.

THE SPECTRUM ANALYZER. A complete spectrum analyzer is shown in Fig. 19-11. The 0.001-in. SEM foils are supported in a unique, spring-loaded, foil holder assembly. The foil holders are mounted on pivoted motor-driven arms. This allows the foils to be retracted or inserted into the beam as necessary.

All electrical connections to the foil holders are shielded by a cover plate. This prevents deposition of any material on the ceramic insulators, which might cause leakage.

The spectrum analyzer electronics system is shown in Fig. 19-12. It is designed to display beam energy spectrum information in three ways: (a) average spectrum, (b) sampled spectrum, and (c) video spectrum.

The signals from the spectrum analyzer include a signal from the current monitor (I-13 or -33) located after the slit. The gain of the amplifier for this current monitor signal is proportional to the inverse of the selected slit opening. The amplitude of the current signal is brought in this way into proportion with the foil signals for various slit openings.

The average spectrum displays use essentially the same electronics as the TSM. One difference is the method of getting the video signal into the integrators. The mixed video signals are connected to thirteen triggered

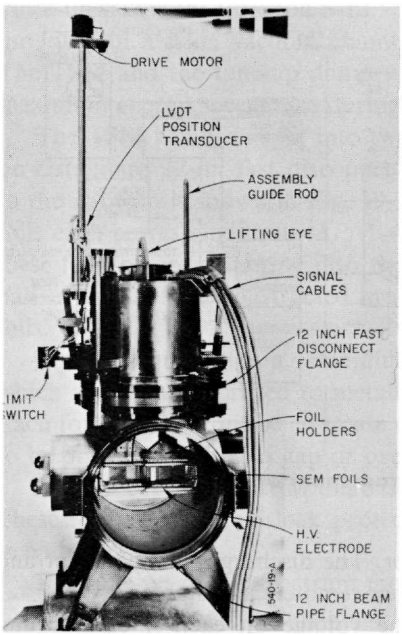

Figure 19-11 Spectrum analyzer.

sample-and-hold circuits. The sampling time of these circuits is 100 nsec, so that many beam pulses are included in the sample.

It is also possible to increase the sample time from 100 nsec to the full beam pulse length. This allows a display of the normal beam spectrum on a pulse-to-pulse basis. The spectrum display signals may be used for plotting a spectrum using the spectrum sweep foil selector.

Figure 19-12 Spectrum analyzer system.

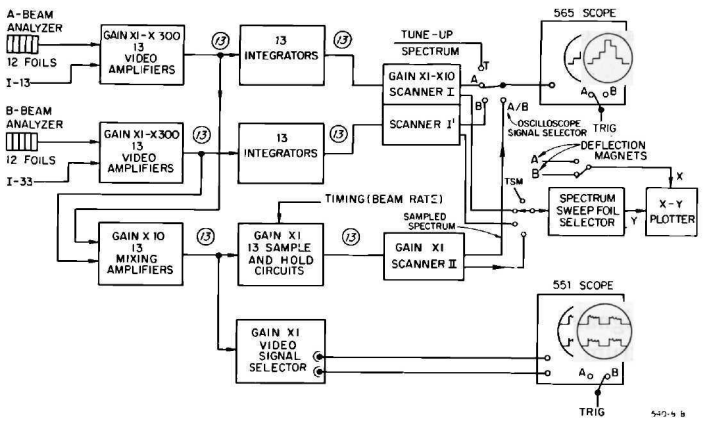

SPECTRUM DRIFT INDICATOR ELECTRONICS. The SDI is used for two purposes: (a) to provide the accelerator operator with a simple monitor showing slow drifts in spectrum during operation and (b) as a backup for the spectrum analyzer in the event of damage to the foils or other delicate parts.

The signals for the SDI are derived from the two SEM foils on the front end of the slits and the current monitor downstream of the slit (I-13 or I-33). These signals are integrated, mixed, and displayed on three panel meters which show both the direction of spectrum drift toward higher or lower energy and the transmitted current.

Meter displays and gain controls are located in the switchyard and accelerator control room.

Transport control (RAS)

The transport control system includes means for switching magnet power supplies on and off and for regulating their current and polarity. It also includes equipment for magnet field and current measurements and for slit and collimator control. Most of the major magnet and slit or collimator adjustments can be made in either of two ways—manually or through the use of a control computer. One element, the long-coil integrator in the reference magnet used for setting the energy analyzing magnets (see "Magnetic Measurements" below), is controllable only through the computer. On the other hand, at the time of writing (July 1967), current adjustments on certain small steering dipoles must be made manually.

MANUAL MAGNET CONTROL. As mentioned above, most magnet currents may be adjusted either manually or by computer. The manual system is used as a backup in case the computer is down for maintenance. All power supplies have internal references that are adjustable by a front panel potentiometer. It is by driving this potentiometer remotely that manual control is achieved. On most of the supplies in the switchyard this is accomplished by the use of a motor mounted on the power supply front panel; a rim drive through a rubber wheel turns the potentiometer. The motors used are the low-voltage dc type and are geared down for better speed control. Two speeds are provided, one by applying full voltage to the motor winding and the other by applying a square wave of full voltage with a 20% duty cycle at 20 counts/sec. The latter method of driving the motor more closely preserves the full speed torque while slowing the motor down. Adjustments are made by the operator with a three-position lever switch (up–off–down with a spring return to the "off" position). The controls are not multiplexed; there is one lever switch for each magnet supply. Certain supplies are operated by a stepping motor, again running at two fixed rates; the operator controls are identical to those just described.

Manual control of the energy-defining magnets is accomplished through the use of a stepping motor, but because of the special requirements on the

rate and magnitude of the current changes (see Chapter 18) the operator controls are different from those described above. In this case a set of rotary switches can be set by the operator to correspond to the number of steps the motor is to take. The motor will start on pushbutton command and stop after having taken the number of steps indicated by the switches. The motor runs at a fixed rate corresponding to a rate of change of current of 6 A/sec in the magnets. One control panel is used for both the A and B magnet systems.

Readback of magnet current is accomplished in two ways, depending upon the type of power supply (dc or pulsed). The dc currents are converted to voltages by ohmic shunts and are subsequently read by a digital voltmeter, switched by a relay scanner. Any dc signal from the switchyard can be read to 0.02% absolute accuracy in this way. Pulsed magnet currents are converted to voltage by a pulse transformer and are read by a sample-and-hold circuit and an analog-to-digital converter capable of reading rates up to 360 pulses sec. This counter is switched by a second relay scanner, and absolute accuracy is better than 0.1%. The pulsed system has one fixed range of 10 V full scale with a resolution of 0.001 V; the dc system has ranges of 1000, 100, 10, 1.0, 0.1. and 0.01 V full scale with a resolution of five digits (0.1 μV on the smallest range).

MAGNETIC MEASUREMENTS (RAS). A system for remote measurement of magnetic fields has been provided. This system includes residual field detectors, NMR probes, and flux loop integrators (an integrator connected to a loop around the magnet yoke).

The residual field detector is a flux-gate magnetometer. The probe consists of a pair of strips of high-permeability magnetic material, each wound with a "primary" coil. The primaries are connected in series, opposing. A 1000-Hz signal applied to the primary windings then alternately saturates the cores in opposite directions. A pickup "secondary" coil is wound around both strips. The signal in this coil (to first order) does not contain any 1000-Hz components because of the opposing primary currents. If a small dc magnetic field is applied parallel to the strips, a 2000-Hz voltage appears across the secondary, because on each half-cycle of the primary current one of the cores is easier to saturate than the other, "unbalancing" the primary currents. This signal is passed through a 2000-Hz, narrow band filter and applied to a high gain amplifier. The output of the amplifier is synchronously detected using the primary signal for phase reference. The resulting dc output is proportional to the field in the probe and is displayed on a panel meter. Sensitivity of the meter is about 2.5 G full scale. This method was chosen to allow the use of a passive probe structure; the probe consists entirely of radiation-resistant materials and can be operated up to 2000 ft from the electronics.

Nuclear magnetic resonance probes are placed in the energy-defining magnets B-10 to B-13 and B-30 to B-32, and in the reference magnets (two reference magnets B-100 and -300 are placed in the control room building

and are electrically in series with the energy-defining magnets in the A-beam and B-beam). The NMR circuit is a modified Pound-Watkins-Knight marginal oscillator[7] and offers no unusual design features. The probe itself consists of a quartz tube with a volume of 0.03 cm^3 surrounded by a solenoid, which acts as the RF circuit of the oscillator. The liquid is a 0.1-mole solution of $MnSO_4$ in saturated $LiCl_2$ in water and provides two resonances: ^1H at 4.2577 MHz/kG and ^7Li at 0.23487 MHz/kG. This double-resonance technique allows coverage of a wider field range without frequency range switching in the electronics. No sweep coils were provided because the dimensions of the probe had to be made as small as possible ($\frac{3}{8}$-in. o.d.) to avoid interaction with the beam in the narrow magnet gaps. A sweep field is obtained by shunting the magnet with a transformer operated from the 60-Hz power line via dc blocking capacitors. A signal-to-noise ratio of 10 to 1 is obtained in the final system with connecting cables as long as 1000 ft.

A simple integrator system has been provided to allow crude field measurements in the dc magnets. The purpose of these measurements is to allow detection of shorts or other changes in the magnet coils at a remote location. The pickup coils (flux loops) consist of several turns around the return yokes of the magnets. These coils are connected by a selector to a stable dc integrator. The system is used as follows. The magnet is turned on to a preset current and the integrating capacitor discharged. The magnet is then turned off, and the resulting output from the integrator is read on a digital voltmeter. The system measures magnet characteristics to better than 1%.

Stationary flux loops on the pulsed magnets PM1 through PM5 are used to integrate the magnetic field in these magnets every beam pulse. The output is used not only to measure the field but also to interlock the beam in the event of misfiring of a magnet modulator (see Section 19-3).

A special rotating flux coil is used in the reference magnets B-100 and -300. This coil can be rotated 180° in the gap of these magnets. The coil output voltage is connected to a voltage-to-frequency converter, and the number of pulses emerging from the converter is proportional to the integral of the field along the coil length. Because the coil is made long enough to include most of the fringing fields, it measures the $\int B\,dl$ to high accuracy. The absolute accuracy of the method is not well defined because of the lack of a suitable comparison standard, but rms deviations in the measurement are typically less than 5 parts in 10^5 over a 1-hour interval. The rotating flux coil is used by the computer (see below) to set the energy acceptance of the BSY.

COMPUTER SYSTEM (RAS, SKH). The transport control system includes a small digital computer to aid in setting up the complex set of parameters in the BSY. The computer (SDS 925) has an 8192-word core memory (24 bits per word) and a 1.75-μsec cycle time; it is a fully parallel, binary oriented machine. Standard peripheral equipment includes a card reader (200 cards/min), a card punch (100 cards/min), and a pair of teletypes, one in the BSY control room and one in the CCR.

Through the use of a number of SLAC-built interfaces, the computer can read, log, and control status information; control magnet, slit, and collimator settings; determine the energy of the various beams in the switchyard to better than 0.05%; and communicate with a larger computer (SDS 9300) in the experimental areas. The operation of these interfaces and associated equipment will be described below.

The interlock and status scanner reads, every beam pulse (2.8 msec), the 1008 two-state status signals in the BSY. The computer scans these signals, detects changes in them, and notifies the operator of the changes. The time required by the computer for scanning, detecting, and identifying the signals is less than 400 μsec. Additional time is required for processing if changes occur.

The scanner is basically a digital multiplexing system controlled by the computer; it transfers 1008 input signals to its output, sixteen signals at a time. Along with each group of sixteen data signals, 6 bits of address information are presented at the output to identify the group being transferred. Thus 22 bits of information are presented to the computer at a time. The computer must accept 63 such transfers to get all of the 1008 signals. When all of the information is stored in the computer memory, the data are compared bit by bit with the previous scan, and the changes recorded. At the time of writing (July 1967) the changes are printed on a small digital printer (maximum speed $\approx$20 lines/sec), but plans are underway to add an oscilloscope display to the system, which would be used to provide a more sophisticated presentation.

Computer magnet control involves five basic equipment modules: digital-to-analog converters to control magnet currents; analog-to-digital conversion equipment to read those currents; the long flux coil (see "Magnetic Measurements," above) interface to read $\int B\,dl$ in the energy-defining magnets; the "tune box" to provide the operator with facility for making small changes in the settings; and a set of status control channels for controlling magnet power supply "on–off" and reversing. Two interfaces are used for digital-to-analog conversion, and each operates a different type of converter. The most common type consists of a 15-bit binary resistor ladder switched by mercury-wetted reed relays. The relays are of the magnetic latching type, and thus form the memory as well as the switching and isolation functions. Reference voltage for the resistor ladder is supplied by a highly stable ($\pm$0.01%/24 hours) power supply that is shielded and guarded from the chassis ground. The resistor ladder contains thirty-one resistors, matched to $\pm$0.002%, and is also guarded. The 15-bit resolution allows steps of 1 part in 32,768 of the full-scale output voltage of 10 V, or about 300 μv. The present system includes twenty-six such converters, with provision to extend this number to sixty-four.

The energy-analyzing magnets, however, have one special requirement which precludes the use of this type of converter. The high energy of the electron beam (24 GeV) requires eight 3-meter magnets to deflect the beam

24° in the analyzing system (for A-beam; the B-beam uses four magnets to deflect the beam 12°). These magnets are connected electrically in series, along with a reference magnet (which is placed in the control room for measurement purposes). In order to ensure accurate tracking of the magnetic field, a necessity if the reference magnet measurements are to be meaningful, the current in these magnets must be changed at a relatively slow rate (0.75%/sec).

The digital-to-analog converters mentioned above inherently produce transients that far exceed this rate. Therefore, these magnets are controlled by a reference voltage from a multiturn potentiometer driven by a digital stepping motor. The mechanical nature of such a system precludes transients larger than about 0.003% in amplitude. The interface contains a pair of counters (one for A-beam and one for B-beam) which are loaded by the computer with the number of steps the motor is to take. The interface detects the sign of the number (it is loaded in two's complement) and, if negative, counts the counter up and the motor counterclockwise; if it is positive, the interface counts the counter down and the motor clockwise. A pulse is counted by the counter for each pulse sent to the motor. When the counter reaches zero, the clock pulses stop (stopping the motor) and the computer is interrupted.

Readback of magnet currents is accomplished by two methods. In the case of dc magnets, the currents are measured by shunts ($\approx 1.2 \times 10^{-3}$ ohm), and the shunt signals are switched through a precision relay scanner to a digital voltmeter, where they are digitized to an accuracy of better than 0.01%. Of course, any dc signal can be read through this system. For the pulsed magnets, a solid-state differential multiplexer and a fast analog-to-digital converter with a sample-and-hold circuit provide the computer with measurement ability. The computer selects both the channel and trigger time of the sample-and-hold circuit.

The long flux coil interface contains circuits to control the motor and clutches on the coil mechanism, and to count the pulses from the voltage-to-frequency converter. The circuits work in the following way. Upon issuance of a command by the computer, the motor starts to turn and the clutch engages, starting the coil in motion. The output of the coil is connected to a voltage-to-frequency converter with high stability. Since the output of the converter is a train of pulses the frequency of which is proportional to the input voltage, the number of pulses is proportional to the integral of the input voltage. These pulses are counted by a register in the interface, and a set of microswitches on the coil mechanism stops the motor and provides an interrupt to the computer when the rotation has ended. Upon interruption the computer reads the number in the register, resets it, and starts the coil rotating in the opposite direction. The program always averages two successive "flips" of the coil to eliminate the effect of zero drift error in the voltage-to-frequency converter. The resulting number is precisely proportional to the $\int B\,dl$ in the magnet, which is, in turn, proportional to the energy of a particle

passing through the center of the slit. Root-mean-square deviations of the measurement are typically less than 5×10^{-5} over a 1-hour period, with the coil making three flips a minute.

The "tune-box," or magnet manual control panel, consists of twenty-four pushbuttons, one lever switch (three position momentary), and a speed control knob. Interrupts are sent to the computer by this panel whenever the lever switch is raised or lowered. The rate at which these interrupts are sent to the computer is controlled by the speed control (1 per switch operation, or a steady 1, 5, or 25 per second). When so programmed, the computer will interpret the selected pushbuttons as magnet supplies, inspect the pushbuttons, and increment or decrement the magnet currents selected depending upon the position of the lever switch. There are two such panels provided. Since the interface is designed such that the interrupt is not required for the computer to inspect the pushbuttons, this panel can also be used in other ways, one of which is to print out on the typewriter the currents (in equivalent gigaelectron volts) of all magnets selected. This is done through a typewriter instruction (see the discussion of the computer program below). The tune-box was provided primarily to allow the operator to make small adjustments to the magnet currents in a manner more natural than typing a series of instructions on the computer typewriter.

The final interface used for magnet control is a set of sixteen mercury-wetted relays (the system is expandable to sixty-four such sets) of which the positions are individually under computer control. This interface allows the computer to turn on and off and reverse power supplies, or to control other status in the switchyard and research areas.

A computer–computer link has been designed between the SDS 925 in the switchyard and the SDS 9300 in the experimental area, about 1000 ft away. The link system contains two buffers, each 24 bits long, to hold data from one computer until the other can respond and read it. The data word is transferred, along with an interrupt, in parallel along coaxial lines. Maximum transfer rate is limited by the speed of response of the computers to the interrupt, but could, in principle, exceed 50×10^3 full computer words per second.

The entire computer system, including the slit and collimator control system, is shown in Fig. 19-13.

Control of the slits and collimators is a complex task involving a separate system. The computer can control them through the slit/collimator (S/C) computer control unit, a portion of the S/C control system. The entire system will be described later.

Communications between the operator and the computer are accomplished either directly by typing the instruction on the typewriter, or by punching the instructions on IBM cards and reading the cards into the computer. The execution of the instructions is accomplished through the use of the "925 system language," the source language for a real-time compiler which is resident in the computer at all times. The real-time compiler reads instructions from the typewriter (or card reader) on-line and in what is essentially

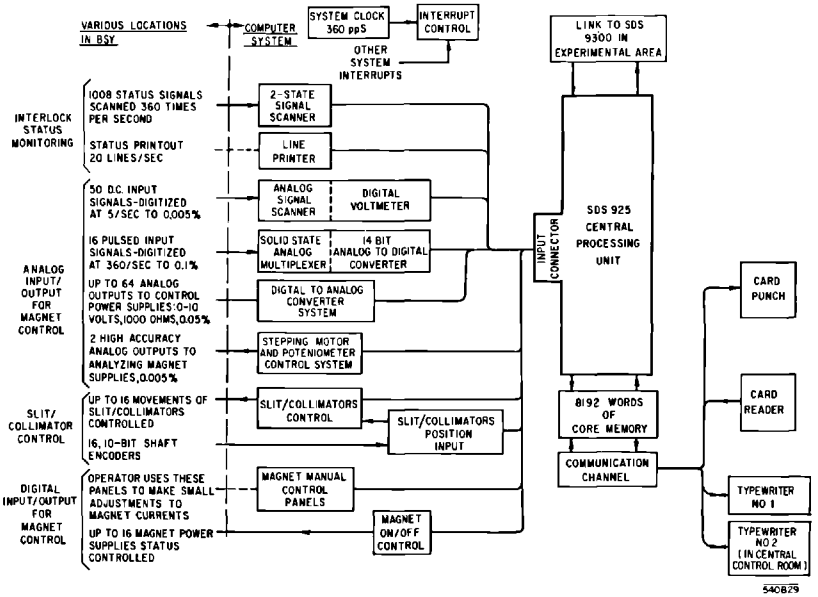

Figure 19-13 Switchyard computer system.

English language. It interprets them, compiles the machine language instructions necessary to execute them, and performs the actual execution, all automatically and in real time. Statements in the instruction may be included to modify or delay the execution time, if desired.

The following section describes the instructions programmed for the switchyard computer system. A list of these instructions is shown in Table 19-5.

An instruction is a series of words, separated by one or more spaces or carriage returns, terminated by a semicolon word, " ; "

In case of confusion, e.g., two instructions before the semicolon, the computer takes the last (or rightmost) one. If there is no meaningful instruction between semicolons, the computer types out " ERR " and is ready for another try.

1. Modifiable instructions

STEP ⟨elt⟩ BY ⟨no. ⟩ ; — Causes specified magnet power supply to increase its current by the specified fraction of its present value.

FLC ; — Starts the flip coil on a single flip, which takes about 20 sec to complete.

CARDS ; — Causes the input source to be the card reader, i.e., the program now takes its input from the card reader until an " end of file " character is sensed. This character is the "$\sqrt{}$" (8-7 punch on cards).

(Continued on p. 681)

Table 19-5 List of computer instructions

Modifiable instructions—clauses may be added.

SET BOX1 = ⟨no.⟩;
STEP BOX1 BY ⟨no.⟩;
TOLSCAN BOX1;
TOLSCAN BOX1 Δ = ⟨no.⟩;
OUTPUT BOX1;
RECORD BOX1;
SET ⟨elt⟩ = ⟨no.⟩;
STEP ⟨elt⟩ BY ⟨no.⟩;
TOLSCAN ⟨elt⟩;
TOLSCAN ⟨elt⟩ Δ = ⟨no.⟩;
OUTPUT ⟨elt⟩;
RECORD ⟨elt⟩;
SEND ⟨string⟩;
TIME;
CLOCK (⟨time⟩);
CARDS;
FLC;

Fixed instructions—all clauses are ignored.

SCALE ⟨elt⟩ BY ⟨no.⟩;
KILL ⟨label⟩;
TUNE ⟨elt⟩ BY ⟨no.⟩;
TUNE ALL BY ⟨no.⟩;
CLEAR;
RESET = ⟨no.⟩;

Clauses

EVERY ⟨time⟩ }
AT ⟨time⟩ } —time clauses
UNTIL ⟨time⟩ }
TO ⟨destination⟩ —destination clause
⟨label⟩: —label clause

⟨time⟩ format examples

(9HR) }
(9 : 00MIN) } refers to 9 o'clock or 9 hours
(9 : 00 : 00SEC) }
(T + 5MIN) } refers to current time plus 5 minutes
(T + 5 : 00SEC) }

⟨destination⟩ list

2—typewriter output
3—card output
4—link output
anything else—typewriter output
no destination clause—typewriter output

⟨string⟩ definition—any sequence of characters, not spaces or carriage returns, the first of which is a letter or the character "*"

⟨label⟩ definition—any string

⟨No.⟩ definition—any sequence of digits with one decimal point somewhere in it. The sequence may be preceded by a minus sign "—"

⟨elt⟩ list

PM1A	AP5	Q14	B29
PM2A	Q10	Q20	Q400
PM3A	Q11	Q21	Q401
PM4A	Q12	ADUM	ABEN
PM5A	Q13	B1A	EFA
		BIT	

OUTPUT ⟨elt⟩ ;	Causes current of specified magnet (or width of specified slit) to be packaged as output.
RECORD ⟨elt⟩ ;	Causes scale factor of specified magnet (or width of specified slit) to be packaged as output in a format which is reloadable, i.e., the format is in the 925 system language.
SCALE ⟨elt⟩ BY ⟨no. ⟩ ;	Causes the SCALE factor of the specified magnet to be loaded with the given number. The assumed units are kilogauss/(GeV/c). This number uniquely determines the "focal length" of the quadrupole and hence all of its focusing characteristics.
SEND ⟨string⟩ ;	Causes specified string (note—a space is the delimiter and hence the string contains no spaces) to be packaged as output.
TIME ;	Causes the time to be packaged as output.
CLOCK (⟨time⟩) ;	Sets the computer clock to the specified time of day.

Examples :

```
STEP B1 BY .01 ;
OUTPUT EFA ;
RECORD Q10 ;
CARDS ;
SEND THIS . IS . A . TEST ;
TIME ;
CLOCK (9:00 MIN) ;
```

2. Clauses

Clauses may be added to these instructions to give them flexibility. The types of clauses are given below. In case of confusion, e.g., two clauses of same kind in a single instruction, the computer takes the last (or rightmost) one.

TIME CLAUSES. Each of the above instructions causes a single action to take place. This action may be taken at a specific time, repeated at periodic intervals, and stopped at another specific time by adding the following clauses (in any order appearing anywhere before the final semicolon).

```
EVERY (⟨time⟩)
AT    (⟨time⟩)
UNTIL (⟨time⟩)
```

Examples:

AT (9:05MIN) EVERY (15SEC) UNTIL (9:20MIN) STEP B1 BY .01 ;
(Causes the current to be increased (by 1% of its value) every 15 sec until 9:20.)

AT (T + 30SEC) EVERY (20SEC) UNTIL (T + 10:30SEC) FLC ;
(Will cause the flip coil to begin a flip every 15 sec for 10 min. Time may be expressed in either HR, MIN, or SEC or PUL (beam pulses).

Thus,

(9HR)
(9:00MIN)
(9:00:00SEC)
(9:00:00:000PUL)

all express the same time.)

DESTINATION CLAUSE.

TO ⟨integer⟩

This clause is used with any of the digital output instructions, that is, with

OUTPUT
RECORD
SEND
TIME
TOLSCAN

and directs the output to the specified destination. If there is no destination clause, the program assumes typewriter output. The destinations currently available are

integer	*destination*
1	no dest (i.e., ignore the output)
2	TWR
3	card punch
4	Link

Example:

AT (9:05:20SEC) EVERY (20SEC) UNTIL (9:20:20SEC) OUTPUT B1 TO 3
(Causes the current in B1 to be punched on cards every 20 sec, but 20 sec behind the execution time of the previous example.)

LABEL CLAUSE. Each of the above instructions may be given a label by the user, so that it may be singled out by the computer later (to be deleted or related to the output produced). Instructions without a label clause are implicitly given the label "XX." The label clause

⟨label⟩ :

may appear anywhere before the final semicolon.

Example:

LABL : EVERY (1 MIN) OUTPUT ADUM ;
(Causes ADUM current to be printed on the typewriter every minute indefinitely.)

3. Fixed instructions

The instructions below ignore any clauses and will be executed just once.

KILL ⟨label⟩ ;	Kills the instruction having the specified label.
SET ⟨elt⟩ = ⟨no.⟩ ;	Set magnet current (or slit width) to specified value.

TUNE ⟨elt⟩ = ⟨no.⟩ ;	Loads scale factor for specified magnet (or for all magnets) connected to the tune box into the computer. Then each time the lever on the tune box is pushed, the current in magnets selected on the tune box panel are increased by (new current) = (1 + scale factor) (old current).

Examples:

KILL LABL ;	Kills the instruction in examples in label clause section.
SET EFA = 4.5 ;	Sets the current in magnet EFA (the BSY 3° bending magnets) so that the design momentum of beam through the switchyard is 4.5 GeV/*c*.
TUNE ALL BY 0.01	Loads scale factor of 1% for all elements connected to TUNE box. Then, on "Magnet Manual Control" panel, buttons for 1 or more elts may be pushed. This activates them for 1% changes. In SINGLE STEP mode, each time the lever is pushed up they are increased by 1%. Each time it is pushed down they are decreased by 1%. The 1% factor is changed by the TUNE instruction.
SET BOX1 = 18.0 ;	Will adjust the currents of all magnets corresponding to buttons pushed on the "Magnet Manual Control" panel so that 18.0-GeV electrons will pass. For quadrupoles the appropriate SCALE factors must have been previously loaded, as they are required to compute the current of the quadrupole.

SLIT/COLLIMATOR CONTROL (MJH). The positions of the slits and collimators must be precisely controlled and accurate measurement of their position made remotely at the control room. The collimators consist of a pair of jaws, one closing in the vertical direction and one in the horizontal direction. A slit is half of a collimator, opening only in the horizontal direction.

The slits and collimators are enclosed in vacuum tanks (see Chapter 20 for a complete discussion of these devices). The various units used in the switchyard are listed in Table 19-6. The mechanical motion to open or close the jaws of the devices inside the tank is obtained by rotating shafts coupled into the tank through bellows. The rotating shafts are linked to drive motors through magnetic clutches and gear trains. The motor housing contains the motor, gear trains, position readout devices, and magnetic clutches, and is mounted in the upper housing of the BSY to minimize radiation damage to its contents.

There are two types of controls. One type controls the open–close motion of the jaws inside the tanks, whereas the other moves the tank itself transversely in a direction parallel to the faces of the jaws. This latter control is

Table 19-6 Data on slit and collimator position control

Name	*Designation*	*Type*	*Speed*	*Motor*	*Encoder*	*Potentiometer*	*Mechanical counter*	*Travel (in in.)*	*Readback precision (in in.)*
High-Z collimator	—	{H / V}	Slow/fast	1	2	2	2	3	0.0029
High-Z slits	SL-11	Single	Slow/fast	1	1	1	1	3	0.0029
	SL-31	Single	Slow/fast	1	1	1	1	3	0.0029
High-power slits	SL-10	{F / R}	Slow/fast	1	2	2	2	3	0.0029
	SL-30	{F / R}	Slow/fast	1	2	2	2	3	0.0029
High-power collimator	C1-H	{F / R}	Slow/fast	1	2	2	2	0.75	0.0007
	C1-V	{F / R}	Slow/fast	1	2	2	2	0.75	0.0007
Photon collimator	C-10	{H / V}	Slow/fast	1	2	2	2	3	0.0029
Photon collimator (tank)	C-10 (T)	{up-down / left-right}	Slow	1	2	2	2	3	0.0029
High-power slits (tank control)	SL-10	Up-down	Slow	1	None	1	1	7	0.01
	SL-30	Up-down	Slow	1	None	1	1	7	0.01
High-power collimator (tank control)	C1-H	Up-down	Slow	1	None	1	1	7	0.01
	C1-V	Left-right	Slow	1	None	1	1	7	0.01

required to extend the life of the jaws by changing and thus extending the beam interaction area. The jaws can be controlled at variable speeds, the tanks at only one speed.

The 16-ft long jaws of the high-power (2-MW) collimator C-1 and the high-power slits SL-10/SL-30 require two independent drive mechanisms, one at the front end of the jaws and one at the rear. Magnetic clutches are required to switch over from high drive speed to low drive speed.

The slit and collimator jaw position is read back digitally by means of shaft encoders. In addition, potentiometers are provided to back up the encoders and to give an analog jaw position signal for readout in the accelerator control room.

The position control and readback system for the slits and collimators is shown in Fig. 19-14 and consists of the following units:

1. Slit and collimator position controller
2. Shaft encoder multiplexer
3. Position readout I and II
4. Position feedback multiplexer
5. Motor/clutch selector
6. Slit/collimator computer control
7. Motor/clutch on–off feedback

The central unit from an operations point of view is the slit and collimator position controller. This panel has a switch to select three modes of control: manual, manual–computer, and computer. The latching selection pushbutton connects both the readout and control electronics to the selected slit or collimator. Two rows of lever switches are used to control speed and direction (open–close). In the manual control mode, the operator is able to select any slit or collimator to be read out and controlled. In the manual–computer mode, the computer samples the position of the slit or the collimator selected by the operator. In this mode the operator is not able to make another

Figure 19-14 Control of slits and collimators.

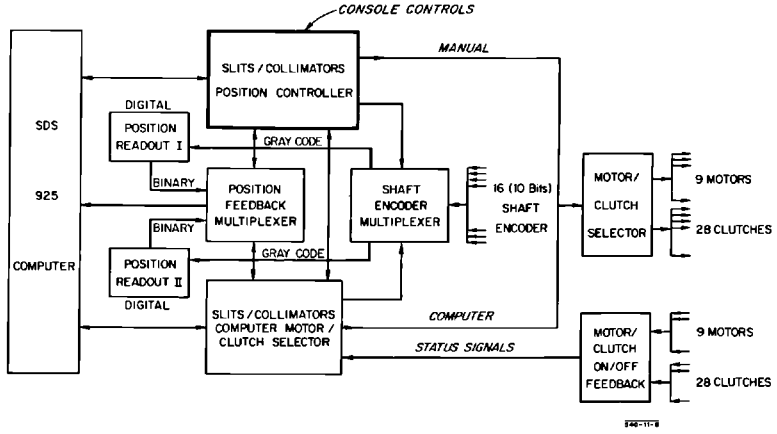

selection until the computer has had a chance to store the previous setting into its memory. In the computer control mode, the operator can selectively control any slit or collimator through the use of the system program language on the typewriter or through the punch-card reader. The computer then makes the necessary decisions required to set the slits or the collimators as specified by the program.

The slit and collimator position controller becomes disabled, in the manual and manual–computer modes, if 3 min have elapsed since the last change was made by the operator. The shaft encoder multiplexer contains sixteen input channels and two output channels. Each input channel is connected to one shaft encoder and the output channels are connected to position readouts I and II, respectively.

The position readout devices I and II receive position information in gray code from the shaft encoder multiplexer. The readout devices convert the 10-bit gray code information into binary form, then from binary into 8421 BCD-code,[8] and finally from 8421 BCD into a decimal display. The 10-bit binary information is sent to the position feedback multiplexer.

The position feedback multiplexer, under computer control, transfers 16 bits of data into the computer memory. Ten of the bits originate in one of the readout devices, whereas 6 bits represent the device code.

The motor/clutch selector receives a control command from either the S/C position controller or the S/C computer control, and controls the appropriate clutches and motor accordingly.

The logical design of the S/C computer motor/clutch selector is such that the computer is able to select any device and to change the speed and direction of the device. Basically, the S/C computer motor/clutch selector works as follows.

A control word, which contains 1-bit read/control, 6-bit slit/collimator device code, 2-bit speed code, and 2-bit open/close code, is sent by the computer to the S/C computer motor/clutch selector. Once the S/C computer motor/clutch selector receives the control word, it decodes the words. If the first bit (read/control) is a zero, then the S/C computer motor/clutch selector allows the computer to sample the S/C position feedback multiplexer. However, if the first bit is a 1, then the S/C computer motor/clutch selector selects the slit or collimator, and waits for an acknowledge signal from that slit or collimator. If the signal returns, it sends the next control command to turn one of the two speed clutches on, and waits for the second acknowledge signal from that speed clutch. Finally, if the clutch signal returns, it sends a signal to turn the motor on. If the motor is turned on, then the S/C computer motor/clutch selector sends a signal to the computer indicating that everything is set, and the computer will proceed to sample the S/C position feedback multiplexer. Suppose, after the computer has sampled a few times, it decides to make a change. The computer would then send another word to the S/C computer motor/clutch selector. The S/C computer motor/clutch selector then, in turn, stops the motor, changes speed if required, changes motor

direction if required, and informs the computer that it has made the change. No matter what signal the S/C computer motor/clutch selector sends out, it always waits to receive a return acknowledge signal from the clutches or the motors. If no signal returns within $\frac{1}{2}$ sec, then the S/C computer motor/clutch selector will send a malfunction interrupt to the computer. The computer will inform the operator.

The motor/clutch on/off feedback provides the S/C computer motor/clutch selector with the necessary information for sequential operation, and also provides the operator with a lamp display showing which clutches and motors are in use.

The entire slit and collimator position control and readout consists of thirteen chassis. The function of each chassis is described in detail by Hu.[9]

19-3 Interlock system—equipment protection (RAS)

In the accelerator, all the interlaced beams traverse a common beam channel —the accelerator waveguide. For this reason if an interlock action for machine protection is sensed, there is usually no way to detect which of the beams "tripped" it, and all beams must be shut off. These interlaced beams are separated by the pulsed magnets in the BSY, however, which send them to different experiments in widely separated end stations through separate beam channels. This separation allows the machine protection system in the BSY to assume an added flexibility by turning off the beam which tripped an interlock, leaving the others on and their associated experiments still running. This flexibility is desirable not only to avoid interruption of experimental time on the unaffected beams but also to allow one experiment to run even if others have been disassembled and their interlock chains broken.

In order to achieve true separation of interlocks, the beams must be separated; this is because the slow nature of many of the sensors (e.g., temperature sensors—response time ≈ 30 msec) precludes distinguishing between two beams only 2.8 msec apart in time and because many interlock functions (e.g., water cooling of protection collimators) are necessary if *any* beam is on. This separation of the beams is a trickier proposition than one might first imagine. Although it is true that the pulsed magnets will (barring failure) separate the beams, they must also always send the right beam to the right place. Suppose the beams are numbered 1 through 6; then if the interlock system is wired to expect beam 1 in the A-analyzing channel, beam 1 will be turned off in the event of water flow failure to slit SL-10, for example. Suppose now that by accident beam 2 enters the A-beam channel, and water flow stops in the slit. The system would turn off beam 1, leaving beam 2 to continue to run, perhaps damaging the slit.

To provide some protection against accidents of the above type, one of several techniques can be adopted. For example, the interlocks could be wired to the switches for the pulsed magnets so that they would always shut off the beam programmed to come into their channel. This is quite complicated,

because the direction and magnitude of deflection is a function of the polarity, number, and setting of the pulsed magnets as well as the sign of the charge of the particle. In addition, the emergency magnets B-1 and B-2 can be used in lieu of (or even conceivably in conjunction with) the pulsed magnets. Also, this scheme would not protect against failure of the deflection magnet systems. Alternatively, a set of switches could be provided, indicated desired beam "destinations" and the interlock system could inspect the *actual* beam geometry (as measured by the various current toroids and ion chambers in the BSY), the beam could be turned off if agreement were not achieved on each beam pulse. If this same set of switches were to "connect" the interlock system to the beam shutoff network, then the interlock circuits would essentially be comparing the actual beam geometry with the one protected. This second method is the one employed in the BSY summary interlock; it is called "errant beam" protection. In the above example, if beam 2 entered the A-beam channel, the interlock system would detect this condition by noting a current in I-10 at the wrong time and would shut off *all* beams until the problem was corrected. Correction could be made either by changing the "geometry selector" so that beam 2 could enter the A channel (the water flow loss in SL-10 would then shut off beam 2 also), or by readjusting pulsed or emergency magnets so that beam 2 could not enter the A channel.

In addition, the interlock system in the BSY must be switchable to handle experimental changes. That is, not all interlocks are used in each of the several possible beam configurations; indeed, some of the interlock conditions are mutually exclusive. Thus, whole areas of the BSY interlock system can be switched out at will by the operator; the summary circuits inspect the conditions that allow the selection, and if at any time they are not satisfied, the beams are switched off.

Electronics

The summary circuit for the BSY inspects the beam conditions selected by the selection circuits on a pulse-to-pulse basis and provides the permissive pulse to the injector circuits, the pattern interlock signals to the CCR, and the necessary status signals to the BSY operators. The permissive pulse and pattern interlock circuits are described fully in Chapter 21, and will only be touched on here.

The permissive pulse gates the injector trigger, and thus if it is absent the beam will be inhibited. It is generated on a pulse-to-pulse basis in the switchyard summary circuits when the switchyard is operating. The accelerator generates its own permissive pulse for accelerator tests (see Chapter 21). It is this signal which allows the beam to be turned off immediately if necessary. There is no time lag involved. However, since the pulse involves only the injector, the klystrons don't "know" there is no beam, and stay on in the "accelerate" mode. Therefore, any stray electrons ("dark current") will be accelerated and produce a small but nonzero beam in the switchyard. The

pattern interlocks have an inherent one-pulse delay—they always allow one pulse to be produced after detection of the fault condition. They, however, remove the accelerate triggers from the klystrons and, thus, reduce the dark current to negligible values. A disadvantage (in addition to the delay) of the pattern interlocks is that the triggers to the BSY equipment and experimental areas are also removed. These two interlock methods are used in conjunction with one another as the situation requires.

The summary circuits for the BSY interlocks work in the following way. The A-beam interlocks are gated by the A-beam pattern (as selected by the "geometry selector"); the B-beam interlocks are gated by the B-beam pattern, and so on. The resultant signals are combined (OR'ed) and gated by the common beam interlocks (those signals from sensors in the area where the beams share a common beam channel, i.e., before the pulsed magnets). The result is an ac signal which, when gated by a 360/sec trigger at the proper delay time, provides the permissive pulse generator with a trigger. Thus a permissive pulse is generated if either the A-beam is OK when the A pattern pulse is "due," *or* the B-beam is OK when the B pattern pulse is "due," *or* the C-beam is OK when the C pattern pulse is "due," and so on, *and* the common gate is OK. The errant beam detector consists of a flip–flop that is actuated if a current is detected in its associated toroid or ion chamber when there is *no* pattern signal for that area. There is one flip–flop for each beam area. The outputs of these flip–flops are connected to the COMMON beam gate.

After most interlock faults, relays in the selector circuits latch out and keep the beam off until reset. These relays do not drop out for certain "suppression functions," such as the pulsed magnet interlock or beam hold during profile monitor movement, to avoid excessive loss of beam time due to repeated resets. Normally, the pattern interlock signal is broken when this relay drops out, but for those cases where loss of triggers cannot be tolerated, a switch is provided that maintains a steady pattern interlock signal independent of the state of the summary circuits. Also, two signals are accepted from each experiment in addition to the interlock circuits. These two signals come from switches in the experimenter's setup. One "suppresses" the beam; that is, it removes his permissive pulses from the permissive pulse train without either dropping out the latch relay (which would require control room reset) or interrupting the pattern interlock circuits (which would remove his triggers). The other breaks the pattern interlock circuit without dropping out the latch relay. The latter interrupts the beam *and* removes the triggers on that pattern. Each experimenter can individually suppress his own beam and triggers without affecting the other experiments.

Ionization chamber interlocks

A few beam pulses at maximum beam power may damage a vacuum chamber or a protection collimator. Since thermal sensors are too slow to detect instantaneous local temperature changes, ionization chambers have been

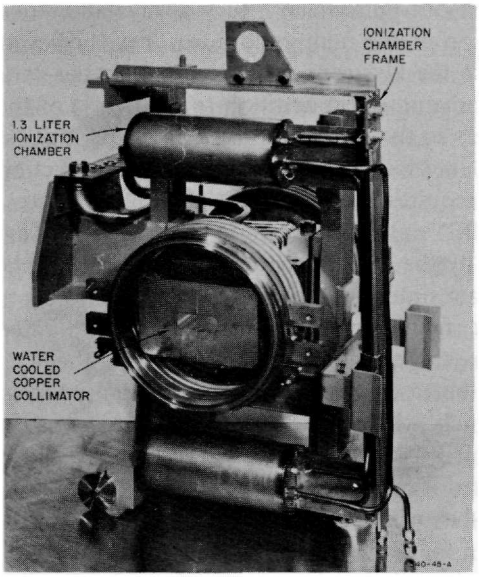

Figure 19-15 Protection collimator with ionization chambers.

used because of their quick response for these purposes. Ionization chambers have the advantages of being simple in construction, easy to make radiation-resistant, and of operating physically independently of the equipment to be protected. Their disadvantages are (1) they saturate easily, (2) they are very sensitive to geometrical arrangement with respect to the radiation source, and (3) they are somewhat difficult to calibrate.

The ionization chambers used in the switchyard (Fig. 19-15) consist of a number of parallel aluminum plates with $\frac{1}{4}$-in. spacing connected alternately to a signal lead and a high-voltage lead (300 V). The welded stainless steel housing contains helium at atmospheric pressure. The active volume is 1.3 liters. The output signal from the ion chamber is roughly proportional to the power of the absorbed beam. For the protection collimator shown in Fig. 19-15, the charge collected by the chamber is of the order of 10^{-10} C/J of absorbed beam in the protection collimator. Thermometers at the inlet and outlet of the cooling water for the protection collimator and a water flowmeter make it possible to calculate the absorbed beam power directly and can be used to calibrate the ionization chambers. The ionization chambers do not saturate if a pulse of a 2-MW beam hits the protection collimator.

Two long, coaxial, ionization chambers are used in the switchyard to protect long drift sections in the vacuum pipe. These coaxial chambers consist of lengths of Andrews Heliax $1\frac{5}{8}$-in. coaxial cable filled with helium (or argon). A positive high voltage is applied to the inner conductor; the charge is collected from the inner conductor through a capacitor.

A gas flow system[10] delivers continuously a small flow of helium slightly above atmospheric pressure to the ionization chambers.

The gas is supplied by a double bank of twelve bottles with automatic changeover. After a 20-psi regulator, the supply line divides into four branches; three branches supply the ion chambers and the fourth branch supplies gas for the Cerenkov cells.

The ion chambers in each branch are connected in series. The flow is metered and controlled by a needle valve at the input side and monitored on the return with a low-flow alarm detector. A back pressure regulator in the return line maintains a constant upstream pressure (referred to vacuum).

The low-flow alarms operate warning lights but do not inhibit the beam.

IONIZATION CHAMBER DETECTOR CIRCUITS. The pulsed current produced in the ionization chambers is roughly proportional to the power absorbed in the protection collimators. The current pulses are integrated in a circuit using an operational amplifier. The ion chamber is a high impedance current source, and, therefore, the input resistor of the integrator has little influence as long as it is low. It is made equal to the cable impedance (95 ohms) to avoid reflections. The integrator is followed by an adjustable discriminator and a latching output circuit. The integrator time constant is 0.1 sec, which is slightly faster than the thermal time constant of the protection collimators. The protection collimators can absorb an average beam power of 20 kW. The trip level at this power absorption level is reached in 100 msec. When the protection collimator is hit by a beam carrying the full 2-MW beam power, the trip level will be reached about 100 times faster (1 msec), so that the beam will be switched off before the accelerator will send the next beam pulse (beam pulses are spaced by 2.78 msec).

The output signals from the integrating circuits are terminated in a plug on the rear of each detector circuit. These signals can be connected to a patch panel for meter readout. The signals are extremely useful for beam-steering purposes.

The detector circuit for the long ionization chamber is slightly different from that of other ion chambers because of a different signal polarity.

Some of the ion chambers located near the collimators and dumps are not used for interlock purposes but for reading the charge intercepted by these absorbers. A special integrator is built for this purpose with a digital display reading out the "charge intercepted" by the devices with which these ion chambers are associated.

Thermal protection

A slow temperature rise may occur from the continuous scraping of the beam on the vacuum chamber wall. In places where this is likely to occur, surface temperature sensors are mounted on the outside of the vacuum chambers and are arranged to trip the beam if the temperature exceeds a preset level.

The sensors used are 100-ohm platinum resistance elements mounted in platinum cases and insulated with ceramic material. Radiation exposure tests have shown that these devices are very reliable up to doses of 10^{13} ergs/g. The sensors are spot-welded to small copper pads which are mounted in many cases against the vacuum chamber with a fitting that allows easy replacement. In other cases the sensors are an integral part of a device, such as those on a magnet chamber.

In addition to vacuum chamber surface temperature measurements, water temperature measurements are made on the cooling water supply and return line of slits, collimators, water-cooled vacuum chambers, and dumps. In areas where the radiation levels are very high and where measurements have to be made in the radioactive cooling water lines, a stainless steel thermal well is welded into the pipe at each measuring location and a radiation-resistant immersion sensor is screwed into the well. These devices have basically the same element as the surface sensor, namely 100-ohm platinum resistance wire, ceramic-insulated, but in this case it is in a stainless steel housing with an integral electrical receptacle. Connection is made through stainless steel-jacketed magnesium oxide-insulated cables.

Where the environment is less severe, similar but slightly less expensive sensors are used as direct immersion devices with no thermal wells. The electrical connections are made through fiberglass-insulated cables.

TEMPERATURE DETECTOR CIRCUITS. The two basic temperature detector interlocks circuits are an absolute circuit (measuring temperature at various locations on vacuum chambers, etc.) and a differential circuit (comparing inlet and outlet temperatures of the cooling water in various beam-absorbing devices). Each of the differential resistance thermometers is connected in one arm of a bridge circuit. The absolute temperature interlock circuit uses a fixed 100-ohm resistor in the second arm of the bridge. The bridge current is limited to 5 mA to prevent self-heating. A 5-mA current results in a sensitivity of 2 mV/°C.

The trip circuit uses a magnetic differential detector. This unit consists of a magnetic current-to-polarized-voltage pulse converter followed by a solid state on–off output stage. The trip level is set by adjusting the bias of the magnetic converter.

The input impedance of this circuit is 2 kohms, which results in a trip accuracy of about 1°C, which is adequate for this application.

An output signal from each resistance thermometer is also brought to a patch panel, which makes it possible to measure the various temperatures by means of a three-digit digital temperature readout.

To increase reliability, a test circuit is built which tests the electronics of the temperature detector circuits and the ion-chamber detector circuits. This test circuit checks the tripping action of the detectors as well as the continuity of the cabling system. The test is done automatically after each beam shutoff, but can also be started manually or on a programmed basis.

Secondary-emission foil signals

The interlock circuit for the SEM devices has been described previously. It is made very flexible to allow for changes that may be required after experience is gained with high-power beams.

Pulsed magnet interlock

A special interlock circuit has been built for the pulsed magnets. It holds the beam pulse if the magnetic field has not reached the proper value shortly before beam injection. A block diagram of this circuit is shown in Fig. 19-16.

When the modulators for the pulsed magnets receive a trigger signal (approximately 416 μsec before beam time), a large transient voltage appears across the pickup coils. This transient is detected by the start circuits, which begin the timing of a 203-μsec delay circuit. Triggers are injected into the start circuit to prevent an output if the modulators fire too early or too late. The delay, in turn, actuates a gate generator, which produces a 10-μsec gate, 203 μsec later or 213 μsec before beam time.

While the delay is in progress, the gated integrator is producing a signal which is proportional to the $\int B\,dl$ through the pulsed magnets. This signal is passed through the analog processing circuits, which divide it by $\sqrt{2}$ and invert it if required by the polarity signals. The resulting processed signal is compared to a reference voltage. The references are derived from the analyzing magnet power supplies and are proportional to the beam energy settings in the A- and B-beams. When the processed analog signal is equal to the reference, a pulse appears at the output of the comparator. This pulse is passed through the gating logic, which ensures that the "A" comparator is inspected during "A" patterns and the "B" comparator during "B" patterns.

Figure 19-16 Pulsed magnet interlock.

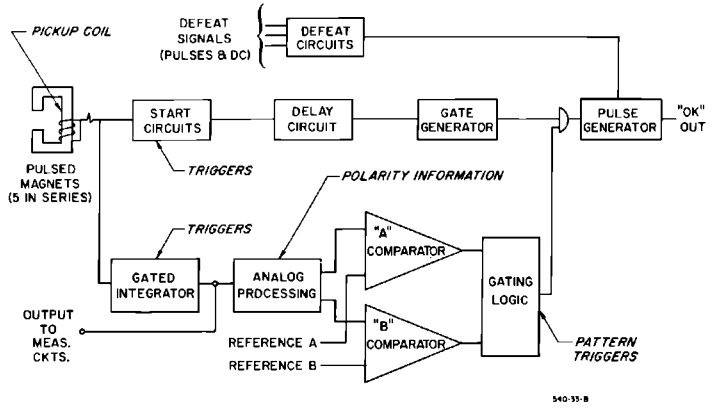

Since the pulsed magnet current waveform is a sine wave with a period of 1666.6 μsec, the $\int B\,dl$ will reach $1/\sqrt{2}$ of its peak value in 208 μsec. The output of the gating circuit is a pulse which occurs when the $\int B\,dl$ reaches $1/\sqrt{2}$ of the desired peak value. If this pulse occurs during the 10-μsec gate (i.e., 20 ± 5 μsec after the start of the waveform), the output pulse generator is enabled. The pulse generator then produces an output signal 208 μsec before the beam injection time. This signal is part of a chain which gives a permissive pulse to the injector.

The defeat circuits shown in Fig. 19-16 allow the beam to be enabled during tune-up periods (e.g., when a third beam is to be deflected to the tune-up dump while the A- and B-beams are on). The system can be defeated on a pulse-to-pulse basis, as required by the above example, or permanently by a dc signal.

Differential current interlock

This circuit provides protection against beam deflection errors and will back up the devices discussed in the previous sections. The circuit uses the signals from two current transformers. One transformer is located in the common beam at the beginning of the switchyard and a second one at the end of each electron beam. The circuit will produce an interlock signal if less than a certain percentage (say 10%) of the beam arrives at its destination. The circuit operates at higher beam currents only; at low currents it switches off automatically.

Instead of a signal from a second transformer, the circuit may also operate with a signal from other reference sources, such as a dc signal.

19-4 Pulsed bending magnet supplies (ICL)

General

The pulsed magnet power supplies have the capability of energizing the magnets with a field of either direction (for right or left beam deflection) on a pulse-to-pulse basis, at repetition rates up to 360 pulses/sec, and of recovering most of the energy at the end of the pulse. The basic circuit used consists of silicon-controlled rectifiers (SCR) to switch energy stored in a capacitor bank to the magnets and back to the capacitor bank with relatively small losses, and a dc supply to recharge the capacitor bank between pulses.

Power supply circuit

The power supply can be divided into three functional blocks: (1) the energy storage capacitor bank with the associated means of regulating the amount of stored energy, (2) the SCR's used to connect the energy storage capacitor bank to the magnet, and (3) the dc charging supply to recharge the capacitor

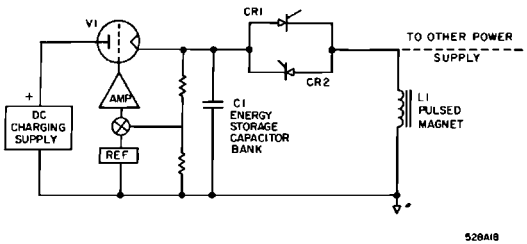

Figure 19-17 Basic circuit of pulsed power supply.

bank at the end of the current cycle. The basic circuit of the pulsed power supply is shown in Fig. 19-17, and the sequence of operation is as follows:

1. A signal is applied to the grid of the series regulator tube (V1) allowing the dc charging supply to charge the energy storage capacitor bank to the desired voltage level; then the grid is biased negative so that the tube is cut off.

2. The SCR switch (CR1) is then triggered, allowing the capacitor bank to discharge into the pulsed magnet (L1). A sine wave of current builds up in the magnet at a resonant frequency determined by the capacitance of the capacitor bank (C1) and the inductance of the pulsed magnet (L1). During this time V1 is kept cut off so that the capacitor bank is isolated from the dc charging supply, and the voltage across the capacitor bank decreases with a cosine wave shape as the energy is transferred from the capacitor bank to the pulsed magnet. When the magnet current reaches its peak value, the voltage on the capacitor bank is zero and all the energy of the system is stored in the pulsed magnet. Because of the relatively high-Q resonant circuit, the magnet now acts as a source of energy and discharges back into the capacitor bank, charging it to a negative polarity. The current continues to flow through CR1 until the energy stored in the magnet has been transferred back to the capacitor bank, at which time CR1 prevents the current from reversing. The capacitor bank remains charged to a negative polarity.

3. The second switch (CR2) is then triggered, allowing the capacitor bank to discharge again into the magnet in order to reverse the polarity of the voltage across the capacitor bank to its original polarity. CR2 conducts until the current tries to reverse, when the energy has been transferred from C1 to L1 and back to C1, at which time CR2 effectively opens the circuit, leaving the capacitor bank charged to its original polarity.

4. A signal is again applied to the grid of V1, which recharges C1 to make up the losses during the previous cycle. When C1 has been recharged to the desired voltage, V1 is biased off and the power supply is ready for the next beam pulse.

A resonant frequency of 600 cycles/sec between C1 and L1 has been chosen so that the above sequence of operation can be accomplished in less than 2.7 msec, thus allowing the pulsed magnets to be pulsed at 360 pulses/sec, the maximum repetition rate of the accelerator. The chosen resonant

frequency of the circuit is a compromise between the peak voltage required on the magnet, the time allowed between pulses, the peak recharge current required, and the amount of heating allowed in the magnet.

Operation

Two power supplies are connected to each pulsed magnet, one typically connected such that its capacitor bank is charged to a positive polarity and the other such that its capacitor bank is charged to a negative polarity, thus allowing a deflection of an electron beam from the accelerator to either the right or left, as desired, on a pulse-to-pulse basis. The power supplies are independent and their capacitor banks can be charged to different voltages, if desired, allowing beam pulses of different energies from the accelerator to be deflected to the two experimental areas.

A "command" pulse is sent to the power supply to trigger the SCR switch only when it is desired to use that power supply to energize the pulsed magnet for a particular beam pulse. This command pulse is derived from the operational pattern signal of the accelerator. In order to assure that the energy storage capacitor bank is kept charged to the desired voltage level, a "recharge" pulse is sent to each power supply and applied to the grid of the series regulator tube at a constant 360-pulses/sec repetition rate. This recharge pulse is derived from the accelerator clock signal.

Energy storage capacitor bank

The energy storage capacitor bank is made up of several pulse capacitors in parallel to give a total capacitance of 32 μF as required to obtain a 600-cycles/sec resonant frequency with the pulsed magnet inductance of about 2.2 mH. The capacitors are built with a polyethylene dielectric and silicon fluid impregnant in order to achieve a low-temperature coefficient of capacitance. Changes in the capacitance of the bank will result in a change in the resonant frequency and, hence, would require a change in the peak voltage required to give the desired peak current in the magnet. The cases of the capacitors have water-cooling tubing soldered to them, through which temperature-regulated water is circulated to eliminate variations due to changes in ambient temperature.

Series regulator tube

The series regulator tube (V1) is a transmitting-type vacuum tube (3W5000) which is capable of supplying the required peak charging current at a reasonable tube drop and of withstanding the high voltage impressed between the filament and plate during the magnet current cycle. During the period available for recharging the capacitor bank, the grid is driven positive about 150 V until the desired voltage level on the capacitor bank has been reached

at which time the grid is driven negative about 2500 V to cut the tube off. The tube is kept cut off during the rest of the time until the next recharge time period. The capacitor bank can be charged to any desired voltage up to 3000 V by the series regulator tube and the associated voltage regulation circuitry. The circuitry is designed to regulate to 0.1 % of the desired voltage between the values of 1500 and 3000 V dc and regulates very well as low as a few hundred volts.

Silicon-controlled rectifier switch

The silicon-controlled rectifier (SCR) switches CR1 and CR2 are each made up of eight, type C181P, SCR's connected in series. These SCR's have a voltage rating of 1000 V dc and a current rating of 235 A rms. Each SCR switch conducts for one-half of the sine wave magnet current cycle. The maximum design value of peak current through each SCR switch is 316 A, the corresponding rms current is 122 A, and the average current is 61 A. The SCR gate pulses are supplied from a pulse transformer having a separate winding for each SCR.

Dc charging supply

The dc charging supply is a solid-state three-phase rectifier power supply operating from 470-V, 3ϕ, ac line voltage. The ouput voltage is constant at about 4000 V dc.

19-5 Pulsed steering magnet supplies (ICL)

The power supplies used with the pulsed steering magnets are of the same design as those used with the pulsed bending magnets. They differ only in that they have smaller ratings on peak current and voltage and have reversing relays built in to reverse the polarity of the voltage on the energy storage capacitor bank when the output current is reduced to zero. The supplies are designed to supply a peak current of 23 A into the steering magnet inductance of 18 mH. The energy storage bank capacitance is about 3.2 μF and the maximum charge voltage is about 1550 V dc. Type 6JE6A vacuum tubes are used as series regulators and the dc charging supply operates from 117-V, 1ϕ, ac line voltage.

19-6 Dc power supplies (CAH)

The power supplies required for the BSY dc magnets were purchased to satisfy various performance specifications. These power supplies are all located in the Data Assembly Building with copper cables carrying the required dc current to the respective magnets for an average distance of 150 ft. The electrical ratings of these power supplies were chosen to minimize

Table 19-7 Beam switchyard dc power supply ratings

Magnet designation	*Required power at 25 GeV* (*A*)	(*V*)	*Power supply ratings* (*A*)	(*V*)	*Specified regulation* (%)
1. A dump B-23, -24, -25, -26	950	380	1050	660	±0.25
2. A bend B-10 to B-17, B-100	765	724	805	832	±0.01
3. Q-10 (8-cm quad)	452	39	550	50	±0.1
4. Q-11 (8-cm quad)	473	41	550	50	±0.1
5. Q-12 (18-cm quad)	315	50	550	50	±0.1
6. Q-13 (8-cm quad)	474	41	550	50	±0.1
7. Q-14 (8-cm quad)	445	39	550	50	±0.1
8. B-1, B-2 (emergency switching)	500	50	850	65	±0.1
9. Q-20 (8-cm quad)	850	65	850	65	±0.1
10. Q-21 (8-cm quad)	850	65	850	65	±0.1
11. B-29 and -29A (clearing)	1000	113	1000	120	±0.1
12. B bend B-30, -32, -33, -35, -300	765	406	805	408	±0.02
13. Q-30 (8-cm quad)	472	40	550	50	±0.1
14. Q-31 (8-cm quad)	500	43	550	50	±0.1
15. Q-32 (18-cm quad)	283	45	550	50	±0.1
16. Q-33 (8-cm quad)	800	64	850	65	±0.1
17. Q-34 (8-cm quad)	800	64	850	65	±0.1
18. B-36 or B-37 (bending)	850	55	850	65	±0.1
19. B-38 (bending)	850	55	Shared with PB36		
20. A-10, -11, -30, -31 (steering)			25	135	±0.1
21. A-400, -401, -12 (steering)			36	200	±0.1
22. B-28 (steering)			81	10	
23. A-16, -36 (steering)			10	18	

the number of types which had to be procured. A comparison of the power supply ratings and the requirement for handling 25-GeV electrons is given in Table 19-7.

The required power supplies may be divided into four main groups according to use:

1. A-beam dump magnets, 693 kW at ±0.25% regulation
2. A- and B-beam bending magnets, 582 and 326 kW at ±0.01% regulation.
3. Quadrupole and other miscellaneous magnets, 27.5, 55, 120 kW at ±0.1% regulation.
4. Steering magnets (dc); ten units ranging from 0.18 to 7.2 kW at ±0.1% regulation.

The main characteristics of each of these groups of power supplies will be discussed in the following sections.

All of the dc power circuits of the magnet power supplies are designed and insulated so that any point of the system may be connected to ground without disturbing the precision of current regulation or causing excessive voltage gradients. The dc system is then grounded at the point desired, usually at the current monitoring shunt, through a resistance of 10 to 100 ohms that serves to limit any ground fault current resulting from an insulation failure of some part of the system. The current through this grounding resistor is monitored with an alarm circuit that turns off the power supply in case of excessive ground currents.

The off and on circuits and control systems in the BSY control room are based upon 24 V dc; therefore, a special relay conversion panel is required to control the 117-V ac interlock circuits of the various power supplies.

The current from each power supply is monitored with a digital voltmeter located in the BSY control room. The shunts (100 mV, 1000 A) used for monitoring the A and B bending magnet currents are mounted in a temperature-regulated oil bath to stabilize these measurements. The other magnet systems use shunts that have a calibration of about 1.2 V at rated current; this higher voltage shunt allows precision current measurements to be made even below 10% of rated output current. They are water cooled for rated currents greater than 100 A.

The regulation system on each power supply system is required to maintain the output current within specified tolerances even when a $2\frac{1}{2}\%$ line voltage transient is experienced. Fast response against line voltage transients was specified to prevent the high-energy electrons from hitting objects in the BSY. Even a single beam pulse wrongly steered can produce enough radiation relative to normal levels to cause the protection circuits in the BSY to trip and result in lost beam time of several minutes.

The SCR's or diodes used in the main dc power circuits were required to have a peak-reverse-voltage rating of $2\frac{1}{2}$ times the normally expected circuit voltages. The number of units used in parallel for the specified current had to be sufficient to allow normal operation with one device disconnected in each leg of the rectifier circuit without exceeding the manufacturer's ratings.

Transistor banks were required to have fast acting fuses for each power transistor and diode isolation on the bases to allow normal operation with up to 10% of the transistors not functioning or shorted.

Motor-driven reversing switches were required on all of the BSY power supplies to allow easy changing of the magnet polarity for handling either an electron or a positron beam. These switches also permit easy degaussing of the magnets.

Reverse diodes were installed across the dc circuits ahead of the reversing switches to protect each of the systems against open circuits from blown fuses in the SCR or transistor circuits. A 10-μF capacitor is connected across the magnet terminals to protect the magnet against voltage transients when the reversing switches operate at currents less than 10 A.

Magnet impedances

The mechanical construction of the magnets used in the BSY is described in Chapter 18. Except for the pulsed magnets, the iron yokes or return paths of these magnets are solid (not laminated); therefore, the inductance of the magnet will vary as a function of frequency. Table 19-8 shows the calculated low-frequency inductance (frequency less than 0.001 Hz). In general the lag in ac current versus the ac voltage applied to a magnet will not exceed 70° for frequencies less than about 2000 Hz, and the impedance will be less than one-tenth of that calculated using the low-frequency inductance for frequencies >5 Hz, because of the lossy nature of the solid iron cores.[11]

The location of the energizing coils of these magnets relative to the gap is such that the percent field variation is about equal to the percent current variation for frequencies less than 5 Hz and is only about a factor of 10 down at the ripple frequencies of 360 Hz.

Dump magnet power system

Four magnets (B- 23, -24, -25, and -26) are connected in series and powered from a single power supply to direct either the electrons or positrons being guided through the A bending system into a water-cooled dump. This dump is used during photon beam experiments and for other special cases to prevent the primary beam from entering the end station A experimental areas.

The power supply is fed from a 480-V, three-phase power line and consists of two three-phase bridge rectifiers using SCR's with separate *LC* filters (20-Hz cutoff), connected in series to provide the rated output with twelve-phase ripple. A single plate transformer is used with a delta primary and water-cooled Y and delta secondary windings.

The power supply uses a transductor as the current sensing element in the slow loop portion of the current regulation system. A voltage feedback loop sensing ahead of the main *LC* filters (20 Hz cutoff) is combined with the slow current loop to give a fast response against sudden line voltage changes.

Table 19-8 Calculated magnet inductances[a]

Magnet system	*Calculated inductance (H)*	*Time constant (sec)*
1. A dump magnets (4 in series)	0.36	1.0
2. A bending magnets (9 in series)	1.5	1.8
3. 8-cm quads	0.04	0.5
4. 18.5-cm quads	0.05	0.4
5. B-1 and B-2 in series	0.17	1.7
6. B-beam magnetic slit (B-36 or B-37)	0.03	0.009

[a] Frequencies less than 0.001 Hz.

The variable phase triggers for control of the SCR's are Schmidt triggers derived from comparison of a variable dc voltage and a well-filtered sine wave from the 60-Hz ac line voltage.

The A bending magnet power system

The A bending magnet system used to guide the accelerated particles through the BSY to the end station A experimental hall consists of eight of the 3° bending magnets in the switchyard and one reference magnet of the same design, located in the Data Assembly Building (DAB). These nine magnets are connected in series with the power supply to guarantee that all the magnets have an identical history of variations of current. (See Fig. 19-18.)

Earlier investigations of the reproducibility of a magnetic field of similar magnets[12] has shown that they will track if the rate of change of current through all of the magnets is held the same.

The dc power for this magnet system consists of two 350-kW (435-V, 805-A) power supplies connected in series with a transistor bank to provide a regulation of $\pm 0.01\,\%$. The transistor bank uses 328 transistors connected in parallel to handle a maximum of 805 A. The bank has a maximum rating of 53 kW but normally operates at 31 kW (38 V drop). The voltages from the two 350-kW power supplies furnishing the main dc power for this system have their output voltages controlled with induction voltage regulators by a slow loop servo system that senses the voltage across the series transistor bank; the regulation system maintains approximately 38 V dc across the series

Figure 19-18 End station A bending magnet—power supply system.

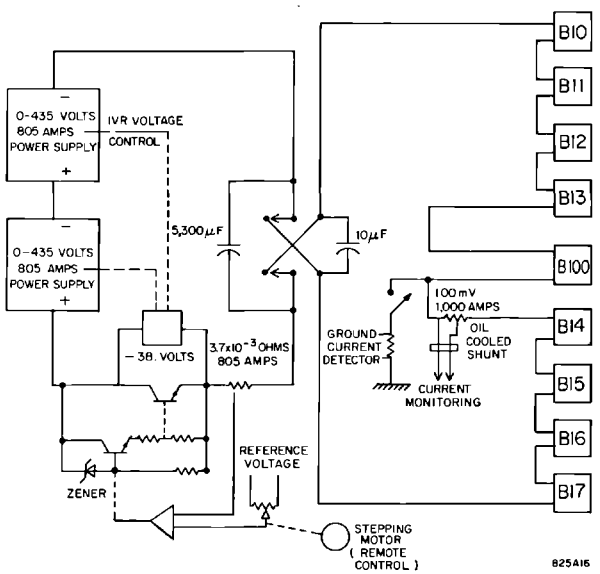

transistors and maintains the current in the bending magnets within $\pm 0.01\%$ from 40 to 100% rated current.

The dynamic range of control is from about 10 to 805 A. The current is controlled from the DAB control room with a stepping motor drive on a multiturn potentiometer that always changes the current in the magnet at a rate of 6 A/sec. This rate was chosen as about the optimum regarding convenience and reproducibility of the field versus current in the magnet.

The B bending magnet power system

The B bending magnet system uses components similar to the A bending system except that only one 350-kW power supply is required to drive four bending magnets in the switchyard and one reference magnet in the DAB. The transistor bank for the B side is rated for 35-kW and operates at a normal voltage drop of 27 V.

Quadrupole and other miscellaneous magnet power supplies

Quadrupole power supplies rated at 27.5 and 55 kW have been provided. They energize magnets of similar impedances but allow for the fact that the beam optics does not require maximum power to be available for all of the magnets. Power supplies of these ratings are also used to energize other magnets, such as the emergency magnets B-1 and -2, the B-beam switching magnets B-36 and -37, and the B-beam pulsed magnet B-38 when the latter is energized with dc (not pulsed) power.

The regulation system of these power supplies is a current-stabilized, voltage-regulated, three-phase bridge, SCR system. The voltage-regulated system is current-stabilized through a slow loop using a transductor as the current sensing element. The voltage regulation part of the system comprises

Figure 19-19 The 27.5- and 55.3-kW quadrupole power supplies.

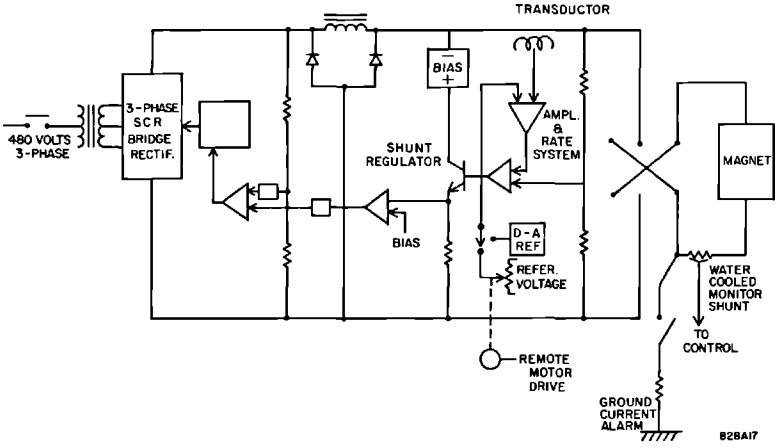

two loops: (1) an SCR regulation system and (2) a shunt transistor bank carrying about 10% of the rated power supply current to extend the frequency response range above the limit of about 10 Hz for the SCR loop (see Fig. 19-19).

The current in these power supplies can be adjusted from the control room by either a dc motor driving a multiturn potentiometer or by the use of a digital-to-analog converter. The regulation loop amplifiers have a built-in rate-limiting system that forces the current to change slowly regardless of the size of step required by the digital-to-analog converter. This rate limiter helps prevent overshooting of the current when making step changes in current with the digital-to-analog converter. The $\pm 0.1\%$ accuracy required for these magnets can be attained using only the current vs field relationships obtained during magnetic measurement.

Steering magnets

The power supplies for the steering magnets must be easily controlled from a positive current to a negative current with as little perturbation as possible at the zero current point. Some of the magnets steer in the vertical plane and others steer in the horizontal plane.

Reversing control is accomplished with reversing switches automatically actuated when the stepping motor-driven multiturn potentiometer used for current control approaches its zero position.

This type of control allowed for the minimum size of required power supply. A lever-type switch is used for the control of the current setting for these steering magnets.

The reversing switch position and current setting potentiometer controls are coordinated so that the position of the potentiometer control handle indicates the direction in which the beam will be steered regardless of the magnitude or sign of the current in the steering magnet. Thus, a left position of a control handle may mean an increase in current in the normal position of the reversing switch, but it would cause the current to decrease if the reversing switch were in the reverse position.

All these power supplies are regulated with series transistor banks to give good control and stability over a dynamic range of 100 to 1 in current.

Some of the power supplies use a narrow range regulator with a motor-driven variable transformer controlled to keep the regulator in range; other units have a fixed power supply voltage with a series transistor bank that can absorb the total voltage when required to operate at low magnet currents.

Acknowledgments

The authors are deeply indebted to D. A. G. Neet, who headed the Instrumentation Group responsible for the work herein described from its inception until September, 1966, when most of the work was completed. He provided the vital direction and leadership necessary to accomplish a project of this

magnitude in the time required. B. de Raad supplied most of the criteria, calculations, and preliminary development of the monitoring instruments in addition to several very valuable suggestions on electronics techniques. H. Dijkhuizen and J. Cole designed and developed most of the original interlock circuits for machine protection.

References

1 D. Olsen, "Beam Position and Intensity Displays in the BSY," Tech. Note No. SLAC-TN-64-92, Stanford Linear Accelerator Center, Stanford University, Stanford, California (November 1964).

2 R. S. Larsen, "Design of Beam Position and Charge Monitoring Circuits for the Stanford Two-Mile Accelerator," Rept. No. SLAC-63, Stanford Linear Accerator Center, Stanford University, Stanford, California (May 1966).

3 D. Olsen, "Design of a Precision Current Integrator for the BSY," Tech. Note No. SLAC-TN-65-56, Stanford Linear Accelerator Center, Stanford University, Stanford, California (July 1965).

4 B. De Raad, "The Application of Synchrotron Light for Beam Observation in the BSY," Tech. Note No. SLAC-TN-63-95, Stanford Linear Accelerator Center, Stanford University, Stanford, California (November 1963).

5 B. De Raad, "Beam Profile Monitors for the Beam Switchyard," Tech. Note No. SLAC-TN-64-77, Stanford Linear Accelerator Center, Stanford University, Stanford, California (September 1964).

6 W. Schulz, "A Multipurpose and Variable-Parameter Microspray Gun and Two of Its Applications at SLAC," Tech. Note No. SLAC-TN-67-3, Stanford Linear Accelerator Center, Stanford University, Stanford, California (January 1967).

7 R. V. Pound and W. D. Knight, *Rev. Sci. Instr.* **21**, 219 (1950).

8 M. J. C. Hu, "Binary to BCD (8421) Converter by Modulo 1010 Method," Tech. Note No. SLAC-TN-65-53, Stanford Linear Accelerator Center, Stanford University, Stanford, California (July 1965).

9 M. J. C. Hu, "Beam Switchyard Slit and Collimator Position Control and Readout System," Tech. Note No. SLAC-TN-66-52, Stanford Linear Accelerator Center, Stanford University, Stanford, California (December 1966).

10 R. Coombes, "Proposed Gas Flow System for the BSY," Tech. Note No. SLAC-TN-64-91, Stanford Linear Accelerator Center, Stanford University, Stanford, California (October 1964).

11 Gustavo R. Gonzalez and Amedeo Brambilla, "Frequency Dependence of the Resistance and Inductance of Solid Core Magnets," Rept. No. CEAL-1019, Cambridge Electron Accelerator Laboratory, Cambridge, Massachusetts (March 1965).

12 C. A. Harris and J. K. Cobb, "Establishing the Magnetic Field of a Solid Pole Magnet to within $\pm$ 0.01%," *Proc. Intern. Symposium on Magnet Technol., Stanford Linear Accelerator Center, September 1965* (H. Brechna and H. S. Jordon eds.), p. 823, CONF-650922, Clearing House for Federal Scientific and Technical Information, Springfield, Virginia.

20

BEAM POWER ABSORPTION DEVICES

A. H. Kilert, L. R. Lucas, W. S. Scott, and D. R. Walz, Editor

The ever-increasing energy and beam intensity of particle accelerators and the resulting high-power densities pose some challenging problems. One such problem is the successful absorption and dissipation of the power from a particle beam incident on matter. The SLAC beam switchyard (BSY) contains two beam transport systems to momentum-analyze the electron beam and to deflect it into physically separated research areas. In the course of traversing the BSY, the electron beam could impinge on many transport system components, such as magnets, beam position and profile monitors, current monitors, vacuum chambers, and targets for production of secondary particle beams. All but the last of these components are not designed for power dissipation and might suffer serious damage or total destruction if exposed to the high-power density beam. High-energy physics experiments often require a precise determination of the beam momentum and acceptance of a narrow momentum band. The bending magnets of the beam transport system serve to analyze the momentum of the beam. This analysis, in turn, allows removal of particles outside of the acceptable momentum band. Thus, devices which can absorb and safely dissipate rather high-power densities are required. Finally, the remaining electron beam leaving a target must be disposed of.

This chapter presents a summary of the research, development, design, and fabrication of beam power absorption devices. The first section treats beam interactions with materials, starting with the electromagnetic cascade shower development, and followed by the resulting power deposition and temperature rise. The pertinent modes of heat transfer are briefly reviewed, and auxiliary problems such as thermal stress and thermal fatigue are dealt with. In the following two sections, high-power and low-power beam dumps for continuous absorption and dissipation of up to 2.2 MW average beam power are discussed and analyzed. Radiolysis and radioactivity in the

cooling-water systems are treated in some detail with the inclusion of experimental results. Then, variable-aperture high-power and low-power slits and collimators are discussed and their final versions and first performance data are presented and illustrated with photographs. The treatment is supplemented by a slit analysis including a numerical example. Next follows a section on protection collimators with emphasis on protection philosophy, beam trajectory, and beam envelope studies. Finally, a few thoughts on future high-power absorption devices are offered. It is hoped that this chapter, in addition to presenting the high-power absorbers as built at SLAC, will serve as a guide for development of such devices at other laboratories. A list of pertinent references completes the chapter.

20-1 Beam interactions with materials (DRW)

The following treatment summarizes the most important phenomena to be considered in the development of high-power absorbing equipment. Electromagnetic cascade shower development, power deposition and temperature rise, heat transfer, thermal stress development, thermal fatigue, and thermal shock are reviewed. The list does not claim to be complete and a number of other important topics such as radiation levels and radiation damage, radiolysis and induced radioactivity, metallurgy and corrosion problems are dealt with using specific examples in the sections below.

Cascade shower development

High-energy electrons such as those produced by the SLAC linac will gradually lose their energy upon traversing matter. This energy is lost primarily as a consequence of electromagnetic interactions in the form of radiation effects and collisions with atomic electrons. Extensive literature[1] exists, and only the most important processes are dealt with here.

The important processes for electrons are radiation or bremsstrahlung and ionization; for photons, pair production and Compton scattering. A multigigaelectron-volt electron beam impinging on matter will cause production of a large number of secondary particles.

Upon traversing the electric field of nuclei, electrons are deflected and radiate photons. This process is referred to either as radiation or as bremsstrahlung. It can occur many times for incident 20-GeV electrons, and the total secondary particle population rises rapidly as a function of depth. As the energy of the electrons decreases the probability of a radiation interaction decreases also, whereas the probability for "absorption" and associated "ionization" increases.

The photons produced in the bremsstrahlung process can have various interactions with matter depending on their energy. A high-energy photon produced by an incident electron will most likely interact with the nucleus in a process in which the photon disappears and two new particles, an electron

and a positron, are released. The energy of the photon appears primarily as kinetic energy of the electron and positron. The process is called "pair production." Both secondary particles are still highly energetic and can liberate more photons by bremsstrahlung. These photons, in turn, can materialize in pair production. Thus, the population of electrons, photons, and positrons increases rapidly at the expense of the average energy of the particles. This phenomenon is called the development of an "electromagnetic cascade shower."

After traversing a certain amount of matter, the particle population reaches a maximum which is referred to as the shower maximum. This is also the location of peak energy deposition in matter, as this quantity is proportional to the shower multiplicity.

As the energy of the photons decreases to the range of 1 to 5 MeV, they interact mainly by elastic scattering with the orbital electrons of the atom; the photon is scattered and the electrons recoil. After several elastic scattering collisions the photon has lost much energy and the probability of its being absorbed in a collision with an atomic electron is greatly increased. When this happens, an electron is ejected from the atom and the photon disappears. This phenomenon is referred to as "photoelectric absorption." Thus, as the radiation shower traverses beyond the shower maximum, the total number of electrons, positrons, and photons decreases; the shower is exponentially attenuated.

Equations to compute the total number of electrons or photons in a shower due to an incident electron or photon, respectively, have been given.[1] At the shower maximum, the number of electrons, $\Pi_{\max}^{(e^-)}$, due to an incident electron of energy E_0 is

$$\Pi_{\max}^{(e^-)} = 0.31\left(\frac{E_0}{\varepsilon_0}\right)\left[\ln\left(\frac{E_0}{\varepsilon_0}\right) - 0.37\right]^{-1/2} \tag{20-1}$$

and the number of photons, $\Pi_{\max}^{(\gamma)}$, due to an incident photon of energy E_0 is

$$\Pi_{\max}^{(\gamma)} = 0.31\left(\frac{E_0}{\varepsilon_0}\right)\left[\ln\left(\frac{E_0}{\varepsilon_0}\right) - 0.18\right]^{-1/2} \tag{20-2}$$

where ε_0 is the critical energy of the target material, i.e., the average energy loss due to ionization (or radiation), per unit radiation length.

The longitudinal distance in radiation lengths to the shower maximum can be computed from

$$T_{\max}^{(e^-)} = 1.01\left[\ln\left(\frac{E_0}{\varepsilon_0}\right) - 1\right] \tag{20-3}$$

and

$$T_{\max}^{(\gamma)} = 1.01\left[\ln\left(\frac{E_0}{\varepsilon_0}\right) - 0.5\right] \tag{20-4}$$

where one radiation length, X_0, is defined as the distance (of matter traversed) in which an electron's energy is reduced by radiation to $1/e$ of its original value. The radiation shower develops not only in the direction of the incident electron beam but also radially. At the beginning of the shower, where the average energy of the particles is still high, scattering angles of the shower particles are small, and secondary electrons, positrons, and photons are also emitted at small angles. Thus, the shower develops mainly in the forward or longitudinal direction. As the average energy of the shower particles decreases, scattering and emission angles become larger, and a significant radial shower development results. This has a profound influence on lateral dimensions of energy-absorbing equipment.

Evaluation of cascade showers is a very difficult mathematical task. Approximations and simplifications have to be introduced to make calculations practical. Relatively few simplifications are made in Monte Carlo calculations, using differential and total cross sections for the various processes described above. The longitudinal shower development has been treated in detail analytically.[1] More recently a Monte Carlo method to calculate the three-dimensional shower has been developed.[2,3] This method was used to study the effectiveness of an aluminum collimator in a 20-GeV electron beam.[4] The results are based on a single incident electron, i.e., a point source; they are thus not particularly useful for practical applications. Assumption of a point source results in unrealistically high energy densities near the origin.

Figure 20-1 Longitudinal shower development of a 20-GeV, 2.18-MW electron beam in water, aluminum, and copper.

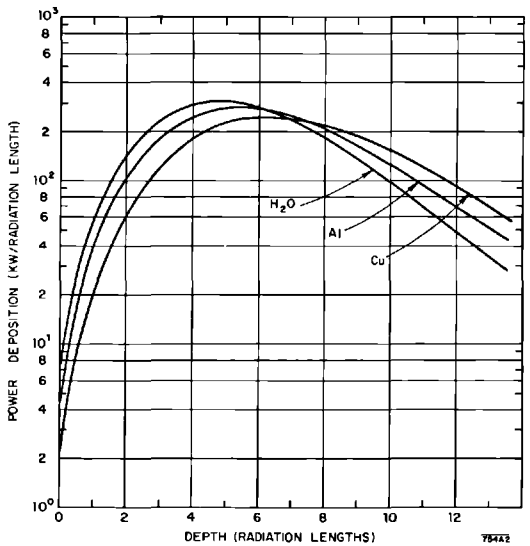

Point source results of the three-dimensional shower in semi-infinite media of copper, aluminum, and water have been transformed into physically realizable finite-sized beams assuming a Gaussian radial beam distribution.[5] Three different incident beam profiles having standard deviations of $\sigma_b = 0.1$, 0.3, and 1.0 cm were treated. All values are for radially symmetric, 20-GeV, incident electron beams with a repetition rate of 360 pulses/sec, a pulse length of 2.1×10^{-6} sec, and an average beam power of 2.18 MW. These beam data allow conversion of the energy densities obtained in the Monte Carlo calculations into power densities. The longitudinal power deposition in Cu, Al, and H_2O is shown in Fig. 20-1. The curves are for $\sigma_b = 0.3$ cm, a beam size closely resembling expected operating conditions. Figure 20-2 presents the corresponding radial power distribution at the shower maximum.

Power deposition and temperature rise

A close examination of the relationships given in Figs. 20-1 and 20-2 reveals some interesting facts. The energy deposition rates at the shower maximum and at the origin, $r = 0$, are very high. Using radiation length values from Table 20-1, volume heat sources of $S = 198$, 16.4, and 2.2 kW/cm^3 for copper, aluminum, and water, respectively, can be computed. The resulting local temperature rise, ΔT, assuming uniform heat source distribution in the volume

Figure 20-2 Radial shower development of a 20-GeV, 2.18-MW electron beam at the shower maximum (for $\sigma_b = 0.3$ cm) in water, aluminum, and copper.

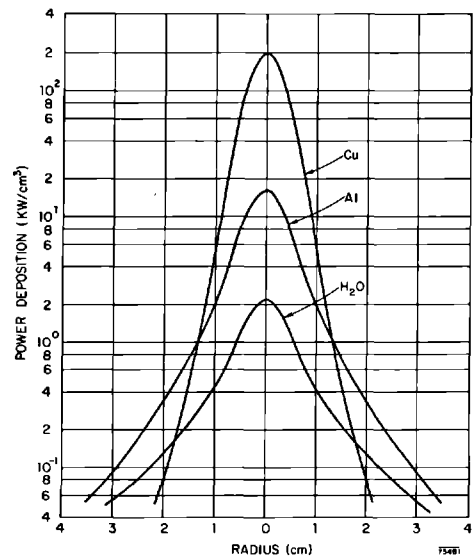

element under consideration, is spectacular. It can readily be calculated from

$$\Delta T = \frac{S}{\rho c(\mathrm{PRR})} \tag{20-5}$$

where S is the heat source from Fig. 20-2 in watts per cubic centimeter, ρ and c are the specific gravity and specific heat of the material in grams per cubic centimeter and watt-seconds per gram-degree centigrade, respectively, PRR is the pulse repetition rate in pulses per second, and ΔT is in degrees centigrade per pulse. For the heat source values at $r = 0$, as presented above, Eq. (20-5) gives for copper $\Delta T_{\max} = 158°\mathrm{C/pulse}$, for aluminum 18°C/pulse, and for water 1.5°C/pulse.

Maximum power densities and calculated peak temperature rises per pulse have been presented[6] and an abstract is given in Table 20-1 for two standard deviations, $\sigma_b = 0.1$ cm and $\sigma_b = 0.3$ cm. For other materials, the maximum power deposition can be determined from

$$S = \frac{\Pi_{\max} P_{\mathrm{AV}} \rho}{AE_0} \frac{dE}{dx} \tag{20-6}$$

where $\Pi_{\max}$ can be evaluated from either Eq. (20-1) or Eq. (20-2), P_{AV} is the average incident beam power, E_0 is the energy of the incident beam, A is the beam-spread area at shower maximum, and $dE/dx = \varepsilon_0/X_0$ is the energy loss of the shower electrons. A number of potentially useful materials for energy absorber applications, including important material constants, have been given.[6] An expanded, slightly altered version is presented in Table 20-2. Calculated values are based on $E_0 = 20$ GeV, $P_{\mathrm{AV}} = 2.2$ MW, and $A = 1\ \mathrm{cm}^2$.

Table 20-1 Maximum power densities and peak temperature rises at the shower maximum in copper, aluminum, and water[a]

	Depth		*$\sigma_b = 0.1$ cm*		*$\sigma_b = 0.3$ cm*	
Material	*Radiation lengths*	*cm*	*S (kW/cm³)*	*ΔT (°C/pulse)*	*S (kW/cm³)*	*ΔT (°C/pulse)*
Cu	0.0– 0.5	0.0 – 0.716	57.2	45.1	6.6	5.2
	6.0– 6.5	8.59– 9.31	920.0	725.5	198.1	156.2
	9.5–10.0	13.60– 14.32	328.8	259.3	86.1	67.9
Al	0.0– 0.5	0.0 – 4.52	14.4	15.7	1.9	2.1
	5.0– 5.5	45.2 – 49.7	56.6	61.7	16.4	17.9
	9.5–10.0	85.8 – 90.3	14.2	15.5	4.4	4.8
H_2O	0.0– 0.5	0.0 – 18.65	4.5	3.0	0.73	0.5
	4.5– 5.0	167.8 –186.5	7.1	4.7	2.2	1.5
	9.5–10.0	354.3 –373.0	1.0	0.7	0.33	0.22

[a] For $E_0 = 20$ GeV, $P_{\mathrm{AV}} = 2.18$ MW.

Table 20-2 **Properties and characteristics of potentially useful materials for energy absorber applications**[a]

Characteristics		Materials									
		Be	*C Pyrolytic*	*H_2O*	*Al*	*Ti*	*Fe*	*Cu*	*Ta*	*W*	*Pb*
Z		4	6	7.23	13	22	26	29	73	74	82
ε_0[b,c]	(MeV)	110.0	79.0	72.8	40.0	24.0	20.6	18.8	8.2	8.1	7.4
X_0[b]	(g/cm²)	66.0	43.3	35.7	24.3	15.1	13.9	13.0	6.9	6.8	6.5
$T_{\max}^{(e^-)}$	(radiation-lengths)	4.24	4.57	4.66	5.28	5.80	5.93	6.06	6.85	6.86	6.98
$\Pi_{\max}^{e^-}$		25.6	34.5	37.0	64.0	103.0	118.0	131.0	277.0	281.0	305.0
$-\frac{dE}{dx}$	(MeV/(g/cm²)	1.67	1.82	2.03	1.64	1.59	1.48	1.44	1.19	1.18	1.14
ρ	(g/cm³)	1.85	2.0	1.0	2.70	4.50	7.87	8.95	16.6	19.3	11.35
$-\rho\frac{dE}{dx}$	(MeV/cm)	3.08	3.64	2.03	4.45	7.17	11.6	12.8	19.8	22.7	12.9
c	(W-sec/g-°C)	1.78	0.97	4.22	0.94	0.54	0.48	0.385	0.129	0.134	0.13
ρc	(W-sec/cm³-°C)	3.3	1.94	4.22	2.54	2.42	3.79	3.45	2.14	2.58	1.48
k	$\left(\frac{\text{W}}{\text{cm}^2\text{-°C/cm}}\right)$	1.68	0.025 2.0	0.006	2.39	0.17	0.63	3.9	0.63	1.46	0.083
T_{melt}	(°C)	1278.0	3600.0		659.0	1800.0	1530.0	1083.0	3000.0	3380.0	327.0
S	(kW/cm³)	8.7	13.8	8.3	31.1	81.5	152.0	186.0	601.0	696.0	431.0
ΔT	(°C/pulse)	7.3	19.7	5.5	34.1	102.0	112.0	150.0	772.0	748.0	807.0
$\alpha\cdot 10^6$	(1/°C)	12.3	$+0.06$ -0.8		25.0	8.7	12.1	16.6	6.7	4.3	29.4
$E\cdot 10^{-6}$	(psi)	44.0	4.4		10.0	15.0	29.0	17.0	27.0	51.0	2.3
αE	(psi/°C)	540.0	$+0.26$ -3.5		250.0	130.0	350.0	282.0	181.0	220.0	68.0

[a] $E_0 = 20$ GeV, $P_{AV} = 2.2$ MW, and $A = 1$ cm².
[b] Most values from O. I. Dovzhenko and A. A. Pomanskii, *J. Exptl. Theoret. Phys.* (*U.S.S.R.*) **45**, 268–278 (1963).
[c] All values take density effect into account.

It should be noted that using $A = \text{const.}$ does not adequately account for the radial shower development as a function of Z; therefore, the temperature rise and power deposition as computed from Eqs. (20-5) and (20-6) are high for low-Z materials, approximately correct for medium-Z materials, and low for high-Z materials.

The values shown in Tables 20-1 and 20-2 indicate clearly that medium- and high-Z materials are not useful for applications requiring continuous exposure to the beam. Energy is deposited at a much higher rate than can be handled by thermal diffusion for practical geometries. The local temperature increases dramatically with each successive pulse, and failure due to gross geometrical changes or melting results for most of these materials within a fraction of 1 sec. Note that the product of ρc, i.e., the specific heat capacity, is essentially constant for all metals.

Further examination of Table 20-2 indicates that low-Z materials offer some promise for successful application in the construction of energy absorbers for high power density beams. In low-Z materials the power is dissipated in a much larger volume, i.e., the heat source is less intense.

Heat transfer problems

In the previous section it was shown how to calculate rates of heat deposition and local temperature rises per pulse. The next step in the course of an energy absorber analysis is the determination of the temperature distribution resulting from the beam power deposition and boundary conditions imposed on the system. Heat transfer between two adjacent particles of matter is the transfer of thermal (heat) energy by virtue of a temperature difference from the hotter to the colder. In any solid energy absorber, heat is transferred solely by thermal conduction. In an isotropic body the law of heat conduction can be stated as

$$q'' = -k \frac{\partial T}{\partial n} \tag{20-7}$$

where q'' is the heat flux in a direction n, and k is the thermal conductivity. Using Eq. (20-7), the most general equation describing the temperature distribution in any solid can be derived. If the thermal conductivity is assumed to be constant the heat equation (Fourier's law of conduction) can be stated as

$$k\nabla^2 T + S = \rho c \frac{\partial T}{\partial \tau} \tag{20-8}$$

where ∇^2 is the Laplacian operator, S is the rate of heat generation per unit volume, and τ is the time; S may be a function of space and time. For steady-state conditions with no internal heat generation, Eq. (20-8) reduces to the familiar Laplace equation. The heat equation has been solved for a wide variety of applications.[7]

Even when low-Z materials are used, so that heat source intensities are greatly reduced, the resulting heat fluxes from a surface are very high for practical geometries. Consider the case of an aluminum slab of thickness $\delta = 0.5$ cm placed normal to the beam direction at the shower maximum. Assume that one side of the slab faces a vacuum and the other side is water cooled. To a first approximation the heat sources are uniformly distributed through the cylindrical volume defined by the thickness of the slab and the effective diameter of the incident particle beam. This volume element for a 1-cm diameter beam is 0.39 cm^3, and the volume heat source is $S \approx 12$ kW/cm^3 (from Fig. 20-2 assuming a beam of 20-GeV energy and 2.18-MW average power). The power dissipated in this space is then $P_{AV} = 4.7$ kW. Neglecting radial conduction for the time being, it is found that the resultant steady-state local heat flux in the beam direction from the slab and into the water is $q'' = 6.0$ kW/cm^2. This is a very high if not excessive heat flux. A solution to Eq. (20-8) will readily yield the temperature rise across the slab as

$$\Delta T = \frac{q''}{k}\left(\frac{\delta}{2}\right) \tag{20-9}$$

which would be approximately 630°C. Consideration of radial conduction[7] will reduce this to about 500°C, a temperature still excessive for practical application. Examination of Eq. (20-9) shows that δ is the only variable since $q'' = \text{const.}\ \phi(\delta)$. For the case of uniform heat sources, δ enters linearly into q''; therefore an increase of δ by a factor of 2 increases the heat flux by a factor of 2 and the temperature difference by a factor of 4.

The high energy deposition rates and resulting large instantaneous temperature rises as given in Table 20-2 dictated the selection of low-Z materials for beam absorption devices. Similarly, high heat fluxes force the adoption of small wall thicknesses and result in a special mode of heat transfer. For heat transfer surfaces at room temperature or slightly above, heat fluxes up to approximately 0.25 W/cm^2 can be handled by natural convection in air and thermal radiation. The Stefan-Boltzmann law for heat transfer by radiation between two surfaces separated by a vacuum is given as

$$q'' = \sigma(C_2 T_2^4 - C_1 T_1^4) \tag{20-10}$$

where $\sigma = 5.77 \times 10^{-12}$ W/(cm^2 °K^4) is the Stefan-Boltzmann constant, and C_1 and C_2 are constants depending on the orientation, distance, absorption, and reflection properties of the two surfaces.

For heat fluxes $0.25 < q'' < 10$ W/cm^2 forced convection with air yields good results and is usually inexpensive. Extensive heat transfer data for various surface geometries cooled by air jets are available.[8] As the heat flux is further increased, forced convection using water will yield satisfactory results. Heat fluxes of 50 W/cm^2 can readily be handled with moderate water velocities.

At water velocities of about 1.5 m/sec and heat fluxes of more than about 65 W/cm^2, another heat transfer mechanism becomes important. It is commonly referred to as boiling heat transfer. Extensive literature is available,[9,10] and only basic mechanisms will be reviewed here.

Air or water vapor bubbles trapped in crevices of the metal surface begin to grow in size as the metal surface temperature and, therefore, the temperature of the thermal boundary layer is increased to a point where bubble growth can be sustained. Depending on the velocity and temperature of the coolant, the bubbles will grow to a size such that they are swept away by viscous drag from the fluid, or they detach themselves due to their buoyancy. Some of the water vapor stays in the cavity and is the nucleus for the next bubble. Once in the main stream the bubbles will collapse more or less rapidly, depending on the subcooling, i.e., the temperature difference between the boiling point and the bulk fluid temperature. In highly subcooled liquids the bubbles can collapse without ever leaving the surface. This has important implications as will be shown later.

The vapor bubbles carry large amounts of energy away from the surface, through the thermal boundary layer and out into the main bulk fluid. Rather high heat fluxes can be handled in this fashion. Moreover, the moving bubbles stir up the thermal boundary layer and fresh bulk fluid reaches the hot surface. This mechanism is referred to as "nucleate boiling" and occurs in all energy absorbers discussed below.

As the heat flux is still further increased, the number of bubbles and the number of nucleation sites increase until adjacent bubbles start to interfere with each other's growth and motion. This is the condition of maximum heat flux, also referred to as critical or burnout heat flux. Any further increase of the surface temperature will result in the formation of a stable vapor film which, in turn, prevents the bulk liquid from reaching the surface and, thus, acts as an insulator. This condition is called "film boiling." It usually results in a rapid rise of the metal surface temperature to the point of destruction.

Unfortunately, the large number of variables, such as surface geometry and condition, fluid velocity and temperature, fluid properties, and radically varying heat transfer mechanisms for different regimes, make a single heat transfer correlation and prediction of burnout a very difficult task. No universally acceptable correlation yet exists. Furthermore, most experimental data reported in the literature are for the case of uniformly heated large surface areas. They do not adequately represent the local heat transfer conditions expected from impingement of high-intensity particle beams into solids. Typical values of burnout heat fluxes for moderate water velocities are in the neighborhood of 1 kW/cm^2.

High local heat fluxes from electron-bombarded water-cooled targets have been reported.[11] The values are much higher than the usual burnout heat fluxes. Boiling heat transfer experiments were also performed at SLAC[12] to establish permissible heat flux values from a local hot spot for different materials. Flat plates of varying thickness were bombarded with 15-keV

electrons from a tungsten filament. Heat fluxes of up to 6 kW/cm^2 were achieved, and the experiments confirmed that at least 2 kW/cm^2 could be assumed for the design and safe operation of energy absorbers, using either copper or aluminum. The experiments demonstrated clearly that the flow velocity parameter is only of secondary importance. It becomes significant only at the lower and upper boiling region limits. For example, an increase in flow velocity increases the burnout heat flux slightly. The subcooling of the fluid is a much more important variable and primarily determines burnout.

At this point an additional deleterious effect of operation at high heat fluxes will be mentioned. As already indicated above, highly subcooled boiling results in the collapse of the vapor bubble either on or very close to the material interface. The collapse or cavitation of a bubble will give rise to a shock wave that expands radially and dissipates its energy as it propagates. If the bubble cavitates very close to the surface, the shock wave is strong enough to work-harden the metal. The surface will become brittle and will eventually fail from fatigue. Cavitation or dynamical erosion can be very severe; it is often accelerated by thermochemical and other corrosion mechanisms. Observed erosion rates per 100 hours and for heat fluxes of 1.5 to 2.0 kW/cm^2 were 0.02 cm for a 1100 series aluminum plate, 0.0012 cm for a 6061-T6 series aluminum plate, and 0.0065 cm for a tungsten plate. Comparable damage was observed for various pure copper plates. Solutions to the erosion problem are proposed in a later section.

Thermal stress development

It has been demonstrated that high rates of energy deposition can be achieved with the accelerator and that the instantaneous energy dissipation during a single pulse gives rise locally to steep temperature gradients in space and time.

If the body under consideration and its properties are continuous, the nonuniform temperature distribution will give rise to thermal stress and strain within it. Each volume element of the body tends to expand (or contract) by a different amount proportional to its temperature rise (or temperature drop). Since the temperature change is nonuniform, adjacent volume elements will change by different amounts. In a continuous body, adjacent volume elements will hold the element under consideration in place and shape, i.e., they represent an internal constraint. The result is what is called "thermal stress." External constraints, i.e., body forces, can also cause thermal stress in a heated body. The designer is warned not to ignore them; they can fundamentally influence the performance of a specific structure! The expansion resulting from the temperature rise is called "strain," denoted by ε. It is the same in all directions in an isotropic body and is related to the temperature change, ΔT, and to the coefficient of linear thermal expansion, α, by the relationship

$$\varepsilon = \alpha \, \Delta T \tag{20-11}$$

The stress, σ, is related to the strain by Hooke's law, assuming a fully elastic system:

$$\sigma = E\varepsilon = E\alpha\,\Delta T \tag{20-12}$$

where E is the modulus of elasticity.

If in addition, external forces are applied, the resulting stresses are superimposed on the thermal stresses. Hooke's law can then be expressed as[13]

$$E\varepsilon_{xx} = \sigma_{xx} - \nu(\sigma_{yy} + \sigma_{zz}) \tag{20-13a}$$

$$E\varepsilon_{yy} = \sigma_{yy} - \nu(\sigma_{zz} + \sigma_{xx}) \tag{20-13b}$$

$$E\varepsilon_{zz} = \sigma_{zz} - \nu(\sigma_{xx} + \sigma_{yy}) \tag{20-13c}$$

$$\varepsilon_{xy} = \frac{1}{2G}\sigma_{xy} \qquad \varepsilon_{yz} = \frac{1}{2G}\sigma_{yz} \qquad \varepsilon_{zx} = \frac{1}{2G}\sigma_{zx} \tag{20-13d}$$

and

$$G = \frac{E}{2(1+\nu)} \tag{20-14}$$

where ν is Poisson's ratio and G denotes the shear modulus. Addition of Eq. (20-12) to Eqs. (20-13a) through (20-13c) yields the total stress.

Thermal stresses are usually compressive (negative) stresses in the center of the heated area, and tensile stresses outside the heated area. For steady-state conditions the designer can allow for combined stresses up to the yield limit of the particular material. In the design of structures the ductility is often allowed to relieve stresses, using typical 0.1 to 1.0% permanent deformation values as design criteria. This may be disastrous in thermal stress applications and does not present a solution to the problem. It should be pointed out, however, that the detrimental effects of thermal stresses are more often than not overestimated. Moreover, stress values can be lower or higher than predicted by Eq. (20-12), depending on geometry or sources of stress concentration. A wide variety of thermal stress problems has been treated analytically.[14]

Thermal fatigue

The pulsing electron beam will result not only in a nonuniform, spatial, temperature distribution but will also cause temperature variations in time. Thus, cyclic stresses of thermal origin are superimposed on the steady-state thermal stress distribution, and thermal fatigue may result. Under these circumstances, structures fail at much lower stresses than predicted by simple stress–strain relationships. Ductile materials relieve stresses in excess of the yield strength by plastic deformation and creep. Thermal fatigue damage then is caused by cyclical yielding or cyclical plastic deformation.

The first signs of onset of thermal fatigue are an elongation of certain crystals and a slip at the grain boundaries. Under continued cyclical load, the slip eventually develops into individual pores, and cracks appear. If additional external constraints exist, fracture of the structure may result. The magnitude of the stress necessary to cause failure in the structure diminishes with increasing number of cycles. The fatigue or endurance limit of the material is determined by the number of cycles required to generate cracks at the given elevated temperature, as described above.

Electron accelerators can typically produce 10^{10} pulses/yr, and long-term fatigue values have to be selected accordingly.

Superposition of cycling and steady-state stresses and prediction of the expected lifetime can be accomplished using, for example, a Goodman diagram, described in more detail in another section below.

Thermal shock

A number of accelerators exist that can produce bursts of very high-power density over short periods of time. The high rates of energy dissipation during the pulse give rise to very steep temperature gradients in space and time, resulting in proportional thermal stress gradients. The latter can cause formation of thermal shock waves which, in turn, may result in fracture and spallation of materials, regardless of how well the part is cooled.

An experiment to determine the importance of this effect on an aluminum collimator module is described in more detail below. The rate of energy deposition during the pulse in the module wall was 600,000 kW/cm^3. No damage was observed. This may be explained by the relatively high ductility of the aluminum; another, more brittle material may have failed.

20-2 High-power beam dumps (DRW)

This section discusses the important design criteria and features of the high-power A-beam dump D-11 (see Fig. 17-1) and beam dump east D-400. Emphasis is given to the three important dump components: the window, the "vortex flow" region, and the plate compartment. The auxiliary but important problems of radiolysis in water, the evolution of free hydrogen and its disposal, are also treated in detail.

Criteria

The high-power beam dumps are to be capable of continuously absorbing and dissipating the full beam power produced by the SLAC linac over a wide range of energies. This includes conditions arising from radiators placed in the beam transport system upstream of a dump. Table 20-3 gives a summary of the most important criteria.

Table 20-3 High-power beam dump criteria

1. Full average beam power	2.2 MW
2. Incident beam energy	$\leq$25 GeV
3. Minimum beam size	
For A-beam dump	$\sigma_{b,x} = 0.1$ cm; $\sigma_{b,y} = 0.25$ cm
For beam dump east	$\sigma_b = 0.25$ cm
4. Entrance window size	15-cm diameter usable area
Thickness	0.127 cm
5. Total length	30 radiation lengths
6. Dump diameter	140 cm
7. Dump shell material	Stainless steel Type 316-L
8. Distance of beam center line from radial boundary	34.5 cm minimum
9. Water pressure at the window	45 psia maximum
10. Cooling water flow velocity in vortex region normal to beam direction	100 cm/sec ($\approx$3 ft/sec) minimum
11. Minimum flow rate	
For high-power operation	2000 liters/min (=550 gal/min)
For low-power operation	1500 liters/min (=400 gal/min)
12. Maximum cooling-water temperature	40°C
13. Window is remotely replaceable	
14. Water drainage is possible in place	
15. Gas is continuously vented from the dump vessel into the closed, radioactive, water loop	

Important design features

An isometric view of a high-power beam dump is shown in Fig. 20-3. One can identify four major components: (1) the beam entrance window; (2) the 10-radiation-length "vortex" flow region; (3) the 20-radiation-length plate compartment; and (4) the support carriage. The window is treated in detail in a separate section below.

It has been demonstrated in a previous section that only low-Z materials can be used to degrade and dissipate a 2.2-MW beam. In order to retain flexibility for beam power or energy variations and to achieve operational safety at a reasonable construction cost, it was decided to dissipate most of the beam power and establish the shower maximum in a large volume of water.

The beam enters into the cylindrical vessel through a thin window which is located off-axis, at $R = 30$ cm. The beam then traverses the vessel parallel to the axis of rotational symmetry. The shower maximum for 20-GeV electrons occurs at a depth of approximately 170 cm. For stagnant water conditions, the temperature would rise rather rapidly. Therefore, good circulation and mixing are required to prevent local overheating near the origin of the beam, particularly at the shower maximum where volume boiling could

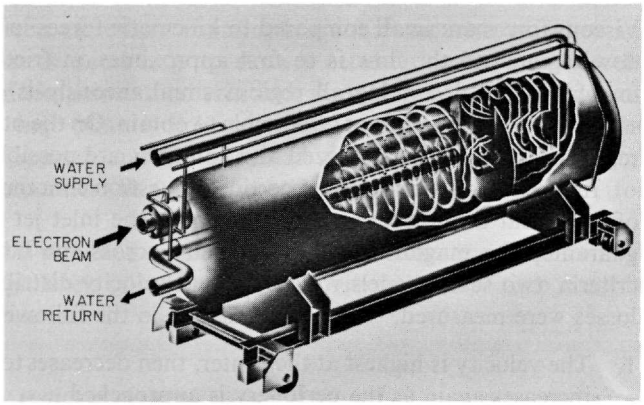

Figure 20-3 Artist's conception of a 2.2-MW ($E_0 = 11$–25 GeV) beam dump.

occur. Formation of a gas space would reduce the effective Z drastically; it would shift the shower maximum downstream and could result in destruction of the plate compartment in the rear of the dump. Hydrogen formed in the radiolysis of water could come out of solution and might present additional complications. Thus, the exposure of a volume element of water to the hot core of the beam has to be limited to a few pulses at most.

Several methods could be applied to exchange the water continuously in the cylinder. In order to economize on the flow rate and to reduce the beam exposure time of a volume element of water, it was decided to use a "vortex" flow. An inlet flow header located at the periphery of the shell induces the vortex flow. Water is injected through a series of holes, equally spaced over the 10 radiation lengths. The water then flows spirally toward the center of the vessel where the exit manifold is located. The velocity normal to the nominal beam center line (at $R = 30$ cm) was set at approximately 100 cm/sec. For this velocity no volume element of water equal in size to the hot core of the beam is exposed to more than about 4 pulses.

Knowledge of the quantitative radial velocity distribution is essential to guarantee safe operation. Seven different flow regions have been identified and are listed as follows:

1. The boundary layer at the cylinder wall
2. The rotational flow as a result of the submerged nozzle
3. The potential vortex flow region (perturbed by the effect of the geometric disturbance due to the inlet nozzle)
4. The interface between regions 2 and 3
5. Regions 4, 2, and 1 for the outlet nozzle in the center.

Losses in the system are mainly frictional losses in the various boundary layer regions due to shearing forces and eddy mixing losses from jets and wakes.

Viscous forces are small compared to kinematic forces in the potential vortex flow region and the flow is to first approximation frictionless. The mathematical model describing all regions simultaneously is complicated and its solution very difficult if not impossible to obtain. On the other hand, individual regions can readily be analyzed and solutions are possible.

In order to answer the most pertinent question concerning the performance of an actual beam dump, namely, what is the inlet jet velocity required to guarantee the magnitude of the velocity across the beam set forth in the criteria, two scale models were built and velocity distributions and pressure losses were measured.[15] The tests resulted in the following conclusions:

1. The velocity is highest at the center, then decreases to a flat minimum and increases again as the periphery is approached.
2. The ratio of the velocity at the beam to the inlet jet velocity is, to first approximation, independent of the Reynolds number over a wide range of N_{Re} (only the velocity was varied, however).
3. The velocity ratio varies linearly with the ratio of nozzle diameter to nozzle spacing.
4. A central outlet nozzle has a stabilizing influence on the flow and its symmetry.

Conclusion 1 indicates that the flow pattern is not just a simple potential vortex, given by $V \cdot r = \text{constant}$, but contains a term for solid angular rotation. This was to be expected due to the presence of other flow regions as described above. On the other hand, angular momentum is conserved to a large degree.

Conclusion 4 deserves some further comments: for the potential vortex under consideration the sink is located at the center of the vessel. In principle, no outlet nozzle has to be present along the center. Omission of the outlet pipe and creation of an outlet nozzle at the end of the vessel would change the two-dimensional vortex into a three-dimensional one. This is analytically predictable and was experimentally verified. In the case of a stable flow pattern the results indicated little difference in the velocity at the beam location between presence and absence of the outlet nozzle. Presence of the pipe, however, stabilized the flow appreciably and reduced asymmetry due to the perturbation caused by the geometric disturbance of the inlet nozzle. The axis of the inlet manifold coincides with a horizontal plane through the rotational symmetry axis of the vessel. This location gave best results at the beam axis. The diameter of the dump cylinder was determined by radial shower development considerations.

The 20-radiation-length plate compartment will now be described. Since space is at a premium and large pieces of equipment are expensive to fabricate and difficult to handle, it is not economical to attenuate fully the cascade shower in water alone. Solid copper plates are introduced downstream of the shower maximum, at a location where the cascade shower is sufficiently attenuated to cause only moderate heat fluxes and temperature rises.

A total of nineteen plates are contained in the compartment. They are graduated in thickness according to shower attenuation to maintain the design heat flux and temperature criteria and, thus, optimize the total length of the vessel. The first plate is 0.32 cm thick, the last one 3.8 cm. The plates are equally spaced and water-cooled at about 200 cm/sec water velocity. The maximum heat flux anywhere in the system is 2 kW/cm^2 (for $P_{AV} = 2.2$ MW).

The dump vessel is mounted on a mobile frame to allow remote placement or removal, since high levels of induced radioactivity will in due time result in inaccessibility of the area.

Window and window removal system

It has already been mentioned that the beam enters the dump through a thin window. The use of a window is necessary because the stainless steel vessel shell, which is approximately 1 cm thick, is not capable of dissipating all the power deposited in it. The size of the window is determined (a) by the maximum possible beam deviations from the nominal center line, (b) by the aperture of a protection collimator upstream of the dump, and (c) by the momentum spread of the residual electron beam due to a 0.01-radiation length target. The effective window area normal to the beam is defined by a 15-cm diameter circle.

High-purity copper (with thin layers of nickel and hard chromium plating as discussed below) was selected as window material. It is compatible with the rest of the system, which contains only copper and stainless steel. Based on peak power deposition, aluminum or titanium would have been superior to copper (see Tables 20-1 and 20-2). However, in an aqueous system aluminum would not be compatible with the copper used in the plate compartment, and titanium presents more fabrication problems than copper. The disadvantage of copper due to its high Z is offset, in part, by its excellent thermal conductivity.

The window thickness was chosen to be 0.127 cm (0.050 in.). The window separates water at elevated pressure from the beam transport vacuum system. To minimize the stress level, a hemispherical shape was adopted. The power deposited in the window can be readily calculated from a modified form of Eq. (20-6):

$$P = 1.6 \times 10^{-19} N \delta \rho \frac{dE}{dx} \tag{20-15a}$$

or

$$P = I_{AV} \delta \rho \frac{dE}{dx} \tag{20-15b}$$

where N is the number of electrons per second, δ is the window thickness, ρ the specific gravity, and I_{AV} is the average beam current.

For $E_0 = 11$ GeV and $P_{AV} = 2.2$ MW, the total power deposited in the window is $P_w = 0.325$ kW. The minimum expected beam size at the A-beam dump (D-11) is approximately 0.1 cm^2. The resulting heat flux into the water is about 2 kW/cm^2 (this includes consideration of lateral conduction in the window). Assuming steady state and the proper boundary conditions, solution of Eq. (20-8) yields a maximum temperature difference across the window of about 32°C. The thermal stresses are moderate (for a water-cooled window, taking into account the temperature difference across the interface) but would be severe if such a small beam cross section existed continuously at full power operation. A separate window-cooling mechanism was developed. Individual jets of water impinge in the area of high heat flux and prevent development of burnout conditions.

The window is expected to be the weakest item in the beam dumps. The production costs of a dump are high and lead times are long. For these reasons, it was decided to make the window exchangeable. Two seals are required: one between water and air, and the other one between vacuum and air. In the high radiation environment, only all-metal joints are useful for extended service. After extensive evaluation of various all-metal joints, the knife-edge-type of vacuum joint was chosen for both the vacuum and the water side of the window. It employs copper for the window, which also serves as the gasket, and stainless steel for the knife-edge flange. These are the same materials as are used in the rest of the dump. The knife-edge gasket has the advantage that it will seal vacuum tight, even with shallow scratches on the knife-edge or the gasket. Thus, neither the knife-edge nor the gasket is critical for a successful seal.

The expected high levels of induced radioactivity will result in inaccessibility of the dump, and, consequently, the window must be remotely exchangeable. For this purpose a hydraulic–pneumatic remote window-removal mechanism was developed and successfully tested. In order to reduce the complexity of this mechanism, only two bolts are used to tighten the flanges and make the seal. The flanges are, therefore, very stiff to achieve successful sealing. The bolts are turned by means of a hydraulically manipulated, pneumatic impact wrench, and windows are exchanged by employing a hydraulically operated mechanism. Detailed instructions for removal of the window unit have been prepared.[16]

A full-size prototype of a window was tested in the National Bureau of Standard's linac.[17] Temperatures were measured with thermocouples attached to the air side of the window. The highest heat transfer rate from the window to the water was approximately 1.25 kW/cm^2 in the area of beam impingement. The highest temperature recorded was 315°C. This thermocouple did not, however, coincide with the beam center line, and temperatures may have been as high as 350°C. Furthermore, the data are not corrected for beam exposure of the thermocouples. This would lower the values. The window showed no spallation effects due to thermal shock, and the hard-chromium plating on the water side appeared to be undamaged.

Material selection and fabrication

The dump vessels, including all the piping, are fabricated from stainless steel, Type 316-L. This material was selected because of its superior corrosion resistance. It is a fully austenitic, low-carbon steel which is Mo-stabilized. Carbide precipitation in the multitude of welds is negligible and corrosion resistance in these areas is very good. Furthermore, Type 316-L appears to be less susceptible than type 304 to stress corrosion cracking, frequently the swift destroyer of stainless steel structures.

All welds were made by the tungsten inert gas arc method (TIG) to highest welding quality standards. Only low-carbon, Type 316-L welding rod was used. Full penetration and fusion were required, since the lack of either may cause crevice corrosion, subsequent stress-corrosion cracking, and pit corrosion. All welds were inspected using x rays and dye penetrants.

The plates located in the rear of the vessel are oxygen-free high-conductivity copper, graduated in thickness as previously described. Without surface treatment the cavitation erosion problem would be a serious limitation on the expected lifetime of a beam dump. Experiments have indicated that hard materials are much less subject to cavitation erosion than soft ones. Good results were achieved by electroplating the copper surface with a sandwich of nickel and hard chromium. The soft nickel layer is approximately 0.0025 cm thick, the hard chromium layer about 0.001 cm. There are two reasons for the nickel substrata. First, it seals the copper surface and protects it from various corrosion mechanisms; this is important, since hard chromium is susceptible to cracking. Second, the soft nickel layer acts as a stress-absorption buffer. Significant differences in the coefficient of linear thermal expansion between copper and chromium would cause large thermal stress concentrations at the interface during operation. The chromium would crack and might even flake off. The nickel layer, in turn, is soft, can yield easily, and has a thermal expansion coefficient which is intermediate to the coefficients of copper and chromium. It is of importance to mention that the hard chromium has to be plated above 55°C, otherwise continuous microcracks are formed and the plating is porous.

The beam dump prior to installation is shown in Fig. 20-4. The right-hand side of this front view shows the water inlet manifold at the top, then the water outlet manifold, and a drainage line at the bottom. Also shown as part of the water outlet manifold is a Venturi for removal of air during the filling procedure and for continuous venting of gases formed in the radiolytic decomposition of water.

The water system and corrosion problems

The radioactive cooling-water loops are described in detail elsewhere in this text, and a brief treatment will suffice here. The water quality of the primary radioactive water loop is monitored daily. A resin ion-exchanger located in

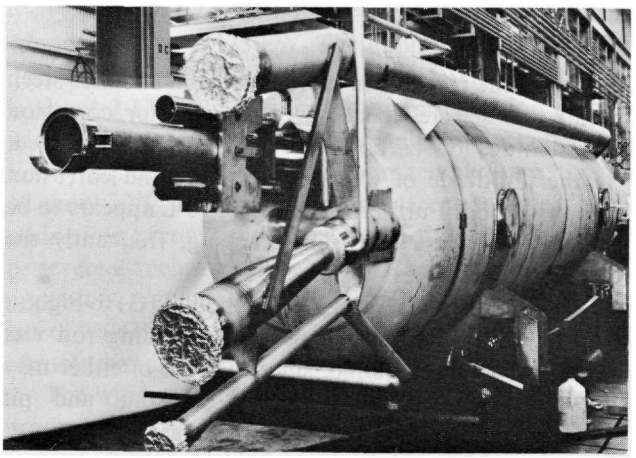

Figure 20-4 Front view of 2.2-MW beam dump (D-400).

a bypass loop serves to keep the water at 1 megohm-cm, or better. The pH is kept slightly acidic, approximately 6.2–6.5, from carbon dioxide dissolved in the aerated water. Particular attention is given to chlorides in the water, since they are a major factor in initiating stress-corrosion cracking in stainless steels. Chloride concentrations are <1 ppm. Based on extensive experimental results from other laboratories, it is felt that chloride concentrations should not exceed 0.1 ppm for safe, long-term operation. Significant amounts of hydrogen peroxide, H_2O_2, are formed in the radiolysis of water. It is an oxidizing agent and, therefore, caused concern about the corrosion resistance of the materials used in the radioactive loops. A study of H_2O_2 chemistry indicated that no problems should exist in the water loops. Stainless steels as well as aluminum alloys derive their superior corrosion resistance from the presence of a dense, more-or-less insoluble, oxide film on the surfaces of these materials. Aluminum containers are often used to store H_2O_2 and keep it from decomposing. It is felt that the presence of H_2O_2 in the radioactive water loops either enhances formation of even denser oxide films or has no influence at all on the corrosion behavior of these systems.

A major concern during maintenance work has been the radiation from curies of ^{7}Be (54 days half-life), a daughter nuclide of ^{16}O. It is formed in not negligible quantities in the beam dumps under high-power operation. Measurements revealed that essentially all ^{7}Be is trapped in the ion exchangers, thus localizing the radiation problem and making it easy to shield against.

The tritium (^{3}H) buildup in the radioactive water systems is also monitored. The total volume of water contained in the A-beam dump radioactive waterloop is approximately 12,000 liters. It was estimated that about 5 MW-hr were dissipated in this volume during the first 9 months of operation. At the end of this period the ^{3}H level was 3×10^{-4} $\mu Ci/cm^3$ or about 4 mCi for

the total system. The maximum permissible concentration (MPC) for disposal of water into sewers is 10^{-3} μCi/cm^3. Thus, drainage of the water at regular intervals is an inexpensive solution to minimize health hazards.

Operational experience

To date (July 1967), after 12 months of continuous operation, no failures have occurred. The highest average power deposited and dissipated in the A-beam dump so far is 240 kW at 17.5 GeV (on March 28, 1967).

Radiolysis and radioactivity in the water

Large quantities of water are used in the beam dumps as the coolant and primary energy absorbant. In the high-power beam dumps, approximately 90% of all the energy entering the dumps is dissipated directly in the water, with the remaining 10% dissipated in the copper plates, and a very small part lost from the system due to radiation. For electrons with energies $E_0 > 0.5$ MeV, the linear energy transfer, i.e., the amount of energy lost per unit distance traveled is $-(dE/dx)\rho \approx 2$ MeV/cm. This energy is lost in discrete amounts averaging about 100 eV per event. The energy usually converts within less than 10^{-12} sec into heat. Water molecules are excited in the region where this energy transfer occurs; such a region is called a spur. The energy deposition reaches a maximum at the end of the track of a charged particle and results in formation of a high-temperature region, called a "thermal spike." For this case, spurs will be an average of 5×10^{-5} cm apart.[18]

During the pulse, high concentrations of free radicals such as H and OH are formed in the spur. Some of these radicals will react with one another; others diffuse out of the spur into the bulk water. The reactions within the spur will yield H_2, H_2O, H_2O_2, and others. They can be symbolically represented as

$$H_2O \rightarrow H, H_2, OH, HO_2, H_2O_2, H_2O, e_{aq}^- \qquad (20\text{-}16)$$

where e_{aq}^- is the hydrated electron.

The radicals diffusing into the bulk can increase in concentration to a point where they not only react with the H_2, H_2O, and H_2O_2, but also with one another to form more H_2 and H_2O_2. Since the solubility of hydrogen in water is only about 0.8×10^{-3} moles/liter, after a certain time there will be a net evolution of free hydrogen. Also, once equilibrium concentration is reached, hydrogen peroxide is expected to decompose due to radiation and other chemical reactions, and a net evolution of O_2 can be expected. Theoretical quantitative prediction of evolution rates is a complicated task. It is thought that at least fourteen rate equations have to be solved simultaneously.

Measurements have been made[19] to determine the amount of free hydrogen produced using an electron linac giving pulses of approximately 7×10^4 g-rads and energies $E_0 \approx 15$ MeV. The dose into the effective irradiated volume

of 15.3 ml of oxygen-free water was approximately 4.5×10^3 rads. A constant yield $G(H_2) = 0.71$ molecule of H_2 per 100 eV of energy absorbed was observed. These authors also calculated the direct yield from oxygen-free water. This yield $g(H_2)$, which does not include contributions from secondary reactions, was found to be 0.41. The calculated result for 0.8 N H_2SO_4 (N stands for normal concentration) was $g(H_2) = 0.45$. Using $G(H_2) = 0.70$, the calculation yields a total rate of H_2 evolution of 1.6 liters/(MW-sec) from the SLAC high-power dump. Whether or not this G value holds at much higher energies and current densities than discussed above has not been determined. However, it is thought[20] that the true value will lie within a factor of 2 of $G(H_2) = 0.70$, which would amount to a range of 0.8 to 3.2 liters H_2/(MW-sec). Impurities contained in any real operating water system have a marked effect on reaction rates and many influence $G(H_2)$ significantly.

Various degassed neutral and alkaline aqueous solutions have been irradiated[21] with γ rays from a ^{60}Co source and with 2-MeV x rays. The results were the same for the neutral and the alkaline solutions, and they were independent of temperature from 4° to 65°C. The direct yield was $g(H_2) = 0.45$. Degassed acidic solutions of light water (0.4 M H_2SO_4, where M denotes molar concentration) and heavy water (0.4 M D_2SO_4) were irradiated with γ rays from a ^{60}Co source,[22] and a direct yield of $g(H_2) = 0.45$ and 0.38 was measured for the light and heavy water samples, respectively.

The hydrogen yield from air-saturated water has been calculated[18] for the initial condition where H_2 and H_2O_2 concentrations are very small compared with O_2. The result is $G(H_2) = 0.16$. This means that if $g(H_2) = 0.45$ as reported above is correct, the difference between 0.45 and 0.16 is lost due to secondary reactions of H_2 with OH. Oxygen-saturated water has been irradiated with γ rays from a ^{60}Co source, and an initial yield of $G(H_2) = 0.20$ was measured.[23]

Experiments have been performed at SLAC[17] to measure the rate of H_2 evolution in the high-power A-beam dump. The beam dump radioactive water system is a closed-loop system with a surge tank, pump, and heat exchanger. Hydrogen produced by radiolysis evolves in the aerated gas space on top of the surge tank and its concentration is measured in a sampling loop. The H_2 evolution has been evaluated for incident electron energies of 10.0, 12.0, and 16.3 GeV; pulses of 6×10^6 to 5.4×10^7 g-rads; and average power deposited in the dump ranging from 20 to 170 kW. The rates of H_2 evolution varied from 0.26 to 0.44 liter/(MW-sec) with an average of 0.31 liter/(MW-sec). The latter corresponds to $G(H_2)_{AV} = 0.14$. It seems that at these high power densities, reactions occur which tend to favor recombination of free radicals to form H_2O. However, agreement with the values for aerated water reported above is quite good.

The free hydrogen evolving in the surge tanks presents significant problems. The lower explosive limit of a hydrogen–air mixture is 4% H_2 for atmospheric conditions (STP). One can consider 2% H_2 as the upper limit for safe, continuous operation. For water already saturated with H_2 it took

only 10 min to reach the safe limit at $P_{AV} = 150$ kW. Unfortunately, even at low average power levels of, for example, 50 kW the amount of radioactivity released into the atmosphere is prohibitive for any long-term venting operation.

The SLAC Health Physics Group has analyzed the gases on top of the surge tank during several experiments and identified ^{15}O (2 min) and ^{11}C (20.5 min) as major contributing isotopes; both are daughter nuclides of ^{16}O. A drying column failed to remove the ^{15}O, suggesting that it is in gaseous form (O_2) rather than in the H_2O molecules of the water vapor. Chemical removal of CO and CO_2 indicated that virtually all ^{11}C is in CO_2. The radiation level at a distance of 100 cm from the top of the surge tank was ≈ 60 R/hour for steady-state dissipation of 170 kW in the dump.

Two solutions have been proposed for removal of evolved hydrogen: a chemical CO_2 removal-storage-venting system and a catalytic recombination system. In the first system gases coming off the surge tanks are diluted to achieve concentrations of $<2\%$ H_2. Then ^{11}C is removed by absorbing CO_2 in a resin bed. Thereafter, the gases pass through a storage tank large enough to guarantee a lapse time of 12 to 15 half-life periods for ^{15}O before they are finally vented into the atmosphere. After careful study, this system was rejected in favor of a catalytic recombination system. It consists of a fully closed system in which the gases are diluted to maintain concentrations of less than 2% H_2. The gases are continuously recirculated through a catalytic bed, in which H_2 and O_2 are recombined to form water. A SLAC-developed recombiner prototype is successfully operating at this time (July 1967). High recombination efficiencies have been obtained at slightly elevated temperatures.

20-3 Low-power beam dumps (DRW)

Two types of low-power beam dumps are discussed in this section: (1) the tune-up beam dump (D-10) and the central beam dump (D-2); and (2) the B-beam dump.

The tune-up dump is located in the space between the central beam and A-beam as indicated in Fig. 17-1. Its horizontal dimensions were chosen so as to allow maximum possible momentum acceptance during accelerator tuning. Crude spectrum measurements are possible by means of a spectrum monitor (S-10) located in front of the tune-up dump. The monitor consists of a row of secondary-emission monitor (SEM) foils and is described in more detail in Chapter 19. The power absorption capacity of the dump was determined by two machine requirements. First, the dump should accept a beam at the full repetition rate (360 pulses/sec) and with a peak current of ≥ 1 mA to satisfy the minimum requirements for proper functioning of the accelerator phasing system and the beam position monitors. Second, it should also accept a tune-up beam at full energy and full current (50 mA for Stage I). For a dump of reasonable size and cost, this requires a reduction in the beam

repetition rate to approximately 10 pulses/sec. With the inclusion of a safety factor, the maximum average power absorption capacity was set at 60 kW.

Although the power absorption specifications for the central beam are somewhat lower than for the tune-up beam, it was decided to duplicate the tune-up beam dump for this application and thus reduce engineering costs.

The B-beam dump is located in the B target room and serves to absorb and dissipate the electron beam and as the μ-meson target. Its power absorption capacity is 120 kW.

Table 20-4 shows a summary of the important criteria of the low-power beam dumps.

Design features, materials, and fabrication

In the tune-up and central beam dumps, beam power is dissipated in a series of water-cooled, high-conductivity copper plates. They are graduated in thickness according to shower development and attenuation, thus optimizing

Table 20-4 Low-power beam dump criteria

Characteristics	*Tune-up and central beam dumps*	*B-beam dump*
Maximum average beam power	60 kW	120 kW
Incident beam energy	$\leq$25 GeV	$\leq$20 GeV
Minimum beam size	$\sigma_b = 0.3$ cm	$\sigma_b = 0.3$ cm
Entrance window size	15 × 48 cm	15 × 30 cm
Thickness	0.16 cm	0.32 cm
Total length	30 radiation lengths	20 radiation lengths
Dump diameter	—	35.5 cm
Width	49.5 cm	—
Height	16.8 cm	—
Dump shell material	Stainless steel Type 316-L	Stainless steel Type 304-L
Window material	Stainless steel Type 316-L	OFHC[a] copper
Plate material	OFHC[a] copper	OFHC[a] copper
Nominal distance of beam center line		
From horizontal boundary	$\geq$1.9 cm	—
From vertical boundary	7.3 cm	—
Water pressure	165 psi	—
Cooling-water velocity between plates	230 cm/sec ($\approx$7.5 ft/sec)	150 cm/sec ($\approx$5 ft/sec)
Minimum flow rate	130 liter/min ($\approx$35 gal/min)	150 liter/min ($\approx$40 gal/min)
Maximum inlet cooling-water temperature	25°C	

[a] Registered trade name of American Metals Climax, Inc.

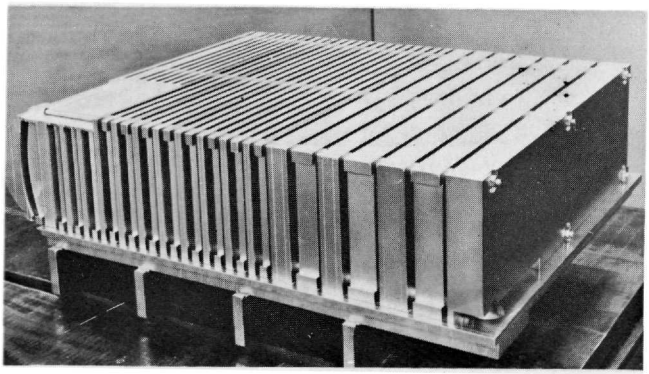

Figure 20-5 Plate compartment of 60-kW tune-up beam dump (D-10).

the dump length. Figure 20-5 shows a partial assembly of a tune-up dump. All plates are covered with electrodeposited layers of nickel and hard chromium for cavitation–erosion protection as described in detail in the previous section. The plates are contained in a Type 316L stainless steel shell.

The lateral dump dimensions were selected to allow a reasonable margin for possible beam excursions, taking into account radial power escape and heat transfer and thermal stress in the stainless steel sidewalls.

The window is a portion of a cylindrical surface to minimize the wall thickness and, consequently, the power absorption. For fabrication reasons, stainless steel has been selected in preference to copper as the window material. The window has been arc welded (TIG) to the stainless steel sidewalls. Copper would have required a more expensive brazing operation. The smaller wall thickness combined with the capacity for operating at much higher thermal stresses partially offsets the disadvantage of stainless steel because of its low thermal conductivity compared to that of copper. Figure 20-6 shows the completed tune-up dump assembly mounted under its support flange and ready for installation in the divergent vacuum chamber.

The B-beam dump is circular in cross section. It has a flat plate copper window, furnace-brazed to a stainless steel flange. The latter is welded to the stainless steel plate compartment. Other features are very similar to the tune-up dump design and are, therefore, not described further.

Operations to date

Experience during the first year of operation of the beam dumps has been flawless. The maximum average powers deposited in the tune-up beam dump and the central beam dump were about 40 and 45 kW, respectively. The B-beam dump has dissipated up to 75 kW.

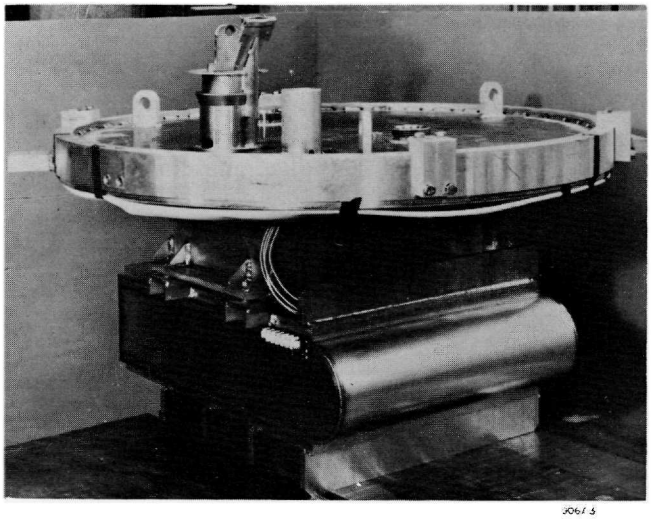

Figure 20-6 Assembly of 60-kW tune-up beam dump (D-10).

20-4 Collimators and slits (DRW)

General considerations and definitions

A list of important components in any beam transport system almost always includes collimators and slits. The functions of these devices may be described as follows: collimators are used to define the spatial extent of the particle beam, to form aperture stops for beam transport systems, and to protect magnets and other equipment from physical damage by the beam; slits are similarly used to provide stops that define momentum transmission in a beam transport system containing dispersive elements.

In the following sections three basically different types of collimators and slits will be treated in detail: (1) the variable-aperture, high-power collimator and slit; (2) the variable-aperture high-Z collimators and slits; and (3) the fixed-aperture protection collimators. Either variable or fixed-aperture collimators are employed depending on their function in the beam transport system. For example, at the beginning of the beam switchyard and the beam transport system, a set of variable-aperture collimators define the beam cross section at the center of the pulsed magnets PM-1 through PM-5. (For locations see Fig. 17-1.)

Under normal operation the power absorption in the collimators should be relatively low compared to the total beam power. However, mis-steering of the beam, beam breakup at the end of the accelerator, or misalignment of the collimators can cause abnormally high-power densities to be absorbed by these devices, which must, therefore, be designed to operate in this condition for an extended period of time without suffering physical damage.

Most components in the beam transport system must be protected from excessive power deposition or excessive exposure to primary radiation. Their location and aperture are usually fixed and, consequently, they may be protected by fixed-aperture collimators installed in front of them.

The slits are of variable aperture to satisfy the varying demands on maximum allowable momentum spread of the beam for different high-energy physics experiments. A relatively high-power absorption may occur when a narrow momentum spectrum of the electrons is desired and significant momentum components must be removed, or when the output of the accelerator is unstable.

Since one of the prime objectives of slits and collimators is the removal of particles of unwanted momenta from beam transport systems, it is of utmost importance to select a proper geometry and/or suitable materials. A poor choice of the latter may result in excessive multiplicity along the beam-defining edges and in the introduction of a new, significant momentum spread into the beam. This could reduce or even nullify the benefits of momentum selection in the beam transport system.

It would seem that optimum results can be achieved by using a high-Z material and a short physical length. This statement contains some element of speculation and more experimental work is needed to determine the effect of physical length on slit scattering. In the paragraph on shower development in Section 20-1, it has been demonstrated that high-Z materials are not useful for continuous dissipation of a full-power SLAC beam. Therefore a compromise has to be made on Z which results in an increase in physical length of the slits.

Ideally, the length of a slit should be zero, i.e., the slit should coincide with the image of the center of the pulse magnet group (PM-1–5) formed by the quadrupole doublet (Q-10, Q-11 or Q-30, Q-31). The size of this image and consequently the resolution at the slit is a function of the particle beam size at the center of the pulse magnet group. After passing through the quadrupoles (Q-10 and Q-11), the beam is bent a total of 12° by the first bending magnet group in the A-beam transport system (B10 through B13), and the beam is thus dispersed for momentum analysis at the slit. The dispersions at the A-beam slit (SL-10) and at the B-beam slit (SL-30) are 0.177%/cm and 0.343%/cm, respectively. Only a horizontal slit is needed to remove dispersive components of the beam, since the beam spectrum is displayed as a function of momentum in the horizontal plane.

20-5 High-power collimator and slits (DRW)

In the following section the high-power collimator (C-1) and slit (SL-10) are discussed. For locations see Fig. 17-1. An analysis of a slit is presented applying the principles and equations given in Section 20-1. Corrosion problems arising in a stainless steel–aluminum–water system are treated in

Table 20-5 High-power collimator and slit criteria

Maximum average beam power	
For minimum beam size	1.0 MW
For average expected beam size	2.2 MW
Incident beam energy	$\leq$25 GeV
Minimum beam size (for $\Delta p/p = \pm\frac{1}{4}\%$; angular divergence $\Delta\theta = 10^{-5}$ radian)	
At collimator C-1	$\sigma_b \geq 0.1$ cm
At slit[a] SL-10	$\sigma_{b,x} = 1.58$ cm; $\sigma_{b,y} = 0.08$ cm
At slit SL-30	$\sigma_{b,x} = 0.79$ cm; $\sigma_{b,y} = 0.07$ cm
Average expected beam size	
At the collimator	$\sigma_b \approx 0.3$ cm
At slit SL-10	$\sigma_{b,x} = 1.58$ cm; $\sigma_{b,y} = 0.24$ cm
At slit SL-30	$\sigma_{b,x} = 0.79$ cm; $\sigma_{b,y} = 0.21$ cm
Maximum aperture opening	
Collimator	$b_x = b_y = 4$ cm
Slits SL-10 and SL-30	$b_x = 15$ cm ($\Delta p/p = 2.66\%$ and 5.13%, respectively)
Total length	30 radiation lengths
Total usable height	$\pm$7.5 cm
Materials	
Modules	Aluminum alloy 6061-T6 and water
Water piping	Stainless steel Type 316-L
Vacuum shells	Stainless steel Type 304-L
Maximum water pressure	75 psia
Water flow velocity in prime heat transfer areas	$\geq$150 cm/sec ($\approx$5 ft/sec)
Minimum flow rate	
For 2.2 MW	950 liter/min ($\approx$250 gal/min)
For 1 MW	750 liter/min ($\approx$200 gal/min)
Maximum water inlet temperature	40°C
Operational vacuum	$\leq 10^{-4}$ torr
The apertures are remotely adjustable during beam operation	

[a] See Reference 6.

some detail. Finally, some fabrication highlights are described and illustrated with photographs.

The high-power collimator (C-1) and A-beam slit (SL-10) are presently in operation. A high-power B-beam slit (SL-30) identical to SL-10 is planned for the future. The important criteria are summarized in Table 20-5.

Slit and collimator analysis

Until recently, accelerator powers and intensities were low enough to permit the use of almost any material and geometry. A collimator was simply a block of medium-Z or high-Z material containing a hole to fix the desired aperture. Similarly, the jaws of a slit consisted of two opposing blocks of such a material. The blocks formed a variable gap and were operated in a vice-like manner.

For multigigaelectron-volt, multimegawatt electron beams, entirely new concepts must be formulated and applied. At SLAC, various collimator concepts were analyzed.[24] It was demonstrated that a water-cooled, rotating-drum-type collimator was feasible in principle as an aluminum structure for up to 2.2-MW average beam power, at least on the basis of evaluation of heat transfer, thermal stress, strain, and fatigue problems. The same geometry, using OFHC copper as the material, could operate safely for average beam powers up to 500 kW. However, the rotating drum-type collimator presents some very difficult problems associated with the operation of bearings and dynamic seals in a vacuum under high radiation doses (up to 10^{14} ergs/g/yr are expected), and a nonrotating device has obvious advantages.

In a quasi-stationary slit, even medium-Z materials must be ruled out, since the thickness of power-absorbing walls becomes too small for practical applications. Walls cannot be made infinitely thin since they separate the vacuum system from the coolant under pressure, i.e., the device is a pressure vessel. The optimum geometry for a given pressure is a hollow circular cylinder, a tube. The feasibility of a modular array of tubes or a "tube forest" as the basic collimator element has been demonstrated.[12,25]

Efforts to fabricate prototype collimator elements of the tube-forest model were not fully successful. The multitude of water-to-vacuum joints presented problems. A modification of the tube-forest concept was, therefore, developed. The idea was to let the spacing for pump-out between the outside diameters of individual tubes in the array shrink to zero, i.e., to bring all tubes into physical contact with all adjacent tubes. A solid block of material, perforated with an array of holes having a diameter identical to the inside diameter of the tubes, closely approaches this concept as shown in Fig. 20-7. The number of water-to-vacuum joints in one plane is thus reduced to one at the periphery.

Figure 20-7 Geometric configuration of high-power slit modules.

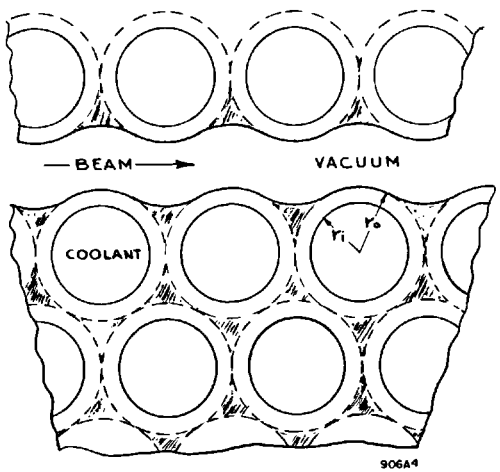

The heat transfer behavior of this new geometry is to first approximation still represented by the hollow circular cylinder geometry. For a wall thickness which is small in comparison to the particle beam size, one can assume uniform heat source distribution as a result of the beam power deposition. To first approximation, axial conduction can be neglected. The temperature distribution is described by Fourier's law of conduction. For steady-state, uniform heat source distribution, Eq. (20-8) may be written in polar coordinates as

$$\frac{d^2T}{dr^2} + \frac{1}{r}\frac{dT}{dr} + \frac{S}{k} = 0 \tag{20-17}$$

with boundary conditions

$$T(r_i) = T_i \tag{20-18a}$$

and

$$q'(r_i) = 2\pi k r_i \left(\frac{dT}{dr}\right)_{r_i} = \pi(r_0^2 - r_i^2)S \tag{20-18b}$$

where q' is the heat transfer rate per unit length across the metal–liquid interface.

The solution to this set of equations is

$$T = T_i + \frac{S}{2k} r_0^2 \ln\left(\frac{r}{r_i}\right) - \frac{S}{4k}(r^2 - r_i^2) \tag{20-19}$$

and the maximum temperature difference across the cylinder wall is

$$\Delta T = \frac{S}{4k}\left[2r_0^2 \ln\left(\frac{r_0}{r_i}\right) - (r_0^2 - r_i^2)\right] \tag{20-20}$$

The heat source S can either be calculated as outlined earlier or it can be extracted from curves such as given in Fig. 20-2. In order to make computational results realistic, an effective beam size has to be defined. Peak power dissipation occurs at the origin, $r = 0$. Values obtained in this fashion would, however, result in unrealistically high temperature gradients. Therefore, an "effective" beam size equal to the "hot core" of the beam is used. It was arbitrarily defined as the space limited by a radius, r_{hc}, at which the local power deposition is 80% of the peak value occurring at the origin. The power deposition is then averaged within this volume element and results in the value for the heat source. For the case of an incident beam of standard deviation $\sigma_b = 0.3$ cm, the corresponding value of the hot core at the shower maximum is $r_{hc} = 0.26$ cm. Knowledge of the radial power deposition distribution in just a few depth locations is sufficient to construct a curve expressing the relationship of the "percent of power" deposited (within r_{hc}) per unit

length versus shower depth. Heat source values can then be calculated readily by using curves given in Fig. 20-1 and multiplying each value obtained by the percentage value for that shower depth. It should be pointed out that this gives conservative values for the slit geometry under consideration, especially up to the shower maximum. This is due to the presence of large quantities of water with a significantly lower Z than aluminum. Moreover, there exists a strong dependence on σ_b at the beginning of the shower development. For increasing depth this factor becomes less important, and scattering and shower-spread dominate.

Note further that, for the case of the slit or collimator geometry, the Monte Carlo calculation for a semi-infinite solid gives excessive heat source values and, therefore, excessive temperatures. In this application the beam will always impinge close to the beam-defining edge, i.e., the system boundary. In that case, no infinite medium exists in the transverse direction. Shower particles will leave the boundary and are lost for further multiplication and power deposition in that area. It has been estimated[26] that this will reduce the power deposition values obtained for an infinite medium by at least a factor of 2. Once S has been determined, the temperature distribution and gradient can be calculated. The heat transfer rate per unit area at the metal–water interface is also readily obtained as

$$q''(r_i) = \frac{q'(r_i)}{2\pi r_i} = \frac{S}{2r_i}(r_0^2 - r_i^2) \tag{20-21}$$

The temperature distribution is slightly perturbed by the presence of heat sources in the triangular space formed by each three adjacent cylinders (see shaded areas in Fig. 20-7). An estimate of the peak temperature in that space can be obtained using Eq. (20-19) and redefining r_0. For a more accurate result an electrical analog would readily give the proper temperature distribution.

Finally, it should be mentioned that the temperature gradient as calculated from Eq. (20-20) gives somewhat excessive values, since it does not account for axial heat conduction. A more accurate value can be obtained from the following form of Eq. (20-8), assuming steady state and no circumferential heat source variation:

$$\frac{\partial^2 T}{\partial r^2} + \frac{1}{r}\frac{\partial T}{\partial r} + \frac{\partial^2 T}{\partial y^2} + \frac{S(y)}{k} = 0 \tag{20-22}$$

where y denotes the axial dimension. Equation (20-22) is a Poisson equation; $S(y)$ has, to first approximation, a Gaussian distribution and can be written as $S(y) = S_0 \exp[-y^2/2\sigma^2]$, where S_0 is the peak power density at the origin. The equation can be solved either by a Laplace transformation or by finite difference methods. Assuming $S(y)$ to be a step function allows a quick solution of the boundary value problem by separation of variables and superposition of results.

The maximum possible principal thermal stress in a fully restrained system due to a temperature gradient may be calculated from Eq. (20-12) using Eqs. (20-20) and (20-21),

$$\sigma_{th} = -E\alpha\,\Delta T_{tot} \tag{20-23}$$

where the effective temperature difference for the thermal stress development consists of two components,

$$\Delta T_{tot} = \Delta T_{film} + \Delta T_{metal} \tag{20-24}$$

Note, this stress is a compressive stress for a positive ΔT, i.e., a temperature increase.

Numerical example: Assume aluminum alloy 6061-T6 as material, $\Delta r = r_0 - r_i = 0.127$ cm ($=0.050$ in.), $\sigma_b = 0.3$ cm, $P_{AV} = 1$ MW. At a depth of 5 radiation lengths, one obtains from Fig. 20-1,

$$P' = 14.3\ \text{kW/cm}\left(= \int_0^\infty 2\pi r P(r)\,dr\right)$$

Approximately 9.5% of P' is deposited within the hot core for $r_{hc} = 0.26$ cm, thus $S = 6.4\ \text{kW/cm}^3$. Equations (20-20) and (20-21) yield $\Delta t = 35.5°\text{C}$ and $q'' = 0.88\ \text{kW/cm}^2$; if axial conduction is considered, Eq. (20-22), ΔT reduces to 32°C. Correction by a factor of 2 due to leakage of particles through the boundary yields a temperature gradient across the wall, from the vacuum to the water, of $\Delta T_{metal} = 16°\text{C}$ (or 35°C for $P_{AV} = 2.2$ MW).

Assuming a bulk water temperature of 40°C and a water pressure of 10 psig, $\Delta T_{film} \approx 74°\text{C}$. The effective total temperature gradient for thermal stress considerations, Eq. (20-24), is $\Delta T_{tot} = 90°\text{C}$, and the maximum metal temperature at the vacuum interface is 130°C. Equation (20-23) yields a thermal stress value of $\sigma_{th} = 22{,}500$ psi for a fully restrained system. The yield strength of alloy 6061-T6 at 135°C is $\sigma_{YT} = 30{,}000$ psi and the endurance limits for 10^6 and 10^{10} cycles are 18,000 and 12,000 psi, respectively. The instantaneous temperature rise due to 1 pulse is $\Delta T \approx 4°\text{C/pulse}$, which results in an additional cyclical thermal stress $\sigma_{alt\,max} = 1000$ psi. Superposition of the cyclical stress and steady-state stress can be accomplished by defining a mean effective stress σ_m as

$$\sigma_m = \tfrac{1}{2}(\sigma_{tot} + \sigma_{th}) = \tfrac{1}{2}(2\sigma_{th} + \sigma_{alt}) \tag{20-25}$$

For this example, $\sigma_m = 23{,}000$ psi. Next a Goodman diagram is constructed. Let the ordinate represent the cyclical stresses and mark $\sigma_E = 12{,}000$ psi for 10^{10} cycles. The abscissa is to represent the steady-state stresses and $\sigma_{YT} = 30{,}000$ psi is marked. The σ_E and σ_{YT} are connected by a straight line. The calculated sample point is located, with σ_{alt} as the ordinate value and σ_m as the abscissa value. Any combination of σ_m and σ_{alt} which results in a point located in the triangular area defined by the origin, σ_E, and σ_{YT} has unlimited life expectancy. For this example, i.e., $P_{AV} = 1$ MW, no fatigue failure is expected. It can also be shown that a 2.2-MW beam can be safely dissipated for $\sigma_b \geq 0.3$ cm.

Material selection and corrosion problems

An evaluation of low-Z fabrication materials resulted in selection of aluminum alloy 6061-T6 for the slit modules. This alloy has good corrosion resistance (as will be shown below), strength, and thermal conductivity. It has been successfully applied for uranium fuel element claddings in nuclear reactors where it experiences similar operating conditions. The strength–temperature relationship is flat and favorable up to 150°C.

For higher temperatures the strength decreases rapidly and small temperature changes result in large strength variations. Design in this region is not recommended unless one can pinpoint the temperature accurately. The alloy is quite immune to radiation-induced lattice structure changes for doses up to 10^{16} ergs/g. Formation of vacancies and interstices slightly increases the yield and ultimate tensile strength. For higher doses a rapid increase in strength is recorded; the material becomes brittle. Some of the alloying constituents are more likely to be displaced from their proper lattice site and chemical property changes in addition to mechanical ones may be of importance. The low-Z of the slit module materials also helps to keep down induced radioactivity, an important factor in accessibility to slit and collimator locations.

Stainless steel Type 316-L was selected for the water piping for reasons stated in the previous section. Important links in the water system are bellows which allow supply and return of water to the adjustable slit jaws. Inconel 600 was selected as the material for this application. It does not appear to be susceptible to stress-corrosion cracking and exhibits good all-around corrosion resistance. This is most important for stressed components with thin walls ($\approx$0.03 cm). Inconel 600 and stainless steel Type 316-L can readily be joined by TIG welding.

All external materials exposed to the beam switchyard atmosphere were carefully selected to withstand this environment. High levels of radioactivity near the power absorbers will result in ionization of the switchyard atmosphere. Oxygen and nitrogen ions will combine to form nitrogen oxides, which, in turn, will form nitric acid with the water vapor in the air. Significant amounts of HNO_3 are expected to be formed at high-power operation[27] according to

$$2H_2O + 2N_2 + 5O_2 \rightarrow 4HNO_3 \qquad (20\text{-}26)$$

One molecule of HNO_3 is formed for each 35 eV absorbed.[28] It has been estimated[29] that at full power operation, approximately 600 W are absorbed by the air in the entire beam switchyard. This results in formation of the equivalent of approximately 1 liter/day of commercial, 70% concentrated nitric acid. At this time it is still difficult to estimate for what percentage of the time one has to expect full power operation in the future. Moreover, the switchyard is not hermetically sealed, and significant amounts of air are exchanged in the course of normal daily atmospheric pressure changes. The switchyard air is also vented irregularly after an appropriate cooling-off

period for maintenance work. Nevertheless, the net amount of HNO_3 left might turn out to be significant and warrants careful selection of materials.

The slit and collimator vacuum shells, flanges, bellows, and other important structural items are fabricated from stainless steel Type 304-L. This material also exhibits less outgassing than mild steel, and pump-down time is shortened. The support structures are very massive, and the use of stainless steel would have been prohibitively expensive. They were fabricated instead from mild steel. Nitric acid corrosion is not expected to jeopardize seriously the proper functioning of these structures.

The usual rust layer formed on mild steel surfaces may, however, present a health hazard. The rust is continuously being irradiated as is the rest of the equipment, and induced radioactivity could make maintenance work dangerous. Radioactive rust particles could be picked up on shoes and clothing. The seriousness of radiation through the soles of the feet is seldom treated with sufficient concern. There is also the remote possibility that under dry conditions rust particles may become airborne and could be inhaled.

All support structures were, therefore, painted with a highly radiation-resistant, corrosion inhibiting paint. For highest resistance the paint has to be baked onto the surface. This operation was combined with a stress-relief operation to increase dimensional stability. Materials painted in this fashion have been exposed to a total dose of 2.4×10^{13} ergs/g. They showed no indications of damage, and adhesion was not impaired.[30]

A cause for concern was the simultaneous presence of aluminum and stainless steel in the slit and collimator radioactive water loops. Stainless steel is cathodic and aluminum with its high anodic potential reacts with most cathodic materials. A literature survey was carried out[31] on the corrosion behavior of aluminum alloys in a closed-loop aqueous system in the presence of stainless steel, nuclear radiation, varying water purity, temperature, and heat flux. Several corrosion mechanisms are active.

1. Aluminum reacts with oxygen-containing water by thermochemical or direct corrosion according to the equation

$$4Al + 3O_2 + 6H_2O \rightarrow 2Al_2O_3 \cdot 3H_2O \qquad (20\text{-}27)$$

This hydrous aluminum oxide is called "bayerite." It adheres well to the aluminum surface and is primarily responsible for the favorable corrosion behavior of aluminum. At elevated temperatures a denser oxide film is formed, $Al_2O_3 \cdot H_2O$, known as "boehmite." The solubility of bayerite in high-purity water[32] is a function of pH and is at a minimum at a pH of approximately 5. At this level of acidity, stainless steels suffer some attack.

2. The presence of cathodic materials, particularly copper, causes electrochemical corrosion. Copper ions in the aqueous system will plate out on the aluminum surface and they will cause pitting of the aluminum. Stainless steel and chromium result in only slight electrolytic attack unless in direct contact, even though both have a cathodic potential. No problem exists if high purity of the water is maintained.

3. Pitting corrosion or formation of little pits or cavities is brought about by a local cell action on a very small scale. Chemical (for example, copper ions) and geometrical discontinuities on the surface are responsible for local destruction of the passivating oxide film, followed by formation of a cell. High local currents and corrosion rates are the result. At elevated temperatures, above 100°C, pitting is not a serious problem.

4. Failures due to stress-corrosion have been encountered. High purity water and the use of certain tempered (heat-treated) aluminum alloys with a fine, random grain pattern are good protection against stress-corrosion.

5. The previously described cavitation erosion phenomenon associated with high heat transfer rates results in accelerated loss from the aluminum surface. This is partly due to increased solubility in the boiling heat transfer zones and partly due to spallation of the brittle oxide film.

6. Aluminum and most of its alloys react favorably with respect to corrosion while irradiated in aqueous systems.[33] Observations of lower corrosion rates than for unirradiated systems were made. The author believes that the difference in the corrosion behavior is due to formation of hydrogen peroxide and oxidizing free radicals in the radiolysis process in water. The oxidizing agents, in turn, will cause formation of an even denser protective oxide film on the aluminum surface which retards further corrosion.

Aluminum alloy 6061-T6 satisfied most of the fabrication, strength, fatigue and corrosion criteria and was selected as module material. Rigid control of water purity is essential for long-term operation. The water should be kept acidic; whereas a pH of 7 would favor the stainless steel, a pH of 5 would be preferable for the aluminum. The systems at SLAC show a pH of 6.2 to 6.5 and resistivity is better than 1 megohm-cm.

Finally, one should mention the transition from aluminum to stainless steel which exists in various locations. Commercially available brazed transition pieces were used. In that application, aluminum is in direct contact with stainless steel, except for the brazing material interface, and a potential hazard exists.

Design feature highlights

Both the collimator and the slit have variable aperture openings. The collimator is formed by placing two slits in series with the second rotated 90° with respect to the first about the common axis. A slit is 30 radiation lengths (≈ 5 meters) long, so each one had to be built up from modular sections for fabrication and alignment reasons. Typical modules are shown in Figs. 20-8 and 20-9.

A total of eleven modules are assembled to a strongback to form a jaw, and two opposing jaws form a slit. Figure 20-10 shows a partially completed horizontal slit. It is desirable to build these devices as short as possible since space is at a premium. The length can be optimized if the governing wall thickness between adjacent holes as well as the vacuum interface is tailored

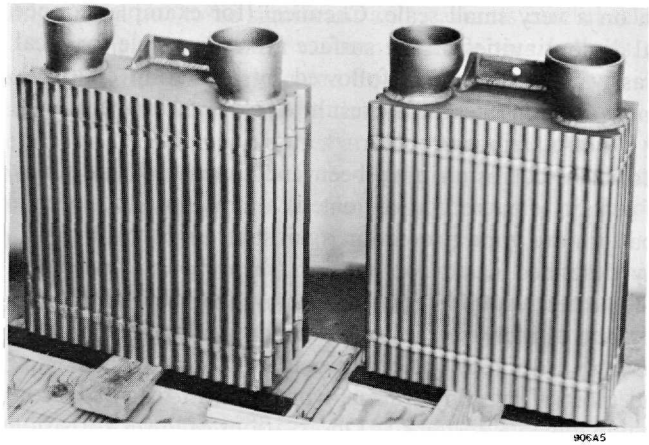

Figure 20-8 Front view of high-power slit modules.

according to shower development and attenuation. This was done for economical reasons in discrete steps rather than continuously. Thus, the ratio of aluminum to water and, therefore, the effective Z is increased downstream from the shower maximum in favor of aluminum according to shower attenuation.

Figure 20-9 Top view of slit modules.

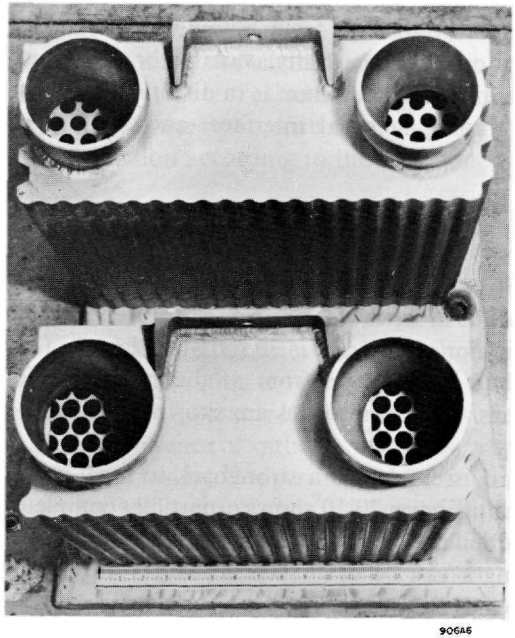

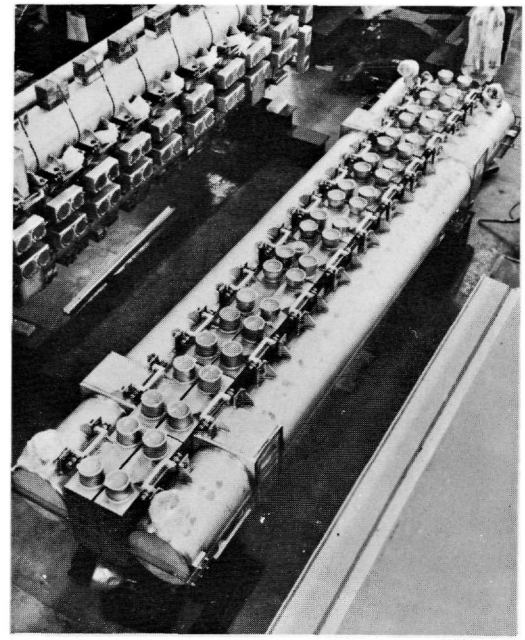

Figure 20-10 Horizontal slit module–strongback assembly (SL-10) with vertical slit assembly (C-1-V) in background.

Each module floats axially with respect to the strongback on linear ball bushings; this allows for thermal expansion between strongback and power-absorbing modules, and the strongback can properly maintain the straightness of the beam-defining edge. The strongback is fabricated from stainless steel Type 316-L as a hollow circular cylinder for maximum torsional rigidity. It is used as water inlet manifold and its temperature remains essentially constant during operation. Only the last module is rigidly connected to the strongback via the water inlet pipe and all modules are in series in the water loop.

A double pantograph assembly (parallelogram linkage) is used to provide center-line stability. The link between two opposing pantographs is made for zero backlash with high-strength, low-stretch aircraft cables, Fig. 20-11. Spherical ball-journals connect pantograph arms and strongback. They allow differential gap opening between front and back of the slit jaws which may be used to accommodate angular divergence of the beam. Proper assembly of two opposing jaws allows nesting of the module convolutions, i.e., no line-of-sight is possible, and a slit can be used as a beam stopper (for principle, see Fig. 20-7). In order to protect equipment downstream of the collimator or slit from excessive radiation and to minimize the possibility of halo (penumbra) formation behind the beam-defining edge due to the low-Z aluminum–water combination, a set of 9.5-radiation-length copper modules

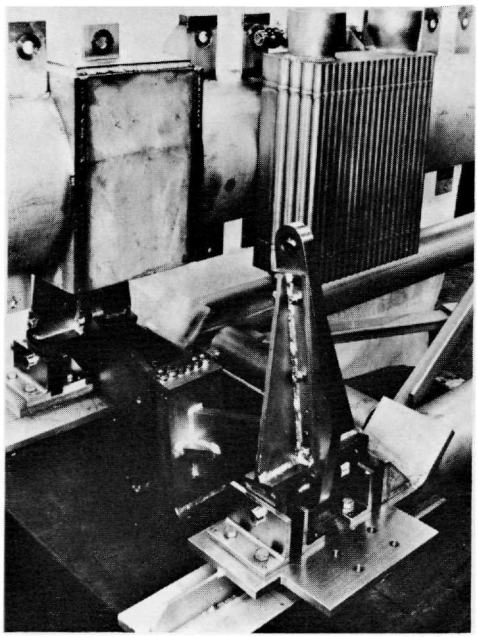

Figure 20-11 Strongback–pantograph assembly of high-power slit.

was installed. They are bolted to the last aluminum module and cooled by conduction only.

The completed slit assemblies were pneumatically pressure tested to 100 psig, using dry nitrogen. They were then placed in a vacuum tank, where they are operated by means of two actuators attached to the front and back of one jaw. The operating vacuum in the slit tank is approximately 10^{-5} torr. The assemblies were leak-checked with a helium mass spectrometer. No leaks were detected at the highest sensitivity of the instrument, 10^{-10} standard-cm^3 He/sec.

Thermocouples are connected to the copper blocks to monitor their temperature. Secondary-emission monitor foils are installed in front and back of each jaw. Figure 20-12 shows SEM foils attached to the front of a slit and the associated copper-jacketed, mineral-insulated (MgO) cables which serve to bring the signals out of the vacuum and radiation environment. The reason for the cable coils is to minimize bending stresses during aperture adjustments and, thus, to prevent fatigue failure. The SEM foils are used for protection of the jaws in front and for monitoring losses at the back. In the case of a slit they can be used for rough monitoring of drift in the momentum spectrum.[34] A more detailed description is presented in Chapter 19.

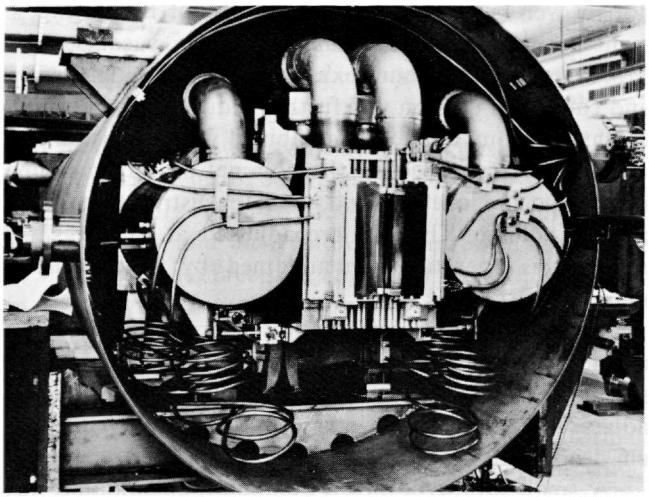

Figure 20-12 Front view of high-power slit (SL-10). Slit assembly placed in the vacuum tank, with secondary-emission monitor foils.

Modules and their fabrication

As already indicated above, eleven individual modular elements make up a slit jaw. The first six modules are identical and the water-to-vacuum wall thickness is $\Delta r = 0.127$ cm (0.050 in.). Note that for 20-GeV electrons the shower maximum occurs at the beginning of module No. 4. Modules No. 7 and 8 are identical and $\Delta r = 0.305$ cm (0.120 in.). Module No. 9 has $\Delta r = 0.760$ cm (0.300 in.), and the last two modules are again identical with $\Delta r = 1.520$ cm (0.600 in.).

The modules were manufactured from high-quality aluminum blocks which were forged, stress-relieved, and tempered to a T-6 condition. Each module consists of 3 parts: a 30-cm-high module body and two flow headers. The machining of 30-cm long holes of 1.6 cm diameter presented many difficult problems. Tolerances on hole position and parallelism had to be held very closely to satisfy temperature, Eq. (20-20), and corrosion criteria. Different techniques were investigated, including gun drilling, electric-discharge milling (EDM), and electrochemical milling (ECM). The problem was finally successfully solved with a tape-controlled, deep-hole drilling technique. The flow headers were welded to the module body with an electric arc (TIG) method for thin walls and with the electron beam welder for thick walls. Full penetration was required to minimize crevice corrosion and notch sensitivity problems. Total leak rates in excess of 10^{-9} standard-cm^3 He/sec were cause for rejection.

The reasons for the height and depth of the modules are as follows: radiation damage due to high-energy electrons penetrating the aluminum is

not yet well known. For doses in excess of 10^{16} ergs/g, significant embrittlement is known to result from dislocations, vacancies, and interstitial atoms. Moreover, the aluminum oxide film may spall in the area of high heat flux, and cavitation erosion will further reduce the wall thickness. An increase in height of the module body combined with provision for vertical adjustment of the slit with respect to the nominal beam center line allows for various beam exposure locations and, thus, for distribution of the radiation dose over a large volume. The slits are adjusted at 10^{10} ergs/g. Center-line stability during this operation is maintained by two guideposts mounted on the main support frame.

The module transverse depth is determined by radial shower development considerations, maximum transverse beam excursion, and beam momentum spread. A maximum transverse flux of 1 W/cm^2 leaving the module plane adjacent to the strongback was set as criterion. The modules were made 16.5 cm deep to satisfy this condition.

A small prototype of an aluminum slit module was tested for thermal shock[17] in the Astron accelerator at Lawrence Radiation Laboratory in Livermore. This high-intensity machine can produce bursts of very high power density over short periods of time. The peak power density was achieved by a beam of $E_0 = 3.8$ MeV, $I_{peak} = 90$A, pulse length $= 0.3 \times 10^{-6}$ sec, pulse repetition rate = 5 pulses/sec, and beam diameter = 1 cm. The resulting local heat flux is low compared to the design criterion. Much more spectacular is the rate of energy deposition during the pulse, which gives rise to very steep temperature gradients in space and time, resulting in proportional thermal stress gradients. For this run the rate of energy deposition during the pulse in the module wall was 600,000 kW/cm^3. Although very high in comparison with such values from other accelerators, this power deposition was not high enough to damage the aluminum. No effect on the module wall was visually detectable after several hours of beam exposure. Thus, even for a well-focused SLAC beam, no thermal shock and spallation problems (beyond spallation of oxide films) are expected for the high-power slit and collimator.

Fabrication and alignment

The slits were assembled in the SLAC fabrication facilities. The internal slit assemblies were built in a clean room, using methods which are considered good practice for handling of vacuum equipment. Particular attention was focused on the alignment of the beam-defining plane formed by the convoluted face of all the modules. The latter were optically aligned flat to ± 0.015 cm. As was mentioned earlier, the dispersion at the slit due to the first bending magnet group is 0.15%/cm. The completed slit assembly was tested for alignment hysteresis under vacuum. Hysteresis up to 0.013 cm was recorded.

The horizontal and vertical slits of the collimator are tied to laser beam stations. The relationship between the slit center line and the laser beam center line was established in the shop. A Fresnel target allows positioning of

the slit such that its center line coincides with the nominal electron beam center line. This is discussed in more detail in Chapter 22.

Assurance concerning the actual location of each slit and its center line is obtained in three different ways:

1. Second level optical survey in the switchyard is used to position each slit with respect to an external reference. Tooling balls and mirror stages (see, for example, Fig. 20-13), rigidly mounted to the external structure of the slit, were set during assembly and have known distances and rotations with respect to the slit center line. Precision alignment jacks allow adjustments to 0.003 cm accuracy.
2. The two slits of the collimator (as well as the high-Z collimator) are connected to laser beam target stations as described above. A laser survey can detect deviations of 0.001 cm.
3. The electron beam can be used as a survey tool to ascertain such information as rotation of the slit about an axis normal to the beam center line and comparison of center-line location of high-Z and high-power collimators or slits. This information is obtained using two steering magnets to deflect the beam across the front face of the slit. The beam current transmission is then measured as a function of magnet current. Differences of 0.005 cm can be detected.

Figure 20-13 High-Z collimator (C-0) with high-power collimator (horizontal slit C-1-H) as installed in the beam switchyard.

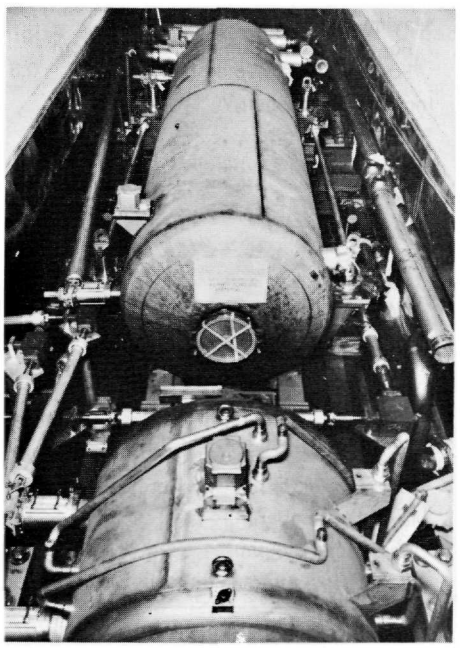

Operations to date

Although power levels encountered to date (July 1967) have been low, operations of high-power slits and collimators for the first 12 months have been essentially faultless. Up to approximately 50 kW of average beam power has been dissipated. Reproducibility of aperture width and center line of a 5-meter long slit of ± 0.03 cm has been achieved.

The primary radioactive water system is similar to the one for the high-power beam dump and will not be discussed in further detail. Hydrogen recombiners are planned for installation in the near future.

The question of whether or not the low-Z and large physical length of these slits have a negative effect on beam analysis and definition has not yet been investigated. However, the limited number of physics experiments conducted so far has not uncovered any deleterious effects.

20-6 High-Z slits and collimators (WSS, DRW)

Variable-aperture, low-power, high-Z slits and collimators were designed and built to serve as backup devices for the high-power units. The slit material is copper and properly only medium Z, but the term "high Z" was used to distinguish these devices from the high-power units described in the previous section. Two collimators and two slits are now in use: a collimator (C-0) immediately upstream of the high-power collimator (C-1), a photon beam

Table 20-6 High-Z collimator and slit criteria

Maximum average beam power	
For minimum beam size, $\sigma_b < 0.3$ cm	20 kW
For average expected beam size, $\sigma_b \geq 0.3$ cm	40 kW
Incident beam energy	$\leq$25 GeV
Pulse repetition rate	1–360 pulses/sec
Beam sizes (see Table 20-5)	
Maximum aperture opening	$b_x = 15.0$ cm
Total length	35 radiation lengths
Materials	
Modules	OFHC copper
Water piping	Everdur 1015, stainless steel Type 316-L
Vacuum shells	Stainless steel Type 304-L
Maximum water pressure	175 psia
Water flow velocity in prime heat transfer areas	$\geq$150 cm/sec ($\approx$5 ft/sec)
Minimum flow rate for full power	34 liter/sec ($\approx$10 gal/min)
Maximum water inlet temperature	40°C
Maximum temperature rise	$\approx$25°C
Operational vacuum	10^{-4} torr or better
Aperture is remotely adjustable during beam operation	

collimator (C-10), and two slits (SL-11, SL-31) for momentum definition in the two beams serving the major research areas. The important criteria are summarized in Table 20-6.

Design features

The high-Z collimator and photon beam collimator (which are in most aspects identical) are formed, as is the high-power collimator, by two slits in series with the second rotated 90° with respect to the first about the common axis. Both the horizontal and vertical slits of a collimator are installed in one vacuum tank because of their small physical size. Two opposing OFHC copper modules form a slit. Figure 20-14 pictures a set of modules for the collimator (C-0). They are 10 cm deep, 20 cm high, and 50 cm long. The volume close to the beam-defining edge is perforated with a row of hole pairs for proper cooling. The water passages are connected in series by means of square flow cavities milled into the copper and closed with a cover plate braced to the module. The cavity reverses the flow direction and promotes good mixing. The minimum wall thickness between the collimating surface and the flow passages is 1.0 cm. The length of the modules is thus 35 radiation lengths up to a transverse depth of 1.0 cm, and it decreases to a minimum of 15.5 radiation lengths at a depth of 1.8 cm, coinciding with the centers of the first row of holes. In order to minimize the possibility of penumbra formation in the case of the slits and the photon beam collimator, the flow channels were altered downstream from the shower maximum. At an axial shower depth such that power deposition has decreased to a low level, the two parallel flow

Figure 20-14 High-Z slit copper modules before furnace brazing.

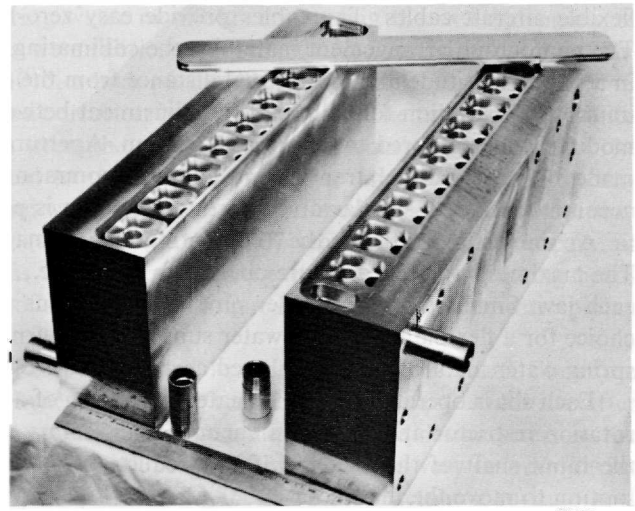

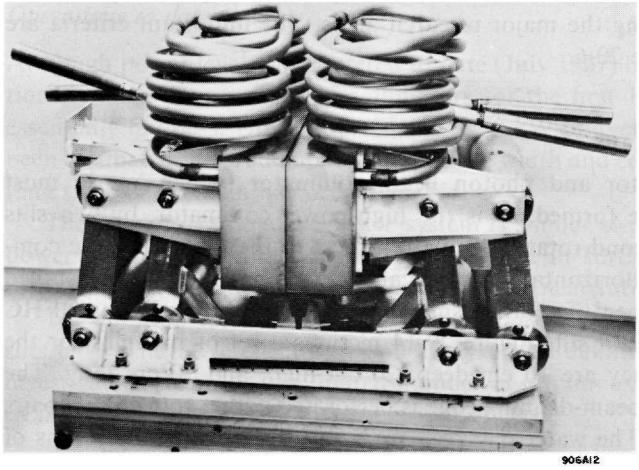

Figure 20-15 Double pantograph assembly with slit modules attached.

passages were combined into one, which is of somewhat larger diameter to keep the velocity constant. Its center is located midway between the two smaller passages. This provides an increase in Z downstream from the shower maximum in the transverse region extending from 1.0 cm to the flow passages.

The modules are mounted to a four-pivot point or double pantograph assembly as illustrated in Fig. 20-15. The pivot points are mounted on tapered roller bearings to allow adjustment for zero backlash. The two halves of the pantograph assembly are cross-connected with low-stretch, high-strength, flexible aircraft cables. The cables provide easy zero-backlash adjustment. The pantograph arrangement maintains the collimating faces of the modules in a parallel attitude and at an equal distance from the center line. The maximum total variation for full aperture adjustment between any two opposing modules was measured to be about 0.006 cm. Aperture adjustments can be made only as parallel translations about a common center line, i.e., no accommodation to angular divergence of the beam is possible.

An interesting feature is the "coil-spring" water manifold, see Fig. 20-16. The maximum possible aperture opening is 15 cm, i.e., 7.5 cm translation for each jaw. Small stroke and other physical limitations make bellows a poor choice for a flexible link in the water supply and return lines. Thus, the coil-spring water manifold was developed as an alternative to bellows.

Each slit is operated by one actuator consisting of a precision jack with a rotation restrictor and a bellows vacuum seal. Rotary motion is supplied to the input shaft of the jack for 100 : 1 reduction and creation of the linear motion to move the modules.

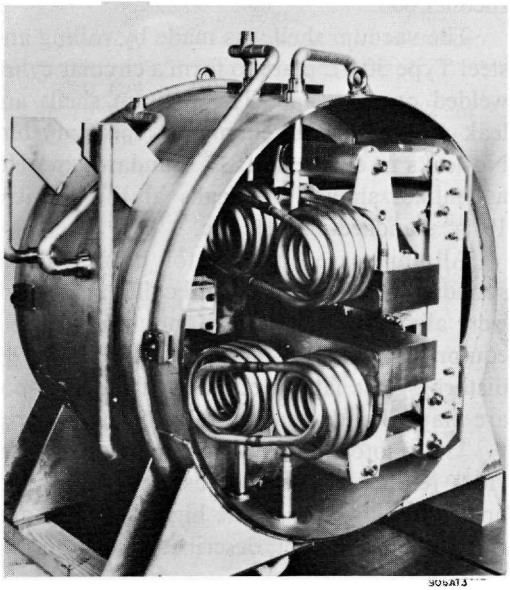

Figure 20-16 High-Z collimator (C-1, C-10); vacuum tank installation with view of "coil-spring" water manifold.

Fabrication and material selection

The modules were machined from solid forgings. To assure soundness in the furnace-brazed joints and prevent hydrogen blistering, OFHC copper was selected. The coil-spring water manifolds connecting the external piping to the movable modules were fabricated from extruded electrical conduit. The material is Everdur 1015, a high-purity silicon bronze. It was selected for its high strength and good corrosion behavior in water. The tube work-hardened and achieved its high strength and elasticity in the coil-bending process. The coils were hand-brazed to the module to confine annealing to the brazing joint. After all brazing was completed, the coil-module assemblies were shot peened with small glass beads (0.002–0.007 cm) propelled by 60 psig air pressure. Brazed areas received prolonged exposure to the impinging beads to assure restoration of strength and fatigue life. The rest of the water piping is stainless steel, Type 316-L.

The pantographs were fabricated as welded structures from aluminum alloy 6061, solution heat-treated and tempered to the T-6 condition after welding. To maintain stability the maximum allowable design stress in the pantograph assembly was set at 3500 psi. This compares very favorably with a yield strength of 40,000 psi for alloy 6061-T6. The actuator vacuum seal

bellows are of the welded diaphragm type, fabricated from 0.015-cm thick Inconel 600.

The vacuum shell was made by rolling and welding 0.8-cm thick stainless steel Type 304-L plate to form a circular cylindrical vessel. Dished heads were welded on each end. The vacuum shells and slit assemblies were vacuum leak checked with a helium mass spectrometer at various stages of fabrication. No leaks in excess of 10^{-8} standard-cm^3 He/sec were allowed and all final assemblies showed no leaks at the sensitivity limit of the spectrometer, 10^{-10} standard-cm^3 He/sec.

All units except the photon beam collimator are mounted on the corresponding high-power slit and collimator support frames; see Fig. 20-13. They were aligned at the time of mounting to be coincident with the high-power equipment. Small lateral adjustments of ± 2.5 cm can be made without disturbing the lateral position of the high-power devices. These adjustments are manual and semiremote from the upper tunnel housing.

The photon beam collimator was installed on a special frame that provides remote powered adjustment of ± 3.75 cm in both the vertical and horizontal directions. The high-Z devices are tied into the magnet cooling-water (LCW) system, described in Chapter 24.

Operational experience

Functioning of all the high-Z units has been faultless to date (July 1967). The significant difference between the Z of the "high-power" and "high-Z" slits as well as a large difference in physical length (10 : 1) should make it possible to partially answer questions concerning the influence of these parameters on slit scattering and beam halo formation.

Magnets were used to deflect the beam across the front of the partially opened high-Z B-beam slit (SL-31) and beam current transmission was measured as a function of magnet current in order to obtain beam spectra. Figure 8-17 shows the spectrum for a 6 GeV beam (obtained on February 1, 1967).

20-7 Collimator actuation and drive system (LRL, DRW)

Two types of adjustments can be made on each slit and collimator: (1) remotely controlled motorized adjustments during beam operation, such as opening and closing the slit aperture, changing the collimator aperture, or changing the beam exposure location on the modules; and (2) semiremote and manual adjustments on maintenance days, performed in the tunnel housing —this covers all alignment operations and is done solely by mechanical precision jacks.

In case of a major disturbance, such as a severe earthquake, it is possible to add or remove spacers up to ± 15 cm. Table 20-7 summarizes the important criteria with identification of individual equipment.

All remotely controlled adjustments are accomplished from the Data Assembly Building (DAB). A group of panels in the DAB houses the

Table 20-7 Actuation and alignment system criteria

Variables	*Device*	*Max. translation*	*Max. tolerance*
Gross manual positioning of support frames, transverse to the beam direction	C-0, C-1 SL-10, SL-11 SL-30, SL-31	±15 cm	±0.3 cm
Semiremote, manual alignment of support frames transverse to the beam direction	C-0, C-1 SL-10, SL-11 SL-30, SL-31	±7.5 cm	±0.05 cm
Semiremote, manual alignment of high-Z support frames in horizontal plane	C-0 SL-11 SL-31	±2.5 cm	±0.010 cm
Maximum possible aperture opening (remotely, motorized)	C-0 SL-10, SL-11 C-10 C-1	15 cm 3.8 cm	
Reproducibility of aperture and center line (including all tolerances)	All Devices		±0.06 cm
Remote, motorized alignment of photon beam collimator support frame	C-10	±3.75 cm	±0.005 cm
Remote, motorized change of beam exposure location (radiation damage distribution)	C-1 SL-10 SL-30	±7.5 cm	±0.15 cm
Maximum allowable time for aperture adjustment for all devices		1 min	
Minimum ambient temperature range capability of equipment		20°–60°C	
Radiation dose expected in close vicinity of high-power devices for full power operation		10^{12}–10^{13} ergs/g/yr	
Atmosphere may contain varying amounts of HNO_3			

controls, readouts, and warning lights. The system is built to be controlled and operated by the SDS-925 computer. This interface of the actuation system is discussed in detail in Chapter 19.

A typical remote-controlled, motorized actuation system comprises the following major components:

1. The electric and electronic interface with the DAB
2. The drive control box containing the prime mover, electromagnetic clutches, shaft encoders, potentiometers, and limit switches
3. The drive train made up of shafts, universal joints, and angle gear boxes (miter gears)
4. The actuator in the form of a precision jack to transform rotary into linear motion.

A typical alignment point is simply a precision jack coupled to an angle gear box for easier adjustment from the upper tunnel of the switchyard housing.

The prime mover and control box

The prime mover for each type of motorized drive system is an ordinary electric gearmotor. The motor and the associated equipment are contained in a partially sealed box in a wall chase in the upper tunnel of the switchyard housing. This location was selected for easy maintenance access and because the radiation levels are two orders of magnitude lower than in the close vicinity of the energy absorbers; the expected dose rate for full power operation is then 10^{10}–10^{11} ergs/g/yr. All the components in the box are of usual materials with normal lubrication. The control box can be flooded with dry instrument air if moisture or nitric acid becomes a problem.

The motor and associated equipment are operated remotely from the DAB, either manually or by computer. In the case of a jaw drive for aperture adjustments either high-speed or low-speed operation is possible. High-speed operation is necessary to satisfy the 1-min criterion for full aperture adjustment. Low-speed operation allows achievement of close tolerances. The usual aperture adjustment procedure is first high-speed operation for fast approach to the vicinity of the desired aperture and then low-speed operation for accurate adjustment. The rate of aperture change of the high-power slit (SL-10), for example, is 0.016 cm/sec for low speed and 9 times faster, or 0.148 cm/sec, for high-speed operation. The front and the rear ends of the high-power slit jaws may be driven independently or in unison.

Figure 20-17 shows a typical drive box with the cover removed. The gearmotor located in the upper-right-hand corner drives a central shaft. This shaft terminates at the high-speed electric clutch. Directly below is the low-speed clutch. The electric clutches at the upper end of the left or right drive output shaft can engage either or both shafts. To the left of each output shaft is the counter shaft. It is coupled on the top to a gray bit shaft encoder and on the bottom to a mechanical counter for local reference. The encoder makes one revolution for the full opening of the slit aperture and gives 1024 counts. Table 20-8 gives a summary of this information. To the right of each output shaft is a threaded shaft that operates the limit switches and also drives a ten-turn potentiometer for a crude aperture opening display in the DAB.

The drive train

The output shaft of a control box is connected to the appropriate actuator, located in some instances 12 meters away, by a combination of drive shafts, miter gear boxes, and universal joints. The fact that rotary motion of the output shaft has to be transmitted around several corners and transformed

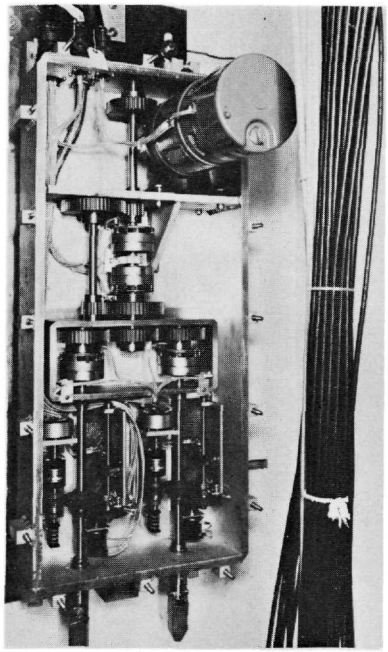

Figure 20-17 Aperture adjustment drive box.

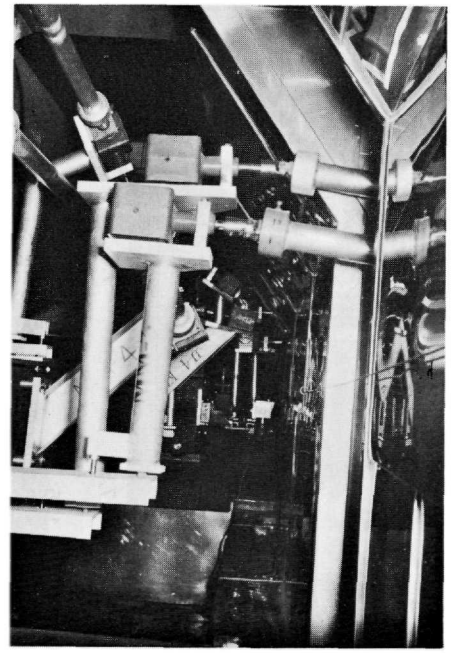

Figure 20-18 Slit, drive train, angle gear boxes and shaft disconnects.

into a linear motion at the slit with a minimum amount of backlash presented some interesting engineering design problems. The allowed accuracy tolerance was the equivalent of 0.005 cm of aperture width or 0.0025 cm of jaw position. The actuator jacks translate each input turn into a linear motion of 0.025 cm. Thus 0.0025 cm output is equivalent to 36° of shaft backlash. The actual shafting backlash achieved is about one-tenth of this figure.

The above problem becomes more complicated with the superposition of the slit tank motion requirements due to alignment and radiation-damage distribution criteria as given in Table 20-7. Figure 20-18 shows the typical solution. Most drive trains include two miter gear boxes but the solution is good for any number of boxes, provided that every second box is pivotally mounted as is the box in the center of the picture. The gear box is rigidly mounted on a stand. The stand can pivot about a pin located at its foot, and an outboard pin fitting in a slotted hole acts as a torque reaction arm. A universal joint is required on each side of the box. The remaining problem is, then, only one of geometry so that each shaft in the limits of its excursion clears the other shafts and equipment; see, for example, Fig. 20-19.

The universal joint ordinarily has one end bored and keyed to attach to a gear box. The other end is a square plug that inserts into the hub of the

Table 20-8 Slit and collimator drive system data

Characteristics	*Horizontal slit of collimator (C-1-H)*	*Vertical slit of collimator (C-1-V)*	*High power A-beam slit (SL-10)*	*All high-Z devices (C-0, SL-11, SL-31, C-10)*	*Photon beam collimator (C-10) support frame*
Maximum jaw travel ($\frac{1}{2}$ full aperture) (cm)	1.9	1.9	7.5	7.5	$x = 7.5$, $y = 7.5$
Drive box output					
Fast (rpm)	175	175	175	175	175
Slow (rpm)	19.5	19.5	19.5	19.5	19.5
Total output turns	75	57	300	327	300
Full-range total turns					
Encoder	1.0	1.0	1.0	1.0	1.0
Counter	150	150	150	150	150
Least count (per jaw)					
Encoder (cm)	0.0018	0.0018	0.0074	0.0074	0.0074
Counter (cm)	0.002	0.002	0.010	0.010	0.010
Full range adjustment time					
Fast (sec)	25.7	19.5	103	112	—
Slow (sec)	231	175	926	1010	926
Aperture closure rate					
Fast (cm/sec)	0.148	0.195	0.148	0.136	—
Slow (cm/sec)	0.0162	0.0217	0.0162	0.0152	0.0162

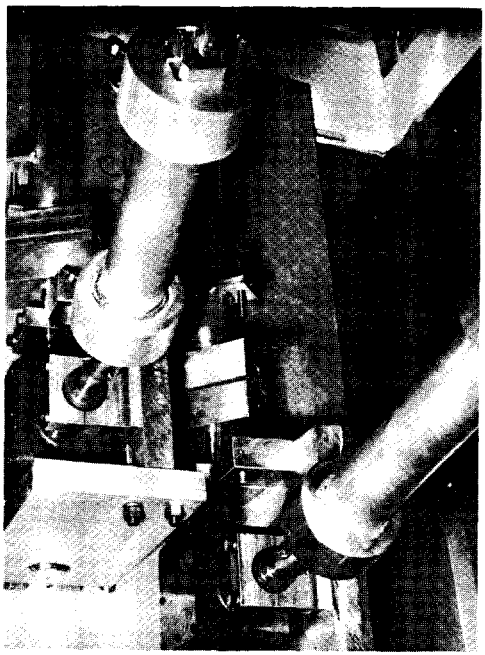

Figure 20-19 Slit drive train components (shafts, universal joints, angle gear boxes).

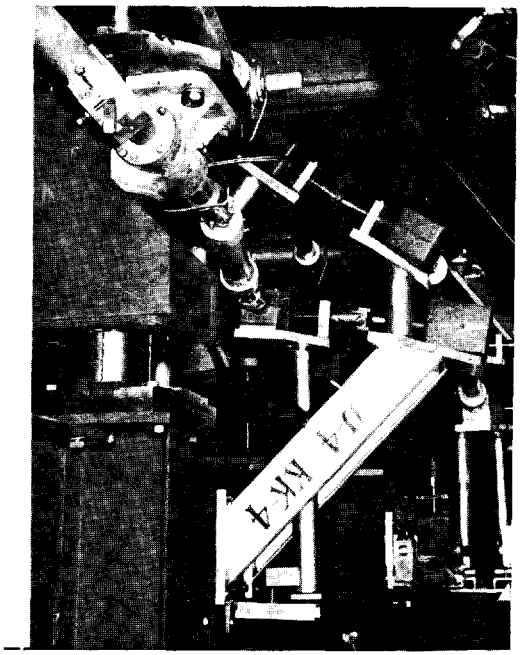

Figure 20-20 Guidepost, support jack and drive train for high-power collimator.

connecting shaft; see Fig. 20-20 at the top of the picture. The insertion depth is determined by a projecting pin on the side of the square and the shaft is retained by a screw bearing across the corner of the square.

In some instances the drive unit at each end of a drive shaft is fixed in location such as between jacks for radiation damage distribution, or between the drive box on the wall and the gear box below and on the same wall. In these applications the shafts are attached at one end with a universal joint, and the other end uses a T-slot termination; see Fig. 20-20 in the middle of the picture. The T-slot may be slid out of engagement after the keeper pin is pulled. Assembly and disassembly of drive train components can be done semiremotely from the upper tunnel housing.

The actuator

A commercial screw jack would be ideal for this service if it could be demonstrated that the mechanism would not jam after the lubricant has deteriorated due to radiation damage. Dose rates of 10^{13} ergs/g/yr are expected near the actuators for full power operation. This is too high for organic lubricants. However, historically accelerators do not operate at full power for the first

year or longer, and in the early stages they are not operated continuously either. Under these conditions a radiation-resistant organic lubricant might last for 6 months, 1 yr, or even longer. Radiation-resistant organic lubricants were irradiated at SLAC[30] with 5-Mev electrons. A polyphenyl ether appeared to be useful for switchyard applications for doses up to 10^{12} ergs/g. Its basic chemical structure is the benzene ring, known to be highly radiation resistant. This lubricant was used in applications where there was sufficient operating moment to shear through the polymerized resinous residue left by the decomposition of polyphenyl ether due to radiation.

Jamming is a combined geometry and lubrication problem. This is true for both rotary machinery and linear devices. A common trick for rotary machinery is, as in the case of the pivot wheel of a watch, to reduce the radius of the bearing to a point. The frictional moment, i.e., force times lever arm, is essentially zero even for high frictions because the lever arm is nearly zero. Unfortunately, for appreciable loads one has to have big bearings and the operating force must be applied at a large radius to prevent self-locking or jamming. Thus, designs for unlubricated applications become extremely bulky.

With these ideas in mind, a commercial jack actuator was modified and tested under various operating conditions. Leaded tin bronze is commercially available to fabricate unlubricated bearings. The jack worm gear was thus made of 10% leaded bronze. This gives control of the friction between the worm and the worm gear, and between the worm gear and the screw. The existing tapered roller bearings were replaced by ball bearings with a leaded bronze ball retainer. A leaded bronze retainer was also added to the thrust bearings. This modified jack operated, then, with input torques 1–3 times that of the normal lubricated jack for a life equal to at least 1 yr of service for the slit application.

The tests proved that the jacks would not suddenly become inoperative when the polyphenyl ether had polymerized. The wear of unlubricated jacks was very severe and it emphasized that the jack should be operated with a lubricant as long as possible. Up to date (July 1967), no jack has failed and all jacks are lubricated with polyphenyl ether. Since the leaded bronze is not resistant to nitric acid, each jack has a connector for admitting dry compressed air in case HNO_3 should become a problem.

Reproducibility

The aperture opening and center-line position are quite critical, particularly in the case of a momentum-defining slit. The drive should be as reproducible as possible. Momentum resolution is desirable to an accuracy of $\pm 0.01\%$ $\Delta p/p$ which amounts to approximately 0.062 cm (A-beam slit, SL-10). This rather generous figure disappears rapidly when all the contributing elements are added. Table 20-9 lists measurements for a high-power slit. One should note that the figures do not include any survey error.

Table 20-9 High-power slit tolerance and reproducibility data

Variables	*Tolerances (cm)*
Looseness of pivot joints in tank	$\leq$0.020
Jack output antibacklash	$\leq$0.005
Jack input (equivalent output backlash)	$\leq$0.010
Encoder least count	0.0075
Drive train backlash	$\leq$0.0025
Tank guidepost clearance	0.010
Frame adjustment ways	0.0075
Frame lateral jack backlash	$\leq$0.005
Lateral jack mount	$\leq$0.010
Total	0.0775

It may seem ridiculous to allow only 0.0025 cm of equivalent jaw error for a drive train from the tunnel below to the drive box in the upper tunnel housing and then at the same time give away 0.010 cm for a simple sliding pair such as the tank guidepost, seen, for example, in the left center of Fig. 20-20. However, the decisions are valid, and will be discussed in more detail directly below.

Dry friction and wear of materials

As has been pointed out above, situations can occur where rolling or sliding parts have to operate in a high-radiation environment containing varying amounts of nitric acid. Experiments were conducted at SLAC[17] to evaluate promising material pairs. The goal was to find corrosion resistant materials that can slide and roll dry, unlubricated, at minimum clearances, without galling or seizing and which show minimum wear. The vital part of the experimental apparatus consisted of a 3.75-cm diameter shaft rotating under 80-lb load in a 3.75-cm long sleeve bearing at 8 rpm. All experiments were conducted in air and at room temperature and were to establish minimum operating clearances.

Selection of material pairs was according to known friction and wear criteria. Dry friction always causes wear, but hard materials wear less than soft ones. Materials should have high moduli of elasticity, high recrystallization temperature, and resistance to plastic flow in order to minimize galling and seizing. A hardness of at least Rockwell C-42 appears to be required. Furthermore, a lamellar structure as found in dry lubricants such as molybdenum and tungsten disulfides and diselenides, graphite, and others is desirable. Slip between low shear strength layers causes formation of lamellar particles, and a hexagonal lattice structure has just this property. The selection

of materials was considerably aided by a recent book.[35] The concept that the equilibrium surface roughness and the wear particle size of a sliding or rolling pair is related to the surface energies of the two materials divided by the surface hardness is extremely useful where it is necessary to hold close tolerances. It is also shown that hexagonal lattice structure metals apparently did not have coefficients of friction higher than 0.6.

Attention was focused on finding and evaluating corrosion resistant, high strength materials having hexagonal lattice structure. Cobalt and titanium alloys performed remarkably well. Stainless steel 440-C hardened to Rockwell C-56, although not of hexagonal structure, made an excellent compatible material with the α-titanium alloy, Ti–5Al–2.5Sn. Stainless steel 440-C and Stellite No. 6 (Co-28 Cr-4W) also formed a very good material pair. Moreover, the experiments have shown that for these hexagonal materials it is not necessary to have dissimilar materials in the pair. Material pairs where both the shaft and the sleeve bearing were composed of stainless steel 440-C, Stellite No. 6 or α-titanium alloy (Ti–5Al–2.5Sn) performed very well. A selected material pair was considered a success if it survived 10^4 cycles without seizing for clearances <0.006 cm. Successful operations with clearances as low as 0.0018 cm were achieved. In contrast, 300 series stainless steels will fail with any practical clearance. For compatible materials, the minimum clearance is determined by the size of the wear particles and equilibrium surface roughness. If a material pair is compatible, it will establish its own characteristic equilibrium surface roughness regardless of the initial surface finish of each individual material. Having thus established compatible material pairs, dry lubricants can be used to lower the coefficient of friction, depending on application. But because of the thinness of dry lubricant films they cannot be relied on for successful operation; they are just an added bonus. The nonwelding properties of hexagonal lattice metals as found above have meanwhile been confirmed.[36]

Material selection

The materials for the drive system components were chosen according to preceding considerations and also according to price, delivery, and commercial availability.

For these reasons the gear boxes were of commercial cast steel frame. The shafts and gears were stainless steel and the bearings were graphite bushings. The graphite bushings require no lubrication; the moisture in the atmosphere is sufficient to keep the coefficient of friction low and the wear reasonable.

The stainless steel miter gear operating against another stainless steel gear was recognized as a poor choice, but delivery and manufacturing costs dictated this compromise. The gear teeth are lubricated with spray-on molybdenum disulfide. Replacements in the future should be a titanium gear against a stainless steel gear.

The universal joints were made of stainless steel with titanium pins and washers so rotating pairs are always stainless steel against titanium. Clearances are 0.012–0.028 cm.

Bearings and friction surfaces within the vacuum shells were surface coated with a low-coefficient of friction layer of tungsten disulfide. The latter was sprayed onto the surface at very high velocities. To date no wear failures or seizures have occurred in the slit and collimator drive system.

20-8 Protection collimators (AHK, DRW)

Protection philosophy and beam transport system problems

The many sizes of apertures through the beam transport system components in the BSY have resulted in a vacuum envelope of rather complex geometry. This fact, coupled with the high-power density characteristics of the accelerator, required that considerable attention be given to the possibility of damage to these components and the vacuum pipes resulting from excessive power deposition or excessive exposure to primary radiation. A protection scheme was developed[34,37] to minimize the probability of serious damage to transport components. It utilizes water-cooled, fixed-aperture protection collimators, ionization chambers, temperature sensors, and threshold current monitors strategically located throughout the BSY. All are interlocked to shut off the accelerator should the local beam losses or local temperature rises exceed predetermined levels or should the total beam loss reach an intolerable level.

There are several operating conditions in which primary beam or radiation can reach the vacuum envelope and beam transport components on either a continuous or transient basis. The most significant source of continuous power deposition in this equipment is due to the presence of particles of unwanted momenta in the spectrum of the beam. If the maximum deviation from a nominal momentum in the A-beam and B-beam transport systems were $\pm 1.3\%$ and $\pm 2.6\%$, respectively, the electrons would pass through the BSY (for slits open) without any power deposition at all. Unfortunately, the beam always has, to varying degrees, low and high momentum tails which become progressively more dispersed as the beam passes through the BSY bending magnets. The amount of power associated with these tails at any time depends on the operating conditions of the accelerator.

When the jaws of the high-power collimator and slits are intercepting the beam, radiation emanates from them and, hence, represents another source of continuous power deposition. Much of this radiation can reach components or vacuum chambers downstream, either because of a large angle of divergence or because of dispersion by bending magnets. An attempt[37] was made to estimate the amount of radiation emitted from the collimator (C-1) during transmission of a high-power beam. For the case of a 20-GeV, 2-MW average power beam, assumed to have a uniform power density to a radius $r_b = 0.3$ cm,

and the center of which is coincident with the edge of one of the aluminum jaws of the collimator, the following estimates were arrived at:

1. Most of the cascade shower particles re-entering the vacuum envelope are of rather high momentum with less than 10% having momenta below 2.5 GeV/c.
2. Leakage out of the jaw in the form of electrons and positrons amounts to 24 kW, and a leakage of 16 kW is due to photons
3. The power figures are order of magnitude but probably low due to the effective low-Z of the aluminum–water composition of the slit modules
4. Further, the power figures are low because the number of particles to be considered will increase with small misalignments and distortions, and they are also low because for a nominal angular divergence of $\Delta\theta = 10^{-4}$ radian, electrons are incident over the full length of the 5-meter long jaw.

Additional conditions that can lead to continuous or transient power deposition in the BSY vacuum envelope are (1) misalignment of components which may expose surfaces to the beam which are normally not exposed; (2) mis-steering of the beam; and (3) magnet malfunction or failure.

The vacuum envelope in the BSY is almost entirely made of 300-series stainless steel. Exceptions are (a) the aluminum vacuum chamber between the bending magnet B-2 and protection collimators PC-10 and 30 (for locations, see Fig. 17-1) and (b) the vacuum chambers in the pulsed magnets PM-1 through PM-5, which are ceramic. The low thermal conductivity of the stainless steel, coupled with its medium-Z property (see Table 20-2) does not permit much power deposition before physical damage occurs from excessive thermal stresses or melting.

To illustrate the heating problem in stainless steel, consider the case of a 20-GeV electron beam with 100-kW average beam power and $\sigma_b = 0.3$ cm impinging on a solid block of 300-series stainless steel. At the shower maximum the average power deposited is readily computed from a modified form of Eq. (20-6) to be $P' = 6.9$ kW/cm (using values for iron, which has approximately the same Z and ρ as stainless steel). For a beam PRR of 360 pulses/sec the temperature rise per pulse in stainless steel is then about 7°C as can be seen either from Eqs. (20-5) and (20-6) or from Table 20-2 by proper scaling. At a repetition rate of 360 pulses/sec, the low thermal conductivity of stainless steel does not permit adequate heat diffusion between individual pulses and, hence, the temperature builds up rapidly.

The power loss from a dispersed or mis-steered beam in most places in the BSY is distributed in the horizontal plane along the length of the vacuum chambers in the magnets and interconnecting vacuum pipes. In general, the beam height is small and, thus, the heat generation may be assumed to take place in a line source along the length of a chamber or pipe.

Assuming power deposition on one side of a pipe, the heat flow from the source in the circumferential direction of the pipe may be deduced from the equation of heat flow in a fin which is of finite length and insulated at

its end.[38] The heat transfer per unit length of pipe to the surrounding atmosphere is

$$q' = 2(t\bar{h}k)^{1/2}(T_s - T_\infty)\tanh \pi R\left[\frac{\bar{h}}{(kt)}\right]^{1/2} \tag{20-28a}$$

where

t is the wall thickness of the pipe
$\bar{h}$ is the average coefficient of heat transfer by natural convection and radiation
k is the thermal conductivity of the pipe material
R is the radius of the pipe
T_s is the maximum metal temperature at the source
T_∞ is the ambient temperature of the surrounding atmosphere.

Since the thermal conductivity of stainless steel is low, this equation reduces to

$$q' = 2(t\bar{h}k)^{1/2}(T_s - T_\infty) \tag{20-28b}$$

for all sizes of pipe over 15 cm diameter. If a metal temperature rise over the ambient of $(T_s - T_\infty) = 150°C$ is permitted and if an average heat transfer coefficient of 1.4 W/(cm^2 °C) is assumed, the power deposition along one side of a stainless steel pipe can be only about $P' = 3.7$ W/cm.

In the BSY there are several hundred vacuum couplings which use an indium gasket to make the vacuum seal. Because of the low melting point of indium, an upper limit of 80°C was placed on the local temperature so that the softening and consequent change in the flow properties of the indium would not result in a vacuum leak. With respect to the ambient, this maximum local temperature corresponds to a temperature rise of about $(T_s - T_\infty) \approx$ 50°C. The radial thickness of the vacuum coupling flange is 2.5 cm and thus provides a larger area to conduct heat away from the source in the circumferential direction than does a pipe. However, with the lower limit on the maximum allowed metal temperature, a local power deposition of only about 3 W/cm can be permitted along the coupling.

In a few areas of the BSY it was possible to minimize the potential amount of power deposition by making the vacuum pipes sufficiently large. Space limitations and availability of quick-disconnect vacuum couplings, however, greatly restricted this design. A nominal 30 cm diameter was the largest-sized coupling used in sufficient numbers to be economical to produce.

In most instances, the beam transport components have very limited aperture sizes. Rather small gaps are used in the bending and quadrupole magnets for reasons of economy. The differential pumping system oil trap which divides the accelerator and BSY vacuum systems had to be restricted to a 2.5-cm aperture for functional reasons, but it introduced a constriction in this area. The microwave beam position monitors in the BSY were limited to a 5-cm diameter aperture which could be increased only at the expense of a great loss in sensitivity. Furthermore, any beam power deposition in these

monitors had to be avoided, since a temperature change[34] of more than 5°C can cause the cavity output voltage to vary more than the desired maximum of $\pm 1.5\%$.

Beam trajectory and beam envelope studies

The devices most effective in providing equipment protection in the BSY are the fixed-aperture protection collimators (PC's). These operate by directly intercepting any beam electrons and/or scattered radiation which have the potential for causing damage. Figure 20-21 is typical of the kind of studies that were made to arrive at the proper choice of apertures and of locations for the PC's. In particular, Fig. 20-21 is a study of the beam trajectories between PC-10 and the symmetry quadrupole Q-12, which led to the specification of the aperture sizes and locations of PC-10, 18, and 11 in the A-beam line. (For layout convenience, the 12° bend in the beam was straightened out and, hence, required that the vacuum chambers through the bending magnets B-10, 11, 12, and 13 be shown curved.) These studies also led to the specification of locations for mounting surface temperature sensors on vacuum chambers and for placing ionization chambers. The design beam used in these studies had a radius of 0.3 cm and a divergence of $\Delta\theta = 10^{-4}$ radian at the pulsed switching magnets PM-1 through PM-5. The layout shows that the horizontal width of the aperture through PC-10 was dictated by both the position monitor P-10 and the quadrupole magnet Q-11. The design momentum deviation that PC-10 passes is $\pm 2.65\%$, assuming it is properly aligned, and it intercepts all electrons on the low-energy side between 2.65 and 20.5%.

Figure 20-21 A-beam trajectory study, PC-10 to Q-12.

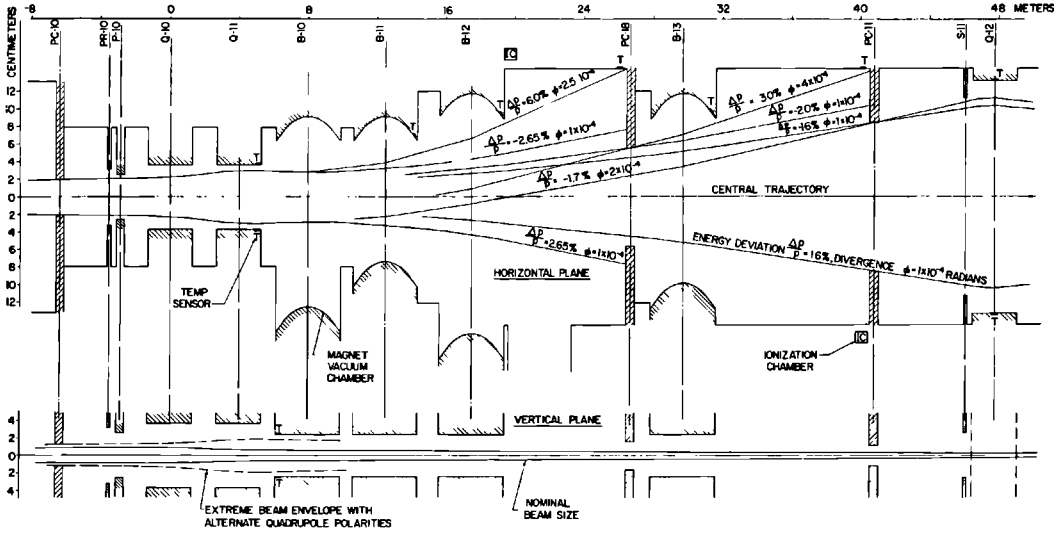

Any lower-energy electrons are incident with a very low power density over the length of the vacuum chamber between the pulsed magnets and PC-10. The electron beam can impinge on the downstream end of the vacuum chamber in Q-11 when there are (1) nonnominal field settings in the quadrupoles (e.g., stronger horizontal defocusing in Q-10) and (2) relative misalignments. Temperature sensors for protection of the vacuum chamber are installed on each side and interlocked to shut off the accelerator if the temperature reaches the trip level.

As the beam passes through the bending magnets B-10 through B-13, it becomes further dispersed. The layout showed that the vacuum chamber in B-13 was quite exposed to power deposition, and, therefore, PC-18 was installed. It passes a momentum deviation of $\pm 2.00\%$. A smaller aperture and resulting transmission of a narrower momentum spectrum would increase the probability of intercepting significantly more power at a very high power density (because of the closeness of the edge of the aperture to the center of the momentum spectrum). It also would make PC-18 more sensitive to transverse misalignments. The PC-11 was installed to protect the quadrupole magnet Q-12 and the instruments located in front of it. It passes a momentum deviation of $\Delta p/p = \pm 1.60\%$ from the design beam. It was located 7 meters upstream from the center of Q-12 in order to eliminate the need to water-cool the vacuum pipe in this area. The pipe size was limited by the largest vacuum coupling size available, i.e., 30 cm diameter. To locate PC-11 further upstream would have made it more sensitive to transverse misalignments, which would result in increased exposure to high power density. Downstream of Q-12, the slits intercept all power arriving outside their aperture but passing through PC-11.

Slight misalignments or bending errors may cause the exit ends of the vacuum chambers in B-11, 12, and 13 to be exposed to small steady power depositions. Therefore, temperature sensors were installed at these locations to detect any abnormal temperature buildup. For the same reasons, temperature sensors were installed near the upstream ends of PC-10, 11, and 18 to protect the indium-sealed vacuum couplings. To guard against any sudden large power depositions due to steering errors or magnet malfunctions, ionization chambers were installed at the exit of B-12 and in front of PC-11.

Because the large bend angles occur only in the horizontal plane, there is no beam dispersion or gross missteering capability to protect against in the vertical plane. Attention was given to effects in the vertical plane caused by possible small missteering or from scattering of electrons caused by insertion of a profile monitor into the beam.

The layout in Fig. 20-21 shows that the vertical aperture in PC-10 was designed to protect the entrance of B-10 when Q-10 and Q-11 are operating opposite to the present polarity (which happens to be the case in the B-beam). Only a small clearance was allowed between the beam and the entrance to the vacuum chamber in B-10 so that the vertical aperture in PC-10 was not unduly reduced. Temperature sensors were installed on the top and bottom

sides of the vacuum chamber to detect any temperature buildup when misalignments permit the beam to reach it. The beam height diminishes in size between B-10 and Q-12 and does not encounter any vertical aperture limitations. However, insertion of the Cerenkov profile monitor PR-10 into the beam causes an increase in the angular divergence due to 2.4×10^{-3} or 6.0×10^{-3} radiation lengths of material through which the beam must pass. The two thicknesses correspond to the use of helium or argon, respectively, in the instrument. The vertical aperture in PC-11 was designed to prevent scattered electrons from reaching and generating heat in the thermally isolated foil supports of the beam energy spectrum monitor S-11. Because of the shape of its aperture, PC-11 also provides protection for the diamond-shaped vacuum chamber of Q-12. In order to observe any temperature buildup from scattered particles or misalignments, temperature sensors were installed at the mid-length of the chamber and in the horizontal plane.

A section of the BSY that was somewhat more difficult to cope with was the region in the A-beam line between the target changer TC-20 and the dump D-11. When a photon beam is required in the end station, a thin target is inserted into the beam at TC-20. The electrons emerging from the target are removed from the photon beam by the dump magnets B-23 through 26. They are bent 12° downward into the window of D-11. The nearly monoenergetic electron beam (maximum momentum deviation $\Delta p/p = \pm 1\%$) which enters the target, however, emerges with a fairly broad momentum spectrum which then is widely dispersed by the dump magnets. Many of these electrons impinge on the dump magnets and on the vacuum pipe following the magnets. For the purpose of engineering the geometry and power absorption capacity of this system, the energy spectrum after the target (to within a few percent of E_0) was assumed to be approximately given by[39]

$$N(E)\,dE = \frac{t\,dE}{E_0 - E} \tag{20-29}$$

for $(E_0 - E)/E_0$ larger than a few percent. $N(E)\,dE$ is the fraction of the total number of electrons in the energy interval dE, E is the energy of an electron emerging from the target, E_0 is the energy of the incident electron beam, assumed to be monoenergetic, and t is the target thickness in radiation lengths. The fraction of the total power in all electrons of which the energy is smaller than E_1 is, then,

$$P = \int_0^{E_1} \frac{t\,dE}{E_0 - E} = t\left[-\frac{E_1}{E_0} - \ln\frac{(E_0 - E_1)}{E_0}\right] \tag{20-30}$$

The dump D-11 was designed with a 15-cm diameter window. The design of the power-absorbing capacity of the system upstream from the dump was predicated on a target having a maximum thickness of 0.01 radiation length for a 2-MW beam (or 0.02 radiation length for a 1-MW beam, etc.). Requiring that the peak of the spectrum enter the dump through the window at a

location 2.5 cm above its geometric center, it was estimated that approximately 83 kW of the dispersed beam would fall outside of the dump window.

Despite the fact that this amount of power is distributed over a fairly large distance (about 30 meters), the local power deposition is too high to depend on the natural convection mode of heat transfer. Lack of space between the magnets made it impossible to use PC's for absorption of all the dispersed beam. Therefore, the bottom sides of the vacuum chambers in the dump magnets B-23 through 26, and the bottom of the drift pipe between B-26 and PC-12 are all water-cooled. The PC-12, having a 10-cm aperture, assures that any beam passing through it will properly pass through the dump window.

The protection system of the entire BSY was developed from geometrical studies similar to the foregoing. Table 20-10 contains a list of the as-built apertures in the water-cooled PC's in the BSY. The various aperture sizes reflect the changing cross-sectional geometry of the beam as it enters and leaves the BSY.

Design features

A total of fourteen PC's were designed to absorb continuously up to 20 kW average power, and a total of six were designed to absorb continuously up to 5 kW. The latter group (PC-3, 4, 5, 7, 8, and 9) protects the ceramic vacuum

Table 20-10 Protection collimator dimensions

Protection collimator No.[a]	*Aperture width (cm)*	*Aperture height (cm)*	*Copper width (cm)*	*Copper height (cm)*	*Aperture length (cm)*	*Average power absorption capacity (kW)*
PC-1	2.077	Circular	20.3	Circular	36.53	20.0
PC-2	2.228	Circular	20.3	Circular	36.53	20.0
PC-3	8.585	2.438	26.0	15.6	32.08	5.0
PC-4	9.911	2.438	26.0	15.6	32.08	5.0
PC-5	11.598	2.438	26.0	15.6	32.08	5.0
PC-6	4.209	Circular	20.3	Circular	36.53	20.0
PC-7, 8, 9	7.038	2.438	26.0	15.6	32.08	5.0
PC-10, 30	3.988	2.479	27.9	17.8	44.91	20.0
PC-11	16.916	2.258	40.6	17.8	44.91	20.0
PC-12, 400[a]	10.173	Circular	29.8	Circular	35.41	20.0
PC-14, 32	8.915	2.248	22.9	17.8	44.91	20.0
PC-15	3.980	Circular	20.3	Circular	36.53	20.0
PC-16	4.623	Circular	20.3	Circular	36.53	20.0
PC-18	11.186	3.200	38.1	17.8	44.91	20.0
PC-31	15.255	2.256	40.6	17.8	44.91	20.0
PC-33	3.820	Circular	20.3	Circular	36.53	20.0

[a] All PC's except PC-400 are shown in Fig. 17-1. PC-400 is located in front of beam dump east.

chambers and the coils in the pulsed magnets (primarily from the scattered radiation emanating from the high-power collimator). Each unit is equipped with two ionization chambers, one mounted above and one below the PC to monitor the power absorbed and to shut off the beam if the power deposition exceeds a preset level. Additionally, platinum resistance-type immersion temperature sensors are installed in the cooling-water supply and return lines. These are also interlocked to shut off the beam should the temperature difference exceed a preset level. In addition to serving as a slow backup to the ionization chambers, the temperature sensors are also used to calibrate them, since the steady-state power deposition can be determined calorimetrically from the water temperature rise. Figure 20-22 shows a typical assembly of a PC with its ionization chambers installed. The quick-disconnect cooling water and vacuum couplings can also be seen.

The ionization chambers respond quickly and roughly proportionally to the amount of power deposition in a PC. Since only a few high-power beam pulses may be sufficient to cause thermal damage, they have a distinct advantage over more slowly responding temperature sensors. Should the entire beam be deposited in a PC, the response time of the electronic circuitry is such that the trip level of the ionization chambers is reached before the next pulse arrives when operating at 360 pulses/sec.

Figure 20-22 Protection collimator with ion chambers.

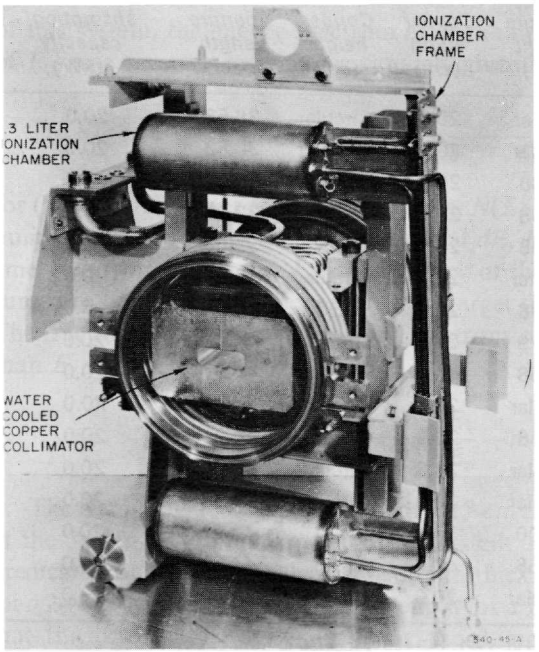

In order to achieve a reasonably compact configuration, it was desirable to mount the ionization chambers as closely as possible to the body of the PC. Because of the close proximity to the radiation source and because the ionization chambers saturate easily, it was necessary to limit the amount of radiation reaching them by shielding. Copper is used as the power-absorbing material in the PC's. Therefore, shielding was most easily accomplished by providing sufficient radial thickness between the region of power deposition and the outside surface of the copper body. For the particular ionization chambers used, this resulted in a radial thickness of approximately 5 radiation lengths or about 7.5 cm between the aperture and the top and bottom surfaces for the 20-kW PC's. The cross-sectional dimensions of the various units are summarized in Table 20-10.

The PC's are a major source of radiation in the BSY. The radial thickness chosen provided sufficient self-shielding to attenuate a large amount of the radiation which would otherwise increase the noise level in the local electronics and accelerate the deterioration of insulation on electrical cables and magnet coils.

The foregoing arguments concerning the specification of the radial thickness of the PC's are also applicable to the specification of the axial length. Since the longitudinal shower development is much more extensive than the radial, the axial length of the copper is correspondingly greater. Furthermore, each one of the microwave position monitors has a PC upstream of it and, therefore, the axial length had to be large enough to minimize the possibility of power deposition in these temperature-sensitive monitors. The length also serves to minimize the radiation deterioration of the ferrite rings in the current intensity monitors, particularly in the monitor I-2; see Fig. 17-1.

In view of the foregoing considerations, the minimum length through the shortest path (i.e., through any cooling-water passages) in the vicinity of the aperture was established as 25 radiation lengths. This is equivalent to 33.5 cm of solid copper. (PC-3, 4, 5, 7, 8, 9 were exceptions because the available space allowed only 24.2 cm of solid copper.) A length of 25 radiation lengths attenuates the power to less than 0.5% of the incident beam power.

The PC's were fabricated in two basic geometries: circular for the units that required a circular aperture and rectangular for those with a rectangular aperture. The circular PC's consist of a 12.5-cm diameter copper core (with the aperture bored through the center) surrounded by a copper sleeve having an outside diameter of 20 cm to satisfy the radial thickness requirement. This core was limited to 12.5 cm diameter so that the cooling-water interface would not be too far from the aperture. For an incident beam of 20 kW average power the longitudinal power deposition at the shower maximum is about 1.65 kW/cm (from Fig. 20-1). Depending on the beam size, the power density can cause metal temperatures in excess of 300°C. The thermal stresses resulting from such a temperature difference exceed the yield strength of copper, and after some cycling may well lead to cracking in the aperture. As long as the cracks do not propagate to the cooling-water interface and admit

water to the vacuum system, the function of the PC's is not impaired. A much lower metal temperature could be realized for the same incident beam power if aluminum were used (see, for example, Table 20-2). However, the radiation length in Al is about 7 times that of Cu and the space requirement for an aluminum protection collimator is far greater than was available. A composite construction was not undertaken for economical reasons, since the PC's are considered to be expendable items.

Fabrication details and materials

As mentioned above, the circular PC's consist of a 12.5-cm diameter copper core surrounded by a copper sleeve. A 1.25 × 1.25-cm cooling-water channel was machined into the outside diameter of the core in the form of a thread with a 2.54 cm (1 in.) lead. Stainless steel, Type 304-L, nipples were inserted into the outside diameter of the sleeve near the ends of the collimator to provide for the cooling-water supply and return lines. Stainless steel, Type 304-L, adaptor rings for welding on the vacuum couplings were added to each end of the core and sleeve assembly. The entire assembly was then brazed together in one operation. PC-12 was fabricated in essentially the same way except that the core was made larger to accommodate the 10-cm diameter aperture. Since the core was also made with a larger radial thickness, stainless steel instead of copper was used for the outer sleeve.

The copper body of the rectangular PC's was made in two halves with the joint running in the axial direction. The rectangular aperture was formed by first machining one-half of the aperture into each piece and then brazing the two halves together. Most of the rectangular PC's are required to absorb power mainly in the horizontal plane. Therefore, twelve 1.58-cm diameter cooling-water holes were drilled vertically through the copper blocks (perpendicular to the beam direction) on each side of the aperture. To form a continuous cooling-water passage between inlet and exit points at the ends, copper elbows and nipples were brazed to the copper bodies on the top and bottom sides such that the flow spirally laced through the external tubes from the holes on one side of the block to those on the other. The brazing of each unit was carried out in two steps, as described below.

Except for the care that had to be exercised in the handling of large pieces of annealed copper, the fabrication of the protection collimators was routine. However, the brazing operation required special care because of the massiveness of the copper pieces and large joint areas involved.

All brazing operations were carried out in a hydrogen atmosphere furnace, and it was, therefore, essential to use certified OFHC copper to prevent embrittlement and blistering. The wrought copper elbows used for the external cooling water passages of the rectangular PC's were the exception, since they are only available as a stock item in phosphorous, deoxidized copper. However, prior to use they were preheated in a hydrogen atmosphere to the brazing temperature to assure that they were oxygen-free.

The OFHC copper was procured in the form of heavily forged shafts and blocks. To ensure that the crystalline structure of the cast billet was completely disintegrated and that the copper structure was completely free of voids and gas, a maximum grain size of 0.150 mm in the interior of the forgings was specified.

The largest copper body was 18 × 40 × 45 cm in size and weighed about 625 lb. The largest surface area to be brazed was in the longitudinal joint which was needed to form the aperture. Its size was 43 × 45 cm minus the height of the aperture. From an experimental test piece it was determined that a surface flatness of 0.005 cm combined with a brazing alloy sheet thickness of 0.01 cm would produce highly reliable joints with full vacuum integrity.

The most essential requirement in selecting the brazing alloys[40] was that they have a melting point in excess of 925°C. Above 925°C, the hydrogen atmosphere in the brazing retort is completely effective in reducing the chromic oxide. The latter remains on the stainless steel parts of the assembly after proper chemical cleaning. The reduced surface assures wetting when the brazing alloy melts. Three alloys were used in the fabrication of the PC's:

Alloy No. 1: 35 Au–62 Cu–3Ni with a liquidus temperature of 1030°C
Alloy No. 2: 35 Au–65 Cu with a liquidus temperature of 1010°C
Alloy No. 3: 50 Au–50 Cu with a liquidus temperature of 970°C

Alloy No. 3 was reserved for reruns to repair any joints that came out of the previous braze with marginal integrity. The melting point of OFHC copper is 1083°C. The PC's having a circular geometry were brazed in one step with alloy No. 2. The PC's with the rectangular geometry were brazed in two steps: in the first step, the longitudinal joint in the copper was brazed with alloy No. 1 and in the second, the stainless steel adaptor flanges and the copper elbows and tubes for the cooling water passage were brazed with alloy No. 2.

The massiveness of the copper bodies in the PC assemblies required heating and cooling cycles in the brazing operation that ranged from 10 to 16 hours depending on the size of the unit. In the heating portion of the cycle (which required about one-third of the time), the temperature rise of various parts of the assembly was monitored with thermocouples so that the brazing alloy at extended thin sections would not melt before that on the massive copper. Because the gold in the gold–copper brazing alloys has an affinity for copper, it will "pick up" copper from the base metal if permitted to remain too long in the liquid state. A small river of alloy can form, drain a joint, and erode the base metal to the extent of cutting through, for example, the thin copper tubes in an assembly. The PC's were allowed to cool to about 100°C before being removed from the sealed retort so that surfaces which were to be subsequently exposed to vacuum would come out oxide-free and bright.

Most stainless steels become sensitized in the temperature range of 500° to 900°C. Sensitization is the result of either carbide precipitation or the formation of a brittle σ phase. Sensitized steels suffer from intergranular corrosion

and are attacked by nitric acid.[41] The low-carbon stainless steels, 0.04% or less carbon, are desirable because they exhibit low carbide precipitation. There are two grades which are commercially available for fabrication: Type 304-L and Type 316-L. Type 304-L was chosen for all stainless steels that must go through the brazing cycle because Type 316-L contains molybdenum, a σ-phase promoter.

Operating experience

To date (July 1967), the protection system as designed and installed has functioned well. Initially all ionization chambers and temperature sensors had their interlock trip levels intentionally set very low. The runs at higher-power levels have, however, already required that some of these trip levels be raised to prevent frequent shutdown of the accelerator, but in no instance have these increases in threshold levels exceeded any design limitations. The system seems to respond particularly well to transient power depositions such as occur from missteering of the beam and sudden increase of beam spectrum width.

The design philosophy of the entire protection system was predicated on a beam power of 2.2 MW. The real test of the effectiveness of the protection system will come when beam power levels significantly above the 240 kW achieved to date are common. The amount of power associated with the off-momentum regions of the spectrum will probably far outweigh all other sources of excessive power deposition which can damage the BSY beam transport system components.

20-9 Future power absorption devices (DRW)

The power absorbers as described in the foregoing sections are designed to satisfy the SLAC requirements for Stage I ($P_{AV} \leq 600$ kW) and Stage II ($P_{AV} \leq 2.2$ MW). In Section 20-1, it has been demonstrated that only low-Z materials can be used as solids to intercept a 2.2-MW beam.

A survey of low-Z metals readily shows that only aluminum and beryllium alloys are useful engineering materials for power absorber applications. The technology of beryllium fabrication, however, is still in its infancy and production costs are high. Moreover, further reduction of Z below that of aluminum combined with an expected future increase of the incident beam energy, requires even longer devices to attenuate adequately the longitudinal cascade shower. The present high-power slit is 5 meters long to satisfy the 30-radiation length criterion for shower attenuation. As stated previously, the slit should have theoretically zero depth and should coincide with the image of the center of the pulsed magnet. Whether or not the long physical length and low Z of the materials have a detrimental effect on the beam in causing slit scattering and halo formation has not yet been investigated.

However, the length combined with the transport system resolution requirements resulted in some rather difficult precision alignment problems and, therefore, high production costs. A further increase in size will jeopardize dimensional stability during operation as a result of unavoidable temperature gradients in the slit and support structures.

The extensive use of water as a primary power absorbant and coolant created new auxiliary problems. Radiolysis and evolution of large amounts of hydrogen, particularly in the high-power beam dumps, demand expensive instrumentation for H_2 detection, including safety interlocks. The handling of the hydrogen mixed with other radioactive gases, and the disposal of large quantities of contaminated water are costly and require the attention of health physics personnel. In short, low-Z power absorbers have many disadvantages, even though they are successfully employed at SLAC at the present time. An advance in the state of the art is needed.

In the design of future accelerators, attention should be focused on improvement of the output by minimizing beam spectrum widths. Next, modifications of existing low-Z designs are needed with emphasis on quick replacement of components which have failed. A small vacuum leak, for example, may render an expensive and complex piece of equipment useless, unless the faulty part can be easily replaced or repaired. The expected increase in induced radioactivity from future high-intensity, high-power machines should be a challenge to the designer of quick-disconnects and remote-handling equipment. Particular emphasis must be given to the problem of minimizing precision alignment time.

Last but not least, the ultimate goal should be the successful employment of high-Z liquid metals as primary beam absorbants and coolants. To name just a few requirements, these liquid metals must be inexpensive, since significant quantities would be needed. They should have a low vapor pressure for application in the beam transport vacuum systems, thus eliminating the need for solid container walls. They should be nonpoisonous and nontoxic. Materials used in the liquid metal loops must be resistant to corrosion and erosion. There may be no liquid metal that satisfies all requirements, but a reasonable compromise probably can be found which would reduce future power absorbers to manageable proportions.

Acknowledgments

The authors would like to express their particular gratitude to D. Coward, E. L. Garwin, Z. Guiragossián, B. de Raad, H. DeStaebler, J. Jurow, E. J. Seppi, R. E. Taylor, and H. A. Weidner for the many valuable suggestions and contributions during the development of the SLAC power absorbers. J. Wagner was the designer and project engineer for the high-power beam dumps. Most of the high-power slit and collimator system was designed by I. Zavialoff and J. Mitchell, and their experience helped greatly to make the program a success. Valuable engineering and design studies were contributed

by L. Cooper to the high-Z collimator program. Under the leadership of A. Eldredge, the SLAC fabrication groups demonstrated a high degree of technical sophistication during the construction phase of the power absorbers. J. Ryan contributed significantly to the development of prototypes and to the experimental programs.

The efforts of the Astronautics Division of General Dynamics/Corvair, San Diego, California in developing the deep-hole drilling technique for the slit modules deserve to be mentioned.

References

1 B. B. Rossi, *High-Energy Particles*, Prentice Hall, New York, 1952.

2 C. D. Zerby and H. S. Moran, "Studies of the Longitudinal Development of High-Energy Electron-Photon Cascade Showers in Copper," Rept. No. ORNL-3329, Oak Ridge National Laboratory, Tennessee (1962).

3 C. D. Zerby and H. S. Moran, "A Monte Carlo Calculation of the Three-Dimensional Development of High-Energy Electron-Photon Cascade Showers," Rept. No. ORNL-TM-422, Oak Ridge National Laboratory, Tennessee (1962).

4 C. D. Zerby and H. S. Moran, "A Collimator Study for a 20-GeV Electron Beam," Rept. No. ORNL-TM-524, Oak Ridge National Laboratory, Tennessee (1963).

5 Z. Guiragossián, "Longitudinal and Radial Distribution of Shower Development in Cu, H_2O, and Al," Rept. No. SLAC-TN-63-85, Stanford Linear Accelerator Center, Stanford University, Stanford, California (1963).

6 Z. Guiragossián, "Peak Power Densities at the Beam Switchyard Collimator and Slits," Rept. No. SLAC-TN-64-16, Stanford Linear Accelerator Center, Stanford University, Stanford, California (1964).

7 H. S. Carslaw and J. C. Jaeger, *Conduction of Heat in Solids*, 2nd Ed., Oxford University Press, London and New York, 1959.

8 D. R. Walz, "Spot Cooling and Heating of Surfaces with High Velocity Impinging Air Jets," Tech. Rept. No. 61, AD 607 727, Department of Mechanical Engineering, Stanford University, Stanford, California (1964).

9 H. A. Johnson, ed., "Lecture Series on Boiling and Two-Phase Flow for Heat Transfer Engineers," University of California, Berkeley, California (1965).

10 J. Jurow, "Boiling Heat Transfer Peak Heat Flux Correlations and References," Rept. No. SLAC-TN-63-84, Stanford Linear Accelerator Center, Stanford University, Stanford, California (1963).

11 C. E. Taylor and J. F. Steinhaus, "High Flux Boiling Heat Transfer from a Flat Plate," Rept. No. UCRL-5414, University of California, Lawrence Radiation Laboratory, Livermore, California (1958).

12 D. R. Walz, J. Jurow, and E. L. Garwin, *IEEE Trans. Nucl. Sci.* **NS-12**, No. 3, 867 (1965).

13 S. Timoshenko, *Strength of Materials*, Vol. 1, p. 66, Van Nostrand, Princeton, New Jersey, 1955.

14 B. A. Boley and J. H. Weiner, *Theory of Thermal Stresses*, Wiley, New York, 1960.

15 J. Jurow, Stanford Linear Accelerator Center, Stanford University, Stanford, California (private communications).

16 L. R. Lucas, "Dump Window Removal Unit Instructions," Rept. No. SLAC-TN-66-43, Stanford Linear Accelerator Center, Stanford University, Stanford, California (1966).

17 D. R. Walz, L. R. Lucas, H. A. Weidner, R. J. Vetterlein, and E. J. Seppi, *IEEE Trans. Nucl. Sci.* **NS-14**, No. 3, 923 (June 1967).

18 A. O. Allen, *The Radiation Chemistry of Water and Aqueous Solutions*, Van Nostrand, Princeton, New Jersey, 1961.

19 A. R. Anderson and E. J. Hart, *J. Phys. Chem.* **66**, 70 (1962).

20 D. K. Nichols, M. T. Simnad, and V. A. J. VanLint, General Atomic Division of General Dynamics, San Diego, California (private communications).

21 H. A. Schwarz, J. P. Losee, and A. O. Allen, *J. Am. Chem. Soc.* **76**, 4693 (1954).

22 H. A. Mahlman and J. W. Boyle, *J. Am. Chem. Soc.* **80**, 773 (1958).

23 J. A. Ghormley and C. J. Hochanadel, *J. Am. Chem. Soc.* **76**, 3351 (1954).

24 D. R. Walz, "Heat Transfer and Thermal Stress Analysis of Slits and Collimators," Rept. No. SLAC-TN-64-29, Stanford Linear Accelerator Center, Stanford University, Stanford, California (1964).

25 L. R. Lucas and D. R. Walz, "Heat Transfer and Thermal Stresses in Tube-Forest Slits and Collimator," Rept. No. SLAC-TN-64-61, Stanford Linear Accelerator Center, Stanford University, Stanford, California (1964).

26 H. DeStaebler, Stanford Linear Accelerator Center, Stanford University, Stanford, California (private communications).

27 G. Rogers, Stanford Linear Accelerator Center, Stanford University, Stanford, California (private communications).

28 S. C. Lind, C. J. Hochanadel, and J. A. Ghormley, *Radiation Chemistry of Gases*, Reinhold, New York, 1961.

29 D. A. G. Neet, "Radiation Exposure in the Switchyard," Rept. No. SLAC-TN-65-9, Stanford Linear Accelerator Center, Stanford University, Stanford, California (1965),

30 D. R. Walz and E. J. Seppi, "Irradiation of Highly Radiation-Resistant Organic Lubricants and a High Temperature Paint," Rept. No. SLAC-TN-67-13, Stanford Linear Accelerator Center, Stanford University, Stanford, California (1967).

31 D. R. Walz, "Corrosion in an Aluminum–Stainless Steel System," Rept. No. SLAC-TN-64-17, Stanford Linear Accelerator Center, Stanford University, Stanford, California (1964).

32 E. Deltombe and M. Pourbaix, *Corrosion* **14**, 496t (1958).

33 U.S. Office of Naval Research, *The Effects of Radiation on Materials* (J. J. Harwood *et al.*, eds.), Reinhold, New York, 1958.

34 D. A. G. Neet, ed., "Instrumentation, Computer Control and Electronic Systems for the SLAC Beam Switchyard," Rept. No. SLAC-68, Stanford Linear Accelerator Center, Stanford University, Stanford, California (1966).

35 E. Rabinowicz, *Friction and Wear of Materials*, Wiley, New York, 1965.

36 D. H. Buckley and R. L. Johnson, "Friction and Wear of Hexagonal Metals and Alloys As Related to Crystal Structure and Lattice Parameters in Vacuum to 10^{-10} Millimeters of Mercury," ASLE Paper No. 65 LC-18, American Society of Lubrication Engineers (1965); Also as Rept. No. NASA-TM-X-52096, National Aeronautics and Space Administration (1965).

37 B. de Raad, "Protection of the BSY Equipment against Overheating by the Electron Beam," Rept. No. SLAC-TN-64-54, Stanford Linear Accelerator Center, Stanford University, Stanford, California (1964).

38 F. Kreith, *Principles of Heat Transfer*, p. 48, International Textbook Co., Scranton, Pensylvania, 1958.

39 B. de Raad, "Beam Profile Monitors for the Beam Switchyard," Rept. No. SLAC-TN-64-77, Stanford Linear Accelerator Center, Stanford University, Stanford, California (1964).

40 H. Soderstrom, Stanford Linear Accelerator Center, Stanford University, Stanford, California (private communication).

41 H. F. Ebling and M. A. Scheil in *Advances in the Technology of Stainless Steels and Related Alloys*, Special Tech. Publ. No. 369, p. 275, ASTM, Philadelphia, Pennsylvania, 1965.

PROTECTION SYSTEMS

G. Babcock, K. E. Breymayer, D. D. Busick,
K. Crook, T. M. Jenkins, K. B. Mallory, Editor,
R. McCall, D. D. Reagan, and G. Warren

This chapter describes the equipment which is provided (a) for the protection of personnel from the hazards of radiation generated by the machine and (b) for the protection of the machine itself from damage caused by a missteered beam.

The procedural rules governing the use of this equipment are discussed in detail.

21-1 System interlocks for accelerator

Although many interlocks for personnel and equipment protection can be confined to the individual piece of equipment they control, e.g., interlocks on high-voltage safety doors and cooling-water circuits, there are some interlock circuits which provide system-wide interactions among injector, accelerator, switchyard, and end stations. The purpose of an interlock is to override operator control. These circuits are, therefore, quite independent of manual control systems. In general, their signals are carried on individual wire-pairs and make no use of the multiplexing systems.

There are six interlock circuits which serve to shut off the machine under irregular circumstances. They are

1. An access control system that prevents entry to a radiation area when the machine is on
2. A machine shut-off system that keeps the beam off and shuts off all RF power to the accelerator in circumstances where there is a possible radiation hazard to personnel
3. An "emergency stop" circuit that changes the geometry of the beam areas by inserting beam stoppers when excessive radiation is detected in the research yard

4. A machine protection system (1-msec network) that shuts off the injector in circumstances where there is a probable radiation hazard to equipment
5. A 50-μsec protection network that shuts off the injector when the switchyard is not ready to accept the programmed pulse
6. Pattern interlocks that shut off the program for a beam in circumstances where the beam is not desired by the experimenter or a beam channel is not ready to accept any beam.

The *access control system* contains a tone loop with a transmitter at Sector 2, interrupts at each variable-voltage substation, and a receiver in central control. If all substations are off, the loop is closed and permissive signals are sent to ventilation and access control relays in each area. When any substation is turned on, the loop is broken, interlock relays are released, and the central control operator has no power to release keys or initiate ventilation.

The major purpose of the access control system is to keep the number of people entering the housing, the number of people entering at one time, and the duration of each entry, to a minimum. The housing should not be cleared because the beam is coming on but because the need for occupancy is finished.

The purpose of the *machine shutoff system* is to limit the hazard of radiation exposure when personnel are in the housing by preventing turn-on of all variable-voltage substations which supply high voltage to the klystron modulators.

The machine shutoff system and the access control system form a complete interlock. If any substation is on, people may not be in the housing. If there are people in the housing, no substation may be turned on.

The machine shutoff system contains two parallel tone loops which indicate that each radiation area is secure. It has as inputs the doors to radiation areas, access keybanks, and "emergency off" pushbuttons.

In order to allow experiments to be carried out in one end station while equipment is being set up in the other, an alternative definition of security is required for the end stations. If appropriate beam stoppers are in position, the end station may be defined secure and access may be permitted without shutting off the variable-voltage substations.

If a person enters a beam area, the entry can be detected by limit switches which are wired into a fail-safe circuit. His entry is made unlikely by appropriate control of door-release circuits. There is, however, no automatic way to remove the person! If, despite all precautions, he is present in a beam area, it is necessary to shut down the machine.

The "*emergency stop*" *circuit* provides a means for removing the beam from the beam switchyard (BSY) and end stations when excessive radiation is observed in the research area outside the end stations, without resorting to the extreme measure of shutting down the entire machine. The primary function is to insert beam stoppers in the path of the beam, thus ensuring

that the beam cannot leave the accelerator housing; the beam itself is also shut off through the machine protection system.

A distinction is maintained between "emergency off" buttons and "emergency stop" switches. The former are located within beam housings and shut off the machine completely through the machine shutoff system. The latter are located outside the end stations, in the research area, and stop only the beam through the "emergency stop" circuit.

The *machine protection system* has as its major component the 1-msec network, which consists of a tone transmitter in Central Control Room (CCR), tone interrupt units in CCR, Data Assembly Building (DAB), and each sector, and a tone receiver at Sector 0 (the injector area). The network shuts off the gun trigger if the circuit is interrupted at any of the tone interrupt units. The major inputs to the machine protection system at each sector are the signals indicating those conditions likely to damage equipment in the accelerator or BSY housing. A long ion chamber which detects excessive beam loss along the accelerator is connected to the system at CCR.

Any breach in the security of any of the radiation areas shuts off the gun through the machine protection system in addition to shutting off the variable-voltage substations through the machine shut-off system. The machine protection system shuts off the injector for a minimum of 1 sec and may be reset by the central control operator only after the trouble has been cleared.

The *50-μsec protection network* provides a pulse-by-pulse permissive signal to the gun which is withheld if any BSY interlock fails or if the pulsed magnets do not approach the proper field strength for the programmed beam. A pulse generator, located at the DAB, generates a 200-μsec pulse approximately 150 μsec in advance of each beam pulse. If the interlock determines that the switchyard is prepared for the beam, the pulse is transmitted to the injector trigger generator and drives a gate which allows trigger pulses to be transmitted to the gun. A beam thus cannot be accelerated unless the permissive pulse is received from the switchyard.

A similar network originates at the positron source. It transmits a permissive signal when the wand target is clear of the beam and also when it is in all respects prepared to produce positrons. A third circuit will be installed later at the take-off magnet for the storage ring.

Interlock signals that must operate on the next beam pulse are handled through the 50-μsec protection network. This network has no lockout feature. Interlock signals which are to be effective for a longer duration and are to affect only one beam shut off the *pattern interlock* for that beam at the pattern generator in central control. Examples of such signals are the experimenter's "on/off" switch for a particular experiment, interlock signals for the experimenter's equipment, and interlock signals for the beam transport system into a target area. Since the other systems generally turn off all beams, this is the simplest system which can handle signals which pertain to a single beam or experiment. The research area inputs to the 50-μsec network and to the pattern interlocks are discussed in more detail in Chapter 19.

21-2 Personnel protection system

Health physics requirements (TMJ)

The health physics requirements concerning personnel around or in the accelerator were formulated early in 1964 and are summarized here with appropriate updating:

1. All entrances to radiation areas, including housing, BSY, and experimental areas will be the responsibility and under direct control of either the CCR or DAB operators.
2. Operators in CCR and DAB will be trained and certified competent in radiation matters by the Health Physics Group so as to be able to make day-to-day decisions within the framework of the established radiation policy.
3. At least one member of the Health Physics Group will be available or on call to give advice or help in nonstandard situations.
4. All entrances to radiation areas will be controlled with a key that is in the interlock chain. For entrances not frequently used, the key may be kept in the CCR or DAB consoles. For other entrances, the key will be locally available within a few feet in a keybank. In both cases, CCR or DAB must give permission to allow removal of the key. Keys may not be removed unless the machine is off.
5. Every person entering a radiation area will carry a key with him while inside to guarantee that the machine cannot be turned on. The only exception to this occurs when the machine is open to unlimited access, in which case a search must be completed before the machine can be turned on.
6. Personnel entering a radiation area will be identified and logged in, and the integrity of the door maintained either by appropriate electronics signals or by posting a guard. If the security of an area is violated, a search must be made before it is locked again and considered secure.
7. Egress from all areas will be possible without a key. Emergency entrance will be possible by breaking a glass and taking a key, which automatically shuts off the beam.

In addition to the above, the following policies are observed:

1. The personnel protection system may operate within seconds, unlike the machine protection system, which must work in milliseconds. This is acceptable because human reaction times are involved, and these are very slow compared to the response times of electronic systems.
2. There must be audible alarms prior to turning on the beam, early enough to allow personnel caught inside to make their way to an "emergency off" button.

3. There must also be visible alarms preceding beam turn-on, such as blinking lights, with the lights being dimmed during actual beam operation.
4. These audible and visible alarms must exist within all radiation areas, but not outside the shielding. A visible indication at each point of entry is sufficient warning there.

It is required that every entrance into a radiation area be suitably identified. Thus, one should not be able to enter the klystron gallery without seeing an appropriate red or green light which identifies the radiation or potential radiation status. The lights installed to meet this requirement are convex so they are seen by someone entering from an adjacent sector. Above every entrance into the housing and BSY are magenta and yellow lights. The magenta signifies a beam or potential beam condition; the yellow signifies that the beam is off, but that the area should be entered with caution for there may remain residual radioactivity. Worded status lights are used at the entrances into the end stations.

In addition to status lights, radiation areas are further identified by placing a fence around them. These areas include the klystron gallery, BSY, and end station areas, but exclude the campus area and cryogenics building. Entrance inside this fence is limited to personnel wearing film badges. Within the radiation fence, areas with radiation levels ≥ 0.75 mrem/hour are roped off.

Design criteria (KBM)

A personnel radiation protection system consists of two major parts: a collection of equipment designed to safeguard personnel and a body of procedural rules for its use. The purpose of this section is to describe the equipment in the personnel radiation protection system. Only brief reference is made to the operational procedures developed by the Operations and Health Physics Groups. These procedures include: (a) the operational rules (e.g., "the operator will make verbal announcement over the public address system before turning on the beam") for use of the protection system, (b) an educational program about the rules and functions of the equipment itself, and (c) a supervisory or disciplinary procedure to assure that the rules are followed.

As at many accelerator installations, interlocks with acceleration power are the primary means used to protect personnel from direct machine-produced activity. These interlocks shut off the variable-voltage substation (VVS) supplies to all klystron modulators. Accessways to beam areas are also interlocked to make it difficult to enter while the accelerator is operating. However, the latter interlocks are regarded as secondary means of protecting personnel, because provisions for emergency entrance bypass the access interlocks.

Protection from residual activity is achieved by health physics procedures including radiation surveys and tagging or temporary blockading of "hot"

areas. The system described below contains no provision for restricting circulation once a person has entered a radiation area. Such restrictions change from day to day or even hour to hour and are imposed and enforced by health physics personnel and the operations groups.

Although security system activities are generally performed locally at the scene by trained and responsible personnel, the geographical extent of the site, the large number of entrances, and the need to allow one area to be entered while another area is secure make it imperative that the chief operator be kept continuously aware of all such activities.

The hazardous areas to be considered are those areas directly exposed to the beam, and also the klystron gallery, the research yard, and certain enclosed spaces adjacent to the housing.

The system design had to take into consideration the fact that there are some ninety entrances to radiation areas spread out over the 2½-mile long site. These include regular entrances to beam areas, any of which may be used during controlled access periods; other openings into beam areas, some of which are normal entrances for maintenance and construction during shutdowns; and entrances to additional areas which are insufficiently shielded from machine-produced activity and which, therefore, may not be occupied while the accelerator is operating. Since many areas remain hazardous when the accelerator is off, the operator must retain independent control of each entrance.

The interlock system is concerned with holding the machine off until the operations crew and the chief operator are assured that the areas are cleared and locked, preventing normal reentry as long as the machine is on, and shutting off the RF acceleration power and the gun if any of the above entrances are used in an emergency.

In the klystron gallery, red–green warning lights automatically inform personnel when the klystrons themselves are operating. Access to the klystron gallery is controlled at the gates of the peripheral fencing (see Chapter 27), rather than at the 150 doors of the gallery itself.

All accelerator entrances, including housing, BSY, and experimental areas are the responsibility and are under direct control of the chief operator.

When an access door is to be opened, it must be monitored by a qualified person, who will log, tag, or otherwise identify personnel entering and leaving. The alternative is to make a search of the accessible area before it is locked up again.

The primary control of access to radiation areas is achieved by a key-release system. For entrances frequently used, the key is stored locally in a keybank adjacent to the door; release of keys from the keybank is by signal from central control or DAB, as appropriate. For other entrances, the keys are kept at central control or DAB.

A person entering a controlled area keeps possession of the key while in that area and returns it to the keybank upon leaving. The keybank interlock thus cannot be closed until all personnel have left the radiation area.

In emergency, any access door may be opened without CCR permission by actuating a mechanical latch inside a "break the glass" enclosure. This latch either unlocks the door directly or releases a key from the keybank.

Except for emergency or forced entry, the interlock cannot be broken without permission from CCR. This insures that no accidental interruption of the machine occurs by thoughtless entry.

Interlocked beam stoppers allow personnel to enter one end station to set up experiments while an experiment is in progress in another target area. Once the chief operator has determined that entry is permissible, he will then delegate responsibility for key release and for search of end stations to an operator in the DAB. When major installation or rebuilding of experimental equipment is in progress, key control may be removed. All entrances will be unlocked and keys will not be released. The end station must be put back under key control and searched before experiments may be resumed.

The system is designed to maintain zero occupancy of the radiation area. Once the interlock system has been signalled that the radiation areas are empty, it can prevent normal entry of personnel and can permit the accelerator to be turned on. Once any person has entered a radiation area, it is the responsibility of the operations crew to restore zero occupancy.

Starting with a housing known to be empty, the operations crew can count all people entering and leaving and know when the housing is again empty. However, if at any time the number of occupants is in doubt, the entire area must be searched and cleared.

Because of the magnitude of the search procedure, the system is designed to minimize unauthorized entrance.

Since emergency shutdown of the accelerator can dump as much as 25 MVA of ac power supplying the klystron modulators, the system has been designed to minimize false alarms due to momentary ac power failures.

System description (KBM)

Each area—injector, sector, switchyard, or end station—is considered a unit for the system. Each area has its own radiation monitors, warning signals, and circuits for determining that its portion of the housing has been secured. The areas are tied together by the access control and machine shutoff circuits. The appropriate interconnections are made in the Central Control Building. The overall system interconnections are briefly described below; the circuits to be found in each area are described in more detail later.

The system consists of two major parts: the *machine shutoff* circuit, which insures that the machine cannot be turned on until the radiation areas are cleared and secured and which turns off the machine if the security of any area is broken, and the *access controls* which prevent entry into radiation areas while the machine is on.

In addition, the system contains warning devices and radiation monitors to help determine the state of the machine. Figures 21-1 and 21-2 are block

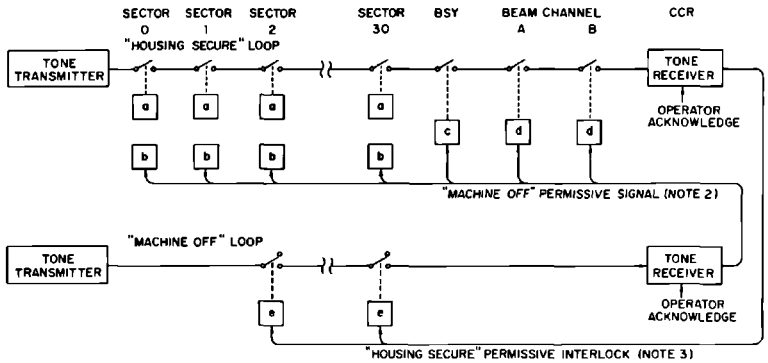

Note 1 : Code letters in boxes refer to Figures 21-2 (a) thru 21-2 (e)

Note 2 : Keys can be released and ventilation initiated by operator only if "MACHINE OFF" permissive signal is present

Note 3 : All VVS's are automatically turned off if "HOUSING SECURE" tone loop is interupted.

Note 4 : Transfer logic for BAS mode of operation is not illustrated.

833A1

Figure 21-1 Personnel protection system block diagram.

Figure 21-2 Personnel protection system logic details.

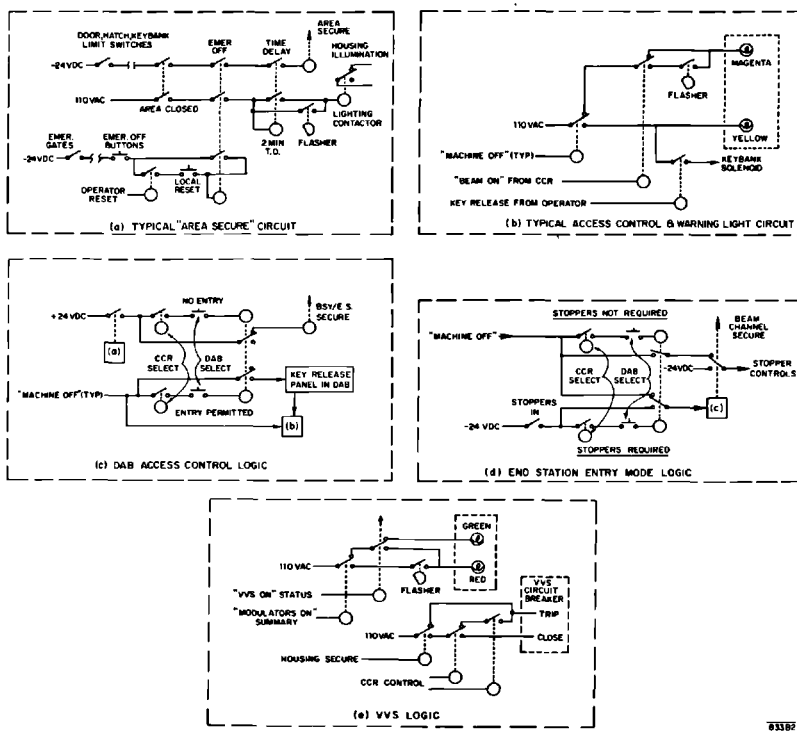

833B2

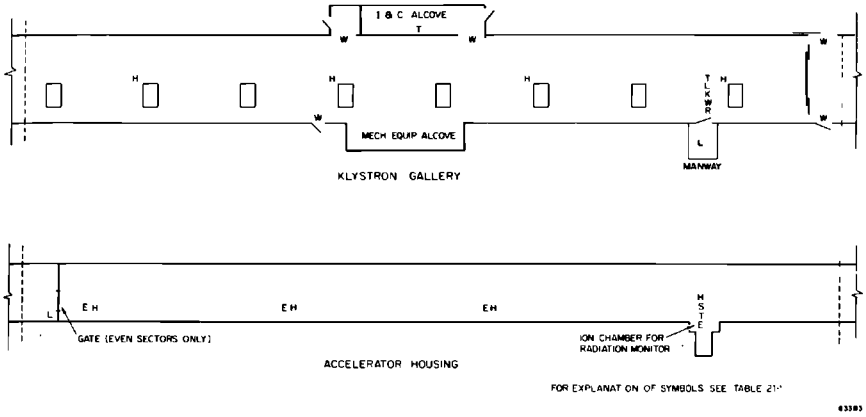

Figure 21-3 Location of personnel protection system components in a typical sector.

and schematic diagrams of the system logic. Figures 21-3 through 21-5 show the locations of system components.

MACHINE SHUTOFF SYSTEM. The machine shutoff system turns off all VVS which supply high voltage to the klystron modulators when the security of any radiation area is broken. As noted elsewhere, the gun is simultaneously shut off through an independent circuit.

Figure 21-4 Location of personnel protection system components in the beam switchyard.

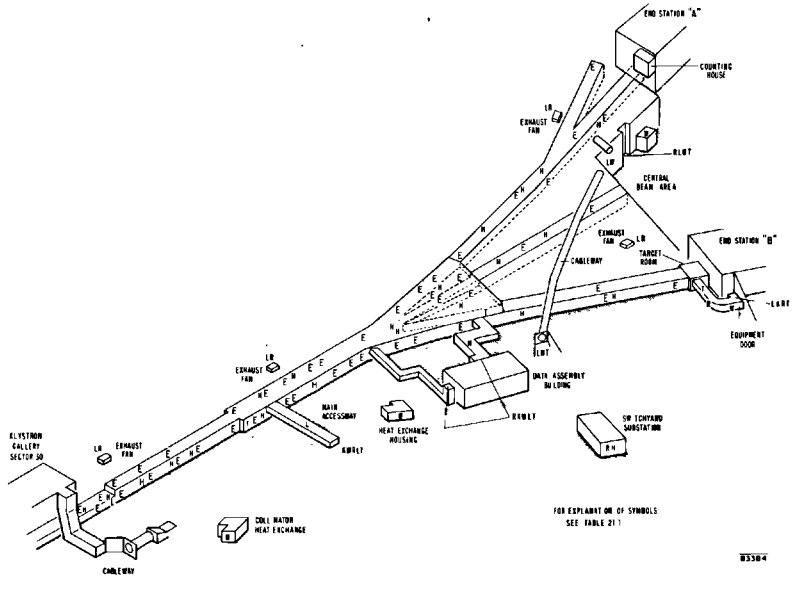

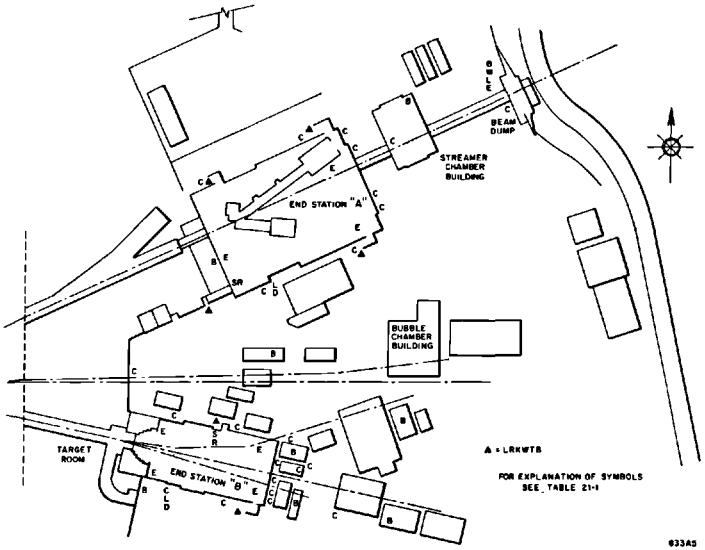

Figure 21-5 Location of personnel protection system components in the research area.

The system contains a "housing secure" tone loop which determines that each radiation area is secure. The tone equipment is identical to that used in the machine protection system. The system recognizes the following separate radiation areas: injector, Sectors 1, 2, ..., 30, BSY, beam channels A and B. If all of the areas have been secured, the tone loops are completed and a permissive interlock ("housing secure") allows the operator to turn on the VVS (Fig. 21-2e). If the tone loop is interrupted, all VVS are automatically turned off.

The machine shut-off system has the following inputs: all doors to radiation areas, certain gates within radiation areas, ventilation hatch covers, access keybanks, and "emergency-off" pushbuttons (Fig. 21-2a). Each time an "emergency-off" button is tripped, the area accessible from the vicinity of that button must be searched. Upon completion of this search a reset button within the area must be operated. Simultaneous acknowledgment by the central control operator is also required to complete the reset process.

In order to allow experiments to be carried out in one end station while equipment is being set up in the other, an alternative definition of security is required for the end stations. If the pulse magnet modulator for that area is interlocked off, a beam stopper is in position and the slits are closed, the beam channel may be defined secure and access to the end station itself may be permitted without shutting off the VVS (Fig. 21-2d).

A second alternative definition of security (the "BAS mode") allows operation of the accelerator to a beam-analyzing station (BAS) at Sector 20 for machine studies, warmup, or modulator adjustment. If the housing is

Table 21-1 Key to symbols used in Figs. 21-3, 21-4, and 21-5

Symbol	*Item*	*Remarks*
L	Limit switch	Two switches and two dc circuits per door.
K	Keybank	One dc status and one ac release circuit per keybank.
R	Radiation monitor	The symbol is used to designate the radiation monitors at accessways, air vents, and cooling-water heat exchangers. Details are given in the text.
W	Warning light boxes, magenta–yellow (radiation), red–green (klystrons)	One common three-wire circuit per area for each type of warning light.
H	Speaker	In public address systems operated from CCR and DAB.
T	Telephone	
V	Television camera	Video cables run to monitors in CCR and DAB. One control circuit and one status circuit per camera.
D	Door release	Electrical latch and local release button for utility tunnel gates and concrete doors. One common control ac circuit for all door releases.
E	Emergency off	One series dc actuating circuit and one parallel dc button illuminating circuit per area.
B	Emergency stop switch	One series dc actuating circuit around each end station.
C	Beam shutoff ion chamber	In series with emergency stop switches. Readout in DAB.
S	Search reset button	One dc circuit.

secure from the injector through Sector 29 and if beam stoppers at the ends of Sectors 20, 21, and 28 are in place, the VVS may be turned on through Sector 28 and access may simultaneously be permitted in Sector 30, the BSY, and the end station. The beam may be turned on if the BAS magnet is energized.

In general, the machine shut-off system has parallel redundancy as far as possible. Circuits arising in single-pole limit switches are being converted to dual circuits as early as practicable. Any normal entrance breaks at least two such circuits. The interlocks are operated from dc batteries so that momentary interruptions of ac power, whether general or local, need not destroy the housing security or unnecessarily turn all VVS off at once.

ACCESS CONTROLS. The access control system contains a tone loop which is completed only if all VVS are turned off. This is the definition of "machine off."

If all substations are off, the loop is closed and permissive signals are sent to relays in each area interlocked with ventilation and access controls. Release of keys and opening of ventilation hatches requires additional explicit signals from the central control operator (Fig. 21-2b). When any substation is turned on, the loop is broken; interlock relays are released and the central control operator has no power to release keys or initiate ventilation.

In the BAS mode of operation, Sector 30, the BSY, and the end stations are no longer beam areas.

When the beam stoppers are in, the chief operator and switchyard operator may, by agreement, set up the alternative state, "stoppers required," for either end station (Fig. 21-2d). This allows the accelerator to deliver a beam to one end station or to the tune-up dump while experimenters are working in the other end station.

When an end station is set for the alternative "stoppers required" mode of operation, the end station is no longer a beam area as long as the stoppers are in. If the end station has been secured, the stoppers may be removed for experiments, but must be replaced before the end station may be entered again. The stoppers cannot be removed unless the end station is secure. When entry to an end station is permitted, the keybank release is at the discretion of the switchyard operator (Fig. 21-2c).

The hatch covers or other air seals may be opened and the exhaust fans may be started by the operator in central control, or by local control in an instrumentation and control (I & C) alcove, or in DAB, only if all VVS are off or if the area is not a beam area.

The operator must assure himself that the housing and/or end stations have been adequately ventilated before releasing any keys.

WARNING SIGNALS. There are several classes of radiation warnings to be considered. The simplest is in the klystron gallery, which has x radiation from the klystrons and from some of the penetrations to the housing.

Facing each outside door of the gallery are boxes with red and green warning lights. Green means VVS off; steady red means VVS on, klystrons potentially operable. Flashing red means one or more klystrons on within the sector (Fig. 21-2e).

In addition to these warnings of local modulator activity, there is a magenta–yellow light box adjacent to each entrance to the accelerator housing, BSY, and heat exchangers.

Yellow indicates machine off; steady magenta means high voltage is being applied to the modulators in one or more sectors—there is potential beam within; flashing magenta indicates that the beam is on. Note that yellow does not guarantee the absence of residual activity (Fig. 21-2b).

Adjacent to end station doors are illuminated warning signs: red "no access" and yellow "controlled access" (doors not locked; the area must be searched before returning to a secure condition).

Adjacent to each normal accessway to accelerator, switchyard, and heat-

exchanger housings are meters indicating the output of a gamma monitor at the inner end of the accessway. The outputs are also displayed at CCR or DAB. These indicate whether it is safe to enter the housing as far as the monitor. Beyond this point portable survey meters must be used.

Audible warnings over the public address system are given by the operators according to operating procedures defined by health physics.

Control of the magenta and yellow lights outside the radiation areas is provided by the "machine off" interlock loop. A tone receiver in central control receives information that all VVS are off. This information is then fanned out to all sectors to turn on the yellow light outside all housing entrances (Fig. 21-2b). When any substation is turned on, the tone receiver output is removed and magenta lights appear outside each housing entrance.

When the injector is ready for pulsing, all beam-inhibit interlocks have been removed and a beam program has been turned "on" by the operator; a control signal is fanned out to all areas to make the magenta warning lamps flash.

WARNING SIGNALS WITHIN RADIATION AREAS (Fig. 21-2a). The general illumination within radiation areas is used as a warning when the area is being closed. The lights in the accelerator housing are interlocked with the manway hatch covers. In the BSY and end stations, they are interlocked with the large concrete doors and with an inner gate at other entrances. As soon as the area is closed, the lights are flashed off and on for 2 min and then left at a low level. This serves to warn any workers in the housing that it is time to proceed to the nearest "emergency-off" button. The "shutoff" buttons and a green exit light are illuminated and remain visible after the housing lights have been dimmed. Full illumination is restored immediately if the emergency-off circuit is tripped. In the end stations, a number of outlets are provided for connection of additional "emergency-off" buttons, as required.

RADIATION MONITORS. None of the radiation monitors is directly interlocked with the machine shutoff system or with the control of access. Some of them are interlocked with the beam through the machine protection system, others with the "emergency stop" circuit.

Five types of radiation monitors are used in the personnel protection system:

1. Portable gamma monitors in each sector and in the DAB.
2. Gamma monitor at all personnel accessways. These meters can be read out in central control as well as locally, so that the operator can determine whether residual radiation is sufficiently low to allow entry.
3. Gamma–beta air monitors at alternate air exhausts along the gallery and at every exhaust in BSY and beam dump east.
4. Gamma monitors in each nonradioactive secondary water loop of the switchyard heat exchangers. These monitors are interlocked with the

cooling tower pumps to shut off the primary water loop in case of leakage of radioactive water from the primary loop to the secondary loop.

5. Research area monitors to operate the "emergency stop" circuit. Readout of these meters is provided in DAB.

These monitors are described in more detail later.

NORMAL PERSONNEL ACCESSWAYS. Normal personnel accessways are characterized by having two interlocked doors and keys in a local keybank. In the accelerator and switchyard housings, one of the doors is airtight. A radiation monitor with readout at each entry is provided to indicate the existing radiation level inside the entry.

Each door uses a different key. A keybank stores only keys for the adjacent door. Release of the keys from the keybank is controlled from CCR or DAB, as appropriate. Interlocks prevent the operators from releasing keys unless the machine is off or appropriate beam stoppers have been inserted. A glass panel provides access to emergency manual release of keys.

In general, the locked door is self-closing so that a person requires a key *each* time he enters. Each person who enters is expected to take a key along with him. The absence of the key from the keybank is the worker's primary assurance that the accelerator cannot be turned on.

Each entrance has an inner gate or door which has no lock but which remains open any time a person is working inside. The inner gate is interlocked with the machine (just as is the keybank) and provides a second assurance that the machine cannot be turned on until the people inside have left the area and closed the inner gate behind them.

The airtight manway hatch covers along the accelerator serve the function of the inner gate for the accelerator housing. A wire screen door within the labyrinth serves the same function in other areas. The flashing light warning is also interlocked with the closing of this inner gate.

Since much of the shielding around the end stations is movable, the end-station entrances are not permanent installations. A portable entrance module furnishes a weather-tight vestibule bolted to the shielding blocks at each labyrinth entrance. The keybank, a TV monitor camera, and illuminated warning signs are located in the module. Its inner door is the locked control door for the end station; its outer door is for weatherproofing only. The inner gate at each entrance is separately bolted to the labyrinth-shielding blocks.

Each time the inner gates to an area are closed, the lights are flashed for about 2 min. After this period, the illumination is dimmed. The remaining illumination is sufficient to allow a person to find the nearest "emergency-off" button and the nearest exit.

SPECIAL ACCESSWAYS FOR EQUIPMENT INSTALLATION. In general, sliding concrete doors and gates in the end-station cable trenches are left open for the

duration of the required access. There is no associated inner gate and a search of the entire accessible area is required after they are closed. Their limit switches are wired in series with the "emergency stop" buttons. Keys are required to open these doors, but the (exterior) local controls are inhibited unless it is safe to enter and the operator has decided to permit unrestricted access to the area.

It is possible to open the door from the inside without regard to interlocks and during temporary power failures. Local controls for emergency entrance are provided behind a glass panel by each door.

Entrances to cableways and some manholes which are not beam areas but which have substandard shielding from the accelerator housing or BSY are padlocked and the keys are kept at Sector 20 or in DAB in a keybank interlocked with the machine.

Special surveys must be made when the radioactive heat exchangers are entered since they will remain radioactive long after the accelerator is turned off. Keys used to control access to the heat exchangers are kept in an interlocked keybank in the DAB.

DAB DISPLAY PANEL. By perusing the display panel, the DAB operator can check the status of each door, ventilation hatch, gate, and keybank in the switchyard and end stations and can determine if the emergency stop circuit for any area has been tripped. He has controls that permit him to set each end station to either the "stoppers required" state or the "stoppers not required" state, and additionally to set each end station and the switchyard to the states "entry permitted" or "no entry." Changing any of these states requires concurrence of the chief operator. The DAB operator also has buttons to select states "controlled access" or "permitted access" for each end station, and a key release and a television monitor which may be switched to any controlled entrance to the switchyard and end stations. The key release is effective only during "controlled access."

A search reset button is provided for switchyard, B target room, and each end station. This reset button is effective only when the local reset button in the housing is pressed simultaneously.

A set of radiation meters allows the DAB operator to estimate the level of residual activity inside the switchyard or B target area before he releases a key.

The controls for the beam stopper and slit are located elsewhere but are interlocked with the state "stoppers required." The status signals: "pulsed-magnet off," "stoppers in," and "slit closed" are displayed.

Controls for the ventilation hatch covers in the switchyard are located elsewhere but are interlocked with the state "entry permitted" for the switchyard. A status signal "hatch closed" is displayed for each hatch cover.

CCR DISPLAY PANELS. The detailed display of the status of door hatch cover, exhaust fan, keybank, and emergency stop circuit for each sector is on the

switched "sector display" panel. Controls for hatch, fan, keybank release, and search reset also appear on this panel.

The fan control is interlocked with the hatch cover; the hatch may be opened if the machine is off. Key release controls are ineffective until the operator has actively acknowledged that the machine is off. The search reset button is effective only when the local reset button in the housing is pressed simultaneously.

The backup console contains an array of meters to allow the operator to monitor the residual radiation at each manway entrance to the accelerator housing. The operator is expected to determine that the radiation is at a safe level before releasing a key. He also is expected to open hatch covers and start the fans to ventilate the housing for 10 min before releasing any keys.

The status signals "sector secure" and "door closed" are repeated on a summary panel in the maintenance console so that the operator may determine the security of the accelerator housing at a glance.

The summary panel contains indicators for the operational states of the switchyard and end stations ("entry permitted–no entry," "stoppers required–no stoppers," "controlled–unrestricted access"). Selector buttons are provided for the CCR operator to set these states by prearrangement with the DAB operator. Certain further indications of the state of closure of each area (keybank summary, door summary, "emergency off–search reset" status, etc.) are also provided.

Other summary panels also have status indications and reset key switches for the major tone loops "housing secure" and "machine off." The reset button for the "machine off" loop is the operator's acknowledgment that the machine is off and must be pressed before he can permit any entry to housing or end stations.

The reset switch for the housing secure loop must be operated before the operator can turn on any VVS. He thus acknowledges that the housing is secure to the best of his knowledge.

INTERLOCK WIRING. The interlocks are hard-wire circuits which prevent access to radiation areas when the accelerator is on and prevent turning on the accelerator before the housing is secured. The circuits have little direct connection with central control. They require, however, the fan-out of information to every sector. The Central Control Room is the place from which this fan-out can most easily be accomplished. Space in CCR has, therefore, been utilized for the equipment which detects interlock status and sends out permissive control information. For example, the tone receivers for the "housing secure" loop are located in central control. They, in turn, transmit signals which permit turning on the VVS. Similarly, a relay which is actuated when all substations are off ("machine off" loop) is located in central control. It transmits permissive signals allowing ventilation hatches to be opened, etc.

"EMERGENCY STOP" CIRCUIT. The "emergency stop" circuit for the research areas is designed to shut off the beam and to insert beam stoppers in Sectors

20, 21, and 29, and ST_{10} and ST_{30} in the switchyard when, through some fault of shielding or operational procedures, excessive radiation is observed in the research area outside the end stations.

The system is designed to protect personnel who must work in peripheral areas during an experimental run. Insertion of beam stoppers is less extreme than total shutdown and allows quicker return to normal operation once the fault is corrected. It is, nevertheless, quite absolute in its manner of removing the beam from the area.

A stopper consists of a 1-in. diameter stainless steel tube, 5 in. long, filled with lead. It is installed in a fail-safe condition such that air cylinders keep the stopper out of the beam path unless the air supply fails or the power is shut off. The means of inserting the stopper is primarily gravity with slight assistance from the atmospheric air pressure against the bellows seal at the stopper stem. Limit switches indicate the position of the stopper and are connected into the personnel protection interlock system. If the stopper is not in the retracted (out-of-beam) position, no beam can get into the switchyard.

The stopper was not designed to absorb any energy. It was designed to prevent stray pulses of the beam from reaching the switchyard and research areas. It is, in turn, protected through the machine protection system both by interlock switches and the long ion chamber.

The "emergency stop" switches are made of commercial parts. Each switch is actuated by two buttons. The "on" button is key-operated. With the key removed, the "on" button is nonfunctional, but the circuit may be tripped by the "stop" button. The key must be inserted and turned to allow resetting the circuit. The switches are located in research trailers and at each end-station entrance, as shown in Fig. 21-5.

The ion chambers are discussed in detail below. Three alarm levels are provided. One of the three alarm levels is a low set point alarm. A source added to the chamber gives a signal of about 2 mrads/hour, and the low set point is used as an indication of the correct operation of the circuit. The second alarm level is at about 25 mrads/hour. It lights an alarm in the DAB as an indication that the radiation level is becoming excessive. The third alarm level is set at about 100 mrads/hour and is used to turn off the gun and insert beam stoppers. Only the third alarm is part of the local unit; the other two alarms are part of the remote metering circuit in DAB.

No special reset circuit is provided. Each "stop" switch will remain open, after actuation, until reset by an operator's key. Each radiation monitor has a local reset, to be operated by health physics personnel. After the circumstances have been investigated to the satisfaction of the BSY operator, he may remove ST_{10} and/or ST_{30}. If CCR is satisfied, beam stoppers in the accelerator housing will be removed. The injector may, then, be turned on and operation may be resumed, with such extra surveys or restrictions as prove desirable.

Operation of system (KBM)

SEARCH PROCEDURE. One of the major functions of the personnel protection system is to make it possible for the chief operator to keep track of the number of people in the radiation areas. The operator in central control has immediate responsibility for the accelerator housing; the DAB operator has immediate responsibility for BSY and end stations.

If the operator knows the housing is empty, lets two people into an area and counts the same two people out, he may immediately secure the area and prepare to turn the accelerator on. After an extended shutdown, the number and the identity of the people in the housing may be unknown. A search is then required in order to clear the housing or at least to determine exactly how many people are left.

A search is also required any time an "emergency off" button has been operated or any time a person leaves an area through an unguarded door. The immediate and primary function of the "emergency off" buttons is to disable the accelerator. This interlock is reset by a "search" circuit linking the "search reset" buttons.

A search of the entire accelerator housing and end stations requires several man-hours of work. The housing is, therefore, subdivided so that it is possible for the operator to keep a separate count on each area. In general, if unrestricted access is allowed to one area, only that area needs to be searched before securing the housing. An area which has not been entered need not be searched. The end stations, the B target room, the switchyard, and groups of sectors are separated by rigid barriers or gates; a separate accounting of occupants may be kept for each area. The gates between accelerator sectors and between the accelerator and switchyard housing are spaced so that there is seldom any need for personnel to pass through. They are not locked and may be opened easily if necessary, but they are interlocked so that a search is required in both adjacent areas if a gate has been opened.

A search is accomplished by a search team which starts at a dead end or a locked gate and sweeps through the area. As the team passes a gate, they either check that the gate is securely locked or they post a guard.

At specified accessways the team captain calls the operator and then actuates a reset button within the accessway. Simultaneous acknowledgment by the operator resets the search circuit. If the area is empty, the search team may lock the final accessway. If personnel have been left behind, they monitor the accessways until all personnel have been logged out.

When the final accessway is closed and the completion of search has been acknowledged, the illumination in the area flashes for 2 min and then dims to a level sufficient for a person to make his way to the nearest "emergency off" button. Should a person be left behind and press the "emergency off" button, the full illumination is immediately restored, the search circuit is upset, and the entire search must be repeated.

GALLERY AND ACCELERATOR HOUSING. The locations of the personnel protection system components in the gallery and housing of a typical sector are shown in Fig. 21-3. A key to the symbols of Fig. 21-3 and later figures is given in Table 21-1.

The basic lockup procedure for the accelerator housing starts with a search of the housing. At the end of the search, the display panel in CCR should show that all entrances to the accelerator housing have been closed and locked.

Once the chief operator has assured himself that the housing has been cleared and that all entrances are secure, the accelerator housing is ready for the beam. After the BSY and the end stations have also been secured, the accelerator may be turned on.

When entry to the accelerator housing is desired, it is first necessary for the chief operator to acknowledge that the accelerator has been turned off (all VVS off). The chief operator may then release keys to individual doors. The housing ventilation may be started as soon as all VVS are off.

BEAM SWITCHYARD. The location of the personnel protection system components in the switchyard are shown in Fig. 21-4.

Once the DAB operator has assured himself that the housing has been cleared and that all entrances are secure, he may signal to the chief operator in central control that the switchyard is ready for beam. *Simultaneous* acknowledgment by the chief operator sets up the state "no entry" for the BSY and operates interlocks to prevent release of keys for doors and to prevent opening of exhaust fan hatch covers.

When it is desired to enter the BSY, it is first necessary to set the state "entry permitted." This cannot be done until the accelerator has been turned off (all VVS off) or the BAS mode of operation has been established. The chief operator may then press his button "entry permitted" for the switchyard. Simultaneous acknowledgment by the DAB operator denotes his acceptance of the responsibility for control of entry to the switchyard housing.

The DAB operator may then initiate ventilation and release keys to individual doors.

B TARGET ROOM. At time of writing, the B Target Room is a part of the switchyard. It has a separate "emergency off" and reset circuit. Keys may be released from the keybank only when entry to the switchyard is permitted. The B Target Room must be secure before the state "no entry" may be set for the switchyard.

Late in 1967, a shielding wall will be installed between the B Target Room and the BSY. The B Target Room will then be interlocked as part of end station B.

END STATIONS. The location of the personnel protection system components in the end stations A and B are shown in Fig. 21-5.

The end stations have two entry modes, "controlled access" and "access permitted." Under "controlled access" personnel may enter the end station only at designed doors with keybanks. Under "access permitted" personnel may operate local release controls for any door to the end station. Before a search may commence, the DAB operator must set the "controlled access" state, thus immobilizing the release mechanisms for the concrete door and for the gates and utility trenches.

When it is desired to enter an end station, it is first necessary to set the state "entry permitted." (This state includes both the "controlled access" and the "access permitted" states described above.) This cannot be done until (1) the accelerator has been turned off (all VVS off), (2) the BAS mode of operation is established, or (3) the stoppers for that end station are in.

The DAB operator may then release keys to individual doors or may choose "access permitted." This activates local release circuits for operating doors; keys will not be required for entrance until "controlled access" is restored. If "access permitted" has been elected, a full search of the end station is required before it can again be secured.

21-3 Radiation monitoring

Introduction (RM)

Radiation monitoring is accomplished by using a combination of fixed detectors and movable detectors, and within that framework, by continuous monitoring and spot-checking or batch sampling. Examples of the different monitoring concepts are as follows:

1. *Batch sampling.* The cooling water for the klystrons and accelerator waveguides passes under the klystron gallery floor to a heat exchanger in the mechanical equipment alcove. There are thirty such alcoves along the klystron gallery. Radiation levels from these return water lines and heat exchangers are monitored only periodically. The heat exchanger itself is a doubly isolated unit; should a leak develop in the radioactive-water side, the chances of this water reaching the cooling tower are sufficiently remote (because there would have to be a corresponding leak in the cooling tower loop) as not to require a continuous monitor in the cooling tower loop. Water in this line is checked on a periodic basis, taking batch samples back to the laboratory for analysis.

2. *Continuous monitoring.* The heat exchangers for the slits, collimators, and dumps are singly isolated; therefore, a leak in one side contaminates the water in the other. The cooling water loop for these units runs from the tower to the individual units in series. After the final heat exchanger, a continuous water radiation monitor is provided, which not only records the levels, but will shut off the water pumps and indirectly the beam if levels rise above a predetermined value. The air exhaust points of the BSY are other examples of continuous monitoring, with the air being monitored

continuously during the period of probable radioactivity (the first 15 min of venting).

3. *Combination of continuous and batch monitoring.* The air monitors in the klystron gallery are examples of this type of monitoring. There are fixed air monitors at every other exhaust point. Those points not continuously checked will be sampled on a spot-checking basis until a pattern has emerged or "hot spots" identified. The ultimate location of the fixed air monitors and their number will await the results of these checks.

Each of the continuous monitors may employ the following readouts: (1) local only, (2) local and remote, (3) a combination of the above plus beam interrupt. Examples of the first type are the air monitors which have a local ratemeter plus chart recorder. These charts are checked periodically by health physics. The manway monitors are examples of the second type, with a local ratemeter and a remote ratemeter located either in CCR or DAB. The water monitor, which stops the water pumps under alarm conditions, is an example of the third type.

The end station areas require special attention. Although the personnel protection system ensures that no one can enter an area without turning the beam off, the end station walls are not thick enough to attenuate the radiation should a significant fraction of the beam be stopped within the end station itself. In cases where a significant power is to be absorbed within an end station, local shielding must be employed. However, even though the local shielding may be adequate for normal running conditions, there are cases where radiation levels outside the end station walls may rise significantly due to beam missteering, magnet failure, and so on. Levels as high as hundreds of rem per hour may result. Two systems have been installed to minimize this hazard to personnel.

The first system is concerned with high radiation levels at the outside walls of the end stations themselves. Discrete, tissue-equivalent ion chambers are installed around the walls which will (a) read locally, (b) alarm locally and in the DAB if a level of 25 mrads/hour is reached, (c) shut off the beam through the "emergency stop" circuit if a level of 100 mrads/hour is reached. These units respond within 1 sec.

The second system is concerned with radiation levels in the vicinity of an experiment and serves to protect the experimenter. Tissue-equivalent ion chambers, positioned according to the particular experiment, will read and alarm locally and in the DAB if the dose rate rises above 1 mrad/hour. In addition, these units will integrate the dose received over a period of 1 hour. If this integrated dose is greater than 0.75 mrad, an alarm lights in the DAB. Both alarms require that the operator take some action, which may be simply sending one of the available health physics technicians to monitor the area.

In addition to fixed monitoring along the machine, health physics maintains eight peripheral monitoring stations, consisting of moderated BF_3 and Geiger counters, which print out once each hour. Information from these stations is used to assess the radiation levels at the SLAC boundary lines.

Research area monitoring system (GB, GW)

The research area monitoring system consists of ten stations and a central readout unit located in the DAB. The monitoring stations are located at strategic points in the research area depending upon the experiments in progress. Each station consists of two four-decade log ratemeters and two ionization chambers. Dose rate information (0.1–1000 mrads/hour) is displayed locally and transmitted to the DAB. If a preset dose rate is exceeded, an alarm light is turned on locally and also in the DAB. Pulses from the tissue equivalent plastic chamber are transmitted to the DAB and integrated for 1 hour. If the dose for 1 hour exceeds a preset level, an alarm is energized.

One chamber at each station is designed to give the total absorbed dose. This ion chamber is a polystyrene container lined with Shonka tissue-equivalent plastic and filled with Shonka tissue-equivalent gas. See Fig. 21-6 for construction details. The outside is coated with silver conducting paint. The chamber has essentially parallel plate geometry with 4-in. plate separation. The collection efficiency has been checked in a constant field of 400 rads/hour and is essentially saturated (90%) at 550 V. Boag[1] gives equations for the collection efficiency for steady radiation fields and also for pulsed radiation fields where the time between pulses is long compared to the transit time of the ions formed and the pulse width is short compared to the transit time. At 1 pulse/sec, this condition is approached. The theoretical collection efficiency for a 1.5-μsec pulse at 1 pulse/sec is 90% at 10^6 R/hour. At higher repetition rates and the same pulse width, this condition is not fulfilled. Theoretical collection efficiencies for repetition rates up to 360 pulses/sec are, nevertheless, greater than 90% at 550-V collection potential, for average dose rates

Figure 21-6 Construction details of tissue-equivalent ionization chambers.

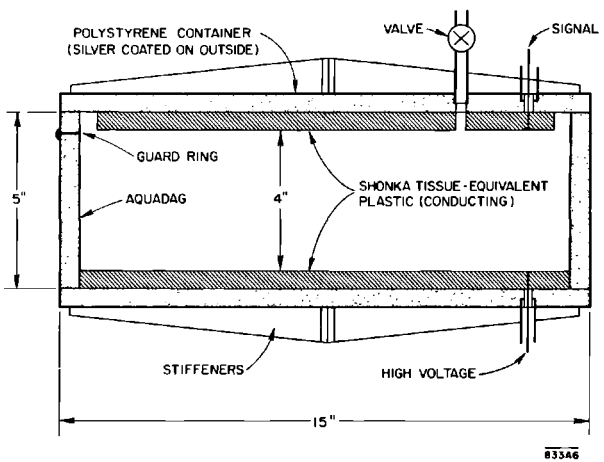

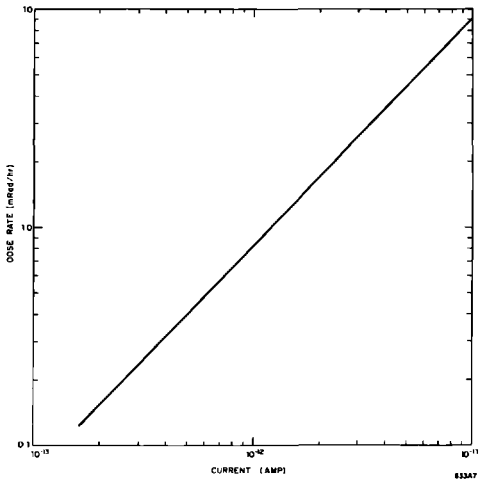

Figure 21-7 Current response of tissue-equivalent chamber to neutrons and gammas.

up to 5 R/hour or more. Figure 21-7 shows a calibration curve of dose rate for Pu–Be neutrons and ^{226}Ra gammas versus current. The dose rate from this chamber is compared with a known tissue-equivalent chamber (Rossi P chamber).

The second ionization chamber is a commercial design, described under manway monitor below.

In order to save on development time, it was decided to modify a commercial instrument for processing the ionization chamber signals. With the exception of two electrometer tubes, the instrument is all solid-state.

Its design concept is as follows: The front end uses one of the electrometer tubes in a common cathode configuration as the input stage of an amplifier the sole function of which is to monitor the charge voltage on a holding capacitor at the input and to maintain a clamp on an otherwise free-running multivibrator. When unclamped, the multivibrator injects a subtractive charge into the holding capacitor through the second electrometer tube connected as a diode. The sense of this subtractive charge is such that the electrometer amplifier reclamps the otherwise free-running multivibrator. Thus, equilibrium is established when the time integral of the subtractive charges exactly equals the time integral of the incoming charges (the signal from the ionization chamber). The digitization is of the order of 1 pulse per picocoulomb. These pulses are used to trigger a circuit which has an analog output proportional to the logarithm of the rate of the input pulses.

This instrument was modified by installing a buffering amplifier in order to bring out the pulses, which are linearly related to the current from the ionization chamber.

These two output signals (a linear signal in digital (pulse) form and a logarithmic signal in analog form ranging from 0 to 5 V) are sent from the remotely located monitoring station via 50-ohm coaxial cable and shielded twisted pairs to the common readout chassis located in the DAB. Analog data from the ten tissue-equivalent chambers are read out on individual meters identical to the ones located in the local instruments. A station selector switch permits analog data from the ten aluminum ionization chambers to be read out on a single meter.

Digital data (from the tissue-equivalent chambers only) are read out on two types of registers. One is a predetermining counter with four significant figure resolutions which can be set to produce an alarm signal at any selected integrated dose level. Each of the ten tissue-equivalent chambers has its own individual predetermining counter.

The second type of register displays the integrated dose and automatically prints a record of the integrated dose every hour. A programmer generates the necessary commands to stop accumulating data, print, and reset the registers hourly. Dead time as a consequence of this program is less than 20 sec each hour. The analog readouts are not affected by this program.

Because of the limited pulse pair resolution of the registers (40 msec minimum), each of the ten channels of digital information is prescaled by a factor of 32. The derandomizing effect of the prescalers and the short-term averaging response of the ionization chambers in conjunction with the use of a "nonparalyzable" pulser to drive the registers enables the digital portion of the system to keep up within the saturation limitations of the ionization chambers for any type of doses (including pulsed) the average rate of which is less than 600 mrads/hour. Due to the nonparalyzable feature just mentioned, higher average fluxes than this maximum will be read out as approximately 650 mrads/hour.

The calibration of the digital channels of information is such that 1 mrad of absorbed dose will be indicated as 100 digits on the digital registers. All channels of information can be individually adjusted so as to exhibit mutual agreement within the limits of reproducibility of this type of instrumentation. A toggle switch permits the operator, at his discretion, either to reset the predetermining registers simultaneously with the automatic hourly resetting of the printing registers or to reset any combination of the predetermining registers at any time with individual pushbuttons. Beyond this one option, the system is entirely automatic. It is completely contained on a single chassis occupying about 15 in. of standard relay rack space.

Peripheral monitoring (TMJ, GB)

The presence of radioactive ground water is monitored through the use of wells. For this purpose there exists a network of eighteen peripheral wells (Fig. 21-8). Samples have been taken from these during the last 18 months to establish background conditions. These wells could also be used to lower the local water table if necessary. The wells are sampled once every 2 months.

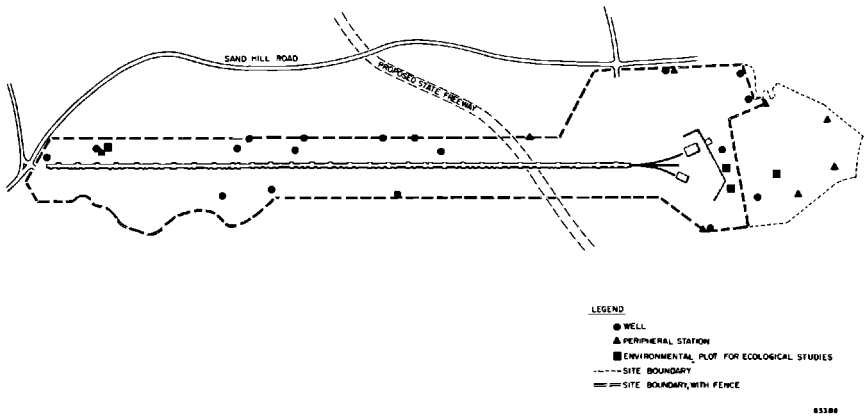

Figure 21-8 Locations of peripheral monitoring stations, water sampling wells, and bio-environmental plots.

In addition, samples are taken from San Francisquito Creek upstream and downstream of the project on a monthly basis. Operating wells in the San Francisquito basin downstream of SLAC are also sampled, including those used by Stanford University. Samples are sent to a commercial laboratory for gross beta and tritium measurements; γ-ray spectra are measured at SLAC.

Finally, there are four environmental plots for ecological studies. Vegetation samples are taken from these on a semiannual basis and compared with similar samples from a distant location. Gamma-ray spectra are measured in-house and gross beta are measured in the ashed samples at a commercial laboratory.

The peripheral monitoring stations serve to provide automatically recorded data concerning radiation levels near the boundaries of the accelerator site. A prototype system was constructed and put in use for approximately 1 year prior to the first turn-on of the accelerator beam, thus giving data on the prior radiation history of the site. Subsequently, three "penultimate" and four "final" versions of this instrument were built, giving a total of eight stations around the site. Seven of these stations are situated relatively near the BSY end of the site, the eighth station is near the injector (see Fig. 21-8).

Convenience, reliability, and cost dictated use of ac power for these stations, supplied from the main facilities through weatherproof cable.

Radiation information is obtained with a Geiger tube and an enriched paraffin-moderated BF_3 tube. Except for sharing a common power supply and a common readout device, the two sources of radiation information are completely independent. The readout device prints and displays ten columns of numbers. The associated circuits assign five of them to the Geiger tube, and five to the BF_3 tube. The resultant display is the equivalent of two independent scalers capable of storing 10^5–1 counts each.

Due to the pulse pair resolution limitation of the register (40 msec minimum), prescaling of the input pulses was again considered necessary. Accordingly, bistable multivibrators were connected serially to provide prescaling coefficients of 8 for the BF_3 tube, and 32 for the Geiger tube. Resultant sensitivity is such that a flux having an average value for 1 hour of 1 mR/hour will be read out as 4800 counts on the Geiger tube channel, and a neutron flux having an average value for 1 hour of 1 mrem/hour will be read out as 48,000 counts on the BF_3 channel. The printout cycle is the same as that for the research area monitors. Although the printed data are usually gathered by health physics personnel once a week, attendance on these stations could be limited to semiannual replacement of roll paper and/or printing ribbon.

An important feature of this system involves the pulser that drives the register. It is of the nonparalyzable type. This means that if the instantaneous rate (20 pulses/sec) is ever exceeded, the register will merely not count the pulses in excess of its maximum rate. It can count at this maximum rate continuously. This rate corresponds to approximately 15 mR/hour for the Geiger channel and about 1.5 mrem/hour for the BF_3 channel. This saturation limit is rarely likely to occur under normal circumstances, since normal readouts are less than one-thousandth of the maximum (7×10^4 counts) that could be acquired in 1 hour.

The Geiger tube can be biased on its plateau with a front panel control switch providing 900–1000 V in 25-V steps. A corresponding front panel control switch provides a bias voltage for the BF_3 tube ranging from 2000 to 2400 V in 100-V steps.

The pulses from the Geiger tube trigger a one-shot multivibrator which, in turn, drives the prescaler (scale of 32) which triggers the nonparalyzable pulser which drives the Geiger portion of the register. Since the pulses from the BF_3 tube are much smaller than those from the Geiger tube and since amplitude discrimination is needed, the BF_3 channel is slightly more complex. A cylindrical extension attached to the BF_3 tube serves as a housing for a bootstrapped field effect source follower amplifier having a gain of approximately 0.95 and an output impedance of about 50 ohms. The output of this amplifier drives a 93-ohm coaxial cable which transmits the signal to a linear amplifier (gain = 100) located within the main chassis. The output of the linear amplifier is presented to a tunnel diode discriminator of which the output drives the BF_3 prescaler (scale of 8). Thereafter the circuitry is identical to the corresponding circuitry in the Geiger channel. Although these stations do not have the sophistication of more elaborate laboratory-type equipment, they appear to accomplish their intended function reliably. They are protected from the weather by being housed in hinged plywood boxes resembling large steamer trunks (see Fig. 21-9).

Tapes are collected monthly from the eight peripheral stations, and the data are fed to a computer which plots the levels in mR/hour for gammas, and mrem/hour for neutrons using a conversion factor of 8 neutrons/cm^2/sec = 1 mrem/hour. This is probably a conservative value and will be revised by

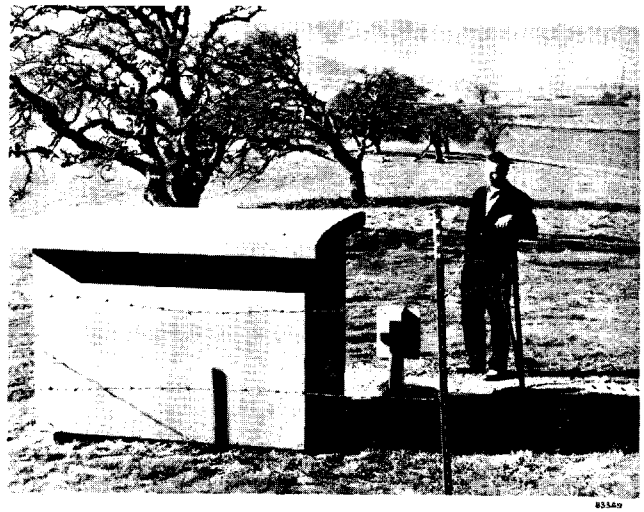

Figure 21-9 Typical weatherproof peripheral monitoring station.

placing a proton-recoil proportional counter at the peripheral monitoring sites to measure an effective average neutron energy. Once this is established, a new conversion factor will be used in the computer to plot dose levels.

The plots are normally made by using values obtained by averaging the readings for a 24-hour period. If a more detailed analysis is desired, the computer will plot out an hourly level. Figure 21-10 is a plot made from one of the monitoring stations during the first quarter of 1967. Peaks corresponding to high radiation level runs in both end station A (ESA) and end station B (ESB) appear clearly on these plots.

Figure 21-10 Radiation levels at peripheral monitoring station No. 1, first quarter of 1967.

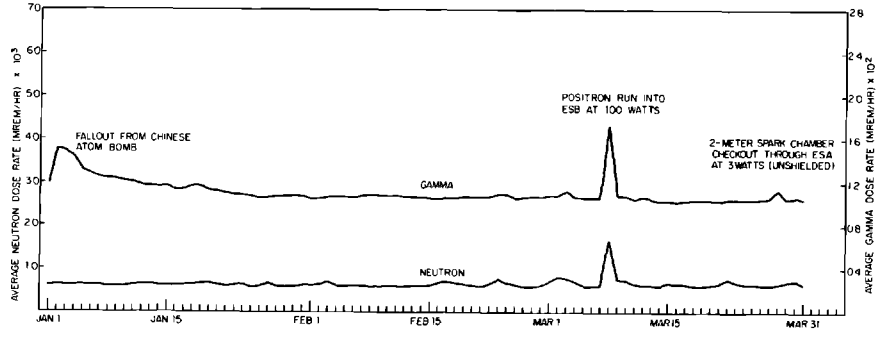

Manway monitors (TMJ)

The primary purpose of the manway monitor is to measure the level of residual radioactivity at the base of a manway penetration to check radiation hazard to which entering personnel will be exposed. A secondary purpose is to determine radiation levels in the tunnel for purposes of shielding evaluation, etc., while the machine is in operation. A manway monitor is located at each manway along the accelerator, each entrance to the BSY, and at the entrances to the heat exchanger pads for slits, collimator, and dumps. Readout is both local (beside the keybank next to the entranceway) and remote (either in CCR or the DAB) to inform both the person entering and the operator of the levels in the vicinity of the detector.

Because the distances involved (up to 2 miles) make frequent checking of these instruments impracticable, the utmost in stability is required. Conventional electrometer circuits have too much drift. The electronics of this system uses a pulse charging technique of which the drift is less than 1 mR/hour over periods of months. (See section on Research Area Monitoring System for details.)

The detector is a 2.5-liter sensitive volume, 4-atm air-filled ionization chamber with an energy response flat to $\pm 10\%$ within the energy range of 80 keV to 3 MeV. An aluminum wall was specified to minimize induced activity in the chamber walls, and the location of the chamber was chosen to give the closest approach to the accelerator possible while maintaining adequate shielding against forward-directed high-energy particles when the beam is on. In the accelerator housing, the detectors are positioned within 8 ft of the waveguide, while they are within 10 ft of the upper housing in the BSY. Their locations are shown in Figs. 21-3 and 21-4.

The range of the meter, located 50 ft from the chamber, is from 1 mR/hour to 10 R/hour with logarithmic readout. The instrument will handle peak intensities greater than 10^3 times full scale, allowing it to be used during machine operation. Typically, when the machine is tuned properly, and with a beam power of about 10 kW, the manway monitors read less than 100 mR/hour, and often less than 10 mR/hour. These units proved extremely helpful during initial beam trials in aiding the operators to locate sectors of maximum beam loss before the long ion chamber was operational. They still serve as a backup to that system.

Water monitor (TMJ)

This section is concerned only with those sources of radioactive water at SLAC that could get into the public water supply. The radioactive cooling-water loops are designed so that a leak to the outside will drain into sumps. A leak into the return water loop of the heat exchanger would be detected by an in-line water monitor and the pumps would be turned off before the contaminated water could reach the cooling tower.

The water monitor consists of ten Geiger tubes with a sensitive volume of 2085 cm^3, immersed in a single stainless steel well through which bypass water flows at a rate of about 1.5 gal/min. The Geiger tubes form two separate detectors, five Geiger tubes per detector. Each detector has its own preamplifier, high-voltage supply, and ratemeter electronics.

Detectors and preamplifiers are located inside the BSY substation building near the return water lines. Readouts of 500 to 2500-V variable supplies and log ratemeters are located in the DAB. When the meter pointer reaches the alarm setting, a relay contact within the ratemeter closes. This is an automatically resetting relay, opening within about 1 sec after closure. If the condition which caused the high level persists, the needle will "chatter" about the alarm point. Also, when this relay closes, a local red light on the ratemeter lights, and then turns off when the relay resets itself.

When both ratemeters alarm in coincidence, a latching relay closes. This lights a local red light as well as a light on the DAB console, and also interrupts a repeater relay of which the normally closed contacts are connected across the cooling tower pump motor "trip" circuit. The pumps cannot be turned on again until the latching relay is reset by pushing the reset button. When reset is accomplished, the red lights are extinguished.

These units were not designed to be fail-safe, so that if one or both units should lose power, the pumps will not shut off. The units are checked daily, and the probability of a leak occurring during the period of a unit failure is sufficiently remote to preclude the failure of the accelerator to shut off in such an event (see Fig. 21-11).

In cooling towers, where water is lost by evaporation, normal radiation levels rise due to the presence in the atmosphere of fallout products which dissolve in the water and are concentrated by the evaporation process. The State of California has estimated that an impurity level of 50 to 3750 pCi/liter will normally occur after a year or so of operation with a waste flow of 5000 gal/day. Thus the alarm level must be set taking into account the normal rise in radioactivity in the cooling water. Normal background from each detector

Figure 21-11 Coincidence and latching relay circuit of water monitor.

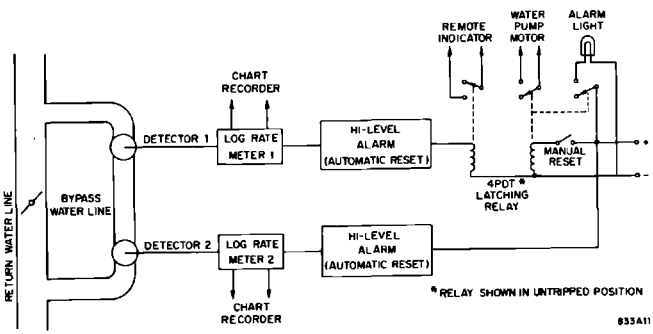

(consisting of five Geiger tubes) immersed in the cooling tower water is about 70 to 100 counts/min. The unit is surrounded by 2 in. of lead so that radiation levels from the accelerator itself will not actuate the pump shut-off system

Radioactive gas monitor (GW)

Radioactive air produced inside the accelerator housing will present a significant hazard to personnel. Using a 3% beam power loss uniformly distributed along the accelerator, DeStaebler[2] has calculated concentrations of various isotopes produced in air. For air the following reactions are of concern: $^{14}N(\gamma, n)^{13}N$; $^{14}N(n, 2n)^{13}N$; $^{16}O(\gamma, n)^{15}O$; $^{40}A(\gamma, p)^{39}Cl$; $^{14}N(\gamma, 2np)^{11}C$. The calculated equilibrium concentrations are shown in Table 21-2. To reduce the hazard, the tunnel which is normally sealed during operation is first vented before entry is permitted. During venting, one complete air change occurs approximately every 10 min.

A radioactive gas monitor is located at alternate exhausts from the accelerator and at every exhaust from the BSY. Monitors are also available to measure the concentration of radioactivity in the tunnel or BSY before venting.

The radioactive gas monitor is a modified commercial design and essentially measures the activity in an 11-liter volume through which air is being pulled at a rate of 3 ft^3/min. The monitor is divided into two sections. One section consists of the GM tube, triggered pulser, pump, and shield and is located in the manway access housing; the remaining section consisting of the ratemeter, recorder, and timer is located in a rack near the manway housing.

The ratemeter and recorder meter movements operate continuously. The air pump starts when the exhaust fan is started and remains on as long as the exhaust fan is on. The recorder drive starts when the fan is turned on and runs for a preset time. The chart drive speed is 2 in./min. The highest concentration occurs in the first few minutes of venting, and then declines. The preset recording time is variable so that the decline in concentration can be followed for a desired length of time (nominally 15 min). The time can be set from 1 to 60 min.

Table 21-2 Calculated equilibrium concentrations of radioactive nuclides

Final nuclide	*Equilibrium concentrations in tunnel (pCi/cm^3)*
^{11}C	3.1
^{13}N	190
^{15}O	220
^{39}Cl	5.5

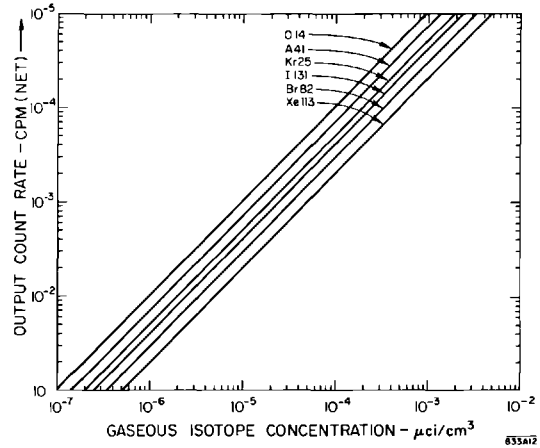

Figure 21-12 Air monitor calibrations.

The unit is calibrated with ^{85}Kr and gives 200 counts/min above background for a concentration of 5×10^{-6} $\mu Ci/cm^3$. Typical calibration curves are shown in Fig. 21-12. The detector is a 50-mg/cm^2 stainless steel Geiger tube filled with a mixture of neon and halogen. The tube is connected to a triggered pulser that provides a 4-V negative pulse, 2 μsec wide, into a 93-ohm load.

The ratemeter is a combination ratemeter and high-voltage supply. The ratemeter is four-decade logarithmic and indicates counts per minute. The high-voltage supply is variable from 500 to 2500 V and provides 100 μamp.

Personnel beam shutoff ionization chambers (GB, GW)

The monitoring station in the research area personnel beam shut-off system ("emergency stop" circuit) consists of an ionization chamber and a four-decade logarithmic ratemeter indicating from 1 to 1000 mrad/hr full scale. The analog information is displayed locally and transmitted to the DAB. There are three alarm conditions: one system failure alarm and two radiation level alarms which are set at 25 mrads/hour (warning) and 100 mrads/hour (beam shutoff). The "system failure" turns on an alarm light in the DAB and requires a manual reset at the DAB alarm panel. The "warning" turns on an alarm light in the DAB and is reset automatically when the radiation level is reduced. The "beam shutoff" turns on an alarm light at the DAB, turns off the injector, and inserts a beam stopper. The "beam shutoff" requires manual reset at the chamber location. A block diagram of one channel is given in Fig. 21-13.

The "system failure" and "warning" level alarms are controlled by a dual optical meter relay used as the analog readout in the DAB. The "beam shutoff" level alarm is controlled by a latching-type contact meter relay in the unit.

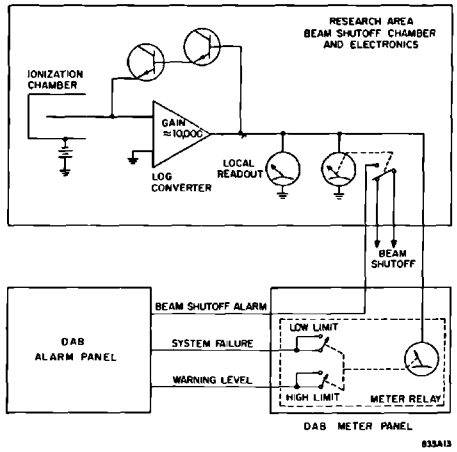

Figure 21-13 Beam shutoff ion chamber and electronics.

The ionization chamber is constructed from aluminum and filled with a tissue-equivalent gas. It is cylindrical, with the collecting electrode supported by a Teflon insulator and the high-voltage electrode supported by a Lucite insulator. Incorporated within the chamber is a 0.4-μCi ^{90}Sr source which produces a current corresponding to 2 mrads/hour for the system failure check. The chamber is designed to produce 1 pA/mrad/hour (10 liter-atm with a collecting potential of 1000 V). It has been checked for saturation in fields up to 100 rads/hour.

Except for two 500-V batteries in series which provide the collecting potential for the ionization chamber, this system is ac-powered and the electronics are all solid-state. The log converter consists simply of two base-to-emitter junctions in series as the major part of a feedback network in an operational amplifier. This amplifier has a dual MOS-FET input and exhibits an open loop gain of the order of 10,000. Primarily because of the temperature dependence of the log converter, this entire circuit is enclosed in an oven operating at approximately 50°C. The proportional controller for this oven uses a thermistor for temperature sensing. Within $\frac{1}{2}$ hour from a cold start, this device has the oven stabilized to within ± 0.1°C. The entire oven temperature control circuit is also located within the oven housing. The oven housing measures approximately $3\frac{1}{2} \times 3\frac{1}{4} \times 2\frac{1}{4}$ in.

A moderate survey of readily available devices quickly led to the discovery that the 2N2484 transistor made by the Texas Instrument Company exhibited a practically ideal logarithmic characteristic (i.e., base-to-emitter voltage versus base-to-emitter current) over the range of 10^{-5} to 10^{-12} A. Surprising uniformity was observed among thirty devices randomly selected, all of them having a conversion slope closely approximating 60 mV per decade of current at room temperature.

The entire monitor unit is enclosed in a weather-tight aluminum housing, 28 in. long and 10 in. in diameter. This housing and the 50°C oven insure that the unit operates with no loss of stability or reliability over the full range of local temperatures (approximately $-5°$ to $+45°$C). The mechanical and electronic layout is such that the unit may be operated in any position and mounted anywhere space allows. This gives a wide choice of location so that the units may be placed to optimize personnel protection for a given set of beam conditions.

Meteorological measurements (DDB)

Early in the design phase, it was recognized that significant amounts of radioactive gas, and possibly radioactive dust particles as well, would be formed by machine irradiation of the air in the accelerator and BSY housings. It was also anticipated that radioactive gas would be evolved from the water used to dissipate beam energy in the switchyard and end station beam dumps. The latter source has since been eliminated by the use of closed-loop catalytic recombiners; however, ^{15}O and ^{11}C isotopes released from dump water prior to the installation of recombiners were used as tracers to measure the atmospheric dilution which occurs between the vent point and the site boundaries.

Atmospheric dilution factors were calculated, using a simplified form of the equation given by Sutton and Pasquill[3]:

$$\frac{\chi_p}{Q} = \frac{8}{\mu}\left(\frac{X}{2}\right) \exp\left[-1.75 + \frac{b(1-C)}{\mu}\right]$$

where

χ_p = the center-line concentration (curies per cubic meter)
Q = the source strength (curies per second)
X = the distance from the source (meters)
C = the fraction of the sky covered by low clouds
$b = +0.5$ at night and -1.2 during the day
μ = the wind speed (meters per second)

The equation holds for $X \leq 2$ km and $\mu > 2$ meters/sec. The night and day values of χ_p were calculated for various values of C and μ with a beam power of 1 MW, and assuming the source to be 400 meters from the site boundary. The relation between beam power and source strength was taken to be $Q \approx 1$ Ci/sec/MW. This was confirmed by measurement (see Fig. 21-14). The results are given in Fig. 21-15. The calculated dilution factor, χ_p/Q is plotted in Fig. 21-16 as a function of X, for constant μ and various values of C.

The maximum permissible concentration (MPC) for ^{15}O and ^{11}C is based on a submersion dose; therefore, total dose for whole-body radiation is used as the limiting criterion. Further, because the MPC is based on the

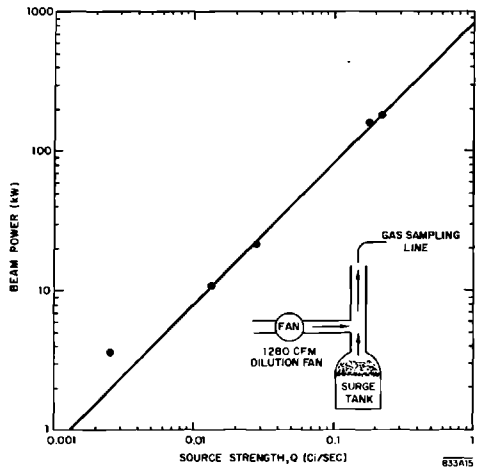

Figure 21-14 Source strength measured at the exhaust stack of a surge tank as a function of power absorbed in a large water dump.

Figure 21-15 Calculated concentration at 400 meters for 1-MW beam absorbed in a large water dump. Curves 1 and 2 for nights; curve 3, overcast day or night; and curves 4, 5, 6, and 7 for days.

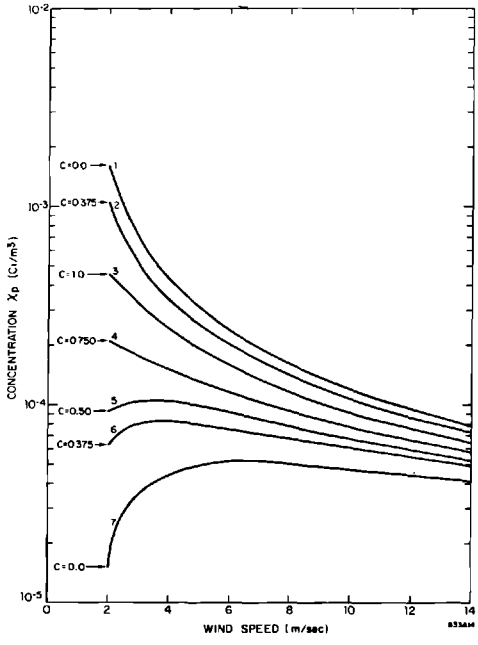

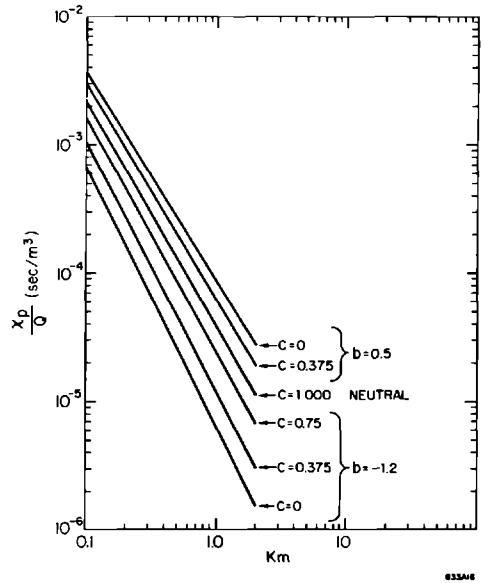

Figure 21-16 Dilution factor vs distance for various atmospheric stability conditions for a 4-meters/sec wind speed. (C, fraction of sky covered by low clouds.)

exposure of a receptor in a semi-infinite cloud, the observed ratio between the maximum dose rate from such a cloud and the measured concentration is used to predict the dose from calculated concentration values at a given distance. This ratio was measured at SLAC and was found to be 0.03 at a distance of 100 meters from the release point. The ratio is not constant because it is dependent upon the vertical and horizontal expansion of the cloud and is also affected by atmospheric turbulence close to large structures. The center-line concentration overestimates by large factors (2–100) the actual ground concentration any receptor might be exposed to at the site boundary. These predictions are, therefore, conservative.

In addition to continuous source strength monitoring, the experimental area is ringed by thermoluminescent γ dosimeters at the site boundary. These dosimeters are collected and evaluated quarterly. As described earlier, there are seven peripheral radiation monitors with BF_3 and Geiger tubes about 700 meters from the point of discharge. These monitors accumulate counts for 1 hour and then print out, giving a measure of integrated n and γ dose on an hourly basis. Only the Geiger measurements are affected by the radioactive gas cloud. These two peripheral monitoring systems will permit a more precise evaluation to be made of the radiation exposure at the SLAC site boundaries. The data will be correlated with wind speed and direction records collected at two on-site weather stations.

Each pair of sectors contains a ventilation fan which removes air from the accelerator housing at the rate of 9000 ft^3/min, making a total of 135,000 ft^3/min from all 30 sectors. This amounts to a complete change of air every 10 min. Each discharge point is slightly above the roof line of the klystron gallery.

The switchyard is vented by five fans having a total capacity of 83,000 ft^3/min, sufficient to change the air every 6 min.

As previously mentioned, radioactive gas monitors are located at alternate vents in the accelerator and at every vent in the switchyard. Exhaust air is continuously monitored while the fans are on.

It has been found that air activation products do not offer serious problems. Under most conditions, atmospheric dilution factors are sufficient to maintain the site boundary dose well below 500 mR/yr.

21-4 Equipment protection systems

General (KEB)

One of the major problems in the development of protective circuits was the evaluation and understanding of all the system interactions. For the purpose of this analysis, it was convenient to define two major systems: (1) the RF system which is used to generate and to distribute the RF energy, and (2) the beam guidance system which injects and guides the beam to the user. The analysis of the relations existing in each system and between the systems defined the protection requirements that had to be implemented.

In the RF system proper, protection is normally confined to a particular piece of equipment with appropriate self-protective features. The requirements for the system transporting the beam were more complex, because both RF power and beam were involved and some interactions extended over the whole length of the machine.

Protection requirements arising from the presence of RF power in the waveguide and accelerator sections and its interactions with the modulator-klystron, vacuum, and cooling-water systems were covered by the modulator–klystron protection system, as detailed in Chapter 15. Protection is provided by turning off individual modulators in case of abnormal operating conditions.

The extended interactions led to the development of the machine protection system, which consists of three major parts: the 1-msec network, the 50-μsec network, and the Panofsky long ion chamber (PLIC). The system is designed to turn off the injector before the start of the beam pulse following detection of trouble. (By the time, say, that beam loss or spill is detected during a pulse, it is too late to do anything about it—indeed, the injector and first few sectors will have already finished their work before any signal could possibly be transmitted back from the point of detection.)

The 1-msec network shuts off the beam in case of failure of components the normal operating state of which is steady during beam operation. The

beam is kept off until normal operation for the component has been restored. The beam can then be turned on by a manual reset and may continue to exist as long as all protected components operate normally. Three types of components are protected. Some are partially or fully exposed to the beam and require water cooling for proper functioning. Such items include protection collimators along the accelerator and the positron targets. Other components, such as vacuum valves, are normally completely out of the beam path, but must be protected against the beam if they close in response to a vacuum fault. Some failures in the RF distribution system can produce beam energy changes that exceed the momentum acceptance of the BSY. Certain of these failures are used to turn off the beam through the 1-msec network and serve as backup to the after-the-fact protection provided through the 50-μsec network.

The 50-μsec network was designed primarily to provide protection for switchyard components. The state of switchyard interlocks is edited between each pair of beam pulses according to the trigger pattern signal specifying where the next beam pulse is to be delivered. (For example, if the beam is to go to end station A, B-beam interlocks are to be ignored.) As late as possible before each beam pulse, a permissive signal is transmitted to the injector if the interlocks are satisfied. The network can also be used to inhibit the beam if the positron wand target is not centered at the correct time during its transit across the accelerator aperture.

The PLIC protects the disk-loaded waveguide from damage by the beam itself. The beam is shut off when radiation due to beam interception by the waveguide exceeds a preset level.

One-millisecond network (KC)

The 1-msec network provides a means of automatically turning off the beam if certain interlocks open. The name derives from the speed of operation of the system. Components of the machine protected are the automatic and manual vacuum valves, the protection collimators, and the accelerator disk-loaded waveguide. Inputs to the system are listed in Table 21-3.

SYSTEM DESCRIPTION. A block diagram of the system is shown in Fig. 21-17. The major assemblies are the tone transmitter at the CCR, a tone interrupt unit (TIU) in CCR, the DAB, all sectors and the injector, and a tone receiver at Sector 0 (injector). Two tones (40 and 50 kHz) are generated by the transmitter. When all interlocks are in the normal state, the TIU's provide a through path, and the tones appear at the receiver input. The receiver output (-20 V dc) is applied as an enable input to the injector trigger generator. When any input to a TIU changes to the alarm condition, the signal path is broken and the receiver output changes from -20 to 0 V. This removes the gun trigger and turns off the beam.

Table 21-3 Machine protection system inputs

A. For Sectors 1–30		
	RF drive OK	
	Sector secure	
	Fast valve open	
	Manual valve open	
	Vertical degaussing power supply[a]	
	Horizontal degaussing power supply[a]	
	Beam scraper (except Sector 1)	
	Sector vacuum (main manifold gauge controller)[a]	
	Fast valve control panel	
B. For Even Sectors (2, 4, etc.)		
	Conventional substation output[a]	
	VVS 600-V circuit breaker status[a]	
C. Special		
	Sector 0:	Sector secure
		Vacuum (main manifold gauge controller)
	Sector 1:	BAS-1 vacuum gauge controller
		Temporary positron source, water flow
	Sector 2:	VVS-V1A 600-V circuit breaker status
	Sector 11:	Flood control, automatic–manual switch status (For other interlocks, see TIU 2)
	Sector 20:	BAS-2 vacuum controller
		BAS-2 electronics
		Beam stopper
	Sector 21:	Beam stopper
	Sector 28:	Beam stopper
	Sector 30:	Drift section vacuum controller G1-0
		Fast valve control panel (30-9)
	DAB:	Radiation emergency stop
	CCR:	Beam off
		PLIC
		BAS magnet current
D. TIU 2 Interlock		
	Sector 11:	Main manifold 2, gauge controller
		Source gauge controller
		Fast valve control panel 2
		Fast valve control panel 3
		Fast valves 2, 3, 4, open status
		Fast valve control panel 4
		Positron water cooling
		Wheel–wand–profile monitor status
		Source gauge, fail status

[a] Will become "resettable" interlocks. They will shut off the beam, but the operator may resume operation if they represent a fault in a sector not in use.

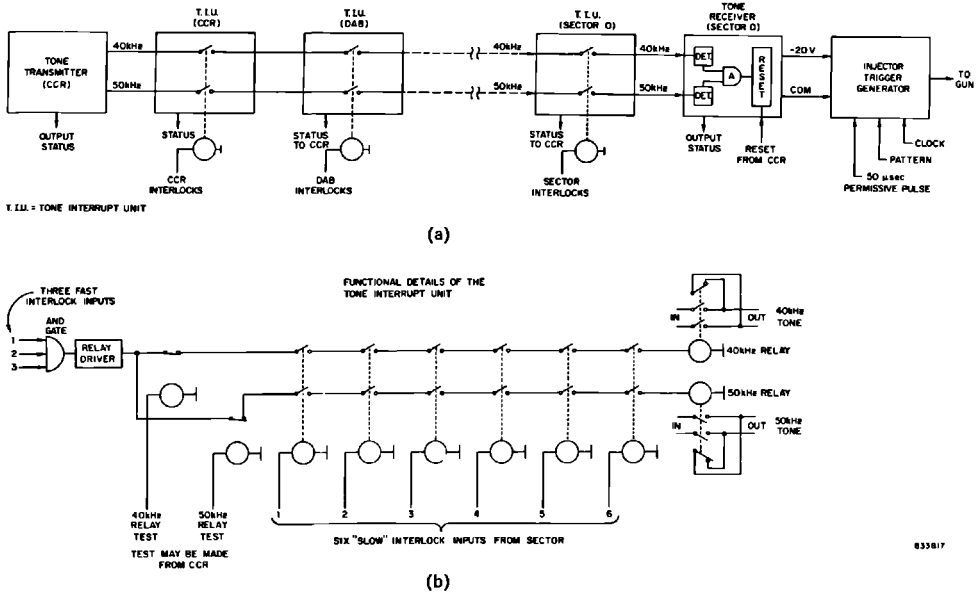

Figure 21-17 One-millisecond network beam shutoff system. (a) Block diagram of 1-msec system. (b) Functional details of the tone interrupt unit.

EQUIPMENT DESCRIPTION. The tone transmitter consists of two independent generators, one at 40 kHz and the other at 50 kHz. The outputs are stable sine waves of 5-V rms amplitude. Each output is transformer-coupled to a 125-ohm balanced wire pair. If either output drops below a preset level, a detector generates an audible and visual alarm.

The tone receiver comprises two independent level detectors, a two-input AND gate, and a reset module. When both tone levels are above the preset value at the receiver input terminals and when a -24-V dc reset signal transmitted from CCR is applied to the reset circuit input, the receiver generates a -20-V dc enabling voltage for the injector trigger generator. The reset signal operates a latching circuit and can be removed once the receiver has been reset. When either or both tones drop below the preset value, the receiver output changes to 0 V, thereby gating off the trigger generator pulses to the injector gun. When the tone inputs have been restored, the receiver has to be reset before the -20-V output can be produced. The delay time between the change of an input tone level and a change in the receiver output voltage is less than 500 μsec. The receiver channel bandwith is ± 1.5 kHz. The input threshold is adjustable from 0.25 to 2.5 V rms, and is set 6 dB down from the normal received input. Line attenuation at 50 kHz is 5 dB/mile.

Provision has been made for operating the receiver with one tone only, thus allowing protection of the machine while the other tone circuit is being tested.

The TIU provides a through path for each tone if all interlock inputs are in the normal state. When any one input goes to the abnormal state, the TIU

opens both tone paths. The input-to-output connection is made or broken by sealed dry reed relay contacts. The contacts open both conductors of each pair and also short each conductor of a pair on the receiver side of the break. Two types of interlock inputs are accommodated: fast inputs (dc levels) operate logic gates in the TIU and open the paths within 500 μsec; slow inputs are applied to relays which release on removal of the input and open the paths within 1 msec. For test purposes, each tone path can be opened independently by remote control from CCR. Whenever the TIU goes to the alarm state, a status change signal is transmitted to CCR.

BAS-2 OPERATION. When the machine is operating in the BAS-2 mode, the tone path bypasses the BSY and Sector 30, and feeds directly from CCR to Sectors 29, 28, etc., and the injector.

Panofsky long ion chamber (DDR)

If missteered at high power, the SLAC electron beam can cause local melting of accelerator components in a fraction of a second. Even relatively low-level irradiation of the accelerator waveguide might ultimately cause harm, gradually changing critical dimensions by altering the crystalline structure of the copper. To protect the accelerator, a system has been installed which is based upon a single long ion chamber[4,5] which runs the whole 2-mile length of the accelerator housing. The signal from the ion chamber operates equipment that turns off the beam when any local radiation level becomes too high. The same signal, observed on an oscilloscope, is sometimes helpful in steering and focusing the beam.

The ion chamber is assembled from some twenty lengths of 4.1-cm diameter RG 319/U coaxial cable, and pressurized to 1 atm gauge with a mixture of argon and 5% carbon dioxide. The facing surfaces of the cable conductors are bare copper spaced by a narrow spiral of polyethylene. The cable is supported by straps near the ceiling of the accelerator housing, 2 meters away from the accelerator disk-loaded waveguide.

When high-energy electrons strike the inner wall of the accelerator structure, a cascade shower is produced in the copper waveguide. The shower density is proportional to the intercepted beam current and to the primary electron energy. The flux of ionizing radiation and the charge collected in the ion chamber are thus proportional to the local electron beam power loss. An ionizing event gives rise to a negative pulse in the cable, which splits with one-half the energy being propagated in the forward direction while the other half is propagated backward toward the injector. The backward pulse travels to the injector end of the cable, which is extended some 500 meters to form a delay line. It is there inverted and reflected by a capacitor, and returns along the cable, which is extended into the CCR and terminated. Each backward pulse arrives in CCR with a relative time delay which is proportional to the distance of its origin from the injector. In CCR, the pulse train from the cable

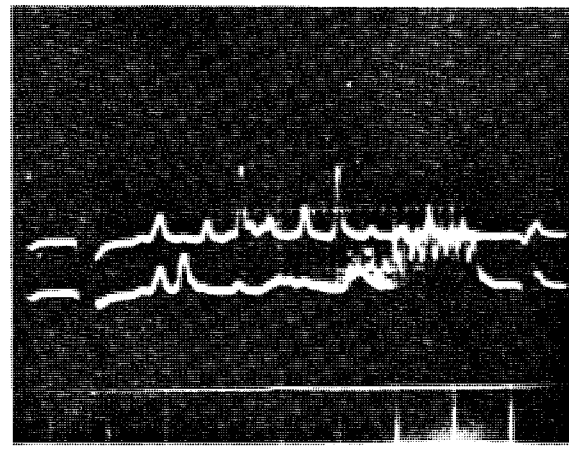

653A18

Figure 21-18 Long ion chamber pulse trains as observed in Central Control Room.

is displayed on an oscilloscope (Fig. 21-18) and fed into a discriminator circuit.

Observation of the backward pulse train at CCR enables one to estimate the magnitude of beam power loss in various regions along the machine and to establish the location of a beam-scraping event to within a few decameters. The closely spaced spikes shown in Fig. 21-18 represent signals from beam scrapers, spaced 100 meters apart. The parameters governing the space resolution are the electron collection time,[6] ~ 0.27 μsec, the electron velocity in the accelerator, c, and the propagation velocity of the cable, 0.92 c. The 0–50% and 10–90% rise times have been measured for pulses making a two-way transit of the whole cable. They have been found to be approximately 0.1 and 2.5 μsec, respectively, in agreement with results cited by Kerns *et al.*[7] The effect of the presence of free electrons and ions upon the propagation of signals in the cable has been estimated[8] and found to be small for the ionization densities usually encountered in practice.

An important advantage of a single long ion chamber is its uniform sensitivity. This uniformity is somewhat impaired in this application by the presence of extra material, such as quadrupoles, dipoles, and beam scrapers between the beam and the ion chamber and by geometrical asymmetry. Multiple scattering of the beam and of secondary electrons tends to reduce the effect of axial asymmetry. When a 10-MW (peak) beam is steered so that it all strikes the inner wall of the accelerator waveguide in a distance of 20 or 30 meters, a pulse amplitude of about 1 V is observed in CCR. By manipulating the location and orientation of missteering, it has been found possible to vary the pulse height through a range of about 30%. A crude calculation indicates that system sensitivity will be about 40% less for an event in which the beam strikes a beam scraper rather than the accelerator waveguide.

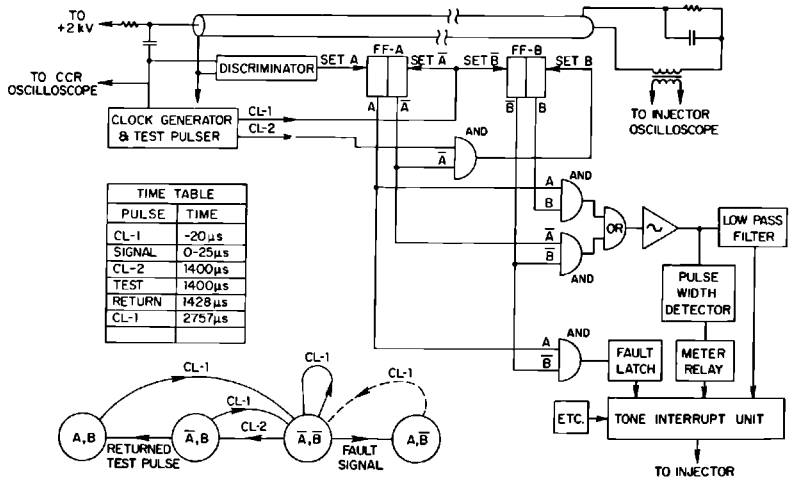

Figure 21-19 Block diagram, time table, and state transition diagram for the long ion chamber logic circuits.

THE DISCRIMINATOR AND PULSE TESTER. Whenever any local beam power loss causes a signal which exceeds a preset value, typically 2 V for 360-pulses/sec operation, the discriminator system turns off the electron beam by operating the 1-msec tone loop system described in the previous section. The tone loop system responds to the loss of one or more input signals by interrupting tone signals in two channels. Absence of tone signal in either channel causes the injector to be turned off within 1 msec. A pulse generator and a system of logical gating circuits, illustrated in Fig. 21-19, test several properties of the ion chamber system during each interpulse interval. In the test, a pulse is transmitted along the cable, its transit time to the injector end and back is measured, and it is verified that the reflected pulse indeed operates the discriminator.

The test circuit consists of a pair of bistable multivibrators, a clock and test pulse generator, and logical gating circuits. The operation of the logic circuits can be understood with the aid of the state transition diagram shown in Fig. 21-19. Flip-flop A is set to state A whenever the signal exceeds the discriminator threshold. Flip-flops A and B are reset to states ($\bar{A}$, $\bar{B}$) by clock pulse CL-1. Flip-flop B is set to state B whenever CL-2 is coincident with state $\bar{A}$. During normal operation, as the system cycles through states ($\bar{A}$, $\bar{B}$), ($\bar{A}$, B), (A, B), ($\bar{A}$, $\bar{B}$), etc., a "fast" enable signal is generated by passing a signal corresponding to ($\bar{A} \cdot \bar{B} + A \cdot B$) through a low-pass filter. Thus during the brief 28-μsec cable transit time interval during which state ($\bar{A}$, B) persists for normal operation, the low-pass filter maintains the fast enable voltage. However, if the transition from ($\bar{A}$, B) to (A, B) fails to occur, state ($\bar{A}$, B) will persist for 1.4 msec. In this event, the enabling signal will decay below an acceptable value in approximately 100 μsec, thereby signaling a system fault

and shutting off the tone signal to the injector. A simple pulse width detector measures the duration of state ($\bar{A}$, B) and produces an analog signal which is applied to a meter relay. Repeated failure to arrive at state ($\bar{A}$, B) will result in a meter relay current of zero. If state ($\bar{A}$, B) persists for approximately 28 μsec during each 2.78-msec interpulse interval, the meter relay will read within its high-low limits. Finally, if ($\bar{A}$, B) repeatedly persists for a half-cycle, the meter-relay reading will exceed its high limit setting. The meter relay is interlocked with other meter relays measuring ion chamber high-voltage and dc current and with a pressure switch actuated by the gas pressure in the ion chamber. These relay circuits interrupt a "slow" enabling signal applied to the TIU.

When a signal fault occurs, the system is set to state (A, $\bar{B}$) and the fast enable signal is removed within 100 μsec. A fault-latching circuit and redundant relay circuit continue to withold the slow enabling signal even though the system again proceeds through its normal cycle after CL-1. The fault-latching circuits must then be manually reset to resume operation.

THE POSITRON GATE. When positrons are being generated, a large signal is produced in the long ion chamber. The discriminator is accordingly provided with a gating circuit which acts to prevent the signal from the positron source from shutting off the injector. The positron gate is normally triggered only when the positron beam is in operation. Its time delay and duration are adjustable, so that the system can retain full sensitivity during those periods when no large burst of radiation is expected from the positron source.

DISABLING THE CIRCUIT. A key-operated switch is provided for disconnecting the system and supplying dummy inputs to the CCR TIU, without disturbing the circuits that produce the oscilloscope signals.

Fifty-microsecond network (permissive pulse system) (KC)

The 50-μsec network establishes the beam permissive condition on a pulse-to-pulse basis. A beam pulse can be released only if the field of the BSY pulse deflection magnet has reached 70% of the final desired value. To allow for rise time and transmission delay associated with the twisted pair cable, the permissive pulse starts at least 50 μsec before the next beam time (hence the system name).

Figure 21-20 shows the system block diagram. In the BSY mode, the permissive pulse is generated in the DAB and transmitted at a 50-V level on a wire pair to CCR. The pulse width is approximately 150–250 μsec and the rise time is 50 μsec. When a positron source pulse (1.5 msec) is present at CCR, the AND gate connects the DAB pulse through to the injector. In the BAS 2 mode, the 150 μsec pulse is generated in CCR and transmitted to the injector on a wire pair.

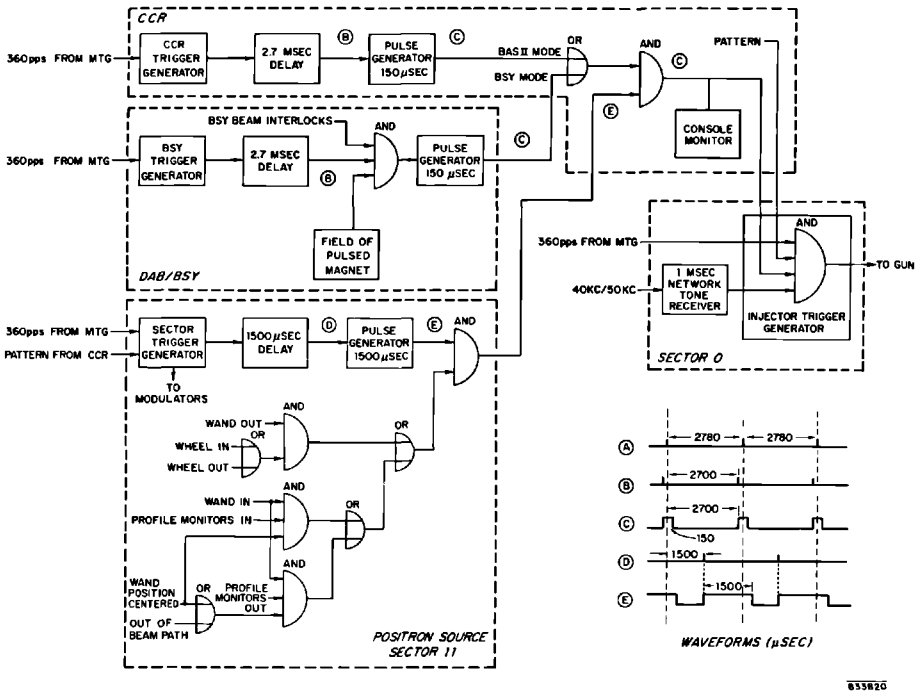

Figure 21-20 Block diagram of 50-μsec network.

The injector trigger generator produces a pulse to the gun when the 1-msec tone receiver output is normal and when the clock, pattern, and permissive pulses are present.

Acknowledgments

We would like to acknowledge the contributions of M. Fishman, who designed the electronics circuits for the long ion chamber protection system. Also, we would like to thank J. Jasberg and V. Waithman for their critical reviews and suggestions for improvement of the personnel protection system.

References

1 J. Boag, in *Radiation Dosimetry, Vol. 2: Instrumentation* (F. Attix, W. Roesch and E. Tochilin, eds.), p. 24, 3rd Ed., Academic, New York, 1966.

2 H. DeStaebler, "Radioactive Gas in the Tunnel," Rept. No. SLAC-TN-62-9, Stanford Linear Accelerator Center, Stanford University, Stanford, California (March 1962).

3 F. Pasquill, *Atmospheric Diffusion*, Van Nostrand, Princeton, New Jersey, 1961.

4 W. K. H. Panofsky, "The Use of a Long Coaxial Ion Chamber along the Accelerator," Rept. No. SLAC-TN-63-57, Stanford Linear Accelerator Center, Stanford University, Stanford, California (July 1963).

5 H. DeStaebler, "Note on Panofsky's Long Ion Chamber," Rept. No. SLAC-TN-63-63, Stanford Linear Accelerator Center, Stanford University, Stanford, California (July 1963).

6 B. Rossi and H. Staub, *Ionization Chambers and Counters*, p. 14, McGraw-Hill, New York, 1949.

7 Q. Kerns, F. Kirsten, and C. Winningstad, in "Radiation Laboratory Counting Handbook," Rept. No. UCRL 3308 (Rev.), Counting Note, File No. CC2-1, Lawrence Radiation Laboratory, University of California, Berkeley, California (1959).

8 D. Reagan, "Plasma Effects in Panofsky's Long Ion Chamber," Rept. No. SLAC-TN-63-91, Stanford Linear Accelerator Center, Stanford University, Stanford, California (November 1963).

SUPPORT AND ALIGNMENT

D. Connell, W. B. Herrmannsfeldt, Editor, M. J. Lee, A. V. Lisin, J. G. Niforopulos, R. C. Sandkuhle, K. Skarpaas, J. J. Spranza, K. R. Trigger, and J. K. Witthaus

This chapter describes the support and alignment systems for both the accelerator and the beam switchyard (BSY). It is divided into three parts which describe successively the laser alignment system, the accelerator support system, and the BSY support and alignment system. The purpose of these systems is to make precision mechanical adjustments for all the beam-carrying elements of the accelerator and the BSY. Thus, the systems include both the measurement and the adjustment features necessary to meet the design tolerances for alignment.

22-1 The laser alignment system (WBH, MJL, JJS, KRT)

Accurate optical alignment over very long lengths requires optics of high resolution and the elimination of atmospheric disturbance. A system of 277 large, long focal length, rectangular Fresnel lenses is used for the alignment of the accelerator. The lenses, also called targets below, are enclosed in a 24-in. diameter vacuum pipe. The system consists of a light source, a detector, and the lenses, one of which is located at each point which is to be aligned.

The tolerance for the alignment of the target points along the accelerator is ± 0.01 in. Conventional optical tooling techniques would require that a very large telescope be pointed at a reference target at the end of the accelerator. The telescope would then have to remain stable until a target at the point to be aligned could be inserted and viewed. The stability requirement would be 0.01 in./120,000 in. or less than 10^{-7} radian, a virtually impossible tolerance.

The three-point method which has been adopted eliminates the high pointing accuracy requirement. Instead, a diverging monochromatic light

source at one end of the accelerator is used to illuminate fully the target of which the position is to be determined. The target, which functions as a simple converging lens, focuses the light source to an image at the opposite end of the accelerator from the source.

The basic idea of the SLAC alignment system is illustrated in Fig. 22-1. A straight line is defined between a point source of light (L) and a detector (D). The light source is a helium–neon laser. The detector consists of a mechanical scanning system and a photomultiplier with suitable output equipment capable of resolving a shift of 0.001 in. at any of the accelerator support points. The actual sensitivity or least-count of the detector is one-tenth of that, or ± 0.0001 in. At each support point, a target T is supported on a remotely actuated hinge. Three additional targets are mounted on monuments, such as the one at M, which are 24-in. diameter pillars supported by rock below the accelerator foundation. To check the alignment at a desired point, the target at that point is inserted into the light beam by actuating the hinge mechanism. The target is actually a rectangular Fresnel lens with the correct focal length so that an image of the light source is formed on the plane of the detector. This image is then scanned by the detector in both the vertical and the horizontal directions to determine the displacement of the lens from the predetermined line.

The lenses are mounted in a 24-in. diameter aluminum pipe (see Fig. 22-2) which is the basic support girder for the accelerator. The support girder is evacuated to about 10^{-2} torr to prevent air refraction effects from distorting or deflecting the alignment image. If any adjustments are required, the support girder is moved by means of a pair of vertical screw jacks and a sidewall screw jack.

The accelerator proper is mounted about 27 in. above the center of the support girder. Because the optical alignment system is only intended to align the support girder in the horizontal and vertical directions, it is necessary to provide an auxiliary system of levels to prevent azimuthal misalignment

Figure 22-1 Schematic diagram of the two-mile linear accelerator alignment light pipe showing position of Fresnel lenses in light pipe girders and monument box.

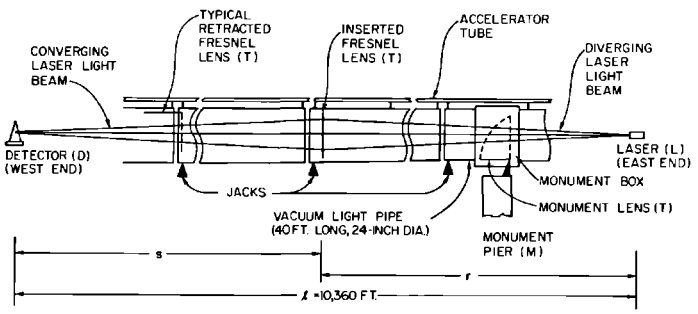

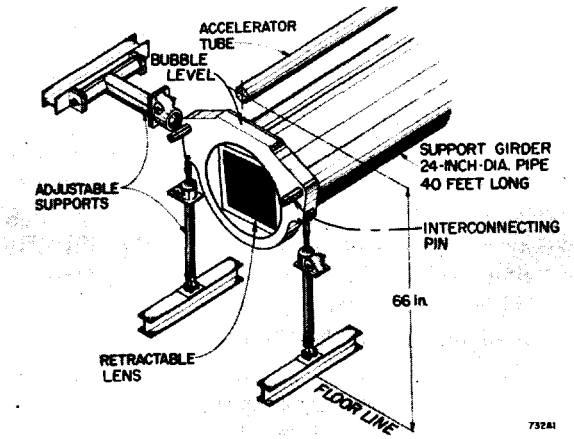

Figure 22-2 Components of alignment system showing the mounting arrangement at the lens end of each accelerator support girder. The lens is shown in the "inserted" position. When "retracted," the lens is in a horizontal position near the top of the pipe.

of the support girder which, to first order, would have the effect of horizontal misalignment of the accelerator. The azimuthal tolerance is about 1 min of arc. Fig. 5-15 is a photograph of an installed 40-ft. accelerator module before the preceding module was moved into place.

The standard accelerator module consists of four 10-ft. long sections of disk-loaded waveguide mounted on top of a 40-ft long section of the 24-in. diameter aluminum support girder. At the end of each sector, which consists of eight 40-ft long modules, there is a special 9-ft long drift section used for steering, focusing, and instrumentation. The standard drift section consists of focusing and steering magnets, beam monitoring devices, and a 0.62-in. diameter collimator, all of which are mounted on a 9-ft long section of support girder. There is a total of thirty such sectors, i.e., 240 of the 40-ft modules and thirty of the 9-ft drift sections, plus three extra modules for the injector and the positron source. As described above, each module is supported at the input end by a pair of precision screw jacks from the floor and by a third jack from the wall, as shown in Fig. 22-2. The output end of a module is attached to the beginning of the next module by a pair of heavy guide pins which allow for thermal expansion. Both the support girders themselves and the four 10-ft long accelerator sections supported by each of them are joined end-to-end by heliarc-welded bellows. A 3-in. thick aluminum end flange is welded to the input end of each section of support girder. The connecting pins from the three jacks are fastened to the outside of this flange. The lens hinge assembly is mounted at the top of the inside of the flange. The accelerator sections are supported on adjustable brackets along the support girder,

except for the first support bracket for the first section. This bracket, which begins above the 3-in. flange, is pinned in place. The whole design of the input flange is intended to provide maximum rigidity between the accelerator sections and the alignment lens.

The alignment lens is mounted on a 14-in. square stainless steel frame. The hinged support plate is spring-loaded to hold the lens firmly against the lower stop when it is inserted in the light beam. A spring-loaded actuator holds the lens horizontally against the top of the support girder, when it is not being used. In this position the lens is hidden behind a square baffle which is mounted in the output end of the adjacent support girder segment. During alignment, one lens at a time is inserted in the light beam produced by the laser. The insertion is obtained by operating a bellows actuator which is mounted in an opening at the top of the support girder. The control panel for the lens actuator is in the klystron gallery directly above the accelerator. Indicator lights wired to microswitches within the support girder show the position of the lens to the operator in the klystron gallery. In addition, the operator of the detection equipment at the end of the accelerator has an indicator showing if any lens in the entire system is not fully retracted. This indicator assures the operator that only one lens at a time is affecting the pattern of the image being viewed. The operator also has control switches to permit him to insert one lens at each drift section in order to make a quick survey of the key points along the accelerator.

Light source

The light source for the alignment system is a standard model commercial helium–neon gas laser. The lenses are designed for the fundamental visible wavelength of 6328 Å. A glass lens of short focal length is mounted on the laser to cause the beam to diverge sufficiently to illuminate fully the closest Fresnel lens, which is about 50 ft away. This lens has a diagonal dimension of about 6 in., but to insure that it is evenly illuminated and further to reduce the pointing requirement, the beam is diverged to about twice that diameter. Even with the diverging lens, the intensity of the images on a ground glass screen is sufficient to be viewed in subdued light. The laser output is from 1.0 to 3.0 mW.

Lens design and fabrication

The targets are rectangular Fresnel-zone plates made out of nickel plated copper. The rectangular design was preferred over the classical circular zone plate primarily for reasons of fabrication. It is easier to rule straight lines than circles, and the circular zones would have required special spiders for supports. The basic scheme would, of course, also have worked with glass lenses. The overwhelming objection to glass was that ordinary glass turns dark in high radiation fields such as are found along the accelerator. Also,

the cost for glass lenses, particularly of radiation-resistant material, would have been much greater.

The one-dimensional Fresnel pattern is shown in Fig. 22-3. The distance from the center line of the target to the nth slot is

$$X_n = \left(\frac{\lambda rs}{2l}\right)^{1/2} (4n)^{1/2} \tag{22-1}$$

This expression is the same as that derived for the radius of the $2n$ Fresnel zone in most standard optics texts.[1] In it, λ is the wavelength, r and s are, respectively, the distances from the lens to the laser and to the detector, and $l = r + s$ (See Fig. 22-1). The edges of the nth slot are at

$$X_{ni} = \left(\frac{\lambda rs}{2l}\right)^{1/2} (4n + d - 1)^{1/2}$$

and

$$X_{no} = \left(\frac{\lambda rs}{2l}\right)^{1/2} (4n + d + 1)^{1/2} \tag{22-2}$$

The subscripts "i" and "o" denote the inner and outer edges of a slot, respectively. The arbitrary constant d selects the point at which the slot edges are located in each Fresnel zone. For example, the values 0.0 and 2.0

Figure 22-3 One-dimensional Fresnel pattern. The spacing is the same as for a circular Fresnel lens with the same product of focal length and wavelength.

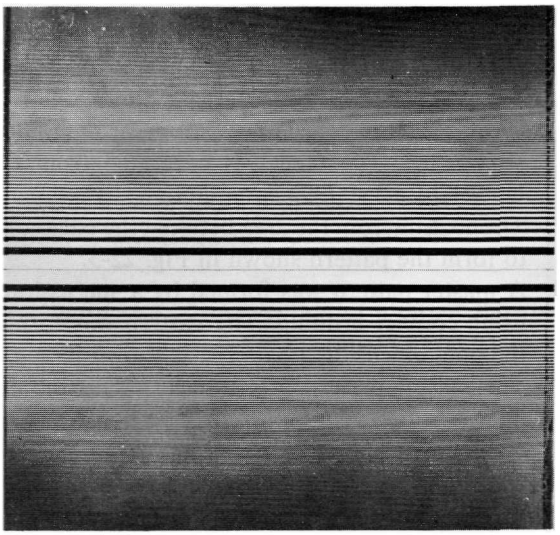

248-4-A

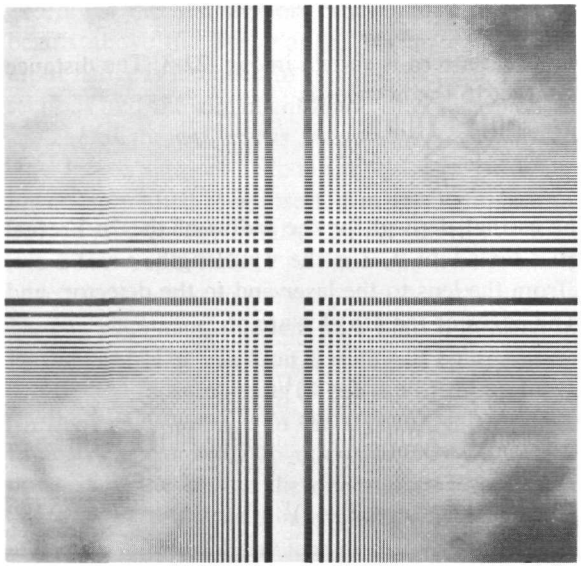

Figure 22-4 Crossed pattern of the rectangular Fresnel lens. The actual lenses have open spaces in the dark areas. The opaque center ribbon, 0.4 in. in width, provides added structural support.

for d have the effect of making two patterns which are inverse or negatives of each other.

The targets are formed by chemically milling an array of rectangular holes into a copper sheet which is about 14 in. square and 0.02 in. thick. The following step-by-step process was developed by the manufacturer*:

1. The complete one-dimensional pattern was ruled on a coated glass plate with an automatic diamond-tipped ruling engine controlled by punched paper tape. The tape was generated from the output of the Stanford University IBM 7090 computer.
2. The coating from the area between the edges of the open slots was stripped to form the pattern shown in Fig. 22-3.
3. A master pattern was formed by a succession of photographic steps, all using contact printing. The pattern was formed from crossed images of the one-dimensional pattern, as shown in Fig. 22-4.
4. The master pattern was transferred to the copper sheet by applying a light-sensitive coating known as photoresist and by exposing the coated copper to the master pattern. The nature of the photoresist coating is

* Metrigraphics Laboratories, Division of Dynamics Research Corporation, Stoneham, Massachusetts.

such that, after developing and fixing, it is possible to use a suitable solvent to wash away the coating where it has been exposed to light. The resulting areas of clean copper may then be used for subsequent plating or etching operations.

5. A 0.002-in. thick layer of nickel was electroplated on the clean copper to form the actual pattern of the target.
6. By chemical milling, the unplated copper was removed to form the required pattern of holes as shown in Fig. 22-4. The chemical milling process was controlled to retain the copper behind the nickel plating wherever possible. Generally, some copper remains if the width of the ribbon is greater than the thickness of the copper sheet.
7. A thin flash-coating of nickel for protection was applied to the target which now resembles the cross-sectional view shown in Fig. 22-5.
8. The target was mounted on the stainless steel frame by match-drilling the target and the frame. The frame has a pair of holes which fit over locating pins on the target hinge, thus completing the connection between the target and the accelerator.

Errors in the position of the edges of the apertures can always be divided into symmetric and asymmetric components. The maximum error that can occur in finding the center of the target is essentially the magnitude of the asymmetric shift of the aperture edges. This conclusion was verified by calculations based on methods which will be used later in this paper. The calculations are detailed in an internal document.[2] The tolerance for the aperture edges is 0.001 in. which is the same as the criterion for the sensitivity of alignment of each lens.

Symmetric errors can only affect the intensity and sharpness of the image, not its position. The only important type of symmetric error is that which is proportional to the distance of the edge of the aperture from the center of the target. This error is equivalent to having the wrong focal length for the target as calculated from Eq. (22-2) where the focal length f is given by $f = rs/l$. The longitudinal distance by which each target can be moved without causing a reduction in alignment sensitivity greater than 10% has been calculated by a digital computer program. In many cases it was found possible to let one target pattern be used in two or more positions without exceeding the 10% limitation. In addition, it was frequently possible to use the same

Figure 22-5 Cross section of a target showing how the apertures are formed by the 0.002-in. thick nickel plating on 0.02-in. thick copper sheets. Where the holes are small and closely spaced, all the copper was often etched away.

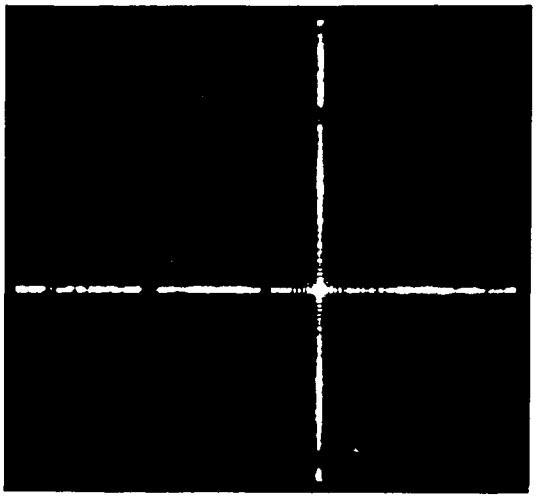

ACTUAL SIZE

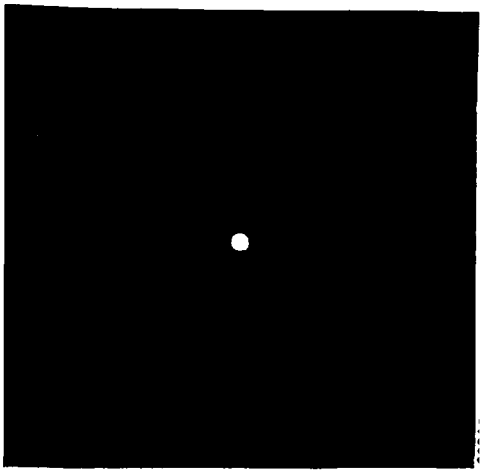

ENLARGED

Figure 22-6a Photograph of image pattern from a Fresnel lens 1000 ft from the focal plane. The point to be aligned is the spot at the center of the crossed lines. The width of the center spot corresponds to the diffraction limit of the Fresnel lens.

target at an exactly symmetrically located position relative to the center of the accelerator. This is equivalent to exchanging r and s in Eq. (22-2). As a result, a total of only 121 different patterns was required for the 277 target locations along the accelerator.

Most of the patterns are 12 in. square. However, a limit of 250 slots was set for ease of fabrication, and as a result, at the ends of the accelerator the targets have 250 lines in less than 12 in. The smallest of the targets, which is the very last one, is only about 4 in. square. The smallest slot in this last target is about 0.004 in. wide. The target with the longest focal length, which is located at the center of the accelerator, has only forty-six slots in each direction of the 12 in. square.

Detector

The spot or line width of the image at the detection station varies from about 0.004 in. for the last target to about 0.5 in. for the target nearest the light source. Figures 22-6a and b show photographs of a typical image pattern. The most difficult targets to align are the ones in the center of the accelerator. In this region, line widths are about 0.2 in. The desired resolution of the alignment system is 0.001 in. With a 2 : 1 enlargement ratio of a lens in the center of the accelerator, it is necessary to find the center of the spot within

Figure 22-6b Photograph of image pattern from a Fresnel lens 9000 ft from the focal plane. The point to be aligned is the spot at the center of the crossed lines. The width of the center spot corresponds to the diffraction limit of the Fresnel lens.

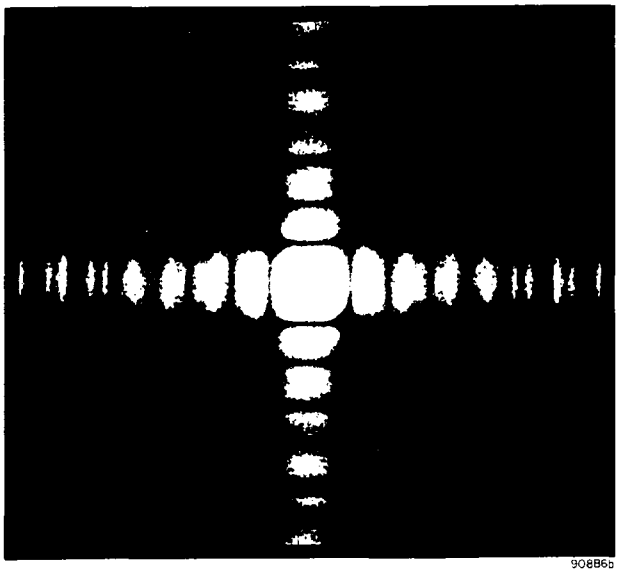

908B6b

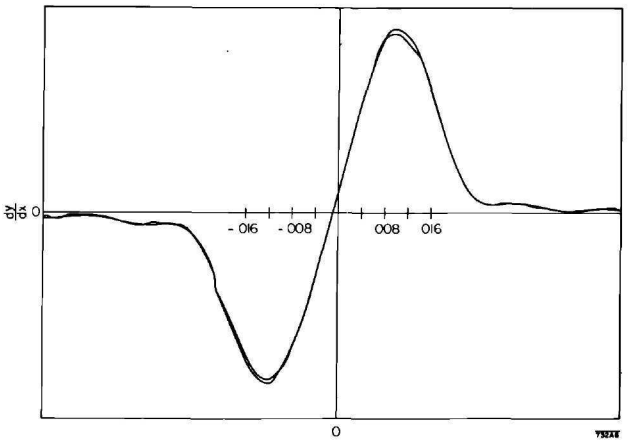

Figure 22-7 Plot of the differentiated signal from the photoelectric scanner. The trace was repeated to show the reproducibility of the output.

0.002 in. or 1 part in 100 of the line width. This is better than a human operator could be expected to do routinely. Therefore, an electromechanical scanning system has been devised which generates the derivative of the spot intensity as a function of detector position in the horizontal and vertical directions. The center of the spot is defined by the point where the derivative is zero. The advantage of using this method is that the steep derivative line intersecting the axis gives an unambiguous determination of the image center. Figure 22-7 shows the actual plot of the differentiated alignment image as obtained from an *x-y* recorder. The curve was traced twice to establish the reproducibility of the results. Figure 22-8 shows an artist's cutaway

Figure 22-8 Variable-amplitude scanner and photomultiplier. The scanner may be rotated to sweep either vertically or horizontally.

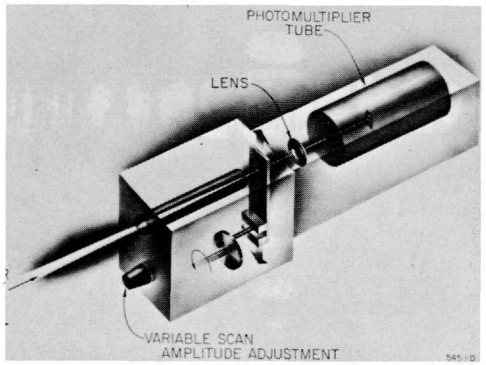

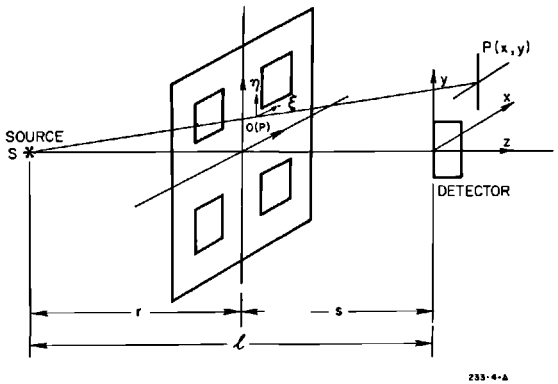

Figure 22-9 Coordinate system for calculating the Fresnel integrals. The amplitude U(P) at the detector is found by integrating from the point O(P) on the target.

of the detector assembly. The detector can be rotated so that it can scan either horizontally or vertically. A switching mirror system at the detector permits the operator to view the image on a ground glass or to direct it into the detector.

Referring to Fig. 22-7, the slope of the trace as it crosses the horizontal axis is proportional to the second derivative of the intensity at the peak of the image spot (d^2I/dx^2), where x is the transverse displacement in the image plane, as shown in Fig. 22-9. When the second derivative of the intensity curve is multiplied by the peak intensity I_0, a measure of the error signal as a function of displacement of the image is obtained. When the square root of this quantity is multiplied by the magnification of the system, l/r, the resulting product is proportional to the signal obtained by displacing the target, thus giving as a measure of the alignment sensitivity

$$\frac{d}{dx}(\text{output signal}) \text{ which is proportional to } \left[I_0\left(\frac{d^2I}{dx^2}\right)\right]^{1/2}_{x=0}\left(\frac{l}{r}\right) \quad (22\text{-}3)$$

Image pattern

The calculation of the image intensity from a pattern of holes in a target plate involves the use of Fresnel integrals. Both Taylor series approximations of the integrals and digital computer programs have been used for calculating the expected images. The analytical approximations will be presented below for the rectangular Fresnel lens.

Referring to Fig. 22-9, the intensity at any point P on the image plane of light which has passed through an arbitrary hole pattern is

$$I(P) = |U(P)|^2 \quad (22\text{-}4)$$

For a point source S, the amplitude $U(P)$ is given by the Fresnel-Kirchoff diffraction integral which, to second order in the variables ξ and η describing the surface is

$$U(P) = \frac{-iAe^{ikl}}{2l} \iint_{\text{target}} \exp\left[i \frac{\pi}{2} (\mu^2 + v^2) \right] d\mu \, dv \tag{22-5}$$

where μ and v are the normalized distances from the origin P on the target and are given by

$$\mu^2 = \frac{2l}{\lambda rs} \xi^2 \qquad \text{and} \qquad v^2 = \frac{2l}{\lambda rs} \eta^2 \tag{22-6}$$

The wave number is $k = 2\pi/\lambda$ and, as in Fig. 22-9, r and s are the source and image distances, respectively, and $l = r + s$. The point $O(P)$ is the point where the line joining S and P intersects the plane of the target. The source intensity is A^2 units-of-power per steradian.

By taking coordinates ξ and η parallel to the edges of the holes, the integrals in Eq. (22-5) can be separated, giving

$$U(P) = \frac{-iAe^{ikl}}{2l} \int_{\mu} e^{i(\pi/2)\mu^2} \, d\mu \int_{v} e^{i(\pi/2)v^2} \, dv \tag{22-7}$$

Substituting Eq. (22-7) back into Eq. (22-4), the expansion for $I(P)$ becomes

$$\begin{aligned} I(P) &= \left(\frac{A}{2l} \right)^2 \{ C^2[\mu(P)] + S^2[\mu(P)] \} \cdot \{ C^2[v(P)] + S^2[v(P)] \} \\ &= \left(\frac{A}{2l} \right)^2 I_\mu I_v \end{aligned} \tag{22-8}$$

There are a variety of ways to design the target within the mechanical limitations. A simple illustration is to attempt to maximize the C integrals while minimizing the S integrals for $P = 0$. If we write

$$C(0) = \int \cos\left(\frac{\pi}{2} \mu^2 \right) d\mu$$

and

$$S(0) = \int \sin\left(\frac{\pi}{2} \mu^2 \right) d\mu \tag{22-9}$$

and allow slots at $(4n-1) < \mu^2 < (4n+1)$ and ribbons at $(4n+1) < \mu^2 < (4n+3)$, the $\cos[(\pi/2)\mu^2]$ function will always be positive during intervals of contribution to the integral while the $\sin[(\pi/2)\mu^2]$ function will oscillate in a manner that causes the integral to be small. The nth slot will then have edges at

$$\xi_+ = \left(\frac{\lambda rs}{2l}\right)^{1/2}(4n+1)^{1/2}$$

and

$$\xi_- = \left(\frac{\lambda rs}{2l}\right)^{1/2}(4n-1)^{1/2} \tag{22-10}$$

In the case of the targets for the main part of the accelerator, a support strip was required through the middle of each target. This prevented inclusion of the center or $n = 0$ slot. The best alternative was to make the central ribbon the same width (0.4 in.) in all targets. Under this condition, the slot edges as defined by Eq. (22-10) do not give optimum peak intensity. It is shown in the Appendix to this chapter that the peak intensity can be maximized by the addition of the constant d under the radical as in Eq. (22-2), with the value of d determined for each target by the central ribbon width. Since $\lambda rs/2l = \lambda f/2$ is different for each target, it is necessary to calculate d from the expression in Eq. (22-2) for the inner edge of the first slot $X_{1i}^2 = (\lambda f/2)(3+d)$, yielding

$$d = \frac{X_{1i}^2}{(\lambda f/2)} - 3 \tag{22-11}$$

where the value for X_{1i} is the half-width of the ribbon, 0.2 in. For the present example, the case for $d = 0$ as in Eq. (22-10), will be considered further, but without the center slot.

Having defined the target pattern as alternating slots and ribbons, the integrals can be rewritten as sums of integrals over the successive slots. Thus,

$$C(\varepsilon) = \sum_{\substack{n=-N \\ n\neq 0}}^{N} \int_{\mu_{n-}(\varepsilon)}^{\mu_{n+}(\varepsilon)} \cos\left(\frac{\pi}{2}t^2\right) dt \tag{22-12}$$

and

$$S(\varepsilon) = \sum_{\substack{n=-N \\ n\neq 0}}^{N} \int_{\mu_{n-}(\varepsilon)}^{\mu_{n+}(\varepsilon)} \sin\left(\frac{\pi}{2}t^2\right) dt \tag{22-13}$$

where ε is the normalized displacement from P at the point where the line from S to the point of interest on the image plane crosses the target. Thus, for the intensity at the peak, the integrals are evaluated for $\varepsilon = 0$. By

measuring ε in the normalized coordinates, as in Eq. (22-6), the slot edges, which are the limits of integration, become

$$\mu_{n-}(\varepsilon) = (4n - 1)^{1/2} - \varepsilon$$

and

$$\mu_{n+}(\varepsilon) = (4n + 1)^{1/2} - \varepsilon \tag{22-14}$$

for $n > 0$, and

$$\mu_{n-}(\varepsilon) = -(4|n| + 1)^{1/2} - \varepsilon$$

and

$$\mu_{n+}(\varepsilon) = -(4|n| - 1)^{1/2} - \varepsilon$$

for $n < 0$.

To analyze the intensity of the image near the central maximum, the one-dimensional intensity of Eq. (22-8) is expressed as a power series in ε. This results in

$$I_\mu(\varepsilon) = C^2(0) + S^2(0) + \varepsilon\left[2C\frac{\partial C}{\partial \varepsilon} + 2S\frac{\partial S}{\partial \varepsilon}\right]_{\varepsilon=0} + \frac{\varepsilon^2}{2}\left[2\left(\frac{\partial C}{\partial \varepsilon}\right)^2 + 2C\frac{\partial^2 C}{\partial \varepsilon^2} + 2\left(\frac{\partial S}{\partial \varepsilon}\right)^2 + 2S\frac{\partial^2 S}{\partial \varepsilon^2}\right]_{\varepsilon=0} + \cdots \tag{22-15}$$

where

$$\frac{\partial C}{\partial \varepsilon} = -\sum_n \left[\cos\left(\frac{\pi}{2}\mu_{n+}^2\right) - \cos\left(\frac{\pi}{2}\mu_{n-}^2\right)\right]$$

$$\frac{\partial^2 C}{\partial \varepsilon^2} = -\pi\sum_n \left[\mu_{n+}\sin\left(\frac{\pi}{2}\mu_{n+}^2\right) - \mu_{n-}\sin\left(\frac{\pi}{2}\mu_{n-}^2\right)\right]$$

$$\frac{\partial S}{\partial \varepsilon} = -\sum_n \left[\sin\left(\frac{\pi}{2}\mu_{n+}^2\right) - \sin\left(\frac{\pi}{2}\mu_{n-}^2\right)\right]$$

and

$$\frac{\partial^2 S}{\partial \varepsilon^2} = \pi\sum_n \left[\mu_{n+}\cos\left(\frac{\pi}{2}\mu_{n+}^2\right) - \mu_{n-}\cos\left(\frac{\pi}{2}\mu_{n-}^2\right)\right]$$

For the range of boundaries of interest, good approximations for the integrals are[3]

$$\int_0^\mu \cos\left(\frac{\pi}{2}t^2\right)dt \approx \frac{1}{2} - \frac{1}{\pi\mu}\left[\frac{\cos\left(\frac{\pi}{2}\mu^2\right)}{\pi\mu^2} - \sin\left(\frac{\pi}{2}\mu^2\right)\right] \tag{22-16}$$

and

$$\int_0^\mu \sin\left(\frac{\pi}{2}t^2\right)dt \approx \frac{1}{2} - \frac{1}{\pi\mu}\left[\frac{\sin\left(\frac{\pi}{2}\mu^2\right)}{\pi\mu^2} - \cos\left(\frac{\pi}{2}\mu^2\right)\right] \tag{22-17}$$

Using Eq. (22-16),

$$C(0) = \sum_{1}^{N} \int_{\mu_{n-}}^{\mu_{n+}} \cos\left(\frac{\pi}{2} t^2\right) dt + \sum_{-1}^{-N} \int_{\mu_{n-}}^{\mu_{n+}} \cos\left(\frac{\pi}{2} t^2\right) dt$$

$$= \frac{1}{\pi}\left[\sum_{1}^{N} \left\{\frac{\pi}{2} - \frac{\cos\left(\frac{\pi}{2}\right)\mu^2}{\pi\mu^3} + \frac{\sin\left(\frac{\pi}{2}\right)\mu^2}{\mu}\right\}_{(4n-1)^{1/2}}^{(4n+1)^{1/2}}\right.$$

$$\left. + \sum_{-1}^{-N} \left\{\frac{\pi}{2} - \frac{\cos\left(\frac{\pi}{2}\mu^2\right)}{\pi\mu^3} + \frac{\sin\left(\frac{\pi}{2}\mu^2\right)}{\mu}\right\}_{-(4|n|+1)^{1/2}}^{-(4|n|-1)^{1/2}}\right]$$

$$= \frac{2}{\pi} \sum_{1}^{N} [(4n+1)^{-1/2} + (4n-1)^{-1/2}] \approx \frac{2}{\pi} \sum_{1}^{N} n^{-1/2} \qquad (22\text{-}18)$$

Similarly, it can be shown that

$$S(0) \approx -\frac{2}{\pi^2} \sum_{1}^{N} [(4n+1)^{-3/2} + (4n-1)^{-3/2}] \approx \frac{-1}{2\pi^2} \sum_{1}^{N} n^{-3/2} \qquad (22\text{-}19)$$

Except for small values of N, the contribution of $S^2(0)$ to $I_\mu(0)$ is negligible. The sum in Eq. (22-18) can be approximated by

$$\sum_{1}^{N} n^{-1/2} \approx \frac{1}{2}\left[\int_{2}^{N+1} n^{-1/2}\, dn + \int_{2}^{N+1} (n-1)^{-1/2}\, dn\right] + 1$$

$$= (N+1)^{1/2} + N^{1/2} - 2^{1/2} \qquad (22\text{-}20)$$

Thus $C^2(0)$ may be expressed as

$$C^2(0) = \frac{4}{\pi^2}[(N+1)^{1/2} + N^{1/2} - 2^{1/2}]^2 \qquad (22\text{-}21)$$

which agrees with computer calculations of $I(0)$ within 0.25% for $N > 25$.

In completing the expansion to second order for Eq. (22-15) using the above method, it is found that

$$\left.\frac{\partial C}{\partial \varepsilon}\right|_0 = \left.\frac{\partial S}{\partial \varepsilon}\right|_0 = \left.\frac{\partial^2 S}{\partial \varepsilon^2}\right|_0 = 0 \qquad (22\text{-}22)$$

The only nonzero term for second order is

$$\frac{\partial^2 C}{\partial \varepsilon^2} = -2\pi \sum_{1}^{N} [(4n+1)^{1/2} + (4n-1)^{1/2}] \approx -8\pi \sum_{1}^{N} n^{1/2}$$

$$\approx -4\pi\left[\int_{1}^{N+1} n^{1/2}\, dn + \int_{1}^{N+1} (n-1)^{1/2}\, dn\right]$$

$$= -\frac{8\pi}{3}[(N+1)^{3/2} + N^{3/2} - 1] \qquad (22\text{-}23)$$

Substituting Eqs. (22-21), (22-22), and (22-23) into Eq. (22-15) gives

$$I_\mu(\varepsilon) \approx \frac{4}{\pi^2}\left[(N+1)^{1/2} + N^{1/2} - 2^{1/2}\right]^2 \cdot \left[1 - \varepsilon^2 \frac{4\pi^2}{3} \frac{(N+1)^{3/2} + N^{3/2} - 1}{(N+1)^{1/2} + N^{1/2} - 2^{1/2}} + \cdots\right] \tag{22-24}$$

For an alignment target formed by superimposing identical patterns at right angles to each other, the symmetry condition

$$I_\mu(0) = I_\nu(0) \tag{22-25}$$

can be used. Then using Eq. (22-8), with $N \gg 1$, Eq. (22-24) becomes

$$I(\varepsilon) = \left(\frac{A}{l}\right)^2 \frac{64N^2}{\pi^4}\left[1 - \varepsilon^2 \frac{4\pi^2 N}{3} + \cdots\right] \tag{22-26}$$

which describes the intensity near the peak along one of the axis lines through the center.

Detector signals

The methods used to analyze the image intensity from the rectangular Fresnel lens will now be extended to study the signal from the detector. The image is scanned in one direction at a time by a linearly oscillating aperture which moves parallel to the direction in which the scanning motion is made. A phase-sensitive detector is used to analyze the signal. To get an analytical expression of the signal amplitude, slope, and line width, the image intensity will be expanded in a Taylor series.

If $H(x, y)$ describes an aperture located at x and y on the image plane, the power into a photomultiplier tube placed behind the aperture is

$$P(x, y) = \left(\frac{A}{2l}\right)^2 \int_{H(x,y)} I(\xi) I(\eta)\, d\xi\, d\eta \tag{22-27}$$

As defined in Eq. (22-6), ξ and η are measured in the target plane. $I(\xi)$ and $I(\eta)$ can be expanded in a Taylor series as

$$I(\xi) = I(0) + \xi I^{(1)} + \frac{\xi^2}{2} I^{(2)} + \cdots \tag{22-28}$$

where

$$I^{(n)} = \left.\frac{\partial^n I}{\partial \xi^n}\right|_{\xi=0}$$

It is convenient to make the calculation using a rectangular aperture with dimensions $2a$ wide by $2b$ high. Then the integral in Eq. (22-27) becomes

$$\int_{H(x\ y)} I(\xi)I(\eta)\,d\xi\,d\eta = \left(\frac{r}{l}\right)^2 \int_{x-a}^{x+a} I(\xi)\,d\xi \int_{y-b}^{y+b} I(\eta)\,d\eta \tag{22-29}$$

where the r/l factors come from measuring ξ and η at the image plane.

If the scan is made in the x-direction exactly through the peak of the image at $y = 0$, then

$$\frac{r}{l}\int_{-b}^{b} I(\eta)\,d\eta = 2I(0)b + \frac{2}{3!}I^{(2)}b^3 + \cdots = G(0) \tag{22-30}$$

and

$$\begin{aligned}\frac{r}{l}\int_{x-a}^{x+a} I(\xi)\,d\xi &= 2I(0)a + \frac{1}{2}[(x+a)^2 - (x-a)^2]I^{(1)} \\ &\quad + \frac{1}{3!}[(x+a)^3 - (x-a)^3]I^{(2)} \\ &\quad + \frac{1}{4!}[(x+a)^4 - (x-a)^4]I^{(3)} \\ &\quad + \frac{1}{5!}[(x+a)^5 - (x-a)^5]I^{(4)} \\ &\quad + \cdots \\ &= 2I(0)a + 2xaI^{(1)} + \left(ax^2 + \frac{a^3}{3}\right)I^{(2)} \\ &\quad + \frac{xa}{3}(x^2 + a^2)I^{(3)} \\ &\quad + \frac{2a}{5!}(5x^4 + 10x^2a^2 + a^4)I^{(4)} + \cdots \\ &= F(x)\end{aligned} \tag{22-31}$$

The motion of the aperture is described by

$$x = x_0 + d\sin\omega t \tag{22-32}$$

where x_0 is the position of the center of oscillation at time t and the amplitude of oscillation is d. From Eq. (22-32),

$$\begin{aligned}x^2 &= x_0^2 + 2x_0\,d\sin\omega t + d^2\sin^2\omega t \\ x^3 &= x_0^3 + 3x_0^2\,d\sin\omega t + 3x_0\,d^2\sin^2\omega t + d^3\sin^3\omega t\end{aligned} \tag{22-33}$$

and

$$x^4 = x_0^4 + 4x_0^3\,d\sin\omega t + 6x_0^2\,d^2\sin^2\omega t + 4x_0\,d^3\sin^3\omega t + d^4\sin^4\omega t$$

The output signal can be obtained in terms of the primary oscillating frequency and harmonics by using the following standard trigonometric identities:

$$\sin^2 \omega t = \tfrac{1}{2} - \tfrac{1}{2}\cos 2\omega t$$

$$\sin^3 \omega t = \tfrac{3}{4}\sin \omega t - \tfrac{1}{4}\sin 3\omega t \tag{22-34}$$

and

$$\sin^4 \omega t = \tfrac{3}{8} - \tfrac{1}{2}\cos 2\omega t + \tfrac{1}{8}\cos 4\omega t$$

The Fourier analysis can then be made by combining Eqs. (22-31) through (22-34) and grouping terms with the same harmonic number. When this is done, the terms with the fundamental frequency are

$$\frac{l}{r}F_1(x_0) = 2I^{(1)}ad + 2I^{(2)}adx_0 + I^{(3)}a\left[x_0^2 d + \frac{a^2 d}{3} + \frac{d^3}{4}\right] + \tfrac{1}{3}I^{(4)}a[x_0^3 d + \tfrac{3}{4}x_0 d^3 + x_0 a^2 d] + \cdots \tag{22-35}$$

To evaluate Eq. (22-35), notice by comparing Eq. (22-21) and (22-24) that

$$I_\mu(\varepsilon) \approx \left[\sum_{\substack{n=-N \\ n\neq 0}}^{N} \int_{\mu_{n-}(\varepsilon)}^{\mu_{n+}(\varepsilon)} \cos\left(\frac{\pi}{2}t^2\right) dt\right]^2 = C^2(\varepsilon) \tag{22-36}$$

From the definition in Eq. (22-6) and from Eq. (22-28)

$$\frac{r}{l}I^{(n)} = \left(\frac{2r}{\lambda ls}\right)^{n/2}\frac{\partial^n I_\mu}{\partial \varepsilon^n} \tag{22-37}$$

where the derivatives are found by successive differentiation of Eq. (22-36).

The derivatives of the $C(\varepsilon)$ integrals follow the pattern used after Eq. (22-15). If the same model target that was assumed in the analysis of the rectangular Fresnel lens is used, then the limits of integration are the same as given by Eq. (22-14).

Predictably, it is found that the odd derivatives are

$$\left.\frac{\partial C}{\partial \varepsilon}\right|_{\varepsilon=0} = \left.\frac{\partial^3 C}{\partial \varepsilon^3}\right|_{\varepsilon=0} = 0 \tag{22-38}$$

$C(0)$ and $\partial^2 C/\partial\varepsilon^2|_{\varepsilon=0}$ are given by Eqs. (22-21) and (22-23), respectively. Continuing to the fourth derivative from Eq. (22-15),

$$\frac{\partial^4 C}{\partial \varepsilon^4} = \frac{32\pi^3}{5}[(N+1)^{5/2} + N^{5/2} - 1] \tag{22-39}$$

is obtained. Combining Eqs. (22-35) through (22-39), the coefficient of the fundamental frequency is found to be

$$F_1(x_0) \approx -\frac{2r}{\lambda ls}(2adx_0)\frac{128N^2}{3}\left[1 - \left(\frac{2r}{\lambda ls}\right)\left(x_0^2 + \frac{3}{4}d^2 + a^2\right)\frac{16\pi^2 N}{15} + \cdots\right] \tag{22-40}$$

The width of the image can be defined as the distance between maximum and minimum of $F_1(x_0)$. As such, it is approximately the distance between

the positive and negative peaks in Fig. 22-7 and is about equal to the full width at half-maximum. If it is assumed that a and d are small compared with the distance to the maximum or minimum, x_m, then by setting $dF_1(x_0)/(dx_0) = 0$,

$$1 - \frac{16\pi^2}{5} N x_m^2 \left(\frac{2r}{\lambda l s}\right) = 0$$

From this one finds

$$x_m = \pm \left[\frac{16\pi^2}{5} N \frac{2r}{\lambda l s}\right]^{-1/2} \tag{22-41}$$

Thus the line width, $x_{max} - x_{min}$, is proportional to $(Nr/s)^{-1/2}$.

In practice the light pipe has constant diameter, thus limiting the targets to a fixed maximum width. Letting $\mu^2 = 4N$ in Eq. (22-6), ξ equals the half-width of a target so that the effective width of a target is

$$D = \left(\frac{8N\lambda r s}{l}\right)^{1/2} \tag{22-42}$$

Combining Eqs. (22-41) and (22-42), the width of the image is found to be

$$w \approx \sqrt{5} \frac{\lambda s}{\pi D} \tag{22-43}$$

which, for the middle of the accelerator, is 0.17 in. Equation (22-43) is strikingly close to the standard expression for resolution of a lens, $\lambda s/D$.

The detection sensitivity is equal to the derivative of the first harmonic coefficient at $x_0 = 0$. Combining Eqs. (22-27) and (22-30) and differentiating, one obtains

$$\left.\frac{dP_1}{dx_0}\right|_{x_0=0} \approx \left(\frac{A}{2l}\right)^2 G(0) \left.\frac{dF_1}{dx_0}\right|_{x_0=0}$$

which, on substituting from Eqs. (22-30) and (22-40), becomes

$$\left.\frac{dP_1}{dx_0}\right|_{x_0=0} \approx -\left(\frac{A}{2l}\right)^2 \left(\frac{16N}{\pi^2} 2b\right)\left(\frac{2r}{\lambda l s}\right)\left(\frac{256N^2}{3} ad\right) \tag{22-44}$$

If it is assumed that the dimensions of the aperture are proportional to the image width such that $b = 2a = Dw$, where D is a constant of proportionality, Eq. (22-44) reduces to

$$\left.\frac{dP_1}{dx_0}\right|_{x_0=0} \approx -17\left(\frac{A}{2l}\right)^2 N^2 D^2 d \tag{22-45}$$

With a laser source that emits 1 mW into a solid angle of $4\pi \times 10^{-4}$ steradian, $(A/2l)^2 \approx 1.3 \times 10^{-11}$ W/in.^{2} for $l \approx 1.2 \times 10^5$ in. Assuming the sweep amplitude d of the scanner is equal to $w/2$, one finds

$$\left|\frac{dP_1}{dx}\right| \approx 1.1 \times 10^{-10} N^2 D^2 w \text{ (W/in.)}$$

In the center of the accelerator, the targets only have 46 lines, or $N = 23$. Putting $D = 1/10$, $|dP_1/dx| \approx 1 \times 10^{-10}$ W/in. Converting to the target coordinates, the alignment sensitivity is

$$\left|\frac{dP_1}{d\xi}\right| = \frac{l}{r}\left|\frac{dP_1}{dx}\right| \tag{22-46}$$

which for the center target is about 2×10^{-10} W/in. To detect a shift of 0.001 in. in the target requires a differentiation of

$$\left|\frac{dP_1}{d\xi}\right|\Delta\xi = (2 \times 10^{-10}) \times (10^{-3}) \text{ watts} \tag{22-47}$$

or 2×10^{-13} W for the middle target. The peak intensity, which is the energy striking the photomultiplier at the center of the image, is, from Eqs. (22-26) and (22-30),

$$I(0) = \left(\frac{A}{2l}\right)^2\left(\frac{256N^2}{\pi^4}\right)(2b)(2a) = \left(\frac{A}{2l}\right)^2 \frac{512N^2}{\pi^4}(Dw)^2 \text{ watts} \tag{22-48}$$

At the center of the accelerator, this is about 8.5×10^{-12} W.

Baffles

A baffle plate with a square opening has been mounted in the light pipe at each target position. The dimensions of the hole in each baffle were determined by the criteria that no light should get around a lens when it is inserted and that no direct rays from the laser should hit the inside surface of the pipe.

The combined diffraction pattern from all the baffles is very complex. It is actually such a diffraction pattern, not a spherical wave, which illuminates a lens. The alignment errors resulting from the baffles were calculated in Reference 2. The method used was to estimate the alignment error as a function of the asymmetry of the diffraction pattern from the baffles. The conclusion is that for any reasonable shift of the baffle, the resulting alignment error is negligible.

Vacuum requirements

The 24-in. light pipe must be evacuated to reduce the magnitude of refractive effects of the residual gas to below the alignment tolerance. Some care was taken during construction to avoid the introduction of heavy solvents or other chemicals with high indices of refraction, so that dry air will be assumed for the following calculations. A large oil diffusion pump with a refrigerated baffle is located at the laser end of the pipe, which has a volume of nearly 33,000 ft^3. The pumping system has proven capable of reducing the pressure to $\approx 10^{-2}$ torr in 8 hours. At this pressure, the system becomes conductance limited by the light pipe itself.

To calculate the effects of the residual gas, it is assumed that the index of refraction has the form

$$n(y) = n_0(1 - \varepsilon y) \tag{22-49}$$

where $n(y)$ is the index of refraction as a function of the vertical position y, and $n_0\,\varepsilon$ is the gradient of n in the vertical direction. The vector form of the differential equation of a light ray is[4]

$$\frac{d}{ds}\left(n\frac{d\mathbf{r}}{ds}\right) = \text{grad } n \tag{22-50}$$

Here $\mathbf{r} = \mathbf{i}x + \mathbf{j}y$, $\mathbf{i}$ and $\mathbf{j}$ are unit vectors, s is the distance along the ray, and y is the transverse coordinate; x is measured along the axis of the light pipe, and thus $s = x$ to a very good approximation. Substituting Eq. (22-49) on the right side of Eq. (22-50) gives

$$\frac{d}{dx}n\left(\mathbf{i} + \mathbf{j}\frac{dy}{dx}\right) = -\mathbf{j}\varepsilon n_0 \tag{22-51}$$

so that

$$\frac{d}{dx}\left(n\frac{dy}{dx}\right) \approx -\varepsilon n_0 \tag{22-52}$$

By integrating Eq. (22-52), it is found that if ε is small,

$$y \approx -\frac{\varepsilon x^2}{2} + Cx + C' \tag{22-53}$$

For a paraxial ray starting on the axis and parallel to it, both constants of integration are zero, and therefore,

$$y = -\frac{\varepsilon x^2}{2} \tag{22-54}$$

which gives the displacement of a light ray due to a gradient of the index of refraction in the light pipe. For the accelerator, the worst case is the middle target for which x is about 5000 ft. Hence, for an error of 0.001 in., which is the permissible tolerance, $\varepsilon \approx 5 \times 10^{-13}$ per inch.

To determine the gradient of the index of refraction, one may use the Lorentz-Lorenz formula in the form[5]

$$A = \frac{RT}{p}\frac{(n^2 - 1)}{3} \tag{22-55}$$

in which A is the molar refractivity, R is the gas constant, T is the temperature, and p is the pressure. Because n is very nearly unity, Eq. (22-55) can be written as

$$n - 1 = \frac{3Ap}{RT(n + 1)} \approx \left(\frac{3A}{2R}\right)\left(\frac{p}{T}\right) \tag{22-56}$$

to obtain the temperature and pressure dependence of $n - 1$. For dry air at standard temperature and pressure, $n - 1 = 3 \times 10^{-4}$. Thus, at any other temperature T and pressure p,

$$n - 1 = 3 \times 10^{-4} \frac{300^{\circ}\text{K}}{760 \text{ torr}} \left(\frac{p}{T}\right) = 1.2 \times 10^{-4} \left(\frac{p}{T}\right) \tag{22-57}$$

where p and T are measured in torr and degrees Kelvin, respectively.

To calculate the gradient of the index of refraction due to vertical temperature and pressure gradients, let

$$p = p_0 + p'y \tag{22-58}$$

and

$$T = T_0 + T'y \tag{22-59}$$

where p' and T' are the derivatives of pressure and temperature with respect to the coordinate y.

By substituting Eqs. (22-58) and (22-59) into Eq. (22-57) and expanding to terms of first order in y, one obtains

$$n - 1 = 1.2 \times 10^{-4} \left(\frac{p_0}{T_0} + \frac{p'y}{T_0} - \frac{p_0 T'y}{T_0^2} + \cdots\right) \tag{22-60}$$

Comparison of terms in Eq. (22-60) and Eq. (22-49) gives

$$n_0 \varepsilon = 1.2 \times 10^{-4} \left(\frac{p_0 T'}{T_0^2} - \frac{p'}{T_0}\right) \tag{22-61}$$

At 10^{-2} torr, $p' = -2.7 \times 10^{-8}$ torr/in. The pressure term then becomes $\varepsilon_p \approx 1 \times 10^{-14}$ per inch which is one-fiftieth of the tolerance derived above and can be neglected. The temperature gradient from top to bottom of the light pipe is not well known. Differences of about 0.1°C have been measured. Solving Eq. (22-61) for T' using the calculated tolerance for $n_0 \varepsilon$ yields

$$T' = \frac{n_0 \varepsilon T_0^2}{1.2 \times 10^{-4} p_0} = \frac{5 \times 10^{-13} \times (300)^2}{1.2 \times 10^{-4} \times 10^{-2}} \approx 0.037^{\circ}\text{C/in.} \tag{22-62}$$

which means that about 1°C differential is allowed from top to bottom of the 24-in. diameter light pipe. It is notable that the temperature term is the one that limits the maximum permissible pressure to stay within the tolerance for alignment.

Detector operation

The theoretical predictions of image size and detector sensitivity have been largely confirmed by experiment. The dimensions of the image patterns agree with the predictions of Eq. (22-43) except in the case of the targets

nearest the laser. For the target closest to the laser, it appears that the assumption of a point source is invalid. The image from the target is about 0.8 in. in diameter instead of the 0.4 in. calculated assuming a point light source. The magnification for this position is about 200, so that the center needs to be found only to within ± 0.2 in. to yield the required accuracy of locating the target. Actually, the sensitivity of determining the position of any target with the photoelectric scanner is ± 0.0001 in., which is the least count of the shaft encoder on the traverse system. The optimum aperture dimensions and scanning amplitudes which were calculated are only partially adhered to in practice. The scanning amplitude is adjusted according to the image width. However, the entire operation is done with a round aperture of 0.004 in. diameter. The photomultiplier has a sufficiently sensitive cathode that even this small aperture is enough to give a very adequate signal.

The detector assembly shown in Fig. 22-8 is mounted on the scanning system shown in Fig. 22-10. The arrangement of the observation equipment is shown in Fig. 22-11. By using the large swing mirror it is possible to divert the image pattern from the detector to a ground-glass screen.

Figure 22-10 Scanning assembly with the large mirror moved to the right to show the large vacuum window. Precision shaft encoders determine the position of the scanner to ± 0.0001 in.

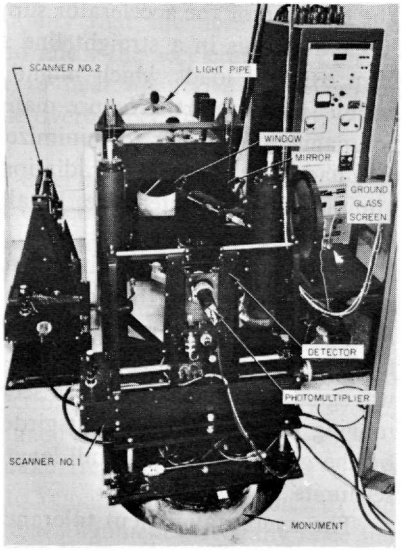

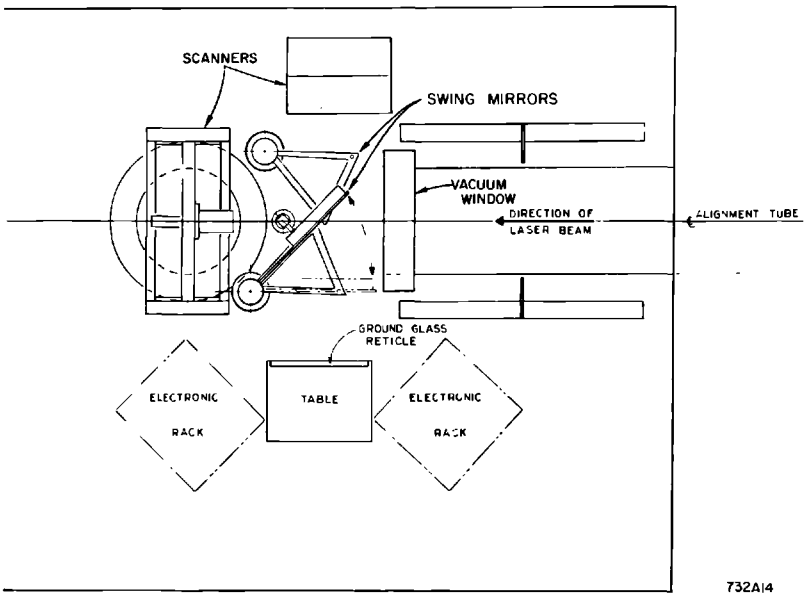

Figure 22-11 Layout of mirrors and observation equipment. By using a beam splitter, two coordinates of alignment can be monitored simultaneously.

22-2 The accelerator support system (DC, WBH, AVL, RCS, KS)

Design criteria

The function of the accelerator support system is twofold: to maintain the accelerator axis in a straight line and to protect the accelerating structure from external loads which might affect its dimensions and, therefore, its tuning. The support structure materials which are near the beam had to be nonmagnetic in order to minimize their interaction with beam optics, and they had to be resistant to radiation. The system had to be stable and require a minimum of maintenance. Finally, it had to have a minimum lifetime of 20 yr and be low in cost.

After initial alignment it had to be expected that the accelerator would move because of earth motions and that realignment would be required. Realignment causes relative motion between the accelerator sections and the klystron gallery. Such relative motion introduces reactions through the waveguides to the accelerator section. Because realignment is achieved by moving the ends of the 40-ft girders, adequate stiffness had to be provided by the girders over their full length to keep transverse deformations within set limits.

The overall alignment tolerance for the 2-mile length of the accelerator is ± 0.040 in. Thus alignment accuracy keeps the need for beam steering to

a minimum. Good alignment is especially important for multiple beams of different energies. The total laser system accuracy is ± 0.010 in., which left ± 0.030 in. for mechanical tolerances in the fabrication and assembly of supporting hardware in the disk-loaded waveguide, the 40-ft optical alignment system, and reading error. The ± 0.030 in. tolerance was allotted as follows. The accuracy of locating the optical tooling holes on the accelerator section at the lens end with respect to the center of the Fresnel lens mounting pins was ± 0.005 in. The tolerance for the location of the optical tooling holes with respect to the center of the accelerator mounting plate was ± 0.005 in. The straightness of an accelerator section mounted on its strongback was supposed to be within ± 0.010 in. Inaccuracies in the alignment tooling and reading error were given another ± 0.002 in. The remaining ± 0.008 in. was allowed as the tolerance for the deflection of the accelerator support structure under external loads.

In addition to the transverse alignment tolerance described above, there was also an axial location tolerance. This tolerance, which applies to the input end of each 10-ft section on a given girder, is ± 0.010 in. This location accuracy was achieved by mounting the input end of the first of the four accelerator sections rigidly to the 40-ft. girder. At this end, the girder is rigidly tied to the ground. The axial location of the successive three accelerator sections on each girder was fixed by spacers between sections.

During operation, the copper accelerator structure temperature is 113°F, whereas the supporting structure is at ambient temperature. Initially, the accelerator housing ambient temperature was approximately 55°F. As of July 1967, the housing temperature is approaching 100°F. Therefore, the support design had to permit a change in length of the supporting aluminum strongback while the accelerator section length remained fixed. Furthermore, it was necessary to recognize the possibility that the accelerator, water temperature, control system could fail and allow the accelerator sections to drop to tunnel ambient temperature or to heat up above the operating temperature to as high as 150°F before the overtemperature interlock would turn off the RF power.

While acting like hinges in the axial direction, the support assemblies had to be sufficiently stiff in the transverse directions to withstand side loads. Side loads could be transmitted to the accelerator sections through the rectangular waveguide in the event that the distance from the klystron to the accelerator changed. In addition to the external loads transmitted through the waveguide, transverse loads can be produced in any direction by an earthquake. The accelerating structure and its supports were designed to withstand an accelerating force in any direction equal in strength to the force of gravity. The structure also had to be designed so that its resonant frequency was outside of the predominant earthquake frequency range of 1 to 10 cycles/sec. The structure is not required to remain within tolerance during an earthquake but must return to its original alignment elastically once the earthquake load is removed.

Because of the radiation environment, the accelerator housing is relatively inaccessible. Thus, materials were chosen which exhibit long-term stability. For the same reason, the support system had to be designed in such a way that small alignment changes could be made quickly with minimum exposure to personnel. After this general discussion of design criteria, individual subsystems will now be described.

Twenty-four-inch light pipe

The 24-inch diameter light pipe serves the dual role of primary support girder for the accelerator and evacuated light pipe for the laser system. A round tube was the most rigid configuration obtainable for a given amount of material. The length of each girder module was determined by the requirement that it support four 10-ft accelerator sections fed with RF power by a common klystron. For the resulting length of 40 ft, a diameter of 2 ft gave the required stiffness. The wall thickness is $\frac{3}{8}$ in.

The girders were made by rolling aluminum plates and welding the longitudinal seam. After welding, each 40-ft segment of pipe was subjected to a fluoroscope inspection (optically magnified, visual x-ray technique). The aluminum pipe was then hydraulically expanded beyond its elastic limit into a 24-in. diameter cavity. This process brought the pipe to its finished form. The pipe dimensions were required to be within $+1/32$ and $-3/32$ in. on diameter, $\pm\frac{1}{4}$ in. on ovality, and straight to $\frac{1}{2}$ in. over the length of the pipe.

A 3-in. thick aluminum plate was used for the upstream end plate. It was called the target plate because it fixed the geometric relationship between the center of the accelerator sections and the center of the alignment target mounted to it. It also secures the pins of the intergirder connection hardware which supports the weight of the downstream end of the adjacent girder, and it provides for connecting the support jacks to the girder. Rather than to cut a full circle in the end flange to match the inside diameter of the pipe, a bridge was left to accommodate the target hinge. A flanged surface outside the pipe was provided for doweling the end plate of the first 10-ft accelerator section. These features are shown in Fig. 22-12. The 3-in. thick target housing was butt-welded directly against the upstream end of the support girder pipe.

The downstream end flange of the support girder pipe was made from a $1\frac{1}{2}$-in. thick aluminum plate. The plate was provided with a cutout hole slightly larger in diameter than the pipe so that it could be slipped over the 24-in. diameter and welded in position to yield the correct girder length to a tolerance of $\pm 1/16$ in.

Brackets for mounting the accelerator sections to the girder were welded to the 24-in. pipe. The accelerator support pads, when fitted with two vertical and one horizontal stud, permitted the alignment of the 10-ft accelerator sections relative to the target plate.

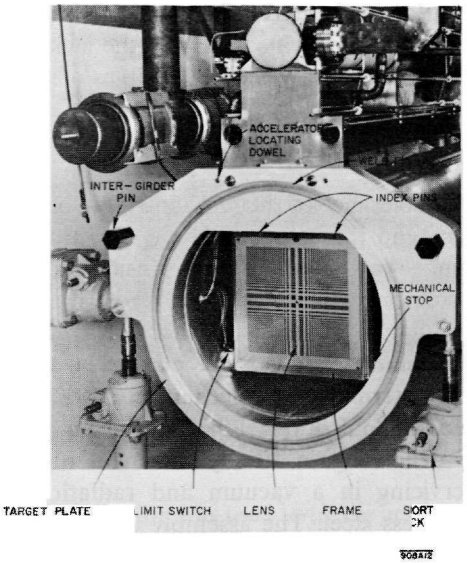

Figure 22-12 View of girder at target end.

The intergirder connection supports the downstream end of the girder. Adjustable rollers were mounted on the downstream end plate of each girder. A pair of hexagonal steel pins were fitted into conical holes in the target plate. The pins mate with the rollers and permit axial expansion of the girder. The joint also permits slight angular adjustments to be made between girders.

A 24-in. diameter aluminum bellows was welded between the adjacent ends of each pair of girders. The welding was done in place in the $2\frac{3}{4}$-in. wide gap between girders. The weld was made to a 1/16-in. thick fin which was left on the face of the end plates. A complete description of the girder fabrication method can be found in Reference 6.

Mechanical worm screw jacks serve as adjustable links between the support girder and the floor and wall of the accelerator housing. The wall jack permits making horizontal adjustments of the girder. This jack was braced to provide the longitudinal constraint. The floor jacks permit making vertical and leveling adjustments to the girder. In the bottom of each floor jack-strut, there is a system of springs that limits the maximum torque that any jack may introduce into the girder system. Ball rod ends connect the jacks to the girder and floor mounting bracket. The floor jacks are provided with a 6-in. adjustment permitting a readily available adjustability of ± 3 in.

To achieve the required axial stability, the wall jacks were provided with short 2-in. adjustment screws. The caps that guide the screw in the jack body were held to a maximum clearance of 0.003 in. Also, to reduce wobble to a tolerable minimum, it was necessary to build a bearing into the base of the jack body to support the jack screw.

For horizontal adjustments to the girder in excess of ± 1 in., 2 in. of shims were provided between the jack and its "A" frame support. They may be removed or added in multiples of $\frac{1}{2}$ in. as required.

Laser alignment hardware

The tolerance of the mechanical tie between the center of the laser alignment lens and the center of the accelerator section is 0.001 in. A spring-loaded hinge was mounted to the inside face of the target housing. A pneumatic actuator drives the hinge from outside the light pipe vacuum system through a vacuum tight mechanical connection. The Fresnel lens in its frame was pinned to the hinge plate. The "in" and "out" positions of the lens are determined by mechanical stops. Limit switches wired to lights in the remote control panel in the klystron gallery indicate the lens position.

The hinge assembly shown in Fig. 22-13, which must operate without servicing in a vacuum and radiation environment, was fabricated from stainless steel. The assembly consists of the lens mounting plate, the shaft, the constant force springs, and the mounting bracket. Constant force springs were attached to the hinge shaft to force the bottom edge of the lens frame against the mechanical stop. The torque is just sufficient to hold the frame firmly against the stop and to actuate the limit switch.

The hinge actuator shown in Fig. 22-14 consists of a pneumatically driven bellows assembly attached to a spring-loaded push rod. A bell crank hook is attached to the slotted end of the push rod. Both the bell crank and the spring cylinder are mounted on a common base bracket. The spring and the bellows work in opposition so that with the air pressure off, the spring retracts the target. As air is applied to the bellows, the pressure on the cylinder exceeds the force of the spring and allows the bell crank to rotate about its shaft and lower the target into the laser system. As the push rod extends forward, it does not apply any force to the bell crank; thus there is no external force on the target.

Figure 22-13 Target hinge.

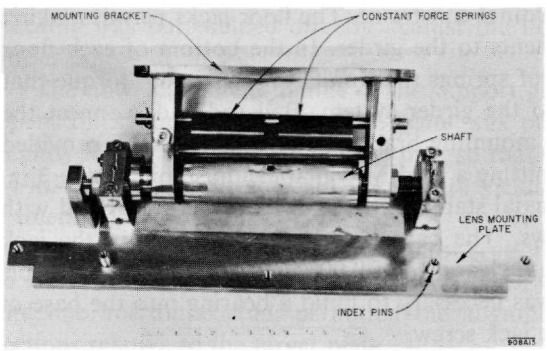

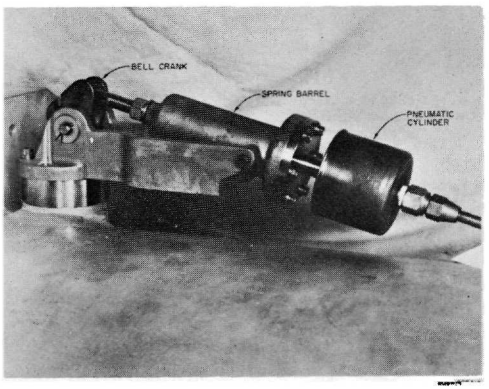

Figure 22-14 Hinge actuator.

A vacuum feedthrough with a universal motion was used to tie the actuator linkage to the hinge mechanism. This motion is achieved with a welded metal bellows arrangement and a rigid connecting rod which ties the hinge to the bell crank pin. The pin was threaded to permit adjustment. The vacuum feedthrough was fabricated of 300-series stainless steel plate and the bellows was made of precipitation-hardened stainless steel. The feedthrough is mounted on the light pipe on a boss welded to the pipe. The vacuum seal between the feedthrough and the light pipe is made by a metal gasket.

The position of the target is referenced by two limit switches. When the target is retracted, it makes contact with the upper switch attached to the hinge. When the target is inserted in the laser light path, the lower limit switch indicates that the target is in the correct vertical position. The switch wires were connected through an electrical feedthrough consisting of a connector sealed in a Pyrex–boro silicate glass insulation mounted in a Kovar flange. The flange was sealed to the light pipe by an indium wire seal.

Accelerator sections

The 4-in. diameter copper accelerator sections were fabricated in 10-ft lengths. The copper was fully annealed and, therefore, the sections could not support their own weight. Hence, immediately after fabrication, all 10 ft sections were permanently mounted on 10-ft aluminum extrusions, called "strongbacks." These extrusions and their mounts were designed to protect the accelerator sections and their input and output transition waveguides during processing and final installation. The mounts were designed to permit differential thermal expansion between the aluminum supporting structures and the accelerator sections. Four of these 10-ft accelerator sections were mounted and aligned on each 40-ft aluminum support girder as shown in Fig. 22-15.

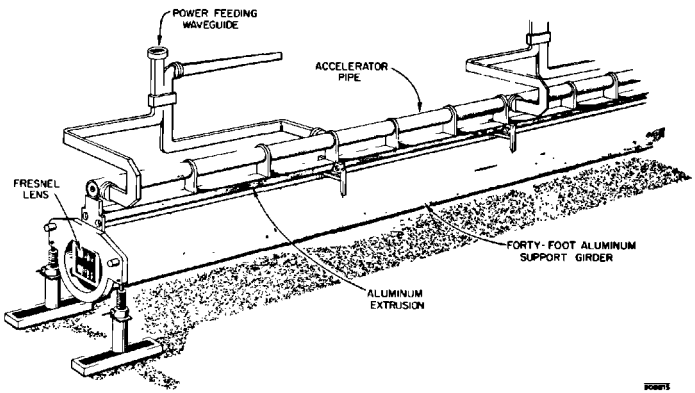

Figure 22-15 Sketch of 40-ft girder.

The specific design criteria placed on the accelerator section support structure were

1. With the accelerator section displaced along its axis by 0.275 in. relative to the strongback and under operating conditions, no combination of the loads shown in Fig. 22-16 should cause a total transverse displacement greater than ± 0.010 in. vertically, ± 0.008 in. horizontally, or a twist greater than 0.2 mradian. (See Fig. 22-17).
2. With the accelerator section displaced along its axis by 0.375 in. relative to the strongback during transportation or other temporary condition, no combination of the loads shown on Fig. 22-16 should cause total transverse displacements exceeding twice the maximum displacements listed in (1) above.
3. The maximum axial force in an accelerator section from all supports used on one 40-ft girder should not exceed 750 lb during accelerator operating conditions.

Figure 22-16 Design loads and axial displacements at the free downstream end of the 40-ft girder.

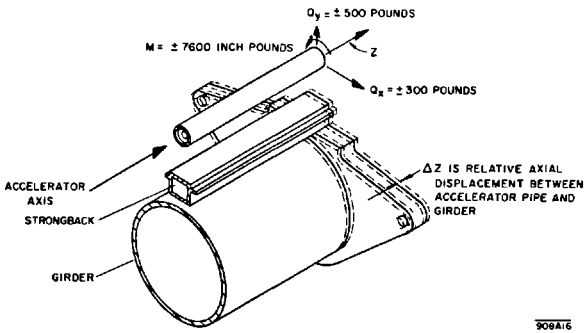

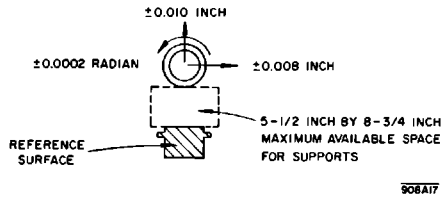

Figure 22-17 Allowable transverse displacements at the downstream end of the 40-ft girder.

4. The supports should be capable of withstanding shock loads of 2 times the design load without permanent deformation.
5. After the supports have been cyled axially 600 times with full design load, between plus and minus 0.372 in., they should still meet criteria (1), (2), (3), and (4).
6. The supports should require no maintenance.
7. The support assembly should be made from nonmagnetic materials.
8. The supports should be of a frictionless and elastic type such that, when all external loads on the accelerator sections are brought back to their original values, the accelerator sections are also restored to their original position.
9. Each 10-ft assembly should provide accurate and easily accessible references for alignment of the accelerator sections on the 40-ft girder.

All the 10-ft support structures were built from assemblies as shown on Fig. 22-18. Interchangeable subassemblies were used to build the support

Figure 22-18 Ten-foot accelerator section mounted on aluminum strongback.

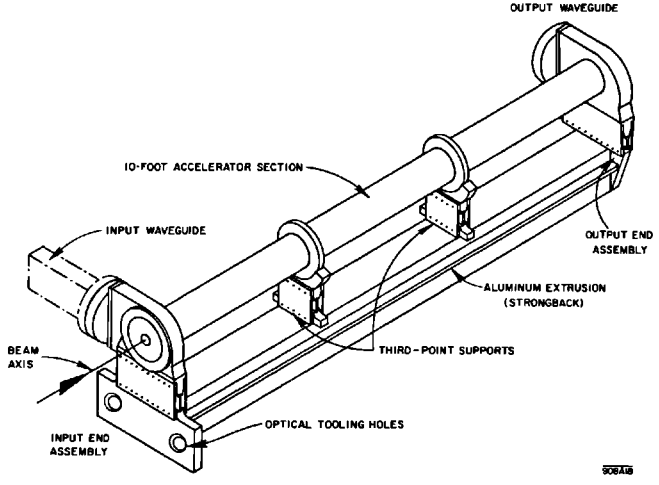

structures for ease of manufacture and cost saving. A typical support structure was made from an aluminum extrusion, an input-end assembly, an output-end assembly, and a pair of one-third point supports.

The input- and output-end assemblies were essentially identical except that only the input-end assembly had optical tooling holes. The optical tooling holes and the locating hole for the disk-loaded waveguide were machined into the end assemblies in a triangular pattern having an 11-in. base line and 10-in. height to a dimensional accuracy of ± 0.001 in. The optical tooling holes were later used in the alignment of the 10-ft assemblies on the 40-ft girders and also in the alignment between girders. Lateral and axial alignment of the downbeam end of each 10-ft section was achieved by the use of stainless-steel locating and spacing rings. These rings aligned one accelerator section with respect to another by mating with concentrically machined recesses at the ends of the accelerator sections.

The first input-end assembly used on each girder was bolted rigidly to the girder target housing. The rigid end assembly was made by using a larger mounting plate and eliminating the flexible section. The last accelerator section on each girder had mounting plates with tooling holes at both the upbeam and downbeam ends. The optical tooling holes of the downbeam end were used to align the accelerator section on the girder and then to make the intergirder cross-joint alignment. Six different end assemblies were produced, all capable of being mounted at either end of the aluminum extrusions. Different combinations of these subassemblies were then used to produce all the required support structures.

Figure 22-19 Flexible support assembly (cross section to scale).

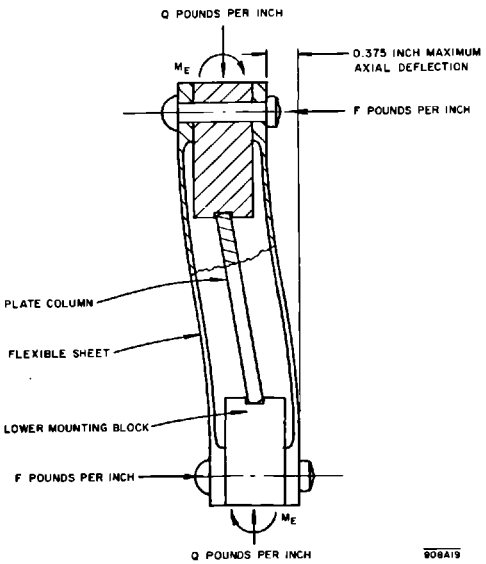

Most of the support subassemblies included a flexible section built as shown in Fig. 22-19. This riveted part of the subassemblies consisted of two flexible aluminum sheets, an upper and a lower mounting block, and a spring-tempered, phosphor, bronze plate column. The plate column, which was rounded at both ends, was inserted with a compressive preload to insure that an external tensile load would not cause separation between the plate column and the mounting blocks. The flexible assemblies carried the weight of the accelerator sections plus any external loads while deflected axially as shown in Fig. 22-19. During this deflection, the plate column rolls on its ends and the sheets bend. This design was chosen since it was capable of providing very high lateral stiffness and almost any chosen axial stiffness.

The 10-ft aluminum extrusion provides support for the 10-ft accelerator section at the one-third and two-third points as well as at the ends. The extrusions are never exposed to external loads, all external loads being carried through the end assemblies directly to the support girder. The aluminum extrusion was designed to limit lateral deflections of the accelerator sections to 0.030 in., when exposed to accelerations of $\sqrt{2}\,g$ in any direction.

The aluminum extrusion was a 10-ft long box beam. A lip on each side was provided for mounting of the third-point supports.

The assembly of the accelerator section to the support structure was performed on a granite block which had special built-in tooling. The accelerator sections were mounted on the preassembled support structures, and the third-point supports were adjusted to bring these two points on the accelerator section in line with the ends to within 0.002 in. For a more complete description of the accelerator support assemblies, see Reference 7.

Drift sections

Drift sections are located at the end of every sector along the two-mile linear accelerator. The drift sections are used for beam guidance and diagnostic purposes. (See Chapter 15 for a more complete description of drift section components.) A typical drift section is shown in Fig. 5-22. Each component is mounted on the strongback by means of support plates which contain optical tooling holes. The support plate position is adjustable for alignment. The entire assembly is approximately 9 ft long and weighs 630 lb. The drift tubes at either end of the drift section contain bellows through which the assembly is connected to the accelerator vacuum system. A manual thin valve at the upbeam end and an automatic thin valve at the downbeam end allow the drift section to be isolated from the remainder of the machine vacuum. A description of the thin valves, their function and operation, is contained in Chapter 23. The drift section assembly is supported by a special 10-ft length of the 24-in. light pipe.

The alignment tolerances of the various components with respect to a theoretical beam axis were: quadrupoles, ± 0.005 in.; beam position monitor assembly, ± 0.024 in.; beam intensity monitor, ± 0.062 in.; steering

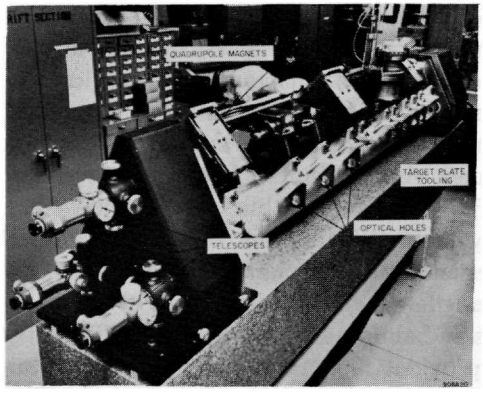

Figure 22-20 Drift section alignment.

dipole, ± 0.030 in.; and beam profile monitor chamber, ± 0.035 in. The beam scraper alignment tolerance with respect to the following accelerator section was ± 0.010 in.

Before installation, the positions of the optical tooling holes in the support plates were fixed relative to the center line of the components. The support plates were, in turn, attached to the strongback by adjusting bolts.

The final alignment was made after all the components were mounted on the strongback so that the strongback was supporting the full weight (510 lb) of the components and had undergone its full deflection. The alignment was carried out on a three-telescope station shown in Fig. 22-20. The telescopes were mounted at the vertices of a triangle having an 11-in. base line and a height of 10 in. The telescope positions were adjusted for translation and angulation within the telescope mounting structure. The telescopes were aligned relative to a pair of special target plates which were mounted at the ends of the drift section. The target mounting plates were made of the same aluminum alloy as the component support plates and the strongback. Each plate held three see-through wire targets in the 11×10 in. triangular pattern. The target holes in the pair of target plates were jig bored together in one operation.

The drift sections were designed to be readily replaceable in the event of failure of a component, and spare full assemblies are being maintained. This approach was chosen because a complete drift section assembly can be replaced more quickly than an individual component. Mounting plates which have supporting surfaces accurately located with respect to optical tooling holes were mounted on each end of a drift section support girder. The support plates were located with respect to the Fresnel lens in the standard fashion described earlier in this chapter.

The optical tooling holes on the magnetic quadrupole lenses were located with respect to the mechanical center of the aperture. The mechanical center

was found by using a self-centering target. Initially, the center of the quadrupoles was determined by inserting a vial containing a colloidal ferrite suspension into the space between pole pieces. The magnet was then energized, and the pattern formed by the colloid[8] was observed. For the initial drift section installation, which contained quadrupole triplets rather than doublets, the quadrupoles were aligned using the colloidal suspension. The drift sections which were removed from the accelerator and reworked to contain quadrupole doublets were aligned mechanically. To within the accuracy of either method (± 0.001 in.), one could not discern a difference between the results of using the colloidal suspension and the results of using a self-centering target.

The beam position monitor assembly is described in Chapter 15. The center line of the position monitor was located by reference to external surfaces which were machined accurately to be concentric with the aperture between cavities. The structure is held by support plates which again have optical tooling target holes.

The alignment tolerance for the steering dipoles was sufficiently loose and the configuration was such that they could be aligned with respect to the drift tube. The dipole supports, therefore, have no optical tooling holes.

The beam profile monitor chamber was designed to house any special beam monitoring equipment which might be required. Seven of them contain profile monitors. The large flange to which equipment housed in the chamber is bolted serves as the reference surface to which that equipment is aligned. The equipment is thereby located accurately with respect to the optical tooling holes in the support plates. The support plates are bolted and doweled in place. The profile monitor chambers in Sectors 5, 13, 21, and 29 have been replaced by pairs of orthogonally mounted C-band waveguide cavities for detecting transverse beam oscillations associated with the beam breakup phenomenon (see Chapter 7).

The beam scraper serves as a fixed protection collimator for the accelerator sections in the sector following the drift section. The scraper bore is 0.673 in. and its effective length is 22 radiation lengths. The smallest aperture in the accelerator section is 0.7517 in., so that the scraper offers good protection against diffuse beams which tend to fill the aperture as well as against misteered beams. The beam scrapers are water-cooled. The support points on the beam scraper o.d. are machined to be concentric with the i.d. of the scraper. The support plates are similar to those used for the beam position monitor assembly.

Monument target system

Monument target girders are located at three places along the accelerator. In addition to their normal function, these girders contain special Fresnel lenses which are mounted to concrete monuments. The monuments are independent of the accelerator housing and extend through the floor of the

housing into the bedrock layer. The four monument lenses are used to observe changes in accelerator alignment relative to the underlying rock. Special girders were fabricated with box sections to house the monument lens and its support structure.

A pair of bellows makes a flexible vacuum connection between the girder and a shaft that runs through the length of the box and supports the lens. The shaft is fixed relative to the concrete monument. The hardware that supports the lens on the shaft is statically balanced so that there is no tendency for the shaft to rotate as the lens is swung in and out of the laser beam on its vertical axis. Outside the bellows, the shaft is positioned relative to the monument on an adjustable support system. This support fixes only the horizontal, vertical, and axial position of the shaft. The shaft is free to rotate on roller bearings in this support. Rotations of the girder relative to the monument, therefore, do not strain the support hardware, but the girder must be level for the position to be correct.

Fixtures were supplied at the time of assembly to maintain the proper target position relative to the girder. When the girders were installed, the connection to the monument was made and the support fixtures were removed. This arrangement is shown in Fig. 22-21.

Each monument girder is provided with a 24-in. diameter access port to permit servicing the monument target hardware. On occasion, these ports have served the additional purpose of providing access for a lean and agile technician to do maintenance inside the girders, as far as 500 ft away.

Figure 22-21
Monument target support.

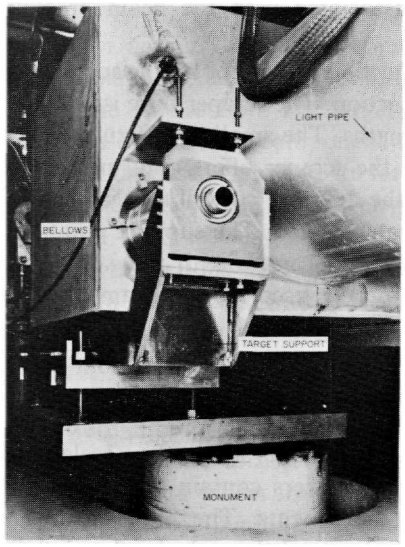

Positron source girders

The positron source station occupies a length of approximately 40 ft in Sector 11 and contains both standard and special beam-monitoring equipment, steering dipoles, focusing solenoids, a pulse deflection magnet, an RF deflector, accelerator sections, in-line thin vacuum valves, and the positron radiator itself. The design of the source and the function of these components is described in Chapter 16. The total positron station weight is approximately 16,000 lb as compared to 4000 lb for a standard girder. To accommodate this weight, the components were distributed among three shorter girders. The first positron girder is 10 ft long and supports 6500 lb. The second girder is also 10 ft long and supports 4000 lb. The third girder is 20 ft long and supports 5500 lb.

The positron wheel source and its drive mechanisms are supported from the floor of the accelerator housing and aligned with respect to the beam axis by means of fiducials placed on the wheel support structure. Any realignment of the first positron source girder requires a realignment of the wheel radiator. The wand radiator source is mounted to a 6-in. flange on the back of the radiator housing and is supported directly from the housing. The alignment of the wand is, therefore, independent of any girder alignment. The initial alignment of both positron source radiators was made by removing the drift tube ahead of the positron source and sighting down the beam line at the inserted target.

A strongback is used to support the positron source components in order to make the installation and removal process for the positron source as fast as possible. The rapidity with which the radiator strongback can be removed is very important because of the high radiation levels in this area. The mounting method is similar to that used for the drift sections. Special equipment must be used for handling the positron source because of its weight. Carriages and hoists traveling on overhead rails are used for handling the source. Additional permanently installed handling equipment is used for removal of either of the source radiators.

The two accelerator sections following the positron source are supported by concentric strongbacks which fit into the solenoid coils. The strongback consists of an 8-in. diameter nonmagnetic stainless steel pipe to which the accelerator section is rigidly attached at the upbeam end. Sliding supports keep the accelerator section straight while allowing it to expand axially with respect to the strongback and the girder. Holes were provided through the wall of the strongback for tuning the accelerator section after it was mounted in the strongback and for measuring the straightness of the accelerator section within the strongback. Alignment of the accelerator section is made by reference to special optical tooling plates which are clamped to each end of the accelerator section.

The solenoid coils are supported by box-like frames. The frames have optical tooling plates on each end. The coils were first mounted on the frames

and rough-aligned mechanically. The coils were then energized and their magnetic center determined. The coil positions on the frame were adjusted to make the magnetic center coincident with the accelerator axis.

Injector girder

The main injector girder is 30 ft long. It supports the gun, parts of the gun modulator, ion pumps, the prebuncher and buncher, an accelerator section, solenoid coils, beam position and intensity monitors, and the beam knockout. A complete description of the injection system can be found in Chapter 8. The accelerator section is mounted in a nonmagnetic stainless steel concentric strongback. The strongback is sufficiently stiff to support both the weight of the accelerator section and the solenoid coils. The accelerator section is rigidly attached to the strongback at the upbeam end and is allowed to slide downbeam within the strongback to permit thermal expansion. The strongback is, in turn, rigidly anchored to the girder at the upbeam end and is supported by flexible supports at its midpoint and downbeam end. The accelerator strongback has a series of holes opposite each cavity so that the accelerator section can be tuned after insertion into the strongback. Additional holes allow for measuring from the strongback o.d. to the accelerator section for centering it inside the strongback. Optical tooling holes are incorporated into the accelerator supports. The components downbeam of the accelerator section are mounted on a strongback similar to that used for the drift sections.

Beam-analyzing stations

The two beam-analyzing stations (BAS) described in Chapter 15 are located in the accelerator housing. BAS-1 is located just downbeam of the injector on girder 1-1; BAS-2 is located on girder 20-1.

Figure 22-22 Beam-analyzing station (BAS-2).

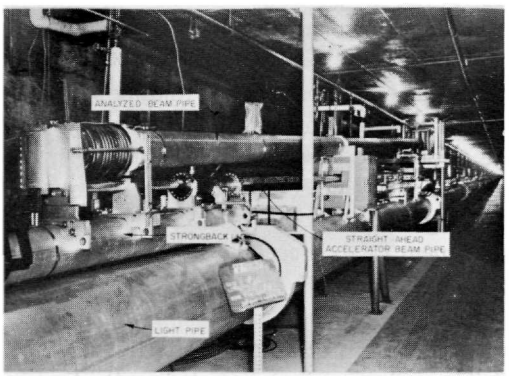

The BAS-1 is approximately 10 ft long and replaces the fourth accelerator section on girder 1-1. It is shown in Fig. 15-16.

The beam-analyzing station at Sector 20 (BAS-2) can be seen in Fig. 22-22.

On both beam-analyzing stations, the components which had to be aligned accurately were mounted on a strongback similar to the drift section strongback and aligned prior to installation on the girder. A three-telescope station was used to align the magnets with respect to the optical tooling holes on the strongback. The deflection magnet pole pieces were aligned parallel to the beam axis and centered on the axis by measuring an offset from one of the pole faces. The magnet angle was set by means of a sine bar and level. Magnet rotation about the beam axis was set using a level.

Quadrupole singlets

Quadrupole singlets were installed at 40-ft intervals in Sectors 1 through 6 as discussed in Chapter 7. They are located between 40-ft girder assemblies, around a drift tube and bellows assembly which joins two girders on the beam line, as shown in Fig. 22-23.

The quadrupoles were attached to a supporting bracket which had two clearance holes at the location of the optical tooling hole. Adjusting screws on the bottom and side of the clearance holes allowed the optical tooling target to be positioned within that hole. After the support bracket was attached to the quadrupole, the assembly was mounted on the drift section

Figure 22-23 Quadrupole singlet installed between two 40-ft girders (Sectors 1 to 6).

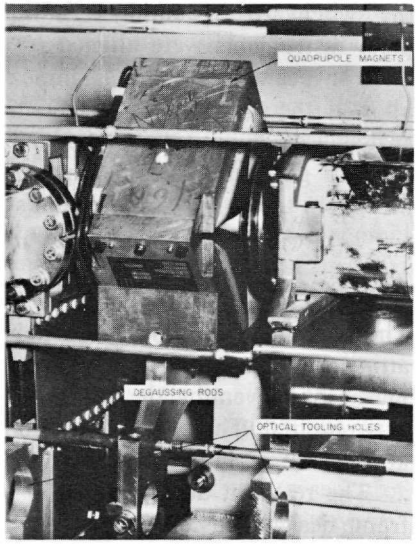

alignment and assembly station which contains the three-telescope stand. The magnet was adjusted until its center lay on the upper optical alignment sight. The magnet was also leveled and adjusted for pitch, roll, and yaw. The target positions were then adjusted to coincide with the two lower lines of sight and the adjusting screws locked in place. The equipment used for this activity was the same as that described previously for the quadrupole alignment in the drift sections. At installation, the quadrupole magnets were disassembled, slipped under the drift tube and bellows assembly, reassembled, and mounted to the target housing plate at the upbeam end of the girder.

The 40-ft quadrupoles were aligned at installation by a mechanical centering alignment tool consisting of an arbor centered on the end-plate target holes by means of centering plugs. A gib in the arbor was tapered 0.005 in./in. Sliding the gib axially changed the radial distance from the arbor center line to the surface of the gib. Calibration marks were placed on the gib to indicate dead center (0.750-in. radius) as well as ± 0.002-in. displacements. The magnet position was adjusted until the optical tooling holes in the magnet support plates were in line with the target holes on the adjacent accelerator support plates. This condition was indicated when the gib just touched the screws in the optical tooling holes. The alignment was carried out on one side of the accelerator. The other side is aligned by using a transverse level going from the wall side target across to the arbor shaft.

Beam switchyard support girders

The final four light pipe girders of the accelerator constitute the beginning of the BSY instrument section. The girders were specifically designed to support the instruments in the same manner as they are supported throughout the switchyard. Mounting rails were welded to the o.d. of the aluminum pipe. Instruments were aligned to the correct position with respect to the electron beam axis by an alignment fixture referenced from the rails. This allowed the diagnostic instruments to be interchangeable throughout the switchyard. A cryogenic differential vacuum baffle is mounted on one of the BSY girders. This baffle separates the high vacuum system of the accelerator from the switchyard vacuum system.

Light pipe vacuum restraints

The vacuum within the 24-in. light pipe creates an external force due to atmospheric pressure of approximately 6500 lb axially along the pipe. A means of preventing the collapse of the intergirder bellows under vacuum was required. Therefore, restraints were attached to the light pipe sections at the extreme ends of the accelerator.

The restraint at the upstream end of the accelerator is of a fixed "A" frame design. This "A" frame is adjacent to one of the accelerator alignment reference points, so that no adjustment features are required.

At the downstream end of the accelerator, the vacuum restraint is designed to permit vertical and horizontal adjustments as required for accelerator realignment. To make this hardware adjustable, rollers similar to those in the pin and roller bearing assemblies were used to permit vertical and horizontal motions with minimum resistance as the floor and wall jacks adjacent to the restraint are adjusted.

In an attempt to eliminate any possibility of failure of the two restraints, a safety factor of approximately 10 was used in the design of the structures and in the method of attaching them to the floor of the accelerator housing.

Installation and initial alignment

The 40-ft modules of the accelerator were assembled on stands as shown in Fig. 6-40. Four accelerator sections were mounted to each module of the light pipe. The alignment operation was performed using the telescopes visible at the near end of the pipe in Fig. 6-41. The first step consisted of positioning the nearest section as accurately as possible relative to the support plate to which the Fresnel lens is fastened. The second step consisted of adjusting the positioning screws for the end supports until the four accelerator sections were aligned along a line parallel to the axis of the light pipe.

Several difficulties were encountered in the above operation which are worth reporting. First, the hinge assemblies which support the Fresnel lenses were found to be sensitive to the force required to insert them. The hinges were modified after about 20% of the installation was complete, but this meant that in those cases in which the hinge had to be replaced by a modified model, the initial position of the lens was lost.

Next, it was found that temperature stability in the assembly area was not good enough to permit accurate adjustment of the position of the four accelerator sections on each girder. There are always difficulties in using optical tooling techniques over distances of more than a few meters. This is particularly true of a system which has not come to temperature equilibrium. Refractive effects due to temperature gradients in the air limited the observations to accuracies of from 0.01 to 0.04 in.

There were also doubts, which turned out to be well founded, that the alignment within each module would remain correct after the assembly was moved to the accelerator housing and installed. Installation included connecting the rectangular waveguides which could put some vertical loading on the girder.

Several times during the assembly process, there were difficulties with the tooling jigs, which were not found until after the module had been installed. The problems involved in returning these modules to the assembly line were such that in almost all cases the rework was done in the field.

The net result of these and other lesser problems was that a series of setups had to be devised to permit repeating effectively all these operations on the installed accelerator. The largest effort was to determine the

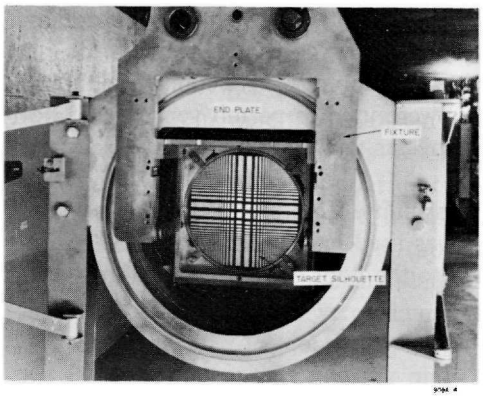

Figure 22-24 Calibration jig being installed on a special calibration girder.

displacement of the accelerator relative to the Fresnel target. A ruled ground-glass reticule plate was suspended in a jig from the optical tooling holes at the end of an accelerator segment. Figure 22-24 shows the jig fixture being installed on a special test and calibration girder. The glass was positioned as close as possible to the target. A light was projected from the other end of the module against the face of the target. The silhouette of the target thus appeared on the glass plate with the rulings superimposed. A set of five photographs was made of each target with a 35-mm camera and a one-to-one closeup lens. A sample of the one-to-one photography is shown enlarged in Fig. 22-25. On the accelerator, the entire operation had to be performed by working through a $2\frac{3}{4}$-in. slot between girders. The vacuum bellows were welded in the gap as soon as the photographs were checked. From the first

Figure 22-25 Photograph used to calibrate position of installed Fresnel target.

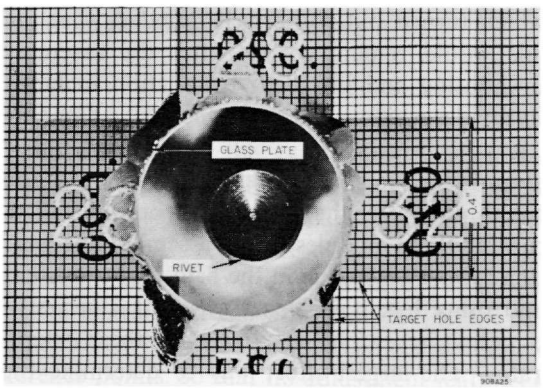

checks with this photographic calibration, it was apparent that the accuracy with which the targets were located on the accelerator was not as good as expected. This meant that it was necessary to carry out the photography on every one of the 272 girders. Counting calibration shots and retakes, about 600 sets of pictures were made. The displacements of the target slot edges from the reticule lines were read on a micrometer microscope. Twelve edge readings were made in both the horizontal and vertical directions for each target. The data were analyzed by computer with a program which checked that the data were consistent within themselves and with the target that was supposed to be installed at that location. It is estimated that the accuracy of determining the target position was about 0.005 in. Repeatability was about ± 0.002 in. No satisfactory explanation was ever found for the failure of the original telescope system to yield consistent results. Errors of ± 0.020 in. were common for a method which should have been 20 times better.

The accelerator was initially installed along a line determined by conventional surveying. Figure 22-26 shows the observed results when the laser system was first activated. Although the spread in vertical and horizontal alignment was about the same, it is possible to see a pattern in the horizontal alignment while the vertical spread appears random. The pattern in the horizontal alignment was probably due to errors in locating secondary reference points by sightings from the surveying towers at the ends of the site. The actual placement of girders was made over marks made from these

Figure 22-26 Accuracy of initial alignment as measured by laser system. Initial alignment was accomplished using conventional surveying techniques.

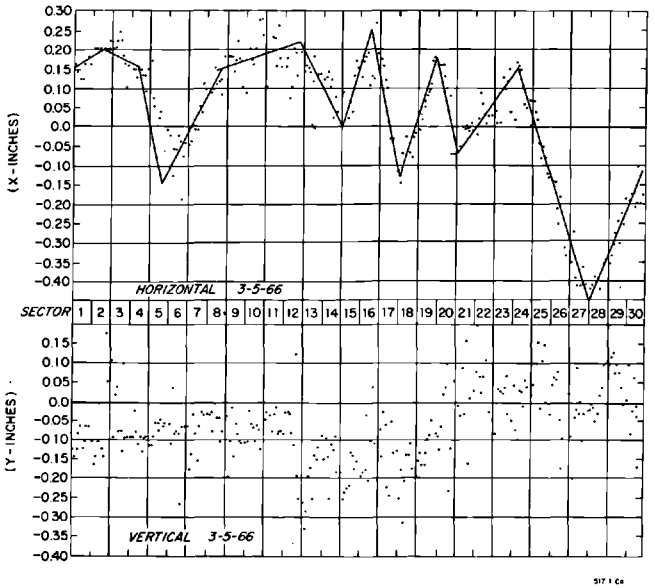

secondary points. The vertical survey used local gravity as a reference and, thus, was probably better. However, the placement of girders vertically was done with less precision.

The process of aligning the accelerator with the laser system required that a two-man team work along the accelerator while in communication with an operator in the alignment observation room. The alignment of the accelerator was dependent on keeping the support girder level in the transverse direction. A precision bubble level was placed between the optical tooling holes so that the differential extension of the two floor jacks could be equalized. The alignment procedure was as follows. The operator in the observation room observed and recorded the position of the laser image. By referring to a table of coordinates, he then set his detector to the correct position and instructed the team to adjust the position of the girder until the detector read a null signal. When the girder was set in both translation and elevation, the level was rechecked. The procedure required about 15 min per station and was accurate to 0.001 in. A record of how far the girder was moved was obtained by using the initial readings in a computer program to determine the alignment error at the point in question. The amount moved was recorded and was equal and opposite to the calculated error.

The alignment results from the first use of the system were checked by stretching a wire through the tooling holes on successive sets of three girders. Thus, if a gross error was made in determining the correction factor on the location of one target, it showed up in a displacement of that girder relative to its neighbors. The wire was observed both vertically and horizontally by a system based on detecting the magnetic field from a 1000-Hz current which was passed through the wire. Modified stereo tape recorder heads were

Figure 22-27 Stretched wire pickups.

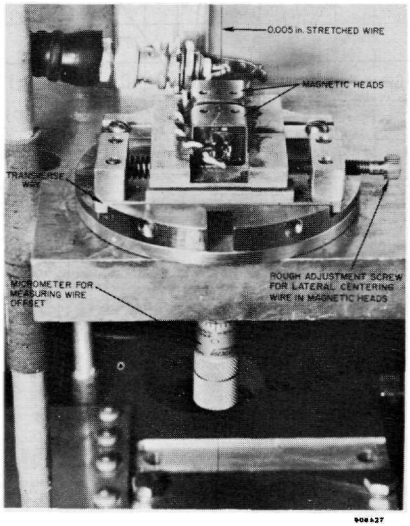

used as pickups for the alternating magnetic field. When the signal was exactly balanced between opposite heads, the discriminator read a null signal. Figure 22-27 shows the detector assembly with the micrometer screws used to position the heads. The head fits into an optical tooling hole. By means of a cam wheel, the head is expanded until it is centered in the hole. The total span of the wire was from 60 to 100 ft. The wire was tensioned by a weight over a pulley. A sufficiently high tension was used so that the catenary sag was of the order of 0.040 in.

The four accelerator sections on each segment were realigned after all the above operations had been completed. By this time, the accelerator was at its normal operating temperature of 113°F, and all waveguides, vacuum manifolds, and water lines were connected. The forces from these loads cause some sag in the girder. This alignment operation could have been done best by the stretched wire method but it was faster to use a pair of conventional alignment telescopes, one on each side of the girder. The telescopes were mounted in the optical tooling holes at the Fresnel lens end of a girder and were bucked into sighting targets in the corresponding holes in the next girder. The targets were then inserted, one at a time, on each side in the holes on each section and indicated adjustments were made.

Figure 22-28a Accumulated horizontal alignment changes, 1 yr after installation.

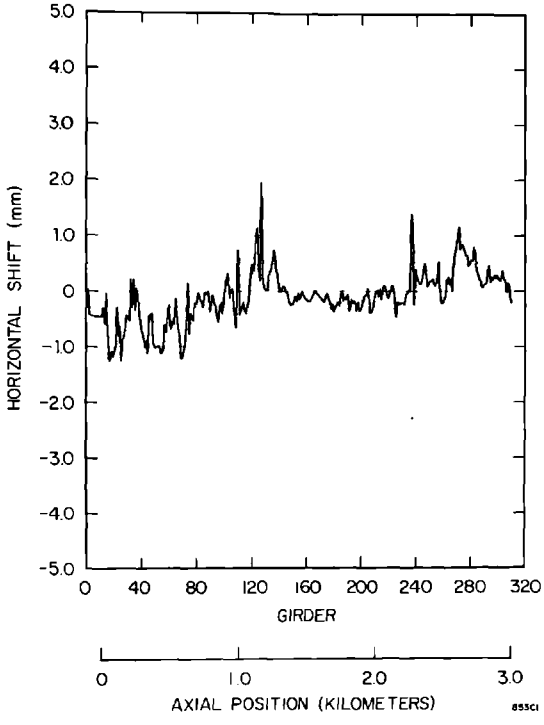

Stability

Information about long-term stability was obtained by referring to four monuments which are located along the accelerator. Three of the monuments have Fresnel lenses mounted as described earlier. The fourth monument was used as the base for the detector. Alignment data taken at any time can be calculated with reference to the straight line determined by any two points along the accelerator. Whenever a pair of the monuments are chosen for this purpose, the results give the total shift since the initial alignment.

The results of the operation of the alignment system for the first year are shown in Figs. 22-28a and b. The changes shown are accumulations of changes which were corrected by periodic realignment. The largest settlements occurred in areas constructed over filled ground. The correspondence between settlement and fill is quite striking. The implication is that those parts of the accelerator which were built directly on subsurface rock are quite stable. Fortunately, the more critical areas of the BSY and the end stations are all built directly on the underlying sandstone.

Figure 22-28b Accumulated vertical alignment changes, 1 yr after installation.

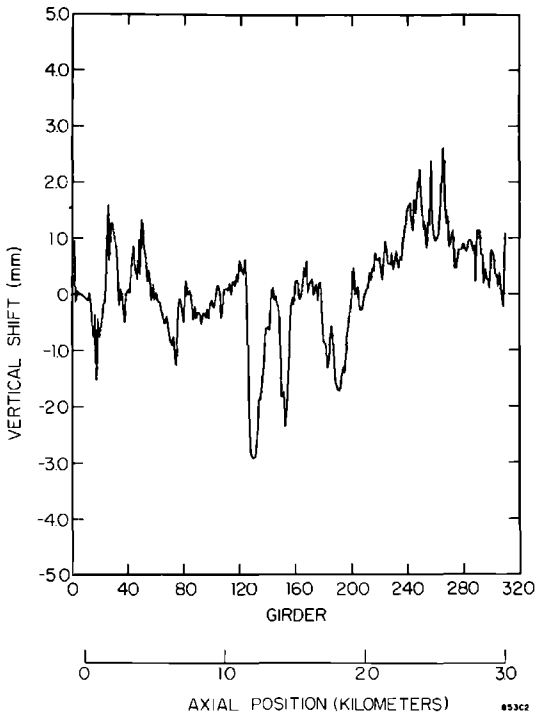

22-3 The beam switchyard support and alignment system (DC, WBH, JKW, JGN)

Summary of requirements

The support and alignment of the BSY is described in this section. It will be recalled from earlier chapters that the purpose of the BSY is to deliver the electron beam from the accelerator to the experimental areas. The switchyard consists of an elaborate system of bending magnets, magnetic quadrupole lenses, protection devices, and diagnostic instruments. These elements are primarily divided among two transport systems* leading to the experimental areas. (See Fig. 17-1.) The two systems, labeled A and B, after the experimental areas they serve, have a common origin in the beam line from the accelerator. A list of the most pertinent design parameters of these two systems is contained in Table 17-2.[9,10] The problems of support and alignment are primarily those of meeting the requirements set forth in this table.

The following procedures were used to insure the utmost accuracy in the alignment and placement of components in the BSY. An extension of the accelerator laser alignment system was used as a primary reference line. Secondary reference points from which measurements could be made were established along the path of each beam by using stretched wires and accurately scribed tapes. The distances between components or between a component and a reference point were set by tapes scribed with the proper distance. A tape bench facility was built for scribing these tapes. When properly installed, most components in the switchyard are tilted. A special optical alignment shop was established for measuring the angles of tilt and for targeting the components to insure proper installation. Finally, the angles and distances required for the correct alignment of components were calculated, taking into account the effect of the curvature of the earth upon these parameters.

The basic optics of transport system A is shown schematically in Fig. 22-29. System B is very similar. Each system lies in a distinct plane (see Fig. 22-30). The exit beam lines are required to be horizontal with respect to local gravity in the experimental areas. The accelerator axis points downward by 4.74 mradians with respect to the local gravity vector at the beginning of the switchyard. The respective exit beam lines for the A and B systems and the common accelerator line define the two planes in which the beams lie. A major part of the alignment effort involves targeting each component so that it can be aligned in its respective tilted plane while a local gravity reference can still be used for making measurements.

The tolerances reported in Reference 9 were calculated using the error analysis features of the TRANSPORT computer program.[11] The criteria

* As this book is being written a third system leading to experimental area C is being installed straight ahead.

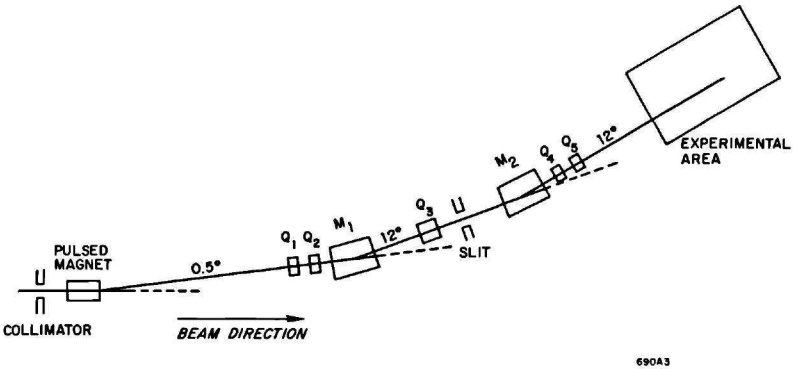

Figure 22-29 Schematic diagram of an achromatic bending system (transport system A) in the BSY.

that place the strongest limitations on the position tolerances are energy resolution (see Table 17-2) and the apertures of the switchyard elements downstream of the element being aligned.[12] The most restrictive translation alignment tolerance applies to the horizontal and vertical positions of either element of the first quadrupole doublet (see Table 17-3). This tolerance is based on the fact that a translated quadrupole is equivalent to a quadrupole plus a dipole. The most restrictive rotational alignment tolerance is ± 0.33 mradian for rotation about the beam line axis for magnets in the first bending group, M_1. This rotational tolerance is necessary to constrain the vertical component of the bend. Although many of the other tolerances are less restrictive, some of them are as difficult to achieve. For example, the switchyard is about 1000 ft long and a longitudinal tolerance of only 0.01 ft represents an alignment precision of 1 part in 10^5.

Figure 22-30 Tilted planes of A- and B-beams in the BSY.

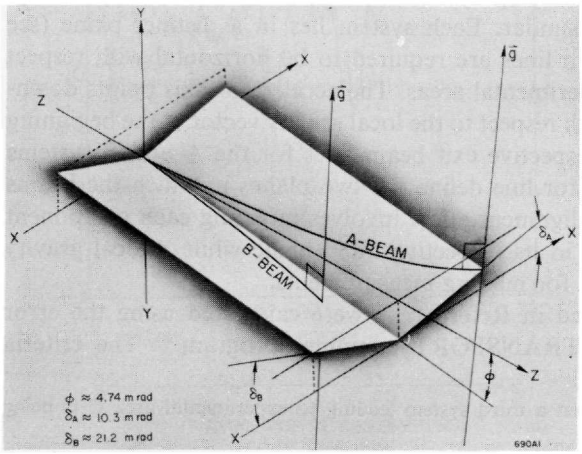

Laser reference line

An extension of the accelerator laser alignment system (see Section 22-1) provides a reference line throughout the first half of the switchyard. The function of this extension is to locate alignment targets with transverse coordinates to within ± 0.002 in. These target positions are then used as references for positioning the components in the beam lines. Figure 22-31 shows a laser alignment target stand and a portion of the vacuum pipe through which the laser beam travels.

The extension has a separate laser located at the east end of a 10-in. diameter vacuum pipe which extends approximately 750 ft beyond the end of the accelerator. It includes twenty alignment positions, each of which has a retractable Fresnel lens, the position of which can be determined by the operator in the Alignment Room at the beam injection (west) end of the accelerator. The Fresnel lenses are similar to the targets in the accelerator system but they are smaller (up to 6×6 in.). The 10-in. switchyard pipe is tangential to the bottom of the 24-in. accelerator pipe at the coupling point. The reduction was required because of the size of the collimators (see Fig. 5-24 and Chapter 20) which prevented use of a 24-in. light pipe throughout the switchyard. In view of the fact that the reference line is centered in the pipe at the beam injection end, 10,000 ft upstream, there is a slight slope which must be compensated for in the measurements.

Calculations

Survey, shop, and installation calculations were necessary for the alignment and placement of beam transport equipment. Each calculation required knowledge of the beam transport geometry calculated by TRANSPORT[11] and criteria defining the BSY inertial reference frame. This BSY reference

Figure 22-31 Laser alignment target stand in BSY.

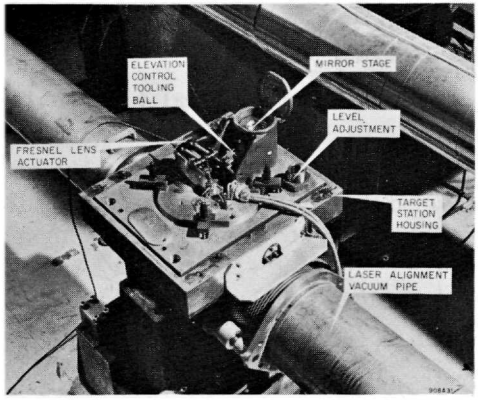

frame (see Fig. 22-30) is defined as follows. The Y axis is parallel to the gravity vector at accelerator station 105 + 08. The Z axis is in a vertical plane containing the accelerator axis and is perpendicular to the Y axis. The X axis is orthogonal to Y and Z. The origin of the system is at station 101 + 75.

Survey calculations preceded shop and installation calculations. Surveys were performed by SLAC and Aetron–Blume–Atkinson (ABA) to establish inertial reference points by creating both horizontal and vertical benchmarks.

Two computer programs, LAYOUT and VERTEX, were developed to compute the BSY component locations and alignment values. These programs were written with options so that equipment locations could be specified in both BSY or local gravity systems and redefined with respect to any previously defined points along any coordinate system. These options made possible the determination of tooling offsets and elevations required for the placement of targets on many of the components. Other computer programs were written to aid in field surveys, to reduce survey field data, and to analyze alignment data from the optical alignment shop.

LAYOUT and VERTEX had different input requirements. This difference insured independent analyses in providing the data. The drift lengths, bending angles in the beam plane, and desired options were required inputs for the VERTEX code. The usual input for LAYOUT was the TRANSPORT code deck used to compute the beam optics, plus other data cards which specified the desired coordinate system, the units, and the parameters of which the values were to be computed. This tie between the beam optics program and a component position program was desirable because it helped to eliminate human error in transcribing or making new data input cards, once the beam optics had been computed.

The A- and B-beam transport parameter values in the beam planes were computed by TRANSPORT. The expressions derived below show the relationships used to associate points in either beam plane to a common reference system, the BSY reference frame. In the beam plane, shown in Fig. 22-32, once an origin is specified, the beam transport parameters

Figure 22-32 Beam plane.

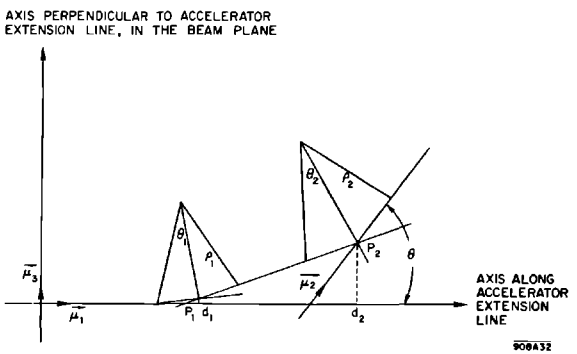

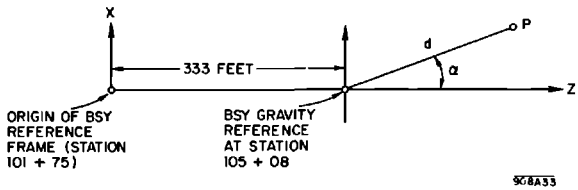

Figure 22-33
Definition of gravity vector parameters.

d_1, θ_1, ρ_1, d_2, θ_2, ρ_2, ... are sufficient to compute the coordinates of the vertices P_1, P_2, ... which define a beam line.

In vector notation, the position of any beam point can be expressed as a linear combination of two unit vectors, $\boldsymbol{\mu}_1$ and $\boldsymbol{\mu}_3$,

$$\mathbf{P}_i = x_i \boldsymbol{\mu}_3 + z_i \boldsymbol{\mu}_1 \tag{22-63}$$

where $\boldsymbol{\mu}_1$ lies along the accelerator extension line and $\boldsymbol{\mu}_3$ is perpendicular to $\boldsymbol{\mu}_1$ in the beam plane.

Then, if $\boldsymbol{\mu}_2$ is a unit vector along the beam exit line in the end station,

$$\begin{aligned} \boldsymbol{\mu}_1 \cdot \boldsymbol{\mu}_3 &= 0 \\ \boldsymbol{\mu}_2 \cdot \boldsymbol{\mu}_3 &= \sin\theta \end{aligned} \tag{22-64}$$

and

$$\boldsymbol{\mu}_1 \cdot \boldsymbol{\mu}_2 = \cos\theta$$

where θ is the angle between the beam exit line and the accelerator extension line. This angle is 24.5° for the A-beam and 12.5° for the B-beam. For the beam exit lines to be normal to local gravity in the end stations, one must have

$$\boldsymbol{\mu}_2 \cdot \mathbf{G}_y = 0 \tag{22-65}$$

where $\mathbf{G}_y$ is the local gravity vector.

In the BSY reference frame where unit vectors **i**, **j**, and **k** are taken along axes X, Y, and Z, the local gravity vector is

$$\mathbf{G}_y = \left(\sin\frac{d}{R}\sin\alpha\right)\mathbf{i} + \left(\cos\frac{d}{R}\right)\mathbf{j} + \left(\sin\frac{d}{R}\cos\alpha\right)\mathbf{k} \tag{22-66}$$

where d is the distance from station 105 + 08, and $1/R$ is the local earth curvature, 4.606×10^{-8} radian/ft. The angle α is defined as the angle between a line from station 105 + 08 to the point P being considered and the Z axis, as shown in Fig. 22-33, and is given by $\alpha = \arctan[x/(z - 333\text{ ft})]$.

Recalling that ϕ is the angle defined in Fig. 22-30, the beam entrance line into the BSY may be expressed as

$$\boldsymbol{\mu}_1 = -\sin\phi \cdot \mathbf{j} + \cos\phi \cdot \mathbf{k} \tag{22-67}$$

Expressions (22-63) through (22-67) may be used to solve for the beam vectors ($\boldsymbol{\mu}_1$, $\boldsymbol{\mu}_2$, $\boldsymbol{\mu}_3$) in terms of the BSY vectors (**i**, **j**, **k**) and thus to obtain the coordinates x, y, and z of a beam point P_i in the BSY reference frame. Equation (22-63) could then be expressed as

$$\mathbf{P}_i = x\mathbf{i} + y\mathbf{j} + z\mathbf{k} \tag{22-68}$$

Both LAYOUT and VERTEX programs used the above relationships to represent beam points in the various coordinate systems which were meaningful to the field, shop, and installation crews.

The external targets which were mounted on the BSY components were set so that the components are at the proper tilt when they are aligned. A mirror target was set on each component so that it is horizontal with respect to local gravity when the component lies in the tilted plane. This targeting procedure will be discussed later in this chapter under the section Shop Alignment.

One of the first required sets of calculations was that capable of supplying the information necessary to make the stretched wire layout shown in Fig. 22-34. The vertex monuments (VT) are the intersections of the beam drift lines entering and leaving a bending magnet group. The programs LAYOUT and VERTEX were used to find these intersection points. Once the values for the stretched wire layout were computed, the field crew required tape length values and elevation differences and offsets from these established lines.

The tape lengths required were the distances from VT to targets which had been placed on the components. These targets were usually preset mirror targets. The tape lengths set the position of the component along the beam. Because the field crews were familiar with possible obstructions for their tape pulls, the most workable procedure was found to be one in which these crews specified the respective monuments and components for which a tape distance was desired. This distance was then computed, checked, scribed on a tape, and given to the field crews for their use.

Figure 22-34 Vertex monument and stretched wire layout for alignment of BSY area.

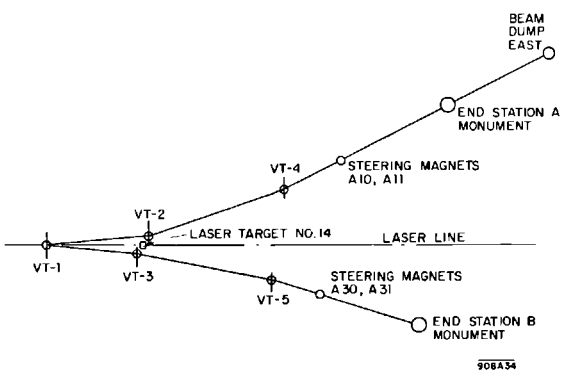

Elevation values for BSY components were computed in a sea level sense, i.e., concentric circles about the center of the earth, because survey crews follow the curvature of the earth with their level readings and sightings. However, to make the BSY a system independent of the earth, all elevation values were given as elevation differences between components. The tooling ball on laser target No. 14 near the center of the BSY was used as the inertial reference point for most elevation measurements.

SLAC tape bench

A tape bench facility was constructed at SLAC for scribing and calibrating the Invar field tapes. More than forty tape marks were scribed for the original equipment installation. Scribing accuracies within 0.003 in. were achieved. Although the actual placement of all components was not required to this accuracy, the gross errors due to tolerance accumulation were reduced by having all tape marks scribed on the tape bench.

The tape bench facility was built in a tunnel accessway in the accelerator housing. Double doors to the housing were installed and insulated so that the tape bench temperature stayed as constant as possible.

A monthly calibration check, made on each scribed tape, shows that the stability of the tapes after handling and general field use has been excellent. The maximum recorded deviation is less than 0.003 in. from the originally scribed length.

The standard tapes were 1200 in. long since most of the distance measurements made in the BSY fell within a 1200-in. range. As temperature stability is of primary concern with regard to mechanical measurements, Invar tapes were used because of the low thermal expansion of Invar. On the other hand, the stability of Invar under a continuous load is questionable; therefore, in order to keep the stress levels to a minimum, the tapes were allowed to hang in a catenary with just enough tension (10 lb) to keep the tapes off the ground over a 1200-in. span. Sometimes, allowing a survey tape to hang in a catenary with light tension can have detrimental effects on the measurements because air currents can cause the tape to vibrate. However, at SLAC, all the work requiring precision tape measurements was done in enclosed areas where wind was not a problem.

A series of tests were run to investigate the possible errors that might occur in long measurements because of creep of the Invar. The test periods were 5 days (120 hours) with the tapes under a 10-lb tensile load. The average stress level was 2000 psi, and the average ambient temperature was 70°F. The results of the tests indicated no measurable creep.

As the field survey tapes were to be used in a catenary configuration, it was necessary to have a calibrated standard tape which was held horizontal on the tape bench to correct for catenary sag. The standard was a graduated steel tape, calibrated by the National Bureau of Standards.

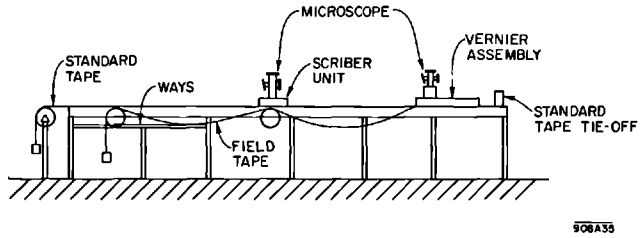

Figure 22-35 Schematic of the tape bench.

The tape bench (Fig. 22-35) consists of five major components: the vernier assembly, the scriber, pulleys, the standard tape, and the bench itself. Both the vernier assembly and scriber are equipped with microscopes for positioning the units over the desired location on the bench relative to the scribe marks on the standard steel tape.

The tape tie-off end of the bench is fabricated of aluminum jig plate which is approximately 10 ft. long. Gauge holes in this plate are set at 20-in. intervals and are used to locate the vernier assembly. These gauge holes correspond to the 20-in. increments of the steel master tape. The remainder of the bench is of hardwood with a steel framework. The entire length of the bench is supported by tubular members with adjustable bases for leveling purposes. These supports are spaced at 4-ft intervals.

The vernier assembly is an independent unit mounted on rollers which guide it along the tape tie-off end of the bench. The assembly has the capability of movement within the 20-in. gauge hole span from 0 to 24-in. increments of 0.0001 in. In this manner, the vernier assembly may be located at the desired 20-in. gauge hole location, and the independent slider mechanism may then be moved along until the desired scribing position is obtained. Attached to the assembly through a cable linkage is the end-supporting pulley for the Invar tape. The pulley is free to follow the travel of the vernier assembly.

The scribing unit mounted on a round steel way travels the full extent of the bench. The scriber houses a cutting tool mounted to the carriage containing the microscope. This tool marks the tapes once the scribing unit is in the desired location along the tape.

The pulleys are 16-in. diameter, $\frac{1}{2}$-in. thick, aluminum plates. Instrument-type ball bearings were used for mounting the pulleys on hardened steel shafts. The bearings were completely degreased and oiled with light clock oil. After mounting the pulleys on their respective shafts, they were balanced so that 1.6×10^{-3} lb applied at the diameter would rotate the pulley. This force is essentially a measure of the friction in the bearings. The net effect on the accuracy of the measurements is negligible since an error of 0.002 in. in an unsupported length of 1200 in. requires an uncertainty of 7×10^{-3} lb in the tension load.

The method for scribing tapes is to clamp the Invar tape into the vernier assembly so that the zero mark on the tape is immediately under the cross-hair reticule on the microscope. The free end of the tape is tensioned and supported over the pulley. The scriber is positioned by microscope over the correct 120-in. increment on the standard tape. The vernier assembly is then moved to the required interval between 0 and 120 in. on the steel standard so that the interval between the scriber and the vernier assembly on the standard is within 20 in. of the desired length. The fine adjustment is then made on the vernier such that the required span between the scriber and zero point on the Invar tape is obtained. The tape is clamped to the pulley on the scriber unit and scribed. The entire procedure is then repeated for calibration.

Support stands for the beam switchyard

Four different basic types of support stands are used in the BSY. These are the quadrupole magnet stands, the 3° bending magnet stands, the pulsed magnet stand, and the instrument stands. The bending magnet and quadrupole magnet stands are designed to support only one magnet. The pulsed magnet stand is required to support five pulsed magnets, six intervening protection collimators, two emergency dc magnets, and a pulsed vertical steering magnet. The instrument stands are designed with support rails so that they may support one or more interchangeable instruments. A few stands made by slightly modifying one of the four basic designs are used throughout the switchyard to accommodate special magnets or instruments.

The support stands are designed with fine adjustments to permit the final alignment of the components with six degrees of freedom, 3 translational and 3 rotational. The adjusting jacks can be operated from the second level of the BSY so that all alignment work can be done while the personnel are protected from residual radiation by a layer of concrete shielding.

Each support stand was designed to withstand specified earthquake shock loading and, of course, to support the BSY component which was to be placed on it. In the case of the 18-cm quadrupole magnet, a weight exceeding 17 tons must be supported.

The base supports for all stands use three jacks arranged in a tripod suspension. In the case of the magnet stands, the components rest on beds which are free to move in the plane determined by the three base jacks. Three other jacks are used to move the beds so that the stands have a total of six jacks to provide movement of the components placed on the stands. The jack design is a modification of the design which was made for the accelerator supports. These modifications increased the range and tightened the tolerances in backlash and translational motion of the jacks. The stands provide for a movement of ± 3 in. from the original center along any axis.

The major difference between the supports for the bending magnets and the quadrupole magnets is in the bed upon which the magnets rest. The

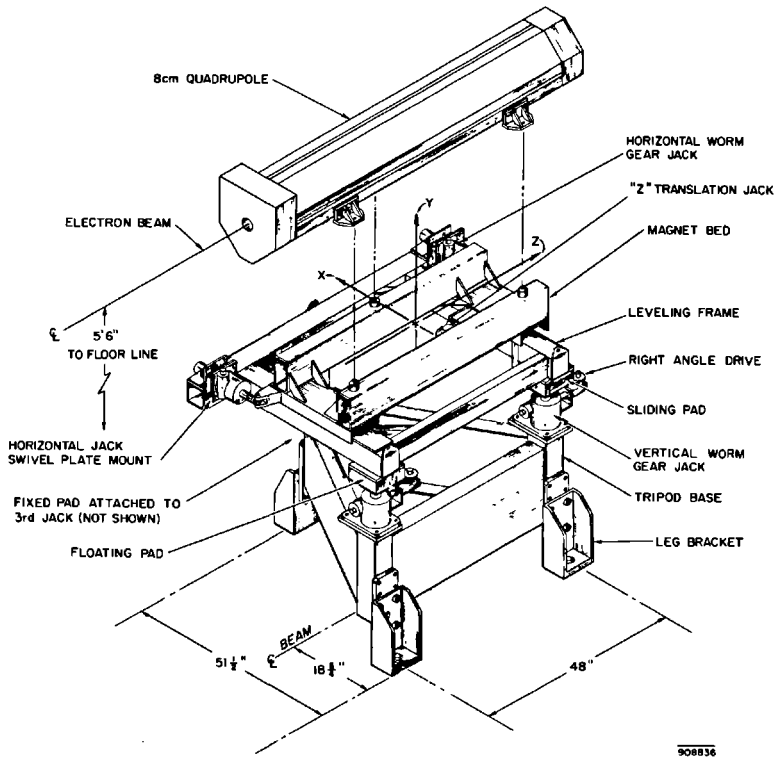

Figure 22-36 Support stand for 8-cm quadrupole magnet.

bending magnet support bed is flat while the quadrupole magnet support bed is in the form of a cradle in which the quadrupole magnet fits. A drawing of the support stand for an 8-cm quadrupole magnet is shown in Fig. 22-36.

The pulsed magnet stand is 44 ft long and supports all of the equipment from the downstream end of the high-power collimator to the beginning of the divergent vacuum chamber. Two laser targets are attached rigidly to the support frame for alignment of the stand in the switchyard. The pulsed magnets and the protection collimators which are also supported by the pulsed magnet stand are placed on reference pads on the stand. These pads are prealigned relative to the laser targets so that when the beam transport equipment is placed on the support and the support is aligned with the laser targets, the equipment is positioned in relation to the ideal beam location within about ± 0.04 in.

The instrument stands were built with level parallel rails instead of beds. The rails were accurately machined so that there are no deviations from straightness, flatness, or parallelism greater than 0.005 in. over their full length. The rails are located at a fixed distance below the electron beam so that instruments can be interchanged on the stands. The instruments are placed

on the rails in the shop and prealigned. The instrument stands cannot be translated along the beam axis and, thus, the stands have only five degrees of freedom; however, the instruments themselves may be moved on the rails so that their position along the beam may be adjusted.

Shop alignment

A special optical alignment shop was set up for the purpose of installing the external alignment targeting on the BSY components. All instruments and magnets that required targeting were processed through this shop before installation in the BSY. Tooling balls and mirror target assemblies were mounted on the exterior of the components to allow accurate installation with a minimum of effort on the part of the field installation crews.

The equipment in the alignment shop consisted of two 7-ft tooling bars and one 15-ft tooling bar, arranged in the form of a "T." The shop layout is shown in Fig. 22-37. Two fixed targets, the locations of which with respect to the tooling bars were precisely measured, were installed in the alignment shop. One was at the base of the "T" and the other under one of the arms of the "T." These targets are on the wall opposite the one shown in Fig. 22-37. They were used to set up a line of sight between the centers of the components to be aligned and the fixed targets. This line of sight simulated the electron beam path through the component during the alignment procedures. A stand with a permanently mounted telescope was installed at the intersection point of the "T." Being at the intersection, this telescope could be rotated to sight along any one of the tooling bars and could, therefore, be used for lining up other jig transits placed on the tooling bars. The transits on the tooling bars were aligned by autocollimation with the permanently installed telescope. A pair of high stands with a cross bar (see Fig. 22-37) were installed so that a jig transit could be placed directly over a component. The shop also contained an optical calibration stand with five collimators for aligning and checking the alignment instruments which were used in the shop and field.

Figure 22-37 Optical alignment shop.

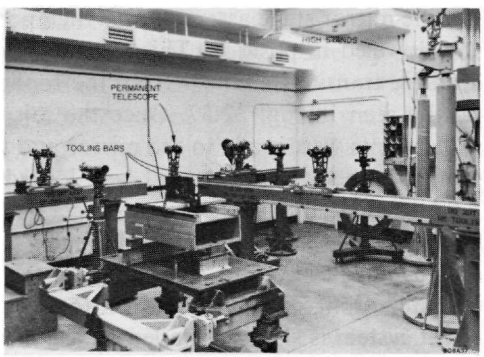

The optical alignment shop was located in a room which was built especially for alignment purposes. This room was in the Heavy Assembly Building where final assembly and magnetic measurement facilities were also located. The room for the alignment shop was constructed with a roof which had removable sections so that the components could be lowered in place and the roof sections could then be replaced. In this manner, the shop was kept relatively dust free and at a controlled temperature.

A magnet stand and an instrument stand were permanently installed in the alignment shop, one on each side of the long central tooling bar. A component to be aligned was placed on the appropriate stand so that the movable telescope on the long central bar could be used to make measurements along the beam axis (G_z axis) of the component. The telescopes on the shorter bars made measurements normal to the simulated beam path axis, i.e., along the component's G_x axis. Measurements along the vertical axis (G_y axis) were made by conventional leveling methods using precision spirit levels and optical tooling scales.

A component brought into the shop for alignment was first leveled and its mechanical or magnetic center located and marked. The exact determination of the centers of the components was important since all shop measurements, including those relating to location of targets for the components, were made using the centers as references. Special jigs were made to locate the mechanical centers. These jigs had a target attached to them so that when properly installed, the target was at the mechanical center. The magnetic centers of the quadrupole magnets were found by the use of a colloidal suspension of ferrosoferric oxide particles. The stand was then adjusted until the center and centerline of the magnet pole face were lined up with the fixed target on the shop wall and a jig transit which was held fixed on the stand at the other end of the magnet. The pole faces were leveled using precision levels and the secondary target tooling balls were then installed. Using the tooling bars, jig transits, a master level and scales, positions of the tooling balls were taken and recorded on the data sheet for the magnet. Then, using the center of the magnet as a rotation point, pitch and roll angles were turned into the magnet. This was accomplished by use of a clinometer, referenced to the leveled position with an accuracy of 2 arcsec or better.

The mirror stage assembly was then positioned on the magnet and bolted and doweled in position. This location was determined by use of the overhead jig transit positioned from the tooling bars. This overhead jig transit can be seen in Fig. 22-37. Once the mirror stage was fixed, final position adjustments were made to the mirror and the mirror leveled by autocollimation from the overhead transit, and locked in place.

A single stainless steel mirror target was used to control the position along the beam and the pitch and roll angles for the component. In conjunction with a bull's-eye target, the mirror also controls yaw. A single tooling ball mounted alongside the mirror on the vernier stage controls elevation. This target system is shown installed on a quadrupole magnet in Fig. 22-38.

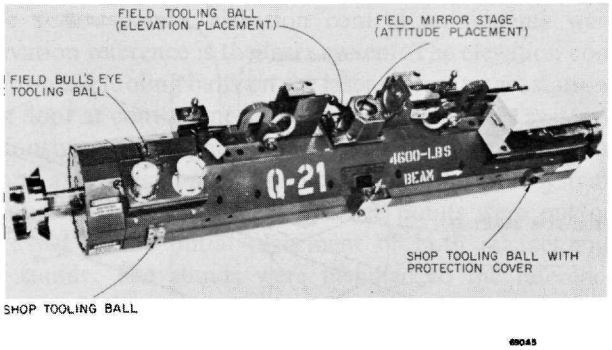

Figure 22-38 Alignment equipment on a quadrupole magnet.

The mirror target is mounted in an assembly called the mirror stage which consists of a series of gimballed cups which can be locked in a tilted position. The mirror has a reticule target etched on its surface face. The bull's-eye target is made from a 0.5-in. diameter stainless steel tooling ball. The ball has been ground flat on top and has concentric rings machined on the flat for a target.

Stainless steel is used for the bull's-eye and mirror targets because of its high corrosion and radiation resistance. A test was performed on a mirror target in which it was exposed to a 20% vapor solution of HNO_3 for 30 hours. After the test, the surface was discolored but the mirror was still useful and the reticule target was still discernible from the second level.

In addition to this primary target system for installation, a secondary system for checking alignment is also employed. It consists of three or four tooling balls, depending upon the component, located and doweled in position on the component. The position of these tooling balls is measured with respect to the mirror target and the tooling bull's-eye target with the component in the level position, and again in the tilted BSY position. With these measurements, the mirror target settings can be checked in the alignment shop and/or, if necessary, while in position in the BSY.

Wires were stretched along the second level of the BSY directly over the beam drift lines. The targets were placed on the components so that the alignment of the components would be correct when the targets were located directly under the stretched wires. On the instrument stands, the center line is obscured by the equipment and the targets had to be offset from center. The center line of the 3° bending magnets are not under the stretched wire. The offset distance from the drift line depends upon the position of the magnet in the bending group and its distance from the vertex point of the bend. Offsets from the magnet center line for the bending magnet mirror stages and tooling balls were computed for each magnet.

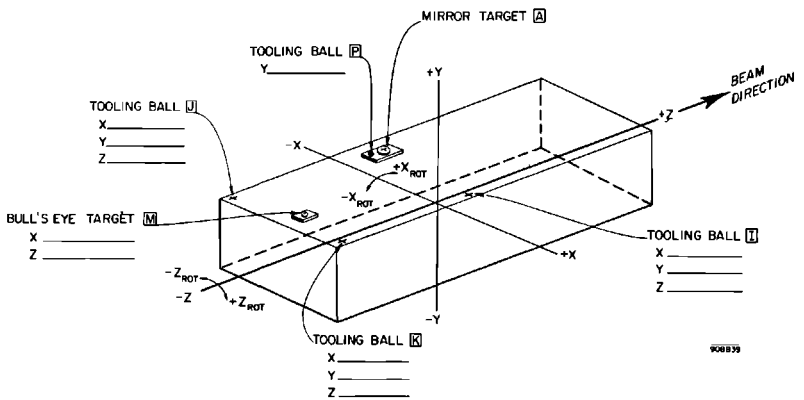

Figure 22-39 Alignment data sheet for a 3° bending magnet.

Shop installation procedures were written for each component to account for all of the above geometric requirements. A series of data sheets was made for each type of equipment to be aligned in the shop. These sheets had a drawing of the component showing the relative location of all alignment targets to be placed upon it. After the targets were installed, their positions were measured and entered on the data sheet. These sheets formed a valuable permanent record for the aligned component which can be used for checking the alignment, for realignment, and for making future changes to component location. A typical data sheet for the 3° bending magnet is shown in Fig. 22-39.

Installation alignment

Brass plates permanently fixed in the housing floor mark the vertex monument points. They are marked with a scribe to indicate their position relative to the laser system. Vertex point 2, VT-2, was set by trilateral measurement from two laser target stations. Because of its close proximity to the center of the BSY, VT-2 served as control point for the establishment of the remaining vertex points throughout the BSY. The other vertex points were defined by trilateral measurement between VT-2 and one of the laser target stations most accessible for horizontal measurement.

In order to align the equipment beyond the final vertex points, VT-4 and VT-5, turning points were established at the steering magnet groups, some 70 ft downstream from each of these vertex points. Since the electron beam was to be steered into the end stations by these magnets, their locations could be used as secondary alignment monuments. To reduce long pulls of the stretched wire, these groups of steering magnets were used as one of the tie-off points. From the end station steering magnet groups, the wires were extended across the end station monuments, thus defining the theoretical beam drift path into the end stations.

In addition to the vertex points, elevation control monuments were required. The basic elevation reference is the laser system. The elevation controls were transferred from the tooling balls on the laser system target stations to rivets in the housing floor at convenient points for both transport systems.

As described previously, each magnet and beam diagnostic instrument was assigned a horizontal and vertical position in the beam transport system. The component positions were surveyed and reference points were put on the housing floor to assist in the initial placement of both magnet and diagnostic instrument stands. The stands were installed to the reference points so that a minimum of adjustment would be required during the final alignment process.

The layout of the BSY was designed so that the optical alignment could be performed through penetration holes in the shielding, corresponding to the alignment targets on the components. Holes were also placed in the shielding to permit operation of the jacks on the alignment stands. Figure 22-40 gives a view of the second-level operation.

The field installation of all components is very similar. The description of the installation of a bending magnet given below should make the installation and field alignment of any component clear. A schematic view of the setup for a magnet is shown in Fig. 22-41. Jig transits are plumbed over the vertex points upstream and downstream of the magnet. A steel wire, 0.004 in. in diameter, is then stretched between the two vertex points. The wire is supported at either end on an adjustable table and is then moved until it

Figure 22-40 Second-level alignment of BSY component.

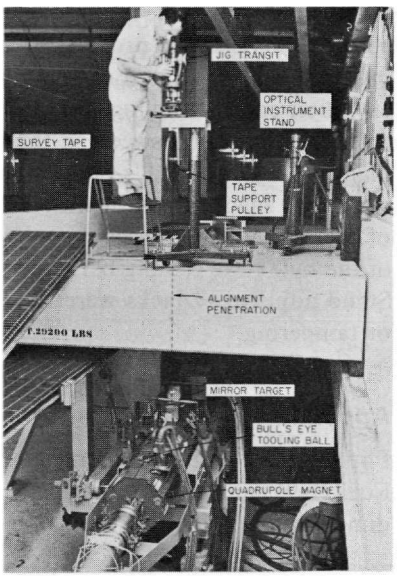

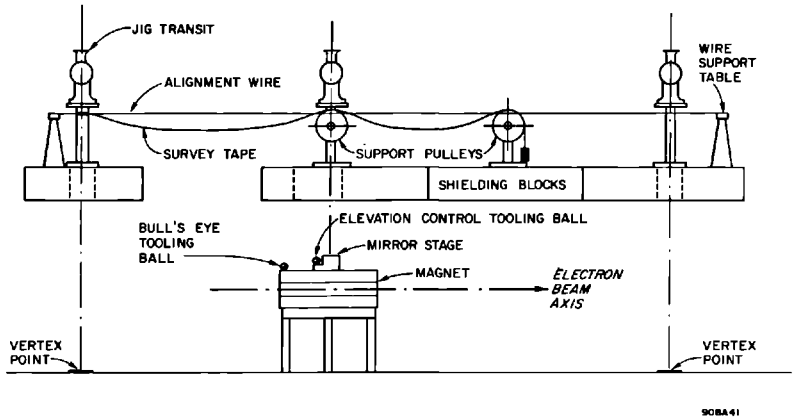

Figure 22-41 Schematic layout of installation alignment setup.

bisects the line of sight of the jig transits. This wire now lies over the theoretical beam drift path through the series of components between the two vertex points. A survey tape is extended over a pulley support system parallel to the stretched wire. The tape defines the horizontal location of the magnet along the beam drift path from one of the vertex points. A third jig transit is plumbed directly over the wire at the scribe mark on the survey tape corresponding to the location of the magnet mirror target.

The component was correctly positioned by making the mirror target coincident with the line of sight of the jig transit and the tape scribe mark. This placed the center of the mirror target directly under the alignment wire. The magnet was then adjusted to autocollimate the transit on the mirror target thus making the mirror perpendicular to the line of sight. This operation gave the magnet the proper tilt to make it parallel to the beam plane. The magnet was then set for elevation by reference to a sight rod set on the elevation control tooling ball on the magnet mirror stage. The correct yaw rotation was set by sweeping the jig transit along the wire and rotating the magnet until the bull's-eye tooling ball was directly under the alignment wire. The magnet was then in its proper position. Final checks were made of the autocollimation of the mirror, the magnet elevation, and the position of the bull's-eye tooling ball and mirror stage center line relative to the wire. Stand adjustment jacks were then lock-wired to prevent further adjustment or tampering.

Appendix: maximization of intensity (MJL)

For a target pattern having alternate slots and ribbons, the integrals in Eq. (22-9) can be written as sums of integrals over the slots. Consider two-dimensional vectors

$$\mathbf{V}_n = (C_n(0), S_n(0))$$

with

$$C_n(0) = \int_{\mu_{n-}}^{\mu_{n+}} \cos\left(\frac{\pi}{2} t^2\right) dt$$

and

$$S_n(0) = \int_{\mu_{n-}}^{\mu_{n+}} \sin\left(\frac{\pi}{2} t^2\right) dt$$

In terms of these vectors, the peak intensity is given by

$$I(0) = \left(\frac{A}{2l}\right)^2 I_\mu I_v$$

where

$$I_\mu = |\mathbf{V}|^2 = \left|\sum_n \mathbf{V}_n\right|^2$$

with a similar expression for I_v. Thus, in order to optimize the peak intensity, the length of the vector V must be maximized.

A procedure for maximizing |V| will be illustrated graphically. On a plot of the Cornu spiral, start from a point μ_{1-}, which corresponds to a given central ribbon width of a target, and draw a straight line through the end point of the spiral, E, as in Fig. 22-42. The points of intersection of the

Figure 22-42 Cornu spiral used to show graphic method of determining the optimum target design. The point μ_{1-} corresponds to the edge of the central ribbon. Subsequent slot edges correspond to the intersections of successive curves of the spiral with the line joining E and μ_{1-}.

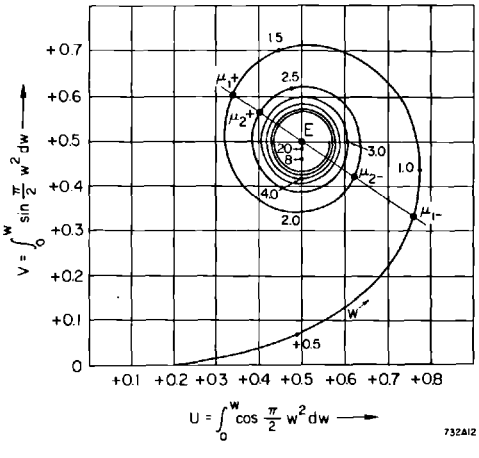

line with the spiral constitute a set of μ_{n+} and μ_{n-} which maximizes $|V|$. It can be seen that each of the vectors $\mathbf{V}_n$ has an optimum length and all vectors lie along the same direction.

It can be shown analytically that the values of μ_{n+} and μ_{n-} are approximately given by

$$\mu_{n\pm} = (4n - d \pm 1)^{1/2}$$

with

$$d = 3 - \mu_{1-}^2$$

where

$$\mu_{1-}^2 = \frac{lw^2}{2\lambda rs}$$

in which w is the width of the central ribbon.

For this, it suffices to show that the slopes of the lines joining $\mu_{n\pm}$ and E are independent of n.

From Eqs. (22-16) and (22-17), the slopes of the lines joining $\mu_{n\pm}$ and E are

$$M_{\pm}(d) = \frac{\left[\dfrac{\sin[(\pi/2)\mu_{n\pm}^2]}{\pi\mu_{n\pm}^2} - \cos\left(\dfrac{\pi}{2}\,\mu_{n\pm}^2\right)\right]}{\left[\dfrac{\cos[(\pi/2)\mu_{n\pm}^2]}{\pi\mu_{n\pm}^2} - \sin\left(\dfrac{\pi}{2}\,\mu_{n\pm}^2\right)\right]}$$

from which

$$M_{\pm}(d) = \frac{\sin[\pi/2(d \pm 1) - \phi]}{\cos[\pi/2(d \pm 1) + \phi]}$$

where

$$\phi = \tan^{-1} \pi\mu_{n\pm}^2$$

Because $d < 3$, $\pi\mu_{n\pm} > 12$ for $n \geq 2$ so that $\phi \approx \pi/2$. Hence,

$$M_{\pm}(d) = \frac{\sin \pi d/2}{\cos \pi d/2}$$

which, being independent of n, proves that the choice of edges is optimized.

Acknowledgments

The authors of this chapter wish to recognize SLAC's director, W. K. H. Panofsky, for his key part in developing the basic concepts of the Fresnel target system. The accelerator assembly and installation work was directed by D. Robertson and C. Rasmussen. The Fresnel lens system was tested and calibrated by O. Turpen. The early design of the switchyard alignment system was made by J. Voss. The BSY assembly and installation work was directed

by H. Weidner and R. O'Keefe. The targeting and field alignment of BSY components was directed by B. Hooley, E. Head, and W. Walsh. One of the computer programs used for BSY alignment was written by S. Howry. Many other workers were needed in all these areas. The contributions of all of them and the cooperation of their department heads is hereby gratefully acknowledged.

References

1 F. A. Jenkins and H. E. White, *Fundamentals of Optics*, 3rd Ed., McGraw-Hill, New York, 1957.

2 K. R. Trigger, "Approximate Solutions of Images Using Fresnel Zone Plates," Rept. No. SLAC-TN-64-19, Stanford Linear Accelerator Center, Stanford University, Stanford, California (1964).

3 Max Born and Emil Wolf, *Principles of Optics*, pp. 428-434, Macmillan, New York, 1964.

4 *Ibid.*, p. 122.

5 *Ibid.*, p. 88.

6 R. Sandkuhle, "Support Girder Fabrication," Rept. No. SLAC-TN-67-24, Stanford Linear Accelerator Center, Stanford University, Stanford, California (1967).

7 K. Skarpaas, "Elasticity Theory and Design of Flexible Supports for Stanford Two-Mile Linear Accelerator," Rept. No. SLAC-TN-67-9, Stanford Linear Accelerator Center, Stanford University, Stanford, California (March 1967).

8 J. K. Cobb and J. J. Murray, *Nucl. Instr. Methods* **46**, 99-105 (1967).

9 H. S. Butler, S. K. Howry, and C. H. Moore, "Specifications for the Beam Transport Systems to End Stations A and B," Rept. No. SLAC-29, Stanford Linear Accelerator Center, Stanford University, Stanford, California (1964).

10 R. E. Taylor, *IEEE Trans. Nucl. Sci.* **NS-12** (No. 3), 84 (June 1965).

11 H. S. Butler, S. K. Howry, and C. H. Moore, "TRANSPORT ... A Computer Program for Designing Beam Transport Systems," Rept. No. SLAC-DOC-12, Stanford Linear Accelerator Center, Stanford University, Stanford, California (1964).

12 A. Kilert, "Position Tolerances for Equipment in the Beam Switchyard," SLAC Engineering Note 000-014, Stanford Linear Accelerator Center, Stanford University, Stanford, California (1966).

23

VACUUM SYSTEMS

M. E. Baldwin, K. G. Carney, Jr., S. R. Conviser, Editor,
A. L. Eldredge, F. F. Hall, W. B. Pierce, and G. I. Skoda

The three major vacuum systems serving the two-mile accelerator, the optical alignment system light pipe, and the beam switchyard (BSY) transport vacuum chambers are located as shown in Fig. 23-1.

The *accelerator vacuum system* must maintain a very high vacuum in the accelerator to prevent RF electrical breakdown and electron scatter. Thirty-two subsystems evacuate the accelerator to a design pressure of 5×10^{-7} torr at the center of the individual 10-ft long sections of disk-loaded waveguide that comprise the beam envelope. Separate subsystems are provided for the injector, for the positron source, and for each of the thirty sectors of the accelerator. The subsystems are interconnected only through the 2-mile length of the disk-loaded waveguide except for a normally closed cross-tie between the injector and Sector 1 subsystem piping. Mobile cryosorption pump sets evacuate the individual subsystems from atmospheric pressure to a level at which the sputter-ion pumps can take over to produce the operating vacuum.

The *alignment light pipe vacuum system* evacuates the tubular aluminum girders which support the two-mile accelerator and the central beam tube in the BSY. The design pressure of 1×10^{-2} torr prevents deflection of light rays used for optical alignment. The girders are interconnected by flexible metal bellows. A single pumping station is located at the end of Sector 30. The initial pumpdown from atmospheric pressure is accomplished using high-capacity mechanical vacuum pumps. The vacuum is maintained at the operating level by a diffusion-ejector vacuum pump backed by a mechanical pump.

The *beam switchyard vacuum system* evacuates the BSY beam transport vacuum chambers to an average design pressure of 1×10^{-4} torr to permit passage of electron and positron beams. Normally open valves are provided by which adjoining chambers can be segregated into seven independently

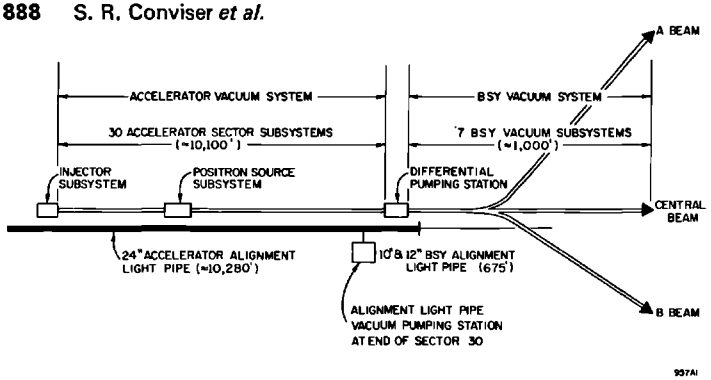

Figure 23-1 Location of vacuum systems.

pumped subsystems. The BSY high vacuum system is separated from the accelerator very high vacuum system by a refrigerated section of accelerator disk-loaded waveguide. The seven subsystems are roughed down from atmospheric pressure using mechanical vacuum pumps. The operating vacuum level is maintained by diffusion pumps.

23-1 The accelerator system

Design criteria (SRC, FFH)

Evacuation of the accelerator is required primarily to prevent electrical breakdown in the high RF fields (2856 MHz) used to accelerate the electrons and to prevent excessive scattering of the electrons by gas molecules during transit through the disk-loaded waveguide. Theoretical considerations borne out by experience on the Mark III and Mark IV accelerators at Stanford University and confirmed at SLAC indicated that a pressure of 1×10^{-6} torr or less would meet the requirement for RF breakdown. As shown by DeStaebler,[1] gas scattering is not significant below pressures of 1×10^{-5} torr. Allowing suitable safety factors, design pressures were established as 5×10^{-7} torr for accelerator sections and 5×10^{-8} torr for the vicinity of the klystron waveguide windows.

Other considerations which influenced the design were as follows. Design pumping speed at the disk-loaded waveguide input coupler was to be approximately 10 liters/sec to provide for gas bursts in the waveguides. The system was to have a design pumping speed of 20 liters/sec at the klystron window pumpout to protect against multipactoring and RF breakdown which are conditions conducive to catastrophic failure of the windows. The presence of a significant amount of hydrocarbon in the waveguides would seriously degrade the ultimate vacuum attainable; the risk of oil contamination would be great if oil diffusion pumps were used. The use of organic materials was to be minimized in the interests of cleanliness, low vapor

pressure, and reliability; these materials deteriorate in the high radiation environment in the accelerator housing, and replacement could result in excessive beam downtime. Equipment requiring servicing, such as pumps, valves, and vacuum gauges, was to be located in the klystron gallery in order to be accessible to maintenance personnel while the accelerator is in operation. Reliability of equipment is extremely important. As a design objective the life of major components was to be at least 10 yr. It was to be possible to restore accelerator operation in less than 24 hours after a maximum of three subsystems had been let up to atmospheric pressure. Provisions were to be made for expansion to Stage 2 with minimum additional expense. In Stage 2 the number of klystrons is increased to 965 from 245 in Stage 1. This increases the number of rectangular waveguides connecting the klystrons with the accelerator from 16 to 32 per sector.

Pumping speeds and pressures (SRC, GIS)

To ascertain the required pumping speed, outgassing rates of RF processed copper and stainless steel were determined by test. The residual outgassing rate of copper is less than 1×10^{-11} torr-liter/sec/cm^2.[2] Over a period of time it should reduce to approximately 1×10^{-12} torr-liter/sec/cm^2 because the system is sealed and under vacuum continuously. It was found that after vacuum processing at 400°C for 24 hours, the residual outgassing rate of stainless steel is less than 1×10^{-12} torr-liter/sec/cm^2.[3] The remainder of this section gives the approximate methods used for estimating system operating parameters.

Basic vacuum system relationships are

$$Q = C \times \Delta P = d \times A = S \times P$$

where

Q = throughput in torr-liters per second
C = conductance in liters per second
ΔP = pressure difference in torr
P = pressure in torr
d = surface outgassing rate in torr-liters per second per centimeter squared
A = total internal surface area of the vacuum system in centimeters squared.
S = pumping speed in liters per second.

Calculations were based on the following assumptions:

1. The design outgassing rate of copper is 1×10^{-11} torr-liter/sec/cm^2. This is a factor of 10 times the anticipated residual rate.
2. Outgassing of stainless steel should be neglected since the outgassing rate is an order of magnitude less than the conservative design rate used for

copper. Along the accelerator, the area of copper is approximately equal to the area of stainless steel. The total copper area per sector is 1.5×10^6 cm^2 for Stage 1 and 1.95×10^6 cm^2 for Stage 2. The stainless steel area per sector is 1.5×10^6 cm^2 for both stages.

3. The point of highest pressure, or null point, in each rectangular waveguide is located halfway between the power dividers. This is because the pressures at pumpouts at each end of the rectangular waveguides are approximately equal and the waveguide conductance is very low (less than 3 liters/sec).
4. The gas load due to leaks is negligible. The maximum tolerable leak rate per joint was separately established as 1×10^{-9} atm-cm^3/second of helium. In practice, leaks were generally less than 2×10^{-10} atm-cm^3/sec even though there are some 200 flanged joints in each sector.
5. The gas load from Viton* "O" rings in valves is negligible. The total area of Viton per sector is 471 cm^2 and the outgassing rate is 2×10^{-9} torr-liter/sec/cm^2. This results in a contribution of approximately 10% of the outgassing load from copper in Stage 1. Although outgassing rates of Viton A have been reported as 1.0×10^{-8} torr-liter/sec/cm^2 after baking and subsequent exposure to air followed by 48 hours of pumping,[4] tests conducted at SLAC by E. L. Garwin and J. Jasberg showed that 2×10^{-9} torr-liter/sec/cm^2 could be attained after 96 hours of pumping.
6. Referring to Fig. 23-2, which represents a typical Stage 1 configuration, the maximum pressure in the accelerator occurs in the middle of a 10-ft section.

The conductance C_{as} of an accelerator section from the center to an end cavity was computed from the formula[5]

$$C = 12.1 \frac{D^3}{L} \alpha$$

where D = the diameter of the tube in centimeters, L = the length of the tube in centimeters, and α = the Clausing factor, dependent on the ratio L/D. The average aperture conductance (see Fig. 23-3) was calculated to be

$$C_0 = 47.8 \text{ liters/sec}$$

and the average cavity conductance was calculated as

$$C_c = 445 \text{ liters/sec}$$

It followed, then, that the conductance of the accelerator section from center to end is

$$C_{as} = \left[\frac{(47.8)(445)}{(42 \times 445) + (43)(47.8)}\right] = 1.0 \text{ liters/sec}$$

* DuPont Company, Wilmington, Delaware.

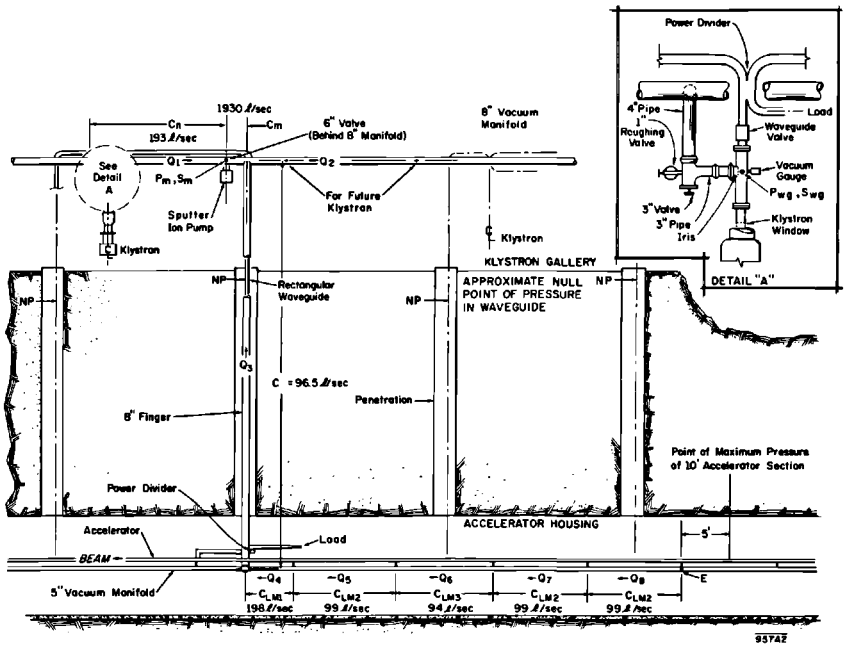

Figure 23-2 Waveguide and manifold configuration for part of a sector.

The conductance of the rectangular waveguide was calculated from the formula[5]:

$$C = 30.9 \frac{a^2 b^2}{(a+b)L} K$$

where a and b are the internal dimensions of the waveguide in centimeters, L is the length of the waveguide in centimeters, and K is a factor depending on the ratio b/a. Hence, the conductance C_{wg} of the waveguide was found to be 66.7 liters/sec for a 1-ft length.

Figure 23-3 Disk-loaded waveguide configuration.

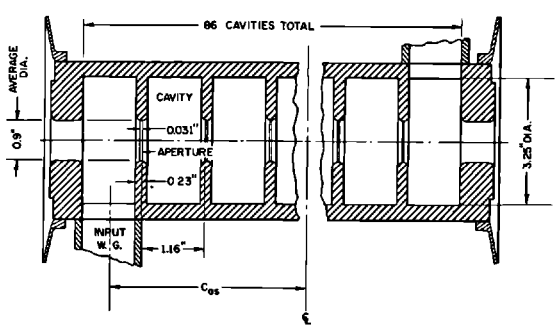

The pressure at the pump, P_p, was computed from

$$P_p = \frac{Q_1 + Q_2 + Q_3}{S_p}$$

where Q_1, Q_2, Q_3 are the gas contributions from the various portions of rectangular waveguide and accelerator section as shown in Fig. 23-2, and S_p is the pump speed.

The pressure at the manifold, P_m, was obtained from

$$P_m = \frac{Q_1 + Q_2 + Q_3}{S_m}$$

where S_m is the effective speed at the manifold, which is given by

$$S_m = \frac{(C_{\text{6-in. valve}})(S_p)}{C_{\text{6-in. valve}} + S_p}$$

$C_{\text{6-in. valve}}$ is the conductance of the valve above the ion pump, and S_p is the speed of the ion pump.

At this point it was possible to write an expression for the pressure at the center of the accelerator section farthest away from the pump:

$$P_{as} = P_m + \left[\frac{Q_2 + Q_3}{C_m} + \frac{Q_3}{C_f} + \frac{Q_4}{C_{\text{LM1}}} + \frac{Q_5}{C_{\text{LM2}}} + \frac{Q_6}{C_{\text{LM3}}} + \frac{Q_7}{C_{\text{LM2}}} + \frac{Q_8}{C_{\text{LM2}}} + \frac{Q_8}{C_{po}} + \frac{Q_{as}}{C_{5'wg}} + \frac{Q_{5'wg}}{2C_{5'wg}} + \frac{\frac{1}{2}Q_{as}}{2C_{as}}\right]$$

In this equation, Q_2, Q_3, Q_4, Q_5, Q_6, Q_7, Q_8, Q_{as}, $Q_{5'wg}$, and $\frac{1}{2}Q_{as}$ are individual gas contributions in torr-liters per second, and C_m, C_f, C_{LM1}, C_{LM2}, C_{LM3}, C_{po}, $C_{5'wg}$, $2C_{5'wg}$, and $2C_{as}$ are the corresponding conductances in liters per second as shown in Figs. 23-2 and 23-4. The latter equation was simplified by introducing the surface outgassing rate, d, yielding

$$P_{as} = d\left[\frac{368 \times 10^3}{S_p} + 20.2 \times 10^3\right]$$

so that for $d = 1 \times 10^{-11}$ torr-liter/sec/cm^2,

$$P_{as} = \frac{3.68 \times 10^{-6}}{S_p} + 2.02 \times 10^{-7}$$

This showed that the lowest pressure attainable at the center of the farthest accelerator section would be 2×10^{-7} torr using an infinitely large pump.

At the time of pump selection, nominal speeds commercially available were 400, 500, and 1000 liters/sec. The 400-liters/sec pump was ruled out because a 500-liters/sec pump cost only 15% more and used the same power supply. The 10% saved per sector by using two 1000-liters/sec pumps and power supplies instead of four 500-liters/sec pumps and power supplies was

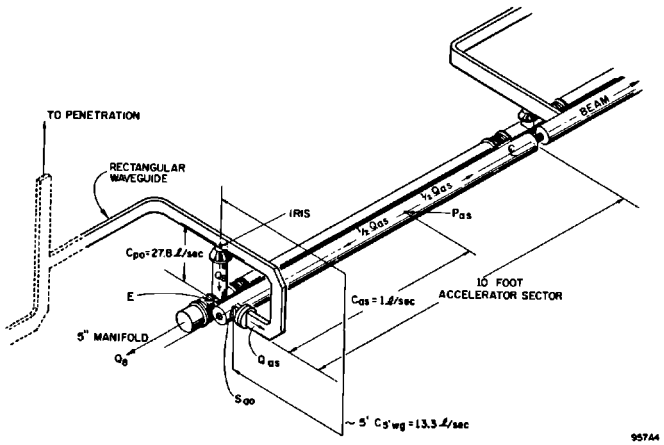

Figure 23-4 Accelerator-waveguide vacuum connection.

more than offset by the added cost of the larger stainless steel manifolds required by the 1000-liters/sec pumps. Therefore, the 500-liters/sec units were considered to be economically optimum. Setting $S_p = 500$ liters/sec, one obtains

$$P_{as} = 2.1 \times 10^{-7} \text{ torr}$$

Therefore, assuming a total copper gas load $Q = 1.5 \times 10^6 \times 1 \times 10^{-11}$ torr-liter/sec per sector, and designing for four standard 500-liters/sec pumps per sector, the pressure at each pump was found to be

$$P_p = \frac{Q}{4S_p} = \frac{1.5 \times 10^{-5} \text{ torr liter/sec}}{4 \times 500 \text{ liters/sec}} = 7.5 \times 10^{-9} \text{ torr}$$

For stage 2 conditions with one klystron per 10-ft accelerator section, the gas load would be increased by additional rectangular waveguides. The pump pressure would increase from 7.5×10^{-9} to 9.5×10^{-9} torr. Pressure in the accelerator section should not be affected appreciably.

The effective pumping speed at the klystron waveguide window, S_{wg}, with a 500-liters/sec pump was calculated as follows:

$$\frac{1}{S_{wg}} = \frac{1}{S_p} + \frac{1}{C_{\text{6-in. valve}}} + \frac{1}{C_n} + \frac{1}{C_{\text{4-in. pipe}}} + \frac{1}{C_{\text{3-in. valve}}} + \frac{1}{C_{\text{3-in. pipe}}} + \frac{1}{C_{\text{iris}}}$$

i.e.,

$$\frac{1}{S_{wg}} = \frac{1}{500} + \frac{1}{1300} + \frac{1}{193} + \frac{1}{176} + \frac{1}{250} + \frac{1}{160} + \frac{1}{100} \text{ sec/liter}$$

or

$$S_{wg} = 29.5 \text{ liters/sec}$$

Thus, the pressure at the waveguide window pumpout is

$$P_{wg} = \frac{\text{area}_{60'wg}\, d}{S_{wg}} = \frac{60 \times 649 \times 1 \times 10^{-11}}{29.5}$$

$$P_{wg} = 1.3 \times 10^{-8} \text{ torr}$$

The effective pumping speed at the accelerator section input coupler as shown in Fig. 23-4 was calculated as follows:

$$\frac{1}{S_{ao}} = \left(\frac{1}{S_p} + \frac{1}{C_{6\text{-in. valve}}} + \frac{1}{C_m} + \frac{1}{C_f} + \frac{1}{C_{5\text{-in. manifold}}}\right)\frac{1}{2} + \frac{1}{C_{po}} + \frac{1}{C_{5'wg}}$$

$$= \left(\frac{1}{500} + \frac{1}{1300} + \frac{1}{1930} + \frac{1}{96.5} + \frac{1}{22}\right)\frac{1}{2} + \frac{1}{27.8} + \frac{1}{13.3} \text{ sec/liter}$$

$$S_{ao} = 7.1 \text{ liters/sec}$$

Although this is some 30% below the value in the design criteria, it was deemed satisfactory and has proven adequate in operation. Also it should be kept in mind that for 16 of 32 accelerator sections the length of waveguide between the vacuum system pumpout and the accelerator section input coupler is reduced from 5 ft in length to only 14 in., which approximately doubles the effective pump speed at the input coupler.

Subsystem arrangement (SRC, KGC)

The accelerator system extends over 10,084 ft including the injector and thirty sectors of accelerator, each 333 ft, 4 in. long. Each of the thirty sectors is handled as an independent subsystem. Except for the cross-tie between the injector and Sector 1, the only connection between subsystems is through the 2-mile length of disk-loaded waveguide. Sector 11 is further subdivided and a separate subsystem is provided to minimize the effect on the rest of the sector of an accident at the positron source. The injector is also served by a separate subsystem with one 500-liter/sec sputter-ion-pump connected to the rectangular waveguide in the klystron gallery and smaller pumps connected to the injector proper in the accelerator housing. To provide backup, this subsystem is also tied through an isolation valve to the Sector 1 manifold in the klystron gallery, as shown in Fig. 23-5.

A typical sector vacuum system for Stage 1 is shown in Fig. 5-19. Four sputter-ion pumps, each rated at 500 liters/sec, adequate for both Stage 1 and Stage 2, are connected by 6-in. valves to an 8-in. manifold in the klystron gallery extending the full length of the sector. A similar 5-in. manifold is located in the accelerator housing. The two manifolds are interconnected by four 8-in. vertical fingers passing through 27-in. diameter service penetrations spaced approximately 80 ft apart.

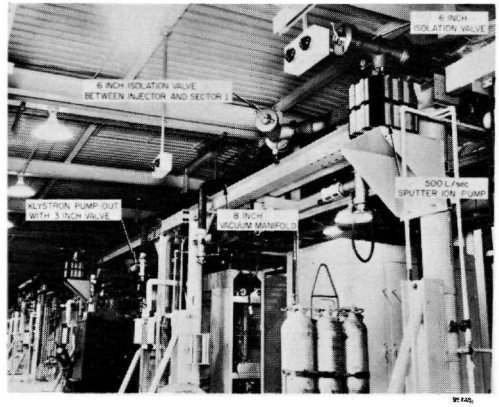

Figure 23-5 Cross-connect valve between injector and Sector 1.

Four-inch branches on approximately 40-ft centers connect the waveguide pumpouts near each klystron window to the 8-in. manifold. A 3-in. manual valve is included in each branch. Provisions are made for the future connection of twenty-four additional klystrons in each sector. In the accelerator housing, a pumpout at each of the thirty-two couplers (rectangular waveguide to disk-loaded waveguide) connects the accelerator to the 5-in. vacuum manifold.

A 5-in. finger connects the 8-in. klystron gallery manifold to the 10-ft drift section at the end of each sector in the accelerator housing. This drift section contains beam-monitoring and guidance apparatus. The drift section can be isolated from the sector vacuum subsystem by closing a 3-in. finger valve (similar to the klystron valves) in the klystron gallery and closing the beam-line valves at each end of the drift section. The upbeam valve is manually operated, but the valve at the downbeam end of the drift section is a spring-actuated fast-acting valve which closes in the order of 9 msec. These fast valves close automatically to isolate a sector in the event of accidental loss of vacuum.

Each klystron is isolated from the sector vacuum subsystem by a waveguide window, as shown in Fig. 23-2. A valve located in the rectangular waveguide approximately 2 ft above this window, used in conjunction with the 3-in. klystron valve, permits replacement of klystrons without interrupting accelerator operation.

The vacuum system in Sector 11, shown schematically in Fig. 23-6, differs from the conventional sector subsystem in the measures taken in anticipation of a water or air leak at the positron source on girder 11-3A.

The 5-in. sector manifold is interrupted and pumpout connections adjacent to girder 11-3A are eliminated to preclude the possibility of bypassing fast valves 11-2 and 11-3. The closing of valves 11-2 and 11-3 establishes a first line of defense against contamination of neighboring accelerator sections by

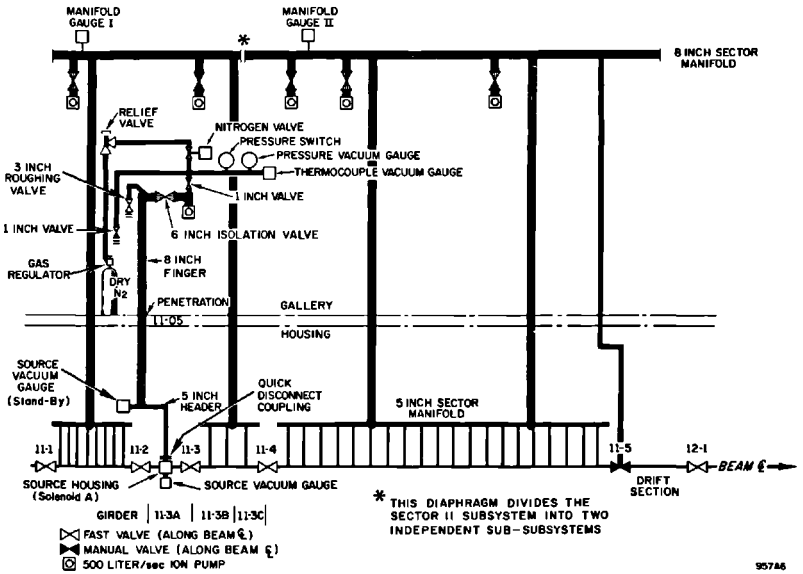

Figure 23-6 Positron source vacuum subsystem.

isolating components particularly vulnerable to leakage, such as quick-disconnect couplings and bellows, along the intervening girder 11-3A drift tube.

Double protection for accelerator sections upbeam from fast valve 11-1 and for accelerator sections downbeam from girder 11-3C is achieved by adding fast valve 11-4 and by interrupting both the 8-in. header in the klystron gallery and the 5-in. manifold in the accelerator housing. The manifold is separated at the downbeam end of girder 11-3C. The header is blocked by a metal diaphragm just downbeam from the finger serving accelerator sections 11-3B and 11-3C. Manifold gauge I monitors the vacuum and operates the interlocks in the downbeam two-thirds of the sector. Manifold gauge II monitors the vacuum and operates the interlocks in the upbeam one-third of the sector.

Pumping capacity between fast valves 11-2 and 11-3 is provided through a separate positron vacuum subsystem, which includes a 500-liters/sec sputter-ion pump, a pair of cold cathode-type ion gauges, a 3-in. roughing valve, a 6-in. pump isolation valve, a combined 8-in. header and finger, and a 5-in. header in the accelerator housing. To facilitate replacement of the radiator strongback carrying the beam line and service equipment on girder 11-3A, a 6-in. indium-sealed quick-disconnect coupling of the type used in the BSY is interposed between the end of the 5-in. header and the source housing to reduce the radiation exposure of personnel working on the joint. To minimize response time, the source vacuum gauge is located on the 5-in. header as near as possible to the points of probable leakage. The standby gauge is mounted in a region of minimum residual radioactivity where it is more readily

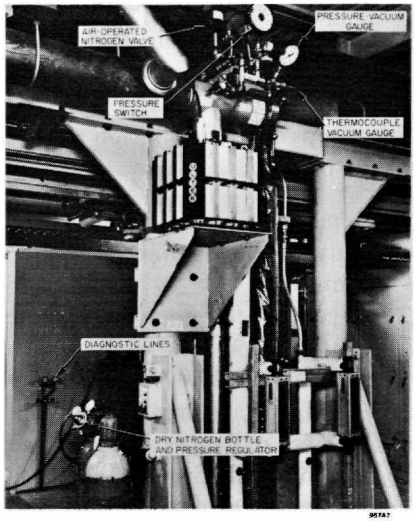

Figure 23-7 Positron source flood control.

accessible for replacement. The cable from either gauge can be plugged into the controller in the klystron gallery.

Rapid application of gas counterpressure in the event of a suspected water leak anywhere in the positron vacuum subsystem is an important feature of the so-called "flood control system." The valves, gauges, and pressure switch used to introduce and control gas flow are mounted on a manifold attached to the positron vacuum subsystem through a 1-in. valve attached to the 6-in. isolation valve body as shown in Figs. 23-6 and 23-7. When the thermocouple gauge controller in the Sector 11 instrumentation and control alcove registers a pressure rise in the subsystem to above 10^{-2} torr, an electrically controlled, air-operated nitrogen valve opens, admitting 30 psig of dry nitrogen in an attempt to stop further entry of water or air. When the gas pressure in the manifolds builds up to 5 psig, actuation of the pressure switch closes the nitrogen valve, opens the drain valve, and stops the solenoid and radiator cooling-water pump. A 1-in. valve, accessible from the klystron gallery floor, can be used for attachment of a leak detector or for introducing gas to let the subsystem up to atmospheric pressure.

Sputter-ion pumps (SRC)

Two types of pumps which appeared to be most applicable were considered during the preliminary design: sputter-ion pumps and oil-diffusion pumps baffled by molecular sieve traps with mechanical backing pumps. Liquid nitrogen baffles were ruled out due to high operating cost and complexity of operation. The cost of the diffusion pump scheme appeared to be 5% less than that

of the sputter-ion pump scheme. However, the total power demand during high-vacuum operation would be 400 kW for diffusion pumps versus 12 kW for ion pumps. This represents a significant saving which, over a 10-yr period, would exceed the initial cost differential. The principal advantages of sputter-ion pumps over oil-diffusion pumps are listed below, not necessarily in order of importance:

1. Replacement of expensive diffusion pump oil is eliminated and the possibility of oil contamination of the waveguides during normal operation is avoided.
2. Once in operation, no attendance is required and the maintenance problems of mechanical equipment and associated controls and safety devices are eliminated.
3. Pump current measurement indicates pressure directly, reducing the number of gauges and gauge controllers required.
4. An inherent advantage is the fact that as vacuum improves, sputter-ion pump power requirements decrease. It was estimated that power costs for the ion pumps would be approximately 3% of that for diffusion pumps.

The applicability of diode-type sputter-ion pumps was proved by a series of tests conducted over a 6-month period at a "tree-house" test facility consisting of one 40-ft module of the accelerator. During these tests, the performance of diffusion pumps was compared with that of sputter-ion pumps. The residual gases were monitored with RF power on, and it was found that the principal gases were H_2, H_2O, CO, and CH_4, with H_2 dominating, particularly during gas bursts resulting from transient effects such as multipactoring. Because H_2 is very active, sputter-ion pumps inherently have a pumping speed for H_2 which is twice that for air. This characteristic enhanced the desirability of their use on the accelerator. Over a period of approximately 9 months at this test facility, a 400-liters/sec sputter-ion pump was repeatedly let up to gaseous nitrogen and air with no serious effect on subsequent pumping speeds or recovery times.

Sputter-ion pumps operate on the principle of the Penning* cold cathode discharge arranged to trap gas molecules in a metallic film. The pumps start at a pressure of approximately 10^{-2} torr and reach full pumping speed at a pressure of approximately 10^{-5} torr. A magnetic field is used to increase the electron path length and the probability of ionizing collisions between electrons and gas molecules. Positive ions are accelerated toward the titanium cathodes where sputtering of the titanium occurs. The gaseous ions are pumped by (1) entrapment in the sputtered material, the majority of which ends up on the anode, (2) burial in the cathode, and (3) chemical reaction with the sputtered titanium. Pumping speeds for the noble gases in diode-type pumps are much lower than for the more active gases, e.g., the speed for argon is

* F. M. Penning, "Coating by Cathode Disintegration," U.S. Patent No. 2146025 (February 7, 1939).

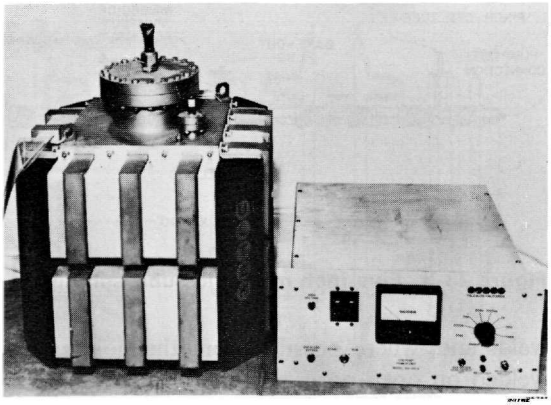

Figure 23-8 Sputter-ion pump and power supply.

approximately 1% of the speed for nitrogen and the speed for helium is about 10% that of nitrogen. Triode pumps have higher speeds for the noble gases. However, the accelerator operates as a sealed system with negligible air leaks so that the presence of noble gases is no problem. For this reason, commercially available and proven diode sputter-ion pumps were selected. The pump and power supply used are shown in Fig. 23-8.

Manifold piping (SRC)

The long pumping paths and low inherent conductances dictated that a clean system with a minimum of real and virtual leaks should be provided in order to minimize the size and related cost of pumps. System materials are (1) 304L stainless steel for piping, flanges, and valves, (2) OFHC* copper for the waveguides and waveguide flange gaskets, and (3) Viton A† "O"-ring seals in klystron gallery valve seats. To improve reliability, welded connections, rather than bolted flanges, were used where feasible. The Viton "O" rings used for valve seals were baked in a vacuum furnace at 150°C for 12 hours prior to installation in the valve. The OFHC copper rectangular and disk-loaded waveguides were chemically cleaned and processed at full RF power prior to installation.

During fabrication, manifold components were handled in pressurized clean rooms with filtered air supply. Individual parts were cut to length, degreased and cleaned, rinsed with city water, rinsed in warm deionized water, and dried in filtered warm air. Parts were then welded by the tungsten inert gas fusion process. An inert atmosphere within the subassembly was ensured by an argon gas purge. Automatic welding techniques were used for butt

* American Metal Climax, Inc., New York, N.Y.

† DuPont Company, Wilmington, Delaware.

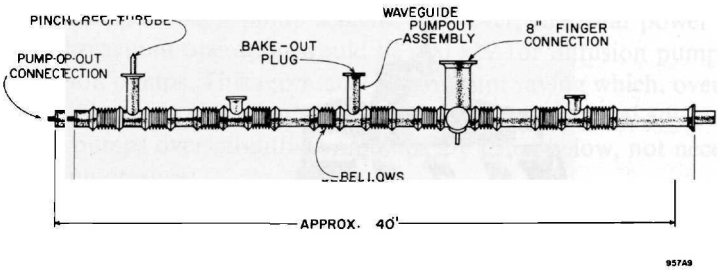

Figure 23-9 Five-inch manifold subassembly.

welds and, where possible, for other joints. Temporary bakeout plugs were welded on open ports of the subassembly. A temporary pumping port was provided for connection to vacuum processing pumps. Eight manifold subassemblies were mounted on a steel cart and connected to a liquid–nitrogen trapped, mercury diffusion pump. The eight manifolds were baked out simultaneously in a special furnace with the temperature maintained at 400° to 425°C for a period of 24 hours. After bakeout, the subassemblies were checked by the rate-of-pressure rise technique for compliance with the specified maximum outgassing rate of 1×10^{-12} torr-liter/sec/cm^2. They were then let up to dry nitrogen through pinch-off tubes on the end opposite the pump connections. The nitrogen purge was maintained while the pumped end was separated from the pumping manifold and a cap welded on. The let-up connection was then pinched off and the subassembly was crated for shipment. A completed 40-ft long, 5-in. manifold subassembly is shown in Fig. 23-9.

Forty-foot long, 8-in. and 5-in. manifold subassemblies were sealed, backfilled with dry nitrogen in the manner described above, and delivered to the field. The 5-in. manifold subassemblies were installed on the 24-in. support girders and connected to the waveguides in the SLAC shops. The completed

Figure 23-10 Forty-foot girder ready for installation.

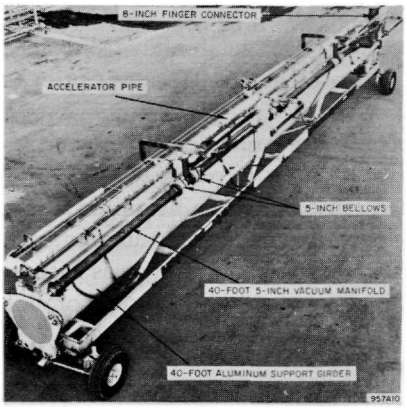

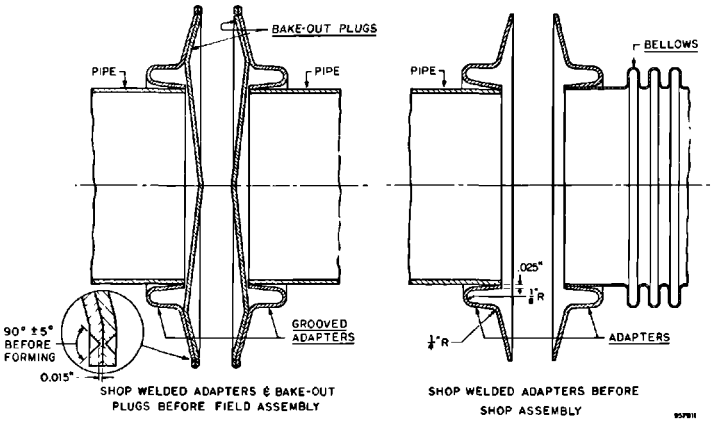

Figure 23-11 Weld joint adapters.

girder assembly ready for installation in the accelerator housing is shown in Fig. 23-10. During field installation, a positive pressure of dry nitrogen was maintained inside the piping.

The special adapters used to connect pipe to bellows and for joints made in the field are shown in Fig. 23-11. In the latter application, both the adapter and the temporary bakeout plug installed in the shop have a 90° V-groove, $\frac{1}{8}$ in. from their outer edges. The bakeout plug is welded to the outer edge of the adapter beyond the groove. In the field, the area between the apex of the groove and the outer edge is peeled off and the field weld connecting the adapters made at the new edge as shown in Fig. 23-12.

Bellows are provided to (1) allow for thermal expansion, (2) prevent excessive loading of the accelerator structure, particularly during accelerator alignment procedures, and (3) to facilitate installation. There is a total of ninety 8-in. bellows and 1920 5-in. manifold bellows in the complete accelerator vacuum system installation.

Figure 23-12 Adapter field weld.

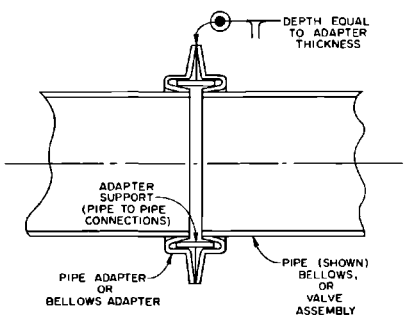

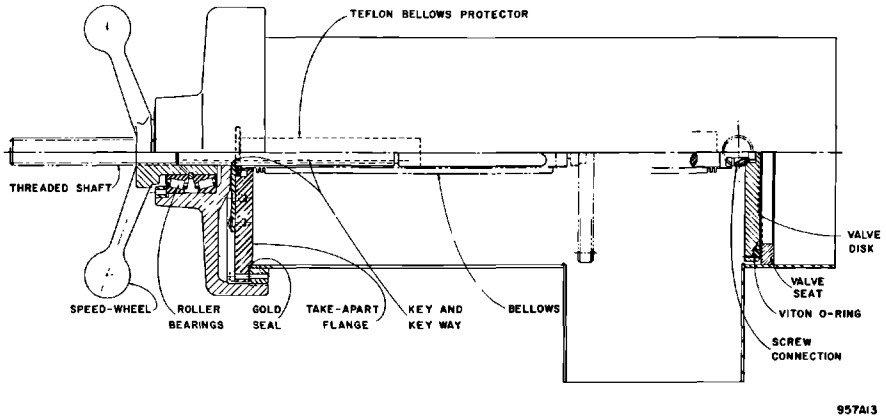

Figure 23-13 Cross section of 6-in. valve.

Klystron gallery valves (SRC)

Valves located in the klystron gallery are used to isolate sputter-ion pumps, klystrons, and drift sections. In addition, a 1-in. roughing valve is attached to each isolating valve. The roughing and isolation valves are of the angle type with a bellows-sealed stem. Inasmuch as there are 150 6-in. valves and 270 3-in. valves, cost considerations precluded the use of all-metal stainless steel valves and led to the selection of Viton A "O" rings for seals at valve seats. Other valve material exposed to vacuum is 304L stainless steel.

A cross section of the 6-in. valve is shown in Fig. 23-13. The 3-in. valves are similar. Flanges with gold-wire seals are used to separate the valve interior from the atmosphere. An unusual feature of this valve is the detachable valve disk held to the stem by means of a screwed connection. This allows the bellows and valve operator, which are the least reliable components, to be replaced with vacuum maintained in the system.

For isolation of the vacuum gauges mounted on the thirty 8-in. manifolds, a bakeable, all-metal, commercially available valve was used, since the presence of an elastomer at the gauge could give erroneous readings. It was also felt that it would be necessary to bake the cold cathode gauges periodically to 400°C. Therefore elastomers are not suitable for this application. A 12-in. long, $\frac{1}{4}$-in. diameter, pinch-off tube is provided to allow roughing of the gauge volume when replacement is necessary.

Beam-line fast-acting valves (ALE)

A fast-acting vacuum valve[6] for applications along the electron beam axis was developed and installed at the downbeam end of each 333-ft, 4-in. sector. The valve closes in 9 msec, affording substantial protection for the disk-loaded waveguides against vacuum failure anywhere in the system. The valve is automatically actuated when the pressure rises to a predetermined value.

The actuating signal is provided by the manifold gauge controller described below. The same signal turns off the electron beam. Thus, an individual sector is isolated by the closure of its fast valve and the fast valve at the downbeam end of the preceding sector.

A cross-sectional view of the fast valve is shown in Fig. 23-14. The valve has a 13/16-in. aperture for the electron beam. The oval disk of the valve has a groove in which a remeltable indium seal is located. When the valve is closed, the knife edge ring on the beam aperture tube indents the indium to effect the seal. After each set of 20 to 30 closure cycles, the indium is remelted under high vacuum while the valve is open.

Good reliability of the valve is achieved by virtue of the fact that no sliding or rolling metal-to-metal contacts are necessary in vacuum for the valve to be closed or opened. The cycling is accomplished by flexible metal hinges that are attached to the oval disk. The actuating force is from the stored energy in the compressed spring. The actuation of the valve is initiated by tripping the solenoid which releases the latch hook, allowing the spring to

Figure 23-14 Cross section of beam-line fast valve.

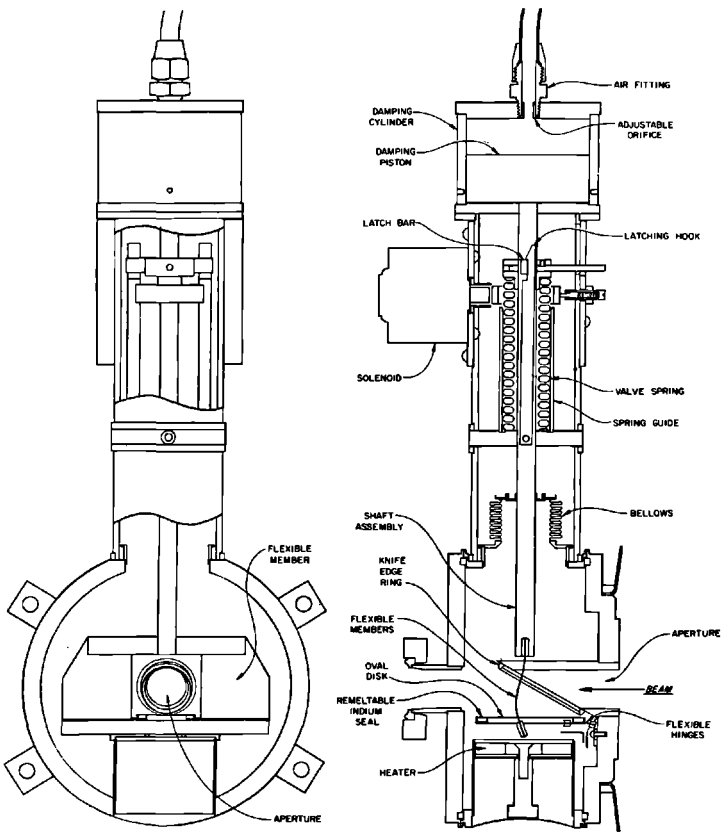

extend and hence move the shaft assembly upward. This action pulls the oval disk closed against the beam aperture seat.

The shaft assembly travels in two bearings and is lubricated by molybdenum disulfide, a permanent lubricant that is relatively unaffected by the radiation environment. The bellows permits the shaft assembly to operate in air at its upper end and in vacuum within the valve body. Molybdenum disulfide is also used as a permanent lubricant for the piston which operates within the cylinder without seals. The air holes in the side of the cylinder provide release of vacuum damping under the piston during the valve closing and also prevent pressure buildup under the piston when it is forced downward to open the valve. An adjustable restriction located in the air fitting at the top of the valve regulates the air escape to achieve the desired damping during valve closure.

Accelerations of 200 to 300 g occur during the operation of the valve, requiring the air damping cylinder to cushion the motion at the instant the oval disk seats against the beam aperture. The air cylinder is also used to reset the valve. The air piston is forced down by compressed air until the latch hook re-engages. Actuation and resetting of the valve are readily accomplished remotely. The parts of the valve needing maintenance, such as the spring, solenoid, and damping cylinder assembly, are all outside the vacuum system, so that repairs can be made without disturbing the vacuum side of the valve.

Gauges and controllers (WBP)

There are approximately 280 vacuum gauges required for accelerator operation. A gauge is located at each of the 245 klystrons. The primary function of these gauges is to protect the klystron and klystron window from damage

Figure 23-15 Klystron gauge logic diagram.

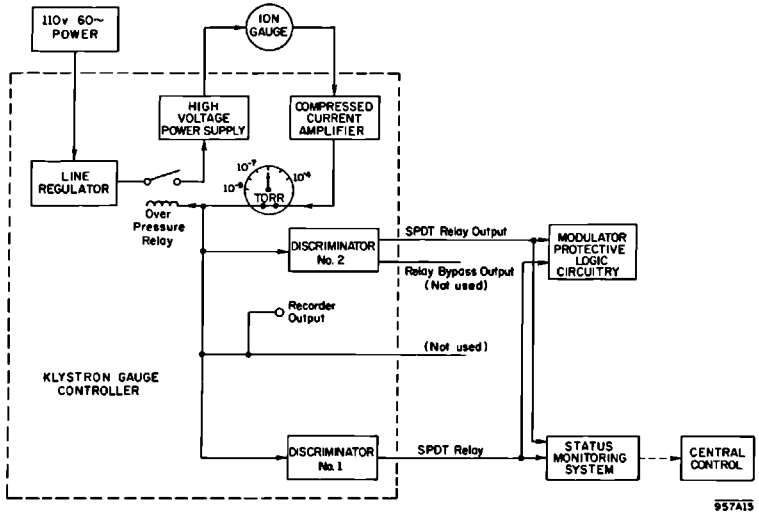

due to operation with a poor vacuum. The gauge senses any degradation in vacuum and the klystron gauge controller opens an interlock chain which takes the klystron modulator and hence the klystron out of operation. As shown in Fig. 23-15, the status of the gauge is also available at central control via the status monitoring system.

A gauge is located in the klystron gallery near the center of each of the thirty sector manifolds. Five gauges are located in the accelerator housing at the positron source and beam-analyzing stations. These thirty-five manifold gauges have two primary functions: to give a representative sector vacuum indication and to sense a vacuum failure and cause the manifold gauge controller to generate a fast response signal closing the beam-line fast valves at each end of the sector. A schematic of the manifold gauge controller appears in Fig. 23-16.

The vacuum gauges selected for the accelerator are of the cold cathode discharge type. These were selected over the more widely used hot filament type because they have greater sensitivity by a factor of 10 to 20, they require simpler electronics because of the higher sensitivity and elimination of the hot filament, construction is more rugged because of the metal envelope, and they have a longer life.

Criteria set for the gauge performance were as follows:

1. Operation should be stable from 10^{-4} to 10^{-9} torr
2. Their sensitivity for nitrogen should be within $\pm 50\%$ of the nominal specified value
3. The maximum sensitivity variation for each individual gauge should be stable within $\pm 25\%$
4. The maximum start-up time at 10^{-8} torr should be 30 seconds
5. All-metal construction bakeable to 400°C should be used
6. The maximum operating voltage should not exceed 4000 V dc.

Figure 23-16 Manifold gauge logic diagram.

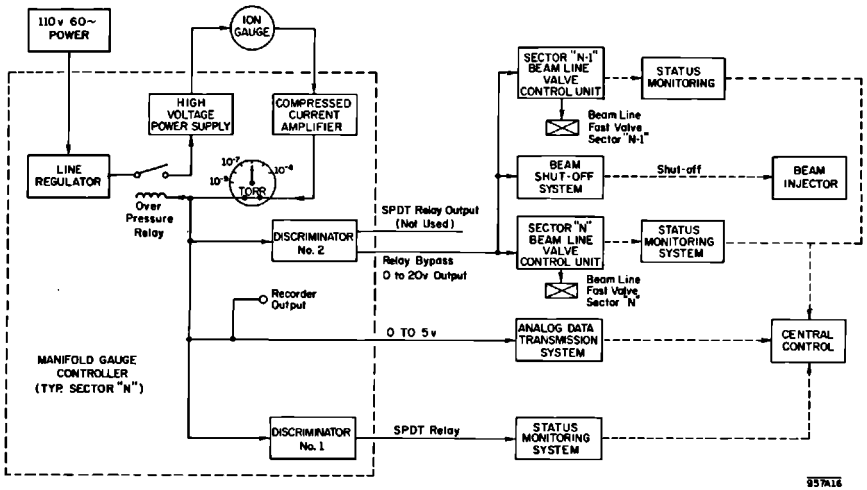

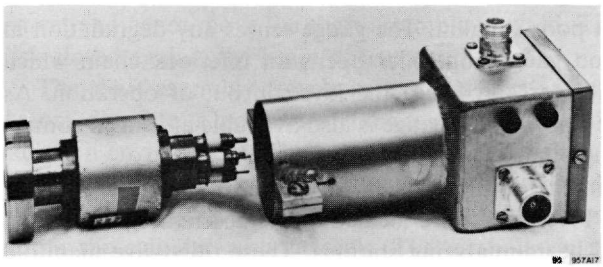

Figure 23-17 Vacuum gauge and guard.

The performances of cold cathode-type discharge gauges supplied by several manufacturers were checked on a test dome and on the previously mentioned "tree house," a 40-ft accelerator hot test facility. The test dome was capable of handling as many as eight gauges simultaneously. The gauge ion current was measured on a calibrated micromicroammeter and compared with the pressure in the test chamber. Pressure measurements in the chamber were obtained by comparison with a gauge calibrated by an independent laboratory and by a "known pumping speed–known volume of gas" method.

Calibration curves compared fairly well over the desired pressure range. Other problems, however, developed with gauges of two different designs. One problem, common to both designs, was instability. This was due to the existence of two different modes of operation which resulted in a change of sensitivity and pressure indication by as much as a factor of 3. Also, gauges of one design frequently extinguished and would not restart at pressures below 10^{-7} torr. After exhaustive tests, the General Electric* all-metal, cold cathode gauge with a permanent magnet and a starting filament was selected as most nearly in conformance with SLAC specifications. This gauge is shown in Fig. 23-17.

Specifications for vacuum gauge controllers were written with the intention of purchasing the controllers from a commercial supplier. Fifteen units were purchased from each of two different manufacturers. After considerable testing and evaluation, it was determined that neither model would satisfy all requirements. As a consequence, an in-house project was initiated to design an acceptable unit.

The design philosophy was to use the best components available and, if at all possible, to use only silicon semiconductors within the controller. The ambient operating temperature for the controllers varies from 0° to 60°C. The relative humidity can be as high as 100%.

The cold cathode gauge chosen for use on the accelerator requires 2500 V and a separate starting filament voltage. The sensitivity of the gauge is approximately 2.5 A/torr. The operating range is from 10^{-9} to 10^{-4} torr, with currents of 2.5×10^{-9} to 2.5×10^{-4} A available for display and control. It

* General Electric Company, Vacuum Products Operation, Schenectady, New York.

was decided that the five-decade range of current should be covered on a single logarithmic meter scale with no range switching.

To meet the interlock requirements, it was necessary that all 280 controllers used with both klystron and manifold gauges be fail-safe and initiate protective action for the system when the vacuum deteriorates below a preset adjustable level. In addition, a fast response output was required from the thirty-five controllers used with the manifold gauges, in order to close the beam-line valves in time to preserve the vacuum in the adjacent sectors. Total closing time from fault-sense to valve closure is less than 12 msec; 9 msec are required for valve closure alone.

As shown schematically in Fig. 23-18, the controller contains a modular, high-voltage power supply. Adjustment over the range of 0 to 5 kV is accomplished by a small adjustable autotransformer across the input. An overcurrent relay protects the unit from destruction due to gauge shorting. To present the five decades of current which will be passed by the gauge as the vacuum varies over the five decades of pressure, a scale compression, or log amplifier, is required. A voltage proportional to the log of the current is obtained by passing the current through a silicon diode and observing the voltage. Ten diodes were placed in series to increase the voltage output level; this also served to reduce the effects of variation in diode characteristics. The series diodes were placed in a proportional control-type oven to maintain a constant temperature and thus keep amplifier drift, measured at the amplifier output, within the required specification of less than 0.25 V, or 5%, over the ambient

Figure 23-18 Schematic of vacuum gauge controller.

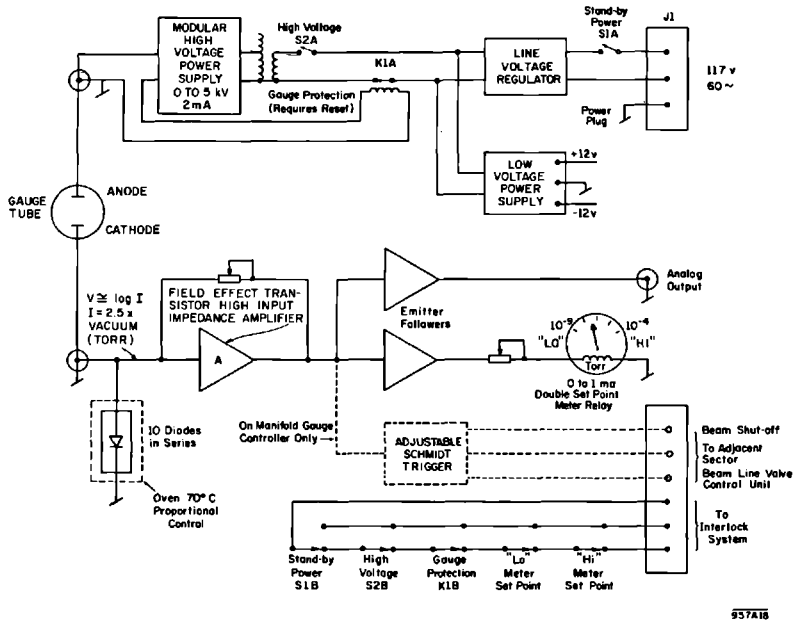

temperature range of 0° to 60°C. The amplifier that follows the diodes is a high-current gain amplifier with considerable voltage feedback. Since very low currents are measured at the input, a high impedance device is necessary. A low leakage field-effect transistor was used with very satisfactory results. The output of the amplifier corresponding to the 10^{-9}–10^{-4} torr range is 0–5 V. This analog output is available for remote indication. Klystron protection is obtained from relay contacts on a front panel meter driven from the 0–5-V analog signal.

Rapid response to vacuum failure is required of the manifold gauge controller. The fast output used to close the valves isolating the sector is a pulse of 2 msec duration and 20 V amplitude derived from a Schmidt trigger-type circuit.

Cryosorption roughing pump sets (GIS)

Roughing pumps are required to reduce the pressure in the accelerator vacuum system to below 10^{-2} torr before the main sputter-ion pumps can be started. This is done by a mobile, three-stage cryosorption pump utilizing molecular sieve material cooled by liquid nitrogen.

The volume of each sector subsystem is approximately 9000 liters and each is roughed separately. A permanent roughing system was originally proposed for each sector. As planning progressed, it became obvious that a reliable vacuum could be maintained with relatively infrequent letups to atmospheric pressure. Sector isolation by fast valves so that not more than three sectors would be affected in the event of a major leak was also a factor in the decision to use portable roughing equipment.

The use of high vacuum equipment such as diffusion and turbomolecular pumps was initially considered for roughing service, since it was felt that sputter-ion pump life and performance could be substantially extended if the starting pressure were limited to a maximum of 1×10^{-6} torr. Tests conducted on the "tree house" facility indicated that sputter-ion pumps operated adequately when repeatedly started at pressures of 10^{-2} to 10^{-3} torr. Consequently, the types of pumps offered for final consideration were multistage cryosorption pumps, liquid nitrogen-trapped mechanical pumps, and Roots blower with liquid nitrogen trap and mechanical pump.

Cryosorption roughing as originally proposed[7] included a combination of mechanical and cryosorption pumps. Tests were conducted with systems utilizing a mechanical pump and a two-stage cryosorption pump. It was found that a pressure of 2×10^{-4} torr was reached in $1\frac{1}{2}$ hours.[8] In this series of tests, 2×10^{-4} torr was reached in $3\frac{1}{2}$ hours using a prototype, three-stage, cryosorption unit without a mechanical pump. After reviewing the design of the large cryosorption pumps with the manufacturer, it was concluded that by incorporating some minor modifications and using a different molecular sieve material (Linde 5AX),* pressures of 2×10^{-4} torr could be reached

* Union Carbide Corporation, Linde Division, New York, New York.

without the mechanical pump in less than 2 hours, including the time required to cool the cryopumps down to operating temperature.

In order to eliminate the possibility that oil from the mechanical pump might contaminate the waveguides, it was finally decided to rely exclusively on molecular sieve cryosorption pumps.

Two identical cryosorption pump sets were procured, each consisting of two large and one small cryopump. The large Stages 1 and 2 pumps contained 125 lb of Linde 5AX molecular sieve material. The small Stage 3 pump contained 12 lb of the same material.

The complete cryosorption pump set is mounted on a mobile frame, including vacuum and liquid nitrogen valves, manometer, thermocouple and cold discharge gauges, and temperature-sensing devices. A schematic of the pump set is shown in Fig. 23-19 and actual equipment is shown in Fig. 23-20. Molecular sieve material in the large pumps is reactivated by compressed air electrically preheated to 315°C. Because the small pump absorbs relatively little gas when used in the third and last stage of the roughing cycle, it is reactivated at ambient temperature. After the sieve material is reactivated and with the sector roughing valve still closed, valves above each pump are opened and the large Stage 1 pump is chilled with liquid nitrogen. When the pressure in the 5-in. roughing manifold reaches approximately 10^{-2} torr, the 2-in. valve above the small Stage 3 pump and the 6-in. valve above the large uncooled Stage 2 pump are closed. These preliminary operations require approximately 25 min. Roughing then begins when the sector roughing valve is opened. While Stage 1 is pumping the other two stages are being chilled.

Figure 23-19 Schematic of sector roughing pump set.

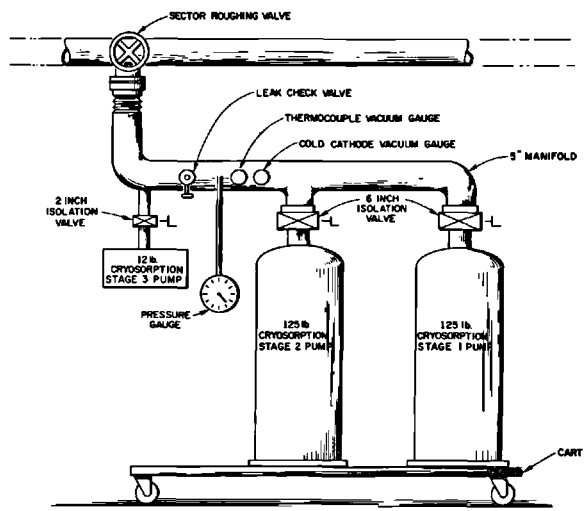

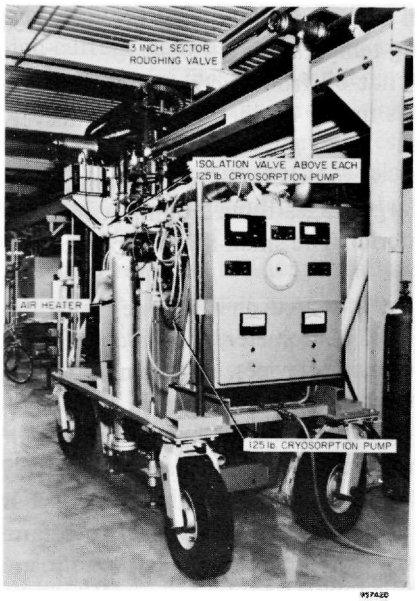

Figure 23-20 Sector roughing pump set.

Stage 1 is valved off when the pressure reaches approximately 200 torr after 50 min of pumping and Stage 2 is valved in. From the curve in Fig. 23-21, it is seen that a pressure of 10^{-3} torr can be reached in about 75 min using two of the three stages. By closing off Stage 2 and valving in the small Stage 3 pump, a further reduction in pressure to 3×10^{-4} torr can be achieved in another 15 min or so.

Liquid nitrogen consumption for a complete pumpdown is 350–400 liters. Each large pump requires about 100 liters for cooldown and 75 liters for pumpdown. The small pump consumes about 40 liters total for cooldown and pumpdown.

Because the useful life of each of the 245 klystrons in Stage 1 is limited to several thousand hours, one or more klystrons may have to be replaced every day. In order to accomplish this without disrupting the vacuum system, two valves were incorporated in the klystron-waveguide system. One is a 3-in. stainless steel valve with a Viton "O" ring seal. It is located in the klystron window pump-out connection. The other is an all-metal, remeltable indium-sealed valve built into the copper waveguide and further described in Chapter 11. The 3-in. valve has a 1-in. roughing valve on the klystron side. A typical arrangement is shown in Fig. 23-22. After klystron replacement, a small portable roughing system is used to evacuate the volume of approximately 9 liters between the 3-in. valve and the waveguide valve. The system consists of a pair of liquid nitrogen-cooled cyropumps, each filled with 2 lb of Linde

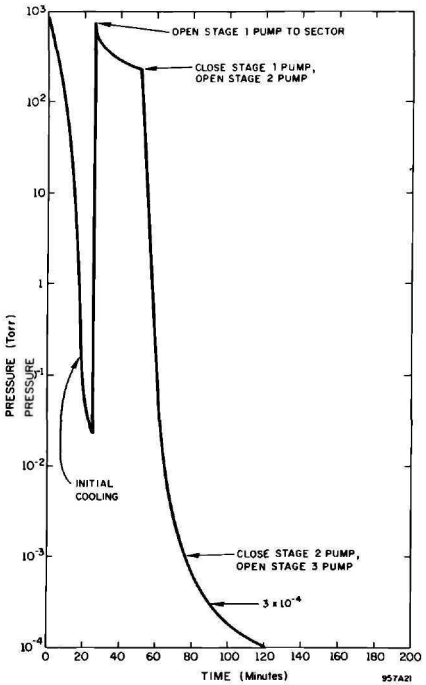

Figure 23-21 Typical sector rough-down cycle.

5A sieve material. Starting at atmospheric pressure, it takes about 5 min to reach 5×10^{-4} torr, assuming letup to dry nitrogen before the previous klystron was removed. At that pressure, the 3-in. valve and the waveguide valve are opened. The momentary rise in subsystem pressure, measured at the window of the nearest klystron, is about two decades.

Figure 23-22 Klystron vacuum arrangement.

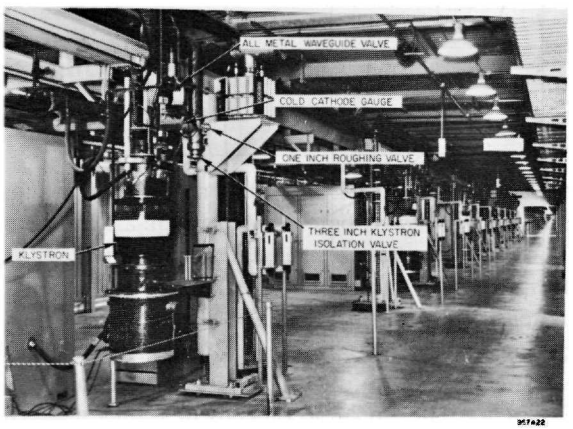

Operating experience (MEB)

The accelerator vacuum system has performed essentially as predicted. The base pressure has continued to improve with time and now is approximately 8×10^{-9} torr at the sputter-ion pumps and 3×10^{-8} at the klystron windows with no RF on. With RF and beam on, these pressures increase by a factor of about 2. As shown in Fig. 23-21, a cryosorption pump set is capable of roughing a typical sector from dry nitrogen at atmospheric pressure to 3×10^{-4} torr in approximately $1\frac{1}{2}$ hours, including the time required for cooldown of the pumps. The additional time required for the four sputter-ion pumps to bring the sector down to operating pressure is shown in Fig. 23-23.

The 500-liters/sec sputter-ion pumps have been trouble-free with one exception. The original high-voltage cable connectors supplied with the pumps were poorly insulated and required replacement with a new type. The old connectors exhibited corona, and the resulting high ozone concentration led to corrosion of the metal end of the power feedthroughs. As a result of this corrosion, a deposit was formed on the ceramic insulators. Cracks then developed in the insulators, causing serious leakage. After many months of continuous operation with the new connectors, no failures of this nature have occurred.

The large cryosorption pump sets have proven extremely useful and reliable. No degradation in their performance has been noticed since the original acceptance tests. During a sector pumpdown, the liquid nitrogen required to cool the cryopumps is supplied from a 600-liter mobile tank. The same tank

Figure 23-23 Sector pumpdown.

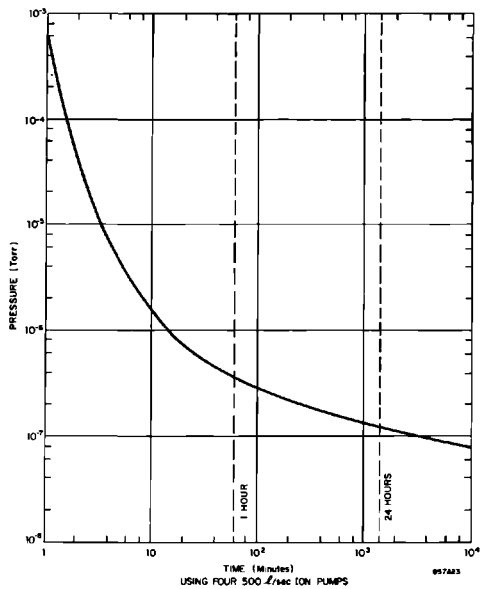

is used for letting a sector up to nitrogen. Letup from high vacuum to 1 psig requires approximately 45 min.

No major problems have been encountered with the "O" ring-sealed 1-in., 3-in., and 6-in. valves or with the indium-sealed waveguide valves. The ion pump power supplies, gauge power supplies, and gauge tubes have also performed as expected with only filter and indicator light replacement being necessary.

Leak detection has not presented any serious problems thus far. Probably the primary reason is that there have been very few problem leaks since installation. In most cases, the location is obviously where a new component or drift section has just been installed. Except for very large leaks, a helium mass spectrometer-type leak detector is used. Large leaks can usually be found by spraying with acetone and noting the response of a thermocouple gauge or by use of an ultrasonic leak detector or, in some instances, by the unaided ear. A differential amplifier connected to the recorder output of a sputter-ion pump or vacuum gauge power supply is also occasionally used for leak detection. The suspected area is sprayed with oxygen and argon, and entry of the gas through the leak results in a current change in the gauge or pump. Argon increases the current and deflects the amplifier meter to the right, whereas oxygen reduces the current and causes a left deflection. This method has been successful when the leak is very close to the gauge or pump being used as the sensing element. It does not work well at distances of over 10 or 15 ft or when large volumes are involved. It is difficult to make a general statement concerning response and cleanup times when the helium leak detector is used. A typical situation involves probing a leak in a drift section between sectors in the accelerator housing with the detector connected to a valve in the klystron gallery. In this instance, the response time is of the order of 5 sec for a subsystem pressure in or below the 10^{-5} torr range. If a very small amount of helium is introduced, cleanup time is 5–10 min. If the leak is sprayed heavily with helium, it can take as long as several hours, due primarily to the sputter-ion pump's low pumping speed for helium.

23-2 The alignment light pipe vacuum system

Design criteria (SRC, FFH)

The 24-in. o.d. aluminum support girder in the accelerator housing supports the disk-loaded waveguide and its appurtenances and serves as an evacuated light pipe for the laser alignment system.

The alignment system light pipe extends from a point 178 ft west of the start of Sector 1 to a point in the BSY 102 ft downbeam from the end of Sector 30, a total of approximately 10,280 ft. A 24-in. pumping finger, approximately 50 ft long, extends from the accelerator housing to the pumping station located in the klystron gallery at the end of Sector 30. Extending into

the BSY and connected to the 24-in. pipe is about 675 ft of 10- and 12-in. o.d., schedule-40, aluminum pipe. The total volume of this light pipe system is approximately 31,000 ft^3 including an allowance for additional volume in the area of the nine bellows per sector used to connect adjacent girders and for the three target boxes for alignment monuments at Sectors 16, 27, and 30. As outlined in Chapter 22, the vacuum requirement for this system was established at 10^{-2} torr. At this pressure, displacement of the laser beam caused by a 1°C/ft average temperature gradient from top to bottom of the aluminium light pipe will be less than 0.001 in.

A maximum of 16 hours was proposed for evacuation of the light pipe, thus permitting overnight pumpdown.

System description (SRC)

For roughing down the system, two 500-ft^3/min mechanical pumps were selected. For continuous pumping of the system, an oil diffusion-ejector pump with a speed of 2000 liters/sec was chosen. A refrigerated baffle operating at −30°C was used to minimize contamination of the alignment light pipe. A 150-ft^3/min mechanical forepump was selected to back the diffusion-ejector pump. The exhaust to outdoors from the three pumps was equipped with oil separators to minimize the oil mist which occurs when roughing from atmospheric pressure.

Calculations indicated that a pumping system using this equipment would reach design pressure of 10^{-2} torr after approximately 10 hours pumpdown time[9]. The outgassing rate for the steam-cleaned, unbaked 24-in. girders was found to be approximately 10^{-7} torr-liter/sec/cm^2.

Figure 23-24 Schematic of light pipe vacuum pumping station.

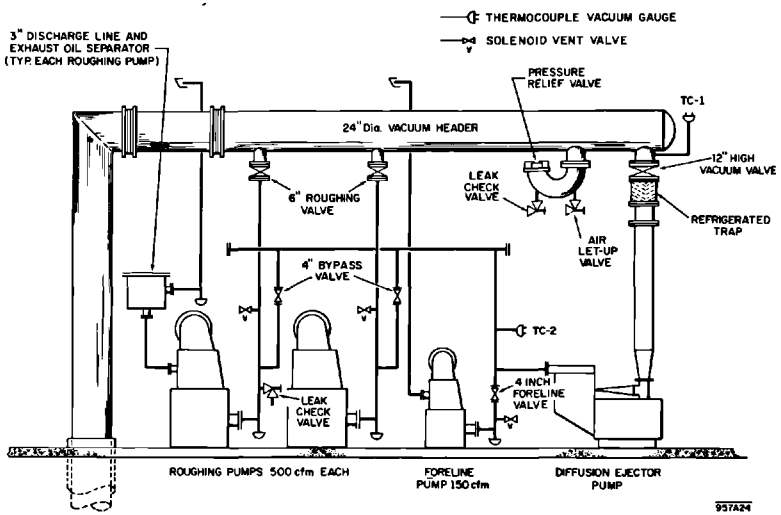

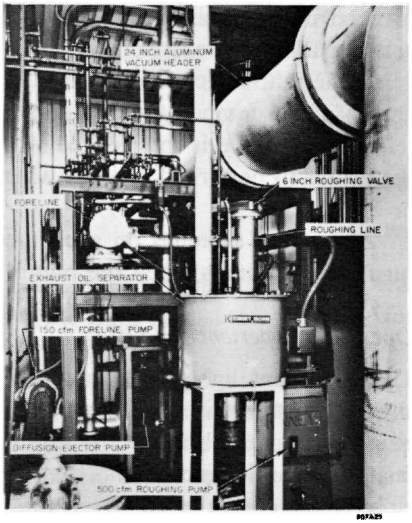

Figure 23-25 Light pipe vacuum pumping station.

All vacuum valves, except for the manual letup and leak test valve, are air operated and controlled as described below.

The arrangement of the pumping station is shown schematically in Fig. 23-24. Figure 23-25 shows the final installation. Provisions have been made for future installation of an additional diffusion-ejector pump and its backing pump, and of an additional 500-ft^3/min roughing pump if leak rates of the system are found to be higher than expected.

Valves are arranged to permit using either one of the roughing pumps to back the diffusion-ejector pump and also to allow roughing with one 500-ft^3/min mechanical pump with the other backing the diffusion-ejector pump.

The motor control center contains all the electrical controls, plus the cooling water, compressed air, vacuum readouts, and relays that are required for operation of the pumping station.

Instrumentation and control (GIS)

The pumping station equipment for the alignment pipe system is protected by pressure, temperature, and shaft speed sensing devices.

Thermocouple vacuum gauges are located so that the pressure on each side of any vacuum valve can be checked before the valve is opened. Referring to Fig. 23-24, gauge TC-1 is on the high vacuum side. Its gauge controller closes the 12-in. valve above the diffusion-ejector pump if the pressure is above a predetermined level. Gauge TC-2 is on the roughing line. Its gauge controller closes the 4-in. foreline valve if the pressure is above a

predetermined level. In turn, the diffusion-ejector pump heater is shut off and the 12-in. valve is closed.

A thermal switch on the diffusion-ejector pump heater de-energizes the heater if the temperature exceeds 150°C. Another thermal switch on the refrigerated baffle is interlocked with the diffusion pump heater and allows the heater to be turned on only when the temperature at the baffle is −20°C or below.

Zero-speed switches on each mechanical pump shaft are interlocked to turn off the pumps when the pump shaft speed falls below 80% of normal.

Operating experience (KGC)

The alignment light pipe vacuum system has been operating satisfactorily since its installation. An overnight pumpdown brings the system to the required vacuum. Although the rate of pressure rise with pumps turned off is faster than anticipated, it has been possible to maintain an operating pressure close to the design level.

23-3 The beam switchyard system

Design criteria (SRC)

The BSY contains a large number of bending magnets, quadrupoles, and various protection and monitoring devices extending over a length of approximately 1000 ft along three major branches. Associated with these devices are extensive, relatively large volume, vacuum chambers. The high level radiation environment results in severe operation and maintenance problems and imposes the necessity for remote handling of components. For these reasons, it was not economically feasible to design for a pressure as low as the accelerator (10^{-6} to 10^{-7} torr). Fortunately, because high RF fields do not exist in the BSY, vacuum requirements are not as rigorous and a design pressure of 1×10^{-4} torr was used.

The general criteria resulting from the above considerations are described in the preliminary design study.[10] No organics were to be used in those parts of the vacuum system located in the BSY housing. The average pressure was to be less than 1×10^{-4} torr. Time to reach operating pressure after letups to atmospheric pressure was to be less than 6 hours. Remote disconnect-type couplings were to be supplied at each end of every magnet, slit, collimator, and other instruments to facilitate their removal and replacement. Provisions were to be made to protect sections of the vacuum chambers containing delicate instruments from accidental ruptures and letups. The vacuum envelope was to be nonmagnetic. It was to be possible to let any section of the BSY between isolating valves up to air without disturbing the other sections.

The optimum pumping system was found to be the oil diffusion type. The use of these pumps obviated the necessity of providing "windows" to separate the BSY vacuum system from the diffusion-pumped target area

vacuum systems. However, it imposed the necessity for an effective means of protecting the "clean" very high vacuum of the accelerator from degradation due to its connection with the "dirty" high vacuum of the BSY. This led to the development of the differential pumping station described in a subsequent section.

Subsystem arrangement (GIS)

Figure 23-26 shows the layout of the BSY. Single or multiple beams enter from the left or west side and exit toward the right or east side along any one or all three of the beam paths.

In order to permit maintenance or replacement of the various instruments without letting the entire switchyard up to air, all-metal isolation valves separate the system into seven distinct volumes, evacuated by eight pumping stations. The stations are located approximately at the center of the separate volumes so as to equalize the gas load and the pressure at the beam line.

To protect delicate instruments from shock waves and flying debris if a vacuum window should break, all-metal fast valves requiring a maximum of 25 msec to close have been located as shown in Fig. 23-26.

Table 23-1 lists approximate areas and volumes pumped by the individual pumping stations, less the areas and volumes of the "fingers" connecting the stations with their respective vacuum chambers in the lower housing of the BSY.

Outgassing rates were assumed to be 10^{-9} torr-liter/sec/cm^2 for unbaked stainless steel and 10^{-8} torr-liter/sec/cm^2 for unbaked aluminum. The average effective pumping speed at the vacuum finger connection to the beam was calculated to be approximately 150 liters/sec.

Figure 23-26 Schematic of beam switchyard vacuum system.

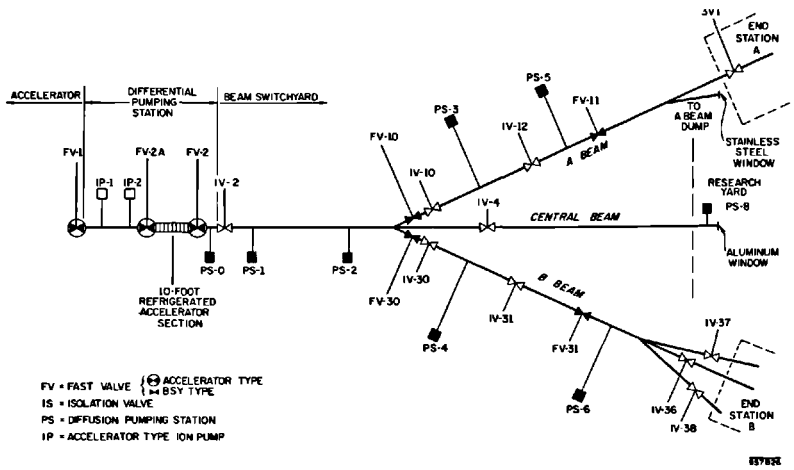

Table 23-1 Surface area and volume of chambers evacuated by beam switchyard vacuum pumping stations

Pumping station	*Area[a] in cm²*	*Volume[a] in liters*
PS-0	45,000	64
PS-1 and PS-2	3,490,000	67,460 (includes divergent chamber)
PS-3	1,420,000	12,600
PS-4	600,000	4,800
PS-5	720,000	1,150
PS-6	720,000	3,700
PS-8	720,000	1,200

[a] Areas and volumes of connecting "fingers" not included.

Taking the divergent chamber as the worst case and assuming pumpdown by PS-2 alone, the pressure at the chamber was calculated as follows:

Q = total gas load (torr-liter/second)
A = internal surface area (2.26×10^6 cm^2) of the divergent chamber
q = outgassing rate (10^{-8} torr-liters/sec/cm^2 for clean unbaked aluminum)
P_1 = pressure at the chamber connection
S_1 = effective pumping speed at the chamber (150 liters/sec)

then

$$Q = A \times q = 2.26 \times 10^6 \text{ cm}^2 \times 10^{-8} \text{ torr-liter/sec/cm}^2$$
$$= 2.26 \times 10^{-2} \text{ torr-liter/sec}$$

and

$$P_1 = \frac{Q}{S_1} = \frac{2.26 \times 10^{-2} \text{ torr-liter/sec}}{150 \text{ liters/sec}} = 1.5 \times 10^{-4} \text{ torr}$$

Diffusion pumping stations (GIS)

Vacuum in the BSY is maintained by eight diffusion pumping stations, seven located at grade about 60 ft above the beam line and one in the research yard at the end of the central beam. The seven stations at grade each consist of a water-cooled 6-in. oil diffusion pump, a 6-in. baffle refrigerated to −25°C, a 65-ft^3/min mechanical pump, and pneumatically operated valves in high vacuum, roughing, and forelines. A photograph of a typical system is shown in Fig. 23-27. The station in the research yard is essentially similar but incorporates a water-cooled baffle and a 15-ft^3/min pump. Pressure is measured by a Bourdon gauge, a thermocouple gauge, and a cold cathode gauge on the

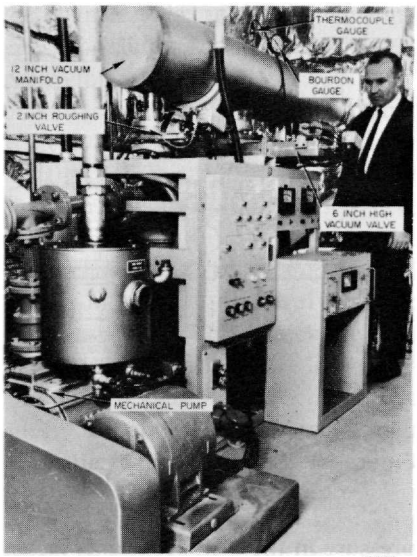

Figure 23-27 Beam switchyard vacuum pumping station.

high vacuum side and a thermocouple gauge on the foreline. Each station is interlocked in such a manner that if the mechanical pump stops, all valves will be closed and the diffusion pump will be shut off. The mechanical pump is interlocked with a cooling-water low-flow switch and a zero-speed switch. High pressure on the high vacuum side will close the 6-in. valve. An air reservoir with a check valve is provided at each station to operate the vacuum valves in the case of failure of the main air supply. Controls and switches for the pumps and valves are all locally mounted. However, the status of the pumps and valves and the indication from each cold cathode gauge is transmitted to the Data Assembly Building control room.

Differential pumping station (GIS)

The problem of connecting the "dirty" BSY system to the "clean" accelerator system and bridging the difference between 1×10^{-4} torr in the BSY and 5×10^{-7} torr in the accelerator was solved by using a differential pumping station. As shown in Fig. 23-28, this consists of a low conductance tube, a diffusion pumping station, a 10-ft accelerator section refrigerated to $-30°C$ which serves as a high impedance oil trap, and a sputter-ion pump. A second sputter-ion pump is located about 100 ft upbeam. Accelerator-type beam-line fast valves FV-2A and FV-2 are located on either end of the refrigerated accelerator section. These valves close when pressure in the BSY rises to 10^{-2} torr, when refrigeration temperature rises above $-10°C$, or when

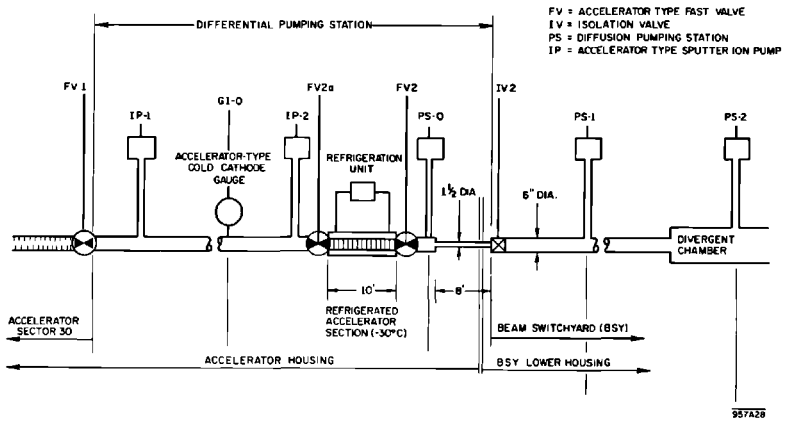

Figure 23-28 Schematic of differential pumping station.

pressure in the drift section as measured on gauge G1-0 rises to about 10^{-5} torr. Valve FV-1 at the end of Sector 30 is tripped simultaneously with FV-2A and FV-2. The refrigerated accelerator section is cooled by triethyl phosphate which is chilled by a conventional mechanical refrigeration system. Triethyl phosphate was selected for use in the BSY lower housing because it is resistant to radiation breakdown.

Tests showed that a pressure differential of five orders of magnitude is possible over the length of the station. The normal pressure differential at the present time is much smaller due to the absence of leaks in the BSY. Typical pressures are as follows:

Drift section between Sector 30 and BSY: 2×10^{-8} torr
First diffusion pumping station, PS-0: 2×10^{-7} torr
Second diffusion pumping station, PS-1: 5×10^{-7} torr

However, when the pressure at the next station downbeam (PS-2) rises due to an occasional leak in the BSY, a differential as great as three decades has been observed between the drift section and PS-1.

Calculations made from laboratory tests indicate that it will take about 20 yr to cover the last 10-ft section of the two-mile accelerator with a single layer of hydrocarbon molecules.[11]

Divergent chambers (FFH)

The divergent chamber is located at the downbeam end of a series of magnets which can be pulsed to switch a single or multiple beam received from the accelerator to one or more of the three beam paths shown in Fig. 23-26. The beams enter the 3-ft diameter chamber as the overall spread along the diverging paths approaches the capacity of the 12-in. upbeam pipe. After

they have traveled the 220-ft length of the chamber, the adjacent beams are far enough apart to accommodate the pipes, couplings, and other equipment necessary to establish a separate vacuum envelope for each.

A 12-in. quick-disconnect coupling joins the upbeam pipe with the chamber. About halfway down the chamber, the cylindrical wall is offset in the direction of the A-beam and a separate 10-in. pipe is added to carry the B-beam. At the downbeam end of the chamber two 10-in. quick-disconnect couplings are provided, one for the A-beam and one for the B-beam, together with a 6-in. coupling for the central beam. The chamber is secured and aligned by two sets of adjustable jacks. One set is floor-mounted for vertical support; the other set is wall-mounted for horizontal restraint. The fourteen jacks in each set are mounted in pairs, one jack on each side of the center line.

Aluminum was selected for the chamber walls because it was believed less likely to fail from overheating than stainless steel should the electron beam accidentally be steered into the wall. The quick-disconnect half-couplings welded to the chamber at each end were also made out of aluminum.

The chamber was manufactured from 20-ft wide, $\frac{1}{2}$-in. thick, 5083 aluminum plates rolled into 20-ft long cylinders. Pairs of cylinders were welded into 40-ft sections which were checked for straightness and leaks before shipping to SLAC. The 40-ft sections were aligned in place at SLAC and preheated at the weld area prior to welding. The tungsten inert-gas process was used in making the five leak-tight circumferential field welds. The root pass was made from the inside. After x-ray examination and repair, subsequent passes were made from the outside. The completed welds were again x-rayed and necessary repairs were made.

Provisions were made to drain the chamber if a vacuum–water interface window at a beam dump should fail. The drain pipes were welded shut but can be cut open in the event of such an accident.

A second smaller divergent chamber was also installed in the B-leg of the BSY. It was fabricated of stainless steel in a manner similar to the vacuum piping described below.

Piping and bellows assemblies (GIS)

The vacuum piping which serves as the beam transport envelope in the BSY generally consists of 6-in., 10-in., and 12-in., schedule-five Type-304L stainless steel pipe. The one exception is the aluminum divergent chamber described in the previous section. Direct current magnet, quadrupole, and instrument chambers were made from Types-304L and -316L stainless steels, chosen for low magnetic permeability. Pulse magnet chambers were ceramic to prevent induction heating.

The three different sizes of pipes for the beam vacuum chambers were chosen to accommodate the various beam profiles. Type-304L stainless steel was chosen for the vacuum piping because it is essentially nonmagnetic, it could be readily welded or brazed to all initially planned BSY vacuum

chambers except the aluminum divergent chamber, it is resistant to all corrosives in the contemplated environment, and its strength is adequate.

Sections of pipes were cut and chemically cleaned at the vendor's facility. Quick-disconnect half-couplings were welded to the pipe sections used to connect the magnets, slits, instrument stands, valves, and other removable beam-line equipment. The subassemblies were then leak-checked. After leak-checking, the ends were covered with plastic protectors and the complete lengths of pipe were wrapped in polyethylene sheet for shipment to SLAC.

Needless to say, the above-mentioned quick-disconnect couplings were quite expensive and for this reason the minimum possible number were used. Pipe sections not fitted with quick-disconnect half-couplings were assembled in the BSY lower housing and welded together. The tungsten inert-gas welding process was used to join stainless steel piping throughout the BSY vacuum system. Filler rod was used only on pipes with wall thicknesses over $\frac{1}{8}$ in.

Water cooling was provided for the chambers of the four bending magnets and the length of vacuum pipe leading into the A-Beam dump. This is an area where appreciable amounts of beam power can be absorbed on the chamber surfaces.

Due to the various sizes of pipes, certain sections had unequal axial loads. These loads were taken up by restraints extended from instrument or magnet stands.

To facilitate the replacement of beam-line equipment, the connection to the vacuum pipe at each end was through a stainless steel bellows fitted with mating quick-disconnect half-couplings. To remove the equipment, the bellows assemblies are first uncoupled and taken out. The equipment can then be unbolted and lifted off its mounting rails.

Connections between the beam chambers and piping in the BSY lower housing and the pumping stations on the top of the fill, some 60 ft above, were made of 20-in. schedule-10 Type-304L stainless steel pipes. These connections are called "vacuum fingers." All-metal $1\frac{1}{2}$ in. angle valves are provided in the upper housing for leak checking each finger.

Ten-inch double stainless steel bellows were used to connect the vacuum fingers in the lower housing to the beam line. These bellows were designed to accommodate a 3-in. radial displacement of the beam line. Because the two sputter-ion pump fingers at IP-1 and IP-2 and the first diffusion pump station finger at PS-0 are offset within the lower housing, the pair of bellows at the foot of each of these three fingers were gimballed to preclude damage to the drift piping due to relative movement of the vertical fingers.

Quick-disconnect couplings (ALE)

The ability to remove and replace vacuum equipment without undue exposure of personnel to a high radiation environment is an essential feature of accelerator design if beam off-time is to be minimized. To meet this

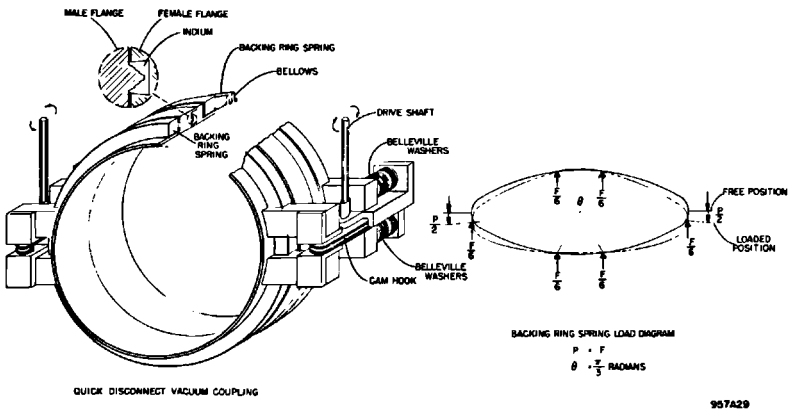

Figure 23-29 Quick-disconnect coupling.

requirement, vacuum equipment such as magnet vacuum chambers, beam analysis instruments, and drift pipes located in the BSY were equipped with quick-disconnect couplings.[6]

The couplings were built in 6-, 10-, and 12-in. pipe sizes. Figure 23-29 illustrates a typical coupling. The design is essentially the same for all three pipe sizes with the exception that the material cross section is changed to keep stresses constant. The couplings consist of two flanges, one containing an annular groove filled with indium. The other mating flange has a circular knife edge of a stepped, triangular cross section protruding from a flat face. The two flanges are pulled together, forcing the knife edge into the indium to make the seal.

The flanges are forced together by two rings which bear against the backs of the flanges at six places equally spaced about the rings. These rings are pulled together by two cam hooks which are operated simultaneously by rotating shafts extending vertically from the cam hooks. As the rings deflect, they distribute the load to the flanges at the six points of contact as shown in Fig. 23-29. The cam hooks are further spring-loaded by Belleville washers to compensate for the cold flow of the indium and to maintain a nominal loading of 100 lb/in. of seal.

To compensate for the lateral and angular misalignment of adjacent pieces of apparatus, the couplings are used in pairs, separated by a bellows as shown in Fig. 23-30. This arrangement accomplishes several things such as providing an allowance for a 3/16-in. lateral misalignment, 3° angular misalignment and a $\frac{1}{4}$-in. variation in the axial location of apparatus.

All pieces of equipment have a male coupling half on each end of their vacuum chambers. The bellows are welded between two female coupling halves. This allows for maximum flexibility in the placement of equipment and also permits remote inspection of the female flange halves of all joints that are uncoupled.

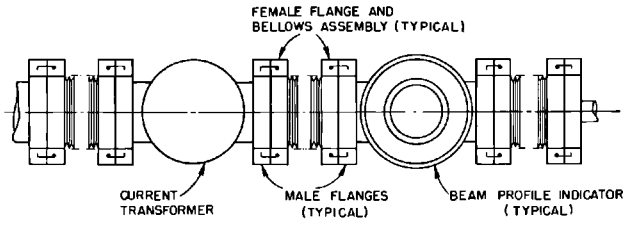

Figure 23-30 Typical coupling installation. 957A30

Beam-line isolation valves (GIS, SRC)

Pneumatic, cylinder-operated, all-metal valves are required in the BSY vacuum system to provide a means of automatically isolating an individual subsystem in the event of a sudden pressure rise and of manually isolating an individual subsystem for maintenance, repairs, equipment changes, and leak-checking.

The following criteria were established for the isolation valves. The valves were to be of all-metal, in-line construction. The minimum opening was to be 4 in. in diameter except for the valve which was initially installed immediately upstream of the A-beam dump and which required a 6-in. opening. Leakage across the seat against atmospheric pressure was to be less than 1×10^{-6} atm-cm^3/sec. The valve was to be remotely operable. A minimum service life of 500 cycles was required.

The valves were purchased to SLAC specifications and consist of a stainless steel welded body in which a carriage moves on roller bearings, carrying a seal plate. The seal consists of a copper sealing disk bearing against a stainless steel seat. Actuation is by means of an air cylinder. Two external microswitches are mounted on the air cylinder for remote indication of the gate position. The seals in the air cylinder are of graphite-filled asbestos. A photograph of a 4-in. valve is shown in Fig. 23-31.

The vacuum seals on the top plate and on the valve ports are of the Batzer[12] type, utilizing aluminum foil for the gaskets. Nine 4-in. valves are now installed in the BSY.

Beam-line fast-acting valves (GIS, SRC)

Fast valves are required downbeam of the differential pumping station to interrupt shock waves and flying debris resulting from sudden ruptures of beam-line windows. The criteria for the fast valves were as follows. They were to be of all-metal construction. The minimum opening was to be 4-in. in diameter. Closure time was to be 20–30 msec, but the valve need not be vacuum-tight. The valves were to be remotely operable. A minimum service life of 500 cycles was required.

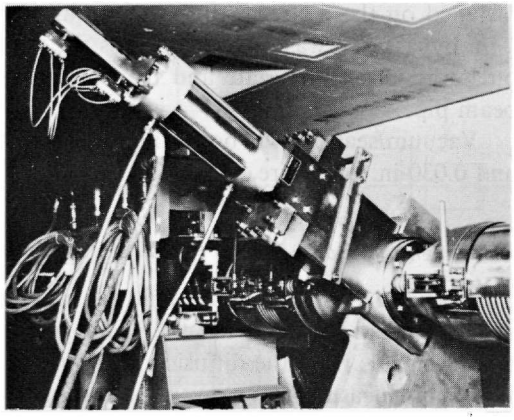

Figure 23-31 Beam switchyard isolation valve.

A photograph of the valve, which was procured commercially, is shown in Fig. 23-32. The valve body is a stainless-steel casting in which a machined aluminum plate, guided by two side rails, slides across the port. The aluminum plate is held in the open position, against the force of a compression spring, by a specially designed solenoid coil and an armature plate. Approximately 400 mA at less than 0.5 V dc is required to hold the gate open. When the current through the solenoid is suddenly interrupted, the compression spring forces the gate to close at a high velocity. Tests indicated a closure time of 22 to 28 msec. The energy of the moving masses is absorbed by Belleville washers. An air cylinder retracts the gate and recocks the spring. The "standard" valve was modified. An additional microswitch was installed in the body to indicate "gate closed." An actuating arm and microswitch were

Figure 23-32 Beam switchyard fast valve.

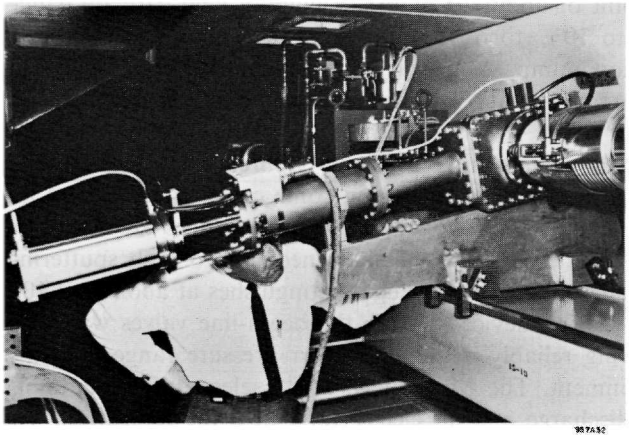

installed on the air recocking shaft to allow automatic recycling. Finally, a $\frac{1}{2}$-in. bypass line was provided across the valve gate to equalize the pressure on both sides of the gate and to eliminate any "trapped" volumes in the beam pipe.

Vacuum seals on the body and flanges of the valve are made from 0.020- and 0.030-in. gold wire.

Instrumentation and control (GIS, WBP)

The vacuum instrumentation and controls in the BSY interlock the valves and the beam and provide the Data Assembly Building with digital and analog signals from the diffusion pumping stations. Pressure at the pumping stations is measured by conventional gauges as described below. Due to the difficulty of maintenance in the high radiation environment, vacuum-sensing devices along the beam line are limited to the switches required to trip the fast and isolation valves.

Accidental letup to atmospheric pressure because of beam-line window rupture or puncture of the vacuum envelopes due to a missteered beam could generate shock waves within the vacuum piping. Under certain conditions, velocities of Mach 6 could be reached in the pipe and cause damage to delicate instruments and foils.[13] As described above, fast valves were, therefore, located at strategic places to protect these instruments.

All beam-line valves are interlocked with the beam permissive system so that the beam cannot be turned on until the valves are all fully open. If a valve gate starts moving toward its closed position, the beam is interrupted.

At the diffusion pumping stations, three sensors measure pressures ranging from 760 torr at the beginning of the roughing cycle to 10^{-7} torr during normal operation. A Bourdon gauge measures from 760 to 1 torr. A thermocouple gauge then measures from 1 to the 10^{-3} torr range. This thermocouple gauge is interlocked with the 6-in. valve on the high vacuum side of the diffusion pump so that the valve closes when the pressure exceeds the set point of about 10^{-2} torr. Finally, a cold cathode gauge measures from 10^{-4} to 10^{-7} torr. This gauge is located on the high vacuum side of the diffusion pump. A special control unit transmits an analog signal of this pressure to a meter with logarithmic readout in the Data Assembly Building control room.

The pressures in the BSY can be three or four orders of magnitude higher than in the accelerator and, in some cases, could extend into the 10^{-2} torr range where conventional hot cathode gauges are not suitable and the life of cold cathode gauges is shortened due to high sputtering rates. The discharge in cold cathode gauges extinguishes at about 2×10^{-2} torr.

A sensing device to close the beam-line valves was required, capable of operating reliably in the 10^{-2} torr pressure range and in a high radiation environment. The McClure switch[14] selected for this application utilizes a cold discharge and an electrostatic field for ionization. The device, shown

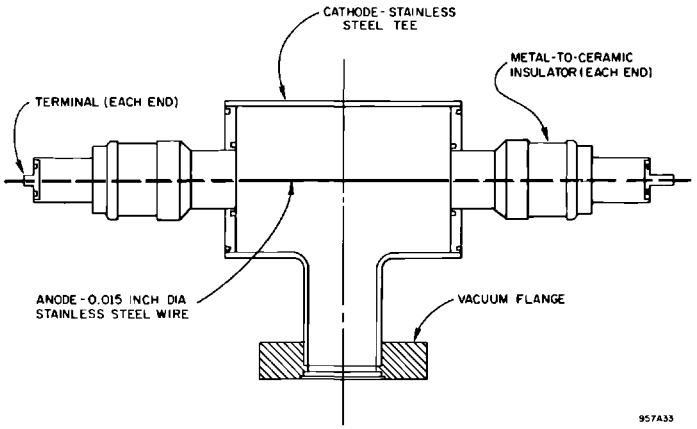

Figure 23-33 McClure switch.

in Fig. 23-33, is set to trip at 1 to 2 × 10^{-2} torr. It operates as a true "switch" with no readout capability.

In order to provide maximum protection for the BSY instruments, the McClure switches were installed at Cerenkov cells and other places particularly vulnerable to window rupture. The fast valves were located far enough away so that there would be time for them to close ahead of the shock waves. In general, each McClure switch closes whatever beam-line valves may be required to contain the pressure rise within a single subsystem. A diagram of the valve interlock chains is shown in Fig. 23-34.

Several interlocks are incorporated in the diffusion pumping stations. The foreline and high vacuum valves close if the pressure in the high vacuum manifold and in the foreline exceeds the set point of about 10^{-1} torr in the

Figure 23-34 McClure switch—valve interlocks.

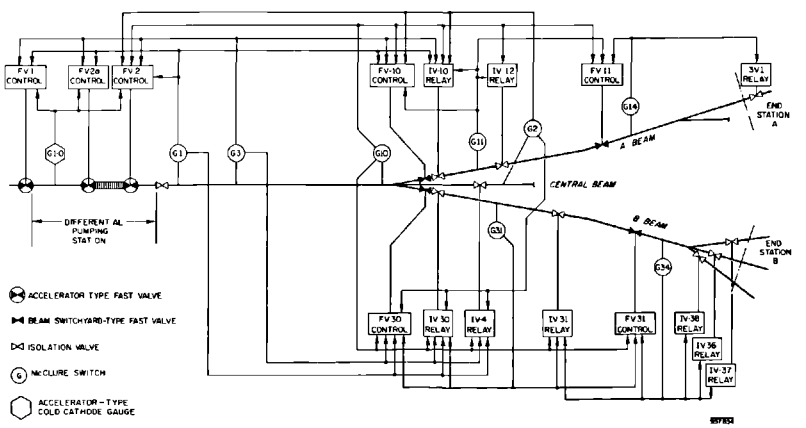

foreline, and 10^{-2} torr in the high vacuum manifold. Temperature and water interlocks also protect the pump. All operations such as starting the pumps and opening the valves are done manually at the pumping stations. Remote indications are provided at the Data Assembly Building control room to indicate whether the mechanical pump is on or off, whether the diffusion pump is on or off, whether the high vacuum valve is closed, open, or moving, and whether the roughing valve is closed, open, or moving. A remote indication is also provided of the pressure at the cold cathode gauge on the high vacuum side of the diffusion pump.

All controls for the beam-line valves and the McClure switches are located in the Data Assembly Building control room. The isolation valves close on a trip signal from the McClure switches. They can also be closed by pressing a pushbutton on the panel. The fast valves close only from a trip signal.

An analog panel with meter readouts indicates pressure at each pumping station and also at the drift section between Sector 30 and the BSY. If the vacuum exceeds the set point, a flashing yellow light warns the operator of a pressure rise. This warning indication is also connected to the scanning system which prints out the fault data.

A temperature readout from the differential pumping station is also located at the Data Assembly Building control room. A relay on this meter closes the two fast valves on either side of the refrigerated accelerator section if the temperature exceeds the preset point of about $-10°C$.

The McClure switch controller contains a 0–2000 V variable high-voltage power supply and the electronics necessary to detect the switch closing. When a switch closure is detected, the controller generates a 25-V amplitude, 10-msec minimum width pulse used to close the fast valves. Each controller has parallel outputs for closing up to six fast valves. The controller also energizes a relay for 3 sec which is used to close the isolation valves. Each controller can close seven isolation valves at once. Once the switch has fired, the high voltage is removed from the switch until the controller is manually reset.

The controller incorporates four electronic components. A 2000-V power supply module with a variac on the input was obtained commercially. Electronic circuits detect the vacuum switch current and trigger a silicon-controlled rectifier used to generate the fast valve pulse and start the 3-sec relay closure. A reed-type relay is used with the interlock system to turn off the beam within 50 μsec of the switch firing. A meter on the front panel indicates the voltage on the switch, which determines the vacuum level at which the switch fires. The meter is of the meter relay type with the lower set point acting as an interlock, affording protection against operation with no high voltage on the switch.

The controllers for the fast valves are completely transistorized units powered from ± 24-V battery power supplies. A schematic diagram of the controller appears in Fig. 23-35.

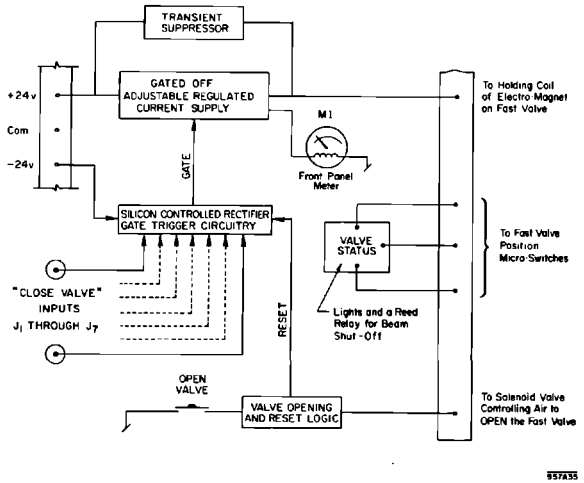

Figure 23-35 Beam switchyard fast valve controller.

The 400-mA current required to hold the valve open is supplied from a variable two-stage transistor constant current power supply. To close the valve, the holding current is reduced to zero in as small as possible time interval. This produces large transients across the solenoid coil and hence across the pass transistors. Two 75-V Zener diodes shunt the solenoid for voltage spike suppression. A 20-V Zener diode is required to permit a voltage drop to develop across the solenoid in the forward direction.

The control has a total of seven inputs and requires a 5-V, 2-μsec pulse. The holding current is reduced to zero by firing the silicon-controlled rectifier and back-biasing the first stage of the constant current power supply.

The front panel meter indicates the solenoid holding current. There are indicating lights showing valve position, open or closed, and $\pm$24-V power on. Also located on the front panel is a "valve open" pushbutton switch which resets the electronics and energizes the necessary air solenoid for opening the valve. Because inadvertent closure of valves is to be avoided insofar as possible, there are no switches on the front panel for closing the valves or turning off the power supplies.

Operating experience (MEB, GIS)

The operating experience acquired since initial startup of the subsystems indicates that all design criteria have been met or exceeded. The diffusion pump stations, using silicon oil and elastomer seals, produce base pressures of approximately 1.5×10^{-7} torr with the 6-in. gate valves closed. When operating with the valves open and with no detectable leaks, the pressures measured at the pump stations range from 2×10^{-7} to 1×10^{-6} torr. The variation is due to differences in the areas, volumes, and conductances.

The pumpdown times for the seven subsystems of the BSY also vary due to the differences in volume. Maintenance or repair work on a beamline component normally requires shutdown of only one, or in certain cases, two pump stations and the isolation of the corresponding subsystem in the lower housing. The time required to pump any one of these subsystems from atmospheric pressure down to an acceptable operating vacuum of, say, 5×10^{-4} torr is approximately 90 min. Pump stations PS-1 and PS-2, which serve the collimator, pulse magnet chambers, and the large divergent chamber, cannot be isolated from each other in the housing. Using these two pump stations only, the pumpdown time for the combined subsystem is approximately $3\frac{1}{2}$ hours, as shown in Fig. 23-36.

The fast valves, isolation valves and vacuum switches installed in the beam line have generally been trouble free. During the first 7 months of operation, there was one fast valve failure due to seizing of internal parts and one isolation valve malfunction caused by a part displaced during shipment or installation. Although no record of closures has been kept, it is estimated that a typical valve might be cycled approximately 250 times per year.

The indium-sealed quick-disconnect couplings used throughout the BSY have proven to be extremely reliable. There have been instances when these

Figure 23-36
Beam switchyard pumpdown.

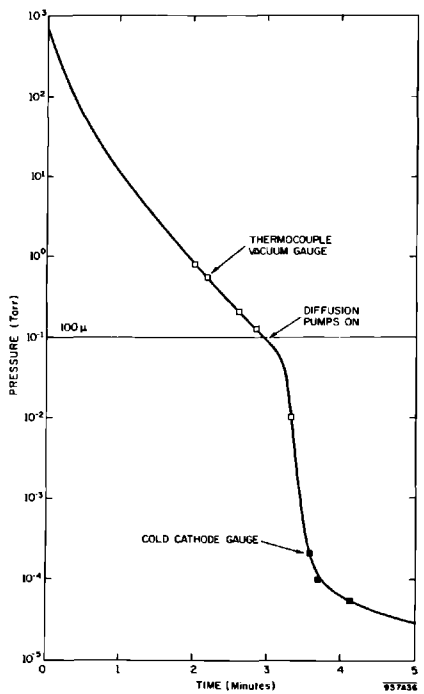

couplings leaked, but in almost all cases the leaks were caused by improper makeup, interference of the male or female pilots, or foreign material embedded in the indium. In some instances, joints have been made up leak-tight and remade as many as 3 or 4 times using the same indium. However, this is not a recommended procedure, particularly for 10- and 12-in. couplings, which leak approximately 50% of the time when the old indium is retained. The best practice is to replace the indium each time a joint is uncoupled. The experience to date has been that over 90% of the quick-disconnect joints made in the BSY are made up tight the first try.

Leak detection in the BSY has proven to be much easier than anticipated. One of the major reasons is that the quick-disconnect couplings either seal completely or leak quite badly. Most leak detection is done with the helium mass spectrometer leak detector connected to a $1\frac{1}{2}$-inch all-metal valve on each vertical finger in the BSY upper housing. A valve has been provided at each pump station enabling the leak detector to be connected to the diffusion pump foreline. The connection in the housing proved to be the most useful simply because the person operating the helium probe can hear the audio response of the leak detector. It is also easier to move the leak detector by means of the overhead crane in the housing than to transport it from one pump station enclosure to another. The time from introduction of helium until a response is noted on the leak indication meter is typically about 5 sec. The time required for the indicator to return to its original or background level is from 1 to 5 min. These times are representative when leak-checking joints in a 6-in. pipe approximately 100 ft from the leak detector.

Acknowledgments

In addition to the authors noted under the chapter heading, many other people made significant contributions to the vacuum design. N. Carter worked on initial studies of vacuum system requirements. K. Trigger consulted on basic vacuum calculations and pump selection. E. L. Garwin was principal advisor on design details and equipment selection. R. B. Neal, H. DeStaebler, A. L. Eldredge, J. V. Lebacqz, and J. Jasberg were invaluable in furnishing design criteria for the accelerator vacuum system. W. Herrmannsfeldt developed design criteria for the alignment light pipe vacuum system. L. Schwarcz, P. Thingstad, and H. Weidner helped prepare beam switchyard vacuum system design criteria. U. K. Cummings conducted the tests for determining outgassing rates of RF processed OFHC copper as well as monitoring fabrication of components and assemblies. E. Hoyt conducted the tests on the "tree house" test facility and studies of outgassing rates for stainless steel. C. Hale was very helpful in preparing specifications for pumps and vacuum system fabrication and installation so that schedules could be maintained. G. Egg was extremely helpful in monitoring fabrication of klystron gallery 3- and 6-in. valves as well as the field installation of the accelerator vacuum system. A. Burch developed the basic design of the gallery

3- and 6-in. valves and was very helpful in working out details of adaptors and restraints for piping and bellows, as well as design of the beam switchyard divergent chamber. D. Cheng designed the refrigeration system for the beam switchyard differential pumping station. M. Heinz developed the basic design for the accelerator beam-line fast acting valves. R. Allyn developed the basic design for the beam switchyard quick-disconnect vacuum couplings. R. Callin is responsible for operation and maintenance of the accelerator vacuum system and K. Welch conducts engineering investigations of its operational problems.

References

1 H. C. DeStaebler, Jr., "Scattering of Beam Electrons by the Residual Gas in the Accelerator," Rept. No. M-281, Stanford Linear Accelerator Center, Stanford University, Stanford, California (October 1961).

2 U. K. Cummings, SLAC internal memorandum, Stanford Linear Accelerator Center, Stanford University, Stanford, California (September 1963).

3 E. Hoyt, "Effect of Surface Treatment and Baking on the Outgassing Characteristics of 304 Stainless Steel Pipe," Rept. No. SLAC-TN-64-5, Stanford Linear Accelerator Center, Stanford University, Stanford, California (January 1964).

4 R. S. Barton and R. P. Govier, "A Mass Spectrometric Study of the Outgassing of Some Elastomers and Plastics," Rept. No. CLM-R-16, UKAEA Research Group, Culham Laboratory, Culham, Abingdon, Berkshire, England (March 1962).

5 A. Guthrie and R. K. Wakerling, Vacuum Equipment and Techniques, 1st Ed., McGraw-Hill, New York, 1949.

6 Arnold L. Eldredge, Albert J. Keicher, Marvin Heinz, and Richard J. Allyn, *IEEE Trans. Nucl. Sci.* **NS-12**, 3, 694 (1965).

7 R. B. Neal, "Absorption Pumping of the Two-Mile Accelerator," Rept. No. SLAC-TN-62-77, Stanford Linear Accelerator Center, Stanford University, Stanford, California (1962).

8 S. R. Conviser and G. Skoda, "Results of Evaluation of Prototype Cryosorption Pumping System," Rept. No. SLAC-TN-65-28, Stanford Linear Accelerator Center, Stanford University, Stanford, California (April 1965).

9 F. Halbo, R. Conviser, and F. Hall, "Vacuum Pumping Station for Alignment System," Rept. No. TR-840-710-R0, Stanford Linear Accelerator Center, Stanford University, Stanford, California (February 1965).

10 L. Schwarcz, E. Hoyt, and P. Thingstad, "BSY Vacuum System Study," Rept. No. SLAC-TN-64-22, Stanford Linear Accelerator Center, Stanford University, Stanford, California (March 1964).

11 E. W. Hoyt and E. L. Garwin, "BSY Beam Tube Oil Trapping Tests," Rept. No. SLAC-TN-64-70, Stanford Linear Accelerator Center, Stanford University, Stanford, California (August 1964).

12 T. H. Batzer, "Flange Design Using Aluminum Foil for UHV Application," Rept. No. UCID 4548 (Rev. 4), University of California, Lawrence Radiation Laboratory, Livermore, California (1966).

13 G. Skoda, SLAC internal memorandum, "Tests on 100-foot Shock Tube," Stanford Linear Accelerator Center, Stanford University, Stanford, California, (August 1965).

14 G. W. McClure, *Appl. Phys. Letters* **2**, 12, 233 (1963).

24

COOLING-WATER SYSTEMS

K. G. Carney, Jr., S. R. Conviser, C. J. Hale, F. F. Hall, Editor, D. B. Robbins, G. I. Ratliff, and G. I. Skoda

The cooling-water systems which serve the accelerator and its RF drive system, the Beam Switchyard (BSY), the research area, and supporting laboratories and shops are described in this chapter. The special problems of radioactive water loops are discussed in detail.

There are three major groups of interrelated cooling-water systems at SLAC. The "general purpose systems" consist of a closed-loop, low-conductivity cooling-water system for laboratories and shops, a distilled water plant, and a cooling tower having a 10 MW rating at 68°F (wet bulb) ambient. The "accelerator systems" consist of a large number of closed-loop, low-conductivity cooling-water systems for accelerator components, a low conductivity water makeup system, and two cooling towers each having an 11 MW rating at 68°F (wet bulb) ambient. The "beam switchyard and end station systems" consist of several closed-loop, low-conductivity cooling-water systems for BSY magnets and power supplies, a large closed-loop, low-conductivity cooling-water system for research equipment, several closed-loop, low-conductivity radioactive cooling-water systems for beam energy-absorbing devices, a low-conductivity water makeup system, and a cooling tower having a 23 MW rating at 65°F (wet bulb) ambient.

All closed-loop, primary cooling-water systems use water which has been filtered and demineralized. This is done to minimize loss of copper from equipment operating at high voltages, to inhibit deposit of scale on important heat transfer surfaces, to prevent plugging small flow passages which may be relatively inaccessible for cleaning, and to reduce corrosion of equipment and piping. Experience to date indicates low-conductivity water at over 1 megohm specific resistance is easy to maintain using about 1% bypass flow through demineralizing cartridges. In a few systems the water has also been deoxygenated to reduce still further deposition of

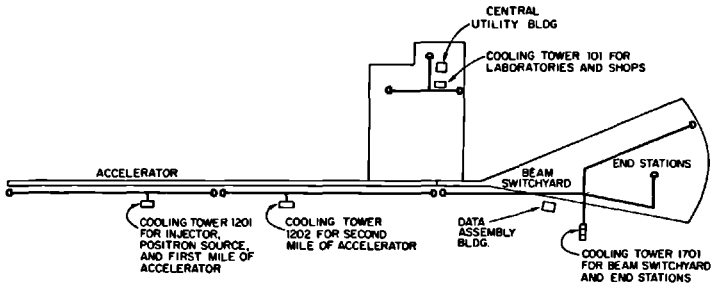

Figure 24-1 Location of cooling tower water systems.

conducting oxides on the inner walls of ceramic connectors to critical magnet coils.

For various reasons no single combination of materials has been used or could conceivably have been used economically throughout SLAC. The following combinations are now in service, and no evidence of serious corrosion has been found up to the present date (July 1967):

1. Low-zinc bronze, stainless steel, and copper
2. All stainless steel
3. Stainless steel and copper
4. Stainless steel and aluminum
5. Low-zinc bronze, stainless steel, aluminum, and copper.

The general purpose systems have been in operation since 1963. The accelerator systems were put into service during 1964 and 1965. The BSY and end station systems were started up in 1966. All systems were designed for continuous service and pumps are shut down only when absolutely necessary. All cooling towers are of the induced draft counterflow type. Cooling tower 101 serves the laboratories and shops. Cooling tower 1201 serves the injector, the positron source, and the first mile of the accelerator. Cooling tower 1202 serves the second mile of the accelerator. Cooling tower 1701 serves the BSY and end stations. The general location of each tower and the system served is shown in Fig. 24-1.

24-1 Laboratory and shop, general purpose systems (GIR)

The laboratory and shop systems comprise a general purpose, closed-loop, low-conductivity cooling-water system, a distilled water plant, and cooling tower 101. The tower, heat exchangers, tanks, pumps, and other equipment are located outdoors, south of the Central Utility Building, as shown in Fig. 24-2.

General purpose system

The general purpose cooling-water system transfers heat from equipment in the Test Laboratory, Central Laboratory, Fabrication Building, and Heavy

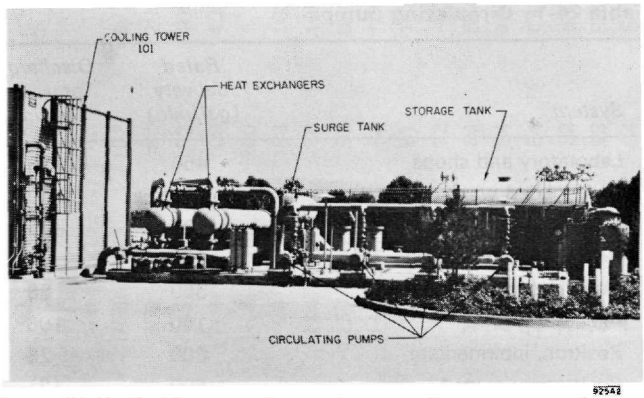

Figure 24-2 Outdoor equipment, general purpose cooling-water system.

Assembly Building to the cooling tower water system. The four circulating pumps are in parallel, with one normally on standby. A flow diagram of the system is shown in Fig. 24-3.

The circulating pumps have a rated delivery of 450 gal/min, a discharge pressure of 110 psig, and a 50-hp drive motor as shown in Table 24-1. The pumps are of the single radial stage centrifugal type. The vertical-split casings and open impellers are low-zinc bronze. The single mechanical shaft seals have carbon rotating faces, ceramic stationary faces, and Teflon secondary seals. Each pump is driven through a flexible coupling.

Figure 24-3 Flow diagram of general purpose cooling-water system.

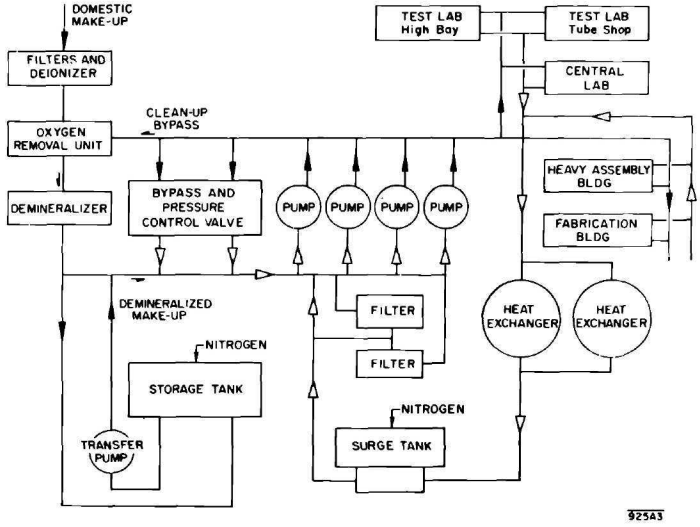

Table 24-1 Circulating pumps

System	*Rated delivery (gal/min)*	*Discharge pressure (psig)*	*Drive motor (hp)*
Laboratory and shops	450	110	50
Disk-loaded waveguide	480	79	30
Injector	100	71	10
Rectangular waveguide–drive line	160	66	10
Main klystron	360	88	25
Injector klystron	160	106	25
Positron, intermediate	600	26	15
Positron, primary 1	500	121	60
Positron, sub-loop	73	246	15
Positron, primary 2	70	87	10
Positron, primary 3	30	87	5
Magnet coil	650	146	75
Magnet power supply	225	117	25
Pulsed magnet power supply	85	79	7.5
Collimators	1020[a]	49	40
A-beam slit	520	49	25
B-beam slit	520	49	25
A-beam dump	520	64	30
Beam dump east	520	64	30
Target area	1500	269	350

[a] Flow is equally divided between a section for horizontal collimation and one for vertical collimation.

The two heat exchangers, each with a surface area of 3510 ft^2, have a rated capacity of 3450 kW. Low-conductivity water enters the tube side of a heat exchanger at 120°F, makes four passes, and leaves at 85°F at a rate of 660 gal/min. The cooling tower water enters the shell side at 78°F at a rate of 1540 gal/min, makes one pass, and leaves at 93°F. (See Table 24-2.) The two exchangers are of the floating head shell and tube type. The 90-10 copper–nickel tubes are $\frac{3}{4}$ in. o.d. The tube sheets, channels, and floating head cover are aluminum bronze. The shell and shell baffles are steel.

Copper is used for piping up to and including 2-in. nominal diameter. Fittings are copper or low-zinc bronze. Aluminum is used for pipe over 2 in. in diameter. Generally, building supply and return headers are aluminum, whereas small branch lines are copper, connected to the headers by dielectric nipples. Makeup water from the domestic supply passes through anthracite and activated carbon filters and cation and anion deionizers. The capacity of the deionizers is 10 gal/min. The 9400-gal storage tank provides a reserve supply of deionized water which can be fed into the system through the

Table 24-2 Heat exchangers

System	Rated capacity (kW)	Low-conductivity water[a]				Cooling tower water[a]				Surface area (ft^2)
		Output			Input	Input			Output	
		Passes	(gal/min)	(°F)	(°F)	Passes	(gal/min)	(°F)	(°F)	
Laboratory and shops	3450	4	660	85	120	1	1540	78	93	3510
Disk-loaded waveguide	173	1	480	110	113	2	92	75	88	75
Injector	147	1	100	102	112	2	24	75	85	75
Rectangular waveguide–drive line	27	1	96	112	114	2	24	75	83	10
Main klystron	3000	1	384	105	158	1	756	75	102	872
Injector klystron	540	1	160	95	119	2	300	75	87	280
Positron, intermediate	1870	2	719	91	109	2	745	75	92	1400
Positron, primary 1	1870	2	500	104	129	2[b]	719	91	109	1400
Positron, sub-loop	38	1	4	152	113	1[b]	4	265	200	2
Positron, primary 2	106	1	360	91	93	2	96	75	83	108
Positron, primary 3	106	1	360	91	93	2	144	75	80	108
Magnet coil	2850	1	570	104	138	1	1150	75	92	1050
Magnet power supply	275	1	174	100	115	1	144	75	88	170
Pulsed magnet power supply	74	1	85	86	92	2	85	75	81	103
B Target	100	1	50	103	120	2	40	75	92	82
Collimators	1000	1	1000	104	111	1	750	75	84	514
A-beam slit	1000	1	500	104	118	1	750	75	84	432
B-beam slit	1000	1	500	104	118	1	750	75	84	432
A-beam dump	2000	1	500	104	131	2	750	75	93	890
Beam dump east	2000	1	500	104	131	2	750	75	93	890
Target area	3190	1	750	95	124	1	1150	75	94	1512

[a] In all heat exchangers, the low-conductivity water passes through the shell side, and the cooling tower water passes through the tube side except for the laboratory and shops system which is just the reverse and except for the target area system where the low-conductivity water passes through tubes mounted in the cooling tower itself.
[b] The tube side in these systems carries low-conductivity water rather than cooling tower water.

transfer pump. The tank is constructed of steel and is lined with Amercoat 23,* a five-coat air-drying vinyl resin system which remains flexible and can be easily repaired. The coating was recently inspected and found to be severely blistered. The tank is equipped with a liquid-level sight glass. Gaskets are Teflon and couplings are stainless steel. The tank is pressurized to 3 psig with nitrogen to prevent oxygen from entering the system.

No temperature control is provided. The water temperature varies with the ambient and load conditions.

The volume above the water level in the surge tank is filled with nitrogen at 10 psig. The surge tank serves three purposes: (1) it accommodates the thermal expansion of the water, (2) it acts as a reservoir to replenish system losses, and (3) it provides a positive pressure to keep air out of the system. The tank has a total capacity of 1020 gal and a design working pressure of 50 psig. The same materials are used in the construction and lining of the surge tank as were used in the storage tank.

System protection is provided by a normally closed 4-in. manual, bypass valve and a parallel automatic 2-in. pressure control valve which minimize pump discharge pressure fluctuations.

To remove oxygen and other impurities, a flow of 10 gal/min is continuously bypassed through an oxygen removal unit and a mixed bed demineralizer. A recording conductivity meter checks the performance of the demineralizer. Two 5-μ filters with a capacity of 540 gal/min each are provided in the return header.

Distilled water plant

Distilled water for use in the Fabrication Building cleaning and plating area is produced in a vacuum-type evaporator with a capacity of 10 gal/min. It is powered by a 75-hp electric motor. Water entering the evaporator is softened by an automatically regenerating water treatment unit consisting of a filter, softener, and brine and salt tanks. A 12,000 gal storage tank holds sufficient distilled water for two-shift operation of the cleaning and plating area. The plant also furnishes the klystron gallery and target area with low-conductivity makeup water produced by passing distilled water through a mixed bed demineralizer. A flow diagram of the plant is shown in Fig. 24-4.

The filter is of the graded sand bed type. Its capacity is 11 gal/min at a flow rate of 3 gal/min/ft^2 of filter bed area. The all-welded steel filter tank is built in accordance with the requirements of the American Society of Mechanical Engineers (ASME) Boiler and Pressure Vessel Code. It is lined with a bitumastic coating.

The softener contains approximately 4 ft^3 of high-capacity polystyrene-base resin. The all-welded steel tank is also built to ASME code requirements and lined with a bitumastic coating. The capacity between regenerations is 32,000 gal of water having a hardness of 3 grains/gal as calcium carbonate.

* Amercoat Corporation, Southgate, California.

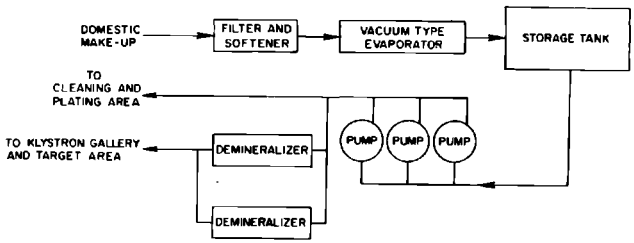

Figure 24-4 Flow diagram of distilled water plant.

Twenty-four pounds of salt are required for regeneration. The brine tank serves as a combination measuring and storage tank. The tank has a storage capacity of about 10 ft^3 and includes a makeup float valve in a separate chamber. It is constructed of steel and lined with a bitumastic coating.

Distilled water is stored in an all-welded stainless steel tank. The present tank replaced an equivalent wound-glass filament-reinforced epoxy resin tank which proved unsuitable because of the contamination of the distilled water by the continuous leaching out of the mold-release agent.

Three stainless steel canned-rotor centrifugal pumps, each rated to deliver 45 gal/min at a discharge pressure of 50 psig, are provided to distribute the water from the storage tank both to the cleaning and plating area and, through a pair of demineralizers, to the line serving the klystron gallery. One pump is normally on standby.

The two demineralizers on the line to the gallery are connected in parallel. The flow rate of each unit is 20 gal/min and the capacity between regenerations to the end point of 1 megohm specific resistance is 12,000 grains as calcium carbonate. The demineralizer resin is furnished as a replaceable cartridge, encased in fiberglass-reinforced polyester. Each cartridge contains $1\frac{1}{2}$ ft^3 of general purpose mixed bed resin. Although the maximum flow rate to the gallery is 40 gal/min, normal flow is less than 20 gal/min. Since the demineralizers handle distilled water, the life between rechargings is more than a year and ample time is available to service the cartridges without the necessity of providing a spare.

The low-conductivity water is piped to the klystron gallery in a 2-in. copper line. A valved connection to a $1\frac{1}{2}$-in. copper header running the length of the gallery is provided near the east end of Sector 29. A 2-in. underground line from the east end of Sector 30 connects the gallery header to the target area cooling-water system.

Cooling tower water system

Cooling tower 101 provides cooling water for the general purpose water system heat exchangers, the main air-conditioning water chiller condensers in the Central Utility Building, and the local air-conditioning chiller condensers at the Fabrication Building and the Test Laboratory. A flow diagram

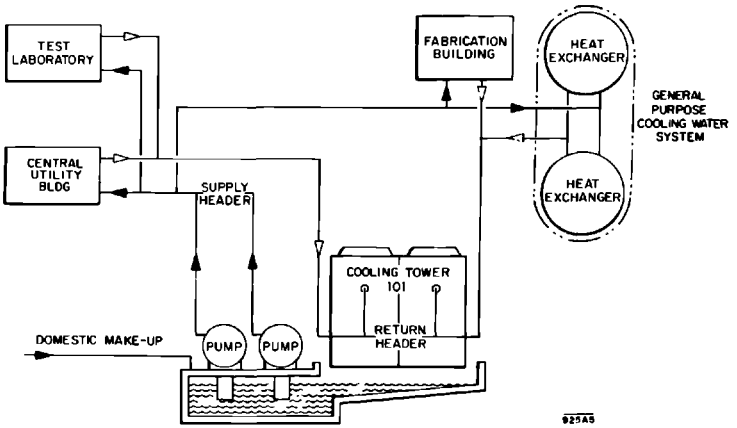

Figure 24-5 Flow diagram of laboratory and shop cooling tower water system.

of the cooling tower water system is shown in Fig. 24-5. The two-cell tower is of the counterflow induced draft type. It is rated at 10 MW, cooling 4600 gal/min from 93 to 78°F at 68°F (wet bulb) ambient. The low profile tower is 60 ft long, 24 ft wide, and 21 ft high. Redwood is used for the structural frame, fill, flumes, drift baffles, fan outlet rings, and top deck. The air-intake louvers and side panels are cement asbestos. The two-speed fan in each cell is driven by a motor which develops alternatively 7.5 and 30 hp to allow for variation in the heat load. The two tower water circulating pumps each deliver a rated 2800 gal/min at 50 psig discharge pressure. A 100-hp motor drives each pump. The pumps are of the two-stage vertical turbine type. A 30-mesh screen protects the suction well of each pump. System makeup water is introduced through an automatic float-controlled valve. Switches are provided that shut the fans down in the event of excessive vibration. An automatic "deluge" system protects the tower against fire.

24-2 Accelerator systems (FFH)

Approximately 80% of the power consumed by the electronic components of the SLAC linear accelerator is rejected as heat energy to one of the following closed-loop low-conductivity, cooling-water systems:

1. Disk-loaded waveguide systems, including the injector constant metal temperature system
2. Rectangular waveguide—drive line system
3. Klystron systems, including the injector klystron system
4. Positron system, including primary and intermediate circuit 1 and primary circuits 2 and 3.

These four accelerator systems and the associated cooling tower water systems are described in subsequent sections.

A branch from a $1\frac{1}{2}$-in. makeup header extending the length of the klystron gallery provides low-conductivity makeup water to each of the thirty sector mechanical alcoves. The branch line is connected to the surge tanks of the accelerator systems in the alcoves through automatic solenoid-operated valves. Water is supplied to the header from the distilled water plant. It can also be supplied from the target area storage tank.

Compressed air is supplied to the east end of the klystron gallery from the central compressed air utility system described in Chapter 27. Air can also be supplied from a separate compressor in the BSY substation. Compressed air passes through automatic duplex drying units before entering the 3-in. steel header extending the length of the gallery. Branch lines carry the air from the header to the mechanical equipment alcove in each sector and to the hatch cover actuating cylinders, beam-line vacuum valves, alignment targets, and wherever it is needed in the gallery and accelerator housing. System pressure is 100 psig. At each mechanical alcove, compressed air from the 3-in. steel header is filtered, reduced to 20 psig, and distributed to the pneumatic controllers used in the water systems.

To insure electrical phase stability, the metal temperature of all 10-ft accelerator sections is held at $113.0° \pm 1.4°$F. To hold critical high-power accelerator sections, such as the one in the injector and the three at the upbeam end of Sector 1, within these limits under all conditions of steady state RF loading, the temperature of cooling water supplied to the sections is automatically controlled by sensors responsive to the metal temperature of the sections themselves. Each sector throughout the rest of the accelerator is held within the same limits by controlling the supply water temperature in the gallery to within 0.2°F of a value preset to maintain the required metal temperature in the housing. The individual rotameter-type flow indicator and globe valve provided for each accelerator section facilitate temperature control by making it possible to equalize the bulk flow rate and water velocity throughout the accelerator. To insure symmetrical temperature distribution, the cooling-water supply and return connections are both located at the midpoint of each accelerator section. Water flows lengthwise to and from each end of the section through four hairpin loops of copper tube brazed to the periphery. The eight legs of the loops are spaced at equal intervals around the sections. Alternate legs carry supply and return water. To minimize temperature variation along the two-mile accelerator, the controller in each sector is calibrated against a very accurate reference standard.

To eliminate operating temperature as a design variable, rotameter-type flow indicators and globe valves are provided to equalize the rate at which water is supplied to each klystron and to each of a number of other machine components.

High purity low-conductivity water was chosen as the coolant offering the best long-term assurance of unrestricted flow through small apertures and

scale-free heat transfer surfaces. Copper pipe was selected for exclusive use throughout the accelerator systems on the basis of economy and compatibility with the accelerator materials and with low-conductivity water.

Going from 245 klystrons in Stage 1 to 965 in Stage 2 will result in a four-fold increase in the load on the heat exchangers of the accelerator systems. The klystrons themselves account for some 75% of the rejected heat. At present the thirty sectors are served by ten klystron cooling-water systems. Each system handles three sectors at eight klystrons per sector or a total of twenty-four klystrons. In Stage 2, each sector of thirty-two klystrons will require a separate cooling-water system. Another 20% of the rejected heat derives from the disk-loaded waveguides and the remaining 5% from the rectangular waveguides and drive lines. New and larger heat exchangers will be needed for the thirty disk-loaded waveguide systems. However, the heat exchangers presently used in the disk-loaded waveguide systems will be more than adequate for the rectangular waveguide–drive line systems in Stage 2. The existing pumps and piping are sized to meet Stage 2 requirements.

A large number of identical components are used in the accelerator water systems. For this reason, time was well spent in reviewing the many possible alternatives in search of the least expensive way of doing a given job. As an example, one proposal was to use a reduced pressure flash tank of special design in which low-conductivity water is evaporated at nominal temperature. The condensate is collected on tube bundles cooled by tower water and is pumped back into the system. Although the surface area is less than that of the equivalent shell and tube exchanger, the more conventional device was finally chosen, primarily because the proposed flash tank had not yet been proved in service. The anticipated economies in fabrication also appeared questionable in comparison with the mass-produced exchangers of the shell and tube type. With some 1400 low flow switches required to protect the accelerator cooling-water systems, the use of the least expensive commercially available type was an important factor in reducing installation costs. However, this choice of switches proved to be a mixed blessing due to the uncertainty of actuation at the marginal flows required in many branch lines and to the tendency for the initial setting to vary with time. Fortunately, it was possible to substitute a hermetically sealed, switching unit of adequate set-point stability while retaining the original body and orifice assembly. The modified switch is still less expensive than any equivalent, commercially available, differential pressure switch.

It was predicted[1] that cooling water passing through the accelerator housing would become slightly radioactive when the beam was on. In an effort to minimize the hazard to personnel in the gallery, the protective features described in subsequent sections have been included in the design of the disk-loaded waveguide and positron cooling-water systems.

Pumps used throughout the accelerator cooling-water systems are close-coupled, single radial stage, centrifugal pumps with vertical-split, low-zinc bronze casings, with open, low-zinc bronze impellers, and with single

mechanical shaft seals. The shaft seals have a carbon rotating face, a ceramic stationary face, and Teflon secondary seals, except for the two primary circuit 1 pumps in the positron system, which have double mechanical seals of the same material and Viton* secondary seals. Pressure gauges are pipe-mounted at the discharge from each pump.

The heat exchangers are shell and tube type. Low-conductivity water is on the shell side, and tower water is on the tube side, except as noted for the positron system. Shells, baffles, and tube sheets are silicon bronze. Tubes are 5/8-in. o.d. 90-10 copper–nickel. Channels and channel covers are steel. The design pressure is 150 psig for both shell and tube sides. Dial-type thermometers and pressure gauges are pipe-mounted at each inlet and outlet.

Piping in the several systems is copper, joined with 95-5 tin–antimony solder, using a water-soluble flux. In the positron system, the joints are made up with self-fluxing silver brazing alloy. Valve bodies, flexible metal hose, and other fittings not generally available in copper, are low-zinc bronze. Unless otherwise noted, flow indicators are all of the rotameter type.

Disk-loaded waveguide systems (DBR)

A closed-loop, low-conductivity cooling-water system is provided to remove heat from all thirty-two disk-loaded waveguides (10-ft accelerator sections) in each of the thirty sectors except Sectors 1 and 11. The injector constant metal temperature system serves the first three accelerator sections in Sector 1 in addition to the beam-line components of the injector. Heat is removed from the accelerator sections on girders 11-3B and 11-3C in Sector 11 by primary circuits 2 and 3 of the positron system. Each disk-loaded waveguide system also cools the beam scraper and the beam position monitor in the drift section at the downbeam end of the preceding sector.

The standard sector system in the diagram in Fig. 24-6 is designed to cool the accelerator sections and their output loads. The water leaving the output load of each odd-numbered section also cools the adjacent rectangular waveguide. Flow rates through the various components are itemized in Table 24-3. The pump, heat exchanger, and auxiliary equipment for each system are located in the mechanical alcove of the respective sector.

A flow diagram of the injector constant metal temperature system appears in Fig. 24-7, with flow rates itemized in Table 24-4. The pump, heat exchanger, and auxiliary equipment are located in the mechanical alcove in Sector 1. Figure 24-8 shows the heat exchanger, together with other cooling-water equipment in the Sector 1 alcove.

Design and operating parameters for the standard sector system and for the injector constant metal temperature system are included in Tables 24-3 and 24-4. Inlet and outlet water temperatures over the range of RF power loading may be taken from the curve in Fig. 24-9. Although the accelerator

* DuPont Company, Wilmington, Delaware.

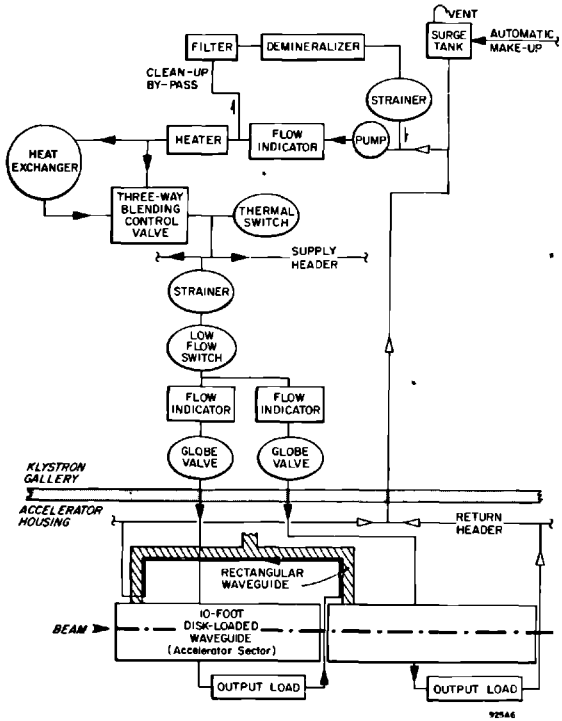

Figure 24-6 Flow diagram of disk-loaded waveguide cooling-water system.

Figure 24-7 Flow diagram of injector constant metal temperature cooling-water system.

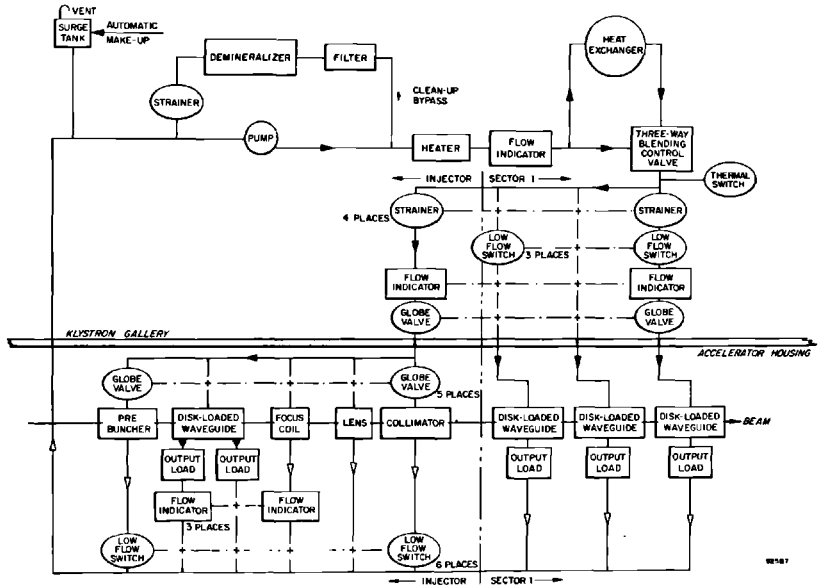

Table 24-3 Design parameters for standard disk-loaded waveguide cooling-water system

Parameters	*Stage 1*	*Stage 2*
Accelerator section		
Flow (gal/min)	13 ± 1	13 ± 1
Heat load, max (kW)	3.1	12.4
Water temperature in, max heat load (°F)	110.3 ± 0.2	101.8 ± 0.2
Water temperature rise (°F)	1.625	6.5
Metal temperature (°F)	113.0 ± 1.4	113.0 ± 1.4
Pressure drop, max (psi)	8	8
Output load		
Flow (gal/min)	13 ± 1	13 ± 1
Heat load, max (kW)	1.5	6.0
Water temperature in, max heat load (°F)	111.9	108.3
Water temperature rise (°F)	0.8	3.2
Pressure drop, max (psi)	5	5
Rectangular waveguide		
Flow (gal/min)	13 ± 1	13 ± 1
Heat load, max (kW)	0.05	0.2
Water temperature in, max heat load (°F)	112.7	111.5
Water temperature rise (°F)	0.025	0.1
Pressure drop, max (psi)	4	2
Totals—Average 10-ft accelerator section		
Flow (gal/min)	13 ± 1	13 ± 1
Heat load, max (kW)	4.65	18.6
Water temperature rise (°F)	2.45	9.8
Water temperature out, max heat load (°F)	112.7	111.6
Pressure drop, max (psi)	17	15
Beam scraper, flow (gal/min)	40	40
Beam position monitor, flow (gal/min)	1	1
Cleanup bypass, flow (gal/min)	8	8
System totals		
Flow (gal/min)	465	465
Design flow (gal/min)	480	480
Heat load less the contribution of the scraper and position monitor, max (kW)	148.8	602
Design heat load (kW)	173	—
Design pressure drop, max (psi)	75	75

Table 24-4 Design parameters of injector constant metal temperature cooling-water system

Component	*Flow (gal/min)*	*Heat load (kW)*
Prebuncher	2	3
Focus coil	26	40
Injector accelerator section, loads and waveguide	13	19
Lens	2	3
Collimator	2	3
Sector 1 accelerator sections, loads and waveguides—three at 13 gal/min and 19 kW each	39	57
Cleanup bypass	8	—
System totals		
Flow (gal/min)	92	92
Design flow (gal/min)	100	100
Heat load, max (kW)	125	125
Design heat load (kW)	147	147
Design pressure drop, max (psi)	67	67

would operate satisfactorily at a metal temperature anywhere between 80° and 120°F, it was necessary to specify the design temperature in order that the proper allowance could be made for dimensional changes due to the difference in metal temperature during fabrication and during operation. If the metal temperature during operation is set too low, the size and cost of the heat exchangers is unduly increased. On the other hand, if it is set too

Figure 24-8 Injector cooling-water equipment.

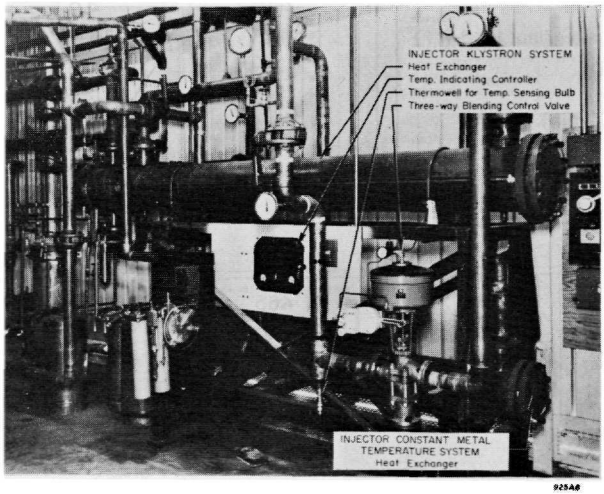

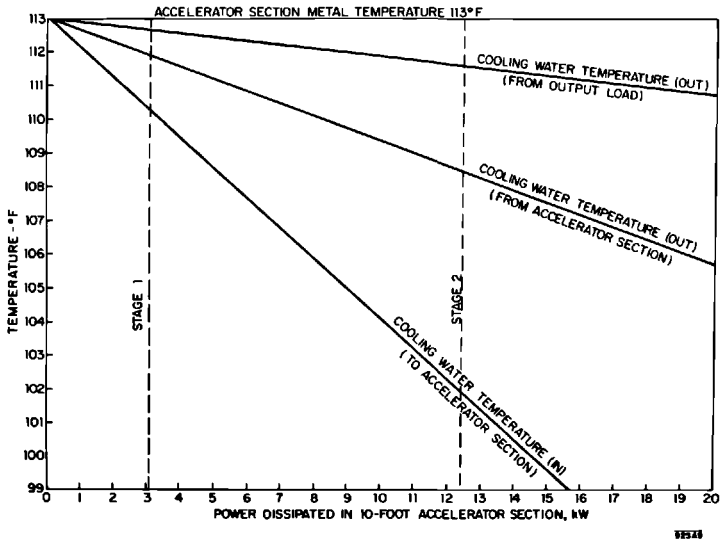

Figure 24-9 Water temperature versus RF power loading.

high, the resistivity of the section increases and the resulting decrease in the Q and shunt impedance reduces the beam energy. An excessive metal temperature could also warm up the surrounding concrete enough to make it uncomfortable to do maintenance work in the accelerator housing during shutdown. As a compromise, a temperature of 113°F was set for the disk-loaded waveguides. During the 8 hours/week that the accelerator housing is open for maintenance, the air temperature runs approximately 80°F with the ventilating fans turned on. When the accelerator is in operation, the air temperature in the closed housing averages 90°F.

Components of all thirty disk-loaded waveguide systems (thirty sectors) are identical. The basic features common to pumps, heat exchangers, and piping of all accelerator cooling-water systems are summarized above. Operating characteristics of the circulating pumps and heat exchangers for the disk-loaded waveguide and for the injector are included in Tables 24-1 and 24-2.

The sector supply headers for the disk-loaded waveguide system are of 4-in. pipe. An in-line strainer and a low flow switch are provided in valved, $1\frac{1}{2}$-in. supply branches located at 20-ft intervals along the header. Each branch feeds a pair of 1-in. risers serving two adjacent accelerator sections through a 27-in. service penetration. A globe valve and flow indicator permit adjustment of the rate at which water is supplied through each riser. The 1-in. risers are connected to the accelerator sections through 4-ft lengths of flexible metal hose with union ends. Water returns through a similar hose to a 4-in. header in the accelerator housing. A 5-in. return riser approximately in the middle of the sector carries the water up through a 20-in. penetration to a trench in the gallery floor leading to the mechanical equipment alcove.

The beam scraper and position monitor are also connected to the return header with flexible metal hose. Block valves are provided in the accelerator housing on the return line from each accelerator section and water-cooled drift section component. Supply headers and risers are insulated.

The injector system serves the first three accelerator sections in Sector 1 through three risers. The arrangement is similar to that of the standard sector except that the risers are fed directly from the 2½-in. supply header instead of being connected in pairs through a 1½-in. branch. Each riser has its own strainer and low flow switch. The system also supplies water through a 2-in. riser equipped with a flow indicator and globe valve to a 2-in. header serving the injector equipment in the accelerator housing. Block valves are included in the branch line to each component, together with a low flow switch on the return side. Flow indicators are provided on the two return lines from the injector accelerator section and on the return line from the focus coil. Water is collected from all components in the housing through a 2½-in. return header. Both supply and return headers in the klystron gallery are insulated.

For temperature control in the disk-loaded waveguide system, each heat exchanger is provided with a bypass and a pneumatically positioned three-way blending control valve. The blending valve is a piston-operated device designed to pass a constant flow irrespective of stem position. A mercury-filled temperature-sensing bulb is mounted in a thermowell downstream of the three-way valve. A capillary tube connects the bulb to a pneumatic transmitter where the temperature signal is converted to a 3–15-psig air signal to the indicating controller on a nearby panel. The controller is preset to the temperature at which the water must leave the gallery to hold the average metal temperature of the disk-loaded waveguides in the sector between 111.6° and 114.4°F. The controller compares the actual water temperature with the preset temperature. An air signal from the controller to the valve positioner readjusts the setting of the three-way valve in proportion to the direction and magnitude of the difference between the two temperatures. As directed by the positioner, the three-way valve combines a stream of cool water from the heat exchanger with a warmer stream bypassing the exchanger to maintain the preset water temperature. During startup and low-power operation when the heat loads are negligible and all the flow is through the bypass, water temperature is maintained by a 50-kW in-line electric heater. The heater is energized through a relay actuated by a set of contacts in the controller.

In Stage 1 operation, as has been described, four accelerator sections in a standard sector share the output of a single klystron. In contrast, the four accelerator sections cooled by the injector system are powered by separate klystrons. To hold these high-power sections within the specified metal temperature limits, the temperature of the cooling water supplied by the injector system is automatically varied to maintain the minimum practicable differential between a preset control point of 113°F and the average metal temperature of the four sections themselves. The control instrumentation

consists of mercury-filled temperature-sensing bulbs in thermowells brazed to the periphery of the four accelerator sections, pneumatic transmitters which convert the temperature signal from each bulb to a 3–15-psig air signal, an averaging relay which forwards a single signal equivalent to the average of the four received from the transmitters, and an indicating controller. The controller compares the actual average metal temperature with the preset temperature of 113°F and, by air signal to the valve positioner, readjusts the setting of the three-way valve in the same manner as in a standard sector. A 25-kW in-line heater maintains the water temperature during startup and low-power operation.

A copper surge tank accommodates thermal expansion of the water in each system. The 35-gal tank is mounted 10 ft above the pump suction in each mechanical equipment alcove. It is connected to the return header by a 2-in. riser. The tank is vented to the atmosphere. Each tank is equipped with a liquid-level sight glass. Automatic control of the water level in the tank and protection against excessive leakage is provided by a float and two limit switches.

As the return water may be slightly radioactive, confining it to a header in the housing and to a single return riser simplifies any problem of shielding that may arise in the klystron gallery. The principal activity is from ^{15}O with a half-life of 2 min. The radiation level in the gallery could be reduced by adding a shielded holdup tank in the return line and by stacking lead bricks over the trench through which the 5-in. riser returns to the alcove. However, it has been unnecessary to resort to either of these expedients as background radioactivity remains below the allowable tolerance. Individual low flow switches are interlocked to shut off the modulator serving the klystron of the corresponding accelerator section if the flow drops to 80% of normal. In the injector system, flow switches on the buncher, focus coil, lens, and collimator cooling-water lines are interlocked with the respective power supplies. A Venturi-type flowmeter is installed in the pump discharge line with the pressure taps connected to an indicator and a differential pressure switch on the control panel in the alcove. The switch is interlocked to shut down the in-line heater and variable-voltage substations if the flow drops to 70% of normal. In addition, a thermal switch mounted on the piping downstream of the three-way valve is interlocked with the variable-voltage substations to interrupt power to the modulators should the system temperature exceed 130°F. As the water level in the surge tank goes down, the first limit switch opens a solenoid valve, admitting low-conductivity makeup water. The second switch shuts down the circulating pump when the level drops to within about an inch of the bottom of the tank, a condition which indicates excessive leakage from the system.

Water is held to a specific resistance of more than a megohm by a 5-μ replaceable cellulose filter and a mixed bed demineralizer located on a bypass between pump discharge and pump suction. The bodies of the filter and the demineralizer tanks are Type 304 stainless steel. Isolating valves are provided

so that the filter elements and the demineralizer resin can be replaced while the system is operating. A 100-mesh strainer in the bypass downstream of the demineralizer prevents resin carryover into the circulating system.

Rectangular waveguide–drive line systems (DBR)

Thirty closed-loop, low-conductivity cooling-water systems serve the rectangular waveguides and RF drive lines. These systems have three functions. They remove the heat generated by the RF losses in the rectangular waveguides, provide constant temperature water for tracing the drive line and the phase monitoring cables, and cool the sub-booster modulators. A typical system is shown diagrammatically in Fig. 24-10. In Sector 1, the system cools the injector rectangular waveguides and one standby sub-booster modulator in addition to the typical sector loads. Although rated for 160 gal/min at 66 psig discharge, the pump is capable of delivering the 185 gal/min required for Stage 2 operation. The corresponding discharge pressure of 59 psig is ample to overcome system impedances. The pumps, heat exchanger, and other auxiliary equipment are located in the mechanical alcove in each sector.

Figure 24-10 Flow diagram of rectangular waveguide–drive line cooling-water system.

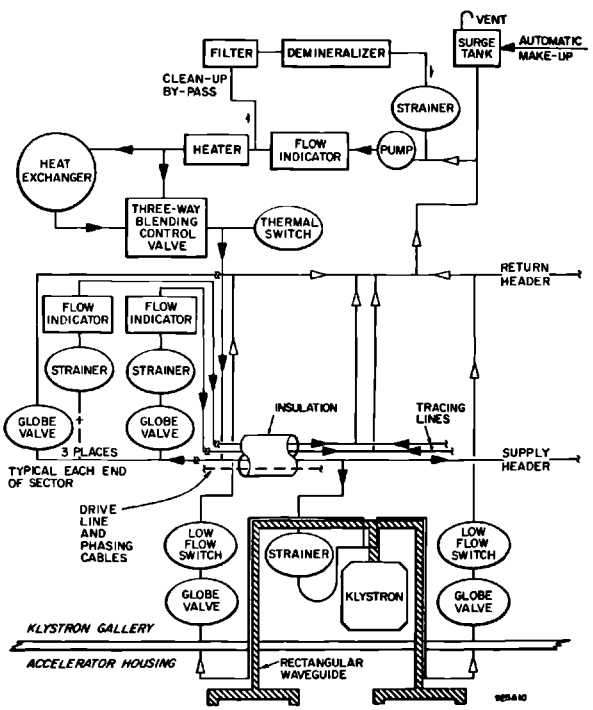

Table 24-5 Design parameters for rectangular waveguide–drive line systems

	Stage 1	*Stage 2*
Waveguide		
Flow per klystron (gal/min)	10	5
Heat load per klystron (kW)	2.75	2.75
Water temperature in (°F)	112 ± 1	112 ± 1
Water temperature rise (°F)	1.87	3.74
	Flow (gal/min)[a]	*Heat load (kW)*[a]
Drive line and phase monitoring cables	10	nil
Subbooster modulator	2	0.5
Supply-to-return header bypass	5	—
Cleanup bypass	8	—
	Stage 1	*Stage 2*
System totals		
Flow (gal/min)	105	185
Design flow (gal/min)	160	185
Heat load (kW)	22.5	88.5
Design heat load (kW)	26.5	—
Design pressure drop, max (psi)	62	55

[a] Quantities apply to both Stage 1 and Stage 2.

Design and operating parameters for the system are included in Table 24-5. The temperature of the cooling water supplied to the rectangular waveguides and drive lines must be held at 112° ± 1°F to maintain electrical phase stability. Water at the same temperature is used to cool the sub-booster modulators. Whereas the temperature along an individual waveguide may vary by more than ±1°F, depending on power level, the temperature variation at corresponding points on the sixteen waveguides in each sector may not exceed ±1°F.

Identical components are used on all thirty systems. The basic features common to the pumps, heat exchangers, and piping of all accelerator cooling-water systems are summarized above. Operating characteristics of the circulating pumps and heat exchangers for this system are included in Tables 24-1 and 24-2.

Hollow copper waveguides carry RF power from the klystrons to the accelerator. A short length of full power waveguide on the klystron couples equally into two half-power branch waveguides of rectangular cross section with a cooling-water channel brazed to the face of each. The thermally insulated waveguides enter the accelerator housing through separate penetrations, one upbeam and one downbeam from the klystron. Within the housing, each waveguide divides through a 3-dB coupler into two one-quarter power waveguides feeding the individual accelerator sections. Water from

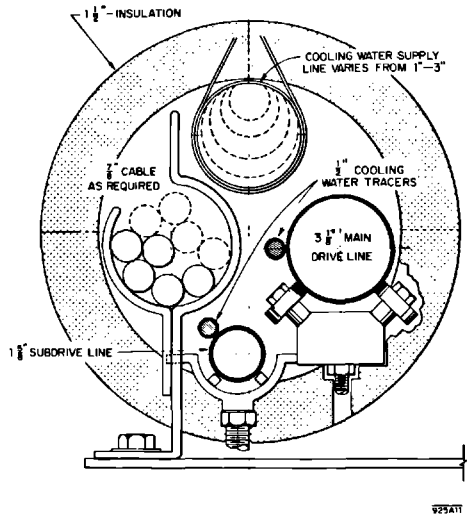

Figure 24-11 Drive line and phase-monitoring cable package.

this system cools the waveguides from the klystron as far as the couplers in the housing. Beyond the couplers, the rectangular waveguides are cooled by the disk-loaded waveguide cooling-water system. The 2½-in. supply header serving each sector is located within the insulated drive line and phase-monitoring cable package shown in cross section in Fig. 24-11. The valved 1-in. supply branch above each klystron includes an in-line strainer. Each branch connects to the cooling channels on the waveguides through a length of flexible metal hose. The cooling channel on each waveguide ends at the lower coupler and a riser carries the water back up through the penetration to the return header in the klystron gallery. A globe valve, low flow switch, and block valve are located near the header end of the riser. Stubs are provided on the supply header for the additional branches required for expansion to Stage 2.

In order to take advantage of the constant temperature environment provided by the supply header of the rectangular waveguide–drive line cooling-water system, the main and subdrive lines and phase-monitoring cables are included in the same insulated package. It was found necessary to fasten "tracers" of ½-in. copper pipe to the two drive lines in order to insure the required degree of temperature stability. Water is supplied to the tracer lines through a globe valve and flow indicator at each end of the sector.

Temperature control for this system is the same as for a standard sector disk-loaded waveguide system. A 20-kW in-line electric heater holds the system at temperature when the beam is off, during startup, and during low-power operation.

The surge tanks, the filter demineralizers, and protection against low flow, against high system temperature, and against low water level in the surge tank are all the same as for the disk-loaded waveguide systems.

Klystron cooling-water systems (DBR)

Eleven closed-loop, low-conductivity cooling-water systems are provided to remove the heat generated in the klystrons, including ten main klystron systems and one injector klystron system. During Stage 1 operation, twenty-four klystrons in three adjacent sectors are connected to a typical main klystron system, as shown in the flow diagram in Fig. 24-12. The pumps, heat exchangers, and other auxiliary equipment are located in the mechanical alcoves of Sectors 2, 5, 8, 11, 14, 17, 20, 23, 26, and 29. A klystron heat exchanger is seen in Fig. 24-13. In addition to the normal complement of twenty-four klystrons, the main system for Sectors 10, 11, and 12 serves an additional klystron in the positron area in Sector 11.

The injector klystron system depicted in Fig. 24-14 cools the two injector klystrons and their RF switches and output loads, the two main boosters and their output load, and the first three klystrons in Sector 1. The pump,

Figure 24-12 Flow diagram of klystron cooling-water system.

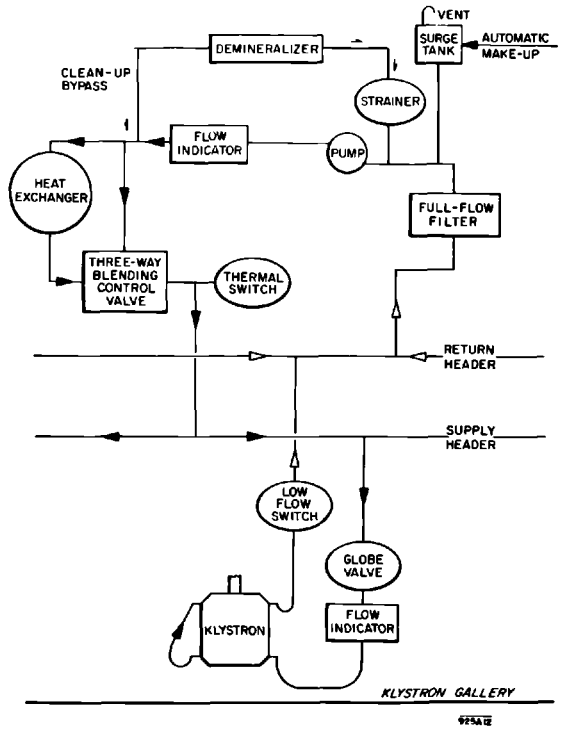

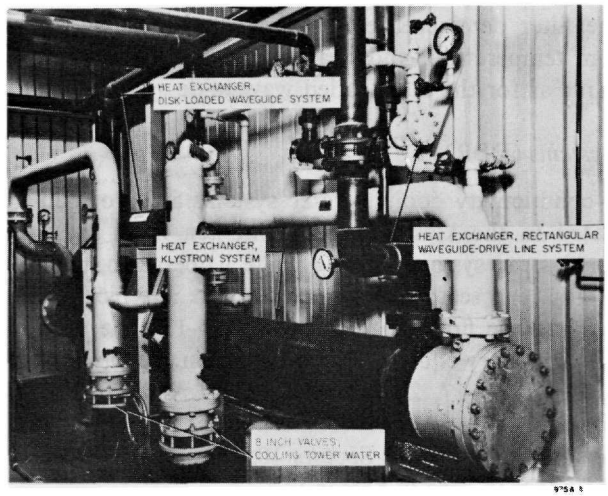

Figure 24-13 Heat exchangers in Sector 11 mechanical alcove.

heat exchanger, and other auxiliary equipment are located in the Sector 1 mechanical alcove. Figure 24-13 includes a view of the heat exchanger and some of the other equipment in the alcove. Adding a standby circulating pump to the system for Sectors 1, 2, and 3 and providing normally closed interconnections between the supply and return headers of this system and the injector klystron system, increases the overall reliability of the klystron water systems at the injector end of the accelerator.

Figure 24-14 Flow diagram of injector klystron cooling-water system.

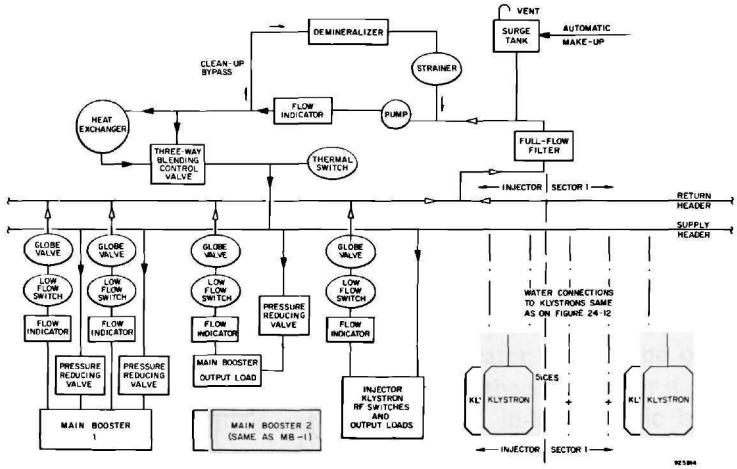

Table 24-6 Design parameters for main klystron cooling-water system

Parameters	*Stage 1*	*Stage 2*
Klystron tube and pulse transformer		
Flow (gal/min)	11	11
Heat load, normal (kW)[a]	57.4	57.4
Heat load, standby (kW)[a]	79.0	79.0
Water temperature, in, normal (°F)	95.0	95.0
Water temperature, out, normal (°F)	129.8	129.8
Water temperature, out, standby (°F)	143.0	147.5
Pressure drop, max (psi)	30	30
Cleanup bypass		
Flow (gal/min)	8	8
System totals		
Sectors per system	3	1
Klystrons per system	24	32
Flow (gal/min)	270	360
Heat load, normal (kW)	1378	1837
Heat load, standby (kW)	1896	2528
Water temperature, in, standby (°F)	95	99.5
Design pressure drop, max (psi)	85	85

[a] Includes 3 kW from pulse transformer.

Stage 2 operation requires thirty main systems, each serving thirty-two klystrons in a typical sector.

Design and operating parameters for the klystron cooling-water systems are summarized in Tables 24-6 and 24-7. Constant-temperature cooling water improves klystron performance, but a few degrees either way is not critical. A flow of 8.1 gal/min is required to hold the bulk temperature rise in the water within allowable limits. The operating flow was set at 11 gal/min to give a margin for resetting the low flow switches and to permit the use of later-model klystrons which can deliver more than the rated 24-MW peak power.

Identical components are used in all ten main klystron systems, and the injector klystron system components are similar to these. The basic features common to the pumps, heat exchangers, and piping of all accelerator cooling-water systems are summarized above. Operating characteristics of the circulating pumps and the heat exchangers for the main klystrons and for the injector klystrons are included in Tables 24-1 and 24-2.

Table 24-7 Design parameters for injector klystron cooling-water system

Components	*Flow (gal/min)*	*Heat load (kW)*
Two main boosters		
Regulator tube at 15 gal/min, 25 kW	30	50
Klystron tube and magnet at 25 gal/min, 50 kW	50	100
Main booster output load	10	25
RF switches and output loads	10	25
Klystrons and pulse transformers, five, at 11 gal/min, 79 kW (standby)	55	395
Cleanup bypass	5	—
Injector klystron system[a]	160	595

[a] Design pressure drop is 62 psi.

The main klystron system headers are 4-in. pipe, with block valves between sectors for easy conversion to Stage 2 operation. Injector klystron system headers are 3-in. pipe. Valved 1-in. branches are provided at each klystron. Capped stubs are included for each Stage 2 klystron. Pressure reducing valves, pressure gauges, and relief valves are incorporated in the $1\frac{1}{2}$-in. branches supplying the injector main boosters to hold the water pressure below the 70-psig rating of ceramic connectors used in the boosters. Each supply branch includes an in-line strainer and a flow indicator. A low flow switch is provided in each return branch. Supply and return connections to the klystrons are through short lengths of reinforced rubber hose fitted with double-valved quick-disconnect couplings.

Temperature control is the same as for the standard sector disk-loaded waveguide systems. However, since a single klystron can deliver 34 kW to the water, in-line heaters are omitted. Surge tanks, system protection, and demineralizers for the klystron systems are the same as for the disk-loaded waveguide systems. The frequent replacement of klystrons during accelerator operation increases the likelihood of contaminating the water system, as compared to the disk-loaded or rectangular waveguide systems. Thus a full-flow 5-μ filter is included at the pump suction to trap any particles entering the return header. The demineralizer is the same as that used in the disk-loaded waveguide systems.

Positron system (KGC)

The positron cooling-water system is made up of three primary circuits and one intermediate circuit. Primary circuit 1 and the intermediate circuit cool the solenoids, positron radiators, and the scraper as shown in Fig. 24-15.

Primary circuit 2 cools accelerator sections 11-3B and 11-3C and the associated output loads and rectangular waveguides in the accelerator housing. During positron generation, primary circuit 3 handles the extra heat developed in fast valve 11-3 and in the coupler end plate and disk-loaded waveguide of accelerator section 11-3B. Primary circuits 2 and 3 appear in Figs. 24-16a and b, respectively.

Each primary circuit includes a pump, a heat exchanger, temperature control, a surge tank, provision for system protection, and a filter and demineralizer. The additional pump and the thirteen parallel-connected, double-wall, spiral-wound heat exchangers serving coil 0 are incorporated in a high-pressure sub-loop of primary circuit 1. The pump supplies the extra head needed to force sufficient water through the thirteen hollow conductors comprising coil 0 to remove over 700 kW of heat without exceeding the maximum allowable operating temperature of the interturn insulation. The thirteen exchangers reduce the bulk temperature of the water as it leaves the accelerator housing to a level compatible with the ratings of rotameter-type flow-monitoring instrumentation. Intermediate circuit 1 follows the same pattern as the primary circuits, but without the heater, three-way valve, filter, and demineralizer.

The pumps, demineralizers, filters, and most of the valves are located in a concrete-shielded cubicle in the positron equipment alcove in the klystron gallery. The four shell and tube heat exchangers are also in the cubicle, but the thirteen coil-type exchangers are installed in the accelerator housing. The cubicle walls are 1-ft thick, barite concrete with a density of 225 lb/ft^3.

Figure 24-15 Flow diagram of primary and intermediate circuit 1, positron cooling-water system.

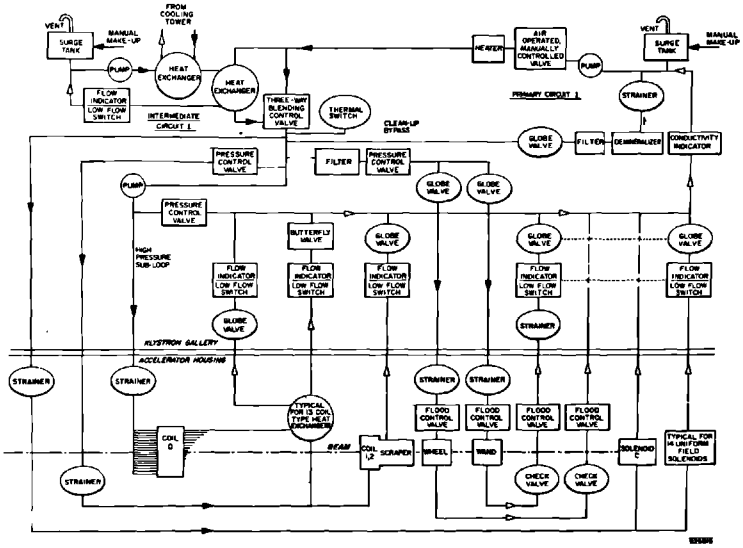

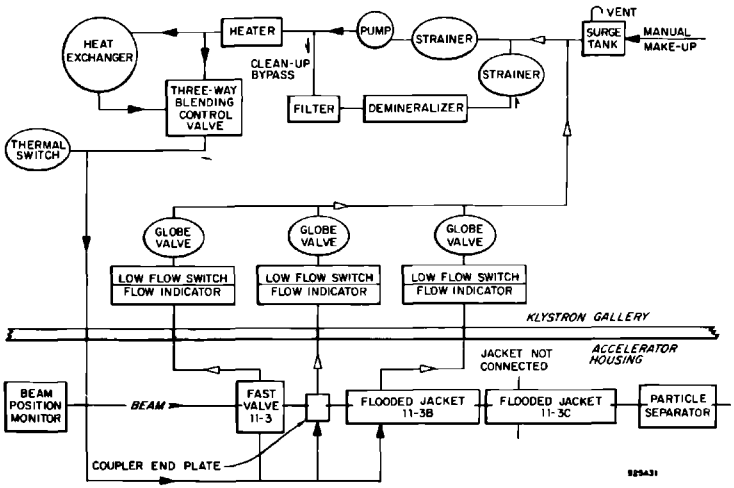

Figure 24-16a Flow diagram of primary circuit 2, positron cooling-water system.

During positron generation, flow control valves are operable from outside through slots in the wall of the cubicle, as shown in Fig. 24-17.

Heat loads and water flow for each circuit are summarized in Table 24-8. The beam positron monitor at the upbeam end of girder 11-3A and the particle separator at the downbeam end of girder 11-3C are cooled by the Sector 11 disk-loaded waveguide cooling-water system.

Figure 24-16b Flow diagram of primary circuit 3, positron cooling-water system.

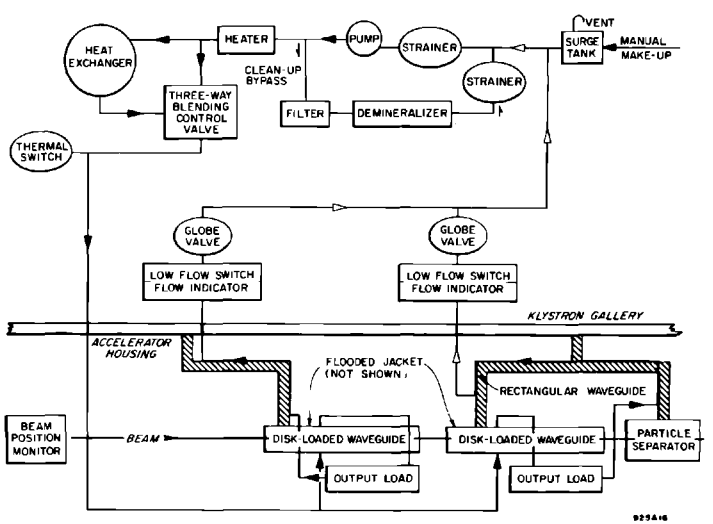

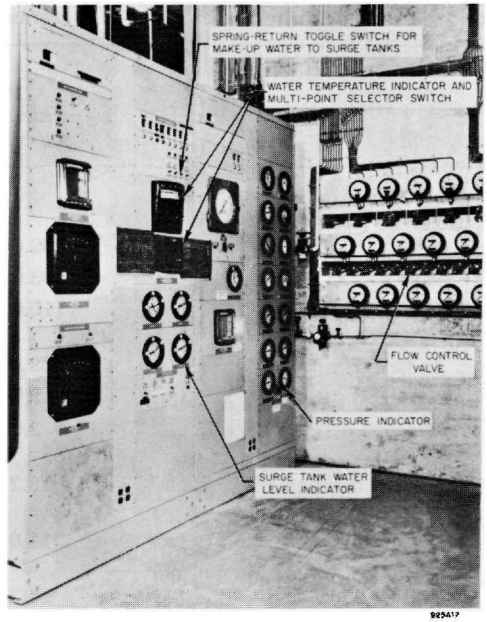

Figure 24-17 Water control center in the positron cooling-water system.

The basic features common to the pumps, heat exchangers, and piping of all accelerator cooling-water systems are summarized above. Characteristics of the positron system circulating pumps are included in Table 24-1. The pump in the sub-loop is of the vertical in-line type, with the pump shaft coupled to the motor shaft. Mechanical, face-type, shaft seals in the pumps in primary circuits 2 and 3 are interchangeable with those used on the pumps in the accelerator cooling-water systems. A pump seal injection circuit with two sub-loops is provided, one sub-loop for the main pump and one for the high-pressure pump. Low-conductivity water at a pressure above the suction pressure of the respective pump is circulated through the annulus between the inside diameter of the packing gland and a pair of face-type mechanical seals mounted back-to-back along the pump shaft. Water level in the supply tank of this auxiliary circuit is monitored by a differential pressure transmitter, a level indicator, and two pressure switches. As the seal injection water absorbs the heat developed by friction between the seal faces, a small branch of the cooling tower system is piped through the supply tank. The seal injection circuit also supplies 175 psig water pressure to stop leakage along the stems of the butterfly valves in primary circuit 1.

Characteristics of the positron system heat exchangers are included in Table 24-2. All heat exchangers except those for the sub-loop are of the shell

Table 24-8 Design and operating parameters for positron system cooling-water systems

Circuit	*Flow (gal/min)*	*Heat load (kW)*	*Water temperature rise (F°)*
Primary circuit 1			
Solenoid A			
Coil 0	39.0	705	123
Coil 1	43.0	81.2	6.5
Coil 2	10.0	17.4	11.9
Scraper—cooled by water from coils 1, 2	53.0	350	44.8
Solenoid C	3.84	17.7	54.0
Solenoid F	3.60	23.3	54.0
Solenoids G, I, N, P, R, T at 2.2 gal/min and 16.5 kW each	13.2	99.0	54.0
Solenoids H, J, O, Q, S at 2.2 gal/min and 16.8 kW each	11.0	84.0	54.0
Solenoids K, M at 2.64 gal/min and 20.0 kW each	5.28	40.0	54.0
Totals	128.9	1417.6	—
Radiators, total for wheel operation[a]	50.0	150.0	—
Primary circuit 1, totals	178.9	1567.6	—
Intermediate circuit, totals	550.0	1567.6	—
Primary circuit 2, totals	26.0	38.0	10.0
Primary circuit 3, totals	83.0	65.0	9.1

[a] Wand requirements at 3.0 GPM and 1.0 kW are considerably less than for the wheel.

and tube type. The inner and outer tubes of the thirteen coil-type, sub-loop exchangers are copper. Water from coil 0 flows through the inner tube. Water from the supply line to coils 1, 2, and the scraper is circulated through the outer annulus. The heat exchanger in primary circuit 1 is shown in Fig. 24-18.

The 6-in. main pump discharge header shown diagrammatically in Fig. 24-15 continues into the housing as one 6-, one 2-, and one $1\frac{1}{2}$-in. supply line to the solenoids and one 2- and one $\frac{1}{2}$-in. supply line to the radiators. In the housing, the 6-in. line branches into a $2\frac{1}{2}$-in. line to coils 1, 2, and the scraper and into a 2-in. header cooling the thirteen coil-type heat exchangers. Thirty-one separate lines return the water to the main pump through a 6-in. suction header in the cubicle. Supply and return lines in primary circuits 2 and 3 are shown in Figs. 24-16a and b. The supply lines in

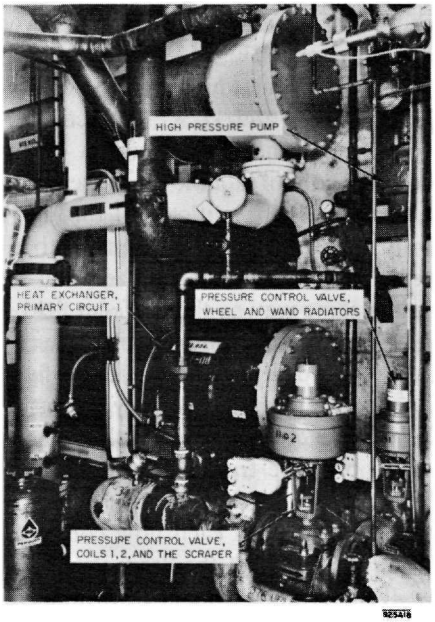

Figure 24-18 Heat exchanger and control valves in the positron cooling-water system.

the three primary circuits are insulated from the three-way valve to a convenient point in the housing. Return lines are not insulated. The drift tube, solenoids A and C, and the beam line and service equipment between fast valves 11-2 and 11-3 are mounted on the horizontal web of an all-welded aluminum I-beam, fabricated of 1-in. plate. The method of locating and supporting the resulting radiator, strongback subassembly on girder 11-3A permits the removal and replacement of the entire subassembly as a single unit.

To keep the girders free for realignment, connections between pipes fixed to the housing and components mounted on the jack-supported girders are made through flexible metal hose. The radiation to which personnel will be exposed in breaking the water lines leading to the strongback is minimized by locating the strongback end of each connection as far upbeam as practicable and by using quick-disconnect-type couplings. The water lines leading to and from coils 1, 2, and the scraper are stainless steel pipe with welded joints.

The two 2000-A power connectors and the associated bus bars on girder 11-3A are cooled by water from the high-pressure sub-loop. The water returns through the two 2000-A feedthroughs to coils 1 and 2 and the scraper or through the 2-in. return header for cooling water from the thirteen heat

exchangers. Ceramic insulators prevent an electrical short-circuit to ground along the water lines.

Water to the uniform field solenoids is delivered to two headers fixed to girders 11-3B and 11-3C, respectively. A short length of flexible bronze hose connects the header through a ceramic insulator to the inlet lead of each coil, or pair of double pancakes, in each of the fourteen solenoids. Water returns from the outlet lead through another ceramic insulator and flexible bronze hose to a header common to all coils in the given solenoid. A separate return line is provided for the water from each solenoid. Solenoid C is cooled in the same way as the uniform field solenoids.

With one exception, globe valves are used for flow control in all return lines. The exception is the butterfly valve used in the cooling-water return line from the thirteen coil-type heat exchangers.

Figure 24-19 shows the close-packed array of pipes, orifice flanges, differential pressure transmitters, and valves on the inside of the shielding wall. The outside of this wall is shown in Fig. 24-17. Air can be introduced through the valve beneath each flow control valve in Fig. 24-19 to blow radioactive water out through the drain valve in the accelerator housing.

Temperature control in primary circuit 1 is accomplished in essentially the same manner as in the disk-loaded waveguide system in a standard sector. The indicating controller returns the water to the solenoids and radiators at a

Figure 24-19 Inside west wall of cubicle, positron cooling-water system.

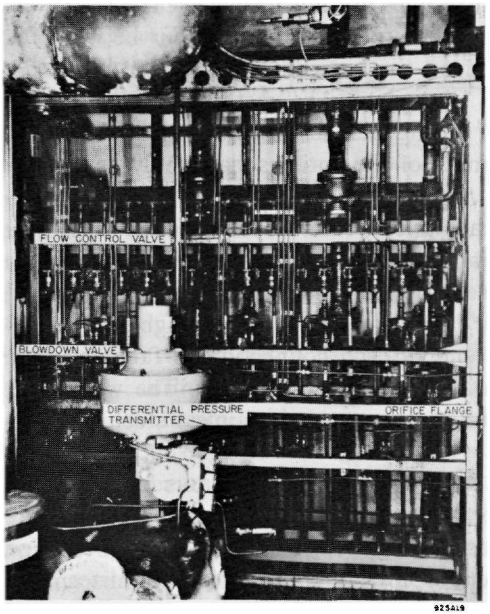

preset temperature of 104°F. An in-line heater keeps the supply water up to temperature during standby in order to prevent condensation on the coils and the uninsulated conductors in the housing and to reduce the severity of the thermal shock to which the circuit components are subjected at the commencement of positron generation.

Each of the four circuits is vented to atmosphere through a 30-gal copper surge tank connected through a 2-in. pipe to the pump suction header. The tanks also provide a reservoir for thermal expansion of the water as it rises to operating temperature. The three tanks in the primary circuits are connected to a common overflow and vent pipe leading up through the roof. Overflow from this line discharges into a concrete trench in the floor of the gallery from where it is drained down into the housing. Overflow and venting from the intermediate circuit is through a hole in the side of its surge tank. The tanks are filled through individual, manually controlled, normally closed, solenoid-operated valves fed off a common low-conductivity, makeup water header. Each tank is equipped with a differential pressure transmitter for water level indication and two pressure switches.

The water in primary circuits 2 and 3 may become slightly radioactive during positron generation. As the pressure in these two circuits is less than that of the cooling tower water, there is no danger of contaminating the tower in the event of leakage through either heat exchanger. Conditions are just the opposite in primary circuit 1. Water in this circuit not only runs at a higher pressure than cooling tower water, but it also becomes highly radioactive during positron generation. To avoid contamination of the tower in the event of leakage through the heat exchanger, primary circuit 1 is cooled by low-pressure intermediate circuit 1, which, in turn, is cooled by tower water. Leakage of radioactive water from the two pumps in primary circuit 1 is prevented by the pump seal injection circuit. One of the two pressure switches provided to monitor the water level in the seal injection supply tank gives a low level alarm, the other shuts off the seal injection pump when the water level drops to within 3 in. of the bottom of the supply tank. Two additional pressure switches in the seal injection sub-loop to each primary pump shut off the seal injection pump if the pressure in the line is either too high or too low. The pumps in primary circuit 1 cannot be started unless the pump in the seal injection circuit is running.

The solenoid-operated flood-control valves in the water lines serving the wheel and wand radiators and the four air-operated drain valves in primary circuit 1 are necessarily located in the accelerator housing. To prolong the life of radiation-resistant elastomeric seals and packing, these valves are grouped within two lead brick enclosures on the floor of the housing. A detailed account of the purpose and operation of the flood-control system is given in Chapter 23. Capped nipples are union-connected to stubs in the return lines of both radiators, providing an emergency vacuum connection between the flood control valves on the wheel and wand supply and return lines in

the housing. The vacuum pump can be located in the gallery, pumping through a $1\frac{1}{2}$-in. copper pipe installed in penetration 11-04. A 2-in. flexible bronze hose runs from the end of the copper pipe to the immediate vicinity of the stubs. The hose is terminated with a "T" and fittings mating with both the 2-in. stub on the wheel radiator line and the $\frac{1}{2}$-in. stub on the wand radiator line. All openings in this emergency vacuum line are capped to keep out dirt. Diagnostic lines running up to the gallery facilitate leak-checking the portions of the wheel and wand supply and return lines isolated in the housing by closure of the flood control valves.

Water released by drain valves is piped downbeam into a 600-gal concrete sump tank built into the alcove at the foot of Sector 11 accessway. A low-crested dam on the floor of the housing just downbeam from girder 11-3C retains any water that leaks or is spilled from the system. Water trapped behind the dam is piped into the sump. Leakage from equipment in the concrete-shielded cubicle is collected in a concrete trench in the gallery floor and drains into the gutter on the south side of the housing floor at a point above the dam. A pump with remote control and level indication makes it possible for personnel in the gallery to empty the contents of the sump into a tank for disposal or storage, depending on the radioactivity of the water.

When power to solenoid C and the uniform field solenoids is interrupted, heat generation in the coils immediately ceases and the temperature of water leaving the coils quickly drops from 158° almost to 104°F, the temperature of the supply water. The ceramic insulators that prevent electrical short-circuits to ground along the water return lines from the individual coils would be subjected to a severe thermal shock by this sudden temperature change. To minimize the shock, the pump motors in primary circuit 1 are interlocked with the three solenoid power supplies. When any one of the power supplies is turned off, the pumps stop, thereby cutting off the supply of "cold" water to the coils. An adjustable time delay, presently set at 5 min, prevents restarting the pumps until the insulators have had a chance to cool down.

The in-line heater in each primary circuit is interlocked with its pump motor to make sure the pump is on before the heater is energized. Heaters are also interlocked so that power is cut off when failure of instrument air results in loss of temperature control.

On solenoid C and the uniform field solenoids, gas-filled, hermetically sealed, bimetallic thermostats are mounted in pairs on the outlet lead from each coil, as close to the body of the coil as possible. A normally closed contact in each thermostat opens at 186°F to break an interlock chain which, in turn, shuts off the power supply. The interlock chain is a series circuit made up of all the thermostats in any given solenoid. The thermostats protect against burnout should the water line serving a particular coil become plugged anywhere between the supply and return header on the solenoid—a condition not readily detectable as a change in the total flow through the five or six coils comprising the solenoid. Thermostats are likewise provided on the

return line from coil 1, 2, and the scraper. Protection against malfunctioning of the three-way valve is afforded by a thermal switch mounted on the piping downstream of the valve. It is set to break the interlock chain, shutting off the power supplies when the system temperature exceeds 130°F. Temperatures at thermocouples on the thirteen outlet leads from coil 0 are indicated in the Sector 11 instrumentation and control alcove.

Primary circuit 1 includes an air-operated manually controlled butterfly valve, spring returned to the normally closed position. The valve and the pump motor are interlocked through a pressure switch in the air line to the valve. The switch does not allow the pump to start until the valve is closed, as evidenced by loss of pressure in the air line. The purpose of the interlock is to protect primary circuit 1 piping from the pressure surges that accompany pump startup. Pushing the "start" button turns on the main pump of primary circuit 1. A pressure switch downstream from the air-operated valve delays startup of the sub-loop pump until the main pump is running and the valve is open.

The pressure of water supplied to the radiators is automatically controlled by an air-operated valve. The pressure of water supplied to coils 1, 2, and the scraper is controlled by a similar valve. Both valves are shown in Fig. 24-18, together with the pump in the high-pressure sub-loop. As a precaution against overpressure in the supply line to the wheel radiator, a pressure switch in the gallery is tied to the supply line in the housing through a small-diameter copper tube. Should the switch setting be exceeded, the pump is shut off. Provision is made for flushing this line with low-conductivity makeup water.

On all lines except those from coil 0, an orifice flange and differential pressure transmitter provide an air signal for indication and alarm. Rotameter-type flow indicators and low flow switches of the type used in the accelerator cooling-water systems are provided in the return lines from coil 0. Monitoring flow in the return instead of the supply line eliminates the possibility that a leak may give a false indication of adequate flow.

One of the pressure switches provided to monitor water level in the surge tank gives a low level alarm light; the other shuts off the pump when the water level drops to within 3 in. of the bottom of the tank.

Each primary circuit has its own 5-μ bypass filter and mixed bed demineralizer. A 100-mesh in-line strainer is installed at the outlet of each demineralizer. Each primary circuit is also equipped with a temperature-compensated conductivity sensor. The supply line to the radiators includes a full-flow filter in the cubicle as well as individual Y-type strainers on the wheel and wand supply lines in the housing. An additional Y-type strainer on the wand return line in the cubicle picks up any particles that may spall off the heat transfer surface of the wand during irradiation. The Y-type strainers are also used in the 6-, 2-, and $1\frac{1}{2}$-in. solenoid supply lines in the housing; similar strainers protect the pump suction on primary circuits 2 and 3.

Cooling tower water (DBR)

The cooling tower water for the two-mile accelerator is supplied from two independent systems. Cooling tower 1201 serves the first mile, through Sector 15. Cooling tower 1202 serves the second mile. The towers are located at Sectors 9 and 22, respectively, on the south side of the klystron gallery. Each tower comprises two cells of the counterflow-induced draft type. Each tower is rated at 11 MW and cools 5000 gal/min from 90° to 75°F at 68°F (wet bulb) ambient. The towers are 60 ft long, 30 ft wide, and 26 ft high. The materials are the same as those used in cooling tower 101 described earlier in the chapter.

The two-speed fan in each cell is driven by a motor which develops alternatively 15 hp and 60 hp to allow for variation in heat load. Each tower has three pumps, one of which serves as a spare. The pumps each deliver 2500 gal/min at 41-psig discharge pressure. Each pump is driven by a 75-hp motor. The pumps are of the two-stage vertical turbine type. A 30-mesh screen protects the suction well of each pump. Cooling tower 1201 appears in Fig. 24-20. The water is distributed through underground headers running along the south side of the klystron gallery. The headers include flanges for adding a tower to each system. The 16-in., cement asbestos pipe used for the headers adjacent to the tower steps down to 10 in. at the ends of each system. Valved supply and return takeoffs of 8-in. steel pipe serve branches feeding the heat exchangers in the mechanical equipment alcove of each sector. Similar $1\frac{1}{2}$-in. takeoffs serve the electrical substation alcoves. Butterfly valves are provided to isolate each exchanger for cleaning and repairs. A flow

Figure 24-20 Accelerator cooling tower 1201.

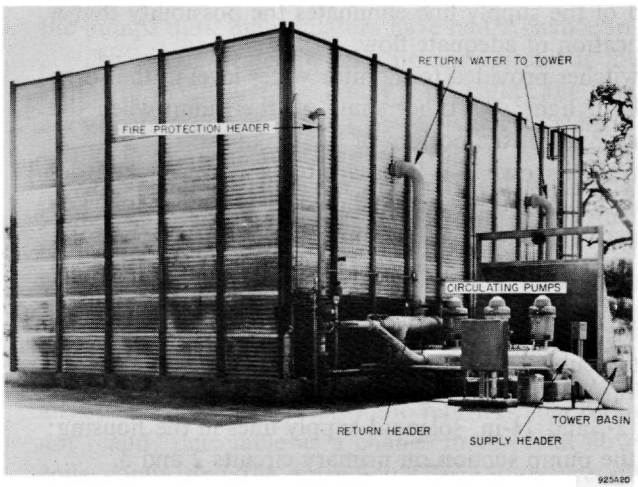

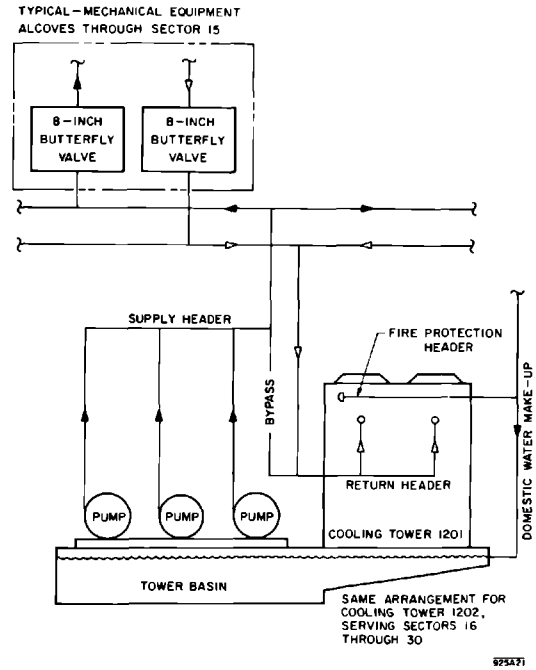

Figure 24-21 Flow diagram of accelerator cooling tower water systems.

diagram typical for the two accelerator cooling tower water systems is shown in Fig. 24-21. A two-step thermostat immersed in the basin of each tower controls the fans. When the fans are turned on, they both run at low speed. A rise in water temperature above 70°F puts one fan on high speed. The second fan goes on high speed when the water exceeds 75°F. Pump discharge pressure is indicated locally and in the Central Control Room (CCR). Makeup water is introduced as it is needed through a float-controlled valve. A low level switch shuts off the pump motors and relays an alarm to the CCR. Switches are provided which shut down the fans in the event of excessive vibration. An automatic "deluge" system protects the tower against fire.

Operating experience—accelerator cooling-water systems (CJH)

Cooling-water systems serving the injector and Sectors 1 and 2 were put into operation in September 1964. All systems through Sector 15 except the positron system were operating by August 1965. Systems in Sectors 16 through 30

were ready by October 1965. The positron system followed early in 1966. The installation subcontract required that the subcontractor flush, clean, rinse, refill, and turn on each system. Upon completion of each system, it was thoroughly flushed with domestic water to wash out bits of solder and to dissolve flux and other water-soluble foreign materials on the inside of the pipes. After flushing, the system was filled with a commercial phosphoric acid-base detergent solution and left to soak for several hours to clean out scale, products of corrosion, and other contaminants remaining after the water flush. The solution was then drained and the system was rinsed with low-conductivity water to remove all traces of the detergent. Filters were replaced, strainers were emptied, and the system was refilled with low-conductivity water. The pump was then turned on and the system was put into operation. The accelerator cooling-water systems have been operating since startup with only minor problems.

Even before all the systems were completed, continued evidence of foreign matter in those accepted as operational led to the decision to reclean and backflush all accelerator cooling-water systems. The debris afterward removed from the filters and strainers included many small droplets of solder, metal chips, fibrous paper-like materials, fragments of Teflon joint tape, pipe sealing compound, and demineralizer resin. This experience and the results from the analysis of many water samples led to the addition of strainers in each supply branch upstream from the low flow switch.

Although equipped with separate temperature controls and three-way valves, the injector constant metal temperature system and the disk-loaded waveguide system for the Sector 1 originally shared a common heat exchanger and heater. The heater was energized only through the Sector 1 controller. With the controller set at 113°F, water temperature excursions ranging between 109° and 115°F were occasionally observed in the injector system during the first months of operation, particularly when the pulse repetition rate was increased to 360 per second. Upon investigation, it was found that the temperatures of the two systems changed at different rates. When one controller called for more heat and the other for less, the temperature of the injector system fluctuated above and below that of the disk-loaded waveguide system. The "hunting" instability was attributed to the existence of separate temperature controls for water from a common recirculating source. Stability could be restored by a manual adjustment of the injector system controller to compensate for the increased range of temperature fluctuation. The problem was ultimately corrected by isolating the two systems and providing each with its own heat exchanger and heater.

Instances of low water temperature observed when the beam was off were caused by early failure of the in-line heaters described earlier. The original heaters incorporated multiple U-shaped copper-clad heating elements, heliarc welded to a stainless steel flange. The heating elements were electrically connected for 480-V delta operation. In eight or ten of the heaters, an open circuit in one leg of the delta was responsible for water temperatures running

5°–7°F below normal when the accelerator was turned off. The problem was solved by substituting stainless-clad heater elements.

A specific resistance of between 2 and 6 megohms is maintained in the various systems by using low-conductivity makeup water and by continuously bypassing 5 to 15 gal/min through a mixed bed demineralizer containing $1\frac{1}{2}$ ft^3 of resin. Regeneration of the resin is necessary about once a year.

Some difficulty was experienced with the low flow switches installed in large numbers along the accelerator to protect components from overheating due to interruption of the cooling-water supply. In practically every instance of switch failure reported, the equipment was turned off when the water flow was normal or was not turned back on when flow was restored after shutdown. Substitution of a hermetically sealed switching unit for the one furnished as original equipment has taken care of this problem.

Cooling tower makeup water is taken from the domestic supply. Although relatively soft (20–40 ppm total hardness), it is corrosive and must be treated to protect pipes and heat exchangers. Tower water is treated with a corrosion inhibitor and a biocide, both of which are commercially available products. The inhibitor contains a blend of active ingredients in a polyphosphate base. The inhibitors cover all metal surfaces with a film protecting them against the formation of anodic and cathodic corrosion cells. The maximum rate of corrosion recorded from test pieces in the several systems was less than 0.004 in./yr. The commercial biocide is toxic to microorganisms and contains a dispersant to retard microbial deposits. It is necessarily nontoxic to animal and fish life, because the overflow from the tower ends up in San Francisquito Creek.

The proper surveillance of tower water requires a number of routine tests. The pH value is measured every day. Total hardness, calcium hardness, and phosphate concentration are checked weekly. The tower baffles and the basin are inspected every month for algae, slime, and deposits of bacterial growth. Every 3 months, samples are submitted to a laboratory for the following tests: tower water microbiological analysis; slime microbiological analysis; makeup water chemical analysis for hardness, pH, and chlorides; tower basin water analysis for hardness, pH, and chlorides; and a chemical analysis of solid deposits taken from the tower piping. The test pieces in the tower system are inspected, measured, and weighed every quarter to determine corrosion rates. The results of the treatment and control of tower water as outlined above have been very satisfactory. There has been little trouble either with heat exchanger fouling or with corrosion in the tower water system.

Experience with the positron system has been much the same as that with the other accelerator systems. On one occasion, the failure of an edge-cooled magnet coil filled the system with copper and copper oxide particles. This rapidly decreased the specific resistance of the water from above 6 megohms to the neighborhood of 0.15 megohm. However, within 72 hours, continued recirculation of the water through the demineralizer cleaned up the system and increased the resistivity to an acceptable level.

24-3 Beam switchyard and end station water systems

Magnet coil cooling-water systems (SRC)

A closed-loop, low-conductivity cooling-water system serves the A-beam magnets, high-Z collimator C-10, high-Z slit SL-11, and tune-up dump D-2. A similar system serves the B-beam magnets, high-Z collimator C-0, high-Z slit SL-31, and tune-up dump D-10. The two systems are cross-connected through normally closed valves. The pump and heat exchanger in each system are designed to handle the aggregate flow of both systems. The pumps, heat exchangers, and other auxiliary equipment are located on the magnet heat exchanger pad, as depicted in Fig. 24-22. A flow diagram typical for both magnet coil, cooling-water systems is shown in Fig. 24-23.

Operating characteristics of the circulating pumps for the magnet coil cooling water systems are included in Table 24-1. The pumps are of the close-coupled single radial-stage centrifugal type. The vertical split casings and open impellers are low-zinc bronze. Shaft seals are mechanical, with a carbon rotating face, a carbide stationary face, and Teflon secondary seals.

Operating characteristics of the heat exchangers are included in Table 24-2. The shells, baffles, and tube sheets are silicon bronze. The $\frac{5}{8}$-in. o.d. tubes are 90-10 copper–nickel. Steel is used for the channels and channel covers.

Piping for the systems is copper. The fittings are copper or low-zinc bronze. Individual lengths of flexible metal hose connect the supply headers on the upper level of the BSY housing with each item of equipment in the

Figure 24-22 Magnet heat exchanger pad.

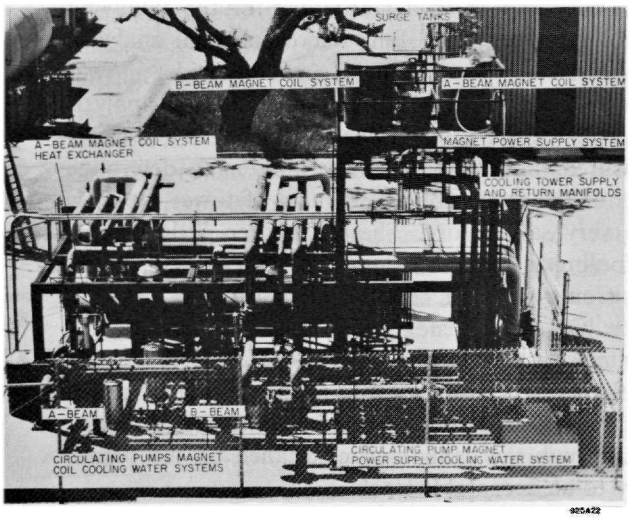

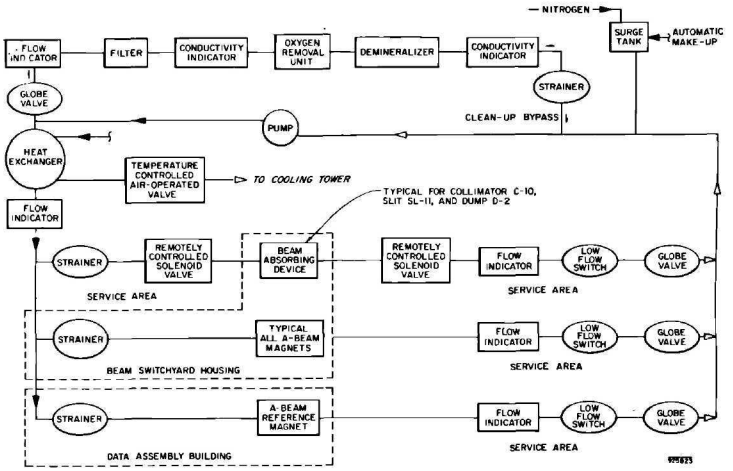

Figure 24-23 Flow diagram of magnet coil cooling-water system.

lower level. The individual return lines are flexible metal hose to the upper level and continue as rigid pipe through the service shafts to a thermometer, rotameter-type flow indicator, and a low flow switch in one of the service areas, as shown in Fig. 24-24. A single header along the cableways returns the water to the heat exchanger pad.

The low-conductivity water temperature is maintained at $95° \pm 2°F$ by an indicating controller through an air-operated butterfly valve which regulates

Figure 24-24 Return lines, magnet coil cooling-water system.

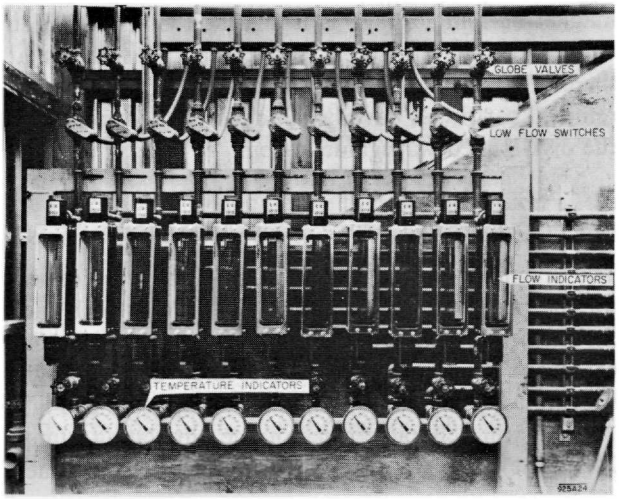

the flow of cooling tower water through the heat exchanger. The temperature-sensing element is a mercury-filled bulb. When the magnets are turned off, the flow of cooling tower water through the heat exchanger is reduced to the point where the energy contributed by the circulating pump is sufficient to hold the water temperature at 95°F to prevent condensation on the magnets and exposed conductors in the BSY housing, which is hermetically sealed during high-power beam operation.

A 115-gal copper surge tank to accommodate the thermal expansion of the cooling water in the system is located above the magnet heat exchanger pad and is connected to the return line at the pump suction. The tank is equipped with an automatic makeup water supply, a liquid level sight glass, and level controller. The makeup water is introduced through a solenoid valve controlled by a pressure switch. A nitrogen atmosphere is maintained above the water in each surge tank.

The differential pressure across an orifice downstream from the circulating pump is converted to a pneumatic signal and transmitted to a flow indicator mounted on the local control panel. When the flow rate drops below a safe level, a pressure switch actuates an alarm in the Data Assembly Building (DAB). Individual supply piping is provided from the service areas to the two collimators, two slits, and two dumps which have water-to-vacuum interfaces. To minimize the amount of water entering the vacuum system in the event of a leak at any point in the water-to-vacuum interface, remotely operated solenoid valves are provided in each supply and return line. The solenoid valves are located in the service areas. When an accident occurs they are closed from switches on the water control panel in the DAB. A pressure switch monitors the water level in the surge tank and turns on a light in the DAB when it reaches the low level alarm point. When it drops a further 6 in., another pressure switch shuts off the circulating pump.

Because of the close tolerances on momentum resolution, the allowable magnet current leakage is less than 1 mA. A buildup of a low-resistance copper oxide film across the ceramic insulators at the magnets would, therefore, be intolerable. In this system, therefore, replaceable oxygen-removal cartridges have been added to the typical cleanup bypass as used in the disk-loaded waveguide system.

Magnet power supply system (SRC)

The magnet power supply, cooling-water system serves the power supplies for the magnets used in the BSY, together with the reference magnets and the incidental test equipment in the DAB. The pump, heat exchanger, and other auxiliary equipment are located at the magnet heat exchanger pad shown in Fig. 24-22. A flow diagram appears in Fig. 24-25.

Operating characteristics of the circulating pump are included in Table 24-1. The basic features of the pump are the same as those given for the

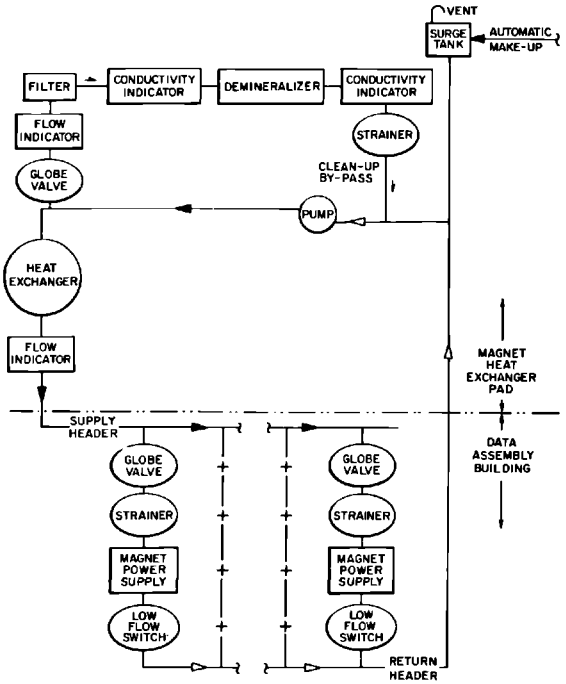

Figure 24-25 Flow diagram of magnet power supply cooling-water system.

pumps used in the magnet coil systems except that the stationary seal face is ceramic.

Operating characteristics of the heat exchangers are included in Table 24-2. The basic features of the heat exchanger are the same as those given for the exchangers used in the magnet coil systems.

The piping is copper. The fittings are copper and low-zinc bronze. The water is distributed through two sets of insulated 2-in. supply and return headers in the DAB, with individual branches to and from each piece of equipment. A block valve is included in each branch.

No temperature control is provided. The temperature varies with the ambient and load conditions.

A 20-gal copper surge tank to accommodate the thermal expansion of the cooling water is located over the magnet heat exchanger pad and is connected to the return line at the pump suction. The tank is equipped with an automatic makeup water supply, a liquid-level sight glass, and a level controller. These are similar to the ones in the magnet coil system. The tank is vented to the atmosphere.

Provision for flow indication and low flow alarm are the same as for the magnet coil system. There are no branch flow indicators. The filter demineralizer is the same as for the disk-loaded waveguide system.

Pulsed magnet power supply system (SRC)

This closed-loop, low-conductivity cooling-water system serves the pulsed magnet power supplies and two regulators. The pump, heat exchanger, and other auxiliary equipment are located in a cabinet adjacent to the power supplies in the DAB.

Operating characteristics of the circulating pump are included in Table 24-1. The basic features of the pump are the same as those given for the pumps used in the magnet coil system.

Operating characteristics of the heat exchanger are included in Table 24-2. The shell is red brass, the baffles yellow brass, the tube sheets forged brass. The $\frac{3}{8}$-in. o.d. tubes are Admiralty Metal. Forged brass is used for the channels and cast iron for the channel covers.

The piping is copper. The fittings are copper and low-zinc bronze. The water is distributed through a $2\frac{1}{2}$-in. insulated supply and return header, with individual branches to and from each power supply and regulator. Block valves are provided in each branch.

Water at a constant temperature of 85°F is required for the operation of the pulsed magnet power supplies. The method of temperature control is the same as that used in the disk-loaded waveguide system for a standard sector. An in-line electric heater of approximately 6 kW capacity brings the system up to 85°F from a cold start and holds it at temperature during periods of low-power operation.

A small copper surge tank to accommodate the thermal expansion of the cooling water in the system is located overhead. The tank is connected to the return line at the pump suction and is equipped with a liquid-level sight glass. The tank is vented to the atmosphere.

When flow drops below 80% of normal in any branch line, a low flow switch de-energizes the power supply or regulator served by that line. The filter demineralizer is the same as for the disk-loaded waveguide system.

B-beam target system (KGC)

The B-beam target, cooling-water system serves a number of small loads in the B-beam target room. Supply and return connections to the system are also provided for end station B. The pump, heat exchanger, and other auxiliary equipment are located in a shielded heat exchanger housing beside the end station, as shown in Fig. 24-26. The circulating pump is the same as used in the rectangular waveguide–drive line systems, with a single-speed motor and a single mechanical seal. Operating characteristics of the heat exchanger are included in Table 24-2. The type, arrangement, and materials are the same as for the exchanger in the pulsed magnet power supply system. The cooling tower water temperatures given in Table 24-2 include no allowance for changes in input temperature due to simultaneous operation of the radioactive systems connected in the same series cooling tower water circuit.

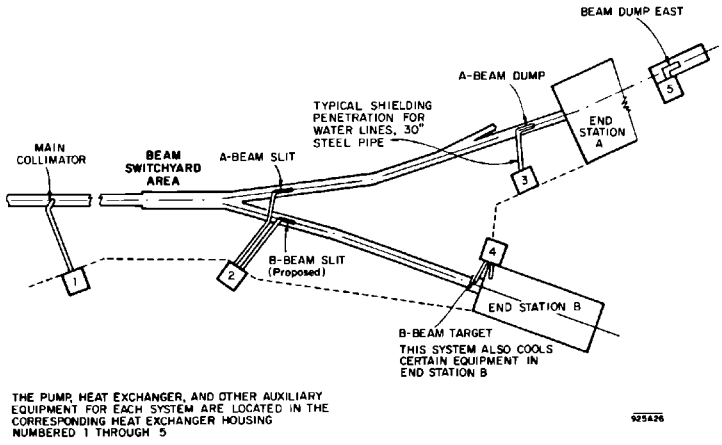

Figure 24-26 Location of B-beam target and radioactive cooling-water systems.

Copper pipe is used throughout. The fittings are copper and low-zinc bronze. A remotely controlled solenoid valve is installed in the supply header to the target room, another in the supply header to the end station. A length of flexible metal hose connects each piece of equipment to a branch from the supply header and to an individual return line. A check valve replaces a second solenoid valve in the return line. The solenoid and check valves are installed within the target room or end station shielding. In the event of a leak of sufficient magnitude to close the solenoid valve, the check valve prevents further loss of water due to reversed flow in the return line.

No temperature control is provided. The water temperature varies with the ambient and load conditions.

A 50-gal surge tank accommodates thermal expansion of the water in the system. The low alarm and pump shutdown levels are 6 and 12 in., respectively, below the operating water level. A 6-in. drop in level is equivalent to a loss of 5 gal from the 120-gal system. Makeup water is introduced through a manually controlled solenoid valve. The sump tank is vented to the atmosphere.

A positive pressure differential is maintained between the tube and shell sides of the heat exchanger. Because of the higher pressure of the cooling tower water on the tube side, any leakage will be into the radioactive shell side, thereby preventing contamination of the cooling tower. Should the pressure differential fall below a preset value, an interlock in the pump motor control circuit shuts down the circulating pump. The pump is also automatically stopped when the water level in the surge tank indicates excessive leakage from the system. Another signal simultaneously closes the two solenoid valves on the supply headers. An alarm light alerts the DAB to low flow in any of the return lines. An air-operated, manually controlled butterfly valve in the pump discharge line protects the system against pressure surges

during startup. Operation of a similar valve is described in connection with primary circuit 1 in the positron system. Pressure, level, and flow instrumentation is pneumatic, with indicators and pressure switches mounted in cabinets outside the heat exchanger housing.

The filter demineralizer is the same as for the magnet coil systems except that no provision is made for deoxygenation. Flow through the cleanup bypass is 10 gal/min.

Radioactive systems (FFH, SRC, GIS)

The radioactive systems comprise the five closed-loop, low-conductivity cooling-water systems serving the main collimator, the A-beam slit, the A-beam dump, beam dump east, and a future B-beam slit. Each system must be capable of absorbing the full energy of the beam. The pump, heat exchanger and other auxiliary equipment for each system are located in one of the heat exchanger housings shown in Fig. 24-26. When the beam strikes water, the water is partly decomposed into hydrogen and oxygen. The gases are carried through the system, eventually collecting above the water surface in the surge tank. Since flame propagation in air requires only 4% by volume of hydrogen, the resulting mixture of free hydrogen and oxygen constitutes a serious explosion hazard.

The beam power may reach 600 kW in Stage 1 and 2.2 MW ultimately. The level of radioactivity will be very high in the 1500 gal of water used to absorb the beam energy in each system. The saturation activity for a 1-MW beam has been estimated[2] as shown in Table 24-9. Hydrogen peroxide and small amounts of tritium will also be generated. Because of the radioactivity of the gases accompanying the hydrogen, particularly the carbon dioxide and tritium, venting is not permissible during high-energy runs. The presence of an explosive gas mixture and the radiation level during operation dictate the requirement for separate shielded water systems. The dangers inherent in piping radioactive water over the relatively long distances between the beam-absorbing devices and the difficulty of scheduling emergency maintenance without shutting down the beam also favors the use of individual systems.

Table 24-9 Saturation activity for a 1-MW beam

Radioactive isotope	*Half-life (min)*	*Activity (Ci)*
Oxygen-15	2	35,000
Nitrogen-13	10	1,390
Carbon-11, present in CO_2	20	1,390
Beryllium-7	(53 days)	280
Total activity		38,060

The two most promising ways of removing the hydrogen were by delayed venting and by recombination with oxygen to form water. In comparison with a recombiner for each closed-loop water system, studies showed that economical removal of the CO_2 would require a costly chemical complex, including a holdup tank and the piping linking the tank with the CO_2 removal equipment, the radioactive cooling-water systems, and the atmosphere. It was found that the ^7Be is effectively removed in the demineralizers, thus greatly reducing the time after shutdown before the system is accessible for maintenance.[3] The metal surfaces in contact with the radioactive water are Type 316L stainless steel except as noted below. This material is compatible with the aluminum used in the collimators and slits and the copper used in the beam dumps. It is also relatively insensitive to carbide precipitation in the heat-affected zones adjacent to welds and is less susceptible than the other 18-8 stainless steels to stress corrosion cracking and pitting corrosion in the presence of chlorides. Where a cast material was required, as for the valve bodies, pump casings, and impellers, cast Type 316 stainless steel was used.

Operating characteristics of the circulating pumps at 1750 rpm are included in Table 24-1. The pumps are of the single-stage radial centrifugal type. The vertical-split casings and open impellers are Type 316 stainless steel. The pumps are driven through flexible couplings by two-speed (875/1750 rpm) motors, since half the rated flow will suffice during most of Stage 1 operation. Calculations also indicate that the life of the beam-line windows in the two dumps can be greatly increased by reducing the water pressure. The double mechanical seal used in each pump is of the type used in the pumps in primary circuit 1 of the positron system, except that the secondary seals are Buna-N. At the dose rate measured along the pump shaft, it is predicted that the carbon and ceramic sealing faces themselves will wear out at least 2 yr before the secondary seals succumb to radiation damage. A pump seal injection circuit similar to that described for the positron system circulates low-conductivity water at 100 psig through the space between the two shaft seals. The seal injection circuit also supplies water to back up the polyurethane O-rings sealing the stem of the air-operated valve in the pump discharge line. The transfer pumps are of the self-priming centrifugal type, with a single mechanical shaft seal. They are used to move the water between the system and a mobile retention tank. Transfer hoses may be attached to blind flanges provided on each system.

Operating characteristics of the heat exchangers are included in Table 24-2. All joints between the tube and shell sides of the exchangers are seal-welded to avoid any possibility of radioactive water diffusing into the cooling tower water system. A mass spectrometer-type leak detector sensitive to less than 1×10^{-7} cm^3/sec of helium at atmospheric pressure was used to establish the integrity of each exchanger.

Type 316L stainless steel pipe of x-ray quality was used throughout. The welds were made by the heliarc process using AWS/ASTM, Type ER 316L

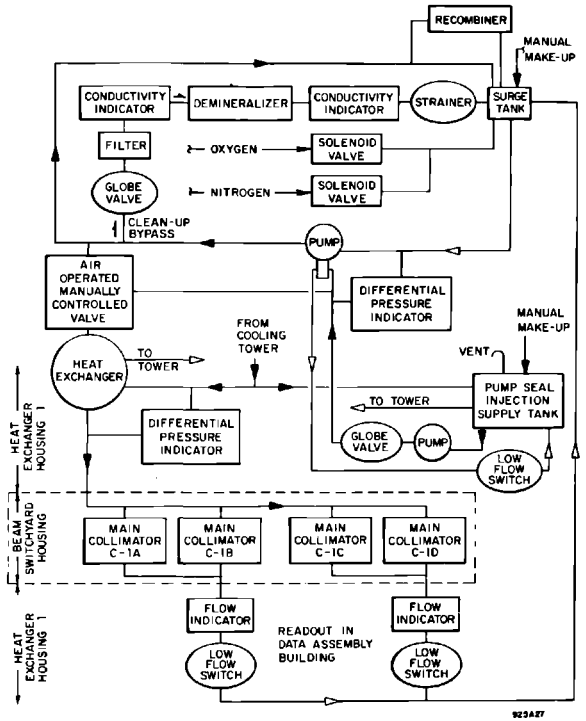

Figure 24-27 Flow diagram of typical radioactive cooling-water system.

filler rod.* Both the welders and the procedures were qualified under the provisions of the American Society of Mechanical Engineers Boiler and Pressure Vessel Code. All welds were radiographically examined. The supply and return headers for each system leave the heat exchanger housing through a large-diameter access sleeve and enter the lower level of the BSY housing near the device they serve. Flexible metal hoses with remote disconnect couplings at both ends connect the supply and return headers to the device. Provision is made for draining each system through a line passing through the access sleeve to the transfer pump. A flow diagram for the system serving the collimator is included in Fig. 24-27. It is typical of the radioactive water systems discussed in this section.

No temperature control is provided. The temperature varies with the ambient and load conditions.

The surge tanks are of all-welded stainless steel construction as shown in Fig. 24-28. To help separate the entrained gases, the return water is introduced tangentially above a perforated plate. The water level is maintained

* American Welding Society/American Society for Testing and Materials.

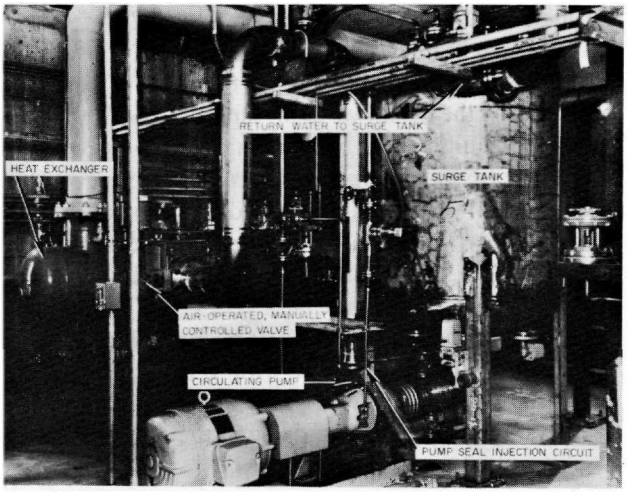

Figure 24-28 Surge tank, radioactive cooling-water system.

below the plate. The water returns to the pump suction through an anti-vortexing arrangement to prevent pump cavitation. The manually operated, makeup valves for each surge tank and seal injection supply tank are located outside the shielded housing.

The recombiner which eliminates the explosion hazard by disposing of the free hydrogen mounts on the top of the surge tank. The gases in the tank are drawn through a heated catalyst which recombines the hydrogen and oxygen. To make sure that there is always a surplus of oxygen, an oxygen sensor is connected to the recombiner. If it reads too low, a solenoid valve is automatically opened, admitting additional oxygen through the bottom of the surge tank. Provision is made for flooding the surge tank with nitrogen should the hydrogen content of the evolved gases rise above 2%.

Five interlocks stop the pump of the respective radioactive system and interrupt the beam under the following conditions:

1. Low differential pressure between the pump seal injection circuit and the main pump suction
2. Low level in the seal injection supply tank
3. Low flow in the seal injection circuit
4. Low level in the surge tank
5. High level in the surge tank.

To keep makeup water from leaking through the supply valves and overfilling the surge tanks and seal injection supply tanks, normally closed valves are installed in pairs, one at each end of a "T" in the supply line. The valve on the tank side is of the spring-return type. During operation, leakage

through the valve on the supply side is drained through a normally open valve on the branch of the "T."

To prevent pressure surges from damaging any part of the system, particularly the windows that separate the water from the vacuum in the two beam dumps, the main pumps are interlocked so that they cannot be started until an air-operated manually controlled butterfly valve in the respective discharge line is closed. The valve is opened after the pump is started. Operation of a similar valve is described more fully in connection with primary circuit 1 in the positron cooling-water system.

The filters and demineralizers are the same as those used in the disk-loaded waveguide systems except that the demineralizer tank is of all-welded construction and is shielded with 1 in. of lead around the periphery. The conductivity of the water is measured before and after the demineralizer in each system. The flow rate through the cleanup bypass is 10 gal/min.

Target area cooling-water system (FFH, SRC)

The 41,500-gal target area system serving end station A, end station B, the research yard, and the cryogenics building is the largest of the low-conductivity, cooling-water systems. The system also supplies low-conductivity makeup water to cooling-water systems in the BSY and the end stations and can be used to supply makeup water to LCW systems in the klystron gallery. A flow diagram is given in Fig. 24-29. At present, the system includes four circulating pumps and six heat exchangers. Provision is made for the addition of a fifth pump. Figure 24-30 shows the pumps and cooling tower 1701, in which the heat exchangers are located.

Figure 24-29 Flow diagram of target area cooling-water system.

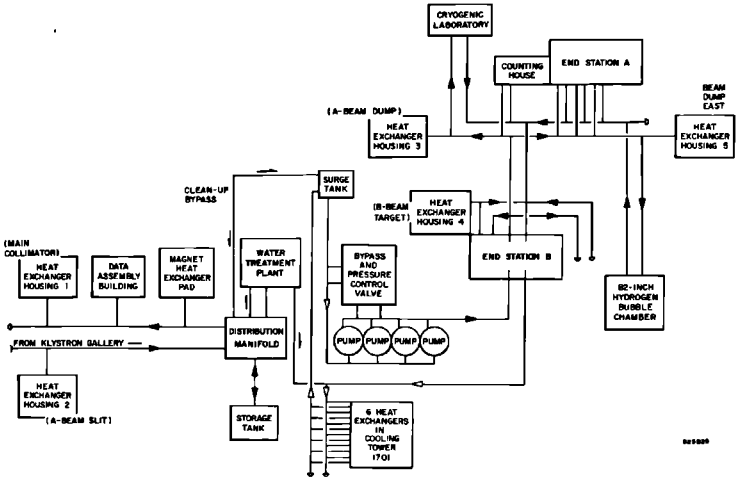

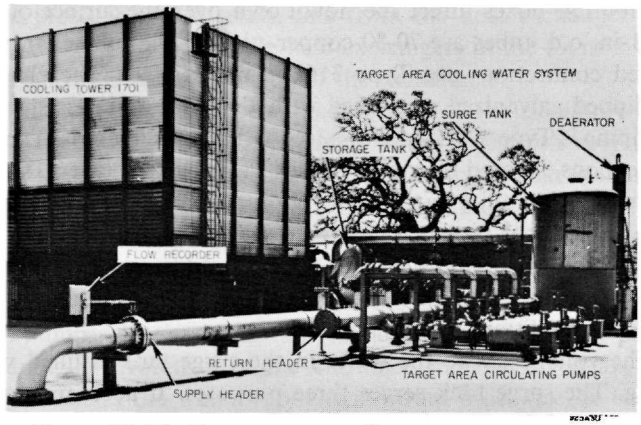

Figure 24-30 Target area cooling-water pumps.

Operating characteristics of the circulating pumps are included in Table 24-1. The pumps are of the single radial stage centrifugal type. The vertical-split casings and open impellers are Type 316 stainless steel. The shaft seals are mechanical, with a carbon rotating face, a ceramic stationary face, and Teflon secondary seals. The pumps are driven through flexible couplings.

Operating characteristics of the heat exchangers are included in Table 24-2. The six exchangers are of the atmospheric coil type. The tubes are formed into rectangular coil sections. Each exchanger is made up of two coil sections. The exchangers are mounted in a common horizontal plane in two of the three cells of cooling tower 1701—four in one cell, two in another—as shown in Fig. 24-31. The cooling tower water is collected in pans above the exchangers.

Figure 24-31 Flow diagram of beam switchyard cooling tower water system.

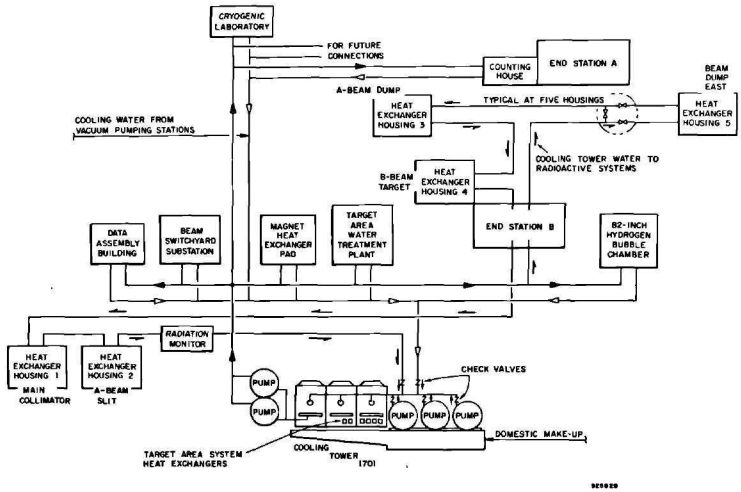

Distribution boxes direct the flow down over the surface of the bare tubes. The 1-in. o.d. tubes are 70-30 copper–nickel. The tube channels, baffles, and flanged connections are Type 316L stainless steel. The channel covers are hot-dipped galvanized steel lined with Type 304 stainless steel sheet.

Piping is Type 304L stainless steel with two exceptions. The heat exchanger connections exposed to cooling tower water are Type 316L stainless steel and the lines in the utility yard in sizes through 4-in. nominal diameter are copper pipe. The copper pipe is joined with self-fluxing silver brazing alloy. A flow recorder is provided in the main supply header.

No temperature control is provided. The temperature varies with ambient and load conditions.

The volume above the water in the surge tank is filled with nitrogen at 2 psig. The surge tank serves three purposes. It accommodates the thermal expansion of the water in the system; it pressurizes the system to prevent the entry of air when the pumps are not operating; and it provides a 4500-gal reservoir immediately available to make up for losses from the system, or, in the event of a major line break, to give the operators time to shut down the research equipment before the circulating pumps stop. The water level in the tank is float-controlled. When the level is low, a valve is opened and make-up water from the storage tank is admitted through the transfer pump. When the system is full, another valve drains excess water back into the storage tank. The surge tank has a total capacity of 6300 gal and a design pressure of 15 psig. A relief valve set at 12 psig protects the tank against overpressure. A vacuum breaker is also provided. The tank is of all-welded construction, using Type 304L stainless steel, and conforms to the requirements of the American Society of Mechanical Engineers Boiler and Pressure Vessel Code. It is mounted vertically on a carbon steel skirt.

The makeup water for the target area system is provided from a storage tank normally containing between 8000 and 12,000 gal of low-conductivity water. The volume above the water in the tank is filled with nitrogen at from 1 to 15 psig. The water level in the tank is float-controlled. When the level is low, a valve is opened admitting low-conductivity, i.e., distilled and demineralized makeup water received from the distilled water plant through the klystron gallery header. A 2-in. hose connection is provided for loading or unloading tank trucks. Should the need arise, water from the storage tank can be pumped back into the klystron gallery header.

The storage tank has a total capacity of 16,900 gal and is mounted horizontally on two steel saddles supported on concrete piers. It is protected against overpressure by a relief valve set at the design pressure of 15 psig. A vacuum breaker is also provided. The tank is of all-welded construction, using Type 304L stainless steel, and conforms to the requirements of the American Society of Mechanical Engineers Boiler and Pressure Vessel Code.

A stable supply pressure is insured by a 4-in. air-operated pressure control valve which bypasses water from the supply header to the return header when the supply pressure exceeds 275 psig. The valve also opens the

bypass when the pressure in the return line from the heat exchanger coils exceeds 100 psig, thereby protecting the heat exchangers in the event a valve should be closed on the downstream side of the exchangers.

The water treatment plant is an enlarged version of the cleanup bypass used to maintain high purity low-conductivity water in the other systems. A 3-in. branch off the 16-in. return header upstream from the heat exchangers carries the water being bypassed through a filter and into a deaerator. The deaerator is an upright cylindrical tank, relatively tall in comparison to its diameter. The water inlet and outlet are through the top and bottom heads, respectively. Another line leads from the top of the tank to a heat exchanger and two vacuum pumps. As the water falls through the deaerator, a partial vacuum encourages the evolution of the entrained and dissolved air. The heat exchanger condenses the water vapor that would otherwise be carried over into the vacuum pumps. A control valve responsive to the water level in the deaerator adjusts the rate at which water flows into the tank to equal the rate at which it is pumped out at the bottom. A transfer pump returns the air-free water through one of the two demineralizers to the surge tank. The 33 ft^3 capacity of each demineralizer is further evidence of the relative size of the target area system. In comparison, the demineralizers used throughout the rest of the system hold only $1\frac{1}{2}$ ft^3 of resin. Two filters and two transfer pumps are also provided, with interconnections affording the maximum operating flexibility.

Cooling tower water (SRC)

Cooling tower 1701 serves the heat exchangers in the BSY and end stations, the air compressor in the BSY substation, and equipment in the data assembly and cryogenic laboratory. It is located southeast of the DAB. The tower includes three cells of the counterflow induced draft type. It is rated at 23 MW when cooling 8700 gal/min from 93° to 75°F at 65°F (wet bulb) ambient. The tower is 92 ft long, 32 ft wide, and 33 ft high. The materials are the same as those used in cooling tower 101 described in a previous section, except that the fill is plastic.

The two-speed fan in each cell is driven by a motor which develops, alternatively, 15 and 60 hp to allow for variation in heat load. The two main circulating pumps each deliver 2400 gal/min at 80-psig discharge. Each is driven by a 150-hp motor. These pumps are of the two-stage vertical turbine type. They circulate water from a pan inside the tower through the cooling tower water system piping to the heat exchanger areas and to buildings throughout the target area. The three tower recirculating pumps each deliver 4600 gal/min at 36-psig discharge. Each is driven by a 125-hp motor. These pumps are of the single-stage vertical turbine type. They take water from the tower basin and recirculate it through the spray heads at the top of the tower. Normally one pump in each set is a spare. The pump suction wells are protected by 30-mesh screens.

Six atmospheric-type heat exchangers are provided within the tower to cool the target area, low-conductivity water. As previously mentioned, the heat exchangers for the radioactive systems and the B-beam target system are connected in series, with cooling tower water flowing successively through the exchangers serving beam dump east, A-beam dump, B-beam target, the main collimator, A-beam slit, and, eventually, B-beam slit. Bypasses are provided so that failure of an exchanger will not interfere with the operation of the system as a whole.

A radiation monitor is located in the cooling tower return line at the BSY substation. Should radioactivity ever be detected in the cooling tower water, the monitor will turn on an alarm light in the DAB and shut down the cooling tower water circulating pumps.

Makeup is taken directly from the domestic water supply or indirectly from vacuum pumping stations PS-0 through PS-6. The domestic water which cools the pumps discharges into the cooling tower return header. A float-controlled valve automatically regulates the amount of water taken from the domestic supply. A flow diagram of the system is shown in Fig. 24-31.

The fans are equipped with excess vibration shutdown switches. An automatic "deluge" system protects the tower against fire.

Operating experience—Beam switchyard and end station systems (CJH)

The magnet coil, magnet power supply, and pulsed magnet power supply, cooling-water systems were put into operation during the summer of 1966 in essentially the same manner as outlined in the section covering accelerator system operating experience. No major problems have been encountered in these systems. The low flow switches protecting the magnets against failure of the cooling-water supply have been modified in the manner previously described. Low-conductivity water has been maintained in the radioactive systems by diverting approximately 10 gal/min through a bypass demineralizer. Specific resistance varies from 0.5 to 1.5 megohms depending on the condition of the demineralizer and the degree of contamination generated in the system. The demineralizers in these systems contain $1\frac{1}{2}$ ft^3 of resin which lasts about 6 weeks between regenerations. Special procedures have been worked out for handling the resins because of the radioactivity of the ^7Be isotope removed from the water.

Hydrogen evolution in the A-beam dump, cooling-water system caused numerous beam shutoffs. With the development and installation of a hydrogen recombiner, operation has become relatively routine.

The full capacity of the four 1500-gal/min pumps in the target area, low-conductivity cooling-water system has yet to be utilized. Pump discharge pressure is 269 psig. Users in the end stations require that a pressure not less that 230 psi be maintained at the pumps and that pressure surges be held as low as possible. Manual operation of the pump controls, supply valves, and the bypass valve between the main supply and return headers are often

necessary to hold the pressure within these limits when user's equipment drawing over 600 gal/min is suddenly thrown on or off the target area system. Load changes up to 600 gal/min are automatically accommodated by an air-operated, pressure control valve on the bypass between the main supply and return headers. A controller adjusts the valve opening to maintain a constant pressure in the supply header.

The water treatment plant serving the target area system includes two demineralizers, each containing 33 ft^3 of mixed bed resin. The demineralizers are used one at a time. When the resin in the first demineralizer is fully depleted, it is removed for regeneration and the second demineralizer is valved into the system. When the system was started up, the first demineralizer lasted 3 months. The second demineralizer was still good after 8 months of operation. Specific resistance of the water normally runs about 4 megohms.

The treatment plant also includes a deaerator. An external heat exchanger is provided to condense the moisture out of the air leaving the deaerator. Due to insufficient cooling, quantities of water vapor were being carried over into the vacuum pumps that remove the air. The original exchanger was replaced with one having a larger cooling capacity.

At one time or another, failure to close the supply valves before the return valves has resulted in damage to a user's equipment and piping, particularly if it was designed to withstand less than the full supply pressure of the target area system. Users who wish to tie into the system are now required to install check and relief valves to protect their equipment against overpressure.

Cooling tower water is chemically controlled, using the same techniques as in the accelerator system cooling towers. It has been much more difficult to hold the water in this system within the desired limits because of the influx of domestic water from several small vacuum pumping stations. When the tower is operating at very light loads, the amount of domestic water discharged into the system as a conservation measure often exceeds the losses due to evaporation and leakage. The constant overflow carries a portion of the treatment chemicals out of the basin into the nearby storm sewer before they become thoroughly mixed into the system.

The graphite-impregnated packing used in the seal injection pumps in the radioactive systems leaked continuously. It was difficult to stop the leak by tightening the packing without causing the shaft to seize. The packing was replaced with mechanical seals.

Acknowledgments

In addition to the authors noted under the chapter heading, many other people made significant contributions to the cooling-water design. P. Warrington was responsible for many system calculations and specifications for equipment. J. Jurow consulted on basic cooling calculations and pump selection. R. B. Neal, E. L. Garwin, A. L. Eldredge, J. V. Lebacqz, and

A. V. Lisin were invaluable in advising on design details and material selection. G. Rogers consulted on corrosion problems and worked on the development of cooling tower water systems. F. Bonaudi and D. Coward consulted extensively on the design of the target area, closed-loop, low-conductivity water system. G. Greske developed a number of system control schemes. F. Leone developed the design of the positron source, closed-loop systems. W. Springhorn was very helpful in establishing piping and equipment layouts. G. Fritzke consulted on metallurgy and radiography. H. Hagaman assisted in designing flexible piping connections to critical beam switchyard equipment. L. Lucas, H. Ross, R. Vetterlein, D. Walz, and H. Weidner assisted in developing criteria for beam switchyard cooling-water systems. J. Anderson was very helpful in piping stress analysis and solving installation problems relating to the beam switchyard remotely operated disconnect couplings for beam energy absorbers. G. Egg assisted in stainless steel welding inspection and related problems. R. Robbers was invaluable in working out field construction problems with the contractors. W. Lusebrink and R. Lingley were very helpful in putting systems into operation and developing maintenance programs.

References

1 H. DeStaebler, Jr., "Activation of the Cooling Water," Rept. No. SLAC-TN-61-19, Stanford Linear Accelerator Center, Stanford University, Stanford, California (November 1961).

2 D. Coward, internal memorandum, Stanford Linear Accelerator Center, Stanford University, Stanford, California (May 21, 1965).

3 R. McCall, "Activation of Water during Beam Tests," Rept. No. SLAC-TN-66-4, Stanford Linear Accelerator Center, Stanford University, Stanford, California (January 1966).

25

ELECTRICAL POWER SYSTEM

P. C. Edwards, F. F. Hall, C. B. Jones, I. L. Krumholz, M. A. Machicao, F. G. Poblenz, and A. A. Tseng, Editor

Before delving into the systems aspects of supplying electric power to the project, it should be noted that the project is a national facility for scientific research. It is anticipated that the present power system will continuously be subjected to unforeseen requirements for expansion, conversion, or change in emphasis of power usage, especially in the research areas.

The two-mile accelerator project as now installed has a connected load of 105 MVA. The peak demand in 1967 is expected to be 60 MVA. The demand is expected to triple within the next 5 yr. The SLAC load experience and forecast of maximum megawatt demands as estimated in 1967 are shown in Fig. 25-1.

A prime consideration in the design of the power system was its reliability of operation. The reliability of the many components was, therefore, studied and analyzed in depth. The major questions to be answered were: (1) how reliable should the system be, and (2) how much of the available funds should be spent to obtain a higher degree of reliability?

In mid-1962, a firm criterion for power system reliability was established. In essence, it was realized that the project is not a critical process plant in which loss of power could cause months of cleaning and rebuilding time. The accelerator needs reliable power, but the project will frequently shut down for readjustment, maintenance, and/or repair. Short-time outages lasting from fractions of a second to a few minutes will turn the accelerator off, but it can be readily restarted. Outages of a few minutes to a few hours will necessitate some readjustment to prevent damage to equipment, but the critical vacuum system can be maintained. Outages of more than a few hours could cause a loss of vacuum in some systems and loss of temperature control which would require vacuum pumping and some adjustments to get the accelerator back into operation.

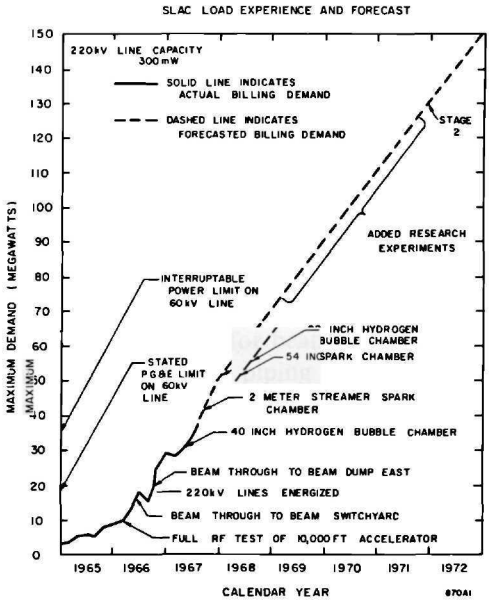

Figure 25-1 SLAC load experience and forecast.

Figure 25-2 Single 220-kV line on tubular steel poles.

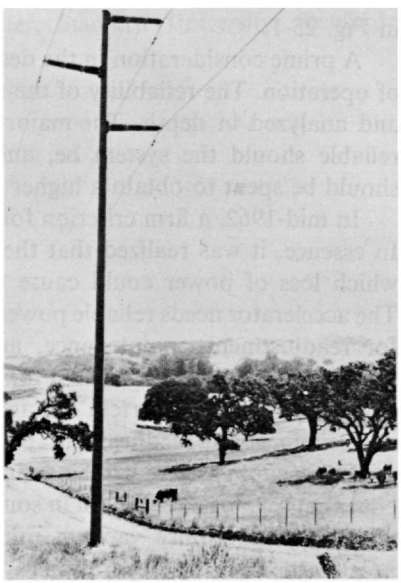

The above concept of reliability led to the following design criteria:

1. Two 220-kV overhead supply circuits, each capable of delivering 300 MVA to the project.
2. Two 40-MVA, 220–12.47-kV transformers.
3. Two 12.47-kV buses connected through a tie circuit breaker.
4. Dual cable service throughout the project.
5. Double-ended substations for critical loads.

The community of Woodside objected to an overhead power line serving the project. Unfortunately, it was necessary to use an overhead power line instead of an underground cable because of its much lower cost. However, their concern resulted in extensive studies to find how best to reduce the impact of such an installation. It was decided to use tubular steel poles (see Fig. 25-2) rather than the conventional trussed towers (see Fig. 25-3), and the design of the line was modified. This provides an installation of greatly improved appearance as compared with a steel lattice-work mast design. In modifying the appearance of the line, the primary service had to be reduced to one 220-kV 300-MVA circuit. The single circuit service concept, together with the limited standby source of 60-kV power and further economic considerations, resulted in a recommendation to use one 83-MVA, 220–12.47-kV transformer and two 15-MVA, 60–12.47-kV transformers. The change in concept for the 220-kV line reduced the reliability of items 1, 2, and 3 above. Items 4 and 5 remained the same.

The final decisions and actual electrical system installation are outlined in this chapter.

Figure 25-3 Conventional trussed tower for 220-kV line.

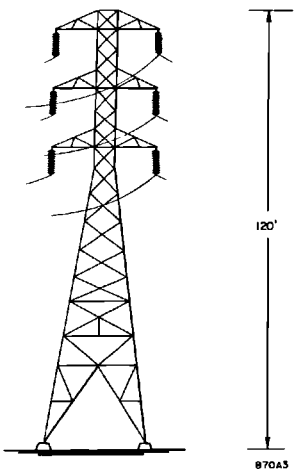

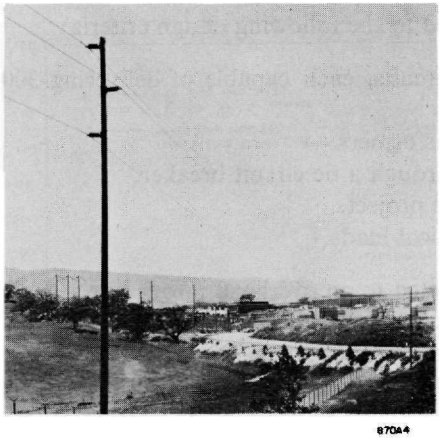

Figure 25-4 Single 60-kV line carried on wood poles.

25-1 Primary services (PCE, AAT)

There are two ac power services to the SLAC site. The first is the 60-kV service. This service supplied power for construction and the initial operational tests of the accelerator. It now serves as a second source of power and provides a backup for the major source. The 60-kV service is classified a second source because the available power is limited to 18 MW with an ultimate capacity of 30 MW. Moreover, the nature of this 60-kV transmission system makes it subject to more interruptions than are acceptable to project operations.

The second is the 220-kV service, which is the major source of power for SLAC. It supplies energy for all the site loads because this service's capacity is adequate for the project power demands and, of the available sources, it is the least subject to unplanned outages.

The 60-kV service will be used when the 220-kV is not available during maintenance work on the project's transmission line or transformer or during the rare instances of 220-kV interruption.

The 220-kV service is tapped from the Pacific Gas and Electric Company (PG & E) Jefferson-Monta Vista transmission line west of the accelerator site and the 60-kV service is connected to SLAC's master substation by a short PG & E transmission line from a nearby 60-kV line east of the accelerator site. This 60-kV line is insulated by post-type insulators which are mounted on wood poles (see Fig. 25-4). The location of the site ac power service sources is shown on Fig. 25-5. The 220-kV tap line (1113 MCM, all aluminum conductor) has an ultimate capability of 300 MVA based on current PG & E system loading limits.

The project's 220-kV service line, which is 6 miles long, utilizes post-type insulators and hollow steel tapered masts where possible. The design of this

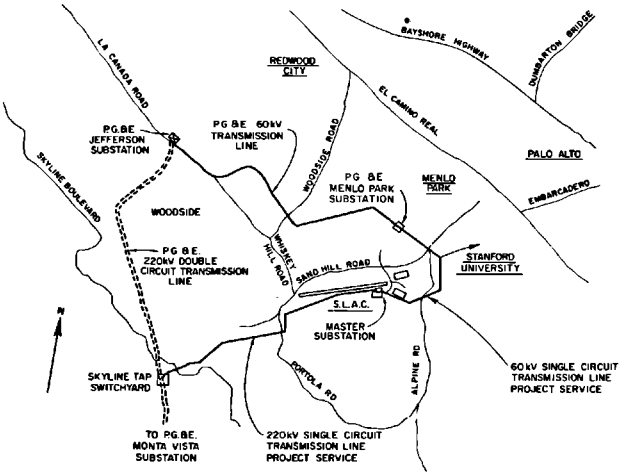

Figure 25-5 Location of site ac power service source.

line is based on considerations of safety, minimum sight impact on neighboring communities, and minimum interference with nearby scientific research activities. The line as constructed blends into the terrain. The adjacent Stanford University radioscience projects are not affected by the operation of the 220-kV line and associated apparatus.

The terminal point for the 220- and 60-kV ac power service lines is the SLAC master substation shown in Fig. 25-6. The site ac power is supplied by

Figure 25-6 Single-line diagram of site ac power service and master substation.

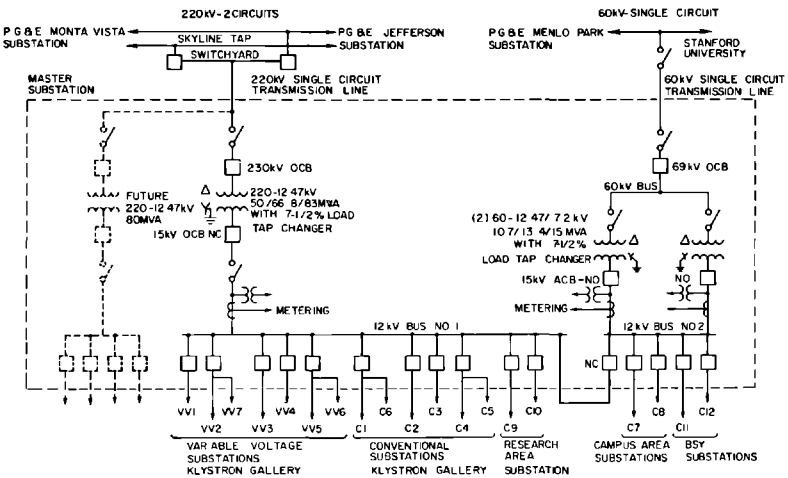

the PG & E at transmission voltages and, therefore, SLAC provides the transformation to 12.47 kV which is distributed throughout the site by an underground cable system. The 60- and 220-kV services cannot be interconnected through the site 12.47-kV system because interconnection at this point is unacceptable from utility operation and safety considerations and because the two high-voltage systems are not in phase.

The project's master substation (see Fig. 25-7) is located near the geographical center of the electrical loads. This substation is a part of the original facilities construction program and is operated by SLAC. The decision favoring project construction and operation as compared with PG & E construction, ownership, and operation is based upon (1) avoiding the commitment of project funds to guarantee to PG & E the installation cost (plus removal expense but minus salvage value) of the substation; (2) the small savings in the power bill resulting from taking the ac power service at transmission voltages; (3) the more effective handling of the fifteen 12.47-kV distribution feeders radiating from the master substation; and (4) the desirability of direct SLAC responsibility for apparatus specification, construction, supervision, and operation management without limitation other than contractual stipulations.

The master substation provides essential features in the receiving, voltage transformation, control, and metering of electric energy. This is briefly described by the one-line diagram, Fig. 25-6. The substation consists of an outdoor high-voltage yard, a switch house, and an outgoing feeder cable vault under the switch house. The substation outline plan is shown in Fig. 25-8.

The high-voltage yard contains the 60- and 220-kV switchgear, the 220–12.47-kV transformer, the two 60–12.47-kV transformers, a 230-kV class oil circuit breaker, a 69-kV class oil circuit breaker, and a 15-kV class oil circuit breaker. All high-voltage apparatus, insulators, energized components, and bus hardware are in accordance with low radio noise influence factor specifications. The 220-kV bus work is designed for 1050-kV basic

Figure 25-7 View of master substation.

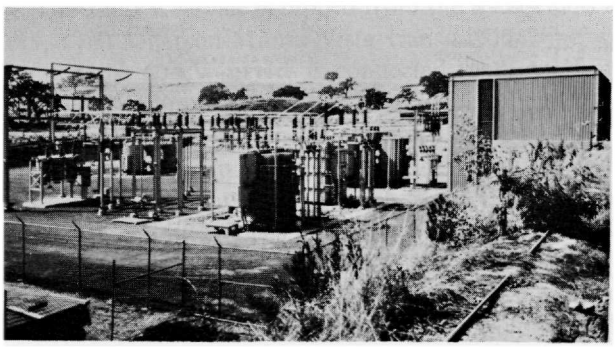

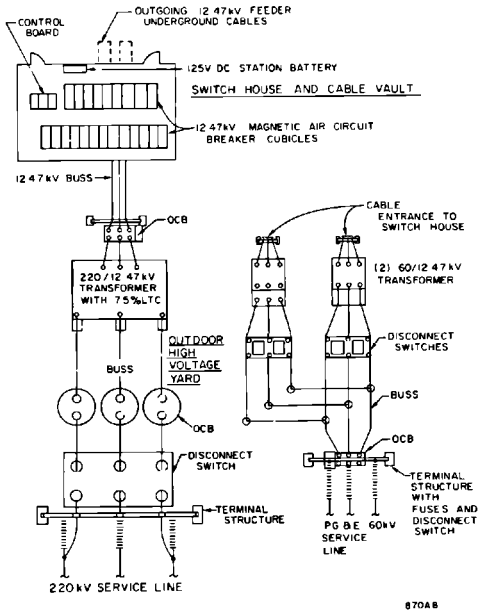

Figure 25-8
Outline plan of master substation.

insulation level (BIL). The 220–12.47-kV transformer is reduced to 825-kV BIL using 75% rated lightning arrestors. The 12.47-kV switchgear is rated at 110-kV BIL. The transmission-line terminal structure, high-voltage buses, support insulators and structure are low profile-type units as shown in the photograph, Fig. 25-7, in order to achieve a more acceptable appearance than that resulting from conventional substation structures. The 12.47-kV distribution voltage at the site matches PG & E's practice, thus increasing the possibility of rapid transformer replacements in the event of failure. Also, PG & E's local area 12-kV distribution is usable if required to supply temporary power to a portion of the project. This low-voltage service was used during initial construction phases prior to the availability of the 60–12.47-kV transformer and switchyard. The power transformer installations are fitted with a high-pressure water sprinkler system, automatically turned on by flame-sensing devices. This provides an effective damage control in the event a power transformer tank ruptures allowing oil to pour out and feed a fire. Rock-filled oil sumps are provided under the major oil filled apparatus. These sumps have adequate capacity for both oil and water and the rock fill insulates the oil from the flame.

The power transformers are oil-insulated and oil-cooled. They are manufactured to rigorous industrial standards and are provided with air cooled radiators through which the oil is circulated. Fans are installed on the radiators to allow an increased power capacity over the self-cooled rating. The

220–12.47-kV transformer has a set of oil pumps that circulate oil through the radiators. This additional circulation feature adds to the cooling effectiveness which increases the rating of the transformer from 50 to 83 MVA.

The switch house contains a 125-volt dc station control battery, dc rectifier, and battery charger. The battery is composed of nickel–cadmium cells, which do not require ventilation hoods, and specially enclosed racks. Included in the switch house are 1600 and 2000-A magnetic blowout air circuit breakers, three PG & E revenue metering sets, switchgear controls, dead front and back switchgear cubicles, and power demand monitoring information transmitters. Provisions are made for portable metering arrangements to monitor incoming or outgoing volts, amperes, watts, and vars.

Protective relaying is included in the apparatus to sense line-to-ground faults, line-to-line short circuits, and low system voltage. Interruptible power is defined by means of underfrequency relays.

The SLAC load requirements are supplied by the PG & E high-voltage transmission network. Present (1967) total generating capacity of this network is 8034 MW. The PG & E maximum demand reported for 1966 is 7392 MW. The project load is of a magnitude that requires consideration in the circuit of the whole PG & E system. For example, uncontrolled switching of the total SLAC load affects the PG & E system stability and produces a transient swing of frequency. Because of the system's reactance, the sudden switching of 26 MVA of load produces a phase angle shift of the voltage at the load bus as compared with the phase angle of the generated voltage. The sudden shift is equivalent to a 0.3-Hz phase modulation for a fraction of a second.

The source impedance of the 220-kV ac power service is 0.5% resistance and 4.85% reactance on a 100-MVA base. The 220–12.47-kV, 50-MVA power transformer adds to this value to make the total at the master substation (bus No. 1) 2.07% resistance and 29.85% reactance on a 100-MVA base. The ohmic values are 0.032 ohm resistance and 0.46 ohm reactance. These values will decrease somewhat as the PG & E system grows. The voltage drop that results from loading the system is automatically compensated by two features that return the voltage to the desired level within 10 to 15 sec. The first is the regulation control of the PG & E system output voltage. The second is the automatic tap changing device on the 220–12.47-kV power transformer. This device operates under load and is designated as a load tap changer (LTC) on Fig. 25-6. Bus No. 1 voltage at the master substation is regulated by these two means to within $\pm 0.8\%$. This provides a stable base from which to operate the system.

The source impedance of the 60-kV ac power service is 2% resistance and 17.4% reactance on a 100-MVA base. The 60–12.47-kV, 10.7-MVA power transformer adds to this value to make the total at the master substation bus No. 2, 7.1% resistance and 87.4% reactance on a 100-MVA base. The

Table 25-1 Tabulation of limited research and accelerator operation with ac power service from 60-kV system

Support and service area	3.0 MW
Klystron gallery house power	5.2 MW
Beam switchyard and Data Assembly Building	1.3 MW
End station house power	1.5 MW
Subtotal	11.0 MW
Accelerator operation, 18 GeV and 60 pulses/sec	3.7 MW
Beam switchyard operation, 18 GeV	0.4 MW
End station B, transport system operation, 12 GeV	2.9 MW
Total	18.0 MW

ohmic values are 0.11 ohm resistance and 1.4 ohms reactance at the 12.47-kV bus No. 2. The 60-kV transformers are supplied with load tap changing features. The PG & E 220–60-kV power transformers in the Jefferson substation are also regulated by load tap changing gear. Bus No. 2 voltage at the master substation is regulated by these two means to within $\pm 0.8\%$.

The limit of 18 MW when power is supplied only by the 60-kV line imposes restrictions on the project's operations. For example, the accelerator can operate at low pulse rate and support limited research as shown in Table 25-1.

25-2 On-site, 12.47-kV power distribution (PCE, FFH)

The present 12.47-kV on-site distribution system was selected through many stages of developments. As noted previously, the 12.47-kV distribution voltage matches PG & E's 12-kV practice, thus increasing the possibility of rapid transformer replacement and permitting use of the local area 12-kV system if required to supply temporary power to a portion of the project. It is interesting to note that early studies of on-site power distribution for the project considered voltages from 480 to 13,800 V, with overhead pole lines, cables through the klystron gallery, direct burial cable, and an underground cable-duct system. The above-grade pole line system while being the least expensive was quickly discarded for aesthetic reasons and because it would be hazardous for cranes and moving equipment. Some consideration was given to serving the klystron gallery complex with a cable system running on trays the length of the gallery. This was dropped because of the high temperature at the gallery roof and because the gallery space was needed for vacuum, water, local power, and control lines. The direct-burial cable system was discarded because of inflexibility and possible lengthy downtime in case of an outage. To meet flexibility, reliability, and minimum maintenance criteria, an underground cable-in-duct bank system was adopted.

Distribution voltage was determined from accelerator equipment requirements. In the early stages of the project it was planned that some 24 MVA of ac power would serve a central dc facility located adjacent to the master substation. Power would be distributed along the klystron gallery at 23-kV dc to the modulators. The central dc facility was to consist of sixteen variable-voltage rectifying units with a range of about $\pm 30\%$ of the nominal voltage. The manufacturing limitations for the induction voltage regulators was 16 kV which would represent the $+30\%$ control point. To satisfy these limitations, a nominal distribution voltage of 12 kV was selected after checking with the equipment manufacturers.

In mid-1962 the central dc facility was abandoned due to technical problems. The 12-kV–480-V Test Laboratory substation and the 60–12-kV substation were on order and, hence, it was too late to change the voltage rating without seriously delaying the overall schedule. With the aim of increasing the distribution voltage within the capability of the Test Laboratory and 60-kV substations, it was recommended that the nominal voltage be increased to 12.47 kV. This increase from 12 to 12.47 kV reduced the duct-bank heating losses by 7% and made better use of the cable equipment rated at 15 kV.

The underground duct-bank and cable system was adopted early in the design. The design objective was to provide a system with component materials which had proven their reliability over a period of years. After careful study it was agreed to use 15-kV three-conductor, paper-insulated, lead-covered cable (PILC) with an exterior jacket of neoprene. PILC cable was chosen over the newer insulation materials such as polyethylene, cross-linked polyethylene, and butyl rubber because of the "year-miles" experience record. PILC cable has greater overload capacity than the newer insulations; also the three-conductor PILC cable costs less.

In accordance with the reliability criteria that were established in mid-1962, the project is served by a dual cable system. Each distribution unit substation is served by two 12.47-kV cables; one is for normal service and one is for emergency service. Both cables, however, normally carry a full load. The emergency cable can be overloaded during the emergency connection period for a maximum of 3 days. This overload condition requirement was considered in the selection of and sizing of the PILC cables.

A detailed analysis was made of each duct-bank system, particularly with regard to thermal capability of each cable and of the duct-bank as a whole. The thermal and cable-sizing studies covered thermal conductivity of the soil, soil moisture content, mass of concrete in the duct-bank, duct materials, cable materials, normal cable loading, emergency 3-day cable loading, and short-circuit current vs time characteristics of the system and of the cable.

Two duct-cable systems were critical: the klystron gallery service and the service to the research area substation. Studies for the klystron gallery system resulted in a cable system with tapered wire size. In areas where the klystron gallery earth fill is high above original grade, additional concrete was added

to the duct-bank to increase the duct surface area to compensate for the below-normal soil thermal conductivity. The design criteria and operating limits for the klystron gallery cable system are outlined in Tables 25-2 and 25-3. The duct-bank system includes thermal capacity to allow for one 5-MVA cable to serve the area at Sector 10 and two 5-MVA cables to serve the area at Sector 20 (the future colliding beam area), but the ducts and cable must be added in the future.

The duct-cable system serving the research area substation is of unusually large capacity. Two 2000-A circuit breakers in the master substation serve the research area substation. For the initial installation, these two circuits each consist of two parallel three-conductor cables. With both circuits in service, the initial system can deliver 30 MVA continuously. With one circuit out of service, the in-service circuit can deliver 30 MVA for a 3-day period.

Table 25-2 Klystron gallery cable loads, conventional substations

Substation			*Feeder cable No.*			
No.	*kVA rating*	*Max. demand (kVA)*	*1*	*2*	*3*	*4*
1A	750	700	N[a]	E[b]	—	—
1B	750	700	E	N	—	—
2	750	700	N	E	—	—
3	750	700	N	—	E	—
4	750	700	N	—	E	—
CT-1	500	500	E	N	—	—
5	1000	1000	—	N	E	—
PSI	1500	1300	—	N	—	—
6	750	700	—	E	N	—
7	750	700	E	—	N	—
8	750	700	E	—	N	—
9	750	700	—	E	N	—
10	1000	1000	—	N	—	E
11	750	700	E	—	—	N
CT-2	500	500	E	N	—	—
12	750	700	E	—	—	N
13	750	700	—	E	—	N
14	1000	1000	—	—	E	N
15	1000	1000	N	—	—	E
Total normal load		17,075	4000 kVA	4100 kVA	4000 kVA	4275 kVA

[a] N = normal.
[b] E = emergency.

Table 25-3 Klystron gallery cable loads, variable-voltage substations

Substation			*Feeder cable No.*				
No.	*kVA rating*	*Max. demand (kVA)*	*VV-1*	*VV-2*	*VV-3*	*VV-4*	*VV-5*
VV-1A	1750	975	N	E	—	—	—
1B	1750	775	E	N	—	—	—
2	1750	1550	N	E	—	—	—
3	1750	1550	N	E	—	—	—
4	1750	1550	E	N	—	—	—
5	1750	1550	E	N	—	—	—
6	1750	1550	—	E	N	—	—
7	1750	1550	—	E	N	—	—
8	1750	1550	E	—	N	—	—
9	1750	1550	E	—	—	N	—
10	1750	1550	—	E	—	N	—
11	1750	1550	—	—	E	N	—
12	1750	1550	—	E	—	—	N
13	1750	1550	—	—	E	—	N
14	1750	1550	—	—	—	E	N
15	1750	1550	—	N	—	—	E
Total normal load		23,450	4075	4225	4650	4650	4650

Figure 25-9 Power distribution of site utilities system.

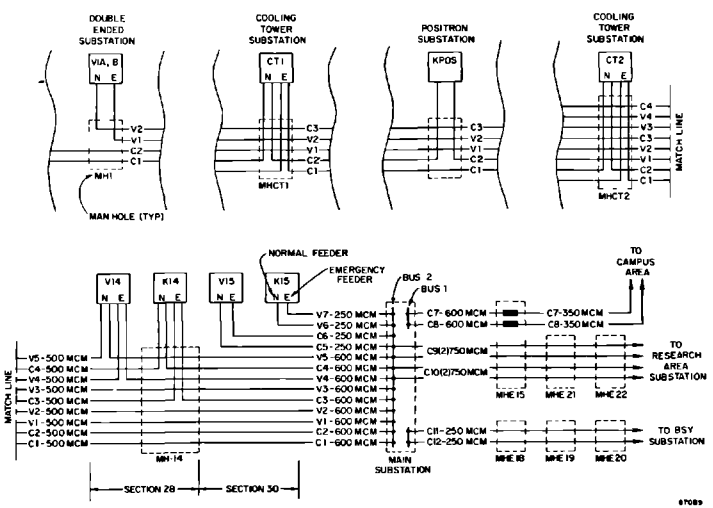

The duct-bank is designed to handle the future maximum loading of the research area substation, when each of the existing two circuits serving the research area substation will be doubled to four three-conductor cables per circuit. With the installation of these cables, the two circuits operating together can deliver about 52 MVA. With one circuit out of service, the in-service circuit consisting of four parallel three-conductor cables will be able to deliver about 43 MVA for a 3-day period.

Figure 25-9 shows the site 12.47-kV utilities system power distribution.

25-3 Secondary distribution

Klystron gallery (ILK, FGP)

Two ac systems serve the accelerator housing and klystron gallery. One furnishes three phase, 480 and 208Y/120 V for building services, vacuum, instrumentation and control, machine cooling water, microwave, alignment, and injection subsystems. The other provides variable voltage (258–595-V) services to modulators.

Sources for each system are unit substations located in alcoves along the klystron gallery, which transform the 12.47-kV distribution voltage to the utilization voltage. Each substation generally serves two sectors of the klystron gallery (666 ft, 8 in.) and the accelerator housing below; hence fifteen substations are required to supply the modulators. One substation supplies the positron source. In addition, each substation at Sector 2 is double-ended to provide extra reliability to the power sources for the main injector and Sectors 1 and 2. Finally, two substations, each in its own alcove, serve the machine water-cooling towers. These substations are equivalent in design and reliability to industrial systems of similar capacity. Standby power is provided only for the vacuum and beam guidance systems. In the case of failure of a sector substation, a second feeder from an adjacent substation may be connected by a manual transfer switch to energize the vacuum and beam guidance systems in the down sectors, permitting the beam to drift through them. Sectors 1 and 2 require continuity of operation for the injector and the first three "beam-stiffening" klystrons. Therefore, they are served by double-ended substations.

Auxiliaries (including cooling towers, but not the positron source) in the klystron gallery are served by an installed transformer capacity of 13,750/18,000 kVA AA/FA (self-cooled/forced air cooled), with a Stage I demand load of 5200 kVA and connected load of 17,000 kVA. Projected Stage II demand is 13,000 kVA and connected load 21,500 kVA.

Modulators served by an installed transformer capacity of 28,000 kVA have a Stage I maximum demand of 22,240 kVA and a connected load of 26,545 kVA. Figure 25-10 is a one-line diagram of a typical variable-voltage substation.

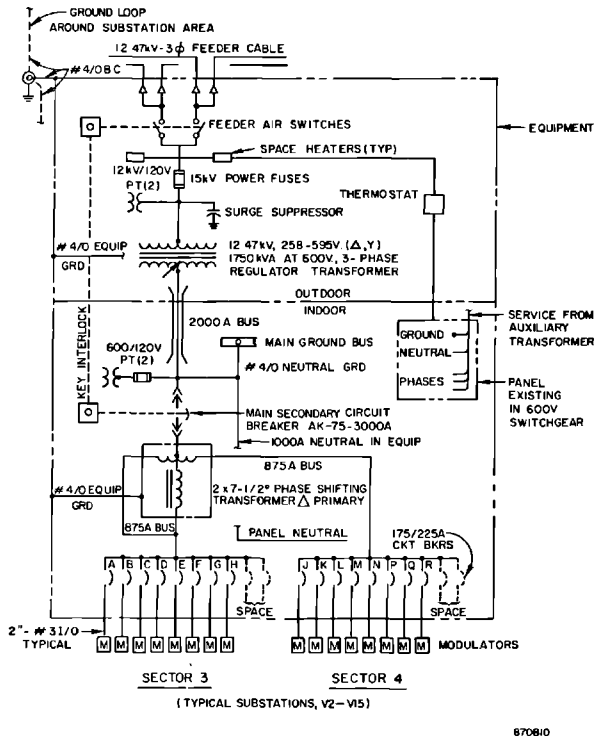

Figure 25-10 One-line diagram of klystron gallery variable-voltage sub-stations.

Figure 25-11 One-line diagram of klystron gallery auxiliary services.

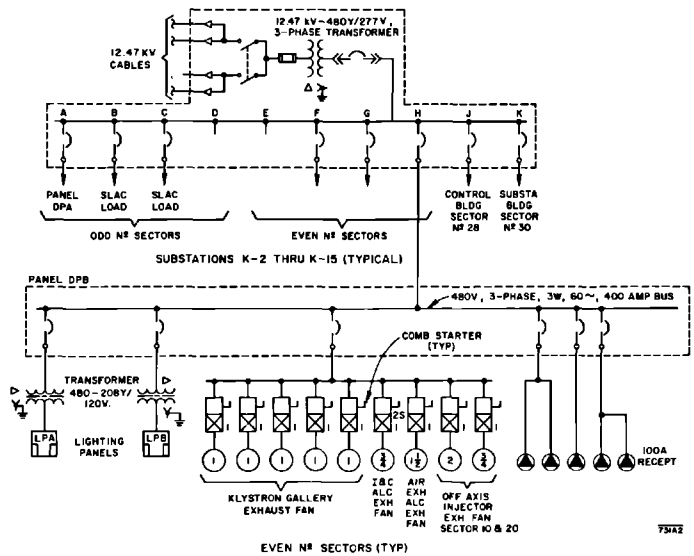

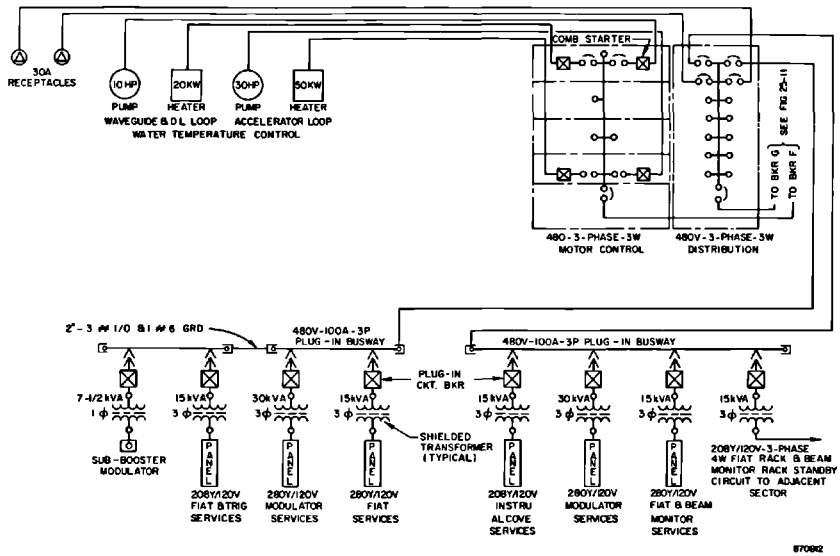

Figure 25-12 One-line diagram of klystron gallery modulator auxiliary services.

Figures 25-11 and 25-12 are one-line diagrams of a typical sector showing auxiliary services and modulator services.

Substations for auxiliary services are ventilated, dry-type, Class H insulated, dual rated, self-cooled or forced air cooled (in sizes over 500 kVA) with 500-MVA power fused primary switches designed to withstand 40,000 A momentary test with secondary breakers in cascade arrangement. Substations are located indoors for architectural reasons.

Variable-voltage substations for modulator services are similar to substations for the auxiliary services except that the primary incorporates a water-cooled oil-insulated induction voltage regulator which is not located indoors. The regulator is bused to a phase-shifting transformer in the indoor section which serves two output buses such that the phase angle on a 60-cycle base between these buses is 15°. Modulator loads provide the equivalent of a twelve-phase system, and the 15° phase shift between buses establishes twenty-four-phase dispersion at the substation secondary. The regulator, controlled by a bistable amplifier, adjusts substation output voltage within ± 2 V of approximately 5 times a reference signal of 50 to 120 V from central control. The main secondary circuit breaker is equipped with adjustable time-delay undervoltage trips.

Power for the auxiliary services (secondary distribution system) in each successive pair of sectors originates at one substation. Distribution, however, is on a per sector basis. Each sector is served by three 480 V, three phase, three wire power feeders. One serves a distribution panel from which subfeeders extend to vent fans, receptacles, and lighting. A second serves a motor

control center which, in turn, feeds water pumps and heaters for machine temperature regulating and cooling. The third distributes 480 V along the sector by means of plug-in bus ducts. The bus duct is used for its economy, salvage value, and to permit maximum flexibility of subfeeder location for modulator auxiliaries, vacuum, instrumentation and control, trigger, and microwave services.

Four hundred and eighty-volt circuit breakers in distribution panelboards and plug-in bus duct have not less than 15-kA asymmetrical interrupting ratings. Where circuit breakers are used in combination with starters, this rating applies to the combination. Circuit breakers used in 208Y/120- and 120/240-V panelboards have a minimum interrupting rating of 7500 A asymmetrical. A 24-V dc, 125-A power supply with a 200-A-hour floating battery provides power for instrumentation and control in each sector. The cables, rated at 600 V, are insulated by cross-linked polyethylene for economy and radiation resistance.[1]

Lighting and receptacle services for each sector's accelerator housing run down that sector's man accessway. All other services to the accelerator are brought down through the penetrations which connect the accelerator housing to the gallery at 20-ft intervals.

Interference is reduced by the use of shielded transformers throughout the installation and by physical separation, i.e., power wiring is run along the south and instrumentation along the north walls of the klystron gallery wherever possible.

Positron source (MAM)

Sector 11 is equipped with one dry-type, indoor, 1500/2000 kVA (self-cooled/forced air cooled), 12.47-kV–480/277-V substation for the positron source. The substation feeds power supplies serving three dc solenoids with a total demand of 1300 kW and two klystron modulators rated at 125 kVA each.

Output voltage to the modulators is controlled by two 125-A, 260–600-V automatic three-phase induction voltage regulators. The regulators perform essentially the same functions as the regulators in the variable-voltage substations described earlier, with the exception that each regulator feeds only one modulator, thus allowing independent voltage control.

Power for positron instrumentation racks as well as for the 150-kVA heat exchanger is derived from the conventional substation in Sector 10 because of economy in feeder length. Unlike the other substations in the klystron gallery, the positron substation is not provided with a 12.47-kV emergency feeder nor is there standby power for the instrumentation and control racks and the special quadrupole triplets associated with the positron source.

In addition to the conventional short circuit and overload protection, phase undervoltage relays trip the main secondary breaker to protect the power supplies from single phase operation.

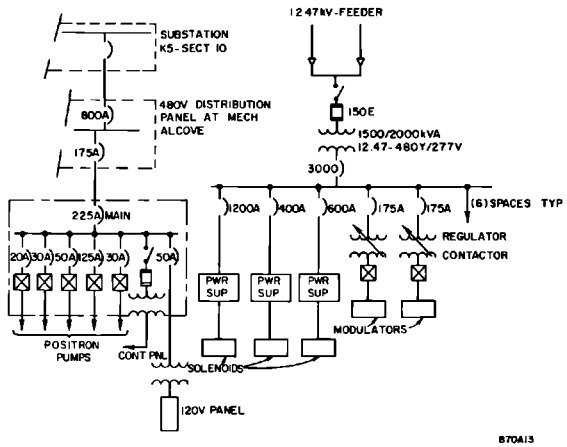

Figure 25-13 One-line diagram of positron area substation.

The induction voltage regulator output contactors are provided with a permissive interlock from the personnel and machine protection system of the accelerator.

Figure 25-13 is the one-line diagram for the positron source electrical services.

Beam switchyard (ILK, AAT)

Two double-ended indoor substations located in a building near the Data Assembly Building (DAB) supply power for the beam switchyard (BSY). One serves power supplies for switchyard magnets, magnet auxiliaries, and instrumentation and control. The other serves A-beam dump magnet power supplies and pumping stations for all switchyard and end-station cooling water. It also supplies house power requirements for the switchyard substation building, DAB, and the switchyard itself, 40 ft below grade.

Emergency power for minimal crane, ventilation, and lighting requirements in the switchyard and end stations is provided by a Diesel generator. Power supplies with batteries in parallel furnish instrumentation and control services.

Power for the BSY is supplied by means of two 250-MCM 3/C PILC, 12.47-kV feeder cables underground from the master substation to BSY substation. Each serves an individual 12.47-kV bus. The two substations are connected to the buses through fused switches to permit one or both substations to be connected to either bus (see Fig. 25-14). Substations are sized for switchyard operation at the 25-GeV beam energy level. At this level, the loads are such that the substations have to be forced air cooled. Switchyard magnets, power supply auxiliaries, and instrumentation requirements

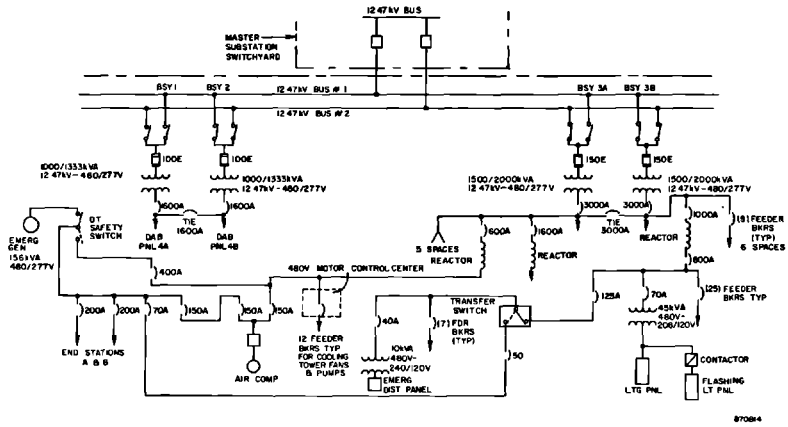

Figure 25-14 Single-line diagram of beam switchyard substation.

are served by substations Nos. 1 and 2, totaling 2000/2666 kVA, AA/FA (self-cooled/forced air cooled) of installed transformer capacity with a demand load of 1760 kVA and a connected load of 1900 kVA. Switchyard site services, cooling-water pumps, and A-beam dump requirements are served by substations Nos. 3A and 3B, totaling 3000/4000 kVA, AA/FA (self-cooled/forced air cooled) of installed transformer capacity with a demand load of 3100 kVA and a connected load of 3900 kVA.

The substations mentioned above are double-ended, ventilated, dry-type, class H insulated. Substations Nos. 1 and 2 each have transformers rated 1000/1333 kVA, AA/FA. Substations Nos. 3A and 3B each have transformers rated 1500/2000 kVA, AA/FA. The primary switches have 500-MVA rated power fuses and are designed to withstand forces due to 40,000-A asymmetrical short circuits. Secondary breakers are in cascade arrangement. Substations Nos. 1 and 2 have a key-interlocked 1600-A tie breaker and 1600-A, main secondary circuit breakers with adjustable time delay, undervoltage, and underfrequency tripping devices. Substations Nos. 3A and 3B have 3000-A main secondary circuit breakers connected to trip on low or unbalanced voltage and automatically close the 3000-A tie. Selection is available for manual or automatic operation. Large pump motors are all controlled directly by circuit breakers. All circuit breakers in feeders to the DAB may be remotely tripped from the DAB.

Secondary distribution at 480 V, three-phase, three-wire serves building needs, cranes, vacuum systems, cooling-water pumps, power supplies, and instrumentation. Dry-type, class H insulated, shielded, 480/208Y/120-V transformers are furnished near application points for lighting, convenience outlets, instrumentation and control, and miscellaneous 120-V needs. Motor and building loads are electrically separated from precision power supplies so far as economically feasible in order to improve regulation and to reduce high-frequency electrical noise.

Four hundred and eighty-volt circuit breakers in the DAB are capable of interrupting not less than 25 kA asymmetrical at 480-V ac. Where breakers are used in combination with starters, this rating applies to the combination. Circuit breakers used for 208Y/120-V circuits are capable of interrupting 7.5 kA asymmetrical at 240-V ac.

Power services outside of the switchyard are run in conduits and ducts using conventional building wire. Inside the switchyard, lighting, receptacle, and crane services use polyethylene-insulated wire in conduit. For convenience and economy, all magnet, instrumentation, and communication cables are run in cable trays from their origin in the DAB to their destination in the BSY. Services are brought into the switchyard through duct banks and through lockable radiation labyrinths. Radiation levels inside the switchyard are such[2,3] as to require that the cabling in the upper housing be cross-linked polyethylene. Cables in the lower housing are, in general, fiberglass- and mica-insulated; in particularly high-radiation areas, such as the vicinity of the slits and collimators, magnesium oxide-insulated (MI) cables are used. The magnesium oxide-insulated cables are stainless steel jacketed to limit corrosion. Terminations at both magnets and instruments are radiation-resistant and are remote operable, e.g., capable of being opened or made up by rods through holes in the floor of a shielded maintenance cab in the upper housing. Where disconnects cannot be remotely opened and closed, the magnet or instrument itself may be drawn into the maintenance cab to be disconnected manually. Sufficient slack is left in all cables at connection points to permit a wide range of remote manipulation.

To maintain service continuity and to isolate the klystron gallery instrumentation from the BSY instrumentation, two 24-V power supplies with parallel batteries are furnished. A 200-A power supply with a 400-A-hour parallel positive-grounded battery serves controls, relays, and both klystron gallery and BSY status needs. A 125-A power supply with a 200-A-hour parallel negative-grounded battery serves computer logic circuits and that part of the interlock system which uses commercially available, solid-state circuits. The battery ground is common and is tied to the main SLAC ground bus.

End station area (PCE, AAT)

Electric energy for the various end station facilities (see Figs. 25-15 and 25-16) and for the research operations is served from the research area substation, except for a limited standby service which is assigned to critical loads requiring emergency service. The emergency service is supplied by a Diesel engine generator set located in the BSY area substation.

The research area substation, located adjacent to the end station A counting house, provides 480-V, 4160-V, and 12.47-kV power for the entire end station area. The substation has two 12.47-kV buses designed to permit transfer of power from one end station area to another with the progression

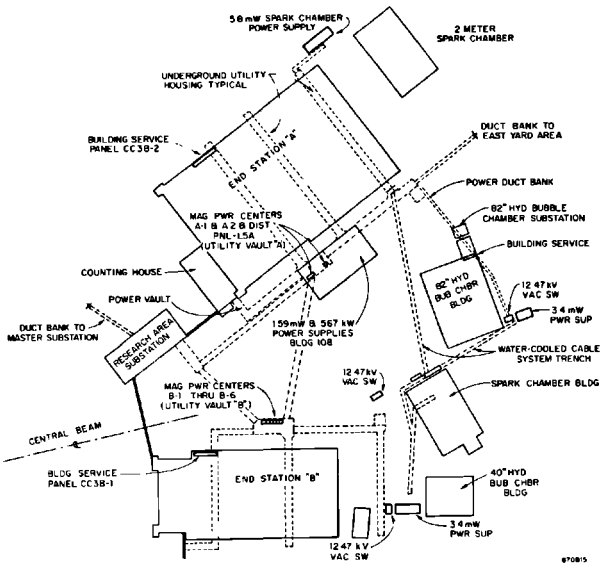

Figure 25-15 Electrical plot plan of end station area.

of research operations. The capability of the installed cables from the master substation is 30 MVA to the research area substation. The duct bank from the master substation is available for future cable installation to carry an ultimate capacity of 52 MVA.

The research area substation houses four 12.47-kV–480-V unit substations, one 12.47-kV–4160-V unit substation, the substation house power services,

Figure 25-16 Single-line diagram of research area substation.

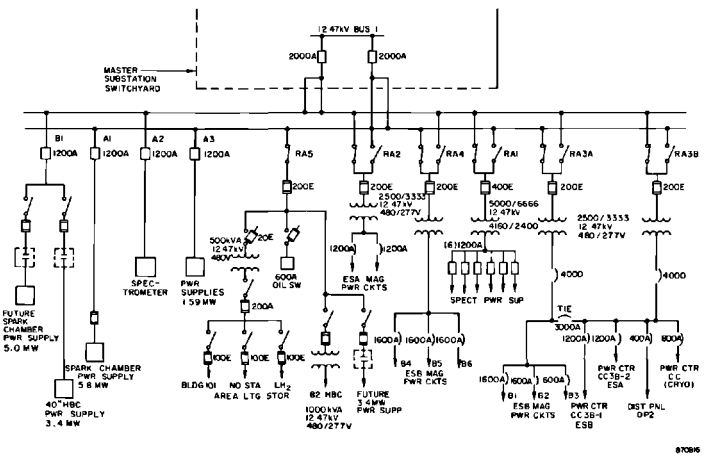

Table 25-4 Transformer capacity

Service	Unit rating (kVA)	Transformer installed capacity	
		Self-cooled (kVA)	Fan-cooled (kVA)
480 V	(4) 2500/3333	10,000	13,333
4160 V	(1) 5000/6667	5,000	6,667
		15,000	20,000

a 125-V dc control power battery bank, a motor control center, six 4160-V feeder circuit breakers, and four 12.47-kV feeder circuit breakers. The end station area electrical secondary distribution plan, Fig. 25-16, shows a single-line diagram of the major features.

The total transformer capacity is 15 MVA on a self-cooled basis and 20 MVA on a forced air-cooled basis (see Table 25-4.)

These transformers are ventilated, dry-type, and air insulated for 50-kV BIL. The materials and construction are class H, which permits operation at 150°C average winding rise above a 40°C ambient within the unit substation metal enclosure. Taps are provided in the high-voltage winding to permit compensation for $2\frac{1}{2}$ and 5% supply voltage above and below 12.47 kV. These can be used also to decrease the output by $2\frac{1}{2}$ and 5%, which decreases the 12.47-kV circuit current by $2\frac{1}{2}$ and 5%. Fans are installed for air cooling to permit operation at a load higher than the self-cooled rating. The 12.47-kV–480-V transformers are manufactured to higher (10.3%) than normal (5.6%) impedance, thus limiting the short-circuit current below 30,000 A at the substation bus and 25,000 A at the load distribution magnet power centers in order to permit use of molded case K frame circuit breakers with 25,000-A interrupting capacity in power distribution panels and in power utilization devices.

The substation's primary switchgear is arranged in a lineup of six 15-kV class, indoor-type, metal-enclosed, load interrupter selector switch assemblies and four 15-kV class, rollout, indoor-type, metal-enclosed, magnetic air circuit breakers. The basic insulation level for this switchgear is 95-kV BIL. The load interrupter selector switches are rated for 600 A continuous and are capable of closing into a 40,000-A momentary current. The 15-kV class power fuses associated with each selector switch have a 500-MVA interrupting rating. The magnetic air circuit breakers are rated for 1200 A continuous and 500-MVA interrupting capacity which is 25,000 A in the 12.47-kV system.

The 480-V unit substations consist of ventilated dry-type transformers, electrically operated drawout-type air circuit breakers and related control circuits. Unit substation 3A-3B is arranged to form a double-ended substation with a common aisle between control faces and an interconnecting overhead

bus duct. The double-ended substation has, not only feeder air circuit breakers, but also a 4000-A main circuit breaker for each of the two transformers and a 3000-A tie circuit breaker. The main and tie circuit breakers provide a means of interchangeably using one or the other of the two transformers to feed the loads. Selection is available for manual or automatic operation. However, the loads must be compatible as to fluctuations, sensitivity to rapid changes, rectifier commutation transient voltages, and undesirable response to harmonic voltages. The single-ended unit substations do not have a main breaker and are, therefore, limited to not over six large power feeders per bus. Phase overcurrent protection is provided by series tripping devices attached to each circuit breaker. These series tripping devices prove to be inadequate on the 4000- and 3000-A main and tie circuit breakers. A satisfactory system of monitoring main bus and bus tie currents is the extremely inverse-type station relay operated from the unit substations current transformers. Ground fault and transformer neutral residual currents are satisfactorily monitored by a separate current transformer mounted in the connection between the transformer secondary neutral and the unit substation's neutral bus which is grounded at the substation. The series tripping devices mounted in the drawout-type feeder circuit breakers are adequate for monitoring feeder line currents for overload and short circuit. However, the tripping time vs current characteristics of drawout circuit breakers are not compatible with the tripping time vs current characteristics of large molded case circuit breakers.

The 4160-V unit substation consists of a ventilated dry-type transformer, six electrically operated rollout magnetic air circuit breakers, and related control circuits. A main circuit breaker is not provided. Phase current and ground fault current protection is obtained through the use of station relays operating from the unit substation current transformers and transformer neutral current transformer. The rollout indoor magnetic air circuit breakers are rated for 1200-A continuous and 75-MVA interrupting capacity, which is 10,500 A in the 4160-V circuit.

All transformer primary 12.47-kV windings are delta and the secondary windings are grounded Y. Distribution-type lightning arrestors protect the 12.47-kV coils and limit the surge voltages to which the 12.47-kV coils may be subjected to a safe value within the 50-kV basic insulation level.

The two single-ended 480-V unit substations, the one 4160-V unit substation, and the four 12.47-kV feeder circuit breakers can be selected to trip by underfrequency relays for purposes of interruptible power contract load shedding. Undervoltage tripping is provided to protect rectifier loads against single phase operation, which is damaging to silicon-controlled rectifier units.

Safety features for personnel in the end stations are provided. The 480-V (except house and emergency power), 4160-V, and 12.47-kV power circuits from the research area substation are arranged to allow selective tripping from either end station A or end station B. Access to the research area substation 12.47-kV fuse cubicles, the 4160-V and 12.47-kV circuit breaker

roll-in ways, the electrical power vaults, the electrical utility tunnels, and the 12.47-kV manhole junction boxes is controlled by a key interlock system.

The initial loads served in the end station area are summarized in Table 25-5.

End station A and end station B house power is supplied from the research area substation at 480 V, three-phase, four-wire, 60 cycles/sec. Distribution of power throughout each end station building is made from a building service

Table 25-5 End station area electrical loads

Facility	*Permanent demand loads 480 V (kVA)*	*Present research operations maximum substation loads*		
		480 V (kVA)	*4160 V (kVA)*	*12.47 kV (kVA)*
End station A building, end station area facilities, and yard house power	800	—	—	—
82-in. bubble chamber house power	300	—	—	—
Counting house power	100	100	—	—
End station B building and adjacent facilities house power	300	—	—	—
Cryogenics facility	300	—	—	—
	1800	100		
End station A				
20-GeV spectrometer magnets 8-GeV spectrometer magnets 1.6-Gev spectrometer magnets	—	1000	4000	3700
2-Meter spark chamber magnet	—	—	—	7000
		1000	4000	10700
Central beam				
82-in. hydrogen bubble chamber magnet	—	—	—	3000
Beam transport magnets	—	2600	—	—
		2600		3000
End station B				
40-in. hydrogen bubble chamber magnet	—	—	—	4000
54-in. spark chamber magnet	—	—	—	3300
Beam transport magnets	—	6700	—	—
		6700		7300
Total: 37,200 kVA	1800	10400	4000	21000

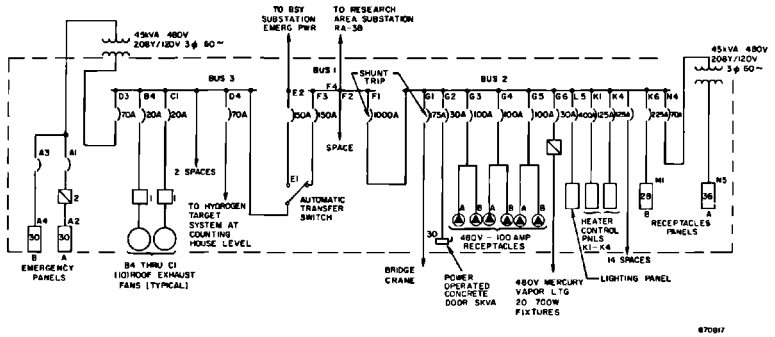

Figure 25-17 One-line diagram of end station A house power.

power center shown in Figs. 25-17 and 25-18. Power at 480 V, three-phase, is provided by this means for the high bay mercury vapor lighting, the 480-V receptacles, the bridge crane service, the motor-operated concrete doors, and the service to the roof ventilation fans. Several 45-kVA, 480-208Y/120-V transformers supply power for incandescent lighting and for the 120-V receptacles. The mercury vapor lighting is turned off as a warning that research operations are to begin. In addition, a major proportion of the incandescent lighting in the high bay and in the utility housings under the building are cycled between dim and bright as a final warning. The four 75-kW heaters in end station A are supplied from the building service power center.

End station A facilities, including the end station A Power Supply Building, the 2-meter spark chamber building, east yard buildings, and the beam dump at the east end of the A-beam line are supplied from the facilities power panel in utility vault A. This panel is supplied from the end station A building service power center.

Power for the end station area is distributed from the research area substation by cables run from the substation down a chase in the retaining wall

Figure 25-18 One-line diagram of end station B house power.

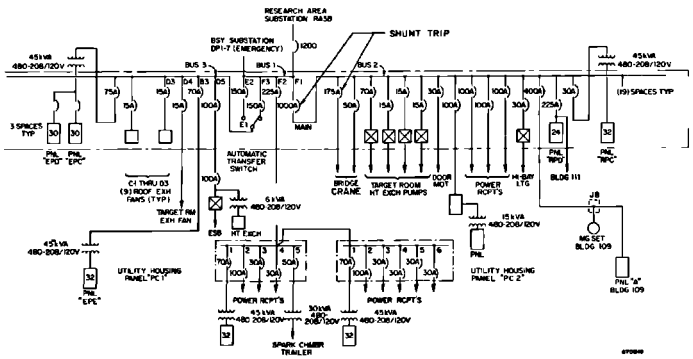

Table 25-6 Distribution capacity, end station area

Facility	*Installed cable and terminal bus capacity*			
	480-V cables (kVA)	*4160-V cables (kVA)*	*12.47-kV cables (kVA)*	*Total kVA*
End station A				
Building and end station area facilities and yard house power	830	—	—	—
Spectrometer magnets	2600	6667	14200	—
2-Meter spark chamber	—	—	7100	—
	3430	6667	21300	31,397
Central beam				
82-in. bubble chamber house power and magnet power	250	—	4000	—
Beam transport magnets	1330	—	—	—
	1580		4000	5,580
End station B				
Building and adjacent facilities house power	830	—	—	—
40-in. bubble chamber magnet and spark chamber magnet	—	—	7100	—
Beam transport magnets	6700	—	—	—
	7530		7100	14,630

to the electrical power cable vault adjacent to the wall footings. A 12.47-kV cable to the north staging area, H frame substation provides 300 kVA of transformation to 480 V. This serves the adjacent building facilities and lighting.

The installed distribution for the end stations is shown in Fig. 251-6 and Table 25-6. Electrical utility housings are located as per Fig. 25-15. These are the underground cableways connecting the electrical power vault with utility vaults A and B (see Fig. 25-19). These cableway housings are corrugated metal off-round culverts having a nominal cross-sectional dimension of 6 ft wide × 8 ft high. The arrangement of the hangers and oiled maple clamps permits forty triplexed or quadruplexed power cables or bundles of control cable. The housing-type cableway is used to minimize the end station yard area underlaid by the cableway as well as to minimize the trench width required. Yard area is at a premium because some research installations require deep borings and foundations that are not compatible with duct banks and housings. The 6-ft below-grade cover over duct banks or the crown of the housings is required by the surface mechanical loading specification

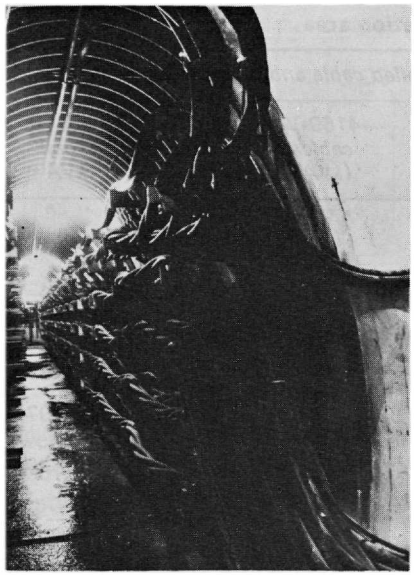

870B19

Figure 25-19 View from outgoing end of electrical utility housing serving utility vault.

for the concrete pad. The housing uses a 7-ft wide trench, 14 ft deep as compared with the less expensive equivalent duct bank which requires a more costly trench, 36 ft wide × 9½ ft deep to accommodate four ten-duct banks.

The utility housing from the electrical power vault to vault A has 52% of available rack space filled with cables. These cables serve the end station A building, the 82-in. bubble chamber magnet, the 2-meter spark chamber magnet, and the area facilities and yard power. The spare rack space available and the thermal capacity of the housing permits an additional 6500 kVA of 480-V services.

The power and control cables installed in the utility tunnel to vault A are listed in Table 25-7.

The utility housing from the electrical power vault to vault B has 73% of available rack space filled with cables. These cables serve end station B, the 40-in. bubble chamber magnet, the spark chamber magnet, the end station B transport magnets, the central beam transport magnets, and the area facilities power. The spare rack space available and the thermal capacity of the housing permits an additional 4000 kVA of 480-V services.

The cables installed in the utility tunnel to vault B are listed in Table 25-8, However, the cable chase in the retaining wall below the research area substation does not have sufficient additional space to allow both 20% more cables in the housing to vault B and 40% more cables in the housing to vault A.

Table 25-7 Capacity of cables in utility tunnel to vault A

Quantity	*Service*	*Total installed cable capacity (kVA)*
1	125-V dc service	—
1	Controls, four-cable bundle	—
3	480-V services: three 750-MCM triplexed or quadruplexed, 90°C Hypalon-insulated, per service	3,430
6	4160-V services: one No. 4/0-triplexed 5-kV, concentric shielded, polyethylene-insulated, per service	6,667
3	12.47-kV services: one 350-MCM triplexed 15-kV, concentric shielded, polyethylene insulated, per service	21,300
1	12.47-kV service: one 350-MCM triplexed 15-kV, metal tape shielded, ethylene propylene insulated, per service	4,000
		35,397

Campus facilities

All conventional unit substations furnished for campus building power and lighting are 12.47 kV to 480Y/277 V. All unit substations are sized for present and planned loads plus 25% capacity for unforeseen load growth. The building power requirements are up to 50% higher than for industrial buildings of the same gross area. This is normal in scientific research buildings where power is often required at greater load density than in most manufacturing processes.

The cable and wire used for 480- and 120-V house power distribution are general, conventional, building wire and conduit systems. These systems

Table 25-8 Capacity of cables in utility tunnel to vault B

Quantity	*Service*	*Total installed cable capacity (kVA)*
1	125-V dc service	—
1	Control, four-cable bundle	—
7	480-V services: three 750-MCM copper triplexed or quadruplexed, 90°C Hypalon-insulated, per service	7,530
1	480-V service: twelve 1000-MCM aluminum, 75°C USE-insulated, per service	1,330
1	12.47-kV service: one 350-MCM triplexed 15-kV, concentric-shielded, polyethylene-insulated, per service	7,100
		15,960

are used in areas such as the Test Laboratory Building, Electronics Building, Heavy Assembly Building, and the Central Laboratory Building. Four hundred and eighty-volt plug-in bus duct at 480 V and 120-V busways are installed for flexibility and field additions.

The electrical control for mechanical equipment has undervoltage protection. In case there is a loss of voltage, the electrical control device drops out and has to be manually reset to allow the mechanical equipment to operate again. This is true for most of the mechanical equipment which does not have automatic control.

Lighting intensity levels were investigated during the conventional facilities design for special areas, office, and laboratory use. After detailed study, the following was established as a minimum standard for the project:

Office areas: 50 ft-c
Laboratories: 50 ft-c
Other areas: 25 ft-c

There are two 12.47-kV air circuit breakers and their associated feeder cables, 350-MCM, 15-kV class, PILC, which originate from the master substations for Campus Building electrical facilities:

C.8 (12.47-kV feeder)
Fabrication Building (1000–1333 kVA), Heavy Assembly Building 5B-W (750–1000 kVA), Test Laboratory B-E (2000–2667 kVA), and Central Laboratory 4B-E (750–1000 kVA)

C.7 (12.47-kV feeder)
Heavy Assembly Building 5A-E (750–1000 kVA), Test Laboratory 1A-W (2000–2667 kVA), Central Laboratory A-W (750–1000 kVA), Construction Office Building (250 kVA), and crafts shop (500 kVA)

25-4 Fire alarm system (CBJ)

The criteria established for the fire alarm system calls for an automatic detection system to protect personnel and to minimize the possibility of loss of equipment. The fire detection system is provided with detection devices at specific points. The master control located in the Fire Station Building has four coded fire-monitoring circuits. The four circuits are as follows: (1) the klystron gallery loop, (2) campus area loop, (3) research area loop, and (4) spare.

There are twenty-nine street-type master fire alarm boxes, strategically located throughout the site. Each one of the boxes is connected to one of three fire-monitoring supervised circuits. Each fire alarm box, when activated by a fire alarm, transmits a pulse-coded signal to the Fire Station master monitoring console. The signals are audibly indicated, recorded, and automatically retransmitted to the Stanford University Fire Department via leased telephone wires. The coded signal directs Fire Department personnel

to the particular box originating the alarm and the annunciator used in conjunction with the master box gives further instruction as to the exact location.

Associated with each master fire alarm box there is a fire alarm subsystem which covers a specific area or building, which, in turn, is normally subdivided into several fire zones. The subsystems are provided with local audible alarms and ventilation fan interlocks when needed.

Each zone is equipped with either heat detector, smoke detector, sprinkler flow switch, manual switch, or combination thereof.

An alarm received at the Fire Station identifies the master fire box, and the fire box, in turn, annunciates the zone in trouble.

All fire alarm systems are equipped with emergency standby power. In addition, all alarm circuits are continually monitored for circuit faults.

In conjunction with the automatic fire detection system, a water sprinkler system was installed in all buildings except in areas where water could cause severe damage to electronic equipment In these areas, portable fire-extinguishing equipment suitable for electronic equipment is provided. Automatic water flow switches are provided to actuate the fire alarm system.

25-5 Grounding (AAT)

The grounding system installed in the project is a unified system combining both high-frequency short rise time pulse and 60-cycle power requirements. Grounding facilities are provided for (1) ac power system equipment grounding, (2) instrument and control requirements, and (3) electrolysis and corrosion damage control. Certain features of each of these three facilities are in conflict as to desirable criteria. However, the system provided herein includes compromises to accomplish the following overall purposes listed in order of importance: (1) personnel safety; (2) reduction of system deterioration resulting from electrolysis; (3) reduction of interference in the instrumentation and control system.

The klystron galley grounding design is intended to furnish a 60-cycle impedance of less than 0.03-ohm resistance and 0.03-ohm reactance and also to present a high-frequency characteristic impedance not greater than 5 ohms. Connections at the klystron tube flange and modulator ground leads are designed to have an impedance not greater than 0.2 ohm at 200 kHz. Normally, the dc current is less than 1 mA.

The grounding scheme is composed of (1) the major ground bus which forms the backbone of the system and runs the full length of the klystron gallery; (2) lateral runs of the same size bus that connect the thirty instrumentation and control alcoves and the accelerator control building; and (3) ac power system equipment grounding (control center, vacuum pump stations, etc.).

The following is a physical description of the above items.

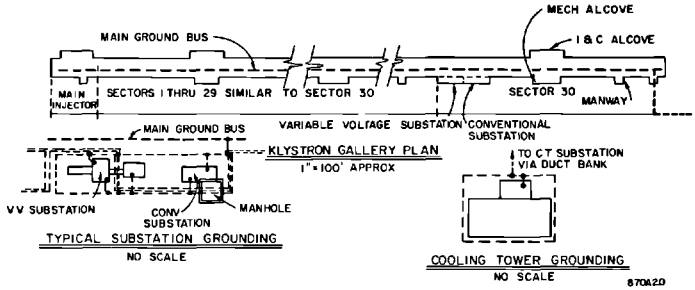

Figure 25-20 Grounding plan of accelerator.

1. The *major ground bus* consists of a copper bus $\frac{3}{16} \times 14$ in. in cross section running the full length of the klystron gallery and extending into the main injector station. Joints between lengths of the bus are thermal fusion butt-welds made by the Cadweld process. Expansion joints of flexible copper strap are made between sectors at the building steel expansion joint locations. The bus is secured to the building steel only at the midpoint of each sector, which allows expansion in both directions as required. Each roof beam is connected to the bus by a flexible copper strip. The main ground bus of each sector is connected to the sector substation grounding system with insulated cable. All connections to the main bus are bolted using silicon bronze lugs and hardware. The same ground bus extends all the way to the BSY and near end station areas as shown on Figs. 25-20 through 25-22.

2. The *lateral ground bus runs* are made from the major ground bus to each instrumentation and control alcove, and each ac power substation

Figure 25-21 Grounding plan of beam switchyard.

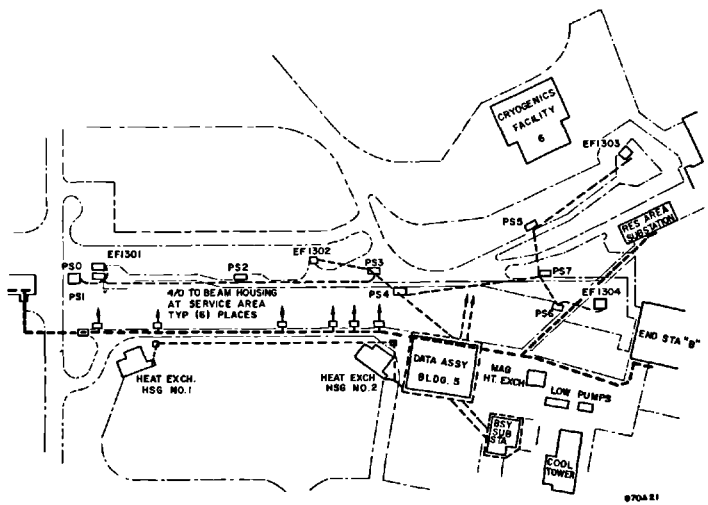

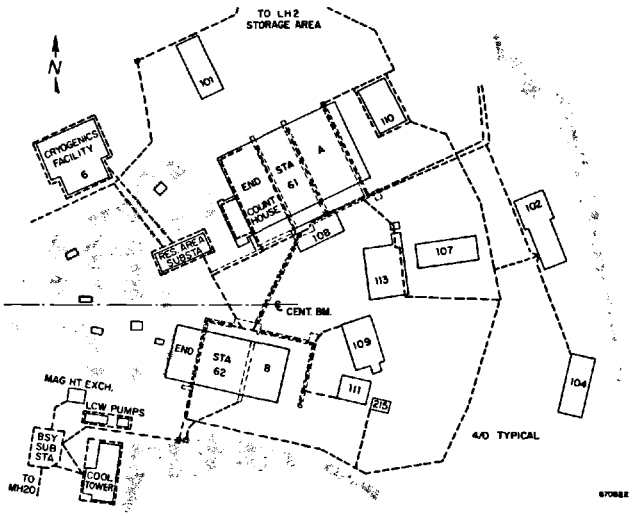

Figure 25-22 Grounding plan of end station.

480-V transformer neutral. They also are made to the monitoring and instrumentation ac power supply transformer shields, the accelerator control building, the receiving substation ground mat, the modulator dc facility ground mat, and the injector. In a depression in the floor, $\frac{3}{16} \times 14$ in. copper sheets are installed.

3. The *ac and dc power system equipment ground* is connected to the 13-kV distribution system cable sheath. The major element of the 12-kV power system ground is No. 4/0 copper cable, bare where the run is in concrete, TW-insulated where the run is in soil. Building columns are connected to the main ground bus by No. 1/0 TW cable run below grade.

Typical grounding and bonding criteria for the project substation and various buildings are as follows:

SUBSTATIONS. Each substation is furnished with a firm peripheral ground loop of not less than No. 4/0 stranded bare copper wire, located not less than 18 in. below grade. Ground rods in wells are set periodically in this loop and connected to the loop by removable pressure clamps. All transformer and switchgear equipment is connected to the loop. The loop is connected to the ground bus by No. 4/0 green "THW" stranded copper cable. The substation neutral is white "THW," insulated, run in wood mold where exposed. A pressure connector fastens the neutral to the ground bus. Each service run from a substation into the service area is routed at the point the service enters the building through not less than 20 ft of rigid, galvanized steel conduit, coated to resist corrosion. At the point where each steel conduit enters the building, the conduit is bonded once only to the ground bus.

BUILDING. The gallery structural steel frame is grounded to the floor slab reinforcement at each column. The floor slab reinforcement material is electrowelded mesh. Grounding connection points on columns are exposed. At each penetration pipe the klystron gallery floor reinforcements are connected to the pipe by a single exposed pigtail. Connections between steel and copper are mastic coated (or epoxy painted) except at the klystron gallery ground bus. Doors are metal or metal encased, not bonded to frame or columns. Each metallic utility service is bonded to the nearest building column at the point of entry.

120/208-V TRANSFORMER NEUTRALS. Each transformer neutral is bolted to the case and the shield at the transformer.

EQUIPMENT GROUNDING. A bare copper bus is run from each transformer housing to the grounding bus. The bus is bolted to the main bus and to transformer neutral, housing, and shielding. A green insulated wire equal in size to the service conductors, but no larger than No. 4/0, accompanies the service conductors in conduit from the transformer to the distribution panel and is connected to the "equipment ground bus" provided in the panel. The equipment ground bus in each panel is a $\frac{1}{4}$-in. thick × 2-in. wide copper bus grounded to the panel structure and equipped with mechanical connectors of the proper number to accommodate all ground wires terminating in the panel. A green insulated wire is carried in the conduit with service to each item and screwed or bolted to the item served. Wires are sized as follows:

No. 4/0. To each item of electrical equipment with a capacity over 600 A
No. 2. To each item of electrical equipment with a capacity between 200 and 600 A
No. 6. To each item of electrical equipment with a capacity between 50 and 200 A
No. 12. To all other items of electrical equipment in the building.

GENERAL GROUNDING AND BONDING. Reinforcing steel bars where required to be bonded are double-welded. Buried connections are thermal-welded.

All connections to ground rods are made with silicon bronze pressure connectors. Equipment connections to the ground bus are made with silicon bronze connectors in such a way as to be removable.

The overall project grounding system is shown in Figs. 25-20 through 25-22.

25-6 Emergency power (CBJ)

Early concepts of reliability called for parallel power services, distribution and transformation, and, in addition, numerous local standby emergency generator plants. The emergency generators were to be located at each

substation along the klystron gallery. After careful analysis, the multiple standby generator concept was reduced to providing facilities for connecting portable generators.

It is difficult to predict the degree of reliability of each of the various areas and components of the power system, such as the 220-kV transmission line, the master substation, the distribution system, the unit substations, and the low-voltage distribution to the utilization devices. Rough cost estimates were made for doubling the transmission, distribution, and transformation system. Judgments on what these costs meant in improved reliability were made. The final choice was to use two Diesel-driven generators to serve the critical loads as outlined below. These generators start automatically upon failure of conventional power. Loads are transferred as soon as the generator voltage is at the correct value, usually about 6 sec from normal power failure. The generators carry their loads until 2 min after restoration of normal power.

One 75-kW generator located in the Central Utility Building supplies selected circuits in the Test Laboratory, Administration and Engineering Building, Control Utility Building, and Permanent Fire House. Minimum lighting is covered in all these buildings as well as telephone, radio, and fire alarm circuits. Vacuum pumps and control circuits associated with klystron processing stations in the Test Laboratory are also protected from power failure. The Diesel prime mover is supplied with fuel from a 10,000-gal tank which also serves two building heating boilers in case of natural gas failure. This tank is kept full, so that it has adequate reserve capacity for 8 hours of operation in case of simultaneous failure of gas and electricity.

The other Diesel generator is rated for continuous duty at 125-kW, 156.5-kVA, 0.8 power factor and is located in the BSY substation building and supplies selected circuits in the BSY, DAB, end stations A and B. Ventilation of end stations A and B and the target room are on emergency power to take care of the escape of hydrogen due to lack of refrigeration during a power outage. Fire alarm circuits and a few lights in end stations A and B and the DAB are protected. A 75-hp air compressor in the BSY substation can be switched to the generator circuit for periodic maintenance loading and checking of the Diesel engine. The Diesel prime mover is supplied with fuel from a 500-gal tank which is kept filled to at least 250 gal, enough for 5 days of operation.

A nonautomatic-start Diesel-driven generator of 50-kW rating supplied power through a manual transfer switch to the Temporary Fire House.

Portable generators of 50-, 25- and 10-kW ratings are available for emergency use in case of equipment failure or of scheduled maintenance outages.

In the klystron gallery, a small amount of emergency power can be obtained in any sector from an adjacent sector which is served from a different substation. Manual transfer switches for this purpose are adequate as the vacuum pumps served by these circuits can be off for an hour without serious deterioration of vacuum.

25-7 Operational experience (CBJ, AAT)

The master substation was designed to carry part of the loads on the 12-kV bus supplied from 220-kV and the remaining loads on the 12-kV bus supplied from 60 kV. Then, in the event of failure of either source, the loads affected are transferred automatically to the other source. This system worked many times when acceptance tests were made and a few times when sources were actually in trouble. However, on one occasion, the automatic transfer was not completed and the loads were energized only after manual switching. Because of this and because the 60-kV line is subject to more voltage dips due to mechanical damage to poles, all loads are presently fed from the 220-kV source.

The 12-kV manually operated load-break-disconnect switches turned out to be of a mechanically poor design. About half of them failed at least once in twenty operations. After two redesigns and the replacement of several operating parts, the sixty switches now work fairly well.

Some of the 12-kV switching (which disclosed the above design troubles) was required to allow work on 12-kV potheads which had been made up incorrectly in spite of detailed instructions. About sixty potheads had to have stress-cone construction corrected and then be repotted.

The 12- and 4-kV circuit breakers in the research area substation were not designed for frequent operation. The loads on their circuits need

Figure 25-23 Typical operating characteristics, 360-kW current regulated power supply, silicon-controlled rectifier, 3000 A, 120 V dc.

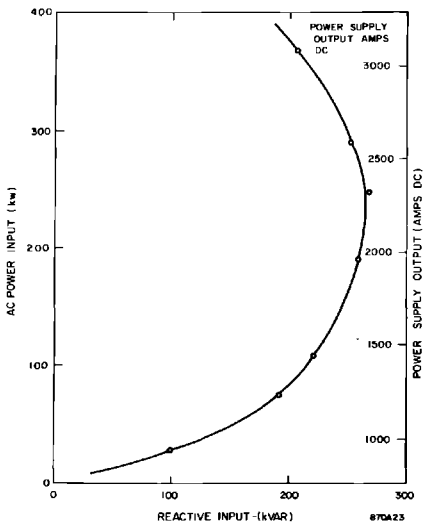

switching more frequently than had been anticipated, sometimes as often as 40 times per week. Electrically operated, vacuum-enclosed, load-break switches are being added to these circuits.

Typical power load characteristics are illustrated in Figs. 25-23 and 25-24 for operation of the end station B beam-transport system power supplies. Nine 360-kW current regulated power supplies are served from one 480-V, 2500/3333-kVA unit substation by feeders B4, B5, and B6 (see Fig. 25-16). These power supplies are silicon controlled solid-state rectifiers supplying the bending and quadrupole magnets in the beam transport line. Current regulation is accomplished by controlling the phase of triggering of the rectifier. Figure 25-23 demonstrates the operation of one of the power supplies which draws not only power but also a wattless reactive load from the ac power system. The reactive load and, hence, the power factor, $kW/(kW^2 + kVAR^2)^{1/2}$, varies as the rectifier ouput is adjusted to different output dc currents. The power demand is proportional to the power load of the magnet plus the small losses in the rectifier. A group of three power supplies served from one of the feeders (B4) shows the same semicircular characteristic (Fig. 25-24). The typical semicircular characteristic results from the process of phase-back control. The 3000-kW load level is the result of operating all the beam transport magnets for 16-GeV particles.

The voltage drop in the 480-V circuits from the research area substation has been too high in some cases. Better operational conditions would have been obtained had an additional substation been placed closer to the loads.

Figure 25-24 Typical group operating characteristics on feeder, three 360-kW current regulated power supplies, silicon-controlled rectifiers, each 3000 A, 120 V dc.

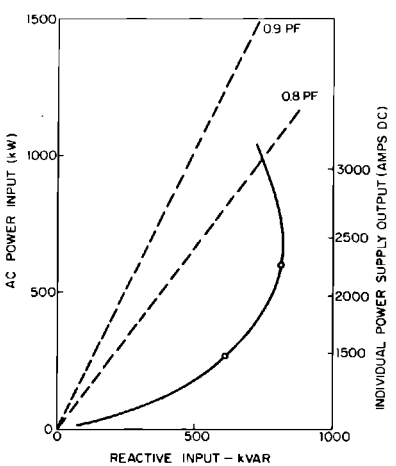

This would have cost more and servicing would have been inconvenient at times due to high radioactivity in this area.

The 480-V circuits are protected from ground fault only at the larger breakers which have a relatively sluggish breaker mechanism. Molded case breakers have no ground current protection. The result is that a small ground fault can trip a larger breaker which needlessly disconnects some loads. Future additions and changes to the wiring will use overcurrent relays for ground current protection in all locations.

Most of the voltage-adjusting motor contactors in the variable-voltage substations have operated as often as one million times in a year. This excessive operation has been reduced by adding a small time delay to the circuit.

Power contracts, energy consumption, and cost (AAT)

There are two power contracts governing the supply of ac power from either 220- or 60-kV lines to the SLAC project.

1. Contract No. AT(04-3)-526, between the U.S. Atomic Energy Commission and the U.S. Bureau of Reclamation, June 16, 1965, calls for the supply of firm power starting at 6 MW for temporary power connections. The firm power supplied under this contract was later increased to 12 MW, then to 18 MW, and, most recently, to 25 MW. The pertinent data, extracted from Schedule R2-F2 of the above contract, are as follows:

Monthly rate: The demand charge is \$0.75 per kilowatt of billing demand. The energy charge is 4 mils/kW-hour for the first 130 kW-hours/kW of billing demand; 3 mils/kW-hour for the next 130 kW-hours/kW of billing demand; and 2 mils/kW-hour for all over 260 kW-hours/kW of billing demand.

Minimum bill: \$1.00 per month per kilowatt of contract rate of delivery.

Billing demand: The billing demand will be the highest 30-min integrated demand measured during the month.

Adjustments: If delivery is made at transmission voltage so that the Bureau of Reclamation is relieved of substation costs, 5% discount will be allowed on the demand and energy charges. If delivery is made at transmission voltage but metered at the low-voltage side of the receiving substation, the meter readings will be increased 2% to compensate for transformer losses. There are no adjustments for power factor; SLAC will normally be required to maintain a power factor at the point of delivery of not less than 90% lagging.

2. Contract AT(04-3)-466, which consists of firm or interruptible power procured from PG & E are from the same line as mentioned above. The rates and charges on this contract, as outlined in PG & E Schedule A-13, are as follows:

Firm service: Firm service energy charge is shown in Table 25-9. The minimum charge per month is \$150.00 but is not to be less than 90 cents/kW of billing demand.

Table 25-9 Firm service energy charge

Energy	*Cents*
First 6000 kW-hour per meter per month	2.64 per kW-hour
For all excess over 6000 kW-hour per month	
First 50 kW-hour kW of billing demand	2.22 per kW-hour
Next 150 kW-hour per kW of billing demand:	
First 100,000 kW-hour	1.28 per kW-hour
Balance	0.91 per kW-hour
Next 100 kW-hour per kW of billing demand	0.91 per kW-hour
All excess	0.65 per kW-hour

Interruptible service: Interruptible on-peak demand is billed at \$0.6832/kW per month; interruptible off-peak demand is billed at \$0.1577/kW per month; the sum of these two shall not be less than a minimum monthly demand charge of \$7000 per month. Interruptible energy is billed at \$0.0062/kW-hour added to the demand charge. The total charge, except the minimum monthly demand charge for any month as computed on the above rates, shall be decreased or increased, respectively, by 0.1% for each 1% that the average power factor is greater or less than 85%, such average power factor to be computed (to the nearest whole percent) from the ratio of lagging kilovolt-ampere hours to kilowatt-hours consumed in the month, provided, however, that no power factor correction charge will be made for any month when the interruptible on-peak demand was less than 10% of the highest such demand in the preceding 11 months.

It is realized that operating costs can be reduced if research experimental loads can be scheduled to minimize short, infrequent, high-power demands each month. Furthermore, by proper negotiation of the firm power and interruptible power allocation of the above power contracts, the power costs can be further reduced. Meters to indicate the project's total megawatt load have been placed in three locations so that operators who control blocks of power can view the instantaneous power consumption and stagger the demands whenever possible.

Typical loads based on various operating conditions (July 1967) are shown in Table 25-10.

Power costs, load factors, and mils per kilowatt-hour for the fiscal years of 1965, 1966, and 1967 are shown in Table 25-11.

Power factor correction

Because of the use of large solid-state rectifiers in the end station power supplies as outlined above, the present average monthly power factor is approximately 86%. It is expected that even lower power factors will result due to added magnet power supply loads and longer operating time of power supply equipment as the SLAC research program is expanded. SLAC is

Table 25-10 Typical loads based on various operating conditions (July 1967)

Facility	*Minimum (MW)*	*Average (MW)*	*Maximum (MW)*
Campus load including conventional substation for klystron gallery	8	9	10
Variable-voltage substations for accelerator operation	2	15	22
End station A	1	7	13
End station B	1	3	8
	12	34	53

obligated to maintain 0.9 power factor or better at the point of delivery as stipulated in Contract AT(04-3)-526, as noted above. The present load characteristics require power factor correction in order to maintain 0.9 power factor or better. Power factor correction devices supplying 3726 kVAR are currently needed to meet the contractual requirements under the present conditions of loading. This amount of correction provides a small margin for the immediate future.

The planned installation of power factor correction apparatus must have a harmonic current control feature. The harmonic current control is essential in operating power factor correction apparatus on feeders serving the silicon-controlled rectifier power supplies. This control prevents excessive heating in existing electrical equipment and unacceptable distortion in the project's line voltage. It also reduces line harmonics to levels acceptable under the power service contract.

SLAC is in the process of procuring a power factor correction device to improve average power factor to 0.9 or better.[4] Negotiations are under way to procure a large, government-surplus, synchronous condenser which will be connected to a 12-kV bus at the master substation.

Acknowledgments

In addition to the authors noted under the chapter heading many other people made significant contributions to the design of electrical systems. T. Turner investigated the possibility of dc distribution to modulators. K. Wilson promulgated a number of project electrical standards and made a number of studies of project power costs and system load growth forecasts. W. K. H. Panofsky, R. B. Neal, G. Loew, J. V. Lebacqz, C. Kruse, K. Mallory, and C. Olson were invaluable in advising on design details and overall system criteria. H. Halperin consulted on transmission and distribution problems. L. Stone consulted on RF interference as did members of the staff

Table 25-11 Power usage and cost experience

Month	Billing demand (kW)	Average P.F.	Billing energy (kW-hour)	Total charge	Load factor	Average cost (mils/kW-hour)
			Fiscal year 1965			
Jul 64	2,654	—[a]	1,258,584	$ 5,267.76	0.644	4.20
Aug 64	2,656	—	1,267,783	5,285.24	0.658	4.15
Sep 64	2,962	—	1,444,057	5,951.55	0.66	4.12
Oct 64	3,635	0.860	1,696,464	7,159.99	0.63	4.21
Nov 64	4,125	0.873	1,837,860	7,959.31	0.61	4.30
Dec 64	4,015	0.875	2,052,526	8,248.04	0.687	4.10
Jan 65	4,125	0.861	2,176,737	8,603.17	0.708	3.94
Feb 65	4,663	0.860	2,198,194	9,226.60	0.70	4.19
Mar 65	5,753	0.877	2,788,969	11,529.54	0.65	4.14
Apr 65	5,985	0.885	3,103,636	12,378.66	0.72	3.99
May 65[b]	6,524	0.870	3,163,563	13,076.27	0.653	4.13
Jun 65	6,348	0.854	2,779,200	12,399.63	0.59	4.45
			25,767,573	$107,085.76		4.16
			Fiscal year 1966			
Jul 65	5.104	0.853	2,706,919	$ 11,400.00	0.69	4.21
Aug 65	5,569	0.866	2,913,138	11,566.19	0.703	3.98
Sep 65	7,430	0.865	3,350,474	14,412.59	0.626	4.30
Oct 65	8,482	0.849	3,893,140	16,582.97	0.617	4.26
Nov 65	8,433	0.875	3,962,186	16,615.44	0.656	4.20
Dec 65	9,486	0.867	4,896,955	19,577.55	0.694	4.00
Jan 66	10,086	—	4,422,758	19,326.38	0.59	4.37
Feb 66[c]	10,404	—	4,835,718	20,455.40	0.69	4.24
Mar 66	12,240	0.852	5,650,841	23,992.52	0.531	4.25
Apr 66	13,709	—	5,802,813	25,872.20	0.588	4.46
May 66	18,482	—	7,776,011	34,790.42	0.566	4.48
Jun 66	18,360	—	7,415,298	33,972.95	0.564	4.57
			57,626,251	$248,564.61		4.31
			Fiscal year 1967			
Jul 66	17,258	—	7,579,069	$ 33,090.65	0.614	4.38
Aug 66	15,178	—	6,885,122	29,519.50	0.610	4.28
Sep 66	20,318	—	6,870,374	35,058.11	0.470	5.11
Oct 66	24,480	—	7,139,408	40,076.72	0.406	5.60
Nov 66	25,826	0.85	8,592,546	45,731.46	0.460	5.34
Dec 66[d]	29,131	0.85	9,343,955	52,142.26	0.432	5.65
Jan 67	28,519	0.85	9,887,717	53,111.37	0.466	5.30
Feb 67	26,561	0.86	8,346,823	43,160.05	0.435	5.15[e]
Mar 67	30,233	0.86	12,885,599	53,537.01	0.575	4.15[e]
Apr 67	30,845	0.87	13,358,685	56,085.74	0.603	4.20[e]
May 67	33,660	0.87	15,039,288	62,627.55	0.600	4.18[e]
Jun 67	33,415	0.85	14,237,262	61,314.34	0.592	4.30[e]
			120,373,398	$565,454.76		4.70

[a] Data not available.

[b] Firm power delivery changes from 6 to 12 MW.

[c] Firm power delivery changes from 12 to 18 MW.

[d] Firm power delivery changes from 18 to 25 MW.

[e] Including $11,685.00 credit to SLAC from PG & E on 220-kV transmission lines.

of the Stanford Radio Sciences Laboratory. U. Lamm consulted on system power factor correction equipment design. M. Grushkin was responsible for overall project communications and developed audio–visual systems for the auditorium. V. Smith and J. Kuypers consulted on physical requirements for the instrumentation and control cable plant and racks for supporting electronic equipment. E. Mortenson, C. Hale, R. Ardnt, and W. Farley were principal contributors to the preparation of drawings and specifications for the cable plant and racks. J. Smith prepared a number of early construction cost studies. E. Keyser and D. Pike expedited the electrical installation work. J. Fish and R. Laughead were responsible for preparation of working drawings for the electrical systems. K. Johnson participated in the design of the test stands power system and electrical distribution systems for the beam switchyard and end stations. R. Robbers was invaluable in working out field construction problems. W. Lusebrink and M. Buenrostro were very helpful in putting systems into operation and developing maintenance programs. Chief J. Marston of the Stanford Fire Department consulted on development of fire alarm system criteria. R. Mizrahi prepared a report on ac distribution to modulators and then collaborated with C. Olson *et al.* on the design of the high-voltage rectifiers for the modulators. J. Casati was very helpful in the design of the variable-voltage substation control equipment and other electrical systems for the accelerator.

References

1 I. Krumholz, "Effect of Radiation in the Accelerator Area on Cable Insulation," Rept. No. SLAC-TN-62-31, Stanford Linear Accelerator Center, Stanford University, Stanford, California (June 1962).

2 R. E. Taylor, *IEEE Trans. Nucl. Sci.* **NS-12** (3), 846 (June 1965).

3 D. A. G. Neet, "Radiation Exposure in the Switchyard," Rept. No. SLAC-TN-65-9, Stanford Linear Accelerator Center, Stanford University, Stanford, California (January 1965).

4 F. Hall and A. Tseng, "Power Factor Correction Status Report," Internal Memorandum, Stanford Linear Accelerator Center, Stanford University, Stanford, California (September 1967).

26

SHIELDING AND RADIATION

H. DeStaebler, T. M. Jenkins, Coeditor, and W. R. Nelson, Coeditor

The purpose of this chapter is to present a simplified logic useful in understanding the shielding around a high-energy electron accelerator. This should be useful in cases where a shield is to be designed for radiation worker tolerance and in cases where a shield already exists and some knowledge of the radiation penetrating that shield is required.

Certain basic assumptions are made which should be discussed here. First, the energy spectrum of radiation penetrating a shield is assumed to be known, or to be approximated in such a way that a flux-to-dose conversion may be made. Second, the problem of distant boundaries is assumed to be secondary to that of the radiation worker in close proximity to the shield, so that to a first-order approximation, skyshine, etc., may be ignored.

Shielding calculations are done in distinct steps:

1. First, one must determine the radiation tolerances. At SLAC this value is 0.75 mrem/hour (steady occupancy). To be conservative, one should design shielding to produce about one-tenth of the steady occupancy value.
2. The amount of average electron beam power stopped within the shield must be estimated.
3. One must derive some information on the development of the electromagnetic cascade.
4. One must determine the production of penetrating particles by the cascade.
5. Finally, the attenuation of these penetrating particles in the shield has to be calculated.

This chapter is concerned with items (3), (4), and (5) above. First, the electromagnetic cascade and the production of penetrating particles by that

cascade will be examined. Then, the shielding problem will be approached from the standpoint of having to shield the least penetrating component (photon radiation) first, go on to the next more penetrating component (neutrons), and finally, take up the problem of shielding muons which are very weakly interacting. A brief discussion concerning radiation streaming up penetrations will follow. And in conclusion, an outline for making practical (order-of-magnitude) calculations will be presented.

26-1 Electromagnetic cascade (HDeS, WRN)

When a high-energy electron or photon enters an absorber, an electromagnetic cascade shower is produced. The basic interactions of the electrons and photons are well established, but analytical solutions of the diffusion equations are prohibitively difficult to obtain. Analytic shower theory[1,2] accounts for the main features of the longitudinal or one-dimensional development of the cascade. Usually for shielding calculations the behavior at great depths is needed where approximation in the theory may have important consequences. Few experiments go deeper than 15 or 20 radiation lengths[3–5] (denoted by X_0), but these experiments and simple theory agree that the shower decreases exponentially with an absorption mean free path of several radiation lengths. This agreement may be accidental, however, because the most penetrating component, which one would expect to control the shower at great depths, consists of photons with energies near the minimum in the interaction cross section* (hence, with the greatest mean free path, denoted by $\Lambda \equiv 1/\mu_{\min}$,

* These are the good geometry values which are given many places, for example, Reference 6.

Figure 26-1 The variation of Λ, λ, X_0, and X_m with atomic number, Z.

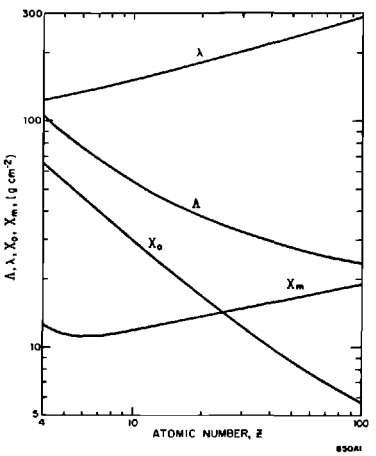

where μ_{min} is the narrow beam, minimum absorption coefficient). In most analytic shower theories, there are approximations that eliminate this minimum in the photon cross section. Figure 26-1 shows that Λ varies from about $2X_0$ at low Z to about $4X_0$ at high Z. Scattering, which decreases the effective absorption length in a real three-dimensional shower, is more important at high Z because the average electron energy is lower, and an absorption mean free path around $3X_0$ is reasonable for all Z.

The radial or transverse spread requires three-dimensional shower theory[7] which is too complicated to be done very accurately analytically and application is limited to high-energy cosmic-ray phenomena. The most useful calculations are the Monte Carlo studies,[8–10] which take into account the important cross-section data and which do not introduce as many oversimplifications. Experiments are complicated by the requirements of large dynamic range in the detector and small sizes for the incident beam and the detector.[3,11,12] For shielding applications a useful way to summarize the Monte Carlo results is to consider the energy absorbed per unit volume, dw/dv. Define the fraction of the total energy E_0 absorbed beyond radius r_0 by

$$\frac{U(r_0)}{E_0} = \frac{\int_0^\infty \int_{r_0}^\infty \frac{dw}{dv} 2\pi r \, dr \, dz}{\int_0^\infty \int_0^\infty \frac{dw}{dv} 2\pi r \, dr \, dz} \tag{26-1}$$

Figure 26-2 gives U/E_0 versus r_0 in Moliere units. A Moliere unit, X_m, is the characteristic measure for radial distributions in analytic shower theory[13] and

Figure 26-2 The fraction of the total shower energy that is absorbed beyond a cylindrical radius, r_0, as a function of r_0/X_m.

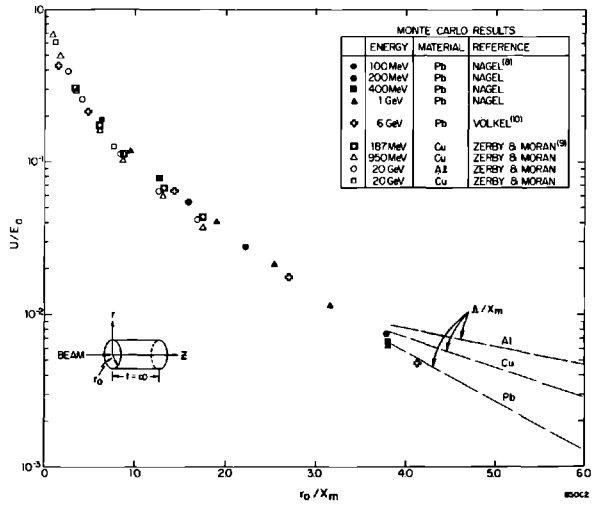

is equal to $X_0 E_s/\varepsilon_0$, where ε_0 is the critical energy of the material and $E_s = 21.2$ MeV. The values of X_0 and X_m used[14] are given in Fig. 26-1. The significance of Fig. 26-2, for shielding purposes, is that a universal curve is formed. The result is independent of incident energy and target material. The behavior of U/E_0 at large r_0 is of interest, but unfortunately the Monte Carlo calculations do not extend far enough out. Again, one would expect the most penetrating component (namely, those photons having a mean free path, Λ) to control the shower at large radial depths. Shown on Fig. 26-2 are the slopes corresponding to Λ (in Moliere units) for aluminum, copper, and lead.

26-2 Production and attenuation of photon radiation from thick targets (TMJ, WRN)

It is of practical interest to determine the angular distribution of photon radiation for high-energy electron beams striking thick targets. Consider a cylindrical target having a length of $\approx 15X_0$ and a radius of $\approx 3X_m$. One would expect, according to Fig. 26-2, that about 1% of the total energy would escape radially. Assuming that this energy is radiated isotropically into 4π steradians, one can make an order of magnitude calculation of the dose rate at 1 meter for 1 kW of incident beam power.

$$\bar{D} = \frac{10^{-2} \times 10^{3}\ \text{W} \times 10^{7}\ \text{ergs-sec}^{-1}\ \text{W}^{-1}}{4\pi(10^{2}\ \text{cm})^{2}\ 30\ \text{g-cm}^{-2}} \times \frac{1\ \text{rad}}{10^{2}\ \text{ergs-g}^{-1}} \times \frac{3600\ \text{sec}}{\text{hour}}$$

$$\sim 10^{3}\ \text{rad/hour}$$

where 30 g-cm^{-2} is an average value for Λ.

Figure 26-3 The photon dose rate from a typical beam absorber as a function of the angle from the beam direction, normalized to 1 kW of beam power and to a source-to-detector distance of 1 meter.

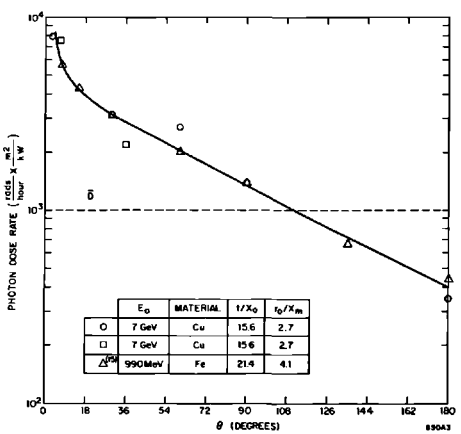

This order of magnitude is verified in Fig. 26-3 where several measurements are plotted versus the angle from the beam direction, the cylinder considered a point source. Measurements at 0° have been made but are not shown in Fig. 26-3 because they are too dependent on incident beam energy, target thickness, and detector size (the dose rate falls off rather sharply with angle, as seen in Fig. 26-3).

For $E_0 = 990$ MeV, $t = 21.4X_0$, and using a Zeus ion chamber, Neet[15] has measured 1.1×10^4 rads/hour at 0° and for 1 kW at 1 meter. On the other hand, we have measured 1.2×10^5 rads/hour for $E_0 = 12$ GeV, $t = 16X_0$, and using a small ($\frac{1}{8}$ in.) capsule of LiF.

Gamma-ray absorption measurements have been made at 0°, 45°, and 90° by placing capsules of LiF powder between lead plates and by exposing the arrangement to the radiation coming from an iron cylinder ($t = 16X_0$, $r_0 = 3.6X_m$) bombarded by a 12-GeV electron beam. The LiF responds to ionizing radiation and its use for this purpose is described elsewhere.[16] Figure 26-4 shows the absorption for these three angles as a function of lead thickness. The 90° measurement was complicated by the presence of the 20-GeV spectrometer, the backscattering from which might account for the departure from a straight line, as indicated in Fig. 26-4 by the broken line.

One would expect, according to the simple theory above, that the most probable gamma-ray energy would be ≈ 8 MeV, corresponding to the

Figure 26-4 Absorption measurements in lead for γ radiation coming from an iron target that is bombarded with a 12-GeV electron beam, for various angles from the beam direction ($t = 16X_0$, $r_0 = 3.6X_m$).

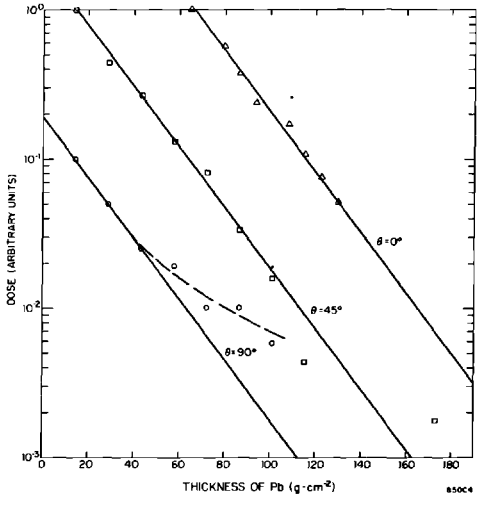

minimum in the narrow-beam absorption curve for iron. The absorption coefficient, μ, in lead at 8 MeV is 0.047 cm^2/g, which is the slope of the straight lines in Fig. 26-4.

One can apply the above curves and theory to a typical shielding situation. Consider a copper target ($t = 15.6X_0$, $r_0 = 2.7X_m$) located in end station A as shown in Fig. 26-5. The beam energy is 7 GeV and the power is 1 kW. Using Fig. 26-3 along with the narrow-beam absorption coefficient in concrete at 9 MeV, one obtains the dose rates around the end station given in Table 26-1. Also given are the actual gamma-ray measurements taken under the above conditions.

At positions B and G the calculation agrees within the measuremental errors. At positions C and F the measurements are higher than the calculations; however, this could very well be due to scattering around the entrance maze. (Using the unattenuated calculated dose rates at the entrance modules and allowing 5% of the photon radiation for each 90° bend, one obtains about the dose rate actually measured.) At positions D and E the calculation fails—although account should probably be taken of the much higher levels at close to zero angle that have scattered in the air path between the target

Figure 26-5 Plan view of end station A, indicating the positions where photon and neutron measurements were made.

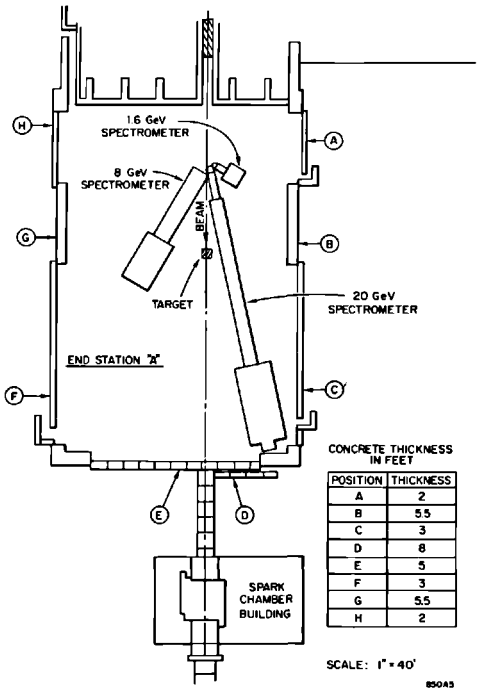

POSITION	THICKNESS
A	2
B	5.5
C	3
D	8
E	5
F	3
G	5.5
H	2

Table 26-1 Comparison of calculated and measured photon dose rates around end station A

Position[a]	*Calculated dose rate (mR/hour)*	*Measured dose rate (mR/hour)*
A	12	5–6
B	0.5	0.5–2.5
C	0.2	4–5
D	0.007	2.5–3.8
E	1.0	18–38
F	0.4	7.5
G	0.7	0–2.5
H	7.5	2.5–4

[a] See Fig. 26-5; $E_0 = 7$ GeV; beam power = 1 kW.

and the end station wall. Also, the method of calculation seems to overestimate the dose rate at position A—particularly if one again accounts for the radiation that comes through the entrance maze. One might expect that the average gamma-ray energy in the backward direction would be considerably lower than 8–9 MeV, and hence, a much larger absorption coefficient should be used. It appears, however, that one can estimate the photon dose rate within a factor of 2 or 3, except in the forward ($\theta \lesssim 10°$) direction.

26-3 Neutron production and attenuation (HDeS, TMJ)

Outline of general calculation

The procedure outlined here for calculating the photonuclear shielding is fairly simple. It is basically the same as that first used for reactor shielding, and in many details it is a direct application of the scheme developed by

Figure 26-6 Schematic of a typical shielding geometry.

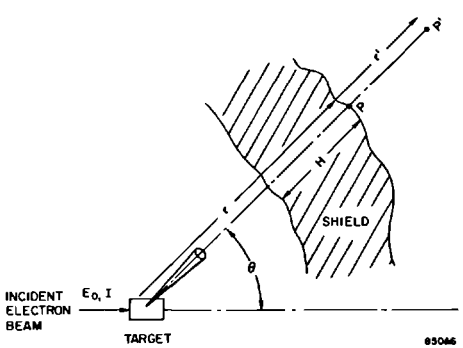

Moyer and co-workers and applied to the 184-in. cyclotron and to the bevatron.[17,18]

Figure 26-6 shows the general layout and defines some symbols. Assuming a point source, the radiation level at a point P on the outside surface of the shield is

$$D_P = \frac{1}{r^2} \int F(T)B(T) \exp\left[\frac{-H(\theta)}{\lambda(T)}\right] \frac{d^2n(T, \theta)}{dT\, d\Omega}\, dT \tag{26-2}$$

where

T = the neutron kinetic energy
r = the distance from target to P
F = the biological conversion factor (rem/neutrons-cm^{-2})
H = the shield thickness
λ = the effective removal mean free path
B = the buildup factor so that $Be^{-H/\lambda}$ represents the tail of the nuclear cascade
$\frac{d^2n}{dT\, d\Omega}$ = the yield of neutrons into (T, dT) and $(\theta, d\Omega)$ arising from the absorption of an electron beam with current I and energy E_0

At low energies $B \approx 1$ and F is well established[19]; at high energies, $BF \equiv G$ may be taken from the work of Neary and Mulvey.[20]

Equation (26-2) may be written

$$D_P = \frac{1}{r^2} \sum G_i \exp\left(\frac{-H}{\lambda_i}\right) \frac{dn_i}{d\Omega} \tag{26-3}$$

where the subscript i denotes a range of neutron energies for which G and λ are fairly constant, and

$$\frac{dn_i}{d\Omega} = \int_{T_i}^{T_{i+1}} \frac{d^2n}{dT\, d\Omega}\, dT \tag{26-4}$$

Moyer approximated the sum in Eq. (26-3) by a single term (since below 200 MeV, λ decreases rapidly as T decreases[18,21]) with $\lambda = 158$ g/cm^2, which is typical of the effective removal mean free path in concrete for neutrons with energies above several hundred million electron volts (see Fig. 26-1), and with

$$\frac{dn(\varepsilon, \theta)}{d\Omega} = \int_{\varepsilon}^{T_{\max}(\theta, E_0)} \frac{d^2n}{dT\, d\Omega}\, dT \tag{26-5}$$

with $\varepsilon = 150$ MeV.

The distribution in angle and energy of photoneutrons has not been measured extensively above roughly 100 MeV. In an approximate calculation,

fictitious two-body reactions replace the actual complicated reactions.[22] Then

$$\frac{d^2n}{dT\,d\Omega} = I \int \frac{N_0}{A} \frac{d\sigma(k, \theta^*)}{d\Omega^*} \frac{\partial(k, \theta^*)}{\partial(T, \theta)} \frac{dl}{dk}\, dk \tag{26-6}$$

where

I = the incident electron current
N_0, A = Avogadro's number, atomic weight
$\frac{d\sigma}{d\Omega^*} = \sigma_{\text{total}}/4\pi$ if isotropy in the center of mass is assumed
$\frac{\partial(k, \theta^*)}{\partial(T, \theta)}$ = the Jacobian from variable transformation
$\frac{dl}{dk}$ = the differential photon track length, $0.57\, E_0 X_0/k^2$

The total cross sections are shown in Fig. 26-7. For thin shields the giant resonance reactions dominate; these have been studied extensively.[23–25] For thick shields, the pion reactions[26] are most important. The pseudodeuteron reaction[23] always contributes but never dominates. The $1/k^2$ variation of the photon track length makes the neutron yields insensitive to the behavior of the cross section at higher energies. Preliminary measurements[27] up to 5 BeV are consistent with σ_{total} roughly constant of the order of 100 mb/nucleon, and there is some evidence that σ_{total} decreases at very high energies.[28]

Figure 26-7 Total photonuclear cross section divided by the atomic weight (millibarns/nucleon) as a function of the photon energy.

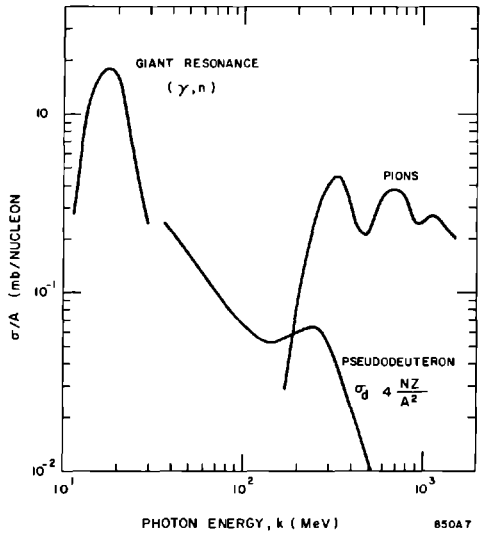

The two-body approach of Eq. (26-6) gives reasonable agreement with the measured spectra of photoprotons with $50° < \theta < 94°$ from 950-MeV bremsstrahlung on copper.[22] Figure 26-8 shows $dn/d\Omega$, essentially Eq. (26-5) from Eq. (26-6), for electrons on copper for $\varepsilon = 100$, 150, and 200 MeV. Note that for electrons, $dn/d\Omega$, and hence D_p is proportional to IE_0 (the incident beam power) and to X_0 (via dl/dk). The values for $\varepsilon = 25$ MeV and $\varepsilon = 700$ MeV were extrapolated from the 100-,150-, and 200-MeV calculations and are included in Fig. 26-8. Figure 26-9 shows $r^2 D_p$ derived from Fig. 26-8 and Eq. (26-3) with five energy groups and Moyer's curve for $\lambda(T)$.

Some comments on this whole procedure may be appropriate.

1. This approach is sometimes called semiempirical because λ is determined from experiment. Although $dn/d\Omega$ and G are based upon reasonable, yet approximate, calculations, various measurements indicate that there are no gross errors.

2. In the model implied by Eq. (26-2) and Fig. 26-6, there is no spreading of the nuclear cascade in the shield. All of the spreading arises from the

Figure 26-8 High-energy neutron production by electrons on copper as a function of angle. The curves indicate the number of neutrons with energies greater than ε.

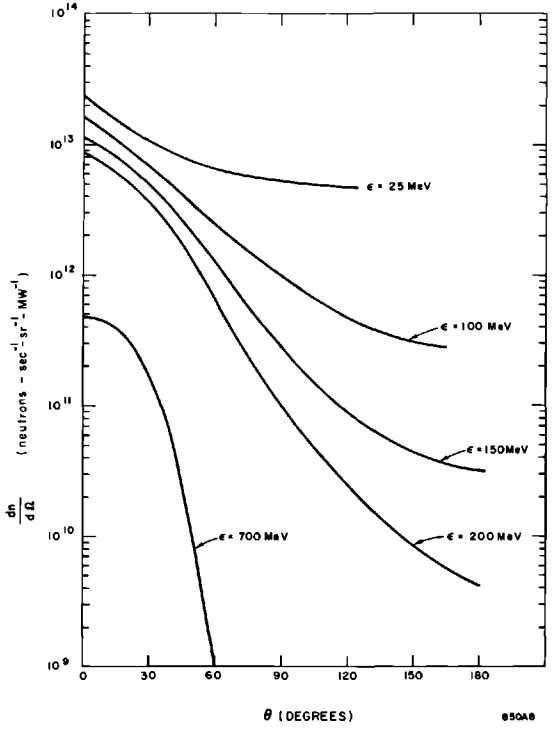

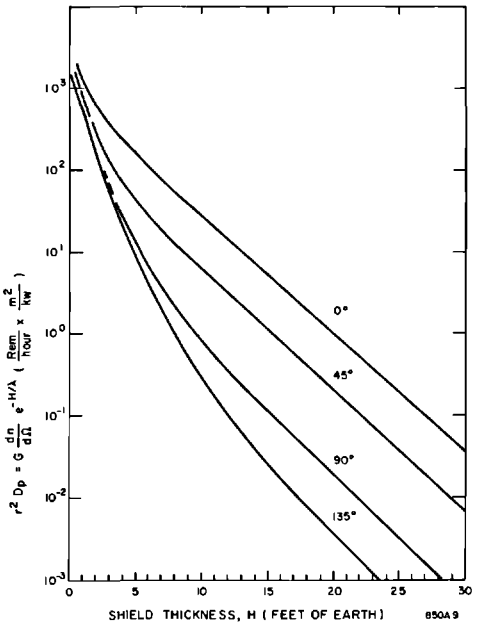

Figure 26-9 Normalized neutron radiation level (r^2D_p, in Eq. (26-3)) for $\theta = 0°$, 45°, 90°, and 135° as a function of the shield thickness, H, in feet of earth-equivalent ($\rho = 1.70$ g-cm^{-3}).

angular distributions of the neutrons from the source. These approximations are better the more uniform the shield thickness and the greater the separation between target and shield.

3. Since the cascade is taken to be one-dimensional ("straight-ahead" approximation), λ should be derived from a bad geometry experiment.

4. Empirically, λ scales with the inelastic σ at high energies and with the total σ at low energies.[18] These cross sections vary approximately[29] as $A^{3/4}$, so for different materials λ is proportional to $A^{1/4}$ (in which case the effective A of concrete is 23.3) and this is the variation of λ shown in Fig. 26-1.

5. Most of the radiation field at the outer surface of the shield consists of low-energy particles, the secondaries in equilibrium with the penetrating high-energy particles. These secondaries have a broad angular distribution so that simply replacing r by $r + r'$ in Eq. (26-2) may not give a good estimate of $D_{P'}$, the radiation level at P' (see Fig. 26-6). A better procedure is to treat the surface of the shield as a new source by integrating D_P over the surface of the shield and letting it reradiate according to some new angular distribution, for example, isotropic into 1 or 2π, or cosine.

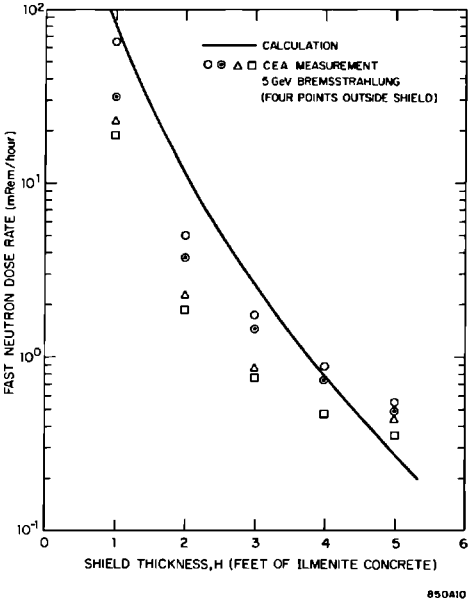

Figure 26-10 Comparison of a Cambridge electron accelerator shielding experiment with calculation. The fast neutron dose rate is plotted versus the shield thickness (Ilmenite concrete, $\rho = 4.0$ g-cm^{-3}). Photon beam intensity $= 2.0 \times 10^{10}$ eq. quanta/sec; see Reference 30.

As an example of the application of all this, Fig. 26-10 compares measurements made at the Cambridge electron accelerator[30] with the present method of calculation. The points are the levels actually measured with a Bonner sphere dosimeter (uncorrected for background) at four points outside the shield. The calculation is based on (1) a rough interpolation between 45° and 90° curves on Fig. 26-9, (2) a factor of 0.5 accounting for the fact that the dosimeter only measures part of the level, and (3) the level at the surface of the shield being integrated over (multiplied by) 2π steradians and reradiated isotropically into one-quarter of a sphere with a radius of 10 ft. Considering the crudeness of this estimate, the agreement is amazingly close.

Measurements of photoneutrons

For shielding against radiation produced in a high-energy accelerator, one would like to know the energy-flux distribution of neutrons incident upon a shield. Except in the forward direction where muons become significant, neutrons with energies between 200 and 500 MeV dominate the shielding

calculations in a high-energy accelerator. Neutrons with higher energies are very rare because there are few high-energy photons, and neutrons with lower energies have short attenuation lengths and are easily absorbed. For areas of thin shielding, such as the end stations where walls may be only a few feet thick, one needs to know the neutron production fairly well in order to make an accurate estimate of radiation penetrating the shield. For these reasons, the accuracy of neutron production calculations, and particularly Fig. 26-8, were checked in a series of experiments using a high-energy electron beam. The yield of neutrons was measured in the 0° direction at an electron energy $E_0 = 10$ GeV with $\varepsilon = 700$ MeV and with $\varepsilon = 25$ MeV. The yield for $E_0 = 7$ GeV with $\varepsilon = 25$ MeV was also measured at 0°, 30°, 60°, and 90°.

Measurements of neutrons with $E_n > 25$ MeV were made using the $^{12}C(n, 2n)^{11}C$ reaction which has a threshold of ≈ 20 MeV. Normally, this reaction has been utilized only outside of shielding where competing reactions from high-energy photons and charged particles are not probable. However, inside the shielding, photons, pions, and protons will tend to mask the $(n, 2n)$ reaction to a degree determined by particle production cross sections and reaction cross sections leading to ^{11}C. Figure 26-11 shows the cross sections for reactions in carbon leading to ^{11}C as given in the literature.[31]

The carbon is in the form of a plastic scintillator 5 in. in diameter and 5 in. high, coated with white paint. The scintillators were first irradiated and then removed for counting on a 5-in. photomultiplier tube encased in a lead-lined iron housing. Sensitivity of the system is such that a unit flux density of neutrons with $E_n > 20$ MeV will give 105 counts/min. Normal background is about 800 counts/min.

Figure 26-11 Reaction cross sections in carbon leading to ^{11}C (taken from Reference 31). Also shown is the reaction leading to ^{7}Be ($T_{1/2} = 53$ days).

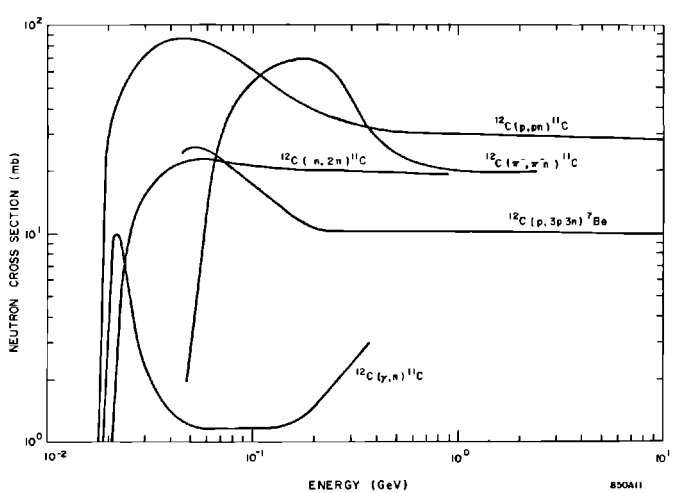

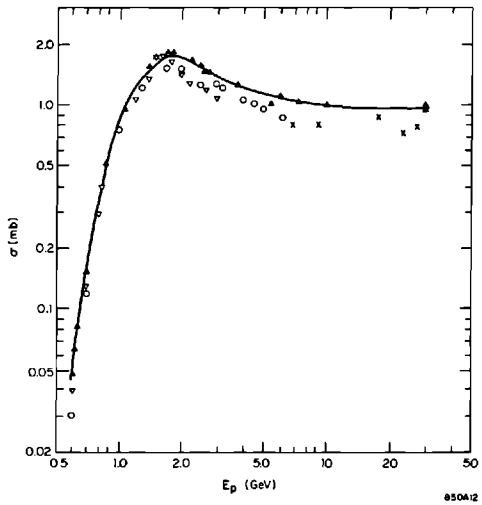

Figure 26-12 Cross section for the reaction $^{197}Au + p \rightarrow {}^{149}Tb$ (taken from Reference 33). The $^{197}Au + n \rightarrow {}^{149}Tb$ cross section is assumed to be the same. The threshold, shape, and magnitude for the reaction in mercury should be similar to gold (Reference 32).

Neutrons with energies greater than 700 MeV were measured with mercury detectors. The high-energy spallation reaction in Hg has been reported by McCaslin *et al.*,[32] with a threshold for producing ^{149}Tb between 300 and 700 MeV. The threshold and cross sections should be essentially the same as that for the spallation of Au leading to ^{149}Tb as reported by Franz and Friedlander[33] (see Fig. 26-12), who give a threshold for the ^{197}Au (p, spallation) ^{149}Tb reaction between 500 and 600 MeV with a cross section of about 1 mb. It is assumed that the reaction cross section for ^{149}Tb production from neutrons is similar to that from protons. Inside shielding, this detector measures the reaction from pions, protons, neutrons, and perhaps high-energy photons. However, in SLAC measurements, a thick copper target ($\approx 16X_0$) was used. There should not be many surviving photons with energies great enough to produce this reaction. Thus, this detector should give numbers closer to calculation than the carbon detector where there may be a significant number of photons with $E_\gamma \gtrsim 20$ MeV, especially in the forward direction. The mercury was irradiated in polyethylene jars and then removed to a laboratory* for analysis. There they were placed in a centrifuge rotating at 1700 g for 1 hour with a cellulose acetate pressure-sensitive tape on top. The tape

* Thanks are due J. B. McCaslin and the Lawrence Radiation Laboratory, Berkeley, for the use of their facilities and experience.

was then removed and counted on a windowless alpha counter with about 33% of 4π geometry. The 1-hour centrifuge time plus 1-hour wait time before centrifuging was sufficient to allow any short-lived products to decay away and the 4.12-hour ^{149}Tb half-life was followed without ambiguity. Figure 26-13 shows the ^{149}Tb decay from a mercury sample irradiated near a target which was bombarded with 10-GeV electrons. The sensitivity of the system used at Lawrence Radiation Laboratory is such that a 500-g sample irradiated to saturation by a unit flux density gives 3×10^{-2} counts/min.

A few sentences describing how this calibration factor was obtained might be in order. The mercury used in the calibration was placed in a 700-MeV proton beam with gold foils in front and to the rear of the sample. The calibration was then determined relative to gold, assuming that the (n, spallation) cross section is the same as the (p, spallation) cross section.

In the SLAC experiment, the electron beam bombarded a thick target, and a mixture of high-energy particles was incident upon the sample. It was expected that secondary particles would have energies up to that of the incident electron energy, which was 10 GeV. The uncertainties in cross section, plus the fact that the system was calibrated at only one energy, were such that

Figure 26-13 Decay of ^{149}Tb activity in a mercury sample irradiated in the SLAC tunnel near a 10-GeV electron beam targeting in copper. Zero decay time corresponds to 3.5 hours after beam shut off. This allowed for the decay of shorter-lived products and also for the 1-hour centrifuging. The solid line is the slope corresponding to the 4.12-hour half-life of ^{149}Tb.

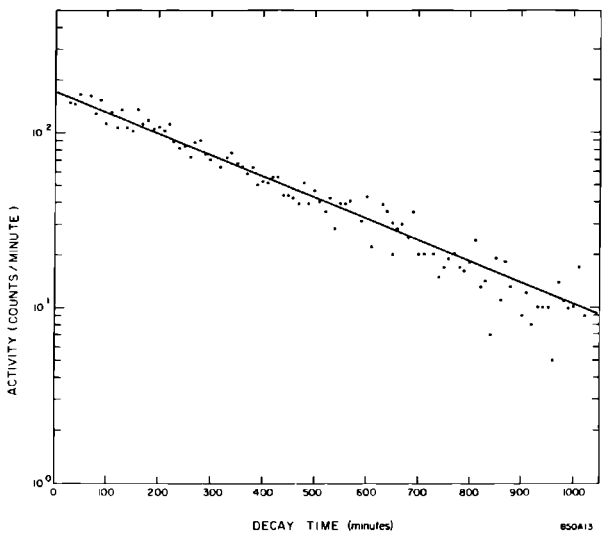

an accurate measurement was improbable, and one had to be satisfied with an order-of-magnitude measurement.

The yield of neutrons with energies above 700 MeV was checked in the forward direction only and compared with the yield of neutrons with energies greater than 25 MeV as measured with the carbon scintillators. With a 10-GeV electron beam incident on a $16X_0$ copper target, the detectors were placed about 5° from beam direction and 10 ft downstream. Twelve inches of lead with a 4-in. hole were located between the target and detectors. From Fig. 26-8, one would estimate the yield of neutrons with energies greater than 700 MeV to be 4.5×10^{11} neutrons/sec-steradian-MW. The measured value, using the mercury detector, was 4×10^{11} neutrons/sec-steradian-MW. With the gross uncertainties in cross section and detector calibration, this is considered excellent agreement.

The yield of neutrons with energies greater than 25 MeV, as measured with the carbon reaction, was 1.4×10^{14} neutrons/sec-steradian-MW which

Figure 26-14 Comparison of measured and calculated values of $dn/d\Omega$ as a function of the angle from the beam direction. The calculations are from Figure 26-8 ($\varepsilon = 25$ MeV). The agreement is good at angles greater than 30°. At 0°, the agreement is poor, due probably to competing reactions.

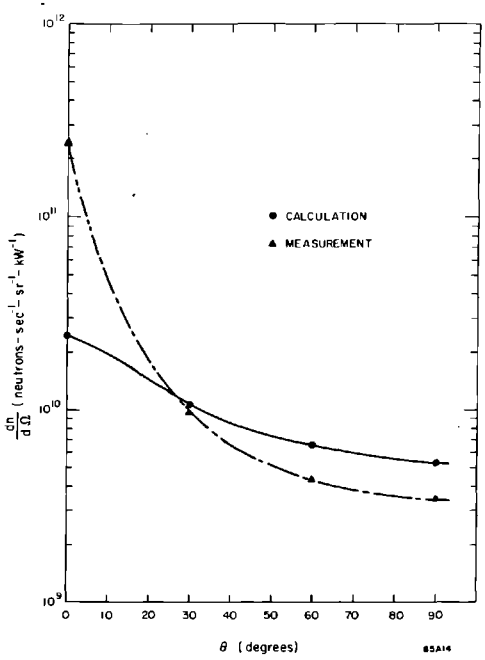

is about 5 times greater than the estimated value of 2.1×10^{13} neutrons/sec-steradian-MW. The high measured value probably indicates the contribution from the (γ, n) reaction.

In another experiment an electron beam of 7 GeV was targeted in end station A in a $16X_0$ copper cylinder ($r_0 = 2.7X_m$) and measurements of neutrons with $E \gtrsim 25$ MeV were made, again using the solid plastic scintillators, at 0°, 30°, 60°, and 90°. In Fig. 26-14, a comparison is made between the measured values at these angles and the calculated curve of Fig. 26-8. As can be seen, there is good agreement at all angles except in the forward direction where the agreement is not expected to be as good due to competing (γ, n) reactions from high-energy photons.

In an effort to generate some information on neutron fluxes in other energy intervals, detectors of bare indium, moderated indium, and aluminum disks were placed at 3°, 30°, 60°, 90°, 135°, and 180° from the beam direction

Figure 26-15 Fast neutron fluxes inside end station A at 20-ft radius from a target bombarded by 7-GeV electrons. Measurements were made using: ○ moderated In foils, □ Al disks, and △ bare In foils. Increased fluxes near the 90° direction are probably due to proximity to the end station walls.

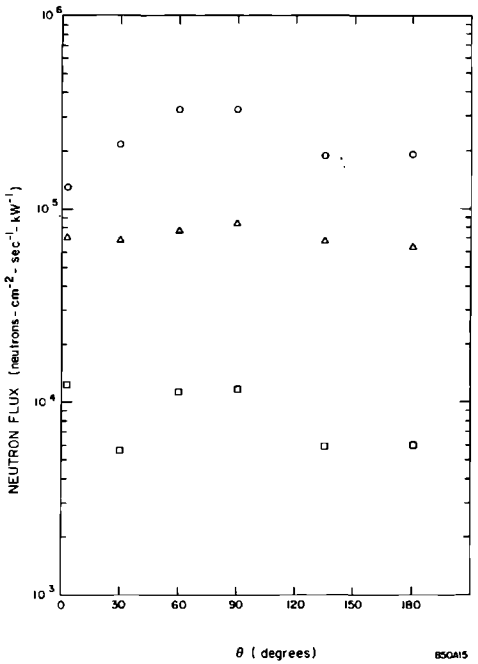

in end station A at a radius of 20 ft. An approximate isotropic yield would be expected for neutrons in the giant resonance region, which is the region encompassed by the moderated indium detectors, and partly by the aluminum detectors, and this is, indeed, what was measured. The thermal neutron flux inside the end station should be more or less uniform, for the walls are the main source of thermal neutrons. Figure 26-15 shows the relative fluxes as measured by bare and moderated indium and the aluminum detectors. The flux is isotropic within a factor of about 2.5 and may be even closer to isotropic when the effect of backscatter is added. The detectors at 90° were only 40 ft from the end station walls whereas those at 0° or 180° were at least 100 ft from the end walls. The source strength at 90°, as measured by the moderated indium foils, was about 1.5×10^{12} neutrons/sec-kW which was in good agreement with previous measurements of 1.25×10^{12} neutrons/sec-kW,[34] and with calculations.[35]

Detectors encompassing only three energy intervals make it difficult to unfold a spectrum. However, some information may be presented in a useful manner if one knows the flux of neutrons in each energy range. It was decided to present the data as ratios of fluxes compared to the fluxes as measured by moderated indium foils. This is done in Table 26-2, with the flux of neutrons as measured by Neet[15] at 1-GeV electron energy in the Mark III accelerator also included. Table 26-2 shows that the neutrons measured by the carbon reaction are definitely forward peaked, falling rapidly with increasing production angle, whereas the neutrons measured by the aluminum reaction are essentially isotropic.

Figure 26-9, showing $r^2 D_p$ derived from Fig. 26-8, was checked using a 1-kW electron beam targeted in the middle of end station A. Radiation from the target penetrated different thicknesses of concrete at different angles, giving an excellent check on Fig. 26-9. Neutron measurements were made

Table 26-2 Ratio of neutron source strength measured with aluminum, carbon, or moderated indium, for a 7-GeV electron beam incident on a $16X_0$ copper target[a]

	Aluminum	*Carbon*	*Q (Moderated indium) (neutrons-sec^{-1}kW^{-1})*	
Angle	*moderated indium*	*moderated indium*	*$E_0 = 7$ GeV*	*$E_0 = 1$ GeV*
0–3°	0.095	4.96	6×10^{11}	1.95×10^{12}
30°	0.026	0.121	9.9×10^{11}	2.9×10^{12}
60°	0.035	0.036	1.51×10^{12}	4.16×10^{12}
90°	0.035	0.028	1.5×10^{12}	3.82×10^{12}
135°	0.032	—	8.5×10^{11}	4.16×10^{12}
180°	0.031	—	8.8×10^{11}	—

[a] The data at 1 GeV is by Neet (Reference 15).

Table 26-3 Comparison of calculated and measured neutron dose rates around end station A[a]

Position	*Calculated dose rate (mrem/hour)*	*Measured dose rate (mrem/hour)*
A	45	25
B	9.8	4.9
C	31.2	8.5
D	—	—
E	50	5
F	24	7.8
G	2.8	2.8
H	22	15.8

[a] See Fig. 26-5.

outside the end station A walls using a moderated BF_3 detector which detects neutrons in the energy range of from 10 keV to 4 MeV. Figure 26-9 gives no indication of which energy range of neutrons is contributing to the dose outside the walls. Calculations, dividing the neutron flux incident upon the walls into $E_n > 100$ MeV and the giant resonance region, indicate that the high-energy neutrons will contribute almost all the dose outside the walls, even where the wall thickness is only about 3 ft. These high-energy neutrons are moderated in passing through the concrete, and will have an energy distribution different from the incident flux. Evaporation neutrons from the outer parts of the walls would be expected as well as a modified high-energy spectrum. Many, perhaps most, of these neutrons will be in the energy range encompassed by the moderated BF_3 detector. Table 26-3 gives the actual measurements at various locations around end station A (see Fig. 26-5) compared with the expected values as derived from Fig. 26-9. There seems to be reasonable agreement, especially at the larger angles.

26-4 Muon production and attenuation (WRN)

The production and absorption mechanisms for muons are rather well known.[36] Because muons essentially lose energy by ionization, a fairly unique range is associated with each energy. At both electron and proton machines the high-energy muons are peaked predominantly in the forward direction because in pair production and in nuclear pion production the transverse momenta are on the order of the particle mass, μ, and the muons are rarely a problem for transverse shielding.[22] The muon flux that is produced when a high-energy electron beam is completely attenuated in matter can be calculated by integrating the pair production cross section over the photon distribution in the electromagnetic shower.[37] The equations given by Drell[38]

can be rewritten as the probability per radiation length (in small angle approximation).

$$\frac{d^2\sigma}{d\Omega\, dE}(E, k, \theta) = \frac{1}{\pi}\left(\frac{m}{E}\right)^2 \frac{\ln(E/\mu)}{\ln(183Z^{-1/3})} \frac{E(k-E)}{k^2} \frac{1}{k} \times \left\{ \frac{\frac{k^2}{E(k-E)}\left[\left(\frac{\mu}{E}\right)^2 + \theta^2\right]^2 - 2\left[\left(\frac{\mu}{E}\right)^4 + \theta^4\right]}{\left[\left(\frac{\mu}{E}\right)^2 + \theta^2\right]^4} \right\}$$

(GeV-radiation length-steradian)$^{-1}$ (26.7)

and

$$\frac{d\sigma}{dE}(E, k) = \left(\frac{m}{\mu}\right)^2 \frac{\ln(E/\mu)}{\ln(183Z^{-1/3})} \frac{1}{k}\left[1 - \frac{4}{3}\frac{E(k-E)}{k^2}\right]$$

(GeV-radiation length)$^{-1}$ (26-8)

where

m = the electron rest mass = 0.511 MeV
μ = the muon rest mass = 106 MeV
E = the muon energy
k = the photon energy
Z = the atomic number of absorber

Equations (26-7) and (26-8) will probably overestimate the muon yield by a factor of 2 according to Tsai.[39]

The differential photon track length as given by Rossi[1] under Approximation A of shower theory is

$$\frac{dl}{dk} = 0.57\frac{E_0}{k^2}\text{(radiation length/GeV)} \qquad (26\text{-}9)$$

A Monte Carlo study of the longitudinal development of electron–photon cascade showers in copper has been done by Zerby and Moran[9] where the track length results are compared with Eq. (26-9). The approximate analytic results fit the Monte Carlo data rather well for photons in the energy range below 0.6 E_0 and above the critical energy for copper ($\approx$20 MeV).

DeStaebler[40] has made a comparison of several track length formulas with the Monte Carlo data. Figure 26-16 shows two of these track length formulas divided by the Approximation A result,[1] Eq. (26-9), as a function of $u = k/E_0$. The simple Approximation A is good to within a factor of 2 except perhaps at the very tip. Equation (26-9) is used in the present calculation with the understanding that the results should give a conservative estimate of muon fluxes for shielding purposes.

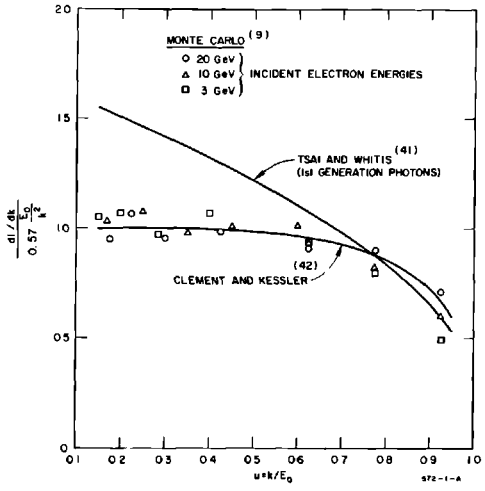

Figure 26-16 Differential photon track length divided by Approximation A (Reference 1) versus the fractional photon energy, $u = k/E_0$.

The *differential* muon flux a distance R from the target is

$$\frac{d\Phi}{dE}(E_0, E, \theta) = \frac{2I}{R^2}\int_E^{E_0} \frac{d^2\sigma}{d\Omega\, dE}\frac{dl}{dk}\, dk \text{ (muon/cm}^2\text{-sec-GeV)} \qquad (26\text{-}10)$$

where I = electron current (e^-/sec) and where the factor of 2 comes from the fact that both μ^+ and μ^- are required. The result of this integration is

$$\frac{d\Phi}{dE}(E_0, E, \theta) = \frac{2IE_0\, 0.57 \ln\left(\frac{E}{\mu}\right)\left(\frac{m}{\mu}\right)^2}{R^2\mu^2\pi(1+\eta^2)^2 \ln(183Z^{-1/3})} H(E_0, E, \theta) \qquad (26\text{-}11)$$

where

$$H(E_0, E, \theta) = \frac{1-x^2}{2} - \frac{1}{6}\left[1 - 4x^3\left(1 - \frac{3}{4}x\right)\right]\left[\frac{1+\eta^4}{(1+\eta^2)^2}\right] \qquad (26\text{-}12)$$

and where $x \equiv E/E_0$, $\eta \equiv \theta/\theta_0$, and $\theta_0 \equiv \mu/E$.

The *integral* muon flux is

$$\Phi(E_0, E, \theta) = \int_E^{E_0} \frac{d\Phi}{dE}\, dE \qquad (26\text{-}13)$$

from Eqs. (26-11) and (26-12). The integration was performed numerically on the B5500 computer using the procedure SIMPS6.* Form factor effects are neglected, as is multiple scattering.

* This program was written and developed by J. Welsch of SLAC.

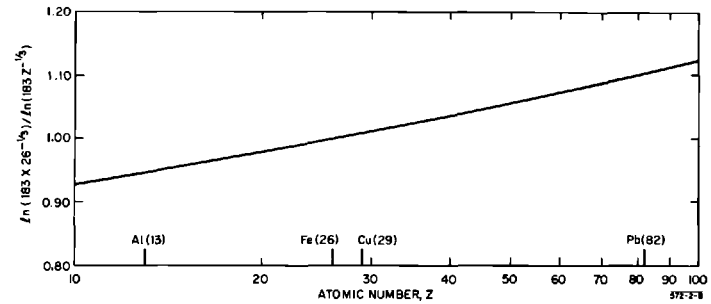

Figure 26-17 Curve showing the slight dependence of the muon flux on the atomic number, Z.

To convert flux to dose rate, it seems reasonable to use the simple conversion factor 1 μ/cm^2-sec = 0.1 mrem/hour, which corresponds to a quality factor (QF) of 1 and an energy loss of 1.75 MeV/g-cm^{-2}.

The Z-dependence of the target material enters in the form $\ln(183Z^{-1/3})$. All these calculations have been done with $Z = 26$ (Fe), and Fig. 26-17 gives the necessary multiplicative factor for other absorbers.

Figure 26-18 The integral muon flux (for 1 kW at 1 meter) versus the fractional muon energy, E/E_0, for several production angles and incident electron beam energies.

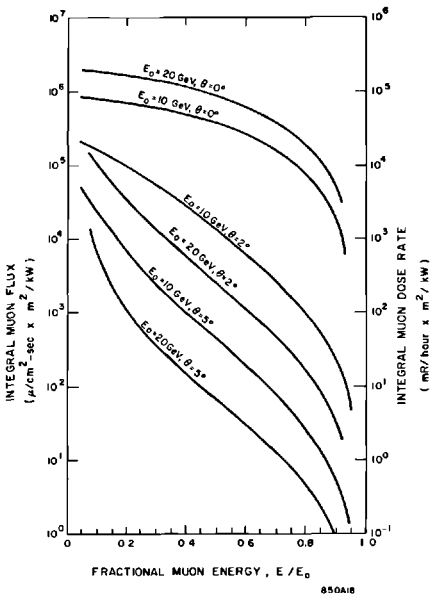

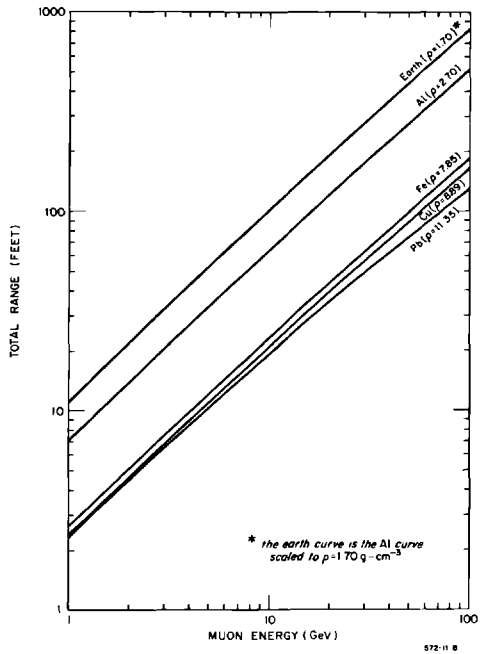

Figure 26-19 Range energy curves for muons in various shielding materials.

The results of the calculation are shown in Fig. 26-18 where both the integral flux and dose rate for $R = 1$ meter and $P = 1$ kW are plotted against the ratio E/E_0 for various values of θ and E_0. In order to calculate the muon flux, one needs to know the lower limit on the muon energy, which is determined by the shielding between the source and the observer. Since multiple scattering has not been included, the calculation will overestimate the flux when thick shields are close to the source. For thick shields at large distances from the source, the calculation should be better since the production angle dominates over the multiple scattering.

A set of range–energy curves for muons in various materials is given in Fig. 26-19 which aid in doing shielding calculations. The curves represent an extension of previous calculations to higher energies and include pair production, bremsstrahlung, and nuclear interaction losses.[43,44] A similar calculation has been done by Thomas.[45]

Integration of the flux over 4π steradians results in the total muon yield shown in Fig. 26-20. Also shown is the yield of muons from a high-energy proton beam[46], which is richer at lower energies partly because lower-energy pions are more likely to decay.

Multiple scattering is also important when the shield is thick but narrow, for then the muon flux can readily escape the sides. A calculation has been made[47] which accounts for the energy loss in the medium in which the

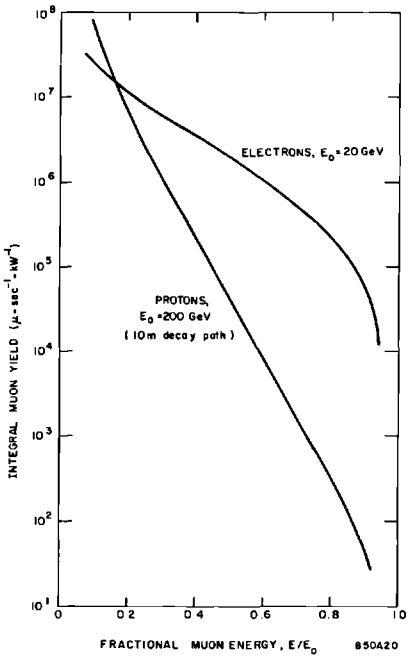

Figure 26-20 Integral muon yield versus the fractional muon energy for incident 20-GeV electrons. Also included for comparison is the muon yield (from pion decay) that is expected from a 200-GeV proton beam.

multiple elastic scattering takes place. The defining equation is the Fermi diffusion equation[1], which has been solved by Eyges[48] with energy loss considered. A second-order polynomial is fitted to existing range–momentum data,[49] and the integral expressions of Eyges are numerically integrated to obtain y_{rms} and θ_{rms}.

The root-mean-square lateral displacement and scattering angle, due to multiple scattering of muons in iron and silicon dioxide for incident momenta of 5, 10, and 20 GeV/c, are shown in Figs. 26-21 and 26-22, respectively.

If we neglect energy loss (i.e., $p\beta$ = constant), the mean square values are

$$\langle \theta^2 \rangle = \frac{1}{2}\left(\frac{E_s}{p\beta}\right)^2 t \tag{26-14}$$

and

$$\langle y^2 \rangle = \frac{1}{6}\left(\frac{E_s}{p\beta}\right)^2 t^3 \tag{26-15}$$

where t = depth of penetration in radiation lengths, and $E_s = 21.2$ MeV.

This special case is compared in Figs. 26-21 and 26-22 for $p\beta = 20$ GeV/c and for SiO_2.

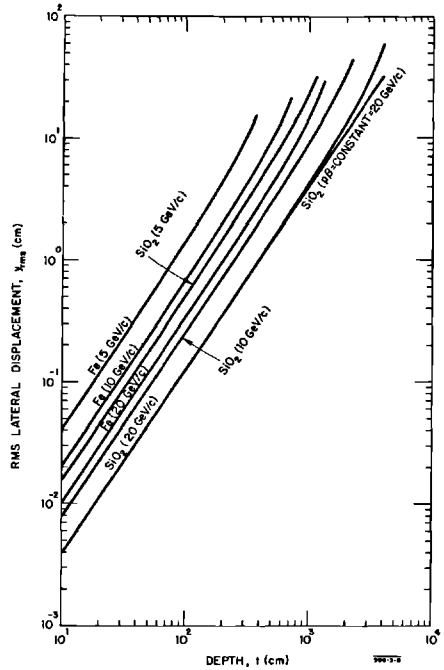

Figure 26-21 Root-mean-square lateral displacement due to multiple elastic scattering of muons of various incident momenta in iron and silicon dioxide.

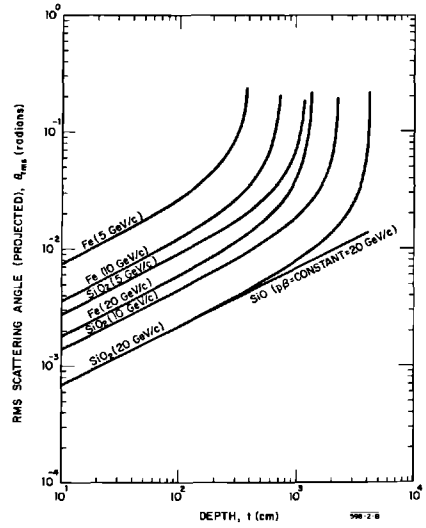

Figure 26-22 Root-mean-square projected angle due to multiple elastic scattering of muons of various incident momenta in iron and silicon dioxide.

26-5 Radiation in the 2-mile tunnel and penetrations (HDeS, TMJ)

Dose determination

In general, the flux at a point in a duct (penetration) consists of a direct part which decreases as $1/z^2$ and a part that has scattered off the walls (depending upon albedo) and decreases faster than $1/z^2$, z being the distance up the duct. The fractional transmission, $g(z)$, in a cylindrical duct for a parallel flux of neutrons is given by[50]

$$g(z) = \frac{\phi(z)}{\phi(0)} = \left(\frac{a}{z}\right)^2 \left[1 + K\frac{a}{z}\right] \qquad \text{for } 4 < z/a < 36 \qquad (26\text{-}16)$$

where

a = the radius of the cylindrical duct
$K = 60$ for photons and thermal neutrons, and closer to 16 for fast neutrons
$\phi(z)$ = the flux at a point z in the duct
$\phi(0)$ = the flux at the entrance to the duct

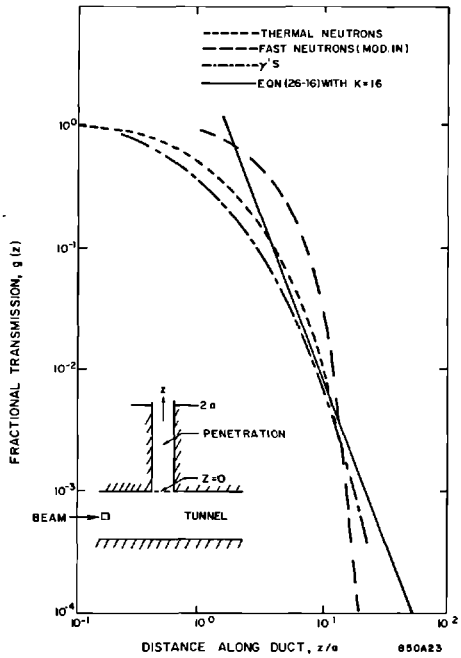

Figure 26-23 Fractional transmission of neutrons and photons in a duct. Measurements of thermal and fast neutrons and photons are shown along with the calculated transmission taken from Eq. (26-16), with $K = 16$. The source was a thick copper target bombarded with 1-GeV electrons.

The fractional transmission has been measured for thermal neutrons by other authors[51] and is shown in Fig. 26-23 which was used in calculating the dose rate at the top of the penetrations at SLAC. The PuBe neutrons closely follow the same curve when measured in a 27-in. diameter service penetration.

The original calculation of DeStaebler,[50] assuming a line source, gave the result

$$D(\text{mrem/hour}) = 3.6 \times 10^6 F g(z) \phi(0) \tag{26-17}$$

where

D = the dose rate at the end of a penetration
3.6×10^6 = a factor which converts rem/sec to mrem/hour
F = the biological effect per fast neutron (3.8×10^{-8} rem/neutron-cm^{-2})
g = the transmission in the duct; for $z/a = 21$ as in the case of a service penetration, $g = 10^{-3}$ from Fig. 26-23
$\phi(0)$ = the fast neutron flux at the bottom of a penetration

A measurement was made at the end of the first 660 ft of accelerator. A 1-GeV, 1.25-kW electron beam was completely absorbed in a target located 16.1 ft from a penetration. Using a source strength of 1.25×10^{12} neutrons/sec-kẆ radiating isotropically,[34] one obtains

$$D = (3.6 \times 10^{6})(3.8 \times 10^{-8})(10^{-3})\left(\frac{1.25 \times 10^{12}}{4\pi(16.1 \times 30.5)^2}\right)$$

$$= 56 \text{ mrem/hour}$$

The measured value was 60 mrem/hour for the above conditions, which agrees with the calculation.

The fractional transmissions, $g(z)$, in a 28-in diameter service penetration were measured for thermal neutrons, fast neutrons, and photons, and are included in Fig. 26-23. The photons entering the 28-in. service penetration are essentially parallel; transmission in a penetration upstream of the target was the same as that downstream.

A different situation exists when a source is placed inside a tunnel and the flux is measured down that same tunnel, such as the case when a beam targets somewhere in the accelerator housing. The high-energy component will be peaked in the forward direction. The giant resonance neutrons, which are isotropic, should give a result similar to a PuBe source suspended in the tunnel. If there were no scattering effects, the flux should decrease according to

$$\phi_0 = \frac{q}{4\pi r^2} \tag{26-18}$$

where r is the straight line distance from the source to the detector, and q is the

Figure 26-24 Transmission of Pu-Be neutrons in the accelerator tunnel [q = constant, $Q = Q(r)$].

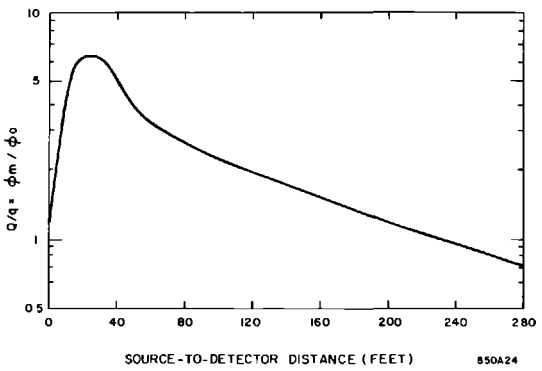

neutron source strength. An effective source strength, Q, can be defined in terms of the actually observed flux, ϕ_m, by

$$\phi_m = \frac{Q}{4\pi r^2} \tag{26-19}$$

and Fig. 26-24 shows $(\phi_m/\phi_0) = (Q/q)$ as a function of r for PuBe neutrons measured in the tunnel. The variation of $Q(r)$ seems plausible. If r is small compared with the cross-sectional dimensions of the tunnel, then $Q \approx q$; at $r \approx 20$ ft, Q builds up to a maximum of about $5q$, presumably owing to scattering from the walls of neutrons that would otherwise never have hit the counter; for r greater than a couple of hundred feet, Q decreases roughly exponentially with a mean free path corresponding to the $\approx$1-MeV scattering cross section in air.

Determination of the neutron spectrum in the penetrations

Nuclear track emulsion (Ilford L4) was placed at the top of a 28-in. service penetration which was located approximately 10 ft downstream from a target. Two inches of lead was placed around the emulsion in order to reduce the γ-radiation level. The beam energy was 10 GeV and the target was 9 in.

Figure 26-25 Neutron energy spectrum in a SLAC penetration near a target that is being struck by 10-GeV electrons.

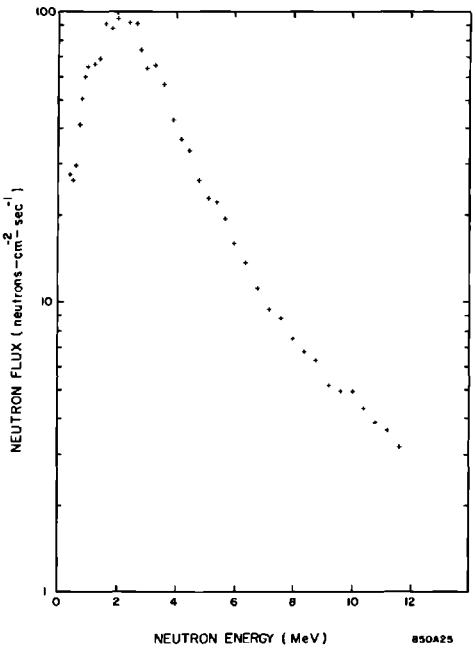

of water-cooled copper. The processing and scanning of the emulsion, and the emulsion itself, were provided by the Health Physics Department of the Lawrence Radiation Laboratory in Berkeley, California. They also obtained the neutron spectrum from the proton recoil data using their computer codes RECOIL I and RECOIL DD.[52] The resultant spectrum is shown in Fig. 26-25. The peak at 2 MeV is not unexpected since the giant resonance spectrum should dominate with such a shielding geometry.

26-6 Residual radiation (TMJ)

Beam loss along the accelerator is estimated to be 3% of the final beam power.[22] This occurs primarily in the thirty beam scrapers and small couplings along the machine. There will be times, especially during tune-up, when local points will intercept more of the beam. An example of this was seen during initial operations on the 660-ft accelerator where, using moderated indium foils to measure the neutron flux, an apparent beam power loss of 8.7% was noted in the collimator at the end of Sector 1.

The accelerator problems are typical, with activation occurring in metal parts, concrete walls, water, and air. In concrete, the principal reaction of concern is $^{23}\text{Na}(n, \gamma)^{24}\text{Na}$ with $T_{1/2} = 15$ hours. In certain areas, activation of the concrete is a significant portion of the radiation inside the tunnel. Boron frit (B_2O_3) has been added to the concrete walls near the positron target and in the beam switchyard; the effectiveness[53] is shown in Fig. 26-26.

Along the accelerator waveguide, the principal reactions are

$$^{65}\text{Cu}(\gamma, n)^{64}\text{Cu}, \quad (T_{1/2} = 13 \text{ hours})$$
$$^{63}\text{Cu}(\gamma, n)^{62}\text{Cu}, \quad (T_{1/2} = 10 \text{ min})$$

with ^{58}Co ($T_{1/2} = 71$ days) and ^{60}Co ($T_{1/2} = 5.3$ yr) becoming important daughter products after long irradiation times, and long (>100 hours) waiting times. Calculations of residual activity are made from the yield formula,[54]

$$R(\text{curies}) = 58\, g\left(\frac{X_0}{A}\right) \int \frac{\sigma dk}{k^2} \text{ per MW of incident beam}$$

where

g = the fractional atomic abundance of parent nuclide
X_0 = the radiation length in grams per square centimeter
A = the atomic weight of the material
$\sigma(k)$ = the cross section in microbarns

Tables 26-4 and 26-5 show some of the radioactive products that will be formed from copper.

For a uniform 3% of 2.4-MW beam power loss along the accelerator and for 10^2 to 10^4 hours irradiation times, the predicted levels inside the tunnel as a function of waiting time are shown in Fig. 26-27.

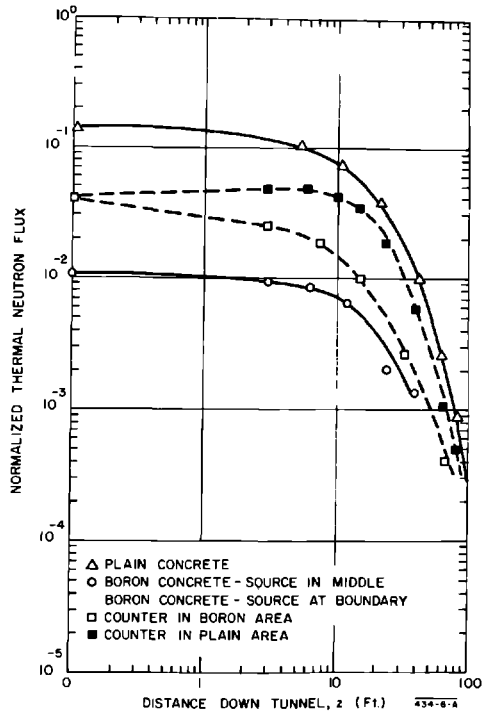

Figure 26-26 Normalized thermal neutron flux versus distance down the accelerator tunnel showing the effect of adding boron to concrete.

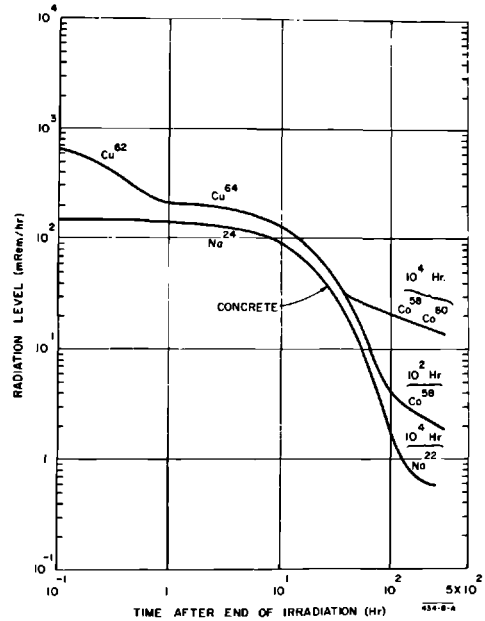

Figure 26-27 Radiation levels in the accelerator tunnel versus waiting time for 10^2 and 10^4 hours irradiation time. SLAC worker tolerance is 0.75 mrem/hour.

Table 26-4 Photon-induced activities in copper

Daughter nuclide element	*A*	*Mean life τ (hour)*	*Radiation (γ energy in MeV)*	E_γ *(MeV)*	*Yield relative[a] to* ^{62}Cu	RE_γ *(Energy) × (Activity)[b] (MeV-Ci)*
Cu	64	18.4	β^+, β^-	0.60	0.58	390.0
	62	0.23	$\sim 2\%\ \gamma, \beta^+$	1.10	1.00	1230.0
	61	4.8	$\sim 10\%\ \gamma, \beta^+$	0.94	0.18	190.0
Ni	57	52.0	1.4, 1.9, β^+	1.99	1.8×10^{-3}	4.0
Co	60	6.6×10^4	1.17, 1.33	2.51	(2.0×10^{-2})	56.0
	58	2.5×10^3	0.80, β^+	0.94	(2.7×10^{-2})	28.0
	56	2.7×10^3	0.89, others, β^+	0.70	(1.2×10^{-2})	9.4
	55	26.0	Many, β^+	2.02	8.5×10^{-4}	1.9
Fe	59	1.56×10^3	1.1, 1.3	1.29	(3.0×10^{-3})	4.3
Mn	56	3.7	0.8, 2.8	1.80	3.0×10^{-3}	6.1
	54	1.0×10^4	0.8	0.84	(5.0×10^{-3})	4.7
	52	2.0×10^2	1.4, β^+	2.45	1.3×10^{-3}	3.6
	51	1.1	β^+	1.02	(1.2×10^{-3})	1.4

[a] Parentheses indicate that yield is inferred, not measured; Reference 55.
[b] For a power absorption of 3% of 2.4 MW.

An ionization chamber lowered down various service penetrations gives a beam loss profile during machine operation. Figure 26-28 is typical for an early period of operation. This profile was a function of many variables, such as focusing, steering, phasing, and so on. Residual activity profiles follow the same shape, with the beam scrapers and small flexible couplings being the main hot spots. After absorbing 1 kW of beam power, levels 2 ft away from a copper target with 2 in. of lead shielding are typically a few roentgen per hour, 5 min after beam shutoff. Levels in the aisle along the accelerator vary from 0.1 mR/hour to over 1 R/hour, and decrease by an order of magnitude within the first 8 hours.

Table 26-5 Activities in copper induced by neutrons

Reaction	*Mean life τ (hour)*	*Radiation (γ energy in MeV)*	E_γ *(MeV)*	*(Energy) × (Activity) RE_γ (MeV-Ci)*
$^{65}Cu(n, 2n)^{64}Cu$	18.4	β^+, β^-	0.60	20.0
$(n, p)^{65}Ni$	3.7	1.1, 1.4	0.59	2.8
$(n, \alpha)^{62}Co$	0.34	$\gtrsim 1.2$	≈ 1.3	—
$^{63}Cu(n, 2n)^{62}Cu$	0.23	$\sim 2\%\ \gamma, \beta^+$	1.10	80.0
$(n, p)^{63}Ni$	$\sim 10^6$	0.0	0.0	0.0
$(n, \alpha)^{60}Co$	6.6×10^4	1.17, 1.33	2.51	—

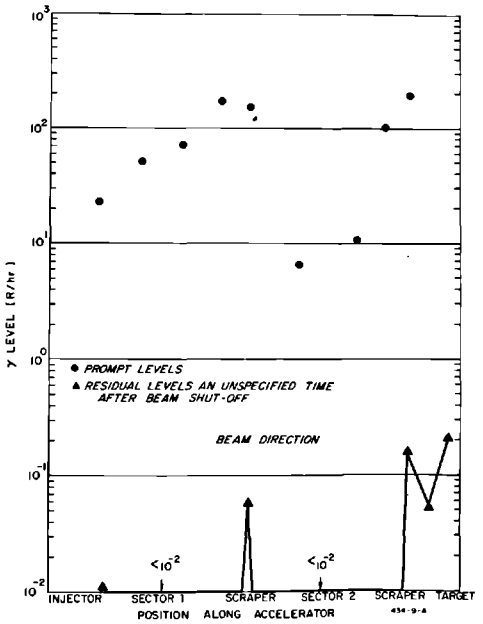

Figure 26-28 A typical beam loss profile for the tune-up period on the 660-ft accelerator as measured with an ionization chamber. Residual activity follows the prompt radiation curve and is primarily localized to beam scrapers and the target. The copper target has a 2-in. Pb jacket around it.

Cooling water along the accelerator, and especially in the slits, collimators, and beam dumps, will become radioactive. Typical levels in the water of a dump[56,57] when irradiated to saturation with 1 MW of beam power are shown in Table 26-6. Water at a heat exchanger associated with beam switchyard components was measured and the radioactive levels were in agreement

Table 26-6 Activity in water[a]

Daughter nuclide	*R (Ci)*	*Mean life τ (hours)*
^{15}O	35,000	0.05
^{13}N	1,390	0.24
^{11}C	1,390	0.5
^{7}Be	280	1.85×10^{3}
^{3}H	400	1.55×10^{5}

[a] Irradiated to saturation with 1 MW of beam power

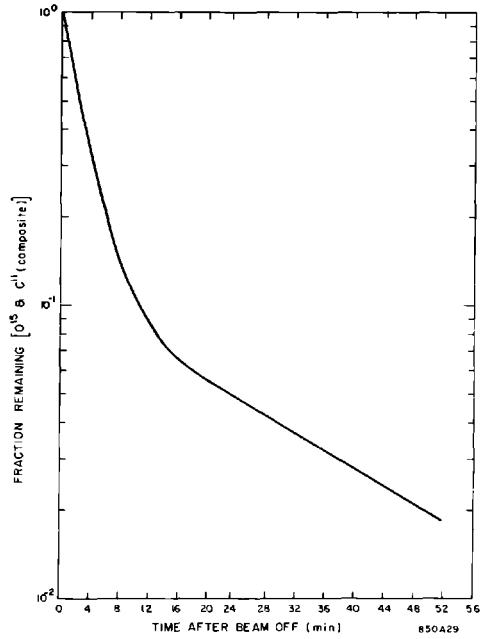

Figure 26-29 Decay of radioactive water at beam switchyard service areas. Half-lives are those of ^{15}O and ^{11}C.

with the predicted values, with the exception of ^{13}N, which was absent. Figure 26-29 shows the decay of the radioactive water as a function of time. It is apparent that this water presents a significant hazard to health and must be carefully shielded and monitored (see Chapter 21). The radioactive water of each unit is contained within a closed loop, with nonradioactive water cooling in a heat exchanger outside the main earth shield. Water in the radioactive side of the loop is monitored on a sampling basis, whereas the nonradioactive water is monitored continuously for ruptures, etc. to ascertain that no significant amounts of radioactivity reach the cooling tower and from there the outside world.

Radioactive and chemically active air produced inside the tunnel presents a significant hazard to personnel. Using a 3% beam power loss uniformly distributed along the accelerator, DeStaebler[58] has calculated the rate of formation of noxious chemicals in the tunnel to be about 1 ppm/day. For radioactive air, the following reactions are of concern[59]: $^{14}N(\gamma, n)^{13}N$, $^{14}N(n, 2n)^{13}N$, $^{16}O(\gamma, n)^{15}O$, with $^{40}A(\gamma, p)^{39}Cl$ and $^{14}N(\gamma, 2np)^{11}C$ also of importance. The equilibrium concentrations in the tunnel are shown in Table 26-7. From this it is calculated that if a person enters the tunnel immediately after beam shutoff and remains for a period significantly long compared with the half-lives of the nuclides involved, he would receive a total

Table 26-7 Equilibrium concentrations of final nuclides after irradiation of air

Final nuclide		*Rate of formation R (nuclides/sec)*	*Equilibrium concentration in tunnel ($\mu\mu Ci/cm^3$)*
^{11}C		0.24×10^{10}	3.1
^{13}N	Incident γ	12.0×10^{10}	
	Incident n	$<3.0 \times 10^{10}$	
	Total	15.0×10^{10}	190.0
^{15}O		17.0×10^{10}	220.0
^{39}Cl		0.42×10^{10}	5.5

exposure of 97 mrem from radioactive gas. A wait time of 20 min before entry would decrease this to 20 mrem. To reduce further this hazard, the tunnel, which is normally sealed from the outside world, is first vented before entry is permitted. During venting, one complete air change occurs approximately every 10 min.

26-7 Outline: order-of-magnitude shielding calculations (TMJ, WRN)

A. Attenuation of the electron–photon shower

1. The longitudinal shower decreases exponentially with an absorption mean free path, Λ, given in Fig. 26-1. The shower maximum occurs at a depth of about $4X_0$ for $E_0 = 1$ GeV and about $10X_0$ for $E_0 = 20$ GeV.
2. The fraction of incident energy (power) that escapes radially can be found using Fig. 26-2, which plots the radius in Moliere units, X_m. Both X_0 and X_m are given in Fig. 26-1. Figure 26-2 is independent of both E_0 and the absorbing material.

B. Photon production and attenuation

1. Use Fig. 26-3 to determine the unshielded photon dose rate coming from a thick target ($t \approx 15X_0$, $r_0 \approx 3X_m$) as a function of angle.
2. Determine the effective photon energy from the minimum in the mass absorption curve (good geometry) for the target material.
3. Determine the absorption coefficient for this energy in the shielding material.
4. Use $D = D_0 e^{-\mu t}$, where D_0 is the unshielded dose rate, μ is the absorption coefficient, t is the shield thickness, and D is the required dose rate.
5. This method is not good for angles less than 10°.

C. Neutron production and attenuation

1. Calculate the shield thickness, H, in feet of earth equivalent ($\rho = 1.7$ g-cm^{-3}).
2. Determine the neutron dose rate through the shield from Fig. 26-9.
3. This estimate should be good to a factor of 2 for angles greater than about 30°.

D. Muon production and attenuation

1. Determine the lowest muon energy, E, by using the shield thickness and Fig. 26-19.
2. With E/E_0, look for the muon dose rate on Fig. 26-18.
3. Divide this dose rate by 2 since the cross section given by Tsai[39] is approximately half as large as that given by Drell.[38]
4. This estimate might be as much as 5 times too high since nuclear form factors and multiple scattering have been neglected.

E. Radiation through penetrations and holes in shields

1. Use Fig. 26-23 to determine the transmission, $g(z)$.
2. Use $D(z) = D(0)g(z)$ to determine the dose rate at the end of the duct, $D(z)$, with a prior knowledge of the dose rate at the entrance to the duct, $D(0)$.

26-8 General discussion (TMJ, WRN)

The preceding sections describe the various shielding calculations and measurements that have been made at SLAC to date (July 1967). A number of subjects have been intentionally omitted, either because the measurements have not been adequately related to theory or because they are too extensive to cover sufficiently in this chapter. A few general statements might be of practical interest, however.

It has been found that Eq. (26-14) does not adequately describe the spread of primary electron beams in thin targets because large-angle scattering turns out to be significant. It is necessary to go to more elaborate theory[60] in order to determine the effective beam cone for shielding purposes.

In areas where roof shielding is thin or contains voids or holes, there will be a component of radiation, both neutrons and photons, that scatters off the atmosphere. This skyshine problem exists at SLAC and is being studied. Similarly, the problem of radiation scattering through a maze is also being looked at. A general rule-of-thumb has been found to work for both photon and neutron radiation, namely, one gets about a factor of 20 reduction with each 90° bend in a thick concrete maze.

References

1 B. Rossi and K. Greisen, *Rev. Mod. Phys.* **13**, 240 (1941); B. Rossi, *High-Energy Particles*, Prentice-Hall, Engelwood Cliffs, New Jersey, 1952.

2 S. Z. Belenkii and I. P. Ivanenko, *Soviet Phys.-Usp.* **2**, 912 (1960).

3 Y. Murata, *J. Phys. Soc. Japan*, **20**, 209 (1965).

4 G. Backenstoss, B. D. Hyams, G. Knop, and U. Stierlin, *Nucl. Instr. Methods* **21**, 155 (1963).

5 W. Blocker, R. W. Kenney, and W. K. H. Panofsky, *Phys. Rev.* **79**, 419 (1950).

6 T. Rockwell, III (Ed.), *Reactor Shielding Design Manual*, p. 447, Van Nostrand, New York, 1956.

7 K. Kamata and J. Nishimura, *Progr. Theoret. Phys. (Kyoto)*, Suppl. No. 6, 93 (1958).

8 H. H. Nagel, *Z. Physik.* **186**, 319 (1965); [English Transl., Rept. No. SLAC-TRANS-28, Stanford Linear Accelerator Center, Stanford University, Stanford, California (1965)].

9 C. D. Zerby and H. S. Moran, *J. Appl. Phys.* **34**, 2445 (1963); "Studies of the Longitudinal Development of High-Energy Electron-Photon Cascade Showers in Copper," Rept. No. ORNL-3329, Oak Ridge National Laboratory, Tennessee (1962); and "A Monte Carlo Calculation of the Three Dimensional Development of High-Energy Electron-Photon Cascade Showers," Rept. No. ORNL-TM-422, Oak Ridge National Laboratory, Tennessee (1962). Also, private communication.

10 U. Völkel, "Elektron-Photon-Kaskaden in Blei für Primärteilchen der Energie 6 GeV," Rept. No. DESY 65/6, Deutsches Elektronen-Synchrotron, Hamburg, Germany (1965); [English Transl., Rept. No. SLAC-TRANS-41, Stanford Linear Accelerator Center, Stanford University, Stanford, California (1966)].

11 A. Kantz and R. Hofstadter, *Phys. Rev.* **89**, 607 (1953); *Nucleonics* **12**, 36 (March 1954).

12 W. R. Nelson, T. M. Jenkins, R. C. McCall, and J. K. Cobb, *Phys. Rev.* **149**, 201 (1966).

13 K. Greisen, "The extensive air showers," *Progr. Elem. Particle Cosmic Ray Phys.*, 3, 22 (1956).

14 O. I. Dovzhenko and A. A. Pomanskiĭ, *Soviet Phys.-JETP* **18**, 187 (1964).

15 D. A. G. Neet, "Radiation Exposure in the Switchyard," Rept. No. SLAC-TN-65-9, Stanford Linear Accelerator Center, Stanford University, Stanford, California (1965).

16 F. H. Attix, "Present Status of Dosimetry by Radiophotoluminescence and Thermoluminescence Methods," Rept. No. NRL Report 6145, Naval Research Laboratory, Washington, D.C. (September 1964).

17 B. J. Moyer, "Evaluation of Shielding Required for the Improved Bevatron," Rept. No. UCRL-9769, Lawrence Radiation Laboratory, Berkeley, California (June 1961).

18 Roger Wallace, *Nucl. Instr. Methods* **18**, **19**, 405 (November 1962).

19 U.S. National Bureau of Standards, "Protection against neutron radiation up to 30 MeV," *Natl. Bur. Std. (U.S.) Handbook* **63**, (November 1957).

20 International Commission on Radiological Protection, "Protection against electromagnetic radiation above 3 MeV and electrons, neutrons and protons," *ICRP Publ. No. 4*, p. 4, Pergamon, New York, 1964.

21 U.S. National Bureau of Standards, "Shielding for high-energy electron accelerator installations," *Natl. Bur. Std. (U.S.) Handbook* **97** (July 1964).

22 H. DeStaebler, Jr., "Transverse Radiation Shielding for the Stanford Two-Mile Accelerator," Rept. No. SLAC-9, Stanford Linear Accelerator Center, Stanford University, Stanford, California (November 1962).

23 A. Wattenberg, "Nuclear reactions at high energies," in *Encyclopedia of Physics*, Vol. XL, p. 450, Springer, Berlin, 1957.

24 M. E. Toms, "Bibliography of Photo- and Electronuclear Disintegrations," Rept. No. NRL-BIB-24, U.S. Naval Research Laboratory, Washington, D.C. (July 1965).

25 V. I. Antonesoc, "Photonuclear Reactions," *Bibliographical Series No. 10*, International Atomic Energy Agency, Vienna (1964).

26 Charles E. Roos and V. Z. Peterson, *Phys. Rev.* **124**, 1610 (1961).

27 H. R. Crouch *et al.*, *Phys. Rev. Letters* **13**, 636 (1964).

28 H. S. Murdoch and H. D. Rathgeber, *Phys. Letters* **13**, 267 (1964).

29 S. J. Lindenbaum, "Shielding of high-energy accelerators," *Ann. Rev. Nucl. Sci.* **11**, 213 (1961).

30 S. Kao and G. Voss, "Effectiveness of Ilmenite-Loaded Concrete in Attenuating Neutron Radiation Produced by a 5-BeV Photon Beam," Rept. No. CEAL-1007, Cambridge Electron Accelerator, Cambridge, Massachusetts (December 1963).

31 St. Charalambus, J. Dutrannois, and K. Goebel, "Particle Flux Measurements with Activation Detectors," Rept. No. CERN/DI/HP-90, European Council for Nuclear Research, Geneva (1966).

32 J. B. McCaslin, H. Wade Patterson, Alan R. Smith, and Lloyd D. Stephens, "Some Recent Developments in Technique for Monitoring High-Energy Accelerator Radiation," Rept. No. UCRL-16769, Lawrence Radiation Laboratory, Berkeley, California (1966).

33 E. M. Franz and G. Friedlander, *Nucl. Phys.* **67**, 123 (1966).

34 H. DeStaebler, T. Jenkins, W. R. Nelson, "Reduction of the Thermal Neutron Flux in Concrete Using Paraffin Moderators," Rept. No. SLAC-TN-65-11, Stanford Linear Accelerator Center, Stanford University, Stanford, California (1965).

35 K. G. Dedrick and H. H. Clark, "Photoneutron Yields from Excitation of the Giant Resonance," Rept. No. M-225, Stanford Linear Accelerator Center, Stanford University, Stanford, California (1960).

36 G. N. Fowler, and A. W. Wolfendale, "The interaction of μ-mesons with matter," *Progr. Elem. Particle Cosmic Ray Phys.* **4**, 107 (1958).

37 W. R. Nelson, "Muon Production Calculations for Muon Shielding," Rept. No. SLAC-TN-66-37, Stanford Linear Accelerator Center, Stanford University, Stanford, California (1966).

38 S. Drell, "Some Aspects of Target Area Design for the Proposed Stanford Two-Mile Linear Electron Accelerator," Rept. No. M-200, Section M-200-7A, W. W. Hansen Laboratories, Stanford University, Stanford, California (Summer 1960).

39 Y. S. Tsai, "Estimates of secondary-beam yields at SLAC," *SLAC Users Handbook*, D.3-3, Stanford Linear Accelerator Center, Stanford University, Stanford, California.

40 H. DeStaebler, private communication, Stanford Linear Accelerator Center, Stanford University, Stanford, California (July 1966).

41 Y. S. Tsai and Van Whitis, *Phys. Rev.* **149**, 1248 (1966).

42 G. Clement and P. Kessler, *Nuovo Cimento* **37**, 876 (1965); G. Clement, *Compt. Rend.* **257**, 2971 (November 1963).

43 W. H. Barkas and M. J. Berger, "Tables of Energy Losses and Ranges of Heavy Charged Particles," NASA-SP-3013, National Aeronautics and Space Administration, Washington, D.C. (1964).

44 P. J. Hayman, N. S. Palmer and A. W. Wolfendale, *Proc. Roy. Soc.* (*London*) **A275**, 391 (1963).

45 R. H. Thomas, private communication, Lawrence Radiation Laboratory, Berkeley, California (July 1964).

46 "200 BeV Accelerator Design Study," Rept. No. UCRL-16000, Lawrence Radiation Laboratory, Berkeley, California (June 1965).

47 W. R. Nelson, "Multiple Elastic Scattering of Muons with Energy Loss," Rept. No. SLAC-TN-66-41, Stanford Linear Accelerator Center, Stanford University, Stanford, California (1966).

48 L. Eyges, *Phys. Rev.* **74**, 1534 (1948).

49 W. H. Barkas, "The Range–Energy Function," Rept. No. UCRL-10292, Lawrence Radiation Laboratory, Berkeley, California (August 21, 1962).

50 H. DeStaebler, "Radiation Problems Arising from Holes in the Transverse Shielding," Rept. No. SLAC-TN-62-71, Stanford Linear Accelerator Center, Stanford University, Stanford, California (1962).

51 B. T. Price, C. C. Horton, and K. T. Spinney, *Radiation Shielding*, Macmillan (Pergamon) New York, 1957.

52 R. L. Lehman and O. M. Fekula, *Nucleonics* **22** (No. 11), 35 (1964).

53 H. DeStaebler and T. Jenkins, "Pu-Be Neutron Measurements in the Accelerator Tunnel," Rept. No. SLAC-TN-65-24, Stanford Linear Accelerator Center, Stanford University, Stanford, California (1965).

54 H. DeStaebler, "Photon-Induced Residual Activity," Rept. No. SLAC-TN-63-92, Stanford Linear Accelerator Center, Stanford University, Stanford, California (1963).

55 R. J. Debs, J. T. Eisinger, A. W. Fairhall, I. Halpern, and H. G. Richter, *Phys. Rev.* **97**, 1325 (1955).

56 H. DeStaebler, "Tritium Production in Water," Rept. No. SLAC-TN-64-6, Stanford Linear Accelerator Center, Stanford University, Stanford, California (1964).

57 D. Coward, private communication, Stanford Linear Accelerator Center, Stanford University, Stanford, California.

58 H. DeStaebler, "Electron-Photon Flux in the Tunnel When the Machine is on: Applications to Chemically Active Air and to Active Cooling Water," Rept. No. SLAC-TN-62-76, Stanford Linear Accelerator Center, Stanford University, Stanford, California (1962).

59 H. DeStaebler, Jr., "Radioactive Gas in the Tunnel," Rept. No. SLAC-TN-62-9, Stanford Linear Accelerator Center, Stanford University, Stanford, California (1962).

60 B. P. Nigam, M. K. Sundaresan, and Ta-You Wu, *Phys. Rev.* **115**, 491 (1959).

PHYSICAL PLANT

J. Anton, D. Browne, Jr., J. W. Crisp, R. S. Gould,
F. F. Hall, Editor, C. R. Johnson, E. P. Lee,
T. E. McLellan, G. I. Ratliff, and W. P. Savage

A large portion of the investment in SLAC lies in its physical plant. This chapter describes the planning and management that went into this part of the program. The development and improvement of the site, the structures built, and the utilities installed are discussed.

27-1 Planning and management

The physical plant consists of the site and site improvements, general site utilities, buildings, accelerator equipment and services, and certain initial experimental equipment.

Three broad programs are covered herein as follows:

1. Initial construction of buildings, utilities, and site improvements. This program is discussed at length and referred to briefly in other chapters. It covers the work which was the responsibility of the Aetron-Blume-Atkinson architect–engineer–manager firm.
2. Installation of the accelerator equipment and services. The broad outline of this SLAC-managed program is discussed briefly in this chapter. Detailed discussions of design, procurement, testing and performance of equipment, and equipment services and systems are all covered under appropriate earlier chapters.
3. More recent construction programs, all managed by SLAC. They are discussed at length herein and referred to briefly in other chapters.

Initial construction of buildings, utilities, and site improvements (DB, EPL)

THE JOINT VENTURE. The design, procurement, construction, and acceptance of initial buildings, utilities and site improvements were managed by

Aetron-Blume-Atkinson (ABA), a joint venture, under subcontract to Stanford University. The joint venture consisted of Aetron, a division of Aerojet General Corporation, Covina, California; John A. Blume and Associates, Engineers, San Francisco, California; and the Guy F. Atkinson Company, (constructors), South San Francisco, California.

The selection of ABA was effected by Stanford University and the U.S. Atomic Energy Commission in December 1960, and preliminary design work started in February 1961. Construction of SLAC buildings was started in July 1962, and substantially completed in June 1966. Sub-contract closeout work was essentially complete by March 1967, except for final cost accounting reports. ABA on-site office activity was completed shortly thereafter.

During the design and construction period, ABA was assisted by a number of consultants of whom the following made major contributions:

Architectural design—Charles Luckman & Associates, Los Angeles, California

Concrete mix design—Professor Raymond E. Davis, University of California, Berkeley, California

Electrical consultant—Herman Halperin, Menlo Park, California

Landscaping design—Royston, Hanamoto, Mayes and Beck, San Francisco, California

Soil mechanics engineering—Dames & Moore, San Francisco, California

Organizationally, ABA had three coequal divisions covering engineering design, quality control, and operations. They used critical path method (CPM)

Figure 27-1 Initial construction schedules.

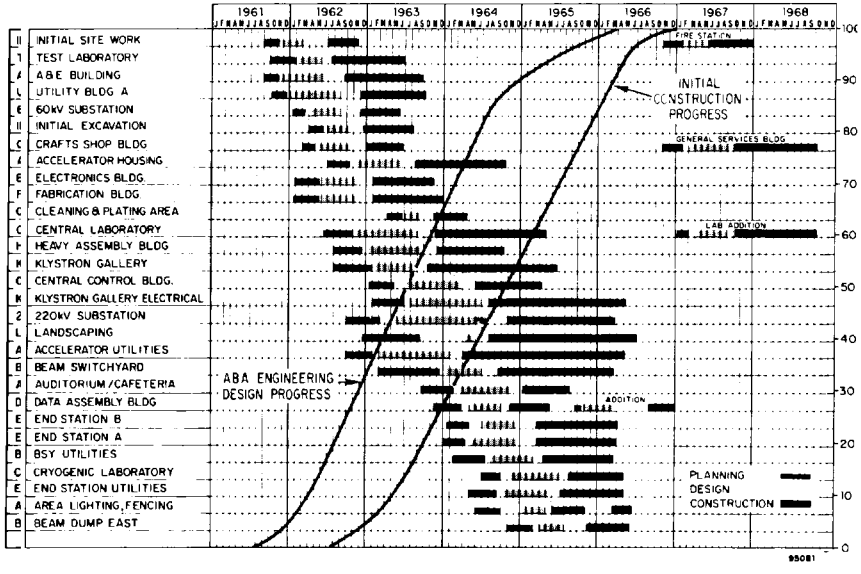

Figure 27-2 SLAC offices, laboratories, and shops.

scheduling for all major subcontracts. The ABA subcontract was administered by the Plant Office of the SLAC Business Services Division and technical liaison between ABA and SLAC was provided by the Plant Engineering Department of the SLAC Technical Division. Detailed descriptions of the conventional buildings, utilities, and site improvements designed and constructed under ABA management follow in subsequent sections of this chapter.

The ABA contractual requirements provided for master planning, architect–engineering design, inspection and quality control, and management of the construction of "conventional facilities" for the project. Prime design areas consisted of engineering studies and development of design criteria, architectural considerations, civil, structural, mechanical, and electrical engineering, general engineering services, planning, and scheduling. The scope of "conventional facilities" included site development, buildings, structures, and on-site utility systems, exclusive of the accelerator proper and its ancillary equipment and services. Figures 5-2, 27-1, and 27-2 and Tables 27-1 and 27-2 provide a synopsis of the ABA program. A comprehensive summation of the ABA designs is furnished in Reference 1.

Installation of accelerator equipment and services (FFH)

SYSTEMS ENGINEERING AND INSTALLATION. The design, procurement, installation, and acceptance testing of accelerator equipment and service systems were managed by SLAC personnel, principally the Business Office of the SLAC Business Services Division, acting as subcontract administrator, and the former Systems Engineering and Installations Department of the SLAC Technical Division, acting as installation manager. These two groups worked closely with a number of SLAC Research Division and Technical Division groups

Table 27-1 Initial construction subcontracts

Contract No.	*Subcontract title*	*Name of subcontractor*	*Date of award*	*Estimated cost*	*Date of beneficial occupancy*	*Actual cost*
1-250	Construction power system	Progress Electric Palo Alto, Calif.	7/62	$ 9,500	11/62	$ 11,858
1-250-2	Accelerator alignment survey towers	Donald C. Pratt Los Altos, Calif.	1/63	10,000	3/63	13,507
1-250-3	12-kV temporary overhead pole line	Bay Area Electric Corp. Redwood City, Calif.	3/63	35,000	9/63	43,063
1-402	Time and materials contract	Hans Stavn Palo Alto, Calif.	7/63	20,000	12/64	51,900
1-402-1	Time and materials contract	Hans Stavn Palo Alto, Calif	1/65	30,000	7/66	150,000
401	Initial site improvements	F F & M Co., Inc. Burlingame, Calif.	6/62	142,160	11/62	129,192
401-1	Loop road and site improvements	L. C. Smith Co. San Mateo, Calif.	6/62	79,400	11/62	87,770
421	New property fence	Embarcadero Fence Co. Mountain View, Calif.	6/62	8,280	7/62	8,272
430-1	Landscaping, increment I	Dennis R. Gibson Palo Alto, Calif.	7/64	32,400	12/64	30,494
430-3	Landscaping, increments II and III	A & J Shooter, Inc. Burlingame, Calif.	4/65	74,200	10/65	61,126
430-4	Landscaping, increment IV	Rudolph Watson, Inc. Redwood City, Calif.	9/65	69,600	1/66	68,505
430-5	Landscaping, increments V and VI	Rudolph Watson, Inc. Redwood City, Calif.	1/66	35,300	5/66	38,487

4-400	Construction office building, parking lot	O. C. Jones & Sons Berkeley, Calif.	8/63	6,070	9/63	8,938
450	Boundary fence construction	Anchor Post Products, Inc. So. San Francisco, Calif.	11/62	9,437	5/63	8,272
450-1	Site fencing	Oakland Fence Co., Inc. San Leandro, Calif.	3/66	70,000	6/66	51,828
501	Accelerator housing, initial excavation	Edwin D. Varwig East Palo Alto, Calif.	12/62	515,914	7/63	459,035
501-1	Equipment rental contract	Edwin D. Varwig East Palo Alto, Calif.	10/62	95,000	2/63	74,879
501-2	Accelerator housing and earthwork contract	Peter Kiewit Sons' Co. Arcadia, Calif.	8/63	4,841,000	10/64	4,387,904
501-3	Initial accelerator housing	Power Construction, Inc. Mountain View, Calif.	6/63	383,000	10/63	313,231
501-4-1	Coating of accelerator housing	Allied Painters & Decorators, Inc. Oakland, Calif.	10/64	44,000	12/65	44,605
502	Klystron gallery	Jasper Construction, Inc. Santa Cruz, Calif.	10/63	3,681,000	6/65	3,804,487
503-435-1	Control building & miscellaneous site improvements	Harrod & Williams, Inc. Sunnyvale, Calif.	6/64	373,700	4/65	418,470
505	Beam switchyard	M. M. Sundt Construction Tucson, Ariz.	9/64	3,608,100	3/66	4,327,411
505-1	Data assembly building	Harrod & Williams, Inc. Sunnyvale, Calif.	11/64	145,900	5/65	141,709
506	Cryogenics facility building	Harrod & Williams, Inc. Sunnyvale, Calif.	8/65	462,000	5/66	470,147

Table 27-1 Initial construction subcontracts (*continued*)

Contract No.	*Subcontract title*	*Name of subcontractor*	*Date of award*	*Estimated cost*	*Date of beneficial occupancy*	*Actual cost*
523-673	Central utility building and heat transfer system	Cortelyou & Cole, Inc. Mountain View, Calif.	12/62	$ 206,900	9/63	$ 242,077
523-4(679)	Cooling tower & cooling tower fire protection system	Fluor Products Co., Inc. Santa Rosa, Calif.	12/62	44,600	4/63	32,006
524-525	Electronics & stores buildings and fabrication building (shops complex)	Cortelyou & Cole, Inc. Mountain View, Calif.	1/63	950,300	12/63	960,830
5-250-2	Plating and cleaning area	Cortelyou & Cole, Inc. Mountain View, Calif.	11/63	166,800	10/64	207,486
525-3-1	Still installation & piping	C. Norman Peterson Co. Berkeley, Calif.	1/64	25,000	4/64	19,017
525-3-2	Cleaning building	Arthur Bros., Inc. San Mateo, Calif.	4/64	39,000	6/64	34,349
525-3-3	Gas storage area	Cortelyou & Cole, Inc. Mountain View, Calif.	12/63	6,000	3/64	8,941
526/540	Research complex—heavy assembly building and central laboratory	Harrod & Williams, Inc. Sunnyvale, Calif	12/63	1,829,800	4/65	2,437,991
535	Construction office building	Arthur Bros., Inc. San Mateo, Calif.	1/63	196,[illegible]00	6/63	199,892
540-1	Completion of second-story addition to one-story wing of central laboratory	Forrest Anderson Construction Co. Palo Alto, Calif.	4/65	121,000	10/65	95,864

541	Administration & engineering building	Morris Daley, Inc. Burlingame, Calif.	9/62	772,300	9/63	774,910
542-1	Shops dining room	Harrod & Williams, Inc. Sunnyvale, Calif.	8/64	22,400	10/64	27,214
542-543	Cafeteria-auditorium	Vanderson Construction, Inc. San Jose, Calif.	1/64	383,600	8/64	373,054
544	Test laboratory building	Cortelyou & Cole, Inc. Mountain View, Calif.	7/62	370,000	6/63	479,036
544-1	Test laboratory electrical	Trans-Pacific Electric, Inc. San Leandro, Calif.	7/62	187,200	6/63	154,606
544-2	Test laboratory mechanical	Nagel Associates, Inc. Redwood City, Calif.	7/62	218,000	6/63	141,939
544-3	Test laboratory fire protection system	California Automatic Sprinkler Co. San Francisco, Calif.	7/62	23,700	6/63	26,013
544-9	Test laboratory cranes	Lypta Cranes, Inc. Houston 36, Texas	12/62	59,500	9/63	37,815
561-1	Beam dump east structure	Harrod & Williams, Inc. Sunnyvale, Calif.	11/65	250,000	6/66	350,782
561-562	End station A and B, buildings and utility housings	M. M. Sundt Construction Tucson, Ariz.	3/65	3,846,000	5/66	3,392,106 (claims not settled)
600-X	Initial site utilities	Cortelyon & Cole, Inc. Mountain View, Calif.	12/62	388,500	7/63	433,785
600Y-1	Klystron gallery utilities, piping, & site improvements	C. R. Fedrick, Inc. Novato, Calif.	4/64	747,000	9/65	693,497
600Y-2	Klystron gallery utilities	C. R. Fedrick, Inc. Novato, Calif.	10/64	819,700	1/66	617,536

Table 27-1 Initial construction subcontracts (*continued*)

Contract No.	*Subcontract title*	*Name of subcontractor*	*Date of award*	*Estimated cost*	*Date of beneficial occupancy*	*Actual cost*
600Y-3	Cooling towers	Ets-Hokin Corp. San Francisco, Calif.	5/64	$ 202,000	12/64	$ 206,656
600Z-1	Beam switchyard site improvements and utilities	Harrod & Williams, Inc. Sunnyvale, Calif.	4/65	975,400	5/66	916,449
600Z-2	End station site improvements and utilities	Cortelyou & Cole, Inc. Mountain View, Calif.	7/65	1,464,000	6/66	1,311,268
615	Area lighting	Golden Gate Electric Co. San Francisco, Calif.	6/65	32,700	11/65	25,644
616-1	Master substation	S & Q Construction Co. So. San Francisco, Calif.	12/64	853,700	1/66	846,828
616-2	Switch house	Arthur Bros., Inc. San Mateo, Calif.	10/64	55,600	5/65	68,941
617	60/12-kV substation	Westinghouse Electric Corp. San Francisco 8, Calif.	11/62	80,000	6/63	75,539
7-925-1	Concrete doors	TRG, Incorporated Menlo Park, Calif.	10/65	203,000	9/66	119,000
7-930-X	Target area cranes	Crane Hoist Engineering & Manufacturing Co. San Leandro, Calif.	6/65	256,000	8/66	254,867
7-931-2	Cranes for shop complex	American MonoRail Co. c/o Buehrer, Inc. Oakland, Calif.	9/63	43,500	2/64	36,700

7-932-2	Heavy assembly building cranes (design)	Crane Hoist Engineering & Manufacturing Co. San Leandro, Calif.	9/64	16,000	2/65	7,289
7-932-3	50-ton crane for heavy assembly building	Crane Hoist Engineering & Manufacturing Co. San Leandro, Calif.	2/65	61,900	8/65	62,300
7-932-4	Cranes for heavy assembly building and cryogenics building	Crane Hoist Engineering & Manufacturing Co. San Leandro, Calif.	2/65	72,435	7/65	66,208
7-936	Beam switchyard materials handling system	American Crane & Hoist Corp. Downey, Calif.	7/64	198,866	4/66	294,016
544-6 (613)	Substation control power battery for test laboratory substation	Nife Incorporated Copiague, Long Island, N.Y.	7/62	4,000	4/63	1,554
544-7 (544)	Control centers for test laboratory	General Electric Co. Schenectady, N.Y.	8/62	6,000	7/63	4,857
544-8 (613)	Distribution center for test laboratory substation	Federal Pacific Electric Co. Newark, N.J.	8/62	4,500	12/62	3,210
613-X-1	Unit substations	Federal Pacific Electric Co. Burlingame, Calif.	11/63	306,900	9/66	330,059
613-Z-1	Indoor electrical switchgear and substations	Federal Pacific Electric Co. Burlingame, Calif.	3/65	379,500	2/67	421,417
792-1	Shielding blocks	Dean C. Buehler, Inc. Palo Alto, Calif.	12/62	13,600	2/63	12,080

Table 27-2 Initial construction costs

Breakdown of Aetron-Blume-Atkinson costs	
Engineering, design, and inspection	$3,776,900
Construction management	1,583,600
Indirect costs	3,093,900
Fee	1,236,500
	$9,690,900
Cost breakdown of conventional facilities	
Site improvements	$ 2,206,500
Accelerator housing	4,710,400
Klystron gallery	3,604,300
Control building	288,300
Beam switchyard	4,257,500
Cryogenic facility	295,700
Central utility building	63,200
Electronics building	341,200
Fabrication building	751,000
Heavy assembly building	764,500
Construction office building	188,300
Central laboratory	1,582,300
Administration & engineering building	774,600
Cafeteria and auditorium	316,500
Test laboratory	892,100
End station A	2,562,500
End station B	988,000
Plant utilities: Electrical	4,033,900
Mechanical	2,664,200
Equipment	857,300
	$32,142,300

having prime responsibility for the design and fabrication of mechanical and electronic components of the accelerator and its beam switchyard, and with the Purchasing Department of the SLAC Business Services Division.

Prior to initiating a SLAC-managed installation program, it was necessary to determine the scope of the program and then obtain approval from the U.S. Atomic Energy Commission to carry out the work. The desirability of having a SLAC-managed installation program for the accelerator equipment and its critical service systems was based on the following considerations:

1. This arrangement would allow design decisions to be deferred in those cases where it would be desirable to do so without disrupting the work of outside agencies.

2. It would provide flexibility to include or not to include specific work items in a given subcontract as information firmed up.
3. It would allow maximum coordination of the activities of SLAC component designers and SLAC installation planners.
4. It would permit SLAC installation supervisors to schedule work in various accelerator areas so as to best meet short-term objectives.
5. It would allow close SLAC control of subcontractor work in the vicinity of critical SLAC equipment, as well as direct SLAC supervision of the installation of such critical equipment.

A report, "Installation Program for the Two-Mile Accelerator" (dated May 14, 1963), was prepared by the Systems Engineering and Installations Department in collaboration with all SLAC technical groups having primary interest in one or more phases of the work. This report was reviewed at length with the U.S. Atomic Energy Commission and their approval to proceed was received. The program may be summarized as follows: (a) SLAC would act as its own general contractor for the accelerator installation; (b) a number of lump-sum installation subcontracts would be awarded "by trade," principally for electrical work and plumbing work; (c) installation of critical accelerator equipment and instrument and control wiring at primary machine control consoles would be accomplished using subcontractors retained on a "time and materials" basis.

Organizationally the work was programmed so as to use a minimum number of people. All lump-sum installation subcontracts were handled through two contract administrators. A third contract administrator handled time and material subcontracts. Overall direction and coordination were handled by the installation manager, an office engineer, a field superintendent, and an assistant field superintendent. Each component or system group furnished a cognizant field engineer together with the necessary number of inspectors to follow properly the group's field work. Component groups also furnished field superintendents and test personnel to direct the installation of critical accelerator equipment, such as the following:

Klystron tubes
Rectangular waveguide assemblies
Main injector
Beam-analyzing station No. 1
Standard 40-ft accelerator assemblies
Sector drift section assemblies
Positron source
Positron solenoid section assemblies
Beam-analyzing station No. 2
Beam switchyard drift tubes
Pulsed magnet assembly No. 1
Special instrument section assemblies
Main beam collimator

Main divergent chamber
Beam tune-up dumps
Beam scrapers
Beam bending magnets
Main beam slits
Main beam dumps
Photon beam section assembly
Magnetic slit
Pulsed magnet assembly No. 2
B-beam divergent chamber

SUBCONTRACTS. Working drawings and specifications were prepared for the following lump-sum installation subcontracts:

Accelerator ac electrical services
Accelerator cooling-water systems
Accelerator high vacuum system
Sectors 1 and 2, electronic equipment rack assembly
Sectors 3–30, electronic fiat rack assembly
Sectors 3–30, electronic control alcove rack assembly
Accelerator instrumentation and control (I & C) cable plant
Accelerator electronic equipment rack installation
Beam switchyard electrical work
Beam switchyard cooling-water systems
Beam switchyard equipment installation

Specifications and instructions were prepared for the following time and materials installation subcontracts:

Accelerator and klystron installation
Electronic control room wiring
Beam switchyard completion work

The accelerator ac electrical services subcontract also provided for the installation of the SLAC-furnished accelerator modulators, personnel communications equipment, main drive line, subdrive line, main trigger line, and I & C battery plants.

The accelerator cooling-water systems subcontract also provided for the installation of compressed air piping in the klystron gallery, the installation of supports for klystron tubes and accelerator girders, as well as pumps and heat exchangers furnished by SLAC.

The accelerator high vacuum system subcontract included the installation of SLAC-furnished gauges, valves, and pumps, but did not include installation of the accelerator alignment vacuum system.

The beam switchyard electrical work subcontract provided for the installation of SLAC-furnished dc magnet power supplies, but did not include installation of the Data Assembly Building control room wiring.

The beam switchyard cooling-water systems subcontract also provided for the installation of compressed air and inert gas systems piping.

The beam switchyard equipment installation lump-sum subcontract provided for the installation of high vacuum pumping systems, chambers and drift tubes and for the delivery of all major equipment to the site prior to June 1966. Equipment delivered later was installed using time and materials subcontractors.

SCHEDULES. The installation of the accelerator and beam switchyard equipment started in April 1964 and was substantially completed in August 1966. Thereafter, a few pieces of equipment were delivered and installed, and by December 1966 only one initial piece of equipment for the beam switchyard had not been delivered. It was installed during January 1967.

On January 7, 1965, a temporary injector delivered an electron beam to Sectors 1 and 2 over a length of 666 ft, 4 in., into a temporary dump. On April 21, 1966, the "permanent" injector delivered an electron beam into beam-analyzing station No. 2 over a distance of about 6400 ft. On May 21, 1966, an electron beam was delivered into a beam tune-up dump in the SLAC beam switchyard, having traveled a distance of almost 11,000 ft. Note the adherence to schedule in that the original planning called for beam tune-up checkout tests during April, May, and June of 1966. As of August 1966, the initial project physical plant was essentially complete. There remained, of course, a lengthy checkout of machine performance and the completion of initial experimental equipment layouts. An overall concept of the SLAC accelerator installation is given in Figs. 5-14, 10-3, 15-16, and 27-3 through 27-8 and in Table 27-3.

It is worth noting that on Friday, April 3, 1964, the first building areas for installation of the machine structures were accepted for SLAC occupancy and that 3 days later, on Monday, April 6, 1964, both electrical and cooling-water subcontractors for installation of these accelerator systems were aboard

Figure 27-3 Main injector.

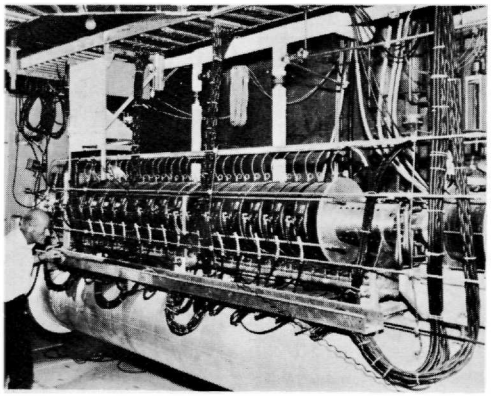

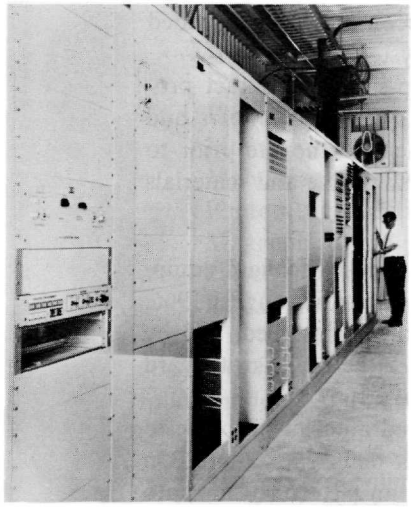

Figure 27-4 Typical sector alcove control room.

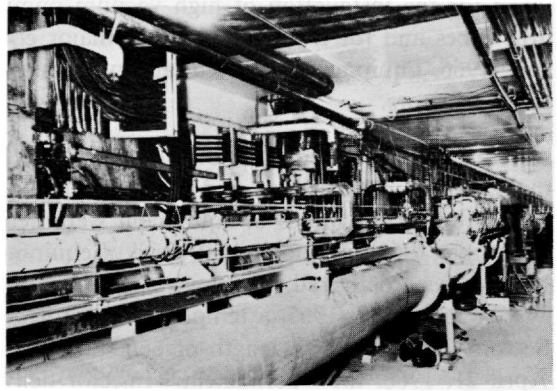

Figure 27-5 Positron source services.

Figure 27-6 First bending magnets upon arrival.

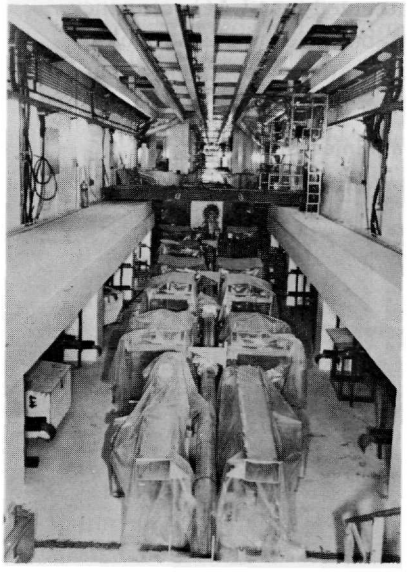

Figure 27-7 Data assembly building control room electronic equipment racks.

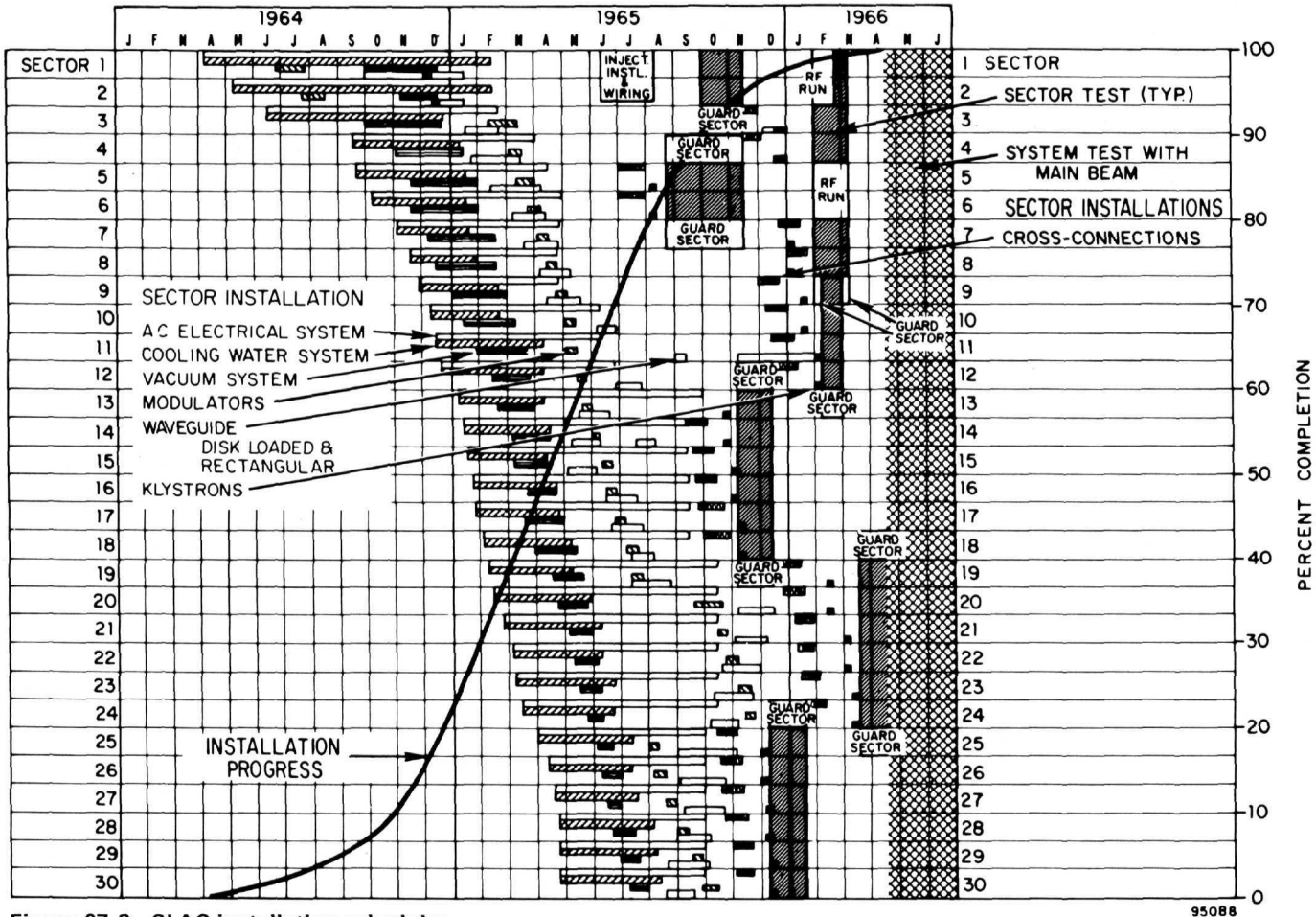

Figure 27-8 SLAC installation schedules.

Table 27-3 SLAC installation subcontract data

Subcontract No.	*Title*	*Subcontractor*	*Engineer's estimate*	*Original bid*	*Final cost*	*Date started*	*Date accepted*
400-S-39	Accelerator ac electrical services	Brayer Electric San Francisco, Calif.	$1,490,400	$999,900	$1,324,940	Mar 64	May 66
400-S-46	Accelerator cooling water	Monterey Mechanical Oakland, Calif.	1,580,000	1,568,000	1,699,018	Mar 64	Sep 66
400-S-40	Accelerator high vacuum system	Cosmodyne Corp. Torrance, Calif.	1,415,900	796,250	1,034,967	Feb 64	Aug 65
400-S-68	Sectors 1 and 2 electronic equipment rack assembly	Ets-Hokin & Galvin San Francisco, Calif.	76,800	40,000	83,000	Jun 64	Apr 65
400-S-71	Time & material, accelerator & klystron installation	Wismer & Becker Sacramento, Calif.	500,000	500,000	405,557	Jul 64	Jun 66
400-S-71R	Time & material, beam switchyard completion	Wismer & Becker Sacramento, Calif.	50,000	50,000	56,525	Jan 66	Jul 66
400-S-92	Sectors 3-30 electronic equipment rack assembly	Keltec Industries, Inc. Santa Clara, Calif.	354,389	163,618	218,662	Jan 65	Jan 66
400-S-111	Accelerator I & C cable plant	Brayer Electric San Francisco, Calif.	714,000	455,555	623,644	Mar 65	Apr 67
400-S-132	Time & material, control room wiring	T. L. Rosenberg Oakland, Calif.	200,000	200,000	200,000	May 65	Apr 66
400-S-135	Time & material, beam switchyard completion	Rosendahl Los Angeles, Calif.	0	0	183,721	Apr 66	Dec 66
400-S-149	Beam switchyard cooling-water systems	Natkin & Co. Santa Clara, Calif.	468,000	482,400	785,568	Aug 65	Apr 67
400-S-155	Beam switchyard electrical work	Trans-Pacific Electric Seattle, Wash.	605,000	944,900	1,201,098	Sep 65	Mar 67
400-S-160	Accelerator electronic equipment rack installation	Brayer Electric San Francisco, Calif.	183,310	217,777	256,006	Jul 65	May 66
400-S-179	Beam switchyard equipment installation	Natkin & Co. Santa Clara, Calif.	84,000	139,540	167,218	Sep 65	Jun 66
			$7,721,799	$6,557,940	$8,239,924		

and underway. For the next 2 yr, SLAC subcontractors entered each increment of construction accepted for beneficial occupancy in periods measured in hours to days, but not in weeks. The installation of the SLAC machine followed very closely the completion of its buildings and utilities.

More recent construction programs (FFH, EPL)

PLANT ENGINEERING. As the construction of initial buildings and utilities and the installation of the accelerator equipment and services approached completion, it was recognized that a revised organization would be needed for the technical management of further modifications and extensions of the SLAC physical plant. During 1966, the former Plant Engineering Department, which had been responsible for SLAC liaison with ABA activities and for initial changes to conventional buildings and utilities, was combined with the Systems Engineering and Installations Department, which was responsible for the installation of accelerator equipment and services, into a single Plant Engineering Department. This department is now responsible not only for completion of initial construction and equipment installation but also for minor modifications to buildings and utilities, general plant projects, new buildings funded under the original construction contract with the U.S. Atomic Energy Commission, and new buildings authorized from subsequent construction funding.

MODIFICATIONS TO EXISTING BUILDINGS. Fiscal year 1967 was the first year of operation and maintenance of the completed SLAC physical plant. Prior to July 1966, changes to SLAC conventional facilities were funded from SLAC initial construction funds, with each change being declared capitalized or not, based on the nature of the change. These changes were managed technically by the plant engineering liaison group, often using the former Systems Engineering Department as its architect–engineer, working in collaboration with the SLAC Plant Office. Since July 1966, the program has been split, with capitalized projects being funded as general plant projects and non-capitalized minor modifications to buildings and utilities being funded as operating costs.

Minor modifications to existing buildings and utilities have been needed from the date of beneficial occupancy of each facility. Reasons for such modifications include the following:

1. Organization of laboratories, workshops, and offices to allow maximum use of space upon initial occupancy by SLAC forces.
2. Change of space requirements by SLAC groups during the initial machine installation period.
3. Change of space utilization as SLAC evolved from the phase of machine installation into the phase of machine operation support of basic research.
4. Conversion of space usage for new SLAC activities not foreseen in detail during the initial scoping of project work.

Table 27-4 Estimated scope of minor modifications projects

Fiscal Year	*Capitalized projects*	*Noncapitalized costs—buildings*	*Noncapitalized costs—utilities*	*Total costs*
1964	$ 20,000	$140,000	$ 30,000	$190,000
1965	190,000	360,000	50,000	600,000
1966	225,000	300,000	75,000	600,000
1967	0	300,000	200,000	500,000
1968	0	300,000	200,000	500,000

Expressed as a percentage of total SLAC construction value, minor modifications to the existing SLAC physical plant have amounted to about 3% to date. Nonetheless, when considered as an annual program, these changes have ranged up to as much as $600,000 a year. For a long time, about $16,000 per month has been expended on an average number of about twenty projects, each of which has an average installed cost of about $800. The balance of work has consisted of a few projects which required the expenditure of about $9000 per month.

The estimated scope of minor modification projects tabulated by fiscal year is shown in Table 27-4.

Looking ahead, the need for minor modifications to existing physical plant is likely to remain constant in the area of modifications to buildings, and to grow slowly in the area of utilities as the scope of SLAC research programs is expanded.

GENERAL PLANT PROJECTS. With the advent of operational budgets starting in fiscal year 1967, it became necessary to segregate projects that must be capitalized and are not properly a part of the initial construction program as general plant projects.

In practice, such projects range in scope from $5000 to approximately $100,000 in installed cost. These projects fall into several categories which include (a) facility conversion which may be considered as an upgrading of space usage, (b) new space, and (c) projects that require additional equipment which, per se, is to be capitalized. The fiscal year 1967 program totaled $350,000 and was carried out as shown in Table 27-5. The fiscal year 1968 program totaled $245,000 and was planned as shown in Table 27-6. Looking ahead, there remain a number of desired projects which properly are to be classified as general plant projects, together with still other projects not being given detailed consideration as of this date. At the present time, the gross scope of these projects, if built, would cost just under $2,000,000, based on current construction costs.

The continuing backlog of projects for both general plant and minor modifications overtaxed the permanent plant engineering staff. In order to

Table 27-5 1967 General plant projects

Description of project	*Engineering costs*	*Construction costs*	*Total costs*
54-in. spark chamber enclosure	$ 300	$ 19,900	$ 20,200
Fire alarm system—target area	1,100	13,600	14,700
Temporary computer facility	27,000	169,000	196,000
Loop road resurfacing	1,000	12,100	13,100
Welding shop	4,700	38,300	43,000
Power supply enclosures	500	15,300	15,800
Power factor correction	0	2,100	2,100
Emergency oil catchment basin	1,400	4,500	5,900
Intercept storm drains	400	0	400
South boundary fence	2,800	24,900	27,700
	$39,200	$299,700	$338,900
Indirects			11,100
			$350,000

obtain increased flexibility, the services of an outside architect–engineer firm were sought to augment the in-house engineering capability. The first such subcontract for architect–engineer assistance was awarded in 1966 to Ackerman-Aronoff-Ruth-Going and Beck, a joint venture, Palo Alto, California. This firm has been very helpful in the execution of medium-sized projects and their work period at present extends through fiscal year 1968.

Table 27-6 1968 General plant projects

Description of project	*Engineering costs*	*Construction costs*	*Total costs*
Chilled water headers	$ 3,200	$ 36,800	$ 40,000
Sand blast facility	1,000	15,000	16,000
Power supply enclosures	0	9,000	9,000
North yard paving	1,500	10,500	12,000
Counting house extension	10,000	83,000	93,000
Addition to temporary computer building	3,900	59,100	63,000
	$19,600	$213,400	$233,000
Indirects			12,000
			$245,000

NEW BUILDINGS. Even as the initial project construction drew to a close, a number of new buildings and facilities were under consideration and these included: a laser room, a fire station, a general services building, an extension to the Central Laboratory, an electron–positron colliding beam storage ring, and a computation building.

To date, the first four items listed above have been authorized from initial SLAC construction funds. The other items are on future funding appropriation lists and are not discussed further. The laser room was designed by the former Systems Engineering Department.

In 1966 the architectural firm of Rockwise and Watson, San Francisco, California, assisted by Gilbert Associates, structural engineers, and Bentley Engineers, electrical and mechanical engineers, also of San Francisco, California, was retained to design the Fire Station and the General Services Building. The Fire Station is scheduled for completion late in 1967 and the General Services Building in mid-1968.

Also in 1966, the engineering firm of John A. Blume Associates, San Francisco, California, assisted by Charles Luckman & Associates, architects, Los Angeles, California, and Keller and Gannon, electrical-mechanical engineers, San Francisco, California, was retained to design the Central Laboratory Extension. This extension to the Central Laboratory will be substantially completed in September 1968.

Looking ahead, it is planned to retain qualified architect–engineer firms for the design of future buildings and facilities as construction is authorized. Daily inspection and coordination of construction subcontractor activities on the SLAC site have been and will be handled by Plant Engineering Department personnel since it is firmly believed that a continuing capability in this area of physical plant work is of importance and value.

27-2 Site and site improvements

Site investigation program (RSG)

At no time during the selection of the site and subsequent design was it assumed that the accelerator would remain in a permanently stable, straight-line condition. Movement is to be expected from seismic and tectonic factors, settlement and consolidation of soils, and the effects of variations in ground water conditions.

The basic task of the site investigation carried out by the Aetron-Blume-Atkinson joint venture was to determine the nature of movements and to predict their magnitudes during the useful life of the machine. Such a program is properly of concern in the early development of any large accelerator project, because of the magnitude of the weights which will be placed on the existing soils. In the case of SLAC, there was also concern because of the nearness of the San Andreas fault.

The basic items of this site investigation program are outlined here.

1. General geology: regional geomorphology, stratigraphy, structure, and paleontology.
2. Engineering geology: Eocene and Miocene rocks; alluvium; soil overburden; soil profile; earthwork; preloading—surcharge and preload fills for minimizing consolidation of foundation materials; ground water.
3. Ground movement and seismic studies: review of previous regional surveys; measurement of slow deformation—horizontal, vertical, tilt; movements caused by construction—rock rebound, settlement, consolidation; seismic studies—seismic design considerations; design parameters for various rock types.

Minor movements which might affect the day-to-day operation of the machine, such as small seismic tremors, traffic-induced vibrations, and earth tides, were investigated. It was concluded that their effect would not be great enough to influence design and no extensive study of them was made.

Means of effecting the program included trenching, bore hole drilling of various types, ground water wells, geologic maps, precise alignment and levels surveys, tilt meters, temperature-measuring devices in backfills and structural concrete, settlement markers (plates at the bases of fills with pipe risers), fluid level settlement indicators, soil moisture instrumentation, deep strata bench marks, and "inverted plumb bobs."*

The largest short-term movements were associated with vertical soil changes. In the measurement of these movements, plates and pipe risers in fills proved more reliable than fluid level indicators, although they were subject to some damage at times during embankment construction.

Other movements can be determined by precise measurements over long time periods (or after earthquakes). SLAC's instrumentation has been designed to provide information on the nature of significant movements occurring during the accelerator's useful life so that effective countermeasures may be devised.

In addition to many private consultants engaged by ABA for this program, a number of institutions, including the University's School of Mineral Sciences, the U.S Coast and Geodetic Survey, and the U.S. Geological Survey, provided valuable data. The subject is covered in detail in References 1, 2, and 3.

Geology (RSG)

The injector end of the accelerator lies about ½ mile from the edge of the San Andreas rift zone running through Portola Valley. Hence, a careful geophysical examination was necessary before a final decision was made on

* Devices patterned after those developed by DeCae at CERN, consisting of floats in vertical wells filled with water, anchored by wires to fixed bases at the well bottoms, to measure relative horizontal shifting of strata.

site selection. Several reports were made by Dr. Perry Byerly and assistants of the University of California in 1959 and 1960 and are included in the report by John A. Blume and Associates.[4] Byerly concluded that the 2-mile original straight line of the accelerator could be expected to curve at a rate producing a displacement of about 2 mm/yr at mid-length. Byerly's conclusion was based largely on triangulation surveys made before and after the 1906 earthquake which disclosed the pattern of elastic strain buildup. It was also based on later surveys showing relative movement between blocks on either side of the fault.

The general geology of the region was described by Atchley and Dobbs in 1960 in their report "Geological Investigation of the Stanford Two-Mile Linear Accelerator Site," and in two subsequent reports by Atchley in the same year. These also are included in Reference 4. Byerly had stated that there appeared to be no geologically recent fault activity within the site boundaries. Atchley, and subsequently Dr. Parker Trask (1961), confirmed this view.[5]

The machine is located, for the most part, in formations of Eocene and Miocene sandstones, the former predominating in the west, and the latter in the east and in the target area. The Eocene is in a chaotic condition in some sections of the machine's length. This necessitated careful engineering geology studies before undertaking final design of the accelerator housing and klystron gallery. The Miocene is superior for engineering purposes and its uniformity and great bearing capacity have made it an excellent base in the end station area* for supporting the massive research equipment.

The physical plant and equipment mountings for the project have been designed to withstand, without major damage, an earthquake with a nearby epicenter and having a Richter scale magnitude of 8.0. The accelerator's lateral alignment adjustment allowance of 12 in. in any direction is expected to be sufficient to permit realignment after such a quake.

For a detailed summary of SLAC's geology, see Reference 2.

Soil mechanics (RSG)

The problem of volumetric changes in soils surrounding the accelerator was critical. It became apparent in the planning stages that the Accelerator Housing would have to be constructed to grades established in accordance with settlement predictions. Accordingly, SLAC established settlement criteria in the fall of 1962 as follows:

> Construct the Accelerator Housing to grades established in accordance with predicted settlement, consolidation and rebound. Regardless of these predicted movements, however, no point along the housing floor is to depart more than four inches above nor two inches below a straight line in October

* During excavation for the end station area, workmen uncovered the near-complete fossil remains of a 9-ft, ½-ton, Miocene age mammal called *Paleoparadoxia*.

1965. Hence, the accelerator tube could be aligned at that time with no point more than four inches below, nor two inches above the optimum position. These departures from straightness should be in directions such that movements during at least the succeeding ten years, due to soil changes only, will be toward straightening of the housing.

If settlement and consolidation during the period is expected to be of a magnitude which would cause movement to pass through a condition of maximum straightness and into a condition of departing from straightness within this period, areas involved should be so reported, indicating their lengths, positions and long-range predicted movements.

It is strongly desired that departures from straightness of the aligned accelerator tube in the overall 10,000-foot length shall not exceed $\frac{1}{4}$ inch in a 90-day period, even though rates of curvature be minute.

The task of meeting these criteria fell upon the firm of Dames and Moore, consulting engineers in applied earth sciences, as consultants to ABA. The October 1965 time-point was chosen because it was anticipated that alignment of the accelerator would be proceeding at that time.

To keep soil movements to a minimum, two areas of least foundation competence were preloaded with earth fills for about a year prior to start of accelerator housing construction. Along the accelerator's length, a couple of locations (not preloaded) departed sharply from the general straightness of the constructed housing, but despite this, the October 1965 tolerances were met.

Maximum recorded fill settlement was $5\frac{1}{2}$ in. measured at the base of an 80-ft fill. Average settlement during earthwork construction (early 1963 to early 1964) was $\frac{3}{4}$ in./10 ft of fill, in fills ranging from 30 to 80 ft deep. Subsequent fill settlements have been very slight and have proved that replacement of alluvia with engineered fills and preloading of weaker areas have been highly effective in reducing or eliminating consolidations.

Scientific use of soil mechanics was made throughout all construction phases of the project. A well-equipped and -staffed soils laboratory was maintained by ABA on site for this purpose.

Further details on the soil mechanics program are described in References 1 and 2.

Roads, yards, and parking (RSG)

Predominant considerations in planning the $8\frac{1}{2}$ miles of site roads were the movement of heavy equipment and materials incident to physics research plus the fact that the ratio of personnel to private cars on site during the working day is almost 1 : 1. Roads between the Heavy Assembly Building and the research yard are of relatively heavy construction with 10 in. of aggregate base and 4 in. of asphalt concrete surfacing. The ratio of parking areas to building areas is large, but costs were kept fairly low by use of asphalt curbs and a light paving consisting of a 6 in. base and of oil and rock-chip seal coat surfacing. Both have stood up well for passenger car parking.

Main roads consist of the main entrance drive, the "Loop Road" circling the main "campus" area, one road on each side of the klystron gallery for the full length of the accelerator, a 2-mile bypass road paralleling the accelerator at a distance of from 200 to 500 ft, and the north and south target area roads.

Maximum grade on these roads is limited to 6% excepting the bypass road paralleling the accelerator. Where wide and heavy loads were anticipated, the inside radii of curves are not less than 40 ft. Because of the need to move buildings occasionally, generous side clearance has been provided. Roads having considerable traffic are 30 ft wide, allowing two lanes of traffic to be maintained when a vehicle is parked.

Yards surrounding buildings are paved with 2 in. of asphalt concrete on aggregate bases varying from 6 to 10 in., depending on the functions of the buildings served. The research yard, having a large percentage of concrete paving, departs somewhat from this standard. It is described later in this chapter.

There are relatively few walks on the site and these are confined to the campus area. One is formed by the top of the concrete utility tunnel serving the campus buildings; others are of asphalt concrete; and some are merely of compacted, graded rock.

Storm drainage system (RSG)

SLAC's underground drainage system consists almost entirely of corrugated metal pipe. Experience has indicated that for those pipes draining shop areas where corrosive liquids could enter the system, a bituminous inner coating would have been advisable.

The use of corrugated metal pipe extends to the culverts under the accelerator. These were sized generously, as marginal hydrologic design could prove to be false economy, considering the total cost of the machine.

Erosion control (RSG)

The side slopes of embankments along the accelerator's length were treated for soil erosion by adding a 6-in. layer of native topsoil and kneading straw into it with compacting rollers equipped with knife-type feet. Seed was added, but the seed contained in the straw predominated and the slopes yielded a lush growth of barley, wheat, and rye. Despite the growth, a heavy rainfall in the winter of the second year of construction caused extensive sloughing of the topsoil layer from the densely compacted fills. Because of this, it was decided to omit the topsoil treatment from the banks of the large beam switchyard fill, and a substitute method was used consisting of a spray application of a mixture of cellulose fiber mulch, seed, and fertilizer. Unfavorable weather conditions following the treatment resulted in a crop failure and the beam switchyard fill entered the winter of 1966–67 with bare banks. A severe storm

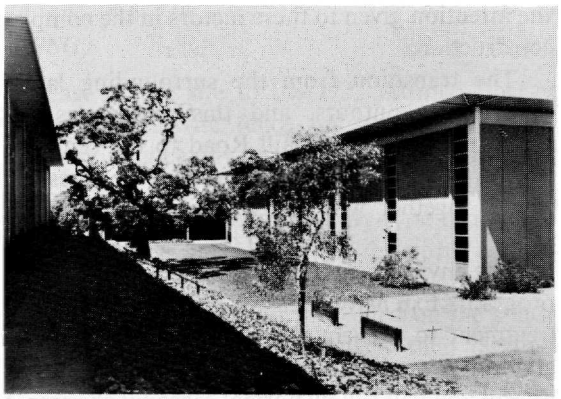

Figure 27-9 Landscaping between shop buildings.

caused the bank surfaces to turn to liquid mud following 36 hours of steady rain. Mud slides developed around the cableway structure on a bench of the slope and behind the Data Assembly Building, necessitating a large cleanup operation, fortunately without serious damage to structures or equipment.

Landscaping (JWC)

Having decided to establish SLAC in the Sand Hill Road area, it was essential, for esthetic, environmental, and political reasons, not to diminish unduly the native beauty, to site the buildings in such a way that their large scale would not dominate the landscape, to restore inevitable construction scars, and to provide landscaping to enhance the buildings. Figures 27-9 and 27-10 show

Figure 27-10 Typical landscaping—looking north of test laboratory.

the attention given to these factors in the completed landscaping and building construction.

The transition from the surrounding land was made without abrupt changes in contours, and this effort was particularly successful in the transition from Sand Hill Road to the central campus area. The retention of the rolling contours permitted the preservation of existing oak trees which, together with native grasses, provide the essential character of the area.

The environmental aspect was, however, only one part of the landscaping program. Extensive areas of cut, fill, and other construction scars required treatment to prevent soil erosion. This has been accomplished with native grasses, ivy, and prostrate shrubs. In the peripheral areas, the native grasses prevail and will follow normal seasonal changes. In the central area, irrigation is used to promote growth, present a fresh, dust-free zone, and serve as a fire-stop to possible grass fires.

In areas around and between the principal buildings, trees provide shade on building walls and foot paths, and occasionally flowering trees are included as accents.

Some of the parking areas and most of the yards are screened by means of earth mounds and dense plantings of trees and shrubs.

The largest building at SLAC, the 2-mile long klystron gallery, is expressed rather than concealed by the landscaping and is flanked by rows of eucalyptus trees which will, in a few years, complement the linear character of the accelerator.

The following categories of plants were used:

GROUND COVER AND VINES—native grasses, turf, *Hedera canariensis*, *Hypericum calycinum*, *Gazania splendens*, *Fiscus repens*

SHRUBS—*Callistemon lanceolatus*, *Ceanothus griseus horizontalis*, *Nerium oleander*, *Prenus laurocerasus*, *Pyracantha crenata*, toyon (*Heteromeles arbutifolia*)

TREES—*Fraxinus uhdei*, *Ginkgo biloba*, *Ligustrum texanum*, *Olea caropea*, *Crataegus phaenopyrum*, *Sequoia sempervirens*, *Pinus muricata*, *Quercus agrifolia*, *Quercus suber*, *Eucalyptus leucoxylon*, *Eucalyptus globulus* (normal and dwarf), *Podocarpus macrophylla*, *Magnolia grandiflora*, *Magnolia soulangeana*.

Irrigation was provided to give the turf, ivy, and *Hypericum* ground cover areas a fresh appearance throughout the year and to promote growth of the trees and shrubs. With few exceptions, plant material was of either 1- or 5-gal size.

In the peripheral areas of pines and eucalyptus, irrigation was provided by means of above-ground piping and quick couplers for hand hose connection to prevent plant loss in the first few summers and to promote growth. In these areas, the irrigation will be discontinued after satisfactory establishment.

Fencing and main entryway (RSG)

Shortly after the University's lease of the site to the U.S. Atomic Energy Commission became effective, a barbed-wire fence on steel pickets was erected along the boundaries, functioning chiefly as a barricade against cattle grazing on adjacent lands.

Near the conclusion of construction, in 1966, a security-type chain-link fence was constructed around the research area and along the north side of the klystron gallery. It was thought that by keeping all south wall doors along the klystron gallery normally locked, no fence would be needed on the south side. However, because access to areas south of the gallery then became difficult for SLAC personnel, in fact far more difficult than for trespassers, it was decided to fence the south side in 1967.

It is project policy to follow the University's precedence of keeping the campus open to the public at most times. SLAC's land areas that are clear of radiation sources are so maintained. The fence location and the main entrance reflect this, the latter being an open road intersecting Sand Hill Road, a city of Menlo Park street. Full-scale development of the entrance has been curtailed by the perpetual imminence of road-widening programs. It is the project's desire that eventually city, state, county, and SLAC road developments will be completed to the mutual advantage of all involved.

27-3 Buildings

The master plan (JWC, FFH)

The decision to build an extensive research establishment in an area of the San Francisco Peninsula associated with Stanford University, large residential estates, and high-priced subdivisions, required esthetic and structural approaches radically different from precedents in more remote and less attractive geographical situations.

From the beginning, Stanford University had assured the neighboring communities that the physical development of the Sand Hill Road site would be executed in a manner sympathetic to the environment. Accordingly, in the Stanford–AEC lease, the University retained architectural control of the development, including landscaping and site planning beyond the limits of the functional needs of the accelerator and target areas.

The basic form of the accelerator and research areas is a "Y" with an elongated tail having an overall length of approximately 12,000 ft. This, together with the required lateral clearance of 500 ft on each side of the accelerator, establishes the land area satisfying accelerator and research area requirements.

In addition to this basic ribbon of land, sufficient additional land was required for several major buildings accommodating light and heavy

laboratories, shops, offices for physicists, engineers, and administrators, an auditorium and cafeteria, and several minor buildings for utility systems. Other land needs included parking for employees and visitors and yards for outdoor storage and assembly of equipment.

After numerous site studies, the decision was made to place the entrance to the project on the north side (connecting to Sand Hill Road) and to provide land on the north side of the accelerator for the support facilities. With this basic land use plan, detailed zoning developed quite naturally with the more public-type buildings for administration and engineering and the auditorium closest to Sand Hill Road. Laboratories for physicists are farther back toward the research area, and the machine shops and electronic laboratories are also farther back but along the north side of the accelerator.

A physics laboratory is by nature dynamic, and provision must be made in the planning for change and growth. For these reasons, the buildings are quite spaciously sited; thus, it will be possible to extend existing buildings and to provide new major buildings in some of the present open spaces.

In 1966, when the existing development was almost completed, an analysis of current building use and anticipated future space needs of the laboratory was made so that growth could proceed in a manner compatible with the established standards of site layout, architecture, and landscaping. This study indicates that the site could accommodate additional buildings, allowing the laboratory population to increase from the current 1200 to approximately 3500 without lowering the quality of the environment.

This study also indicated that the original master plan developed by ABA is still being followed. The current land use plan for the SLAC physical plant is shown in Fig. 5-3.

Space requirements (TEM)

BASIC PLAN. When construction started at SLAC, the laboratory staff program provided for 723 people and these were to be housed in laboratories, offices, and shops with a gross area of 196,800 ft^2, excluding the cafeteria and auditorium and the uninhabited structures such as end stations and accelerator buildings.

As plans for the scope and organization of the laboratory developed, it became evident that the laboratory staff at beam turn-on would be approximately 1100 people and that the extent of the permanent habitable buildings, including those to be constructed in 1967–1968, would be approximately 318,000 ft^2. Table 27-7 summarizes the current building space requirements.

The population density varies considerably with building function. The guide lines for density for offices were established by the AEC general design criteria.[6] These standards allow 200 net ft^2 for each division director, 100–150 ft^2 for each scientist or engineer, 60–75 ft^2 for each secretary, and 75 ft^2 for each draftsman. For office-type occupancy, these standards limit the gross building area per occupant to 200 ft^2 and, with a normal efficiency

Table 27–7 Summary of building space requirements

Building No.	*Facility*	*Gross area (ft^2)*	*Net area (ft^2)*
001	Accelerator housing	154,355	124,355
002	Klystron gallery	361,483	355,913
003	Central control building	13,842	5,925
005	Beam switchyard	50,256	47,256
	Data assembly building	8,000	7,390
	Beam switchyard substation	2,275	2,175
	Research area substation	3,280	3,080
006	Cryogenic laboratory	8,000	6,700
023	Central utility building	3,600	3,534
024	Electronic building	26,500	24,900
025	Fabrication building	32,250	30,950
	Fabrication building substation	475	430
026	Heavy assembly building	34,850	30,856
	Heavy assembly building substation	650	600
027	Shops dining room	1,000	860
035	Craft shops	15,000	13,350
040	Central laboratory	60,275	43,100
	Central laboratory substation	615	565
041	Administration & engineering building	44,023	35,630
042	Cafeteria	3,875	3,450
043	Auditorium	7,550	6,650
044	Test laboratory	41,500	37,900
	Test laboratory substation	3,550	3,120
061	End station A	30,360	28,321
062	End station B	17,000	13,000

ratio of 60 to 70%, this provides approximately 130 ft^2 of net usable space per occupant.

The space requirements for individual laboratories and shops vary with function and equipment and cannot be analyzed on an occupancy basis.

The initial staff was first housed in University buildings on the Stanford campus and moved to the site as beneficial occupancy of the structures was obtained from ABA.

INITIAL SPACE REQUIREMENTS. In the early stages of planning, it became obvious that it was necessary to increase manpower for the design and development effort more rapidly than the construction effort could complete permanent facilities to house this manpower. In order to sustain the major research activities as fully as possible, office, laboratory, and shop space was given construction priority over certain support functions. These support

functions were housed in "temporary" buildings until such time as permanent facilities for crafts shop, receiving and stores, transportation, and salvage function could be completed.

As a first step, temporary quarters were obtained on the Stanford campus proper, where 55,000 ft^2 of shop and warehouse-type buildings were provided by Stanford University to house SLAC during its embryonic period.

The second step consisted of leasing approximately 10,000 ft^2 of office-trailers for approximately 2 yr and purchasing another 8000 ft^2 of light shop buildings to meet SLAC's temporary needs until permanent facilities could be completed. It was planned that these shop buildings would later be moved into the research area as support buildings.

As a third step, a future crafts shop building was hastened to completion at the SLAC site for initial, temporary use by ABA as a construction office building.

TEMPORARY BUILDINGS. At the start of the move into the first completed permanent construction, it was found that it would not be feasible to wait approximately 3 yr until final construction was complete to provide maintenance and repair shops and salvage and transportation facilities. Three temporary buildings of steel frame and metal siding, totaling approximately 20,000 ft^2, were procured for temporary housing of these facilities, subject to later transfer to the research yard area as research support buildings. To date, 17,000 ft^2 of these light shop-type buildings have been moved into the research area and are utilized as planned.

A second problem was to provide adequate engineering, drafting, and physics office space to house the increased staff requirements during the construction period. Such space was provided using relocatable classroom-type buildings as developed for the California Public School System. These were used for this purpose during the peak design period and later became available for use as field offices, control rooms, and field shops in the research area. Approximately 10,000 ft^2 of this type of structure were purchased to fill this need. To date, 6500 ft^2 have been transferred to the research area as planned.

Initial plans for computer support for research anticipated a remote tie-in with the Stanford Computation Center. Between the time of initial planning and approval of SLAC as a project, computer technology and computer service to the University and local industry increased so rapidly that the Stanford Computation Center indicated they would exceed their capacity before SLAC research could be activated. SLAC took steps to order a computer and to add a new Computation Building as a line item for future expansion. Simultaneously, steps were taken to procure 8000 ft^2 of relocatable classroom-type space suitably equipped as a temporary computation facility. It is anticipated that these buildings will be relocated and used as research support buildings when the permanent computation facility becomes available.

Architectural considerations (JWC)

The architectural expression at SLAC is an endeavor to achieve structures appropriate for a laboratory of international stature by using attractive economical materials, and to recall, in color, form, and texture, some of the character of the nearby Stanford main campus.

The architectural detail which unifies the buildings and site includes seven basic elements: exposed structure, fluted metal siding, glass in aluminum sash, sight screens for roof-mounted mechanical equipment, roof overhang, tinted concrete masonry, and, finally, a coordinated color scheme.

Maximum use has been made of consistent details and methods of construction in order to achieve economy and harmony of appearance. In order to maintain scale, the spacing of columns and widths of doors and windows were generally similar everywhere.

The coordinated color scheme is centered around an earthy color for exterior walls, aptly named "homespun brown." This predominating color resembles the tone of the Stanford sandstones and blends well with the seasonal landscape colors. Other colors in the palette include charcoal for handrailings and window panels, a beige tone for spandrels and exposed columns, and a lighter shade for fascia. Sight screens and roof gravel are both rich terra cotta.

The design of the buildings falls into three categories, each incorporating appropriate elements of the architectural concept. First, the Central Laboratory, and Administration and Engineering Building, which house administrative, engineering, and research activities, include textured columns, roof overhangs, and sight screens.

Second, those buildings such as the Heavy Assembly Building, Fabrication Building, Electronics Building, craft shops, and Central Control Building are similar in expression to the first group but lack the textured masonry veneer on columns.

Third, buildings housing general service facilities, such as substations, and the Central Utility Building are without roof overhangs and sight screens.

Exceptions to these rules include the Cryogenic Laboratory which lacks roof overhangs and sight screens at the high bay, the Cafeteria–Auditorium Building and Fire Station which utilize load-bearing concrete masonry walls and exposed wood framing, and the klystron gallery which has no roof overhang or sight screen.

The end stations, because of function and size, do not fit into any of these categories but, because of their importance and mass, deserved special consideration and understanding. Functionally, both buildings required concrete envelopes with a minimum thickness of 2 ft for radiation purposes. Both required extensive wall openings to permit flexibility in placing beam transport structures. The architectural appearance is a direct expression of structural needs and consists of massive corner piers and horizontal beam elements with ribbed panel infilling. Both buildings have parapets vigorously

expressed, and these serve as sight screens for present and future roof-mounted equipment and as protection for maintenance workers. Concrete surfaces are exposed throughout with the granite aggregate heavily exposed on major columns and beam elements and a finer sandblast finish on other exterior surfaces.

Structural design (WPS)

The choice of structural materials and systems was based on occupancy needs, structural requirements, economy, esthetics, and, in some instances, on the provision of flexibility for future modifications.

The materials used are reinforced concrete, reinforced concrete masonry, structural steel, and timber. These materials are often left exposed and become architectural features.

Generally, structural steel frames are used wherever large open spaces are required as in shops and heavy and light laboratories. Framing systems of reinforced concrete are used in office-type buildings where there are no requirements for large spans.

Heavy timber roof framing is used in the cafeteria and shops dining room in conjunction with load-bearing walls of reinforced concrete masonry.

Generally, lateral forces are resisted by exposed reinforced concrete shear walls. The principal exception to this system is the Test Laboratory where the structure is a steel rigid-frame system without shear walls or cross-bracing.

Suspended floors are of concrete, formed with pan joists, ribbed steel decking, and wood formwork.

Roof decks are of either ribbed steel decking or conventional reinforced concrete. Roof decks and suspended floors are used as diaphragms for the transfer of lateral forces to shear walls.

Building foundations are generally spread-type reinforced concrete with grade beams, bearing on undisturbed ground or engineered fills.

Considerable attention was given to the quality of concrete to assure minimum shrinkage by the use of select granite aggregate, water-reducing admixtures, and water curing.

Because of the close proximity of the San Andreas fault, earthquake-induced forces were given serious design consideration. It should be noted, however, that generally wind and not earthquake forces controlled the design of the steel-framed, high bay shop buildings.

Laboratories and office buildings (JWC, DB)

The site plan recognizes the importance of the Central Laboratory as the "headquarters" of the research effort, and places this building and its occupants at the center of gravity of the other principal buildings at SLAC.

Most of the theoretical and experimental physicists have offices and laboratories in the Central Laboratory, and their principal outside areas of interest are the research area, including end stations, associated facilities, and

the computers presently in temporary structures. A permanent computation facility will be erected on a site southeast of the Central Laboratory. The Central Laboratory and research areas have direct cable connections with the computers.

The Cryogenic Laboratory Building contains another important research facility. It is placed in the research area but because of its heavy laboratories and yard requirements, it is located near the end stations rather than near the central campus.

The Administration and Engineering Building, Central Laboratory, and Test Laboratory are physically oriented so as to provide convenient pedestrian communications. Together with the cafeteria and auditorium, these buildings create an informal quadrangle in academic tradition. They have the highest degree of architectural finish and landscaping of all SLAC buildings. The computation facility, when constructed, will conform to this architectural quality.

TEST LABORATORY. The design and construction of the accelerator required considerable development and testing of klystrons and modulators. To enable this work to be expedited, the Test Laboratory was the first building to be designed and constructed at SLAC. As a research facility, the building is sited near the Central Laboratory and incorporates similar architectural features, viz., roof overhang, concrete tile veneer on columns, and a roof sight screen. Figure 27-11 shows a view of the Test Laboratory from the center of the quadrangle. It is flanked on the left by the Central Laboratory and on the right by the Administration and Engineering Building.

As shown in Fig. 27-12, the Test Laboratory plan consists of a high bay wing, 90 ft × 250 ft × 30 ft high, and a two-story wing, 75 ft × 125 ft × 27 ft high, connected by a one-story link 25 ft × 50 ft. One longitudinal bay of the

Figure 27-11 Test laboratory—view from central quadrangle.

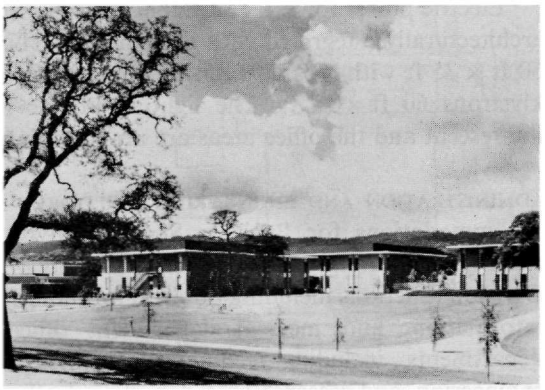

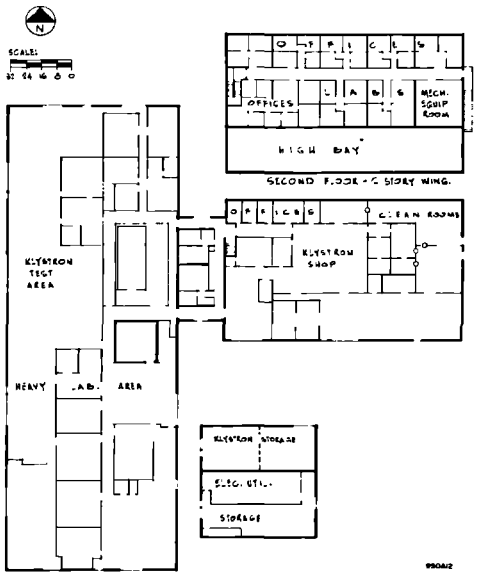

Figure 27-12 Floor plan of test laboratory.

two-story wing, 25 ft × 125 ft, reaches the full height of the building and is equipped with a 3-ton overhead crane. This area has been used as a machine and assembly shop for klystrons. The remainder of this wing is occupied by offices and light laboratories.

The main high bay wing is provided with two 10-ton overhead traveling cranes. During development and construction of the accelerator, this area was principally used for klystron and modulator development and testing. During the operational phase, some of this space has been assigned to accelerator physics, electronics, and research activities, but the development, testing, and maintenance of klystrons continues to occupy a large part of the building.

Electric power for the Test Laboratory is provided from a substation area architecturally integrated with the building. This wing includes a utility area 60 ft × 35 ft with a cable vault of similar dimensions and a storage area for klystrons 60 ft × 25 ft. The lighting in the Test Laboratory is generally fluorescent and the office areas are air-conditioned.

ADMINISTRATION AND ENGINEERING BUILDING. This building provides office accommodations for Business Services Division functions including purchasing, accounting, plant, budget, and safety offices; Administrative Services Division functions including public information, personnel, reports, technical information, and medical department offices; and Technical Division departments, including technical planning, plant engineering, mechanical engineering, and research area department offices.

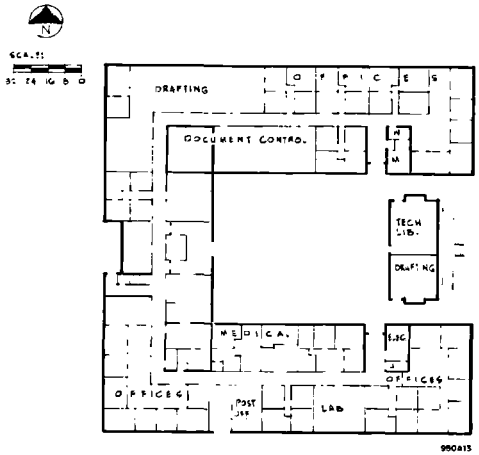

Figure 27-13 First-floor plan of administration and engineering building.

Figures 27-13 and 27-14 are floor plans of this building. The building is in the form of a hollow square with an interior court 70 ft × 70 ft and external dimensions 175 ft × 175 ft. There are two stories, both with direct access to ground level. The reception area for visitors is at the upper level, but the entrance towards the quadrangle, cafeteria, auditorium, and Central Laboratory is at the lower level, supplemented by a portico having an exposed double staircase ascending to the upper level. This staircase and view of the building as seen from the center of the quadrangle is shown in Fig. 27-15.

Figure 27-14 Second-floor plan of administration and engineering building.

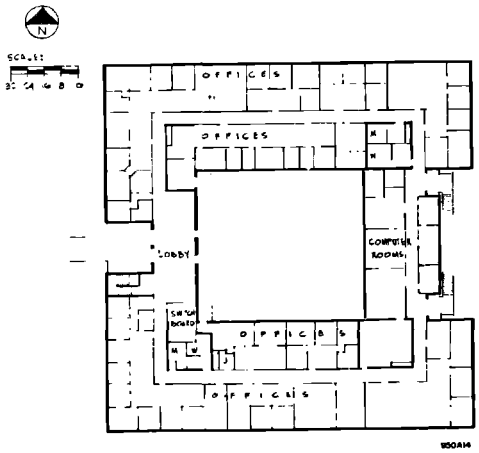

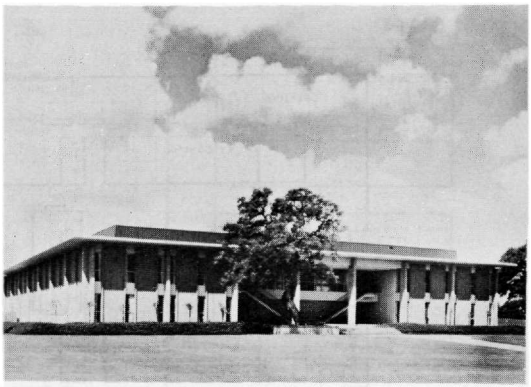

Figure 27-15 Administration and engineering building.

The structure is a reinforced concrete frame with precast concrete tile veneer on exterior columns, wall panels of insulated ribbed metal siding and aluminum windows. Lateral forces are resisted by reinforced concrete, shear walls at toilets and stair wells. The roof and wall slabs are of reinforced concrete and the roof overhangs the walls approximately 4 ft. Interior wall surfaces and partitions are of gypsum wallboard with glazed areas to permit light to enter interior offices.

The lighting and air-conditioning system is integrated with a modular suspended T-bar and glass fiber ceiling, permitting relocation of office partitions. This arrangement has presented many acoustic problems due to noise transfer between offices. In later buildings, particularly the Central Laboratory, some improvement has been accomplished by using ceiling board of higher density.

AUDITORIUM AND CAFETERIA. In early studies of the site planning, these two buildings were separately located on the north and east sides, respectively, of the central quadrangle. They were subsequently combined to provide an integrated center for seminars, to leave the north side of the quadrangle open for a possible future major building, and to commit this desirable site to a use other than offices or laboratories. The site is an oak-covered knoll with a view of the central campus, glimpses of the research area, and commanding views of the surrounding countryside. Figure 27-16 shows a view of this building across the quadrangle from the steps of the Administration and Engineering Building.

The program included an auditorium with 300 seats, lobby, toilets, control room for audio–visual equipment, dining room, kitchen, and "scramble"-type self-service cafeteria area. As shown in Fig. 27-17, the two functions, auditorium and cafeteria, are joined by a partially enclosed lobby used

Figure 27-16 Auditorium and cafeteria.

for occasional assemblies and exhibitions. An area east of the building has informal paving and is used for outdoor eating when weather permits.

The buildings are constructed with reinforced concrete foundations, load-bearing concrete masonry walls, steel roof girders over the auditorium, glued laminated wood girders elsewhere, 3-in. × 6-in. tongue and groove wood

Figure 27-17 Floor plan of auditorium and cafeteria.

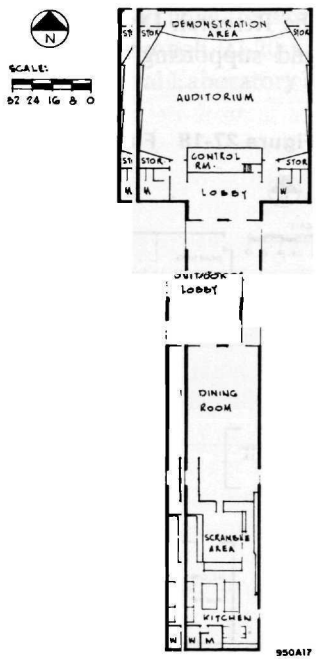

decking throughout with suspended ceiling in the auditorium and toilets and exposed wood decking elesewhere. Windows and exterior doors are of aluminum. Lighting in the cafeteria is fluorescent. In the auditorium, fluorescent tubes in 4-ft diameter flush-mounted ceiling fixtures provide lighting for lectures and seminars. Supplemental incandescent lighting is provided for blackboards and aisles.

Considerable attention has been given to auditorium seating arrangements to ensure good sight lines, comfort, and ease of access. The floor is stepped with ten risers, the lower five, 10½ in., and the upper five, 15 in. The seat platforms are 3 ft, 8 in. wide. A continuous table 2 ft, 5 in. high on pipe legs is placed along the front edge of the platforms. The seats pivot on pipe supports and also have a few inches slide action. Fabric upholstery is used over polyurethane foam on a moulded glass fiber shell. The continuous table is provided with 24-V lamps for note-taking at each seat position and these are individually switched. The table surface is white linoleum. The auditorium is equipped with double-hung blackboards providing 320 ft^2 of visible surface, and a motor-operated projection screen. The acoustics of the auditorium provide good audibility of a normal human voice with reinforcement.

The cafeteria service is operated by a private subcontractor, using kitchen equipment provided by SLAC. The dining room has an area of 1900 ft^2, a scramble area of 550 ft^2, and kitchen area including storage and dishwashing of 1000 ft^2.

CENTRAL LABORATORY. The Central Laboratory serves as headquarters for the Research Division and includes the director's office, offices for physicists and supporting engineers and clerical staff, the main SLAC library, light

Figure 27-18 First-floor plan of central laboratory.

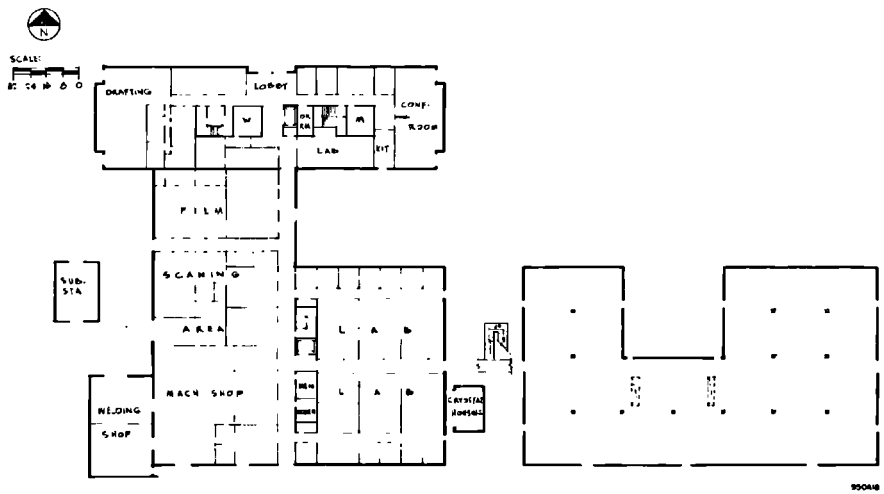

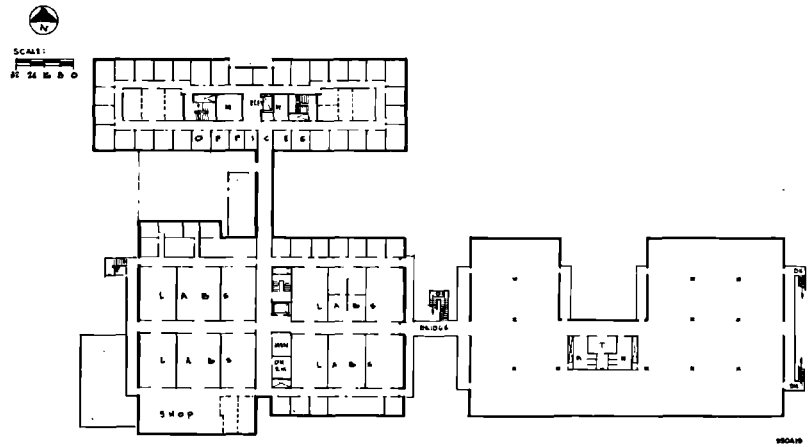

Figure 27-19 Second-floor plan of central laboratory.

laboratories, and machine shops. Offices and the library are placed in a three-story office-type structure, 49 ft × 171 ft × 38 ft high. Laboratories, related offices, and machine shops occupy a two-story wing, 96 ft × 143 ft × 25 ft high. The two wings are linked by a one-story area 48 ft × 70 ft, on the roof of which is an enclosed corridor joining the second floors.

A two-story addition, 96 ft × 175 ft, scheduled for completion in late 1968, will be constructed adjacent to the existing two-story wing. The addition will have a small basement area for storage but otherwise will have the same heights as the existing two-story portion. Figures 27-18 through 27-20 are floor plans of the above described areas. A view of the Central Laboratory as

Figure 27-20 Third-floor plan of central laboratory.

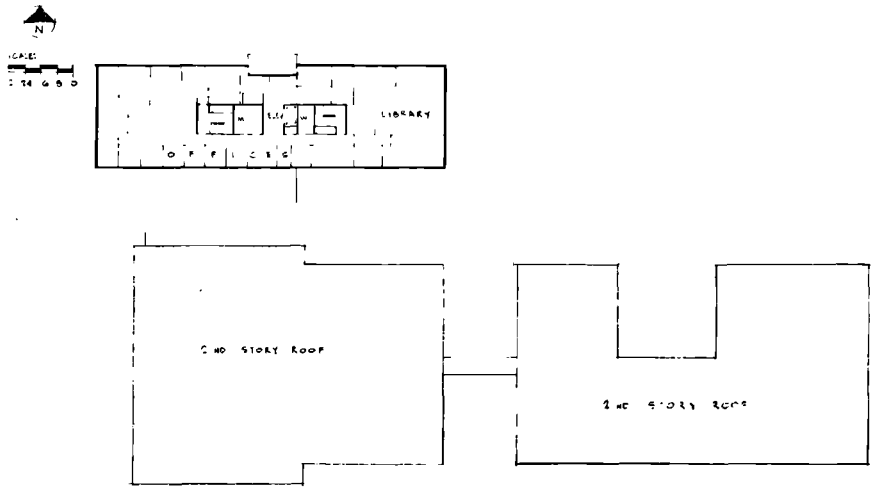

Figure 27-21 Central laboratory.

seen from the cafeteria with the Test Laboratory in the right background is shown in Fig. 27-21.

The addition mentioned above will be constructed with reinforced concrete framing and two-way ribbed slabs. Lateral forces are carried by the perimeter concrete walls formed to match the ribbed metal siding of the existing building. This structural system has been selected to provide maximum flexibility in placing interior partitions.

Services in the addition have been designed for ease of alteration and maximum flexibility. The mechanical ventilation system will provide heating and some cooling, and individual fan coil units in the offices and laboratories will provide the supplemental cooling. The fluorescent lighting fixtures will be chain-supported, plugged in a bus duct, and switched by pull cords. Similarly, laboratory equipment will be plugged into separate overhead bus ducts.

TEMPORARY COMPUTER FACILITY. The temporary computer facility serves as the computation center for the project and houses staff offices plus computers, key punches, electronic scanning equipment, service and dispatch areas. The facility is situated south of the Central Laboratory and adjacent to the planned site for the permanent computation facility.

The principal building in the facility houses the computer. It consists of sixteen prefabricated classroom-type units placed on elevated concrete perimeter footings with one permanent partition down the middle formed by the ends of the units. The building units are 10 ft, 3 in. × 32 ft each, and the complex is 82 ft × 64 ft and contains 5248 gross ft^2. The elevated footings permit underfloor access required for power distribution to the computer equipment. This Computer Building, as well as the surrounding staff offices of similar construction, are shown in plan on Fig. 27-22.

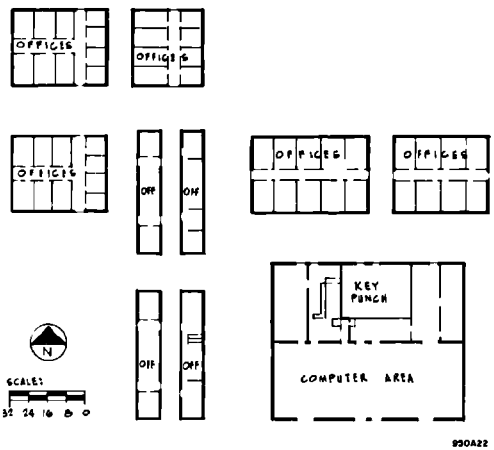

Figure 27-22 Floor plans of temporary computer facility building.

The prefabricated units have a structural steel frame augmented with wood roof joists and sidewall studding. Exterior end walls are steel framed, accommodating windows and doors. The roofing consists of metal sheathing. Floor joists of steel support a plywood floor covered with vinyl asbestos floor tile. The suspended ceiling houses recessed light fixtures and air-conditioning ducts. The $1\frac{1}{2}$-in. thick, glass fiber, ceiling panels serve as roof insulation.

Air conditioning is accomplished by roof-mounted heat pumps. In the case of the Computer Building, heat pumps air-condition the north half of the building, but the south half, containing the largest heat load, is serviced by a 45-ton air-cooled refrigerant compressor alongside the building. This unit supplies refrigerant to direct expansion coils in two roof-mounted fan-coil units. The system is automatically controlled to maintain desired temperature and humidity settings.

Power for the computer equipment is supplied by two special shielded transformers of 90 kVA each, located on pads outside the building. Conventional power requirements are serviced by a separate distribution system.

A raised computer-type floor has been installed in the south half of the Computer Building. This floor consists of 2 ft square removable metal panels supported by adjustable jacks. It provides space for interconnecting computer cabling.

CRYOGENIC LABORATORY. The research programs at SLAC include many facilities for low-temperature development work on accelerators, magnets, bubble chambers, and other devices. This work is performed in this heavy laboratory-type building. For functional reasons, the site is related to the research area. Because of the elevation of the site and the required building height for crane purposes, this building posed architectural problems and

Figure 27-23 Cryogenic laboratory.

these were increased by the need to provide a pitched roof and roof fans for hydrogen exhaust. The solution provides a high bay roof with a one-in-ten slope, without roof overhang, thereby reducing the building profile, and a low bay area containing laboratories with typical roof overhang and sight screen around roof-mounted mechanical equipment. Figure 27-23 shows these architectural considerations.

The high bay area is 41 ft × 60 ft with an eave height of 32 ft, 6 in., and is equipped with a 20-ton overhead traveling crane, with hook height of 25 ft. The high bay is separated from the remainder of the building by a 12-in. thick reinforced concrete wall and a 7-ft wide service corridor. A floor plan of the structure is shown in Fig. 27-24. The structure of the building is of steel, with columns and spandrels exposed as architectural elements. The

Figure 27-24 Floor plan of cryogenic laboratory.

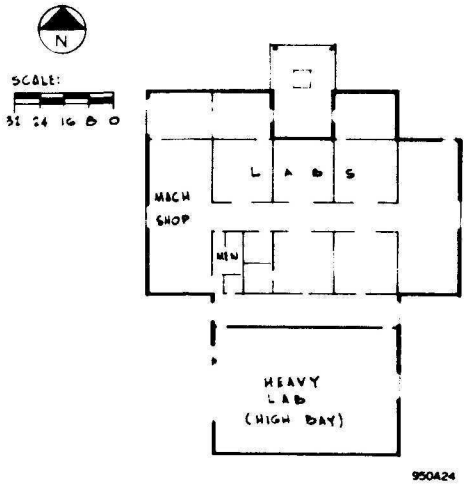

walls are of ribbed metal siding in the high bay, and gypsum wallboard on wood studs elsewhere. All walls are insulated with exposed, rigid, Styrofoam material in the high bay and insulation between wood studs. The metal siding at the high bay is attached to the structure with permanent fastenings on one entire edge for hinge action, and elsewhere with explosion-vent fasteners for immediate pressure release. Floor slabs are concrete.

As an additional safety measure, membrane roofing of polyisobutylene is used instead of a flammable type. The roof insulation applied over the steel decking is of asbestos fiber type. The finish color of the roof is terra cotta to match the other buildings.

Lighting throughout the building is fluorescent. Heating and ventilating are provided by roof-mounted equipment utilizing hot water from the central system.

Shops and support buildings (JWC)

The shops, together with the General Services Building, are situated in a strip of land approximately 400 ft × 1700 ft, immediately north of the klystron gallery. Figure 27-25 shows a photograph of the shops complex. The buildings are surrounded by paved yards of asphalt concrete with minimum widths of 50 ft. The yards are used for material storage, assembly, parking for service vehicles, and sites for temporary relocatable buildings. By the use of mounds of earth, grade changes, and dense landscaping, a considerable degree of screening has been achieved.

The architectural expression used for the shops includes exposed structural steel frames, ribbed metal siding, roof overhangs, aluminum sash, and metal sight screens around roof-mounted mechanical equipment.

The interior face of the ribbed metal siding is covered by an 8-ft high wainscot of hardboard. This provides a clean working surface, protection against mechanical damage, and a measure of thermal insulation at work level.

Figure 27-25 Shops complex.

Lighting in the shops is by fluorescent fixtures, generally mounted just below the roof to provide maximum head room for traveling cranes. In some areas, such as the Electronics Building, lights are mounted at approximately 10 ft above the floor together with plug-in bus ducts for assembly testing and calibration of electronic devices. Heating and ventilation of the shops is by hot water unit heaters using hot water piped from the Central Utility Building. Services including compressed air, low conductivity water, cooling tower water, and domestic water from central sources are distributed in the buildings according to specific needs.

HEAVY ASSEMBLY BUILDING. This building houses machine shop, welding, and assembly functions of greater capacity than the other shop buildings. The effort in this building is principally in direct support of the experimental physics program.

During construction of the accelerator, approximately one-third of the building was used for magnet assembly, alignment, and testing. This work took place in the east bay of this facility and required the use of a temperature-controlled room with an area of about 1500 ft^2 and power supplies and test manifolds, all served by a 20-ton overhead electric crane. The remainder of the building is occupied by heavy machine tools served by a second 20-ton crane and a precision erection floor, served by a 50-ton bridge crane with two 25-ton trolleys with hook heights of 32 ft.

Figure 27-26 Floor plan of heavy assembly building.

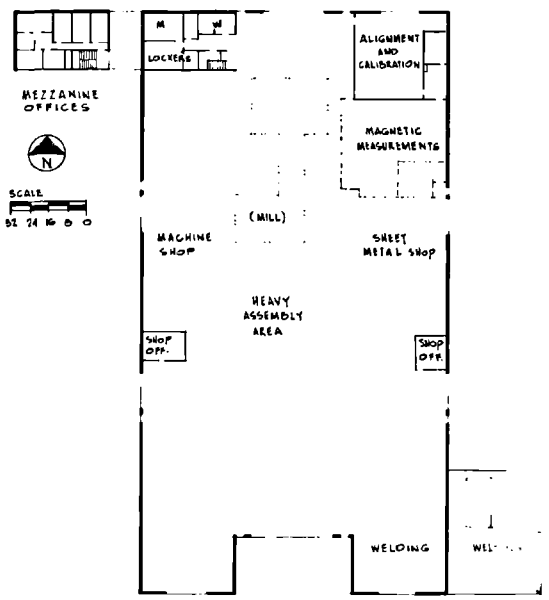

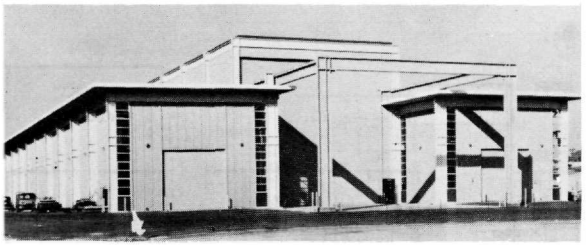

Figure 27-27 Heavy assembly building.

The building consists of a center bay 50 ft × 225 ft and two side bays each 40 ft × 250 ft (see Fig. 27-26). The crane supports in the center bay are extended 50 ft through a large 40-ft × 40-ft rollup door to the exterior to handle large loads, as shown on Fig. 27-27. The gross area of the building is 34,850 ft^2 including 1000-ft^2 office mezzanine and 1000 ft^2 for toilet and locker facilities. The clear interior height of the center bay is 43 ft and 25 ft, 3 in., in the side bays.

The heavy-duty floor is of reinforced concrete, 9 in. thick, over 6-in. thick aggregate base and was designed to provide for uniform floor loading of 5000 lb/ft^2 on a 5-ft square crib. The major machine tools are placed on massive concrete bases isolated from the structure by means of cork insulation.

The building is provided with electric power from a detached substation building. Heating and ventilation are by means of hot water unit heaters and low-profile gravity roof ventilators augmented by operable sash. Welding and other shop gases are piped to the building from a gas storage facility in the building yard.

FABRICATION BUILDING. The Fabrication Building accommodates a medium machine shop, horizontal and vertical brazing furnaces, assembly space, metal-cleaning and plating facilities, and installations for testing and tuning waveguides. All the components of the accelerator proper were manufactured, tested, and/or assembled in this building. Basic materials and components, such as high-purity copper stock, extruded aluminum support girders, vacuum pipes, and cooling-water pipes were processed, machined, and assembled, finally emerging as a 40-ft long accelerator segment ready for installation.

The main building (see Figs. 27-28 and 27-29) consists of three bays, each 40 and 120 ft with a clear height of 22 ft, 6 in. There are four minor external additions—the furnace building, cleaning building, and saw shop. The cleaning building is 42 ft × 75 ft × 12 ft high and accommodates tanks for metal cleaning. This area, together with an area 40 ft × 60 ft in the Fabrication Building, provides an integrated metal-cleaning and plating activity. The furnace building is 20 ft × 20 ft × 20 ft high, over a pit 18 ft deep. It

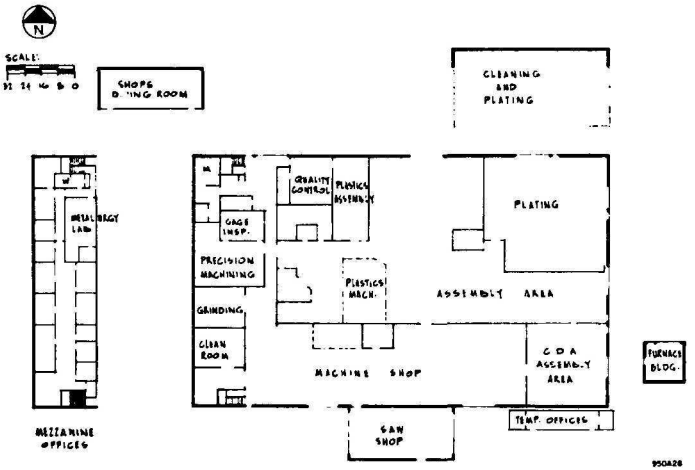

Figure 27-28 Floor plan of fabrication building.

houses an electric pit furnace which was used for brazing subassemblies of the accelerator. The saw shop, 20 ft × 50 ft × 12 ft high, houses saws for cutting metal stock. The Fabrication Building is equipped with two 5-ton electric overhead traveling cranes.

During construction of the accelerator, large quantities of hydrogen were used as fuel for brazing. Other gases, such as oxygen and nitrogen, were used in large quantities for welding and inert environments. To support these activities, an outdoor gas storage area was provided with underground piping to the Fabrication Building for distribution.

ELECTRONICS BUILDING. The Electronics Building has the same overall dimensions and structural form as the Fabrication Building. In the original SLAC space layout, one-half of this building was to be devoted to stores, and it was known as the Electronics and Stores Building. However, as the

Figure 27-29 Fabrication and electronics buildings.

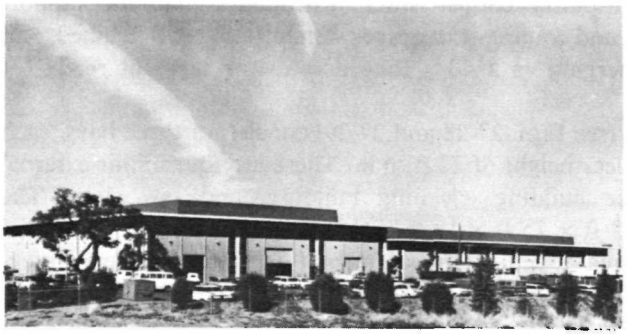

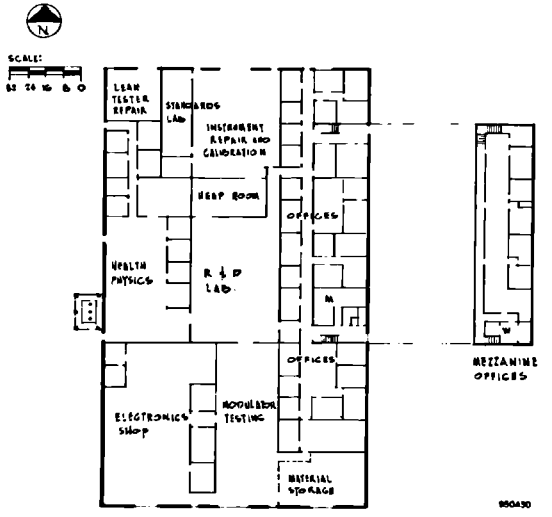

Figure 27-30 Floor plan of electronics building.

space requirements of electronics became larger, general stores were moved on an interim basis to a temporary metal building. Most of the Electronics Building was occupied by electronics and health physics personnel, including physicists, engineers, and technicians. Figure 27-29 shows a photograph of this building and the Fabrication Building, and Fig. 27-30 shows the floor plan to accommodate these activities.

SHOPS DINING ROOM. This small building provides lunch room facilities in a landscaped court between the electronics and fabrication buildings. To provide a change of environment from the working areas, the lunch room is constructed of concrete masonry and heavy timber, similar to the cafeteria.

The dimensions of the shops dining room are 20 ft × 50 ft × 11 ft high, with a covered terrace 14 ft × 43 ft for outdoor eating. The room is equipped with tables and chairs and several vending machines.

CRAFTS SHOP. This building occupied by crafts shop is 100 ft × 150 ft × 13 ft high (see Fig. 27-31). During construction of the accelerator, this building was occupied by ABA, the architect–engineer–manager for construction of the conventional facilities, and it was called the Construction Office Building. Initially, the 1961 SLAC space plan indicated that a portion of the machine shop area in the Fabrication Building would be available for crafts after completion of the accelerator; however, the machine shop and assembly requirements of the research program have shown that all the existing shops are required for future programs. Consequently, the former Construction Office Building was converted to shops for carpenters, electricians, plumbers, painters, vacuum equipment maintenance, and for the associated office staff.

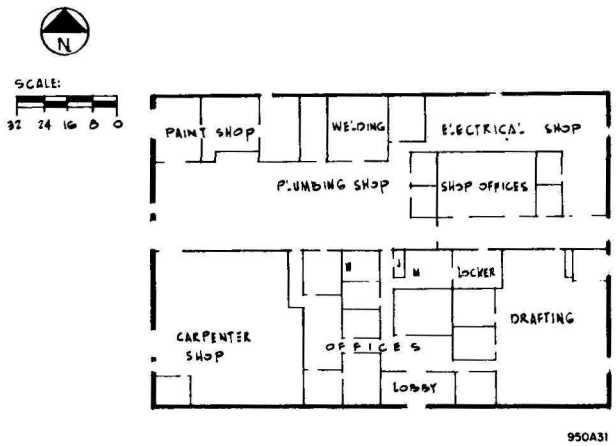

Figure 27-31 Floor plan of crafts shop building.

In land use planning, this building is ideally situated as a part of a support complex including the crafts shop sandblasting facility, the General Services Building, and a common storage yard. Its conformance to standard SLAC architectural expression can be noted (see Fig. 27-32).

GENERAL SERVICES BUILDING. This building is due to be completed in the latter half of 1968 and will provide accommodation for central stores, shipping and receiving, property control, salvage, vehicle maintenance, transportation, labor crew, gardeners, and tool storage. The site is adjacent to the crafts shop, which allows joint use of service yards and construction material storage facilities. The General Services Building, however, has the distinction of being the only Stanford University structure adjacent to a state freeway and for this reason, considerable care was necessary in its planning and design.

Figure 27-32 Crafts shop building.

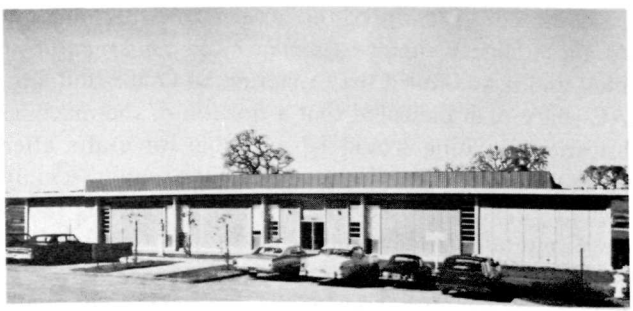

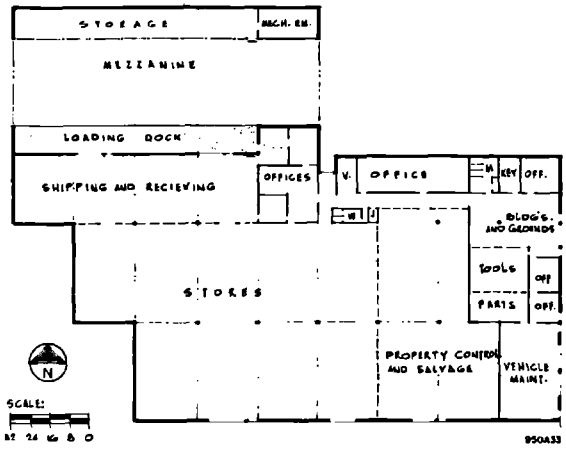

Figure 27-33 Floor plan of general services building.

The building plan (see Fig. 27-33) includes 24,000 ft^2 of fully enclosed building 24 ft high, 7000 ft^2 of covered but not fully enclosed sheds, and 41,000 ft^2 of fenced yard for outdoor storage. To accommodate the building program and to present a satisfactory exterior, the storage sheds and main building create a screen around the storage yards. Earth mounding and landscaping with fast-growing pines and eucalyptus supplement the screening.

Architectural details include exposed structural steel framing, ribbed metal siding, roof overhang, operable aluminum sash, and a sight screen at the roof to screen present and future roof-mounted equipment. The roofmg is of builtup asphalt and gravel over an insulated ribbed steel deck. The columns and spread footings are designed to support future mezzanine loads. Interior partitions are made of wood stud and gypsum wallboard for offices and fire separations. Storage areas are defined by chain link-type fences. The loading dock is equipped with load levelers and scale, and ramps are provided for use of fork lift trucks.

The vehicle maintenance area will be principally used for servicing fork lift trucks and other special vehicles, and is provided with a fuel pump, 10,000-gal underground gasoline tank, service pit, steam cleaning, compressed air, lubrication, and battery-charging facilities. Accommodation in the sheds includes a masonry block building for storage of volatile solvents, a fenced concrete slab at yard elevation for hazardous chemicals, with sump for accidental spillage, and a raised, fenced, concrete dock for storage of gas bottles. Lighting is fluorescent throughout and heating is by gas-fired unit heaters in high bay areas and by gas-fired multizone units for offices.

CENTRAL UTILITY BUILDING. This building, located in the Test Laboratory yard, is the heart of the utility complex serving the buildings of the campus

area (Test Laboratory, cafeteria–auditorium, Administration and Engineering Building, Central Laboratory, Central Control Building, computation facility, and Cryogenic Laboratory). It houses two water chillers and pumps, two hot water generators and pumps, two air compressors, and space for an extra unit of each of these.

It is a steel-framed, steel-sided building conforming with the standard SLAC architectural detail. It is 60 ft × 60 ft in plan, 16 ft high, and divided in half by a concrete block wall to form two rooms. One room is for the hot water generators and the other for mechanical equipment. The latter room is further partitioned to form an 8-ft × 12-ft shop and an 11-ft × 12-ft office. Access to the hot water generator room is through a 12-ft wide door, 8 ft high. A 7-ft × 8-ft door serves the machinery room. This building has a gravity ventilation system with two $7\frac{1}{2}$-ft × $9\frac{1}{2}$-ft roof vents and louver panels in the east and west walls.

ELECTRICAL SUBSTATION BUILDINGS. The major power substations of the project are all housed in covered steel buildings with the exception of the master substation which is enclosed in an open fenced area, but with its switchgear housed in a steel building. Buildings are provided for the Test Laboratory, beam switchyard, and research area substations, plus the master substation switch-house. They function as shelters for foul weather protection, maintenance, and architectural sight screens. To some extent, they permit somewhat lower equipment costs. All are gravity-ventilated (roof vents and wall louvers) and conform to standard SLAC architectural detail.

The buildings house forced air cooled, dry-type transformers, secondary switchgear, and related equipment as follows:

Test Laboratory—two 2667-kVA substations
Beam switchyard—two 2000-kVA substations; two 1333-kVA substations
Research area—four 3333-kVA substations and one 5000/6666-kVA substation plus 12-kV switchgear
Master switch-house—instrumentation power transformer only, plus sixteen 12-kV breakers and metering equipment.

The Test Laboratory substation is located adjacent to that building. It is a two-story building, 34 ft × 60 ft in plan. The lower floor is a concrete underground structure, $9\frac{1}{2}$ ft high, functioning as a cable vault for the underground duct banks entering it. The upper floor is a conventional SLAC steel building with a height to tops of roof beams of 12 ft, 8 in., to 13 ft. Its floor is a 9-in. reinforced concrete slab. Its equipment door is 8 ft wide by 10 ft high.

The beam switchyard substation is a single-story steel building, located near the beam switchyard's Data Assembly Building. Its interior height is 14 ft, and equipment doors are 8 ft × 9 ft.

The Research Area Substation Building is similar in construction and of equal height, but is 83 ft, 4 in. × 38 ft, 6 in. in plan. It is distinctive in being perched at the top of 40-ft high retaining walls, overlooking the research area yard. It was desired to have it somewhat centrally located with respect to research loads without having it located within the yard itself, where it would form a restriction to research activity. Cables enter and exit via a 9-ft × 9-ft pit in the floor, 8ft deep. The major research loads reach the yard through a 10-ft × 3-ft niche in the retaining wall face. Doors 8 ft × 8 ft, at either end, allow movement of equipment.

The master substation switch-house is a two-storied structure situated south of the klystron gallery and in its fill bank, with the lower floor having access to the substation yard and the upper floor opening onto the gallery level. The building is 30 ft × 50 ft with heights of 13 ft for the lower cable gallery and 15 ft for the upper switchgear room.

FIRE STATION. The fire-fighting services at SLAC are provided by the Stanford Fire Department. The SLAC Fire Station is a substation of the Stanford Fire Department.

The site is central with the final selection based on ease of access to possible disaster areas. The building program (see Fig. 27-34) required an apparatus room to house two vehicles, a 500-gal/min pumper and a 1000 gal/min triple combination pumper. It also provided living accommodations for a shift of one officer and three firemen, and a utility room for minor repairs, hose racks, and dryer. The gross building area is 2600 ft^2, and its construction has reinforced concrete spread footings, grouted exposed concrete masonry walls, laminated wood roof girders, a plywood deck, builtup roofing, wood stud and gypsum wallboard partitions, operable aluminum sash. The apparatus room doors are of translucent fiberglass and are electrically operated. Heating is by hot water unit heaters in the apparatus room and by baseboard convectors elsewhere.

The Fire Station communication systems include radio, telephone, and fire alarm. Fire alarm boxes are placed at convenient locations throughout the site. Alarms originating at SLAC are received at the main Stanford

Figure 27-34 Floor plan of fire station.

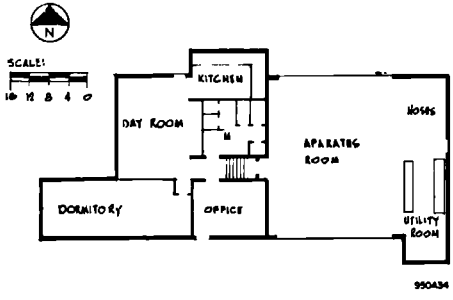

University Station and equipment at SLAC is dispatched by instruction from this station.

Fire protection at SLAC includes the services of the Stanford Fire Department, fire hydrants connected to the domestic water system, automatic wet sprinkler systems in most buildings, rate of rise heat detectors in others, and portable CO_2 extinguishers distributed throughout the buildings, all in accordance with the AEC design criteria, Uniform Building Code (Fire Zone III), and other recognized standards, such as those of the National Board of Fire Underwriters. The last-mentioned is used as a guide only because SLAC buildings are self-insured by the AEC.

The water mains used for fire protection include a 12-in. loop around the Administration and Engineering Building and Test Laboratory, a 10-in. loop along the accelerator between Sectors 7 and 30, and 8-in. loops serving the Central Laboratory, research area, Cryogenic Laboratory, and shops complex. Sectors 1 through 6 are served by a single 6-in. water main. Automatic fire sprinklers are installed in all required areas, except where their use in conjunction with electrical installations would actually increase the hazard. In these cases, rate of rise detectors are used.

Accelerator buildings (JA, RSG, FFH, CRJ)

The housing of the accelerator consists of five principal structures plus a small structure housing the alignment system laser.

1. *The accelerator housing*—a concrete tunnel of rectangular cross section, 2 miles long, enclosing the accelerator tube and its support and alignment pipe. It is situated in an earth fill directly below the klystron gallery with its ceiling 25 ft below the gallery floor.
2. *The klystron gallery*—a steel building, probably the world's longest, which houses the accelerator's klystrons, modulators, and all other associated components.
3. *The central control building*—from which the 10,000-ft accelerator is operated.
4. *The beam switchyard housing*—a large, concrete structure of complex shape under 32 ft of earth and concrete.
5. *The data assembly building*—from which the beam switchyard equipment is operated.
6. *The laser room*—a small steel underground capsule located at the level of the accelerator housing and at the east end of the accelerator.

The accelerator tube and the alignment pipe are supported by the floor of the accelerator housing. The stability of this structure is an important factor in the operation of the machine. Soil mechanics, geology, hydrology, and careful control of concrete construction were key design considerations in securing this stability.

The klystron gallery houses the electrical and electronic components supplying energy to the machine as well as vacuum, cooling, and control systems necessary to its function. Connections to the accelerator are made through vertical 27-in. diameter steel pipe service shafts located at approximately 20-ft intervals over the length of the accelerator. There are also vertical manway shafts between the two structures, located near the end of each of the thirty sectors.

The Central Control Building is located adjacent to Sector 27, one-tenth of the accelerator's length from its junction with the beam switchyard. This point was selected as an optimum point for economy of control cable lengths for the overall length of the machine from main injector to end stations.

The beam switchyard housing forms a system of large concrete ducts for the several beam runs into the research area. It houses the components controlling these research beams. Steering and collimation of these beams result in energy losses from the beams causing radiation and heat transfer problems which, in turn, complicated the design of the structure.

The functions of the beam switchyard are controlled from the Data Assembly Building which also houses the magnet power supplies. It receives signals from the equipment in the beam switchyard and the end station buildings which enable operators to provide beams refined to specifications necessary for the research experiments in progress. The Data Assembly Building also receives from and transmits to the Central Control Room appropriate control and status signals necessary for beam control and coordination. These facilities are described more fully in the following pages.

ACCELERATOR HOUSING. The functions of the accelerator housing are to provide a stable support for the accelerator, a corrosion-inhibiting environment, and, together with the superimposed earth-fill, adequate radiation shielding.

The basic criteria for the accelerator housing suggested a box culvert-type section with internal height of 10 ft and width of 11 ft. The required accuracy of alignment was to be within $\frac{1}{4}$ in. of a straight line for the entire length of the accelerator.

The environmental radiation standards adopted by SLAC required that the housing be covered by 23 ft of earth. Because of the rolling terrain of the accelerator alignment, a cut and fill technique was selected. Because of existing contours and geology, this meant that in some places cuts of up to 80 ft and compacted fills of up to 30 ft of height were necessary to obtain the correct elevation for the housing foundation. A study of the excavation and fill requirements for the entire SLAC building program, including shielding beams at the research area, indicated that economies would be possible if the accelerator housing were constructed with a 0.5% decline from west to east. The klystron gallery follows the same slope, with the structure perpendicular to the incline.

During the planning phase of the accelerator, other public agencies proposed major construction projects in the area which would affect construction at SLAC. First, construction of the Junipero Serra Freeway (Interstate Route 280) included a bridge crossing over the accelerator in the vicinity of Sectors 25 to 26. With the cooperation of the State of California Division of Highways, this bridge was completed in advance of the road construction and before completion of the accelerator.

The bridge foundations used pile-supported footings spaced sufficiently far from the accelerator housing to avoid appreciable influence on earth pressures against the housing. Vibration studies made on a similar bridge in the Bay Area indicated that traffic vibrations would not affect accelerator operation.

Second, the Corps of Engineers has proposed a 100-ft high dam on San Francisquito Creek for flood control. If the dam is constructed, its reservoir area would extend to the accelerator earthwork between Sectors 11 and 21, with a possible water elevation of 287 ft adjacent to a minimum accelerator housing floor elevation of 265 ft. It was estimated that maximum flood levels would be of short duration and that the normal water level would be below that of the housing floor. Studies of local geology and soil mechanics indicated that the stability of the housing and earthwork would not be adversely affected by the construction of this flood control dam, although if it is constructed in the future, the accelerator earthwork would probably have to be protected by rip-rapping the slopes.

The accelerator housing is alternately on cut and fill, with cut areas predominating. In areas of cut, the bedrock foundation materials provided fair-to-excellent conditions for minimum settlement. In the fill areas, however, softer soil layers were overexcavated and replaced with compacted fills of sandy materials. Special treatment in the area of Sectors 18 and 19 in particular was necessary because predicted settlements would have been excessive on account of the depth of the alluvium and open fractured claystone and the required depth of fill. To reduce settlement substantially in this area, the unsatisfactory materials were removed, and prior to construction of the housing, replaced with suitable compacted fill. A surcharged condition was then created, by placing compacted fill to the elevation of the top of the accelerator housing and uncompacted fill to a level 10 ft above the klystron gallery floor level. The surcharge remained in place for approximately 6 months to accelerate consolidation of the fill and underlying earth and rock. Similar but less extensive procedures were used in other problem areas.

The typical box section of the housing has 18-in. thick sidewalls, 24-in. roof slab, and 27-in. floor slab. The section is designed for earth loads without hydrostatic pressure because drains are provided at both sides to suppress the water table. The outfalls for this drain system are located so that the effluent can be monitored for radioactivity.

The exterior surfaces of the walls and roof are covered with a 10-mil polyvinyl membrane protected from mechanical damage by $\frac{1}{2}$-in. fiberboard.

The specifications for concrete for the housing were developed to obtain minimum cracking by reducing drying shrinkage and thermal shocks to a practical minimum. Specifications required modified Type II cement with tricalcium aluminate content limited to 6%, tricalcium silicate content between 42% and 50%, and a 28-day mortar strength test of 4500 lb/in^2. A low shrinkage aggregate, crushed granite rock from the Watsonville area, was used. The additional cost for aggregate was approximately balanced by savings in cement quantities.

Concrete temperature at the time of placement was limited to 60°F. During the summer months, this requirement involved addition of ice to the mix. Also, during the summer months, concrete was placed only in the late afternoon and at night time. All concrete was fog spray cured until just before backfilling.

Construction joints are spaced at 80- to 90-ft intervals and these, together with the few minor cracks that developed, were injected with epoxy. In order to provide a dust-free interior and to facilitate cleaning, the interior surfaces are epoxy-sealed.

To provide a conduit for accelerator waveguides, piping for vacuum, and cooling between housing and klystron gallery, 27-in. diameter steel service shafts occur at approximately 20-ft centers. These were placed in oversized holes bored in the shielding fill and welded to a sleeve cast integrally with the roof slab. The bored hole was then backfilled with granular material.

At each sector, a personnel accessway is provided in the form of a vertical steel shaft, 39 in. in diameter, containing a ladder. At less frequent intervals, a material access shaft with internal dimensions of 6 ft × 12 ft is provided. It terminates ouside the klystron gallery.

The accelerator housing is similar throughout its length except at the west end injector, at the access structures at Sectors 10 and 20, and at the east end alignment station. At the west end, the housing is terminated by an exposed portal at ground level.

Figure 27-35 shows the accelerator housing under construction at Sector 20, the two-thirds beam takeoff point. The vertical structure in the center rear of the photograph is a material accessway located at Sector 19.

Because of the radiation level, there can be no personnel in the housing during accelerator operation. Furthermore, the contained air becomes contaminated with short-lived radioactivity. Following shutdown and radiation decay, air is exhaused by fans at alternate personnel accessways. The remaining accessways serve as filtered air inlets.

At Sector 11, additional radiation shielding was required at the positron radiator. This was accomplished by placing a 7-ft thickness of salvaged naval armor plate directly over the housing in the earth fill. In the same area, boron frit (calcium borate) was added to the concrete to reduce the residual radiation in the concrete adjacent to the positron source.

Channel inserts were imbedded in the ceiling at 10-ft centers to support piping and cables. Pairs of channel inserts were imbedded in the floor

950435

Figure 27-35 Accelerator housing under construction at two-thirds beam takeoff point.

and one wall at 40-ft, 6-in. centers to provide anchorage for accelerator supports.

Lighting in the housing is incandescent with porcelain sockets for 150-W bulbs located on 10-ft centers. In four sectors with highest predicted radiation, mineral-insulated metal-sheathed wiring was used. Elsewhere, polyethylene-insulated wire was used in preference to other organic materials.

KLYSTRON GALLERY. The klystron gallery and end stations A and B are unique elements in the SLAC building program. The end stations are monumental in scale, but only the parapet of end station A is apparent from off-site view. The klystron gallery, 2 miles long, is quite exposed to off-site view and, therefore, was the subject of intensive architectural and structural studies. It was essential in order to minimize cost of such a large building that its elements be simplified and optimized to the best extent possible. A report "Klystron Gallery Design Criteria—Report TR-860-079" (dated June 14, 1962) was prepared by the former Systems Engineering and Installations Department and reflected the minimum requirements as established with the various SLAC occupant groups. It was subsequently furnished to ABA to be used as a guide in the preparation of their design documents. The as-built unit cost of the klystron gallery was $\$10/ft^2$ exclusive of outside utilities, roadways, and landscaping.

The functional requirements of the building dictated the overall dimensions, 10,081 ft long, 30 ft wide, 15 ft high. The building provides shelter for klystrons, modulators, and associated equipment. The structural frame, including rigid frame bents on 10-ft centers, was designed to support piping, conduits, and cable trays. These contribute uniformly distributed loads of 30 lb/ft^2 for a strip 8 ft wide, the full length of the klystron gallery. The

remainder of the roof structure will support 5 lb/ft^2 in addition to normal live and dead loads. The longitudinal walls of the klystron gallery provide support capacity of 300 lb/linear ft for cable trays.

The spacing of the structural bents at 10 ft on center was established to satisfy piping, conduit, and cable tray spans. The construction photograph, Fig. 27-36, shows the structural bent framing. Alternate columns are 8-in. wide flange sections and 14-in. wide flange sections of approximately the same weight per foot. The larger column is exposed on the exterior and the smaller column is concealed by the ribbed metal siding. This arrangement satisfied structural considerations and at the same time provided better external scale with exposed columns at 20-ft centers. Steel purlins, at 7-ft centers, transversely span between 10-in. wide flange top members of the bent framing and support the roof deck.

The length of the klystron gallery is punctuated by alcoves on both sides and these generally occur at sector intervals. An instrumentation and control alcove, 52 ft × 11 ft, occurs at each sector on the north side, opposite a mechanical equipment alcove 41 ft × 11 ft. Electrical equipment alcoves, 50 ft × 11 ft, coupled with screened electrical equipment yards, 30 ft × 11 ft, occur on the south side of even-numbered sectors. Also at each sector, on the south side, there are smaller alcoves, 10 ft × 10 ft, to cover the vertical manway access to the accelerator housing.

The external skin of the klystron gallery consists of two types of ribbed metal. The ribbed metal used for walls on other SLAC buildings is here used for roofing and is extended down as a heavy fascia, 5 ft deep. The lower part of the wall, approximately 9½ ft high, is of ribbed metal with a smaller rib. The heavy fascia is interrupted by the various alcoves which are all enclosed with the small-ribbed metal siding to eave height.

Figure 27-36 Klystron gallery under construction.

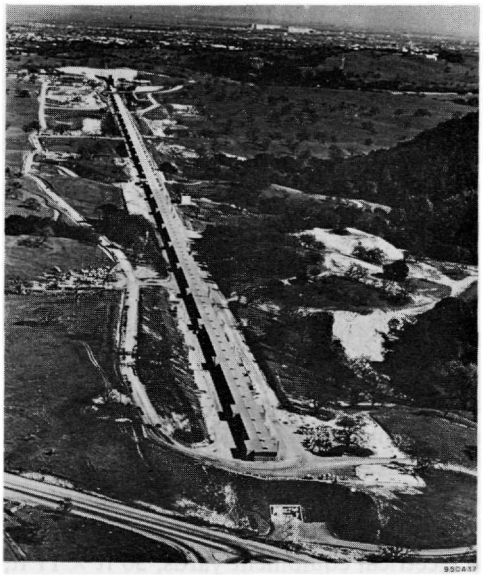

Figure 27-37 Klystron gallery completed.

A regular pattern of painted concrete shear walls occurs on both sides of the klystron gallery. These have vertical grooves at 30-in. centers.

The alcoves, fascia, shear walls, wall, and roof textures present a rhythm of architectural elements that add interest and scale and reduce the monotony of a 2-miles long structure of uniform height. The ridge line of the almost flat roof is punctuated by low-profile gravity ventilators at 70-ft centers. These elements of design are clearly visible in Fig. 27-37, which is an aerial photograph, looking east along the completed klystron gallery, with the injector station, or west end, in the foreground. Visible, also in the foreground below the klystron gallery, is the west entrance to the accelerator housing.

The floor slab is provided with expansion joints at each sector. High quality concrete was obtained by the use of low shrinkage granite aggregate and strict temperature control of concrete during mixing, placing, and curing. All lighting in the klystron gallery is incandescent to avoid interferences with sensitive control systems.

CENTRAL CONTROL BUILDING. The Central Control Building houses the central controls and instrumentation for the operation and maintenance of the accelerator including communication systems linking the Data Assembly Building, the experimental areas, and the accelerator.

The site selection was a compromise of considerations, including economy of cable length, convenience to the Electronics Building for support work, and accessibility for visitors. The contours of the site at the slope of the klystron gallery cut dictated a three-story structure with the uppermost level

Figure 27-38 Central control building.

at the level of the Electronics Building yard and the lowest at klystron gallery level. The exterior face of the third level office wing is depicted in Fig. 27-38.

The uppermost floor has an area of 7000 ft^2 and contains staff offices, toilets, and a large room 54 ft × 90 ft for consoles and electronic equipment racks. The lowest floor area is used for mechanical equipment, battery, and battery chargers. The intermediate floor area, 54 ft × 90 ft, serves as a plenum space and cable distribution gallery for the console and racks above. Floor plans for the building are shown in Fig. 27-39. Connection to the cable system in the klystron gallery is by way of a concrete tunnel, with internal dimensions of 6 ft, 6 in. × 6 ft, 6 in., under the north road alongside the klystron gallery.

The designers of the instrumentation and control systems were concerned about the possibility of RF interference from accelerator component and overhead power line sources, and since the magnitude of these interferences could not be determined accurately in advance of construction, the Central Control Building was designed so that, if necessary, an RF shielding enclosure could be constructed within the building without structural alteration. It was assumed that if this requirement should arise in the future, the rack area and cable gallery would be included within the RF shield. The Central Control Building was, therefore, designed so that the rack area floor system, slab, beams, and columns are electrically isolated from the rest of the building. This was accomplished by provision of a 6-in. gap between the rack area floor slab and the perimeter wall, and a requirement that steel column anchorage for this floor would be at least 2 in. clear of foundation reinforcement. In addition, laminated plastic sheet was placed under the column base plates and sleeves, and washers of similar material were provided at all anchor bolts. The middle floor of the building, known as the cable gallery, serves as a plenum space for the air-conditioning system and also as a work space for installation, maintenance, and modification of the cable systems.

Cable and chilled air to each rack penetrate the rack area floor slab through 6-in. diameter holes at approximately 28-in. centers under the rows of racks. The clear headroom in the cable gallery is 8 ft high, in order to

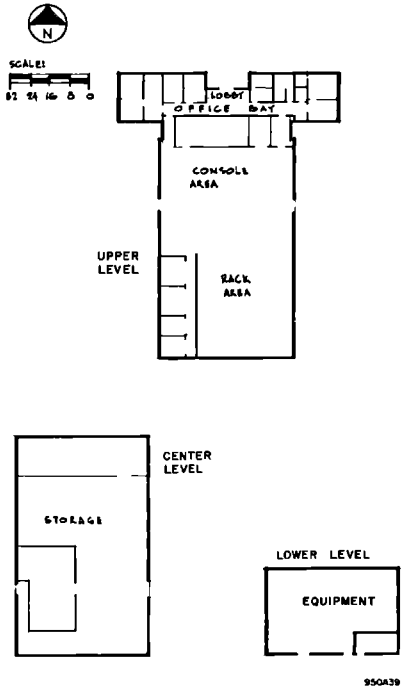

Figure 27-39 Floor plan of central control building.

provide ease of working for installation and maintenance and as a possible expansion space for future control systems.

The exterior walls of the Central Control Building, below the rack area floor, are of reinforced concrete. Above this level, the structure, walls, and roof deck are of steel. The columns supporting the free-standing rack area are square steel tubes. All lighting is incandescent in order to minimize possible electrical interference. The building is air-conditioned by utilizing chilled water from a chiller in the mechanical equipment room. Cooling water for the condenser and hot water are from central sources.

LASER ROOM. During design of the machine's laser beam alignment system, it became apparent that it would be necessary to direct this light beam from a laser source at the east end of the accelerator to the injector end. The laser itself would be at beam level and offset to one side where it could be reasonably well shielded from radiation. Since by the time this decision was made the accelerator housing, klystron gallery, and beam switchyard housing were completed, some ingenuity was necessary to provide a suitable underground structure.

Thirty feet beyond the east end of the klystron gallery, an 11-ft diameter hole was drilled to clear the north wall of the accelerator housing. The depth

of this hole was 3 ft below that structure's floor level and 38 ft below road level. A steel pipe casing was used to prevent cave-ins. Within this casing, a prefabricated steel housing, 8 ft in diameter and 9 ft high, was installed on a concrete base, with a connection to the accelerator housing through a drilled hole in that structure's wall. Access to the Laser Room is obtained by means of a 3-ft diameter steel pipe shaft enclosing a ladder and connecting to a concrete vault, $8\frac{1}{2}$ ft × $4\frac{1}{2}$ ft × $6\frac{1}{2}$ ft high, near the surface. A conventional manhole provides entry from the road level. The structure was backfilled with pea gravel to the accelerator housing level and with earth above that. As the excavation caused release of some of the easily flowing gravel backfill around the accelerator housing, it was necessary to use an extensive amount of fluid cement and fine aggregate grout to fill voids within the area. Alignment observation is conducted at the west end of the accelerator in a space partitioned, shielded, and air-conditioned in a conventional manner.

BEAM SWITCHYARD. The beam switchyard, an underground concrete structure, is an extension to the 10,200-ft long accelerator housing and terminates near the end stations. The structure contains 31,000 ft^2 of floor area with a total volume of 690,000 ft^3. It houses the beam bending magnets, collimators, and beam-analyzing equipment which are used to divert the beam into the proper experimental areas. This complex connecting link between the accelerator proper and the research area is shown in Fig. 27-40. Subsequent Figs. 27-41 through 27-43 show the construction progress of the beam switchyard.

Figure 27-40 Beam switchyard rendering.

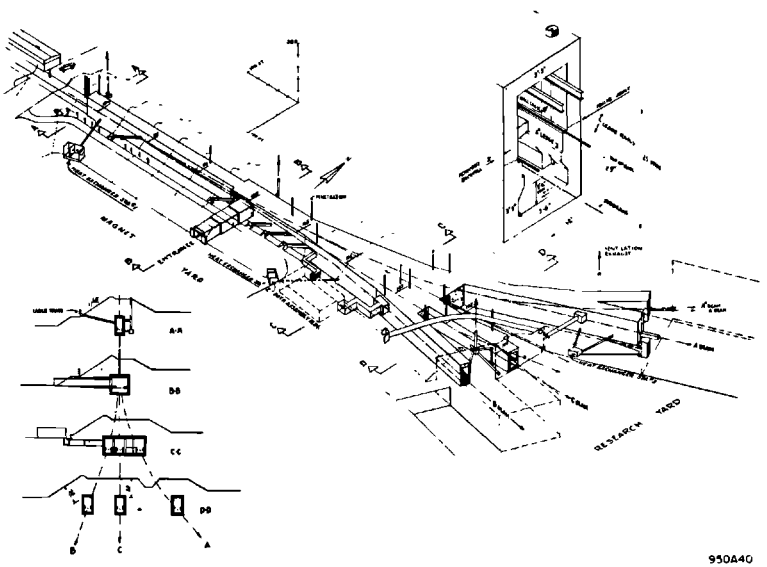

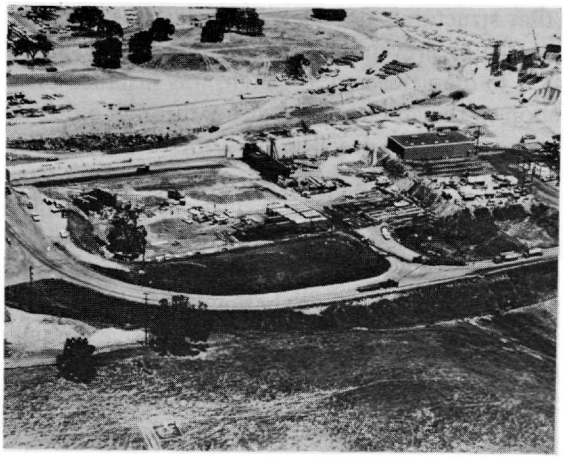

Figure 27-41 Beam switchyard backfill under construction.

The establishment of the basic housing alignment was dictated by the beam line geometry. However, the cross-sectional shape of the housing was determined by operational considerations. Primary among these was the prediction of extremely high-radiation areas and the possibility of having to do all routine maintenance and modifications by the use of remote-handling equipment. This consideration resulted in a two-story layout (see Figs. 27-44 and 27-45), with the beam line equipment below and handling equipment

Figure 27-42 Beam switchyard nearing completion.

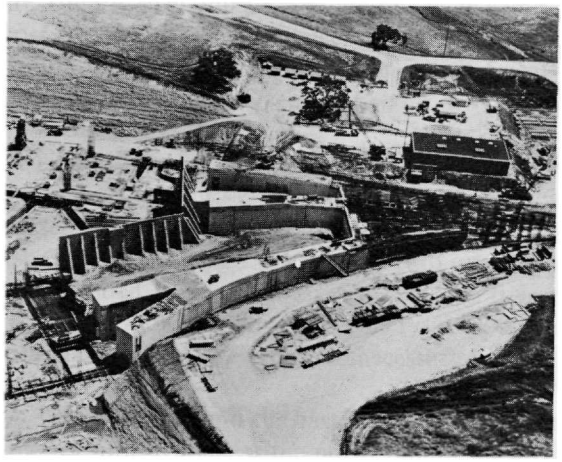

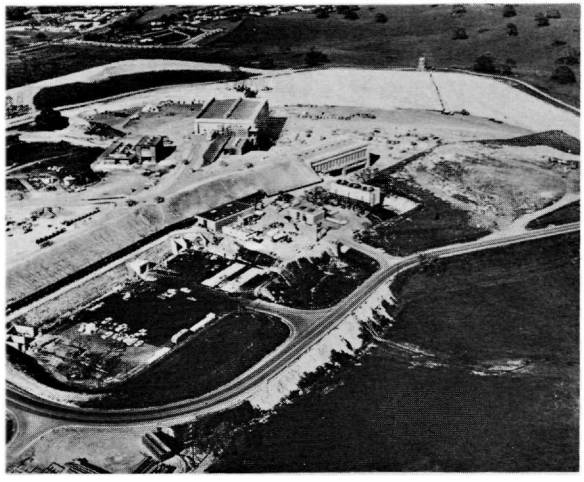

Figure 27-43 Beam switchyard completed.

above, separated by a floor of removable concrete shielding. In the upper level, there is a rail system designed for future use by a 50-ton shielded rail car to be equipped with remote-handling tools.

The height of the structure was determined by the minimum hook height requirements of the 16-ton overhead bridge cranes which traverse the lengths of all three legs of the beam switchyard. This layout resulted in a height of 25 ft from floor to ceiling. The width was determined by the size of the equipment and by the requirement that space be provided to shift the beam alignment a maximum of 9 in. in any direction. This resulted in a basic width of 12 ft.

Figure 27-44 Interior of beam switchyard diverging area, looking west.

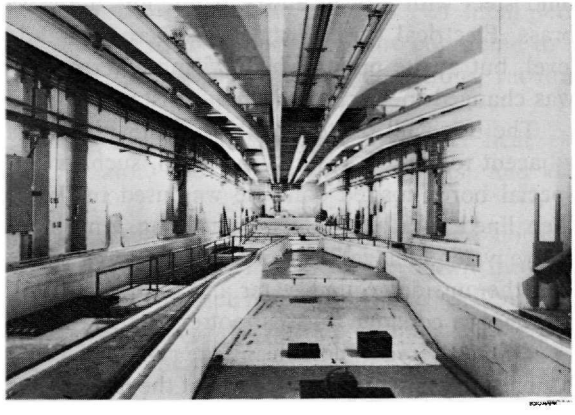

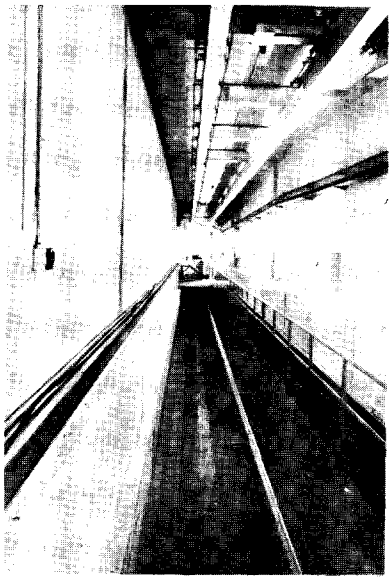

Figure 27-45 Interior of beam switchyard A channel, looking east.

The selection of materials was predicated upon the assumption of high radiation, creation of secondary radiation of air and dust particles, and generation of a nitric acid atmosphere. These considerations eliminated the use of all materials other than concrete for the structure itself. Special precautions were used to avoid concrete dusting. Special phenolic resin paint was used on floor and walls of the lower housing under the shielding floor. The upper housing was painted with a less expensive vinyl base because of the lower radiation levels expected. No galvanized metal was permitted because of the nitric acid atmosphere. All metals were either stainless steel, aluminum, mild steel with special epoxy paint, low alloy weathering steel, copper, or brass. Electrical wiring insulations were of standard materials in the upper level, but at the points where wiring entered the lower level, the insulation was changed to special radiation-resistant material.

The earth fill on top of the housing is 32 ft above the ceiling. In areas adjacent to sources of high radiation, such as slits, collimators, and dumps, special boron-loaded concrete was used in the structure. These areas were then lined with a stainless steel lining. The lining serves to prevent radioactive water spillage from entering the pores of the concrete or from escaping into the outside ground water and to prevent dusting of the concrete so that radioactive concrete dust cannot enter the atmosphere.

Utilities serving the housing are run outside along its length on a cableway bench. They enter the upper level of the housing through a series of horizontal

utility ducts. Vertical wall chases are provided at periodic intervals for utility access from the upper to the lower level. All utilities are routed to avoid known radiation sources and over the shortest feasible paths between the upper and lower housing levels.

The following structural design criteria were used for the concrete housing: The foundation modulus for shale was to be 1.1×10^6 lb/ft^3 and for sandstone, 8.3×10^6 lb/ft^3. The minimum ultimate compressive strength of the concrete was to be 4000 psi at 28 days. Reinforcement was to be in accordance with American Society of Testing Materials (ASTM) Specification A-432, with a design bending stress of 20,000 psi. The earth load on the roof was to be between 1.0 and 1.6 times the nominal vertical overburden pressure depending upon the width of the section under consideration. The earth load on the walls was to be either 0.5 or 0.6 times the nominal vertical overburden pressure, the lesser value applied to the bottom of the wall and the greater value to the top of the wall.

Housing ventilation is provided by four strategically placed exhaust ducts which extend vertically through the 32 ft of shielding fill above the housing ceiling. The main entrance way is equipped with a filter bank which filters the intake air. The exhaust ducts are equipped with fans sized to provide six air changes per hour. The housing is sealed during actual beam operation to prevent the escape of radioactive air into the outside atmosphere. After a beam run is completed, the air is monitored and when a safe level is reached, it is exhausted into the atmosphere.

The crane system in the beam switchyard is complicated by the diverging beam lines. Three 16-ton cab-operated bridge cranes are used, one for each beam line. A transfer system is available to move the cranes from one set of rails to another. All of the cranes are capable of running on any rail system within the switchyard. Two cranes can be used on one set of tracks and can be used in tandem to lift 32 tons.

BEAM SWITCHYARD APPURTENANT STRUCTURES. To avoid the radiation atmosphere within the beam switchyard housing and to provide access to critical items of equipment during beam operation, a number of small peripheral structures are located external to the housing and are connected to it by duct systems. These structures consist of heat exchanger stations, vacuum pumping stations, and utility alcoves.

There are four heat exchanger stations, serving the magnet heat exchangers, the high-power collimator, the A- and B-beam slits, and the A-beam dump.

There are seven vacuum pumping stations located above the housing on top of the shielding fill. Vertical vacuum fingers extend down into the housing through vertical shafts to provide the beam line vacuum. In addition, there are a number of utility alcoves along the cable bench to provide areas for instruments to monitor utility services entering the housing.

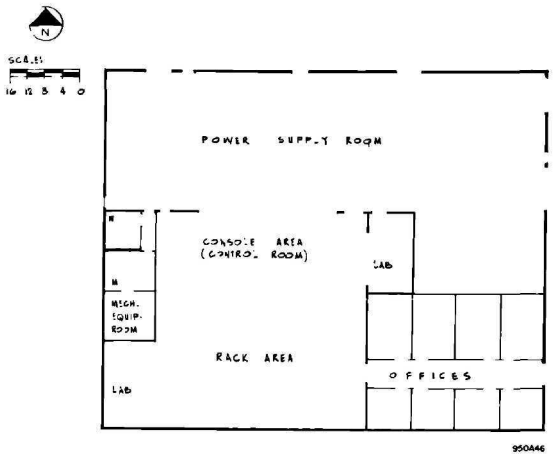

Figure 27-46 Floor plan of data assembly building.

DATA ASSEMBLY BUILDING. The Data Assembly Building serves as the control center for the beam switchyard. The building is 80 ft × 100 × 15 ft high, and is situated on the south side of the beam switchyard shielding fill. The site selection was based on the economics of cable and utility costs related to the function of the building.

As shown on Fig. 27-46, the building provides 2300 ft^2 of control room, 1200 ft^2 of offices, and 3750 ft^2 of power supply space. The balance of the building includes toilets and a light laboratory.

The architectural form is the same as the utility buildings without roof overhang or roof sight screen (see Fig. 27-47). The power supply area (see Fig. 27-48) required maximum wall space for cable racks and for electrical control panels. The control room is equipped with a luminous ceiling for controlled illumination and a raised computer-type floor to provide space for interconnecting cables. Windows are provided only in the office area.

Figure 27-47 Data assembly building.

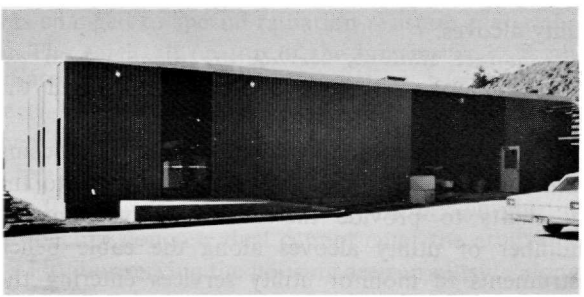

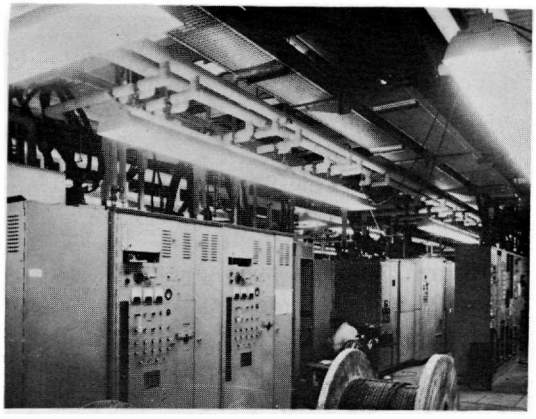

Figure 27-48 Data assembly building interior —power supply room.

The construction is made of a structural steel frame with diagonal bracing, ribbed metal siding and roof deck, and builtup asphalt and gravel roofing. A considerable quantity of conduits, cables, and piping is suspended from the roof girders and, because of the uniqueness of the beam switchyard control problems, complete data on suspended loads were not available for the initial structural design. Some reinforcement of the roof structure was required later.

The control room and office area are air-conditioned by means of local equipment. Gravity roof ventilators are provided for the unheated power supply room.

Research area buildings (RSG, GIR, WPS)

The diverging beam lines, starting at the beam switchyard, continue on into the research area creating a fan-shaped yard area of approximately 10 acres of concrete and asphalt. This research yard was scooped out of the gently rolling hillside to form a flat-bottomed bowl-shaped excavation completely surrounded by either native or artificially created earthen embankments approximately 40 ft high. Within this fan-shaped bowl are located the two large end station buildings and roughly a dozen smaller research and support-type buildings and facilities. The principal buildings are located along the beam paths. As of July 1967, the following major units are in service:

A-beam line
Counting house
End station A
2-Meter streamer chamber enclosure
Beam dump east

C-beam line
82-In. bubble chamber enclosure
Bubble chamber offices and shop
B-beam line
End station B
40-In. bubble chamber enclosure
54-In. spark chamber enclosure

Figure 27-49 is a photograph of the research area yard looking north. Figure 27-50 is a photograph of the research area yard looking west with end station A at the right and end station B at the left. Buried underneath the research area yard is a network of approximately 1700 linear ft of utility tunnels providing utility service to the end station buildings and other experimental areas within the yard. The research area yard thereby fulfills its function of providing adequate work space where high-energy physics experiments can be conducted in an area shielded from the surrounding community and capable of adequate personnel access controls.

Because of the constantly changing nature of the research activities within the research area yard, all the special project buildings had to be designed for maximum flexibility as to their present and future use. They had to be capable of being relocated. They had to be inexpensive. Many of them house heavy magnets. Provision had to be made for crane access. Because of these requirements and the fact that the research yard is shielded from view from the neighboring community, the project architectural standards have been relaxed for research yard buildings under 35 ft in height. This has permitted

Figure 27-49 Research yard.

950A49

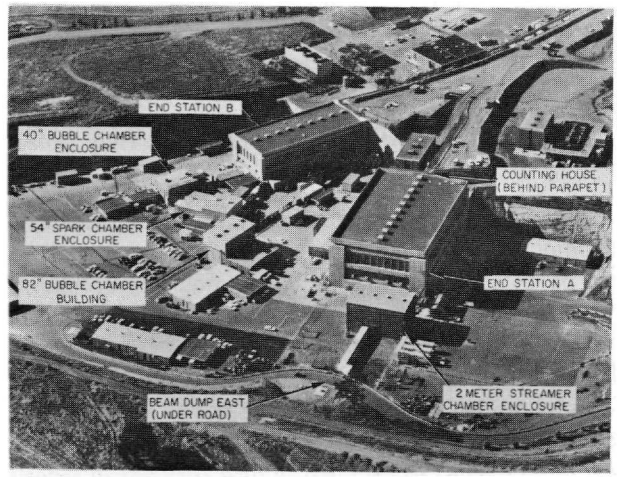

Figure 27-50 End stations.

the use of "pre-engineered" steel buildings with rigid steel structural framing and galvanized sheet steel roof decks and siding.

YARD AREA. The substratum of the research yard is Miocene sandstone with recommended design bearing values as shown in Fig. 27-51. Approximately 1.1 million yd^3 of this material (maximum excavated depth of 70 ft) were removed. Most of this was used to form the compacted radiation shielding fill over the beam switchyard. The shielding dikes on the north and south rims of the research yard and between the experimental area and the outside community are constructed in accordance with the project requirement of 400 ft of embankment in the forward (easterly) direction at the height of the electron beam (approximately 7 ft above yard surface).

A surface area of approximately 10 acres is covered with concrete and asphalt pavement. The area nearest the end stations has a 6-in. nonreinforced concrete slab on an untreated base of 6 in. of compacted rock material. This area lies between the end stations and extends approximately 50 ft beyond the end stations at the remaining two open sides. A midportion of the yard adjacent to the concrete slab is paved with 3 in. of hot-mixed asphaltic concrete on 9 in. of base rock. The remainder of the yard, a strip nearest the eastern earthen bank, is treated with an asphalt seal coat over a similar base material as for the asphaltic concrete.

The yard is underlaid with a storm drain system connected to inlet structures placed on a uniform grid. This surface is sloped to each drain inlet in a grid or waffle pattern except for a level area adjacent to the two end stations (approximately 50 ft). The inlets are spaced at 100-ft intervals. The asphalt surface has a 6-in. vertical variation from high to low. This slope is twice as

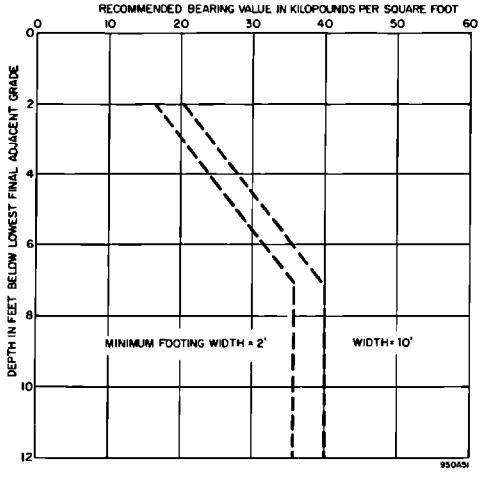

Figure 27-51 Research yard recommended design bearing values (dead loads) for footings founded in poorly cemented, fine-grain, Miocene sandstone. (These bearing pressures are based on Miocene sandstone extending below the footing at least one footing width.)

steep as the concrete paved area. The storm drain system is sized to handle the runoff from the maximum rainstorm expected to occur within a 10-yr span of time. Pipe sizes range from 12 to 42 in. in diameter. The material is galvanized corrugated steel. Catch basins are cast-in-place reinforced concrete boxes with lift-out subway-type heavy-duty grating.

Underground utility housings extend under both end station buildings. They project at right angles from longitudinal housings located alongside the exterior of each building. The housings are constructed of reinforced concrete and are rectangular in cross section. They vary in height from 7 to 10 ft and are 7 ft wide. There are approximately 4 ft of compacted select backfill between housing roofs and the floors of the end station buildings. Housing roofs can withstand a uniform live loading of 3000 lb/ft^2. The housings have underfloor drains sloping to a common sump pump. The longitudinal housings are interconnected by two corrugated metal utility housings, oval-shaped in cross section, buried under the yard area between the two buildings. The intersections of the metal housings with the concrete housings occur in vaults which are essentially a widening-out of the housings. The vault roofs are part of the experimental pad area and are structurally supported by steel columns. Access to the underground utilities is obtained through 3-ft × 6-ft manhole openings. The manholes within the two buildings

also serve as floor drains. A recessed lip around the perimeter of the manhole serves as a gutter. This gutter is connected to a drain pipe which spills waste water at the floor level of the utility housings.

Provision has been made for the future extension of the utility housings into the eastern part of the research yard by means of knockout end walls.

COUNTING HOUSE. The counting house serves as the control center for the spectrometers located within end station A and as the point of experimental data accumulation and computer analysis. It is located on top of the beam switchyard fill, 45 ft above the floor of the end station. The upper portion of the end station A west wall acts as a common wall between the two buildings. The building is a steel frame structure with 1900 ft^2 of main floor area and 1600 ft^2 of mezzanine floor. The main floor consists largely of removable panels over a 2-ft deep space for cabling. Cables can enter the counting house through sleeves in the west wall at the level of this underfloor space. Cabling also enters the underfloor cavity at the south wall by means of cable trays attached to the outside face of the retaining wall.

Viewing ports in the common wall allow experiments in progress in the end station to be viewed from the counting house level.

An industrial freight elevator, 5 ft × 7 ft × 10 ft high, is used for transporting pieces of experimental apparatus from end station floor level to the counting house level. The elevator is of a hydraulic, piston-type with a 3500-lb capacity and an up-and-down speed of 50 ft/min. A steel stairway is also provided for personnel use. The counting house is fully air-conditioned to accommodate temperature-sensitive electronic equipment.

END STATION A. End Station A is located in the north part of the research yard straddling the A-beam as it emerges from the beam switchyard. It is a large concrete building used to house the spectrometers and provide crane, utilities, radiation shielding, and personnel access controls to the experimental area within the building.

The building is rectangular in plan with its west wall abutting the end of the beam switchyard. This wall also acts as a retaining wall for the earth shielding fill over the beam switchyard. The long axis of the building is parallel with and offset 17.5 ft to the south of the A-beam. The direction of the A-beam through the end station is at an angle of 24°29′30″ north of the C-beam. The inside dimensions of the building are 200 ft × 125 ft. As shown by the building cross section (see Fig. 27-52), the clear height from the floor to the highest position of the crane hook is 50 ft. Large openings through the north and south walls, 32 ft high by 40 ft wide, are designed for bringing in equipment. The opening on the south side has a motorized 2-ft thick, concrete door weighing approximately 450,000 lb. The door is mounted on wheeled trucks which roll on a single crane rail. A compressed air tank and motor are provided for auxiliary, emergency power operation of this door.

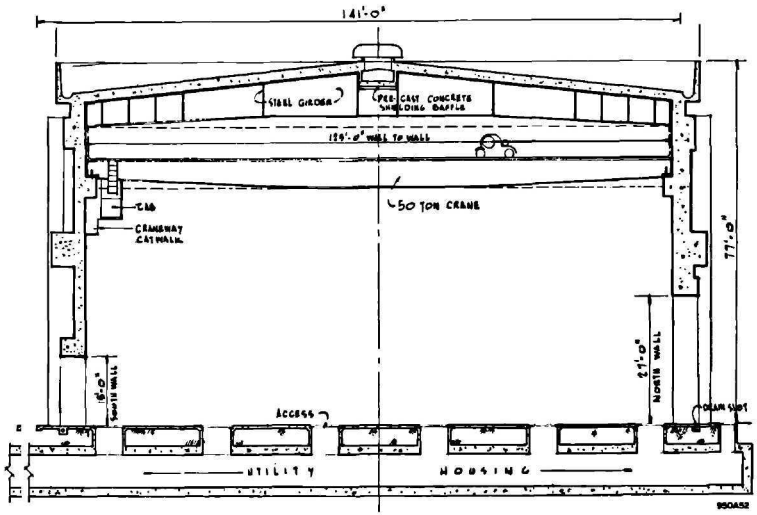

Figure 27-52 Cross section of end station A.

The corresponding opening on the north wall is covered by 2-ft thick, portable concrete blocks. Another opening in the north walls, 27 ft high by 105 ft long, is provided to accommodate the 20-GeV spectrometer. This opening is covered by 3-ft thick, portable concrete blocks. Other openings in the east and south walls are, respectively, 14 ft high × approximately 95 ft wide, with 5-ft thick, portable concrete blocks and 15-ft high × 105-ft wide with 3-ft thick, portable concrete blocks. Many of the feâtures described in this paragraph can be seen in Fig. 27-53.

Figure 27-53 End station A interior.

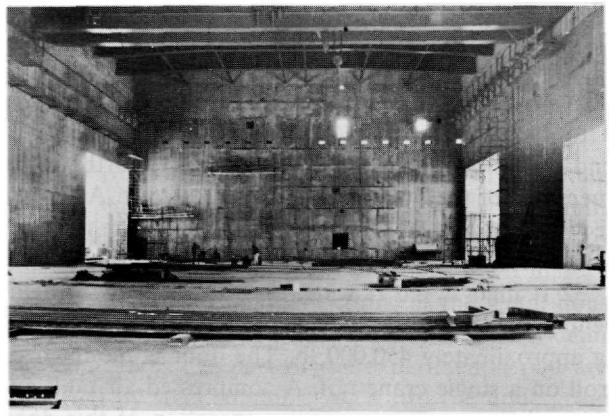

Specific features are constructed in the floor of the end station to accommodate the three spectrometers and these are noted on the floor plan (see Fig. 27-54). A central pivot, about which the spectrometers rotate, is a 28-ft long muzzle section of a 16-in. naval rifle. Eleven and one-half feet of this barrel extends above the floor of a circular utilities pit, 16 ft in radius × 13 ft deep. Radiating outward from this pivot, in concentric circular segments, are crane rails on reinforced concrete grade beams for supporting heavy spectrometer and shielding loads. Several of the concrete grade beams are deepened or are supported on 30-in. diameter × 30-ft deep, drilled-in concrete caissons to carry heavy loads without affecting the adjacent underfloor utility housings.

The structural design of the building was influenced to a large extent by the radiation criteria for the walls and roof. A minimum of 300 lb/ft^2 of mass was required to maintain safe radiation levels outside the building. As a result, all walls and roofs are of concrete, having a minimum thickness of 2 ft.

Wall thickness varies above the minimum as required by structural considerations. Granite rock aggregate was used extensively because of its proven, economic property of reducing shrinkage cracking. Generally, concrete surfaces are not painted. Large equipment and the necessity for unobstructed beam lines dictated the column-free interior.

The floor slab is made of 6-in. thick, unreinforced concrete on a 6-in. untreated base of coarse graded aggregate. It is structurally independent from the walls. The thickness is a compromise between requirements for the expected high floor loading and the ease in removing sections of the floor as required for future utilities. Undisturbed soil (Miocene sandstone) beneath

Figure 27-54 Floor plan of end station A.

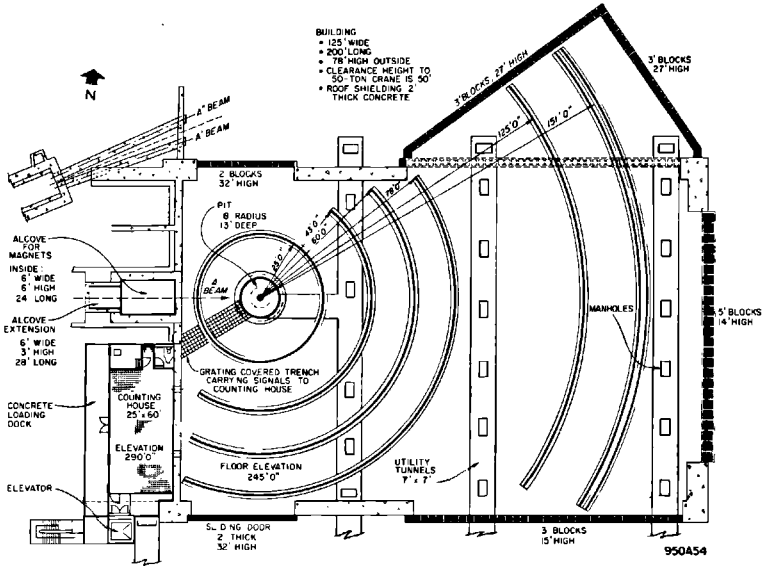

the floor has an exceedingly high load bearing value and care was exercised in the design and construction to minimize disturbance. Where it was necessary to disturb natural soil to install utility ducts and housings, compacted, select, imported backfill of high quality was used.

The building is a large single-story concrete structure designed as a rigid frame. There are large sections of uninterrupted walls carrying large earthquake-induced shear forces into the sandstone foundation. One of these walls is over 5 ft thick, 47 ft wide, and extends 18 ft into the ground. The unusually firm foundation material in this area allowed a maximum design loading of 40,000 lb/ft^2. Because of the large mass of building walls and roof and the proximity of the San Andreas fault, the possible lateral forces induced by an earthquake served as a controlling design factor. The building is designed for a ground acceleration of 0.5 g which corresponds to an earthquake of magnitude 8.0 on the Richter scale. A computer analysis of the structures indicated they were quite stiff regardless of the large wall openings. End station A has a vibration period of 0.06 sec in the transverse direction and 0.14 sec longitudinally. Project-accepted seismic design criteria, based on the foregoing factors, established a coefficient for base shear of 0.2 g.

Roof slabs are supported on steel girders. These girders are designed for composite action with the concrete roof slab. The roof slab was cast in place on top of 8-in. thick, precast concrete planks. The steel girders were shored up temporarily by intermediate posts or shores to support the weight of the roof until the concrete had gained sufficient strength. The shores consisted of groups of four wooden telephone poles lashed together. The shores were systematically removed by jacking the roof down in small uniform increments.

End station A is equipped with a top-riding, 50-ton, overhead electric bridge crane. This crane has a 15-ton auxiliary hoist mounted on the same trolley with the main 50-ton hoist. Main and auxiliary hoists are controlled by a stepless General Electric silicon-controlled rectifiers (SCR) system. Extremely low speeds of 2 in./min on the main hoist can be maintained indefinitely regardless of the load on the hook. The maximum speeds are 10 and 20 ft/min for the main and auxiliary hoists, respectively. Maximum bridge speed is 100 ft/min through a 5-step, wound-rotor motor. Maximum trolley speed is 50 ft/min in 5 steps. Inching speed of 1½ ft/min is obtained through pony motors on both bridge and trolley drives. The crane is operated from either a fixed cab or a movable pendant push-button control station suspended from a separate motorized trolley. The maximum height of the main hook above floor is 50 ft.

End station A is heated by four electric heating units, one in each corner of the building. The electric heating elements have low surface temperatures to reduce the possibility of igniting hydrogen in case of an accidental spill. Heater units discharge forced air picked up near the roof at a height of approximately 13 ft above the floor. Each heater is divided into three separate subunits (one air-handling fan). The heating capacity of each heater unit is 75 kW and the air-handling capacity is 7000 ft^3/min. It is necessary to heat

this building to reduce the distortion and consequent misalignment of the spectrometers due to temperature changes.

Ventilation is provided by ten roof-mounted, 25,000 ft^3/min, belt-driven, exhaust fans located along the length of the building. The fans draw air from the highest point of the building through shielded openings in the 2-ft thick, roof slab and exhaust it through automatic back-draft dampers. The fan motors are totally enclosed, explosion-proof, belt-drive type. The roof has a 10% slope toward the fans for positive movement of light gas. Air movement is based on a 2-min air change of the upper 20 ft of the building. The exhaust fans are manually controlled with controls located in the counting house as well as at the house power panel. A relay in the control circuit provides automatic override control for full capacity operation when activated by the hydrogen detection system. Normal ventilation requirements are met by drawing air supplied from the utility housings through the grate-covered floor openings. Interchangeable solid coverings are available when required for equipment and shielding support. A few manholes into the exterior utility housings are fitted with portable air intake structures.

Local ventilation over hydrogen targets is provided by the use of portable exhaust ducting, hood, and fan. The fan is actuated by a local hydrogen-detecting device. The ducts pass through a system of shielded exhaust ports through the walls of the end station above the portable shielding blocks. All ventilation fans contain backdraft dampers to prevent natural chimney action when the fans are not operating.

2-METER STREAMER CHAMBER ENCLOSURE. This building is used to house the 2-meter streamer chamber. It is a rigid frame building with sheet metal roof and siding, has a floor area of 4000 ft^2 and an eave height of 45 ft. Because of the height of this building, it was subject to architectural review. This resulted in special fluted siding and roofing, special roof ventilators, and exterior paint. The 2-meter streamer chamber is mounted on tracks and rollers and can be towed out of the building through a large door, thus eliminating the need for special heavy crane handling facilities within the building.

This building is equipped with a top-riding 5-ton overhead electric bridge crane. The crane has ac induction motors driving through variable-speed electric clutches for all three motions (hoist, trolley, and bridge). This system gives accurate speed variations, regardless of load, through SCR controls in conjunction with signals from a feedback generator connected to the load side of the clutches. The crane is controlled through pendant-mounted push buttons. Clutch current is controlled through push buttons connected to a resistor with taps for five speeds. A selector switch gives an inching range to all motions. Comfort heat in this building is provided by portable heat lamps.

BEAM DUMP EAST. Beam dump east is a heavily shielded concrete structure located on the A-beam line at the extreme easterly edge of the research yard. The purpose of the structure is to house the water-cooled beam dump that

absorbs the residual A-beam. Shielding is provided to reduce the radiation from the dump to the external areas. A stainless steel lined sump is provided to hold dump water in case of accidental leakage. Other features include rails for handling the dump vessel, a crane for handling equipment and shielding blocks, and a secondary heat exchanger system to water-cool the closed primary cooling system.

The structure is similar in cross section to the beam switchyard. It has a corbelled ledge on which concrete shielding blocks rest, giving it a two-story configuration. It measures 96 ft long × 10 ft wide by approximately 18 ft high (plus sump). The concrete walls, roof, and floor have an average thickness of about 3 ft. The structure is nestled into a sandstone bank and is completely covered by shielding fill. Figure 27-55 shows these features plus the concrete shield blocks defining the A-beam path to beam dump east. To increase the density of the top fill (because of a paved access roadway), two layers of concrete filled and encased gun barrels are placed between the roof and the compacted rock fill. Approximately sixty-five 105-mm World War II "Long Toms" are so used. The approximate depth of fill between the top of concrete housing and the roadway subgrade is 6 ft.

The interior surfaces are painted by means of the same scheme used for the beam switchyard, as follows: the lower portion (below layer of concrete shielding) is painted with special phenolic resin paint; the upper portion (lower radiation exposure above concrete shielding blocks) is painted with vinyl paint. The exterior surface is covered with a 20-mil thickness of polyvinyl chloride membrane to prevent entry of ground water.

Beam dump east is equipped with a top riding, 10-ton, overhead electric bridge crane. Speed regulation of bridge and hoist is obtained through wound-rotor main motors for normal speeds and inching motors are used to provide a speed of $1\frac{1}{2}$ ft/min. The hoist trolley is driven with a two-speed

Figure 27-55 Beam dump east.

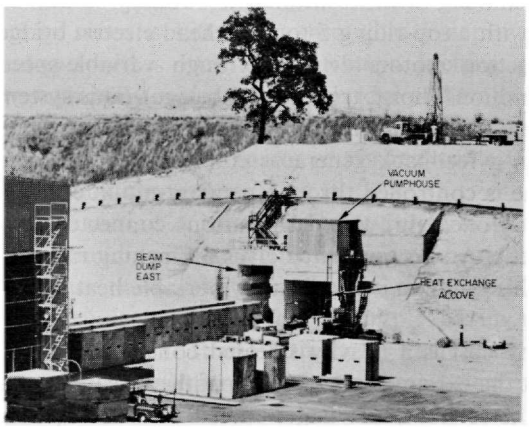

motor. The hook height above floor is approximately 15 ft; the length of the craneway is approximately 96 ft. The crane is controlled from a pendant-mounted push-button station. Because it contains no temperature-sensitive equipment, beam dump east has not been provided with any source of heat.

Beam dump east has a manually operated, exhaust fan to purge its atmosphere before personnel entry. The discharge end of the ventilator duct has a pneumatically controlled lid to prevent unwanted air circulation when the fan is off. The fan is a 5-hp, belt-drive, vane-axial type.

END STATION A POWER SUPPLY SHELTER. This building is used to house the electrical power supply equipment that powers the electromagnets associated with the spectrometers inside end station A. It is a rigid frame building with painted, galvanized sheet metal, roof siding. There are 3300 ft^2 of floor area and an eave height of 16 ft. The roof slopes from the ridge at 1 in. in 12 in. Translucent plastic panels occupy the upper 5 ft of the side walls, which allows natural daylight to enter without windows. This building is unheated and the walls are not insulated. The siding and framing are bolted to the flat level concrete yard area, using it as a floor slab. There are two roof-mounted 2500 ft^3/min powered exhaust fans.

82-IN. BUBBLE CHAMBER ENCLOSURE. The Lawrence Radiation Laboratory's 72-in. bubble chamber was modified and enlarged to an 82-in. unit. It was then disassembled and transported to SLAC. In preparation for this move, the 82-in. bubble chamber building was erected to house the chamber and associated equipment. The building is a rigid frame-type with a gross area of approximately 5600 ft^2. A 40-ft high bay with a floor area of 2500 ft^2 is used to house the bubble chamber. The remaining areas, shown in Fig. 27-56, have ceiling heights of approximately 15 and 9 ft high. These areas house the chamber ancillary equipment and the control room.

Figure 27-56 Floor plan of 82-in. hydrogen bubble chamber building.

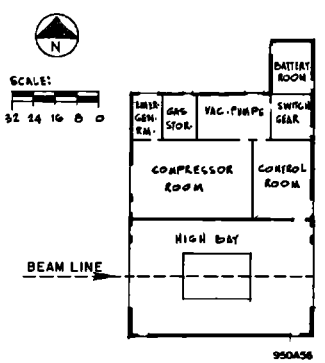

Adjacent to the north side of the building is an outdoor storage area for liquid nitrogen, Dewar, compressor and oil processing facilities. One 720-ft^2 concrete assembly pad is provided east of the high bay of the building. The pad was used to assemble the heavy components of the chamber prior to its move into the building. A 15-ton crane is provided in the high bay for the assembly of the remaining components and for the future maintenance of the chamber.

The high bay area of the building is provided with plastic blowout panels on the top 16 ft. Roll-up doors are provided at each end of the high bay section to facilitate moving the bubble chamber in and out of the building for future experiments. The interior wall between the high bay area and the compressor and control rooms is designed for 216 lb/ft^2 static loading to afford blast protection to the personnel in the compressor and control rooms. The electrical equipment and installation in the high bay and compressor room conform to the requirements of the National Electrical Code for Class 1, Division 2, Group B, to meet the hydrogen safety requirements.

END STATION B. End station B is located in the south part of the research area yard with its west wall abutting the beam switchyard. It is located almost south of end station A. The building is rectangular in plan with inside dimensions of 150 ft × 75 ft at the floor and 183 ft × 75 ft at a mezzanine level formed by the beam port funnel. The long axis of the building is oriented with and centered on the B-beam. The direction of the B-beam through the end station is at an angle of 12°29′32″ south of the C-beam. The north and south walls of the end station B (similar to end station A) are provided with large openings for bringing in equipment. These large openings and the

Figure 27-57 Cross section of end station B.

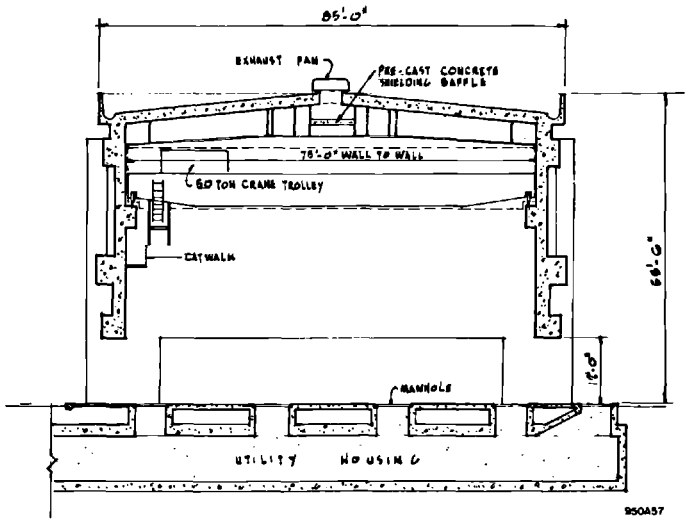

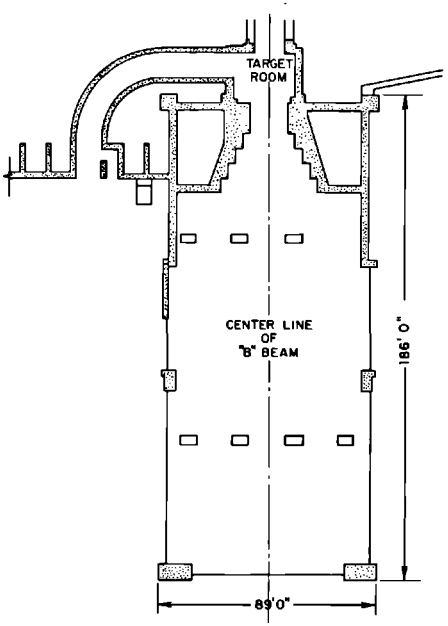

Figure 27-58 Floor plan of end station B.

funnel-shaped beam port can be noted on Figs. 27-57 and 27-58. A portion of the south opening, 20 ft × 20 ft, has a motorized 2-ft thick, concrete door. The door has auxiliary emergency power operation. Other openings in the north, south, and east walls, 12 ft × 70 ft, 12 ft × 70 ft, and 12 ft × 62 ft, respectively, are covered with 2-ft thick portable concrete blocks.

The structural design features of this building are similar to end station A with a 2-ft minimum wall and roof thickness. Earthquake structural design parameters and type of floor slab and rigid frame construction are all identical to those used in end station A except for the bridge crane span. This span was scaled down to fit the smaller building. The maximum height of the hook above the floor is $35\frac{1}{2}$ ft. The crane and the massive concrete blocks which it is required to handle are shown on Fig. 27-59.

Unlike end station A, there is no heat-sensitive equipment located in end station B; therefore, there is no provision for heat in this building. Ventilation consists of nine roof-mounted 25,000 ft^3/min, belt-driven, exhaust fans (compared to ten fans in end station A). Air-handling design and controls are similar to those used in end station A. Local ventilation over hydrogen targets is also provided in this building.

The beam port funnel is located at the upstream end of the building and is shaped as a stepped funnel in plan, open at the top. The narrow opening through the upstream wall has dimensions of 15 ft wide by approximately $26\frac{1}{2}$ ft high. The funnel opens in uniform 3-ft × 6-ft steps until the width of

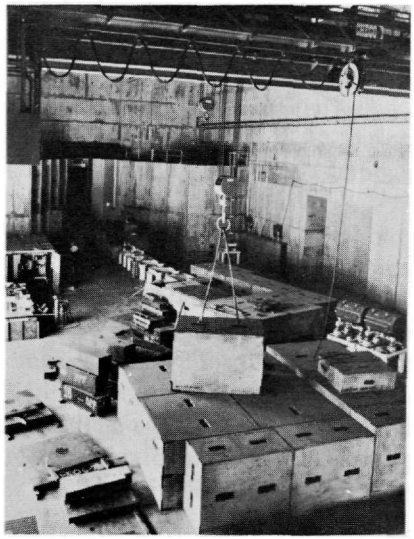

Figure 27-59 End station B, interior photograph, looking west toward target room funnel.

39 ft is attained at the downstream end. The space under the mezzanine, behind the stepped funnel wall, is filled solidly with compacted rock of approximately 150 lb/ft^3 density. The mezzanine surface is 25 ft above the floor of the end station.

The beam port funnel is preceded by the B-beam target room, which is 25 ft wide × 20 ft long × 26½ ft high. This room is covered by a shielding fill of compacted rock having the same high density as that behind the beam port funnel sides.

The target room is served by two 24-in. diameter steel penetrations in the roof and through the dense rock shielding fill. The penetrations will carry cabling necessary for controlling experimentation into the room. The south wall of the target room opens into a forward-curving access structure which is 10 ft wide × 12 ft high. The exterior opening of this access structure is shielded with portable concrete blocks. A personnel door is provided at the main opening. The target room end of end station B is equipped with a 15-ton, underslung, overhead electric bridge crane. Speeds of hoists, bridge, and trolley are controlled through two-speed motors at 4½ and 1½ ft/min. All motions are controlled from a wall-mounted push-button station. The maximum hook height above the floor is 21 ft.

The target room and the access tunnel are equipped with a 12,000 ft^3/min electrical fan. The fan is operated manually for purging prior to personnel entry. Controls are located at the exterior of the mazed man-door. A

backdraft damper located over the man-door allows the fan to draw in fresh air. There are no provisions for heating this area.

54-IN. SPARK CHAMBER BUILDING. This building is used to house the μ-beam spark chamber. It is a rigid frame building with sheet metal roof and siding, it has a floor area of 4200 ft^2 and eave heights of 22 and 28 ft. Special attention was paid in this building to make the structure as light-proof as possible. This was necessary to accommodate the light-sensitive nature of the photographic film associated with the spark chamber. To provide access for a mobile crane, a portion of the siding and subframing was made removable. This building is not equipped with a bridge crane. It does not have a source of building heat.

40-IN. BUBBLE CHAMBER BUILDING. This building is used to house the 40-in. bubble chamber. It is made out of a rigid frame with sheet metal roof and siding, has a floor area of 2000 ft^2 and an eave height of 27 ft. It is mounted on rubber-tired casters which allow the entire building to be rolled away from the bubble chamber in the event that crane access is required to the heavy magnets. This arrangement also permits the building to be relocated anywhere within the yard. The building is windowless; but daylight is allowed to enter through a band of translucent corrugated plastic placed along the upper few feet of the siding. The walls and ceiling incorporate a system of blow-off panels designed to swing open at an internal pressure of 30 lb/ft^2. This safety precaution is taken because of the large volume of liquid hydrogen used by the bubble chamber.

The building is equipped with a 7½-ton top riding overhead electric bridge crane. The crane has ac induction motors driving through variable-speed electric clutches which control the hoist, trolley, and bridge motions. This system gives accurate speed variations, regardless of load, through SCR controls in conjunction with signals from a feedback generator connected to the load side of the clutches. The crane is controlled through pendant-mounted push buttons. Clutch current is controlled through push buttons connected to a resistor with taps for five speeds. A selector switch gives an inching range to all motions. Building heat is provided by four 12-kW space heaters.

PORTABLE EQUIPMENT SHELTERS. These shelters are multipurpose units used as shelters for any system that can fit inside them, including power supplies, magnets, instruments, etc. They are small (16-ft × 32-ft) units with an eave height of 12 ft. They have no floor and hence can be lifted by a crane and set down over any object requiring protection from the weather. There are approximately one dozen of these units in use in the research area yard. They are constructed of self-framing interlocking panels on both roof and walls. The units are prewired for both lights and utility outlets. There is no source of heat. Ventilation is provided by wall louvers.

Table 27-8 Small, temporary buildings

Building No.	*Area (ft^2)*	*Purpose*
101	3920	Spectrometer staging area
102	5370	Research area shops and test area
104	3840	General storage
107	4000	Bubble chamber crew quarters and shop

OTHER SUPPORT BUILDINGS As noted previously, a number of small buildings used for temporary purposes during construction have since been relocated to the research area yard in support of experimental activities (see Table 27-8).

27-4 Utilities (FFH, GIR)

Cooling-water systems

Closed-loop, low-conductivity cooling-water systems and cooling tower water systems are described separately in Chapter 24.

Electric power system

The electric power system is described separately in Chapter 25.

Fire alarm system

The criteria established for the fire alarm system provide for an automatic detection system to protect personnel and to minimize the possibility of loss of equipment. The fire detection system is provided with detection devices at specific points. Master coded boxes are tied into a series-parallel, supervised circuit. The master control, located in the Fire Station Building, has four, coded, master box circuits—the klystron gallery loop, the campus loop, the research area loop, and the tie line to Stanford University Fire Station.

Pulse-coded alarm signals from the master fire alarm boxes are audibly indicated and permanently recorded at the master control panel and, through the tie line, at the Stanford University Fire Station. The coded signal directs the Fire Department to the particular box originating the alarm and the annunciator used in conjunction with the master box gives further instructions for the exact location. Noncoded stations and automatic devices are installed throughout the buildings for actuating the master boxes.

In conjunction with the automatic fire detection system, a water sprinkler system was installed in all buildings except in areas where water could cause severe damage to electronic equipment. In these areas, portable

fire-extinguishing equipment suitable for electronic equipment is provided. Automatic water flow switches are included to actuate the fire alarm system.

There are twenty-nine street-type fire alarm boxes strategically located throughout the site. Every one of the boxes is connected to one of the four fire-monitoring circuits which originate in the Fire Station. Associated with each fire alarm box is a fire alarm subsystem which covers a specific area or building which, in turn, is normally subdivided into several fire zones. The subsystems are provided with local audible alarms and ventilation fan interlocks where needed.

Each zone is equipped with either a heat detector, a smoke detector, a sprinkler flow switch, a manual switch, or combination thereof. All fire systems are equipped with emergency standby power. In addition, all alarm circuits are continually monitored for circuit faults.

Domestic water

Domestic water is obtained from the city of Menlo Park system. In 1963, a 2-million-gal reservoir was constructed about 2 miles north of the main injector end of the machine. One million gallons capacity in the reservoir is reserved for SLAC use and provides for 2 days of normal domestic usage at 140,000 gal/day plus 3000 gal/min for fire-fighting for 4 hours.

Domestic water is supplied to the project through two supply pipes. The main supply is a 16-in. pipe connecting to the project meter box located adjacent to the main SLAC entryway off Sand Hill Road. The second supply is normally valve-closed and is a 10-in. pipe connecting to the domestic water main serving the 2-mile long Klystron Gallery Building at the beginning of Sector 7, or about 2000 ft east of the main injector.

Fire protection requirements were established as 1500 gal/min at 60 psig minimum pressure for hose streams and 1500 gal/min at 20 psig residual pressure for sprinkler systems. These requirements were the controlling factor in sizing the distribution system piping.

All water lines in the fire protection system were looped for added reliability except for the main serving the klystron gallery, which can be supplied from either end. Within the site, mains are 12, 10, 8, or 6 in. All pipes larger than 3 in. in size are Class 150 asbestos cement. Branch lines to buildings or other loads, 3 in. and smaller, are Schedule 40 galvanized steel.

The principal demands for domestic water are domestic use, fire protection, cooling tower makeup, a small amount for diffusion vacuum pump cooling, and irrigation. Water usage at SLAC averages 267,000 gal/day in dry weather when irrigation systems are in use and 167,000 gal/day during wet weather.

The annual average consumption has been about 90 million gal of which 15 million leave via the sanitary sewer and 75 million are used for irrigation or evaporated at the cooling towers. The cooling tower makeup demand is estimated at 45 million gal/yr and is the principal load served.

Sanitary sewer system

Sanitary sewage from the site is disposed of by the Menlo Park sanitary district. An annexation fee was charged for this service, plus a unit rate for any excess over 15,000 gal/day. The average flow rate is 41,000 gal/day. The flow is metered at the point of entry into the sanitary district's sewage lines.

A minimum of 8-in. diameter for the outfall and 6-in. diameter for all other mains was established and in most cases was the controlling factor in sizing the pipes.

The entire collection system, with the exception of three small areas, has gravity flow to the outfall. The three areas that require lift stations are small and serve individual comfort stations. The Data Assembly Building is one such instance. It is served by a pneumatic ejector station housed in a reinforced concrete vault below grade with a capacity of 50 gal/min at 50 ft of dynamic head. It also serves as an intermediate lift station for the pneumatic ejector serving the south side of the research area yard. This ejector is a factory-built packaged unit with a capacity of 30 gal/min at 33 ft of dynamic head. It serves one comfort station and a photographic dark room. The third unit is located in the north side of the research area yard. It is identical to the packaged unit described above. It also has very nominal use.

The majority of the gravity-type sewers are of asbestos cement, Class 1500. The force mains are asbestos cement, Class 150.

Central heating water

A central hot water heating system serves all of the permanent buildings in the "campus area." Located in the Central Utility Building are two natural gas, fire tube, hot water generators, each rated at 10,050 MBtu/hour, which supply 400 gal/min of 235°F hot water. Three hot water pumps are used to maintain a supply pressure of 65 psig. The return pressure is 33 psig. The hot water generators are designed for pressure of 60 psig, but because of the safety requirements for unattended, fully automatic units, the pressure relief valves are set at 30 psig. Ten thousand gallons of Diesel fuel are provided for standby use. This amount is adequate for 3 days' supply, based on estimated January requirements. Provision was made for one additional unit.

The distribution system is made of black iron pipe with molded glass fiber insulation. Exposed piping and piping in the concrete utility tunnels have canvas-jacketed insulation. Buried insulated pipe is protected from water damage by a $\frac{3}{16}$-in., glass fiber reinforced resin coating. All main headers are oversized at least 50% above foreseeable requirements. All high points in the distribution system are provided with vent valves. Drains are provided at low points. In addition to providing the general building heating requirements, the hot water is used at the water distillation facility and at the cleaning and plating shop for heating the various cleaning tanks.

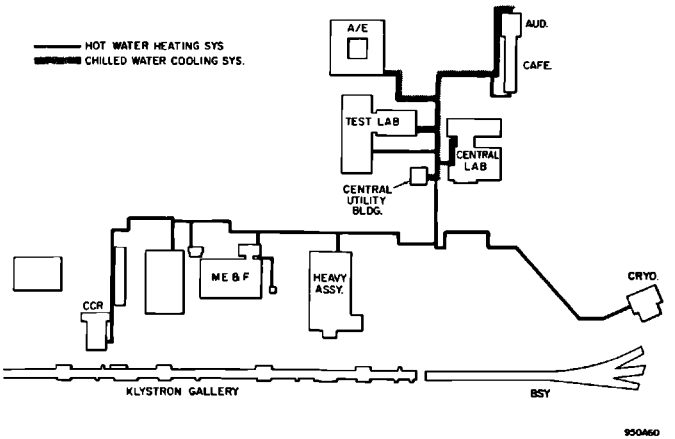

Figure 27-60 Central heating and chilled water distribution systems.

Figure 27-60 shows the layout of distribution piping for this utility service.

Central chilled water

The air-conditioning requirements of the campus buildings contained within the loop road are supplied by a central chilled water system located in the Central Utility Building. Two 200-ton centrifugal compressor water chillers provide 400 gal/min of 40°F chilled water. Condenser water for the system is provided from the central two-cell cooling tower. Two pumps rated at 450 gal/min each provide 66 psig for the supply side of the distribution system. The return pressure is 33 psig. The air-conditioning units are designed for a 10°F rise in water temperature. Provision was made for one additional chiller and pump.

The distribution system is made of black iron pipe with molded glass fiber insulation. Exposed piping in the concrete utility tunnel has canvas-jacketed insulation. Buried insulated pipe is protected from water damage by a $\frac{3}{16}$-in., glass fiber reinforced resin coating. Under paving and roadways, a metal shield covers the glass fiber reinforced resin coating.

Figure 27-60 shows the layout of the distribution piping for this utility service.

Natural gas

Natural gas is supplied to the site by the Pacific Gas & Electric Company. A 3- and a 6-in. line extend onto the site from the main along Sand Hill Road. The 3-in. line is for future firm gas connections to laboratories. It is presently capped off at its point of entry into the utility tunnel east of the Administration

and Engineering Building. The 6-in. line is for interruptible gas and serves the Central Utility Building, the Test Laboratory, and other buildings on the site.

The pipe is of black iron and is wrapped for direct burial.

Compressed air

The compressed air used on the site is generated and distributed by two rather distinct systems with cross-ties for emergency backup.

The larger of the two systems supplies the "campus area" and klystron gallery. Two 300-SCFM compressors, located in the Central Utility Building, supply air at 100 psig. The compressors are of oil-free construction with Teflon rings. The after-cooler uses 40°F chilled water to dry the air. The result is an oil- and water-free air which approaches instrument air quality. Provision was made for the future addition of one more 300-SCFM compressor.

The distribution piping ranges in size up to 6 in. in diameter and serves the General Services Building, craft shops, and the electronics, fabrication, and heavy assembly buildings. A $1\frac{1}{2}$-in. line connects to the klystron gallery and master substation switch house.

The second and smaller system supplies the research area yard. One 300-SCFM compressor is located in the Beam Switchyard Substation Building. It is practically identical to the two units described above. This air is supplied to the beam switchyard, Data Assembly Building, end stations A and B, counting house, and research area yard. This system is tied into the Central Utility Building system at the klystron gallery. Air quality is comparable to that produced at the Central Utility Building.

Telephones and radio

VOICE COMMUNICATIONS. Three main methods of voice intercommunication have been provided for general use by project personnel: the telephone, the service channel system, and the paging system. They cover the klystron gallery, accelerator housing, beam switchyard, and research areas. In addition, there are systems not employed for general usage, such as local paging and several specialized radio networks.

TELEPHONE SYSTEM. Telephones in the areas noted above are owned, installed, and maintained by SLAC. Service is extended to all locations from the Central Control Building on SLAC cables as part of the instrumentation and control system. All telephones in these areas are connected to the telephone company's project central switchboard and are identical in function and operation to all other telephones on the project. They are located approximately 100 ft apart along the full length of the klystron gallery.

There are four telephones in each sector: (1) beside each access door to the accelerator housing, (2) in every instrumentation and control alcove, (3) on the north wall near column 5, and (4) in the accelerator housing in each manway access alcove. Telephones in the beam switchyard are located outside all accessways where personnel may enter and at various locations inside. Telephones are also placed at convenient locations on both the inside and outside walls of the end stations and in all other buildings in the experimental areas.

SERVICE CHANNEL SYSTEM. As the name implies, service channels are used for servicing and maintenance work. They allow maintenance and test personnel to communicate among themselves and with the control rooms for extended periods of time and to coordinate their efforts without loading other communication facilities or being subject to interruption by other traffic. Each channel consists merely of a telephone line with common battery applied and a multiplicity of access points.

There are six channels available. Access to them is at jack panels on each fiat and trigger rack in the klystron gallery and at boxes spaced every 40 ft along the south wall of the accelerator housing. Three channels of the available six (channels 4, 5, and 6) appear at the boxes in the accelerator housing.

Service channel boxes in the beam switchyard contain six channels and are located at 40-ft intervals along the upper housing. The six channels in the beam switchyard and experimental areas are separate and distinct from the klystron gallery and accelerator housing service channels.

Users of the service channels are issued a headset assembly consisting of an operator-type headset, a 25-ft retractile cord, and a small belt-clipped box. The box also contains a slide switch to disable the microphone for monitoring purposes and push buttons marked "CNTL" and "SWBD" for signaling the control room and the telephone switchboard operator, respectively. Extension cords of various lengths are available when required.

There are several ways in which communications may be established on service channels. Someone may be "met" by prearrangement on a specified channel. It is then just necessary to plug in and talk. The switchboard operator may be signaled and instructed to page a desired party to plug into the channel in use. The control operators can also operate the paging system to call certain personnel to a service channel.

The service channels are not used as a substitute for the telephone system; however, there are occasions when it is necessary for maintenance people to converse with someone on the project from the location of the equipment on which they are working. The telephone operator can dial a call for them within the project while they are on a service channel. The operator, however, cannot extend a call outside the project.

PAGING SYSTEM. A single paging system covers the accelerator, beam switchyard, and research areas. These areas may be paged individually as required.

The system is used for locating personnel and for routine or emergency announcements. Access to the system is restricted to three locations: the project telephone switchboard and the central and beam switchyard control rooms. All paging equipment operates from the existing 24-V battery sources and is independent of ac power.

RADIO SYSTEM. There are at present four radio networks in operation on separate frequencies. The utility network is used for dispatching the SLAC taxi service, maintenance forces, surveillance guards, and other administrative services. The fire protection network is part of the Stanford University Fire Department system. Health physics personnel and groups concerned with the operation of the accelerator employ the operations network for radiation safety, personnel search, and other business involving machine operation. The experimenters have a low-power network to coordinate setup and alignment of test apparatus. Individual, electronic, pocket-size, paging devices are used by several of the using groups to increase the effectiveness of radio communication at SLAC.

Temporary communications

When a voice communication link is needed for short-term use, a pool of equipment, consisting of sound-powered telephones, military field telephones, citizens' band portable radios, wireless intercom units, paging amplifiers, speakers, and microphones, is available.

Acknowledgments

Many people made significant contributions to the design and construction of the buildings and utilities and to the installation of the accelerator. W. K. H. Panofsky, E. L. Ginzton, M. Sands, J. Ballam, F. V. L. Pindar, R. H. Moulton, Jr., and R. B. Neal were most effective in assuring development of the physical plant in accordance with the objectives of the University and the government. D. B. Adams, Manager of the Stanford Business Office, and M. H. L. Sanders, Jr., Director of the Stanford Planning Office, were very helpful in the processing of SLAC presentation material forwarded for the approval of the Board of Trustees of Stanford University. The ABA staff, including G. Bawden, manager, R. Sharpe, technical director, R. Hawkins, operations director, H. James, H. Crofts, L. Swanson, and W. Harris; the late D. Wilcox and C. Lewis of Charles Luckman Associates; and the staff of Royston, Hanamoto, Mayes and Beck, landscape architects, contributed to the design and construction of SLAC buildings and utilities and their siting. K. Copenhagen was head of plant engineering during most of the construction period. W. Kinst contributed to the development of the SLAC architectural detail. John A. Blume consulted on seismic considerations and structural design concepts. G. Loew, R. Miller, K. Mallory, J. V. Lebacqz,

A. Eldredge, E. Westbrook, R. Helm, L. Schwartz, D. Coward, H. DeStaebler, R. Taylor, E. Garwin, J. Gunn, K. Trigger, J. O'Ryan, F. Bonaudi, R. Sandkuhle, and R. Blumberg were invaluable in advising on design details and criteria for buildings and concepts for equipment. E. Seppi, H. Weidner, C. R. Johnson, D. Neet, C. Harris, H. Ross, and E. K. Johnson were very helpful in developing beam switchyard requirements. J. Anton, R. Vaerst, and F. Halbo contributed to the initial design coordination for the klystron gallery and accelerator housing and installation planning of the machine. W. McCormish, G. Tenney, and J. Pulis coordinated the development of project standards, specifications format, and document control. R. Gould as staff civil engineer, W. Savage as staff structural engineer, J. Crisp as staff architect, T. McLellan in the area of project space utilization, D. Browne, Jr., in the area of the initial construction of buildings and site improvements, G. Rogers and G. Ratliff in the area of mechanical utilities, and P. Edwards, I. Krumholz, and A. Tseng in the area of electrical utilities, accomplished much toward the development of the SLAC physical plant as it is today. W. Oblak was in charge of design of the Laser Room. J. Bougher, W. Springhorn, G. Hughes, and J. Fish were principal drafting supervisors for the layout of the accelerator equipment and its services. F. F. Hall was head of the former Systems Engineering and Installations Department, installation manager for the accelerator, and head of plant engineering for recent construction programs. R. Conviser was assistant head of the Systems Engineering and Installations Department. F. Poblenz was invaluable in processing all accelerator installation subcontract specifications and drawings including all design changes for final submittal to SLAC Business Services Division during the accelerator installation program. R. Robbers was chief field superintendent for the accelerator installation work. C. Rasmussen of the mechanical engineering fabrication shop supervised the installation of accelerator beam line components. E. Rickansrud and F. Mahan of the SLAC Business Office were very effective in the administration of SLAC installation subcontracts. R. B. Neal, associate director of the SLAC Technical Division, furnished invaluable counsel in technical matters, and his staff, including L. Kral, W. Beeger, E. Stockbridge, K. Barriger, and G. Smith were most helpful in the areas of budgets and scheduling. L. Gallagher of the SLAC Plant Office and his staff were most cooperative in processing subcontract documents for time and material subcontractors, minor modifications to buildings and utilities, general plant projects, and new construction projects. In addition, L. Gallagher was administrator for the ABA subcontract. R. Jamtgaard often advised in the area of cost control. E. Lee was helpful in the administration of plant engineering programs. W. Lusebrink and A. Mainwaring were helpful in the establishment and development of the SLAC crafts shop which provides electrical, plumbing, mechanic, instrument, rigging, and paint shop services and operates the accelerator utilities. R. McCall, T. Jenkins, and W. Nelson of the Health Physics Group were helpful in establishing radiation shielding requirements. Appreciation is

expressed for the cooperation in resolving problems and helpful design reviews furnished by the staff of the Palo Alto Area Office of the U.S. Atomic Energy Commission, including L. Mohr, J. Ryan, L. Kelley, J. Legerski, M. Smith, A. Gordon, V. Kinney, and J. Kuhta.

References

1 "Engineering Design Summary for the Stanford Linear Accelerator Center," ABA Rept. 107, Aetron-Blume-Atkinson, Stanford Linear Accelerator Center, Stanford, California (1966). (This document contains a complete bibliography of all ABA reports prepared for the project.)

2 "Geologic Site Investigation," ABA Rept. 88, Aetron-Blume-Atkinson, Stanford Linear Accelerator Center, Stanford, California, 1965.

3 "Earth Movement Investigations and Geodetic Control," ABA Rept. 106, Aetron-Blume-Atkinson, Stanford Linear Accelerator Center, Stanford, California (1966).

4 "Report for the U.S. Atomic Energy Commission," Volumes II, III, and IV, John A. Blume and Associates, Stanford Linear Accelerator Center, Stanford, California (1960).

5 Parker D. Trask, "Engineering Geology, Proposed Linear Electron Accelerator, Sand Hill Site, Stanford University, California," Stanford Linear Accelerator Center, Stanford University, Stanford, California (June 30, 1961).

6 "AEC General Design Criteria," Appendix 6301 to *AEC Manual*, U.S. Atomic Energy Commission, Washington, D.C.

INDEX